

SUBTERRANEAN ESTUARIES

EDITED BY: Carlos Rocha, Henry Bokuniewicz, Clare Robinson, Isaac R. Santos and Hannelore Waska

PUBLISHED IN: Frontiers in Environmental Science, Frontiers in Earth Science and Frontiers in Marine Science



frontiers Research Topics

Frontiers eBook Copyright Statement

The copyright in the text of individual articles in this eBook is the property of their respective authors or their respective institutions or funders. The copyright in graphics and images within each article may be subject to copyright of other parties. In both cases this is subject to a license granted to Frontiers.

The compilation of articles constituting this eBook is the property of Frontiers.

Each article within this eBook, and the eBook itself, are published under the most recent version of the Creative Commons CC-BY licence. The version current at the date of publication of this eBook is CC-BY 4.0. If the CC-BY licence is updated, the licence granted by Frontiers is automatically updated to the new version.

When exercising any right under the CC-BY licence, Frontiers must be attributed as the original publisher of the article or eBook, as applicable.

Authors have the responsibility of ensuring that any graphics or other materials which are the property of others may be included in the CC-BY licence, but this should be checked before relying on the CC-BY licence to reproduce those materials. Any copyright notices relating to those materials must be complied with.

Copyright and source acknowledgement notices may not be removed and must be displayed in any copy, derivative work or partial copy which includes the elements in question.

All copyright, and all rights therein, are protected by national and international copyright laws. The above represents a summary only. For further information please read Frontiers' Conditions for Website Use and Copyright Statement, and the applicable CC-BY licence.

ISSN 1664-8714
ISBN 978-2-88976-626-0
DOI 10.3389/978-2-88976-626-0

About Frontiers

Frontiers is more than just an open-access publisher of scholarly articles: it is a pioneering approach to the world of academia, radically improving the way scholarly research is managed. The grand vision of Frontiers is a world where all people have an equal opportunity to seek, share and generate knowledge. Frontiers provides immediate and permanent online open access to all its publications, but this alone is not enough to realize our grand goals.

Frontiers Journal Series

The Frontiers Journal Series is a multi-tier and interdisciplinary set of open-access, online journals, promising a paradigm shift from the current review, selection and dissemination processes in academic publishing. All Frontiers journals are driven by researchers for researchers; therefore, they constitute a service to the scholarly community. At the same time, the Frontiers Journal Series operates on a revolutionary invention, the tiered publishing system, initially addressing specific communities of scholars, and gradually climbing up to broader public understanding, thus serving the interests of the lay society, too.

Dedication to Quality

Each Frontiers article is a landmark of the highest quality, thanks to genuinely collaborative interactions between authors and review editors, who include some of the world's best academicians. Research must be certified by peers before entering a stream of knowledge that may eventually reach the public - and shape society; therefore, Frontiers only applies the most rigorous and unbiased reviews.
Frontiers revolutionizes research publishing by freely delivering the most outstanding research, evaluated with no bias from both the academic and social point of view. By applying the most advanced information technologies, Frontiers is catapulting scholarly publishing into a new generation.

What are Frontiers Research Topics?

Frontiers Research Topics are very popular trademarks of the Frontiers Journals Series: they are collections of at least ten articles, all centered on a particular subject. With their unique mix of varied contributions from Original Research to Review Articles, Frontiers Research Topics unify the most influential researchers, the latest key findings and historical advances in a hot research area! Find out more on how to host your own Frontiers Research Topic or contribute to one as an author by contacting the Frontiers Editorial Office: frontiersin.org/about/contact

SUBTERRANEAN ESTUARIES

Topic Editors:
Carlos Rocha, Trinity College Dublin, Ireland
Henry Bokuniewicz, The State University of New York (SUNY), United States
Clare Robinson, Western University, Canada
Isaac R. Santos, University of Gothenburg, Sweden
Hannelore Waska, University of Oldenburg, Germany

Citation: Rocha, C., Bokuniewicz, H., Robinson, C., Santos, I. R., Waska, H., eds. (2022). Subterranean Estuaries. Lausanne: Frontiers Media SA.
doi: 10.3389/978-2-88976-626-0

Table of Contents

05 ***Editorial: Subterranean Estuaries***
Carlos Rocha, Henry Bokuniewicz, Clare E. Robinson, Isaac R. Santos and Hannelore Waska

ADVANCING SUBTERRANEAN ESTUARY CHARACTERIZATION

09 ***Effects of Multiconstituent Tides on a Subterranean Estuary With Fixed-Head Inland Boundary***
Xiayang Yu, Pei Xin, Chengji Shen and Ling Li

23 ***A Multi-Method Approach for Quantification of In- and Exfiltration Rates from the Subterranean Estuary of a High Energy Beach***
Nele Grünenbaum, Janis Ahrens, Melanie Beck, Benjamin Silas Gilfedder, Janek Greskowiak, Michael Kossack and Gudrun Massmann

38 ***Submarine Groundwater Discharge From Sediments and Sand Boils Quantified by the Mean Residence Time of a Tracer Injection***
Michael Schlüter and Philipp Maier

48 ***Mixed-Convective Processes Within Seafloor Sediments Arising From Fresh Groundwater Discharge***
S. C. Solórzano-Rivas, Adrian D. Werner and Dylan J. Irvine

61 ***A Multi-Tracer Study of Fresh Water Sources for a Temperate Urbanized Coastal Bay (Southern Baltic Sea)***
Cátia Milene Ehlert von Ahn, Jan C. Scholten, Christoph Malik, Peter Feldens, Bo Liu, Olaf Dellwig, Anna-Kathrina Jenner, Svenja Papenmeier, Iris Schmiedinger, Mary A. Zeller and Michael Ernst Böttcher

81 ***A State-Of-The-Art Perspective on the Characterization of Subterranean Estuaries at the Regional Scale***
Nils Moosdorf, Michael Ernst Böttcher, Dini Adyasari, Ercan Erkul, Benjamin S. Gilfedder, Janek Greskowiak, Anna-Kathrina Jenner, Lech Kotwicki, Gudrun Massmann, Mike Müller-Petke, Till Oehler, Vincent Post, Ralf Prien, Jan Scholten, Bernhard Siemon, Cátia Milene Ehlert von Ahn, Marc Walther, Hannelore Waska, Tina Wunderlich and Ulf Mallast

ORIGIN AND TURNOVER OF ORGANIC MATTER IN STES

107 ***Saltwater Intrusion and Submarine Groundwater Discharge: Acceleration of Biogeochemical Reactions in Changing Coastal Aquifers***
Willard S. Moore and Samantha B. Joye

121 ***Molecular Traits of Dissolved Organic Matter in the Subterranean Estuary of a High-Energy Beach: Indications of Sources and Sinks***
Hannelore Waska, Heike Simon, Soeren Ahmerkamp, Janek Greskowiak, Janis Ahrens, Stephan L. Seibert, Kai Schwalfenberg, Oliver Zielinski and Thorsten Dittmar

138 ***Rare Earth Element Behavior in a Sandy Subterranean Estuary of the Southern North Sea***
Ronja Paffrath, Katharina Pahnke, Melanie K. Behrens, Anja Reckhardt, Claudia Ehlert, Bernhard Schnetger and Hans-Jürgen Brumsack

156 ***Does Nitrate Enrichment Accelerate Organic Matter Turnover in Subterranean Estuaries?***
J. Severino P. Ibánhez, Xosé Antón Álvarez-Salgado and Carlos Rocha

174 ***Response of Nitrate Processing to Bio-labile Dissolved Organic Matter Supply Under Variable Oxygen Conditions in a Sandy Beach Seepage Face***
Shan Jiang, Jie Jin, Ying Wu, Yixue Zhang, Yongjun Wei, Carlos Rocha, Juan Severino Pino Ibánhez and Jing Zhang

189 ***Reactive Solute Transport Through Two Contrasting Subterranean Estuary Exit Sites in the Ría de Vigo (NW Iberian Peninsula)***
Elisa Calvo-Martin, Xosé Antón Álvarez-Salgado, Carlos Rocha and J. Severino Pino Ibánhez

208 ***Drivers and Seasonal Variability of Redox-Sensitive Metal Chemistry in a Shallow Subterranean Estuary***
Alison E. O'Connor, Elizabeth A. Canuel and Aaron J. Beck

LIFE IN STES

225 ***The Beach Aquifer Microbiome: Research Gaps and Data Needs***
Anand Archana, Christopher A. Francis and Alexandria B. Boehm

238 ***The Three Domains of Life Within the Discharge Area of a Shallow Subterranean Estuary at a High Energy Beach***
Julius Degenhardt, Sahar Khodami, Felix Milke, Hannelore Waska, Bert Engelen and Pedro Martinez Arbizu

253 ***Changes in Organic Matter Deposition Can Impact Benthic Marine Meiofauna in Karst Subterranean Estuaries***
David Brankovits, Shawna N. Little, Tyler S. Winkler, Anne E. Tamalavage, Luis M. Mejía-Ortíz, Christopher R. Maupin, German Yáñez-Mendoza and Peter J. van Hengstum

270 ***Habitat Partitioning in the Marine Sector of Karst Subterranean Estuaries and Bermuda's Marine Caves: Benthic Foraminiferal Evidence***
Jacquelyn N. Cresswell and Peter J. van Hengstum

frontiers | Frontiers in Environmental Science

TYPE Editorial
PUBLISHED 08 September 2022
DOI 10.3389/fenvs.2022.988723

Check for updates

OPEN ACCESS

EDITED AND REVIEWED BY
Aaron J. Beck,
Helmholtz Association of German Research Centres (HZ), Germany

*CORRESPONDENCE
Carlos Rocha,
rochac@tcd.ie

SPECIALTY SECTION
This article was submitted to Biogeochemical Dynamics, a section of the journal Frontiers in Environmental Science

RECEIVED 07 July 2022
ACCEPTED 20 July 2022
PUBLISHED 08 September 2022

CITATION
Rocha C, Bokuniewicz H, Robinson CE, Santos IR and Waska H (2022), Editorial: Subterranean estuaries.
Front. Environ. Sci. 10:988723.
doi: 10.3389/fenvs.2022.988723

COPYRIGHT
© 2022 Rocha, Bokuniewicz, Robinson, Santos and Waska. This is an open-access article distributed under the terms of the Creative Commons Attribution License (CC BY). The use, distribution or reproduction in other forums is permitted, provided the original author(s) and the copyright owner(s) are credited and that the original publication in this journal is cited, in accordance with accepted academic practice. No use, distribution or reproduction is permitted which does not comply with these terms.

Editorial: Subterranean estuaries

Carlos Rocha[1]*, Henry Bokuniewicz[2], Clare E. Robinson[3], Isaac R. Santos[4,5] and Hannelore Waska[6]

[1]Biogeochemistry Research Group, School of Natural Sciences, Trinity College Dublin, Dublin, Ireland, [2]School of Marine and Atmospheric Sciences, Stony Brook University, Stony Brook, NY, United States, [3]Civil and Environmental Engineering, University of Western Ontario, London, ON, Canada, [4]Department of Marine Sciences, University of Gothenburg, Gothenburg, Sweden, [5]National Marine Science Centre, Southern Cross University, Coffs Harbour, NSW, Australia, [6]Research Group for Marine Geochemistry (ICBM-MPI Bridging Group), Institute for Chemistry and Biology of the Marine Environment (ICBM), University of Oldenburg, Oldenburg, Germany

KEYWORDS

nutrients, eutrophication, submarine groundwater discharge, SGD, coastal ecosystem, coastal zone management, ICZM, climate and environmental change

Editorial on the Research Topic
Subterranean Estuaries

Advancing subterranean estuary characterization

Groundwater flows in STEs are complex and driven by dynamic marine and continental forces acting on the land-ocean interface. The convergence of these forces in the subsurface translates into the variable morphology of STEs, regulates the timing of sub-estuarine circulation and physically constrains the residence time of water, regulating STE biogeochemistry, like their surface analogues. To characterize STEs in a way that is useful for fully integrated coastal monitoring and management, we need to untangle the different ways in which the multiple forces acting on STEs interact, driving morphodynamics, mixing regimes, and biogeochemical and microbiological zonation. In parallel, research must extend to probe the influence of STE dynamics on both oceanic and freshwater compartments so that the full aquatic continuum is covered. Achieving this objective requires improving our ability to characterize STEs and monitor net water flows into and out of STEs, from local to global scales, as well as to explore and document life within these subsurface environments.

Modelling has been useful to conceptualize groundwater flow and transport in STEs under different physical constraints, guiding research in real-world systems. Here, Yu et al. show that the salinity distributions in STEs exposed to a multi-constituent tidal signal depends on antecedent tidal oscillations, as well as on the inland extent of the freshwater aquifer. This finding implies that groundwater resource management landward of the littoral zone will affect the biogeochemical dynamics of STEs, changing net mass fluxes seaward, and impact coastal ecotones that may be distant from the decision in time and in space, thus stressing the importance of joined-up thinking in ICZM (Rocha et al., 2021).

It is well established that Submarine Groundwater Discharge (SGD) rates are highly variable in time and space. However, accurate estimates of both infiltration and exfiltration rates are key to determine net mass outflow from STEs and gauge the contribution of SGD to the biogeochemical budgets of coastal surface and subsurface water bodies. Grünenbaum et al. combine an array of methods to assess infiltration and exfiltration across the land-ocean interface in a high energy beach. Their results can be generalized to show that at the littoral zone, STE exchange rates are linked to beach topography, which in turn is affected by weather and by coastal management decisions including erosion control. This information is important to evaluate the impact of coastal management choices on ecosystem function and plan monitoring programmes. Due to the high spatial and temporal variability, monitoring SGD rates effectively for coastal management requires flexible and accurate methodologies that overcome the large human resource requirement. To this end Schlüter and Maier develop and test a scalable, inexpensive automated seepage meter, based on the dilution of tracer (saline water) injections. They use the mean residence time concept to determine SGD rates by modelling tracer breakthrough curves. This system may yet provide a means to develop efficient, networked monitoring of land-ocean transfer of materials in coastal environments *via* SGD.

The capacity for routine, continuous (and affordable) monitoring would contribute to holistic coastal management incorporating the complete water continuum, filling large knowledge gaps in our understanding of the coast, since SGD has an impact on the ecology of coastal systems. Because STE exfiltration zones may extend beyond the intertidal and proximal subtidal zone, far into the continental shelf area, it is critical to develop a physical understanding of STE circulation even when advection of continental groundwater becomes relatively less important. By examining the mixed-convective processes that occur when freshwater rises into a saline groundwater body of water, Solorzano-Rivas et al. set the basis for better understanding of fresh groundwater circulation in regions of sandy seafloor sediments where convection is more important than Darcian flow. Von Ahn et al. show in their Baltic Sea study that where it is necessary to cover both the littoral zone and the contiguous shelf area to monitor the ecosystem-level impact of STEs, combining environmental tracers and geophysical methods is promising. While logistic limitations still constrain regular, sustained, and high frequency sampling and monitoring of STE outflows across field, basin, and regional scales, Moorsdorf et al. show how the combination of different environmental tracer methodologies, geophysical approaches, remote sensing, and hydrogeological modelling could unravel the measurable signatures of STE processes to resolve their regional-scale impact on solute fluxes to the coastal ocean.

Origin and turnover of organic matter in subterranean estuaries

Knowledge of the origin, transfer, turnover, and fate of organic matter in STEs is essential to assign ecosystem-level function to these subsurface units. This information is needed to quantify mass transport across the land-ocean interface and understand the impacts of climate and environmental change on one of the most anthropogenically pressured portions of the Earth system. As with (surface) estuarine science in the past, achieving this aim requires we accept the unique functional identity of STEs and integrate research efforts traditionally conducted by different disciplines under this new praxis. To refocus the scientific community on this point, Moore and Joye emphasise how local changes to land and water use have expanded STEs over the last century, changing the environment in which continental carbon had been stored for millennia. They predict climate-driven sea level rise will accelerate fluid turnover within STEs, conceivably catalysed by higher net groundwater recharge. This acceleration triggers higher chemical mobility near the land-ocean interface and enhances elemental fluxes from aquifers to the coastal oceans. These changes disrupt the balance between soil organic matter burial and mobilization achieved before the growth of groundwater mining in the last century and foretell profound alterations to aquatic and terrestrial biomes that will affect how coastal ecosystems support humanity's needs for food, transport, and recreation.

This emerging higher-order understanding is consistent with findings in a wide variety of STEs in different settings. Waska et al. find evidence of enhanced mineralization of organic matter at STEs in barrier islands of the southern North Sea accompanying high dissolved organic matter (DOM) diversity in the local freshwater lens. Paffrath et al. show how net SGD fluxes of both fresh groundwater and recirculated seawater are a source of rare Earth elements (REEs) to the ocean because of enhanced mineralization rates in the STE. Further South, Ibanhez et al. present evidence of how nitrate enrichment enhances the metabolic turnover of sedimentary organic matter (SOM) in the STE, implying that DIN (dissolved inorganic nitrogen) pollution of coastal aquifers may reduce the residence time of aged organic C within the STE, driving carbon from continental storage into the coastal ocean.

In Sanggou Bay, Jiang et al. combine flow reactor experiments with 16S rDNA probing and stable isotopes to show how nitrate processing in STEs relies on a highly flexible bacterial community that adapts more readily to terminal electron acceptor than DOM availability. The results reveal a specialized microbial community endemic to STEs, rather than a transient one comprising a mix of continental or marine populations arriving onsite with STE mixing endmembers–thus supporting the thesis that STEs are unique habitats. In complementary fashion, Calvo-Martin et al. show

how sedimentary structure of STEs controls biogeochemical zonation by directing water flow, which regulates availability of terminal electron acceptors for OM oxidation. Hence the function of STEs as sources or sinks of N may change depending on structural aspects of the coastal subsurface. Similarly, O'Connor et al. show how the speciation and mobility of redox-sensitive metals depends on oxidation-reduction dynamics within the STE, which in turn drive microbial activity, OM composition and heterogeneous reactions.

The mounting evidence indicates that STEs are efficient, permeable, biogeochemical reactors with internal process dynamics and reaction kinetics set by the prevalent flow regimes. Substrate availability along circulation pathways depends on the biogeochemical legacy of the mixture. This depends on how internal circulation navigates an internal structure shaped by sedimentary morphodynamics that supports a highly adaptable, endemic ecology.

Life in subterranean estuaries

Surface (open water) and subsurface estuaries (STEs) belong in the marine biome. Whilst the biogeochemistry of STEs is driven by the coastal and beach aquifer microbiome, very little is still known about the microbes that populate these systems. Archana et al. critically review the narrow literature available on the subject to reveal that the beach aquifer microbiome is dominated by Proteobacteria, followed by Chloroflexi and Bacteroidetes. Insights from their critical synthesis reveal important blind spots on research conducted so far. For example, understanding how STEs outflows might contribute to eutrophication of the coastal ocean has justified most research on the subject to date, but it would also be important to figure out what impact eutrophication has on microbial communities and genetic composition. Yet, we have poor understanding of the impacts of pollution on STE microbiomes. Still, the full arsenal of the microbiologist has yet to be trained on the problem, since the beach microbiome has mostly been studied with 16S ribosomal DNA sequencing. Metagenomics and metatrasncriptomics would help understand both metabolism and ecology of microorganisms in STEs, necessary to comprehend biogeochemical dynamics.

Even if microbiology and microbial ecology are the poor relatives of Research Topic on STEs, Degenhardt et al. point out that Archean and meiofaunal diversity have been even more neglected. They find archaea contribute ~1%–4% to the 16S rRNA gene sequence bank of prokaryotes, while nematodes made most of the eukaryotes in a southern North Sea STE. Importantly, the study supports insights derived from studies of organic matter turnover by providing direct evidence of the existence of a core prokaryotic community in STEs. This community adapts quickly to SGD compositional dynamics, triggering biogeochemical feedback loops that in turn structure the spatial distribution and composition of eukaryotic communities. Brankovits et al. adds that soil organic matter distribution and deposition dynamics also impact meiofauna composition in karst STEs (previously classified as anchialine systems, Bishop et al., 2015). The evidence so far indicates that prokaryotic community composition and patchiness help shape the local eukaryotic community and biomass distribution within STEs, irrespective of type. The same picture is reconstructed over time by Cresswell and Hengstun. In a breakthrough study conducted in Bermuda, they show that spatiotemporal heterogeneity in POM source, quantity, and mode of delivery drives the co-existence of benthic foraminifera species in karst STE's. The emerging global picture is that POM deposition dynamics and patchiness is the main structural driver of marine benthic community composition and distribution in STEs.

Conclusion

To further our understanding of the function of subterranean estuaries in global biogeochemical cycling, future research must focus on:

1) Physically and mathematically describing internal structures of STEs, classifying their manifestation at diverse sites in terms of hydraulics, the physico-chemical drivers of mixing, as well as the spatiotemporal scales at which they operate.
2) Describing real-life STEs in time and space and moving beyond a focus on either the seepage face or the landward edge. We need better integration of forcing functions and more effective monitoring techniques. Future studies require a better amalgamation of functional drivers, rather than describing features. This focus on function rather than form would be an essential step toward an STE typology across different spatial scales.
3) Exploring what controls the distribution and function of microbial populations in STEs and consequently their biogeochemistry. For instance, it has been valuable to study the factors affecting availability and exchange of carbon in STEs. A focus on carbon will uncover the role of STEs in the atmosphere, land and ocean carbon cycles and their interactions.
4) Increased study of the biology and ecology of STEs, including the description of structure and function of microbial food webs as well as the meiofauna. Ecosystem engineers such as nematodes are likely to link STE food webs and coastal system ecology. We should aim to understand intrinsic and specific characteristics of STEs and how they might be considered biomes on their own right.

Overall, this e-book sheds light on an invisible, subsurface coastal ecotone that has received increasing attention since the term was coined in 1999 (Moore, 1999). Coasts are, more than any ecosystem on Earth, the showcase of the increasing connectivity between human activity and ecosystem function defining the Anthropocene. Almost all the known issues affecting the unadulterated function of socio-ecological coastal systems converge on STEs, making them critical components of the coast. To further advance subterranean estuary science, we need a refined, integrated understanding of how feedbacks between the physics, chemistry, and biology of STEs will affect coastal system function. This understanding will provide more options to adapt and manage the increasing impact of climate and environmental change on natural services on which we all depend.

Summary

Subterranean estuaries (STEs) are an important driver of coastal and marine ecosystem function. Understanding their hydraulics, biogeochemistry, and ecology is critical for the success of integrated coastal zone management (ICZM). Yet, STEs remained largely unexplored as unique, functioning components of the land-ocean continuum until recently. This lack of recognition is in part because STEs are generally invisible, structurally complex, and difficult to sample or even detect, in some cases—in contrast to their better understood surface counterparts. Nevertheless, research into groundwater-seawater interactions resulted in thousands of studies published with the keyword "subterranean estuary" since the term was introduced by Willard Moore in 1999. The field is maturing, following the steps taken in the historical development of estuarine science. A community of dedicated researchers has come into focus, addressing common problems from a toolbox of proven methods. They have now produced undeniable evidence demonstrating the importance of STE and the need to include them as essential components of coastal ecosystem function research, monitoring, policy, and management.

This Research Topic provides a synthesis of knowledge on STEs, including the interplay between physics, chemistry and biology that determines their biogeochemical function at the coast. It provides evidence that STEs constitute distinct habitats, puts forward new methodologies and identifies important aspects of carbon and nitrogen cycling within. Following the early impetus provided by Willard Moore, this Research Topic builds on decades of research by the SGD community to highlight knowledge gaps in our understanding of STEs and draw attention to emerging research opportunities.

Author contributions

All authors listed have made a substantial, direct, and intellectual contribution to the work and approved it for publication.

Conflict of interest

The authors declare that the research was conducted in the absence of any commercial or financial relationships that could be construed as a potential conflict of interest.

Publisher's note

All claims expressed in this article are solely those of the authors and do not necessarily represent those of their affiliated organizations, or those of the publisher, the editors and the reviewers. Any product that may be evaluated in this article, or claim that may be made by its manufacturer, is not guaranteed or endorsed by the publisher.

References

Bishop, R. E., Humphreys, W. F., Cukrov, N., Žic, V., Boxshall, G. A., Cukrov, M., et al. (2015). 'Anchialine' redefined as a subterranean estuary in a crevicular or cavernous geological setting. *J. Crustacean Biol.* 35 (4), 511–514. doi:10.1163/1937240X-00002335

Moore, W. S. (1999). The subterranean estuary: A reaction zone of ground water and sea water. *Mar. Chem.* 65 (1–2), 111–125. doi:10.1016/S0304-4203(99)00014-6

Rocha, C., Robinson, C. E., Santos, I. R., Waska, H., Michael, H. A., and Bokuniewicz, H. J. (2021). A place for subterranean estuaries in the coastal zone. *Estuar. Coast. Shelf Sci.* 250, 107167. doi:10.1016/j.ecss.2021.107167

frontiers in Environmental Science

ORIGINAL RESEARCH
published: 19 January 2021
doi: 10.3389/fenvs.2020.599041

Effects of Multiconstituent Tides on a Subterranean Estuary With Fixed-Head Inland Boundary

Xiayang Yu[1], *Pei Xin*[1]*, *Chengji Shen*[2] *and Ling Li*[3]

[1]State Key Laboratory of Hydrology-Water Resources and Hydraulic Engineering, Hohai University, Nanjing, China, [2]Jiangsu Key Laboratory of Coast Ocean Resources Development and Environment Security, Hohai University, Nanjing, China, [3]School of Engineering, Westlake University, Hangzhou, China

While tides of multiple constituents are common in coastal areas, their effects on submarine groundwater discharge (SGD) and salinity distributions in unconfined coastal aquifers are rarely examined, with the exception of a recent study that explored such effects on unconfined aquifers with fixed inland freshwater input. For a large proportion of the global coastline, the inland areas of coastal aquifers are topography-limited and controlled by constant heads. Based on numerical simulations, this article examines the variation of SGD and salinity distributions in coastal unconfined aquifers with fixed-head inland boundaries at different distances from the shoreline (i.e., 50, 100, 150, and 200 m). The results showed that the fluctuation intensity of freshwater input was enhanced as the inland aquifer extent decreased, e.g., the range of tide-induced fluctuations in freshwater input increased by around 5 times as the inland aquifer extent decreased from 200 to 50 m. The frequency spectra of the fluctuations of SGD and salinity distributions showed that the coastal aquifer of a shorter inland aquifer extent smoothed out fewer high-frequency tidal constituents but enhanced interaction among different tidal constituents. The interaction among tidal constituents generated new low-frequency signals in the freshwater input and salinity distributions. Regressions based on functional data analysis demonstrated that the inland freshwater input and salinity distributions at any given moment were related to the antecedent (previous) tidal conditions weighted using the probability density function of the Gamma distribution. The influence of the antecedent tidal conditions depended on the inland aquifer extent.

Keywords: submarine groundwater discharge, seawater intrusion, coastal aquifer, functional data analysis, numerical modeling

OPEN ACCESS

Edited by:
Carlos Rocha,
Trinity College Dublin, Ireland

Reviewed by:
Anupma Sharma,
National Institute of Hydrology (Roorkee), India
Pedro Giovâni Da Silva,
Federal University of Minas Gerais, Brazil

***Correspondence:**
Pei Xin
pei.xin@outlook.com

Specialty section:
This article was submitted to Freshwater Science, a section of the journal Frontiers in Environmental Science

Received: *28 August 2020*
Accepted: *14 December 2020*
Published: *19 January 2021*

Citation:
Yu X, Xin P, Shen C and Li L (2021) Effects of Multiconstituent Tides on a Subterranean Estuary With Fixed-Head Inland Boundary. Front. Environ. Sci. 8:599041. doi: 10.3389/fenvs.2020.599041

Abbreviations: SGD, submarine groundwater discharge; USP, upper saline plume; SW, saltwater wedge; H_I, inland watertable elevation; H_I, inland aquifer thickness; H_S, seaward aquifer thickness; L_I, inland aquifer extent; L_S, seaward aquifer extent; SM_{SW}, amount of salt stored in saltwater wedge; SM_{USP}, amount of salt stored in upper saline plume; M_2, principal lunar semidiurnal tidal constituent; S_2, principal solar semidiurnal tidal constituent; K_1, lunisolar declinational diurnal tidal constituent; N_2, larger lunar elliptic semidiurnal tidal constituent

HIGHLIGHTS

Salinity distributions fluctuated intensively as the inland aquifer extent decreased.
Aquifer of a shorter inland aquifer extent smoothed out fewer tidal constituents.
Inland aquifer extent regulated the tidal effects on salinity distributions.

INTRODUCTION

Ocean tides are identified as an important driving force that controls the hydrodynamic and biogeochemical processes in coastal aquifers (Werner et al., 2013; Robinson et al., 2018). In subterranean estuaries (i.e., mixing zones between terrestrially derived fresh groundwater and recirculating seawater in coastal aquifers), tides significantly affect submarine groundwater discharge (SGD) and salinity distributions (Werner et al., 2013; Robinson et al., 2018). Tidal forcing, in combination with the density contrast between terrestrial fresh groundwater and nearshore seawater, can lead to the formation of two saltwater recirculation zones in unconfined aquifers: a lower saltwater wedge (SW) and an upper saline plume (USP) (Boufadel, 2000; Robinson et al., 2006).

While tidal effects on SGD and salinity distributions in subterranean estuaries have been studied extensively, previous studies predominately considered single-frequency (monochromatic) tides (Robinson et al., 2007b; Kuan et al., 2019; Shen et al., 2019; Yu et al., 2019a), bichromatic spring-neap tides (Robinson et al., 2007a; Abarca et al., 2013; Heiss and Michael, 2014; Buquet et al., 2016), or fitted tidal variations with several primary constituents (Levanon et al., 2016; Geng and Boufadel, 2017; Levanon et al., 2017; Yu et al., 2019b). Coastal aquifer systems are commonly subjected to oceanic tidal fluctuations, which likely contain tens of constituents with different fluctuation frequencies and amplitudes (Pawlowicz et al., 2002). This would lead to complex and irregular SGD and salinity distributions.

Recently, Yu et al. (2019b) numerically examined the effect of multiconstituent tides on both SGD and salinity distributions in a subterranean estuary. They found that the response of water exchange (e.g., SGD) across the aquifer-sea interface to tides is almost instantaneous. As such, the present (at any given moment) water exchange is mainly influenced by the present (i.e., at the same time) tidal conditions. However, the response of salinity distributions to tides is delayed; thus, salinity distributions are dependent on the antecedent (previous) tidal conditions.

Yu et al. (2019b) found that coastal aquifers behave as a low-pass filter smoothing-out tidal signals, particularly high-frequency tidal constituents (e.g., semidiurnal and diurnal tidal signals). Furthermore, the combination of high-frequency tidal constituents generates new low-frequency signals when the tidal signals propagate in the aquifer, as determined by Li et al. (2000) using analytical solutions for groundwater tidal propagation. These generated low-frequency signals, combined with the primary tidal fluctuations created directly by the ocean tide, jointly affect the salinity distributions (e.g., SW and USP) in unconfined aquifers (Yu et al., 2019b). With the antecedent tidal conditions weighted in the form of convolution using the probability density function of the Gamma distribution, Yu et al. (2019b) demonstrated that the prolonged and cumulative effects of antecedent tidal conditions on the present salinity distributions in unconfined aquifers could be quantified.

Yu et al. (2019b) studied multiconstituent tides within a coastal unconfined aquifer with a fixed-flux inland boundary and inland extent of 150 m. Both fixed-flux (Michael et al., 2005; Robinson et al., 2007c; Kuan et al., 2012; Evans and Wilson, 2016) and fixed-head (Li et al., 1997; Ataie-Ashtiani et al., 1999; Heiss and Michael, 2014; Geng and Boufadel, 2015) inland boundaries have been widely adopted in previous studies of SGD and salinity distributions. The former assumes that freshwater discharge to the sea is constant, whereas the latter applies to topography-controlled aquifers (Werner and Simmons, 2009; Michael et al., 2013). In low-elevation coastal areas, the watertable is often shallow, leading to the overlying unsaturated zone being thin. Under this condition, the rainfall-induced infiltration would be inhibited, i.e., once the soil is saturated, surface water runoff would occur and the watertable tends to be fixed to the local surface elevation. This likely forms a fixed-head inland boundary (Michael et al., 2013; Sawyer et al., 2016). Michael et al. (2013) suggested that approximately 70% of the world's coastlines are topography-controlled. Coastal aquifers with fixed-head landward boundaries are recognized to be more vulnerable to seawater intrusion, as salinity distributions are more responsive to changes to ocean boundary conditions (Werner and Simmons, 2009; Michael et al., 2013). Despite the commonality of fixed-head inland boundaries, the question remains open as to how they regulate the SGD and salinity distributions in subterranean estuaries subjected to multiconstituent tides.

In this study, we focused on the effects of multiconstituent tides on SGD and salinity distributions in unconfined aquifers with fixed-head inland boundaries at different landward positions, under the assumption that the yearly averaged inland freshwater input is the same in aquifers of alternative landward extent. The following key questions were explored based on numerical simulations: 1) How does a change in the inland aquifer extent affect the SGD and salinity distribution responses to multiconstituent tides? 2) How do multiconstituent tides affect inland freshwater input in inland fixed-head aquifers? 3) How does the inland aquifer extent influence the role of antecedent tidal conditions on salinity distributions?

Conceptual Model and Simulations

Similar to Yu et al. (2019b), a 2D cross-shore section of a coastal unconfined aquifer was considered in this study, as shown in **Figure 1**. Boundary DEF was set as the time-variant head boundary (aquifer-sea interface) affected by multiconstituent tides. To investigate the response of the aquifer to multiconstituent tides, we used six years (2011–2016) of real tide data measured from Brisbane Bar tidal station (website: http://data.qld.gov.au/dataset/brisbane-bar-tide-gauge-archived-interval-recordings). The measurement interval was 600 s. Four dominant tidal constituents were detected in this dataset based on

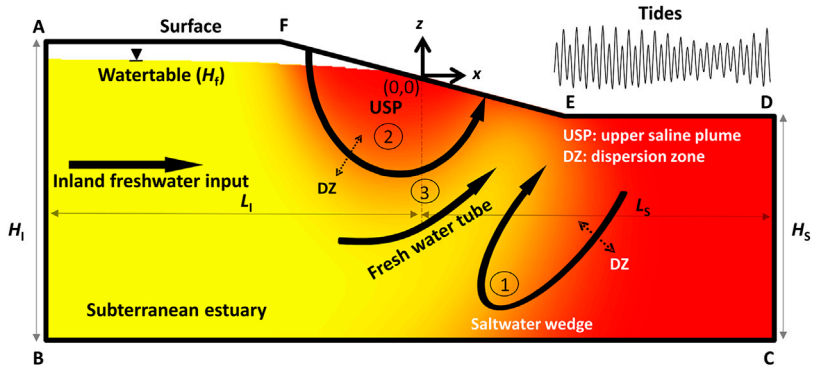


FIGURE 1 | Conceptual diagram of a subterranean estuary of an unconfined aquifer. Flow processes considered in this article are as follows: 1) density-driven seawater circulation, 2) tide-induced seawater circulation, and 3) terrestrial groundwater discharge. The colors represent the salinity (yellow for freshwater and red for saltwater). Boundary ABCDEF represents the model domain. The *x*-*z* coordinate origin was set at the mean shoreline. L_I and L_S are the inland and seaward aquifer extents, respectively. H_I and H_S are the inland and seaward aquifer thicknesses, respectively. H_f is inland watertable elevation at the inland boundary.

spectral analysis: 1) principal lunar semidiurnal tidal constituent (M_2, T (tidal period) = 12.42 h, A (tidal amplitude) = 0.73 m); 2) principal solar semidiurnal tidal constituent (S_2, T = 12 h, A = 0.19 m); 3) lunisolar declinational diurnal tidal constituent (K_1, T = 23.93 h, A = 0.19 m); 4) larger lunar elliptic semidiurnal tidal constituent (N_2, T = 12.66 h, A = 0.15 m).

Boundaries BC and CD were set to no-flow boundaries. Rainfall and evaporation were excluded and thus AF was also set as a no-flow boundary. Different from Yu et al. (2019b), the landward boundary AB was set to a fixed-head boundary. The fresh groundwater recharged from the inland boundary AB and discharged into the ocean through the aquifer-sea interface DEF. It is worth noting that to make the simulation results comparable, inland watertable elevations (H_f) were adjusted to get a similar yearly averaged freshwater input (around 2.1 m^3/m/d). We focused on four cases with the fixed-head inland boundary located at different locations as follows:

(1) Fixed-head and L_I = 50 m (L_I is the inland aquifer extent, which measures the horizotal distance from the inland boundary to the shoreline), with the seaward aquifer extent L_S = 50 m, the seaward aquifer thickness H_S = 27 m, and the inland aquifer thickness H_I = 33 m (note that the same L_S, H_S, and H_I were set in all the cases). H_f was fixed at 0.81 m.
(2) Fixed-head and L_I = 100 m, H_f was fixed at 1.15 m.
(3) Fixed-head and L_I = 150 m, H_f was fixed at 1.50 m.
(4) Fixed-head and L_I = 200 m, H_f was fixed at 1.83 m.

In addition to these four cases with fixed-head inland boundaries, one case with fixed-flux inland boundary (L_I = 150 m, similar to that used in Yu et al. (2019b)) was also considered for comparing the behavior of aquifers with different inland boundaries. We tested the effect of inland aquifer extent (L_I) on salinity distributions in the aquifers with fixed-flux inland boundaries. The results showed that the inland aquifer extent did not remarkably affect the variation of the USP and SW in the aquifers. Therefore, only the results from one case with fixed-flux inland boundary (fixed-flux and L_I = 150 m) were included in this article. The aquifer properties were similar to those used in Yu et al. (2019b). That is, the model setup was based on a homogeneous sandy beach with hydraulic conductivity K_s = 10 m/d and porosity ϕ = 0.45. The beach slope was 0.1. The longitudinal and transverse dispersivities were set to 0.5 and 0.05 m, respectively (Hunt et al., 2011). The residual water saturation S_{Wres} was set to 0.1 and water retention parameters α and n were set to 14.5 m^{-1} and 2.68 (typical values for sand (Carsel and Parrish, 1988)) for the van Genuchten (1980) equations.

The numerical simulations were conducted using SUTRA (Voss and Provost, 2010), which simulates variably saturated and density-dependent pore-water flow and associated solute transport. In the inland subdomain, a mesh with Δx = 1.5 m and Δz = 0.5 m was used, while in the intertidal and seabed subdomain, the mesh was refined ($\Delta x \approx$ 0.33 m and $\Delta z \approx$ 0.1 m). For all the simulations, the model was initially run to the steady states (pressure and salinity unchanged) with a static sea level (0 m). The measured tidal conditions (2011–2016) were then introduced as the boundary conditions in the model with a time step of 300 s. Here, we focused on the analysis of the last two years (2015–2016). As suggested by Yu et al. (2019b) and will be discussed later, after 4 years (2011–2014), the behavior of the system was independent of the initial conditions subjected to the static sea level.

RESULTS AND ANALYSIS

SGD and Salinity Distribution Fluctuations Induced by the Multiconstituent Tides

As mentioned earlier, for the five considered cases (four with fixed-head inland boundaries and one with fixed-flux inland boundary), the averaged inland freshwater input was similar. The two-year (2015–2016) averaged salinity distributions in the aquifers were similar for the five cases, e.g., the 50% isohaline of the seawater (17.5 ppt) largely overlapped (**Figure 2**). This suggests that the yearly averaged inland freshwater input

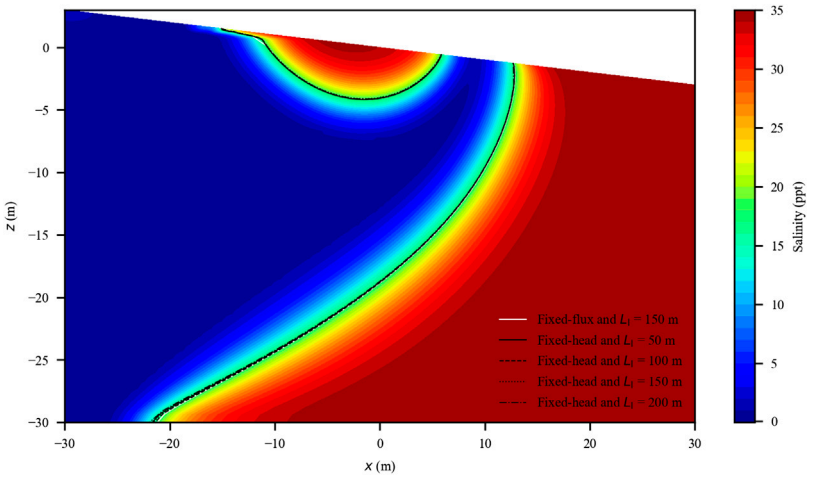


FIGURE 2 | Two-year averaged salinity distribution in the aquifer (note that only the beach section is presented). The salinity is shown by different colors (the case of fixed-head (L_l = 50 m) was used). The different types of lines represent the 50% isohaline of the seawater for the different cases (largely overlapped). The salinity distributions are similar in the cases with fixed-flux (L_l = 150 m) and fixed-head (L_l = 50, 100, 150, and 200 m) inland boundaries.

TABLE 1 | Key results of the flux and salinity distributions affected by different inland boundaries[a].

	L_l(m)	Landward boundary		Water influx (m^3/m/d)						Water efflux (SGD) (m^3/m/d)		Amount of salt stored in the aquifer (kg/m)			
		Head (m)	Flux (m^3/m/d)	Q_f		Q_t		Q_d				Saltwater wedge		Upper saline plume	
				μ	σ	μ	σ	μ	σ	μ	σ	μ	σ	μ	σ
Fixed-flux	150	NA	2.10	2.10	0	1.46	1.11	1.11	0.27	4.67	0.62	8,425	150	872	83
Fixed-head	50	0.81	NA	2.11	0.47	1.42	1.10	0.96	0.26	4.49	0.61	8,316	218	868	154
	100	1.15	NA	2.09	0.21	1.41	1.08	0.96	0.25	4.46	0.62	8,368	180	854	107
	150	1.50	NA	2.11	0.12	1.40	1.08	0.96	0.25	4.47	0.61	8,330	167	840	95
	200	1.83	NA	2.09	0.08	1.41	1.08	0.96	0.25	4.46	0.61	8,352	162	846	90

[a]L_l *is the inland aquifer extent;* Q_f *is the inland freshwater input;* Q_t *is the tide-induced seawater circulation;* Q_d *is the density-driven seawater circulation; SGD is the submarine groundwater discharge;* μ *and* σ *are the averaged result and the standard deviation over the last two years (years 2015–2016), respectively; NA means not applicable. Note that the values of flux and salt mass are calculated per unit width of the aquifer.*

rather than the inland aquifer extent significantly affected the salinity distributions at a long-time scale. For the four cases with fixed-head inland boundaries, the calculated yearly averaged amounts of salt stored in (per unit width) saltwater wedge (SM_{SW}) and upper saline plume (SM_{USP}) were also close to those for the case with fixed-flux inland boundary (8,425 and 872 kg/m, respectively) (**Table 1**). The averaged tide-induced (around 1.4 m^3/m/d) and density-driven (around 1 m^3/m/d) seawater circulation fluxes were also similar for all the cases (**Table 1**). Since the yearly averaged inland freshwater input was similar, the inland aquifer extent did not remarkably affect the averaged SGD and salinity distributions in the aquifers subjected to the multiconstituent tides.

We further investigated the variation of fluxes and salinity distributions (both water flux and amount of salt stored) in response to the multiconstituent tides by presenting the variation in the last two years (2015–2016). To quantify the fluctuations for the different cases, the averaged value (μ) and the standard deviation (σ) over each principal semidiurnal lunar tidal cycle (12.42 h) in these two years were calculated.

The calculated standard deviations for the tide-induced and density-driven influx were similar among the four cases with fixed-head inland boundaries and differed slightly from that for the case with fixed-flux inland boundary (**Table 1**). The SGD, as the total efflux across the aquifer-sea interface, varied intensively in response to the multiconstituent tides (**Figure 3**). The averaged values of the SGD over each principal semidiurnal lunar tidal cycle for the five cases largely overlapped. Consistently, the calculated standard deviations were quite similar and around 0.62 m^3/m/d. This suggests that, for the simulated cases with similar averaged freshwater input, SGD was predominantly affected by the present tidal conditions. The response of SGD to the tidal fluctuations was mostly instantaneous; thus, the effect of the inland aquifer extent was not obvious.

In contrast, the fluctuations of freshwater input differed case by case (**Figure 4**). As the inland aquifer extent decreased,

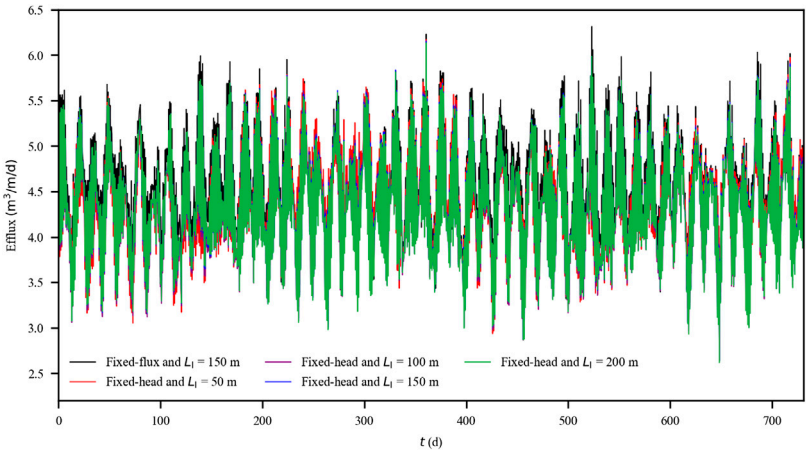


FIGURE 3 | Averaged per unit width water efflux (i.e., submarine groundwater discharge) every 12.42 h for the cases with fixed-flux (L_I = 150 m) and fixed-head (L_I = 50, 100, 150, and 200 m) inland boundaries. Note that the lines are largely overlapped.

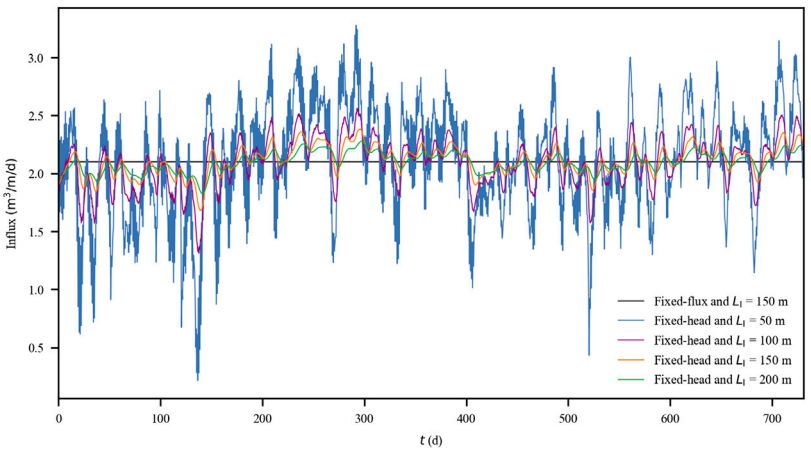


FIGURE 4 | Averaged inland freshwater input every 12.42 h for the cases with fixed-flux (L_I = 150 m) and fixed-head (L_I = 50, 100, 150, and 200 m) inland boundaries.

the averaged values of the freshwater input over each principal semidiurnal lunar tidal cycle started to fluctuate around that for the case with fixed-flux inland boundary (2.1 m^3/m/d). As L_I reduced from 200 to 150, 100, and 50 m, the standard deviation increased from 0.08 to 0.12, 0.21, and 0.47 m^3/m/d, respectively. It is worth noting that the equal reduction in L_I led to unequal increase in the standard deviation of the freshwater input, leading to an accelerating trend. The inland freshwater input was controlled by the lateral hydraulic gradient. As setup in the simulations, a similar yearly averaged inland freshwater input was produced (**Table 1**). It is expected that the instantaneous hydraulic gradient was continuously modified by the inland watertable and seaward tidal level. The multiple tidal constituents propagated into the aquifer and thus affected the hydraulic gradient in a complex fashion. In particular, the low-frequency signals would propagate further inland and obviously affect the freshwater input (details in ***Analysis on Amplitude Spectrums***).

For both the cases with fixed-head and fixed-flux inland boundaries, SM_{SW} and SM_{USP} fluctuated remarkably (**Figures 5**, **6**). Overall, the cases with fixed-head inland boundaries were related to intensive fluctuations in the averaged value over each principal semidiurnal lunar tidal cycle (**Table 1**). As L_I reduced from 200 to 150, 100, and 50 m, the standard deviation for SM_{SW} increased from 162 to 167, 180, and 218 kg/m, respectively, whereas the standard deviation for SM_{USP} increased from 90 to 95, 107, and 154 kg/m, respectively. Clearly, the fluctuation intensity for SM_{SW} was more obvious than that for SM_{USP}, suggesting that SM_{SW} tended to be more affected by the low-frequency tidal signals (details in ***Analysis on Amplitude Spectrums***).

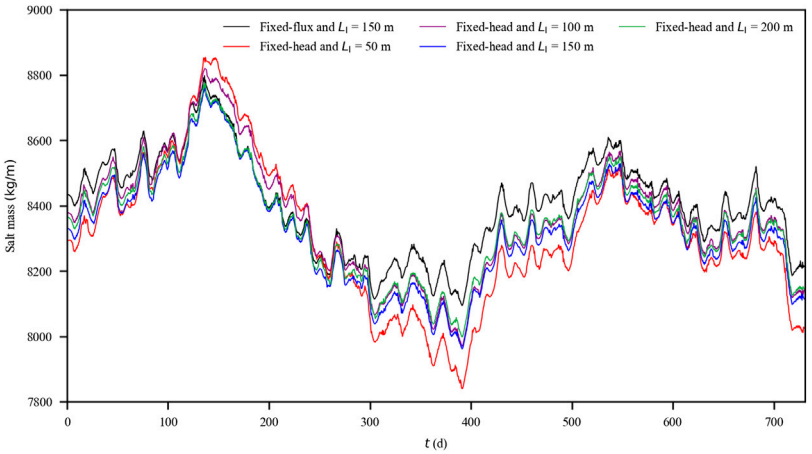


FIGURE 5 | Averaged amount of salt stored in the saltwater wedge every 12.42 h for the cases with fixed-flux (L_I = 150 m) and fixed-head (L_I = 50, 100, 150, and 200 m) inland boundaries.

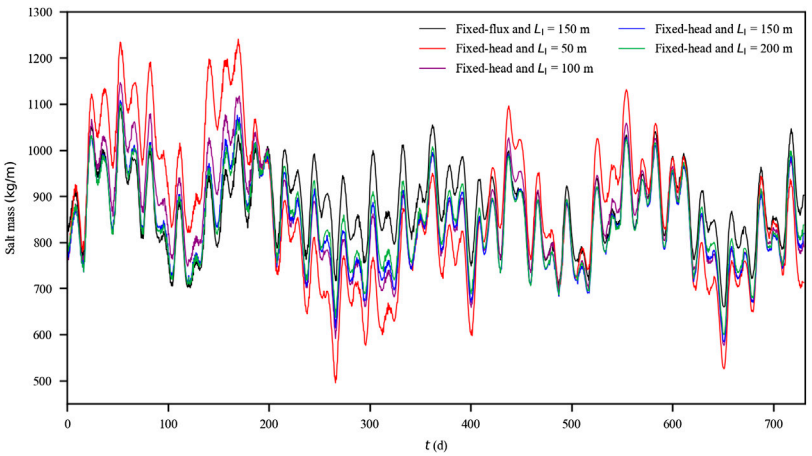


FIGURE 6 | Averaged amount of salt stored in the upper saline plume every 12.42 h for the cases with fixed-flux (L_I = 150 m) and fixed-head (L_I = 50, 100, 150, and 200 m) inland boundaries.

Analysis of Amplitude Spectra

The variations of the SGD and salinity distributions could be reflected by amplitude spectra. Similar to Yu et al. (2019b), the instantaneous results were selected with a 2 h time interval (X). We also used the following standardized and nondimensional variables (X^*).

$$X^* = \frac{X - \text{mean}(X)}{\max(X) - \min(X)}. \quad (1)$$

As expected, four dominant frequencies (M_2, S_2, K_1, and N_2) appeared in the tidal series (**Figure 7A**) and also in the SGD variations (**Figure 7B**). As pointed out by Yu et al. (2019b), in the SGD, two new signals with frequencies of 7.83×10^{-7} Hz (spring-neap tidal cycle, 14.8-day period) and 4.24×10^{-7} Hz (27.3-day period) were generated by the combinations of M_2 and S_2 tidal constituents ($f(S_2)$–$f(M_2)$) and M_2 and N_2 tidal constituents ($f(M_2)$–$f(N_2)$), respectively. These two new signals also appeared in the freshwater input, SM_{SW} and SM_{USP} (**Figures 7C–E**).

Different from the tidal and SGD series, the low-frequency signals started to play important roles in the freshwater input, SM_{SW} and SM_{USP} (**Figures 7C–E**). The contributions (defined as the ratio of a specific nondimensional amplitude to the sum of all the nondimensional amplitudes) of these signals changed in different ways as L_I reduced. For example, for the freshwater input, the contribution of the signal of the 365-day period decreased from 7.21% to 6.10%, 4.51%, and 1.83% as L_I reduced from 200 to 150, 100, and 50 m, respectively. The contribution of the signal of the 365-day period kept unchanged for SM_{SW}, whereas for SM_{USP}, it increased from 2.44% to 3.43%, 5.35%, and 9.33% as L_I reduced from 200 to 150, 100, and 50 m, respectively.

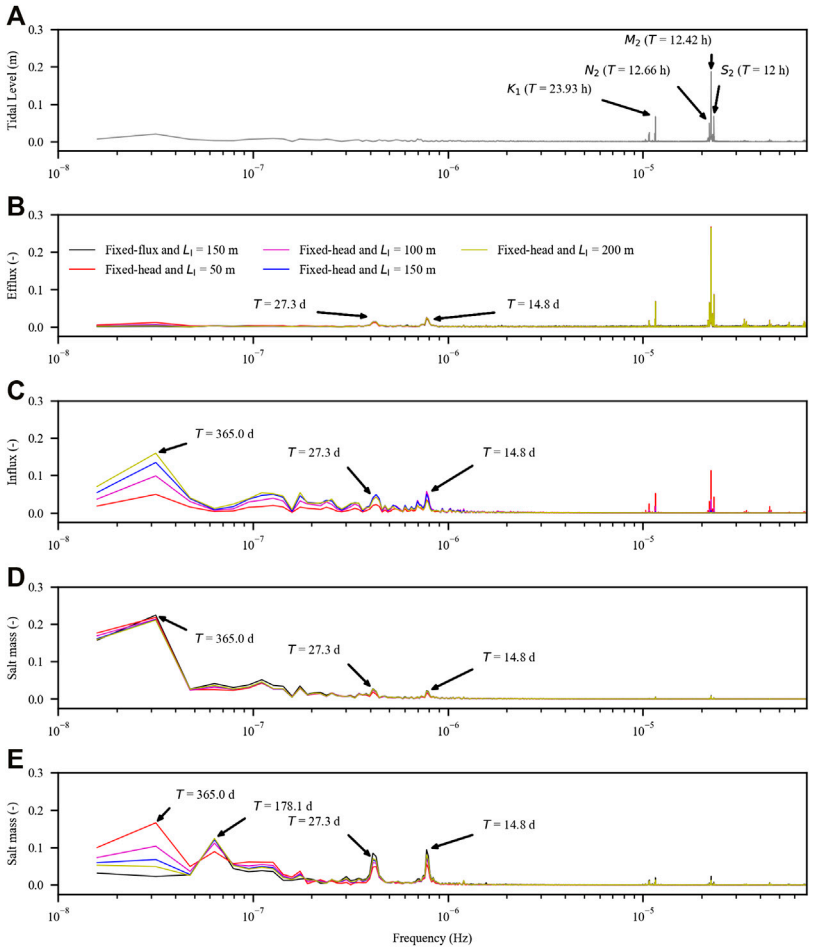


FIGURE 7 | Amplitude spectra of **(A)** tidal level variation, **(B)** submarine groundwater discharge (SGD), **(C)** inland freshwater input, **(D)** amount of salt stored in the saltwater wedge (SM_{SW}), and **(E)** amount of salt stored in the upper saline plume (SM_{USP}). The results are standardized.

As mentioned earlier, the low-frequency signals likely propagated further landward and thus interacted more with the inland boundary. The boundary reflections would damp these signals. The extent of damping depended on the inland aquifer extent and the tidal frequencies. With respect to the variation of the freshwater input, the low-frequency signal of the 365-day period was not apparent with L_I = 50 m, where the high-frequency signals (M_2, S_2, K_1, and N_2) were relatively strong. Thus, the fluctuation intensity of the freshwater input was significantly enhanced in the case with L_I = 50 m.

Similar to Yu et al. (2019b) considering the fixed-flux inland boundary, the combination of M_2, S_2, and N_2 tidal constituents ($3f(M_2)$ -$2f(N_2)$- $f(S_2)$) generated a new signal with a frequency of 6.50 × 10^{-8} Hz (178.1-day period) in SM_{USP} (**Figure 7E**). However, for the cases with fixed-head inland boundaries, this signal of the 178.1-day period competed with that of the 365-day period, both affecting SM_{USP} (**Figure 7E**). The contribution of the former decreased, whereas that of the latter increased as L_I decreased. This was significantly different from the case with fixed-flux inland boundary, in which no signal of the 365-day period was detected for SM_{USP}.

Quantification of SGD and Salinity Distributions Affected by Multiconstituent Tides

From the spectrum analysis, it can be seen that the variations of the SGD and salinity distributions were more complex for the cases with fixed-head inland boundaries, in comparison with the case with fixed-flux inland boundary. The question of whether these variations can be quantified remained interesting, and the regression modeling approaches in Yu et al. (2019b) were tested.

Similar to the results of Yu et al. (2019b), the response of SGD to the multiconstituent tides was instantaneous. As such, the present SGD could be quantified by a linear regression model without considering the effect of the antecedent tidal conditions.

$$Y = a_0 + a_\sigma X_\sigma + a_M X_M + e, \quad (2)$$

where Y is the output of the regression model. X_σ and X_M are the standard deviation of tidal level and the averaged tidal level over each semidiurnal lunar tidal cycle (12.42 h), respectively, which denote the extent of tidal fluctuations over the tidal cycle and the averaged sea level. σ and M indicate the standard deviation of

TABLE 2 | Summary of regression results for submarine groundwater discharge (SGD)[a].

	L_I(m)	Regression model	Goodness of fitting	Coefficients of regression model		
			Adjusted R^2	a_σ(m/d)	a_M(m/d)	a_0(m^2/d)
Fixed-flux	150	$Y = a_0 + a_\sigma X_\sigma + a_m X_m + e$	0.60	1.71	−3.64	3.58
Fixed-head	50		0.78	2.03	−4.11	3.26
	100		0.69	2.11	−3.87	3.21
	150		0.66	2.03	−3.80	3.26
	200		0.65	2.01	−3.77	3.26

[a]L_I *is the inland aquifer extent;* a_σ, a_M, *and* a_0 *are the coefficients of the regression model;* X_σ *is the standard deviation of tidal level per 12.42 h;* X_M *is the averaged tidal level per 12.42 h.*

tidal level and the averaged tidal level over 12.42 h, respectively.a_0, a_σ, and a_M are coefficients of the regression model and e represents the error. The performance of the regression model was indicated by the adjusted R^2, which was 0.78, 0.69, 0.66, and 0.65, respectively, for the cases with L_I = 50, 100, 150, and 200 m (**Table 2**, **Supplementary Figures S1, S2**). With increased inland aquifer extent, the weight of the averaged tidal level (a_M) in the regression model decreased and the performance of the regression model slightly declined.

As expected, the response of the freshwater input, SM_{SW} and SM_{USP}, to the tides was delayed, which failed the regression model in **Eq. 2** excluding the antecedent tidal conditions. Similar to Yu et al. (2019b), we defined the cumulative effect of antecedent multiconstituent tides (X_σ and X_M) in the regression models based on functional data analysis (Ramsay and Silverman, 2005). The cumulative effect was weighted in the form of the following convolution:

$$DTL_i = \frac{\sum_{j=n}^{m} \zeta_{i,j} X_{i,t-j\Delta t}}{\sum_{j=n}^{m} \zeta_{i,j}}, \tag{3}$$

where DTL_i is the parametric regressor, i.e., the weighted antecedent tidal conditions combined in a cumulative fashion. The subscript i indicates the independent value. t is the present time and $t - j\Delta t$ is the past time associated with the quantified antecedent tidal condition. The increment Δt of each time step was set to 12.42 h. $X_{i,t-j\Delta t}$ is the variable at that past time. The subscript j indicates the past time period considered in the convolution, with the minimum and maximum values of n and m, respectively (set to 1 and 1,411 (two years), respectively). $\zeta_{i,j}$ is a time-dependent weighting factor described by the following probability density function of the Gamma distribution:

$$\zeta_{i,j} = \mathrm{Gamma}(\alpha_i, \beta_i, j\Delta t) = \beta_i^{\alpha_i} \frac{1}{\Gamma(\alpha_i)} (j\Delta t)^{\alpha_i - 1} \exp(-\beta_i j\Delta t), \tag{4}$$

where α_i and β_i are the shape and scale factors, respectively. The ratio α_i/β_i is the mean of the Gamma distribution, which indicates a tail of the distribution (a large α_i/β_i indicates a long tail). In addition, it reflects the overall contribution of the antecedent tidal conditions.

The freshwater inputs, SM_{SW} and SM_{USP}, were then quantified using a linear combination of DTL_σ and DTL_M. Firstly, we tested the freshwater input using the regression model as follows:

$$Y = a_0 + a_\sigma DTL_\sigma + a_M DTL_M + e. \tag{5}$$

For the cases with fixed-head inland boundaries, this regression model well captured the variation of the freshwater input for the cases with L_I = 200, 150, and 100 m (**Table 3** and **Supplementary Figures S3, S4**; adjusted R^2 = 0.99, 0.99, 0.96, respectively). However, the regression result (adjusted R^2 = 0.65) for the case with L_I = 50 m was not as good as the other cases with longer inland aquifer extents. The freshwater input was affected by the lateral hydraulic

TABLE 3 | Summary of regression results for inland freshwater input[a].

	L_I(m)	Regression model	With discounted standard deviation		With discounted averaged sea level		Goodness of fitting	Coefficients of regression model		
			α_σ(-)	$\alpha_\sigma/\beta_\sigma$(d)	α_M(-)	α_M/β_M(d)	Adjusted R^2	a_σ(m/d)	a_M(m/d)	a_0(m^2/d)
Fixed-head	50	$Y = a_0 + a_\sigma DTL_\sigma + a_M DTL_M + e$	1.52	1.44	1.67	2.25	0.65	−2.47	−4.39	3.35
	100		2.24	2.38	1.85	2.44	0.96	−1.23	−2.45	2.76
	150		2.73	4.48	1.94	4.87	0.99	−0.74	−1.66	2.52
	200		2.97	7.02	2.12	8.43	0.99	−0.50	−1.26	2.37

[a]L_I *is the inland aquifer extent;* a_σ, a_M, *and* a_0 *are the coefficients of the regression model;* DTL_σ *and* DTL_M *are the parametric regressors relevant to* X_σ *and* X_M*;* α_i *and* β_i *are, respectively, the shape and scale factors of the Gamma distribution function; the ratio* α_i/β_i *is the mean of the Gamma distribution function.*

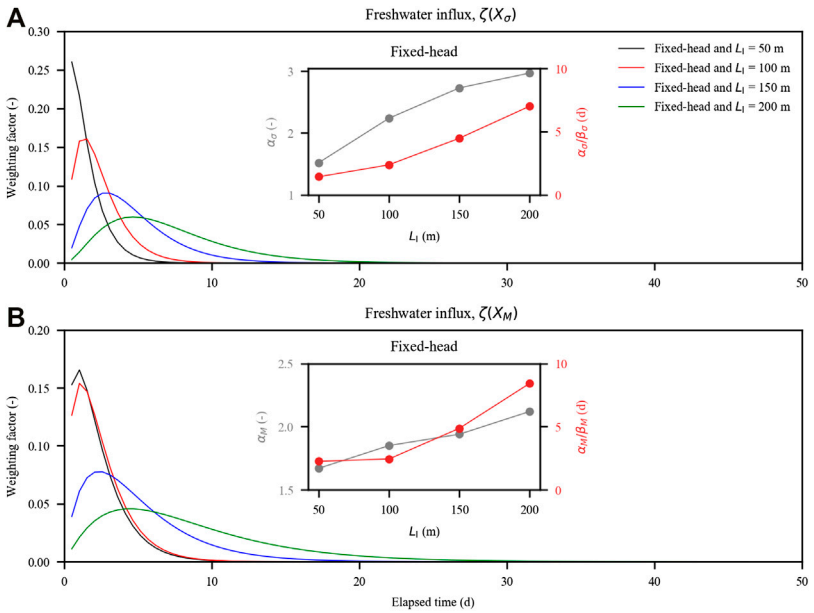


FIGURE 8 | Probability density functions of inland freshwater input quantified with the antecedent tidal conditions on the aquifer: **(A)** time-dependent weighting factor for the standard deviation of tidal level (X_σ) and **(B)** time-dependent weighting factor for the averaged tidal level (X_M). The shape and mean parameters (α and α/β) of the Gamma distribution functions are given in the inserts.

gradient, which was a combination of the inland watertable and tidal level. Given a short inland aquifer extent, the lateral hydraulic gradient was more responsive to the tidal fluctuation as it took less time for tidal signals to propagate into the inland boundary. The signal reflection would thus moderate the inland freshwater input. In this way, the contribution of the antecedent tidal conditions would decrease, whereas that of the present tidal conditions would increase. This was clearly shown by α_i/β_i values for both DTL_σ and DTL_M; for example, with L_I reduced from 200 to 150, 100, and 50 m, α_i/β_i for DTL_σ decreased from 7.02 to 4.48, 2.38, and 1.44 days, respectively (**Table 3** and **Figure 8**). As the regression model considered the antecedent tidal conditions only, it became poor for the cases with a short inland aquifer extent (e.g., that with L_I = 50 m).

Overall, α_i/β_i values for both DTL_σ and DTL_M were less than 10 days, suggesting that the recent tidal conditions were affected more on the freshwater input (**Figure 8**). Both the variation of α_i and α_i/β_i were monotonic. In particular, for all the cases with fixed-head inland boundaries, α_i values were larger than 1, suggesting that the maximum effect of the antecedent tidal conditions was delayed. With L_I reduced from 200 to 150, 100, and 50 m, α_σ for DTL_σ decreased from 2.97 to 2.73, 2.24, and 1.52, respectively, whereas α_M for DTL_M decreased from 8.43 to 4.87, 2.44, and 2.25 days, respectively. These trends were consistent with the tidal propagation; that is, it took less time for tidal signals to reach the inland boundary and moderate the freshwater input with the reduced L_I.

Secondly, we examined SM_{SW}. The regression model for the freshwater input (**Eq. 5**) well captured the variation of SM_{SW} for the cases with fixed-head inland boundaries (**Table 4** and **Supplementary Figures S5, S6**) as well as that for the case with fixed-flux inland boundary (all the R^2 values were larger than 0.95). As L_I increased, both α_i and α_i/β_i values increased monotonously (**Figure 9**), suggesting that the effect of the antecedent tidal conditions on SM_{SW} was further delayed and prolonged as the inland aquifer extent increased.

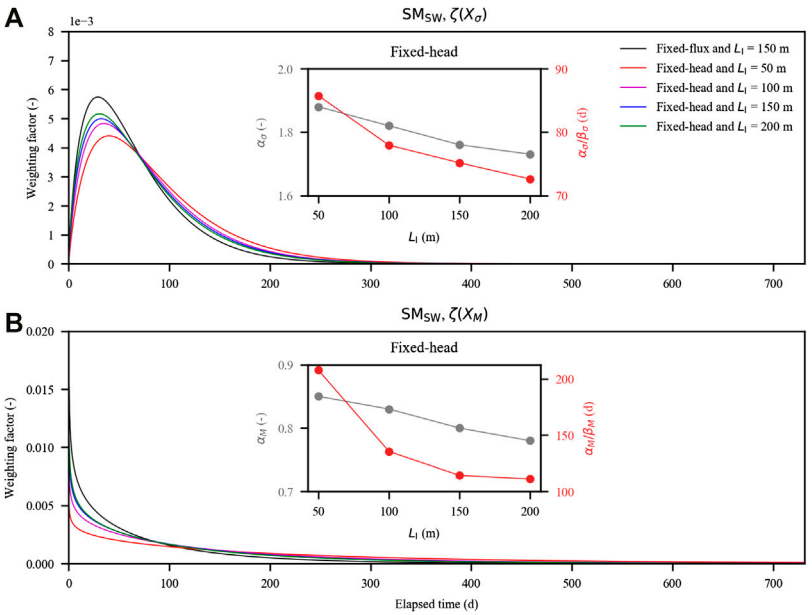


FIGURE 9 | Probability density functions of the amount of salt stored in the saltwater wedge (SM_{SW}) quantified with the antecedent tidal conditions on the aquifer: **(A)** time-dependent weighting factor for the standard deviation of tidal level (X_σ) and **(B)** time-dependent weighting factor for the averaged tidal level (X_M). For the cases with fixed-head inland boundaries, the shape and mean parameters (α and α/β) of the Gamma distribution functions are given in the inserts.

TABLE 4 | Summary of regression results for SM_{SW}[a].

	L_I(m)	Regression model	With discounted standard deviation		With discounted averaged sea level		Goodness of fitting	Coefficients of regression model		
			α_σ(-)	$\alpha_\sigma/\beta_\sigma$(d)	α_M(-)	α_M/β_M(d)	Adjusted R^2	a_σ(kg/m^2)	a_M(kg/m^2)	a_0(kg/m)
Fixed-flux	150	$Y = a_0 + a_\sigma DTL_\sigma + a_M DTL_M + e$	1.80	65.49	0.76	74.73	0.95	−9,321	4,043	13,500
Fixed-head	50		1.88	85.75	0.85	207.72	0.98	−8,026	13,370	12,650
	100		1.82	77.92	0.83	135.47	0.96	−8,725	7,522	13,110
	150		1.76	75.15	0.80	114.21	0.96	−9,686	6,028	13,600
	200		1.73	72.61	0.78	111.01	0.96	−9,783	5,670	13,670

[a]*SM_{SW} is the amount of salt stored in the saltwater wedge (per unit width aquifer); L_I is the inland aquifer extent; a_σ, a_M, and a_0 are the coefficients of the regression model; DTL_σ and DTL_M are the parametric regressors relevant to X_σ and X_M; α_i and β_i are, respectively, the shape and scale factors of the Gamma distribution function; the ratio α_i/β_i is the mean of the Gamma distribution function.*

Finally, we checked SM_{USP} using the regression model given in Yu et al. (2019b) for the cases with fixed-flux inland boundaries.

$$Y = a_0 + a_\sigma DTL_\sigma + a_A \sin(\omega t + \delta) + e, \quad (6)$$

where ω is the angular frequency related to the low-frequency of 6.50×10^{-8} Hz (period of 178.1 d). a_A and δ are the amplitude and the phase shift of this signal, respectively.

This regression model failed to capture the variation of SM_{USP}, particularly under the conditions of L_I = 50 and 100 m (**Table 5** and **Supplementary Figures S7, S8**). The adjusted R^2 values for L_I = 50 and 100 m were, respectively, 0.23 and 0.47. This further demonstrated that the hydrodynamic process in the aquifers with fixed-head inland boundaries was more complicated than that with fixed-flux inland boundaries. As discussed earlier, in the former, the inland freshwater input was variable and affected by both the standard deviations and the averaged values of the antecedent tidal conditions. Therefore, we introduced the following new regression model with DTL_M included to account for the varying freshwater input.

$$Y = a_0 + a_\sigma DTL_\sigma + a_M DTL_M + a_A \sin(\omega t + \delta) + e. \quad (7)$$

Then, the variation of SM_{USP} was well captured in both trend and magnitude for the cases with fixed-head inland boundaries (**Table 5** and **Supplementary Figures S9, S10**). The fitted results were improved in the new regression model (adjusted R^2 of 0.23, 0.47, 0.63, and 0.70 for the old model (**Eq. 6**) in comparison with adjusted R^2 of 0.92, 0.88, 0.87, and 0.87 for the new model (**Eq. 7**). It is interesting that α_i/β_i values for both DTL_σ and DTL_M monotonically increased as L_I increased (**Figure 10**). However, α_i values for DTL_σ and DTL_M showed opposite trends. The former decreased but the latter increased. This suggests that as

TABLE 5 | Summary of regression results for SM_{USP}[a].

	L_l(m)	Regression model	With discounted standard deviation		With discounted averaged sea level		Goodness of fitting	Coefficients of regression model				
			α_σ(-)	$\alpha_\sigma/\beta_\sigma$(d)	α_M(-)	α_M/β_M(d)	Adjusted R^2	a_σ kg/m^2	a_M kg/m^2	a_A kg/m	δ	a_0 kg/m
Fixed-flux	150	$Y = a_0 + a_\sigma DTL_\sigma + a_A \sin(\omega t + \delta) + e$	0.92	13.69	NA	NA	0.86	2,862	NA	64.13	0.72	−653
Fixed-head	50	$Y = a_0 + a_\sigma DTL_\sigma + a_A \sin(\omega t + \delta) + e$	0.92	7.55	NA	NA	0.23	1,559	NA	67.80	0.86	54
	100		0.90	7.88	NA	NA	0.47	1840	NA	67.34	0.75	−112
	150		0.91	8.57	NA	NA	0.63	1826	NA	67.21	0.74	−118
	200		0.92	9.95	NA	NA	0.70	2,103	NA	66.40	0.73	−264
Fixed-head	50	$Y = a_0 + a_\sigma DTL_\sigma + a_M DTL_M + a_A \sin(\omega t + \delta) + e$	0.98	7.25	3.15	31.70	0.92	1,742	2,732	66.11	0.67	−58
	100		0.95	7.75	3.20	36.80	0.88	1,749	1,506	65.82	0.67	−70
	150		0.92	8.76	3.25	39.32	0.87	1,944	1,062	65.21	0.67	−186
	200		0.91	9.65	3.30	39.69	0.87	2,125	854	64.77	0.68	−276

[a]*SM_{USP} is the amount of salt stored in the upper saline plume (per unit width aquifer); L_l is the inland aquifer extent; a_σ, a_M, a_A, δ, and a_0 are the coefficients of the regression models; DTL_σ and DTL_M are the parametric regressors relevant to X_σ and X_M; α_i and β_i are, respectively, the shape and scale factors of the Gamma distribution function; the ratio α_i/β_i is the mean of the Gamma distribution function. NA means not applicable.*

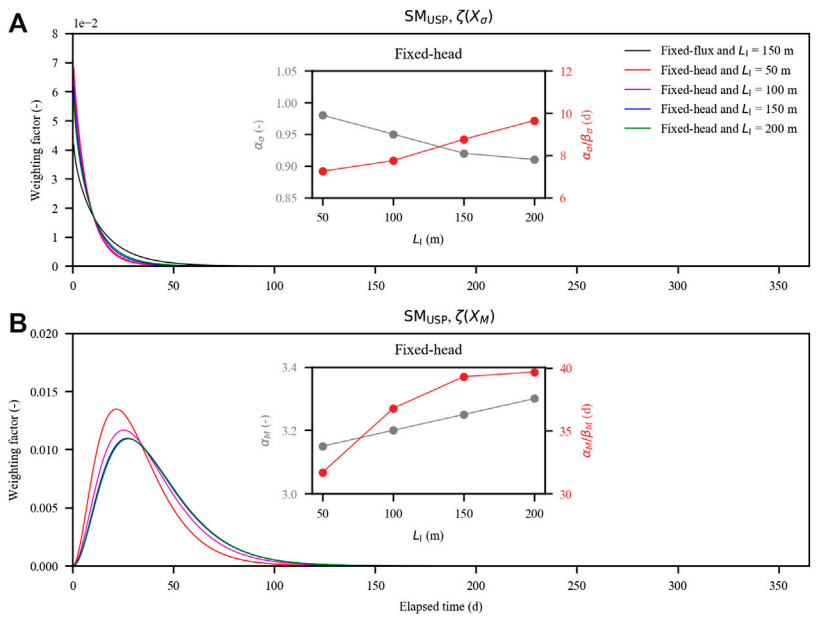


FIGURE 10 | Probability density functions of the amount of salt stored in the upper saline plume (SM_{USP}) quantified with the antecedent tidal conditions on the aquifer: **(A)** time-dependent weighting factor for the standard deviation of tidal level (X_σ) and **(B)** time-dependent weighting factor for the averaged tidal level (X_M). For the cases with fixed-head inland boundaries, the shape and mean parameters (α and α/β) of the Gamma distribution functions are given in the inserts.

the inland aquifer extent increased, the effect of the mean tidal level on the USP was further delayed, whereas the effect of standard deviation was further enhanced. The USP developed in the seaside aquifer and was altered by both the fluctuation intensity of tides and the inland freshwater input. The opposite trends of the enhanced tidal effect and the reduced effect of the inland boundary on the USP are consistent with the previous studies (Werner et al., 2013; Robinson et al., 2018).

DISCUSSIONS

There are generally two types of inland boundary conditions for coastal unconfined aquifers: topography-controlled and constant freshwater discharge, to which the fixed-head and fixed-flux inland boundaries could be applied, respectively (Werner and Simmons, 2009). Given the similar freshwater input, the yearly averaged SGD and salinity distributions remained similar in the

aquifers subjected to the multiconstituent tides. However, with the fixed-head inland boundary, the multiconstituent tides led to more remarkable fluctuations of the USP and SW, in comparison with those for the case with fixed-flux inland boundary. This reflects intensive mixing between freshwater and seawater, which was shown to intensify as the inland aquifer extent decreased. As chemical compositions of seaward seawater and land-sourced fresh groundwater are apparently different, these enhanced mixing between freshwater and seawater would favor biogeochemical reactions in coastal aquifers (Robinson et al., 2018).

With the fixed-head inland boundaries, the lateral hydraulic gradient varied in response to the multiconstituent tides. This led to a varying inland freshwater input, which was more remarkable as the inland aquifer extent decreased. However, the SGD, as the total water efflux, kept a similar fluctuation trend for all the cases and was not significantly altered by the inland aquifer extent. Based on the principle of mass conservation, it is expected that the varying inland freshwater input would moderate the storage of both the freshwater and land-sourced chemicals stored in the aquifer.

The spectrum analysis of the SGD and SM_{SW} showed that the importance of different signals was similar for the aquifers with fixed-head or fixed-flux inland boundaries. The spectrum of freshwater input demonstrated the significant effect of low-frequency signal (365-day period) in the fixed-head inland aquifers and its influence increased as the inland aquifer extent increased. This suggests that the signal of the year-long period in the tidal series was enhanced in the inland freshwater input. The influence of this signal also increased with the increased inland aquifer extent for the size of USP in the aquifers with fixed-head inland boundaries. Consistently, the 365-day period signal did not appear in the spectrum of SM_{USP} for the aquifer with fixed-flux inland boundary. These results were overall consistent with previous studies that coastal aquifers with fixed-head inland boundaries are more responsive to changes to ocean boundary conditions as groundwater discharge and salt distributions can be easily changed (Werner and Simmons, 2009; Michael et al., 2013). Our results further highlighted the importance of low-frequency tidal fluctuations. Not only the SW but also the USP was affected by low-frequency signals. In particular, the USP was affected more by low-frequency signals as the inland aquifer extent increased. At a longer-time scale, the location of the fixed-head inland boundary in a natural aquifer depends on the local topography and mean sea level. A relative sea-level rise, as a combination of the two, is expected to reduce the inland aquifer extent. In this way, the high-frequency tidal signals would play a more important role in affecting salinity distributions (both the SW and USP).

SGD is extensively recognized for delivering considerable land-sourced chemicals to the sea and thus affects marine ecosystems such as inducing coastal eutrophication. Salinity distributions in aquifers affect terrestrial ecosystems and fresh groundwater use in coastal areas. Based on our results, the response of the SGD to multiconstituent tides is mostly instantaneous. This suggests that an intensified oceanic forcing condition may instantaneously lead to large input of chemicals to the sea. The variations of the SW and USP are insensitive to the present tidal conditions but related to the antecedent tidal conditions. Oceanic forcing conditions would affect the salinity distributions in aquifers in a prolonged fashion. This suggests that the management of coastal groundwater resources such as control of seawater intrusion could carefully consider antecedent oceanic forcing conditions and long-lasting impacts of human activities (e.g., groundwater extraction and recharge). The regression models presented in this study provide a way for predicting salinity distributions in coastal aquifers under different scenarios and would help guide decision-making.

CONCLUSIONS

This article has examined the SGD and salinity distributions in coastal aquifers with fixed-head inland boundaries and subjected to the influence of multiconstituent tides. The numerical simulations with different inland aquifer extents represented the typical topography-controlled unconfined coastal aquifers. The following conclusions can be drawn:

- Given a similar yearly averaged freshwater input, the SGD responded instantaneously to the multiconstituent tides. The effect of the inland aquifer extent on SGD was minor. However, the USP and SW fluctuations were enhanced as the inland aquifer extent decreased.
- Inland freshwater input was affected by the combination of the inland aquifer extent and multiconstituent tides. Filtering effect of the aquifer on the high-frequency tidal signals was weakened as the inland aquifer extent decreased and that led to enhanced fluctuations of the freshwater input. The varying freshwater input in turn affected remarkably the salinity distributions in the aquifer.
- The regression modeling approaches developed in Yu et al. (2019b) were shown to be able to quantify the variation of the SGD and SW but did not work well for the USP. The cumulative influence of the antecedent lateral hydraulic gradients (as a combination of inland watertable and tidal level) was further included in the new regression model for the USP.

In natural systems, the inland condition is more complex than that of either fixed-head or fixed-flux inland boundary as the inland freshwater input is commonly irregular in response to local rainfall, evapotranspiration, and anthropic groundwater use. While our regression models well captured the SGD and salinity distributions in both aquifers with fixed-head and fixed-flux inland boundaries, they remain to be tested for real aquifer systems. It is worth noting that most natural aquifers are also affected by high-frequency waves and episodic rainfall. All these forcing factors would affect SGD process and salinity distributions in a prolonged fashion (Xin et al., 2014; Yu et al., 2017). Long-term investigations are necessary for applying our regression models in real coastal aquifers. With available long-term datasets, possible quantitative analysis on the interaction among these forcing factors would help to uncover complex SGD

process and salinity distributions. Nevertheless, the present study has provided guidance for future research, including field investigations that aim to establish the principle link of SGD and salinity distributions to hydrological forcing factors.

DATA AVAILABILITY STATEMENT

The raw data supporting the conclusions of this article will be made available by the authors, without undue reservation.

AUTHOR CONTRIBUTIONS

XY: methodology, formal analysis, data curation, conceptualization, and writing the original draft. PX: conceptualization, methodology, supervision, and writing, review and editing. CS: methodology and supervision. LL: methodology and writing, review and editing.

FUNDING

This work was supported by the National Natural Science Foundation of China (U2040204 and 41807178) and the Fundamental Research Funds for the Central Universities (2019B80414 and 2019B12314).

SUPPLEMENTARY MATERIAL

The Supplementary Material for this article can be found online at: https://www.frontiersin.org/articles/10.3389/fenvs.2020.599041/full#supplementary-material

REFERENCES

Abarca, E., Karam, H., Hemond, H. F., and Harvey, C. F. (2013). Transient groundwater dynamics in a coastal aquifer: the effects of tides, the lunar cycle, and the beach profile. *Water Resour. Res*. 49 (5), 2473–2488. doi:10.1002/wrcr.20075

Ataie-Ashtiani, B., Volker, R. E., and Lockington, D. A. (1999). Tidal effects on sea water intrusion in unconfined aquifers. *J. Hydrol*. 216 (1–2), 17–31. doi:10.1016/S0022-1694(98)00275-3

Boufadel, M. C. (2000). A mechanistic study of nonlinear solute transport in a groundwater-surface water system under steady state and transient hydraulic conditions. *Water Resour. Res*. 36 (9), 2549–2565. doi:10.1029/2000wr900159

Buquet, D., Sirieix, C., Anschutz, P., Malaurent, P., Charbonnier, C., Naessens, F., et al. (2016). Shape of the shallow aquifer at the fresh water–sea water interface on a high-energy sandy beach. *Estuarine. Coast. Shelf Sci*. 179, 79–89. doi:10.1016/j.ecss.2015.08.019

Carsel, R. F., and Parrish, R. S. (1988). Developing joint probability distributions of soil water retention characteristics. *Water Resour. Res*. 24 (5), 755–769. doi:10.1029/WR024i005p00755

Evans, T. B., and Wilson, A. M. (2016). Groundwater transport and the freshwater–saltwater interface below sandy beaches. *J. Hydrol*. 538, 563–573. doi:10.1016/j.jhydrol.2016.04.014

Geng, X., and Boufadel, M. C. (2015). Impacts of evaporation on subsurface flow and salt accumulation in a tidally influenced beach. *Water Resour. Res*. 51 (7), 5547–5565. doi:10.1002/2015WR016886

Geng, X., and Boufadel, M. C. (2017). Spectral responses of gravel beaches to tidal signals. *Sci. Rep*. 7 (1), 40770. doi:10.1038/srep40770

Heiss, J. W., and Michael, H. A. (2014). Saltwater-freshwater mixing dynamics in a sandy beach aquifer over tidal, spring-neap, and seasonal cycles. *Water Resour. Res*. 50 (8), 6747–6766. doi:10.1002/2014WR015574

Hunt, A. G., Skinner, T. E., Ewing, R. P., and Ghanbarian-Alavijeh, B. (2011). Dispersion of solutes in porous media. *Eur. Phys. J. B* 80 (4), 411–432. doi:10.1140/epjb/e2011-10805-y

Kuan, W. K., Jin, G., Xin, P., Robinson, C., Gibbes, B., and Li, L. (2012). Tidal influence on seawater intrusion in unconfined coastal aquifers. *Water Resour. Res*. 48 (2), W02502. doi:10.1029/2011WR010678

Kuan, W. K., Xin, P., Jin, G., Robinson, C. E., Gibbes, B., and Li, L. (2019). Combined effect of tides and varying inland groundwater input on flow and salinity distribution in unconfined coastal aquifers. *Water Resour. Res*. 55 (11), 8864–8880. doi:10.1029/2018WR024492

Levanon, E., Shalev, E., Yechieli, Y., and Gvirtzman, H. (2016). Fluctuations of fresh-saline water interface and of water table induced by sea tides in unconfined aquifers. *Adv. Water Resour* 96, 34–42. doi:10.1016/j.advwatres.2016.06.013

Levanon, E., Yechieli, Y., Gvirtzman, H., and Shalev, E. (2017). Tide-induced fluctuations of salinity and groundwater level in unconfined aquifers – field measurements and numerical model. *J. Hydrol* 551, 665–675. doi:10.1016/j.jhydrol.2016.12.045

Li, L., Barry, D. A., and Pattiaratchi, C. B. (1997). Numerical modelling of tide-induced beach water table fluctuations. *Coast. Eng*. 30 (1–2), 105–123. doi:10.1016/S0378-3839(96)00038-5

Li, L., Barry, D. A., Stagnitti, F., Parlange, J-Y., and Jeng, D-S. (2000). Beach water table fluctuations due to spring–neap tides: moving boundary effects. *Adv. Water Resour*. 23 (8), 817–824. doi:10.1016/S0309-1708(00)00017-8

Michael, H. A., Mulligan, A. E., and Harvey, C. F. (2005). Seasonal oscillations in water exchange between aquifers and the coastal ocean. *Nature* 436 (7054), 1145–1148. doi:10.1038/nature03935

Michael, H. A., Russoniello, C. J., and Byron, L. A. (2013). Global assessment of vulnerability to sea-level rise in topography-limited and recharge-limited coastal groundwater systems. *Water Resour. Res*. 49 (4), 2228–2240. doi:10.1002/wrcr.20213

Pawlowicz, R., Beardsley, B., and Lentz, S. (2002). Classical tidal harmonic analysis including error estimates in MATLAB using T_TIDE. *Comput. Geosci* 28 (8), 929–937. doi:10.1016/S0098-3004(02)00013-4

Ramsay, J. O., and Silverman, B. W. (2005). *Functional data analysis*. New York, NY: Springer.

Robinson, C., Gibbes, B., Carey, H., and Li, L. (2007a). Salt-freshwater dynamics in a subterranean estuary over a spring-neap tidal cycle. *J. Geophys. Res*. 112 (C9), C09007. doi:10.1029/2006JC003888

Robinson, C., Li, L., and Barry, D. A. (2007b). Effect of tidal forcing on a subterranean estuary. *Adv. Water Resour* 30 (4), 851–865. doi:10.1016/j.advwatres.2006.07.006

Robinson, C., Li, L., and Prommer, H. (2007c). Tide-induced recirculation across the aquifer-ocean interface. *Water Resour. Res*. 43 (7), W07428. doi:10.1029/2006WR005679

Robinson, C., Gibbes, B., and Li, L. (2006). Driving mechanisms for groundwater flow and salt transport in a subterranean estuary. *Geophys. Res. Lett*. 33 (3), L03402. doi:10.1029/2005GL025247

Robinson, C. E., Xin, P., Santos, I. R., Charette, M. A., Li, L., and Barry, D. A. (2018). Groundwater dynamics in subterranean estuaries of coastal unconfined aquifers: controls on submarine groundwater discharge and chemical inputs to the ocean. *Adv. Water Resour*. 115, 315–331. doi:10.1016/j.advwatres.2017.10.041

Sawyer, A. H., David, C. H., and Famiglietti, J. S. (2016). Continental patterns of submarine groundwater discharge reveal coastal vulnerabilities. *Science*. 353 (6300), 705–707. doi:10.1126/science.aag1058

Shen, C., Zhang, C., Kong, J., Xin, P., Lu, C., Zhao, Z., et al. (2019). Solute transport influenced by unstable flow in beach aquifers. *Adv. Water Resour* 125, 68–81. doi:10.1016/j.advwatres.2019.01.009

Van Genuchten, M. T. (1980). A closed-form equation for predicting the hydraulic conductivity of unsaturated soils. *Soil Sci. Soc. Am. J.* 44 (5), 892–898. doi:10.2136/sssaj1980.03615995004400050002x

Voss, C. I., and Provost, A. M. (2010). SUTRA, A model for saturated-unsaturated variable-density ground-water flow with solute or energy transport. Available at: http://pubs.er.usgs.gov/publication/wri024231.

Werner, A. D., Bakker, M., Post, V. E. A., Vandenbohede, A., Lu, C., Ataie-Ashtiani, B., et al. (2013). Seawater intrusion processes, investigation and management: recent advances and future challenges. *Adv. Water Resour* 51, 3–26. doi:10.1016/j.advwatres.2012.03.004

Werner, A. D., and Simmons, C. T. (2009). Impact of sea-level rise on sea water intrusion in coastal aquifers. *Ground Water* 47 (2), 197–204. doi:10.1111/j.1745-6584.2008.00535.x

Xin, P., Wang, S. S. J., Robinson, C., Li, L., Wang, Y-G., and Barry, D. A. (2014). Memory of past random wave conditions in submarine groundwater discharge. *Geophys. Res. Lett.* 41 (7), 2401–2410. doi:10.1002/2014GL059617

Yu, X., Xin, P., Lu, C., Robinson, C., Li, L., and Barry, D. A. (2017). Effects of episodic rainfall on a subterranean estuary. *Water Resour. Res.* 53 (7), 5774–5787. doi:10.1002/2017WR020809

Yu, X., Xin, P., and Lu, C. (2019a). Seawater intrusion and retreat in tidally-affected unconfined aquifers: laboratory experiments and numerical simulations. *Adv. Water Resour*. 132, 103393. doi:10.1016/j.advwatres.2019.103393

Yu, X., Xin, P., Wang, S. S. J., Shen, C., and Li, L. (2019b). Effects of multi-constituent tides on a subterranean estuary. *Adv. Water Resour* 124, 53–67. doi:10.1016/j.advwatres.2018.12.006

Conflict of Interest: The authors declare that the research was conducted in the absence of any commercial or financial relationships that could be construed as a potential conflict of interest.

Copyright © 2021 Yu, Xin, Shen and Li. This is an open-access article distributed under the terms of the Creative Commons Attribution License (CC BY). The use, distribution or reproduction in other forums is permitted, provided the original author(s) and the copyright owner(s) are credited and that the original publication in this journal is cited, in accordance with accepted academic practice. No use, distribution or reproduction is permitted which does not comply with these terms.

frontiers in Earth Science

ORIGINAL RESEARCH
published: 09 December 2020
doi: 10.3389/feart.2020.571310

A Multi-Method Approach for Quantification of In- and Exfiltration Rates from the Subterranean Estuary of a High Energy Beach

Nele Grünenbaum[1], Janis Ahrens[2], Melanie Beck[2], Benjamin Silas Gilfedder[3], Janek Greskowiak[1], Michael Kossack[4] and Gudrun Massmann[1,2]*

[1]Institute for Biology and Environmental Sciences (IBU), Carl von Ossietzky University of Oldenburg, Oldenburg, Germany, [2]Institute for Chemistry and Biology of the Marine Environment (ICBM), Carl von Ossietzky University of Oldenburg, Oldenburg, Germany, [3]Limnological Research Station, Bayreuth Center of Ecology and Environmental Research (BAYCEER), University of Bayreuth, Germany, [4]MARUM, Center for Marine Environmental Sciences, University of Bremen, Bremen, Germany

Accurate SGD (submarine groundwater discharge) mass export calculations require detailed knowledge of the spatial and temporal variability in SGD rates. In coastal aquifers, SGD includes a terrestrial freshwater component as well as a saline component originating from circulating seawater. Representative field measurements of SGD rates are difficult to conduct, because SGD is often patchy, diffuse, and temporally variable, especially under tidal influence and high wave activity. In this study, a combination of lysimeters, seepage meters, temperature sensors, pore water radon, and numerical modeling was used to estimate the volumes of infiltrating seawater and exfiltrating groundwater in the intertidal zone of a mesotidal, high energy beach on Spiekeroog Island, northern Germany. Additionally, a 3D-laser scanner was used over short (days) and medium time scales (months) to determine changes in beach topography. The results showed net water infiltration above mean sea level (MSL) and net exfiltration below MSL. Water exchange rates fluctuated between 0.001 and 0.61 m day^{-1}, showing similar ranges within the multiple method approaches. The beach topography was subject to strong fluctuation caused by waves, currents, wind driven erosion and sedimentation, even over short time scales. A comparison of extrapolated in- and exfiltrating water volumes along a beach transect from the mean high water to mean low water line at different times highlights the variability of total in or outflow. The results show that exchange rates depend on beach topography, which in turn changes significantly over time.

Keywords: exchange rates, submarine groundwater discharge, meso-tides, seepage meter, radon, temperature/heat as a tracer

OPEN ACCESS

Edited by:
Isaac R. Santos,
Southern Cross University, Australia

Reviewed by:
Joseph James Tamborski,
Woods Hole Oceanographic Institution, United States
Pei Xin,
Hohai University, China

****Correspondence:***
Nele Grünenbaum
nele.gruenenbaum@uni-oldenburg.de

Specialty section:
This article was submitted to Hydrosphere, a section of the journal Frontiers in Earth Science

Received: *10 June 2020*
Accepted: *11 November 2020*
Published: *09 December 2020*

Citation:
Grünenbaum N, Ahrens J, Beck M, Gilfedder BS, Greskowiak J, Kossack M and Massmann G (2020) A Multi-Method Approach for Quantification of In- and Exfiltration Rates from the Subterranean Estuary of a High Energy Beach. Front. Earth Sci. 8:571310. doi: 10.3389/feart.2020.571310

INTRODUCTION

Over the last decades several studies have suggested that, in addition to riverine inputs, the nutrient fluxes entering the ocean via submarine groundwater discharge (SGD) play an important role for marine ecology and elemental cycles (Johannes, 1980; Swarzenski, 2007; Moore et al., 2008; Kwon et al., 2014; Cho et al., 2018). However, estimates of elemental fluxes to nearshore waters require detailed knowledge of the spatial and temporal variability of SGD rates (Miller and Ullman, 2004;

Urish and McKenna, 2004) and volumes of water circulating through the STE. On local to regional scales the concentrations of nutrients can even be high enough to directly influence near-shore productivity (Burnett et al., 2003) and may cause harmful algal blooms or impact on benthic community structure (Hwang et al., 2005).

In coastal aquifers, the subsurface mixing zone between terrestrial freshwater and circulating seawater was termed subterranean estuary (STE) (Moore, 1999). Under the influence of tides, the STE commonly includes a freshwater discharge tube, an upper saline plume (USP), and a saltwater wedge (Robinson et al., 2006). Seawater infiltrates around the high-water line (HWL), travels through the USP, before exfiltrating as saline to brackish groundwater at the low water line (LWL). Other discharge stems from circulating seawater in the saltwater wedge and terrestrial groundwater from the freshwater discharge tube. Hence, the water either flows in or out across the sea floor, which has been termed as submarine groundwater recharge or SGD, respectively, by Burnett et al., (2003). In general, the total outflow across sea floor often exceeds the total inflow because of additional terrestrial freshwater contributing to SGD. Groundwater in the STE has a wide range of residence times and therefore the chemical composition can also be very variable (Seidel et al., 2015; Beck et al., 2017; Heiss et al., 2017). Additionally, the STE is highly biogeochemically active (Anschutz et al., 2009; Seidel et al., 2015; Waska et al., 2019) with a characteristic redox zonation and salinity distribution (McAllister et al., 2015; Beck et al., 2017; Waska et al., 2019). Fluxes of SGD generally depend on hydro(geo)logical parameters, i.e. beach slope, aquifer depth, hydraulic conductivity, tidal amplitude, or the terrestrial freshwater flux (e.g., Michael et al., 2005; Robinson et al., 2007; Abarca et al., 2013; Greskowiak, 2014; Evans and Wilson, 2016). This makes precise SGD measurements in the field difficult to conduct as SGD predominantly occurs patchy, diffuse, as well as being spatially and temporally variable (Burnett et al., 2006; Röper et al., 2014). Under high energy conditions, conducting field measurements is particularly challenging.

Groundwater in- or outflow to or from the STE has often been measured using seepage meters (e.g., Michael et al., 2003). In its simplest form with an attached plastic bag on top of the chamber, seepage meters are cost-efficient. However, the small chamber diameter limits their spatial coverage and a large number of replicates is necessary to accurately reflect the spatial variability of SGD (Cable et al., 2006). Additionally, tides and waves impede their applicability in highly dynamic coastal ecosystems and require reasonable adaption times in the field (Tirado-Conde et al., 2019).

Pan lysimeters offer another possibility to estimate fluxes during infiltration events. They have been used in non-permanently saturated beach areas by Heiss et al. (2014) in order to determine volumes of infiltrating water during swash events at two sandy beaches at Cape Henlopen (tidal range of 1.4 m). The study demonstrated that lysimeters provide infiltration rates that are comparable to rates estimated based on changes in water content and can additionally be useful to characterize subsurface saturation in sandy beach aquifers.

Another method to calculate exchange rates is dissolved radon-222 (^{222}Rn), a chemically inert noble gas, as a natural tracer for pore water residence times. ^{222}Rn activities in seawater are often close to instrument detection limits. This is due to seawater being naturally low in the parent isotope radium-226 (^{226}Ra; half-life of 1,602 years), which is produced by particle-associated thorium. In addition ^{222}Rn is also lost to the atmosphere, driven by molecular diffusion and wind driven turbulent exchange (Burnett and Dulaiova 2003). In contrast, sediments are enriched in ^{226}Ra, which decays to ^{222}Rn (Swarzenski, 2007). As a consequence, pore waters are enriched in ^{222}Rn compared to seawater. Assuming a homogeneous distribution of ^{226}Ra in the sediment and a closed-system (i.e., no degassing), the ingrowth of ^{222}Rn as a function of time can be calculated up until steady state between production and decay. This can be used to calculate pore water residence times (Colbert et al., 2008; Tamborski et al., 2017; Gilfedder et al., 2018). By determining the increase of residence time with depth and assuming 1D vertical flow it is possible to estimate seawater infiltration rates.

Temperature as a tracer for quantifying water fluxes between ground- and surface water has frequently been used in terrestrial systems. This is due to temperature loggers being increasingly affordable, having a high sensitivity and small size, all stemming from technological advances in the microelectronics (Anderson, 2005). This has allowed deployment of vertical temperature sensors in stream and lake beds (Constantz, 2008; Blume et al., 2013), with measurements being used to either map the spatial distribution of water fluxes (Schmidt et al., 2006) or to capture the temporal dynamics of fluxes in response to external forcing such as precipitation (Rau et al., 2014). The application of temperature for qualitative mapping of groundwater discharge zones is common (e.g., Röper et al., 2014). However, despite its relatively simple application and ability to quantify both infiltration and exfiltration rates, temperature has seldom been quantitatively used in SGD studies. Some exceptions include Taniguchi et al. (2003), who used a steady state and transient approach to quantify water fluxes in the Cockburn Sound (Australia) and Befus et al. (2013), who applied temperature profiles to assist in calibrating a 2D model of the intertidal zone of a tropical Island.

Most of the methods described above were predominantly used at low-energy environments (e.g., Michael et al., 2003; Santos et al., 2012; Heiss et al., 2014). To date, they have rarely been applied in highly dynamic environments, such as high energy beach systems (e.g., Goodridge and Melack, 2014), where mixing of water from different origins and ages is large. Previous studies predominantly focused on one or two independent methods to estimate SGD, whereas Giblin and Gaines (1990), Mulligan and Charette (2006), or Burnett et al. (2006) used a multiple method approach in order to compare methods and respective SGD rates. Results showed that method-dependent differences between rates occur, which is why the simultaneous use of different techniques is recommended. This applies especially at high energy beaches, where spatial and temporal heterogeneity is assumed to be high due to the strong interplay of wind, waves, and tides.

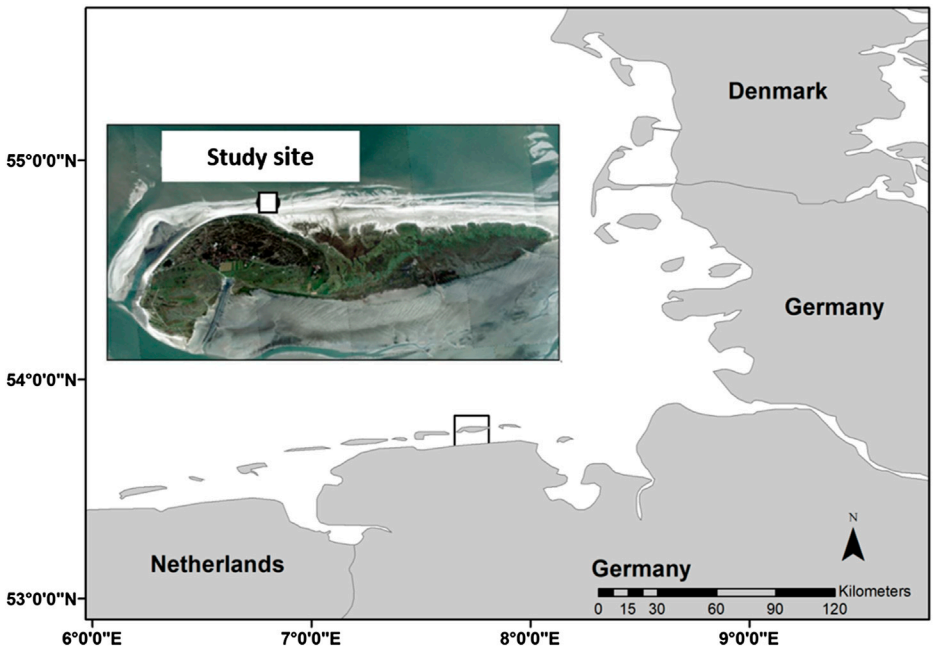


FIGURE 1 | Location of the field site. The aerial picture was provided by the NLPV (2011).

In the presented study, our aim was 1) to apply a suite of field methods to determine the in- and exfiltration rates in the intertidal zone of a high energy beach (Spiekeroog Island, Germany) across all seasons and 2) to compare field results with flux rates obtained from an existing flow and transport model. We tested 3) the applicability and limitations of different methods under transient, highly dynamic conditions and used topographical information of a 3D laser scanning 4) to investigate the spatial dependency of the rates on morphodynamic conditions.

METHODOLOGY

Study Site

The study site is located in the intertidal zone at the northern beach of Spiekeroog, a barrier island with a size of ~21 km^2 in front of the North German coastline (**Figure 1**). Spiekeroog predominantly comprises fine- to medium grained Holocene sands above Pleistocene deposits (Streif, 1990). In the absence of considerable surface runoff, precipitation surplus can infiltrate almost completely into the permeable dune sediments with an estimated recharge rate of 350 mm a^{-1} (Röper et al., 2012). Density differences between fresh and saline groundwater enabled the formation of a freshwater lens overlying seawater in the subsurface, which is limited by a confining clay layer at a depth of approximately 40 m below sea level (Röper et al., 2012) and used for the islands drinking water supply. Groundwater ages in the lens increase vertically up to 50 years (Seibert et al., 2018).

Previous studies observed exfiltrating brackish water containing freshwater from the lens in the intertidal zone at the northern beach of Spiekeroog where the beach is exposed toward the open North Sea and affected by semidiurnal tides with an amplitude of 2.7 m (mesotidal) (Beck et al., 2017; Reckhardt et al., 2017; Waska et al., 2019).

The beach morphology is predominantly characterized by sandbanks and troughs, which generally exist during all seasons (Flemming and Davis, 1994; Beck et al., 2017), but change their position and extension over the year (Waska et al., 2019). In the following, these morphodynamical characteristics are referred to as runnel and ridge structures, even though the original criteria by King and Williams (1949) are not completely fulfilled with respect to macrotidal conditions. The uppermost ridge is temporarily inundated (high tide) or exposed (low tide). Shallow porewater data and numerical simulations for the study site suggested the typical hydrological zonation of a tidally influenced STE (Beck et al., 2017; Reckhardt et al., 2017). Initial modeling approaches suggested that freshwater discharge occurs exclusively into the runnel (Beck et al., 2017). However, further extensive hydrochemical investigations from Waska et al. (2019) as well as apparent ^{3}H-^{3}He ages from Grünenbaum et al. (2020) indicated additional freshwater discharge at the LWL. Beck et al. (2017), Waska et al. (2019), and Grünenbaum et al. (2020) presumed the ridge to function as a groundwater divide during unsaturated conditions (low tide). Recent numerical simulations based on measured salinities and ^{3}H-^{3}He data from Grünenbaum et al. (2020) showed that the strength of the groundwater divide can regulate the groundwater flow in the STE leading to the formation of either a single freshwater exfiltration zone in the runnel (referred to as the "one-plume system") or two freshwater

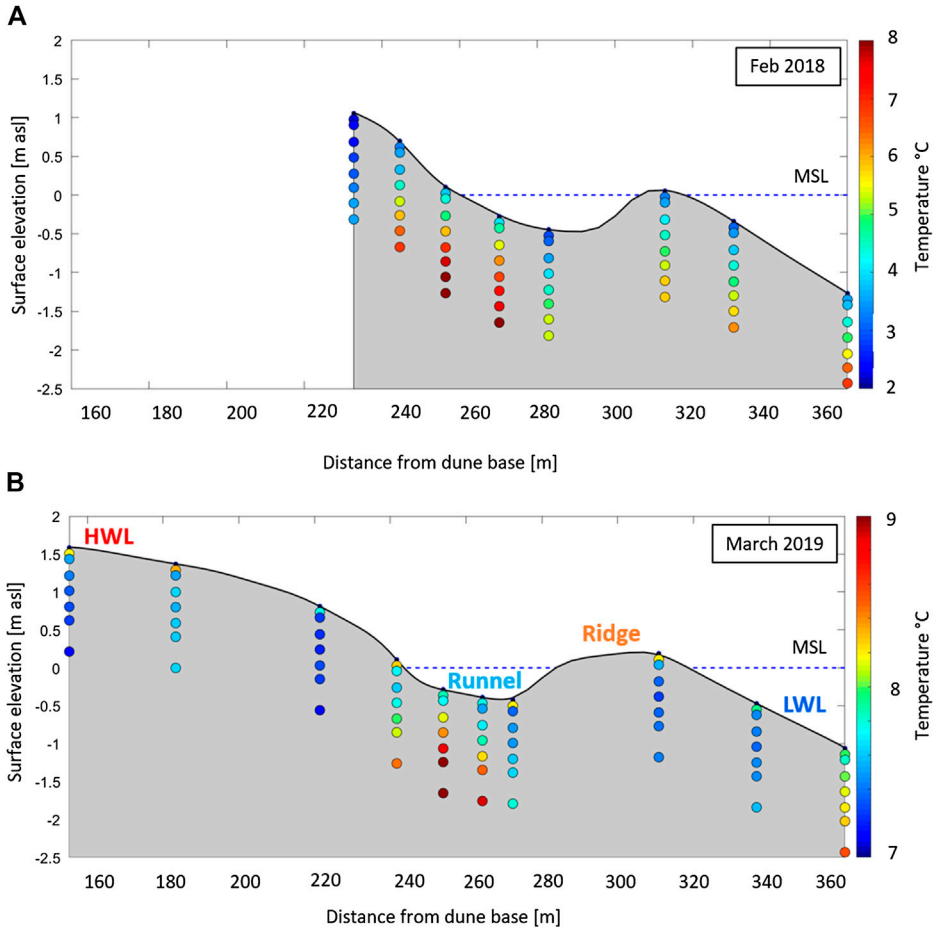


FIGURE 2 | Measured temperature profiles for **(A)** February 2018 and **(B)** March 2019. Exfiltrating conditions are assumed to occur, where porewater's temperatures are higher in ~2 m depth compared to the top and decreases toward the surface. Infiltration conditions are assumed to occur, where temperature sensors show almost continuous temperature of seawater from top to 2 m depth.

exfiltration zones at both runnel and LWL ("two-plume system"). The topography of such a high energy beach is subject to strong changes depending on erosion and sedimentation processes, especially during the storm flood season in winter (Dobrynin et al., 2010). Grünenbaum et al. (2020) concluded that changes between a one- and two-plume system over time, as well as overlapping conditions at the study site as a function of beach topography, are likely.

According to the findings of Beck et al. (2017) and Waska et al. (2019), the intertidal zone of Spiekeroog can be separated into 4 zones, with either infiltrating (HWL, Ridge) or exfiltrating (Runnel, LWL) conditions (see **Figure 2B**).

Quantifying In- and Exfiltration Rates

Different techniques were used to determine the volumes of in- and exfiltrating water. In general, seepage meters and/or lysimeters were installed during spring tide, while ^{222}Rn and temperature were measured simultaneously or within the ensuing week to ensure the mean LWL during low tide could be reached. To compare estimates of different methods, all measurements were reported in Darcy-velocities [m day^{-1}]. Assumptions made for up-scaling are described below for each method.

Handheld Lysimeter Construction and Sampling

Infiltration was measured using a modified pan lysimeter based on the work of Jordan (1968) and Heiss et al. (2014) above the permanently saturated beach areas within the intertidal zone up to the mean spring tide mark.The lysimeters were constructed using a PE-cylinder (Ø 110 mm, height: 500 mm), whose bottom closed conically toward a tube connection (FEP-tube 4 mm × 6 mm, **Supplementary Figure S1A**). This allowed a complete drainage of the buried lysimeters. The upper part of the cylinder was closed with a porous filter plate (PE, 200 μm, thickness = 5 mm), which was protected by a filter sleeve. The remaining space was filled up with sediment from the site (predominantly fine sand). Previous lab experiments by Heiss et al. (2014) revealed that this approach limits the preferential flow into the lysimeter. A second tube connection (4 mm × 6 mm) was attached directly below the porous plate to ensure atmospheric pressure inside the device in order to enable water infiltration.

In October 2016, March 2017, and August 2017, six lysimeters were buried in the unsaturated beach around the HWL at a depth of approximately 20 cm. To limit disturbance of the system, a hole was dug down to the groundwater level and the lysimeters were inserted horizontally into the undisturbed sediment, thereby maintaining an undisturbed sediment cover (**Supplementary Figure S1B**). Sediment gaps were carefully filled with sand before the hole was completely refilled. The lysimeters were left in the sand for 1 day (24 h) to adapt before they were regularly emptied after one tidal cycle using a peristaltic pump (Peristaltic Pump VDC 12 Standard, Eijkelkamp Soil & Water) connected to the tubing system. In order to prevent surface water from entering the drainage or venting tube during high water, both tubes were equipped with wooden swimmers and fixed on a wooden beam. Shallow piezometers (high-density polyethylene, Ø 63/51.4 mm) equipped with pressure loggers were installed close to the lysimeters in order to continuously measure the groundwater level. This way, misinterpretation as a result of unintentional inflow of groundwater into the lysimeters was prevented. Sand accumulations inside the piezometers were impeded by the usage of short filter screens (Ø 63/51.4 mm × 500 mm) with a slot width of 0.3 mm surrounded by a filter sleeve. The lysimeters provided volumes in m^3 per tidal cycle per m^2 beach, which were doubled (semidiurnal tides) to determine a rate in m per day.

Seepage Meter Construction and Sampling

Seepage meters were constructed from PE-cylinders (150 mm height, Ø 670 mm) after Lee (1977) and were unilaterally closed with an unlockable tube port on top (12 mm, **Supplementary Figure S2A**). In October 2016 and August 2017, four seepage meters were carefully placed slightly inclined into the saturated sediment from the LWL to the HWL (protruding ~5 cm from the sediment surface) (**Supplementary Figure S2B**). The locations of seepage meters were varied several times along the transect to reflect the entire intertidal zone. The port was left open for adapting to the environment for at least 30 min. Subsequently, a 3 L PE bag was attached to the outlet for a minimum of 30 min (up to several hours) without changing. Longer adaption or collecting times were not possible for the study site, because strong wave movement threatened to displace the seepage meters. Note that due to the short adaption times we suppose that the water collected in the bags was not pure SGD but seawater which was displaced by discharging groundwater. This means that further geochemical water analysis (e.g., for salinity) would not have been meaningful. Hence, we could not distinguish between fresh and saline SGD in the field using seepage meters. The bags were filled with 500 ml of seawater to impede underestimation of fluxes as mentioned in Shaw and Prepas (1989) and to enable infiltration from the seepage meter into the sediment (Michael et al., 2003). Volume loss or gain was determined after the respective sampling time for each seepage meter. Seepage meters only provided point measurements over a certain period of time and no information about the temporal development of the rates during a tidal cycle as they could not remain in the sediment for long. Additionally, it was not possible to recover them during high tide as they were submerged by ~3 m water depth. To upscale to daily infiltration rates the measured rates (m^3 per m^2 per hour) were assumed to be representative for the time period when the respective beach location was inundated. The inundation time for each sampling point was determined from surface water level and respective surface elevation. In order to calculate exfiltration rates, point measurements were assumed to be representative for the entire tidal cycle, regardless of rising or falling water levels. Measured rates were then extrapolated for 1 day.

Analysis of ^{222}Rn in Pore Water

To analyze ^{222}Rn, multiple discrete 1.5 L pore water samples were extracted in a range of 0.5–2.0 m depth below the surface during five field campaigns in March, May, August and September 2017 as well as in February 2018. Per campaign two to three pore water profiles were sampled. Each profile consisted of at least two and up to 4 samples (**Supplementary Figure S3**). The sampling sites covered the entire intertidal zone, but only samples taken in infiltration zones are discussed in this study. In exfiltration zones, where the groundwater discharging is relatively old, ^{222}Rn cannot be applied as tracer due to its short half-life of 3.8 days and mixing of water masses of different origin. Fresh groundwater deriving from the freshwater lens is assumed to be in equilibrium with surrounding sediments or may deliver even higher loads of ^{222}Rn released by lithologies other than beach sand. Samples were assumed to be a mixture of seawater and freshwater, when the salinity deviated by > 10% from seawater salinity and were subsequently excluded from rate calculations. Porewater was extracted using stainless steel push point samplers and a peristaltic pump (Peristaltic Pump VDC 12 Standard, Eijkelkamp Soil & Water) at low flow rates (<0.5 L/min) to avoid degassing. The polyethylene terephthalate (PET) sample bottle was purged by about one bottle volume and filled without headspace.

^{222}Rn activities were measured in a closed air-loop setup, using a radon-in-air monitor (RAD 7 Radon Monitor, Durridge Company, Inc.; **Supplementary Figure S4**). Prior to measurement, about 7 ml of the sample were carefully discarded to create a headspace. Air was bubbled through the water sample using the internal pump of RAD7 and the stripped ^{222}Rn was transferred in a closed air loop to the detection chamber. From March to September 2017, an active moisture exchanger was implemented in-line with the drying column. In February 2018, the air-loop setup was used without an active moisture exchanger. Counts were integrated from 5 to 8 cycles with each 10–15 min counting time. To convert RAD7 counts into radon-in-water concentrations air loop ^{222}Rn-concentrations were multiplied by a conversion coefficient. This coefficient takes into account sample and air-loop volumes as well as temperature and salinity. The samples were corrected individually for the decay, which occurred between sampling and analysis. Yet, all samples were measured within 24 h after sampling.

Infiltration rates were deduced from the depth distribution of pore water residence times assuming 1D-vertical flow with the latter derived from measured ^{222}Rn activities. Under the assumption that the half-life of the parent isotope ^{226}Ra is

much longer (1,602 years) than of ^{222}Rn (3.8 days), the Bateman Equation (Bateman, 1910) can be simplified to describe the ingrowth of ^{222}Rn in a closed system:

$$^{222}Rn = {}^{222}_{eq}Rn\left(1 - e^{-\lambda_{222Rn}\tau}\right) \quad (1)$$

Here the pore water ^{222}Rn activity is a function of the equilibrium activity ${}^{222}_{eq}Rn$, the specific decay constant $\lambda_{222Rn} = 0.1813\,[d^{-1}]$ and the residence time τ.

Rearranged, the residence time can be calculated:

$$\tau = \frac{1}{\lambda_{222Rn}} ln\left(1 - \frac{^{222}Rn}{^{222}_{eq}Rn}\right) \quad (2)$$

In this study, ${}^{222}_{eq}Rn$ was defined by the activity of a groundwater sample, that was retrieved from 2 m below surface in the runnel exfiltration zone in September 2018 (**Supplementary Figure S3**). According to modeling results from Beck et al. (2017) and Grünenbaum et al. (2020), pore water residence times at this location ranged between several months up to years and are, thus, sufficiently long to approximate ${}^{222}_{eq}Rn$.

According to Tamborski et al. (2017), residence time calculations have reasonable uncertainties when residence times are longer than 0.5 days, but shorter than 7 days. The lower limit is based on radon detectability and background activities such as the seawater radon end-member, whereas the upper limit results from the asymptotical approach of ${}^{222}_{eq}Rn$ during ^{222}Rn ingrowth.

Assuming the uniform distribution of the parent isotope ^{226}Ra in the sediment and steady-state pore water velocities at seawater infiltration sites, the slope of the linear regression function of the ^{222}Rn residence time vs. depth represents the fluid velocity, which was multiplied by the effective porosity ($n_e = 0.3$) to obtain the Darcy flux.

Temperature Sensors

The quantitative use of temperature is based on solving the advection-conduction-dispersion equation for heat transport in porous media and relies on solutions (depending on boundary conditions) to the partial differential equation for heat transport (Anderson, 2005).

This can be written as (Anderson, 2005; Schmidt et al., 2006):

$$\frac{k_e}{\rho c}\nabla^2 T - \frac{\rho_w c_w}{\rho c}\nabla \cdot (T q_z) = \frac{\partial T}{\partial t} \quad (3)$$

Where T is temperature (°C), t is time (s), ρc is the volumetric heat capacity of the fluid-solid system (J m^{-3} K^{-1}) and is often written as $\rho c = n\rho_w c_w + (1 - n)\,\rho_s c_s$ with $\rho_w c_w$ (J m^{-3} K^{-1}) being the volumetric heat capacity of the liquid phase and $\rho_s c_s$ (J m^{-3} K^{-1}) the volumetric heat capacity of the solid phase, q_z (m s^{-1}) is the Darcy seepage velocity, while k_e (J s^{-1} m^{-1} K^{-1}) is the effective thermal conductivity of the saturated sediment with no advective flow.

This equation can be solved analytically or numerically for 1D heat transport assuming 1D vertical flow for either steady state or non-steady state boundary conditions (Lapham, 1989; Rau et al., 2014; Munz and Schmidt, 2017). For steady state 1D heat transport and Dirichlet-Type boundary conditions at the upper and lower ends, the solution of **Eq. 3** can be written as (Bredehoeft and Papaopulos, 1965):

$$T(z) = \frac{\exp\left(z\frac{q_z \rho_w c_w}{k_e}\right) - 1}{\exp\left(L\frac{q_z \rho_w c_w}{k_e}\right) - 1} \times (T_L - T_0) + T_0 \quad (4)$$

L is the depth (m) of the lower boundary condition (m), while T_L is the temperature (°C) at depth L and is usually assumed to be the regional groundwater temperature, T_0 is the temperature (°C) of the upper boundary condition, usually the surface water temperature or, as in our case, just below the sediment-water interface. As the name implies this solution assumes that there is no temporal change in either boundary condition or the groundwater flux and that sediment properties are constant and uniform in time and space.

Typically, the steady state model is fitted to a measured temperature profile by minimizing the root mean square error by varying the Darcy velocity, assuming all other parameters are known. Negative Darcy velocities indicate groundwater exfiltration while positive values are infiltration of seawater into the subsurface.

The BT-lances were made of pointed stainless steel tubing with a diameter of 1 cm and equipped with eight high sensitivity thermistors (5 kΩ NTC thermistor, 0.2% from Reichelt GMBH) (**Supplementary Figure S5**). The thermistors were attached to a stainless steel rod at intervals of 0.08, 0.15, 0.37, 0.57, 0.78, 0.96, 1.16, and 1.37 m that was inserted into the stainless steel housing. The free space was back-filled with fine quartz sand with a similar grain size to the field site. This was an attempt to replicate the thermal characteristics of the beach and to avoid convection that can occur within an air-filled or water-filled tube. Each sensor was attached to a circuit board that measured the resistance of the thermistors. Resistivity was converted to a digital value using an 18 bit ADC and stored to flash memory. Resistivity was converted to temperature values using the function supplied with the thermistors. The electronic setup was based on Arduino architecture and was developed as part of our push towards low-cost high-resolution measurement devices for environmental applications. Tests in the laboratory have shown that each sensor has a resolution of ~0.003°C, and the difference between sensors was around 0.007°C. The high resolution can be attributed to the high-resolution ADC and high quality thermistors.

Temperature profiles were measured from the LWL towards the HWL in February 2018 and March 2019. We did not extend the temperature mapping to the HWL to avoid complications due to heat transport in the unsaturated sands. The temperature lance was driven into the sediment and then left to equilibrate (for ~10 min). In total nine temperature profiles were made along the transect. The steady state model was fitted to each profile by varying the Darcy flux to minimize the Root-mean-square error (RMSE) between the model and the measurements as in Schmidt et al. (2006), see **Supplementary Figure S6**. The thermal parameters were largely taken from Rau et al. (2012), who conducted detailed heat transport experiments on saturated clean quartz sand in the laboratory. The thermal conductivity and volumetric heat capacity

of saturated sand were 3.8 J s^{-1} m^{-1} K^{-1} and 3.23 × 10^6 J m^{-3} K^{-1} respectively. Despite groundwater temperatures never being truly stationary, especially in small island aquifers, we have defined the lower boundary as the depth at which the yearly amplitude in temperature variations is less than 1°C. Based on an evaluation of nested bores located about 3 km to the east of the site (Holt et al., 2019) we set the lower boundary condition as the mean yearly temperature from bore DN-d at a value of 10.6 °C from a depth of 6.4 m. The standard deviation (1σ) in temperatures at this depth was 0.3°C.

Numerical Model

Grünenbaum et al. (2020) developed a two-dimensional cross-sectional model of the study site (from dune base 700 m toward the sea) in order to estimate the groundwater flow, residence times, and salinity distribution at the site, thereby using a time-averaged topography (**Supplementary Figure S7**). Several model cases were set up with the density-dependent groundwater flow model SEAWAT, in order to display the model's sensitivity against changes in model parameters such as dispersivity, hydraulic conductivity, and the groundwater flux from the island's freshwater lens. The existence and extension of a groundwater divide below the ridge was considered in the tide-averaged head calculation in different scenarios. The analysis of the water budget of one selected model provided approximated fluxes through the STE per day along 1 m of shoreline. The model chosen was considered the most realistic one based on shallow salinity measurements, the conceptual model proposed by Waska et al. (2019), and hydraulic parameters by Beck et al. (2017). Note that the influence of waves was not considered in the presented modeling approach. Further model assumptions were the use of tide average heads neglecting storm flood events or spring/neap tides, the estimation of fresh groundwater flux, as well as the uncertainty of the calibration parameters. SGD fluxes can be assumed to be between 0.5 to 2 times the provided rates as also stated in Beck et al. (2017). This estimation is based on findings from Xin et al. (2010), who compared tide-resolved modeling approaches without and with wave setup. The latter resulted in an increase of 33% in the total SGD rates plus a doubled saline SGD rate through the USP.

Morphodynamic Changes and Upscaling

The change in beach topography was measured with a 3D Laser scanner (FARO Focus 3D X 130) in several campaigns (March 2017, May 2017, August 2017, and February 2018). A point distance of 3.068 mm per 10 m was used, recommended for outdoor scans with a distance between the scanner and the object of interest greater than 20 m. In total, eight scans per sampling campaign were conducted and combined, in order to completely cover the study site (200 m × 200 m). Post-processing was done with the FARO software Scene 5.4. The accuracy was strongly dependent on environmental conditions during scanning in the field, but was always under 10 cm.

The measured and modeled in- and exfiltration rates (Darcy-velocities obtained with the various methods) were correlated to the respective topographic heights. Using the areal topography from the 3D laser scans, these rates were transformed to volumetric fluxes for the whole study area. The scanning results were subsequently assigned to the respective in- or exfiltration zone (HWL, Runnel, Ridge, LWL) for the individual campaigns based on relative position in the intertidal zone (**Figure 5**; **Supplementary Figure 8**) and findings from **Figure 3**. The resulting volumetric in- and exfiltration rates between mean HWL (1.37 m **A**bove **S**ea **L**evel) and mean LWL (−1.37 m ASL) were normalized to 1 m shoreline.

RESULTS AND DISCUSSION

Spatial Variability of Exchange Rates

Temperature profiles can be used to qualitatively identify in- or exfiltration zones. As sampling was done in winter, warmer water near the surface should indicate discharge areas. Such upwelling of warm groundwater was observed in the runnel and at the LWL. In contrast, very low SGD rates or infiltrating conditions are indicated by little increase of temperature with depth. This was observed at the ridge and at the HWL (**Figure 2**). These effects were particularly pronounced in February 2018 due to the higher temperature difference between ground and surface water compared to March 2019. Hence, the temperature profiles allow to rapidly screen a field site for potential SGD areas and relate this to the site morphology in a runnel-ridge system (**Figure 2B**).

Groundwater exchange rates were estimated based on seepage meters, lysimeters, ^{222}Rn measurements, and heat modeling of the temperature sensors (**Supplementary Table S1**). Note that the subsequent discussion of measured exchange rates is limited to their spatial variability at the beach as the techniques were used over different seasons, under varying environmental conditions, at various locations, and not all simultaneously. As such the present data, though extensive, is not sufficient to clearly attribute exchange rates to factors of influence such as seasonality reflected by tidal variation or a change in the terrestrial groundwater flow.

Infiltration rates at the site were found to span over two orders of magnitude and ranged between 0.001 and 0.61 m day^{-1}. Measured exfiltration rates were mostly lower and were also less variable, fluctuating between −0.007 and −0.13 m day^{-1}. Similar SGD rates were determined, for example, at Waquoit Bay (~0.05–0.3 m day^{-1}) based on radon and radium time series in bay waters and seepage meters measurements from 2002 to 2003 (Mulligan and Charette, 2006).

The water exchange rates plotted vs. surface elevation using all methods and measurements showed that net infiltration predominantly occurred above MSL, while net exfiltration prevailed below MSL (**Figure 3**). The high fluctuations of infiltration rates in temporally unsaturated beach areas (≥1 m ASL) were likely caused by a spatial variability in the position of the HWL. Thereby, smaller infiltration rates might be attributed to single swash events instead of constant infiltration of seawater over a certain period. In contrast to the partly unsaturated HWL zone, infiltration rates in saturated beach areas (~<1 m ASL) were mostly lower (≤0.1 m day^{-1}).

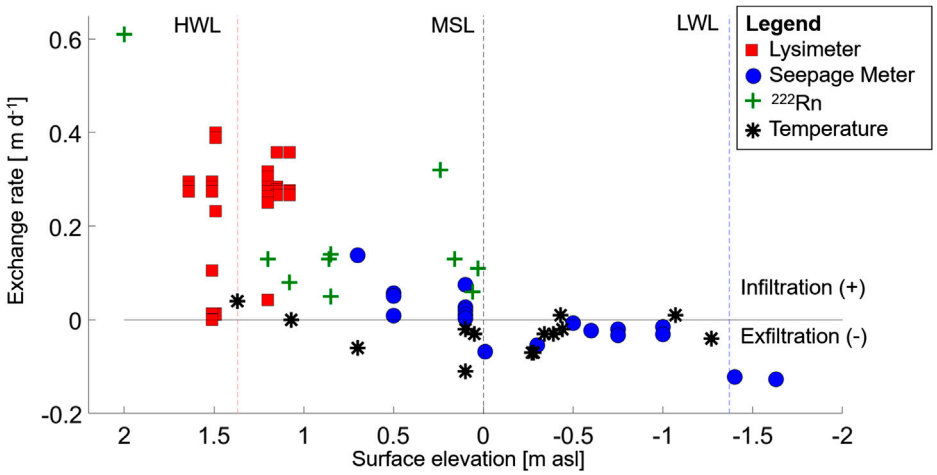


FIGURE 3 | Measured exchange rates plotted vs. surface elevation. Positive rates indicate infiltration and negative rates exfiltration. The different techniques are illustrated with red squares (lysimeters), blue circles (seepage meters), green crosses (^{222}Rn), and black stars (temperature sensors). Mean HWL (red), MSL (black), and mean LWL (blue) are shown as dashed lines.

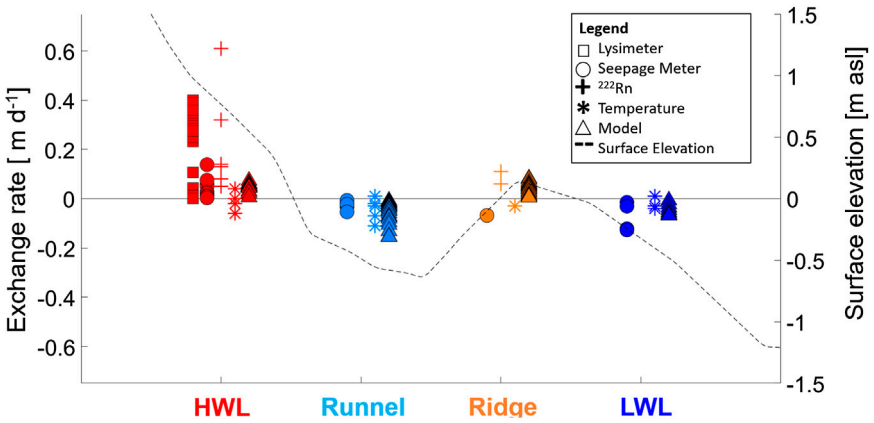


FIGURE 4 | Comparison of all measured exchange rates across respective in- or exfiltration zones (HWL = red, Runnel = light blue, Ridge = orange, LWL = blue). The different methods are indicated with squares (lysimeters), circles (seepage meters), crosses (^{222}Rn), and stars (temperature sensors). Model results are also included (triangles). The exemplary surface elevation from October 2016 is added to visualize the principal zone distribution along the cross-section.

Figure 4 shows how the rates varied along the cross-section visualizing the different in- and exfiltration zones (HWL, Runnel, Ridge, LWL, compare **Figure 2A**). Infiltration rates at the HWL were found to fluctuate the most, i.e., covering rates from 0.001 to 0.61 m day^{-1}, while infiltration rates at the ridge were mostly lower and varied between 0.03 and 0.11 m day^{-1}. Predominately exfiltrating conditions were encountered in the runnel and at the LWL spanning rates between −0.007 and −0.06 m day^{-1} (runnel) and −0.02 and −0.13 m day^{-1} (LWL). Compared to measured exchange rates, numerical modeling by Grünenbaum et al. (2020) displayed the same spatial distribution of in- and exfiltration zones, but infiltration rates at the HWL were generally lower (~0.1 m day^{-1}). Note that only one model run with averaged beach topography was used for flux calculation.

In order to visualize the topography changes and the spatial distribution of in- and exfiltration zones, representative selected LIDAR scan results of two seasons (August 2017 and February 2018) are shown in **Figure 5**. Whereas the runnel-ridge system was always present, the location and extension of both runnel and ridge differed significantly for the two seasons. In August 2017, two separate ridges existed, a long-shore ridge and a ridge-like feature striking in 45° from the HWL towards the LWL. Conversely, the beach topography in February 2018 showed a typical long-shore runnel-ridge sequence from the HWL towards the sea. Corresponding exchange rates plotted into the scans mostly showed infiltrating conditions at the HWL and the ridge and exfiltrating conditions at the LWL and the runnel. Deviations were occasionally observed, e.g., in February 2018 at the LWL and in the HWL zone. Based on the temperature distribution in **Figure 2**, it appears that the fact that exfiltration rates were calculated above MSL from temperature data is possibly the result

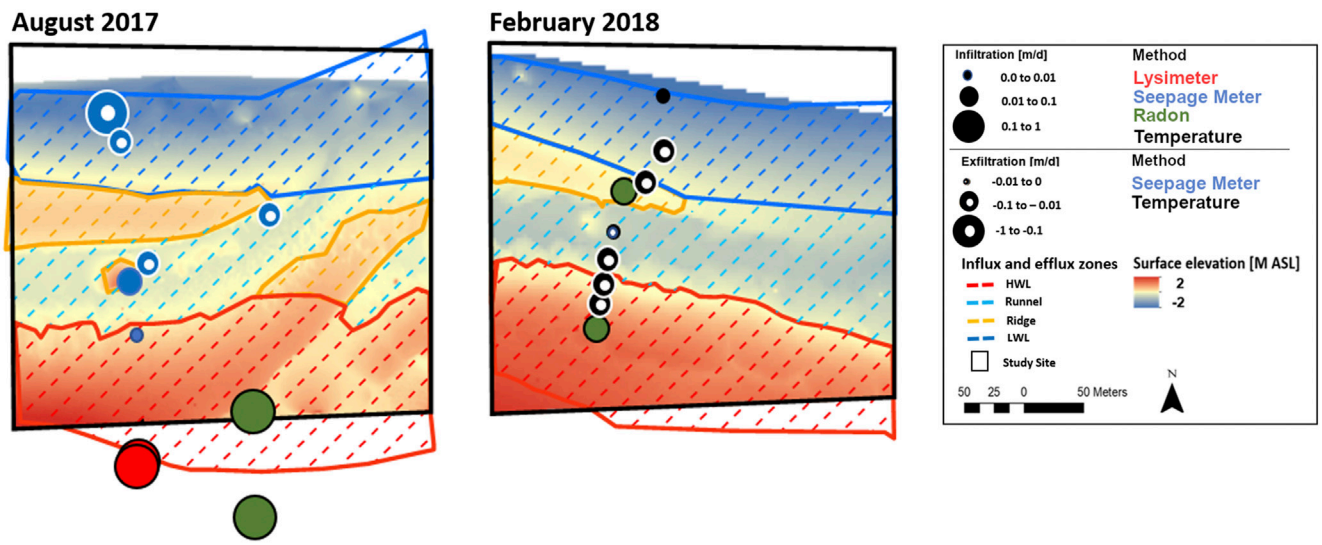


FIGURE 5 | Determination of beach topography (~200 m × ~200 m, black box) for August 2017 and February 2018 including both location and extent of measured exchange rates. Infiltration rates based on lysimeters measurements (red circles) were displayed as mean value from all measurements for respective sampling campaign at same location. Dashed polygons indicate topography-based classification of in- and exfiltration zones (HWL, Runnel, Ridge, LWL) for the study site based on results from **Figure 3** suggesting net infiltration above MSL and net exfiltration below MSL. Zones for HWL and LWL were linearly extended or reduced beyond the boundaries of the study site (black box) to cover the entire area between mean high water (+1.37 m ASL) and mean low water (–1.37 m ASL). Infiltration rates outside the black box were partially measured due to a shift in HWL during sampling.

of the assumption of 1D flow, while in reality it is 2-(or 3) dimensional.

In order to extrapolate the point measurements to the entire study area mapped by the scans, the respective zones (HWL, Runnel, Ridge, LWL) were allocated in all topography scans (**Figure 5**, **Supplementary Figure S8**). This was done based on results from **Figure 3** suggesting net infiltration above MSL and net exfiltration below MSL. Zones for HWL and LWL were linearly extended or reduced to cover the entire area between mean high water (+1.37 m ASL) and mean low water (–1.37 m ASL).

Spatial Extrapolation of Exchange Rates

Figure 6A shows the areal size in m^2 normalized to 1 m shoreline of the respective in- and exfiltration zones based on all scan results (**Supplementary Figure 8**), in the following referred to as "zone length" in m.

Whereas the zone length of HWL and LWL varied between ~30 and ~70 m, and ~50 and ~95 m respectively, the size of the runnel and ridge zones fluctuated between 35 and 50 m, and 15 and 40 m, respectively (**Figure 6A**).

Subsequently, the areal size was multiplied with all the rates measured (**Figure 6B**) to get an idea on the volumes of in- and exfiltrating water along 1 m of shoreline for each in- or exfiltration zone. Note that the number of measurements is significantly different for each zone.

Figure 7 shows that the variation of water volumes circulating through the intertidal zone was relatively high. Especially at the HWL, the total infiltration fluxes ranged between almost zero and 35 m^3 per day and m shoreline. Most of the rates were measured at the HWL, i.e., not equally distributed over the entire infiltration zone. Single point measurements below the HWL suggested the infiltration rates to decrease toward topographical lower laying beach areas (**Figure 3**). Thus, it is possible that the extrapolation of point measurements to the entire zone leads to an overestimation of inflow. The total infiltration into the ridge is indicated to be generally lower compared to the HWL, with a total infiltration of maximum 20 m^3 per day and m shoreline. Total exfiltration within the intertidal zone consists of up to −1.9 m^3 per day and m shoreline into the runnel and −13 m^3 per day and m shoreline at the LWL.

These results suggest that total infiltration (~12 m^3 per day and m shoreline) exceeds total exfiltration (~4.5 m^3 per day and m shoreline). This is the case for both field measurements and the numerical simulation (In: 6 m^3 per day and m shoreline/Out: −5.5 m^3 per day and m shoreline), with modeling limited to the intertidal zone. During field work, the terrestrial groundwater flux was not determined as an inflow component. If it is considered as an additional inflow proportion of approximately 0.75 m^3 per day and m shoreline (Beck et al., 2017) as partially done in the simulations from Grünenbaum et al. (2020), the discrepancy between total in- and outflow is even larger. One explanation could be possible overestimation of total infiltration in the infiltration zone around the HWL, as discussed above. Another reason for the difference could be that the subtidal area below the LWL was neither investigated by flux measurements in the field nor considered within areal extrapolation, while model results suggest that a proportion of the water discharges below the LWL (Grünenbaum et al., 2020).

To assess the relevance of SGD on a larger scale, water fluxes determined at the northern beach of Spiekeroog were assumed to

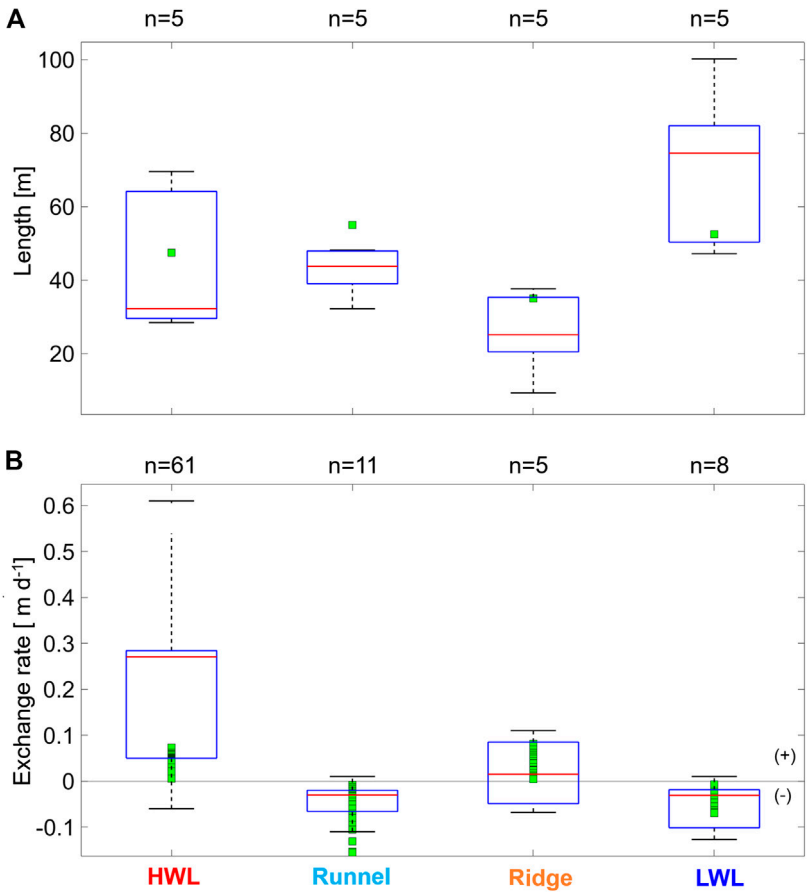


FIGURE 6 | (A) Areal variation of respective in- and exfiltration zone (HWL, Runnel, Ridge, LWL) in the intertidal zone normalized to 1 m shoreline for sampling campaigns March (1) 2017, March (2) 2017, May 2017, August 2017, and February 2018 based on **Supplementary Figure S8**. Green squares indicate model results. **(B)** Variation of measured exchange rates within respective in- and exfiltration zone (HWL, Runnel, Ridge, LWL) in the intertidal zone. Positive rates indicate infiltration, negative rates exfiltration, respectively. Green squares indicate model results. Black dots are values that are more than 1.5 times the interquartile range away from the top or bottom of the box. Red line indicates median of boxplot. Number of statistics (*n*) is given above.

be representative for the beaches of all barrier islands, which are facing the open North Sea and are connected to a freshwater lens. Measured rates were extrapolated to the entire East Frisian barrier island chain from Borkum to Wangerooge (~56 km) based on previous estimations from Beck et al. (2017). In comparison to medium runoff from the rivers Weser, Elbe and Ems into the German Bight, which is about 1,200 m^3 per second (Becker et al., 1999), the SGD proportion (fresh and salty) from the East Frisian barrier island chain is up to 0.8% of the riverine discharge. The median SGD proportion is even lower (0.2%) and matches water budget calculations (0.3%) based on the numerical simulation from Grünenbaum et al. (2020).

Method Applicability and Limitations at a High Energy Beach

In general, the exchange rates measured by the different techniques at the study site agreed reasonably well. Problems arise from the temporal variations of rates over a tidal cycle, up-scaling, the sampling dates that were not consistent between methods and especially the high-energy setting itself. The latter aggravates the use of commonly applied methods, e.g., seepage meter measurements over longer time scales and requires assumptions regarding the rates' temporal development.

Direct Measurements

Lysimeters

The results suggest that the use of lysimeters to determine unsaturated infiltration in high-energy settings for a limited timeframe is suitable. In sufficiently thick unsaturated beach zones, they are easy to install and (after a reasonable adaption time of ~1 day) resistant to the wave dynamics that periodically occur at the sampling site. The lysimeters were able to cover a range of infiltration rates between 0.001 and almost 0.6 m day^{-1}, whereas replica measurements at the same location provided reliable results (**M**ean **A**bsolute **D**eviation of ~0.005 m day^{-1}). In order to resolve the temporal development during a tidal cycle, the lysimeters should be equipped with pressure transducers as done in Heiss et al. (2014) in future studies. Difficulties arise from the continuous sediment relocation at high energy beaches

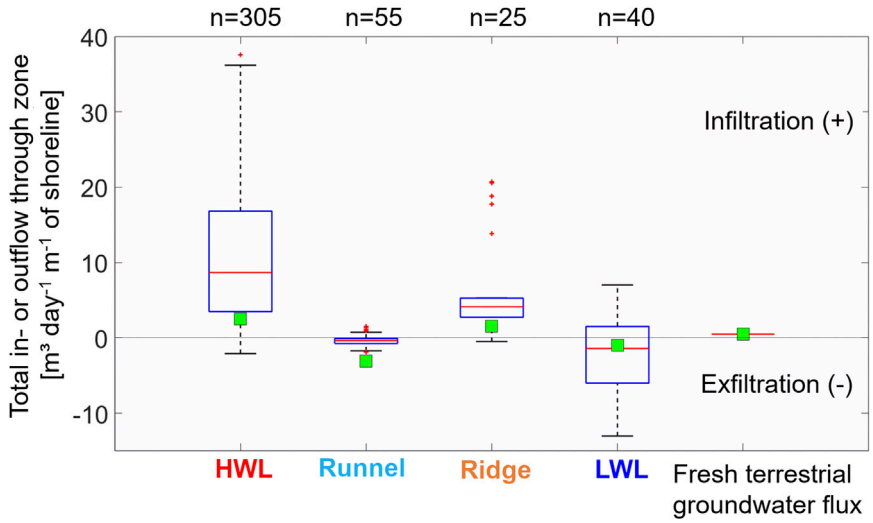


FIGURE 7 | Total in- and outflow within the in- and exfiltration zones at the northern beach of Spiekeroog (intertidal zone) for 1m shoreline. For total water budgeting, fresh groundwater flux (estimated with 0.75 m^3 per day and meter of shoreline from Beck et al. (2017)) has to be considered as additional proportion infiltration. Green squares indicate results from models water budget (Grünenbaum et al., 2020). Red dots are values that are more than 1.5 times the interquartile range away from the top or bottom of the box. Red line indicates median of boxplot. Number of statistics (*n*) is given above.

resulting in an uncontrolled shrinkage or growth of the unsaturated zone within days to weeks and burial of equipment. This means that long-term measurements of unsaturated infiltration are impeded at high energy beaches.

Seepage Meters

Seepage meters provided overall comparable (saturated) infiltration and exfiltration rates from HWL to LWL between replica measurements. Nevertheless, applicability in the field was difficult due to weather and wind conditions. Indeed, seepage meter measurements could not be conducted during all campaigns, because the attached plastic bags were influenced by stronger wave activity, which was reported in previous studies (e.g., Libelo and MacIntyre, 1994; Burnett et al., 2006). Wave activity and resulting equipment loss prevent longer adaptation times to the field site. As a result, only measurements over short times (hours) could be conducted, which does likely not lead to unrealistic fluxes, but inhibits further chemical investigations of the collected (exfiltrating) water, e.g., to determine the salinity, because the water under the seepage meter is not completely exchanged yet. For the study site, automatic seepage meters equipped with flow meters, as done in terrestrial studies (e.g., Krupa et al., 1998), would be more appropriate in order to collect long-term information over several tidal cycle. To stabilize the position of seepage meter and protect it for flipping in the waves, it should be additionally weighted down.

Indirect Measurements

At the study site, the flow field in the intertidal zone appears to be rather complicated considering the effect of tidal pumping, a strong wave-set up, and a changing beach topography (Waska et al., 2019 or **Supplementary Figure S8**). Indirect methods using radon residence times and temperature profiles complement direct volumetric methods but rely on a set of assumptions (e.g., steady state, respective flow conditions). Assumptions and related problems are discussed below.

^{222}Rn in Pore Waters

The infiltration rates obtained by the ^{222}Rn tracer approach are in good agreement to those of lysimeters, temperature sensors, and seepage meters. Most radon derived infiltration rates were lower than respective lysimeter infiltration rates and higher than those derived from temperature sensors or seepage meters (**Figure 3**).

Infiltration rates were obtained by fitting a linear regression function to pore water residence times derived from distinct ^{222}Rn pore water measurements. Sediment inhomogeneity, i.e. a non-uniform distribution of sediment-bound ^{226}Ra or varying grain sizes and mixing of water masses of different ages or salinity will affect the ^{222}Rn distribution within the sediment and have been identified as major constraints for the applicability of this method (Tamborski et al., 2017). Furthermore, ^{226}Ra accumulation is likely regulated by the presence of manganese (hydr)oxides (Dulaiova et al., 2008). Therefore, active manganese cycling within the sediment body may cause a non-uniform distribution of sediment bound ^{226}Ra. Beck et al. (2017) reported rather small variations in grain size for the Spiekeroog study site, with however some carbonate shell layers affecting sediment permeability, porosity, and pore water flow conditions. Generally, as sediment bound ^{226}Ra is the source of pore water radon, smaller grain sizes would lead to a higher specific surface and finally to a higher radon emanation to pore waters. Nonetheless, beach sediments from Spiekeroog Island are redistributed by erosion and sedimentation, e.g., on

seasonal timescales (Flemming and Davis, 1994; Waska et al., 2019). Thus, pronounced redox-driven Mn oxide enrichments are unlikely and the overall effect of sediment inhomogeneity on calculated residence times and infiltration rates is suggested to be rather small for Spiekeroog sediments. Additionally, the pore water receives an integrated ^{222}Rn signal of the sediment through which it has traveled. This may further compensate small scale sediment heterogeneities. Radon evasion across the saturated-unsaturated sediment interface, as reported by Colbert et al. (2008), might be of minor importance for the rate calculations at Spiekeroog because ^{222}Rn samples extracted from the temporally unsaturated part of the sediment do not show a significant radon deficit compared to samples from permanently saturated sediments.

In general, the restriction to a small ingrowth period of 0.5–7 days (Tamborski et al., 2017) limits the applicability of this method to zones of seawater infiltration (HWL, Ridge) at the Spiekeroog study site. If background activities in seawater are low, the lower restriction derives from detection limits of ^{222}Rn. This limit may be lowered by increasing the analytical sensitivity, for example by increasing sample volumes, detector size or reducing air volumes. However, the upper limit derives from the theoretical temporal evolution of ^{222}Rn (**Eq. 1**), which asymptotically approaches the equilibrium activity $^{222}_{eq}Rn$. As a consequence, model uncertainties are amplified, when ^{222}Rn activities are close to $^{222}_{eq}Rn$, producing large errors in residence times (**Supplementary Figure S3**).

In this study, the equilibrium activity $^{222}_{eq}Rn$ was approximated by sampling deep pore water from a representative exfiltration site. This is in contrast to other studies, which determined the equilibrium activity experimentally (Goodridge and Melack, 2014; Colbert et al., 2008; Tamborski et al., 2017). This approach was chosen as the hydrogeological setting is well known (Beck et al., 2017; Grünenbaum et al., 2020) and experimental approaches are often influenced by artefacts as they require an accurate imitation of natural conditions in the laboratory. However, a limitation of our method is that the equilibrium activity $^{222}_{eq}Rn$ was only determined once and not for each sampling event separately, although intertidal pore water temperatures are highly variable throughout the year (Waska et al., 2019). $^{222}_{eq}Rn$ was determined based on analyses in September (summer), when pore waters were comparably warm. However, we are not able to assess any seasonal effects based on our dataset.

Temperature Sensors (1D-Heat Transport Solution)

The use of temperature as a tracer in the coastal zone is limited, but it offers a useful addition to other tracer methods as it can quantify infiltration and exfiltration in saturated sediments, is cheap to measure directly in the field, and is ubiquitous in natural systems. Taniguchi et al. (2003) used temperature profiles to estimate vertical groundwater fluxes in the Cockburn sound (Australia) using the 1D steady state and non-steady state models while Tirado-Conde et al. (2019) recently compared exchange fluxes using the steady state temperature model and direct seepage meter measurements at a calm lagoon of the North Sea coast in Denmark. In the later study fluxes based on temperature measurements better matched seepage meter values in areas with a higher proportion of freshwater discharge than in areas dominated by recirculating seawater. This was explained by the complexity of the flow field in zones of circulating seawater, which is not limited to one dimension. The temperature profiles from the site studied here (**Figure 2**) show that temperature sensors can clearly delineate upwelling warm groundwater during winter in the runnel and LWL as well as locations with either low SGD flux or infiltrating conditions. This qualitative pattern in temperature profiles can be used as an additional tool to rapidly screen a field site for potential SGD and submarine groundwater recharge areas and relate this to the site morphology. This could assist in an optimized sampling strategy for detailed and time-consuming method such as seepage meters. This SGD mapping approach becomes especially important for highly dynamic environments, where the sampling at the LWL is often difficult and prior planning is required. As previous studies have suggested already (Röper et al., 2014; Tirado-Conde et al., 2019), a large difference between seawater temperature and exfiltrating groundwater is necessary in order to distinguish between the different endmembers and set realistic boundary conditions. This generally occurs either in summer- or wintertime. Winter is preferred due to the low to moderate diurnal oscillations in sea water temperature, which makes the use of steady-state models more applicable. While the SGD fluxes calculated using the temperature lances are similar to the other methods, more work is needed to better understand how the assumptions of 1D heat transport and steady-state conditions influence the results. These are clearly a strong simplification, as flow and transport at such a highly dynamic beach site is in reality both transient and 3-dimensional. Despite this temperature offers a currently underutilized tracer in the coastal zone and with further refinement is likely to assist in quantifying SGD rates in the future (Kurylyk and Irvine 2019).

CONCLUSION AND OUTLOOK

This study provides insights into the spatial variability of exchange rates within a STE in a meso-tidal, highly dynamic environment. It is one of a few studies that presents a multiple-method approach with direct (lysimeter, seepage meter) and indirect measurements (radon and temperature as tracer) as well as a numerical model in order to determine in- and exfiltration rates across all seasons to give a general idea about the range of fluxes occurring at a high energy beach.

The results suggest the existence of two exfiltration areas (Runnel, LWL) and two infiltration areas (HWL, Ridge) in the intertidal zone of the respective northern beach of Spiekeroog Island, which were induced by beach topography. Predominantly infiltrating conditions were found above MSL and mostly exfiltrating conditions below MSL. Infiltration rates at the HWL covered the highest range and varied between 0.001 and

0.61 m day^{-1}. Exfiltration rates generally fluctuated around −0.1 m day^{1}. The exchange rates measured by different methods were over all comparable. This was a promising finding as some of the techniques have rarely been applied in coastal aquifers or were found to be error-prone in dynamic environments.

An analysis of spatially and temporally highly resolved exchange rates at a high-energy beach has so far not been conducted and is certainly challenging. Yet, flow and transport patterns can be expected to be highly transient, as are likely the in- and exfiltration rates. To conduct continuous measurements would hence be a valuable yet elaborate task for future investigations.

Topographic information in combination with measured exchange rates showed a significant movement of influx and efflux zones within the intertidal zone over time. Thereby, not only the location but also the extensions of the zones varied, which in turn influenced the up-scaling of total in- or outflow. Extrapolated total SGD fluxes into the southern North Sea from the East Frisian barrier island chain contribute to terrestrial runoff with less than 1%.

DATA AVAILABILITY STATEMENT

The original contributions presented in the study are included in the article/**Supplementary Material**, further inquiries can be directed to the corresponding author.

AUTHOR CONTRIBUTIONS

Planning of field work was carried out by all authors. JG, GM, and I carried out lysimeter and seepage meter measurements at the northern beach of Spiekeroog in October 2016, March and August 2017. JA, MB, and MK were responsible for analysis of ^{222}Radon in pore water from March, May, August, September 2017, and February 2018. BG conducted temperature measurements in February 2018 and March 2019. I conducted the modeling work myself in a previous study, with the support of JG. Data interpretation, as well as manuscript and figure preparation were performed in joint discussion with all co-authors.

FUNDING

We want to thank the Lower Saxony Ministry of Science and Culture for funding the study as part of the BIME project ("Assessment of ground- and porewater-derived nutrient fluxes into the German North Sea – Is there a "Barrier Island Mass Effect?", VW ZN 3184 MWK).

ACKNOWLEDGMENTS

We thank the *Nationalparkverwaltung Niedersächsisches Wattenmeer (NLPV)*, in particular G. Scheiffart and C. Schulz, for permitting investigations at the northern beach site of Spiekeroog, as well as for the aerial image of the island. Many thanks to the *Niedersächsicher Landesbetrieb für Wasserwirtschaft-, Küsten-und Naturschutz (NLWKN)*, especially J. Ihnken and his colleages, as well as H. Nicolai, G. Behrens and K. Schwalfenberg from the Institute for Chemistry and Biology of the Marine Environment (ICBM) in Wilhelmshaven, for their help during the campaigns planning progress and equipment transport. We thank the local community and employees of the researcher house *Wittbülten*. The students, L. Diehl, A. Harms, C.H. Lünsdorf, J. Otten, and J. Schulz are thanked for assistance during sampling. Many thanks to the *Wasser-und Schifffahrtsverwaltung des Bundes* (WSV) and the *Bundesamt für Seeschifffahrt und Hydrographie* (BSH) for providing data of the tide gauges. Finally, we want to thank the *Ministry for Science and Art* (lower Saxony) for funding the study as part of the BIME project ("Assessment of ground- and porewater-derived nutrient fluxes into the German North Sea – Is there a Barrier Island Mass Effect?") and the participating colleges from the ICBM in Oldenburg/Wilhelmshaven and the Max-Planck Institute (MPI) in Bremen. BG is especially grateful for H. Waska funding and organizing his participation in the SGD experiments on Spiekeroog as part of the BIME project.

SUPPLEMENTARY MATERIAL

The Supplementary Material for this article can be found online at: https://www.frontiersin.org/articles/10.3389/feart.2020.571310/full#supplementary-material.

REFERENCES

Abarca, E., Karam, H., Hemond, H. F., and Harvey, C. F. (2013). Transient groundwater dynamics in a coastal aquifer: the effects of tides, the lunar cycle, and the beach profile. *Water Resour. Res.* 49 (5), 2473–2488. doi:10.1002/wrcr.20075

Anderson, M. P. (2005). Heat as a ground water tracer. *Groundwater* 43 (6), 951–968. doi:10.1111/j.1745-6584.2005.00052.x

Anschutz, P., Smith, T., Mouret, A., Deborde, J., Bujan, S., Poirier, D., et al. (2009). Tidal sands as biogeochemical reactors. *Estuar. Coast Shelf Sci.* 84 (1), 84–90. doi:10.1016/j.ecss.2009.06.015

Bateman, H. (1910). Solution of a system of differential equations occurring in the theory of radioactive 815 transformations. *Proc. Cambridge Phil. Soc.* 15, 423–427.

Beck, M., Reckhardt, A., Amelsberg, J., Bartholomä, A., Brumsack, H.-J., Cypionka, H., et al. (2017). The drivers of biogeochemistry in beach ecosystems: a cross-shore transect from the dunes to the low-water line. *Mar. Chem.* 190, 35–50. doi:10.1016/j.marchem.2017.01.001

Becker, G., Giese, H., Isert, K., König, P., Langenberg, H., Pohlmann, T., et al. (1999). Mesoscale structures, fluxes and water mass variability in the German Bight as exemplified in the KUSTOS-experiments and numerical models. *Dtsch. Hydrografische Z.* 51 (2–3), 155–179. doi:10.1007/BF02764173

Befus, K. M., Cardenas, M. B., Erler, D. V., Santos, I. R., and Eyre, B. D. (2013). Heat transport dynamics at a sandy intertidal zone. *Water Resour. Res.* 49, 3770–3786. doi:10.1002/wrcr.20325

Blume, T., Krause, S., Meinikmann, K., and Lewandowski, J. (2013). Upscaling lacustrine groundwater discharge rates by fiber-optic distributed temperature sensing. *Water Resour. Res.* 49, 7929–7944. doi:10.1002/2012WR013215

Bredehoeft, J. D. and Papaopulos, I. S. (1965). Rates of vertical groundwater movement estimated from the Earth's thermal profile. *Water Resour. Res.* 1 (2), 325–328. doi:10.1029/WR1001i1002p00325

Burnett, W., Aggarwal, P., Aureli, A., Bokuniewicz, H., Cable, J., Charette, M., et al. (2006). Quantifying submarine groundwater discharge in the coastal zone via multiple methods. *Sci. Total Environ.* 367 (2–3), 498–543. doi:10.1016/j.scitotenv.2006.05.009

Burnett, W. C. and Dulaiova, H. (2003). Estimating the dynamics of groundwater input into the coastal zone via continuous radon-222 measurements. *J. Environ.* 69 (1–2), 21–35. doi:10.1016/S0265-931X(03)00084-5

Burnett, W. C., Dulaiova, H., Huettel, M., Moore, W.S., and Taniguchi, M. (2003). Groundwater and pore water inputs to the coastal zone. *Biogeochemistry* 66 (1–2), 3–33. doi:10.1023/B:BIOG.0000006066.21240.53

Cable, J. E., Martin, J. B., and Jaeger, J. (2006). Exonerating Bernoulli? On evaluating the physical and biological processes affecting marine seepage meter measurements. *Limnol. Oceanogr. Methods* 4 (6), 172–183. doi:10.4319/lom.2006.4.172

Cho, H.-M., Kim, G., Kwon, E. Y., Moosdorf, N., Garcia-Orellana, J., and Santos, I. R. (2018). Radium tracing nutrient inputs through submarine groundwater discharge in the global ocean. *Sci. Rep.* 8 (1), 2439. doi:10.1038/s41598-018-20806-2

Colbert, S., Berelson, W., and Hammond, D. (2008). Radon-222 budget in Catalina Harbor, California: 2. Flow dynamics and residence time in a tidal beach. *Limnol. Oceanogr.* 53 (2), 659–665. doi:10.4319/lo.2008.53.2.0659

Constantz, J. (2008). Heat as a tracer to determine streambed water exchanges. *Water Resour. Res.* 44, W00D10. doi:10.1029/2008WR006996

Dobrynin, M., Gayer, G., Pleskachevsky, A., and Günther, H. (2010). Effect of waves and currents on the dynamics and seasonal variations of suspended particulate matter in the North Sea. *J. Mar. Syst.* 82 (1), 1–20. doi:10.1016/j.jmarsys.2010.02.012

Dulaiova, H., Gonneea, M. E., Henderson, P. B., and Charette, M. A. (2008). Geochemical and physical sources of radon variation in a subterranean estuary—implications for groundwater radon activities in submarine groundwater discharge studies. *Mar. Chem.* 110 (1–2), 120–127. doi:10.1016/j.marchem.2008.02.011

Evans, T. B. and Wilson, A. M. (2016). Groundwater transport and the freshwater–saltwater interface below sandy beaches. *J. Hydrol.* 538, 563–573. doi:10.1016/j.jhydrol.2016.04.014

Flemming, B. W. and Davis, R. (1994). Holocene evolution, morphodynamics and sedimentology of the Spiekeroog barrier island system (southern North Sea). Senckenbergiana maritima. *Frankfurt/Main* 24 (1), 117–155.

Giblin, A. E. and Gaines, A. G. (1990). Nitrogen inputs to a marine embayment: the importance of groundwater. *Biogeochemistry* 10 (3), 309–328. doi:10.1007/BF00003150

Gilfedder, B., Peiffer, S., Poeschke, F., and Spirkaneder, A. (2018). Mapping and quantifying groundwater discharge to Lake Steißling and its influence on lake water chemistry. *Grundwasser* 23, 155–165. doi:10.1007/s00767-017-0386-8

Goodridge, B. M. and Melack, J. M. (2014). Temporal evolution and variability of dissolved inorganic nitrogen in beach pore water revealed using radon residence times. *Environ. Sci. Technol.* 48 (24), 14211–14218. doi:10.1021/es504017j

Greskowiak, J. (2014). Tide-induced salt-fingering flow during submarine groundwater discharge. *Geophys. Res. Lett.* 41, 6413–6419. doi:10.1002/2014GL061184

Grünenbaum, N., Greskowiak, J., Sültenfuß, J., and Massmann, G. (2020). Groundwater flow and residence times below a meso-tidal high-energy beach: a model-based analyses of salinity patterns and 3H-3He groundwater ages. *J. Hydrol.* 58, 124948. doi:10.1016/j.jhydrol.2020.124948

Heiss, J. W., Post, V. E., Laattoe, T., Russoniello, C. J., and Michael, H. A. (2017). Physical controls on biogeochemical processes in intertidal zones of beach aquifers. *Water Resour. Res.* 53 (11), 9225–9244. doi:10.1002/2017WR021110

Heiss, J. W., Ullman, W. J., and Michael, H. A. (2014). Swash zone moisture dynamics and unsaturated infiltration in two sandy beach aquifers. *Estuar. Coast Shelf Sci.* 143, 20–31. doi:10.1016/j.ecss.2014.03.015

Holt, T., Greskowiak, J., Seibert, S., and Massmann, G. (2019). Modeling the evolution of a freshwater lens under highly dynamic conditions on a currently developing barrier island. *Geofluids* 2019, 9484657. doi:10.1155/2019/9484657

Hwang, D. W., Lee, Y. W., and Kim, G. (2005). Large submarine groundwater discharge and benthic eutrophication in Bangdu Bay on volcanic Jeju Island, Korea. *Limnol. Oceanogr.* 50 (5), 1393–1403. doi:10.4319/lo.2005.50.5.1393

Johannes, R. (1980). Ecological significance of the submarine discharge of groundwater. *Marine Ecol.- Prog. Ser.* 3 (4), 365–373. doi:10.3354/meps003365

Jordan, C. F. (1968). A simple, tension-free lysimeter. *Soil Sci.* 105 (2), 81–86. doi:10.1097/00010694-196802000-00003

King, C. and Williams, W. (1949). The formation and movement of sand bars by wave action. *Geogr. J.* 113, 70–85. doi:10.2307/1788907

Krupa, S. L., Belanger, T. V., Heck, H. H., Brock, J. T., and Jones, B. J. (1998). Krupaseep—the next generation seepage meter. *J. Coastal Res.*, 210–213.

Kurylyk, B. L. and Irvine, D. J. (2019). Heat: an overlooked tool in the practicing hydrogeologist's toolbox. *Groundwater* 57, 517–524. doi:10.1111/gwat.12910

Kwon, E. Y., Kim, G., Primeau, F., Moore, W. S., Cho, H. M., DeVries, T., et al. (2014). Global estimate of submarine groundwater discharge based on an observationally constrained radium isotope model. *Geophys. Res. Lett.* 41 (23), 8438–8444. doi:10.1002/2014GL061574

Lapham, W. W. (1989). *Use of temperature profiles beneath streams to determine rates of vertical ground-water flow and vertical hydraulic conductivity*. Denver, Colorado: Department of the Interior, US Geological Survey; USGPO; Books and Open-File.

Lee, D. R. (1977). A device for measuring seepage flux in lakes and estuaries 1. *Limnol. Oceanogr.* 22 (1), 140–147. doi:10.4319/lo.1977.22.1.0140

Libelo, E. L. and MacIntyre, W. G. (1994). Effects of surface-water movement on seepage-meter measurements of flow through the sediment-water interface. *Appl. Hydrogeol.* 2 (4), 49–54. doi:10.1007/s100400050047

McAllister, S. M., Barnett, J. M., Heiss, J. W., Findlay, A. J., MacDonald, D. J., Dow, C. L., et al. (2015). Dynamic hydrologic and biogeochemical processes drive microbially enhanced iron and sulfur cycling within the intertidal mixing zone of a beach aquifer. *Limnol. Oceanogr.* 60 (1), 329–345. doi:10.1002/lno.10029

Michael, H. A., Lubetsky, J. S., and Harvey, C. F. (2003). Characterizing submarine groundwater discharge: a seepage meter study in Waquoit Bay, Massachusetts. *Geophys. Res. Lett.* 30 (6), 1297. doi:10.1029/2002GL016000

Michael, H. A., Mulligan, A. E., and Harvey, C. F. (2005). Seasonal oscillations in water exchange between aquifers and the coastal ocean. *Nature* 436 (7054), 1145. doi:10.1038/nature03935

Miller, D. C. and Ullman, W. J. (2004). Ecological consequences of ground water discharge to Delaware Bay, United States. *Groundwater* 42 (7), 959–970. doi:10.1111/j.1745-6584.2004.tb02635.x

Moore, W. S. (1999). The subterranean estuary: a reaction zone of ground water and sea water. *Mar. Chem.* 65 (1), 111–125. doi:10.1016/S0304-4203(99)00014-6

Moore, W. S., Sarmiento, J. L., and Key, R. M. (2008). Submarine groundwater discharge revealed by 228Ra distribution in the upper Atlantic Ocean. *Nat. Geosci.* 1 (5), 309–311. doi:10.1038/ngeo183

Mulligan, A. E. and Charette, M. A. (2006). Intercomparison of submarine groundwater discharge estimates from a sandy unconfined aquifer. *J. Hydrol.* 327 (3–4), 411–425. doi:10.1016/j.jhydrol.2005.11.056

Munz, M. and Schmidt, C. (2017). Estimation of vertical water fluxes from temperature time series by the inverse numerical computer program FLUX-BOT. *Hydrol. Process.* 31 (15), 2713–2724. doi:10.1002/hyp.11198

Rau, G. C., Andersen, M. S., and Acworth, R. I. (2012). Experimental investigation of the thermal dispersivity term and its significance in the heat transport equation for flow in sediments. *Water Resour. Res.* 48, W03511. doi:10.1029/2011WR011038

Rau, G. C., Andersen, M. S., McCallum, A. M., Roshan, H., and Acworth, R. I. (2014). Heat as a tracer to quantify water flow in near-surface sediments. *Earth Sci. Rev.* 129, 40–58. doi:10.1016/j.earscirev.2013.10.015

Reckhardt, A., Beck, M., Greskowiak, J., Schnetger, B., Böttcher, M. E., Gehre, M., et al. (2017). Cycling of redox-sensitive elements in a sandy subterranean estuary of the southern North Sea. *Mar. Chem.* 188, 6–17. doi:10.1016/j.marchem.2016.11.003

Robinson, C., Gibbes, B., and Li, L. (2006). Driving mechanisms for groundwater flow and salt transport in a subterranean estuary. *Geophys. Res. Lett.* 33 (3), L03402. doi:10.1029/2005GL025247

Robinson, C., Li, L., and Barry, D. (2007). Effect of tidal forcing on a subterranean estuary. *Adv. Water Resour.* 30 (4), 851–865. doi:10.1016/j.advwatres.2006.07.006

Röper, T., Greskowiak, J., and Massmann, G. (2014). Detecting small groundwater discharge springs using handheld thermal infrared imagery. *Groundwater* 52 (6), 936–942. doi:10.1111/gwat.12145

Röper, T., Kröger, K. F., Meyer, H., Sültenfuss, J., Greskowiak, J., and Massmann, G. (2012). Groundwater ages, recharge conditions and hydrochemical evolution of a barrier island freshwater lens (Spiekeroog, Northern Germany). *J. Hydrol.* 454–455, 173–186. doi:10.1016/j.jhydrol.2012.06.011

Santos, I. R., Eyre, B. D., and Huettel, M. (2012). The driving forces of porewater and groundwater flow in permeable coastal sediments: a review. *Estuar. Coast. Shelf Sci.* 98, 1–15. doi:10.1016/j.ecss.2011.10.024

Schmidt, C., Bayer-Raich, M., and Schirmer, M. (2006). Characterization of spatial heterogeneity of groundwater-stream water interactions using multiple depth streambed temperature measurements at the reach scale. *Hydrol. Earth Syst. Sci.* 10, 849–859. doi:10.5194/hess-5110-5849-2006

Seibert, S. L., Holt, T., Reckhardt, A., Ahrens, J., Beck, M., Pollmann, T., et al. (2018). Hydrochemical evolution of a freshwater lens below a barrier island (Spiekeroog, Germany): the role of carbonate mineral reactions, cation exchange and redox processes. *Appl. Geochem.* 92, 196–208. doi:10.1016/j.apgeochem.2018.03.001

Seidel, M., Beck, M., Greskowiak, J., Riedel, T., Waska, H., Suryaputra, I. N., et al. (2015). Benthic-pelagic coupling of nutrients and dissolved organic matter composition in an intertidal sandy beach. *Mar. Chem.* 176, 150–163. doi:10.1016/j.marchem.2015.08.011

Shaw, R. and Prepas, E. (1989). Anomalous, short-term influx of water into seepage meters. *Limnol. Oceanogr.* 34 (7), 1343–1351. doi:10.4319/lo.1989.34.7.1343

Streif, H. (1990). *Das ostfriesische Küstengebiet: nordsee, Inseln, Watten und arschen; mit 10 Tabellen*. Berlin-Stuttgart: Borntraeger.

Swarzenski, P. (2007). U/Th series radionuclides as coastal groundwater tracers. *Chem. Rev.* 107 (2), 663–674. doi:10.1021/cr0503761

Tamborski, J. J., Cochran, J. K., and Bokuniewicz, H. J. (2017). Application of 224Ra and 222Rn for evaluating seawater residence times in a tidal subterranean estuary. *Mar. Chem.* 189, 32–45. doi:10.1016/j.marchem.2016.12.006

Taniguchi, M., Turner, J. V., and Smith, A. J. (2003). Evaluations of groundwater discharge rates from subsurface temperature in Cockburn Sound, Western Australia. *Biogeochemistry* 66, 111–124. doi:10.1023/B:BIOG.0000006099.50469.b3

Tirado-Conde, J., Engesgaard, P., Karan, S., Müller, S., and Duque, C. (2019). Evaluation of temperature profiling and seepage meter methods for quantifying submarine groundwater discharge to coastal lagoons: impacts of saltwater intrusion and the associated thermal regime. *Water* 11 (8), 1648. doi:10.3390/w11081648

Urish, D. W. and McKenna, T. E. (2004). Tidal effects on ground water discharge through a sandy marine beach. *Groundwater* 42 (7), 971–982. doi:10.1111/j.1745-6584.2004.tb02636.x

Waska, H., Greskowiak, J., Ahrens, J., Beck, M., Ahmerkamp, S., Böning, P., et al. (2019). Spatial and temporal patterns of pore water chemistry in the inter-tidal zone of a high energy beach. *Front. Marine Sci.* 6, 154. doi:10.3389/fmars.2019.00154

Xin, P., Robinson, C., Li, L., Barry, D. A., and Bakhtyar, R. (2010). Effects of wave forcing on a subterranean estuary. *Water Resour. Res.* 46 (12), W12505. doi:10.1029/2010WR009632

Conflict of Interest: The authors declare that the research was conducted in the absence of any commercial or financial relationships that could be construed as a potential conflict of interest.

The reviewer (JJT) declared a past co-authorship with several of the authors (JA and MB) to the handling editor.

Copyright © 2020 Grünenbaum, Ahrens, Beck, Gilfedder, Greskowiak, Kossack and Massmann. This is an open-access article distributed under the terms of the Creative Commons Attribution License (CC BY). The use, distribution or reproduction in other forums is permitted, provided the original author(s) and the copyright owner(s) are credited and that the original publication in this journal is cited, in accordance with accepted academic practice. No use, distribution or reproduction is permitted which does not comply with these terms.

frontiers in Earth Science

ORIGINAL RESEARCH
published: 14 September 2021
doi: 10.3389/feart.2021.710000

Submarine Groundwater Discharge From Sediments and Sand Boils Quantified by the Mean Residence Time of a Tracer Injection

Michael Schlüter[1]* *and Philipp Maier*[2]

[1]Marine Geochemistry, Alfred Wegener Institute, Bremerhaven, Germany, [2]Department of Maritime Technologies University of Applied Sciences, Bremerhaven, Germany

To quantify submarine groundwater discharge, we developed an inexpensive automated seepage meter that applies a tracer injection and the computation of the mean residence time. The SGD-MRT is designed to measure a wide range of discharge rates from about 30 to 800 cm^3/min and allows minimizing backpressures caused by pipe friction or flow sensors. By modifying the inner volume of the flow-through unit, the range of measurement is adjustable to lower or higher discharge rates. For process control and data acquisition, an Arduino controller board is used. In addition, components like temperature, conductivity, and pressure sensors or pumps extend the scope of the seepage meter. During field tests in the Wadden Sea, covering tidal cycles, discharge rates of more than 700 cm^3/min were released from sand boils. Based on the measured discharge rates and numerical integration of the time series data, a water volume of about 400 dm^3 with a seawater content of less than 12% was released from the sand boil within 7 h.

Keywords: submarine groundwater discharge, sand boil, residence time, sgd, coastal zone, fluid flow, arduino

OPEN ACCESS

Edited by:
Henry Bokuniewicz, The State University of New York (SUNY), United States

Reviewed by:
Matt Charette, Woods Hole Oceanographic Institution, United States
Joseph James Tamborski, Old Dominion University, United States

***Correspondence:**
Michael Schlüter
michael.schlueter@awi.de

Specialty section:
This article was submitted to Hydrosphere, a section of the journal Frontiers in Earth Science

Received: *21 May 2021*
Accepted: *16 August 2021*
Published: *14 September 2021*

Citation:
Schlüter M and Maier P (2021) Submarine Groundwater Discharge From Sediments and Sand Boils Quantified by the Mean Residence Time of a Tracer Injection. Front. Earth Sci. 9:710000. doi: 10.3389/feart.2021.710000

INTRODUCTION

The release of fresh or brackish waters from sediments, karst channels, or pockmarks into bottom waters has been reported for numerous coastal regions, river beds, or lakes (Zektzer et al., 1973; Lee, 1977; Bokuniewicz, 1980; Cherkauer and McBride, 1988; Moore, 1996; Burnett et al., 2003; Rosenberry, 2008; Judd and Hovland 2009; Povinec et al., 2012). Submarine groundwater discharge (SGD) flows through the pore space of sediments or along fluid conduits such as karst structures. The relevance of SGD for the transport and release of nutrients, trace elements or gases such as methane or radon from sediments into the groundwater of coastal regions or lakes has already been emphasized by Johannes (1980), Zimmermann et al. (1985), Shaw and Prepas (1990), Simmons (1992) and Bugna et al. (1996).

In order to quantify fluid discharge from the seafloor, the calculation of radon or radium budgets in the water column, pore water studies, different types of flow sensors, or seepage meters are applied (Taniguchi and Fukuo, 1993; Vanek 1993; Moore, 1999; Burnett et al., 2006; Rocha et al., 2009; Santos et al., 2009).

According to the broad range of flow rates, different sediment types, or modes of fluid transport like the dispersed flow-through permeable sediments or the focused flow along conduits, various methods and flow sensors are used to quantify fluid discharge (Sholkovitz et al., 2003; Martin et al., 2004; Schlüter et al., 2004; Seeberg-Elverfeldt et al., 2005; Koopmans and Berg, 2011; Solomon et al.,

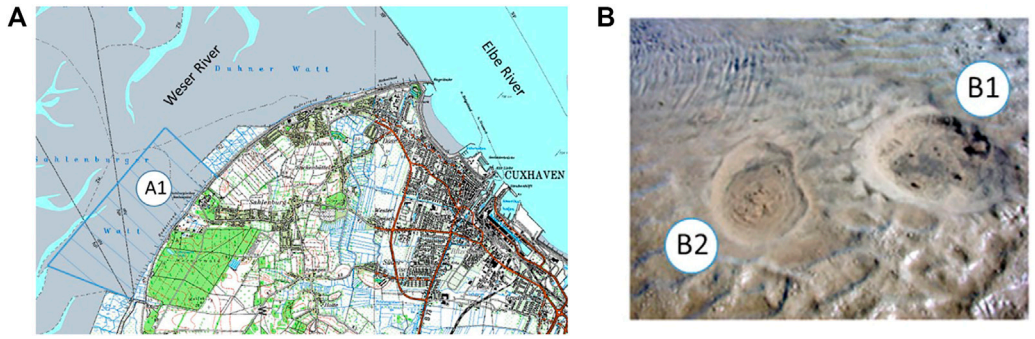


FIGURE 1 | Study area **(A)** in the Elbe-Wester estuary in the southeastern North Sea, where groundwater discharge is observed in numerous places in the Sahlenburg mudflat (A1). (https://nibis.lbeg.de/cardomap3/?TH=534). **(B)**. The effect of backpressure created during the deployment of a seepage meter at a discharge site with an intense release of fluids. A Lee-type chamber equipped with an impeller flow sensor was installed at location B1. About 2 hours after the seepage meter was installed at B1, the backpressure caused by the Lee-type chamber (not shown) caused the fluid discharge to gradually decrease. At the same time, a new active discharge site (B2) formed about 40 cm from site B1.

2020). Overviews of different types of flow meters for quantifying fluid discharge from sediments are provided by Taniguchi et al. (2019), Rosenberry et al. (2020), and Duque et al. (2020).

Most of these flow sensors primarily develop to quantify volume flows of fluids in technical or industrial applications such as domestic water treatment, food industry, process engineering, or the chemical industry. For such applications, mechanical or electronic feedback loops are used to regulate pressure changes and flow rates caused by narrow cross-sections or bottlenecks within flow meters, pipes, or valves.

In contrast to confined flow, under free surface flow conditions such as SGD, the flow patterns and flow lines in porous sediments or karst structures can change when the backpressure exceeds certain thresholds. This might cause shifts in flow lines and changes in discharge rates. Such effects have been demonstrated – for example – by Murdoch and Kelly (2003) and Cable et al. (2006).

We observed the effect of backpressure on measured discharge rates while using a Lee-type chamber (L 30 × W 30 × H 12 cm) equipped with an impeller flow sensor on the Sahlenburg mudflat (**Figure 1A**). About 2 h after the deployment of the seepage meter, the fluid discharge at the sampling site significantly decreased, and a new discharge site with intensive fluid release built up about 40 cm aside from the primary discharge site (**Figure 1B**). The relocation of the subsurface water transport from B1 to B2 and the formation of a new active sand boil mainly result from the backpressure created by the impeller flow sensor deployed at site B1. This observation underlines the need to minimize flow resistance when measuring fluid discharges from sediments.

A method for quantifying discharge rates that minimizes the drawbacks of flow resistances caused by technical restrictions like narrowing cross-sections inside of tube connectors or orifices inside of flow sensors is the computation of the mean residence time (MRT). The MRT computation was developed in the 1950s by Danckwerts (1953), Levenspiel (1999), and others. The MRT computation is widely used in chemical transport and reaction engineering to optimize the contact time of chemical components to produce substances (Fogler, 2006). In hydrogeology or environmental technology, MRT calculations are used to quantify groundwater flow rates or renewal rates or quantify the amount of undesirable substances entering rivers or lakes (Clark, 1996).

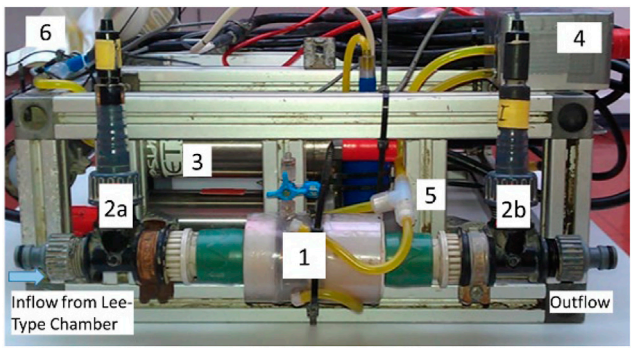


FIGURE 2 | Front view of the SGD-MRT: 1. Flow-through unit (FTU), 2 a, b. Conductivity probe at the inflow and outflow of the FTU, 3. Circulation pump to stir fluids inside the FTU, 4. Tracer injection unit (TIU), 5. Three-way tube connector for injection of the saline solution into the FTU, 6. Flexible bag (300 ml) filled with saline water applied for the tracer injection into the FTU. The carrier frame size is L 45 × W 45 × H 18 cm with a weight of about 8 kg.

To quantify the MRT, an inert tracer is injected into a chemical reactor or flow-through unit (FTU), and the concentration-time function of the tracer is recorded at the outflow of the FTU. Based on this data, the integral of the amount of tracer injected into the FTU is calculated, and the cumulative residence time distribution and the volume flow of the fluid are quantified. Detailed information and examples for calculating the MRT and the volume flow are provided by Fogler (2006) and Clark (1996).

MATERIALS AND METHODS

The SGD-MRT seepage meter is of modular design and applies components like conductivity probes, pressure or temperature

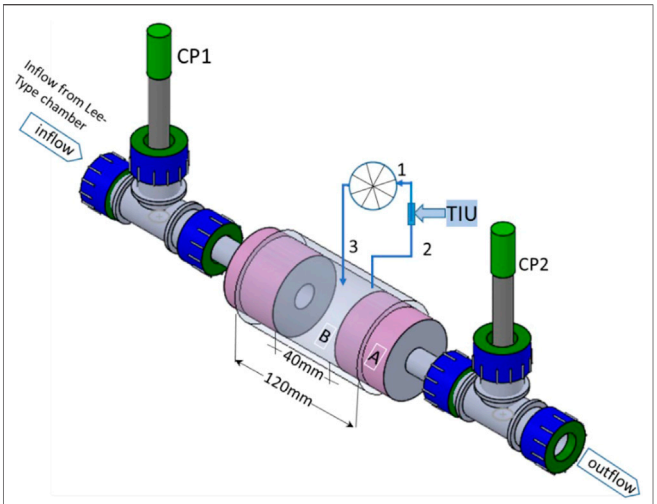


FIGURE 3 | Flow-through unit equipped with conductivity probes CP1 and CP2 at the inflow and outflow of the FTU. The water volume inside the FTU is continuously mixed by the circulation pump (1). The TIU (2) injects the saline tracer into the mixing unit (3) to determine the MRT and quantify the fluid discharge rate. The measuring range of the SGD-MRT is adjustable by sliding the Delrin end caps **(A)** inwards or outwards of the elastic PVC tube **(B)**.

sensors, or inexpensive positive displacement pumps applied for model making. Arduino controller boards and sensors are used for process control, data acquisition, or data storage. The list of the electronic components applied for the SGD-MRT is part of the **Supplementary Material**.

Materials

Figure 2 shows the front view of the SGD-MRT seepage meter designed for deployments on mudflats or shallow water regions (< 10 m water depth). The components of the SGD-MRT are mounted inside a rack built from standard strut profiles, which allows a flexible and extensible design of the seepage meter.

The main components of the SGD-MRT are the flow-through unit (FTU), conductivity probes (CP), a circulation pump, tracer injection unit (TIU), Arduino controller board, battery pack, and a flexible water bag holding a volume of about 300 ml saline water applied for the tracer injection. A Lee-type chamber collects the fluid discharge from the seabed and connects to the inlet of the FTU *via* a flexible hose.

One of the central components of the SGD-MRT meter is the FTU (**Figures 2**, **3**), which comprises elastic PVC tubing (ID 50 mm, length 110 mm) and endcaps made from a standard size Delrin rod, which forms the inlet and outlet of the FTU. We installed three-way tube connectors inside each end cap to mound the conductivity probes. The end caps fit into the PVC tubing and can be fixed by pipe clamps. For mixing the fluid inside the FTU, holes (ID 6 mm) were drilled into the PVC pipe and connected by hose to a circulation pump (**Figure 3**). By shifting the Delrin end caps inside or outside, the inner volume of the FTU for measurements of lower and higher fluid discharge rates can be adjusted.

To quantify the conductivity within the inflow and the outflow of the FTU, conductivity probes are used. We decided on a cell constant of K 1.0 and an electronic unit (Atlas Scientific), combining the conductivity probe with the Arduino controller board. The list of components is part of the **Supplementary Material**.

The TIU – triggered by the Arduino controller – injects a small volume (6 ml) of the sodium chloride solution stored in an elastic storage bag into the FTU (**Figure 4**). For injection of the tracer, an inexpensive positive displacement gear pump applies (e.g., ModelCraft™). The volumetric flow rate of the gear pump was calibrated in the lab using a laboratory balance and weighing of the water volume pumped for time intervals of 5, 10, or 20 s. For additional quality control, an impeller flow sensor is installed inside the TIU to quantify the saline tracer volume injected into the FTU. We used this procedure as an additional quality control, as the amount of tracer injected is determined during the calculation of the mean residence time.

The components of the TIU reside inside an electric junction box (L 10 × W 10 × H 6 cm), used in households for outdoor electricity cables, for example (**Figure 4**). We applied such housings for deployments down to 10 m water depths.

Figure 5 shows the schematic wiring diagram and electronic components of the SGD-MRT. The Arduino mega board applies for process control of the SGD-MRT, data acquisition, or data storage. Additional sensors or actuators can extend the controller board. Specific information about the deployment schedule – i.e., the start and end time, the delay time between measurement cycles, and acquired data – are stored on the SD card part of the Arduino controller board.

Process Flow

Beginning with the deployment of the SGD-MRT at the discharge site, the data acquisition starts according to the schedule stored on the Arduino controller board. During the deployment, the conductivity of the fluid at the inlet and outlet of the FTU, the conductivity of the seawater, the hydraulic pressure, or the temperature in the benthic chamber are measured and stored on the SD card. Furthermore, three self-recording Schlumberger CTD divers and temperature probes are installed inside and outside the Lee-type chamber for data acquisition and additional quality control.

In addition to sensors and electronic circuits required to quantify discharge rates, components such as differential pressure gauges (range from 0 to 5 m), temperature sensors, or conductivity probes connect to the Arduino controller board of the SGD-MRT (**Figure 5**). For example, a conductivity probe is mounted at the bottom of the carrier frame to detect the beginning and end of the inundation of the mudflat.

Triggered by the Arduino controller, a measurement cycle begins with the injection of the saline solution (6 cm^3) into the FTU, continuously mixed by a centrifugal pump (**Figure 6**). The TIU is used for this purpose. The conductivity at the inlet and outlet of the FTU, the time stamp, and additional data are measured every second and stored on the SD card.

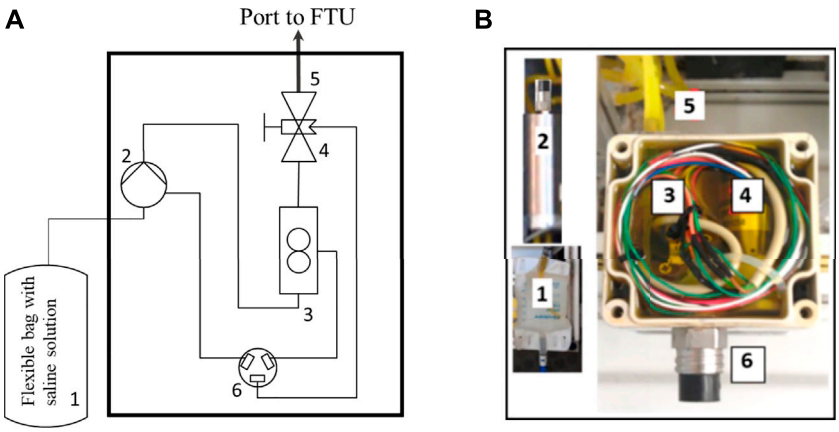


FIGURE 4 | Diagram **(A)** and image **(B)** of the tracer injection unit (TIU, L 10 × W 10 × H 6 cm). The components of the TIU are 1. a flexible bag filled with the saline solution, 2. gear pump, 3. flow sensor, 4. pinch valve, 5. tracer injection port to the FTU, and 6. cable connector to the Arduino controller.

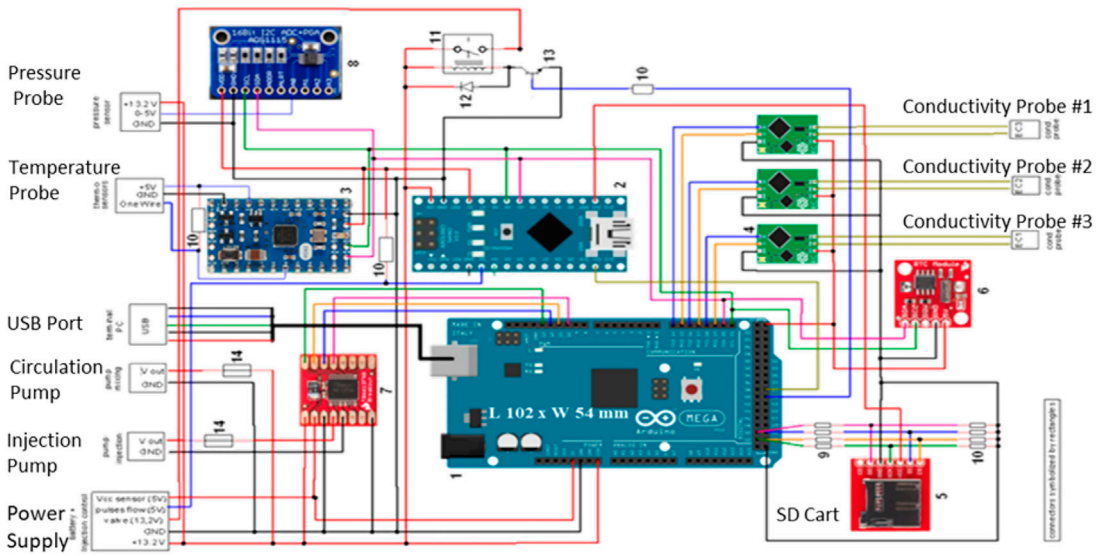


FIGURE 5 | Wiring diagram and electronic components of the SGD-MRT. The list of electronic components and the Arduino shields is part of the **Supplementary Material**.

RESULTS

Laboratory Tests

The suitability of the SGD-MRT for quantifying the volumetric flow of submarine groundwater discharge was tested first in the laboratory. For this purpose, we applied a simplified constant head tank (Graebel, 2001) to assess the relationship between the volume flow-through the FTU and the computed MRT.

The constant head tank is built from a water drain pipe (L 150 cm, OD 11 cm), available in hardware stores. The pipe is mounted vertically on the laboratory bench and sealed at the lower end of the pipe with an end cap. About 5 cm above the lower end cap of the drainpipe, we installed a pipe connector to couple the drainpipe with the inlet of the FTU and the SGD-MRT by a hose. Above the hose connector, at a vertical distance of 5 cm, we drilled a set of holes (ID 6 mm) with a vertical distance of 5 cm into the drainpipe, which rubber plugs can seal.

To achieve a constant hydraulic pressure and volume flow, we installed the drainpipe vertically on the laboratory bench, closed the boreholes with rubber stoppers up to the desired water level, and filled the pipe continuously from above with water from the tap. The water volume flowing into the drainpipe is slightly higher than the water volume leaving the drainpipe at the bottom. The excess water flows out of the open borehole located above those closed by rubber plugs into the laboratory sink. In this way, we

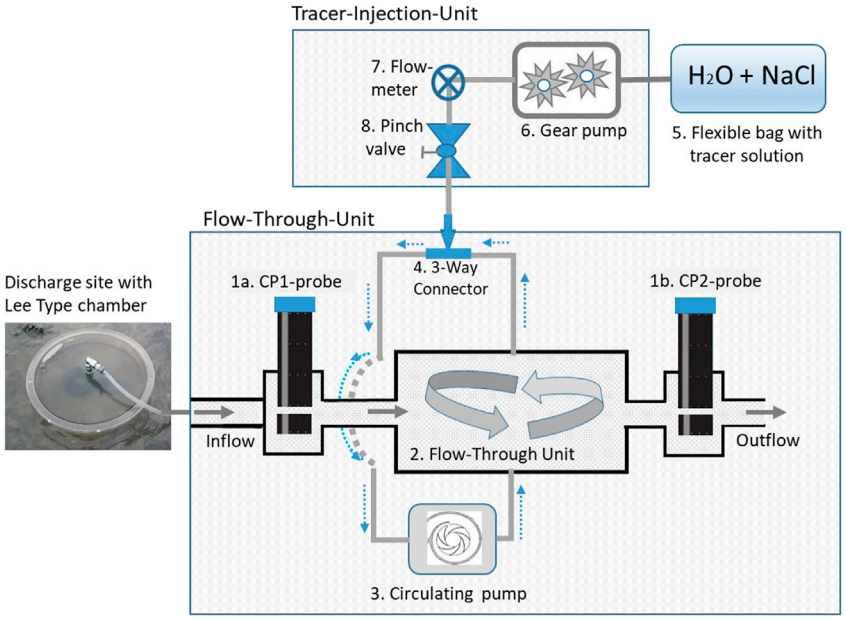


FIGURE 6 | Schematic diagram of the process flow: 1a, b. Conductivity probe at inflow (CP1) and outflow (CP2) of the FTU, 2. Flow-through unit (FTU), 3. Circulating pump, 4. Three-way tube connector for tracer injection by the TIU, 5. Flexible bag holding the tracer solution, 6. Gear pump, 7. Impeller flowmeter, and 8. Pinch valve.

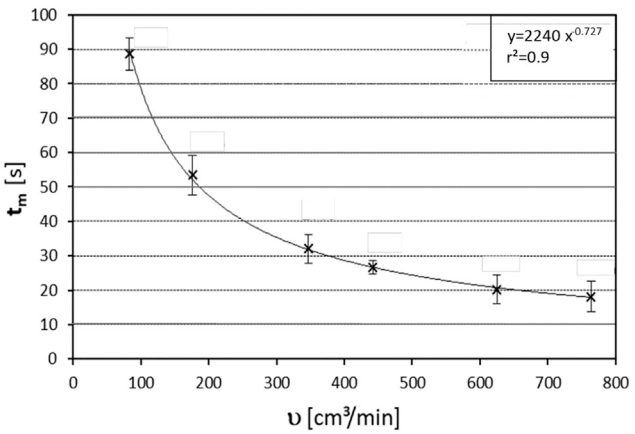


FIGURE 7 | Relationship between the volume flow (υ [cm³/min]) and the mean residence time (tm [s]) quantified by the SGD-MRT. The comparison is considered an independent validation of the mean residence time suitability to quantify volume flows.

created constant volume flows unaffected by pressure fluctuations caused by other faucets in the laboratory. Furthermore, this procedure mimics the free flow mode of fluid discharge.

For quality control of measurements, the lower outlet of the drain pipe connects to the inlet of the FTU by a hose, and the volume flow leaving the FTU is quantified by the SGD-MRT and by application of a volumetric flask and stopwatch. Through this practice, the volume flow of water is measured simultaneously by two independent methods.

Figure 7 shows an example of the relation between the volumetric flow (υ [cm³/s]) measured by the volumetric cylinder and by the MRT (tm [s]) computed by the SGD-MRT. For example, volume flows of about 80 cm³/min to 780 cm³/min are created by the drainpipe and related to the MRTs of the injected tracer of about 18–90 s (**Figure 7**). The correlation coefficient and the repeatability of the measurement – indicated by error bars – confirm the suitability of the SGD-MRT to quantify fluid discharge from sediments. We applied these tests as independent validation for the MRT suitability for quantification of volume flows. It should be mentioned that regression analysis is not obligatory for calculating volume flows by the SGD-MRT.

On-Site Measurements of Fluid Discharge

For the on-site assessment of the SGD-MRT, we deployed the device on the Sahlenburg mudflat on the Elbe-Weser estuary in the southeastern North Sea (**Figure 1**). This study region is characterized by SGD, extending over an area of at least 1.3 × 4.2 km. Discharge rates of more than 400 cm³/min were measured by Lee-type chambers equipped with flexible sampling bags or impeller flowmeters (Kurtz, 2004; Scharf, 2008; Bartsch, 2009).

For on-site measurements, we selected a discharge site located at the GPS position 53°51′10 ”/8°34′56, and flagged it with a pole for later revisiting this site. At this site, the SGD-MRT was deployed on March 23, 2016 (Sahl#1), for about 6:40 h and June 4, 2016 (Sahl#2), for about 8:20 h. During the deployments, the fluid discharge rates were recorded based on a sampling rate of 6 min.

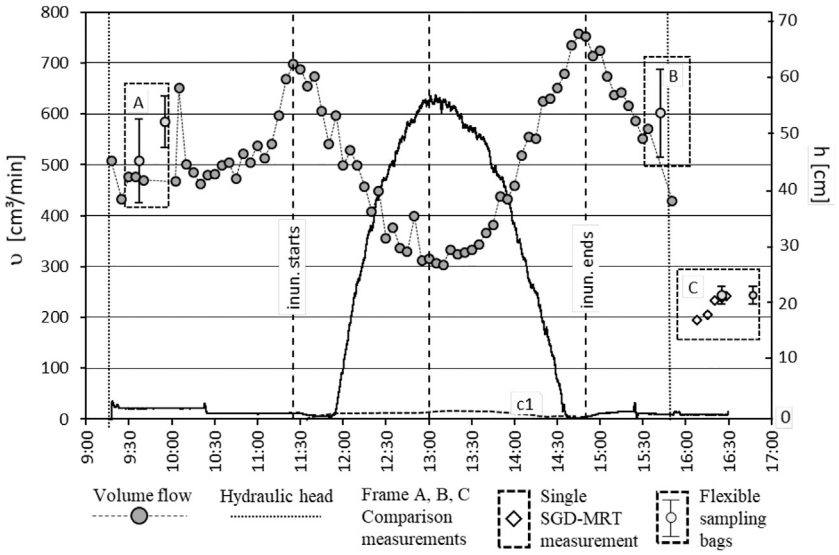


FIGURE 8 | Time series data at *Sahl#1* of fluid discharge rates (cm³/min) and hydraulic head (cm) measured by the SGD-MRT and the salinity inside the benthic chamber (c1, 2.3 mS/cm) recorded by a CDT diver. The data frames A and B compare discharge rates measured by the SGD-MRT and the flexible sampling bags. Frame C compares discharge rates located aside from the main location. Conventional Lee-type seepage meter measurements are indicated by a grey circle with an error bar. The period of the inundation of the discharge site is indicated by inun.starts and inun.ends.

At the beginning of the time series measurement Sahl#l (**Figure 8**), the seepage meter measured discharge rates of about 460–500 cm^3/min for a period of 96 min during low tide (9:18–10:54). In the following period (10:54–11:24), before inundation reaches the sampling site, a considerable increase of volume flow from about 500 cm^3/min to 690 cm^3/min within 35 min is observed.

During the inundation (11:24–13:06), detected by the conductivity probe mounted at the bottom of the carrier frame, discharge rates decrease from about 690 cm^3/min to 310 cm^3/min within 95 min. With the beginning of the ebb tide (13:06–14:48), a considerable increase in discharge rates from 310 cm^3/min to more than 760 cm^3/min in about 100 min is recorded. Subsequently, with the end of the inundation (14:48–15:54), discharge rates lowered to about 420 cm^3/min, a value comparable to the discharge rate measured at the beginning of the time series measurement (**Figure 8**).

For comparison purposes, we measured discharge rates at Sahl#1 at the beginning and end of the time series applying the SGD-MRT and flexible sampling bags (**Figure 8**, frame A and B). This reveals the close comparability of measured volume flows. Additionally, we relocated the Lee-type chamber to a different discharge site in the vicinity, about 5 m aside, of position Sahl#1 to measure discharge rates by the SGD-MRT and flexible sampling bags (**Figure 8**, frame C). The error bars in frames A, B, and C shows the spread of discharge rates measured by flexible sampling bags. This spread is partially caused by the manual unmounting of the SGD-MRT and mounting of flexible bags. Besides pressure fluctuations, the manual handling close to the discharge sites could cause short-term fluctuations of fluid release, which might cause scatter.

We revisited the discharge site for an additional time series study (**Figure 9**) on June 4, 2016 (Sahl#2). At low tide, at the beginning of the measurement (9:30–10:36), the SGD-MRT recorded flow rates of about 350 cm^3/min. Subsequently, during the transition from low tide to flood tide and inundation of the SGD-MRT, a significant increase of fluid discharges from about 350 cm^3/min to 660 cm^3/min was observed (10:36–11:12). During the flood tide (11:12–13:42), the water level rose from about 10 to 74 cm, and discharge rates decreased from about 610 cm^3/min to less than 70 cm^3/min. With the beginning ebb tide, the discharge rate increased to more than 700 cm^3/min within 70 min (13:42–15:54). At the end of the inundation, the fluid discharge lowered and reached a value of approximately 400 cm^3/min (15:54–17:12). In the following period (17:12–18:00), discharge rates were close to those recorded at the beginning of the deployment.

For comparison purposes, the outflow rates were quantified with the SGD-MRT and flexible sampling bags at the beginning and at the end of the time series measurement (**Figures 8**, **9**). Due to the uncoupling and coupling of the flexible bags to the Lee-Type chamber, counter pressures influence the discharge of fluid from the sand boil. Despite these effects, the measurements with flexible bags are close to the discharge rates that were quantified by the time-series measurements of the SGD-MRT.

During the period of 15:45–16:15, the tidal height at the discharge site rose to 74 cm, and the salinity measured by the CTD diver mounted in the benthic chamber increased from approximately 2.9 mS/cm to 5.2 mS/cm and back to 2.9 mS as at the beginning of the ebb (**Figure 9**). The slight increase in salinity in the Lee-Type chamber indicates a small volume of bottom water entering the benthic chamber along with the FTU.

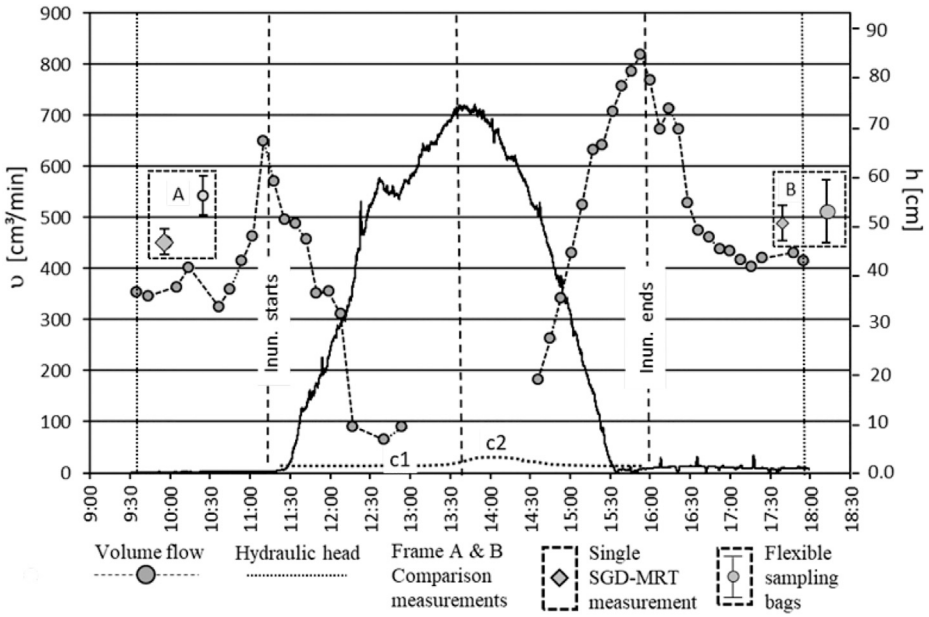


FIGURE 9 | Time series data (*Sahl#2*) of fluid discharge rates (cm³/min), and the hydraulic head (cm) measured by the SGD-MRT and the salinity inside the benthic chamber (c1: 2.9 mS/cm, c2: 5.2 mS/cm) recorded by a CDT diver. In data frames A and B, discharge rates measured with the SGD-MRT and flexible sampling bags compare conventional Lee-type seepage meter measurements indicated by a grey circle with an error bar. The period of the inundation of the discharge site is marked by inun.starts and inun.ends.

DISCUSSION

The main driving forces for the release of groundwater from sediments are hydraulic pressure gradients between the landward aquifer and the intertidal zone or pressure fluctuations caused by tidal cycles. The pressure-driven transport of fluids occurs as a dispersed flow through the pore space of unconsolidated sediment or as conduit flow along pipe-like transport pathways. The latter could cause the formation of boils, discharge sites with intensive release of fluids, or sand boils (**Figure 1B**), areas with an intensive discharge of fluids and washing out of fine-grained particles into bottom waters (Kolb, 1976; Bardet and Kapuskar, 1991; Holzer and Clark, 1993; Li et al., 1996; de Louw et al., 2010; Sassa and Takagawa, 2018). Despite the number of sand boils observed on land or in shallow waters of coastal regions, lakes, or rivers, it appears that discharge rates are rarely quantified to the best of our knowledge.

Sand boils (**Figure 1B**), sites with an intensive fluid discharge are observed in coastal waters, lakes, dams, or polders (de Louw et al., 2010). For example, for landward saline sand boils on a Polder region in the Netherlands, discharge rates of 500–1,000 dm^3/day were quantified by hydrogeological techniques (de Louw et al., 2010; Pauw et al., 2012). In contrast to the onshore sand boils, almost fresh water released from sand boils on the Sahlenburg Mudflat with discharge rates of more.

To account for the broad range of fluid discharges with volume flows of less than 5 cm^3/min to more than 20 cm^3/min and different transport modes like the dispersed or the conduit transport of fluids, numerous techniques have been developed. For the quantification of fluid releases of less than 5 cm^3/min, for example, techniques such as pore water analysis of chloride profiles and calculation of advection rates or methods such as heat pulse injection or dye displacement methods are in use (Vanek, 1993; Schlüter et al., 2004; Seeberg-Elverfeldt et al., 2005; Taniguchi et al., 2007; Koopmans and Berg, 2011; Taniguchi et al., 2019). Quantifying discharge rates of more than 20 cm^3/min, mainly seepage meters are used, comprising a Lee-type chamber and a flexible sampling bag or an automated, self-recording flow sensor. This includes impeller-based flow meters or techniques such as the heat pulse injection, or dye dilution method.

Both the automated dye-dilution based seepage meter and the SGD-MRT apply a tracer injection method, suitable for quantification of discharge rates of more than 60 cm^3/min. For the dye dilution method, an exponential curve fitting routine is required to determine the flow rates based on the absorption measurements recorded by the underwater photometer. Furthermore, concentration of the dye solution needs to be adjusted according to the volume of the dye-mixing chamber to provide a strong initial absorbance signal for the dyed solution without exceeding the linear response (Beer's Law) range of the photometer.

In contrast to most other tracer injection methods, we apply the computation of the Mean Residence Time for quantifying flow rates. A specific flow sensor is not required for this purpose, instead, the concentration-time distribution of the electric conductivity measured at the outflow of the FTU is recorded and analyzed. By this means, the total amount of tracer injected is quantified by numerical integration. This allows analyzing the concentration-time distribution over the entire sampling period

in order to quantify the mean residence time and volume flow of fluids.

For the data derived from deployments Sahl#1 and Sahl#2, we calculated the total amount of water released from the discharge by numerical integration of the measured flow rates. Considering the time-series record of Sahl#1, about 400 dm^3 of water was released from the discharge site within 6:30 h. At Sahl#2 a water volume of about 360 dm^3 was released over a period of 8:30 h. On a daily basis, this suggests an SGD volume of more than 700 dm^3/day released from a discharge site. For groundwater management in coastal regions, boils and sand boils seem to be efficient transport routes between land and sea, which can change the direction of flow depending on the hydraulic pressure conditions.

Process Control and Data Acquisition

Applying the MRT, a designated flow sensor is not required for quantifying discharge rates. Instead, the combination of FTU, tracer injection, conductivity probes, Arduino controller, and the software builds the measuring unit. In addition to these components, differential pressure sensors, temperature probes, or conductivity probes are installed inside the benthic chamber or on the carrier frame and connected to the controller unit (**Figure 5**). These components are used for additional quality control or to extend the scope of the SGD-MRT. Due to this design, the measuring range, the sampling rate, or other settings could be adjusted.

The Arduino controller runs the source code – which is part of the **Supplementary Material** – and manages the process control, data acquisition, or data storage. The sampling rate and other settings could be modified by editing the ini-file stored on the SD card. Furthermore, actuators like an injection pump, differential pressure sensors, temperature probes, or conductivity probes are installed inside the benthic chamber or on the carrier frame and connected to the controller board. By this means, the tidal height, conductivity of fluids, or temperature inside the Lee-type chamber, bottom water, or sediment are recorded. For the time series recording of the tracer concentration at the outflow of the FTU and calculation of the discharge rates, the conductivity in the inlet and outlet of the FTU is measured every second.

Due to the modular concept and the comparatively inexpensive electronic components, Arduino microcontrollers are applied in numerous applications and fields spanning the arts to science or industry. In contrast to terrestrial environmental studies, Arduino or similar microcontrollers seem to have only been used for a few studies on marine or limnology research. An example is the development-inexpensive Arduino-based CDT probe for studies in coastal waters (Lockridge, 2016). Due to the large community of users applying Arduino boards, the modular concept, and the comparatively inexpensive electronic components, these microcontrollers can be easily expanded with SD memory cards, motor controllers, peristaltic pumps for water sampling, or sensors for numerous applications.

The estimated system costs for the SGD-MRT – excluding the CDT diver, pressure housings, and underwater cables – might be about 1,500 €. A re-design concerning the number of pressure housings or cables is feasible (**Figure 5**).

Seawater Fresh Water Ratio

On sampling date Sahl#1, applying a CDT diver, a conductivity of about 2.1 mS/cm was recorded for fluids inside the benthic chamber, and a conductivity of 28.5 mS/cm was recorded for the bottom water aside from the benthic chamber. According to the conductivity ratio calculated, the released fluids comprise more than 93% fresh water.

During the field trials on Sahl#2, the CDT diver mounted at the bottom of the carrier frame recorded a conductivity of 27 mS/cm. Inside the benthic chamber, a conductivity of 2.5 mS/cm was measured for the periods from 9:30 to 12:50 and from 14:30 to 18:00 (**Figure 9**). In the time interval from 12:50 to 14:30, when the hydraulic head exceeded 74 cm, conductivity inside the benthic chamber increased from 2.5 mS/cm to 5.2 mS/cm, indicating a low input of seawater into the benthic chamber. Based on the internal volume of the benthic chamber of around 9 dm^3, a seawater conductivity of 27 mS/cm, and the increase in conductivity inside the benthic chamber from 2.5 to 5.0 mS/cm, the estimated input of seawater into the benthic chamber results in approximately 1.2 dm^3.

The time series data of fluid discharge was interrupted at Sahl#2 on 12:50 at a discharge rate of 97 cm^3/min and continued from 14:40 at a flow rate of about 195 cm^3/min. During this period, the conductivity inside the benthic chamber – measured by the CTD diver – increased from 2.7 mS/cm to 5.1 mS/cm at 14:00 and levels back to the initial conductivity at 14:40 (**Figure 9**). In the following, the measurement of discharge rates steadily continued. As indicated by the slight increase of conductivity of 2.4 mS/cm, related to the bottom water conductivity of 25 mS/cm, only a small volume of seawater might intrude into the benthic chamber.

For more detailed considerations about the data gap, the conductivities measured every second at the inlet and outlet of the FTU were investigated. During the time interval of the data gap, the fluid conductivity inside the FTU varies in a bell-shape mode, from 2.7 mS/cm at 12:50 to 12.2 mS/cm at 13:45 and back to 2.7 mS/cm at 14:45. The increase of conductivity is caused by the TIU, injecting the saline tracer into the FTU every 6 min. Due to the nearly stagnant flow conditions inside the FTU, the conductivity increases and masks the saline tracer and conductivity inside the FTU. With the restart of the fluid discharge from the discharge site, the FTU flushed, and the measurement of discharge rates continue. By modifying the Arduino source code, for example, by adding a feedback loop, this situation can be avoided.

Fluid Discharge From Sand Boils

Sand boils are observed offshore and landward in rivers, lakes, water reservoirs, harbor areas, or low-lying coastal regions. For example, at landward, at polders along the Dutch coastline, numerous sand boils with intense fluid discharge are observed (de Louw et al., 2010). In this region, saline waters with an average chloride concentration of 1,100 mg/L are released from the

landward sand boil, and discharge rates of 500–1,000 dm^3/day are reported.

For the Sahlenburg mudflat, we computed the total volume of water released from the discharge site by numerical integration of the measured flow rates. At the date Sahl#1, a water volume of 400 dm^3 was released from the discharge site within 6:30 h, and during a period of 8:30 h a water volume of 360 dm^3 was released from Sahl#2. On a daily basis, this suggests a SGD of more than 700 dm^3/day. Regarding groundwater management in coastal regions, sand boils seem to be efficient transport routes between land and sea, which can change the direction of flow according to the hydraulic pressure conditions.

CONCLUSION

The motivation for developing SGD-MRT was our demand for an inexpensive and extensible seepage meter suitable for recording time series data of fluid discharge from sand boils. Previous attempts to quantify discharge rates of more than 200 cm^3 were only partially successful. Systems like the scalable SGD-MRT, with a measuring range of up to 700 cm^3/min, might support such objectives.

The modular structure of the SGD-MRT and the use of microcontrollers such as the Arduino offers numerous possibilities for additional applications. In particular, the studies on fluid transport along sand boils connecting the land and coastal waters could support local studies on groundwater management in coastal areas.

DATA AVAILABILITY STATEMENT

The raw data supporting the conclusion of this article will be made available by the authors, without undue reservation.

AUTHOR CONTRIBUTIONS

MS developed the tracer inject method concept and built the first versions of the seepage meter, including the electronics and Arduino software. PM compiled the final version of the SGD-MRT, improved and updated the existing software, and operated the field trials.

ACKNOWLEDGMENTS

We acknowledge the support by the "Wadden Sea World Heritage Center" (Sahlenburg, Germany; https://www.waddensea-worldheritage.org/), the two reviewers, and Henry Bokuniewicz (Stony Brook University) for their very constructive advice.

SUPPLEMENTARY MATERIAL

The Supplementary Material for this article can be found online at: https://www.frontiersin.org/articles/10.3389/feart.2021.710000/full#supplementary-material

REFERENCES

Bardet, J. P., and Kapuskar, M. (1991). *The Liquefaction Sand Boils in the San Francisco Marina District during the 1989 Loma Prieta Earthquake*. Los Angeles, California: Second International Conference on Recent Advances in Geotechnical Earthquake Engineering University of Southern California. Available at: https://scholarsmine.mst.edu/cgi/viewcontent.cgi?article=3629&context=icrageesd.

Bartsch, S. (2009). *Erfassung von Porenwasservariationen in Wattsedimenten und der Einfluss von Grundwasseraustritt im Sahlenburger Watt*. Bremen: Geoscience, FB5, 178.

Bokuniewicz, H. (1980). Groundwater Seepage into Great South Bay, New York. *Estuar. Coast. Mar. Sci.* 10, 437–444. doi:10.1016/S0302-3524(80)80122-8

Bugna, G. C., Chanton, J. P., Cable, J. E., Burnett, W. C., and Cable, P. H. (1996). The Importance of Groundwater Discharge to the Methane Budgets of Nearshore and continental Shelf Waters of the Northeastern Gulf of Mexico. *Geochim. Cosmochim. Acta* 60, 4735–4746. doi:10.1016/s0016-7037(96)00290-6

Burnett, W. C., Aggarwal, P. K., Aureli, A., Bokuniewicz, H., Cable, J. E., Charette, M. A., et al. (2006). Quantifying Submarine Groundwater Discharge in the Coastal Zone via Multiple Methods. *Sci. Total Environ.* 367, 498–543. doi:10.1016/j.scitotenv.2006.05.009

Burnett, W. C., Bokuniewicz, H., Huetel, M., Moore, W. S., and Taniguchi, M. (2003). Groundwater and Pore Water Inputs to the Coastal Zone. *Biogeochemistry* 66, 3–33. doi:10.1023/B:BIOG.0000006066.21240.53

Cable, J. E., Martin, J. B., and Jaeger, J. (2006). Exonerating Bernoulli? on Evaluating the Physical and Biological Processes Affecting marine Seepage Meter Measurements. *Limnol Ocean Methods* 172–183, 4–6. doi:10.4319/lom.2006.4.172

Cherkauer, D. A., and McBride, J. M. (1988). *A Remotely Operated Seepage Meter for Use in Large Lakes and Rivers*. Westerville, Ohio, USA: Ground Water, 165–171. doi:10.1111/j.1745-6584.1988.tb00379.x

Clark, M. M. (1996). *Transport Modelling for Environmental Engineers and Scientists*. Wiley-Interscience, 559.

Danckwerts, P. V. (1953). Continuous Flow Systems: Distribution of Residence Times. *Chem. Eng. Sci.* 2, 1–13. doi:10.1016/0009-2509(53)80001-1

de Louw, P. G. B., Essink, O. G. H. P., Stuyfzand, P. J., and van der Zee, S. E. A. T. M. (2010). Upward Groundwater Flow in Boils as the Dominant Mechanism of Salinization in Deep Polders, *The Netherlands*. *J. Hydrol.* 394, 494–506. doi:10.1016/j.jhydrol.2010.10.009

Duque, C., Russoniello, C. J., and Rosenberry, D. O. (2020). History and Evolution of Seepage Meters for Quantifying Flow between Groundwater and Surface Water: Part 2 – Marine Settings and Submarine Groundwater Discharge. *Earth-Science Rev.* 204, 1. doi:10.1016/j.earscirev.2020.103168

Fogler, S. (2006). *Elements of Chemical Reaction Engineering*. 3. ed. Hoboken, New Jersey, USA: Prentice-Hall.

Graebel, W. P. (2001). *Engineering Fluid Mechanics*. Taylor & Francis, 675.

Holzer, T. L., and Clark, M. M. (1993). Sand Boils without Earthquakes. *Geology* 21 (10), 873–876. doi:10.1130/0091-7613(1993)021<0873:sbwe>2.3.co;2

Johannes, R. E. (1980). The Ecological Significance of Submarine Discharge of Groundwater. *Mar. Ecol.* 3, 365–373. doi:10.3354/meps003365

Judd, A., and Hovland, M. (2009). *Seabed Fluid Flow*. Cambridge University Press. doi:10.1017/CBO9780511535918

Kolb, C. R. (1976). "Geologic Control of Sand Boils along Mississippi River Levees," in *Geomorphology and Engineering: Stroudsburg*. Editor D. R. Coates (Pennsylvania: Halstead Press), 99–114. Available at: https://erdc-library.erdc.dren.mil/jspui/bitstream/11681/20960/1/MP-S-75-22.pdf.

Koopmans, D., and Berg, P. (2011). An Alternative to Traditional Seepage Meters: Dye Displacement. *Water Resour. Res.* 47, W01506. doi:10.1029/2010WR009113

Kurtz, S. (2004). *Grundwasseraustrittsstellen im Sahlenburger Watt: Methoden zur Beprobung von Fluiden und Bilanzierung des Grundwasserausstroms*. Bremen: Univ. Bremen, FB5.

Lee, D. R. (1977). A Device for Measuring Seepage Flux in Lakes and Estuaries. *Limnol.Oceanogr.* 22, 140–147. doi:10.4319/lo.1977.22.1.0140

Levenspiel, O. (1999). *Chemical Reaction Engineering*. Wiley, 668p. 0-471-25424-X.

Li, Y., Craven, J., Schweig, E. S., and Obermeier, S. F. (1996). Sand Boils Induced by the 1993 Mississippi River Flood: Could They One Day Be Misinterpreted as Earthquake-Induced Liquefaction? *Geology* 24, 171–174. doi:10.1130/0091-7613(1996)024<0171:sbibtm>2.3.co;2

Lockridge (2016). Development of a Low-Cost Arduino-Based Sonde for Coastal Applications. *Sensors* 16, 528. doi:10.3390/s16040528

Martin, J. B., Thomas, R. G., and Hartl, M. K. (2004). An Inexpensive, Automatic, Submersible Water Sampler. *Limnol. Oceanogr. Methods* 2, 398–405. doi:10.4319/lom.2004.2.398

Moore, W. S. (1996). Large Groundwater Inputs to Coastal Waters Revealed by 226Ra Enrichments. *Nature* 380, 612–614. doi:10.1038/380612a0

Moore, W. S. (1999). The Subterranean Estuary: a Reaction Zone of Ground Water and Seawater. *Mar. Chem.* 65, 111–125. doi:10.1016/S0304-4203(99)00014-6

Murdoch, L. C., and Kelly, S. E. (2003). Factors Affecting the Performance of Conventional Seepage Meters. *Water Resour. Res.* 39, 1. doi:10.1029/2002WR001347

Pauw, P., de Louw, P. G. B., and Oude Essink, G. H. P. (2012). Groundwater Salinisation in the Wadden Sea Area of the Netherlands: Quantifying the Effects of Climate Change, Sea-Level Rise and Anthropogenic Interferences. *Neth. J. Geosciences* 91, 373–383. doi:10.1017/s0016774600000500

Povinec, P. P., Burnett, W. C., Beck, A., Bokuniewiczc, H., Charette, M., Gonneead, M. E., et al. (2012). Isotopic, Geophysical and Biogeochemical Investigation of Submarine Groundwater Discharge: IAEA-UNESCO Intercomparison Exercise at Mauritius Island. *J. Environ. Radioactivity* 104, 24–45. doi:10.1016/j.jenvrad.2011.09.009

Rocha, C., Ibanhez, J. B., and Leote, C. (2009). Benthic Nitrate Biogeochemistry Affected by Tidal Modulation of Submarine Groundwater Discharge (SGD) through a sandy beach Face, Ria Formosa, Southwestern Iberia. *Mar. Chem.* 115, 43–58. doi:10.1016/j.marchem.2009.06.003

Rosenberry, D. O. (2008). A Seepage Meter Designed for Use in Flowing Water. *J. Hydrol.* 359 (1–2), 118–130. doi:10.1016/j.jhydrol.2008.06.029

Rosenberry, D. O., Duque, C., and Lee, D. R. (2020). History and Evolution of Seepage Meters for Quantifying Flow between Groundwater and Surface Water: Part 1 – Freshwater Settings. *Earth-Science Rev.* 204, 1. doi:10.1016/j.earscirev.2020.103167

Santos, I. R., Burnett, W. C., Chanton, J., Dimova, N., and Peterson, R. N. (2009). Land or Ocean?: Assessing the Driving Forces of Submarine Groundwater Discharge at a Coastal Site in the Gulf of Mexico. *J. Geophys. Res.* 114, 2156–2202. doi:10.1029/2008JC005038

Sassa, S., and Takagawa, T. (2018). "Liquefied Gravity Flow-Induced Tsunami: First Evidence and Comparison from the 2018 Lndonesia Sulawesi Earthquake and Tsunami Disasters," in *News/Kyoto Commitment. Ministry of Land, Infrastructure, Transport and Tourism (MLIT)* (Japan: MLIT). doi:10.1007/s10346-018-1114-x

Scharf, F. (2008). *Der Grundwasseraustritt im Sahlenburger Watt bei Cuxhaven: Datenerhebung und GIS-basierte Untersuchung der Ursachen und Charakteristiken*. Bremen: Uni. Bremen, Geoscience, FB5, 137 p.

Schlüter, M., SauterAndersen, E. J. C. E., Dahlgaard, H., and Dando, P. R. (2004). Spatial Distribution and Budget for Submarine Groundwater Discharge in Eckernfoerde Bay (Western Baltic Sea). *Limnol. Oceanogr.* 49 (1), 157–167. doi:10.4319/lo.2004.49.1.0157

Seeberg-Elverfeldt, J., Schlüter, M., Feseker, T., and Kölling, M. (2005). Rhizon Sampling of Porewaters Near the Sediment-Water Interface of Aquatic Systems. *Limnol. Oceanogr Methods* 3, 361–371. doi:10.4319/lom.2005.3.361

Shaw, R. D., and Prepas, E. E. (1990). Groundwater-lake Interactions: I. Accuracy of Seepage Meter Estimates of lake Seepage. *J. Hydrol.* 119 (1–4), 105–120. doi:10.1016/0022-1694(90)90037-X

Sholkovitz, E. R., Herbold, C. W., and Charette, M. A. (2003). An Automated Dye-Dilution Based Seepage Meter for the Time-Series Measurement of Submarine Groundwater Discharge. *Limnol. Oceanogr. Methods* 1, 16–28. doi:10.4319/lom.2011.1.16

Simmons, G. M. (1992). Importance of Submarine Groundwater Discharge (SGWD) and Seawater Cycling to Material Flux across Sediment/water Interfaces in marine Environments. *Mar. Ecol. Prog. Ser.* 84, 173–184. doi:10.3354/meps084173

Solomon, D. K., Humphrey, E., Gilmore, T. E., Genereux, D. P., and Zlotnik, V. (2020). An Automated Seepage Meter for Streams and Lakes. *Water Resour. Res.* 1, 1–11. doi:10.1029/2019WR026983

Taniguchi, M., Dulai, H., Burnett, K. M., Santos, I. R., Sugimoto, R., Stieglitz, T., et al. (2019). *Submarine Groundwater Discharge: Updates on its Measurement Techniques, Geophysical Drivers, Magnitudes, and Effects*. Westerville, Ohio, USA: Frontiers in Environmental Science. doi:10.3389/fenvs.2019.00141

Taniguchi, M., and Fukuo, Y. (1993). Continuous Measurements of Groundwater Seepage Using an Automatic Seepage Meter. *Groundwater* 31, 675–679. doi:10.1111/j.1745-6584.1993.tb00601.x

Taniguchi, M., Ishitobi, T., Burnett, W. C., and Wattayakorn, G. (2007). Evaluating Ground Water-Sea Water Interactions via Resistivity and Seepage Meters. *Ground Water* 45 (6), 729–735. doi:10.1111/j.1745-6584.2007.00343.x

Vanek, V. (1993). Groundwater Regime of a Tidally Influenced Coastal Pond. *J. Hydrol.* 151 (2-4), 317–342. doi:10.1016/0022-1694(93)90241-z

Zektzer, I. S., Ivanov, V. A., and Meskheteli, A. V. (1973). The Problem of Direct Groundwater Discharge to the Seas. *J. Hydrol.* 20, 1–36. doi:10.1016/0022-1694(73)90042-5

Zimmermann, C. F., Montgomery, J. R., and Carlson, P. R. (1985). Variability of Dissolved Reactive Phosphate Flux Rates in Nearshore Estuarine Sediments: Effects of Groundwater Flow. *Estuaries* 8, 228–236. doi:10.2307/1352203

Conflict of Interest: The authors declare that the research was conducted in the absence of any commercial or financial relationships that could be construed as a potential conflict of interest.

Publisher's Note: All claims expressed in this article are solely those of the authors and do not necessarily represent those of their affiliated organizations, or those of the publisher, the editors and the reviewers. Any product that may be evaluated in this article, or claim that may be made by its manufacturer, is not guaranteed or endorsed by the publisher.

Copyright © 2021 Schlüter and Maier. This is an open-access article distributed under the terms of the Creative Commons Attribution License (CC BY). The use, distribution or reproduction in other forums is permitted, provided the original author(s) and the copyright owner(s) are credited and that the original publication in this journal is cited, in accordance with accepted academic practice. No use, distribution or reproduction is permitted which does not comply with these terms.

frontiers in Environmental Science

ORIGINAL RESEARCH
published: 22 April 2021
doi: 10.3389/fenvs.2021.600955

Mixed-Convective Processes Within Seafloor Sediments Arising From Fresh Groundwater Discharge

S. C. Solórzano-Rivas[1], Adrian D. Werner[1] and Dylan J. Irvine[2]*

[1] College of Science and Engineering and National Centre for Groundwater Research and Training, Flinders University, Adelaide, SA, Australia, [2] Research Institute for Environment and Livelihoods, College of Engineering, IT and Environment, Charles Darwin University, Casuarina, NT, Australia

The dependence of near-shore ecosystems on the freshwater component of submarine groundwater discharge (SFGD) is well recognized. Previous studies of SFGD have typically assumed that SFGD occurs through aquitards that are in direct contact with seawater. These studies provide no guidance on the distribution of freshwater discharge to the seafloor where SFGD occurs through sandy sediments, even though in most situations, seabed sediments are permeable. We find that SFGD may occur in unconfined, seafloor sediments as density-driven flow in the form of fingers, or otherwise, diffusive freshwater discharge is also possible. Unstable, buoyancy-driven flow within seabed sediments follows similar patterns (except inverted) to the downward free convection of unstable (dense over less-dense groundwater) situations. Consequently, the same theoretical controlling factors as those developed for downward mixed-convective flow are expected to apply. Although, there are important differences, in particular the boundary conditions, between subsea freshwater-seawater interactions and previous mixed-convective problems. Simplified numerical experiments in SEAWAT indicate that the behavior of fresh buoyant plumes depends on the aquifer lower boundary, which in turn controls the rate and pattern of SFGD to the seafloor. This article provides an important initial step in the understanding of SFGD behavior in regions of sandy seafloor sediments and analyses for the first time the mixed-convective processes that occur when freshwater rises into an otherwise saline groundwater body.

Keywords: submarine fresh groundwater discharge, coastal aquifer, free convection, mixed convection, Rayleigh number

OPEN ACCESS

Edited by:
Clare Robinson,
Western University, Canada

Reviewed by:
Reza Soltanian,
University of Cincinnati, United States
James Heiss,
University of Massachusetts Lowell, United States

****Correspondence:***
S. C. Solórzano-Rivas
cristina.solorzano@flinders.edu.au

Specialty section:
This article was submitted to Freshwater Science, a section of the journal Frontiers in Environmental Science

Received: *01 September 2020*
Accepted: *19 March 2021*
Published: *22 April 2021*

Citation:
Solórzano-Rivas SC, Werner AD and Irvine DJ (2021) Mixed-Convective Processes Within Seafloor Sediments Arising From Fresh Groundwater Discharge. Front. Environ. Sci. 9:600955. doi: 10.3389/fenvs.2021.600955

INTRODUCTION

Subsea fresh groundwater discharge (SFGD) is the release of freshwater from seafloor sediments, and has been identified as an important means to transport dissolved nutrients to the ocean, thereby having a significant influence on marine ecology and benthic organisms (e.g., Johannes, 1980; Moore, 1999). Knowledge of the salinity patterns in subsea sediments is important for several reasons, including for the understanding of benthic ecosystems in regions of SFGD, and for the design of SFGD measurement approaches. The distribution of groundwater discharge to the sea depends on the characteristics of geological formations. Fresh groundwater discharge to intertidal zones is often associated with unconfined aquifers, whereas SFGD, occurring beyond the intertidal zone, typically requires low-permeability confining units that act to limit freshwater-seawater

mixing that would otherwise occur near the shoreline (e.g., Jiao et al., 2015; Michael et al., 2016). Predictions of the extent of subsea fresh groundwater typically assume that the low-permeability layers that preserve freshwater and allow SFGD to occur are in direct contact with seawater (e.g., Kooi and Groen, 2001; Bakker et al., 2017; Solórzano-Rivas and Werner, 2018; Werner and Robinson, 2018; Solórzano-Rivas et al., 2019). However, the seafloor more often comprises high-permeability sediments (>50% of the global shelf sediments have high permeability; Riedl et al., 1972). Yet, this configuration has not been widely considered in studies of SFGD.

The occurrence of freshwater in high-permeability sediments overlain by seawater, as occurs when SFGD passes through permeable seafloor sediments, creates a mixed-convective condition. That is, flow processes are expected to be controlled by both buoyancy-driven flow (i.e., free convection) driven by water density differences and hydraulic-driven flow (i.e., forced convection) arising from groundwater heads in subsea sediments that exceed those of the sea. Thus, solute distributions in subsea aquifers may resemble those of other mixed-convective situations. However, studies of mixed-convective or free-convective processes where buoyancy is created by salinity gradients usually involve descending plumes of higher-density fluid that contaminate underlying lower-density groundwater (e.g., Webster et al., 1996; Smith and Turner, 2001; Stevens et al., 2009; Xie et al., 2011). Conversely, the upward movement of lower-density groundwater (e.g., as expected to arise during SFGD) is rarely explored in the solute transport context, although upward, buoyancy-driven groundwater flow has received significant attention in the field of heat transport and geothermal phenomena. For example, Kurylyk et al. (2018) utilized temperature-based methods to quantify submarine groundwater fluxes in seafloor sediments offshore of eastern Canada. However, their study suggested that the flow patterns inferred from seafloor temperature-depth profiles appear to be influenced by both density-driven and geothermal processes.

Perhaps the most pertinent prior investigation of mixed-convective transport accompanying SFGD is that of Moore and Wilson (2005), who were perhaps the first to recognize that SFGD may be driven by upward buoyancy forces. Based on temperature measurements of subsea groundwater (1.5 m below the seabed), Moore and Wilson (2005) interpreted that a sudden drop in the ocean temperature produced upward motion of warmer (i.e., less dense) groundwater to the ocean. However, previous research offers little guidance on the characteristics of free-convective or mixed-convective flow within seafloor sediments. In particular, whether mixed-convective flow within seafloor sediments can be characterized according to buoyancy theory developed for other unstable, solute transport conditions (e.g., leading to downward-moving fingers of higher density; e.g., Wooding et al., 1997) is unclear. This includes the application of several dimensionless variables that are used to categorize mixed-convective problems (e.g., Wooding et al., 1997; Simmons et al., 2010). Additionally, to our knowledge, no quantitative evaluation of mixed convection driven by the upward movement of lower-salinity groundwater has been reported in the literature. Rather, upward convection of lower-density groundwater has only been explored where buoyancy is created by temperature gradients (e.g., Irvine et al., 2015).

The aim of this study is to undertake a review of the existing buoyant theory, including non-dimensional numbers used to characterize mixed-convective flow, and explore whether this theory can be applied to SFGD through high-permeability seafloor sediments. A small number of highly idealized numerical simulations are used to provide an initial demonstration of freshwater-seawater mixing accompanying the rise of fresh buoyant plumes through permeable seafloor sediments. We expect that the upward movement of less-dense groundwater will show similar, albeit inverted, characteristics (e.g., buoyancy-driven fingers of freshwater) to the downward movement of more dense saltwater that has been comprehensively assessed in numerous prior investigations.

CONCEPTUAL MODEL

Two hypothetical conceptual models of SFGD are considered, both of which involve freshwater-seawater mixing within high-permeability, seabed sediments, as shown in **Figure 1**. Model A represents the situation where the seafloor sediments are underlain by a higher-permeability freshwater source, whereas Model B involves underlying sediments of lower permeability (i.e., an aquitard). The former is intended to reflect the situation of SFGD where an underlying aquifer sub-crops to the seafloor and is overlain by sand, while the latter represents SFGD passing through a leaky aquitard into more permeable seafloor sediments.

An important unknown for the conceptual models considered here is the distribution of freshwater within the seafloor sediments. While **Figure 1** shows buoyant freshwater plumes that take the shape of fingers, similar to classic unstable flow patterns for downward free convection, freshwater-seawater mixing may alternatively be dominated by dispersive process (at least theoretically), leading to different salinity patterns to those represented in **Figure 1**. Most field studies of SFGD adopt methods that assume that SFGD occurs in a distributed form (i.e., presuming dispersive freshwater-seawater mixing in seafloor sediments), with devices located on the seafloor (i.e., seepage meters) in regular grid patterns (e.g., Taniguchi et al., 2003; Michael et al., 2005; Kurylyk et al., 2018). However, the buoyant freshwater plumes that are hypothesized here (**Figure 1**) may require alternative measurement strategies. For example, the spacing between, and size of, freshwater plumes, should they occur, may influence the deployment of seepage meters.

Although freshwater plumes within seafloor sediments are expected to behave similarly to the well-studied downward-moving saltwater plumes of prior studies (e.g., Xie et al., 2011), there are important differences between the conceptual model of **Figure 1** and previous analyses of downward-moving plumes. Consider for example, the Elder problem (e.g., Elder et al., 2017), which was transformed to free-convective solute motion by Voss and Souza (1987), and is a common benchmarking problem for assessing numerical models. Various modifications of the Elder problem have occurred to explore other aspects of free convection problems. For example, Xie et al. (2010) introduced mechanical

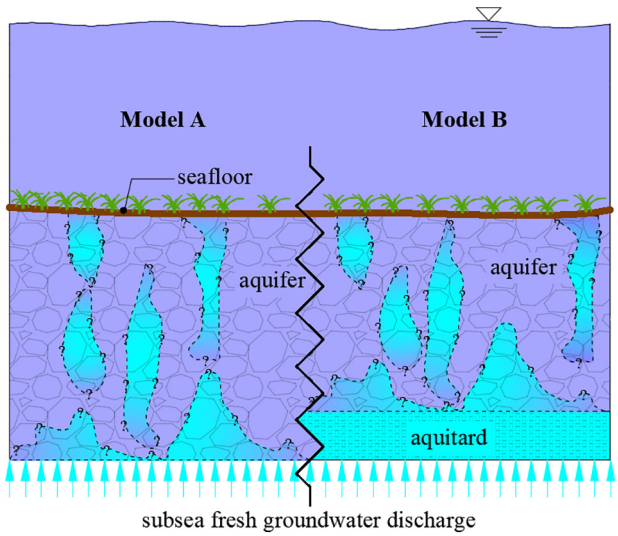


FIGURE 1 | Two conceptual models of a subsea unconfined aquifer subject to SFGD. Blue is freshwater, and purple is seawater. Model A (left) involves sandy sediments overlying a subcropping, higher-permeability aquifer, and Model B represents an aquitard overlain by sand.

dispersion and changed the lower boundary condition to represent more realistic conditions, similar to the approach of Post and Kooi (2003). The conceptual model applied to SFGD (**Figure 1**) is, conceptually at least, an "inverse" of the solute-based Elder problem, where the aquifer is initially seawater-filled and a source of constant freshwater is introduced at the bottom boundary. The initial seawater conditions in the aquifer allow for the transience of salinization to be observed. However, the boundary conditions differ to those of the Elder problem to improve the representation of the expected SFGD process. That is, specified-head boundaries are imposed at the top (seawater) and the bottom (freshwater), whereas the Elder problem uses no-flow boundary conditions at all edges and specified hydraulic heads at the top corners (e.g., Guo and Langevin, 2002). Thus, the behavior of SFGD within seafloor sediments, under the conditions presented in **Figure 1**, cannot be inferred from previous studies. Further details of numerical models are provided in section "Numerical Simulation of SFGD."

REVIEW OF MIXED-DENSITY NON-DIMENSIONAL NUMBERS APPLICABLE TO SFGD THROUGH SEAFLOOR SANDY SEDIMENTS

The characterization of buoyancy-induced flow associated with unstable systems has been the subject of extensive research. One the most common non-dimensional numbers applied for this purpose is the Rayleigh number (*Ra*) (e.g., Simmons et al., 2010). *Ra* is the ratio between buoyancy forces (inducing instabilities in the form of solute fingers) and dispersion forces (tending to resist the formation of unstable solute fingers). When freshwater and seawater interact, *Ra* can be defined as (e.g., Post and Kooi, 2003):

$$Ra = \frac{K\Delta\rho H}{\rho_f D} \quad (1)$$

where K is the aquifer hydraulic conductivity (L T^{-1}), $\Delta\rho$ is the difference between the seawater (ρ_s) and freshwater (ρ_f) densities (M L^{-3}), H is the aquifer thickness (L), and D is hydrodynamic dispersion (L^2 T^{-1}). D is equal to the sum of molecular diffusion [D_0, (L^2 T^{-1})] and mechanical dispersion, which is often simplified to $\alpha_L v_L$, where α_L is the longitudinal dispersivity (L) and v_L the advective flow velocity (L T^{-1}) (i.e., transverse dispersivity, α_T, is often neglected).

There are several alternative *Ra* formulations that have been reported in the literature. For example, some studies have presumed that D consists only of D_0, with mechanical dispersion neglected (e.g., Post and Kooi, 2003; Stevens et al., 2009; Simmons et al., 2010; Xie et al., 2011). These cases involve only free convection, i.e., hydraulic-driven convection is not considered. Alternative expressions for *Ra* have been developed for mixed-convection processes. For example, in mixed- convective problems examined by Simmons and Narayan (1997) and Smith and Turner (2001), both mechanical dispersion and molecular diffusion were included in their definitions of D. However, Simmons and Narayan (1997) adopted α_T and Smith and Turner (2001) adopted α_L in defining D. This study adopts the Smith and Turner (2001) definition of D.

The value of *Ra* has been used to predict the occurrence of unstable solute motion, typically in the form of solute fingers (e.g., Wooding et al., 1997). The critical *Ra* is defined as the threshold value at which buoyancy forces overcome dispersion forces that inhibit finger formation. This threshold value differs depending on conditions in which free convection occurs. For example, in the case of free convection in hydrogeological settings, Stevens et al. (2009) and Moore and Wilson (2005) refer to the critical *Ra* of $4\pi^2$ (i.e., for the appearance of solute fingers) reported by Lapwood (1948) for temperature gradients in porous media. However, alternative critical *Ra* values are offered by other authors for free convection problems. According to van Reeuwijk et al. (2009), the historical incongruency in critical *Ra* estimates is related to such aspects as the numerical approach, governing equations, and slight differences in the initial conditions. They suggest that the critical *Ra* for free convection involving solutes is zero (in other words, solute fingers form without the need for a "dispersive boundary layer"; see below).

Applications of *Ra* theory to mixed-convective processes include the study of Simmons and Narayan (1997), who imposed linearly varying hydraulic heads across the top boundary, to induce lateral flow (i.e., flow parallel to the solute source boundary). The transverse dispersion created by this lateral flow was incorporated into the stabilizing dispersive force in assessing the critical *Ra*. By incorporating $\alpha_T v_L$ in D, Simmons and Narayan (1997) include forced convection (i.e., v_L) in the definition of *Ra*. They found that the critical *Ra* ranged between 300 and 500 under these conditions. Smith and Turner (2001) considered a somewhat similar situation to that

of Simmons and Narayan (1997), except fresh groundwater discharged to the upper solute boundary condition (i.e., the estuary) in Smith and Turner's (2001) analysis of estuary-aquifer interaction. They obtained a critical *Ra* value of 5 for the onset of finger development. Solórzano-Rivas and Werner (2018) adopted the Smith and Turner (2001) formulation for the analysis of freshwater discharge through subsea aquifers, and found a critical *Ra* of about 2 for the salinization of submarine aquitards overlying fresh offshore aquifers. The application of *Ra* to mixed-convection problems introduces challenges in establishing general values for the critical *Ra*, given differences in the representation of forced convection in defining *Ra* across the abovementioned studies.

Wooding et al. (1997) analyzed the development of boundary layers within mixed-convective flow systems (i.e., where freshwater flows upwards towards a saltwater boundary). They derived an expression for the steady-state boundary layer thickness, δ (L), defined as the thickness of solute formed (by dispersion) in the presence of upward freshwater flow, q_z (L T^{-1}), as:

$$\delta = \frac{D_0}{q_z} \tag{2}$$

Wooding et al. (1997) combined **Equations 1** and **2**, by equating H to δ (i.e., conceptually, this is the case where the boundary layer encompasses the entire aquifer thickness), to define a boundary-layer Rayleigh number, Ra_δ, namely:

$$Ra_\delta = \frac{K\Delta\rho\delta}{\rho_f D} \tag{3}$$

The thickness of δ that leads to the onset of unstable solute fingers defines the critical Ra_δ. Wooding et al. (1997) undertook laboratory experiments using a Hele-Shaw cell to determine the critical Ra_δ, including different rates of lateral inflow at the right boundary and vertical outflow to the top, and using various inclination angles of the cell. They also performed numerical experiments that reproduced the two-dimensional flow and solute transport behavior observed in the Hele-Shaw experiment. From the laboratory and numerical experiments, they found Ra_δ values between 8.9 and 9.8, concluding that a good estimate for the critical Ra_δ is approximately 10.

Another widely used non-dimensional parameter for the characterization of mixed-convective processes is the mixed convection ratio (M). M describes the relationship between buoyancy-driven forces and hydraulic-driven forces as (e.g., Simmons et al., 2010):

$$M = \frac{\left(\frac{\Delta\rho}{\rho_f}\right)}{\left(\frac{\Delta h}{\Delta l}\right)} \tag{4}$$

where $\frac{\Delta h}{\Delta l}$ (-) is the hydraulic gradient over a distance Δl. An alternative expression for M, through substitution of Darcy's Law, is given by Smith (2004), as:

$$M = \frac{K\Delta\rho}{\rho_f q_z} \tag{5}$$

By combining **Equations 2** and **3**, it is apparent that Ra_δ and the formulation for M given in **Equation 5** are the same, i.e., $M = Ra_\delta$. Surprisingly, this has not been reported previously to the authors' knowledge. The implications of this are that critical values for Ra_δ also apply to M. However, there is no evidence that the equilibrium value of M = 1 suggested by Simmons et al. (2010) (whereby if M is larger than 1 the problem is said to be free-convection dominated, and forced convection is thought to be the dominant process if M is less than 1) has application in terms of Ra_δ. That is, Ra_δ = 1 has not been reported as a significant value previously. It follows that the onset of instabilities is not predictable through comparison of free and forced convective forces (i.e., through the use of M), as expected given the role that dispersion plays in instability initiation. Nevertheless, Stevens et al. (2009) applied M to the assessment of the occurrence of unstable solute fingering processes that accompany free convection on Padre Island (United States). The site experiences intense evaporation rates and shallow water table conditions, creating large density gradients and low horizontal hydraulic gradients. They found values of M, based on application of **Equation 4**, that were much larger than 1 (i.e., by one and two orders of magnitude), although numerical values of M were not reported. Stevens et al. (2009) interpreted unstable flow structures from resistivity surveys, although these were difficult to conclusively establish. Thus, the application of M to the prediction of unstable fingering remains unproven.

NUMERICAL SIMULATION OF SFGD

Here, the conceptual models illustrated in **Figure 1** are adopted, except the situation is assessed whereby the sandy seafloor sediments are presumed to be originally filled with seawater. Numerical modeling, using SEAWAT (governing equations are found in Guo and Langevin, 2002; not repeated here for brevity), was used to assess two simple situations of SFGD through sandy seafloor sediments. The two cases (Models A and B; see **Figure 2**) involve contrasting mixed-convective forces arising from the inclusion or omission of an underlying aquitard. This is reflected in the corresponding values of *Ra* and Ra_δ, which are reported for each case and compared to previously reported critical values (Wooding et al., 1997; Smith and Turner, 2001) in section "Review of Mixed-Density Non-dimensional Numbers Applicable to SFGD Through Seafloor Sandy Sediments." The calculation of *Ra* and M for Model B does not include the aquitard thickness (i.e., only H is regarded as per the **Equation 1** definition).

Figure 2 is a simplified section showing two possible configurations of a subsea aquifer subjected to SFGD, which is homogeneous, isotropic, and of length L (L) and thickness H (L). The upper boundary represents seawater immediately above the seafloor, simulated by a high hydraulic conductivity (i.e., 100,000 m/d) and a specified-head condition equal to z_s, assigned to the top row of the model. SEAWAT converts z_s to a constant pressure (Langevin et al., 2008) reflecting the column of overlying seawater, of density ρ_s. The solute concentration condition in this top layer depends on the flow direction,

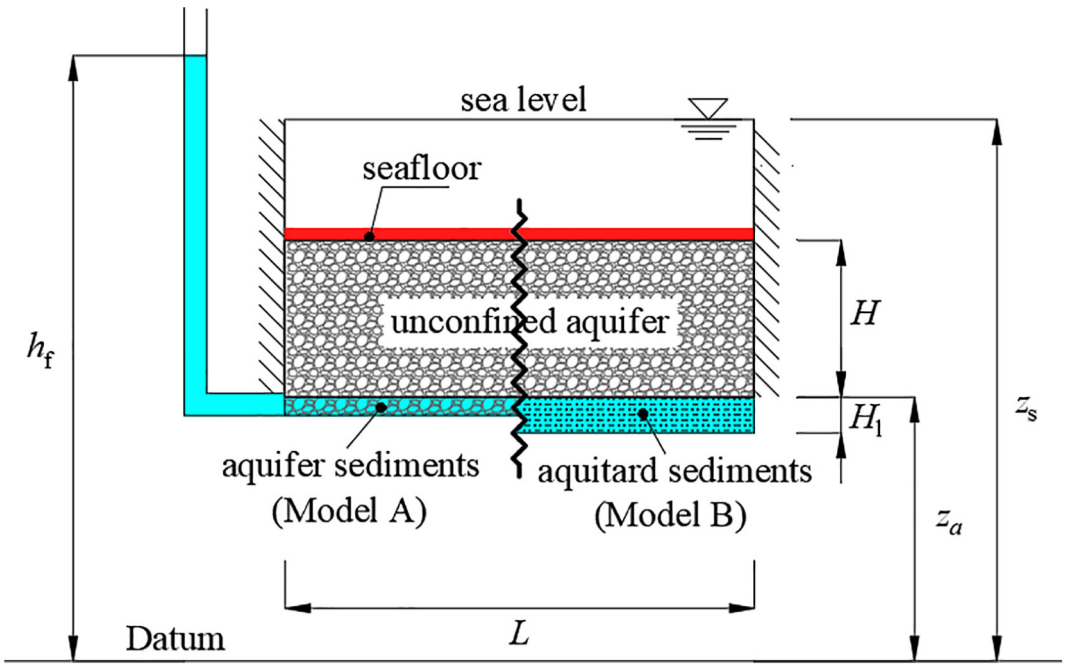


FIGURE 2 | Conceptual models for the numerical implementation of SFGD through an unconfined subsea aquifer, where the left side shows sandy sediments overlying a subcropping, higher-permeability aquifer, and Model B represents an aquitard overlain by sand. Red and blue represent seawater and freshwater boundary conditions, respectively. The equivalent freshwater head at the base of the aquifer, when the aquifer is seawater-filled (i.e., the initial condition), is shown as h_f.

whereby seawater concentration (i.e., solute concentration = 1) was assigned to any inflowing water, whereas discharge to the sea occurs at the ambient groundwater concentration. This type of solute concentration condition avoids salt accumulation at the boundary in an unrealistic manner (i.e., upstream dispersion; Irvine et al., 2021) and is consistent with the approach of Solórzano-Rivas and Werner (2018). The lower freshwater boundary condition differs between Models A and B. In Model A, the lower boundary reflects a situation where an underlying layer of higher permeability occurs, containing freshwater. That is, there is no restriction to the entry of freshwater through the lower boundary of Model A, represented by a specified-head condition equal to h_f, which was converted to a constant pressure (by SEAWAT) based on a water density of ρ_f, as shown in **Figure 2**. In Model B, the lower boundary is composed of lower-permeability sediments (i.e., reflecting aquitard material) of thickness H_L, with the specified head h_f imposed on the bottom row of the model (i.e., the base of the aquitard). The solute concentration of the lower boundary for both Models A and B was set to freshwater (i.e., solute concentration = 0), although this depends on the flow direction in a similar manner to the upper boundary.

No-flow boundaries on the left and right edges of the model domain reflect mostly vertical flow processes. Post et al. (2007) and Langevin et al. (2008) offer the following formulation for vertical flow, q_z, under mixed-density conditions:

$$q_z = -K\left[\frac{\Delta h_f}{\Delta l} + \frac{\rho_a - \rho_f}{\rho_f}\right] \quad (6)$$

where ρ_a is the average density between ρ_s and ρ_f (M L^{-3}) and $\frac{\Delta h_f}{\Delta l}$ is the hydraulic gradient (in terms of equivalent freshwater heads) over a distance Δl.

The aquifer is assumed to be initially full of seawater but is underlain by a fresh groundwater source. The lower boundary head of both models is chosen so that the initial condition is hydraulically stable, primarily to reflect the free-convective situation (i.e., neglecting forced convection) that occurs in the Elder problem and its many variants, thereby providing opportunities to compare upward buoyancy-driven flow to the downward movement of solute fingers observed by others (e.g., Xie et al., 2011). That is, the hydraulic head of the fresh groundwater source is equal to the equivalent freshwater head, h_f, at the bottom of aquifer (at the beginning of each scenario). Considering an initial seawater hydrostatic condition, h_f is given by $\frac{\rho_s}{\rho_f} z_s - \frac{\rho_s - \rho_f}{\rho_f} z_a$ (where z_s and z_a are defined in **Figure 2**). Consequently, the only forces driving flow (initially) are buoyancy forces, because the hydraulic gradient is initially zero. Thus, at the beginning of the scenarios, **Equation 6** reduces to:

$$q_z = -K\left[\frac{\rho_a - \rho_f}{\rho_f}\right] \quad (7)$$

Equation 7 is usually referred to as the convective velocity (e.g., Simmons et al., 2010). Vertical flow velocities in the numerical model, from the initial time-step, were found to be consistent with **Equation 7** (results not shown for brevity).

Although the initial condition is a free convective condition, density changes due to the introduction of freshwater through the lower boundary create head gradients that induce boundary inflows, and the system becomes mixed convective. This differs to the free convection Elder problem, which is bounded by no-flow conditions, including the upper salt source boundary. Thus, although our situation is initially free convective, the situation becomes mixed convective during the course of simulations.

The model is a two-dimensional domain represented by a finite-difference grid of uniform discretization, both vertically and horizontally, of $\Delta z = \Delta x = 0.1$ m. Three cases are evaluated for each model (i.e., a total of six numerical simulations) to briefly explore the role of dispersion in the mixed-convective processes associated with SFGD through the seafloor sediments, namely a Base Case with $\alpha_L = 0.1$ m, Case 1 with $\alpha_L = 0.5$ m, and Case 2 with $\alpha_L = 1$ m. These values fall within the range of "moderate" and "high" reliability values recommended by Zech et al. (2015). Other parameters used in all three cases for Model A are: $\{H, L, z_a, z_s, h_f, K, \rho_f, \rho_s, D_0, \alpha_L/\alpha_T, \varepsilon\}$ = {50 m, 100 m, 80 m, 160 m, 162 m, 2.5 m/d, 1000 kg/m^3, 1025 kg/m^3, 8.64 $\times$ 10^{-5} m^2/d, 10, 0.2}, where ε (-) is effective porosity. The three cases of Model B differ to those of Model A in that K_a is 0.001 m/d and H_L is 1 m. The parameters adopted here correspond to typical, field-scale values used in other SFGD-related studies (e.g., Knight et al., 2018; Solórzano-Rivas and Werner, 2018). Timescales for numerical models to reach steady state or quasi-steady state conditions differed between Models A and B, as shown in section "Results and Discussion." Consequently, Model A was simulated for 5 years and Model B for 100 years. Timescales for freshwater to reach the seafloor depend on the velocities of rise of buoyant freshwater fingers. We adopted the tip of the highest buoyant finger (HBF) to characterize mixed convective velocities (assuming time-constant velocities) in a similar way to the approach of Xie et al. (2011). The tip was defined by the 0.85 isochlor (i.e., 85% of seawater concentration).

RESULTS AND DISCUSSION

The Influence of the Lower Boundary

Figures 3–5 show simulations results from the Base Case, Case 1, and Case 2, respectively. Each figure presents the results of Model A (i.e., where no aquitard is included; left column) and Model B (i.e., where an aquitard underlies the aquifer; right column) at different times. The bottom row in all three figures represents the steady-state conditions, which in the case of Model B is a dynamic equilibrium, also referred to as quasi-steady sate. That is, the Model B distribution of SFGD within seafloor sediments is temporally unstable, involving finger patterns that change in time.

Figures 3–5 highlight substantial differences in mixed-convective processes caused by the existence (or not) of a leaky aquitard below the subsea aquifer. The most important difference between Models A and B, in the context of SFGD characteristics, is that unstable solute patterns persist under quasi-steady state in Model B, whereas in Model A, the flow instabilities are temporary, and the system reaches a steady state condition in which the aquifer is completely fresh. The occurrence of the leaky aquitard creates other important differences in mixed convective processes. For example, freshwater fingers produced from Model A are fresher, for fingers of a comparable height, to those produced by Model B (e.g., **Figures 3c,g**). This leads to sharper freshwater-saltwater interfaces in Model A results. The timescales for the rise of buoyant fingers also differ between Models A and B. For example, the time to obtain freshwater fingers of a roughly similar height differs substantially, as evident in the timing of 292.3 days for **Figure 4c** (Model A) and 2191.9 days for **Figure 4g** (Model B). Thus, the lower aquitard in Model B significantly restricts finger speeds, which is an intuitive outcome. HBF in Model A for the Base Case, Case 1, and Case 2 reaches elevations of 119.15, 110.95, and 110.75 m in **Figures 3c**, **4c**, **5c**, respectively. These represent average finger speeds of 48.9, 38.7, and 38.4 m/year. Lower velocities are produced in all three cases of Model B. That is, HBF heights were 129.85, 127.15, and 120.95 m in **Figures 3g**, **4g**, **5g**, leading to velocities of 8.31, 7.86, and 6.82 m/year, respectively. There is evidence of boundary effects in Model A, associated with the vertical no-flow boundaries, that was also observed by Xie et al. (2011). Greater velocities of fingers adjacent to no-flow boundaries are attributed to the absence of the host fluid (i.e., seawater) moving in the opposite direction to the buoyant fingers, which is otherwise expected to retard the finger upwelling speed. For that reason, fingers adjacent to vertical boundaries were neglected in assessing HBF speeds.

According to Xie et al. (2011), the theoretical velocity of fingers is 13.1 m/year, based on $(\triangle \rho K/\rho_f \varepsilon) \times f$, where f (0.115) is the Xie et al. (2011) corrective factor to the theoretical convective velocity (i.e., the ratio between **Equation 7** and ε). Interestingly, the Xie et al. (2011) corrected convective velocity, which neglects the leaky layer in Model B, is closer to the results in Model B (i.e., 8.31, 7.86, and 6.82 m/year), compared to the finger velocities in Model A (i.e., 48.9, 38.7, and 38.4 m/year). However, finger velocities in Model A could be better predicted applying values of f that fall within the range of corrective factors proposed by Post and Kooi (2003) and Wooding (1969) (i.e., 0.22 and 0.446, respectively).

Figure 6 illustrates the temporal variability in total solute mass within model domains, for the six scenarios considered in this study. The fluctuations in total mass in Model B are caused by mixed-convective instabilities, which persist as quasi-steady state conditions, as discussed above. The time for Model A to reach steady-state conditions (approximately 2 years) is much less than the time required for Model B to reach quasi-steady state conditions (approximately 10 years). This is consistent with the difference between buoyant fingering speeds found in Models A and B, as discussed above. The larger velocities in Model A (e.g., 48.9 m/year, 38.7 m/year, and 38.4 m/d in **Figures 3c**, **4c**, **5c**) led shorter timescales to reach steady state compared to Model B, in which velocities were 8.31, 7.86, and 6.82 m/year (**Figures 3g**, **4g**, **5g**).

The Influence of Dispersion

Figure 6 shows that variations in dispersion had no noticeable impact on the time required to reach steady and quasi-steady state conditions. This is consistent with the relatively

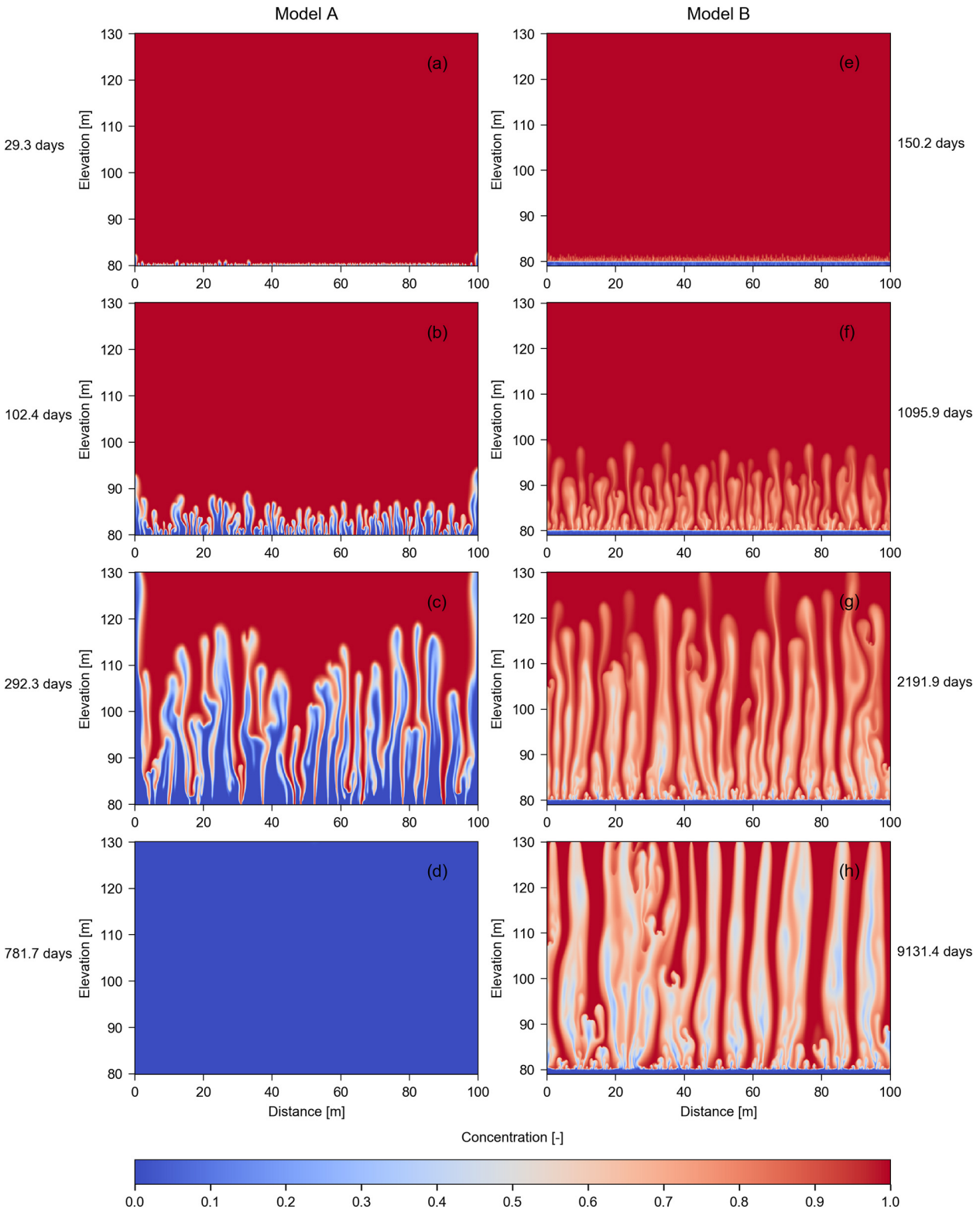


FIGURE 3 | Salinity distributions in seafloor sediments obtained from simulations of the Base Case (i.e., α_L = 0.1 m; α_T = 0.01 m) of Model A (left column) and Model B (right column) at various simulation times. Concentration values represent the relative seawater concentration, where 0 and 1 are freshwater and seawater, respectively. The bottom left subplot depicts steady state results, while the bottom right subplot shows a quasi-steady state salinity distribution. **(a)** 29.3 days; **(b)** 102.4 days; **(c)** 292.3 days; **(d)** 781.7 days; **(e)** 150.2 days; **(f)** 1095.9 days; **(g)** 2191.9 days; **(h)** 9131.4 days.

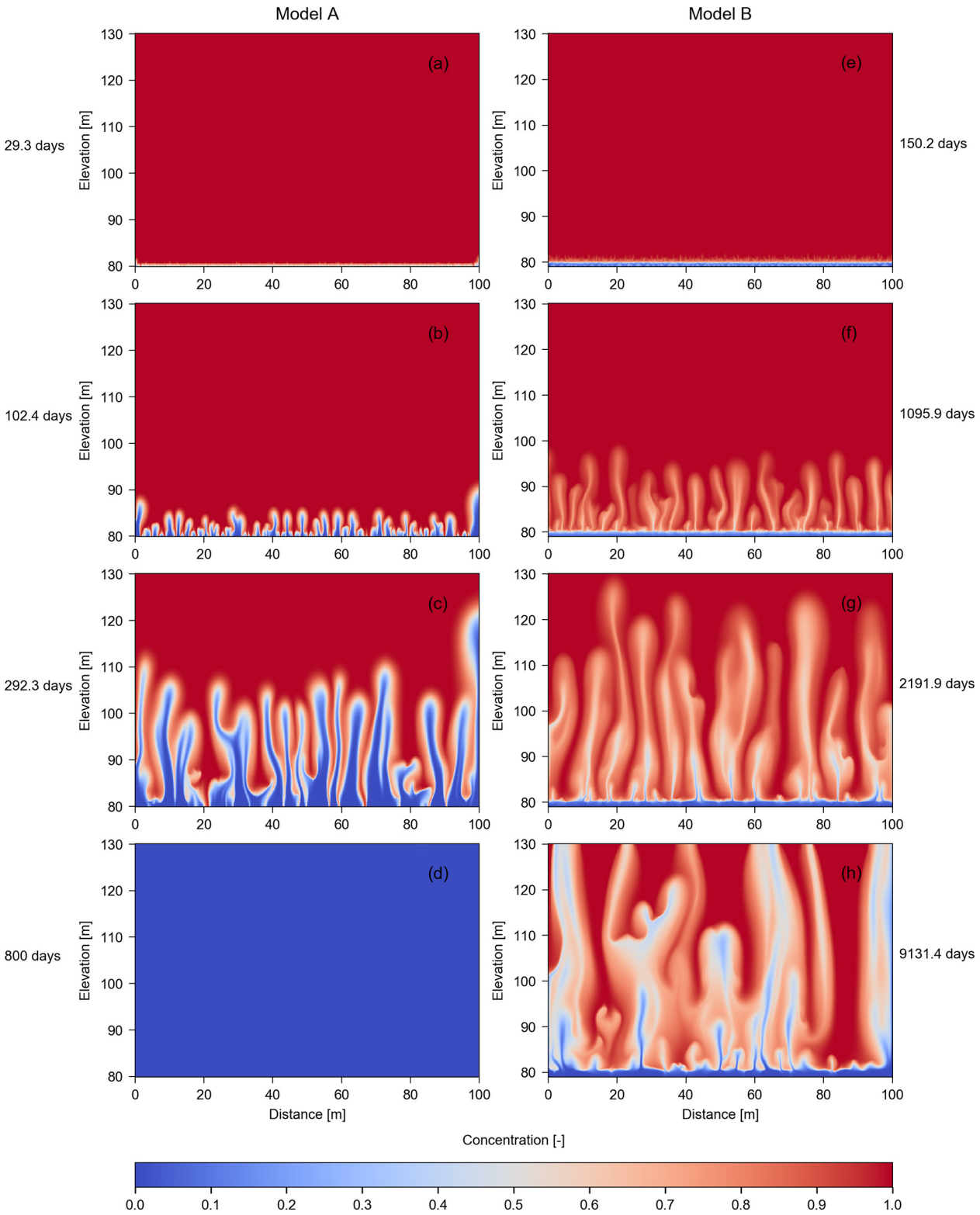


FIGURE 4 | Salinity distributions in seafloor sediments obtained from simulations of Case 1 (i.e., α_L = 0.5 m; α_T = 0.05 m) of Model A (left column) and Model B (right column) at various simulation times. Concentration values represent the relative seawater concentration, where 0 and 1 are freshwater and seawater, respectively. The bottom left subplot depicts steady-state results, while the bottom right subplot shows a quasi-steady state salinity distribution. **(a)** 29.3 days; **(b)** 102.4 days; **(c)** 292.3 days; **(d)** 800 days; **(e)** 150.2 days; **(f)** 1095.9 days; **(g)** 2191.9 days; **(h)** 9131.4 days.

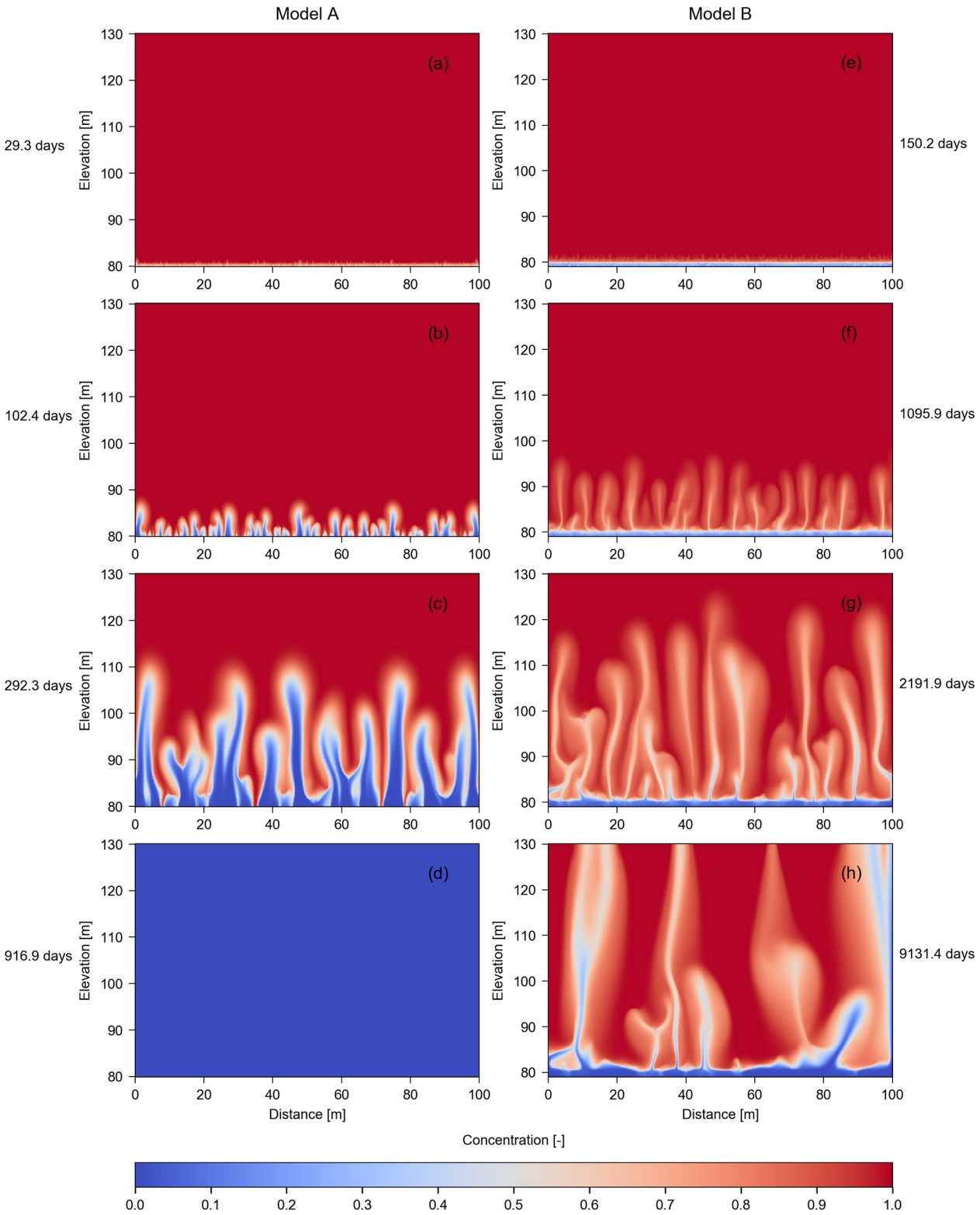


FIGURE 5 | Salinity distribution in seafloor sediments obtained from simulations of Case 2 (i.e., α_L = 1 m; α_T = 0.1 m) of Model A (left column) and Model B (right column) at various simulation times. Concentration values represent the relative seawater concentration, where 0 and 1 are freshwater and seawater, respectively. The bottom left subplot depicts steady-state results, while the bottom right subplot shows a quasi-steady state salinity distribution. **(a)** 29.3 days; **(b)** 102.4 days; **(c)** 292.3 days; **(d)** 916.9 days; **(e)** 150.2 days; **(f)** 1095.9 days; **(g)** 2191.9 days; **(h)** 9131.4 days.

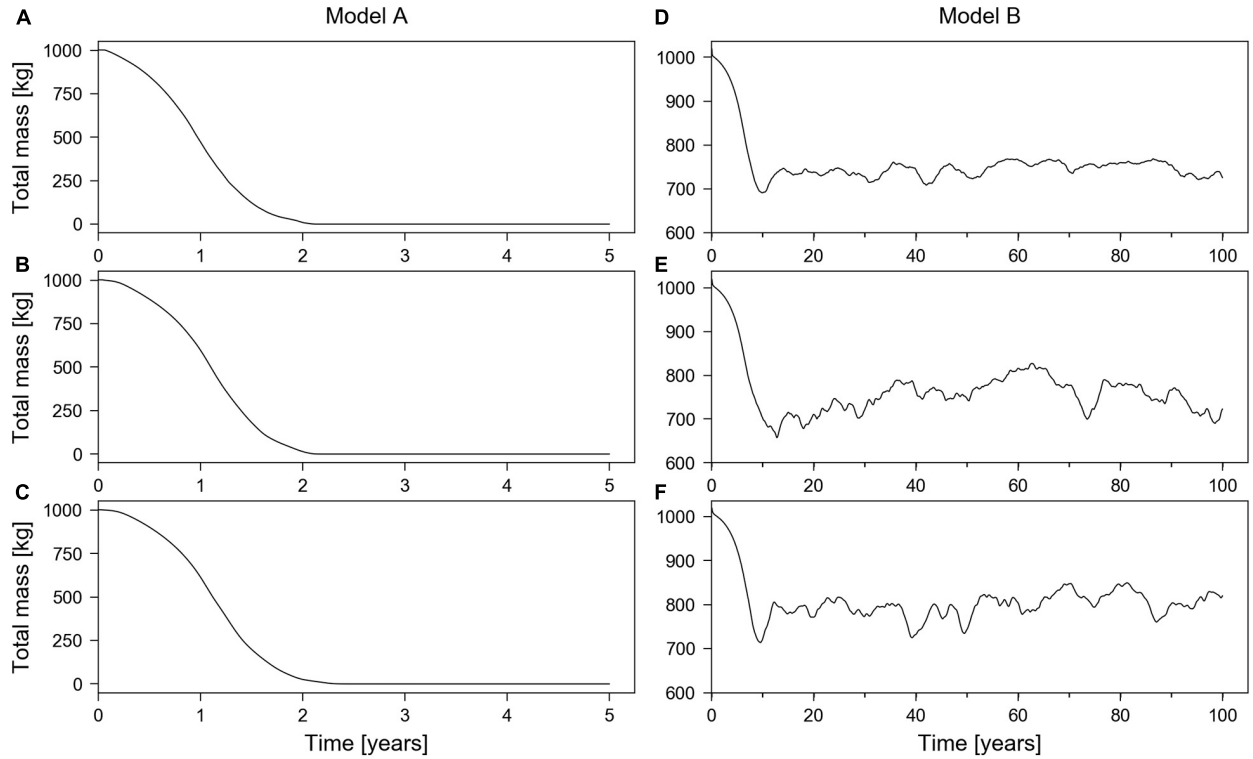


FIGURE 6 | Numerical model results of total solute mass with time. **(A,D)** Base Case (i.e., α_L = 0.1 m; α_T = 0.01 m); **(B,E)** Case 1 (i.e., α_L = 0.5 m; α_T = 0.05 m); and **(C,F)** Case 2 (i.e., α_L = 1 m; α_T = 0.1 m). The left column represents cases of Model A and the right column represents cases of Model B.

small change between cases (i.e., from Base Case to Case 2) in buoyant fingering speeds, as observed also by Xie et al. (2011). The little influence of dispersion on buoyant fingering speeds is also in accordance with the definition of the theoretical convective velocity proposed by Xie et al. (2011), which neglects dispersion. While dispersion has an unimportant role in the speed of buoyant finger rise, dispersion does appear to influence the quasi-steady state buoyant fingering patterns associated with mixed-convective processes (**Figures 3**–**5**).

Figure 7 compares the three cases (i.e., Base Case, Case 1, and Case 2) of Model B, showing quasi-steady state salinity distributions in profile, and the temporal variation in SFGD solute concentration at the seafloor using a timeframe of 85 years. Subplots **Figures 7a–c** correspond to **Figures 3h**, **4h**, **5h**, respectively.

Figure 7 shows that the number of fingers reaching the seafloor decreases with increasing dispersion due to the widening of fingers; a similar observation to those of Xie et al. (2011) for dense, downward-moving fingers.

The temporal and spatial variability in the salinity distribution across the sea floor have important implications for the direct measurement of SFGD. For example, the deployment and size of seepage meters (e.g., Burnett et al., 2006) in areas where mixed-convective processes occur require consideration of the spatial variability in freshwater discharge, given the irregular distributions of SFGD in **Figures 3**–**7**. Mixed-convective flow leads to regions of freshwater upwelling and seawater downwelling, and therefore, SFGD measurement methods that can detect seafloor fluxes in both directions (inflow and outflow) may assist in detecting mixed-convective phenomena. Additionally, the duration of seepage meter placement should consider the temporal variation of SFGD created by mixed convective processes. Freshwater upwelling appeared to be relatively stable over durations of days-to-weeks, but may vary substantially over longer timeframes, at least for the cases illustrated in **Figure 7**.

The non-dimensional parameters *Ra* and *M* were determined, using **Equations 1** and **5**, respectively, from the quasi-steady state results of Model B. The steady-state solution of Model A has no density gradients within the aquifer (i.e., the aquifer is freshwater-filled), and therefore, both *Ra* and *M* (and Ra_δ) are zero. Given that the system is forced-convection dominated, SFGD to the seafloor under the Model A conditions will be diffusive or uniformly distributed.

For the application of **Equation 5** to estimate *M* for Model B, an average q_z (across the bottom aquifer) over about 85 years of quasi-steady state conditions was used, based on the numerical results. The need to know q_z in applying **Equation 5** to estimate *M* (or Ra_δ), as a predictor of buoyancy-driven flow, is potentially problematic for the purposes of designing SFGD monitoring systems (e.g., deployment of seepage meters), because rates of SFGD are typically not known prior to seepage meter deployment. For example, Stevens

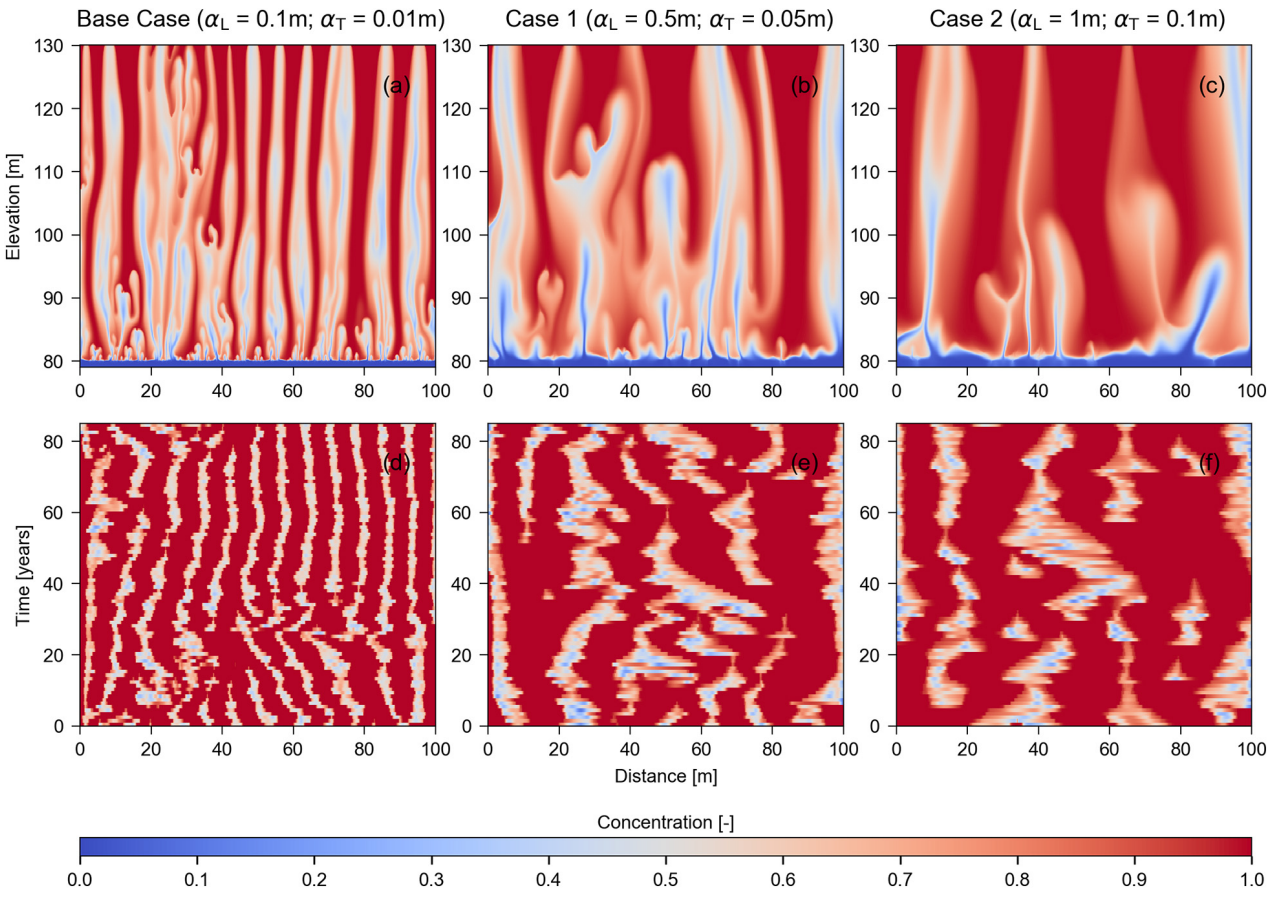


FIGURE 7 | Salinity distribution in profile [subplots **(a–c)**; top row] and temporal variation of solute concentration [subplots **(d–f)**; bottom row] in seafloor sediments obtained from Model B simulations: Subplots are (from left to right) the Base Case, Case 1, and Case 2. Concentration values represent the relative seawater concentration, where 0 and 1 are freshwater and seawater, respectively. All subplots show a quasi-steady state salinity distribution.

et al. (2009) estimated M by applying **Equation 4**, which requires the vertical hydraulic gradient (based on localized measurements of hydraulic heads and salinities from bore data) rather than q_z. Nevertheless, where mixed convective processes occur in seafloor sediments, the vertical hydraulic gradient is also difficult to ascertain considering the changes in location and temporal variations of SFGD caused by buoyancy forces. Alternative approaches to estimating q_z, such as the application of geochemical tracers (e.g., Taniguchi et al., 2019), may overcome difficulties in measuring hydrogeological variables within seafloor sediments.

The steady-state value of q_z is 2.9×10^{-3} m/d in the Base Case (**Figure 7a**), 2.9×10^{-3} m/d in Case 1 (**Figure 7b**), and 2.3×10^{-3} m/d in Case 2 (**Figure 7c**). While the values of M for the three cases of Model B vary within the same order of magnitude (i.e., 22–27), the range of values of Ra is wider (i.e., 2031, 431, and 264 for the Base Case, Case1, and Case 2, respectively). These values indicate that the flow system in Model B is free-convection dominated. That is, $M > 1$, and the critical values of Ra_δ (or M) and Ra (i.e., 10 and 5, respectively) are also exceeded, indicating that unstable solute motion is likely to occur. Therefore, the occurrence of unstable flow in the current cases are consistent with critical values proposed in the literature for downwards salinization (e.g., Wooding et al., 1997; Smith and Turner, 2001). However, further investigation is warranted to ascertain if those critical values can be generally applied to SFGD through sandy seafloor sediments.

CONCLUSION

This research highlights that the occurrence of SFGD in permeable seafloor sediments potentially involves unstable flow processes, with important implications for SFGD measurement and the understanding of seafloor ecosystems. This study provides insight into SFGD measurement approaches, since we have demonstrated that for the cases considered here, SFGD measurements through the deployment of seepage meters will depend on the placement and measurement duration of seepage meters. Predicting whether unstable flow processes occur is theoretically plausible based on our overview of the most common non-dimensional numbers (i.e., Ra_δ, Ra, and M) used previously to characterize mixed-convection processes

in groundwater. Simplified numerical models that represent submarine aquifers settings show that SFGD can occur in the form of upward freshwater fingers, analogous to the inverse downward movement of dense solute fingers. We found that the critical values of Ra_δ and Ra proposed in the literature for solute convection apply to the two cases analyzed in this study, although, further investigation is needed to generalize the use of those critical values to SFGD through sandy seafloor sediments. That is, further research into SFGD through high-permeability sediments is warranted to constrain the application of non-dimensional numbers for predicting unstable conditions, given the substantial differences between stable and unstable salinity patterns and distributions of SFGD to the seafloor. The results of this study show that the pattern of SFGD through high-permeability sediments containing seawater is controlled by the lower boundary, intended to represent either an underlying aquifer or aquitard. The numerical results also showed quasi-steady temporal fluctuations in the SFGD pattern behavior, for the case involving a low-permeability layer beneath the seafloor aquifer.

DATA AVAILABILITY STATEMENT

The raw data supporting the conclusions of this article will be made available by the authors, without undue reservation.

AUTHOR CONTRIBUTIONS

SS-R: numerical modeling, investigation, analysis, visualization, and writing – original draft and editing. AW: conceptualization, supervision, visualization, and writing – review and editing. DI: supervision, visualization, and writing – review and editing. All authors contributed to the article and approved the submitted version.

FUNDING

SS-R was supported by a Research Training Program scholarship. AW was the recipient of an Australian Research Council Future Fellowship (project number FT150100403).

REFERENCES

Bakker, M., Miller, A. D., Morgan, L. K., and Werner, A. D. (2017). Evaluation of analytic solutions for steady interface flow where the aquifer extends below the sea. *J. Hydrol.* 551, 660–664. doi: 10.1016/j.jhydrol.2017.04.009

Burnett, W. C., Aggarwal, P. K., Aureli, A., Bokuniewicz, H., Cable, J. E., Charette, M. A., et al. (2006). Quantifying submarine groundwater discharge in the coastal zone via multiple methods. *Sci. Total Environ.* 367, 498–543. doi: 10.1016/j.scitotenv.2006.05.009

Elder, J. W., Simmons, C. T., Diersch, H., Frolkoviè, P., Holzbecher, E., and Johannsen, K. (2017). The elder problem. *Fluids* 2:11. doi: 10.3390/fluids2010011

Guo, W., and Langevin, C. D. (2002). *User's Guide to SEAWAT: A Computer Program for the Simulation of Three-Dimensional Variable-Density Ground-Water Flow: Techniques of Water-Resources Investigations of the U. S. Geological Survey*. Book 6, Chapter A7, Open File, 01-434. Tallahassee: US Geological Survey, 77.

Irvine, D. J., Sheldon, H. A., Simmons, C. T., Werner, A. D., and Griffiths, C. M. (2015). Investigating the influence of aquifer heterogeneity on the potential for thermal free convection in the Yarragadee Aquifer, Western Australia. *Hydrogeol. J.* 23, 161–173. doi: 10.1007/s10040-014-1194-1

Irvine, D. J., Werner, A. D., Ye, Y., and Jazayeri, A. (2021). Upstream dispersion in solute transport models: a simple evaluation and reduction methodology. *Groundwater* 59, 287–291. doi: 10.1111/gwat.13036

Jiao, J. J., Shi, L., Kuang, X., Lee, C. M., Yim, W. W. S., and Yang, S. (2015). Reconstructed chloride concentration profiles below the seabed in Hong Kong (China) and their implications for offshore groundwater resources. *Hydrogeol. J.* 23, 277–286. doi: 10.1007/s10040-014-1201-6

Johannes, R. E. (1980). The ecological significance of the submarine discharge of groundwater. *Mar. Ecol. Prog. Ser.* 3, 365–373.

Knight, A. C., Werner, A. D., and Morgan, L. K. (2018). The onshore influence of offshore fresh groundwater. *J. Hydrol.* 561, 724–736. doi: 10.1016/j.jhydrol.2018.03.028

Kooi, H., and Groen, J. (2001). Offshore continuation of coastal groundwater systems; predictions using sharp-interface approximations and variable-density flow modelling. *J. Hydrol.* 246, 19–35. doi: 10.1016/S0022-1694(01)00354-7

Kurylyk, B. L., Irvine, D. J., Mohammed, A. A., Bense, V. F., Briggs, M. A., Loder, J. W., et al. (2018). Rethinking the use of seabed sediment temperature profiles to trace submarine groundwater flow. *Water Resour. Res.* 54, 4595–4614. doi: 10.1029/2017WR022353

Langevin, C. D., Thorne, D. T. Jr., Dausman, A. M., Sukop, M. C., and Guo, W. (2008). *SEAWAT Version 4: A Computer Program for Simulation of Multi-Species Solute and Heat Transport. U.S. Geological Survey Techniques and Methods*. Book 6, Chap. A22. Reston: US Geological Survey, 39.

Lapwood, E. R. (1948). Convection of a fluid in a porous medium. *Math. Proc. Cambridge Philos. Soc.* 44, 508–521. doi: 10.1017/S030500410002452X

Michael, H. A., Mulligan, A. E., and Harvey, C. F. (2005). Seasonal oscillations in water exchange between aquifers and the coastal ocean. *Nature* 436, 1145–1148. doi: 10.1038/nature03935

Michael, H. A., Scott, K. C., Koneshloo, M., Yu, X., Khan, M. R., and Li, K. (2016). Geologic influence on groundwater salinity drives large seawater circulation through the continental shelf. *Geophys. Res. Lett.* 43, 10782–10791. doi: 10.1002/2016GL070863

Moore, W. S. (1999). The subterranean estuary: a reaction zone of ground water and sea water. *Mar. Chem.* 65, 111–125. doi: 10.1016/S0304-4203(99)00014-6

Moore, W. S., and Wilson, A. M. (2005). Advective flow through the upper continental shelf driven by storms, buoyancy, and submarine groundwater discharge. *Earth Planet. Sci. Lett.* 235, 564–576. doi: 10.1016/j.epsl.2005.04.043

Post, V., Kooi, H., and Simmons, C. (2007). Using hydraulic head measurements in variable-density ground water flow analyses. *Groundwater* 45, 664–671. doi: 10.1111/j.1745-6584.2007.00339.x

Post, V. E. A., and Kooi, H. (2003). Rates of salinization by free convection in high-permeability sediments: insights from numerical modeling and application to the dutch coastal area. *Hydrogeol. J.* 11, 549–559. doi: 10.1007/s10040-003-0271-7

Riedl, R. J., Huang, N., and Machan, R. (1972). The subtidal pump: a mechanism of interstitial water exchange by wave action. *Mar. Biol.* 13, 210–221. doi: 10.1007/BF00391379

Simmons, C. T., and Narayan, K. A. (1997). Mixed convection processes below a saline disposal basin. *J. Hydrol.* 194, 263–285. doi: 10.1016/S0022-1694(96)03204-0

Simmons, C. T., Bauer-Gottwein, P., Graf, T., Kinzelbach, W., Kooi, H., Li, L., et al. (2010). "Variable density groundwater flow: from modelling to applications," in *Groundwater Modelling in Arid and Semi-Arid Areas*, eds H. Wheater, S. A. Mathias, and X. Li (Cambridge: Cambridge University Press), 87–118.

Smith, A. J. (2004). Mixed convection and density-dependent seawater circulation in coastal aquifers. *Water Resour. Res.* 40:W08309. doi: 10.1029/2003WR002977

Smith, A. J., and Turner, J. V. (2001). Density-dependent surface water-groundwater interaction and nutrient discharge in the swan – canning estuary. *Hydrol. Process.* 15, 2595–2616. doi: 10.1002/hyp.303

Solórzano-Rivas, S. C., and Werner, A. D. (2018). On the representation of subsea aquitards in models of offshore fresh groundwater. *Adv. Water Resour.* 112, 283–294. doi: 10.1016/j.advwatres.2017.11.025

Solórzano-Rivas, S. C., Werner, A. D., and Irvine, D. J. (2019). Dispersion effects on the freshwater–seawater interface in subsea aquifers. *Adv. Water Resour.* 130, 184–197. doi: 10.1016/j.advwatres.2019.05.022

Stevens, J. D., Sharp, J. M. Jr., Simmons, C. T., and Fenstemaker, T. R. (2009). Evidence of free convection in groundwater: field-based measurements beneath wind-tidal flats. *J. Hydrol.* 375, 394–409. doi: 10.1016/j.jhydrol.2009.06.035

Taniguchi, M., Burnett, W. C., Smith, C. F., Paulsen, R. J., O'Rourke, D., Krupa, S. L., et al. (2003). Spatial and temporal distributions of submarine groundwater discharge rates obtained from various types of seepage meters at a site in the Northeastern Gulf of Mexico. *Biogeochemistry* 66, 35–53. doi: 10.1023/B:BIOG.0000006090.25949.8d

Taniguchi, M., Dulai, H., Burnett, K. M., Santos, I. R., Sugimoto, R., Stieglitz, T., et al. (2019). Submarine groundwater discharge: updates on its measurement techniques, geophysical drivers, magnitudes, and effects. *Front. Environ. Sci.* 7:141. doi: 10.3389/fenvs.2019.00141

van Reeuwijk, M., Mathias, S. A., Simmons, C. T., and Ward, J. D. (2009). Insights from a pseudospectral approach to the elder problem. *Water Resour. Res.* 45:W04416. doi: 10.1029/2008WR007421

Voss, C. I., and Souza, W. R. (1987). Variable density flow and solute transport simulation of regional aquifers containing a narrow freshwater−saltwater transition zone. *Water Resour. Res.* 23, 1851–1866. doi: 10.1029/WR023i010p01851

Webster, I. T., Norquay, S. J., Ross, F. C., and Wooding, R. A. (1996). Solute exchange by convection within estuarine sediments. *Estuar. Coast. Shelf Sci.* 42, 171–183. doi: 10.1006/ecss.1996.0013

Werner, A. D., and Robinson, N. I. (2018). Revisiting analytical solutions for steady interface flow in subsea aquifers: aquitard salinity effects. *Adv. Water Resour.* 116, 117–126. doi: 10.1016/j.advwatres.2018.01.002

Wooding, R. A. (1969). Growth of fingers at an unstable diffusing interface in a porous medium or Hele-Shaw cell. *J. Fluid Mech.* 39, 477–495. doi: 10.1017/S002211206900228X

Wooding, R. A., Tyler, S. W., and White, I. (1997). Convection in groundwater below an evaporating salt lake: 1. Onset of instability. *Water Resour. Res.* 33, 1199–1217. doi: 10.1029/96WR03533

Xie, Y., Simmons, C. T., and Werner, A. D. (2011). Speed of free convective fingering in porous media. *Water Resour. Res.* 47:W11501. doi: 10.1029/2011WR010555

Xie, Y., Simmons, C. T., Werner, A. D., and Ward, J. D. (2010). Effect of transient solute loading on free convection in porous media. *Water Resour. Res.* 46, 389–400. doi: 10.1029/2010WR009314

Zech, A., Attinger, S., Cvetkovic, V., Dagan, G., Dietrich, P., Fiori, A., et al. (2015). Is unique scaling of aquifer macrodispersivity supported by field data? *Water Resour. Res.* 51, 7662–7679. doi: 10.1002/2015WR017220

Conflict of Interest: The authors declare that the research was conducted in the absence of any commercial or financial relationships that could be construed as a potential conflict of interest.

Copyright © 2021 Solórzano-Rivas, Werner and Irvine. This is an open-access article distributed under the terms of the Creative Commons Attribution License (CC BY). The use, distribution or reproduction in other forums is permitted, provided the original author(s) and the copyright owner(s) are credited and that the original publication in this journal is cited, in accordance with accepted academic practice. No use, distribution or reproduction is permitted which does not comply with these terms.

frontiers in Environmental Science

ORIGINAL RESEARCH
published: 15 October 2021
doi: 10.3389/fenvs.2021.642346

A Multi-Tracer Study of Fresh Water Sources for a Temperate Urbanized Coastal Bay (Southern Baltic Sea)

Cátia Milene Ehlert von Ahn[1], Jan C. Scholten[2], Christoph Malik[1,3], Peter Feldens[4], Bo Liu[5], Olaf Dellwig[1], Anna-Kathrina Jenner[1], Svenja Papenmeier[4], Iris Schmiedinger[1], Mary A. Zeller[1] and Michael Ernst Böttcher[1,6,7]**

[1]Geochemistry and Isotope Biogeochemistry Group, Leibniz Institute for Baltic Sea Research (IOW), Warnemünde, Germany, [2]Institute of Geosciences, Kiel University, Kiel, Germany, [3]Department of Hydrogeology, UmweltPlan GmbH Stralsund, Stralsund, Germany, [4]Marine Geophysics Group, Leibniz Institute for Baltic Sea Research (IOW), Warnemünde, Germany, [5]Section of Marine Geochemistry, Alfred Wegener Institute Helmholtz Centre for Polar and Marine Research, Bremerhaven, Germany, [6]Marine Geochemistry, University of Greifswald, Greifswald, Germany, [7]Maritime Systems, Interdisciplinary Faculty, University of Rostock, Rostock, Germany

OPEN ACCESS

Edited by:
Henry Bokuniewicz, The State University of New York (SUNY), United States

Reviewed by:
Aaron J. Beck, GEOMAR Helmholtz Center for Ocean Research Kiel, Germany
Olivier Radakovitch, Institut de Radioprotection et de Sûreté Nucléaire, France

***Correspondence:**
Cátia Milene Ehlert von Ahn
catia.vonahn@io-warnemuende.de
Michael Ernst Böttcher
michael.boettcher@io-warnemuende.de

Specialty section:
This article was submitted to Biogeochemical Dynamics, a section of the journal Frontiers in Environmental Science

Received: *15 December 2020*
Accepted: *03 September 2021*
Published: *15 October 2021*

Citation:
von Ahn CME, Scholten JC, Malik C, Feldens P, Liu B, Dellwig O, Jenner A-K Papenmeier S, Schmiedinger I, Zeller MA and Böttcher ME (2021) A Multi-Tracer Study of Fresh Water Sources for a Temperate Urbanized Coastal Bay (Southern Baltic Sea). Front. Environ. Sci. 9:642346. doi: 10.3389/fenvs.2021.642346

Terrestrial surface waters and submarine ground water discharge (SGD) act as a source of dissolved substances for coastal systems. Solute fluxes of SGD depend on the ground water composition and the water-solid-microbe interactions close to the sediment-water interface. Thus, this study aims to characterize and evaluate the hydrogeochemical gradients developing in the fresh-salt water mixing zone of the Wismar Bay (WB), southern Baltic Sea, Germany. Sampling campaigns covering the WB, the fresh-salt water mixing zone at the beach of the WB shoreline, terrestrial surface and ground waters near the WB as well sediments pore water were carried out. In these different waters, the distribution of dissolved inorganic carbon, nutrients, major ions, trace elements, stable isotopes (H, O, C, S), and radium isotopes have been investigated. Enhanced concentrations of radium isotopes together with dissolved manganese, barium in the surface waters of the eastern WB indicated benthic-pelagic coupling via the exchange between pore water and the water column. Salinity, stable isotopes, and major ions in sediment pore water profiles identified the presence of fresh ground water below about 40 cmbsf in the central part of the bay. Geophysical acoustic techniques revealed the local impact of anthropogenic sediment excavation, which reduced the thickness of a sediment layer between the coastal aquifer and the bottom water, causing, therefore, a ground water upward flow close to the top sediments. The fresh impacted pore water stable isotope composition ($\delta^{18}O$, $\delta^{2}H$) plot close to the regional meteoric water line indicating a relatively modern ground water source. The calculated organic matter mineralization rates and the dissolved inorganic carbon sediment-water fluxes were much higher at the fresh impacted site when compared to other unimpacted sediments. Therefore, this study reveals that different fresh water sources contribute to the water balance of WB including a SGD source.

Keywords: urbanized coastal bay, submarine ground water discharge, subterranean estuary, hydrogeochemistry, stable isotope, radium isotope, acoustic survey, Wismar Bay

INTRODUCTION

Coastal regions are great of interest because they receive water and elements from the continents. Water drains the watershed towards the sea through surface water flow like rivers, coastal lagoons, and streams. In addition, ground waters may act as a further transport route for land-derived dissolved matter via submarine ground water discharge (SGD) (e.g., Johannes, 1980; Church, 1996; Burnett et al., 2003, Burnett et al., 2006; Moore 2010; Jurasinski et al., 2018).

A combination of the enhanced material transport and high pelagic productivity in coastal regions lead to an intensive benthic biogeochemical element recycling (Jørgensen and Kasten, 2006) and steep pore water gradients of, e.g., dissolved carbon species, nutrients, and major and trace elements to surface waters. SGD has been found to contribute to the overall oceanic water and element budget (e.g., Burnett et al., 2003; Santos et al., 2012), however, processes impacting the flux and associated solutes along the land-ocean continuum are considered as one of the unsolved problems in hydrology (Blöschl et al., 2019).

In contrast to rivers, where water discharge and their compositional variations are known in sufficient resolution and precision, the quantification of SGD entering coastal waters remains a challenge (e.g., Stieglitz et al., 2008; Rodellas et al., 2012; Douglas et al., 2020; Moosdorf et al., 2021). Therefore, more studies are needed combining different techniques to understand the dynamics in SGD and its role for water and element transfer on different scales (Burnett et al., 2006; Taniguchi, et al., 2019; Moosdorf et al., 2021; Rocha et al., 2021).

Common approaches to calculate SGD fluxes often rely on measurements of dissolved constituents in riverine and nearshore fresh ground water as endmembers, and assume conservative behavior of dissolved constituents across the mixing zone (Oberdorfer et al., 1990; Burnett et al., 2008; Rodellas et al., 2015; de Souza et al., 2021). However, due to the complexity of coastal aquifer mixing zones between ground water and sea water, it is a challenge to characterize the actual composition of solutions that finally discharge to the marine bottom waters (Cerdà-Domènech et al., 2017; Bejannin et al., 2020). This challenge is fostered by biogeochemical and associated physicochemical processes (e.g., mineralization of organic matter, ionic ad/desorption, mineral dissolution/precipitation) between fresh and saline pore water within the aquifer mixing zone that may lead to substantial changes in the composition of SGD-born element fluxes (e.g., Beck et al., 2007; Donis et al., 2017). These mostly redox-dependent processes in the subterranean estuary are more pronounced than those taking place in the oxic mixing zone of surface water estuaries (e.g., Moosdorf et al., 2021).

In many coastal areas, anthropogenic interventions may impact flow conditions and water balance (Stieglitz et al., 2007; Stegmann et al., 2011). For instance, dredging of canals in coastal areas may reduce the sediment cover on top of unconfined aquifers, thereby, enhancing the discharge of SGD and associated substances (Santos et al., 2008; Macklin et al., 2014; Teatini et al., 2017), or may promote salt water intrusions into aquifers (Moore, 1996). Moreover, an enhancement of coastal ground water exchange, e.g., caused by anthropogenic activities, may lead to an indirect enhancement of dissolved nutrient and carbon loads reflecting in changes in the biogeochemistry of surface waters (Lee et al., 2009).

Coastal areas of the southern Baltic Sea (BS) offer great opportunities to investigate the role of different fresh water inputs. Besides surface water inflows, SGD has been observed, for instance, in the Eckernförde Bay in the south-western BS (Whiticar and Werner, 1981; Schlüter et al., 2004). Other studies are focusing on the Puck Bay, in the southern BS (Jankowska et al., 1994; Szymczycha et al., 2012, 2020; Kotwicki et al., 2014; Donis et al., 2017; Böttcher et al., 2021) where significant discharge has been observed. The hydrogeology in these areas differs from those in the northwestern part of the BS, where multiple submarine fresh water sources were described that are only under minor impact by human activities (Krall et al., 2017; Virtasalo et al., 2019).

In the present study, investigations were conducted in the urbanized Wismar Bay (WB), southern BS (**Figure 1**). During a first survey carried out in 2012 along parts of the southern BS coastline comparably higher ^{224}Radium (^{224}Ra) activities were observed in surface waters of the WB (**Figure 2**). This suggested an enhancement of benthic-pelagic coupling, likely driven by SGD, which would agree with a tentative water balance for the WB (Schafmeister and Darsow, 2004). Moreover, the semi-enclosed WB is an interesting site to investigate inputs of water and substances, since the bay is under multiple anthropogenic impacts including port activities (VSW, 2018), making it similar to other modern coastal areas.

We combined a multi-isotope hydrochemical approach including a geophysical characterization of sedimentary structures to improve our understanding of fresh water sources into the WB. In addition, the biogeochemical processes taking place in the top sediments were modeled and investigated to understand the impact of SGD on their release of elements. The results show that different fresh water sources exist for the WB. SGD takes place at different areas through the bay, e.g., near the coastline, and in the central part of the bay. Anthropogenic activities, such as the creation of a navigation channel may cause a connection to unconfined aquifers and, therefore, promoting the exchange of water and associated elements with the WB bottom water.

METHODS

Study Area

The north-eastern part of Germany is characterized by a generally flat topography consisting of unconsolidated glacial sediments, humid climate conditions, urbanized cities, and often agricultural land use in the catchment basin. The present study was carried out in the WB (**Figure 1**), which is a coastal embayment in the southern BS, separated from the open BS by two shallow banks (Prena, 1995). Sediments in the bay are composed of quaternary glaciofluvial sands and intercalated tills (Schafmeister and Darsow, 2004). Maximum water depths of 10 m are in the western part of WB where muddy sediments are found, with

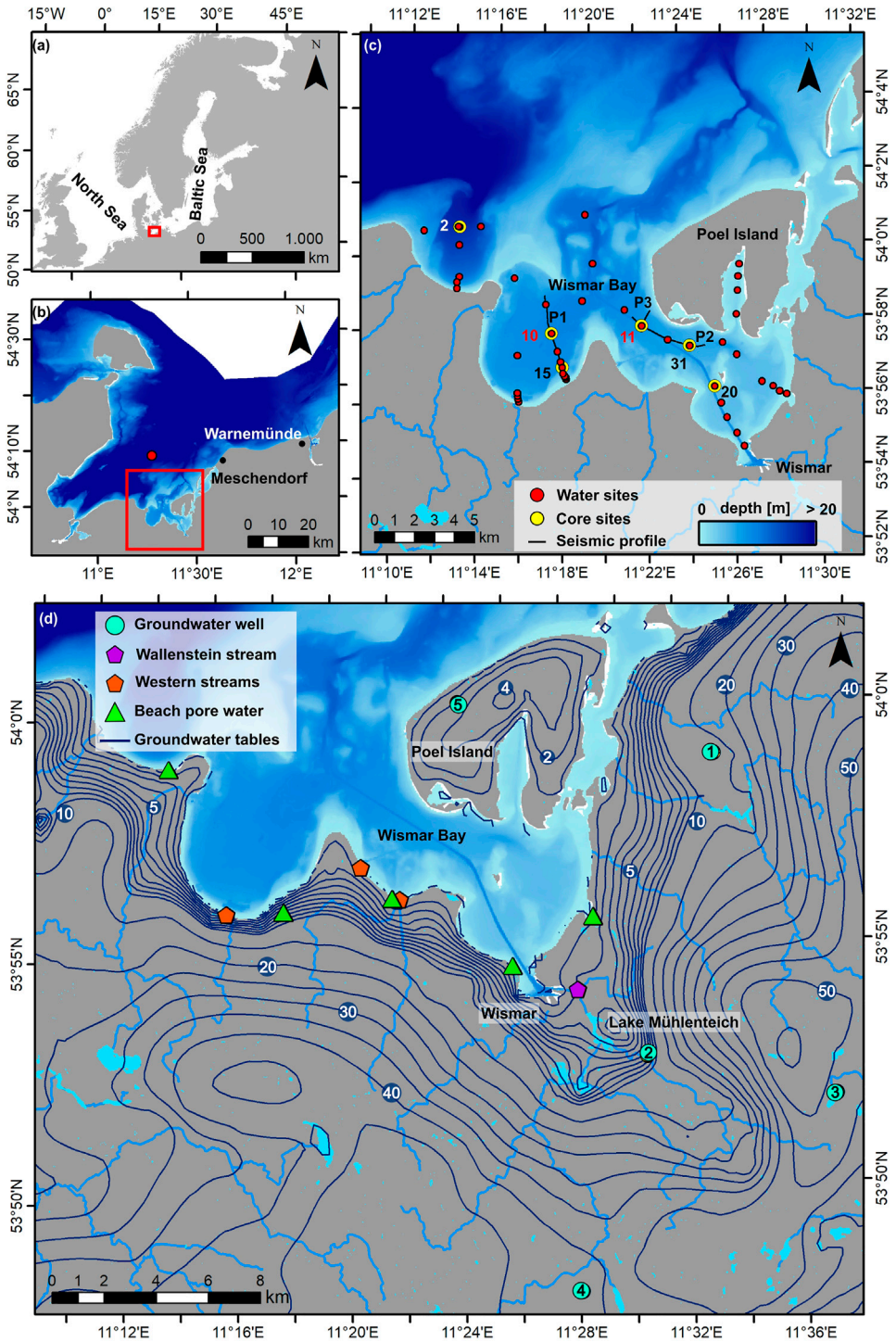


FIGURE 1 | Map of Baltic Sea and North Sea showing the location of the Wismar Bay **(A)**. Southern Baltic Sea, Germany shoreline showing the location of the Wismar Bay, including the adjacent investigated areas: Meschendorf, Warnemünde and, the surface water site at open Baltic Sea waters (red dot). Map of Wismar Bay with the sampling sites: surface water (red dots), sediment cores (yellow dots), the tracks of the seismic profiles (black line). The sediment cores are labeled, and the red numbers are the locations where SGD was found. **(C)**. Map of Wismar Bay and surrounding showing the ground water table (m), the streams discharging into the bay, and the lakes, as well as the ground water wells (cyan circles) also labeled, the sites at the western streams (orange diamond), Wallenstein stream (purple diamond), and the beach pore water sites (green triangle). The bathymetry highlighted the location of the navigation channel in the Wismar Bay. SOURCE: BSH, LUNG.

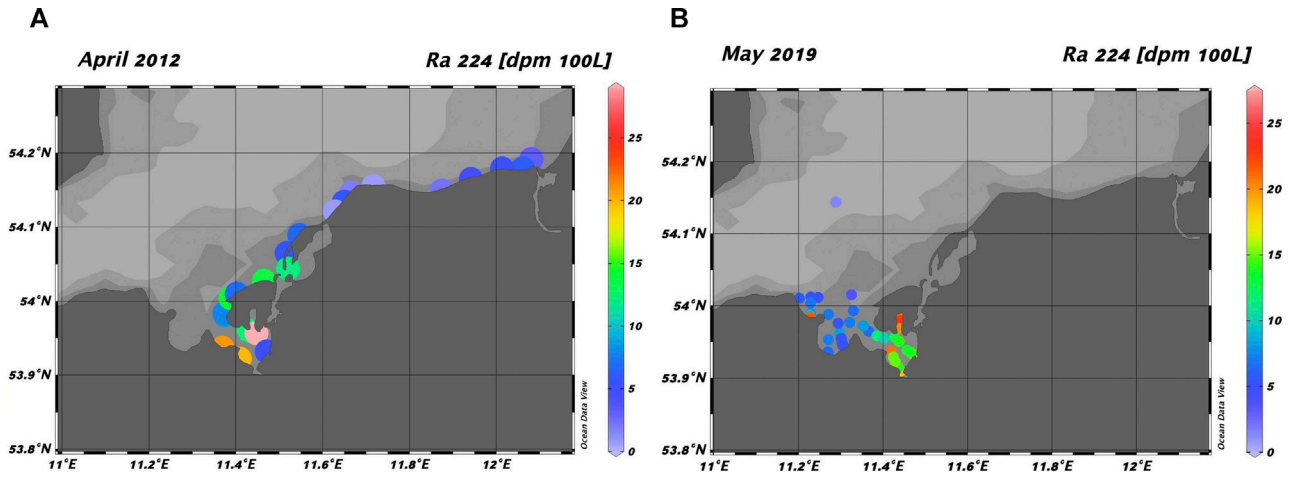


FIGURE 2 | Map of Germany coastline from WB to Warnemünde showing the activities of $^{224}Ra_{ex}$ in surface water from WB until Warnemünde carried out on April 2012 **(A)** and $^{224}Ra_{ex}$ in WB from the present study **(B)**.

sedimentary organic matter of up to 10% (Prena, 1995). Sandy sediments occur in the shallower areas.

The port of the town of Wismar is located on the east side of the bay, and ship navigation to the open BS is via an about 27 km long channel (**Figure 1**) (VSW, 2018).

The surrounding area of WB has three, each approximately 10 m thick aquifers in glaciofluvial sands of Saalian and Weichselian ages. The uppermost and partly phreatic aquifer is separated from the deeper aquifer by up to 20 m thick glacial till layers, which locally pinch out. Hydraulic gradients of up to 0.5% are slightly steeper than reported for other NE German areas (**Figure 1**, Schafmeister and Darsow, 2004, Jordan and Weder, 1995; Jurasinski et al., 2018).

Based on the regional flow dynamics, ground water is entering the WB area from 3 hydraulic height maxima, situated at least 10 km away from the WB (Hennig and Hilgert, 2007). Within the catchment area (about 200 km^2), a lake Mühlenteich and other small streams act as routes of surface water flow into the WB.

The Mecklenburg Western-Pomeranian mean annual ground water recharge is about 123 mm/a, estimated by Hilgert (2009) and Hennig and Hilgert (2007). In combination with a mass balance approach, this leads to a rough daily SGD estimation of 60.000 m^3 to the WB (Schafmeister and Darsow, 2004). Ground water recharge rates in the western part of the WB are lower compared to the SE part (Hilgert, 2009; LUNG, 2009).

Ship and boat based fieldwork took place during the spring and summer of 2019. Meteoric water inputs to WB during this period made up 6% of the annual precipitation 548 mm - Germany Weather Station - Wismar (DWD, 2020).

No large rivers drain into WB, but streams such as the Wallenstein located in the eastern part of the coast and the Tarnewitzer on the western part contribute to the fresh water inputs. The average discharge of both streams based on 10-years data are 0.76 and 0.39 $m^3\ s^{-1}$ respectively (Stalu-MV, 2019). In addition to these streams, smaller ones are also present, however, no hydrologic data are available for them.

Sampling Strategy

Sampling in the WB was performed using RV LITTORINA (L19-06) between 20 and 25 May, 2019. Surface water samples were collected at 47 sites spanning the whole bay (**Figure 1**), and additional bottom water samples at four sites (**Supplementary Figure S1**). For sampling in shallow waters (<5 m) a rubber boat was used (20 sites). At six sites, short sediment cores were retrieved for pore water and sediment analyses (**Figure 1**). The coordinates of all sites in the WB are compiled in **Supplementary Table S1**.

At sites exceeding water depths >3 m, CTD profiles were obtained and surface water samples (1 m) were sampled using a submersible pump. The water was pumped through a filter cartridge (1 µm pore size) into 100 L barrels. Water subsamples were taken via syringe and filtered (0.45 µm, cellulose acetate disposable filters, Carl Roth) for analyses of major and trace elements, dissolved inorganic carbon (DIC), $\delta^{13}C_{DIC}$, and stable isotopes of water ($\delta^{18}O$ and $\delta^{2}H$). Samples for DIC and $\delta^{13}C_{DIC}$ were filled without headspace into 12 ml Exetainer® tubes, previously cleaned with 2% HNO_3 washed, dried, and pre-filled with 100 µl saturated $HgCl_2$ solution. Samples for major and trace element analysis were filled into acid cleaned 2 ml reaction tubes and acidified with concentrated HNO_3 to 2 vol.% and samples for $\delta^{18}O$ and $\delta^{2}H$ analyses were collected in 1.5 ml vials glass sealed with a PTFE-coated septum cap. All samples were stored dark and cool until further analyses.

Water samples in the barrels were pumped, using a submersible pump through manganese-coated acrylic fibers at a flow rate of 1 L min^{-1} to quantitatively extract radium (Ra) isotopes. The fibers were washed to remove salts and partly dried for further measurements.

Short sediment cores were collected at six different sites in the WB (**Figure 1**) using a Rumohr-Lot (60 cm length, inner diameter: 10 cm). For pore water sampling, Rhizons (Rhizosphere Research Products, 0.12 µm pore size (Seeberg-Elverfeldt et al., 2005)) were inserted in pre-drilled holes of the plastic liner and attached to 10 ml plastic syringes. Salinity and pH of pore waters were

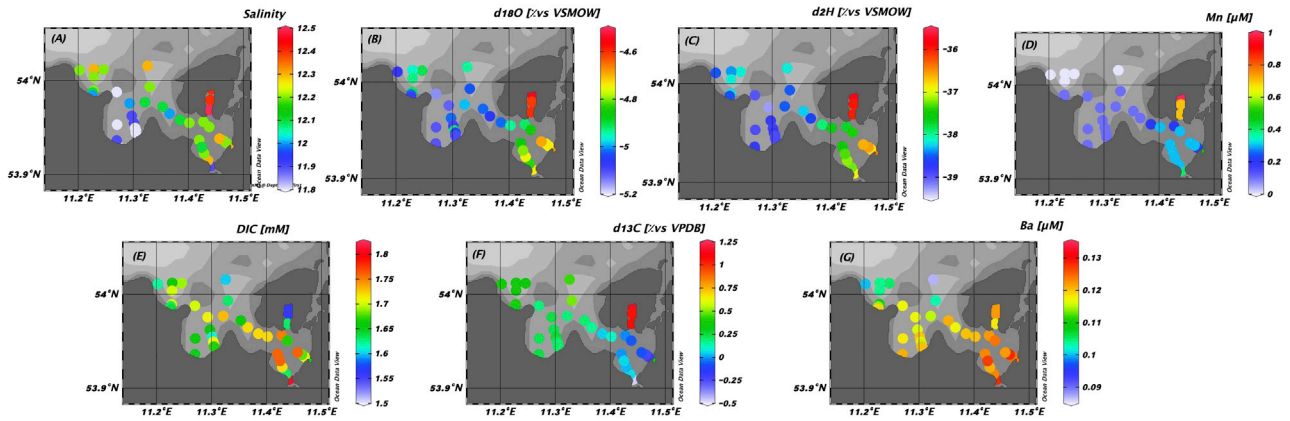


FIGURE 3 | Areal distribution of selected variables in surface waters of the Wismar Bay. Salinity **(A)**, $\delta^{18}O_{H2O}$ **(B)**, $\delta^{2}H_{H2O}$ **(C)** of water, dissolved Mn **(D)**, DIC **(E)**, $\delta^{13}C_{DIC}$ **(F)**, and Ba **(G)**.

measured immediately after recovery using a refractometer and hand-held pH meter (Schott handylab pH meter 11—calibrated with Mettler Toledo Buffer solutions), respectively. Pore water was fixed with 5% Zn-acetate solution for later analysis of total sulphide (H_2S) concentrations. Additional pore water samples were taken for major and trace elements, DIC, $\delta^{18}O$, and $\delta^{2}H$ of water, and preserved and stored as described above. Parallel sediment cores were (sites 10, 11, 15, 20, and 31), sliced at 2–4 cm intervals for geochemical analyses of sediments. Sediments at site 2 were sampled on the same core after pore water extraction. Sediment aliquots were transferred into 50 ml centrifuge tubes (Sarstedt) and kept frozen (−20°C) until further preparation.

Between July and August 2019 along the shoreline pore water samples were collected at five different sites in 0.4–1.8 m depth using push-point lances (MHE products) (**Figure 1**). In addition, four streams draining to the WB were sampled at the mixing zone with BS water. For major and trace elements, and stable isotopes analyses using the same methods as described for surface water of WB. In addition, samples for chloride (Cl) analysis were filled into 500 ml plastic bottles. pH, conductivity, and temperature were measured *in situ* using Schott handylab pH 11 and Schott handylab LF 11 devices. For Ra isotope measurements, 25 L of pore water was collected using a peristaltic pump, while 60 L of stream surface waters were collected and filtered through a 25 µm filter into pre-cleaned gallon containers for further filtration through the Mn fibers.

To identify the potential impact of SGD on coastal waters a pre-survey of Ra isotope distribution in surface water was carried in April 2021 along the shoreline between WB and Warnemünde (~50 km east of WB, **Figure 3**). Water samples for Ra measurements were taken at 23 sites, with 6 sites within WB and the remainder between WB and further east along the coastline (**Figure 3**). The sampling method is the same as described above.

The isotope-hydrochemical composition of ground waters emerging on a nearby coastal beach (Site Meschendorf–**Figure 1**) was considered for comparative purposes in the discussion of this study. The sampling was conducted in the same way as for the surface water campaign in the WB and took place in September 2018.

In addition, fresh ground water samples collected from monitoring wells located adjacent to the WB are presented for comparison purposes. Ground water sampling was carried out in 2014 and followed the protocol described by Jenner (2018). The ground water well at Poel Island (**Figure 1**) and the ground water well 2 are located in a confined aquifer with more than 10 m of soil layer above the filter screen. The other 3 ground water wells (1, 3, and 4) are located in an unconfined aquifer with sampling depths less than 5 m below the surface (Jenner, 2018).

Geophysical acoustic investigations of the subsurface sediments were carried out from July 29th to 31st 2019 using an Innomar SES96 parametric echo sounder mounted on the IOW research catamaran Klaashahn. Seismic data were collected at three frequencies, of which only the 8 kHz dataset is presented here. Results were corrected for ship movements using a motion sensor during data acquisition. The processing of the seismic data was done using Seismic Unix, which involved threefold stacking of the data for the signal to noise ratio improvement, and application of a time-varied gain. The time-depth conversion was calculated using a constant sound velocity of 1,500 m s^{-1}.

Analytical Methods

Water contents of the sediment samples were determined gravimetrically after freeze-drying (considering the water loss due to pore water extractions at Site 2). About 1 g of each sediment sample was pre-treated for grain size analysis by removing carbonate and organic matter using hydrochloric acid (HCl) and hydrogen peroxide, respectively to prevent the binding of the small particles. Grain size measurements in the range from 0.01 to 3.500 µm were performed using a Mastersizer 3,000 with a wet dispersion unit (Hydro EV; Malvern Panalytical). Grain size statistics (including the first mode) were calculated using the program GRADISTAT (Blott and Pye, 2001), applying the volume percentage data and a geometric graphical method modified after Folk and Ward (1957).

Freeze-dried sediments were analyzed for total carbon (TC), total nitrogen (TN), and total sulphur (TS) content with a CHNS Elemental Analyzer (Euro Vector EuroEA 3,052). The

combustion was catalyzed by V_2O_5, the resulting gaseous products were chromatographically separated and quantified via infrared spectrophotometry. Total inorganic carbon (TIC) was determined with an Elemental Analyzer multi-EA (Analytik Jena) after reaction with phosphoric acid 40% followed infrared spectrophotometry quantification of CO_2. The precision of the method were ±3, ±10, ±7.6, and ±4.3% for TC, TN, TS, and TIC respectively, using MBSS- (CNS) and OBSS-$CaCO_3$ (TIC) as in-house standards. The content of total organic carbon (TOC) was calculated from the difference of TC and TIC. The contents of total Mercury (Hg) were analyzed using a DMA-80 analyzer with a detection limit of about 0.15 μg kg^{-1}, as described by Leipe et al. (2013). The precision and accuracy of the measurement were ±8 and ±1.3%, respectively. The calibration was carried out with the 142R MBSS standards.

For the analysis of the acid extractable fraction of several metals (identified in the text with *) about 200 mg of freeze-dried and homogenized sediment was treated with 10 ml 0.5 M HCl agitated for 1 h (Kostka and Luther, 1994). The extracts were filtered with 0.45 μm disposable surfactant-free cellulose acetate membrane filters (Carl Roth), and analyzed by inductively coupled plasma optical emission spectrometry, ICP-OES (Thermo, iCAP, 7,400 Duo Thermo Fischer Scientific), after 10-fold dilution with 2% HNO_3 using external calibration and Sc as an internal standard. The international reference material SGR-1b (USGS) revealed precision and accuracy of better than 2.1 and 3.8%, respectively (Dellwig et al., 2019).

Major ions (Na, Mg, Ca, K, S) and trace elements (Ba, Fe, Li, Mn, Sr) in the water samples were analyzed by ICP-OES using matrix-matched external calibration (diluted OSIL Atlantic Sea water standard spiked with Ba, Fe, Li, Mn, and Sr) and Sc as internal standard. Precision and accuracy were checked with spiked SLEW-3 (NRCC) and were better than 4.7 and 7.6%, respectively.

Concentrations of H_2S were determined by the methylene blue method (Cline, 1969) using a Spekord 40 spectrophotometer (Analytik Jena). The chloride concentration of the water samples was determined by an electric potentiometric precipitation titration (Schott instruments), which utilizes the changing electrical potential difference of the solution by quantitative precipitation of Cl ions due to titration with 0.05 M $AgNO_3$. Analytical accuracy was constantly checked with the international reference standard OSIL Atlantic Seawater 35.

$\delta^{13}C_{DIC}$ values were determined as described by Winde et al. (2014) by means of continuous-flow isotope-ratio-monitoring mass spectrometry (CF-irmMS) using a Thermo Finnigan MAT253 gas mass spectrometer attached to a Thermo Electron Gas Bench II via a Thermo Electron Conflo IV split interface. Solutions were allowed to react for at least 18 h at room temperature before introduction into the mass spectrometer. The international calibration materials IAEA Ca carbonate standard and Solnhofer Plattenkalk were used for calibration of measured isotope ratios towards the V-PDB scale. $\delta^{18}O$ and $\delta^{2}H$ values of water were analysed with a CRDS system (laser cavity-ring-down-spectroscopy; Picarro L2140-I; Böttcher and Schmiedinger, 2021). The reference materials SLAP and VSMOW were used for calibration of measured isotope ratios towards the V-SMOW scale. All stable isotope results are giving in the δ-notation. The given '‰' values are equivalent to mUr (milli Urey; Brand and Coplen, 2012).

Ra isotopes (^{223}Ra, $t_{1/2}$ = 11.4d, and ^{224}Ra $t_{1/2}$ = 3.7d) were measured with radium-delayed coincidence counters (RaDeCC) (Moore and Arnold, 1996) within 3 days after sampling. After about a month, a further measurement was conducted for the determination of ^{224}Ra supported by ^{228}Th ($t_{1/2}$:1.9 years), this measurement is then subtracted from the initial ^{224}Ra to obtain the excess of ^{224}Ra activities ($^{224}Ra_{ex}$). Activities of ^{223}Ra, ^{224}Ra, and $^{224}Ra_{ex}$ were calculated and the expected error of the measurement is 12 and 7% for ^{223}Ra and ^{224}Ra respectively (Garcia-Solsona et al., 2008). The calibration of the detectors is done once a month using ^{232}Th with certificate activities. In this study, we do not discuss ^{223}Ra, but the data can be found in the **Supplementary Table S2**.

The isotope-hydrochemical analysis of the ground water from the wells was carried out by the department of "Strahlen und Umweltschutz" at the "Landesamt für Umwelt, Naturschutz und Geologie". As for methods used, all methods and DIN standards are given in **Supplementary Table S3**. The data was kindly provided by LUNG Güstrow and further details can be found at Jenner (2018).

Numerical Model

Steady-state modeling of pore water profiles was performed to assess the transport mechanism, i.e., diffusive or advective fluxes. The model further evaluates the essential geochemical reactions and the transformations rates. Net-release of a solute into the bottom water leads to positive transformation rates while net consumption results in negative transformation rates (Schultz, 2006).

Pore water sulphates (SO_4) and DIC concentration profiles were computed as a function of sedimentation rate, organic matter degradation, and diffusion rates using the reactive transport model described in (Meister et al., 2013). The following general equation was used:

$$\frac{\partial(\varphi C)}{\partial t} = -\frac{\partial(\omega\varphi c)}{\partial z} + \frac{\partial}{\partial z}\left(\frac{D_0}{\tau^2}\varphi\frac{\partial C}{\partial Z}\right) + \varphi\sum R_i \qquad (1)$$

where C is the concentration, t is time, ω is the sedimentation rate, z is the depth below seafloor, φ is the porosity, and D_0 is the diffusion coefficients corrected by tortuosity (τ^2), which was calculated according to Boudreau (1997) as $\tau^2 = 1–2\cdot\ln\varphi$. The mean sedimentation rate ω was taken as 2 mm yr^{-1} (Lampe et al., 2013) and an average porosity was taken as 0.88 derived from the sediment water content. The diffusion coefficients for SO_4 and DIC were calculated as 0.0236 and 0.0257 $m^2\,yr^{-1}$ respectively, based on the average temperature of 12°C and an average salinity of 13 (Boudreau, 1997).

Sources and sinks of SO_4 and DIC are stoichiometrically coupled to rates of organic carbon decay via the following simplified reaction for organoclastic sulphate reduction:

$$SO_4^{2-} + 2CH_2O \rightarrow HS^- + 2HCO_3^- + H^+ \qquad (2)$$

The organic matter decay rate R_G was followed by the reactive continuum (RC) model of Boudreau and Ruddick (1991).

$$R_G(t) = -\nu(a+t)^{-1}G(t) = -\frac{\nu a^{\nu}}{(a+t)^{\nu+1}}\frac{\rho_s(1-\varphi)G_0}{100\varphi M_C} \quad (3)$$

where the free parameters and a ν determine the shape of the initial distribution of organic matter reactivity. The parameter a describes the average life-time of the more reactive components of the spectrum whereas ν defines the shape of the distribution. The dry density of the sediment is ρ_s (ρ_s = 2.6 g cm^{-3}), M_C is the molecular weight of carbon (M_C = 12) and G_0 is the initial TOC upon sedimentation (wt%). Thus, the SO_4 reduction and DIC production rate can be given by $0.5R_G$ and R_G, respectively.

The isotopic composition was calculated from the measured ratios R and referred to the VPDB according to Hoefs (2018):

$$\delta^{13}C = \left(\frac{Rsample}{R_{VPDB}} - 1\right) \cdot 1000 \quad (4)$$

The absolute concentrations of [^{13}DIC] and [^{12}DIC] were computed by separated reaction-transport equations (**Eq. 1**) for each isotope. Negligible carbon isotope fractionation was assumed during organoclastic sulphate reduction (cf. Claypool and Kaplan, 1974). Therefore, this source of inorganic carbon was assumed to show the same isotopic composition as the organic source.

Initial conditions were 0 mM SO_4 and DIC at all depths. The computer domain was set to be 50 cm. The Dirichlet boundary condition was applied at both the sediment/water interface (z = 0 cm) and bottom (z = 50 cm) according to the observed data. All parameters used in the model are listed in **Supplementary Table S4**.

Data Presentation

The figures presenting the vertical profiles were created using Sigma Plot 10.0 software (Systat Software, Inc., United States). The concentration maps were plotted using Ocean Data View (Schlitzer, 2001). The study area map was created using the Qgis development Team.

RESULTS

Results of all chemical elements measured in the Wallenstein stream, western streams, beach pore water, fresh ground water from the wells, fresh surface water from springs in Meschendorf are listed in **Table 1**. To place these data in a context, the data of surface water and pore water from the WB were also compiled in this table. The parameters of these different waters were plotted against salinity to assess the behavior of the parameter along the salinity gradient and the contribution of mixing and biogeochemical processes (**Supplementary Figure S2**).

Water Composition

Surface Waters in the Wismar Bay

The salinity of the WB surface waters ranged between 11.8 and 12.5 (**Figures 3A**), which is in the range of previously observed (Prena, 1995). The WB water column was well mixed, showing a slight salinity increase in bottom waters at some sites (**Supplementary Figure S3**). All conservative elements followed expected trends by covarying with salinity.

The δ^2H_{H2O} and $\delta^{18}O_{H2O}$ varied between −35.7 and −39.3‰ and between −4.5 and −5.2‰, respectively. Heavier isotopic compositions were found in the sheltered eastern part of the bay, mainly near Poel Island. Towards the western part of the WB, the isotope values were lighter, but show a trend of decreasing values close to the coastline (**Figures 3B,C**).

In surface waters, DIC ranged from 1.5 to 1.8 mM (**Figure 3E**) and $\delta^{13}C_{DIC}$ varied between -0.5 and 1.1‰ (**Figure 3F**). We found a W-E trend increasing concentrations in DIC and an inverse relationship between concentrations and its stable isotope composition. Only the waters close to Poel Island showed the lowest concentrations and the highest $\delta^{13}C_{DIC}$.

The concentrations of manganese (Mn) and barium (Ba) varied between 0.03 and 0.1, 0.07, and 0.1 μM, respectively, (**Figure 3D,G**). The eastern area was characterized by higher concentrations of Mn and Ba compared to the western parts (**Figure 3E**).

The activities of $^{224}Ra_{ex}$ ranged between 3 and 28 dpm 100 L^{-1} with an average of 7 L dpm 100 L^{-1}, presenting also higher activities in the eastern area. The site located in open BS waters presented a ^{224}Ra activity of 1.5 dpm 100 L^{-1} (**Figure 2**).

Streams

The Wallenstein stream discharges into the eastern part of the bay and showed $\delta^{18}O_{H2O}$ and δ^2H_{H2O} values of −4.0‰ and −33.2‰, respectively, which were heavier than the other streams in the western part of the WB. All isotopic compositions plot below Local Meteoric Water Line (LMWL) established for the southern BS at Warnemünde (**Figure 4**) in contrast with the results for ground waters in the WB region that fall on LMWL (**Table 1**; **Figure 4**).

For a general characterization, the hydrochemical composition of the investigated waters is compiled in a Piper diagram (Piper, 1944) (**Figure 5**). Most of the streams can be characterized as Na-Cl, and one of them as CaMg-HCO_3 waters (**Figure 5**), with the Na-Cl type being impacted by mixing with BS water at the sampling site.

The western streams were enriched in DIC compared to the Wallenstein stream. The DIC concentration in the western streams reached 5.8 mM and the $\delta^{13}C_{DIC}$ values were around −13.2‰ whereas the Wallenstein stream had a concentration of 2.5 mM and a $\delta^{13}C_{DIC}$ value of 6.5‰.

The activities of $^{224}Ra_{ex}$ in the western streams (salinities 0.1–1.8) discharging to the western WB ranged from 7 to 24 dpm 100 L^{-1}, which is within the range of the activities measured in the WB surface waters. The activities for the Wallenstein stream were found to be slightly higher (36 dpm 100 L^{-1}).

Ground Water

Ground waters from the WB catchment are characterized by a water isotopic composition ranging from −8.6 to −8.3‰ ($\delta^{18}O_{H2O}$) and −58.8 to −56.7‰ (δ^2H_{H2O}), similar to the composition of the ground water escaping at the Site Meschendorf, which showed average values of −8.5 and 58‰ respectively (**Table 1**- springs; **Figure 4**).

TABLE 1 | Average, minimum, maximum, and number of samples of the WB surface water (WB), Wallenstein stream, small streams, beach pore water (PW), ground water (GW) from the wells near Wismar, GW from a well in Poel Island, springs located close to Wismar, sediment pore water (PW). The pore waters from the beach and from Wismar were extrapolated to 1 mM Na, which is the concentrations found in the fresh ground waters, and termed as central SGD and beach SGD.

Variables	Unit	WB	Wallenstein stream	Small streams	Beach pore water	GW well 1	GW well 2	GW well 3	GW well 4	GW well 5	Springs Meschendorf	PW st. 10 and 11	PW st. 2, 15, 20 and 31	Central SGD	Beach SGD
Salinity		12.1	7.2	1.7	5.5						0.1	13	14		
		11.8/ 12.6 (46)	(1)	0.1/1.8 (3)	3.1/10.2 (5)						0.1/0.3 (6)	1/15 (30)	12–17 (57)		
Cond.	mS. cm^{-1}		12.6	1.4	9.7	0.8	0.7	0.7	1.0	0.7	0.8				
			(1)	0.8/3.6 (3)	5.7/17.4 (5)	(1)	(1)	(1)	(1)	(1)	0.6/1.1 (6)				
pH		8.3	7.9	8.2	7.38	7.2	7.4	7.3	7.0	7.3	7.3	7.7	7.5		
		8.2/9.0 (17)	(1)	8.1/8.7 (3)	7.1/7.8 (5)	(1)	(1)	(1)	(1)	(1)	7.1/7.4 (6)	7.0/8.2 (30)	7.1/8.3 (57)		
Temp.	°C	14.2	23.7	21.0	20.3	10.2	10.2	10.2	10.9	10.0					
		11.7/20.0 (46)	(1)	16.5/23.5 (3)	19.9/24.7 (5)	(1)	(1)	(1)	(1)	(1)					
DIC	mM	1.67	2.5	4.9	8.6		6.1	5.5		5.4	6.1	7.1	3.5	6.4	13.4
		1.51/1.80 (49)	(1)	4.3/5.8 (3)	4.0/9.4 (5)	(1)	(1)	(1)	(1)	(1)	5.50/6.70 (6)	1.49/ 16.38 (29)	1.51/13.57 (55)	(1)	13.30/13.39 (2)
$\delta^{13}C_{DIC}$	‰ VPDB	0.21	-6.46	–13.23	–15.34	–13.77		–13.79	–14.24		–13.75	–9.29	–6.59	–6.63	–26.30
		–0.46/1.15 (49)	(1)	–13.92/ –10.95 (3)	–17.52/ –8.56 (5)	(1)	(1)	(1)	(1)	(1)	–14.4/–13.61 (2)	=–14.4/ 0.1 (29)	–13.4/0.2 (55)	(1)	–26.50/–26.10 (2)
$\delta^{18}O_{H2O}$	‰ VSMOW	–5.0	–4.0	–7.4	–6.1	–8.4	–8.3	–6.7	–8.4	–8.6	–8.5	–4.9	–4.78	–8.5	–7.14
		–5.2 /–4.5 (49)	(1)	–7.3/ –8.1 (3)	– 7.2/–5.2 (5)	(1)	(1)	(1)	(1)	(1)	–8.7/– 8.4 (4)	–7.2/–4.4 (29)	–5.15/–3.9 (55)	(1)	–8.34/6.26 (5)
$\delta^{2}H_{H2O}$	‰ VSMOW	–38.2	–33.2	–52.3	–43.8	–58.0	–56.7	–48.9	–57.3	–58.8	–57.7	–37.7	–36.4	–56.6	–49.4
		–39.3/–35.7 (49)	(1)	–55.4/ –51.5 (3)	–49.4/–39.3 (5)	(1)	(1)	(1)	(1)	(1)	–58.8/–57.2 (4)	–50.2/ 33.8 (29)	–39.5/–29.5 (55)	(1)	–55.35/–44.74 (5)
Cl	mM		124.5	25.1	74.3	1.21	1.30	0.79	0.99	1.32	0.53				
			(1)	1.45/26.30 (3)	39.40/ 165.09 (5)	(1)	(1)	(1)	(1)	(1)	0/0.66 (3)				
Na	mM	162.2	98.4	23.50	66.9	0.7	2.2	1.0	0.8	0.83	1.03	165.6	176.7	1.0	1.0
		150.5/169.2 (49)	(1)	1.35/36.5 (3)	23.7/142.4 (5)	(1)	(1)	(1)	(1)	(1)	0.9/1.1 (5)	30.9/ 207.4 (23)	148.7/244.2 (55)	(1)	(5)
Mg	mM	18.3	11.4	2.9	9.2	0.5	0.6	0.4	0.6	0.7	0.7	18.64	19.0	0.0	0.3
		17.1/19.9 (49)	(1)	0.7/5.6 (3)	3.0/16.9 (5)	(1)	(1)	(1)	(1)	(1)	0.6/0.9 (5)	2.4/21.8 (23)	16.7/24.2 (55)	–1	0/7.6(5)
Ca	mM	4.0	3.3	2.9	8.0	3.7	2.1	2.5	4.0	3.1	3.5	4.2	4.5	2.4	10.1
		3.7/4.1 (49)	(1)	2.6/3.1 (3)	2.8/14.2 (49)	(1)	(1)	(1)	(1)	(1)	2.7/4.8	3.0/5.3 (23)	3.7/5.6 (55)	(1)	2.6/38.9 (4)
K	mM	3.5	2.2	0.9	1.7	0.0	0.1	0.3	0.3	0.1	0.1	3.7	3.87	0.6	0.3
		3.3/3.7 (49)	(1)	0.1/2.2 (3)	0.6/3.4 (5)	(1)	(1)	(1)	(1)	(1)	0.1/ 0.2 (5)	1.2/4.2 (23)	3.3/5.4 (55)	(1)	0/2.7 (5)
SO_4	mM	9.9	5.8	0.7	4.4	0.6	0.2	0.5	2.3	1.0	1.5	0.0	10.0	0.0	1.0
		9.2/10.4 (49)	(1)	0.6/2.2 (3)	0.8/8.9 (5)	(1)	(1)	(1)	(1)	(1)	1.1/2.7 (5)	0/10.25 (23)	5.3/12.1 (55)	(1)	0/3.4 (5)
Si	µM	6.1	0.1	0.4	0.4						0.4	622.3	258.5	887.3	0.0
		4.4/10.6 (49)	(1)	0.2/0.5 (3)	0.1/0.5 (5)						0.3/0.4 (5)	6.8/ 756.28 (23)	6.2/685.5 (55)	(1)	(3)
P	µM	0	9.9	13.5	11.3						4.2	76.8	38.8	22.0	13.7
		0.0/0.0 (49)	(1)	6.6/284.7 (3)	4.1/22.6 (5)						2.3/5.3 (5)	1.7/269.4 (20)	4.2/89.2 (55)	(1)	4.9/185.0 (5)
Ba	µM	0.1	0.4	0.2	1.1	0.3	0.8	0.3	0.5	0.9	1.1	0.3	0.2	1.4	1.1
		0.1/0.1 (49)	(1)	0.2/0.6 (3)	0.2/2.9 (5)	(1)	(1)	(1)	(1)	(1)	0.8/2.0 (5)	0.12/1.79 (24)	0.1/1.3 (55)	(1)	0.4/7.7(5)
Fe	µM	0.1	1.6	1.1	1.3						55.6	0.7	0.3	10.2	2.1
		0.1/1.8	(1)	0.4/2.1 (3)	0.2/2.1						44.7/124.1 (5)	0.1/624.2 (23)	0.0–5.2 (55)	(1)	1.1/3.5 (5)
Li	µM	8.6	6.4	2.9	8.3						2.0	9.2	9.9100	5.8	4.8
		8.2/9.1 (46)	(1)	2.1/3.0 (3)	2.3/9.9 (5)						1.5/2.1 (5)	6.9/11.5 (23)	8.4/ 13.2 (55)	(1)	2.4/13.0 (5)
Mn	µM	0.1	3.5	2.6	12.0	0.0	0.0	0.0	0.0	0.0	3.0	2.3	1.9	4.2	17.4
		0.0/1.5 (46)	(1)	0.7/4.3 (3)	1.5/24.4	(1)	(1)	(1)	(1)	(1)	2.8/4.6 (5)	0.2/58.2 (23)	0.1/9.5 (55)	(1)	1.7/44.5 (5)
Sr	µM	32.0	21.6	9	28.7						5.6	34.2	35.6	6.9	9.9
		29.9/33.3 (49)	(1)	6.4/13.9 (3)	8.4/34.0 (5)						5.0/9.7 (5)	14.01/ 40.7 (23)	31.0/ 44.3 (55)	(1)	4.6/39.0 (5)
^{224}Ra	dpm $100L^{-1}$	8.01	36.2	15.6	362.2										
		2.8/27.4 (49)	(1)	6.8/24.3 (3)	25.8/ 547.1 (5)										
^{223}Ra	dpm $100L^{-1}$	0.9	0.9	0.4	10.6										
		0/1.7 (26)	(1)	01/0.6 (3)	0.5/18.0 (5)										
$^{224}Ra_{ex}$	dpm $100L^{-1}$	7.3	34.9	15.4	350.6										
		2.3/26.5 (49)	(1)	6.3/23.7 (3)	17.6/530.0 (5)										

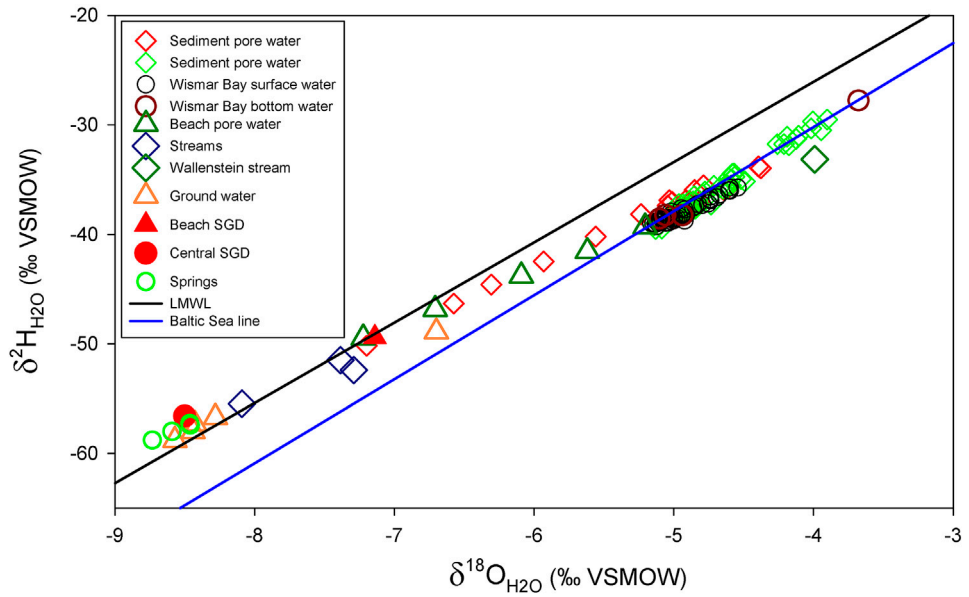


FIGURE 4 | Scatter plot of δ^2H_{H2O} versus $\delta^{18}O_{H2O}$ for sediment porewaters, both impacted (red diamonds) and non-impacted by SGD (green diamonds), Wismar Bay surface (black circles) and bottom (brown circles) waters, beach porewater (green triangles), streams (blue diamond), river (large dark green diamond), ground water (yellow triangle), Beach porewater extrapolated to 1 mM Na called Beach SGD (filled red triangle). The Local Meteoric Water line (LMWL) and the Baltic Sea surface water line from (Böttcher et al., 2020) are also presented.

The hydrogeochemical ground water composition in the region around the WB and of Meschendorf can be classified as Ca-Mg-HCO_3 type (**Figure 5**). Based on the classification scheme by Löffler et al. (2010) it can be further characterized as a relatively young confined ground water.

Sediment Pore Water at the Beachline of Wismar Bay

Salinities of beach pore waters ranged between 3 and 10 (**Table 1**), representing different relative mixtures between fresh (salinities <1) and brackish waters (salinities of the WB: 11.8–12.5). Metabolites were enhanced when compared with the composition of the WB surface water, streams, and fresh ground waters around the WB (**Supplementary Figure S2**).

The water isotope data varied from −7.2 to −5.2 ($\delta^{18}O_{H2O}$) and −49.4 to −39.3‰ (δ^2H_{H2O}), reflecting also a mixture between two different endmembers (**Figure 4**).

The average $^{224}Ra_{ex}$ activity was 351 ± 188 dpm 100 L^{-1} (n = 5), which is one order of magnitude higher than those found in the surface waters from either WB or in the streams (**Table 1**).

Sediment Pore Water in the Wismar Bay

The downcore variation in the pore waters composition from six sediment sites in the WB is presented in **Figure 6** as a function of sediment depths. Sites 2, 15, 20, and 31 are presented separately from sites 10 and 11.

Sediments at sites 2, 15, 20, and 31 showed pore water profiles with constant salinity, except for a slight maximum at around 6 to 15 cmbsf, (**Figure 6A**). At Site 10 and in particular Site 11 (**Figure 1**), a strong downcore decrease in salinity was found. Relative to the bottom water conditions, the pore water salinities at Site 10 decreased by about 30% at 40 cmbsf. At the same depth, the salinity gradient at Site 11 reached essentially fresh water conditions (**Figure 6A-2**). In agreement with the salinity changes, the other conservative elements (Na, Mg, and K) also decreased with depth.

The δ^2H_{H2O} and $\delta^{18}O_{H2O}$ isotope values of the pore water at sites 2, 15, 20, and 31 varied from −39.5 to −29.5‰ and −5.1 and −3.9‰ respectively (**Figures 6B,C**). Due to the freshening by ground water at depth, the down core variations at sites 10 and Site 11 are much more pronounced, −50.2 and −36.9‰ (δ^2H_{H2O}) and −7.2 and −4.9‰ ($\delta^{18}O_{H2O}$), and at 40 cmbsf at sites 11 and 10, respectively (**Figures 6B-2,C-2**).

All pore waters were enriched in metabolites when compared to the bottom waters (**Table 1**), with increase concentrations at depth. A pronounced maximum concentration in the top 10 cmbsf was found at Site 11 (**Figures 6K-2–M-2, O-2**).

Pore water concentrations of SO_4 at the sediment-water interface were between 8 and 12 mM and decreased with depth, reaching 2 mM at most sites, and reaching even complete depletion at the base of Sites 10 and 11 (fresh water influenced sites) (**Figure 6I-2**). H_2S was determined at all sites showing net accumulation below about 16 cmbsf. At site 11, no H_2S accumulation was observed (**Figure 6J-2**).

The concentrations of DIC increased with depth up to 16 mM at all sites except for Site 11 where again a maximum was found in 10 cmbsf (**Figure 6-O2**). The increase in DIC concentrations was associated with a decrease in $\delta^{13}C_{DIC}$ values (**Figure 6P-2**).

Results from the modeling downcore profiles of SO_4, DIC, and $\delta^{13}C_{DIC}$ were indicated by dashed lines in the panels I, I-2, O, O-2, P, P-2 of **Figure 6**. The corresponding fluxes and accumulated mineralization rates in depth intervals of 10 cm are given in

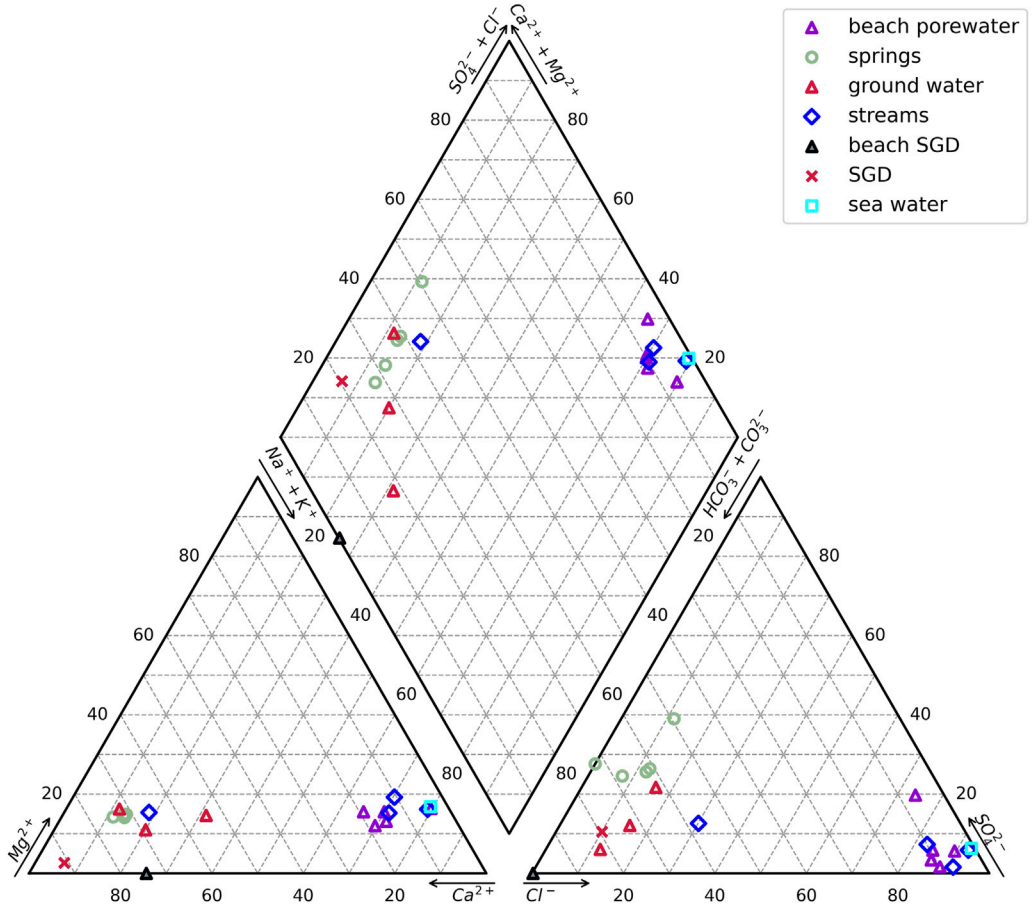


FIGURE 5 | Piper diagram of the major ions of the Wallenstein stream and western streams (blue diamond), springs (green circle), fresh ground water (red triangle), beach porewater (purple diamond) and sea water of Wismar Bay (turquoise square), extrapolated beach porewater (beach SGD—black triangle) and porewater of site 11 (SGD—red cross) to 1 mM Na.

Table 2. The modeled SO_4 fluxes both in the top and bottom sediment are positive and similar at all the sites. In contrast, the modeled DIC fluxes are negative, except at Site 11 which shows positive fluxes. In addition, the results of the model show that in the first 10 cmbsf of the majority of the sites there is a high OM accumulation, especially in Site 11, which is caused by a reactive metal oxide other than sulphate reduction. To verify the additional OM mineralization rate by reactive metal oxide on this site, different mineralization rates at 6–10 cm were tested (**Supplementary Figure S4**). It becomes obvious that an enhanced OM mineralization rate is required to fit the $^{13}C_{DIC}$ values.

Sediment Composition

Sediment Geochemistry

All sediment cores comprised a dark gray to black color with muddy texture covered by a brown fluffy layer on top.

Grain-size analyses show an uni-to bimodal distribution in the upper sediment. The vertical grain-size characteristics represented here by the first mode are given in **Supplementary Figure S5**. The samples first mode ranges between 8 and 100 µm. Fine to medium silt dominate at sites 10 and 11 (<40 µm) and at the surface of site 2 (subsurface), while sites 15 and 31 consist of coarse silt with a second mode around 8 µm. At site 20, in the southeastern part of WB, sediments consist of very fine sand. At sites 10 and 11 grain-size becomes finer with depth, whereas the mean grain-size increases at the other sites. The water content of the sediments ranged between 44 and 87% and generally decreased with sediment depth (**Supplementary Figure S5**).

The total organic carbon (TOC) contents ranged from 1 to 8% dwt. Organic matter-rich sediments (TOC >4 %wt.) were found at sites 10, 11, and 31, whereas sediments at other sites contained less TOC (**Figure 7C**). The molar TOC/TN ratios varied between 6 and 12 (**Figure 7D**) with increasing ratios with sediment depth. Total sulphur (TS) contents ranged from 0.3 to 2.4 wt. % (**Figure 7B**), typical for marine sediments (**Figure 8**) (Berner and Raiswell, 1983). Reactive Fe and Mn were generally pronounced in the top layers and mostly decreased at larger depths (**Figure 9**). Site 11 was characterized by the relatively highest values.

In brackish-marine sediments, microbial sulphate reduction limited by the availability of OM (Berner, 1980) which may be reflected by a positive co-variation of TOC with pyrite sulphur as found for Holocene sediments (Berner, 1982). The TS contents (taken here as a measure for pyrite sulphur) found in the shallow sediments of WB are positioned on or below the relationship

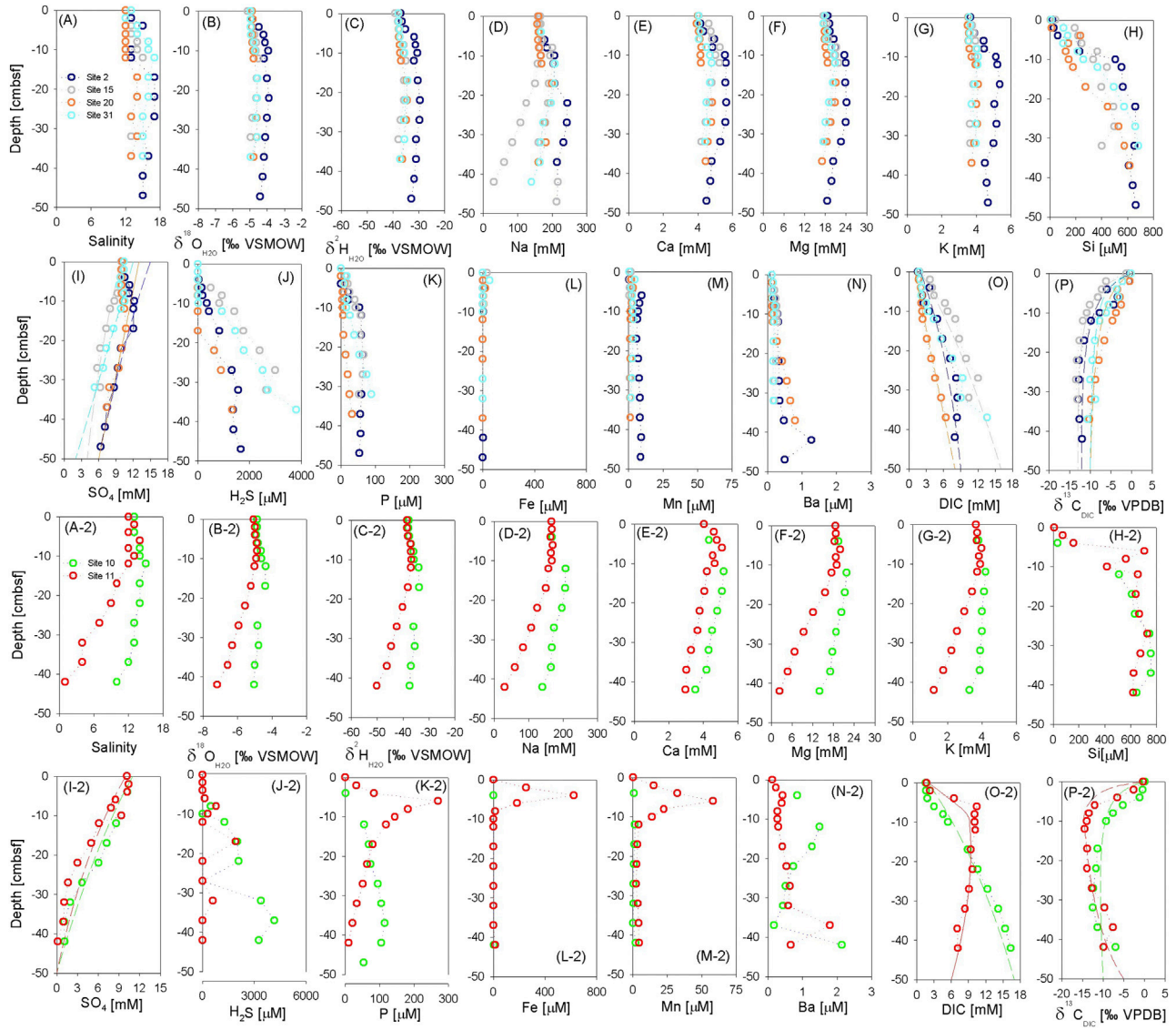


FIGURE 6 | Pore water profiles in sediment cores from WB showing salinity **(A)**, $^{18}O_{H2O}$ **(B)**, $^{2}H_{H2O}$ **(C)**, and different dissolved components Na **(D)**, Ca **(E)**, Mg **(F)**, K **(G)**, Si **(H)**, SO_4 **(I)**, H_2S **(J)**, P **(K)**, Fe **(L)**, Mn **(M)**, Ba **(N)**, DIC **(O)**, $^{13}C_{DIC}$ **(P)**, of sites 2, 15, 20, and 31. The sites impacted by freshening at depth are presented in the panels: salinity **(A-2)**, $^{18}O_{H2O}$ **(B-2)**, $^{2}H_{H2O}$ **(C-2)**, and different dissolved components Na **(D-2)**, Ca **(E-2)**, Mg **(F-2)**, K **(G-2)**, Si **(H-2)**, SO_4 **(I-2)**, H_2S **(J-2)**, P **(K-2)**, Fe **(L-2)**, Mn **(M-2)**, Ba **(N-2)**, DIC **(O-2)**, $^{13}C_{DIC}$ **(P-2)**. The additional dashed lines in the panels I, I-2, O, O-2, P, P-2 are the diagenetic modeling results.

proposed for siliciclastic sediments deposited beneath an oxygenated water column (**Figure 8**) (Berner, 1982).

The typical anthropogenic contaminants as Hg and acid-extractable lead (Pb*), showed pronounced variations reaching maximum contents of 156 µg kg^{-1} and 60 mg kg^{-1}, respectively, mostly in the shallower part of the cores (**Figure 9**). Here, relatively similar concentrations may be related to bioturbation, probably caused by different activities of macrozoobenthos (Lipka et al., 2018b; Gogina et al., 2018). At Site 11, lateral sediment supply from the flanks of the channel, sediment redistribution caused by the channel excavation, and fresh water flow from below may have cause relative constant concentrations. At Site 11, both Hg and Pb* concentrations show no trend with depth.

Geophysical Characterization

The position of transects within WB are displayed in (**Figure 1**) and the results of the acoustic measurements are presented in **Figures 10**, **11**. In the western transect, a steep drop in the bathymetry from less than 3 m water depth to approximately 9 m water depth is observed (**Figure 10**). In shallow waters of 3 m water depth and less no subsurface structures can be recognized in the seismic data.

Directly below the seafloor at the base of the steep drop (near site 15), mostly acoustically transparent sediments with weak horizontal internal layering are deposited (S2). Within this unit, gas fronts prohibited further penetration of the acoustic signal, and are recognized along the profile by high acoustic turbidity. At

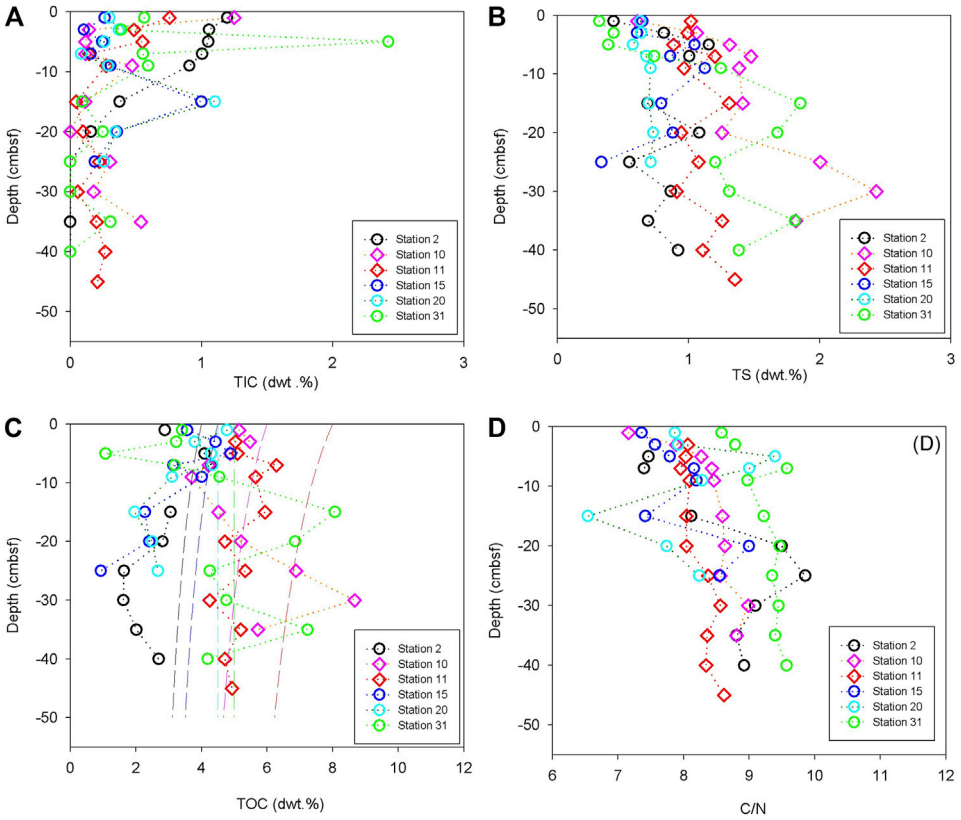


FIGURE 7 | Vertical profiles of the bulk geochemical parameters TIC **(A)**, TS **(B)**, TOC **(C)**, and C/N **(D)** ratios in sediments cores from the WB. The dashed lines in panel C (TOC) display the results from the diagenesis transport model (see discussion).

two locations (Site 13 and between sites 13 and 14), chimneys rise from the gas front to the seafloor. Between sites 13 and 15, the gas front was penetrated and the seismic units S3 and S4 can be observed. A distinct reflector is forming a low angle unconformable boundary of S3 with the overlying unit S2. Within unit S3, a faint and distorted internal lamination is observed. Unit S3 is separated from unit S4 by an unconformable high-amplitude reflector that is strongly undulating. Unit S4 is acoustically transparent and forms the base of acoustic penetration, corresponding to the onset of glacial deposits.

In the central WB, a channel dredged for ship traffic to approx. 10 m water depth is visible (**Figure 11**). At the flank of this artificial depression, seismic unit S1 is observed in the top meter of the subsurface. Based on the acoustic measurement, the unit has a chaotic texture but may be separates into sub-units by an unconformity (near site 31). A medium to high amplitude reflector separated unit S1 from S2, which again shows a weak, horizontal internal lamination with a thickness of up to 3 m. Along the majority of the profile, free gas fronts are observed at a depth of approx. 9 m. Near site 30, a gas chimney reaches the seafloor. Closer to the channel and on a perpendicular profile, unit S3 occurs with a thickness of approx. 1 m. Seismic unit S4, separated from the overlying units by a marked unconformity, forms the base of acoustic penetration.

DISCUSSION

Fresh Water in the Catchment Area and Inlets at the Margins of Wismar Bay

Fresh ground waters from the catchment in the southern part of the WB and from a well on Poel Island (**Figure 1**) display a water isotope composition positioned on the LMWL of Warnemünde (**Table 1**; **Figure 4**). These data are also close to the composition of ground waters escaping at beach spring in Meschendorf (**Figure 1**), which has been shown water of age about 30 years (Lipka et al., 2018a). The hydrogeochemical ground water composition of the majority of investigated wells and the springs fall into the field for relatively "young" ground waters (**Figure 5**).

The Wallenstein stream and the other western streams carry different isotope-hydrochemical signatures, thus representing different surface waters sources entering the southern WB.

The western streams showed a water isotopic composition and $\delta^{13}C_{DIC}$ signatures similar to those found in the well waters of the catchment area (**Table 1**). The slight shift towards heavier isotope values is likely the result of an impact by evaporation and CO_2 degassing when stream waters get in contact with the atmosphere (Michaelis et al., 1985; Clark and Fritz, 1997).

The Wallenstein stream, on the other hand, is enriched in heavy water isotopes and dissolved ions when compared to well waters

TABLE 2 | Modeled diffusive and advective fluxes of DIC and SO_4 and the accumulated OM mineralization rate for all the 6 sediment core sites. The fluxes and the rates are given in mmol m^{-2} d^{-1}.

	Advective and diffusion fluxes					
Sites	**2**	**10**	**11**	**15**	**20**	**31**
			Top (z= 0 cm)			
			SO4 flux			
Advective flux	0.07	0.05	0.05	0.05	0.06	0.06
Diffusive flux	1.18	1.55	1.66	1.66	0.62	0.89
Total flux	1.25	1.60	1.70	1.70	0.68	0.94
			DIC flux			
Advective flux	0.01	0.01	0.01	0.01	0.00	0.00
Diffusive flux	−1.46	−2.62	−4.30	−2.24	−0.68	−1.36
Total flux	−1.45	−2.61	−4.29	−2.22	−0.68	−1.36
			Bottom (z= 50 cm)			
			SO4 flux			
Advective flux	0.03	0.00	0	0.02	0.03	0.01
Diffusive flux	0.60	0.66	0.44	0.29	0.65	0.93
Total flux	0.63	0.66	0.45	0.31	0.68	0.94
			DIC flux			
Advective flux	0.04	0.08	0.03	0.08	0.04	0.07
Diffusive flux	−0.23	−0.81	1.01	−0.89	−0.72	−1.43
Total flux	−0.19	−0.73	1.04	−0.81	−0.68	−1.36
			Accumulated OM mineralization rate			
0-10 cm	0.44	0.66	3.70	0.49	0.00	0.00
10-20 cm	0.29	0.44	0.59	0.33	0.00	0.00
20-30 cm	0.22	0.32	0.43	0.24	0.00	0.00
30-40 cm	0.17	0.26	0.34	0.19	0.00	0.00
40-50 cm	0.14	0.21	0.28	0.16	0.00	0.00
0-50 cm	1.26	1.89	5.34	1.42	0.00	0.00

and western streams (**Figure 4**; **Table 1**). Besides the mixing with BS surface waters during the time of sampling, this could also be the result of surface water evaporation (e.g., Gat, 1996; Clark and Fritz, 1997) that took place during the origin of this stream in Lake Schwerin and a further crossing through Lake Mühlenteich before reaching the WB coastline (**Figure 1**).

The impact of stream waters on the composition of the WB surface waters is most pronounced in the western part of the bay. There the water isotopic composition decreased towards the coastline (**Figures 3B,C**), due to mixing between open BS water, containing heavier isotopes, and a fresh water component characterized by lighter isotopes. In addition, higher concentrations of DIC together with the depleted $\delta^{13}C_{DIC}$ found near the western coastline (**Figures 3E**) are probably related to fresh water sources (Winde et al., 2014). The surface water of the WB in the western part showed water isotopes values decreasing close to the coastline (**Figures 3B,C**), probably due to mixing between open BS water containing heavier isotopes, and a fresh water component characterized by lighter isotopes coming from the small streams located in this region. These streams showed a water isotopic composition similar to those found in the ground water recovered from wells near Wismar (**Table 1**, GW) and fresh water springs at Meschendorf (**Table 1**–springs). The slight trend to heavier isotopes is likely the result of an impact by evaporation and CO_2 degassing when stream waters become in contact with the atmosphere (Clark and Fritz, 1997). The $^{13}C_{DIC}$ isotopic signatures of the western streams are similar to the values in the ground water as well, which reinforces the idea that the streams are supplied by ground water from unconfined aquifers.

Within the western part of the WB, ^{224}Ra activities showed a decrease towards the open BS (**Figure 2B**). Since the ^{224}Ra activities in the streams were comparable to those measured in the surface water of the WB (**Figure 2**; **Table 1**), further sources may are contributing to the observed spatial patterns. Besides the ground water below the central part of the bay (see 4.3), which has not been analyzed for ^{224}Ra, the permeable sediments along the bay may act as a further fresh water and ^{224}Ra source to the WB. The pore water at the beach showed average $^{224}Ra_{ex}$ activities that were about one order of magnitude higher than the activities found in the surface water of WB. These findings, therefore, suggest, that SGD can enter the WB from the boundaries and contributing as a further source to the water balance of the WB.

Beach pore water consist of a mixture between fresh water and a brackish water component. To estimate the fresh water endmember the beach pore water compositions were extrapolated based on actual measurements and using Na as conservative mixing tracer (boundary conditions: average WB and 1 mM for the fresh water, which is the mean concentration found in the ground water wells). These values can be found in **Table 1**—Beach SGD. For the majority of the dissolved compounds a composition close to ground waters was found (**Table 1**). Only some non-conservative constituents, like DIC and Ca were enhanced in the estimated fresh water component, likely due to corrosion processes of carbonates present in the coastal sands (e.g., Smellie et al., 2008).

Although a ^{224}Ra gradient was not established in the eastern part of the WB (**Figure 2**), the generally higher activities in this part may indicate a source of ^{224}Ra. This source may originate from the exchange with pore water or resuspended sedimentary particles or SGD, besides the Wallenstein stream. Moreover, enhancement of Mn and Ba compared to the open BS surface water confirms strong benthic pelagic fluxes.

Tentative Radium Mass Balance for Wismar Bay

A mass balance is constructed, based on Rodellas et al. (2021), to estimate SGD in the WB. The Ra mass balance relies on the assumption that the most important Ra sources and sinks are in steady state, and then SGD can be evaluated by the difference of supply and removal according **Eq. 5**.

$$F_{SGD} * A_{SGD} + Q_{str}C_{str} + F_{sed} * A_{WB} = \lambda VC + Q_{out}C \qquad (5)$$

Where V and A_{WB} are the water volume (m^3) and surface area (m^2) of where samples were collected (**Figure 1**). We assume for the balance that SGD is taking place at 27 km of the shoreline and 10 m offshore (A_{SGD}). Q_{str} is the discharge from streams (m^3 d^{-}). We consider here the Wallenstein stream and the three western streams. Q_{out} is the water outflow to the open BS (m^3 d^{-1}) determined by using the water mass ages, the activity difference between WB and open-sea water and the volume of the study area. The water ager was calculated following (Moore and de Oliveira, 2008). C is the weighted average of $^{224}Ra_{ex}$ of the WB, determined by the $^{224}Ra_{ex}$ inventory. C_{str} are the mean concentrations of $^{224}Ra_{ex}$ in the surface water inlets (Bq m^{-3}). F_{sed} is the $^{224}Ra_{ex}$ diffusion from sediments. λ is the radioactive decay constant of ^{224}Ra. F_{SGD} is the fluxes of $^{224}Ra_{ex}$ per unit area associated with SGD (Bq m^{-2} d^{-1}), respectively. Terms used in the mass balance together with the units are summarized in **Table 3**.

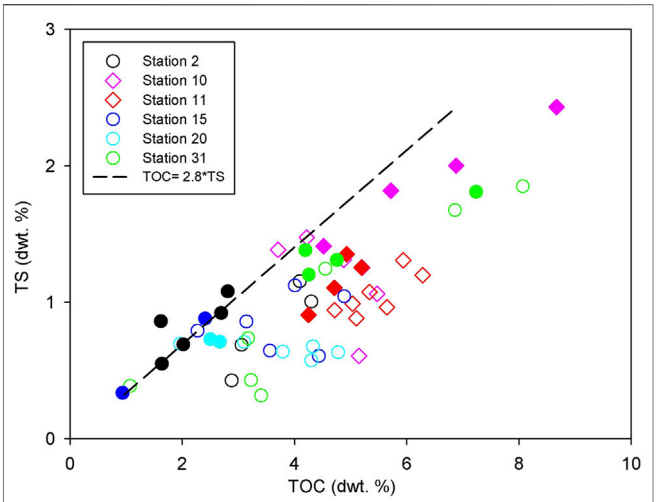


FIGURE 8 | Covariations of TS versus TOC including the relationship suggested for Holocene siliciclastic sediments (Berner, 1982). It is assumed that TS essentially consists in the investigated samples essentially of pyrite sulfur. Surface sediments <20 cmbsf are open symbols and >20 cmbsf are filled symbols.

Solving **Eq. 5** a $^{224}Ra_{ex}$ flux from SGD (F_{SGD}—**Table 3**) of 261.7 Bq m^{-2} d^{-1} was obtained.

This flux was converted into a water flow by dividing it by the $^{224}Ra_{ex}$ activities in different endmembers which were derived from four beach pore water samples with activities of 51, 65, 84, and 88 Bq m^{-3}. The resulting estimated volumetric SGD flow is 3.8 ± 0.7 cm d^{-1} (**Table 3**).

The estimated flow is higher compared to the flow obtained by (Schafmeister and Darsow, 2004). These authors applied a numeric ground water flow model (about 0.02 cm d^{-1}). This is due to the model only considering the fresh water component, whereas the Ra mass balance applied in the present study includes recirculated sea water. However, the SGD rate from WB is considered low when comparing to other SGD rates from different regions in the world, where SGD rates can reach up to 280 cm d^{-1} (Santos et al., 2021).

Benthic Processes and Submarine Fresh Water Source in the Central Wismar Bay

The composition of sediments investigated in the WB is typical for silty/muddy deposits along the North-German coastline

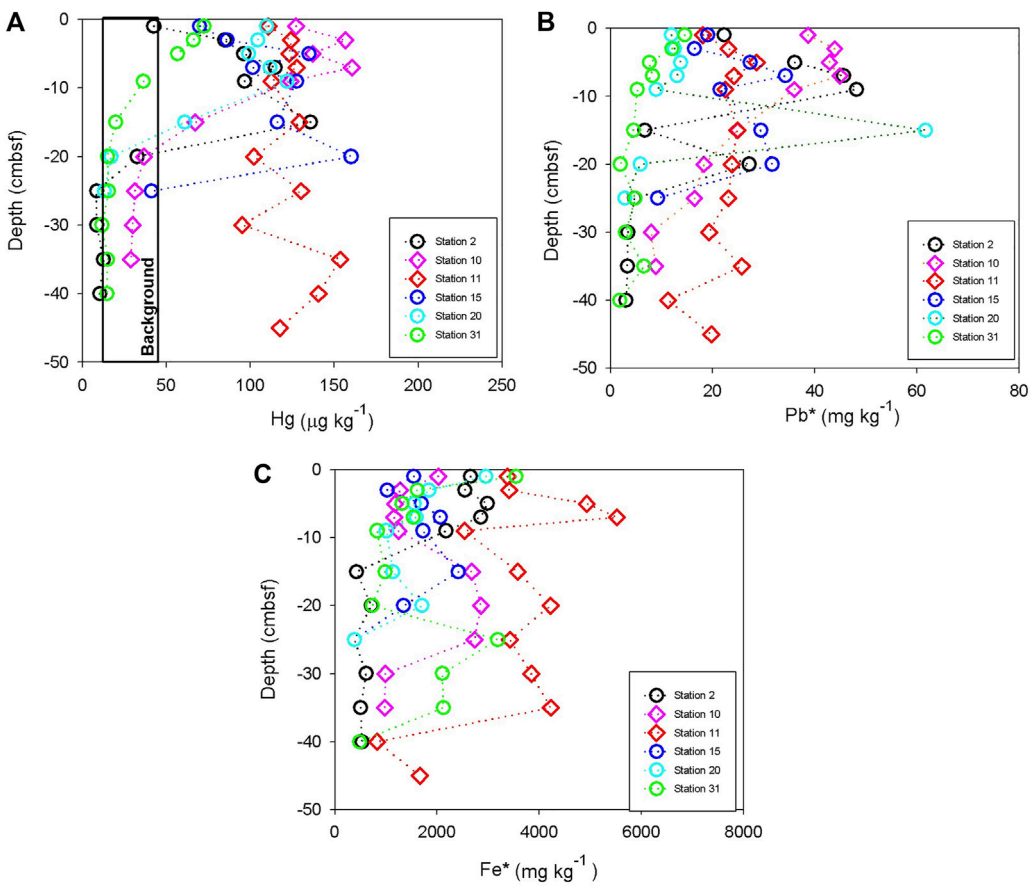


FIGURE 9 | Vertical profiles of the contents of total Hg, **(A)**, including the background level for Baltic Sea (Leipe et al., 2013), and Pb **(B)** and Fe **(C)** of sediment cores from WB. *HCl extractable fraction.

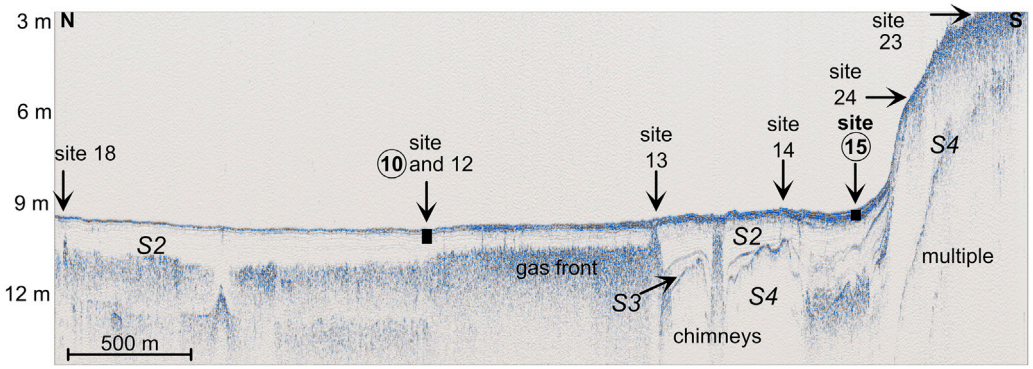


FIGURE 10 | Sediment acoustic profile of the western N-S transect in WB. The cores are represented as a circle around the site number, and the length of each core is indicated by the black bar.

(e.g., Böttcher et al., 2000; Al-Raei et al., 2009; Lipka et al., 2018b).

Except for sites 10 and 11 (**Figure 1**), pore water salinities in the WB sediments were characterized by relatively constant values (**Figures 6A**). Slight maxima around 10 to 15 cmbsf were observed at all sites and are due to past changes of bottom water salinities which are consequence of intrusion of salty North Sea water intrusions into the southern BS (Matthäus and Lass, 1995; Mohrholz, 2018).

Pore water salinities at Site 10 and in particular at Site 11 show a different pattern. Below the surface maxima, they decrease, and at Site 11 the values even reach fresh water conditions at the lowermost depth (salinity of about 1). It suggests that the sediments below the surface muds may host an aquifer containing fresh water, situated above glacial deposits and potentially part of seismic unit 3 (**Figure 11**). The pore water gradients of Site 11 (**Figure 6A-2**) result from mixing between endmembers (e.g., ground water and BS), superimposed by diagenetic reactions leading to further accumulation of some elements in the top sediments.

The pore waters at sites not impacted by freshening (sites 2, 15, 20, and 31) are characterized by a continuous increase in metabolite concentrations and a decrease in SO_4 and $\delta^{13}C_{DIC}$ values (**Figures 6J–O**). These vertical profiles are shaped by intense OM mineralization catalyzed by microorganisms using in particular SO_4 as terminal electron acceptors (Froelich et al., 1979; Jørgensen, 1982).

The maxima in Si, P, DIC, Mn, and Fe concentrations at Site 11 at around 10 cmbsf are in agreement with higher loads of top sediments in metabolizable organic matter leading to enhanced mineralization when compared to the other sites (**Figures 6K-2–M-2,O-2**). These observations also demonstrate that the fresh ground water is not substantially enriched in those substances. The pore water at Site 11 is depleted in SO_4 due to both, microbial sulphate reduction in the upper part of the sediment, but in particular due to the dilution with the underlying ground water that is free of SO_4.

The high dissolved Fe and Mn concentrations observed in the top sediments (**Figures 6L-2,M-2**) may accumulate due to the chemical reaction of metal ox (yhydrox)ides by biogenic sulphide

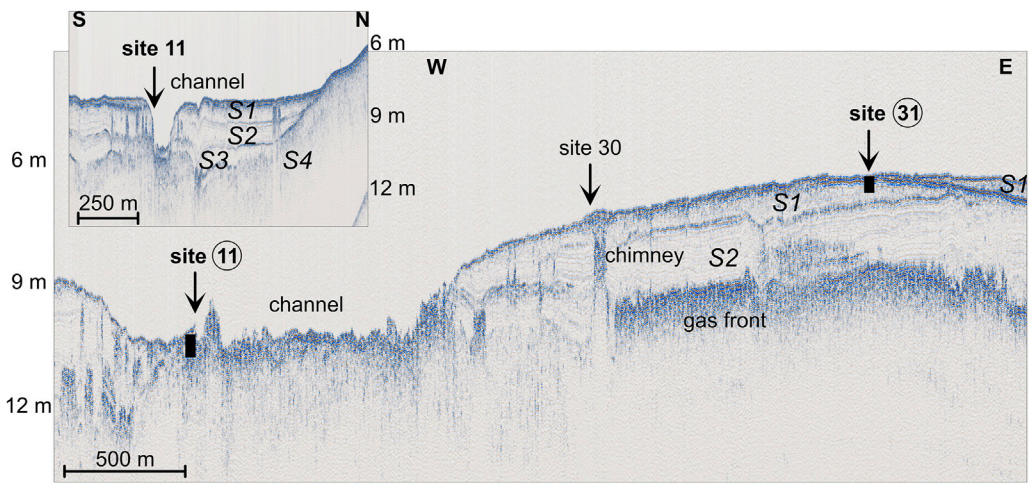


FIGURE 11 | Sediment acoustic profile of the eastern W-E transect. The cores are marked as a circle around the site number, and the length of each core is denoted by the black bar. Inset: perpendicular S-N transect highlighting site 11.

TABLE 3 | Summary of the terms used in the Ra mass balance.

Term	Definition	Value	±	Units	Source
A_{WB}	WB surface area–study area	81,472,500		m^2	Calculated from the bathymetry (GDI-BSH, 2020)
A_{WB}	assumed area where SGD take place	270,000		m^2	
V	WB volume - study area	430,812,610		m^3	Calculated from the bathymetry (GDI-BSH, 2020)
h	average depht of the bay	5		m	V/A_{WB}
Q_{str}	Discharge for the 3 western streams	1,515		$m^3\ d^{-1}$	Because there were no hydrologic data available for these streams, the value was taken from another stream close to area (LUNG, 2020)
Q_{str}	Discharge from Wallenstein stream	26,524		$m^3\ d^{-1}$	LUNG, (2021)
WA	Water age	5	1	d	(ln ($^{224}Ra/^{223}Ra$)WB–ln ($^{224}Ra/^{223}Ra$)beach pore water)/λ223 - λ223
Q_{out}	Water outflow	0.3		$Bq\ d^{-1}$	($^{224}Ra_{WB}$–$^{224}Ra_{offshore}$) *v/RT
C_{str}	$^{224}Ra_{ex}$ concentration in Wallenstein stream	5.8		$Bq\ m^{-3}$	this study–**Table 1**
C_{str}	$^{224}Ra_{ex}$ concentration in the western stream	1.1		$Bq\ m^{-3}$	this study–**Table 1**
C_{str}	$^{224}Ra_{ex}$ concentration in the western stream	2.6		$Bq\ m^{-3}$	this study–**Table 1**
C_{str}	$^{224}Ra_{ex}$ concentration in the western stream	4.1		$Bq\ m^{-3}$	this study–**Table 1**
$C_{offshore}$	$^{224}Ra_{ex}$ concentration in the open BS (Site 1)	0.2		$Bq\ m^{-3}$	this study
C	Average of ^{224}Ra inventory concentration in the WB	1.4	0.8	$Bq\ m^{-3}$	this study
λ	$^{224}Ra_{ex}$ decay constant	0.189		d^{-1}	
F_{sed}	Sediment diffusion from seabed	0.5	0.03	$Bq\ m^{-2}\ d^{-1}$	Krall et al. (2017)
F_{SGD}	$^{224}Ra_{ex}$ inputs from pore water fluxes	261.7		$Bq\ m^{-2}\ d^{-1}$	this study–**Table 1**
$C_{endmember}$	$^{224}Ra_{ex}$ of beach pore water (endmember)	51		$Bq\ m^{-3}$	this study–**Table 1**
$C_{endmember}$	$^{224}Ra_{ex}$ of beach pore water (endmember)	65		$Bq\ m^{-3}$	this study–**Table 1**
$C_{endmember}$	$^{224}Ra_{ex}$ of beach pore water (endmember)	84		$Bq\ m^{-3}$	this study–**Table 1**
$C_{endmember}$	$^{224}Ra_{ex}$ of beach pore water (endmember)	88		$Bq\ m^{-3}$	this study–**Table 1**
V_{SGD}	Volumetric SGD flow	3.8	0.7	$cm\ d^{-1}$	$F_{SGD}/C_{endmember}$

(e.g., Moeslund et al., 1994; Thamdrup et al., 1994; Böttcher et al., 2000). At the sediment-water interface, Fe and in part Mn may are oxidized by NO_3 and/or O_2, whereas in deeper sediment layers Fe and Mn may react with H_2S and DIC to form Fe sulphides and MnCa carbonate solid-solutions, respectively (Froelich et al., 1979; Berner, 1980; Huckriede and Meischner, 1996; Böttcher and Dietzel, 2010). The observed near-surface maximum in dissolved P at Site 11 is due to the parallel release from OM and reduction of Fe ox(yhydrox)ides that acted previously as sorption substrate for P (e.g., Haese, 2006).

The surface sediments at all sites are low in accumulating TS (considered to reflect essentially pyrite contents) when compared to the predicted Holocene saturation line (**Figure 8**), indicating the impact of sulphate-independent mineralization processes in the top sediments and the impact of bioturbation-driven-re-oxidation of sedimentary sulphur species (e.g., Jørgensen and Kasten, 2006). This is in line with previous observations (Mossmann et al., 1991; Böttcher et al., 2000) that gave evidence that for modern sediments some burial at depth and associated time is necessary to establish a constant TOC/S ratio. However, the freshening of pore water at Site 11 establishes SO_4 limited conditions and caused the TOC/TS ratio to remain below 2.8 (**Figure 8**).

Overall, the modeled mineralization rates at the WB are at the lower end when compared to measured gross sulphate reduction rates in muddy sediments from German coastal areas (Böttcher et al., 2000; Llobet-Brossa et al., 2002; Al-Raei et al., 2009; Lipka et al., 2018b) which is likely due to some H_2S reoxidation by metal oxy (hydrox)ides taken place in the surface sediments (Jørgensen, 1982). The highest net anaerobic mineralization rates are found at Site 11 (**Table 2**). The excavation of sediment (**Figure 11**) formed a local sediment trap and led to a fast accumulation of sediments as reflected by the homogeneous distribution of sedimentary organic matter, reactive metals like Fe and Mn, and anthropogenic tracers (Hg, Pb*) (**Figure 9**). This accumulation further leads to enhanced availability of fresh organic matter fostering microbial activity (Aller and Blair, 1996; Jørgensen and Kasten, 2006), and therefore, higher diagenetic element fluxes across the sediment-water interface (**Table 2**).

Moreover, the modeled fluxes indicate that advective and diffuse components are taking place, however, the last one has been more pronounced. DIC is liberated from deeper sediments to the bottom waters, especially at Site 11 (**Table 2**). The pore water at Site 11 was physicochemically evaluated by the Phreeq-C package (Parkhurst and Appelo, 1999). Assuming an equilibrium with

calcite at depth (Morse and Mackenzie, 1990) all solutions are characterized by an enhanced CO_2 partial pressure higher than atmospheric pressure. Therefore, the impact of fresh water at Site 11 on the bottom water of WB will enhance the capability of surface water to act as a potential CO_2 source for the atmosphere.

An Anthropogenic Bottle Opener for SGD?

A stronger decrease in salinity, and therefore an indication of fresh water occurrence is observed at Site 11 compared to the other sites (**Figure 6A-2**). The main morphological difference between this sites is the presence of an excavated navigation channel. This is an about 3–4 m deep artificial sedimentary depression (**Figure 11**) which was built for ship navigation channel between the open BS and the port of Wismar (VSW, 2018).

Based on the geophysical profiles, the dredging removed the previously overlying muddy sediments (units S1 and S2), thereby touching the underlying aquifer in unit 3 (**Figure 11**). The removal of the mud cover at Site 11 promotes the exchange of solutes and water between the aquifer and the bottom water. A more continued excavation this structure in the future, may enhance the direct impact of SGD on the WB. On the other hand, depending on the hydrographic boundary conditions, the artificial channel may also temporarily allow brackish water to penetrate the aquifer.

CONCLUSION AND OUTLOOK

The multi-tracer approach used in the present study demonstrated the impact of different fresh water sources on the Wismar Bay (WB), southern Baltic Sea, and in particular to prove the occurrence of SGD at the center of the bay. In addition, the change in the radium gradient towards the open sea suggests potential ground water leaking from the coastal borders in agreement with direct observations at the shoreline.

The sediment cores retrieved from the central part of the bay together with the acoustic survey discovered fresh water discharge at the sea bottom in the central part of the bay. The discovered SGD site (Site 11) is located in a navigation channel, which demonstrates that the dredging activity may have caused a change in the pressure gradient, thereby allowing ground water to penetrate the sediments overlying the aquifer and the bottom waters of the WB, respectively. Using a tentative Ra mass balance, we estimate a potential contribution from SGD to the WB of about 3.8 ± 0.7 cm d^{-1}.

Diagenesis in the surface sediments results in the enhancement of metabolites in the pore waters at depth. At Site 11, however, enhanced concentrations of metabolites were found in the top sediments which may also be related to the remineralization of fresh organic matter added by dredging in the past that lead to higher mineralization rates.

From the geochemical profiles it can be inferred that SGD is not just limited to the central part of, but can also occur in other places of the WB, which may or may not be associated with dredging activities. Therefore, explorations to determine the number of SGD sites are necessary.

Possible future engineering to impact the WB benthic structure may have impacts on benthic-pelagic coupling and, thereby, change the element fluxes into the bottom waters. Further studies, however, are required to investigate the potential impact of local sediment properties as a source for nutrients and dissolved carbon species for the WB water column.

DATA AVAILABILITY STATEMENT

The raw data supporting the conclusions of this article will be made available by the authors, and graphically presented data will be stored in the PANGEA data base.

AUTHOR CONTRIBUTIONS

MB, CVA, and JS developed the scientific concept and design of the study. CVA, JS, and PF, conducted the field campaigns and on-site measurements. IS, CVA, OD, SP, and PF carried out the analytical data measurements and processing. BL performed the reaction-transport modeling. CM and A-KJ contributed to the groundwater hydrogeochemistry and -geology and MZ was involved in data discussion. CVA and MB wrote the article with contributions and revisions from all co-authors. All authors agreed about the submission of the final version.

FUNDING

The study was supported by the German Academic Exchange Service (DAAD) via a PhD stipend for CvA to work in the Geochemistry & Isotope Biogeochemistry Group at IOW (project no. 57381412), and the Deutsche Forschungsgemeinschaft (DFG) to MB and A-KJ within the framework of the Research Training Group 'Baltic TRANSCOAST' funded by under grant number GRK 2000. This is Baltic TRANSCOAST publication no. GRK2000/0046. It is also supported by DFG to MB and JS within the KiSNet project. JS was further supported by the BONUS SEAMOUNT project funded jointly by the EU and the Federal Ministry of Education and Research of Germany (BMDF, grant no. 03F0771B) and by a FP7 EU Marie Curie Career Integration Grant (grant PCIG09-GA-2011-293499). MZ is supported by BMBF during DAM-MGF. BL acknowledges additional support from the Helmholtz Association (Alfred Wegener Institute Helmholtz Centre for Polar and Marine Research). We acknowledge financial support by Leibniz IOW for Open Access Publishing.

ACKNOWLEDGMENTS

The authors wish to thank the crew and captain of RV LITTORINA and M. Staniek for their expert technical on-board support, and S.

Plewe for his expert support during the field campaigns. We also wish to thank A. Köhler for expert ICP-OES support and I. Scherff for further laboratory assistance, B. Schnetger for providing a Th Standard, and J. Deepen (Stalu-MV) for providing the hydrological data. Aaron J. Beck and Olivier Radakovitch for the careful reviews that helped to improve the manuscript, and Henry Bokuniewicz for the editorial handling. MB further wishes to thank H.-J. H. Dohrenkamp, C.S. Henn, and The United Jazz + Rock ensemble for their culinary and musical inspirations during manuscript preparation. He dedicates this publication to the memory of T.G.P. Jones, C. Reiner, and U. Steinfurth, who recently passed away, for their inspiring and vital sense of humor.

SUPPLEMENTARY MATERIAL

The Supplementary Material for this article can be found online at: https://www.frontiersin.org/articles/10.3389/fenvs.2021.642346/full#supplementary-material

REFERENCES

Al-Raei, A. M., Bosselmann, K., Böttcher, M. E., Hespenheide, B., and Tauber, F. (2009). Seasonal Dynamics of Microbial Sulfate Reduction in Temperate Intertidal Surface Sediments: Controls by Temperature and Organic Matter. *Ocean Dyn.* 59, 351–370. doi:10.1007/s10236-009-0186-5

Aller, R. C., and Blair, N. E. (1996). Sulfur Diagenesis and Burial on the Amazon Shelf: Major Control by Physical Sedimentation Processes. *Geo-Marine Lett.* 16, 3–10. doi:10.1007/bf01218830

Beck, A. J., Tsukamoto, Y., Tovar-Sanchez, A., Huerta-Diaz, M., Bokuniewicz, H. J., and Sañudo-Wilhelmy, S. A. (2007). Importance of Geochemical Transformations in Determining Submarine Groundwater Discharge-Derived Trace Metal and Nutrient Fluxes. *Appl. Geochem.* 22, 477–490. doi:10.1016/j.apgeochem.2006.10.005

Bejannin, S., Tamborski, J. J., van Beek, P., Souhaut, M., Stieglitz, T., Radakovitch, O., et al. (2020). Nutrient Fluxes Associated with Submarine Groundwater Discharge from Karstic Coastal Aquifers (Côte Bleue, French Mediterranean Coastline). *Front. Environ. Sci.* 7, 205. doi:10.3389/fenvs.2019.00205

Berner, R. A. (1982). Burial of Organic Carbon and Pyrite Sulfur in the Modern Ocean; its Geochemical and Environmental Significance. *Am. J. Sci.* 282, 451–473. doi:10.2475/ajs.282.4.451

Berner, R. A. (1980). *Early Diagenesis: A Theoretical Approach*. Princeton, NJ: Princeton University Press.

Berner, R. A., and Raiswell, R. (1983). Burial of Organic Carbon and Pyrite Sulfur in Sediments over Phanerozoic Time: a New Theory. *Geochimica et Cosmochimica Acta* 47 (5), 855–862. doi:10.1016/0016-7037(83)90151-5

Blöschl, G., Bierkens, M. F. P., Chambel, A., Cudennec, C., Destouni, G., Fiori, A., et al. (2019). Twenty-three Unsolved Problems in Hydrology (UPH) – a Community Perspective. *J. Hydrol. Sci.* 64, 1141–1158.

Blott, S. J., and Pye, K. (2001). GRADISTAT: a Grain Size Distribution and Statistics Package for the Analysis of Unconsolidated Sediments. *Earth Surf. Process. Landforms* 26, 1237–1248. doi:10.1002/esp.261

Böttcher, M. E., and Dietzel, M. (2010). Metal-ion Partitioning during Low-Temperature Precipitation and Dissolution of Anhydrous Carbonates and Sulphates. *EMU Notes in Mineralogy* 10 (4), 139–187.

Böttcher, M. E., Hespenheide, B., Llobet-Brossa, E., Beardsley, C., Larsen, O., Schramm, A., et al. (2000). The Biogeochemistry, Stable Isotope Geochemistry, and Microbial Community Structure of a Temperate Intertidal Mudflat: an Integrated Study. *Continental Shelf Res.* 20, 1749–1769. doi:10.1016/s0278-4343(00)00046-7

Böttcher, M. E., Mallast, U., Massmann, G., Moosdorf, N., Mueller-Pethke, M., and Waska, H. (2021). "Coastal-Groundwater Interfaces (Submarine Groundwater Discharge)," in *Ecohydrological Interfaces*. Editors S. Krause, D. M. Hannah, and N. Grimm (New York, NY: Wiley & Sons).

Böttcher, M. E., and Schmiedinger, I. (2021). The Impact of Temperature on the Water Isotope ($^{2}H/^{1}H$, $^{17}O/^{16}O$, $^{18}O/^{16}O$) Fractionation upon Transport through a Low-Density Polyethylene Membrane. *Isotopes Environ. Health Stud.* 57, 183–192. doi:10.1080/10256016.2020.1845668

Boudreau, B. P., and Ruddick, B. R. (1991). On a Reactive Continuum Representation of Organic Matter Diagenesis. *Am. J. Sci.* 291, 507–538. doi:10.2475/ajs.291.5.507

Boudreau, B. P. (1997). *Diagenetic Models and Their Implementation: Modelling Transport and Reactions in Aquatic Sediments*. New York: Springer.

Brand, W. A., and Coplen, T. B. (2012). Stable Isotope Deltas: Tiny, yet Robust Signatures in Nature. *Isotopes Environ. Health Stud.* 48, 393–409. doi:10.1080/10256016.2012.666977

Burnett, W. C., Aggarwal, P. K., Aureli, A., Bokuniewicz, H., Cable, J. E., Charette, M. A., et al. (2006). Quantifying Submarine Groundwater Discharge in the Coastal Zone via Multiple Methods. *Sci. Total Environ.* 367, 498–543. doi:10.1016/j.scitotenv.2006.05.009

Burnett, W. C., Bokuniewicz, H., Huettel, M., Moore, W. S., and Taniguchi, M. (2003). Groundwater and Pore Water Inputs to the Coastal Zone. *Biogeochemistry* 66, 3–33. doi:10.1023/b:biog.0000006066.21240.53

Burnett, W. C., Peterson, R., Moore, W. S., and Oliveira, J. (2008). Radon and Radium Isotopes as Tracers of Submarine Groundwater Discharge – Results from the Ubatuba, Brazil SGD Assessment Intercomparison. *Est., Coast., Shelf Sci.* 76, 501–511. doi:10.1016/j.ecss.2007.07.027

Cerdà-Domènech, M., Rodellas, V., Folch, A., and Garcia-Orellana, J. (2017). Constraining the Temporal Variations of Ra Isotopes and Rn in the Groundwater End-Member: Implications for Derived SGD Estimates. *Sci. Total Environ.* 595, 849–857. doi:10.1016/j.scitotenv.2017.03.005

Church, T. M. (1996). An Underground Route for the Water Cycle. *Nature* 380, 579–580. doi:10.1038/380579a0

Clark, I., and Fritz, P. (1997). *Environmental Isotopes in Hydrogeology*. Boca Raton: Lewis Publishers, 138–140.

Claypool, G. E., and Kaplan, I. R. (1974). "The Origin and Distribution of Methane in Marine Sediments," in *Natural Gases in Marine Sediments*. Editor I. R. Kaplan (New York: Plenum Press), 99–140. doi:10.1007/978-1-4684-2757-8_8

Cline, J. D. (1969). Spectrophotometric Determination of Hydrogen Sulfide in Natural Waters. *Limnol. Oceanogr.* 14, 454–458. doi:10.4319/lo.1969.14.3.0454

de Souza, G. K., von Ahn, C. M. E., Niencheski, L. F. H., and de Andrade, C. F. F. (2021). Effects of Coastal Lagoon Water Level on Groundwater Fluxes of Nutrients to the Coastal Zone of Southern Brazil. *J. Mar. Sys.* 213, 103459. doi:10.1016/j.jmarsys.2020.103459

Dellwig, O., Wegwerth, A., Schnetger, B., Schulz, H., and Arz, H. W. (2019). Dissimilar Behaviors of the Geochemical Twins W and Mo in Hypoxic-Euxinic Marine Basins. *Earth-sci. Rev.* 193, 1–23. doi:10.1016/j.earscirev.2019.03.017

DWD (2020). Deutscher Wetterdienst 2019. Climate Data Germany – Wismar Station. Available at: https://cdc.dwd.de/portal/ (Accessed January 10, 2020).

Donis, D., Janssen, F., Liu, B., Wenzhöferö, F., Dellwig, O., Escher, P., et al. (2017). Biogeochemical Impact of Submarine Groundwater Discharge on Coastal Surface Sands of the Southern Baltic Sea. *Est., Coast., Shelf Sci.* 189, 131–142. doi:10.1016/j.ecss.2017.03.003

Douglas, A. R., Murgulet, D., and Peterson, R. N. (2020). Submarine Groundwater Discharge in an Anthropogenically Disturbed, Semiarid Estuary. *J. Hydrol.* 124369, 124369. doi:10.1016/j.jhydrol.2019.124369

Folk, R. L., and Ward, W. C. (1957). Brazos River Bar: a Study in the Significance of Grain Size Parameters. *J. Sed. Petrol.* 27, 3–26. doi:10.1306/74d70646-2b21-11d7-8648000102c1865d

Froelich, P. N., Klinkhammer, G. P., Bender, M. L., Luedtke, N. A., Heath, G. R., Cullen, D., et al. (1979). Early Oxidation of Organic Matter in Pelagic Sediments of the Eastern Equatorial Atlantic: Suboxic Diagenesis. *Geochim Cosmochim Acta* 43, 1075–1090. doi:10.1016/0016-7037(79)90095-4

Garcia-Solsona, E., Garcia-Orellana, J., Masqué, P., and Dulaiova, H. (2008). Uncertainties Associated with ^{223}Ra and ^{224}Ra Measurements in Water via a Delayed Coincidence Counter (RaDeCC). *Mar. Chem.* 109, 198–219. doi:10.1016/j.marchem.2007.11.006

Gat, J. (1996). Oxygen and Hydrogen Isotopes in the Hydrological Cycle. *Annu. Rev. Earth Planet. Sci.* 24, 225–262. doi:10.1146/annurev.earth.24.1.225

Gdi-Bsh (2020). GeoSeaPortal. Bundesamt fürfur Seeschiffahrt und Hydrographie. Available at: www.geoseaportal.de.

Gogina, M., Lipka, M., Woelfel, J., Liu, B., Morys, C., Böttcher, M. E., et al. (2018). In Search of a Field/based Relantioship between Benthic Macrofauna and Biogeochemistry in a Modern Brackish Coastal Sea. *Front. Mar. Sci.* 5, 489. doi:10.3389/fmars.2018.00489

Haese, R. R. (2006). in *The Biogeochemistry of Iron. Marine Geochemistry*. Editors H. D. Schulz and M. Zabel (Berlin: Springer-Verlag), 207–240.

Hennig, H., and Hilgert, T. (2007). Dränabflüsse – Der Schlüssel zur Wasserbilanzierung im nordostdeutschen Tiefland. – *Hydrologie und Wasserbewirtschaftung* 51 (6), 248–257.

Hilgert, T. (2009). Grundwasserneubildung Mecklenburg-Vorpommern-Aktualisierung und ergänzende Beschreibung, internal project report.

Hoefs, J. (2018). *Stable Isotope Geochemistry*. Springer-Nature, Science Ltd.

Huckriede, H., and Meischner, D. (1996). Origin and Environment of Manganese-Rich Sediments within Black-Shale Basins. *Geochimica et Cosmochimica Act* 8, 1399–1413. doi:10.1016/0016-7037(96)00008-7

Jankowska, H., Matciak, M., and Nowacki, J. (1994). Salinity Variations as an Effect of Groundwater Seepage through the Seabed (Puck Bay, Poland). *Oceanologia* 36, 33–46.

Jenner, A-K. (2018). Ground Water Development in North-Eastern Germany as Deduced from the Hydrogeochemical and Stable Isotopic Composition of Selected Drinking Waters. Griefswald: University of Greifswald and Leibniz IOW. [MSc thesis].

Johannes, R. E. (1980). The Ecological Significance of the Submarine Discharge of Groundwater. *Mar. Ecol. Prog. Ser.* 3, 365–373. doi:10.3354/meps003365

Jordan, H., and Weder, H. J. (1995). *Hydrogeologie – Grundlagen und Methoden und Regionale Hydrogeologie: Mecklenburg-Vorpommern, Brandenburg und Berlin, Sachsen-Anhalt, Sachsen, Thüringen*. Stuttgart: Enke Verlag, 603.

Jørgensen, B. B., and Kasten, S. (2006). in *Sulfur Cycling and Methane Oxidation. Marine Geochemistry*. Editors H. D. Schulz and M. Zabel (Springer), 271–309.

Jørgensen, B. B. (1982). Mineralization of Organic Matter in the Sea Bed: the Role of Sulphate Reduction. *Nature* 296, 643–645.

Jurasinski, G., Janssen, M., Voss, M., Böttcher, M. E., Brede, M., Burchard, H., et al. (2018). Understanding the Coastal Ecocline: Assessing Sea-Land-Interactions at Non-tidal, Low-Lying Coasts through Interdisciplinary Research. *Front. Mar. Sci.* 5 (342), 1–22. doi:10.3389/fmars.2018.00342

Kostka, J. E., and Luther, G. W. (1994). Partitioning and Speciation of Solid Phase Iron in Saltmarsh Sediments. *Geochim. Cosmochim. Acta* 58, 1701–1710. doi:10.1016/0016-7037(94)90531-2

Kotwicki, L., Grzelak, K., Czub, M., Dellwig, O., Gentz, T., Szymczycha, B., et al. (2014). Submarine Groundwater Discharge to the Baltic Coastal Zone: Impacts on the Meiofaunal Community. *J. Mar. Sys.* 129, 118–126. doi:10.1016/j.jmarsys.2013.06.009

Krall, L., Garcia-Orellana, J., Trezzi, G., and Rodellas, V. (2017). Submarine Groundwater Discharge at Forsmark, Gulf of Bothnia, provided by Ra Isotopes. *Mar. Chem.* 162, 162–172. doi:10.1016/j.marchem.2017.09.003

Lampe, R., Luebke, H., Endtmann, E., and Harff, J. (2013). A New Relative Sea-Level Curve for the Wismar Bay, N-German Baltic Coast. *Meyniana* 57, 5–35.

Lee, Y. W., Hwang, D-W., Kim, G., Lee, W-C., and Oh, H-T. (2009). Nutrient Inputs from Submarine Groundwater Discharge (SGD) in Masan Bay, an Embayment Surrounded by Heavily Industrialized Cities, Korea. *Sci. Tot. Env.* 407, 3181–3188. doi:10.1016/j.scitotenv.2008.04.013

Leipe, T., Moros, M., Kotilainen, A., Vallius, H., Kabel, K., Endler, M., et al. (2013). Mercury in Baltic Sea Sediments – Natural Background and Anthropogenic Impact. *Chem. der Erde* 73, 249–259. doi:10.1016/j.chemer.2013.06.005

Lipka, M., Böttcher, M. E., Wu, Z., Sültenfuß, J., Jenner, A-K., Westphal, J., et al. (2018a). Ferruginous Groundwaters as a Source of P, Fe, and DIC for Coastal Waters of the Southern Baltic Sea: (Isotope) Hydrobiogeochemistry and the Role of an Iron Curtain. *E3s Web Conf.* 54, 1–5. doi:10.1051/e3sconf/20185400019

Lipka, M., Woelfel, J., Gogina, M., Kallmeyer, J., Liu, B., Morys, C., et al. (2018b). Solute Reservoirs Reflects Variability of Early Diagenetic Processes in Temperate Brackish Surface Sediments. *Front. Mar. Sci.* 5, 413. doi:10.3389/fmars.2018.00413

Llobet-Brossa, E., Rabus, R., Böttcher, M. E., Könneke, M., Finke, N., Schramm, A., et al. (2002). Community Structure and Activity of Sulfate-Reducing Bacteria in an Intertidal Surface Sediment: A Multi-Method Approach. *Aquat. Microb. Ecol.* 29, 211–226. doi:10.3354/ame029211

Löffler, H., Adam, C. G. B., Brinschwitz, D., Gieseler, W., Ginzel, G., Grunske, K.-A., et al. (2010). Hydrochemische Typisierung für Grundwasser im Lockergesteinsbereich des norddeutschen Flachlandes. *Schriftenreihe für Geowissenschaften.* 18, 369–399. doi:10.1787/9789282102701-13-fr

Lung, M. V. (2009). Landesamt für Umwelt, Naturschutz und Geologie Mecklenburg-Vorpommern. Map of groundwater recharge, German: "Grundwasserneubildung", gwn.shp. Available at: https://www.umweltkarten.mv-regierung.de/script/ (Accessed December 14, 2019).

Lung, M. V. (2020). Landesamt für Umwelt, Naturschutz, und Geologie Mecklenburg-VorpommernKartenportal Umwelt Mecklenburg-Vorpommern. Data set "Grundwasserhöhengleichen". Available at: https://www.umweltkarten.mv-regierung.de/atlas/script/index.php (Accessed December 15, 2020).

Lung, M. V. (2021). Landesamt für Umwelt, Naturschutz, und Geologie Mecklenburg-Vorpommern. Lake Network Map of Mecklenburg Western-Pomerania: Gewässernetz M-V: Standgewässer: Seen, dlm25w_sg_seen.shp. Available at: https://www.umweltkarten.mv-regierung.de/atlas/script/index.php (Accessed December 14, 2020).

Macklin, P. A., Damien, T. M., and Santos, I. R. (2014). Estuarine Canal Estate Waters: Hotspots of CO_2 Outgassing Driven by Enhanced Groundwater Discharge? *Mar. Chem.* 167, 82–92. doi:10.1016/j.marchem.2014.08.002

Matthäus, W., and Lass, H. U. (1995). The Recent Salt Inflow into the Baltic Sea. *J. Phys. Oceanograph.* 25, 280–286. doi:10.1175/1520-0485(1995)025<0280:trsiit>2.0.co;2

Meister, P., Liu, B., Ferdelman, T. G., Jørgensen, B. B., and Khalili, A. (2013). Control of Sulphate and Methane Distributions in Marine Sediments by Organic Matter Reactivity. *Geochim. Cosmochim. Acta* 104, 183–193. doi:10.1016/j.gca.2012.11.011

Michaelis, J., Usdowski, E., and Menschel, G. (1985). Partitioning of ^{13}C and ^{12}C on the Degassing of CO_2 and the Precipitation of Calcite Rayleigh-type Fractionation and a Kinetic Model. *Am. J. Sci.* 285, 318–327. doi:10.2475/ajs.285.4.318

Moeslund, L., Thamdrup, B., and Jørgensen, B. B. (1994). Sulfur and Iron Cycling in a Coastal Sediment: Radiotracer Studies and Seasonal Dynamics. *Biogeochemistry* 27, 129–152. doi:10.1007/bf00002815

Mohrholz, V. (2018). Major Baltic Inflow Statistic – Revised. *Front. Mar. Sci.* 5, 384. doi:10.3389/fmars.2018.00384

Moore, W. S. (1996). Large Groundwater Inputs to Coastal Waters Revealed by ^{226}Ra Enrichments. *Nature* 380, 612–614. doi:10.1038/380612a0

Moore, W. S., and Arnold, R. (1996). Measurement of ^{223}Ra and ^{224}Ra in Coastal Waters Using a Delayed Coincidence Counter. *J. Geophys. Res.* 101, 1321–1329. doi:10.1029/95jc03139

Moore, W. S., and de Oliveira, J. (2008). Determination of Residence Time and Mixing Processes of the Ubatuba, Brazil, Inner Shelf Waters Using Natural Ra Isotopes. *Est.Coast. Shelf Sci.* 76, 512e521. doi:10.1016/j.ecss.2007.07.042

Moore, W. S. (2010). The Effect of Submarine Groundwater Discharge on the Ocean. *Annu. Rev. Mar. Sci.* 2, 59–88. doi:10.1146/annurev-marine-120308-081019

Moosdorf, N., Böttcher, M. E., Adyasari, D., Erkul, E., Gilfedder, B., Greskowiak, J., et al. (2021). A State-Of-The-Art Perspective on the Characterization of Subterranean Estuaries at the Regional Scale. *Front. Earth Sci.* 9, 601293.

Morse, J., and Mackenzie, F. T. (1990). *Geochemistry of Sedimentary Carbonates*. New York: Elsevier, 707.

Mossmann, J-R., Aplin, A. C., Curtis, C. D., and Coleman, M. L. (1991). Geochemistry of Inorganic and Organic sulphur in Organic-Rich Sediments from the Peru Margin. *Geochim. Cosmochim. Acta* 55, 3581. doi:10.1016/0016-7037(91)90057-c

Oberdorfer, J. A., Valentino, M. A., and Smith, S. V. V. (1990). Groundwater Contribution to the Nutrient Budget of Tomales Bay, California. *Biogeochemistry* 10, 199–216. doi:10.1007/bf00003144

Parkhurst, D., and Appelo, C. (1999). User's Guide to PHREEQC (Version 2): A Computer Program for Speciation, Batch-Reaction, One-Dimensional Transport, and Inverse Geochemical Calculations. *Water-Resources Invest. Rep.*, 99–4259. doi:10.3133/wri994259

Piper, A. (1944). A Graphic Procedure in the Geochemical Interpretation of Water Analyses. *Eos, Trans. Am. Geophys. Union* 25, 914–928. doi:10.1029/tr025i006p00914

Prena, J. (1995). Temporal Irregularities in the Macrobenthic Community and Deep-Water Advection in Wismar Bay (Western Baltic Sea). Estuarine. *Coastal Shelf Sci.* 41, 705–717. doi:10.1006/ecss.1995.0085

Rocha, C., Robinson, C. E., Waska, H., Holly, M. A., and Bokuniewicz, H. (2021). A Place for Subterranean Estuaries in Coastal Zone. Estuarine. *Coastal Shelf Sci.* 250, 107167. doi:10.1016/j.ecss.2021.107167

Rodellas, V., Garcia Orellana, J., Garcia-Solsona, E., Masque, P., Dominguez, J. A., Ballesteros, B. J., et al. (2012). Quantifying Groundwater Discharge from Different Sources into a Mediterranean Wetlandwetland by Using ^{222}Rn and Ra Isotopes. *J. Hydrol.* 466-467, 11–22. doi:10.1016/j.jhydrol.2012.07.005

Rodellas, V., Garcia-Orellana, J., Masqué, P., Feldman, M., and Weinstein, Y. (2015). Submarine Groundwater Discharge as a Major Source of Nutrients to the Mediterranean Sea. *PNAS March* 112 (13), 3926–3930. doi:10.1073/pnas.1419049112

Rodellas, V., Stieglitz, T. C., Tamborski, J. J., van Beek, P., Andrisoa, A., and Cook, P. G. (2021). Conceptual Uncertainties in Groundwater and Porewater Fluxes Estimated by Radon and Radium Mass Balances. *Limnol. Oceanogr.* 9999, 1–19. doi:10.1002/lno.11678

Santos, I. R., Chen, X., Lecher, A. L., Sawyer, A. H., Moosdorf, N., Rodellas, V., et al. (2021). Submarine Groundwater Discharge Impacts on Coastal Nutrient Biogeochemistry. *Nat. Rev. Earth Environ.* 2, 307–323. doi:10.1038/s43017-021-00152-0

Santos, I. R., Eyre, B. D., and Huettel, M. (2012). The Driving Forces of Porewater and Groundwater Flow in Permeable Coastal Sediments: A Review. *Estuarine, Coastal Shelf Sci.* 98, 1–15. doi:10.1016/j.ecss.2011.10.024

Santos, I. R., Niencheski, F., Burnett, W., Peterson, R., Chanton, J., Andrade, C. F. F., et al. (2008). Tracing Anthropogenically Driven Groundwater Discharge into a Coastal Lagoon from Southern Brazil. *J. Hydrol.* 353, 275–293. doi:10.1016/j.jhydrol.2008.02.010

Schafmeister, M-T., and Darsow, A. (2004). "Potential Change in Groundwater Discharge as Response to Varying Climatic Conditions – an Experimental Model Study at Catchment Scale," in *The Baltic Sea Basin*. Editors J. Harff and S. Bjorck (Springer), 449.

Schlitzer, R. (2001). Ocean Data View. Availableat: http://www.awi-bremerhaven.de/GEO/ODV.

Schlüter, M., Sauter, E., Andersen, C. E., Dahlgaard, H., and Dando, P. R. (2004). Spatial Distribution and Budget for Submarine Groundwater Discharge in Eckernförde Bay (Western Baltic Sea). *Limnol. Oceanogr.* 49 (1), 157–167. doi:10.4319/lo.2004.49.1.0157

Schultz, H. D. (2006). "Quantification of Early Diagenesis: Dissolved Constituents in Marine Pore Water," in *Mar. Geoch.* Editors H. D. Schulz and M. Zabel (Berlin, Heidelberg: Springer-Verlag).

Seeberg-Elverfelds, J., Schlüter, M., Feseker, T., and Kölling, M. (2005). Rhizon Sampling of Porewaters Near the Sediment-Water Interface of Aquitic Systems. *Limnol. Oceanogr.: Methods* 3, 361–371. doi:10.1002/lom3.v3.11

Smellie, J., Tullborg, E -L., Nilsson, A. C., Sandström, B., Waber, N., Gimeno, M., et al. (2008). *Explorative Analysis of Major Components and Isotopes—SDM-Site Forsmark*. SKB R- 08-84. Stockholm, Sweden: SKB.

Stegmann, S., Sultan, N., Kopf, A., Apprioual, R., and Pelleau, P. (2011). Hydrogeology and Ist Effect on Slope Stability along the Coastal Aquifer of Nice, France. *Mar. Geology* 280, 168–181. doi:10.1016/j.margeo.2010.12.009

Stieglitz, T. C., Rapaglia, J., and Kruoa, S. C. (2007). An Effect of Pier Pillings on Nearshore Submarine Groundwater Discharge from a (Partially) Confined Aquifer. *Estuaries and Coasts* 30 (3), 543–550. doi:10.1007/bf03036520

Stieglitz, T., Taniguchi, M., and Skyler, N. (2008). Spatial Variability of Submarine Groundwater Discharge. *Ubatuba, Brazil. Estuarine Coastal Shelf Science* 76, 493–500. doi:10.1016/j.ecss.2007.07.038

Szymczycha, B., Klostowska, Z., Lengier, M., and Dzierzbicka-Glowacka, L. (2020). Significance of Nutrients Fluxes via Submarine Groundwater Discharge in the Bay of Puck, Southern Baltic Sea. *Oceanologia* 62, 117–125. doi:10.1016/j.oceano.2019.12.004

Szymczycha, B., Vogler, S., and Pempkowiak, J. (2012). Nutrient Fluxes via Submarine Groundwater Discharge to the Bay of Puck, Southern Baltic Sea. *Sci. Total. Environ.* 438, 86–93. doi:10.1016/j.scitotenv.2012.08.058

Taniguchi, M., Dulaim, H., Burnett, K. M., Santos, I. R., Sugimoto, R., Stieglitz, T., et al. (2019). Submarine Groundwater Discharge Updates on its Measurement Techniques, Geophysical Drivers, Magnitudes, and Effects. *Front. Environ. Sci.* 7, 141. doi:10.3389/fenvs.2019.00141

Teatini, P., Isotton, G., Nardean, S., Ferronato, M., Mazzia, A., Da Lio, C., et al. (2017). Hydrogeological Effects of Dredging Navigable Channels Canals through Lagoon Shallows. A Case Study in Venice. *Hydrol. Earth Syst. Sci.* 21, 5627–5646. doi:10.5194/hess-21-5627-2017

Thamdrup, B., Fossing, H., and Jørgensen, B. B. (1994). Manganese, Iron, and Sulfur Cycling in a Coastal Marine Sediment, Aarhus Bay, Denmark. *Geochim. Cosmochim. Acta* 58, 5115–5129. doi:10.1016/0016-7037(94)90298-4

Virtasalo, J. J., Schroeder, J. F., Luoma, S., Majaniemi, J., Mursu, J., and Scholten, J. (2019). Submarine Groundwater Discharge Site in the First Salpausselkä Ice-Marginal Formation, South Finland. *Solid Earth-EGU* 10, 405–432. doi:10.5194/se-10-405-2019

VSW (2018). Wasserstrassen und Schiffahrtsverwaltung des Bundes. Anpassung der seewaertigen Zufahrt zum Seehafen Wismar. Availableat: https://www.gdws.wsv.bund.de/SharedDocs/Downloads/DE/Planfeststellungsverfahren/100_Anpassung_Wismar/Scopingunterlage.pdf?__blob=publicationFile&v=2 (Accessed July 10, 2020).

Whiticar, M. J., and Werner, F. (1981). Pockmarks: Submarine Vents of Natural Gas or Freshwater Seeps? *Geo-Marine Lett.* 1, 193–199. doi:10.1007/bf02462433

Winde, V., Böttcher, M. E., Escher, P., Böning, P., Beck, M., Liebezeit, G., et al. (2014). Tidal and Spatial Variations of DI^{13}C and Aquatic Chemistry in a Temperate Tidal basin during winter Time. *J. Mar. Syst.* 129, 394–402. doi:10.1016/j.jmarsys.2013.08.005

Conflict of Interest: The authors declare that the research was conducted in the absence of any commercial or financial relationships that could be construed as a potential conflict of interest.

The reviewer (AB) declared a past co-authorship with one of the authors (JS) to the handling Editor.

Publisher's Note: All claims expressed in this article are solely those of the authors and do not necessarily represent those of their affiliated organizations, or those of the publisher, the editors and the reviewers. Any product that may be evaluated in this article, or claim that may be made by its manufacturer, is not guaranteed or endorsed by the publisher.

Copyright © 2021 von Ahn, Scholten, Malik, Feldens, Liu, Dellwig, Jenner, Papenmeier, Schmiedinger, Zeller and Böttcher. This is an open-access article distributed under the terms of the Creative Commons Attribution License (CC BY). The use, distribution or reproduction in other forums is permitted, provided the original author(s) and the copyright owner(s) are credited and that the original publication in this journal is cited, in accordance with accepted academic practice. No use, distribution or reproduction is permitted which does not comply with these terms.

frontiers in Earth Science

REVIEW
published: 14 May 2021
doi: 10.3389/feart.2021.601293

A State-Of-The-Art Perspective on the Characterization of Subterranean Estuaries at the Regional Scale

Nils Moosdorf[1,2,3], Michael Ernst Böttcher[4,5,6], Dini Adyasari[1], Ercan Erkul[2], Benjamin S. Gilfedder[7], Janek Greskowiak[8], Anna-Kathrina Jenner[4], Lech Kotwicki[9], Gudrun Massmann[8], Mike Müller-Petke[10], Till Oehler[1], Vincent Post[11], Ralf Prien[12], Jan Scholten[2], Bernhard Siemon[11], Cátia Milene Ehlert von Ahn[4], Marc Walther[13], Hannelore Waska[14], Tina Wunderlich[2] and Ulf Mallast[15]*

[1]Department for Biogeochemistry / Geology, Leibniz Centre for Tropical Marine Research (ZMT), Bremen, Germany, [2]Institute of Geosciences, University of Kiel, Kiel, Germany, [3]Southern Cross Geoscience, Southern Cross University, Lismore, NSW, Australia, [4]Geochemistry and Isotope Biogeochemistry, Leibniz Institute for Baltic Sea Research (IOW), Warnemünde, Germany, [5]Marine Geochemistry, University of Greifswald, Greifswald, Germany, [6]Department of Maritime Systems, Interdisciplinary Faculty, University of Rostock, Rostock, Germany, [7]Department of Hydrology, Bayreuth Center of Ecology and Environmental Research (Bayceer), University of Bayreuth, Bayreuth, Germany, [8]Institut für Biologie und Umweltwissenschaften, University of Oldenburg, Oldenburg, Germany, [9]Institute of Oceanology, Polish Academy of Sciences, Sopot, Poland, [10]Leibniz Institute for Applied Geophysics (LIAG), Hannover, Germany, [11]Federal Institute for Geosciences and Natural Resources, Hanover, Germany, [12]Marine Chemistry, Leibniz Institute for Baltic Sea Research (IOW), Warnemünde, Germany, [13]Technische Universität Dresden, Faculty of Environmental Sciences, Department of Forest Sciences, Chair of Forest Biometrics and Forest Systems Analysis, 01062 Dresden, Germany, [14]Institute for Chemistry and Biology of the Marine Environment (ICBM), University of Oldenburg, Oldenburg, Germany, [15]Helmholtz Centre for Environmental Research (UFZ), Leipzig, Germany

Subterranean estuaries the, subsurface mixing zones of terrestrial groundwater and seawater, substantially influence solute fluxes to the oceans. Solutes brought by groundwater from land and solutes brought from the sea can undergo biogeochemical reactions. These are often mediated by microbes and controlled by reactions with coastal sediments, and determine the composition of fluids discharging from STEs (i.e., submarine groundwater discharge), which may have consequences showing in coastal ecosystems. While at the local scale (meters), processes have been intensively studied, the impact of subterranean estuary processes on solute fluxes to the coastal ocean remains poorly constrained at the regional scale (kilometers). In the present communication, we review the processes that occur in STEs, focusing mainly on fluid flow and biogeochemical transformations of nitrogen, phosphorus, carbon, sulfur and trace metals. We highlight the spatio-temporal dynamics and measurable manifestations of those processes. The objective of this contribution is to provide a perspective on how tracer studies, geophysical methods, remote sensing and hydrogeological modeling could exploit such manifestations to estimate the regional-scale impact of processes in STEs on solute fluxes to the coastal ocean.

Keywords: subterranean estuary, submarine groundwater discharge, coastal aquifer, upscaling, biogeochemistry, geophysics, numerical modeling, ecology

OPEN ACCESS

Edited by:
Frédéric Frappart, UMR5566 Laboratoire d'études en géophysique et océanographie spatiales (LEGOS), France

Reviewed by:
Andrea Pain, University of Maryland Center for Environmental Science (UMCES), United States
David Brankovits, Texas A&M University at Galveston, United States
Gwénaëlle Chaillou, Université du Québec à Rimouski, Canada

****Correspondence:***
Nils Moosdorf
nils.moosdorf@leibniz-zmt.de

Specialty section:
This article was submitted to Hydrosphere, a section of the journal Frontiers in Earth Science

Received: *31 August 2020*
Accepted: *04 February 2021*
Published: *14 May 2021*

Citation:
Moosdorf N, Böttcher ME, Adyasari D, Erkul E, Gilfedder BS, Greskowiak J, Jenner A-K, Kotwicki L, Massmann G, Müller-Petke M, Oehler T, Post V, Prien R, Scholten J, Siemon B, Ehlert von Ahn CM, Walther M, Waska H, Wunderlich T and Mallast U (2021) A State-Of-The-Art Perspective on the Characterization of Subterranean Estuaries at the Regional Scale. Front. Earth Sci. 9:601293. doi: 10.3389/feart.2021.601293

INTRODUCTION

Along global coastlines, meteoric groundwater discharges into the ocean (Church, 1996; Taniguchi et al., 2002; Zhou et al., 2019; Luijendijk et al., 2020). The subsurface zone where meteoric groundwater mixes with saltwater was termed the subterranean estuary (STE) by Moore (1999). This term was defined as "a coastal aquifer where groundwater derived from land drainage measurably dilutes saltwater that has invaded the aquifer through a free connection to the sea" (Moore, 1999). The relevance of STEs for matter cycling and coastal ecology is increasingly recognized by the scientific community (Rocha et al., 2021).

The term estuary originates from hydrology and is defined as the area where fresh river water and saline seawater mix (Prandle, 2009). Riverine estuaries are biogeochemical reactors that, amongst other processes, filter out about 20% of the dissolved silicon through reverse weathering (Tréguer and De La Rocha, 2013) or degas substantial amounts of riverine transported organic carbon as CO_2 (Laruelle et al., 2010). By now, it is accepted that riverine solute fluxes to the coastal realm cannot be meaningfully quantified without considering transformations in the mixing zone of river estuaries (e.g., Kipp et al., 2020). For submarine groundwater discharge (SGD), the same should hold for subterranean estuaries (Robinson et al., 2018).

STEs are characterized by waters with geochemical signatures controlled by steep (physico-)chemical gradients of mixing terrestrial groundwater and seawater (Moore, 1999). The groundwater-seawater mixing zone embraces thematically different scientific fields, sometimes leading to confusion in terminologies. The term STE, for instance, is partly overlapping with the term 'coastal aquifers', which describes a groundwater system at the interface of land and sea in hydrogeology (Duque et al., 2020; Jiao and Post, 2019). Mixing of fresh and saline groundwater occurs differently in porous sedimentary aquifers than in karst or volcanic aquifers since the former have longer residence times and a higher reaction area between solid and fluid phase. STEs of the latter type are termed 'anchialine' (Bishop et al., 2015). Other studies use the term STE for karstic environments (e.g., Gonneea et al., 2014). In these situations, hydrology plays a major role in biogeochemical reactions (Brankovits et al., 2018), which is amplified by the karst's hydrogeological conditions. However, if karstic aquifers discharge in submarine springs with sufficient discharge rates, this can lead to freshwater mixing with seawater in the ocean itself in the form of plume-like structures (e.g., Fleury et al., 2007), whose nutrient fluxes can trigger algal blooms (Chen et al., 2020). Karst areas cover large parts of the global coastline (Goldscheider et al., 2020) and are essential groundwater-ocean interaction areas. Nevertheless, since processes in these conduit-systems differ sharply from those in porous sediments, we focus our assessment on STEs composed of porous sediments (**Figure 1**). Thus, we here use the term STE to describe the zone where fresh and saline groundwater mix in porous coastal aquifers in the subsurface, which is in line with the marine scientific literature (Robinson et al., 2018; Duque et al., 2020).

While STEs share the name estuary and the freshwater-saltwater mixing zone, they differ sharply from their riverine counterparts. The term "estuary" itself is questionable for STEs, since some definitions of estuaries also encompass the shape of the water body, e.g., as "semi-enclosed", basically referring to rivers (Wolanski, 2007). One crucial difference is residence time, which is in the order of days in riverine estuaries (Rasmussen and Josefson, 2002) and can be decades in STEs (e.g., Grünenbaum et al., 2020). The different residence time leads to different mixing processes: while in rivers, mixing can be in turbulent flow driven by wind, flow in STEs is generally linear and advection-dispersion driven. While in river estuaries, water-solid interaction is mostly limited to suspended or surface sediment as solid phase, STEs provide a wide range of minerals and solids to interact due to a lower water/rock ratio. In some STEs, anoxic conditions develop along subsurface flow-paths or be promoted by the inflow of O_2-free groundwater, which changes the biogeochemical reactions compared to STEs where oxic conditions prevail (Slomp and Van Cappellen, 2004) or to oxic surface waters flowing through riverine estuaries. Thus, despite river estuaries and STEs sharing parts of their name, the processes involved can be very different. Also, while rivers can be treated as point sources of solutes and particulates to the coastal ocean, STEs can occur along long stretches of coast, and their geochemistry can vary substantially at the meter scale (e.g., Beck et al., 2016; Ehlert et al., 2016; Beck et al., 2017; Waska et al., 2019b) and even more at the regional scale.

In general, biogeochemical reactions alter the composition of terrestrial groundwater and saltwater that flow through STEs. Thus, the biogeochemical composition of the resulting SGD will not represent a conservative mixing between the fresh and saline waters entering the STE. In many STEs, the contribution of marine water circulating through the sediment ("marine SGD") to the total water fluxes exceeds that of terrestrial groundwater (e.g., Lopez et al., 2020). Groundwater of marine origin in the seafloor sediment and STEs will here be called "saline groundwater." Flow and transport in STEs are highly dynamic and locally variable. While discharge from unconfined shallow aquifers occurs near the shoreline, discharge from confined aquifers has been observed several kilometers offshore, depending on the hydrogeological conditions (Burnett et al., 2003; Gustafson et al., 2019). Mixing of fluids triggers biogeochemical reactions that can change the discharge composition compared to the original end-members (i.e., fresh groundwater and saltwater). Understanding the coupling between the physical and biogeochemical processes is the prerequisite to understand the role of STEs in controlling the geochemical composition of SGD (Robinson et al., 2018). Processes in STEs can substantially influence the water quality of the receiving water bodies and the biological processes in coastal waters (e.g., productivity, food web structure) and the full spectrum of the species inhabiting them, from bacteria (Adyasari et al., 2019a), algae, through grazers, detritivores, to invertebrates (Miller and Ullman, 2004), predatory fish (Pisternick et al., 2020), and birds (Kotwicki et al., 2014; Lecher and Mackey, 2018). The processes controlling the solute fluxes through STEs have been



FIGURE 1 | Examples of beach settings in which active STEs developed. Left panel: Varkala Beach, India, where SGD seeps through the pore space below the waterline (Oehler et al., 2019b) (Photograph: T. Oehler). Middle panel: Trou aux Biches, Mauritius, where SGD is seeping out of the beach face during low tide (Photograph: J. Scholten). Right panel: SGD seeping along preferential flow-paths into the Wadden Sea near Cuxhaven, Germany (Photograph: Nils Moosdorf). Note that an STE often is not directly visible from the surface.

named among the main currently unsolved problems in hydrology (Blöschl et al., 2019).

Groundwater salinity distribution in STEs is typically characterized by a wedge of dense, saline groundwater that thins from the ocean inland underneath a fresh water body at the bottom of an aquifer (**Figure 2**). Along these water bodies' interface, the fresh and saline groundwater mix and a zone of intermediate salinities forms. Another saline recirculation cell, where saltwater infiltrates into the sediment, the so-called 'upper saline plume' (USP), can occur in settings with a sloping land surface where tides and waves run up along the beach (e.g., Lebbe, 1981; Robinson et al., 2007). Between the USP and the saltwater wedge, a 'freshwater discharge tube' evolves, focusing fresh SGD along the low water line under an active SGD seepage zone. These distinct water bodies have been described to shift, expand and contract as a consequence of seasonal groundwater recharge variations (Michael et al., 2005), spring-neap tidal cycles (Abarca et al., 2013; Heiss and Michael, 2014) or intensified wave conditions (Robinson et al., 2014). The shape of the STE is controlled by a large number of factors, such as geological heterogeneity (Geng et al., 2020), terrestrial groundwater discharge (Heiss and Michael, 2014), tidal amplitude (Abarca et al., 2013), sediment topography (Robinson et al., 2006; Waska et al., 2019b; Grünenbaum et al., 2020), or even seawater temperature (Kim et al., 2020).

STEs have been investigated from local, regional (Beck and Brumsack, 2012; Jurasinski et al., 2018) to global perspective (Beck et al., 2013; Rahman et al., 2019), and groundwater dynamics and driving forces have been reviewed (Santos et al., 2012; Robinson et al., 2018). For example, in Waquoit Bay, a comprehensive suite of STE studies related to biogeochemistry (Charette et al., 2005; Charette and Sholkovitz, 2006; Saenz et al., 2012; Gonneea et al., 2014), hydrology (Michael et al., 2005; Spiteri et al., 2008b), and tracer application (Dulaiova et al., 2008) has been conducted. The coastline of the Gulf of Mexico has provided a diverse geological background for local STE studies: from sandy beaches and lagoon systems in Florida (Santos et al., 2008; Roy et al., 2011; Pain et al., 2019), via an organic-rich STE in the eastern part of Mobile Bay, Alabama (Montiel et al., 2019), to developed karst system in Yucatan, Mexico (Gonneea et al., 2014; Brankovits et al., 2017; Brankovits et al., 2018). Biogeochemical STE studies in North America have also been conducted in the eastern (Hays and Ullman, 2007; O'Connor et al., 2018; Tamborski et al., 2017) and western (Santoro et al., 2008; Boehm et al., 2014; Brown and Boehm, 2016) coastal areas of the contiguous United States, as well as boreal parts of Alaska (Lecher et al., 2016a) and Canada (Couturier et al., 2016; Sirois et al., 2018).

Many relevant field studies have been conducted outside North America. The development of an upper saline plume and the freshwater tube underneath was first demonstrated in Belgium by Lebbe (1981). He developed the conceptual model for the salinity distribution in unconfined aquifers influenced by tides based on field measurements and mathematical modeling. The Wadden Sea, located in the southern North Sea, is a well-studied system where various geochemical (Beck et al., 2017; Linkhorst et al., 2017; Reckhardt et al., 2017; Rullkötter, 2009; Seidel et al., 2015; Waska et al., 2019b), hydrological (Moore et al., 2011; Seibert et al., 2019), as well as microbiological and biogeochemical (Musat et al., 2006; Al-Raei et al., 2009) studies have been conducted. Here, STEs have been shown to function as a coastal filter for material exchange and transformation. They are characterized by a high input of organic matter, intensive nutrient recycling, and organic matter remineralization rates (Billerbeck et al., 2006; Al-Raei et al., 2009). Other studied STEs in Europe are the Baltic Sea coast (Szymczycha et al., 2012; Donis et al., 2017; Jurasinski et al., 2018; Virtasalo et al., 2019) and the coast of France (Anschutz et al., 2009; Charbonnier et al., 2013; Oehler et al., 2017). In Asia-Pacific, STE studies were conducted in South Korea (Kim et al., 2012; Lee et al., 2017) with particular attention paid to the volcanic Jeju Island (Kim et al., 2011; Kim et al., 2013), China (Liu et al., 2012; Wang et al., 2015; Yang et al., 2015; Jiang et al., 2020), Japan (Uchiyama et al., 2000; Nakada et al., 2011), Indonesia (Adyasari et al., 2019b), Cook Island (Erler et al., 2014), and Australia (Robinson et al., 2006; Robinson et al., 2007; Sanders et al., 2012).

The delivery of nutrients by terrestrial groundwater has been plentifully addressed also at continental to global scales (e.g., Beusen et al., 2013; Sawyer et al., 2016; Luijendijk et al., 2020), typically by multiplying the estimated water flux by the nutrient concentration of the fresh groundwater to obtain the nutrient mass flux. Such estimates do not consider the biogeochemical reactions in the STE that modulate the actual inputs to the coastal ocean. Local-scale studies have revealed the critical influence of biogeochemical reactions in the STE on land-ocean solute fluxes

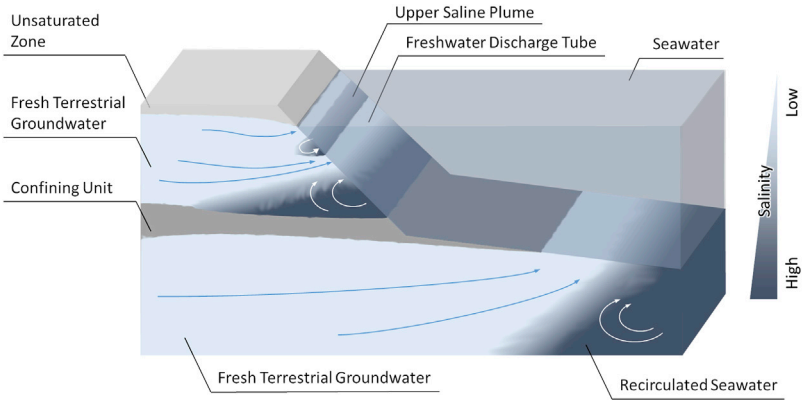


FIGURE 2 | Cross-section of a coastline highlighting the different parts of a subterranean estuary (STE).

and coastal ecology, even though STEs only cover a narrow stretch of the coast. This influence happens most certainly on a local and regional scale and is likely to have a significant effect on global scales. However, what remains unclear is how the knowledge and process descriptions at the local scale can be translated to the regional scale so that the impact of terrestrial SGD on the marine environment can be better quantified. We define the local scale as coastline lengths between 10^0–10^2 m and the regional scale at 10^3–10^5 m. Here, we summarize local scale knowledge about processes in STEs and outline perspectives toward the representation and extrapolation of these processes at the regional scale.

BIOGEOCHEMICAL CYCLING IN SUBTERRANEAN ESTUARIES

Subterranean estuaries are biogeochemically active, characterized by microbially mediated element release, fixation and transformation reactions (Charette et al., 2005; Spiteri et al., 2008a; McGrath et al., 2012; Beck et al., 2017; Duque et al., 2020). Biogeochemical reactions within the STE and the export of reaction products into coastal waters can have wide-reaching consequences for ecologically detrimental coastal processes such as eutrophication and associated oxygen depletion of bottom waters (Slomp and Van Cappellen, 2004; Dybas, 2005), modification of ocean derived substances (e.g., detrital matter including POC and S species: Shum and Sundby, 1996), buffering or enhancing ocean acidification (Wang et al., 2014; Santos et al., 2015; Liu et al., 2017), and transport of contaminants from the land to the sea (Brovelli et al., 2007; Wang et al., 2012). Depending on redox conditions and water flux rates, this can be crucial in determining element speciation and balances in coastal waters with effects for phytoplankton productivity and potentially eutrophication (Taniguchi et al., 2019). Increased primary productivity can further intensify the transfer of nutrients and possible contaminants from lower to higher trophic levels.

Organic carbon forms a primary electron donor in the coastal subsurface, which interacts with various electron acceptors (e.g., O, N, S, Fe and Mn species) derived from the sea or transported within the aquifer. Organic carbon stimulates a cascade of biogeochemical reactions relevant for local to global element turnover rates and budgets at the land-sea interface (Goodridge and Melack, 2014; Couturier et al., 2017; Cho et al., 2018; Seibert et al., 2019). Organic carbon quality, i.e., the fitness of organic molecules for microbial use as an electron donor (and sometimes acceptor), is dependent on its molecular composition, which is usually a complex mixture of terrestrial and marine-derived chemical moieties (Seidel et al., 2015).

The steep physicochemical gradients and enhanced microbial activity in STEs can also lead to mineralization processes of organic matter and hydrocarbons (Akam et al., 2020) as well as reoxidation reactions (Roy et al., 2013). These processes alter the redox conditions and the proton activity and may lead to the formation of authigenic solid phases, like carbonate, sulfide, sulfate or phosphate minerals (O'Connor et al., 2018; Riechelmann et al., 2020; Roy et al., 2013). Mineral formation may limit the concentrations of dissolved trace elements like metals being co-precipitated during iron sulfide formation (e.g., Huerta-Diaz and Morse, 1992). However, mineral formation also adds to the STE function as a filtering barrier between the terrestrial groundwater system and the sea for harmful chemical compounds. A well-known example of this is the so-called 'iron curtain,' an iron oxide rich zone that forms when oxic seawater is cycled through the beach sediments and mixes with anoxic or sub-oxic terrestrial groundwater (Chambers and Odum, 1990; Charette and Sholkovitz, 2002; Spiteri et al., 2006; Linkhorst et al., 2017; Sirois et al., 2018). The large sorption capacity of these iron oxides can be responsible for fixating aqueous pollutants, such as P and As species, before they become entwined in coastal food webs (Chambers and Odum, 1990; Bone et al., 2006; Beck et al., 2010).

Biogeochemically active areas can be unevenly distributed within the STE. This effect is amplified by the geological heterogeneity of flow regimes (Geng et al., 2020). Typically, certain conditions lead to the formation of biogeochemical 'hot-spots', areas of enhanced microbiological and chemical

activity that drive the modification and transformation of ions and molecules in the subsurface (Santos et al., 2008). Microbial activity and community changes with salinity (Adyasari et al., 2019a). While the processes causing the observed spatial distribution of hot-spots are still poorly understood, an appropriate substrate (chemical and physical) is needed, as is an active flux of reactive electron acceptors and donors to maintain an energy flux for the microbial metabolism.

Thus, knowing the hydrogeology of a site (water origin, flow paths, residence times, mixing processes, and aquifer properties) is crucial for understanding the distribution of hot spots in STEs (Goodridge and Melack, 2014). Modeling suggested that density-driven flow can enhance mixing in an STE when dense saline water from the upper saline plume or periodic flooding sinks into the underlying freshwater lens due to 'salt fingering' (Greskowiak, 2014). Other studies show the importance of heterogeneity of hydrogeological parameters in controlling an STE's shape (Weinstein et al., 2007) and the associated biogeochemical reactions (Heiss et al., 2020).

The temporal equivalent of 'hot-spot' is often termed 'hot moment'. The recognition that high element turnover (reactivity) areas are temporally dynamic is important (Liu et al., 2017; Waska et al., 2019b). Hot moments imply that enhanced biogeochemical activity areas are stationary neither in time nor location and will fluctuate depending on hydrological and chemical boundary conditions (Seidel et al., 2015). The incorporation of hot moments into the framework of biogeochemical activity in the subsurface has helped understand the previously ambiguous distributions of elements and molecules, e.g., in the framework of groundwater-river interaction (Vidon et al., 2010). At the coast, storms may, for instance, physically impact the freshwater input, the availability of substrates, or the seafloor morphology, which would change STE behavior. Due to storms, SGD rates can strongly change in a matter of days (Cho et al., 2021). More generally, hot moments in STE can be created through movements of the salinity gradient, when, e.g., phosphorus can desorb from aquifer sediment with increasing salinity and cause a spike of P fluxes to the ocean that is not directly connected to terrestrial or marine inputs (Flower et al., 2017). Hot moments can also result from shifts in groundwater flow paths due to changed wave activity, which have been hypothesized to trigger pulses of arsenic transport into coastal waters due to instability of iron oxyhydroxides under changing redox conditions (Rakhimbekova et al., 2018). Water residence time is an essential factor influencing chemical reaction kinetics in the STE. For instance, in Waquoit Bay, longer residence times during winter caused attenuation of the groundwater nutrient load within the STE, whereas during periods of shorter residence time, SGD was nutrient-enriched (Gonneea and Charette, 2014).

The characterization of mineral authigenesis and its proxy potential in the STE requires sediment core material from the coastal and hinterland zone, best vertically resolved along transects through the STE to gain regional information. Whereas the physicochemical characterization of the aqueous solutions may allow for the identification of the current situation, the solid phases, when combined with appropriate age control, provide information about past SGD (Böttcher and Dietzel, 2010) as well as the movement of the geochemical mixing zone within the STE in response to sea-level change (Roy et al., 2010; Hong et al., 2018). The sea-level rise since the last glacial maximum caused a landward movement of STEs. Isotopic composition of authigenic minerals documents past changes in the land-sea hydrological conductivity and the evolution of the paleoenvironment.

In the following, the biogeochemical cycling of individual compounds in STEs will be discussed.

Carbon

Subterranean estuaries receive carbon (C) from both terrestrial and marine sources. Terrestrial dissolved inorganic carbon (DIC) is principally derived from biological processes taking place in the soil, and further influenced by biogeochemical processes in the groundwater (Bögli, 1980; Clark and Fritz, 1997; Deines et al., 1974). Terrestrial dissolved organic carbon (DOC) in STEs is either transported from the soil zone of the surrounding watersheds to the coast via groundwater or leached from vascular-plant material buried in coastal aquifers, such as paleosols (Sirois et al., 2018) or peat layers. Marine DOC is supplied to STEs by infiltrating seawater and produced locally in the STEs through remineralization of particulate organic matter (POM), for example, from coastal phytoplankton and macrobenthic beach wrack (Kim et al., 2019). DOC from both sources is transformed in STEs by microbial activity into CO_2 and CH_4.

Generally, terrestrial groundwater contributions will enhance the regional potential of coastal seawater to degas CO_2 to the atmosphere and contribute to primary productivity. However, DIC from terrestrial groundwater may also induce intense carbonate mineral dissolution (if terrestrial groundwater is oversaturated in CO_2) or lead to the precipitation of secondary carbonates (Deines et al., 1974; Wigley et al., 1978). The dissolution of carbonates in beach sands could be a substantial pH-buffer preventing acidic groundwater from changing coastal marine environments. Mixing between different water masses may impact the saturation states of carbonate minerals in an aqueous solution (Bögli, 1980; Hanshaw and Back, 1979), which amplifies the STE effect on the carbon cycle. Carbonate dissolution in the groundwater-seawater mixing zone can form caves and caverneous structures (Mylroie and Carew, 1990). At the regional scale, the total amount of carbonate dissolution through saturation effects of mixing groundwater and seawater was estimated on the Yucatan Peninsula (Hanshaw and Back, 1980). Therefore, carbonate dissolution structures may potentially be used to derive information about STE activity at regional scales or trace back STEs over geological time scales. Precipitation or dissolution of authigenic carbonate minerals could develop characteristic C and O isotope as well as trace metal signatures that can be used to deduce the composition of past solute gradients in an STE (Böttcher and Dietzel, 2010).

SGD can also be a source of methane (CH_4) to coastal waters (Lecher et al., 2016b; O'Reilly et al., 2015), and CH_4 gradients have been used to identify sites of SGD (e.g., Cable et al., 1996; Böttcher et al., 2021). In the Baltic Sea, seepage of terrestrial

groundwater associated with CH_4 releases was observed (Whiticar and Werner, 1981; Whiticar, 2002). STEs, both in karstic and porous settings, can be hotspots for CH_4 oxidation that removes CH_4 from groundwater before discharging into surface waters (Schutte et al., 2016; Brankovits and Pohlman, 2020). High variability in temporal (seasonal) and spatial (among geographically similar STEs) CO_2 and CH_4 concentrations and fluxes have been observed (Pain et al., 2019; Pain et al., 2020), complicating extrapolations to the regional scale.

Mineralization of DOM and CH_4 in STEs changes ratios of total alkalinity (TA) over DIC depending on the involved electron acceptors and superimposing biogeochemical processes (Akam et al., 2020). The mineralization can result in characteristic carbon isotope signatures (Deines et al., 1974; Meister et al., 2019). Sheltered, organic-rich STEs with sulfate reduction as a dominant remineralization pathway may become enriched with DOC and TA (e.g., Sippo et al., 2016). The mineralization of organic carbon in STEs is often linked to several overlapping mechanisms, which can vary over seasonal cycles, such as the advective flow of terrestrial groundwater and saltwater and the availability of organic carbon (Kim and Kim, 2017; Liu et al., 2017; Kim et al., 2019). Marine-derived organic matter is assumed to be more abundant and more labile than terrestrially derived organic matter (Seidel et al., 2015) and is accompanied by an injection of oxygen, which accelerates mineralization rates. This "priming" by labile organic carbon and supply of oxygen may impact remineralization of groundwater-imported terrestrial DOC, but how and to which extent is weakly known. Since seawater circulation volumes exceed terrestrial groundwater throughputs in many STEs, marine DOC inputs could primarily determine the activity of the STE microbial reactor. Hence, most DOC released back into the coastal water column could be recycled/transformed. However, the relative contributions of terrestrial and marine organic carbon, as well as the function of the STE as a net source or net sink of organic carbon, are highly variable in space and time (Webb et al., 2019).

Carbon cycling in the STE on a local scale is best understood based on parallel profiling on land and at the seaside of the groundwater-seawater mixing zone since both terrestrial- and marine processes can control DIC and DOC fluxes. Besides direct tracking and benthic measurements of SGD leaving an STE (Donis et al., 2017), stable C isotope compositions of DIC, DOC and CH_4 are useful variables in the characterization and even quantification of internal processes and modulations in STEs (e.g., Winde et al., 2014; Donis et al., 2017; Meister et al., 2019; Pain et al., 2019; Pain et al., 2020). Also, DOM molecular traits can elucidate organic carbon cycling in STEs (Seidel et al., 2015). At the regional scale, the C cycle is particularly complex to represent because of the considerable heterogeneity of unconfined aquifers and the formation of metabolically diverse 'hot spots'. Therefore, an abundance of information is necessary both from the land- and marine sides of the STE.

Nitrogen

Subterranean estuaries may act as either a source or sink of nitrogen (N). Microorganisms catalyze different reactions of reactive N, which include nitrate (NO_3^-), nitrite (NO_2^-), and ammonium (NH_4^+). The core nitrogen cycle involves four reductions [N fixation ($N_2 \rightarrow NH_4^+$), denitrification ($NO_3^- \rightarrow N_2$)], assimilatory nitrate reduction ($NO_3^- \rightarrow NH_4^+$), and dissimilatory nitrate reduction to ammonium (DNRA, $NO_3^- \rightarrow NH_4^+$) as well as two oxidation pathways [nitrification ($NH_4^+ \rightarrow NO_3^-$)] and anaerobic ammonium oxidation (anammox, $NH_4^+ \rightarrow N_2$) (Kanehisa and Goto, 2000). The nitrogen cycle further includes organic nitrogen mineralization, or ammonification, which is the breakdown of organic N (N_{org}), leading to the release of NH_4^+.

Nitrogen usually enters the system via N fixation (Fulweiler et al., 2007; Rao and Charette, 2012), organic input from terrestrial and marine sources, or terrestrial groundwater in the form of nitrate (Weinstein et al., 2011). STEs were classified as nutrient-contaminated STEs when they receive elevated amounts of nitrate from terrestrial groundwater and uncontaminated STEs when they produce nitrate internally from the mineralization of organic matter (Santos et al., 2009b; Loveless and Oldham, 2010; Robinson et al., 2018). In the latter case, tidal pumping provides N_{org} to the STE, which later is remineralized into NH_4^+ or nitrified to create NO_2^- and NO_3^- (Ullman et al., 2003; Santos et al., 2008; Charbonnier et al., 2013). The nitrifying microorganisms are aerobic chemoautotrophs; thus, nitrification generally occurs at the oxic surface layer of STEs where the ammonification rate is high, and N_{org} input and oxygen concentration are abundant (Santoro et al., 2008).

It has been shown that nitrate may be removed in permeable intertidal sediments from circulating seawater (Marchant et al., 2016), in some locations by up to 70% (Wong et al., 2020). Permanent biological removal of reactive N (NO_3^- and NH_4^+) from the STE may be achieved through biological assimilation, denitrification and anammox, provided that contact time between the aqueous and solid phase of an STE is sufficient. Denitrification is reportedly the primary biogeochemical process responsible for N loss in coastal and marine systems (Canfield et al., 2010) and performed by a wide range of bacteria and archaea, mostly heterotrophic microorganisms. Particulate organic carbon (POC) in the coastal aquifer was reported as a major control on denitrification in STE (Kim et al., 2020). Under conditions where NO_3^- inputs exceed the availability of carbon substrate for denitrification, DNRA may occur (Tiedje, 1988; Gardner et al., 2006), which, however, preserves N in the system as NH_4^+. Anammox, another process of biological N removal (Jetten et al., 1998), may occur in an anaerobic, NH_4^+-abundant, low organic matter environment (Sáenz et al., 2012). The co-occurrences of N transformation processes, such as simultaneous nitrification-denitrification, has been found in the STE due to the oxygen and organic matter stratification (Hays and Ullman, 2007; Erler et al., 2014) or rapid mixing of different water masses, creating both oxic and anoxic microzones (Uchiyama et al., 2000; Kroeger and Charette, 2008).

The N transformation processes are controlled mainly by groundwater residence time (Santos et al., 2008; Gonneea and Charette, 2014), redox condition (Slomp and Van Cappellen, 2004), availability of electron donors (Santoro, 2010), and mixing

rate of freshwater and saltwater (Kroeger and Charette, 2008). They have been detected and measured by geochemistry or molecular biology approaches. Stable isotopes ($\delta^{15}N$) and concentrations of reactive N help understand N behavior in STEs (Kroeger and Charette, 2008) and can also be manipulated as a tracer (Erler et al., 2014). Denitrification rates can also be calculated from STE sediment cores (DeSimone and Howes, 1996; Nowicki et al., 1999). Microbial N transformation can be determined by molecular detection, which involves extracting the microbial DNA from water or sediment samples (Santoro et al., 2006; Rogers and Casciotti, 2010; Hong et al., 2018; Adyasari et al., 2020).

Reactions in the nitrogen cycle in STEs are controlled primarily by microbiology. While at the local scale geochemistry or molecular biology assessment methods exist, regional scale tracers for these processes have yet to be identified. They could be indirectly inferred from STE physical properties (e.g., organic matter content and quality in host sediment, residence time, redox conditions) that control reaction rates and types. One example is the use of hyperspectral imaging to identify phytoplankton and CDOM concentration or total suspended solids (e.g., Brando and Dekker, 2003) and benthic information (e.g., Vahtmäe et al., 2020) in coastal waters if the signal is strong and clear enough given possible depth and turbidity. Lastly, if substantial quantities of gaseous N_2 are produced by denitrification, it could be detected by geophysical methods under favorable conditions.

Phosphorus

Phosphorous (P) inputs into terrestrial groundwater are mainly derived from fertilizers, waste and sewage (Slomp and Van Cappellen, 2004), to a minor extent from the mineralization of organic matter (Froelich et al., 1979) or released from minerals as geogenic sources (Kazmierczak et al., 2020; Tao et al., 2020). Geogenic P sources are mostly of local importance and depend on the aquifer mineralogy. In saline groundwater, P is usually derived from the mineralization of organic matter (Froelich et al., 1979). In karstic STEs, where groundwater can reach surface waters via rapid conduit flow pulse, inputs of P are associated with high-intensity rainfall events. In such a system in southern Java (Indonesia), elevated P concentrations were linked to events with high groundwater discharge rates, leading to exceptionally high P inputs into coastal waters (Oehler et al., 2018).

Dissolved P has a high affinity to adsorb at mineral surfaces of carbonates (Gaudette and Lyons, 1980; Burton and Walter, 1990) and iron oxyhydroxides (Einsele, 1936; van der Grift et al., 2014). These minerals can precipitate in STEs, which thereby would reduce the amount of P that is transported via SGD (Pain et al., 2020). In Waquoit Bay, P concentrations are 5–7 times higher in iron oxide rich sands than in the overlying surface sands, indicating how effectively processes in STEs can bind P (Charette and Sholkovitz, 2002).

Phosphorus concentrations along the salinity gradient of STEs usually behave non-conservatively. Elevated P concentrations are often associated with elevated groundwater salinity (Gaudette and Lyons, 1980), e.g., due to desorption from particles (Suzumura et al., 2000), Fe reduction associated with organic matter mineralization, direct P liberation (Froelich et al., 1979), or the release of colloid-bound nutrients (Prouty et al., 2017a). Sporadic P release can also follow occasional saltwater intrusions. Thus, to understand the temporal P transport behavior in an STE, the mobility of the groundwater-seawater mixing zone needs to be known. Depending on the distance to the sediment surface and the SGD flow regime, particulate and dissolved P may be transported to coastal waters (e.g., Lipka et al., 2018). Therefore, the mobility and final release of P to surface waters indirectly depend on redox conditions and the specific composition of the aquifer (Gaudette and Lyons, 1980; Lewandowski et al., 2015).

Phosphorous cycling in the STE is on a local scale best investigated based on the analysis of pore waters and sediments along transects across the terrestrial groundwater end-member through the mixing zone. Porewater analyses should be combined with continuous monitoring of the composition in the pelagic system and complemented by element budgeting. Care has to be taken in separating P in porewater derived from the groundwater against that derived from processes within an STE (Suzumura et al., 2000; Price et al., 2010; Prouty et al., 2017b). Redox conditions in the terrestrial groundwater, as well as the abundance of iron oxyhydroxides and carbonate minerals in the STE sediment need to be known or approximated to estimate the regional scale effect of STEs on P transport and release to the coastal ecosystem.

Sulfur

Subterranean estuaries gain most sulfur (S) from seawater, of which sulfate (SO_4^{2-}) is a major constituent. In brackish-marine sediments, microbial dissimilatory SO_4^{2-} reduction is the primary anaerobic process responsible for the mineralization of organic matter (Jørgensen, 1982), leading to the formation of dissolved sulfide. Sulfate reduction is also responsible for the oxidative conversion of methane into dissolved carbon dioxide (Boetius et al., 2000). Nevertheless, STEs also receive S from terrestrial groundwater, where dissolved SO_4^{2-} may originate from the dissolution of aquifer minerals like gypsum or oxidation of iron sulfides, like pyrite (Zhang et al., 2012). In young water bodies, anthropogenic sources, like acid rain, acid mine drainage and fertilizers, may further enhance SO_4^{2-} loads (Clark and Fritz, 1997; Alorda-Kleinglass et al., 2019).

In STEs containing sufficient electron donors, SO_4^{2-} reduction might be enhanced and can outcompete methanogenesis (Slomp and Van Cappellen, 2004). These systems can differ substantially in their biogeochemical processes and thereby in their release of climate-relevant gas emissions (Böttcher et al., 2021). Hydrogen sulfide may furthermore be re-oxidized by solid and aqueous species or be precipitated as iron sulfides (Luther et al., 1991; Rickard, 1997), thus acting as a sink for other dissolved metals (Huerta-Diaz and Morse, 1992). Overall, the dissolved SO_4^{2-} availability controls the biogeochemical element cycling in the groundwater-seawater mixing zone and specifically the coupled sulfur-carbon-metal cycle. In particular, the coupled stable sulfur and oxygen isotope composition of dissolved SO_4^{2-} in the STE pore waters provides information about sources, sinks and

cycling of sulfur (Fritz et al., 1989; Zhang et al., 2012) that may even be traced in an impacted shallow water column. Using sulfur isotopes as a tracer will be difficult at the regional scale due to the many involved controls and high sampling effort necessary.

Metals

Dissolved metal concentrations in pore waters of STEs (e.g., Ba, Cd, Cu, Fe, Mn, Mo, Pb, Zn) depend strongly on the mineralogy of the aquifer and may be enriched by anthropogenic contamination (Bone et al., 2007; Knee and Paytan, 2011). Many of the trace metals have particular ecological relevance as (micro)nutrients or toxins (Salt et al., 1995; Beck et al., 2010), and their signatures may be recognizable in near-shore STE sediments (Knee and Paytan, 2011). Submarine groundwater discharge is relevant for marine alkaline earth metal composition (Mayfield et al., 2021), a significant source of rare earth elements to the ocean and could be the missing link in the global distribution of Neodynium (Nd), a key proxy for oceanic water-mass mixing (Johannesson and Burdige, 2007; Chevis et al., 2015; Paffrath et al., 2020). Formation of complexes and colloids, sorption on the surface of particles, ion exchange, and changes in speciation are some of the relevant processes that control metal mobility, reactivity and toxicity (Charette and Sholkovitz, 2006; Waska et al., 2019a). The interactions between solutes and aquifer particles exert a firm control on trace metal transport in STEs and are strongly influenced by redox and pH conditions, salinity, and ligand availability (Knee and Paytan, 2011).

One of the quantitatively most abundant metals in STEs is iron (Fe). Its mobility is highly sensitive to changes in redox milieu and pH (Spiteri et al., 2006). Upon precipitation, iron-oxyhydroxides (FeOOH) and iron sulfides (FeS) provide a substrate for sorption and incorporation of metals, Si, As, DOM, and especially P (Huerta-Diaz and Morse, 1992; van der Grift et al., 2014). Furthermore, a substantial impact of FeOOH precipitation on the fractionation of different DOM fractions was described (Linkhorst et al., 2017). Iron mineral formation in the STE may remove selected trace metals from the aqueous solution (Charette and Sholkovitz, 2002; Charette and Sholkovitz, 2006; Böttcher and Dietzel, 2010) and release them later, when the reactive front may have shifted. Karst systems, in particular, can be efficient pathways for the exfiltration of metal-enriched waters through an STE into the coastal zone due to short aquifer residence times, enhanced flow rates, and a low mineral surfaces to groundwater volume ratio (Knee and Paytan, 2011; Pain et al., 2020).

The use of trace metals to identify SGD in the coastal waters depends on their reactivity in redox and pH gradients. Mn, for instance, remains mobile for some time even under oxic conditions (Kowalski et al., 2012; Winde et al., 2014), whereas Fe is efficiently fixed in the STE. This stability difference leads to fractionation of these metals (Balzer, 1982) and the trace metals that sorb on them. On a regional scale, selected trace metals like Mn or Ba in the water column may help to detect and even quantify SGD in tidal areas (Kowalski et al., 2012; Winde et al., 2014).

APPROACHES TO ASSESSING STE PROCESSES AT THE REGIONAL SCALE

Geochemical Tracers

Geochemical tracers can help to identify locations of STEs as well as processes within them. In general, tracers are characterized by distinct differences in concentrations or isotopic compositions between groundwater and seawater. Salinity or conductivity is a ubiquitous tracer since freshening of coastal ocean waters without a nearby surficial terrestrial source is an indicator of STE influence. However, traces of freshening diminish quickly due to mixing with seawater, and interpretations can be ambiguous due to other potential freshwater sources, such as rain.

Thus, other geochemical tracers with higher sensitivity, i.e., large concentration differences between groundwater and seawater, are applied. These are e.g. the natural radionuclides of radon (^{222}Rn; $t_{½}$ = 3.8 days; Rn in following) and radium (^{224}Ra; $t_{1/2}$ = 3.7 days; ^{223}Ra; $t_{1/2}$ = 11.4 days; ^{228}Ra; $t_{1/2}$ = 5.75 years; ^{226}Ra; $t_{1/2}$ = 1,600 years, Ra in the following), which are generally enriched in STE groundwater compared to surface waters. They can provide qualitative and quantitative information on sources and types of water sources to the STE, estimates of seawater residence times in the STE, as well as an overall quantification of the water flux out of the STE (i.e., SGD) into the coastal sea and open ocean (Taniguchi et al., 2019), while the results often include large uncertainties (Rodellas et al., 2021).

In addition to imports by sea- and groundwater, a fraction of the Ra and Rn in STEs pore waters is produced locally in sediment mineral grains by the decay of the radioactive parents Thorium (Th) and ^{226}Ra, respectively. In pore waters with low chloride content Ra is typically immobilized by sorption to clay and Fe and Mn oxide surfaces whereas, at salinities > ~3 practical salinity units (PSU), it behaves conservatively and can be used to trace water flow paths and fluxes (Webster et al., 1994). As an inert noble gas, Rn is not affected by the chemical composition of pore waters and geochemical reactions within the STE. The Ra and Rn pore water concentration will depend on the thorium/radium content of aquifer sediments, the recoiled efficiency, the residence time (i.e., the time elapsed since the water entered the STE) as well as Mn and Fe redox cycling. As seawater Ra and Rn concentrations usually are low, enrichment of these isotopes in coastal waters can be used to locate water fluxes out of the STE and quantify them in a mass balance approach assuming a known groundwater endmember (e.g., Garcia-Solsona et al., 2008).

A sampling of radionuclides can be done by boat at regional scales (Moore, 2000; Schubert et al., 2019; Stieglitz et al., 2010) (**Figure 3**). Time series measurements provide information on the temporal component of Ra and Rn fluxes and thus can be used to understand the dynamics of SGD in response to changing boundary conditions such as tides or storm events (Burnett and Dulaiova, 2003; Santos et al., 2009a). However, identifying STEs and associated terrestrial groundwater flux remains very challenging due to overlapping groundwater circulation processes and pathways, which are difficult to differentiate based on Rn and Ra only.

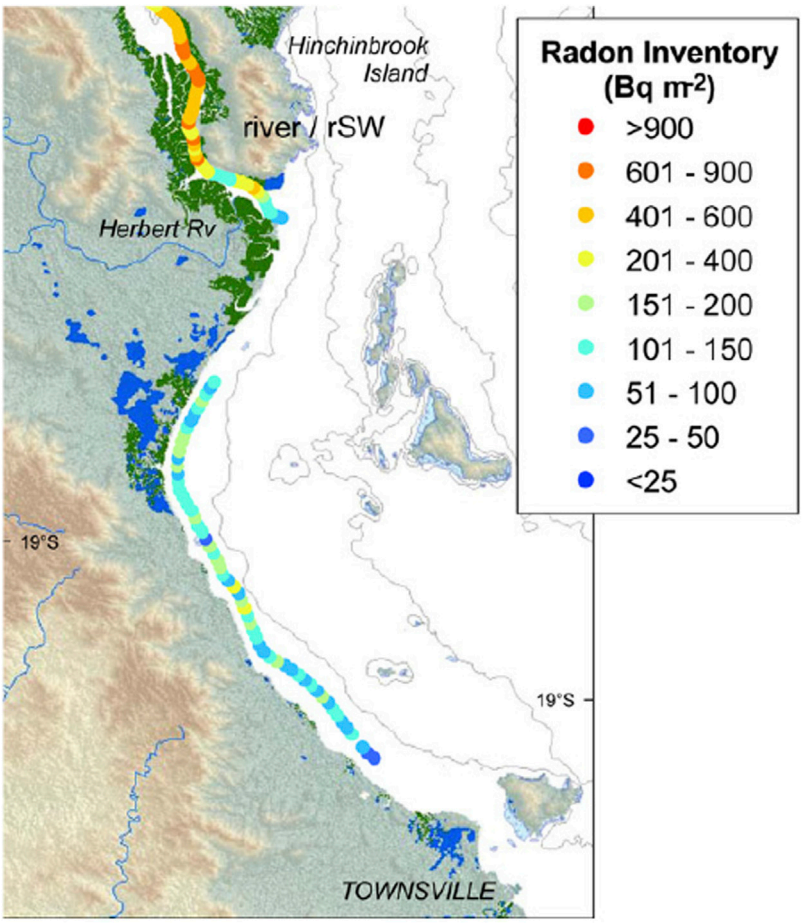


FIGURE 3 | Example of a regional scale Rn survey in Queensland, Australia (Stieglitz et al., 2010). Permission for reprint was provided by the copyright-holder.

The quantification of SGD using Rn and Ra is based on solving a mass balance of these radionuclides, considering all their major sources and sinks. It is usually done on sub-regional scales of up to 100s of meters, with notable exceptions for the Atlantic Ocean (Moore et al., 2008), the Mediterranean Sea (Rodellas et al., 2015) and the global oceans (Kwon et al., 2014). The quantification can be done either assuming a steady-state or using a non-steady-state approach when influxes from the STE are transient (Burnett et al., 2003; Moore, 2003; Hwang et al., 2005; Burnett et al., 2006). The steady-state assumption needs to be critically appraised when analyzing field data used in the mass-balance calculation, especially when using Rn. Turbulent conditions caused by wind and wave action can lead to excessive degassing before and during field campaigns so that the assumption of steady state between source and loss terms is not met. Indeed, it can be difficult to measure any Rn in surface waters following rough conditions. The 'memory' effect of variable degassing for the Rn balance tends to be around 5 days, but depends on factors such as water depth. In general, a non-steady state mass-balance together with continuous Rn measurements is better suited to dynamic conditions in the coastal zone (e.g., Santos et al., 2009c; Gilfedder et al., 2015).

The concentrations of tracers in SGD, i.e., the end-member concentrations of Ra and Rn, must be known to translate a mass flux into a water flux. Constraining these end-member concentrations is one of the most critical and uncertain steps of mass balance approaches. Groundwater concentrations may have substantial temporal and spatial variations caused by the heterogeneity of parent isotopes, different groundwater circulation pathways, hydrological and marine forcing, changes of geochemical processes within the STE as well as variability in terrestrial sources (Gonneea et al., 2013; Cho and Kim, 2016; Rocha et al., 2016; Cerda-Domenech et al., 2017). To overcome this problem, averaging a large number of end-member concentration measurements or taking the maximum and minimum end-member concentration to provide an envelope of possible SGD flux rates are common approaches (Moore, 1996; Beck et al., 2007). Nevertheless, the variability in the end-member concentrations remains the primary challenge for reliable quantification of SGD since shortcomings in accounting for the heterogeneity of end-members at local- and regional scales remain unsolved.

On a local scale, seepage meter measurements, as well as water balances, allow independent verifications of radionuclide-based

SGD rates (Povinec et al., 2012). However, on regional scales, verifications are still lacking or show systematic differences between tracer and model approaches (Prieto and Destouni, 2011). Nevertheless, Ra and Rn isotopes can be applied to map spatial and temporal changes in SGD, which under certain conditions would be a first indicator for the potential presence of an STE. Ra and Rn isotopes were used in regional scale SGD estimates.

Another isotopic tracer that can be applied for STE studies is the stable isotope composition of water ($^{2}H/^{1}H$, $^{18}O/^{16}O$, here shortly called "water isotopes"), which is a well-established tracer in hydro (geo)logical studies for the quantification of mixing processes and the deduction of water mass sources. Terrestrial groundwater is substantially more depleted in the heavier isotopes than seawater (Gat, 1996; Hoefs, 2018) and contains further information about the integrated meteorological conditions in the recharge area. Therefore, water isotopes are widely used in studies of SGD or STE (e.g., Burnett et al., 2006; Povinec et al., 2011; Rocha et al., 2016; Oehler et al., 2017; Duque et al., 2019). Time series can reveal the variability of terrestrial groundwater inputs on different time scales, particularly in dynamic karst STEs. Although still in its infancy, the extension of stable isotope characterization toward a triple isotope approach considering ^{17}O (resp. ^{17}O excess Sharp et al., 2018) may allow freshwater sourcing on the scale of regional STEs. Minerals formed in the mixing zone may record the parent solution's isotopic signature, providing opportunities for studies of past STE conditions.

Besides the stable isotopes of water, groundwater formed after the early 1960s may contain tritium (^{3}H), which has been used for dating purposes (Begemann and Libby, 1957; Bethke and Johnson, 2008). Meanwhile, the anthropogenic component, the atmospheric contamination of the water cycle by surface nuclear tests, has reached a natural background level. However, combined with its daughter isotope ^{3}He and Ne (Tolstikhin and Kamenskii, 1969; Sültenfuss et al., 2009), tritium still can be used for regional age estimation of the freshwater component in STEs (Röper et al., 2012; Post et al., 2019; Grünenbaum et al., 2020). The accumulation of ^{4}He is furthermore used in older groundwater dating (Bethke and Johnson, 2008). Other noble gas isotopes useful in the hydrogeology of STEs are ^{39}Ar and ^{85}Kr (e.g., Sánchez-Úbeda et al., 2018).

Local-scale geochemical investigation of STEs ideally includes vertical transects through the STE, a detailed physicochemical analysis, and solid-phase profiles from core material for a further microanalysis to identify precipitated authigenic solid phases. Measuring transects along the beach face enables mapping the spatial distribution of the biogeochemical environment, reactions and residence times over distances from tens to hundreds of meters. Larger scale mapping is challenging due to labor-intensive field sampling and increasing heterogeneity of the subsurface at larger scales meaning that extrapolation between transects is difficult.

Different circulation pathways in the STE can also be examined by exploiting the different half-lives of Ra isotopes, ranging from tidal to seasonal time scales. Assuming a steady-state hydrological situation, residence times can be estimated applying a general advective transport model in which the concentration of Ra and Rn in pore waters is a function of the supply of the radionuclides and their loss by decay and advection (Bokuniewicz et al., 2015; Tamborski et al., 2017). One of the main uncertainties in this approach is the lithological composition (mineral content, grain size, porosity) of the STE, which is assumed to be homogenous in space and in time throughout the STE. In reality, however, the heterogeneity in the STE causes a wide range of radionuclide supply rates (Beck and Cochran, 2013). Furthermore, temporally and spatially variable geochemical cycling of Fe and Mn and associated oxides profoundly influence the Ra pore water release (Gonneea et al., 2008). Since Ra is conservative in saline waters only, Ra-based residence times are only meaningful when seawater dominates the circulation through the STE. In contrast, Rn can be applied in both the fresh and brackish parts of the STE but is sensitive to ^{226}Ra distributions in the sediments as the parent isotope. Short term hydrological forcing like tides, wave set-up and induced circulation may also cause non-steady-state situations resulting in biases in residence times estimates. Finally, mixing of waters with different ages can lead to errors in the residence time estimates (which is similar to the real mean age of a water parcel) (Post et al., 2013; Gilfedder et al., 2019). As mixing is a linear process while radioactive decay and radioactive ingrowth are exponential (Bethke and Johnson, 2002), a systematic underestimation of the real mean age can occur if waters of different ages mix. One approach to circumvent this problem is the use of isotope ratios like, e.g., $^{224}Ra/^{223}Ra$. This method is very accurate if one water mixes with another one having zero activity (e.g., negligible Ra in freshwater) but does not work if the age difference between the water masses is large.

Residence time measurements tend to be point measurements at specific times. Verification of residence times based on radioisotopes is complicated to obtain. Comparing Ra- and Rn-based residence times may be one approach (Tamborski et al., 2017). Alternatively, pore water residence times may be compared to those derived by the ratio of water volume in the STE and the water flux out of the STE (Colbert et al., 2008).

Ra and Rn isotopes can be combined with other tracers, such as temperature (Cranswick et al., 2014), salinity (Example in **Figure 3**), or dissolved silicon (DSi) (Waska and Kim, 2011; Oehler et al., 2019b). Since DSi behaves rather conservatively during transport through the STE, it can be used to trace processes that change other solutes in groundwater in STE, such as N or P (Oehler et al., 2019b). Another example is the combination of CO_2 measurements and Rn measurements (e.g., Cyronak et al., 2014; Santos et al., 2015; Macklin et al., 2019). While this ties CO_2 concentrations to SGD intensity, it does not yet differentiate if the CO_2 is a product of STE processes or if the coastal groundwater just has elevated CO_2 concentrations that originated from the terrestrial groundwater. Similarly, CH_4 was combined with Rn as a tracer of SGD (Cable et al., 1996; Dulaiova et al., 2010) but could also be used for tracing processes in STE that generate CH_4. Using C stable isotopes as a tracer (Winde et al., 2014; Donis et al., 2017) and considering elemental mass balances (Deines et al., 1974) may be a successful approach.

The measurement of chemical tracers of STE processes at larger scales is associated with the problem to observe and measure the parameters with sufficient temporal and spatial resolution to resolve the underlying processes. Because tracer concentrations are modified upon emerging from the subsurface, sensors near the sea bottom are best suited to detect STE processes. The metabolites of typical benthic biogeochemical anaerobic OM degradation processes, like Mn^{2+} and NH_4^+, may, after benthic-pelagic coupling, survive the oxidation within the oxic water column for some time (Kowalski et al., 2012; Winde et al., 2014). Since some liberated trace elements will be reoxidized and sorbed to suspended particles, regional investigations will have to consider both the dissolved and the solid phases (Kowalski et al., 2012). Whereas the dissolved substances may be detected using discrete or continuous sampling techniques (Petersen et al., 2011; Kowalski et al., 2012), solid-phase sampling for geochemical analysis is limited to discrete sampling. Measurements can also be performed by autonomous underwater vehicles, which could automatically trace signals, like temperature, conductivity or Rn-isotopes, of groundwater discharge and scout for STEs (Tholen et al., 2019).

New combinations of sensors would help to detect STEs. Optical spectrometers in the UV-visible range of the light spectrum can be used to determine the concentration of nitrate, nitrite, HS^-, humic acids or DOC rapidly and without the use of reagents. It is to be expected that the optical absorption spectra will allow identifying water influenced by STEs. Sensors for the oxidation-reduction-potential (or, when referenced to the potential of a Standard Hydrogen Electrode, E_h) have been used for the estimation of concentrations of redox-sensitive elements in the redoxcline of the Baltic Sea (Meyer et al., 2014) or detecting hydrothermal plumes in the deep ocean (e.g., Baker et al., 2005). Combining several sensor types should allow the detection of STE signals in waters close to the bottom.

Geochemical tracers can help to regionally assess the amounts of SGD and point to the presence of STEs. They can also be applied at the local scale to draw quantitative conclusions about residence times in STEs and thus infer information about their reaction kinetics. At the regional scale, discrete and continuous measurements can be done. Still, these measurements will consist of discrete sampling points, and the feasibility of sampling will limit their resolution and coverage, which needs to be scaled according to the variability of the processes and tracers considered.

Ecological Tracers

Biodiversity in terrestrial groundwater recently received increased scientific attention (e.g., Hancock et al., 2005; Humphreys, 2008). Environmental gradients affect marine organisms in coastal waters. N and P are growth-limiting nutrients for most phytoplankton and macrophytes species that form the primary producers of the marine food web. Externally added nutrients alter the cycles of energy-flow between the pelagic and benthic zones, changing the community structure and population dynamics of both pelagic and benthic systems (Johannes, 1980; Sugimoto et al., 2017; Grzelak et al., 2018). A similar adaption to an increase in the concentration of nutrients can also be observed in the case of changes in other physical or chemical parameters of the environment: salinity, amount of light in the water column, amount of C species, heavy metals, O_2 concentration, the presence of hydrogen sulfide, or changes in pH. For example, observed changes in the chemical composition of bioavailable C in the Yucatan coastal waters result in lower coral cover, smaller size and reduced species richness (Crook et al., 2012). Benthic meio- and macrofaunal organisms may react to changes in the environment. Differences in benthic microbiology were observed in STE compared to purely saline beach waters, but little is known about microbial communities in STE (Santoro et al., 2006; Santoro et al., 2008; Santoro, 2010; Adyasari et al., 2019a; Adyasari et al., 2020). Thus, depending on location or environmental factors, STE may change species richness and diversity of meiofauna (Kotwicki et al., 2014; Encarnação et al., 2015; Welti et al., 2015; Grzelak et al., 2018). Similarly, macrofaunal communities can respond; their biodiversity can increase due to food supply (Waska and Kim, 2010; Pisternick et al., 2020) or may be reduced due to salinity stress or changes in pH (Zipperle and Reise, 2005; Migné et al., 2011; Utsunomiya et al., 2017). However, while the named ecological responses can highlight an STE presence, they will be hard to interpret as tracers of processes within that STE.

Since the impact of microbially mediated biogeochemical processes in the physicochemical gradients of STEs can be diverse (e.g., Beck et al., 2011), it is useful to apply the established methods to study the communities of organisms and associated biogeochemical processes occurring in the entire ecosystem. Methods of assessing abundance, activity, biomass and diversity include taxonomic phytoplankton analyses in water samples, fauna and microbial activity analyses in sediment cores, or fish assessment in the water. For ecological studies on the impacts of processes in STEs, these methods are combined with thermal infrared cameras or Ra/Rn tracing (Sugimoto et al., 2017; Grzelak et al., 2018). Simultaneous measurements of ^{222}Rn with other biological parameters allow assessing the reaction of biota activity on products of STEs (Taniguchi et al., 2019). Stable isotopes of N and C can also be used to trace STE products in the food web. Several studies have traced the behavior and fate of groundwater DIN using the isotope $\delta^{15}N$ of seagrass and macroalgae (Winde et al., 2017; Andrisoa et al., 2019) and gradients in the stable carbon isotope ratio between fresh and marine end-members (Gramling et al., 2003; Winde et al., 2017).

Consistent integration of hydrographic and biogeochemical research with bio-monitoring, elementary approaches and stable isotope analyses while considering higher trophic levels like fish and trophic flows in coastal ecosystems would enable the estimation of the direct impact of processes in STEs on ecosystems. While not yet done, specific species may have the potential to indicate STE processes in specific environments. Research in this direction is emerging (Lecher and Mackey, 2018), but additional knowledge is required before ecology can be used as a tracer for STE processes.

Geophysical Methods

From a geophysical perspective, the changes of physical and geochemical conditions under the seafloor associated with the presence of STEs are detectable by measuring properties such as electrical conductivity (EC), acoustic impedance (AI), or temperature. STEs can affect 1) the seafloor itself, e.g., its morphology, 2) the sediment or rock below it and 3) the properties of the water column, e.g., turbidity or sea-surface temperature.

At the local scale, geophysical methods can delineate the shape of an STE in detail. The EC difference between the terrestrial groundwater and saltwater is the most prominent parameter for local scale geophysical STE observation. The EC of freshwater varies depending on the total amount of dissolved ions, and literature puts it below 300 µS/cm (Kirsch, 2006), 1,000 µS/cm (Jiao and Post, 2019), or 2000 µS/cm (Langguth and Voigt, 2004). The EC of surficial seawater is orders of magnitude higher, > 40,000 µS/cm, depending on the temperature and thus latitude (Tyler et al., 2017). However, mineral grains, clay aggregates and organic matter in the STE also affect EC and need to be considered. Particularly sediment porosity and clay content strongly influence the overall EC of the bulk (rocks plus groundwater) volume (Archie, 1942). The high EC of clay leads to the general challenge of distinguishing freshwater saturated clays from brackish water saturated sands that may have very similar EC values. Gamma radiation of potassium, thorium and uranium at the surface helps to distinguish between clayey and sandy sediments (Siemon et al., 2020), as does an acoustic impedance contrast that seismic methods can show.

Many approaches that use electromagnetic fields (EM) emitted and detected by coils are available to represent subsurface properties (frequency-domain EM, time-domain-EM and slingram/ground-conductivity meter: Kirsch, 2006). Frequency-domain (sinusoidal transmitter currents) and time-domain EM (on/off transmitter currents) are typically used to obtain depth resolution at a single measurement point or along transects (Auken et al., 2003). Moving ground-conductivity meters are used for fast lateral mapping of EC but with limited depth resolution (e.g., De Smedt et al., 2013). Locating freshwater and thus STEs, at the regional scale can be realized using airborne or ship-based EC measuring methods.

Airborne methods use helicopters or fixed-wing aircraft to carry the geophysical systems at about 20–100 m above ground, covering 100–200 km of profiles or typically 10–50 km^2 per hour (**Figure 4**). In airborne EM, frequency-domain systems focus on near-surface (1–100 m) investigation of the spatial bulk EC (Siemon et al., 2015; Siemon et al., 2019; Siemon et al., 2020), whereas time-domain systems enable some deeper (5–500 m) investigation (Siemon et al., 2009; Steuer et al., 2009), depending on the conductivity distribution of the subsurface. Apart from electrical conductivity or resistivity, airborne radiometry maps the gamma radiation of the upper few decimeters of the surface (Wilford et al., 1997; IAEA, 2003). This technique has not yet been applied toward Ra/Rn concentrations in seawater but might be a pathway forward to map those isotopes with broader spatial coverage. Besides, semi-airborne methods using a ground-based transmitter and a helicopter-borne receiver have been developed recently to increase the penetration. While deep penetration is less important for STE investigation, UAV-based concepts can supplement the helicopter by a drone carrying the EM sensor in the future and hopefully enable cheaper investigations at the several kilometer scale. Finally, ship-based EM measurements have been applied to detect SGD (Müller, 2010; Müller et al., 2011).

Another EC method is electrical resistivity tomography (ERT), which, on land, uses steel electrodes pinned to the ground measuring the resistivity (the reciprocal of electrical conductivity) of the sediment by injecting a direct current (Stieglitz, 2005; Swarzenski et al., 2006). ERT has been used to observe the saltwater recirculation zone (Morrow et al., 2010) and its temporal changes (e.g., Johnson et al., 2015; Sutter and Ingham, 2017). ERT also can detect induced polarization effects caused by iron oxides (Mansoor and Slater, 2007). While this has not yet been applied to STEs, it could analyze Fe-cycling in the mixing zone. Measurements of magnetic-resonance also provide information on iron oxides and their concentrations (Keating and Knight, 2007; Costabel et al., 2018) and provide subsurface porosity and hydraulic conductivity (e.g., Müller-Petke and Yaramanci, 2015).

Marine ship-based measurements of ERT tow floating or submerged streamers behind a boat (Manheim et al., 2004; Day-Lewis et al., 2006; Hermans and Paepen, 2020). A profile of 5 km length can be measured in 1 h, but the conductive seawater limits penetration depth and therefore, streamer lengths of several hundred meters are needed to achieve sufficient penetration depth.

Seafloor morphological SGD proxies, such as pockmarks (e.g., Hoffmann et al., 2020), submarine terraces (Jakobsson et al., 2020), and depressions in carbonate rocks (Oehler et al., 2019a), are visible in the bathymetry. There are several techniques available to map the seafloor. Sidescan sonar data can reveal the location of pockmarks (e.g., Schlüter et al., 2004; Virtasalo et al., 2019), and echo sounders generally can also be applied for this task (Feldens et al., 2018; Papenmeier et al., 2020). Multibeam echo sounders provide high lateral coverage across-track on the seafloor, which is several times the water depth, enabling a fast mapping of larger scales.

Obtaining information on the geological structures by using high-resolution seismic profiling can be relevant for delineating the geometry of STEs (Mosher and Simpkin, 1999). The resulting image shows the reflection amplitudes and times (or depths) resulting from material interfaces with an impedance contrast, where the acoustic impedance is the product of bulk density and compressional velocity. Seismic profiles can be measured simultaneously with geoelectric streamers providing the same estimated profile length of 5 km per hour.

Geophysical methods also allow analyzing biogeochemical processes that occur within STEs, since some products can be identified. Shallow free gas accumulations (e.g., CH_4, N_2) can be mapped on larger scales using multibeam echo sounders. Gas is visible as acoustic blanking, bright spots, acoustic turbidity, or gas chimneys in seismic data (Hovland and Judd, 1988; Judd and Hovland, 1992). Free gas can have multiple origins in the ocean, so SGD does not necessarily cause its occurrence. However, gas-related features along the Belgian coast (Missiaen et al., 2002), in

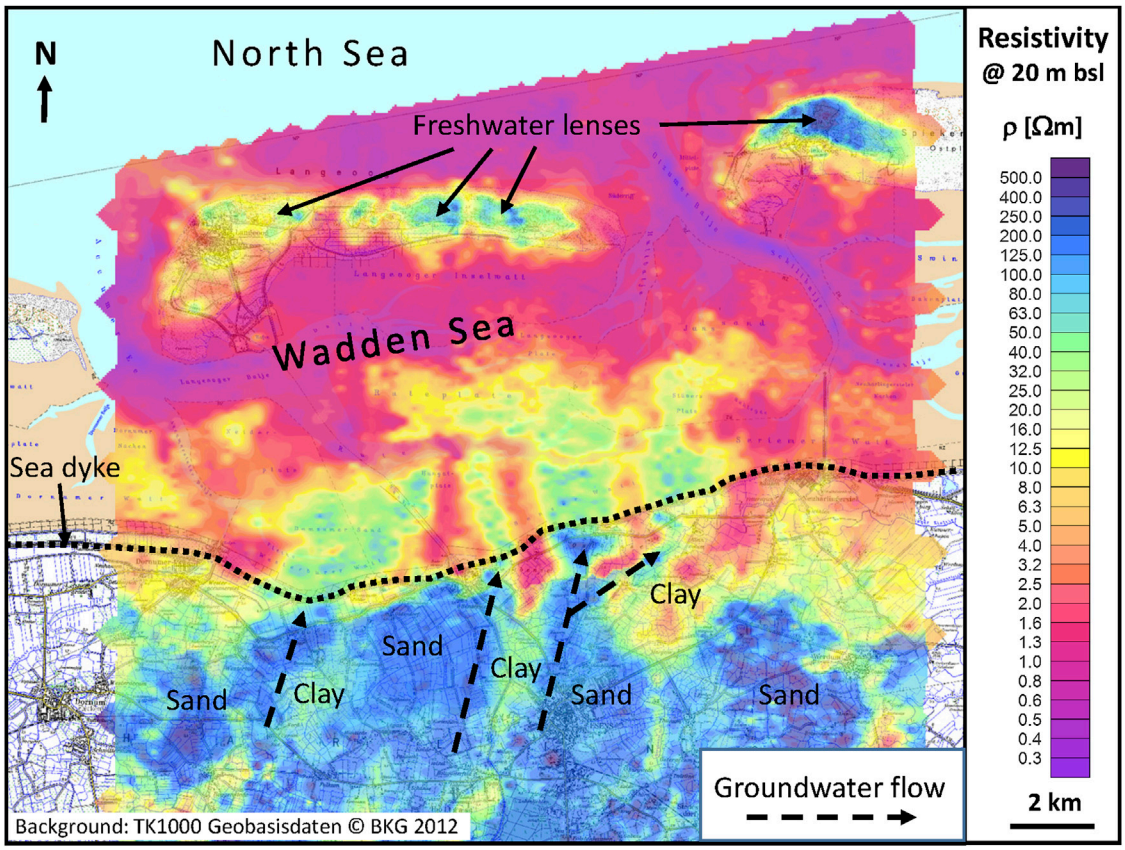


FIGURE 4 | Resistivities at 20 m below sea level derived from HEM inversion models indicating sandy and clayey areas, freshwater lenses on the islands of Langeoog and Spiekeroog and groundwater flow (dashed arrows) towards the Wadden Sea. The sea dyke is indicated by a dotted black line (data from BGR, 2017, background topographic map: BKG, 2012).

Brazil, *Argentina* and South Africa (Weschenfelder et al., 2016) and the North Yellow Sea (Wang et al., 2018) were linked to localized groundwater discharge.

Finding transfer functions linking discrete biogeochemical data and continuous geophysical methods is a promising methodology to extrapolate STE processes to the regional scale. In particular, methods going beyond the "classical" mapping of resistivity (**Figure 4**), which would allow to spot offshore freshening of pore water and thus STEs, have only rarely been applied to characterizing biogeochemical processes in STEs but show a substantial potential. A critical challenge is integrating local information into regional mapping by connecting different scales (point-like measurements, ground-based spatial information, airborne and satellite). Recent developments allow to include point-like or drilling information into ground-based geophysics using different concepts (e.g., Wunderlich et al., 2018) and coupling ground-based geophysics with airborne data (Dickson et al., 2014), providing perspectives for regional-scale assessments that are unviable based on ground-based measurements alone.

Remote Sensing

Remote sensing provides spatially continuous information on a scale from 10^1 to 10^9 m^2 (Böttcher et al., 2021), depending on the platform (ground-based application, remotely operated vehicle, uncrewed erial vehicle (UAV), kite gyrocopter, airplane, satellite). The chosen scale constrains the ground resolution (ground sampling distance), which may vary between 10^0 to 10^2 m. Scale and ground resolution intrinsically determine which STE indicator may be observed (Böttcher et al., 2021). Diffuse discharging groundwater is unlikely to be observed using satellite-based remote sensing, but can be observed with close-range applications or UAVs. However, the effort to cover regional scales is unequally larger for UAVs than for airplane- or satellite-based applications. Given the negligible depth penetration of remote sensing earth observation techniques in most situations, remote sensing can only investigate STE processes indirectly through its surface expressions. Remote sensing can detect terrestrial SGD, map seafloor and coastline morphology to find potential STEs, indicate hydrogeological STE characteristics, and identify STE processes by, e.g., classifying submerged aquatic vegetation that may be influenced by STEs.

Available sensors cover a wide range of the electromagnetic spectrum and can detect/differentiate surface properties that may act as indicators for STE processes or characteristics. The most commonly applied sensor in STE investigations is the thermal infrared (TIR) sensor, which can exploit temperature differences between seawater and terrestrial groundwater at the sea-surface (**Figure 5**). TIR detects groundwater inflow locations by

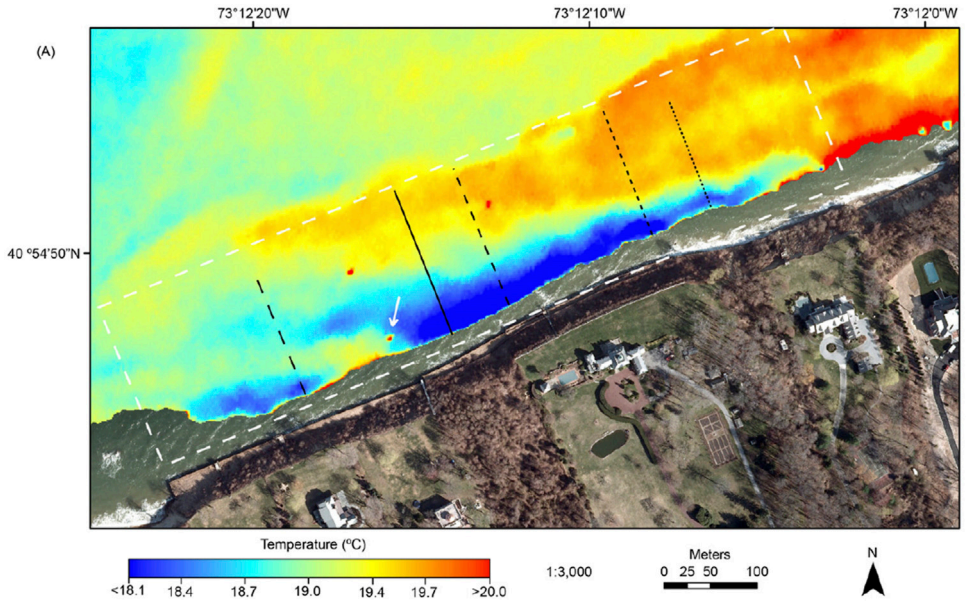


FIGURE 5 | TIR map displaying an area of cool diffuse seepage of terrestrial SGD that indicates an STE (Tamborski et al., 2015). Permission for reprint was provided by the copyright-holder.

identifying a thermal anomaly based on mono-temporal investigations (Fischer et al., 1964; Mejias et al., 2012; Wilson and Rocha, 2012; Kelly et al., 2013; Mallast et al., 2014; Xing et al., 2016), or multi-temporal investigations (Schubert et al., 2014; Oehler et al., 2018), and can be used to quantify freshwater fluxes given *in-situ* reference data of currents and bathymetry (Roseen, 2002; Johnson et al., 2008; Danielescu et al., 2009; Tamborski et al., 2015). The extent and shape of sea-surface temperature anomalies can indicate specific STE processes and characteristics (Chen, 1991; Jirka, 2004). Elongated anomalies oriented perpendicular to the coastline (Shaban et al., 2005) or extensive areas of thermal anomalies (Kelly et al., 2013) point to focused groundwater discharge at a high rate, suggesting a low residence time in STEs. Areas with smaller anomalies close to the coastline distributed over tens of meters alongshore (Tamborski et al., 2015) suggest diffuse discharge. The former is typical for karst or volcanic aquifers from which groundwater discharges along conduits, whereas the latter is commonly associated with sedimentary aquifers. Since higher temperature differences and distinct anomalies are easier to measure by TIR sensors, focused, high-volume discharge is more easily detected than slow, diffuse discharge.

Besides thermally identifying terrestrial groundwater discharge, remote sensing can classify benthic microbiology (e.g., Kazemipour et al., 2012) and submerged aquatic vegetation, which has been found to allow inferences about STEs (e.g., Leitão et al., 2015; Welti et al., 2015). While these observations are connected to local scale *in-situ* investigations, optical remote sensing using multi- and hyperspectral sensors (Klemas, 2016) has successfully been applied in shallow waters but not yet linked to potential terrestrial groundwater influence.

The relationship between STE characteristics indicated by seabed morphology and even operationally provided seafloor maps over regional scales using air- and satellite-borne platforms is similarly unexploited (Siermann et al., 2014; Eugenio et al., 2015). Remotely sensed bathymetry would allow a first-order approximation of potential pockmark sites. Since one of the forces that can produce pockmarks is fluid flow (Hovland et al., 2002), which can be an STE defining process, pockmarks can be seen as hinting toward the potential existence of STEs. Coastline morphology can be shaped by the same processes and may represent a similar indicator (Johannes, 1980).

A drawback of remote sensing methods is that it is challenging to link discrete, *in-situ* measurements to remote sensing data that integrate a multitude of effects other than those caused by an STE presence (e.g., ocean currents, chlorophyll presences). This weakness calls for a multi-scale approach (Lausch et al., 2013) in which an identified STE location is observed synchronously and over long periods with an appropriate *in-situ* sensor array and various airborne to satellite platforms covering different spatial scales. Such long-term sites could be associated with coastal observatories (Schofield et al., 2003) equipped with sensors to measure, e.g., turbidity, EC, pH, oxygen level, and thus be investigated through interdisciplinary approaches (Mollenhauer et al., 2018).

Second, since the temporal variability of the STE-associated processes is high, an interesting approach would be to have a TIR remote sensing approach that enables a multi-temporal observation possibility. The recent advance of UAVs do provide such a possibility, as shown in Mallast and Siebert (2019), but cannot cover a regional scale simultaneously. The revisiting times will be reduced for Landsat with the launch of Landsat-9 in spring 2021 and the Indian-French THRISHNA mission, whose launch is planned for 2024 (Lagouarde et al., 2018). Nano-to mini-satellites can even revisit individual

locations several times per day (Van Ryswyk, 2020). If these vehicles would also carry a TIR sensor and resemble a similarly very high ground resolution of <3 m, a regional to global scale localization of SGD sites and thus STE locations could become possible.

Hydrogeological Modeling

Another way to investigate STEs is through reactive transport models (RTMs), which remains underutilized in STE research (Robinson et al., 2017). Published modeling studies analyzed STEs as a high reactivity zones for, e.g., organic contaminants, nitrate and sulfate (Robinson et al., 2009; Anwar et al., 2014; Kim et al., 2017). The extent to which reactions proceeded was dependent on the degree of dispersive mixing and residence time in the STE, which was controlled by hydrological boundary conditions, such as terrestrial groundwater flux, beach slope and tidal amplitude. Another modeling study also showed the importance of dispersive mixing in STE on organic contaminant removal from groundwater (Nick et al., 2013).

The RTMs mentioned above provided process understanding but lacked confirmation by field data. There are only two field sites where RTMs and observations were integrated. The studies at Waquoit Bay by Spiteri et al. (2008a), Spiteri et al. (2008b), and Spiteri et al. (2008c), formed the earliest applications of RTMs of the STE and showed that the pH change at the interface between terrestrial groundwater and the lower saltwater wedge is an essential factor that controls the oxidation of Fe^{2+} and subsequent adsorption of land derived phosphorus (Spiteri et al., 2008a). Further, model results suggested that enhanced nutrient turnover occurs close to the SGD exit point due to high transverse dispersive mixing of oxic and anaerobic groundwater, resulting from converging groundwater flow toward the sea (Spiteri et al., 2008b; Spiteri et al., 2008c). The other site where model simulations were used to support field data interpretation is at Cape Henlopen, Delaware, USA (Kim et al., 2017). At this site, the field data showed that aerobic respiration led to a depletion of oxygen within the upper saline plume and that nitrate concentrations were lowest where ammonium and particulate organic carbon were highest. Even though their numerical model was able to simulate the general spatial O_2 and N_2 concentration trends, discrepancies remained evident, which the authors attributed to uncaptured heterogeneity and transient processes, as well as the omission of iron and sulfate reduction processes in the model. Thus, this is an example of the difficulties to model STEs due to their high spatial complexity. Modeling can also be applied in combination with isotopic data to elucidate reliable dating information on the STE water age (Bethke and Johnson, 2008; Post et al., 2019), which could provide information for reaction rates.

It is unlikely that numerical, reactive transport models of biogeochemical reactions in STEs can be applied with any reasonable expectation of success at the regional scale. The first reason is that the computational resources required will remain prohibitive in the foreseeable future. The second and perhaps foremost reason is that the input data requirements are unattainable at the regional scale due to the high spatial and temporal variability of STEs. Therefore, regional-scale models of STE nutrient transformations will have to rely on simplified process representations that can be parametrized with input data obtainable at a reasonable effort and cost. There are several essential questions to consider, including: What is an appropriate spatial level of heterogeneity for capturing regional scale processes that could be similar to the representative elementary volume (REV) concept for groundwater flow (cf. Freeze, 1975)? How can processes be integrated along the vertical dimension? How to account for local-scale variability? What is the temporal variability at the intra- and inter-annual scale? Can coastal landscape units be classified according to their geochemical reactivity?

Concerning the last question, one feasible approach to upscale modeling of STE processes might be to identify distinctive zones where controlling factors on the reactions are relatively uniform and then use small-scale model information to extrapolate to a regional-scale area. Working with distinctive uniform zones would imply a classification (e.g., Bokuniewicz et al., 2003). However, levels of homogeneity representative for larger areas are not yet adequately defined, as is the answer to whether and how small-scale temporal variations extrapolate into a larger scale. The terrestrial component of SGD was already modeled at the regional scale (Jarsjö et al., 2008; Befus et al., 2017; Hajati et al., 2019) and global scale (Zhou et al., 2019; Luijendijk et al., 2020) using similar approaches. These models produce spatially explicit estimates of terrestrial SGD that is a necessary prerequisite for STEs. Local scale RTMs highlight the importance of understanding mixing (hydrodynamic dispersion) and sediment organic carbon content, so it would seem reasonable to expect that these at least will have to be accounted for at the regional scale as well. Both are linked to sediment heterogeneity (regarding hydraulic properties and geochemistry) and the variability of hydraulic gradients so that the starting point would be a deterministic understanding of the longshore geological variability and a mechanistic description of the driving forces.

Data products of sufficient quality that represent controls of STE processes are required to model STE processes on the regional scale. The amount of data available at a global scale and high resolution is quickly increasing, but many aspects are not yet adequately covered. Foremost, since STEs occur along the coast, a high-resolution coastline is necessary and available (Sayre et al., 2018). STE sediment properties can be represented by recent datasets focusing on coastal sediment heterogeneity (de Graaf et al., 2017; Zamrsky et al., 2020). Other datasets focusing on the terrestrial aquifer (Gleeson et al., 2014) or marine sediment thickness (Straume et al., 2019) and its properties (Dutkiewicz et al., 2016) are hardly useable at the coast due to their global focus and low spatial resolution. Additional hydrogeological background knowledge would be, e.g., tectonic activity or stress maps, where areas of high tectonic activity would contain more faults and thus more potential pathways for groundwater.

Mixing intensity and processes in STEs will also be controlled by the amount of freshwater discharging (Luijendijk et al., 2020) or the amount of seawater recirculating (Mayfield et al., 2021). Water quality of the incoming freshwater is not known at a global

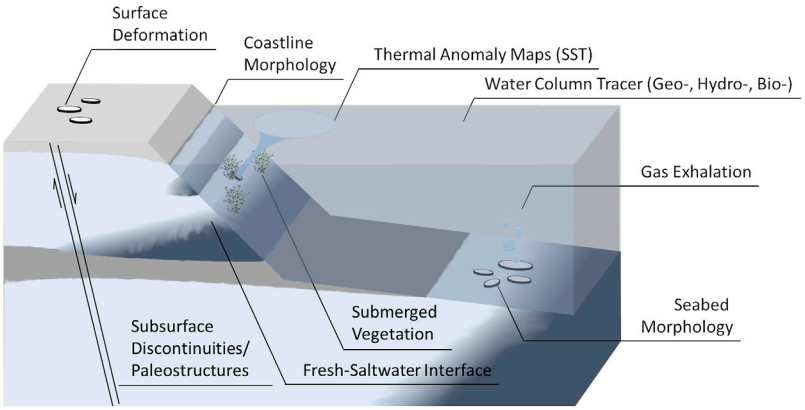


FIGURE 6 | Consequences of hydro (geo)logical and biogeochemical processes in STEs that can be used for extrapolation to the regional scale.

scale, but, as a first crude guess, could be inferred by proxy, e.g., from land-cover (e.g., Arino et al., 2007) or soil (FAOIIASA, ISRIC et al., 2009) datasets. Another option would be to extrapolate from datasets of multiple local groundwater quality measurements (e.g., NAWQA from USGS). In any case, groundwater quality is far less constrained than aquifer properties at large scales. Synthesized data sets of geological and geochemical properties of the subsurface below the seafloor on a regional scale are virtually absent.

Any of the large-scale datasets available have problems resolving the spatial heterogeneity of coasts, so the resulting estimates will not be applicable at the local scale (Geng et al., 2020) but provide first-order estimates for larger scales. This problem is not unique to the coast (e.g., Moosdorf et al., 2010) but amplified by the steep gradients in that setting. Given that the uncertainty of any model-based estimate is going to be very large, rather than focusing on the accuracy of the absolute numbers, it would be preferable to develop approaches that reveal the lateral differences. Such an approach would allow the ranking of different areas in terms of their effect on the coastal systems, highlighting hotspots to be targeted by more detailed investigations or specific measures.

CONCLUSIONS AND PERSPECTIVE

This review of biogeochemical processes in subterranean estuaries highlighted the spatial and temporal variability of these systems. Their reactions and corresponding rates depend on the hydrology of the STEs and the chemical composition of sediments and source waters (terrestrial groundwater and seawater). These controls have to be constrained to budget the processes within STEs and estimate the regional scale effects of STEs.

Characterizing STEs at the regional scale can be achieved through their products (**Figure 6**). The first step of estimating STE activity at a regional scale is to identify locations, amount, and the general extent of STEs. Locations can be identified through continuous measurements of geochemical tracers, e.g., electrical conductivity or Ra/Rn isotopes in the ocean. Biological indicators can point to the existence of STEs. Geophysical methods can provide information about freshened pore water and gas occurrences below the seafloor. Hydrogeological modeling can also estimate the flow behavior, but the necessary data are usually not available to represent larger areas in numerical 3D models realistically. Remote sensing information, for example, TIR images, can additionally show thermal signatures of freshwater influx. Combining observational methods from different disciplinary backgrounds, paired with modeling and hydrogeological data, is most promising for a regional scale effort to locate STEs.

Products of biogeochemical processes can be used to trace processes occurring in STEs (**Figure 6**). These products can be specific chemicals, like, e.g., CO_2, N_2 gas or Mn^{2+}, but also isotopic tracers like δ13C in DIC, δ18O and δ15 N in nitrate, as well as δ2D and δ18O in water. With geophysical methods, gaseous products of STEs can be identified, as well as iron oxides in the sediment, which are an essential control on the biogeochemistry of STEs. Remote sensing allows tracing changes in sea bottom that could indicate properties of the STEs in some cases. Nevertheless, since processes in STEs are spatially and temporally highly variable, discrete *in-situ* observations of specific STE products (e.g., CO_2, N_2, or Mn^{2+}) need to be combined with temporally and spatially continuous and temporally higher resolved data (e.g., remote sensing) using transfer functions.

Reactive transport models (RTM) can act as temporal and spatial link between discrete local scale *in-situ* measurements and spatially continuous regional scale data to extrapolate STE processes onto larger scales. To account for the high variability, quantitative local scale measurements will have to be combined with the concept of representative elementary volume (REV) based on regional-scale data sets such as from geophysical measurements or maps containing hydrogeological information. An RTM would represent each REV to quantify fluxes at scales relevant to the coastal zone and coastal zone management. On that basis, it would be even possible to sort STEs in classes when discussing their regional impact. Particularly, STEs with diffuse porous flow need to be distinguished from STEs in conduits, e.g., in karstic or volcanic settings.

A combination of methods from the presented disciplines promises a pathway toward regional scale estimates of processes in STEs and their impact on land-ocean matter fluxes. That impact may be substantial since local scale studies strongly hint toward their relevance. The processes are known; the products are known; the methods are available. Now is the time to combine methods across disciplines and understand these critical processes.

AUTHOR CONTRIBUTIONS

NM conceived the paper and wrote about upscaling; NM and UM coordinated the paper; UM, HW, and NM got funding for the project; MEB, BG, DA, A-KJ, TO, RP, JS, CE, and HW, contributed the biogeochemical part; LK contributed the biological part; EE, MM-P, BS, and TW, contributed the geophysical part; JG, GM, VP, and MW, contributed the hydrogeological modeling part; UM contributed the remote sensing part. All authors contributed to writing the manuscript and discussing the concept and formulating the overarching themes.

ACKNOWLEDGMENTS

This publication is a result of the DFG supported KiSNet project (MA7041/6-1). MEB and AKJ wish to thank DFG for financial support during research training group BALTIC TRANSCOAST (GRK 2000) and MEB and CvA the DAAD for a Ph.D. stipend for a stay of CvA at IOW. This is BALTIC TRANSCOAST publication No. GRK 2000/0045. HW was funded by the Niedersächsisches Ministerium für Wissenschaft und Kultur (MWK) in the scope of project "BIME" (ZN3184). JS acknowledges the support through the SEAMOUNT BONUS project (art. 185), which is funded jointly by the EU and the Federal Ministry of Education and Research of Germany (BMBF, Grant Nos. 03F0771B). The authors acknowledge the helpful review comments by D. Brankovits, G. Chaillou and A. Pain, and the editorial handling by F. Frappart. Finally, the authors would like to express their gratitude to Bill Burnett, who turns 75 this year. Bill inspired many of us to pursue research in the field of SGD and supported wherever he could. Thank you, Bill.

REFERENCES

Abarca, E., Karam, H., Hemond, H. F., and Harvey, C. F. (2013). Transient groundwater dynamics in a coastal aquifer: the effects of tides, the lunar cycle, and the beach profile. *Water Resour. Res.* 49 (5), 2473–2488. doi:10.1002/wrcr.20075

Adyasari, D., Hassenrück, C., Montiel, D., and Dimova, N. (2020). Microbial community composition across a coastal hydrological system affected by submarine groundwater discharge (SGD). *PLOS ONE* 15 (6), e0235235. doi:10.1371/journal.pone.0235235

Adyasari, D., Hassenrück, C., Oehler, T., Sabdaningsih, A., and Moosdorf, N. (2019). Microbial community structure associated with submarine groundwater discharge in northern Java (Indonesia). *Sci. Total Environ.* 689, 590–601. doi:10.1016/j.scitotenv.2019.06.193

Adyasari, D., Oehler, T., Afiati, N., and Moosdorf, N. (2019). Environmental impact of nutrient fluxes associated with submarine groundwater discharge at an urbanized tropical coast. *Estuarine, Coastal Shelf Sci.* 221, 30–38. doi:10.1016/j.ecss.2019.03.009

Akam, S. A., Coffin, R. B., Abdulla, H. A. N., and Lyons, T. W. (2020). Dissolved inorganic carbon pump in methane-charged shallow marine sediments: state of the art and new model perspectives. *Front. Mar. Sci.* 7. doi:10.3389/fmars.2020.00206

Al-Raei, A. M., Bosselmann, K., Böttcher, M. E., Hespenheide, B., and Tauber, F. (2009). Seasonal dynamics of microbial sulfate reduction in temperate intertidal surface sediments: controls by temperature and organic matter. *Ocean Dyn.* 59 (2), 351–370. doi:10.1007/s10236-009-0186-5

Alorda-Kleinglass, A., Garcia-Orellana, J., Rodellas, V., Cerdà-Domènech, M., Tovar-Sánchez, A., Diego-Feliu, M., et al. (2019). Remobilization of dissolved metals from a coastal mine tailing deposit driven by groundwater discharge and porewater exchange. *Sci. Total Environ.* 688, 1359–1372. doi:10.1016/j.scitotenv.2019.06.224

Andrisoa, A., Stieglitz, T. C., Rodellas, V., and Raimbault, P. (2019). Primary production in coastal lagoons supported by groundwater discharge and porewater fluxes inferred from nitrogen and carbon isotope signatures. *Mar. Chem.* 210, 48–60. doi:10.1016/j.marchem.2019.03.003

Anschutz, P., Smith, T., Mouret, A., Deborde, J., Bujan, S., Poirier, D., et al. (2009). Tidal sands as biogeochemical reactors. *Estuarine Coastal Shelf Sci.* 84 (1), 84–90. doi:10.1016/j.ecss.2009.06.015

Anwar, N., Robinson, C., and Barry, D. A. (2014). Influence of tides and waves on the fate of nutrients in a nearshore aquifer: numerical simulations. *Adv. Water Resour.* 73, 203–213. doi:10.1016/j.advwatres.2014.08.015

Archie, G. E. (1942). The electrical resistivity log as an aid in determining some reservoir characteristics. *Trans. Am. Inst. Mining Metallurgical Eng.* 146, 54–62. doi:10.2118/942054-g

Arino, O., Gross, D., Ranera, F., Bourg, L., Leroy, M., Bicheron, P., et al. (2007). GlobCover: ESA service for global land cover from MERIS. Proceedings of the international geoscience and remote sensing symposium (IGARSS) 2007. Barcelona: IEEE International, 2412–2415.

Auken, E., Jørgensen, F., and Sørensen, K. I. (2003). Large-scale TEM investigation for groundwater. *Exploration Geophys.* 34 (3), 188–194. doi:10.1071/eg0318

Baker, E. T., Massoth, G. J., Nakamura, K.-i., Embley, R. W., de Ronde, C. E. J., and Arculus, R. J. (2005). Hydrothermal activity on near-arc sections of back-arc ridges: results from the mariana trough and lau basin. *Geochem. Geophys. Geosystems* 6 (9). doi:10.1029/2005gc000948

Balzer, W. (1982). On the distribution of iron and manganese at the sediment/water interface: thermodynamic versus kinetic control. *Geochim. Cosmochim. Acta* 46 (7), 1153–1161. doi:10.1016/0016-7037(82)90001-1

Beck, A. J., Charette, M. A., Cochran, J. K., Gonneea, M. E., and Peucker-Ehrenbrink, B. (2013). Dissolved strontium in the subterranean estuary - implications for the marine strontium isotope budget. *Geochim. Cosmochim. Acta* 117, 33–52. doi:10.1016/j.gca.2013.03.021

Beck, A. J., Cochran, J. K., and Sanudo-Wilhelmy, S. A. (2010). The distribution and speciation of dissolved trace metals in a shallow subterranean estuary. *Mar. Chem.* 121 (1-4), 145–156. doi:10.1016/j.marchem.2010.04.003

Beck, A. J., and Cochran, M. A. (2013). Controls on solid-solution partitioning of radium in saturated marine sands. *Mar. Chem.* 156, 38–48. doi:10.1016/j.marchem.2013.01.008

Beck, A. J., Kellum, A. A., Luek, J. L., and Cochran, M. A. (2016). Chemical flux associated with spatially and temporally variable submarine groundwater discharge, and chemical modification in the subterranean estuary at gloucester point, VA (USA). *Estuaries Coasts* 39 (1), 1–12. doi:10.1007/s12237-015-9972-0

Beck, A. J., Tsukamoto, Y., Tovar-Sanchez, A., Huerta-Diaz, M., Bokuniewicz, H. J., and Sañudo-Wilhelmy, S. A. (2007). Importance of geochemical transformations in determining submarine groundwater discharge-derived trace metal and nutrient fluxes. *Appl. Geochem.* 22 (2), 477–490. doi:10.1016/j.apgeochem.2006.10.005

Beck, M., and Brumsack, H.-J. (2012). Biogeochemical cycles in sediment and water column of the Wadden Sea: the example Spiekeroog Island in a regional context. *Ocean Coastal Manag.* 68, 102–113. doi:10.1016/j.ocecoaman.2012.05.026

Beck, M., Reckhardt, A., Amelsberg, J., Bartholomä, A., Brumsack, H.-J., Cypionka, H., et al. (2017). The drivers of biogeochemistry in beach ecosystems: a cross-

shore transect from the dunes to the low-water line. *Mar. Chem.* 190, 35–50. doi:10.1016/j.marchem.2017.01.001

Beck, M., Riedel, T., Graue, J., Köster, J., Kowalski, N., Wu, C. S., et al. (2011). Imprint of past and present environmental conditions on microbiology and biogeochemistry of coastal Quaternary sediments. *Biogeosciences* 8 (1), 55. doi:10.5194/bg-8-55-2011

Befus, K. M., Kroeger, K. D., Smith, C. G., and Swarzenski, P. W. (2017). The magnitude and origin of groundwater discharge to eastern U.S. And Gulf of Mexico coastal waters. *Geophys. Res. Lett.* 44 (20), 396–410. doi:10.1002/2017gl075238

Begemann, F., and Libby, W. F. (1957). Continental water balance, ground water inventory and storage times, surface ocean mixing rates and world-wide water circulation patterns from cosmic-ray and bomb tritium. *Geochim. Cosmochim. Acta* 12 (4), 277–296. doi:10.1016/0016-7037(57)90040-6

Bethke, C. M., and Johnson, T. M. (2008). Groundwater age and groundwater age dating. *Annu. Rev. Earth Planet. Sci.* 36 (1), 121–152. doi:10.1146/annurev.earth.36.031207.124210

Bethke, C. M., and Johnson, T. M. (2002). Paradox of groundwater age. *Geology* 30 (2), 107–110. doi:10.1130/0091-7613(2002)030<0107:poga>2.0.co;2

Beusen, A. H. W., Slomp, C. P., and Bouwman, A. F. (2013). Global land-ocean linkage: direct inputs of nitrogen to coastal waters via submarine groundwater discharge. *Environ. Res. Lett.* 8 (3), 034035. doi:10.1088/1748-9326/8/3/034035

BGR (2017). *Helicopter-borne Electromagnetics (HEM) German North Sea coast – Models*. Bundesanstalt für Geowissenschaften und Rohstoffe (BGR), Hannover, Germany: doi:10.25928/bgr2017heminv_22v5-bg06

Billerbeck, M., Werner, U., Polerecky, L., Walpersdorf, E., deBeer, D., and Huettel, M. (2006). Surficial and deep pore water circulation governs spatial and temporal scales of nutrient recycling in intertidal sand flat sediment. *Mar. Ecol. Prog. Ser.* 326, 61–76. doi:10.3354/meps326061

Bishop, R. E., Humphreys, W. F., Kršinić, F., Sket, B., Iliffe, T. M., Žic, V., et al. (2015). 'Anchialine' redefined as a subterranean estuary in a crevicular or cavernous geological setting. *J. Crustacean Biol.* 35 (4), 511–514. doi:10.1163/1937240x-00002335

BKG (2012). *Rasterdaten Topographische Karte 1:100000 (DTK1000)*. Bundesamt für Kartographie und Geodäsie (BKG), Frankfurt, Germany: Available at https://www.geodatenzentrum.de [Last accessed on July 3, 2012].

Blöschl, G., Bierkens, M. F. P., Chambel, A., Cudennec, C., Destouni, G., Fiori, A., et al. (2019). Twenty-three unsolved problems in hydrology (UPH)—a community perspective. *Hydrol. Sci. J.-J. Des Sci. Hydrologiques* 64 (10), 1141–1158.

Boehm, A. B., Yamahara, K. M., and Sassoubre, L. M. (2014). Diversity and transport of microorganisms in intertidal sands of the California coast. *Appl. Environ. Microbiol.* 80 (13), 3943–3951. doi:10.1128/AEM.00513-14

Boetius, A., Ravenschlag, K., Schubert, C. J., Rickert, D., Widdel, F., Gieseke, A., et al. (2000). A marine microbial consortium apparently mediating anaerobic oxidation of methane. *Nature* 407 (6804), 623–626. doi:10.1038/35036572

Bokuniewicz, H., Buddemeier, R., Maxwell, B., and Smith, C. (2003). The typological approach to submarine groundwater discharge (SGD). *Biogeochemistry* 66 (1, 2), 145–158. doi:10.1023/b:biog.0000006125.10467.75

Bokuniewicz, H., Cochran, J. K., Garcia-Orellana, J., Rodellas, V., Daniel, J. W., and Heilbrun, C. (2015). Intertidal percolation through beach sands as a source of 224,223Ra to Long Island Sound, New York, and Connecticut, United States. *J. Mar. Res.* 73, 123–140. doi:10.1357/002224015816665570

Bone, S. E., Charette, M. A., Lamborg, C. H., and Gonneea, M. E. (2007). Has submarine groundwater discharge been overlooked as a source of mercury to coastal waters?. *Environ. Sci. Technol.* 41 (9), 3090–3095. doi:10.1021/es0622453

Bone, S. E., Gonneea, M. E., and Charette, M. A. (2006). Geochemical cycling of arsenic in a coastal aquifer. *Environ. Sci. Technol.* 40 (10), 3273–3278. doi:10.1021/es052352h

Böttcher, M. E., and Dietzel, M. (2010). Metal-ion partitioning during low-temperature precipitation and dissolution of anhydrous carbonates and sulphates. *EMU Notes in Mineral.* 10, 139–187. doi:10.1180/EMU-notes.10.4

Böttcher, M.E., Mallast, U., Massmann, G., Moosdorf, N., Mueller-Pethke, M., and Waska, H. (2021). "Coastal-Groundwater interfaces (submarine groundwater discharge)," in *Ecohydrological interfaces*. Editors S. Krause, D. M. Hannah, and N. Grimm (New York, NY: Wiley & Sons).

Bögli, A., (1980). *Karst hydrology and physical speleology*. Berlin, UK: Springer, xiii, 284

Brando, V. E., and Dekker, A. G. (2003). Satellite hyperspectral remote sensing for estimating estuarine and coastal water quality. *IEEE Trans. Geosci. Remote Sensing* 41 (6), 1378–1387. doi:10.1109/tgrs.2003.812907

Brankovits, D., Pohlman, J. W., Niemann, H., Leigh, M. B., Leewis, M. C., Becker, K. W., et al. (2017). Methane- and dissolved organic carbon-fueled microbial loop supports a tropical subterranean estuary ecosystem. *Nat. Commun.* 8, 1835. doi:10.1038/s41467-017-01776-x

Brankovits, D., Pohlman, J. W., Ganju, N. K., Iliffe, T. M., Lowell, N., Roth, E., et al. (2018). Hydrologic controls of methane dynamics in karst subterranean estuaries. *Glob. Biogeochem. Cycles* 32 (12), 1759–1775. doi:10.1029/2018gb006026

Brankovits, D., and Pohlman, J. W. (2020). Methane oxidation dynamics in a karst subterranean estuary. *Geochim. Cosmochim. Acta* 277, 320–333. doi:10.1016/j.gca.2020.03.007

Brovelli, A., Mao, X., and Barry, D. A. (2007). Numerical modeling of tidal influence on density-dependent contaminant transport. *Water Resour. Res.* 43 (10). doi:10.1029/2006wr005173

Brown, K. I., and Boehm, A. B. (2016). Transport of fecal indicators from beach sand to the surf zone by recirculating seawater: laboratory experiments and numerical modeling. *Environ. Sci. Technol.* 50 (23), 12840–12847. doi:10.1021/acs.est.6b02534

Burnett, W. C., Aggarwal, P. K., Aureli, A., Bokuniewicz, H., Cable, J. E., Charette, M. A., et al. (2006). Quantifying submarine groundwater discharge in the coastal zone via multiple methods. *Sci. Total Environ.* 367 (2, 3), 498–543. doi:10.1016/j.scitotenv.2006.05.009

Burnett, W. C., and Dulaiova, H. (2003). Estimating the dynamics of groundwater input into the coastal zone via continuous radon-222 measurements. *J. Environ. Radioact.* 69 (1, 2), 21–35. doi:10.1016/S0265-931X(03)00084-5

Burnett, W. C., Bokuniewicz, H., Huettel, M., Moore, W. S., and Taniguchi, M. (2003). Groundwater and pore water inputs to the coastal zone. *Biogeochemistry* 66 (1-2), 3–33. doi:10.1023/b:biog.0000006066.21240.53

Burton, E. A., and Walter, L. M. (1990). The role of pH in phosphate inhibition of calcite and aragonite precipitation rates in seawater. *Geochim. Cosmochim. Acta* 54 (3), 797–808. doi:10.1016/0016-7037(90)90374-t

Cable, J. E., Bugna, G. C., Burnett, W. C., and Chanton, J. P. (1996). Application of 222 Rn and CH4 for assessment of groundwater discharge to the coastal ocean. *Limnol. Oceanogr.* 41 (6), 1347–1353. doi:10.4319/lo.1996.41.6.1347

Canfield, D. E., Glazer, A. N., and Falkowski, P. G. (2010). The evolution and future of Earth's nitrogen cycle. *Science* 330 (6001), 192–196. doi:10.1126/science.1186120

Cerdà-Domènech, M., Rodellas, V., Folch, A., and Garcia-Orellana, J. (2017). Constraining the temporal variations of Ra isotopes and Rn in the groundwater end-member: implications for derived SGD estimates. *Sci. Total Environ.* 595, 849–857. doi:10.1016/j.scitotenv.2017.03.005

Chambers, R. M., and Odum, W. E. (1990). Porewater oxidation, dissolved phosphate and the iron curtain - iron-phosphorus relations in tidal freshwater marshes. *Biogeochemistry* 10 (1), 37–52. doi:10.1007/bf00000891

Charbonnier, C., Anschutz, P., Poirier, D., Bujan, S., and Lecroart, P. (2013). Aerobic respiration in a high-energy sandy beach. *Mar. Chem.* 155, 10–21. doi:10.1016/j.marchem.2013.05.003

Charette, M. A., Sholkovitz, E. R., and Hansel, C. M. (2005). Trace element cycling in a subterranean estuary: Part 1. Geochemistry of the permeable sediments. *Geochim. Cosmochim. Acta* 69 (8), 2095–2109. doi:10.1016/j.gca.2004.10.024

Charette, M. A., and Sholkovitz, E. R. (2002). Oxidative precipitation of groundwater-derived ferrous iron in the subterranean estuary of a coastal bay. *Geophys. Res. Lett.* 29 (10). doi:10.1029/2001gl014512

Charette, M. A., and Sholkovitz, E. R. (2006). Trace element cycling in a subterranean estuary: Part 2. Geochemistry of the pore water. *Geochim. Cosmochim. Acta* 70 (4), 811–826. doi:10.1016/j.gca.2005.10.019

Chen, H.-B. (1991). *Turbulent buoyant jets and plumes in flowing ambient environments*. Aalborg, Denmark: Department of Civil Engineering, University of Aalborg.

Chen, X., Cukrov, N., Santos, I. R., Rodellas, V., Cukrov, N., and Du, J. (2020). Karstic submarine groundwater discharge into the Mediterranean: radon-based nutrient fluxes in an anchialine cave and a basin-wide upscaling. *Geochim. Cosmochim. Acta* 268, 467–484. doi:10.1016/j.gca.2019.08.019

Chevis, D. A., Johannesson, K. H., Burdige, D. J., Tang, J., Bradley Moran, S., and Kelly, R. P. (2015). Submarine groundwater discharge of rare earth elements to a tidally-mixed estuary in Southern Rhode Island. *Chem. Geol.* 397 (0), 128–142. doi:10.1016/j.chemgeo.2015.01.013

Cho, H.-M., and Kim, G. (2016). Determining groundwater Ra end-member values for the estimation of the magnitude of submarine groundwater discharge using Ra isotope tracers. *Geophys. Res. Lett.* 43 (8), 3865–3871. doi:10.1002/2016gl068805

Cho, H. M., Kim, G., Kwon, E. Y., Moosdorf, N., Garcia-Orellana, J., and Santos, I. R. (2018). Radium tracing nutrient inputs through submarine groundwater discharge in the global ocean. *Sci. Rep.* 8 (1), 2439–2446. doi:10.1038/s41598-018-20806-2

Cho, H. M., Kim, T. H., Moon, J. H., Song, B. C., Hwang, D. W., Kim, T., et al. (2021). Estimating submarine groundwater discharge in Jeju volcanic island (Korea) during a typhoon (Kong-rey) using humic-fluorescent dissolved organic matter-Si mass balance. *Sci. Rep.* 11 (1), 941. doi:10.1038/s41598-020-79381-0

Church, T. M. (1996). An underground route for the water cycle. *Nature* 380 (6575), 579–580. doi:10.1038/380579a0

Clark, I. D., and Fritz, P. (1997). *Environmental isotopes in hydrogeology*. London, NewYork, CRC Press.

Colbert, S. L., Berelson, W. M., and Hammond, D. E. (2008). Radon-222 budget in Catalina Harbor, California: 2. Flow dynamics and residence time in a tidal beach. *Limnol. Oceanogr.* 53 (2), 659–665. doi:10.4319/lo.2008.53.2.0659

Costabel, S., Weidner, C., Müller-Petke, M., and Houben, G. (2018). Hydraulic characterisation of iron-oxide-coated sand and gravel based on nuclear magnetic resonance relaxation mode analyses. *Hydrol. Earth Syst. Sci.* 22 (3), 1713–1729. doi:10.5194/hess-22-1713-2018

Couturier, M., Nozais, C., and Chaillou, G. (2016). Microtidal subterranean estuaries as a source of fresh terrestrial dissolved organic matter to the coastal ocean. *Mar. Chem.* 186, 46–57. doi:10.1016/j.marchem.2016.08.001

Couturier, M., Tommi-Morin, G., Sirois, M., Rao, A., Nozais, C., and Chaillou, G. (2017). Nitrogen transformations along a shallow subterranean estuary. *Biogeosciences* 14 (13), 3321–3336. doi:10.5194/bg-14-3321-2017

Cranswick, R. H., Cook, P. G., and Lamontagne, S. (2014). Hyporheic zone exchange fluxes and residence times inferred from riverbed temperature and radon data. *J. Hydrol.* 519, 1870–1881. doi:10.1016/j.jhydrol.2014.09.059

Crook, E. D., Potts, D., Rebolledo-Vieyra, M., Hernandez, L., and Paytan, A. (2012). Calcifying coral abundance near low-pH springs: implications for future ocean acidification. *Coral Reefs* 31 (1), 239–245. doi:10.1007/s00338-011-0839-y

Cyronak, T., Santos, I. R., Erler, D. V., Maher, D. T., and Eyre, B. D. (2014). Drivers ofpCO2variability in two contrasting coral reef lagoons: the influence of submarine groundwater discharge. *Glob. Biogeochem. Cycles* 28 (4), 398–414. doi:10.1002/2013gb004598

Danielescu, S., MacQuarrie, K. T. B., and Faux, R. N. (2009). The integration of thermal infrared imaging, discharge measurements and numerical simulation to quantify the relative contributions of freshwater inflows to small estuaries in Atlantic Canada. *Hydrol. Process* 23 (20), 2847–2859. doi:10.1002/hyp.7383

Day-Lewis, F. D., White, E. A., Johnson, C. D., Lane, J. W., and Belaval, M. (2006). Continuous resistivity profiling to delineate submarine groundwater discharge-examples and limitations. *The Leading Edge* 25 (6), 724–728. doi:10.1190/1.2210056

de Graaf, I. E. M., van Beek, R. L. P. H., Gleeson, T., Moosdorf, N., Schmitz, O., Sutanudjaja, E. H., et al. (2017). A global-scale two-layer transient groundwater model: development and application to groundwater depletion. *Adv. Water Resour.* 102, 53–67. doi:10.1016/j.advwatres.2017.01.011

De Smedt, P., Saey, T., Lehouck, A., Stichelbaut, B., Meerschman, E., Islam, M. M., et al. (2013). Exploring the potential of multi-receiver EMI survey for geoarchaeological prospection: a 90ha dataset. *Geoderma* 199, 30–36. doi:10.1016/j.geoderma.2012.07.019

Deines, P., Langmuir, D., and Harmon, R. S. (1974). Stable carbon isotope ratios and the existence of a gas phase in the evolution of carbonate ground waters. *Geochim. Cosmochim. Acta* 38 (7), 1147–1164. doi:10.1016/0016-7037(74)90010-6

DeSimone, L. A., and Howes, B. L. (1996). Denitrification and nitrogen transport in a coastal aquifer receiving wastewater discharge. *Environ. Sci. Technol.* 30 (4), 1152–1162. doi:10.1021/es950366p

Dickson, N. E. M., Comte, J.-C., McKinley, J., and Ofterdinger, U. (2014). Coupling ground and airborne geophysical data with upscaling techniques for regional groundwater modeling of heterogeneous aquifers: case study of a sedimentary aquifer intruded by volcanic dykes in Northern Ireland. *Water Resour. Res.* 50 (10), 7984–8001. doi:10.1002/2014wr015320

Donis, D., Janssen, F., Liu, B., Wenzhöfer, F., Dellwig, O., Escher, P., et al. (2017). Biogeochemical impact of submarine ground water discharge on coastal surface sands of the southern Baltic Sea. *Estuarine Coastal Shelf Sci.* 189, 131–142. doi:10.1016/j.ecss.2017.03.003

Dulaiova, H., Camilli, R., Henderson, P. B., and Charette, M. A. (2010). Coupled radon, methane and nitrate sensors for large-scale assessment of groundwater discharge and non-point source pollution to coastal waters. *J. Environ. Radioact* 101 (7), 553–563. doi:10.1016/j.jenvrad.2009.12.004

Dulaiova, H., Gonneea, M. E., Henderson, P. B., and Charette, M. A. (2008). Geochemical and physical sources of radon variation in a subterranean estuary - implications for groundwater radon activities in submarine groundwater discharge studies. *Mar. Chem.* 110 (1, 2), 120–127. doi:10.1016/j.marchem.2008.02.011

Duque, C., Jessen, S., Tirado-Conde, J., Karan, S., and Engesgaard, P. (2019). Application of stable isotopes of water to study coupled submarine groundwater discharge and nutrient delivery. *Water* 11 (9), 842. doi:10.3390/w11091842

Duque, C., Michael, H. A., and Wilson, A. M. (2020). The subterranean estuary: technical term, simple analogy, or source of confusion? *Water Resour. Res.* 56 (2), e2019WR026554. doi:10.1029/2019wr026554

Dutkiewicz, A., O'Callaghan, S., and Müller, R. D. (2016). Controls on the distribution of deep-sea sediments. *Geochem. Geophys. Geosyst.* 17 (8), 3075–3098. doi:10.1002/2016gc006428

Dybas, C. L. (2005). Dead zones spreading in world oceans. *Bioscience* 55 (7), 552–557. doi:10.1641/0006-3568(2005)055[0552:dzsiwo]2.0.co;2

Ehlert, C., Reckhardt, A., Greskowiak, J., Liguori, B. T. P., Böning, P., Paffrath, R., et al. (2016). Transformation of silicon in a sandy beach ecosystem: insights from stable silicon isotopes from fresh and saline groundwaters. *Chem. Geology* 440, 207–218. doi:10.1016/j.chemgeo.2016.07.015

Einsele, W. (1936). Über die Beziehungen des Eisenkreislaufs zum Phosphatkreislauf im eutrophen See. *Archiv für Hydrobiologie* 29, 664–686.

Encarnação, J., Leitão, F., Range, P., Piló, D., Chícharo, M. A., and Chícharo, L. (2015). Local and temporal variations in near-shore macrobenthic communities associated with submarine groundwater discharges. *Mar. Ecol.* 36 (4), 926–941. 10.1111/maec.12186

Erler, D. V., Santos, I. R., Zhang, Y., Tait, D. R., Befus, K. M., Hidden, A., et al. (2014). Nitrogen transformations within a tropical subterranean estuary. *Mar. Chem.* 164, 38–47. doi:10.1016/j.marchem.2014.05.008

Eugenio, F., Marcello, J., and Martin, J. (2015). High-resolution maps of bathymetry and benthic habitats in shallow-water environments using multispectral remote sensing imagery. *IEEE Trans. Geosci. Remote Sensing* 53 (7), 3539–3549. doi:10.1109/tgrs.2014.2377300

Feldens, P., Schulze, I., Papenmeier, S., Schönke, M., and Schneider von Deimling, J. (2018). Improved interpretation of marine sedimentary environments using multi-frequency multibeam backscatter data. *Geosciences* 8 (6), 214. doi:10.3390/geosciences8060214

Fisher, W. A., Moxham, R. M., Polcyn, F., and Landis, G. H. (1964). Infrared Surveys of Hawaiian Volcanoes: aerial surveys with infrared imaging radiometer depict volcanic thermal patterns and structural features. *Science* 146 (364), 733–742. doi:10.1126/science.146.3645.733

Fleury, P., Bakalowicz, M., and de Marsily, G. (2007). Submarine springs and coastal karst aquifers: a review. *J. Hydrol.* 339 (1–2), 79–92. doi:10.1016/j.jhydrol.2007.03.009

Flower, H., Rains, M., Lewis, D., Zhang, J.-Z., and Price, R. (2017). Saltwater intrusion as potential driver of phosphorus release from limestone bedrock in a coastal aquifer. *Estuarine Coastal Shelf Sci.* 184, 166–176. doi:10.1016/j.ecss.2016.11.013

Freeze, R. A. (1975). A stochastic-conceptual analysis of one-dimensional groundwater flow in nonuniform homogeneous media. *Water Resour. Res.* 11 (5), 725–741. doi:10.1029/wr011i005p00725

Fritz, P., Basharmal, G. M., Drimmie, R. J., Ibsen, J., and Qureshi, R. M. (1989). Oxygen isotope exchange between sulphate and water during bacterial reduction of sulphate. *Chem. Geol. Isotope Geosci. Sect.* 79 (2), 99–105. doi:10.1016/0168-9622(89)90012-2

Froelich, P. N., Klinkhammer, G. P., Bender, M. L., Luedtke, N. A., Heath, G. R., Cullen, D., et al. (1979). Early oxidation of organic matter in pelagic sediments

of the eastern equatorial Atlantic: suboxic diagenesis. *Geochim. Cosmochim. Acta* 43 (7), 1075–1090. doi:10.1016/0016-7037(79)90095-4

Fulweiler, R. W., Nixon, S. W., Buckley, B. A., and Granger, S. L. (2007). Reversal of the net dinitrogen gas flux in coastal marine sediments. *Nature* 448 (7150), 180–182. doi:10.1038/nature05963

Garcia-Solsona, E., Masque, P., Garcia-Orellana, J., Rapaglia, J., Beck, A. J., Cochran, J. K., et al. (2008). Estimating submarine groundwater discharge around Isola La Cura, northern Venice Lagoon (Italy), by using the radium quartet. *Mar. Chem.* 109 (3-4), 292–306. doi:10.1016/j.marchem.2008.02.007

Gardner, W. S., McCarthy, M. J., An, S., Sobolev, D., Sell, K. S., and Brock, D. (2006). Nitrogen fixation and dissimilatory nitrate reduction to ammonium (DNRA) support nitrogen dynamics in Texas estuaries. *Limnol. Oceanogr.* 51 (1part2), 558–568. doi:10.4319/lo.2006.51.1_part_2.0558

Gat, J. R. (1996). Oxygen and hydrogen isotopes in the hydrologic cycle. *Annu. Rev. Earth Planet. Sci.* 24 (1), 225–262. doi:10.1146/annurev.earth.24.1.225

Gaudette, H. E., and Lyons, W. B. (1980). *Phosphate geochemisty in nearshore carbonate sediments a suggestion of apatite formation*, Durham.

Geng, X., Michael, H. A., Boufadel, M. C., Molz, F. J., Gerges, F., and Lee, K. (2020). Heterogeneity affects intertidal flow topology in coastal beach aquifers. *Geophys. Res. Lett.* 47 (17), e2020GL089612. doi:10.1029/2020gl089612

Gilfedder, B. S., Cartwright, I., Hofmann, H., and Frei, S. (2019). Explicit modeling of radon-222 in HydroGeoSphere during steady state and dynamic transient storage. *Ground Water* 57 (1), 36–47. doi:10.1111/gwat.12847

Gilfedder, B. S., Frei, S., Hofmann, H., and Cartwright, I. (2015). Groundwater discharge to wetlands driven by storm and flood events: quantification using continuous Radon-222 and electrical conductivity measurements and dynamic mass-balance modelling. *Geochim. Cosmochim. Acta* 165, 161–177. doi:10.1016/j.gca.2015.05.037

Gleeson, T., Moosdorf, N., Hartmann, J., and van Beek, L. P. H. (2014). A glimpse beneath earth's surface: GLobal HYdrogeology MaPS (GLHYMPS) of permeability and porosity. *Geophys. Res. Lett.* 41 (11), 3891–3898. doi:10.1002/2014gl059856

Goldscheider, N., Chen, Z., Auler, A. S., Bakalowicz, M., Broda, S., Drew, D., et al. (2020). Global distribution of carbonate rocks and karst water resources. *Hydrogeol J.* 28 (5), 1661–1677. doi:10.1007/s10040-020-02139-5

Gonneea, M. E., and Charette, M. A. (2014). Hydrologic controls on nutrient cycling in an unconfined coastal aquifer. *Environ. Sci. Technol.* 48 (24), 14178–14185. doi:10.1021/es503313t

Gonneea, M. E., Charette, M. A., Liu, Q., Herrera-Silveira, J. A., and Morales-Ojeda, S. M. (2014). Trace element geochemistry of groundwater in a karst subterranean estuary (Yucatan Peninsula, Mexico). *Geochimica Et Cosmochimica Acta* 132, 31–49. doi:10.1016/j.gca.2014.01.037

Gonneea, M. E., Morris, P. J., Dulaiova, H., and Charette, M. A. (2008). New perspectives on radium behavior within a subterranean estuary. *Mar. Chem.* 109 (3-4), 250–267. doi:10.1016/j.marchem.2007.12.002

Gonneea, M. E., Mulligan, A. E., and Charette, M. A. (2013). Seasonal cycles in radium and barium within a subterranean estuary: implications for groundwater derived chemical fluxes to surface waters. *Geochim. Cosmochim. Acta* 119, 164–177. doi:10.1016/j.gca.2013.05.034

Goodridge, B. M., and Melack, J. M. (2014). Temporal evolution and variability of dissolved inorganic nitrogen in beach pore water revealed using radon residence times. *Environ. Sci. Technol.* 48 (24), 14211–14218. doi:10.1021/es504017j

Gramling, C. M., McCorkle, D. C., Mulligan, A. E., and Woods, T. L. (2003). A carbon isotope method to quantify groundwater discharge at the land-sea interface. *Limnol. Oceanogr.* 48 (3), 957–970. doi:10.4319/lo.2003.48.3.0957

Greskowiak, J. (2014). Tide-induced salt-fingering flow during submarine groundwater discharge. *Geophys. Res. Lett.* 41 (18), 6413–6419. doi:10.1002/2014gl061184

Grünenbaum, N., Greskowiak, J., Sültenfuß, J., and Massmann, G. (2020). Groundwater flow and residence times below a meso-tidal high-energy beach: a model-based analyses of salinity patterns and 3H-3He groundwater ages. *J. Hydrol.* 587, 124948. doi:10.1016/j.jhydrol.2020.124948

Grzelak, K., Tamborski, J., Kotwicki, L., and Bokuniewicz, H. (2018). Ecostructuring of marine nematode communities by submarine groundwater discharge. *Mar. Environ. Res.* 136, 106–119. doi:10.1016/j.marenvres.2018.01.013

Gustafson, C., Key, K., and Evans, R. L. (2019). Aquifer systems extending far offshore on the U.S. Atlantic margin. *Sci. Rep.* 9 (1), 8709. doi:10.1038/s41598-019-44611-7

Hajati, M. C., Sutanudjaja, E., and Moosdorf, N. (2019). Quantifying regional fresh submarine groundwater discharge with the lumped modeling approach CoCa-rfsgd. *Water Resour. Res.* 55 (7), 5321–5341. doi:10.1029/2018wr024248

Hancock, P. J., Boulton, A. J., and Humphreys, W. F. (2005). Aquifers and hyporheic zones: towards an ecological understanding of groundwater. *Hydrogeol J.* 13 (1), 98–111. doi:10.1007/s10040-004-0421-6

Hanshaw, B. B., and Back, W. (1980). Chemical mass-wasting of the northern yucatan Peninsula by groundwater dissolution. *Geology* 8 (5), 222–224. doi:10.1130/0091-7613(1980)8<222:cmotny>2.0.co;2

Hanshaw, B. B., and Back, W. (1979). "Major geochemical processes in the evolution of carbonate-aquifer systems," in *Developments in water science*. Editors W. Back and D. A. Stephenson (New York, NY: Elsevier), 287–312.

Hays, R. L., and Ullman, W. J. (2007). Dissolved nutrient fluxes through a sandy estuarine beachface (Cape Henlopen, Delaware, USA): Contributions from fresh groundwater discharge, seawater recycling, and diagenesis. *Estuaries Coasts* 30 (4), 710–724. doi:10.1007/bf02841967

Heiss, J. W., Michael, H. A., and Koneshloo, M. (2020). Denitrification hotspots in intertidal mixing zones linked to geologic heterogeneity. *Environ. Res. Lett.* 15 (8), 084015. doi:10.1088/1748-9326/ab90a6

Heiss, J. W., and Michael, H. A. (2014). Saltwater-freshwater mixing dynamics in a sandy beach aquifer over tidal, spring-neap, and seasonal cycles. *Water Resour. Res.* 50 (8), 6747–6766. doi:10.1002/2014wr015574

Hermans, T., and Paepen, M. (2020). Combined inversion of land and marine electrical resistivity tomography for submarine groundwater discharge and saltwater intrusion characterization. *Geophys. Res. Lett.* 47 (3). doi:10.1029/2019gl085877

Hoefs, J. (2018). *Stable isotope geochemistry*. Göttingen, German: Springer-Nature. doi:10.1007/1978-3-319-78527-1

Hoffmann, J. J. L., von Deimling, J. S., Schroder, J. F., Schmidt, M., Held, P., Crutchley, G. J., et al. (2020). Complex eyed pockmarks and submarine groundwater discharge revealed by acoustic data and sediment cores in Eckernforde Bay, SW Baltic Sea. *Geochem. Geophys. Geosystems* 21 (4). doi:10.1029/2019gc008825

Hong, Y., Wu, J., Wilson, S., and Song, B. 2018). Vertical stratification of sediment microbial communities along geochemical gradients of a subterranean estuary located at the Gloucester Beach of Virginia, United States. *Front. Microbiol.* 9, 3343. doi:10.3389/fmicb.2018.03343

Hovland, M., Gardner, J. V., and Judd, A. G. (2002). The significance of pockmarks to understanding fluid flow processes and geohazards. *Geofluids* 2 (2), 127–136. doi:10.1046/j.1468-8123.2002.00028.x

Hovland, M., and Judd, A. (1988). *Seabed pockmarks and seepages: impact on geology, biology and the marine environment*. Sterling House London: Graham & Trodman. doi:10.13140/RG.2.1.1414.1286

Huerta-Diaz, M. A., and Morse, J. W. (1992). Pyritization of trace metals in anoxic marine sediments. *Geochimica Et Cosmochimica Acta* 56 (7), 2681–2702. doi:10.1016/0016-7037(92)90353-k

Humphreys, W. F. (2008). Rising from Down Under: developments in subterranean biodiversity in Australia from a groundwater fauna perspective. *Invert. Syst.* 22 (2), 85–101. doi:10.1071/is07016

Hwang, D. W., Kim, G. B., Lee, Y. W., and Yang, H. S. (2005). Estimating submarine inputs of groundwater and nutrients to a coastal bay using radium isotopes. *Mar. Chem.* 96 (1-2), 61–71. doi:10.1016/j.marchem.2004.11.002

IAEA (2003). *Guidelines for radioelement mapping using gamma ray spectrometry data*. Vienna: International Atomic Energy Agency (IAEA).

FAOIIASA, ISRIC; ISSCAS; JRC (2009). "Harmonized World Soil Database (version 1.1)," in *Rome and laxenburg*. Editor I. FAO.

Jakobsson, M., O'Regan, M., Mörth, C.-M., Stranne, C., Weidner, E., Hansson, J., et al. (2020). Potential links between Baltic Sea submarine terraces and groundwater seeping. *Earth Surf. Dynam.* 8 (1), 1–15. doi:10.5194/esurf-8-1-2020

Jarsjö, J., Shibuo, Y., and Destouni, G. (2008). Spatial distribution of unmonitored inland water discharges to the sea. *J. Hydrol.* 348 (1, 2), 59–72. doi:10.1016/j.jhydrol.2007.09.052

Jetten, M. S., Strous, M., Van de Pas-Schoonen, K. T., Schalk, J., van Dongen, U. G., van de Graaf, A. A., et al. (1998). The anaerobic oxidation of ammonium. *FEMS Microbiol. Rev.* 22 (5), 421–437. doi:10.1111/j.1574-6976.1998.tb00379.x

Jiang, S., Zhang, Y. X., Jin, J., Wu, Y., Wei, Y. J., Wang, X. L., et al. (2020). Organic carbon in a seepage face of a subterranean estuary: Turnover and microbial interrelations. *Sci. Total Environ.*, 725, 138220. doi:10.1016/j.scitotenv.2020.138220

Jiao, J., and Post, V. (2019). *Coastal hydrogeology*. Cambridge: Cambridge University Press.

Jirka, G. H. (2004). Integral model for turbulent buoyant jets in unbounded stratified flows. Part I: Single round jet. *Environ. Fluid Mech.* 4 (1), 1–56. doi:10.1023/a:1025583110842

Johannes, R. (1980). The ecological significance of the submarine discharge of groundwater. *Mar. Ecol. Prog. Ser.* 3 (4), 365–373. doi:10.3354/meps003365

Johannesson, K. H., and Burdige, D. J. (2007). Balancing the global oceanic neodymium budget: evaluating the role of groundwater. *Earth Planet. Sci. Lett.* 253 (1, 2), 129–142. doi:10.1016/j.epsl.2006.10.021

Johnson, A. G., Glenn, C. R., Burnett, W. C., Peterson, R. N., and Lucey, P. G. (2008). Aerial infrared imaging reveals large nutrient-rich groundwater inputs to the ocean. *Geophys. Res. Lett.* 35 (15), 6. doi:10.1029/2008gl034574

Johnson, T. C., Versteeg, R. J., Day-Lewis, F. D., Major, W., and Lane, J. W. (2015). Time-lapse electrical geophysical monitoring of amendment-based biostimulation. *Ground Water* 53 (6), 920–932. doi:10.1111/gwat.12291

Jørgensen, B. B. (1982). Mineralization of organic-matter in the Sea Bed - the role of Sulfate reduction. *Nature* 296 (5858), 643–645.

Judd, A. G., and Hovland, M. (1992). The evidence of shallow gas in marine sediments. *Continental Shelf Res.* 12 (10), 1081–1095. doi:10.1016/0278-4343(92)90070-z

Jurasinski, G., Janssen, M., Voss, M., Böttcher, M. E., Brede, M., Burchard, H., et al. (2018). Understanding the coastal ecocline: assessing sea-land interactions at non-tidal, low-ling Coasts through interdisciplinary research. *Front. Mar. Sci.* 5. doi:10.3389/fmars.2018.00342

Kanehisa, M., and Goto, S. (2000). KEGG: kyoto encyclopedia of genes and genomes. *Nucl. Acids Res.* 28 (1), 27–30. doi:10.1093/nar/28.1.27

Kazemipour, F., Launeau, P., and Méléder, V. (2012). Microphytobenthos biomass mapping using the optical model of diatom biofilms: Application to hyperspectral images of Bourgneuf Bay. *Remote Sensing Environ.* 127, 1–13. doi:10.1016/j.rse.2012.08.016

Kazmierczak, J., Postma, D., Müller, S., Jessen, S., Nilsson, B., Czekaj, J., et al. (2020). Groundwater-controlled phosphorus release and transport from sandy aquifer into lake. *Limnol. Oceanogr.* 65 (9), 2188–2204. doi:10.1002/lno.11447

Keating, K., and Knight, R. (2007). A laboratory study to determine the effect of iron oxides on proton NMR measurements. *Geophysics* 72 (1), E27–E32. doi:10.1190/1.2399445

Kelly, J. L., Glenn, C. R., and Lucey, P. G. (2013). High-resolution aerial infrared mapping of groundwater discharge to the coastal ocean. *Limnol. Oceanogr. Methods* 11, 262–277. doi:10.4319/lom.2013.11.262

Kim, G., Kim, J.-S., and Hwang, D.-W. (2011). Submarine groundwater discharge from oceanic islands standing in oligotrophic oceans: Implications for global biological production and organic carbon fluxes. *Limnol. Oceanogr.* 56 (2), 673–682. doi:10.4319/lo.2011.56.2.0673

Kim, J., and Kim, G. (2017). Inputs of humic fluorescent dissolved organic matter via submarine groundwater discharge to coastal waters off a volcanic island (Jeju, Korea). *Sci. Rep.* 7, 7921. doi:10.1038/s41598-017-08518-5

Kim, K. H., Heiss, J. W., Geng, X., and Michael, H. A. (2020). Modeling hydrologic controls on particulate organic carbon contributions to beach aquifer biogeochemical reactivity. *Water Resour. Res.* 56 (10), e2020WR027306. doi:10.1029/2020wr027306

Kim, K. H., Heiss, J. W., Michael, H. A., Cai, W.-J., Laattoe, T., Post, V. E. A., et al. (2017). Spatial patterns of groundwater biogeochemical reactivity in an intertidal beach aquifer. *J. Geophys. Res. Biogeosci.* 122 (10), 2548–2562. doi:10.1002/2017jg003943

Kim, K. H., Michael, H. A., Field, E. K., and Ullman, W. J. (2019). Hydrologic shifts create complex transient distributions of particulate organic carbon and biogeochemical responses in beach aquifers. *J. Geophys. Res. Biogeosci.* 124 (10), 3024–3038. doi:10.1029/2019jg005114

Kim, T.-H., Kwon, E., Kim, I., Lee, S.-A., and Kim, G. (2013). Dissolved organic matter in the subterranean estuary of a volcanic island, Jeju: Importance of dissolved organic nitrogen fluxes to the ocean. *J. Sea Res.* 78, 18–24. doi:10.1016/j.seares.2012.12.009

Kim, T.-H., Waska, H., Kwon, E., Suryaputra, I. G. N., and Kim, G. (2012). Production, degradation, and flux of dissolved organic matter in the subterranean estuary of a large tidal flat. *Mar. Chem.* 142–144, 1–10. doi:10.1016/j.marchem.2012.08.002

Kipp, L. E., Henderson, P. B., Wang, Z. A., and Charette, M. A. (2020). Deltaic and estuarine controls on mackenzie river solute fluxes to the arctic Ocean. *Estuaries and coasts*. 42, 1992-2014. doi:10.1007/s12237-020-00739-8

Kirsch, R. (2006). *Groundwater Geophysics—a tool for hydrogeology*. Flintbek, Germany, Springer.

Klemas, V. V. (2016). Remote Sensing of Submerged Aquatic VegetationSeafloor mapping along continental shelves, *Res. Tech. Visualizing Benthic Environments*. 13, 125–140. doi:10.1007/978-3-319

Knee, K. L., and Paytan, A. (2011). "4.08 - Submarine groundwater discharge: a source of nutrients, metals, and pollutants to the coastal ocean", in *Treatise on estuarine and coastal science*. Waltham: Academic Press, 205–233.

Kotwicki, L., Grzelak, K., Czub, M., Dellwig, O., Gentz, T., Szymczycha, B., et al. (2014). Submarine groundwater discharge to the Baltic coastal zone: Impacts on the meiofaunal community. *J. Mar. Syst.* 129, 118–126. doi:10.1016/j.jmarsys.2013.06.009

Kowalski, N., Dellwig, O., Beck, M., Grunwald, M., Dürselen, C.-D., Badewien, T. H., et al. (2012). A comparative study of manganese dynamics in the water column and sediments of intertidal systems of the North Sea. *Estuarine Coast. Shelf Sci.* 100, 3–17. doi:10.1016/j.ecss.2011.03.011

Kroeger, K. D., and Charette, M. A. (2008). Nitrogen biogeochemistry of submarine groundwater discharge. *Limnol. Oceanogr.* 53 (3), 1025. doi:10.4319/lo.2008.53.3.1025

Kwon, E. Y., Kim, G., Primeau, F., Moore, W. S., Cho, H.-M., DeVries, T., et al. (2014). Global estimate of submarine groundwater discharge based on an observationally constrained radium isotope model. *Geophys. Res. Lett.* 41 (23), 2014GL061574. doi:10.1002/2014gl061574

Lagouarde, J.-P., Bhattacharya, B. K., Crebassol, P., Gamet, P., Babu, S. S., Boulet, G., et al. (2018). The Indian-French Trishna mission: Earth observation in the thermal infrared with high spatio-temporal resolution. IGARSS 2018-2018 IEEE international geoscience and remote sensing symposium. IEEE, 4078–4081.

Langguth, H. R., and Voigt, R. (2004). *Hydrogeologische methoden*. Berlin, Heidelberg: Springer, 1014.

Laruelle, G. G., Dürr, H. H., Slomp, C. P., and Borges, A. V. (2010). Evaluation of sinks and sources of CO2in the global coastal ocean using a spatially-explicit typology of estuaries and continental shelves. *Geophys. Res. Lett.* 37 (15), doi:10.1029/2010gl043691

Lausch, A., Pause, M., Merbach, I., Zacharias, S., Doktor, D., Volk, M., et al. (2013). A new multiscale approach for monitoring vegetation using remote sensing-based indicators in laboratory, field, and landscape. *Environ. Monit. Assess.* 185 (2), 1215–1235. doi:10.1007/s10661-012-2627-8

Lebbe, L. (1981). *The subterranean flow of fresh and salt water underneath the western Belgian beach*. Uppsala, Sweden: Proceedings of the 7th Salt Water Intrusion Meeting, 193–219.

Lecher, A. L., Chien, C.-T., and Paytan, A. (2016a). Submarine groundwater discharge as a source of nutrients to the North Pacific and Arctic coastal ocean. *Mar. Chem.* 186, 167–177. doi:10.1016/j.marchem.2016.09.008

Lecher, A. L., Kessler, J., Sparrow, K., Garcia-Tigreros Kodovska, F., Dimova, N., Murray, J., et al. (2016b). Methane transport through submarine groundwater discharge to the North Pacific and Arctic Ocean at two Alaskan sites. *Limnol. Oceanogr.* 61 (S1), S344–S355. doi:10.1002/lno.10118

Lecher, A., and Mackey, K. (2018). Synthesizing the effects of submarine groundwater discharge on Marine Biota. *Hydrology* 5 (4), 60. doi:10.3390/hydrology5040060

Lee, E., Shin, D., Hyun, S. P., Ko, K.-S., Moon, H. S., Koh, D.-C., et al. (2017). Periodic change in coastal microbial community structure associated with submarine groundwater discharge and tidal fluctuation. *Limnol. Oceanogr.* 62 (2), 437–451. doi:10.1002/lno.10433

Leitão, F., Encarnação, J., Range, P., Schmelz, R. M., Teodósio, M. A., and Chícharo, L. (2015). Submarine groundwater discharges create unique benthic

communities in a coastal sandy marine environment. *Estuarine Coastal Shelf Sci.* 163, 93–98. doi:10.1016/j.ecss.2015.06.007

Lewandowski, J., Meinikmann, K., Nützmann, G., and Rosenberry, D. O. (2015). Groundwater - the disregarded component in lake water and nutrient budgets. Part 2: effects of groundwater on nutrients. *Hydrol. Process.* 29 (13), 2922–2955. doi:10.1002/hyp.10384

Linkhorst, A., Dittmar, T., and Waska, H. (2017). Molecular fractionation of dissolved organic matter in a shallow subterranean estuary: the role of the iron curtain. *Environ. Sci. Technol.* 51 (3), 1312–1320. doi:10.1021/acs.est.6b03608

Lipka, M., Böttcher, M. E., Wu, Z., Sültenfuß, J., Jenner, A.-K., Westphal, J., et al. (2018). Ferruginous groundwaters as a source of P, Fe, and DIC for coastal waters of the southern Baltic Sea: (Isotope) hydrobiogeochemistry and the role of an iron curtain. *E3s Web Conf.* 54, 00019. doi:10.1051/e3sconf/20185400019

Liu, Q., Charette, M. A., Breier, C. F., Henderson, P. B., McCorkle, D. C., Martin, W., et al. (2017). Carbonate system biogeochemistry in a subterranean estuary - Waquoit Bay, USA. *Geochim. Cosmochim. Acta* 203, 422–439. doi:10.1016/j.gca.2017.01.041

Liu, Q., Dai, M., Chen, W., Huh, C.-A., Wang, G., Li, Q., et al. (2012). How significant is submarine groundwater discharge and its associated dissolved inorganic carbon in a river-dominated shelf system? *Biogeosciences* 9 (5), 1777–1795. doi:10.5194/bg-9-1777-2012

Lopez, C. V., Murgulet, D., and Santos, I. R. (2020). Radioactive and stable isotope measurements reveal saline submarine groundwater discharge in a semiarid estuary. *J. Hydrol.* 590, 125395. doi:10.1016/j.jhydrol.2020.125395

Loveless, A. M., and Oldham, C. E. (2010). Natural attenuation of nitrogen in groundwater discharging through a sandy beach. *Biogeochemistry* 98 (1–3), 75–87. doi:10.1007/s10533-009-9377-x

Luijendijk, E., Gleeson, T., and Moosdorf, N. (2020). Fresh groundwater discharge insignificant for the world's oceans but important for coastal ecosystems. *Nat. Commun.* 11 (1), 1260. doi:10.1038/s41467-020-15064-8

Luther, G. W., Church, T. M., and Powell, D. (1991). Sulfur speciation and sulfide oxidation in the water column of the Black Sea. *Deep Sea Res. A. Oceanographic Res. Pap.* 38, S1121–S1137. doi:10.1016/s0198-0149(10)80027-5

Macklin, P. A., Suryaputra, I. G. N. A., Maher, D. T., Murdiyarso, D., and Santos, I. R. (2019). Drivers of CO2 along a mangrove-seagrass transect in a tropical bay: Delayed groundwater seepage and seagrass uptake. *Continental Shelf Res.* 172, 57–67. doi:10.1016/j.csr.2018.10.008

Mallast, U., Gloaguen, R., Friesen, J., Rödiger, T., Geyer, S., Merz, R., et al. (2014). How to identify groundwater-caused thermal anomalies in lakes based on multi-temporal satellite data in semi-arid regions. *Hydrol. Earth Syst. Sci.* 18 (7), 2773–2787. doi:10.5194/hess-18-2773-2014

Mallast, U., and Siebert, C. (2019). Combining continuous spatial and temporal scales for SGD investigations using UAV-based thermal infrared measurements. *Hydrol. Earth Syst. Sci.* 23 (3), 1375–1392. doi:10.5194/hess-23-1375-2019

Manheim, F. T., Krantz, D. E., and Bratton, J. F. (2004). Studying ground water under delmarva coastal bays using electrical resistivity. *Ground Water* 42 (7), 1052–1068. doi:10.1111/j.1745-6584.2004.tb02643.x

Mansoor, N., and Slater, L. (2007). On the relationship between iron concentration and induced polarization in marsh soils. *Geophysics* 72 (1), A1–A5. doi:10.1190/1.2374853

Marchant, H. K., Holtappels, M., Lavik, G., Ahmerkamp, S., Winter, C., and Kuypers, M. M. M. (2016). Coupled nitrification-denitrification leads to extensive N loss in subtidal permeable sediments. *Limnol. Oceanogr.* 61 (3), 1033–1048. doi:10.1002/lno.10271

Mayfield, K. K., Eisenhauer, A., Santiago Ramos, D. P., Higgins, J. A., Horner, T. J., Auro, M., et al. (2021). Groundwater discharge impacts marine isotope budgets of Li, Mg, Ca, Sr, and Ba. *Nat. Commun.* 12 (1), 148. doi:10.1038/s41467-020-20248-3

McGrath, G. S., Paik, K., and Hinz, C. (2012). Microtopography alters self-organized vegetation patterns in water-limited ecosystems. *J. Geophys. Research-Biogeosciences* 117. doi:10.1029/2011jg001870

Meister, P., Liu, B., Khalili, A., Böttcher, M. E., and Jørgensen, B. B. (2019). Factors controlling the carbon isotope composition of dissolved inorganic carbon and methane in marine porewater: An evaluation by reaction-transport modelling. *J. Mar. Syst.* 200, 103227. doi:10.1016/j.jmarsys.2019.103227

Mejías, M., Ballesteros, B. J., Antón-Pacheco, C., Domínguez, J. A., Garcia-Orellana, J., Garcia-Solsona, E., et al. (2012). Methodological study of submarine groundwater discharge from a karstic aquifer in the Western Mediterranean Sea. *J. Hydrol.* 464-465, 27–40. doi:10.1016/j.jhydrol.2012.06.020

Meyer, D., Prien, R. D., Dellwig, O., Waniek, J. J., and Schulz–Bull, D. E. (2014). Electrode measurements of the oxidation reduction potential in the Gotland Deep using a moored profiling instrumentation. *Estuarine Coastal Shelf Sci.* 141, 26–36. doi:10.1016/j.ecss.2014.02.001

Michael, H. A., Mulligan, A. E., and Harvey, C. F. (2005). Seasonal oscillations in water exchange between aquifers and the coastal ocean. *Nature* 436 (7054), 1145–1148. doi:10.1038/nature03935

Migné, A., Ouisse, V., Hubas, C., and Davoult, D. (2011). Freshwater seepages and ephemeral macroalgae proliferation in an intertidal bay: II. Effect on benthic biomass and metabolism. *Estuarine, Coastal Shelf Sci.* 92 (1), 161–168. doi:10.1016/j.ecss.2010.12.023

Miller, D. C., and Ullman, W. J. (2004). Ecological consequences of ground water discharge to Delaware Bay, United States. *Ground Water* 42 (7), 959–970. doi:10.1111/j.1745-6584.2004.tb02635.x

Missiaen, T., Murphy, S., Loncke, L., and Henriet, J.-P. (2002). Very high-resolution seismic mapping of shallow gas in the Belgian coastal zone. *Continental Shelf Res.* 22 (16), 2291–2301. doi:10.1016/s0278-4343(02)00056-0

Mollenhauer, H., Kasner, M., Haase, P., Peterseil, J., Wohner, C., Frenzel, M., et al. (2018). Long-term environmental monitoring infrastructures in Europe: observations, measurements, scales, and socio-ecological representativeness. *Sci. Total Environ.* 624, 968–978. doi:10.1016/j.scitotenv.2017.12.095

Montiel, D., Lamore, A. F., Stewart, J., Lambert, W. J., Honeck, J., Lu, Y., et al. (2019). Natural groundwater nutrient fluxes exceed anthropogenic inputs in an ecologically impacted estuary: lessons learned from Mobile Bay, Alabama. *Biogeochemistry* 145 (1), 1–33. doi:10.1007/s10533-019-00587-0

Moore, W. S., Beck, M., Riedel, T., Rutgers van der Loeff, M., Dellwig, O., Shaw, T. J., et al. (2011). Radium-based pore water fluxes of silica, alkalinity, manganese, DOC, and uranium: A decade of studies in the German Wadden Sea. *Geochim. Cosmochim. Acta* 75 (21), 6535–6555. doi:10.1016/j.gca.2011.08.037

Moore, W. S. (2000). Determining coastal mixing rates using radium isotopes. *Continental Shelf Res.* 20 (15), 1993–2007. doi:10.1016/s0278-4343(00)00054-6

Moore, W. S. (1996). Large groundwater inputs to coastal waters revealed by 226Ra enrichments. *Nature* 380 (6575), 612–614. doi:10.1038/380612a0

Moore, W. S., Sarmiento, J. L., and Key, R. M. (2008). Submarine groundwater discharge revealed by 228Ra distribution in the upper Atlantic Ocean. *Nat. Geosci.* 1 (5), 309–311. doi:10.1038/ngeo183

Moore, W. S. (2003). Sources and fluxes of submarine groundwater discharge delineated by radium isotopes. *Biogeochemistry* 66 (1, 2), 75–93. doi:10.1023/b:biog.0000006065.77764.a0

Moore, W. S. (1999). The subterranean estuary: a reaction zone of ground water and sea water. *Mar. Chem.* 65 (1, 2), 111–125. doi:10.1016/s0304-4203(99)00014-6

Moosdorf, N., Hartmann, J., and Dürr, H. H. (2010). Lithological composition of the North American continent and implications of lithological map resolution for dissolved silica flux modeling. *Geochem. Geophys. Geosyst.* 11, . doi:10.1029/2010gc003259

Morrow, F. J., Ingham, M. R., and McConchie, J. A. (2010). Monitoring of tidal influences on the saline interface using resistivity traversing and cross-borehole resistivity tomography. *J. Hydrol.* 389 (1-2), 69–77. doi:10.1016/j.jhydrol.2010.05.022

Mosher, D. C., and Simpkin, P. G. (1999). Environmental marine Geoscience 1. Status and trends of marine high-resolution seismic reflection profiling: Data acquistion. *Geosci. Can.* 26, 174–188.

Müller, H. (2010). *Characterization of marine near-surface sediments by electromagnetic profiling*. Bremen: University of Bremen.

Müller, H., von Dobeneck, T., Nehmiz, W., and Hamer, K. (2011). Near-surface electromagnetic, rock magnetic, and geochemical fingerprinting of submarine freshwater seepage at Eckernförde Bay (SW Baltic Sea). *Geo-mar Lett.* 31 (2), 123–140. doi:10.1007/s00367-010-0220-0

Müller-Petke, M., and Yaramanci, U. (2015). "11.13 - Tools and Techniques: Nuclear Magnetic Resonance," in *Treatise on geophysics*. Editor G. Schubert. Second Edition (Oxford: Elsevier), 419–445.

Musat, N., Werner, U., Knittel, K., Kolb, S., Dodenhof, T., van Beusekom, J. E., et al. (2006). Microbial community structure of sandy intertidal sediments in the North Sea, Sylt-Rømø Basin, Wadden Sea. *Syst. Appl. Microbiol.* 29 (4), 333–348. doi:10.1016/j.syapm.2005.12.006

Mylroie, J. E., and Carew, J. L. (1990). The Flank Margin model for dissolution cave development in carbonate platforms. *Earth Surf. Process. Landforms* 15 (5), 413–424. doi:10.1002/esp.3290150505

Nakada, S., Yasumoto, J., Taniguchi, M., and Ishitobi, T. (2011). Submarine groundwater discharge and seawater circulation in a subterranean estuary beneath a tidal flat. *Hydrol. Process* 25 (17), 2755–2763. doi:10.1002/hyp.8016

Nick, H., Raoof, A., Centler, F., Thullner, M., and Regnier, P. (2013). Reactive dispersive contaminant transport in coastal aquifers: numerical simulation of a reactive Henry problem. *J. Contam. Hydrol.* 145, 90–104. doi:10.1016/j.jconhyd.2012.12.005

Nowicki, B. L., Requintina, E., Van Keuren, D., and Portnoy, J. (1999). The role of sediment denitrification in reducing groundwater-derived nitrate inputs to Nauset Marsh Estuary, Cape Cod, Massachusetts. *Estuaries* 22 (2), 245–259. doi:10.2307/1352981

O'Connor, A. E., Krask, J. L., Canuel, E. A., and Beck, A. J. (2018). Seasonality of major redox constituents in a shallow subterranean estuary. *Geochim. Cosmochim. Acta* 224, 344–361. doi:10.1016/j.gca.2017.10.013

O'Reilly, C., Santos, I. R., Cyronak, T., McMahon, A., and Maher, D. T. (2015). Nitrous oxide and methane dynamics in a coral reef lagoon driven by pore water exchange: Insights from automated high-frequency observations. *Geophys. Res. Lett.* 42 (8), 2885–2892. doi:10.1002/2015gl063126

Oehler, T., Bakti, H., Lubis, R. F., Purwoarminta, A., Delinom, R., and Moosdorf, N. (2019a). Nutrient dynamics in submarine groundwater discharge through a coral reef (western Lombok, Indonesia). *Limnol. Oceanogr.* 64 (6), 2646–2661. doi:10.1002/lno.11240

Oehler, T., Eiche, E., Putra, D., Adyasari, D., Hennig, H., Mallast, U., et al. (2018). Seasonal variability of land-ocean groundwater nutrient fluxes from a tropical karstic region (southern Java, Indonesia). *J. Hydrol.* 565, 662–671. doi:10.1016/j.jhydrol.2018.08.077

Oehler, T., Mogollón, J. M., Moosdorf, N., Winkler, A., Kopf, A., and Pichler, T. (2017). Submarine groundwater discharge within a landslide scar at the French Mediterranean coast. *Estuarine Coastal Shelf Sci.* 198, 128–137. doi:10.1016/j.ecss.2017.09.006

Oehler, T., Tamborski, J., Rahman, S., Moosdorf, N., Ahrens, J., Mori, C., et al. (2019b). DSi as a Tracer for Submarine Groundwater Discharge. *Front. Mar. Sci.* 6 (563). doi:10.3389/fmars.2019.00563

Paffrath, R., Pahnke, K., Behrens, M. K., Reckhardt, A., Ehlert, C., Schnetger, B., et al. (2020). Rare earth element behavior in a sandy subterranean estuary of the southern North Sea. *Front. Mar. Sci.* doi:10.3389/fmars.2020.00424

Pain, A. J., Martin, J. B., and Young, C. R. (2019). Sources and sinks of CO_2 and CH_4 in siliciclastic subterranean estuaries. *Limnol. Oceanogr.* 64 (4), 1500–1514. doi:10.1002/lno.11131

Pain, A. J., Martin, J. B., Young, C. R., Valle-Levinson, A., and Mariño-Tapia, I. (2020). Carbon and phosphorus processing in a carbonate karst aquifer and delivery to the coastal ocean. *Geochim. et Cosmochim. Acta* 269, 484–495. doi:10.1016/j.gca.2019.10.040

Papenmeier, S., Darr, A., Feldens, P., and Michaelis, R. (2020). Hydroacoustic mapping of geogenic hard substrates: challenges and review of German approaches. *Geosciences* 10 (3), 100. doi:10.3390/geosciences10030100

Petersen, W., Schroeder, F., and Bockelmann, F.-D. (2011). FerryBox - Application of continuous water quality observations along transects in the North Sea. *Ocean Dyn.* 61 (10), 1541–1554. doi:10.1007/s10236-011-0445-0

Pisternick, T., Lilkendey, J., Audit-Manna, A., Dumur Neelayya, D., Neehaul, Y., and Moosdorf, N. (2020). Submarine groundwater springs are characterized by distinct fish communities. *Mar. Ecol.*, 41 (5), e12610. doi:10.1111/maec.12610

Post, V. E. A., Houben, G. J., Stoeckl, L., and Sültenfuß, J. (2019). *Behaviour of tritium and tritiogenic helium in freshwater lens groundwater systems: insights from Langeoog island*. Germany: Geofluids, 1494326

Post, V. E. A., Vandenbohede, A., Werner, A. D., and Maimun, M. D. (2013). Groundwater ages in coastal aquifers. *Adv. Water Resour.* 57, 1–11. doi:10.1016/j.advwatres.2013.03.011

Povinec, P. P., Burnett, W. C., Beck, A., Bokuniewicz, H., Charette, M., Gonneea, M. E., et al. (2012). Isotopic, geophysical and biogeochemical investigation of submarine groundwater discharge: IAEA-UNESCO intercomparison exercise at Mauritius Island. *J. Environ. Radioact* 104, 24–45. doi:10.1016/j.jenvrad.2011.09.009

Prandle, D., (2009). *Estuaries: dynamics, mixing, sedimentation, and morphology*. Cambridge: Cambridge University Press, ix, 236

Price, R. M., Savabi, M. R., Jolicoeur, J. L., and Roy, S. (2010). Adsorption and desorption of phosphate on limestone in experiments simulating seawater intrusion. *Appl. Geochem.* 25 (7), 1085–1091. doi:10.1016/j.apgeochem.2010.04.013

Prieto, C., and Destouni, G. (2011). Is submarine groundwater discharge predictable?. *Geophys. Res. Lett.* 38. doi:10.1029/2010gl045621

Prouty, N. G., Cohen, A., Yates, K. K., Storlazzi, C. D., Swarzenski, P. W., and White, D. (2017a). Vulnerability of Coral Reefs to Bioerosion From Land-Based Sources of Pollution. *J. Geophys. Res.*122 (12), 9319–9331. doi:10.1002/2017JC013264

Prouty, N. G., Swarzenski, P. W., Fackrell, J. K., Johannesson, K., and Palmore, C. D. (2017b). Groundwater-derived nutrient and trace element transport to a nearshore Kona coral ecosystem: Experimental mixing model results. *J. Hydrol. Reg. Stud.* 11, 166–177. doi:10.1016/j.ejrh.2015.12.058

Rahman, S., Tamborski, J. J., Charette, M. A., and Cochran, J. K. (2019). Dissolved silica in the subterranean estuary and the impact of submarine groundwater discharge on the global marine silica budget. *Mar. Chem.* 208, 29–42. doi:10.1016/j.marchem.2018.11.006

Rakhimbekova, S., O'Carroll, D. M., Andersen, M. S., Wu, M. Z., and Robinson, C. E. (2018). Effect of Transient Wave Forcing on the Behavior of Arsenic in a Nearshore Aquifer. *Environ. Sci. Technol.* 52 (21), 12338–12348. doi:10.1021/acs.est.8b03659

Rao, A. M. F., and Charette, M. A. (2012). Benthic nitrogen fixation in an eutrophic estuary affected by groundwater discharge. *J. Coast. Res.* 280 (2), 477–485. doi:10.2112/jcoastres-d-11-00057.1

Rasmussen, B., and Josefson, A. B. (2002). Consistent estimates for the residence time of micro-tidal estuaries. *Estuarine Coastal Shelf Sci.* 54 (1), 65–73. doi:10.1006/ecss.2001.0836

Reckhardt, A., Beck, M., Greskowiak, J., Schnetger, B., Böttcher, M. E., Gehre, M., et al. (2017). Cycling of redox-sensitive elements in a sandy subterranean estuary of the southern North Sea. *Mar. Chem.* 188, 6–17. doi:10.1016/j.marchem.2016.11.003

Rickard, D. (1997). Kinetics of pyrite formation by the H2S oxidation of iron (II) monosulfide in aqueous solutions between 25 and 125°C: The rate equation. *Geochim. Cosmochim. Acta* 61 (1), 115–134. doi:10.1016/s0016-7037(96)00321-3

Riechelmann, S., Mavromatis, V., Buhl, D., Dietzel, M., and Immenhauser, A. (2020). Controls on formation and alteration of early diagenetic dolomite: A multi-proxy δ44/40Ca, δ26Mg, δ18O and δ13C approach. *Geochim. Cosmochim. Acta* 283, 167–183. doi:10.1016/j.gca.2020.06.010

Robinson, C., Brovelli, A., Barry, D. A., and Li, L. (2009). Tidal influence on BTEX biodegradation in sandy coastal aquifers. *Adv. Water Resour.* 32 (1), 16–28. doi:10.1016/j.advwatres.2008.09.008

Robinson, C. E., Xin, P., Santos, I. R., Charette, M. A., Li, L., and Barry, D. A. (2017). Groundwater dynamics in subterranean estuaries of coastal unconfined aquifers: Controls on submarine groundwater discharge and chemical inputs to the ocean. *Adv. Water Resour.*

Robinson, C. E., Xin, P., Santos, I. R., Charette, M. A., Li, L., and Barry, D. A. (2018). Groundwater dynamics in subterranean estuaries of coastal unconfined aquifers: Controls on submarine groundwater discharge and chemical inputs to the ocean. *Adv. Water Resour.* 115, 315–331. doi:10.1016/j.advwatres.2017.10.041

Robinson, C., Gibbes, B., and Li, L. (2006). Driving mechanisms for groundwater flow and salt transport in a subterranean estuary. *Geophys. Res. Lett.* 33 (3). doi:10.1029/2005gl025247

Robinson, C., Li, L., and Barry, D. A. (2007). Effect of tidal forcing on a subterranean estuary. *Adv. Water Resour.* 30 (4), 851–865. doi:10.1016/j.advwatres.2006.07.006

Robinson, C., Xin, P., Li, L., and Barry, D. A. (2014). Groundwater flow and salt transport in a subterranean estuary driven by intensified wave conditions. *Water Resour. Res.* 50 (1), 165–181. doi:10.1002/2013wr013813

Rocha, C., Robinson, C. E., Santos, I. R., Waska, H., Michael, H. A., and Bokuniewicz, H. J. (2021). A place for subterranean estuaries in the coastal zone. Estuarine. *Coastal Shelf Sci.* 250, 107167. doi:10.1016/j.ecss.2021.107167

Rocha, C., Veiga-Pires, C., Scholten, J., Knoeller, K., Gröcke, D. R., Carvalho, L., et al. (2016). Assessing land-ocean connectivity via submarine groundwater discharge (SGD) in the Ria Formosa Lagoon (Portugal): combining radon measurements and stable isotope hydrology. *Hydrol. Earth Syst. Sci.* 20 (8), 3077–3098. doi:10.5194/hess-20-3077-2016

Rodellas, V., Garcia-Orellana, J., Masqué, P., Feldman, M., and Weinstein, Y. (2015). Submarine groundwater discharge as a major source of nutrients to the Mediterranean Sea. *Proc. Natl. Acad. Sci. USA* 112 (13), 3926–3930. doi:10.1073/pnas.1419049112

Rodellas, V., Stieglitz, T. C., Tamborski, J. J., van Beek, P., Andrisoa, A., and Cook, P. G. (2021). Conceptual uncertainties in groundwater and porewater fluxes estimated by radon and radium mass balances. *Limnol. Oceanogr.* 11, 676. doi:10.1002/lno.11678

Rogers, D. R., and Casciotti, K. L. (2010). Abundance and diversity of archaeal ammonia oxidizers in a coastal groundwater system. *Appl. Environ. Microbiol.* 76 (24), 7938–7948. doi:10.1128/AEM.02056-09

Röper, T., Kröger, K. F., Meyer, H., Sültenfuss, J., Greskowiak, J., and Massmann, G. (2012). Groundwater ages, recharge conditions and hydrochemical evolution of a barrier island freshwater lens (Spiekeroog, Northern Germany). *J. Hydrol.* 454-455, 173–186. doi:10.1016/j.jhydrol.2012.06.011

Roseen, R. M. (2002). *Quantifying groundwater discharge using thermal imagery and conventional groundwater exploration techniques for estimating the nitrogen loading to a meso-scale inland estuary. Durham.*

Roy, M., Martin, J. B., Cable, J. E., and Smith, C. G. (2013). Variations of iron flux and organic carbon remineralization in a subterranean estuary caused by inter-annual variations in recharge. *Geochim. Cosmochim. Acta* 103, 301–315. doi:10.1016/j.gca.2012.10.055

Roy, M., Martin, J. B., Cherrier, J., Cable, J. E., and Smith, C. G. (2010). Influence of sea level rise on iron diagenesis in an east Florida subterranean estuary. *Geochim. Cosmochim. Acta* 74 (19), 5560–5573. doi:10.1016/j.gca.2010.07.007

Roy, M., Martin, J. B., Smith, C. G., and Cable, J. E. (2011). Reactive-transport modeling of iron diagenesis and associated organic carbon remineralization in a Florida (USA) subterranean estuary. *Earth Planet. Sci. Lett.* 304 (1, 2), 191–201. doi:10.1016/j.epsl.2011.02.002

Rullkötter, J. (2009). The back-barrier tidal flats in the southern North Sea-a multidisciplinary approach to reveal the main driving forces shaping the system. *Ocean Dyn.* 59 (2), 157–165. doi:10.1007/s10236-009-0197-2

Sáenz, J. P., Hopmans, E. C., Rogers, D., Henderson, P. B., Charette, M. A., Schouten, S., et al. (2012). Distribution of anaerobic ammonia-oxidizing bacteria in a subterranean estuary. *Mar. Chem.* 136, 137, 7–13. doi:10.1016/j.marchem.2012.04.004

Salt, D. E., Blaylock, M., Kumar, N. P., Dushenkov, V., Ensley, B. D., Chet, I., et al. (1995). Phytoremediation: a novel strategy for the removal of toxic metals from the environment using plants. *Biotechnology (NY)* 13 (5), 468–474. doi:10.1038/nbt0595-468

Sánchez-Úbeda, J. P., Manuel, L.-C., Calvache, M., Purtschert, R., Engesgaard, P., Martín-Montañés, C., et al. (2018). *Groundwater age dating in motril-salobreña coastal aquifer with environmental tracers 3H/3He, 4He, 85Kr, and 39Ar)*, Spain. Granada. δ18O/δ2H, 287–295.

Sanders, C. J., Santos, I. R., Barcellos, R., and Silva Filho, E. V. (2012). Elevated concentrations of dissolved Ba, Fe and Mn in a mangrove subterranean estuary: Consequence of sea level rise?. *Continental Shelf Res.* 43, 86–94. doi:10.1016/j.csr.2012.04.015

Santoro, A. E., Boehm, A. B., and Francis, C. A. (2006). Denitrifier community composition along a nitrate and salinity gradient in a coastal aquifer. *Appl. Environ. Microbiol.* 72 (3), 2102–2109. doi:10.1128/AEM.72.3.2102-2109.2006

Santoro, A. E., Francis, C. A., de Sieyes, N. R., and Boehm, A. B. (2008). Shifts in the relative abundance of ammonia-oxidizing bacteria and archaea across physicochemical gradients in a subterranean estuary. *Environ. Microbiol.* 10 (4), 1068–1079. doi:10.1111/j.1462-2920.2007.01547.x

Santoro, A. E. (2010). Microbial nitrogen cycling at the saltwater-freshwater interface. *Hydrogeol J.* 18 (1), 187–202. doi:10.1007/s10040-009-0526-z

Santos, I. R., Beck, M., Brumsack, H.-J., Maher, D. T., Dittmar, T., Waska, H., et al. (2015). Porewater exchange as a driver of carbon dynamics across a terrestrial-marine transect: Insights from coupled 222Rn and pCO2 observations in the German Wadden Sea. *Mar. Chem.* 171, 10–20. doi:10.1016/j.marchem.2015.02.005

Santos, I. R., Burnett, W. C., Chanton, J., Dimova, N., and Peterson, R. N. (2009a). Land or ocean?: Assessing the driving forces of submarine groundwater discharge at a coastal site in the Gulf of Mexico. *J. Geophys. Res.-Oceans* 114, 11. doi:10.1029/2008jc005038

Santos, I. R., Burnett, W. C., Dittmar, T., Suryaputra, I. G. N. A., and Chanton, J. (2009b). Tidal pumping drives nutrient and dissolved organic matter dynamics in a Gulf of Mexico subterranean estuary. *Geochim. Cosmochim. Acta* 73 (5), 1325–1339. doi:10.1016/j.gca.2008.11.029

Santos, I. R., Dimova, N., Peterson, R. N., Mwashote, B., Chanton, J., and Burnett, W. C. (2009c). Extended time series measurements of submarine groundwater discharge tracers (222Rn and CH4) at a coastal site in Florida. *Mar. Chem.* 113 (1, 2), 137–147. doi:10.1016/j.marchem.2009.01.009

Santos, I. R., Eyre, B. D., and Huettel, M. (2012). The driving forces of porewater and groundwater flow in permeable coastal sediments: a review. *Estuarine Coastal Shelf Sci.* 98, 1–15. doi:10.1016/j.ecss.2011.10.024

Santos, I. R. S., Burnett, W. C., Chanton, J., Mwashote, B., Suryaputra, I. G. N. A., and Dittmar, T. (2008). Nutrient biogeochemistry in a Gulf of Mexico subterranean estuary and groundwater-derived fluxes to the coastal ocean. *Limnol. Oceanogr.* 53 (2), 705. doi:10.4319/lo.2008.53.2.0705

Sawyer, A. H., David, C. H., and Famiglietti, J. S. (2016). Continental patterns of submarine groundwater discharge reveal coastal vulnerabilities. *Science* 353 (6300), 705–707. doi:10.1126/science.aag1058

Sayre, R., Noble, S., Hamann, S., Smith, R., Wright, D., Breyer, S., et al. (2018). A new 30 meter resolution global shoreline vector and associated global islands database for the development of standardized ecological coastal units. *J. Oper. Oceanogr.*, 12, 1–10. doi:10.1080/1755876X.2018.1529714

Schlüter, M., Sauter, E. J., Andersen, C. E., Dahlgaard, H., and Dando, P. R. (2004). Spatial distribution and budget for submarine groundwater discharge in Eckernförde Bay (Western Baltic Sea). *Limnol. Oceanogr.* 49 (1), 157–167. doi:10.4319/lo.2004.49.1.0157

Schofield, O., Glenn, S., Bissett, P. W., Frazer, T. K., Iglesias-Rodriguez, D., and Moline, M. A. (2003). Development of regional coastal ocean observatories and the potential benefits to marine sanctuaries. *Mar. Technol. Soc. J* 37 (1), 54–67. doi:10.4031/002533203787537456

Schubert, M., Petermann, E., Stollberg, R., Gebel, M., Scholten, J., Knöller, K., et al. (2019). Improved approach for the investigation of submarine groundwater discharge by means of radon mapping and radon mass balancing. *Water* 11 (4), 749. doi:10.3390/w11040749

Schubert, M., Scholten, J., Schmidt, A., Comanducci, J., Pham, M., Mallast, U., et al. (2014). Submarine groundwater discharge at a single spot location: evaluation of different detection approaches. *Water* 6 (3), 584–601. doi:10.3390/w6030584

Schutte, C. A., Wilson, A. M., Evans, T., Moore, W. S., and Joye, S. B. (2016). Methanotrophy controls groundwater methane export from a barrier island. *Geochim. Cosmochim. Acta* 179, 242–256. doi:10.1016/j.gca.2016.01.022

Seibert, S. L., Greskowiak, J., Prommer, H., Böttcher, M. E., and Massmann, G. (2019). Modeling of biogeochemical processes in a barrier island freshwater lens (Spiekeroog, Germany). *J. Hydrol.* 575, 1133–1144. doi:10.1016/j.jhydrol.2019.05.094

Seidel, M., Beck, M., Greskowiak, J., Riedel, T., Waska, H., Suryaputra, I. N. A., et al. (2015). Benthic-pelagic coupling of nutrients and dissolved organic matter composition in an intertidal sandy beach. *Mar. Chem.* 176, 150–163. doi:10.1016/j.marchem.2015.08.011

Shaban, A., Khawlie, M., Abdallah, C., and Faour, G. (2005). Geologic controls of submarine groundwater discharge: application of remote sensing to north Lebanon. *Environ. Geol.* 47 (4), 512–522. doi:10.1007/s00254-004-1172-3

Sharp, Z. D., Wostbrock, J. A. G., and Pack, A. (2018). Mass-dependent triple oxygen isotope variations in terrestrial materials. *Geochem. Persp. Let.* 7, 27–31. doi:10.7185/geochemlet.1815

Shum, K. T., and Sundby, B. (1996). Organic matter processing in continental shelf sediments - The subtidal pump revisited. *Mar. Chem.* 53 (1, 2), 81–87. doi:10.1016/0304-4203(96)00014-x

Siemon, B., Auken, E., and Christiansen, A. V. (2009). Laterally constrained inversion of helicopter-borne frequency-domain electromagnetic data. *J. Appl. Geophys.* 67 (3), 259–268. doi:10.1016/j.jappgeo.2007.11.003

Siemon, B., Costabel, S., Voss, W., Meyer, U., Deus, N., Elbracht, J., et al. (2015). Airborne and ground geophysical mapping of coastal clays in Eastern Friesland, Germany. *Geophysics* 80 (3), Wb21–Wb34. doi:10.1190/geo2014-0102.1

Siemon, B., Ibs-von Seht, M., Steuer, A., Deus, N., and Wiederhold, H. (2020). Airborne Electromagnetic, Magnetic, and Radiometric Surveys at the German North Sea Coast Applied to Groundwater and Soil Investigations. *Remote Sensing* 12 (10). doi:10.3390/rs12101629

Siemon, B., van Baaren, E., Dabekaussen, W., Delsman, J., Dubelaar, W., Karaoulis, M., et al. (2019). Automatic identification of fresh-saline groundwater interfaces from airborne electromagnetic data in Zeeland, the The Netherlands. *Near Surf. Geophys.* 17 (1), 3–25.

Siermann, J., Harvey, C., Morgan, G., and Heege, T. (2014). *Satellite derived bathymetry and digital elevation models (DEM), international petroleum technology conference*. Qatar: International Petroleum Technology ConferenceDoha, 10.

Sippo, J. Z., Maher, D. T., Tait, D. R., Holloway, C., and Santos, I. R. (2016). Are mangroves drivers or buffers of coastal acidification? Insights from alkalinity and dissolved inorganic carbon export estimates across a latitudinal transect. *Glob. Biogeochem. Cycles* 30 (5), 753–766. doi:10.1002/2015gb005324

Sirois, M., Couturier, M., Barber, A., Gélinas, Y., and Chaillou, G. (2018). Interactions between iron and organic carbon in a sandy beach subterranean estuary. *Mar. Chem.* 202, 86–96. doi:10.1016/j.marchem.2018.02.004

Slomp, C. P., and Van Cappellen, P. (2004). Nutrient inputs to the coastal ocean through submarine groundwater discharge: controls and potential impact. *J. Hydrol.* 295 (1–4), 64–86. doi:10.1016/j.jhydrol.2004.02.018

Spiteri, C., Cappellen, P. V., and Regnier, P. (2008a). Surface complexation effects on phosphate adsorption to ferric iron oxyhydroxides along pH and salinity gradients in estuaries and coastal aquifers. *Geochim. Cosmochim. Acta* 72 (14), 3431–3445. doi:10.1016/j.gca.2008.05.003

Spiteri, C., Regnier, P., Slomp, C. P., and Charette, M. A. (2006). pH-Dependent iron oxide precipitation in a subterranean estuary. *J. Geochem. Explorat.* 88 (1–3), 399–403. doi:10.1016/j.gexplo.2005.08.084

Spiteri, C., Slomp, C. P., Charette, M. A., Tuncay, K., and Meile, C. (2008b). Flow and nutrient dynamics in a subterranean estuary (Waquoit Bay, MA, USA): Field data and reactive transport modeling. *Geochim. Cosmochim. Acta* 72 (14), 3398–3412. doi:10.1016/j.gca.2008.04.027

Spiteri, C., Slomp, C. P., Tuncay, K., and Meile, C. (2008c). Modeling biogeochemical processes in subterranean estuaries: Effect of flow dynamics and redox conditions on submarine groundwater discharge of nutrients. *Water Resour. Res.* 44 (2), 18. doi:10.1029/2007wr006071

Steuer, A., Siemon, B., and Auken, E. (2009). A comparison of helicopter-borne electromagnetics in frequency- and time-domain at the Cuxhaven valley in Northern Germany. *J. Appl. Geophys.* 67 (3), 194–205. doi:10.1016/j.jappgeo.2007.07.001

Stieglitz, T. C., Cook, P. G., and Burnett, W. C. (2010). Inferring coastal processes from regional-scale mapping of 222Radon and salinity: examples from the Great Barrier Reef, Australia. *J. Environ. Radioact* 101 (7), 544–552. doi:10.1016/j.jenvrad.2009.11.012

Stieglitz, T. (2005). Submarine groundwater discharge into the near-shore zone of the Great Barrier Reef, Australia. *Mar. Pollut. Bull.* 51 (1–4), 51–59. doi:10.1016/j.marpolbul.2004.10.055

Straume, E. O., Gaina, C., Medvedev, S., Hochmuth, K., Gohl, K., Whittaker, J. M., et al. (2019). GlobSed: Updated Total Sediment Thickness in the World's Oceans. *Geochem. Geophys. Geosyst.* 20 (4), 1756–1772. doi:10.1029/2018gc008115

Sugimoto, R., Kitagawa, K., Nishi, S., Honda, H., Yamada, M., Kobayashi, S., et al. (2017). Phytoplankton primary productivity around submarine groundwater discharge in nearshore coasts. *Mar. Ecol. Prog. Ser.* 563, 25–33. doi:10.3354/meps11980

Sültenfuss, J., Roether, W., and Rhein, M. (2009). The Bremen mass spectrometric facility for the measurement of helium isotopes, neon, and tritium in water. *Isotopes Environ. Health Stud.* 45 (2), 83–95.

Sutter, E., and Ingham, M. (2017). Seasonal saline intrusion monitoring of a shallow coastal aquifer using time-lapse DC resistivity traversing. *Near Surf. Geophys.* 15 (1), 59–73. doi:10.3997/1873-0604.2016039

Suzumura, M., Ueda, S., and Sumi, E. (2000). Control of phosphate concentration through adsorption and desorption processes in groundwater and seawater mixing at sandy beaches in Tokyo Bay, Japan. *J. Oceanogr.* 56 (6), 667–673. doi:10.1023/a:1011125700301

Swarzenski, P. W., Burnett, W. C., Greenwood, W. J., Herut, B., Peterson, R., Dimova, N., et al. (2006). Combined time-series resistivity and geochemical tracer techniques to examine submarine groundwater discharge at Dor Beach, Israel. *Geophys. Res. Lett.* 33 (24), 6. doi:10.1029/2006gl028282

Szymczycha, B., Vogler, S., and Pempkowiak, J. (2012). Nutrient fluxes via submarine groundwater discharge to the Bay of Puck, southern Baltic Sea. *Sci. Total Environ.* 438, 86–93. doi:10.1016/j.scitotenv.2012.08.058

Tamborski, J. J., Cochran, J. K., and Bokuniewicz, H. J. (2017). Application of 224Ra and 222Rn for evaluating seawater residence times in a tidal subterranean estuary. *Mar. Chem.* 189, 32–45. doi:10.1016/j.marchem.2016.12.006

Tamborski, J. J., Rogers, A. D., Bokuniewicz, H. J., Cochran, J. K., and Young, C. R. (2015). Identification and quantification of diffuse fresh submarine groundwater discharge via airborne thermal infrared remote sensing. *Remote Sensing Environ.* 171, 202–217. doi:10.1016/j.rse.2015.10.010

Taniguchi, M., Burnett, W. C., Cable, J. E., and Turner, J. V. (2002). Investigation of submarine groundwater discharge. *Hydrol. Process* 16 (11), 2115–2129. doi:10.1002/hyp.1145

Taniguchi, M., Dulai, H., Burnett, K. M., Santos, I. R., Sugimoto, R., Stieglitz, T., et al. (2019). Submarine Groundwater Discharge: Updates on Its Measurement Techniques, Geophysical Drivers, Magnitudes, and Effects. *Front. Environ. Sci.* 7 (14), 141. doi:10.3389/fenvs.2019.00141

Tao, Y., Deng, Y., Du, Y., Xu, Y., Leng, Z., Ma, T., et al. (2020). Sources and enrichment of phosphorus in groundwater of the Central Yangtze River Basin. *Sci. Total Environ.* 737, 139837. doi:10.1016/j.scitotenv.2020.139837

Teubner, P. P., Breier, R., Coppola, L., Groening, M., Jeandel, C., Jull, A. J. T., et al. (2011). Tracing of water masses using a multi isotope approach in the southern Indian Ocean. *Earth Planet. Sci. Lett.* 302 (1-2), 14–26. doi:10.1016/j.epsl.2010.11.026

Tholen, C., Nolle, L., and Werner, J. (2019). "On the Influence of Localisation and Communication Error on the Behaviour of a Swarm of Autonomous Underwater Vehicles", in *Recent advances in soft computing*. Cham: Springer International Publishing, 68–79.

Tiedje, J. M. (1988). Ecology of denitrification and dissimilatory nitrate reduction to ammonium. *Biol. anaerobic Microorg.* 717, 179–244.

Tolstikhin, I. N., and Kamenskii, I. L. (1969). Determination of groundwater age by the T- 3He method. *Geochem. Int.* 6, 810–811.

Tréguer, P. J., and De La Rocha, C. L. (2013). The World Ocean Silica Cycle. *Annu. Rev. Mar. Sci.* 5 (1), 477–501. doi:10.1146/annurev-marine-121211-172346

Tyler, R. H., Boyer, T. P., Minami, T., Zweng, M. M., and Reagan, J. R. (2017). Electrical conductivity of the global ocean. *Earth Planets Space* 69 (1), 156. doi:10.1186/s40623-017-0739-7

Uchiyama, Y., Nadaoka, K., Rölke, P., Adachi, K., and Yagi, H. (2000). Submarine groundwater discharge into the sea and associated nutrient transport in a sandy beach. *Water Resour. Res.* 36 (6), 1467–1479. doi:10.1029/2000wr900029

Ullman, W. J., Chang, B., Miller, D. C., and Madsen, J. A. (2003). Groundwater mixing, nutrient diagenesis, and discharges across a sandy beachface, Cape Henlopen, Delaware (USA). *Estuarine, Coastal Shelf Sci.* 57 (3), 539–552. doi:10.1016/s0272-7714(02)00398-0

Utsunomiya, T., Hata, M., Sugimoto, R., Honda, H., Kobayashi, S., Miyata, Y., et al. (2017). Higher species richness and abundance of fish and benthic invertebrates around submarine groundwater discharge in Obama Bay, Japan. *J. Hydrol. Reg. Stud.* 11, 139–146. doi:10.1016/j.ejrh.2015.11.012

Vahtmäe, E., Paavel, B., and Kutser, T. (2020). How much benthic information can be retrieved with hyperspectral sensor from the optically complex coastal waters?. *J. Appl. Remote Sensing* 14 (1), 016504. doi:10.1117/1.jrs.14.016504

van der Grift, B., Rozemeijer, J. C., Griffioen, J., and van der Velde, Y. (2014). Iron oxidation kinetics and phosphate immobilization along the flow-path from groundwater into surface water. *Hydrol. Earth Syst. Sci.* 18, 4687–4702. doi:10.5194/hess-18-4687-2014

Van Ryswyk, M. (2020). *Planet announces 50 cm SkySat imagery, tasking dashboard and up to 12x* Available:https://www.planet.com/pulse/tasking-dashboard-50cm-12x-revisit-announcement/.Revisit Planet News.

Vidon, P., Allan, C., Burns, D., Duval, T. P., Gurwick, N., Inamdar, S., et al. (2010). Hot Spots and Hot Moments in Riparian Zones: Potential for Improved Water Quality Management1. *JAWRA J. Am. Water Resour. Assoc.* 46 (2), 278–298. doi:10.1111/j.1752-1688.2010.00420.x

Virtasalo, J. J., Schröder, J. F., Luoma, S., Majaniemi, J., Mursu, J., and Scholten, J. (2019). Submarine groundwater discharge site in the First Salpausselkä ice-marginal formation, south Finland. *Solid Earth* 10 (2), 405–423. doi:10.5194/se-10-405-2019

Wang, B., Zhang, X., Luan, Z., Chen, C. A., and Yan, J. (2018). Seabed domes with circular depressions in the North Yellow Sea. *J. Ocean. Limnol.* 36 (6), 2154–2165. doi:10.1007/s00343-019-7173-6

Wang, D., Lin, W., Yang, X., Zhai, W., Dai, M., and Arthur Chen, C.-T. (2012). Occurrences of dissolved trace metals (Cu, Cd, and Mn) in the Pearl River Estuary (China), a large river-groundwater-estuary system. *Continental Shelf Res.* 50–51, 54–63. doi:10.1016/j.csr.2012.10.009

Wang, G., Jing, W., Wang, S., Xu, Y., Wang, Z., Zhang, Z., et al. (2014). Coastal Acidification Induced by Tidal-Driven Submarine Groundwater Discharge in a Coastal Coral Reef System. *Environ. Sci. Technol.* 48 (22), 13069–13075. doi:10.1021/es5026867

Wang, G., Wang, Z., Zhai, W., Moore, W. S., Li, Q., Yan, X., et al. (2015). Net subterranean estuarine export fluxes of dissolved inorganic C, N, P, Si, and total alkalinity into the Jiulong River estuary, China. *Geochimica Et Cosmochimica Acta* 149, 103–114. doi:10.1016/j.gca.2014.11.001

Waska, H., Brumsack, H.-J., Massmann, G., Koschinsky, A., Schnetger, B., Simon, H., et al. (2019a). Inorganic and organic iron and copper species of the subterranean estuary: Origins and fate. *Geochim. Cosmochim. Acta* 259, 211–232. doi:10.1016/j.gca.2019.06.004

Waska, H., Greskowiak, J., Ahrens, J., Beck, M., Ahmerkamp, S., Böning, P., et al. (2019b). Spatial and temporal patterns of pore water chemistry in the inter-tidal zone of a high energy beach. *Front. Mar. Sci.* 6 (154), 12. doi:10.3389/fmars.2019.00154

Waska, H., and Kim, G. (2010). Differences in microphytobenthos and macrofaunal abundances associated with groundwater discharge in the intertidal zone. *Mar. Ecol. Prog. Ser.* 407, 159–172. doi:10.3354/meps08568

Waska, H., and Kim, G. (2011). Submarine groundwater discharge (SGD) as a main nutrient source for benthic and water-column primary production in a large intertidal environment of the Yellow Sea. *J. Sea Res.* 65 (1), 103–113. doi:10.1016/j.seares.2010.08.001

Webb, J. R., Santos, I. R., Maher, D. T., Tait, D. R., Cyronak, T., Sadat-Noori, M., et al. (2019). Groundwater as a source of dissolved organic matter to coastal waters: Insights from radon and CDOM observations in 12 shallow coastal systems. *Limnol. Oceanogr.* 64 (1), 182–196. doi:10.1002/lno.11028

Webster, I. T., Hancock, G. J., and Murray, A. S. (1994). Use of Radium Isotopes to Examine Pore-Water Exchange in an Estuary. *Limnol. Oceanogr.* 39 (8), 1917–1927. doi:10.4319/lo.1994.39.8.1917

Weinstein, Y., Yechieli, Y., Shalem, Y., Burnett, W. C., Swarzenski, P. W., and Herut, B. (2011). What is the role of fresh groundwater and recirculated seawater in conveying nutrients to the Coastal Ocean? *Environ. Sci. Technol.* 45 (12), 5195–5200. doi:10.1021/es104394r

Weinstein, Y., Burnett, W. C., Swarzenski, P. W., Shalem, Y., Yechieli, Y., and Herut, B. (2007). Role of aquifer heterogeneity in fresh groundwater discharge and seawater recycling: An example from the Carmel coast, Israel. *J. Geophys. Res.-Oceans* 112 (C12), 12. doi:10.1029/2007jc004112

Welti, N., Gale, D., Hayes, M., Kumar, A., Gasparon, M., Gibbes, B., et al. (2015). Intertidal diatom communities reflect patchiness in groundwater discharge. *Estuarine, Coastal Shelf Sci.* 163, 116–124.doi:10.1016/j.ecss.2015.06.006

Weschenfelder, J., Klein, A. H. F., Green, A. N., Aliotta, S., de Mahiques, M. M., Ayres Neto, A., et al. (2016). The control of palaeo-topography in the preservation of shallow gas accumulation: Examples from Brazil, Argentina and South Africa. *Estuarine Coastal Shelf Sci.* 172, 93–107. doi:10.1016/j.ecss.2016.02.005

Whiticar, M. J. (2002). Diagenetic relationships of methanogenesis, nutrients, acoustic turbidity, pockmarks and freshwater seepages in Eckernforde Bay. *Mar. Geol.* 182 (1, 2), 29–53. doi:10.1016/s0025-3227(01)00227-4

Whiticar, M. J., and Werner, F. (1981). Pockmarks: Submarine vents of natural gas or freshwater seeps?. *Geo-Marine Lett.* 1 (3), 193–199. doi:10.1007/bf02462433

Wigley, T. M. L., Plummer, L. N., and Pearson, F. J. (1978). Mass transfer and carbon isotope evolution in natural water systems. *Geochim. Cosmochim. Acta* 42 (8), 1117–1139. doi:10.1016/0016-7037(78)90108-4

Wilford, J., Bierworth, P. N., and Pearson, M. A., C. (1997). Application of airborne gamma ray spectrometry in soil/regolith mapping. *J. Aust. Geol. Geophys.* 17, 201–216.

Wilson, J., and Rocha, C. (2012). Regional scale assessment of Submarine groundwater discharge in Ireland combining medium resolution satellite imagery and geochemical tracing techniques. *Remote Sensing Environ.* 119 (0), 21–34. doi:10.1016/j.rse.2011.11.018

Winde, V., Böttcher, M. E., Voss, M., and Mahler, A. (2017). Bladder wrack (Fucus vesiculosus) as a multi-isotope bio-monitor in an urbanized fjord of the western Baltic Sea. *Isotopes Environ. Health Stud.* 53 (6), 563–579. doi:10.1080/10256016.2017.1316980

Winde, V., Böttcher, M. E., Escher, P., Böning, P., Beck, M., Liebezeit, G., et al. (2014). Tidal and spatial variations of DI^{13}C and aquatic chemistry in a temperate tidal basin during winter time. *J. Mar. Syst.* 129, 396–404. doi:10.1016/j.jmarsys.2013.08.005

Wolanski, E., (2007). *Estuarine ecohydrology*. Amsterdam; Oxford, Elsevier, xi, 157.

Wong, W. W., Applegate, A., Poh, S. C., and Cook, P. L. M. (2020). Biogeochemical attenuation of nitrate in a sandy subterranean estuary: insights from two stable isotope approaches. *Limnol Oceanogr* 65 (12), 3098–3113. doi:10.1002/lno.11576

Wunderlich, T., Fischer, P., Wilken, D., Hadler, H., Erkul, E., Mecking, R., et al. (2018). Constraining electric resistivity tomography by direct push electric conductivity logs and vibracores: an exemplary study of the Fiume Morto silted riverbed (Ostia Antica, western Italy). *Geophysics* 83 (3), B87–B103. doi:10.1190/geo2016-0660.1

Xing, Q., Braga, F., Tosi, L., Lou, M., Zaggia, L., Teatini, P., et al. (2016). Detection of low salinity groundwater seeping into the Eastern Laizhou Bay (China) with the aid of landsat thermal data. *J. Coastal Res.* 74, 149–156. doi:10.2112/si74-014.1

Yang, L., Chen, C.-T. A., Hong, H., Chang, Y.-C., and Lui, H.-K. (2015). Mixing behavior and bioavailability of dissolved organic matter in two contrasting subterranean estuaries as revealed by fluorescence spectroscopy and parallel factor analysis. *Estuarine Coastal Shelf Sci.* 166, 161–169. doi:10.1016/j.ecss.2014.10.018

Zamrsky, D., Karssenberg, M. E., Cohen, K. M., Bierkens, M. F. P., and Oude Essink, G. H. P. (2020). Geological heterogeneity of coastal unconsolidated groundwater systems worldwide and its influence on offshore fresh groundwater occurrence. *Front. Earth Sci.* 7 (339). doi:10.3389/feart.2019.00339

Zhang, Y.-C., Slomp, C. P., Broers, H. P., Bostick, B., Passier, H. F., Böttcher, M. E., et al. (2012). Isotopic and microbiological signatures of pyrite-driven denitrification in a sandy aquifer. *Chem. Geol.* 300–301, 123–132. doi:10.1016/j.chemgeo.2012.01.024

Zhou, Y., Sawyer, A. H., David, C. H., and Famiglietti, J. S. (2019). Fresh submarine groundwater discharge to the near-global coast. *Geophys. Res. Lett.* 46, 5855–5863. doi:10.1029/2019gl082749

Zipperle, A., and Reise, K. (2005). Freshwater springs on intertidal sand flats cause a switch in dominance among polychaete worms. *J. Sea Res.* 54 (2), 143–150. doi:10.1016/j.seares.2005.01.003

Conflict of Interest: The authors declare that the research was conducted in the absence of any commercial or financial relationships that could be construed as a potential conflict of interest.

Copyright © 2021 Moosdorf, Böttcher, Adyasari, Erkul, Gilfedder, Greskowiak, Jenner, Kotwicki, Massmann, Müller-Petke, Oehler, Post, Prien, Scholten, Siemon, Ehlert von Ahn, Walther, Waska, Wunderlich and Mallast. This is an open-access article distributed under the terms of the Creative Commons Attribution License (CC BY). The use, distribution or reproduction in other forums is permitted, provided the original author(s) and the copyright owner(s) are credited and that the original publication in this journal is cited, in accordance with accepted academic practice. No use, distribution or reproduction is permitted which does not comply with these terms.

frontiers in Earth Science

REVIEW
published: 08 April 2021
doi: 10.3389/feart.2021.600710

Saltwater Intrusion and Submarine Groundwater Discharge: Acceleration of Biogeochemical Reactions in Changing Coastal Aquifers

Willard S. Moore[1]* *and Samantha B. Joye*[2]

[1] School of the Earth, Ocean and Environment, College of Arts and Sciences, University of South Carolina, Columbia, SC, United States, [2] Department of Marine Sciences, Franklin College of Arts and Sciences, University of Georgia, Athens, GA, United States

Intrusion of saltwater into freshwater coastal aquifers poisons an essential resource. Such intrusions are occurring along coastlines worldwide due largely to the over-pumping of freshwater and sea level rise. Saltwater intrusion impacts drinking water, agriculture and industry, and causes profound changes in the biogeochemistry of the affected aquifers, the dynamic systems called subterranean estuaries. Subterranean estuaries receive freshwater from land and saltwater from the ocean and expose this fluid mixture to intense biogeochemical dynamics as it interacts with the aquifer and aquiclude solids. Increased saltwater intrusion alters the ionic strength and oxidative capacity of these systems, resulting in elevated concentrations of certain chemical species in the groundwater, which flows from subterranean estuaries into the ocean as submarine groundwater discharge (SGD). These highly altered fluids are enriched in nutrients, carbon, trace gases, sulfide, metals, and radionuclides. Seawater intrusion expands the subterranean estuary. Climate change amplifies sea level variations on short and seasonal time scales. These changes may result in higher SGD fluxes, further accelerating release of nutrients and thus promoting biological productivity in nutrient-depleted waters. But this process may also adversely affect the environment and alter the local ecology. Research on saltwater intrusion and SGD has largely been undertaken by different groups. We demonstrate that these two processes are linked in ways that neither group has articulated effectively to date.

Keywords: saltwater intrusion, submarine groundwater discharge, subterranean estuary, coastal aquifer, nutrient dynamics, sulfate reduction

OPEN ACCESS

Edited by:
Hannelore Waska, University of Oldenburg, Germany

Reviewed by:
William Patrick Gilhooly III, Indiana University–Purdue University Indianapolis, United States
Vincent Post, Federal Institute For Geosciences and Natural Resources, Germany

***Correspondence:**
Willard S. Moore
moore@geol.sc.edu

Specialty section:
This article was submitted to Biogeoscience, a section of the journal Frontiers in Earth Science

Received: *30 August 2020*
Accepted: *18 March 2021*
Published: *08 April 2021*

Citation:
Moore WS and Joye SB (2021) Saltwater Intrusion and Submarine Groundwater Discharge: Acceleration of Biogeochemical Reactions in Changing Coastal Aquifers. Front. Earth Sci. 9:600710. doi: 10.3389/feart.2021.600710

INTRODUCTION: SALTWATER INTRUSION AND SUBMARINE GROUNDWATER DISCHARGE

Saltwater intrusion, the landward excursion of seawater in coastal aquifers, has been recognized since the 19th century as water in impacted aquifers became non-potable (Werner and Simmons, 2009). Extensive efforts have aimed to understand and eliminate this problem; nevertheless, groundwater salinization is accelerating along many coastlines. The primary cause of saltwater

intrusion is over-pumping of fresh groundwater from coastal aquifers, thereby reducing the hydrostatic pressure and drawing saltwater into the aquifer. The source of the saltwater may be the ocean or relic saltwater residing deeper in the aquifer or in an adjacent aquifer. As little as 1% seawater will render groundwater non-potable by taste.

Besides over-pumping, other factors exacerbate saltwater intrusion. Sea level rise alters the hydrostatic balance between the aquifer and the coastal ocean. A massive sea level rise at the end of the last glacial period inundated continental shelves worldwide and drove seawater into coastal aquifers. On a coastal plain with a slope of 1:1000, a 10 cm rise in sea level can lead to a 100 m inland intrusion of seawater into the aquifer (Werner and Simmons, 2009). Future sea level rise of a meter or more during this century (Hansen et al., 2016) will further intensify the expansion. Processes that channel precipitation into surface runoff rather than groundwater recharge also exacerbate saltwater intrusion. These processes include canal construction to drain freshwater coastal wetlands, sewers to drain golf courses, and the replacement of permeable surfaces with impermeable surfaces linked to sewers, e.g., roads, parking lots, buildings. Additionally, pier and bridge construction, installation of pilings for buildings, and harbor dredging may breach confining layers above coastal aquifers, allowing seawater to invade the aquifer. These human impacts are significantly altering coastal aquifers across the globe, accelerating saltwater intrusion at unprecedented–and largely unrealized–rates (Werner et al., 2013).

Most of the concern with saltwater intrusion focuses on the universal needs of local populations for potable water as well as demands from industry and agriculture for freshwater. As such they focus on sodium and chloride. Here we examine additional consequences of saltwater intrusion into coastal aquifers, namely desorption of adsorbed ions and the plethora of reactions linked to sulfate reduction.

During the past 25 years, considerable research, (summarized by Burnett et al., 2003; Moore, 2010; Jiao and Post, 2019), has advanced knowledge of the regulation, dynamics, and biogeochemical importance of submarine groundwater discharge (SGD). Bratton (2010) described three scales of SGD including nearshore and embayment scale processes as well as discharge throughout the continental shelf. Though SGD and seawater intrusion may seem intuitively to be opposing processes, Taniguchi et al. (2006) recognized that they are, in fact, complementary. Much of the seawater that intrudes into the aquifer actively circulates between the aquifer and the ocean in response to periodic forcing functions, including tides (Moore et al., 2002; Robinson et al., 2007), storms (Wilson et al., 2011), persistent wind events (George et al., 2020), seasonality in precipitation and recharge (Michael et al., 2005), seasonality in sea level (Wahl et al., 2014), and seasonality in freshwater withdrawal (Moore, 1999). The water discharging as SGD has a radically different chemical signature compared to the fresh or saltwater that entered the aquifer (Moore, 1999, 2010). Thus, SGD is not simply fresh groundwater flowing into the ocean; instead, it represents a mixture of saltwater and freshwater containing the byproducts of intense biogeochemical reactions between the fluids and aquifer solids.

SUBTERRANEAN ESTUARIES

To emphasize the processes of saltwater-freshwater circulation and reactions with aquifer solids, these affected coastal aquifers are called subterranean estuaries (Moore, 1999). The concept of subterranean estuaries frames coastal aquifers as a dynamic biogeochemical analog of surface estuaries, where fresh water, particles and ocean water mix, fueling a plethora of biogeochemical dynamics and generating unique biogeochemical signatures. Fluids within subterranean estuaries become enriched in the products of biogeochemical reactions, including nutrients, carbon (dissolved inorganic and organic), hydrogen sulfide and other trace gasses, reduced metals, and radionuclides (Moore, 2010). Through SGD, these dramatically altered fluids are delivered to surface estuaries and the coastal ocean. Well over 100 studies focusing on the role of SGD in supplying nutrients, carbon, and metals to coastal waters have concluded, in large part, that SGD is a more important source of these materials than local rivers (Moore, 2010).

Moore (1999) coined the term "subterranean estuary" to help explain why the circulation of seawater through coastal aquifers was important. At the time many scientists equated SGD with subsurface flow of freshwater into the ocean. In a comment to Moore (1996); Younger (1996) argued that if SGWD (now called SGD) is largely of marine origin, its input to the ocean is "unremarkable." Because there is a vast estuarine literature, it is easy to convey why the circulation of brackish water within a surface estuary is important: It creates unique environments for a wide array of organisms and accelerates biogeochemical processes. By tapping into the estuarine literature, Moore (1999) was able to convey the importance of circulation through the subterranean estuary and the reactions of salty groundwater with the solids in the system, thereby creating unique environments rich in nutrients, carbon and metals. This concept drew the attention of coastal scientists and many chose to explore this system.

Some have argued that there is no need for the term "subterranean estuary" because this term is already described by hydrologists as a "transition zone" within a coastal aquifer (Jiao and Post, 2019). They consider the term "confusing and misleading" by wrongly stating that subterranean estuary means "subsurface river mouth." The confusion is due to their misunderstanding of the term "estuary," which they claim must be located at a river mouth. This is not the case. The most widely used definition of estuary by scientists who study them is: *"A semi-enclosed coastal body of water which has a free connection with the open sea and within which seawater is measurably diluted with fresh water derived from land drainage"* (Pritchard, 1967). Thus, a coastal bay that has measurable freshwater land drainage is considered an estuary; a river is not required. Of the four geomorphologic classes of estuaries (Duxbury, 1977; Saegar, 2012), three do not necessarily occur at river mouths. Bar-built estuaries are semi-confined by offshore islands or sandbars.

They usually have low surface freshwater flow and high SGD flow, such as Pamlico and Albemarle Sounds along the North Carolina, United States, coast and Port Royal Sound on the South Carolina, United States, coast (Crotwell and Moore, 2003). Fjords are associated with coastlines where glaciers scoured deep valleys during low sea level stands. Continued glacial melt on the surrounding countryside and in some cases river input dilutes the fjord salinity. Fjords abound on the Greenland and Scandinavia coasts. Tectonic estuaries such as San Francisco Bay may or may not be associated with a river mouth. With the increased recognition of SGD, Conley et al. (2000) proposed redefining an estuary as "*a partially enclosed body of water open to saline water from the sea and receiving freshwater from rivers, land run-off or seepage*." On Hawaii there are few significant rivers, but there are many estuaries including harbors, coves and fishponds that derive freshwater from SGD (Johnson et al., 2008; Adolf et al., 2019). Equating surface estuaries with river mouths is incorrect. By extension a subterranean estuary need not be located only at a river mouth.

In addition to "transition zone" Jiao and Post (2019) suggested that the term "mixing zone" or "coastal aquifer" would be adequate to describe the system. Duque et al. (2020) proposed changing the term "subterranean estuary" to "subterranean mixing and reaction field." We do not advocate these changes. The significant problem in abandoning the term "subterranean estuary" would be to lose the connection to the rich estuarine literature that has described physical, chemical and biological processes that occur in this distinctive geological environment. In elementary oceanography texts (e.g., Duxbury, 1977; Saegar, 2012) students learn that estuaries are classified by morphology and by circulation. The circulation is primarily an interplay between the freshwater flow and tidal energy. These forces control the residence time of water in most surface estuaries, a critical parameter that modulates their biogeochemistry. Framing the subterranean estuary in these terms immediately conveys the importance of circulation in a way that "coastal aquifer," "mixing zone," "transition zone," or "subterranean mixing and reaction field" do not. We agree with Rocha et al. (2021) who "strongly advocate for the inclusion of subterranean estuaries as essential components of coastal ecosystem function research, monitoring, policy and management."

Robinson et al. (2007) introduced a classification system for subterranean estuaries based on salinity stratification (stratified, partially stratified, or well-mixed), a system widely used in surface estuaries where freshwater flow (Q_f) as a fraction of the tidal prism (Q_t) largely determines stratification. Substituting fresh groundwater flow for surface freshwater flow, they found that when Q_f/Q_t was >1.0 the subterranean estuary was stratified. When Q_f/Q_t was between 0.1 and 1 the subterranean estuary was partially stratified and when Q_f/Q_t was <0.1, the subterranean estuary was well mixed. They pointed out that Schultz and Simmons (1957) found similar ranges of Q_f/Q_t determined stratification in coastal plain surface estuaries.

In addition to salinity there are other transition zones within the subterranean estuary. One is between oxic and anoxic regions where sulfate becomes the primary electron acceptor, i.e., SO_4^{2-}–S^{2-}. Within this region are suboxic transition zones: NO_3^-–NO_2^-–NH_4^+, Mn^{4+}–Mn^{3+}–Mn^{2+}, Fe^{3+}–Fe^{2+}. Charette and Sholkovitz (2002) described the Fe^{3+}–Fe^{2+} transition as the "iron curtain" transition zone in subterranean estuaries where soluble Fe^{2+} is oxidized to Fe^{3+} and precipitates, adsorbing important components such as phosphate. After sulfate is consumed there is a transition to methanogenesis. Each of these transition zones is populated by specific organisms, which mediate the measured reactions.

These transition zones within the subterranean estuary migrate in response to changes in circulation patterns (Charette and Sholkovitz, 2002). This migration stimulates different species of bacteria and archaea, which catalyze the biogeochemical reactions. For example, in studies of an intertidal aquifer, McAllister et al. (2015) found that the availability of chemical species controlled microbial populations along groundwater flow paths. They demonstrated that seasonal changes in the relative supply of fresh and saline groundwater affect microbial populations and noted that every pore water sample had a significant portion of sulfate reducers, making this the predominant recognized metabolism within the intertidal mixing zone. Degenhardt et al. (2020) described a "core community" of microbes in the upper meter of a high-energy intertidal area where stable redox transitions were driven by porewater advection and sediment reworking. This equilibrium community was disturbed by a "subsurface spring bloom," probably due to deeper penetration of oxygen and nitrate, but reverted to the "core community" during summer. Such dynamics illustrate the rapidity with which generalist microorganisms can respond to changing conditions within these transition zones.

In 2012 leaders in studies of anchialine environments decided to redefine the definition of their field of study. The title of the paper was "'Anchialine' redefined as a subterranean estuary in a crevicular or cavernous geological setting" (Bishop et al., 2015). This study and the ones by Charette and Sholkovitz (2002) and Robinson et al. (2007) are but three examples of the evolving rich literature on subterranean estuaries. As Moore (2010) pointed out, many surface estuarine processes have an analog in the subterranean estuary. Elucidating some of these processes is the purpose of this paper.

Expansion of the Subterranean Estuary

As saltwater intrusion brings more seawater into coastal aquifers, the subterranean estuary expands inland, significantly altering biogeochemical dynamics over wide regions. For example, in the early 1900's, a 100–500 m wide zone of brackish water lay at the base of the Biscayne aquifer in southern Florida (Barlow and Reichard, 2010). By 1946, canals constructed to drain the coastal wetlands above the unconfined aquifer resulted in the movement of brackish water 2 to 16 km inland, primarily beneath the canals, increasing the size of the subterranean estuary along this 25 km coastline from ∼20 to over 120 km^2 (Barlow and Reichard, 2010). This example has been repeated along coastlines worldwide.

Depletion of fresh groundwater through active pumping has accelerated during the past 50 years. For example, prior to 1950, there was less than 1 km^3 $year^{-1}$ of groundwater depletion from the United States Gulf and Atlantic coastal plain

aquifers; by 2008 this rate had increased to almost 9 km^3 $year^{-1}$ (**Figure 1**; Konikow, 2011). Industrial use of groundwater places major demands on coastal aquifers, as evidenced by the changes occurring along coastal Georgia, United States, in the past ∼60 years. Prior to October 1962, the Upper Floridan aquifer below the city of Brunswick, GA, had a hydraulic head of +3 to +5 m. In 1963, a paper mill began pumping roughly 1.4×10^5 m^3 freshwater day^{-1} from the aquifer and within 14 months the head in the aquifer had dropped to −3 m (Wait and Gregg, 1973). Within 30 years, a 5 km^2 subterranean estuary developed beneath the city, rendering the city wells non-potable due to 1–2.5 g/L chloride concentrations (Joiner, 1991). In China, saltwater intrusion along the coastline of the Laizhou Gulf in Shandong Province covered a total area of 16 km^2 in 1979; 10 years later the area of saltwater intrusion was 238 km^2 (Xu et al., 2002). By 2000, the extent of saltwater in the aquifer reached 1870 km^2, causing over 1500 wells to be abandoned (Qi and Qui, 2011). During the past century such examples have been repeated with similar consequenes along most populated coastlines (Werner et al., 2013).

The thawing of marine permafrost has the potential to produce new subterranean estuaries in the Arctic as ice is replaced with water. For example, Shakhova et al. (2010) suggested that the East Siberian Arctic Shelf (ESAS), an area of 2.1×10^6 km^2 on the Arctic Ocean margin, is potentially more vulnerable to thawing than is terrestrial permafrost. The annual average temperature of ESAS bottom seawater ranges from −1.8 to +1°C; this is 12–17°C warmer than the annual average surface temperature over terrestrial permafrost. On the South Kara Sea shelf in the Arctic, Portnov et al. (2013) found continuous subsea-bed permafrost extending to water depths of ∼20 m offshore. The permafrost created a seal through which gas could not migrate. Further offshore they found discontinuous permafrost up to 115 m water depth where methane ebullition was occurring. They concluded that within this 7500 km^2 area, seafloor gas release is widespread and permafrost degradation is an ongoing process. These are just examples of the thawing processes that are taking place around the Arctic Ocean margin. As ice is replaced with water in these permeable sediments, we posit that water exchange will take place between the sediments and the ocean, bringing these carbon-laden sediments into contact with seawater in new subterranean estuaries. This will substantially alter the biogeochemical dynamics of these systems, almost assuredly increasing the fluxes of carbon, nutrients, metals, and trace gases to the coupled ocean waters.

There is no doubt that the subterranean estuary is expanding rapidly as freshwater and ice are replaced by saltwater. The biogeochemical consequences of this expansion are significant globally.

Biogeochemical Reactions in Coastal Aquifers

Adding saltwater to a coastal aquifer changes the chemical environment dramatically. The increased ionic strength causes some particle-associated, surface-active ions to be released to solution. This increases the dissolved concentrations of desorbable ions such as ammonium, phosphate, barium, and radium (Moore, 1996; Shaw et al., 1998; Price et al., 2006). Another major change is reflected in the increased oxidation capacity of the saltwater. In terms of free energy, oxygen is the most powerful oxidant in natural waters. However, its oxidizing capacity is limited by its poor solubility (∼0.28 mmol/L in freshwater). The reaction

$$CH_2O + O_2 \rightarrow CO_2 + H_2O \quad (1)$$

will cease when 0.28 mmoles/L of organic carbon have been oxidized in a closed system. If this carbon has a typical marine C:N ratio = 6.6, a maximum of 42 μmol/L dissolved inorganic N (DIN) would be regenerated. This places a constraint on the maximum DIN concentration in unpolluted, oxic freshwater aquifers. But once dissolved oxygen is depleted in saltwater, the sulfate ion (∼28 mmol/L in seawater) becomes the primary electron acceptor for organic carbon oxidation. For example

$$2CH_2O + H^+ + SO_4^{2-} \rightarrow 2CO_2 + HS^- + 2H_2O \quad (2)$$

For each mole of sulfate reduced, 2 moles of organic carbon are oxidized and 2 moles of CO_2 are produced. If enough labile organic matter is present to deplete sulfate completely by oxidizing 56 mmol carbon with C:N = 6.6, this reaction could potentially release 8.5 mmol DIN/L in unpolluted aquifers containing marine organic carbon. Terrestrial organic matter contains a lower C:N ratio; its oxidation would produce a lower concentration of DIN. The presence of sulfate minerals could provide additional sulfate ions and increase the DIN released from subterranean estuaries or from freshwater aquifers after oxygen is depleted (Chapelle and McMahon, 1991).

Early studies of sulfate reduction coupled to oxidation of marine organic matter (Martens et al., 1978) found that pore waters of anoxic marine sediments contained up to about 10 mmol ammonia per liter. Riedel et al. (2011) reported NH_4 concentrations of 7 to 9 mmol/L in pore waters from tidal flat sands in the German Wadden Sea in which the sulfate concentration had been reduced to ∼0 and there was no source of DIN pollution. Wang and Jiao (2012) measured NH_4 concentrations of 10–20 mmol/L in a non-polluted Quaternary salty aquifer in the Pearl River delta, China, in which all sulfate had been reduced.

Figure 2 illustrates some differences between freshwater oxic coastal aquifers (**Figure 2A**) and anoxic subterranean estuaries (**Figure 2B**), where sulfate becomes the primary oxidizing agent after oxygen is exhausted. Because of its high sulfate concentration, saltwater has a far greater oxidizing capacity than freshwater. The reaction products of sulfate reduction coupled to organic matter oxidation include both inorganic and organic forms of dissolved C, N, and P as well as hydrogen sulfide. The creation of sulfidic conditions in an aquifer stimulates reduction of iron and manganese oxides, which increases concentrations of Fe^{2+} and Mn^{2+}, as well other metals and non-metals bound to these oxides. Increases of PO_4, Ba, Ra, Hg, Mo, V, rare earth elements (REE), and As are expected. As this chemically altered saltwater is discharged into coastal waters as SGD, it carries a high

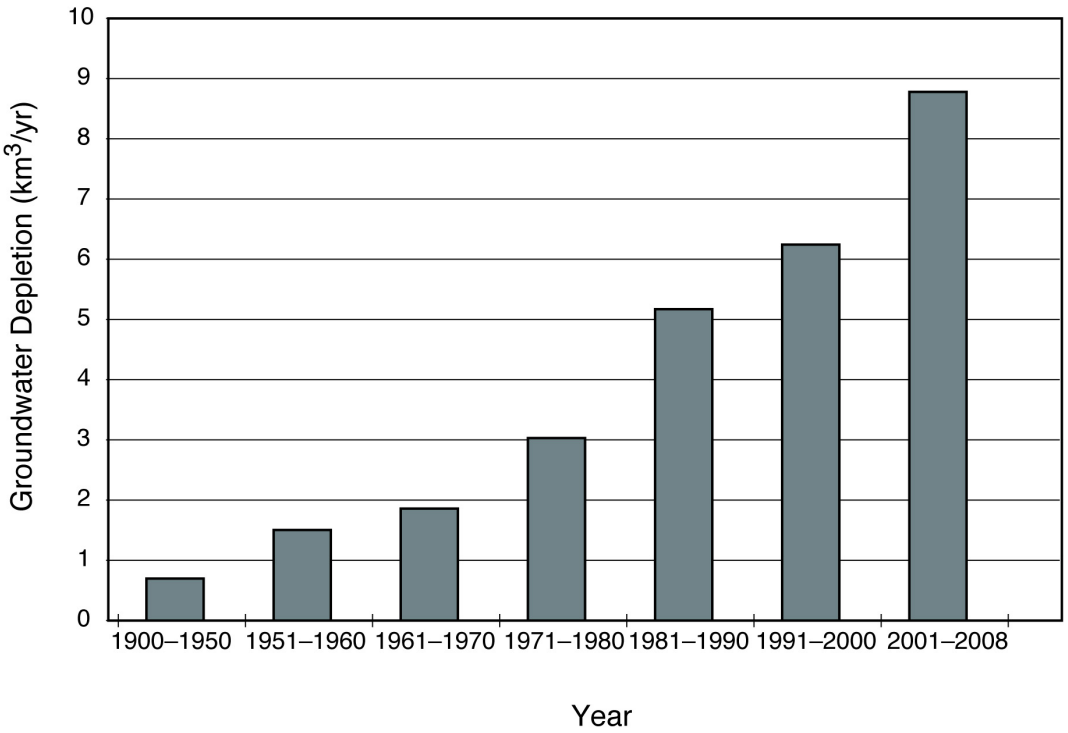


FIGURE 1 | The depletion of groundwater in the United States Gulf and Atlantic Coastal plain aquifers. Before 1950 depletion rates were less than 1 km^3/year. Early in the 21st century this increased to almost 9 km^3/yr. Data from Konikow (2011).

load of nutrients, carbon, metals, and sulfides. While nutrient, carbon and metal concentrations in SGD may be augmented by anthropogenic contamination, even pristine systems may have highly elevated concentrations due to the stimulation of anaerobic microbial metabolisms.

Once oxygen is consumed, a biogeochemical cascade ensues, with nitrate reducing, iron and manganese reducing, sulfate reducing, and methanogenic microorganisms. Thermodynamic energy yield and kinetic constraints interact to dictate the net pattern metabolism: typically, nitrate reduction and metal oxide reduction occur before sulfate reduction which occurs before methanogenesis. Sulfate is typically present in higher concentration than the other electron acceptors, leading to the domination of sulfate reduction in anaerobic metabolism in these systems. However, biologically mediated reactions occur in tandem with abiotic reactions, making it difficult in some cases to assess the driving force behind the observed biogeochemical reactions (Joye and Kostka, 2020).

There are a number of ways to assess the importance of abiotic versus microbially mediated processes in aquifers. Assessing microbial community composition using genomics data (Joye and Kostka, 2020) provides information on genomic capacity for a particular reaction by tracking gene abundance (e.g., probing for genes or assessing metagenomes) or by tracking the presence of transcripts associated with a particular process (e.g., metatranscriptomics). While some studies utilized such techniques in coastal aquifers (Santoro et al., 2006, 2008; Rogers and Casciotti, 2010; Sáenz et al., 2012; Adyasari et al., 2019, 2020), this approach holds tremendous potential. Adyasari et al. (2019) found that temperature and salinity were the main factors driving microbial community composition in shallow aquifers. Adyasari et al. (2020) studied the microbial community in an aquifer near Mobile Bay, AL., which becomes hypoxic during the dry season due to discharge of NH_4^+-rich groundwater. They observed a robust community of organisms associated with dissimilatory nitrate reduction to ammonia in the aquifer and proposed that these organisms may contribute to NH_4^+-loading in the estuary.

Rogers and Casciotti (2010) found a unique population of ammonia oxidizing archaea in well ventilated sediments in a coastal aquifer on Cape Cod and suggest a role for these organisms in nitrification. Sáenz et al. (2012) studied the anaerobic oxidation of ammonium (anammox) in a subterranean estuary in Waquoit Bay MA. They found anammox bacteria were present in redox transition zones where ammonium and nitrate coexist. Santoro et al. (2006) examined the population of denitrifying bacteria in a beach aquifer near Huntington Beach, CA, and were able to resolve population shifts over small spatial scales. They suggest that subtle differences in aquifer chemistry can result in microbial community shifts. In a subsequent paper (Santoro et al., 2008) they compared the abundance of ammonia oxidizing bacteria with that of ammonia oxidizing archaea, revealing that the ammonia oxidizing archaea preferred lower salinities (brackish and freshwater) than the ammonia oxidizing bacteria.

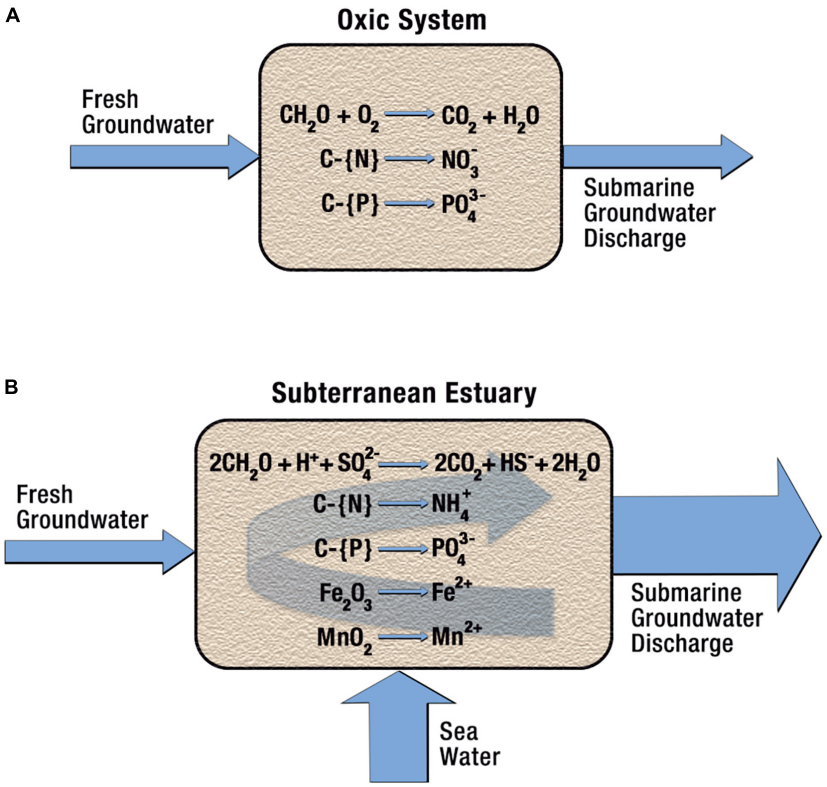


FIGURE 2 | Chemical differences between an oxic freshwater aquifer and an anoxic subterranean estuary. **(A)** As fresh oxygenated groundwater passes through an aquifer containing organic carbon, some carbon may be oxidized and release CO_2 as well as nitrate and phosphate ions. The maximum concentration of nitrate produced (~42 μM) is controlled by the solubility of oxygen (~0.28 mM) and the C:N ratio of the organic matter (~6.6 for marine organic matter). **(B)** The addition of saltwater to this system greatly increases the oxidizing capacity after O_2 is exhausted due to sulfate ion (~28 mM in ocean water). Here the reaction products include significantly greater concentrations of CO_2, ammonium and phosphate as well as sulfide, which can reduce metal oxides, liberating Fe^{2+} and Mn^{2+} and other metals and non-metals to solution.

While genomics methods provide information about metabolic potential and about active gene expression, another way to assess microbial activity directly involves using metabolic inhibitors in combination with radiotracer rate assays. Metabolic inhibitors specifically block enzymes associated with a particular process and hence can be used to separate microbial activity from abiotic processes (Segarra et al., 2013), but again such approaches are rarely applied to aquifer systems. Pairing genomics and targeted rate assays with standard geochemical approaches offers a robust way to advance a number of research areas related to SGD in the coastal zone. Much of the work to date has focused on nitrogen cycling but there is tremendous potential for advancing the understanding in carbon and sulfur cycling using these approaches as well.

RESULTS: CASE STUDIES

To illustrate the processes we have just described on different spatial and temporal scales, as posited by Bratton (2010), we offer three case studies of radically different environments: a small river–salt marsh system in South Carolina, offshore tidal flats in the German Wadden Sea, and a section of the Potomac Subterranean Estuary, a 45,000 km^2 system beneath the United States east coast. Here we reinterpret published data from each system.

Okatee, South Carolina (United States)

The Okatee subterranean estuary lies in southeastern South Carolina, northwest of Hilton Head Island. Previous studies revealed large SGD fluxes of nutrients and carbon (Moore et al., 2006; Weston et al., 2006b; Porubsky et al., 2014). These studies used data collected when the area had a low population density before a large-scale housing development was built in the upper reaches of the system. Monitoring wells along the creek bank were sampled for numerous constituents including dissolved nutrients, carbon, chloride, sulfate, and radium (Moore et al., 2006). The salinity of these well waters ranged from ~25 to >40, the higher values arising from evapotranspiration. **Figure 3** shows the relationship between some of these constituents and the degree of sulfate depletion, via microbial sulfate reduction, observed in groundwater from the monitoring wells. Sulfate depletion is defined as the sulfate concentration observed in the groundwater minus the sulfate concentration predicted from the Cl^- concentration. Here we assume seawater entered the aquifer

with the oceanic SO_4:Cl molar ratio (0.0514) and is the only source of SO_4. Following Martens et al. (1978), who developed this concept in anoxic mud, we call the depletion of SO_4 "ΔSO_4"; this term becomes more negative with increased sulfate depletion.

As predicted by reaction (2), the concentration of dissolved CO_2 increases with a 2:1 ratio as sulfate is depleted. The concentration of dissolved NH_4^+ reaches 400 μM in samples showing the greatest (about 50%) sulfate depletion. This is an order of magnitude greater than the concentration expected from the oxidation of marine organic matter by dissolved oxygen, illustrating the dramatic effect that saltwater intrusion has on the biogeochemistry of coastal aquifers. The scatter is likely caused by differences in the C:N ratio of the material being oxidized [literature values for Spartina, the primary marsh grass in this system, show C:N of 14–74 (Porubsky et al., 2014)]; the soils may also contain terrestrial plant components with even higher C:N ratios and NH_4^+ may exhibit non-conservative behavior after it is released. Dissolved ^{226}Ra (half-life = 1600 years) also increases strongly with increased sulfate depletion. Because ^{226}Ra regenerates very slowly after being desorbed from particles, the increased ^{226}Ra activity in the sulfate-depleted water must be due to its release from the diagenesis of solids in the aquifer. Whether this is due to oxidation of organic matter directly or to subsequent reactions involving Fe-Mn coatings or other components is unknown. Porubsky et al. (2014) demonstrated strong correlations between ^{226}Ra and dissolved DIN, DIP, DIC, and DOC in these wells, reinforcing the idea of stoichiometry in the release of ^{226}Ra during organic matter oxidation. Unlike ^{226}Ra, dissolved ^{228}Ra (half-life = 5.7 years) shows an irregular pattern with high activities occurring at high and low sulfate depletion. This must be due to the continued regeneration of ^{228}Ra from ^{232}Th decay on particles within the flow-path of the groundwater (∼30% of ^{228}Ra regenerates in 1 year from ^{232}Th decay). On a timescale of months to years, the high ionic strength of the water desorbs regenerated ^{228}Ra irrespective of the sulfate depletion. These high ^{226}Ra and ^{228}Ra activities provide effective tracers of SGD that enters estuarine and coastal waters.

Wadden Sea Tidal Flats, Germany

Within the Wadden Sea in northern Germany, some tidal flats are exposed only during low tide. Numerous studies of pore waters within the sandy tidal flats near Spiekeroog Island have documented high concentrations of NH_4, PO_4, DIC, DOC, Mn, Fe, Ba, and Ra and the release of these components to tidal waters during low tide (Billerbeck et al., 2006; Beck et al., 2008a,b; Moore et al., 2011). Here we focus on a study by Riedel et al. (2011) who mapped the interstitial water chemistry down to 2.5 m sediment depth along a transect on an inter-tidal creek bank that is subject to a periodic advective flow. They documented high rates of diagenetic reactions in sites subject to advection compared to sites controlled by diffusion. On a timescale of 200 days, SO_4 was almost completely depleted, while DIC, NH_4, Ba, Mn, and V became highly elevated (Riedel et al., 2011). When plotted against ΔSO_4 (**Figure 4**), these increases follow the same trends observed in the Okatee dataset (**Figure 3**). Again, the DIC increases with a 2:1 ratio as SO_4 is depleted. The NH_4 concentration reaches 8.5 mmol/L, the predicted concentration based on the Redfield Ratio for marine organic material of C:N = 6.6. Ba shows irregular but significant increases, while the V increase is very linear. All of these concentrations are orders of magnitude greater than North Sea water (Moore et al., 2011) and further underscore the role of anaerobic microbial metabolisms in enriching groundwater with reduced metabolites.

The Potomac Subterranean Estuary Offshore New Jersey, United States

The Potomac aquifer lies within the Northern Atlantic Coastal Plain aquifer system, which comprises much of the subterranean coastal area from North Carolina to New Jersey. The aquifer extends under the land and beneath the continental shelf. There has been significant saltwater intrusion into this aquifer in response to multiple sea level cycles (Barlow, 2003). This has created an enormous (∼45,000 km^2) subterranean estuary. The IODP Expedition 313 collected a series of deep cores into this system along an inshore to offshore transect off the coast of New Jersey (Mountain et al., 2010). The chemistry of the pore water extracted from these cores was presented by van Geldern et al. (2013). The pore water had salinities as low as 1–2 in some fine-grained silty and clay-rich sediments. The δ^{18}O and δ^2H values of the water were similar to modern precipitation, indicating recharge by meteoric water via onshore outcrops at times of high sea level. The authors could not determine if this freshwater recharge occurred in modern times or at a time when conditions were similar to the present, i.e., the last interglacial, 120,000 years ago; they concluded recharge did not occur during low glacial sea level as some had suggested.

The more permeable sediments contained saltier water, ranging from brackish to hypersaline. The highest salinity samples probably represent upward migration of a deep brine (van Geldern et al., 2013). Based on stable isotope data, van Geldern et al. (2013) concluded that the porewaters in the upper layers with salinity less than 35 resulted from mixing of meteoric waters with seawater; in deeper layers where salinity was greater than 35, the deep brine was a significant component. Overall, the geochemical results for major ions and stable isotopes in the lower salinity porewaters were in good agreement with modern meteoric and seawater values, indicating possible connections to the seafloor through channels in less permeable layers or through outcrops at the shelf margin (van Geldern et al., 2013). However, not all of the chemical parameters could be described by simple mixing, as the porewaters were high in alkalinity, ammonium, and phosphate and depleted in sulfate. These observations fit the concept of the diagenetic reactions in the subterranean estuary very well.

Here we use the pore water data for Expedition 313 reported on the IODP website (Integrated Ocean Drilling Program [IODP], 2020). To avoid the effect of the deep brine component, we restrict our attention to samples from the upper 340–450 m sections, which van Geldern et al. (2013) interpret as primarily mixing between meteoric recharge and seawater. These samples contained less than seawater concentrations of 550 μM chloride. As in the other systems, we observe significant increases in NH_4 as ΔSO_4 decreases (**Figure 4**). The NH_4

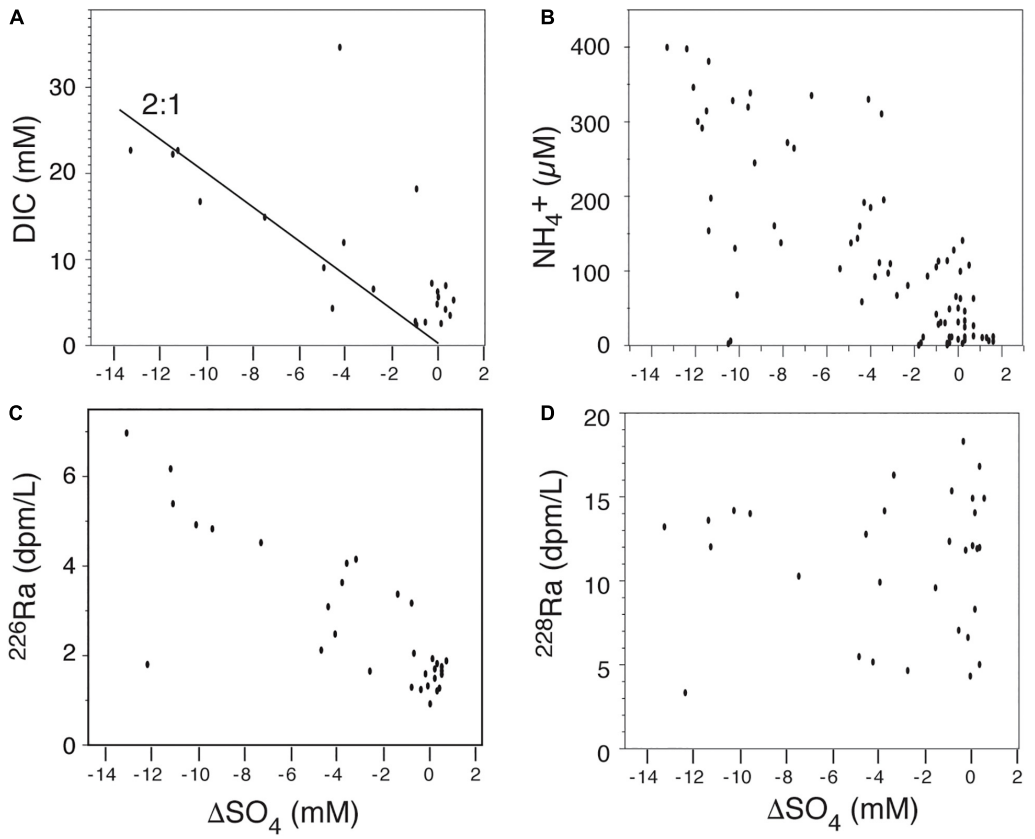


FIGURE 3 | Data from the Okatee subterranean estuary, South Carolina, showing the relationship between sulfate depletion by C oxidation (see text) and dissolved species. **(A)** The concentration of dissolved CO_2 increases with a 2:1 ratio as sulfate is depleted (Eq. 2). **(B)** The concentration of dissolved NH_4^+ reaches 400 μM in samples with the greatest sulfate depletion. **(C)** Dissolved ^{226}Ra increases with increased sulfate depletion, implying organic matter degradation either directly or due to secondary reactions releases significant ^{226}Ra. **(D)** Dissolved ^{228}Ra shows an irregular pattern with high activities occurring at high and low sulfate depletion, implying that desorption of ^{228}Ra regenerated from ^{232}Th decay governs its behavior. Data from Moore et al. (2006) and Porubsky et al. (2014).

increase is intermediate between systems containing primarily marine organic matter like the Wadden Sea and systems where the material being oxidized has a higher C:N ratio. If the increased NH_4 is due to its release from organic matter, its C:N ratio is probably between 6 and 23, based on the slope of the ΔSO_4 curve. This seems reasonable for the oxidation of a mixture of terrestrial (high C:N) and marine (low C:N) organic matter. Obviously, there are other processes at work in these porewaters. For example, the very high NH_4 and Ba values in cases where there is no sulfate deficiency (**Figure 5**) may be due to desorption from the solid phase rather than re-mineralization. It could also be due to the addition of new sulfate from the dissolution of sulfate minerals such as gypsum in the sediments.

DISCUSSION

Earlier Studies

There have been earlier studies linking seawater intrusion with biogeochemical reactions in the subterranean estuary; we will cite a few. Sivan et al. (2005) investigated chemical changes in seawater intrusions along the Mediterranean coast of Israel. They used nuclear bomb-derived ^{3}H to verify that the intruding water 50–100 m onshore had been in the ocean 15–30 years ago. These samples contained total alkalinity and total dissolved inorganic carbon (DIC) in excess of that predicted from aerobic metabolism, indicating anaerobic oxidation of organic matter. In the Florida Everglades, Price et al. (2006) proposed that phosphorus discharge to the surface water was influenced by saltwater intrusion. In the Indian River Lagoon, Florida, Roy et al. (2010) studied the effect of sea level rise on the Fe flux to ocean surface waters through SGD. Fifteen km seaward of the North Carolina coast, Moore et al. (2002) found high nutrient concentrations in 2–4 m deep seabed monitoring wells; both total dissolved N and P correlated strongly with ^{226}Ra, as they did in the Okatee system.

It is clear that saltwater intrusion accelerates biogeochemical dynamics in subterranean estuaries, with potentially profound impacts on the geochemistry of SGD. Luo et al. (2018) reached the same conclusion in their study of the Pearl River aquifer, China, where they documented increased ^{226}Ra and NH_4 with ΔSO_4 similar to our case studies. In their system, NH_4 reached 22 mM, clearly exceeding the 8.5 mM theoretical

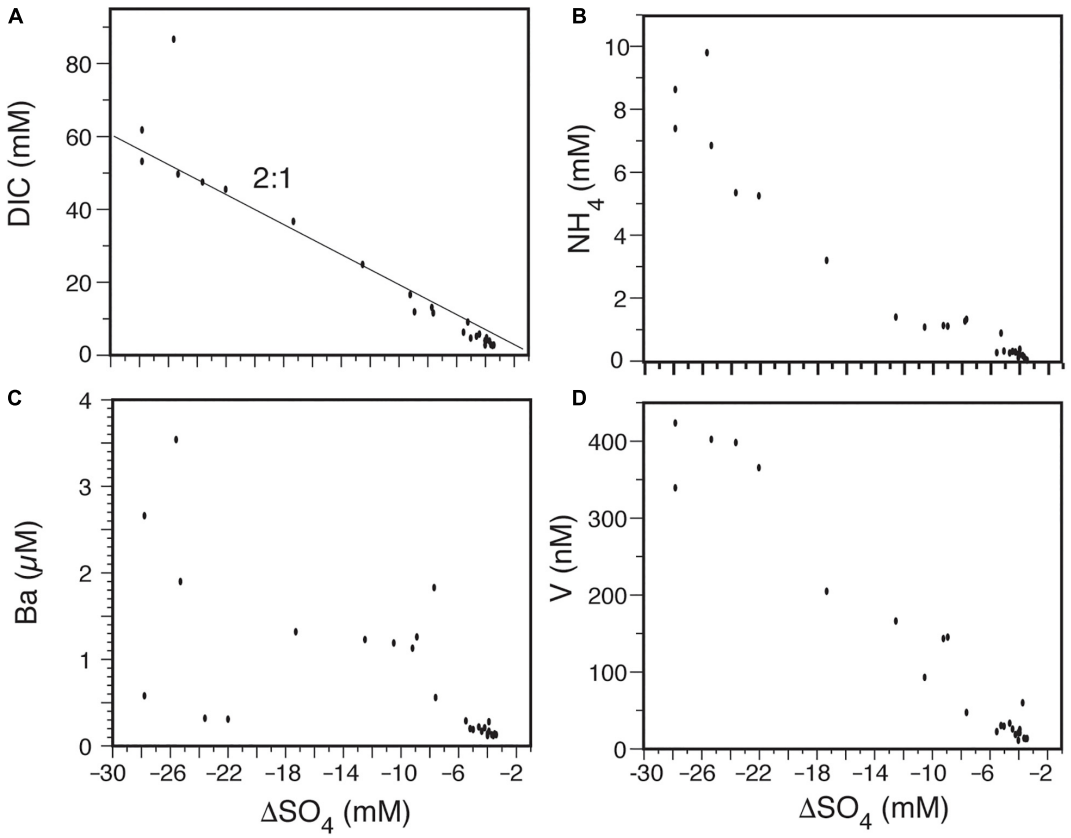


FIGURE 4 | Data from the Wadden Sea tidal flats, Germany, showing the relationship between sulfate depletion by C oxidation (see text) and dissolved species. **(A)** The concentration of dissolved CO_2 increases with a 2:1 ratio as sulfate is depleted (Eq. 2). **(B)** The concentration of dissolved NH_4^+ reaches 8.5 mM in samples with the greatest sulfate depletion as predicted using the Redfield Ratio. **(C)** Dissolved Ba increases irregularly with increased sulfate depletion, implying organic matter degradation releases significant Ba either directly or due to secondary reactions. **(D)** Dissolved vanadium shows a highly linear increase with sulfate depletion, implying organic matter degradation releases significant V. Data from Riedel et al. (2011).

value for the oxidation of marine organic carbon. Because there is no evidence for anthropogenic pollution on a large scale in this system (Wang and Jiao, 2012), Luo et al. (2018) postulated that the high concentrations were likely caused by excess NH_4 in initial fresh groundwater through other remineralization processes–such as Fe-Mn oxide reduction and methanogenesis–before mixing with saltwater and experiencing sulfate reduction. These high concentrations could also reflect ammonia adsorption to the organic-rich sediments during initial stages of saltwater intrusion when the salinity of the water was low, followed by its release when salinity increased. Wang and Jiao (2012) reported the exchange of Mg^{2+} and NH_4^+ in the aquitard of the Pearl River delta, possibly reflecting this process. The presence of gypsum in the sediments could provide another source of sulfate unrelated to saltwater in this or other systems.

Changing Subterranean Estuaries and SGD

Local changes in water and land use have led to enormous expansions of subterranean estuaries in the last 100 years. This expansion has brought high ionic strength seawater containing sulfate into contact with old sediments. Sudden exposure of aquifer sediments to high ionic strength water may mobilize surface-bound ions and organic matter adsorbed onto sediments and alter the mineralogy of metal oxides (Weston et al., 2006a). Both of these effects may further accelerate biogeochemical reactions in aquifers impacted by saltwater intrusion by mobilizing the components of organic matter and increasing the availability of iron and manganese oxides for microbial reduction.

In effect, the introduction of sulfate ion transforms these aquifers from oxidant-limited to almost oxidant-unlimited, allowing extensive amounts of organic carbon to be oxidized. These changes stimulate the biogeochemical reactions that degrade organic matter via anaerobic metabolisms, leading to increased concentrations of nutrients, dissolved carbon (DIC and DOC), hydrogen sulfide and metals in the subterranean estuary. Fluids expelled from subterranean estuaries as SGD enrich coastal waters in nutrients, carbon, sulfide, and metals. In some cases, the excess nutrients can be linked to harmful algae blooms, eutrophication and hypoxia. For example, SGD has been cited as the most likely source of excess nutrients

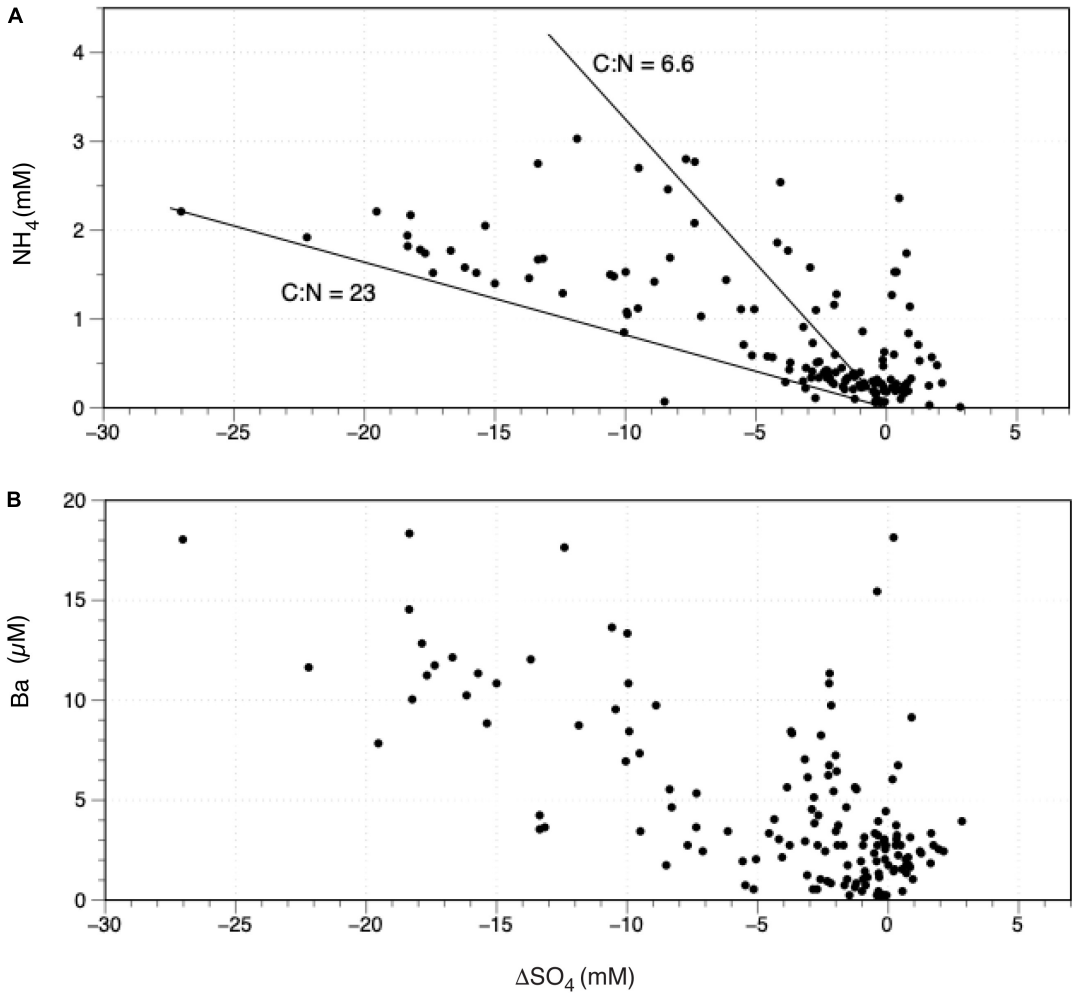


FIGURE 5 | Data from the IODP Exp 313, holes M0027A, M0028A, and M0029A on the continental shelf off New Jersey, showing the relationship between sulfate depletion by C oxidation (see text) and dissolved species in the upper levels of these cores. **(A)** The concentration of dissolved NH_4^+ increases with sulfate depletion in a range between that predicted by oxidizing carbon with a 6.6 C:N ratio (Redfield Ratio) and a much higher ratio (23), implying the oxidation of non-marine carbon. **(B)** Dissolved Ba increases substantially with increased sulfate depletion, implying organic matter degradation releases significant Ba either directly or due to secondary reactions. High concentrations of NH_4 and Ba also exist in multiple samples showing no sulfate depletion, indication that other processes such as desorption or the release of sulfate from solid phases also play a role. Data from van Geldern et al. (2013), Integrated Ocean Drilling Program [IODP] (2020).

in Yeoja Bay (Hwang et al., 2005) and Masan Bay (Lee et al., 2009), South Korea, where harmful algae blooms are common. Hu et al. (2006) observed that nutrient fluxes from local rivers were insufficient to support a harmful algae bloom in coastal waters off west Florida; they concluded that the most likely source of the required nutrients was high fluxes of SGD resulting from a hurricane.

Discharge of high-nutrient groundwater has also been implicated in eutrophication in Tolo Harbor, Hong Kong (Tse and Jiao, 2008). Recently Peterson et al. (2016) reported a near-hypoxic event on the South Carolina coast that was caused by the release of cold, salty, anoxic water from the offshore subterranean estuary. This discharged water formed a high-density benthic boundary layer that largely maintained its identity for several weeks as it spread to a nearshore monitoring station. Thus, SGD fluxes may have significant ecological impacts locally, and in some cases may have global impacts on ocean chemistry (Moore, 2010).

We want to be clear that the ΔSO_4 correlations that we present do not apply to all subterranean estuaries. We have examined data from systems where there are no correlations. The chemical signatures are not simple mixtures of groundwater and seawater but depend on the composition and reactivity of the aquifer and aquiclude solids, the residence time of fluids in the system, and the time that has elapsed since seawater first intruded the system. Understanding what regulates the chemical composition of fluids in subterranean estuaries is a complex and ongoing challenge.

Seawater intrusion into coastal aquifers will likely accelerate as coastal populations increase and sea levels continue to rise. Recent projections of multi-meter sea level rise over the next 50–200 years (Hansen et al., 2016) will cause enormous additional inland expansion of subterranean estuaries. New subterranean

estuaries will emerge in coastal aquifers and in the Arctic as ice is replaced with seawater. These processes will affect portions of aquifers that have not been in contact with saltwater for thousands of years, causing increased production of dissolved nutrients, carbon, sulfide, and metals, and possibly dissolved greenhouse gases, like methane, which accumulate in coastal aquifers (Schutte et al., 2016, 2020) and are trapped in permafrost (Shakhova et al., 2010). The increased biogeochemical reactions that affect these concentrations will operate over larger spatial scales, providing new sources of organic carbon for oxidation.

We must also consider what happens when aquifers that have accumulated saltwater are abandoned as water supplies. As Qi and Qui (2011) point out, seawater intrusion has caused over 1500 wells to be abandoned along the Laizhou Gulf coastline. If the natural flow of groundwater into these systems has not changed, they will recharge with freshwater and discharge the salty water containing the products of anaerobic metabolisms into estuaries or coastal waters. This would cause a release of nutrients, carbon, sulfide, and metals, and possible radiative trace gases like methane and nitrous oxide, to the adjacent coastal waters, potentially leading to or exacerbating eutrophication of the receiving waters over periods of years to decades. The rate of release will depend on the aquifer permeability and whether this has been affected by the saltwater-induced reactions. Jiao and Post (2019) cite examples of such flow reversal as wells are abandoned and point out that because of its higher density saltier water may collect in the deeper regions of the aquifer in spite of renewed recharge. Following the designations of Robinson et al. (2007), the renewed influx of freshwater may transform subterranean estuaries from well- or partially-mixed systems into stratified systems. Similar changes occur on a much shorter timescale in surface estuaries following a large discharge event.

These observations linking the recent expansion of subterranean estuaries with a mechanism for producing high concentrations of nutrients, carbon and metals in their fluids raises a significant question regarding SGD: Has the current supply of nutrients, carbon and metals to the ocean via SGD changed significantly in the past 100 years? We suggest that it may have increased even if the net freshwater flow may have decreased. Roy et al. (2010) concluded that accelerated sea level rise is likely to increase the Fe flux to ocean surface waters along coastlines where groundwater discharges through permeable sediments. This may be true for nutrients also. Because they lack high concentrations of sulfate ion, unpolluted freshwater springs are generally limited to a maximum of 42 μM DIN. Compare this to orders of magnitude higher N concentrations in fluids in subterranean estuaries (up to 10 mM). Small increases in SGD from subterranean estuaries can more than compensate for diminished freshwater springs in terms of N delivery to the coast. Besides tides, other periodic changes in sea level constitute effective drivers of SGD. Seasonal sea level changes result from summertime heating, which expands the ocean and causes sea level to rise and intrude further into subterranean estuaries. During winter sea level falls causing a return flow of fluids that have become enriched in metabolic products. These seasonal changes are being amplified by climate change. Wahl et al. (2014) used seasonal sea level harmonics throughout the 20th and early 21st centuries to document a significant amplification of the annual sea level cycle in the eastern Gulf of Mexico of up to 30% (average 22%) from the 1990s, brought on by both higher summer and lower winter sea levels. Shorter-term changes in sea level result from cyclones and other major storms (Moore and Wilson, 2005; Wilson et al., 2011) or persistent offshore wind events (George et al., 2020). There is growing evidence that cyclones are increasing in intensity and perhaps numbers. We speculate that persistent offshore wind events may also be linked to a warmer ocean. The combined effects of these sea level changes should drive increased exchange between the subterranean estuary and ocean, resulting in increased delivery of nutrients, carbon, and metals to the coastal ocean.

Looking to the Future by Studying the Past

Climate change is certainly affecting SGD forcing functions. Although we cannot determine how this will be affecting SGD globally at present, a future answer may be provided by proxy records in corals. These records offer promise in the future to address this question.

Horta-Puga and Carriquiry (2012) measured Ba/Ca ratios in a 52-year old coral colony in Yucatan, Mexico. They found strong correlations between annual precipitation and the Ba/Ca coral time-series and concluded that Ba/Ca ratios can be used as a proxy of precipitation, which in the Yucatan is a direct indicator of SGD as there is minimal surface runoff (Young et al., 2008). Jiang et al. (2018) measured variations of REE/Ba and REE/Ca ratios in coral samples from Hainan Island, China, and used these as a long-term (>100 year) proxy for SGD in the study area. They observed an increase in the reconstructed SGD corresponding to the escalating trend of local rainfall and suggested that "coral paleohydrological records can contribute to model-data comparisons in SGD models under different pumping scenarios."

Chen et al. (2020) measured Ba/Ca, $\delta^{18}O$, and $\delta^{13}C$ in coral skeletal material from the nearshore reef environment in the Kimberley Region of Northwestern Australia. They concluded the skeletal material contained significant terrestrial signatures of Ba/Ca, residual $\delta^{18}O$, and to a lesser extent $\delta^{13}C$ on a monthly time scale. These signatures as well as the observational coastal sea surface salinity exhibited a consistent lag with respect to river discharge of 1–2 months. They listed groundwater input as a possible cause for this lag but could not verify this possibility. Michael et al. (2005) observed that SGD often lags high precipitation events by several months. It is conceivable that the coral signatures were tracing SGD rather than river discharge.

Erler et al. (2018) analyzed coral skeletons from a reef core dating over 100 years in Rarotonga, Cook Islands, in the South Pacific for tracers of agriculture-related groundwater nitrogen, which is enriched in $\delta^{15}N$. They related increases in the $\delta^{15}N$ of coral skeletal material between 1960 and 2000 to rapid agricultural development that occurred between 1960 and 1985, which increased aquifer N concentrations leading to the elevated $\delta^{15}N$ of groundwater NO_3. They realized the discharge of this N-enriched groundwater continued for at least 15 years after the end of the agricultural boom, highlighting the important

implications for the management of groundwater contamination. Erler et al. (2020) extended these studies to a 333-year composite record of $\delta^{15}N$ in coral skeleton-bound organic matter to understand how nitrogen cycling in the coastal Great Barrier Reef, Australia, has responded to increased anthropogenic nutrient inputs. They concluded that increased nitrogen fixation was the primary cause of increases N supply to the region.

We encourage similar studies to reconstruct the history of SGD along other coastlines and specifically to evaluate its effect on the receiving waters. Although the measurement of ^{226}Ra in small samples is time-consuming (Hsieh and Henderson, 2011; Yaala et al., 2019), the $^{226}Ra/Ca$ ratios in corals may provide a direct link to the numerous studies of SGD using radium isotopes (Charette et al., 2008; Tan et al., 2018; Tamborski et al., 2020).

CONCLUSION

Reactions between fluids and solids in coastal aquifers are amplified dramatically upon the intrusion of seawater. This intrusion causes desorption of adsorbed ions and the oxidation of organic carbon via sulfate reduction in subterranean estuaries. These fluids become enriched in dissolved nutrients, inorganic carbon, organic carbon, sulfide, metals, radiative gases and radionuclide tracers. Circulation of these fluids between the subterranean estuary and the coastal ocean enriches coastal waters in these reaction byproducts, where they may enhance biological productivity and lead to increased biomass. The increased biomass may have positive societal results if it leads to increased seafood production or negative consequences if it leads to eutrophication, harmful algae blooms, and hypoxia. In some cases, the discharge of anoxic groundwater may directly cause hypoxia (Peterson et al., 2016). We conclude that the well-documented accelerating intrusion of seawater into coastal aquifers will increase the concentrations of these reaction products and suggest that continued circulation between the subterranean estuary and coastal ocean will release increasing concentrations of these byproducts. We argue that the effects of climate change will increase this circulation due to short-term and seasonal sea level changes. This circulation may also be temporarily enhanced if the rate of freshwater withdrawal from the aquifer diminishes and the normal flow of fresh groundwater into the aquifer continues, causing more SGD.

AUTHOR CONTRIBUTIONS

Both authors listed have made a substantial, direct and intellectual contribution to the work, and approved it for publication.

FUNDING

This work was funded by South Carolina (NA960PO113, the LU-CES program) and Georgia (NA06RG0029-R/WQ11 and R/WQ12A) Sea Grant and the National Science Foundation (EAR-1316250, OCE-1458424, and OCE-1736321).

ACKNOWLEDGMENTS

We thank Carolyn Ruppel, Nat Weston, Bill Porubsky, and Virginia Saunders for assistance with sample collections, analysis and figure preparation.

REFERENCES

Adolf, J. E., Burns, J., Walker, J. K., and Gamiao, S. (2019). Near shore distributions of phytoplankton and bacteria in relation to submarine groundwater discharge-fed fishponds, Kona coast, Hawai'i, USA. *Estuar. Coast. Shelf Sci.* 219, 341–353. doi: 10.1016/j.ecss.2019.01.021

Adyasari, D., Hassenrück, C., Oehler, T., Sabdaningsih, A., and Moosdorf, N. (2019). Microbial community structure associated with submarine groundwater discharge in northern Java (Indonesia). *Sci.Total Environ.* 689, 590–601. doi: 10.1016/j.scitotenv.2019.06.193

Adyasari, D., Hassenrück, G., Montiel, D., and Dimova, N. (2020). Microbial community composition across a coastal hydrological system affected by submarine groundwater discharge (SGD). *PLoS One* 29:e023523. doi: 10.1371/journal.pone.0235235

Barlow, P. M. (2003). *Groundwater in Freshwater-Saltwater Environments of the Atlantic Coast.* Reston, VA: U.S. Dept. Interior, USGS.

Barlow, P. M., and Reichard, E. G. (2010). Saltwater intrusion in coastal regions of North America. *Hydrogeol. J.* 18, 247–260. doi: 10.1007/s10040-009-0514-3

Beck, M., Dellwig, O., Holstein, J. M., Grunwald, M., Liebezeit, G., Schnetger, B., et al. (2008a). Sulphate, dissolved organic carbon, nutrients and terminal metabolic products in deep pore waters of an intertidal flat. *Biogeochemistry* 89, 221–238. doi: 10.1007/s10533-008-9215-6

Beck, M., Dellwig, O., Liebezeit, G., Schnetger, B., and Brumsack, H.-J. (2008b). Spatial and seasonal variations of sulphate, dissolved organic carbon, and nutrients in deep pore waters of intertidal flat sediments. *Estuar. Coast. Shelf Sci.* 79, 307–316. doi: 10.1016/j.ecss.2008.04.007

Billerbeck, M., Werner, U., Polerecky, L., Walpersdorf, E., de Beer, D., and Huettel, M. (2006). Surficial and deep pore water circulation governs spatial and temporal scales of nutrient recycling in intertidal sand flat sediment. *Mar. Ecol. Progr. Ser.* 326, 61–76. doi: 10.3354/meps326061

Bishop, R. E., Humphreys, W. F., Cukrov, N., Žic, V., Boxshall, G. A., Cukrov, M., et al. (2015). 'Anchialine' redefined as a subterranean estuary in a crevicular or cavernous geological setting. *J. Crustacean Biol.* 35, 511–514. doi: 10.1163/1937240X-00002335

Bratton, J. F. (2010). The Three Scales of Submarine Groundwater Flow and Discharge across Passive Continental Margins. *J. Geol.* 118, 565–575. doi: 10.1086/655114

Burnett, W. C., Bokuniewicz, H., Huettel, M., Moore, W. S., and Taniguchi, M. (2003). Groundwater and pore water inputs to the coastal zone. *Biogeochemistry* 66, 3–33. doi: 10.1023/b:biog.0000006066.21240.53

Chapelle, F. H., and McMahon, P. B. (1991). Geochemistry of dissolved organic carbon in a coastal-plain aquifer. 1. Sulfate from confining beds as an oxidant in microbial CO_2 production. *J. Hydrol.* 127, 85–108. doi: 10.1016/0022-1694(91)90110-4

Charette, M. A., Moore, W. S., and Burnett, W. C. (2008). "Uranium-and thorium-series nuclides as tracers of submarine groundwater discharge," in *Chapter-5 Uranium-and Thorium-Series Nuclides as Tracers of Submarine Groundwater Discharge. U-Th Series Nuclides in Aquatic Systems*, eds S. Krishnaswami and J. Kirk Cochran (Oxford: Elsevier).

Charette, M. A., and Sholkovitz, E. R. (2002). Oxidative precipitation of groundwater-derived ferrous iron in the subterranean estuary of a coastal bay. *Geophys. Res. Lett.* 29, 1444–1447. doi: 10.1029/2001GL014512

Chen, X., Deng, W., Wei, G., and McCulloch, M. (2020). Terrestrial signature in coral Ba/Ca, $\delta^{18}O$, and $\delta^{13}C$ records from a macrotide-dominated nearshore reef environment, Kimberley region of northwestern Australia. *J. Geophys. Res. Biogeoscie.* 125, e2019JG005394. doi: 10.1029/2019JG005394

Conley, D. J., Kaas, H., Møhlenberg, F., Rasmussen, B., and Windolf, J. (2000). Characteristics of Danish Estuaries. *Estuaries* 23, 820–837. doi: 10.2307/1353000

Crotwell, A. M., and Moore, W. S. (2003). Nutrient and Radium Fluxes from Submarine Groundwater Discharge to Port Royal Sound, South Carolina. *Aqu. Geochem.* 9, 191–208. doi: 10.1023/b:aqua.0000022954.89019.c9

Degenhardt, J., Dlugosch, L., Ahrens, J., Beck, M., Waska, H., and Engelen, B. (2020). Seasonal dynamics of microbial diversity at a sandy high energy beach reveal a resilient core community. *Front. Mar. Sci.* 7:573570. doi: 10.3389/fmars.2020.573570

Duque, C., Michael, H. A., and Wilson, A. M. (2020). The subterranean estuary: technical term, simple analogy, or source of confusion? *Water Resour. Res.* 56:e2019WR026554. doi: 10.1029/2019WR026554

Duxbury, A. C. (1977). *The earth and its oceans*. Maryland: Addison-Wesley Publishing Co.

Erler, D. V., Farid, H. T., Glaze, T. D., Carlson-Perret, N. L., and Lough, J. M. (2020). Coral skeletons reveal the history of nitrogen cycling in the coastal Great Barrier Reef. *Nat. Commun.* 11:1500. doi: 10.1038/s41467-020-15278-w

Erler, D. V., Shepherd, B. O., Linsley, B. K., Lough, J. M., and Cantin, N. E. (2018). Coral skeletons record increasing agriculture-related groundwater nitrogen inputs to a South Pacific reef over the past century. *Geophys. Res. Lett.* 45, 8370–8378. doi: 10.1029/2018GL078656

George, C., Moore, W. S., White, S. M., Smoak, E., Joye, S. B., and Wilson, A. M. (2020). A new mechanism for submarine groundwater discharge from continental shelves. *Water Resour. Res.* 56:e2019WR026866. doi: 10.1029/2019WR026866

Hansen, J., Sato, M., Hearty, P., Ruedy, R., Kelley, M., Masson-Delmotte, V., et al. (2016). Ice melt, sea level rise and superstorms: evidence from paleoclimate data, climate modeling, and modern observations that 2° C global warming could be dangerous. *Atmos. Chem. Phys.* 16, 3761–3812. doi: 10.5194/acp-16-3761-2016

Horta-Puga, G., and Carriquiry, J. D. (2012). Coral Ba/Ca molar ratios as a proxy of precipitation in the northern Yucatan Peninsula, Mexico. *App. Geochem.* 27, 1579–1586. doi: 10.1016/j.apgeochem.2012.05.008

Hsieh, Y.-T., and Henderson, G. M. (2011). Precise measurement of $^{228}Ra/^{226}Ra$ ratios and Ra concentrations in seawater samples by multi-collector ICP mass spectrometry. *J. Anal. At. Spectrom.* 26, 1338–1346. doi: 10.1039/c1ja10013k

Hu, C., Muller-Karger, F. E., and Swarzenski, P. W. (2006). Hurricanes, submarine groundwater discharge, and Florida's red tides. *Geophys. Res. Lett.* 33:L11601. doi: 10.1029/2005GL025449

Hwang, D. W., Kim, G., Lee, Y. W., and Yang, H. S. (2005). Estimating submarine inputs of groundwater and nutrients to a coastal bay using radium isotopes. *Mar. Chem.* 96, 61–71. doi: 10.1016/j.marchem.2004.11.002

Integrated Ocean Drilling Program [IODP] (2020). *Integrated Ocean Drilling Program*. Available online at: http://publications.iodp.org/proceedings/313/103/103_t9.htm. [accessed on Aug 30, 2020]

Jiang, W., Yu, K., Yinxian, S., Jian-xin, Z., Yue-xing, F., Yinghui, W., et al. (2018). Coral geochemical record of submarine groundwater discharge back to 1870 in the northern South China Sea. *Paleogeogr Palaeoclimat Palaeoecol.* 507, 30–38. doi: 10.1016/j.palaeo.2018.05.045

Jiao, J. J., and Post, V. (2019). *Coastal Hydrogeology*. Cambridge: Cambridge University Press.

Johnson, A. G., Glenn, C. R., Burnett, W. C., Peterson, R. N., and Lucey, P. G. (2008). Aerial infrared imaging reveals large nutrient-rich groundwater inputs to the ocean. *Geophys. Res. Lett.* 35:L15606. doi: 10.1029/2008GL034574

Joiner, C. N. (1991). *Chloride concentrations in the upper water-bearing zone of the Upper Floridan aquifer in the Brunswick area, Georgia, October-November 1990*. Reston, VA: U.S. Geological Survey. 91–174.

Joye, S. B., and Kostka, J. E. (2020). *Microbial Genomics of the Global Ocean System. American Academy of Microbiology. Colloquium Report*. Washington, DC: American Geophysical Union.

Konikow, L. F. (2011). Contribution of global groundwater depletion since 1900 to sea-level rise. *Geophys. Res. Lett.* 38:L17401.

Lee, Y. W., Hwang, D. W., Kim, G., Lee, W. C., and Oh, H. T. (2009). Nutrient inputs from submarine groundwater discharge (SGD) in Masan Bay, an embayment surrounded by heavily industrialized cities. *Korea. Sci. Total Environ.* 407, 3181–3188. doi: 10.1016/j.scitotenv.2008.04.013

Luo, X., Jiao, J. J., Moore, W. S., Cherry, J. A., Wang, Y., and Liu, K. (2018). Significant chemical fluxes from natural terrestrial groundwater rival anthropogenic and fluvial input in a large-river deltaic estuary. *Water Res.* 144, 603–615. doi: 10.1016/j.watres.2018.07.004

Martens, C. S., Berner, R. A., and Rosenfield, J. K. (1978). Interstitial water chemistry of anoxic Long Island Sound sediments. 2. Nutrient regeneration and phosphate removal. *Limnol. Oceanog.* 23, 605–617. doi: 10.4319/lo.1978.23.4.0605

McAllister, S. M., Barnett, J. M., Heiss, J. W., Findlay, A. J., MacDonald, D. J., Dow, C. L., et al. (2015). Dynamic hydrologic and biogeochemical processes drive microbially enhanced iron and sulfur cycling within the intertidal mixing zone of a beach aquifer. *Limnol. Oceanogr.* 60, 329–345. doi: 10.1002/lno.10029

Michael, H. A., Mulligan, A. E., and Harvey, C. F. (2005). Seasonal oscillations in water exchange between aquifer and the coastal ocean. *Nature* 436, 1145–1148. doi: 10.1038/nature03935

Moore, W. S. (1996). Large groundwater inputs to coastal waters revealed by ^{226}Ra enrichments. *Nature* 380, 612–614. doi: 10.1038/380612a0

Moore, W. S. (1999). The subterranean estuary: a reaction zone of ground water and sea water. *Mar. Chem.* 65, 111–126. doi: 10.1016/s0304-4203(99)00014-6

Moore, W. S. (2010). The Effect of Submarine Groundwater Discharge on the Ocean. *Ann Rev. Mar. Sci.* 2, 345–374.

Moore, W. S., Beck, M., Reidel, T., van der Loeff, M., Dellwig, O., Shaw, T. J., et al. (2011). Radium-based pore water fluxes of silica, alkalinity, manganese, DOC, and uranium: a decade of studies in the German Wadden Sea. *Geochim. Cosmochim. Acta.* 75, 6535–6555. doi: 10.1016/j.gca.2011.08.037

Moore, W. S., Blanton, J. O., and Joye, S. B. (2006). Estimates of Flushing Times, Submarine Groundwater Discharge, and Nutrient Fluxes to Okatee River, South Carolina. *J. Geophys. Res.* 111:C09006. doi: 10.1029/2005JC003041

Moore, W. S., Krest, J., Taylor, G., Roggenstein, E., Joye, S., and Lee, R. (2002). Thermal evidence of water exchange through a coastal aquifer: implications for nutrient fluxes. *Geophys. Res. Lett.* 29:1704. doi: 10.1029/2002GL014923

Moore, W. S., and Wilson, A. M. (2005). Advective flow through the upper continental shelf driven by storms, buoyancy, and submarine groundwater discharge. *Earth Planet. Sci. Lett.* 235, 564–576. doi: 10.1016/j.epsl.2005.04.043

Mountain, G., Proust, J.-N., McInroy, D., and Cotterill, C. (2010). "Proc. IODP, 313: Tokyo," in *Proceedings of the Integrated Ocean Drilling Program*, eds, D. A. V. Stow, F.J. Hernández-Molina, C.A. Alvarez Zarikian, (Tokyo: Integrated Ocean Drilling Program Management International, Inc).

Peterson, R. N., Moore, W. S., Chappel, S. L., Viso, R. F., Libes, S. M., and Peterson, L. E. (2016). A New Perspective on Coastal Hypoxia: the Role of Saline Groundwater. *Mar. Chem.* 179, 1–11. doi: 10.1016/j.marchem.2015.12.005

Portnov, A., Smith, A. J., Mienert, J., Cherkashov, G., Rekant, P., Semenov, P., et al. (2013). Offshore permafrost decay and massive seabed methane escape in water depths >20 m at the South Kara Sea shelf. *Geophys. Res. Lett.* 40, 3962–3967. doi: 10.1002/grl.50735

Porubsky, W. P., Weston, N. B., Moore, W. S., Ruppel, C., and Joye, S. B. (2014). Dynamics of groundwater discharge and associated fluxes of dissolved nutrients, carbon, and trace gases to the coastal zone (Okatee River estuary, South Carolina). *Geochim. Cosmochim. Acta.* 131, 81–97. doi: 10.1016/j.gca.2013.12.030

Price, R. M., Swart, P. K., and Fourqurean, J. W. (2006). Coastal groundwater discharge – an additional source of phosphorus for the oligotrophic wetlands of the Everglades. *Hydrobiologia* 569, 23–36. doi: 10.1007/s10750-006-0120-5

Pritchard, D. W. (1967). "What is an estuary: Physical viewpoint," in *Estuaries*, ed. G. H. Lauff (Washington: DC Pub).

Qi, S.-Z., and Qui, Q.-L. (2011). Environmental hazard from saltwater intrusion in the Laizhou Gulf, Shandong Province of China. *Nat. Hazards* 56, 563–566. doi: 10.1007/s11069-010-9686-3

Riedel, T., Lettmann, K., Schnetger, B., Beck, M., and Brumsack, H.-J. (2011). Rates of trace metal and nutrient diagenesis in an intertidal creek bank. *Geochim. Cosmochim. Acta.* 75, 134–147. doi: 10.1016/j.gca.2010.09.040

Robinson, C., Li, L., and Barry, D. A. (2007). Effect of tidal forcing on a subterranean estuary. *Adv. Water Resor.* 30, 851–865. doi: 10.1016/j.advwatres.2006.07.006

Rocha, C., Robinson, C. E., Santos, I. R., Waska, H., Michael, H. A., and Bokuniewicz, H. J. (2021). A place for subterranean estuaries in the coastal zone. *Estuar. Coast. Shelf Sci.* 250:107167. doi: 10.1016/j.ecss.2021.107167

Rogers, D. R., and Casciotti, K. L. (2010). Abundance and diversity of archaeal ammonia oxidizers in a coastal groundwater system. *Appl. Environ. Microbiol.* 76, 7938–7948. doi: 10.1128/aem.02056-09

Roy, M., Martin, J. B., Cherrier, J., Cable, J. E., and Smith, C. G. (2010). Influence of sea level rise on iron diagenesis in an east Florida subterranean estuary. *Geochim. Cosmochim. Acta* 74, 5560–5573. doi: 10.1016/j.gca.2010.07.007

Saegar, D. A. (2012). "Introduction to Ocean Sciences, 4th edition," in *Creative Commons, 444 Castro Street, Suite 900, Mountain View*, (California: Ever Green).

Sáenz, J. P., Hopmans, E. C., Rogers, D., Henderson, P. B., Charette, M. A., Schouten, S., et al. (2012). Distribution of anaerobic ammonia-oxidizing bacteria in a subterranean estuary. *Mar. Chem.* 13, 7–13. doi: 10.1016/j.marchem.2012.04.004

Santoro, A. E., Boehm, A. B., and Francis, C. A. (2006). Denitrifier community composition along a nitrate and salinity gradient in a coastal aquifer. *Appl. Environ. Microbiol.* 72, 2102–2109. doi: 10.1128/aem.72.3.2102-2109.2006

Santoro, A. E., Francis, C. A., De Sieyes, N. R., and Boehm, A. B. (2008). Shifts in the relative abundance of ammonia-oxidizing bacteria and archaea across physicochemical gradients in a subterranean estuary. *Environ. Microbiol.* 10, 1068–1079. doi: 10.1111/j.1462-2920.2007.01547.x

Schultz, E. A., and Simmons, H. B. (1957). *Fresh Water-Salt Density Currents, A Major Cause of Siltation in Estuaries*. US Army Corps of Engineers Technical Bulletin No. 2

Schutte, C. A., Moore, W. S., Wilson, A. M., and Joye, S. B. (2020). Groundwater-driven methane export reduces salt marsh blue carbon potential. *Glob. Biogeochem. Cycl.* 34:e2020GB006587. doi: 10.1029/2020GB006587

Schutte, C. A., Wilson, A. M., Evans, T., Moore, W. S., and Joye, S. B. (2016). Methanotrophy controls groundwater methane export from a barrier island. *Geochim. Cosmochim. Acta.* 179, 242–256. doi: 10.1016/j.gca.2016.01.022

Segarra, K. E. A., Comerford, C., Slaughter, J., and Joye, S. B. (2013). Impact of electron acceptor availability on the anaerobic oxidation of methane in coastal freshwater and marine sediments. *Geochim. Cosmochim. Acta.* 115, 15–30. doi: 10.1016/j.gca.2013.03.029

Shakhova, N., Semiletov, I., Salyuk, A., Yusupov, V., Kosmach, D., and Gustafsson, O. ¨ (2010). Extensive Methane Venting to the Atmosphere from Sediments of the East Siberian Arctic Shelf. *Science* 327, 1246–1250. doi: 10.1126/science.1182221

Shaw, T. J., Moore, W. S., Kloepfer, J., and Sochaski, M. A. (1998). The flux of barium to the coastal waters of the southeastern United States: the importance of submarine groundwater discharge. *Geochim. Cosmochim. Acta.* 62, 3047–3052. doi: 10.1016/s0016-7037(98)00218-x

Sivan, O., Yechieli, Y., Herut, B., and Lazair, B. (2005). Geochemical evolution and timescale of seawater intrusion into the coastal aquifer of Israel. *Geochim. Cosmochim. Acta.* 69, 579–592. doi: 10.1016/j.gca.2004.07.023

Tamborski, J. J., Cochran, J. K., Bokuniewicz, H., Heilbrun, C., Garcia-Orellana, J., Rodellas, V., et al. (2020). Radium mass balance sensitivity analysis for submarine groundwater discharge estimation in semi-enclosed basins: the case study of Long Island Sound. *Front. Environ. Sci.* 8:108. doi: 10.3389/FENVS.2020.00108

Tan, E., Wang, G., Moore, W. S., Li, Q., and Dai, M. (2018). Shelf-Scale Submarine Groundwater Discharge in the Northern South China Sea and East China Sea and its Geochemical Impacts. *J. Geophys. Res. Oceans* 123, 2997–3013. doi: 10.1029/2017jc013405

Taniguchi, M., Ishitobi, T., and Shimada, J. (2006). Dynamics of submarine groundwater discharge and freshwater–seawater interface. *J. Geophys. Res.* 111:C01008. doi: 10.1029/2005JC00292

Tse, K. C., and Jiao, J. J. (2008). Estimation of submarine groundwater discharge in Plover Cove, Tolo Harbour, Hong Kong by222 Rn. *Mar. Chem.* 111, 160–170. doi: 10.1016/j.marchem.2008.04.012

van Geldern, R., Hayashi, T., Böttcher, M. E., Mottl, M. J., Barth, J. A. C., and Stadler, S. (2013). Stable isotope geochemistry of pore waters and marine sediments from the New Jersey shelf: methane formation and fluid origin. *Geosphere* 9, 96–112. doi: 10.1130/GES00859.1

Wahl, T., Calafat, F. M., and Luther, M. E. (2014). Rapid changes in the seasonal sea level cycle along the US Gulf coast from the late 20th century. *Geophys. Res. Lett.* 41, 491–498. doi: 10.1002/2013gl058777

Wait, R. L., and Gregg, D. O. (1973). "Hydrology and chloride contamination of the principal artesian aquifer in Glynn County, Georgia," in *GA Geol. Survey Hydrologic Report** 1, (Atlanta, GA: USGS).

Wang, Y. J., and Jiao, J. J. (2012). Origin of groundwater salinity and hydrogeochemical processes in the confined Quaternary aquifer of the Pearl River Delta. *China. J. Hydrol.* 43, 112–124. doi: 10.1016/j.jhydrol.2012.03.008

Werner, A. D., Bakker, M., Post, V. E. A., Vandenbohede, A., Lu, C., Ataie-Ashtiani, B., et al. (2013). Seawater intrusion processes, investigation and management: recent advances and future challenges. *Adv. Water Resour.* 51, 3–26. doi: 10.1016/j.advwatres.2012.03.004

Werner, A. D., and Simmons, C. T. (2009). Impact of Sea-Level Rise on Sea Water Intrusion in Coastal Aquifers. *Ground Water* 47, 197–204. doi: 10.1111/j.1745-6584.2008.00535.x

Weston, N. B., Porubsky, W., Samarkin, V., Erickson, M., MacAvoy, S., and Joye, S. (2006b). Porewater stoichiometry of terminal metabolic products, sulfate, and dissolved organic carbon and nitrogen in estuarine intertidal creek-bank sediments. *Biogeochemistry* 77, 375–408. doi: 10.1007/s10533-005-1640-1

Weston, N. B., Dixon, R., and Joye, S. B. (2006a). Microbial and geochemical ramifications of salinity intrusion into tidal freshwater sediments. *J. Geophys. Res. Biogeosci.* 111:G01009.

Wilson, A. M., Moore, W. S., Joye, S. B., Anderson, J. L., and Schutte, C. A. (2011). Storm-driven groundwater flow in a salt marsh. *Water Resour. Res.* 47:W02535.

Xu, J., Shi, B., and Cheng, X. (2002). Study on major ecological environment problems and its survey method. *Shandong Geol.* 18, 95–99.

Yaala, H. B., Fniter, R., Fouchera, D., and Clarisse, O. (2019). Direct analysis of radium-226 in sediment by ICP-MS: an analytical challenge? *J. Anal. At. Spectrom* 34, 1597–1605. doi: 10.1039/c9ja00156e

Young, M. B., Gonneea, M. E., Fong, D. A., Moore, W. S., Herrera-Silveira, J., and Paytan, A. (2008). Characterizing sources of groundwater to a tropical coastal lagoon in a karstic area using radium isotopes and water chemistry. *Mar. Chem.* 109, 377–394. doi: 10.1016/j.marchem.2007.07.010

Younger, P. L. (1996). Submarine groundwater discharge. *Nature* 382, 121–122.

Conflict of Interest: The authors declare that the research was conducted in the absence of any commercial or financial relationships that could be construed as a potential conflict of interest.

Copyright © 2021 Moore and Joye. This is an open-access article distributed under the terms of the Creative Commons Attribution License (CC BY). The use, distribution or reproduction in other forums is permitted, provided the original author(s) and the copyright owner(s) are credited and that the original publication in this journal is cited, in accordance with accepted academic practice. No use, distribution or reproduction is permitted which does not comply with these terms.

frontiers in Marine Science

ORIGINAL RESEARCH
published: 04 February 2021
doi: 10.3389/fmars.2021.607083

Molecular Traits of Dissolved Organic Matter in the Subterranean Estuary of a High-Energy Beach: Indications of Sources and Sinks

Hannelore Waska[1], Heike Simon[1], Soeren Ahmerkamp[2], Janek Greskowiak[3], Janis Ahrens[4], Stephan L. Seibert[3], Kai Schwalfenberg[5], Oliver Zielinski[5,6] and Thorsten Dittmar[1,7]*

[1] Research Group for Marine Geochemistry (ICBM-MPI Bridging Group), Institute for Chemistry and Biology of the Marine Environment, University of Oldenburg, Oldenburg, Germany, [2] Max Planck Institute for Marine Microbiology, Bremen, Germany, [3] Hydrogeology and Landscape Hydrology Group, Institute for Biology and Environmental Sciences, University of Oldenburg, Oldenburg, Germany, [4] Microbiogeochemistry Group, Institute for Chemistry and Biology of the Marine Environment, University of Oldenburg, Oldenburg, Germany, [5] Marine Sensor Systems Group, Institute for Chemistry and Biology of the Marine Environment, University of Oldenburg, Oldenburg, Germany, [6] Marine Perception Research Group, German Research Center for Artificial Intelligence, Oldenburg, Germany, [7] Helmholtz Institute for Functional Marine Biodiversity at the University of Oldenburg, Oldenburg, Germany

OPEN ACCESS

Edited by:
Clare Robinson, University of Western Ontario, Canada

Reviewed by:
Martin Andersen, University of New South Wales, Australia
Gwénaëlle Chaillou, Université du Québec à Rimouski, Canada

***Correspondence:**
Hannelore Waska
hannelore.waska@uni-oldenburg.de

Specialty section:
This article was submitted to Marine Biogeochemistry, a section of the journal Frontiers in Marine Science

Received: *16 September 2020*
Accepted: *13 January 2021*
Published: *04 February 2021*

Citation:
Waska H, Simon H, Ahmerkamp S, Greskowiak J, Ahrens J, Seibert SL, Schwalfenberg K, Zielinski O and Dittmar T (2021) Molecular Traits of Dissolved Organic Matter in the Subterranean Estuary of a High-Energy Beach: Indications of Sources and Sinks. Front. Mar. Sci. 8:607083. doi: 10.3389/fmars.2021.607083

Advective flows of seawater and fresh groundwater through coastal aquifers form a unique ecohydrological interface, the subterranean estuary (STE). Here, freshly produced marine organic matter and oxygen mix with groundwater, which is low in oxygen and contains aged organic carbon (OC) from terrestrial sources. Along the groundwater flow paths, dissolved organic matter (DOM) is degraded and inorganic electron acceptors are successively used up. Because of the different DOM sources and ages, exact degradation pathways are often difficult to disentangle, especially in high-energy environments with dynamic changes in beach morphology, source composition, and hydraulic gradients. From a case study site on a barrier island in the German North Sea, we present detailed biogeochemical data from freshwater lens groundwater, seawater, and beach porewater samples collected over different seasons. The samples were analyzed for physico-chemistry (e.g., salinity, temperature, dissolved silicate), (reduced) electron acceptors (e.g., oxygen, nitrate, and iron), and dissolved organic carbon (DOC). DOM was isolated and molecularly characterized via soft-ionization ultra-high-resolution mass spectrometry, and molecular formulae were identified in each sample. We found that the islands' freshwater lens harbors a surprisingly high DOM molecular diversity and heterogeneity, possibly due to patchy distributions of buried peat lenses. Furthermore, a comparison of DOM composition of the endmembers indicated that the Spiekeroog high-energy beach STE conveys chemically modified, terrestrial DOM from the inland freshwater lens to the coastal ocean. In the beach intertidal zone, porewater DOC concentrations, lability of DOM and oxygen concentrations, decreased

while dissolved (reduced) iron and dissolved silicate concentrations increased. This observation is consistent with the assumption of a continuous degradation of labile DOM along a cross-shore gradient, even in this dynamic environment. Accordingly, molecular properties of DOM indicated enhanced degradation, and "humic-like" fluorescent DOM fraction increased along the flow paths, likely through accumulation of compounds less susceptible to microbial consumption. Our data indicate that the high-energy beach STE is likely a net sink of OC from the terrestrial and marine realm, and that barrier islands such as Spiekeroog may act as efficient "digestors" of organic matter.

Keywords: high-energy beach, dissolved organic matter, subterranean estuary, porewater, barrier island, North Sea, coastal aquifer

INTRODUCTION

Subterranean estuaries (STEs) underlying beaches are underground mixing zones of fresh, meteoric groundwater with seawater, which is pumped through the beach aquifer by waves and tides (Moore, 1999). Porewater flow constantly supplies the beach aquifer with organic matter and electron acceptors, making STEs highly active biogeochemical reactors (Anschutz et al., 2009). Along these advective flowpaths, organic matter is degraded and remineralization products accumulate, before they enter the coastal ocean as submarine groundwater discharge (SGD). Therefore, STEs are characterized by both strong salinity and redox gradients (Rocha, 2008; Reckhardt et al., 2015).

Since the turn of the millennium, the steadily growing recognition of STEs as global, ubiquitous land-ocean interfaces (Ma and Zhang, 2020) has led to a wealth of investigations (e.g., Charette and Sholkovitz, 2006; Robinson et al., 2006; Santos et al., 2009; Roy et al., 2010; Kim et al., 2012; Beck et al., 2017). In particular, the topic of sources and fate of organic matter in STEs has received increasing attention in the past decade, as organic matter is the fuel that drives the STE microbial biogeochemical reactor. Especially, novel spectrophotometric and mass spectrometric techniques have elucidated organic matter inputs and processing in subterranean estuaries (e.g., Kim et al., 2012; Seidel et al., 2015; Suryaputra et al., 2015; Jiang et al., 2020; McDonough et al., 2020a).

Most STEs receive aged dissolved organic matter (DOM) of low bioavailability from soils via the fresh groundwater endmember. However, fresh groundwater in a beach STE can also be a carrier of marine DOM from beach wrack and other particulate organic matter (POM; Santos et al., 2009; Suryaputra et al., 2015; Kim et al., 2019). The seawater endmember provides newly produced DOM from phytoplankton, which is considered more bioavailable compared to aged, groundwater-derived DOM (Seidel et al., 2015). In addition, recirculating seawater was found to leach and transport DOM from particulate marine organic matter buried in the sediment (Kim et al., 2019), as well as from terrestrial paleosols (Seidel et al., 2014; Couturier et al., 2016).

In microtidal, sheltered beaches with a high hydraulic gradient from inland groundwater, terrestrial DOM can be supplied to the STE in large proportions (McAllister et al., 2015; Couturier et al., 2016; Meredith et al., 2020). Contrastingly, in meso-to macrotidal regions, large volumes of marine, labile DOM are pumped through the STE, with models predicting seawater infiltrations up to several tens of meters depth into the beach aquifer (Robinson et al., 2006; Grünenbaum et al., 2020). On the global scale, the volumes of seawater-SGD are several fold higher than those of the fresh groundwater flux (Santos et al., 2012; Kwon et al., 2014; Luijendijk et al., 2020; note that the latter authors did not take into account tidally recirculated fluxes). Taking marine DOM and POM, coastal paleosols, and coastal beach wrack into account, a high-volume throughput of the marine endmember will therefore largely define the source functions and processing of both, terrestrial and marine DOM, in STEs worldwide. Yet, only a few studies of organic matter inputs into meso-to macrotidal STEs are available to date (e.g., Goñi and Gardner, 2003; Kim et al., 2012; Seidel et al., 2015), and only two of those have investigated a site additionally exposed to high-energy waves (Reckhardt et al., 2015; Beck et al., 2017).

Once DOM has entered the STE from different sources, it is abiotically or biologically processed, for example by adsorption/desorption to/from mineral phases, and microbial respiration, respectively. Adsorption of DOM on iron minerals occurs when source water flows through sediments which are rich in iron oxides, and DOM compounds are filtered out (Kaiser and Guggenberger, 2000). DOM may also co-precipitate with iron at oxic-anoxic interfaces commonly found in STEs (Linkhorst et al., 2017; Sirois et al., 2018). Both processes are compound-selective, targeting comparatively less saturated, more aromatic compounds with high oxygen content (Riedel et al., 2012). In addition, they are reversible and may release DOM once reduced conditions are restored (Lalonde et al., 2012; Linkhorst et al., 2017), therefore posing a transient storage pool of organic matter. So far, data on DOM-iron mineral interactions in STEs are scarce (Linkhorst et al., 2017; Sirois et al., 2018). Hence, the magnitudes, and temporal and spatial dynamics of these processes are not well known.

On the biological side, microbes feed on DOM and sequentially consume electron acceptors based on energy yield from oxygen to nitrate, manganese and iron oxides, sulfate, and finally inorganic carbon (Froelich et al., 1979). In parallel to the sequential exhaustion of the electron acceptors, organic matter too is assumed to be degraded along an intrinsic reactivity continuum (Benner and Amon, 2015). As a result,

along the advective flowpath in the STE, accumulation of reduced electron acceptors is accompanied by a decrease in the (relative) abundance of more bioavailable, saturated compounds and carbohydrates, and an increase of abundances of less bioavailable, less saturated, more aromatic compounds (Seidel et al., 2015; Beck et al., 2017). In reactive transport models, this degradation is acknowledged in a simplified manner, attributing decreasing reactivity to increasing age of organic matter (Van Cappellen and Wang, 1996; Spiteri et al., 2008; Anderson et al., 2019). However, heterogeneous flow patterns and additions of DOM from buried patches of POM can disrupt continuous degradation pathways and produce a non-steady state DOM distribution (Rocha, 2008; Santos et al., 2009; Kim et al., 2019). Therefore, more qualitative and quantitative data on DOM sources and sinks are needed to assess and predict organic matter turnover in the STE and calibrate site-specific reactive transport models. Another uncertainty is associated with temporal and spatial dynamics of physical disturbances, and how they might impact the efficiency of the STE microbial community to degrade DOM. In sheltered environments, DOM appears to accumulate along advective water flowpaths due to increasing degradation of POM while at the same time energy-rich electron acceptors are consumed and not replenished fast enough (Roy et al., 2011; Seidel et al., 2014). On the other hand, wave action and large tidal amplitudes may speed up organic matter respiration due to high oxygen supply via sediment re-distribution and fast water circulation. The question is then, whether too high disturbance amplitudes or frequencies, for example by storm events or high-energy waves, have a negative influence on the adaptation capacities of the microbial community. So far, a comparison of research literature from different types of environments indicates that frequent disturbances of flow paths and sediment structures enhance, rather than restrict, microbial remineralization processes in high-energy STEs (McLachlan, 1982; Charbonnier et al., 2013; Reckhardt et al., 2015; Ibánhez and Rocha, 2016; Waska et al., 2019b). If there is no upper limit to microbial resilience against physical disturbances (Novitsky and MacSween, 1989; Degenhardt et al., 2020), then meso- to macrotidal STEs with strong wave action should be particularly active sites of organic matter turnover along the world's coastlines.

In this study, we set out to investigate DOM sources and sinks in a mesotidal, high-energy beach STE on Spiekeroog Island. This STE is characterized by a rather uniform geology and (terrestrial) hydrology (Röper et al., 2012), but complex tidal, wave, and storm flood patterns on the marine side (Beck et al., 2017). Previous research at the study site hinted at a surprisingly high DOM heterogeneity in groundwater, probably stemming from ancient peat layers and surficial influences of dune vegetation (Beck et al., 2017). In 2019, we reported so far unknown brackish porewater patches at the low water line, and suggested that they stem from inland groundwater (Waska et al., 2019b). Furthermore, a decrease of DOC concentrations along the underground flowpaths was attributed to rapid remineralization, indicating that this site may be a net sink for organic carbon (OC; Reckhardt et al., 2015). Therefore, we set out to answer the following questions: (1) What are the molecular signatures of the various types of terrigenous DOM on the island, and are they comparable to those found in brackish porewaters at the low water line? (2) What are the likely abiotic and biotic sinks of DOM, and can they be disentangled by characteristic molecular traits? (3) Is this high-energy, mesotidal system a net source or net sink of organic matter to the coastal North Sea?

To answer these questions, we conducted endmember sampling of seawater, groundwater, and porewater over four sampling campaigns across different seasons and tied their molecular DOM characteristics to electron acceptor distributions and dynamics (Ahrens et al., 2020). In addition, we investigated the co-evolution of DOC and DOM with the accumulation of the groundwater-tracer dissolved silicate (DSi; Oehler et al., 2019) and a DOM fluorescence marker which is known to accumulate in aged groundwater (Nelson et al., 2015; Kim and Kim, 2017). Finally, we investigated DOC and DOM release from the shallow STE over a tidal cycle in two different seasons. The assembly of these large and diverse datasets has enabled us to provide a comprehensive picture of DOM sources and sinks in the shallow STE.

MATERIALS AND METHODS

Study Site

Our study site is located on the northern coast of Spiekeroog Island, which is part of a barrier island chain in the southern North Sea at the German coast of Lower Saxony (**Figure 1A**). The islands' freshwater lens (**Figure 1B**), as well as the beach site itself, have been subject to numerous investigations (for example Röper et al., 2012; Reckhardt et al., 2015; Beck et al., 2017; Reckhardt et al., 2017; Seibert et al., 2018, 2019a; Waska et al., 2019a,b; Ahrens et al., 2020). Briefly, the beach aquifer consists of medium- to fine-grained sands. A clay layer borders the freshwater lens at ∼40–50 meter below sea level (mbsl), but it is not known whether it extends underneath the whole beach aquifer as well (cf., Röper et al., 2012, and references cited therein). The beach length from dune base to low water line is approximately 200–300 m. In the intertidal zone, a shore-parallel runnel can be found downslope of the high water line, then the beach ascends to a ridge before descending toward the low water line (**Figures 1C**, **2**). Both, ridge and runnel undergo strong topographic changes due to wave impact and winter storm floods (Waska et al., 2019b). Numeric models, as well as *in situ* porewater sampling campaigns, indicated that groundwater from the inland fresh water lens exfiltrates into the runnel as well as into the surf zone at the low water line (Beck et al., 2017; Grünenbaum et al., 2020). The high water line and ridge serve as main seawater infiltration zones, which drain into runnel and low water line during receding tide (**Figure 2**). Several studies have characterized the inorganic and organic geochemistry of the study site (e.g., Reckhardt et al., 2015; Beck et al., 2017; Waska et al., 2019b; Ahrens et al., 2020; Paffrath et al., 2020). Overall, the upper intertidal zone between high water line and runnel is dominated by a

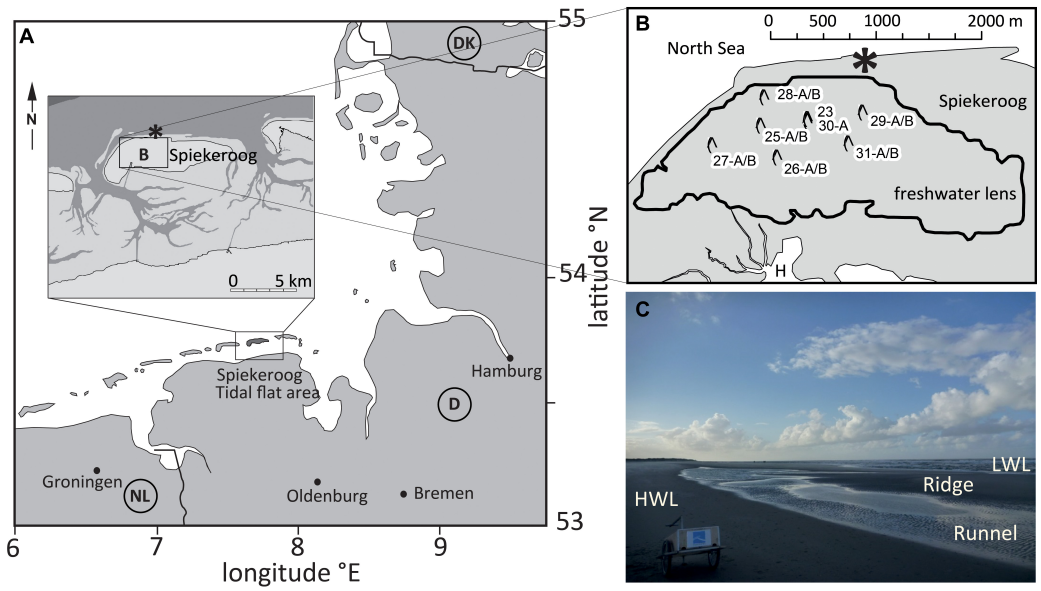


FIGURE 1 | (A) Location of Spiekeroog Island in the German North Sea. **(B)** Enlarged map of box B, with central Spiekeroog in gray and the surrounding sea in white (H = Harbour of Spiekeroog, which faces the Wadden Sea to the South). The black line indicates the borders of the freshwater lens. The well sites sampled for this study are marked with a symbol and with numbers (modified from Seibert et al., 2018). The asterisk denotes the beach sampling site. **(C)** Typical beach morphology. HWL, high water line; LWL, low water line.

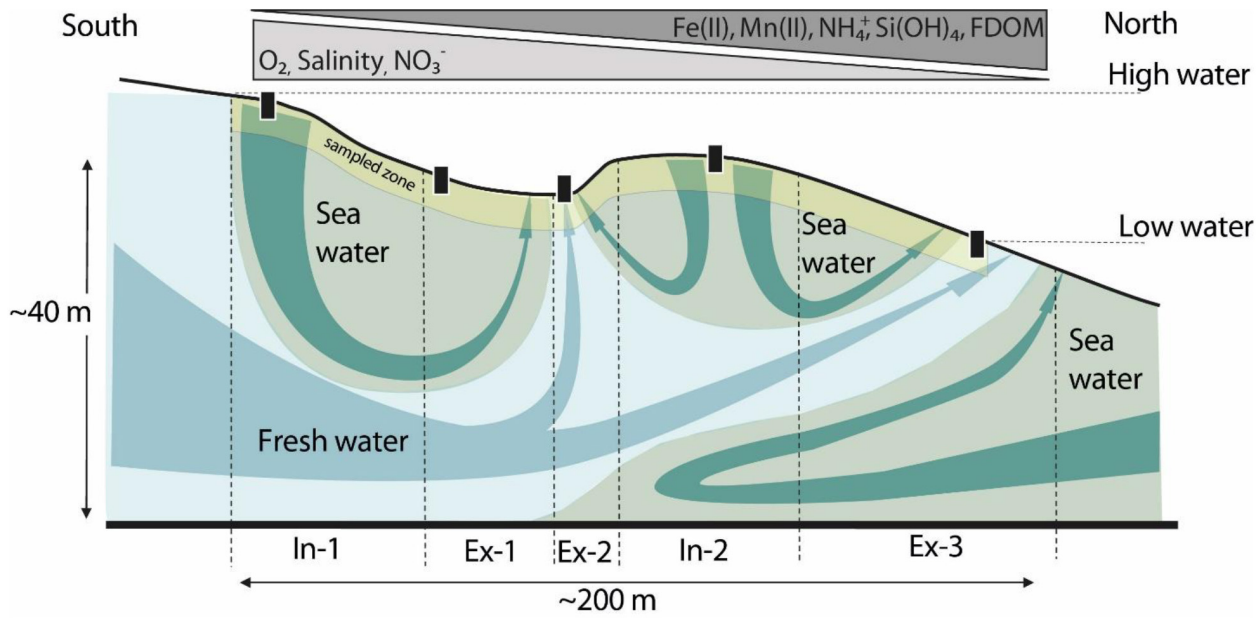


FIGURE 2 | Schematic diagram of a beach cross-section at the study site, modified from Waska et al. (2019b) and Ahrens et al. (2020). The landward side is South, the North faces the open North Sea. The gray–blue arrows depict flow from the islands fresh water lens, the green arrows show seawater circulation through the beach aquifer. In-1 and Ex-3 bracket the intertidal zone of the beach. The triangles on top indicate the direction in which the respective constituent concentrations increase, i.e., concentrations of reduced compounds increase toward the low water line. The yellow section is an approximation of the sampling depths covered in this study compared to the overall extent of the beach aquifer. Black boxes indicate the location of the transect stations. A detailed map of the transect points can be found in Ahrens et al. (2020), **Figure 1C** and Degenhardt et al. (2020), **Figure 1**.

sharp oxic gradient. Between runnel and ridge, active nitrogen cycling (denitrification–nitrification) takes place, while Mn and Fe reduction prevail from the ridge toward the low water line. The horizontal succession of electron acceptors expands across the beachface width during winter and contracts during summer, thus shifting the borders of redox zones in

the cross-shore direction between high and low water line (Ahrens et al., 2020).

Sampling

Intertidal Transects

Samples were collected in four campaigns: October 2016, March 2017, August 2017, and February 2018. With the exception of the March 2017 campaign, all campaigns took place during spring tide. In October 2016, porewaters from two cross-shore transects, approximately 60 m apart, with five stations and four depths (10, 30, 50, and 100 cm below surface) each were sampled. These stations spanned across the whole intertidal zone and covered the main morphological features (e.g., high water line, runnel, ridge, and low water line) and associated in-and exfiltration zones (Waska et al., 2019b). Further details on transect locations and sampling point distributions can be found in Ahrens et al. (2020), **Figure 1C**, and Degenhardt et al. (2020), **Figure 1**. Several stations from the October campaign were re-visited in March and August. Additionally, a third transect, parallel to the other two, was sampled ∼200 m further eastward in March 2017. In February 2018, transect sampling occurred in the vicinity of the most westward transect from October, but not at the exact same stations.

At the sampling stations, porewater was drawn using polyethylene (PE) syringes and stainless steel push-point samplers. Temperature, conductivity, oxygen, and fluorescent DOM (FDOM, excitation center-wavelength 375 nm, emission wavelength range >420 nm) were measured on site using hand-held multimeters (WTW Multi 3430/WTW pH/Cond 340i with TetraCon 925 Conductivity Sensor; FireStingGO2, Pyro-Science; Aquafluor, Turner Instruments). Details on instrument calibration can be found in Waska et al. (2019b) and Ahrens et al. (2020). FDOM measurements were conducted with filtered samples using Whatman Acrodisc GHP 0.2 μm syringe filters. Porewater samples for nutrients and trace metal analyses were collected with the syringes, filtered directly into low-density polyethylene (LDPE) bottles with 0.45 μm cellulose acetate syringe filters, and poisoned with mercury chloride (nutrients) or acidified with ultra-clean HNO_3 to 1% (v/v) (trace metals, Ahrens et al., 2020). For DOC and DOM, porewater samples were collected from the samplers with a 12V-battery driven ceramic piston pump (Fluid Metering, Inc., NY, United States) and Norprene chemical tubing, and directly filtered into acid-washed high-density polyethylene (HDPE) sample bottles. The polypropylene (PP) inline filter holders were equipped with a sandwich of 0.8/0.2 μm acid-washed SUPOR filter membranes (Pall). From each station, 200 mL sample volumes were collected. Filtered samples were acidified with suprapur HCl to pH 2 in a University-associated local laboratory on Spiekeroog (Umweltzentrum Wittbülten) after each day of sampling, and stored in the dark at 4°C. In total, we extracted a maximum of ∼400 mL from each sampling depth for line purging, *in situ* measurements, and samples for processing in the laboratory. Using a sediment porosity of 0.3 (Grünenbaum et al., 2020), this would correspond to a sampling halo with a radius of ∼7 cm. Therefore, we assume that the sample radii of the different depths did not overlap substantially.

Seawater and Groundwater Endmembers

Seawater samples were collected from the nearshore surf zone using acid-washed Nalgene 2 L polycarbonate (PC) bottles, and kept onsite in cool boxes. They were either filtered in between porewater stations during the day, or at the end of the sampling day in the laboratory, using the same pump and filter setup as the porewater samples. In September 2016, groundwater samples were extracted from eight monitoring wells located at different depths (∼6–40 m) in the unconfined aquifer of the islands' freshwater lens (**Figure 1B**; Seibert et al., 2018). The direct distance between the well locations and the beach sampling site ranged from ∼900 to 1,400 m (**Figure 1B**). Fourteen samples were collected in total, which were not filtered but directly acidified, and stored cool in the dark (4°C). Although groundwater travel times from the wells to the beach site (range of decades) are expected to largely exceed the time scale between groundwater and beach porewater sampling campaigns (1–2 years), we acknowledge that differences in sampling dates and sample treatment (filtered vs. non-filtered) may impact DOM composition, and thus the interpretation of endmember data has to be done with caution. In August 2017, porewater was sampled from ∼2 m depth at the dune base of Spiekeroog beach. Samples from this site had a salinity of <1 and represented a shallow groundwater source to the beach STE (hereafter named "dune porewater"). They were filtered, acidified, and stored together with the intertidal porewater samples.

Runnel Time Series

In March and September 2019, time series sampling was conducted to assess the geochemical impact of exfiltrating beach porewater on the nearshore water column. Both March and September sampling campaigns took place during morning low tides (9:58 and 9:43, respectively), with spring tidal ranges (2.8 and 3.5 m, respectively). Water samples were collected from the runnel which serves as a tidal channel, draining first the seawater from tidal inundation and then increasing amounts of exfiltrating porewater as the upper sediment layers are drained. For each of the two campaigns, water from the runnel was sampled approximately every hour over one tidal cycle, filtered on site, and acidified and stored at 4°C in the dark. In the March 2019 campaign, 200 mL samples were collected, in September 60 mL samples were collected, due to a change in the solid-phase extraction procedure for DOM.

Sample Processing and Analyses

Nutrients, Trace Metals, DOC, and TDN Analyses

Details on measurement of dissolved nitrogen species, as well as dissolved Fe and Mn, are published in Ahrens et al. (2020). The data are available on PANGAEA (doi.pangaea.de/10.1594/PANGAEA.905932). Phosphate was determined spectrophotometrically according to the methods of Itaya and Ui (1966) for phosphate <2.1 μM,

and Laskov et al. (2007) for phosphate >2.1 μM. Dissolved silicate ($Si(OH)_4$) in beach samples (porewater, seawater, runnel water, and dune base groundwater) was analyzed spectrophotometrically (Grasshoff et al., 1999) with a precision and trueness better than 10%. In the groundwater samples from the inland wells, $Si(OH)_4$ was measured by ICP-OES, with a precision better than 5% and trueness better than 15%. Further, total alkalinity was analyzed using spectrophotometric method according to Sarazin et al. (1999). DOC and total dissolved nitrogen (TDN) were measured with a Shimadzu TOC-VCPH against a deep sea Atlantic reference material (Hansell Lab, FL, United States), with precision and trueness better than 5%.

Molecular Characterization of DOM

For molecular analysis of DOM, 200 mL (seawater, porewater, and groundwater) acidified samples were desalted and concentrated by solid-phase extraction with help of 200 mg Agilent BOND ELUT cartridges following the protocol by Dittmar et al. (2008). For the runnel time series of March and September 2019, 40 mL samples were extracted onto 100 mg cartridges. This change in DOM isolation procedure was implemented in the late stage of the project to decrease sample collection and processing times. After repeated (3–4x of sample volume) washing with ultrapure water (UPW) acidified with HCl to pH 2, cartridges were dried with Argon gas. All samples were then eluted from the cartridges with Optima grade methanol (Fisher Scientific) into acid-washed, methanol-conditioned 4 mL HDPE bottles, and stored at −20°C in the freezer. Thereafter, samples were analyzed on a 15 Tesla Bruker solariX XR FT-ICR-MS (Fourier transform ion cyclotron resonance mass spectrometer) equipped with an electrospray ionization (ESI) source. For analysis of the beach porewater, sea water, and groundwater endmember samples, mass spectra were acquired using hand injection. The samples were adjusted to 5 ppm DOC with a 1:1 methanol–UPW mixture, filtered through 0.2 μm PTFE filters, and measured in broadband ESI negative ionization mode, with a flow rate of 20 μL min^{-1} and an ion accumulation time of 0.2 s. For each sample, 500 scans were acquired. For analysis of runnel time series, mass spectra were acquired using a HyStar Autoanalyzer, which was installed and hyphenated to the FT-ICR-MS at a later stage of the project, and which uses a higher injection flow rate. The samples were adjusted to 2.5 ppm DOC with a 1:1 methanol-UPW mixture and then measured in broadband ESI negative ionization mode, with a flow rate of 40 μL min^{-1} and an ion accumulation time of 0.2 s. For each sample, 200 scans were acquired. Together with the samples, an in-house deep-sea reference sample (North Equatorial Pacific Intermediate Water, NEqPIW) was measured daily to control instrument drift.

Acquired mass spectra were calibrated internally against a NEqPIW-based mass list of confirmed molecular formulae with an error of <0.1 ppm. Thereafter, the mass spectra were processed using the ICBM-OCEAN freeware (Merder et al., 2020) to remove noise, align samples along matching masses, and assign unique molecular formulae to each mass. Formula assignment was done with an error of <0.5 ppm, with the elemental setting $C_{1-100}H_{1-200}O_{1-70}N_{0-6}S_{0-2}P_{0-1}$. To yield unique formula assignments, the ICBM-OCEAN program applies a hierarchy of knock-out criteria as follows: isotopologue verification > homologous series length > assignment error. All assigned unique molecular formulae were classed into distinct molecular groups based on their elemental ratios (**Supplementary Figure 1**).

Data Processing

We assembled two main datasets of DOM molecular composition and environmental parameters: Dataset one contained all groundwater, dune porewater, seawater and beach porewater samples, and dataset two contained the two runnel time series. Therefore, all data processing as described below was done on each of the two sets individually. For DOM, the acquired mass cross tables were filtered to retain only the monoisotopic mass of each assigned molecular formulae. This approach increases the relative contribution of less abundant masses, as series of ^{13}C-containing masses of more abundant compounds are removed before further statistical analyses. Thereafter, samples were normalized against the sum of their intensities. The weighed sums of molecular properties (e.g., elemental composition, compound group classification) were calculated based on the distribution of relative signal intensities in the mass spectrum. In addition, we retrieved and applied four source-based and processing-based DOM molecular indices from the literature, which had been developed previously in other environmental settings (**Supplementary Figure 1**):

i A molecular degradation index ("Ideg"), which consists of ten ubiquitous molecular formulae, and which was developed in an open ocean setting and calibrated against the $\Delta^{14}C$ radiocarbon age of DOM (Flerus et al., 2012).
ii A broad DOM lability index ("MLB_l") which considers the H/C ratio of all molecular formulae in a sample, dividing them along a "molecular lability boundary" of H/C = 1.5 (D'Andrilli et al., 2015).
iii A terrestrial index ("ITerr") consisting of 80 ubiquitous molecular formulae, which were significantly correlated with the salinity gradient of the Amazon estuary (Medeiros et al., 2016).
iv A bioproduction index ("Ibioprod") of ten ubiquitous molecular formulae which were associated with fresh DOM release from aquatic primary production in a controlled marine mesocosm (Osterholz et al., 2015; Seibt, 2017).

Statistical analyses and plotting were done in R Studio (R version 3.5.3), using the packages *vegan*, *ggplot2*, *plyr*, and *corrplot*. Multivariate statistics primarily consisted of principal coordinate (PCoA) analyses of normalized DOM mass spectra using Bray-Curtis dissimilarities. The DOM-based distributions were correlated with environmental data (e.g., geographical location, physical properties, inorganic parameters) and weighed sums of molecular properties (e.g., elemental composition, compound group classification) using *vegan*s envfit function (Oksanen et al., 2013). Co-variations between relative intensities of molecular formulae and environmental parameters [e.g., salinity, $Si(OH)_4$] were done with Spearman's rank

correlation. Group comparisons were conducted with pairwise Wilcoxon rank-sum tests.

RESULTS

Endmember Geochemistry and DOM Characteristics

Salinities increased in the order groundwater < dune porewater < beach porewater < seawater, whereas concentrations of dissolved oxygen increased in the order groundwater < beach porewater < dune porewater < seawater (**Supplementary Table 1**). Furthermore, nitrate concentrations in dune porewater were 10- to 100-fold higher, and phosphate concentrations up to 10-fold higher, compared to the other endmembers. Beach porewater displayed the highest levels of dissolved Fe and Mn concentrations compared to groundwater, dune porewater, and seawater. On the other hand, freshwater lens groundwater had the highest ranges for DOC, $Si(OH)_4$, and FDOM concentrations (**Supplementary Table 1**).

A large DOM molecular dataset (>50,000 assigned unique molecular formulae) was produced from a total of 211 samples (groundwater, dune porewater, seawater, and beach porewater). Overall, groundwater samples yielded on average the highest number of assigned molecular formulae, and seawater samples the lowest (**Supplementary Table 2**). Similarly, DOM from groundwater samples had the highest average mass, and DOM from seawater the lowest. While no distinct trend in elemental O/C ratios could be found, average H/C ratios were overall highest in seawater and lowest in dune porewater. In line with the H/C ratios, unsaturated, aliphatic compounds, as well as the indicator for molecular lability (MLB_l; D'Andrilli et al., 2015), displayed the highest values in seawater ($p < 0.001$, Wilcoxon rank-sum test between seawater and groundwater). On the other hand, indicators of less saturated compounds, for example the aromaticity index (AI.mod) and the calculated double bond equivalents (DBE) were generally lower in seawater compared to groundwater and beach porewater ($p < 0.05$, Wilcoxon rank-sum test between seawater and groundwater). The relative abundances of aromatic compound groups, and the terrestrial index (ITerr) were also lower in seawater and beach porewater compared to groundwater, and reached their maximum values in the dune porewater samples.

The freshwater lens samples displayed a large heterogeneity with regards to $Si(OH)_4$, DOC, and FDOM concentration ranges, as well as ranges of DOM molecular indices (**Figure 3**

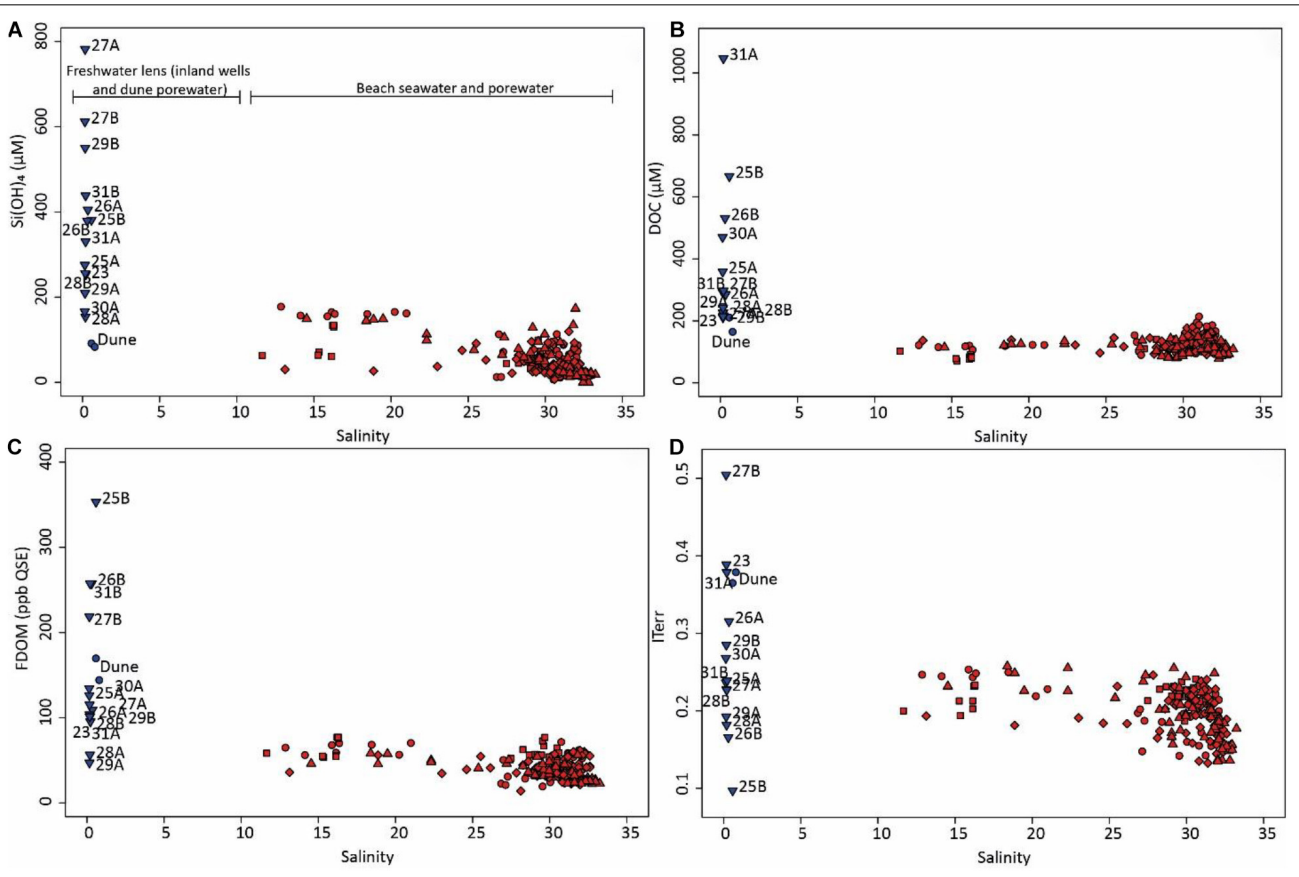


FIGURE 3 | (A) $Si(OH)_4$, **(B)** DOC, **(C)** FDOM, and **(D)** ITerr vs. salinity. The blue and red colors indicate fresh (groundwater and dune porewater) and brackish/saline (beach porewater and seawater) samples, respectively. Symbols indicate campaign season (see also **Figure 4**): Triangles = October, diamonds = March, squares = February, upside down triangles = September. Numbers indicate groundwater wells (see also **Figure 1**).

and **Supplementary Figure 2**). Spearman rank tests revealed no significant correlation of the chemical parameters with groundwater ages (Seibert et al., 2018; **Figure 4**), well locations, or well depths. In beach porewater samples, $Si(OH)_4$, and FDOM concentrations, as well as ITerr values slightly increased with decreasing salinities, while DOC concentrations were relatively low throughout (**Figure 3**). All four molecular indices were significantly correlated with DOC concentrations in beach porewaters and seawater (**Supplementary Figure 2**), most notably Ideg (**Supplementary Figure 2B**) with a $p < 0.001$ and a negative correlation coefficient of $\rho = -0.79$ (**Supplementary Figure 2B**, insert).

Via PCoA of DOM molecular composition, we condensed the extensive molecular information of all endmember water samples, i.e., relative abundances of all assigned molecular formulae, into two coordinates (PC1 and PC2). Together, the two principal coordinates explained 43.5% of DOM molecular composition. In the PCoA bivariate plot, three sample groups were distinguished along the first coordinate (PC1): A relatively compact aggregation of beach porewater samples, a widely distributed assembly of groundwater samples from the freshwater lens, and brackish beach porewater samples from the low water line plotting in between (**Figure 4**). In addition, dune porewater occupied a niche separated from the beach seawater, porewater, and groundwater samples along the second coordinate (PC2). This group was associated with high abundances of aromatic indicators (Ar, AI.mod) and ITerr. PC1 was significantly positively correlated with salinity, and significantly negatively correlated with $Si(OH)_4$ and FDOM concentrations. Seawater and beach porewater samples associated with high salinity were also linked with unsaturated compounds, particularly those containing nitrogen, and with high abundances of the lability index MLB_l. PC2 was negatively correlated with O_2 concentrations and relative abundances of highly unsaturated compounds (HU), and positively correlated with Fe and NH_4^+ concentrations, and relative abundances of aromatic compounds (Ar).

In addition to sample-specific DOM molecular fingerprints, we also found distinct molecular properties correlating (Spearman rank test) in their relative abundances to concentrations of the environmental parameters DOC, FDOM, $Si(OH)_4$, Fe, and O_2 (**Figures 5A–E**) in beach porewater and

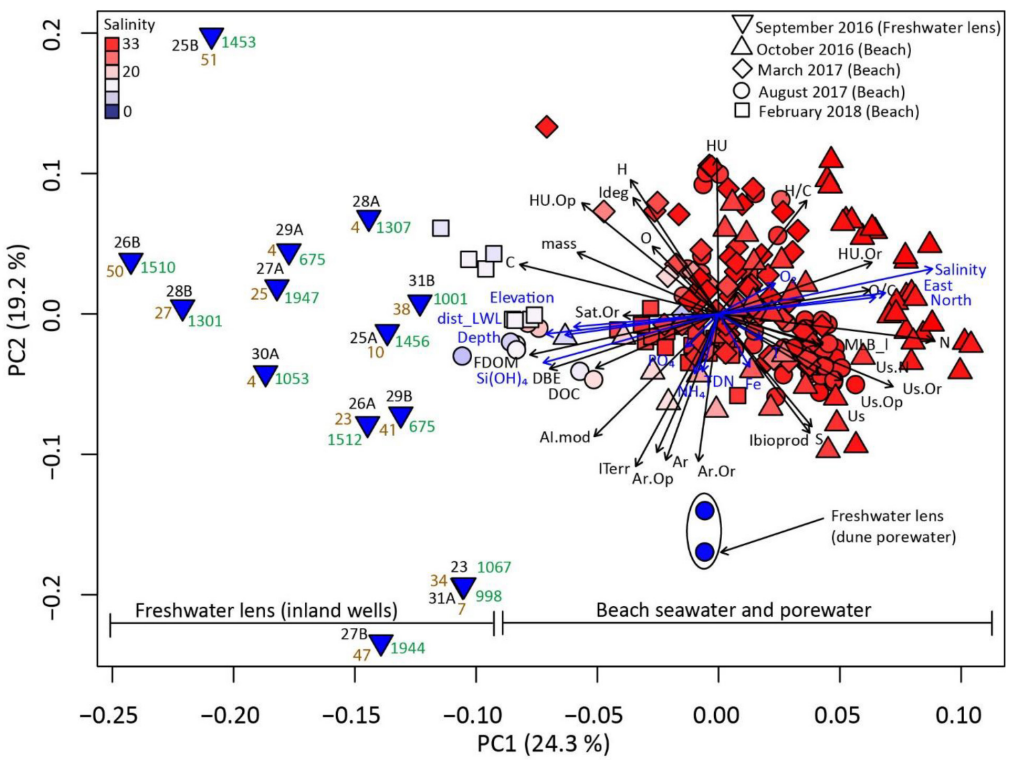


FIGURE 4 | Principal coordinate analysis (PCoA) using Bray-Curtis similarities of DOM molecular composition. Numbers next to inland well samples correspond to well locations as in **Figure 1**, with A and B indicating shallow (~6–10 mbsl) and deep (~20–40 mbsl) wells, respectively. Tan numbers denote $^3H/^3He$ dated groundwater ages (Seibert et al., 2018). Green numbers denote direct distance of well sites from the low water line. Blue arrows display significant ($p < 0.05$) correlations of environmental parameters with the principal coordinates, with the direction of the arrow indicating positive correlation, and its length indicating strength of the correlation coefficient. Environmental parameters contain geographic (Universal Transverse Mercator coordinates, elevation, sampling depth), and physico-chemical data (NH_4^+, TDN, PO_4^{3-}, $Si(OH)_4$, O_2, NO_2^-, Salinity, Mn, Temperature, Fe). Black arrows display significant ($p < 0.001$) correlations of DOC and FDOM concentrations, and chemical DOM properties (intensity-weighed) with the principal coordinates. These include (i) relative abundances of elements and elemental ratios (e.g., C, H/C, O, N) of assigned molecular formulae, (ii) relative abundances of compound classes (**Supplementary Figure 1**, e.g., Ar.Or = Aromatic oxygen-rich, HU = highly unsaturated), (iii) relative distribution of indices (e.g., AI.mod, double bond equivalents = DBE, MLB_l, ITerr).

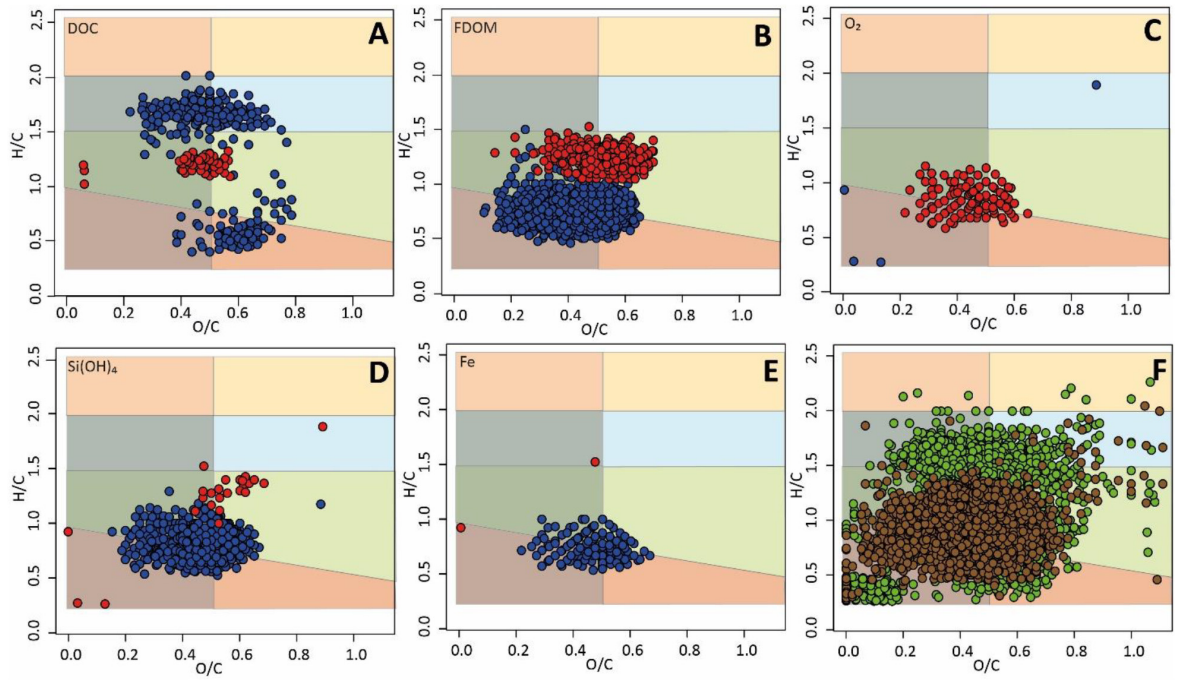


FIGURE 5 | (A–E) Van Krevelen plots of compounds significantly correlating with environmental parameters (Spearman rank test, $p < 0.05$). Blue color indicates positive correlations ($\rho > 0.5$) and red color negative correlations ($\rho < -0.5$). **(F)** van Krevelen plot of compounds associated with beach porewaters from the high water line (green color) *vs.* compounds associated with beach porewaters from the runnel (Ex-2, tan color). Only compounds are shown which are significantly higher in either compartment (Wilcoxon rank-sum test, $p < 0.05$, ratio > 1). The background colors of the plots refer to compound group classes as described in **Supplementary Figure 1A**.

seawater samples. DOC concentrations were significantly positively correlated with relative abundances of unsaturated compounds and aromatic, oxygen-rich compounds, and significantly negatively correlated with relative abundances of highly unsaturated compounds (**Figure 5A**). In contrast, FDOM, $Si(OH)_4$, and Fe concentrations were significantly positively correlated with relative abundances of aromatic compounds and highly unsaturated compounds with an H/C ratio lower than ∼1.2 (**Figures 5B,D,E**). FDOM and $Si(OH)_4$ were furthermore significantly negatively correlated with relative abundances of highly unsaturated compounds with an H/C ratio higher than ∼1.2 (**Figures 5B,D**). O_2 concentrations showed a contrasting pattern to that of FDOM, Fe, and $Si(OH)_4$ concentrations, and were significantly negatively correlated with relative abundances of aromatic compounds and highly unsaturated compounds with an H/C ratio lower than ∼1.2 (**Figure 5C**). A pairwise Wilcoxon rank-sum test comparing DOM composition in beach porewaters from the high water line (In-1) and runnel (Ex-3) revealed relative enrichment of In-1 with unsaturated and aromatic compounds, and relative enrichment of Ex-3 with highly unsaturated compounds (**Figure 5F**).

Spatial and Temporal Variations of Beach Porewater Physico-Chemistry

Seawater temperatures were 12.4°C in October, 7.5°C in March, 18.5°C in August, and 3.2°C in February. Beach porewater temperatures were 11.8 ± 1.1°C in October, 8.8 ± 1.3°C in March, 18.1 ± 0.8°C in August, and 4.5 ± 1.0°C in February. No significant differences (pairwise Wilcoxon rank-sum test, $p < 0.05$) were found between concentrations of the groundwater tracer $Si(OH)_4$ (Oehler et al., 2019) of the four sampling campaigns, although concentrations in August were slightly elevated compared to the rest (**Figure 6A**). On the other hand, $Si(OH)_4$ concentrations from all campaigns combined differed significantly between in- and exfiltration compartments in the cross-shore direction (**Figure 6B**). $Si(OH)_4$ concentrations generally increased with sampling depth (**Figure 6C**), but the differences between the depths were not statistically significant. In contrast to $Si(OH)_4$, FDOM distributions showed an overall trend of increasing concentrations from October 2016 to February 2018 (**Figure 6A**, green color code). Nevertheless, FDOM mostly co-varied with $Si(OH)_4$ on a spatial scale, and FDOM and $Si(OH)_4$ concentrations in beach porewaters were significantly positively correlated across all seasons and depths (Spearman rank test, $p < 0.001$, $\rho = 0.64$).

Dissolved organic carbon concentrations of all stations and depths were significantly different between seasons (pairwise Wilcoxon rank-sum test, $p < 0.05$), increasing in the order February < October < March < August (**Figure 7A**). In addition, DOC concentrations were significantly different amongst cross-shore compartments, with highest concentrations in seawater and lowest concentrations in Ex-2 porewater

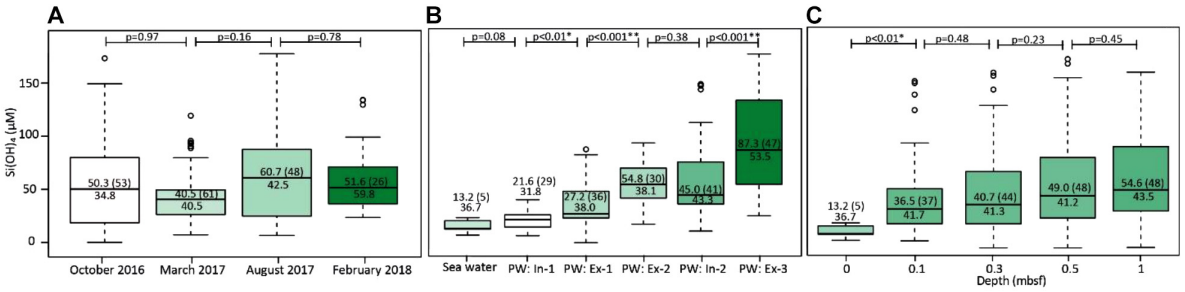


FIGURE 6 | Boxplots of $Si(OH)_4$ concentrations **(A)** for the four campaigns, **(B)** along the cross-shore transects, and **(C)** at sampled sediment depths (0 m represents seawater). Numbers next to brackets denote median $Si(OH)_4$ concentrations, numbers in brackets indicate number of samples. Numbers above display p-values for pairwise Wilcoxon rank-sum tests. The white to green color scale corresponds to increasing FDOM concentrations (also denoted by the numbers in the boxes below the median line). The captions in plot **(B)** refer to in- and exfiltration zones defined in **Figure 2**.

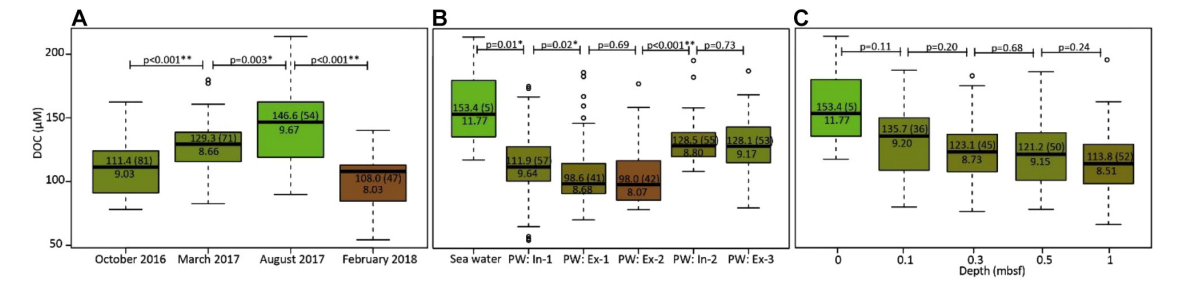


FIGURE 7 | Boxplots of DOC concentrations **(A)** for the four campaigns, **(B)** along the cross-shore transects, and **(C)** at sampled sediment depths (0 m represents seawater). Numbers next to brackets denote median DOC concentrations, numbers in brackets indicate number of samples. Numbers above display *p*-values for pairwise Wilcoxon rank-sum tests. The green to tan color scale corresponds to decreasing MLB_l values (also denoted by the numbers in the boxes below the median line). The captions in plot **(B)** refer to in- and exfiltration zones defined in **Figure 2**.

(**Figure 7B**). Overall, DOC concentrations decreased with increasing sediment depth (**Figure 7C**). Across all temporal and spatial scales, the MLB_l was significantly positively correlated with DOC concentrations (Spearman rank test, $p < 0.001$, $\rho = 0.36$).

Concentrations of total alkalinity (TA) were only determined in beach porewater, seawater, and dune porewater samples and ranged from 1.75 to 6.74 mM. They were highest in dune porewater and lowest in seawater (**Supplementary Table 1**). In beach porewater, TA was significantly negatively correlated with concentrations of dissolved O_2 (Spearman rank test, $p < 0.001$, $\rho = -0.33$), and significantly positively correlated with concentrations of dissolved Fe ($p < 0.001$, $\rho = 0.49$) and Mn $p < 0.001$, $\rho = 0.50$). Overall, highest TA concentrations were found in the August campaign (**Supplementary Figure 3A**). Analogous to $Si(OH)_4$, TA concentrations increased in beach porewaters in the cross-shore direction and with increasing sediment depth (**Supplementary Figures 3B,C**). The degradation index Ideg displayed some contrasting patterns to TA: Although it generally increased together with TA in the cross-shore direction and with increasing sediment depths, it decreased again at the infiltration zone In-2, in parallel with increasing DOC concentrations and increasing MLB_l values. Additionally, it was lowest in the August campaign when TA was highest (**Supplementary Figure 3A**).

Runnel Time Series

The runnel water temperature in March 2019 ranged between 8.3 and 8.7°C, whereas in September 2019, runnel water temperature ranged from 16.3 to 19.1°C. Overall, water levels in the runnel decreased from ∼1 m during high tide to ∼10–20 cm during low tide. During both campaigns, $Si(OH)_4$ concentrations were ∼4–6 fold higher in the runnel during low tide compared to high tide, while DOC concentrations were ∼30–40% lower (**Figures 8A,B**). Amongst DOM molecular indices, Ideg showed diverging trends, with decreasing values toward low tide in March and increasing values toward low tide in September (**Figures 8C,D**). Finally, the MLB_l decreased toward low tide in both campaigns (**Figures 8E,F**). An apparent time lag between tidal heights and temporal geochemical gradients was observed in March, but not in September (**Figures 8A–F**).

DISCUSSION

Sources of Terrestrial DOM to Spiekeroog STE

In line with a previous campaign at the same study site (Beck et al., 2017), DOM molecular composition of beach porewaters was distinctly different from that in the freshwater lens, both from inland and the dune site (**Figure 4**). Surprisingly, the DOM

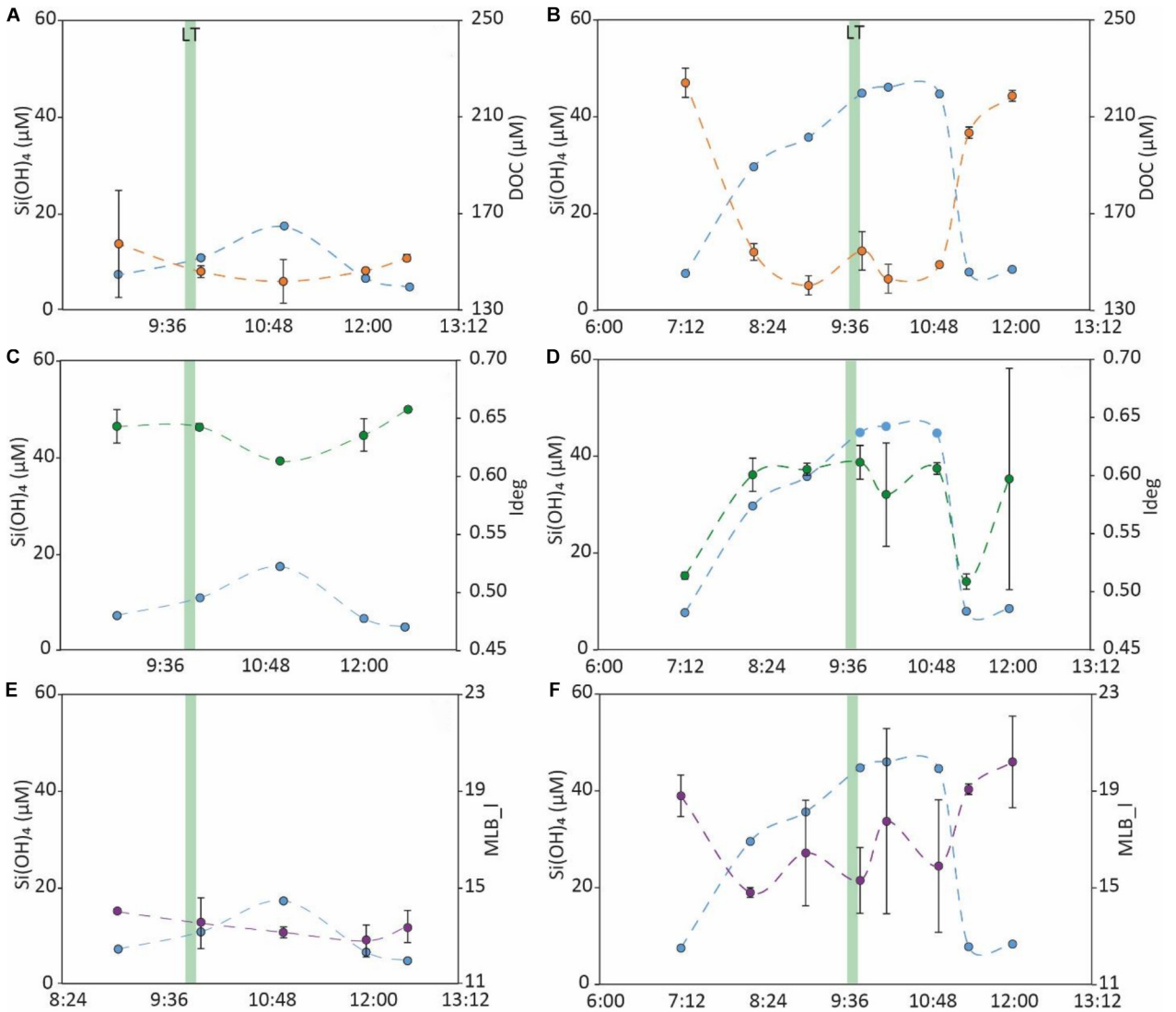


FIGURE 8 | Temporal trends in concentrations of $Si(OH)_4$, a well-known SGD tracer (Oehler et al., 2019) [light blue, **(A–F)**] and DOC [orange, **(A,B)**] and magnitudes of Ideg [green, **(C,D)**] and MLB_I [purple, **(E,F)**], in runnel water samples collected in March 2019 **(A,C,E)** and September 2019 **(B,D,F)**. The green bar indicates time of low tide.

composition in the brackish porewater sites at the low water line was more similar to that in the wells from the freshwater lens (distances of ∼600–2,000 m) compared to the samples collected from the dune base onsite (distance of ∼300 m). Therefore, at the low water line, DOM was likely a mixture of groundwater from the main lens below the island and the discharging recirculated seawater (**Figure 3**). It should be noted that amongst the groundwater well samples, there was no group or cluster formation based on e.g., location, groundwater age or sampling depth (shallow wells "A" vs. deep wells "B"). Furthermore, the wells' distances from the low water line did not appear to influence their distribution relative to the brackish low water line samples in the PCoA plot (**Figure 4**). Although the average of the terrestrial index ITerr was higher in well groundwater compared to beach porewater (**Supplementary Table 2**), it did not display a pronounced trend with salinity and differed vastly between wells (**Figure 3D**). All sampled wells are located in the same vegetation zone (Röper et al., 2012): Gray dunes, dominated by grass, for example *Corynephorus canescens,* herbaceous plants, moss, and lichens) with the exception of well 26, which is in the brown dune zone (dominance of perennial shrubs, mostly *Empetrum nigrum*). Because of the relatively homogeneous local vegetation patterns, together with the long flowpaths associated with the sampled depths (∼6-40 m) we do not assume a direct link between current plant communities and the very high DOM heterogeneity between the wells. Overall, the geology of the island consists of pre- and postglacial sand deposits, with a clay aquitard at ∼40 m depth, and peat and salt marsh deposits occurring in patches throughout the island (Streif, 2002) which likely affect groundwater well DOM composition locally. Peat porewater is

enriched in aromatic compounds compared to seawater (Riedel et al., 2012), and peat-influenced groundwater will have a higher ITerr compared to groundwater not in contact with peat, because the ITerr index is positively influenced by compounds of a higher aromaticity (Medeiros et al., 2016). Variations in the contribution of soil horizons to groundwater DOM can also influence ITerr, as topsoil DOM often has higher aromaticity compared to subsoil DOM (Shen et al., 2015; Anderson et al., 2019). On the other hand, DOM adsorption to mineral phases decreases ITerr, because it also targets more aromatic compounds of the DOM pool (Shen et al., 2015; Linkhorst et al., 2017). Originally, ITerr was developed using Amazon estuarine samples (Medeiros et al., 2016) and it may not be applicable as an unambiguous terrestrial endmember marker for subterranean estuaries. However, it could reveal mineral-water interactions along groundwater flowpaths, or be a valuable indicator of local peat or paleosol deposits in the coastal aquifer. In line with our study from the German North Sea coast, peat and/or paleosol leaching by groundwater was observed in coastal aquifers in Australia and North America (Goñi and Gardner, 2003; Couturier et al., 2016; McDonough et al., 2020b). This process can enrich coastal groundwater DOC concentrations up to tenfold compared to the global average (McDonough et al., 2020c; Meredith et al., 2020). Therefore, the transfer of ancient organic matter deposits from deep aquifers to surficial environments (with high degradation potential) could be an important process in the global coastal carbon cycle.

The similarities of DOM molecular properties between brackish beach porewater and freshwater lens groundwater were quite astonishing, and differed mainly by the much higher DOC concentrations in the latter (∼200–1,000 μM) compared to the former (∼100–150 μM). Previous research on Spiekeroog beach (and other STEs worldwide) has mainly focused on characterizing the freshwater endmember directly at the shoreline (Reckhardt et al., 2015; Seidel et al., 2015; Beck et al., 2017). In agreement with Anschutz et al. (2016), our data indicates that information about the inland watershed is necessary to constrain endmembers to the beach STE. However, a substantial unknown in our study, as well as in the current STE literature, is the fate of DOM on its transport between the inland wells and the beach STE. For example, we do not have any detailed information about the quantity and quality of the sedimentary organic matter below the dune belt. Even the particulate OC content of <0.03–0.04%% found in Spiekeroog beach sands (Beck et al., 2017; Seibert et al., 2019b) would correspond to several hundred fold higher DOC concentrations than the ones we measured in any of our samples. Therefore, it is likely that a continuous addition via the solid phase occurs along the decade-long flowpaths of the inland groundwater toward the shoreline. Based on the molecular similarities of the groundwater and brackish porewater DOM, we propose that any added DOM below the dune belt likely has comparable sedimentary sources (soils, peat, and vascular plant material) as the wells, and is processed under similar conditions. Employing a numerical density-dependent groundwater flow and transport model of the site, Grünenbaum et al. (2020) calculated a water travel time from the dune to the low water line of 16–18 years. With a mean $^{3}H/^{3}He$ age of 20–30 years of the freshwater lens (Röper et al., 2012; Seibert et al., 2018) and adding another 10–20 years to pass the STE, the mean age of the discharging fresh groundwater must be around 30–50 years. Further, numerical modeling of the reactive transport processes within the freshwater lens revealed a low sulfate reduction rate of maximum 0.015 nmol/mL/day (Seibert et al., 2019a). Therefore, it is possible, that the low availability of electron acceptors, together with the aged DOM, result in a low reactivity along the flowpath. Using this maximum sulfate reduction rate and assuming a maximum mean age of 50 years, this would yield a degradation of ∼140 μM DOC, which is less than the observed difference between the average DOC concentrations of the groundwater and beach porewater, respectively (**Supplementary Table 1**). Another DOM removal process could be adsorption onto reactive iron oxides (Linkhorst et al., 2017), which are found in small but constant amounts (∼10 mmol/kg) in surface (<2 m) sediments from our study site (Ahrens, 2016) as well as in sediment cores (up to 10 m) from a dune site in the Eastern part of the island (Seibert et al., 2019a). Considering the affinity of terrestrial, plant-derived DOM for Fe-Oxide binding, the potential of the solid phase as a (transient) storage of OC could be substantial and needs to be investigated in more detail in future studies, similar to Sirois et al. (2018). We also suspect decreases of freshwater lens-derived organic matter under the dune belt, as it mixes with dune porewater, which is in contact with the atmosphere, and which has lower DOC, higher oxygen, and higher FDOM concentrations (**Supplementary Table 1**; **Figures 3B,C**; Anschutz et al., 2016). Finally, degradation of terrestrial DOM could be accelerated once it reaches the intertidal zone, due to the deep injection of seawater rich in labile DOM ("priming"; Bianchi, 2011) and electron acceptors (e.g., oxygen, nitrate, and sulfate; Ahrens et al., 2020; Grünenbaum et al., 2020).

At the dune base, DOM was remarkably enriched with aromatic compounds compared to all other endmember samples (**Figure 4** and **Supplementary Table 2**). As we only sampled this endmember in August, it may not be representative for the remainder of the year. In the area of the dune base, so-called "Winterspülsaum" was observed, a beach wrack deposition area mainly composed of kelp (*Fucus* sp.) and dune grass (*Ammophila arenaria*) washed high up the shore during winter storms. It appears that this buried plant material, which is not reached during regular tidal inundation, influences dune porewater composition as it is leached into the aquifer by infiltrating rainwater. Unfortunately, it was not possible in the scope of this study to access deeper layers of the beach fresh groundwater endmember. Effectively, we are treating the deep beach aquifer as a "black box" of which only the infiltrating seawater, and the exfiltrating porewater (brackish and saline), are well-characterized (**Figure 2**). The relative contributions of different groundwater layers are unknown, since the brackish porewater samples contain a processed composite of groundwater from the entire freshwater lens. In a study on Spiekeroog South Beach, groundwater DOC concentrations varied between ∼100 and 400 μM over a sampling depth of only 1.5 m (Waska et al., 2019a). Little is known about vertical distributions of groundwater DOM in STEs, since spatial and temporal observations of DOC and DOM endmembers are often discussed in the context of seawater-groundwater mixing (e.g., Santos et al., 2009; Seidel et al., 2015). Most STE studies focus on the upper ∼2–3 m (e.g., Roy et al., 2010; Kim et al., 2012; Seidel et al., 2015; Yang et al., 2015;

Couturier et al., 2016) although sampling of 4 m depth or more (Charette and Sholkovitz, 2006; Beck et al., 2017; Kim et al., 2019; Meredith et al., 2020) revealed, in some cases, variations in DOC of up to 100-fold between sampling depths at the same station (Charette and Sholkovitz, 2006; Meredith et al., 2020). On Spiekeroog, the upper saline plume(s) alone reach (modeled) depths of ∼20 m (**Figure 2**; Grünenbaum et al., 2020). Therefore, probing of groundwater layers at the dune site up to 20–30 m depth may be necessary to capture all sources of terrestrial organic matter to the beach STE.

DOM Turnover in the STE

Our DOC and DOM data confirm earlier findings that seawater provides relatively fresh, labile organic matter to beach aquifers (e.g., **Figures 2**, **7** and **Supplementary Tables 1, 2**; Seidel et al., 2015). Across the beach STE, a general inverse relationship between DOC concentrations and Ideg could be found (**Supplementary Figure 2D**), whereas higher DOC concentrations were associated with higher values of molecular lability and bioproductivity indices. Environmental parameters indicative of relative water residence time in the STE in a qualitative sense, i.e., O_2, Fe, and $Si(OH)_4$ (Reckhardt et al., 2015; Oehler et al., 2019; Ahrens et al., 2020) revealed increasing relative contributions of highly unsaturated and aromatic compounds to the DOM pool with increasing porewater age. Furthermore, FDOM increased with increasing water residence times, making this fluorescence component a potential groundwater tracer as previously proposed in other coastal environments (Kim et al., 2012; Nelson et al., 2015; Kim and Kim, 2017). It should be noted that $Si(OH)_4$ and FDOM concentrations are highly influenced by the relative contributions of the fresh groundwater endmember (**Supplementary Table 1**; **Figure 6**; Ehlert et al., 2016), and that is difficult to separate patterns of accumulation along the flowpath from additions of our fresh groundwater endmember due to its large concentration ranges (**Figure 3**). On the other hand, compounds positively correlated with Fe concentrations could be not only the result of accumulation due to water age, but also from release of sedimentary OC due to reduction of reactive Fe oxides (Waska et al., 2019b).

As a general paradigm, the average H/C ratio of DOM molecular formulae is often considered an indicator of DOM lability, with compounds of H/C ratios >1.5 being degraded more rapidly than those with H/C ratios <1.5 (D'Andrilli et al., 2015), and with aromatic compounds being the most resistant to degradation due to the stability of the aromatic ring structures. However, environmental and experimental data from open ocean to freshwater environments showed that increased degradation is characterized by increased relative abundances of highly unsaturated compounds with intermediate H/C ratios of ∼1.2 and O/C ratios of ∼0.5, at the cost of both, less and more saturated compounds ("island of stability"; Lechtenfeld et al., 2014; Mostovaya et al., 2017). **Figures 5A,F** show DOM composition changes toward the "island of stability" with decreasing DOC concentrations and increasing water residence times. Therefore, degradation of both, aliphatic and aromatic compounds appears to take place in the beach STE. In addition, removal of aromatic compounds due to adsorption onto reactive iron oxides may occur along the advective porewater flowpath (Linkhorst et al., 2017; Sirois et al., 2018).

We are aware that water residence time and porewater age are inherently difficult to define in the beach STE. Based on groundwater age dating and numerical models of the local flowpaths (Röper et al., 2012; Beck et al., 2017; Grünenbaum et al., 2020), we posit that groundwater from the freshwater lens is the oldest endmember, and infiltrating seawater at the high water line the youngest, with regards to autochthonous DOM contribution. The combination of beach seawater circulation and old groundwater would then result in an overall increase of water age from high to low water line, particularly from the runnel onward, where increasing contributions of fresh groundwater are to be expected (Beck et al., 2017; Waska et al., 2019b). Tidal inundation may "reset" water age in the intertidal zone, most prominently at the ridge. Indeed, **Figures 6**, **7** show some similarities between In-1 and In-2. Nevertheless, the overall higher elevation, together with an overall higher hydraulic gradient, between high water line and runnel compared to that between ridge and low water line, seems to ensure that the largest seawater volumes are circulating through the upper intertidal zone of the beach (**Figures 2**, **5F**, **7B**). This geochemical pattern is supported by numerical models calculating fourfold higher discharge volumes in the runnel compared to the low water line (Waska et al., 2019b).

Even with fresh groundwater influence, DOC concentrations in beach porewater (across all samples and seasons) were consistently lower compared to those in both seawater (by ∼40 μM) and groundwater (by ∼160 μM when using the average of well groundwater and dune porewater, **Supplementary Table 1**). At the same time, oxygen concentrations decreased by >200 μM and nitrate concentrations by >100 μM (using average dune porewater and seawater, **Supplementary Table 1**), which would correspond to a respiration of ∼280 μM OC assuming stoichiometric reactions of only these dissolved reaction partners (Van Cappellen and Wang, 1996), and which would be more than sufficient to account for the observed loss of DOC. Of course, this very simple comparison of temporally and spatially averaged electron acceptor and electron donor budgets contains several large uncertainties: on the electron acceptor side, oxygen and nitrate participate in the chemical oxidation of reduced nitrogen, metal, and sulfur species, and could be added to shallow porewater throughout the intertidal zone via diffusion (contact with the atmosphere) as well as skin circulation during tidal inundation (Billerbeck et al., 2006; Ahmerkamp et al., 2017). Furthermore, manganese, iron, and sulfate reduction also occur on Spiekeroog beach, albeit to a lesser extent compared to oxic respiration and nitrate reduction (Ahrens et al., 2020). On the electron donor side, the concentration of the deep fresh groundwater endmember is not entirely known, and contributions of sedimentary and beach wrack OC to the porewater DOC pool could exceed DOC concentrations from sea- and groundwater by several fold in deeper (>1 m) parts of the beach STE, especially during spring and summer (Kim et al., 2019). In general, high-energy beaches are known as remineralization hot spots of marine-derived OC (McLachlan, 1982; Anschutz et al., 2009; Charbonnier et al., 2013), but the role of fresh groundwater as an additional substrate for the

beach microbial community is not well understood. In this study, our data indicate that the "aged" DOM from groundwater still undergoes degradation before it discharges into the coastal ocean. Dynamic beach hydrology could enhance microbial respiration of terrestrial DOC by supplementing the fresh groundwater endmember with oxygen, nitrate, and labile marine organic matter ("priming"; Bianchi, 2011). It is not possible to determine, based on our environmental study, which effect (supply of oxygen vs. labile OC) is more prominent on Spiekeroog beach; laboratory mesocosms are needed in future study to disentangle electron acceptor and electron donor effects on beach OC respiration.

Exfiltration of DOM and Impact on Water Column

Our runnel time series support the observations in DOC concentrations found for the different endmembers, and indicate that exfiltrating beach porewater is generally DOC-depleted compared to surface seawater (**Figure 8**). This trend occurred parallel to the reliable increase of $Si(OH)_4$, a well-known groundwater tracer (Oehler et al., 2019) during or after low tide, and was remarkably consistent in both runnel time series. Some concentration fluctuations occurred in our runnel time series data, as indicated by comparably larger standard deviations for some points in **Figure 8**. We attribute these to heterogeneities in the runnel water column, which had a dynamically changing water level and which may receive different water parcels from the draining sediments. However, such runnel time series seem to be a valuable asset to trace SGD impact in a high-energy environment where SGD-related chemical signals are diluted rather quickly by the adjacent coastal seawater. In line with our findings, a recent study on a diverse set of coastal zones, attributed dependency of STE source-sink functions to high OC loads in adjacent surface waters (Webb et al., 2019). This effect may be further exacerbated in high-energy beach STEs with high advective water throughput, which prevent efficient accumulation of DOC.

We emphasize that on a qualitative level, the Spiekeroog beach STE is still a source of terrestrial, as well as recycled, chemically modified, marine DOM (**Supplementary Tables 1, 2** and **Figure 7**) to the nearshore water column. This modified DOM is enriched in humic-like FDOM and highly unsaturated compounds (**Supplementary Tables 1, 2**) and likely has contributed to the discharging inorganic nutrient pool, e.g., ammonium (Ahrens et al., 2020). In one of our runnel time series in March 2019, which took place shortly after the spring phytoplankton bloom, exfiltrating beach porewater appeared to be more labile (as indicated by Ideg) than the surrounding seawater, although it had less DOC (**Figure 8C**). This pattern was contradictory to our other results from the seasonal transects, as well as a runnel time series in September 2019 (**Figures 7**, **8**). It could imply that a lag in sedimentary microbial response during times of high coastal water column productivity causes inverse patterns of DOM degradation, i.e., a more labile DOM pool found in the porewaters compared to a less labile, more degraded DOM pool in the seawater. In addition, we cannot present any porewater exfiltration data from the low water line, because time-series sampling and seepage meter placement in a high-energy surf zone presents a formidable, yet-to-overcome challenge. However, future DOM characterization of SGD from the low water line will be necessary to fully elucidate the impact of Spiekeroog beach porewater onto the adjacent coastal North Sea.

CONCLUSION

Our study indicates that the Spiekeroog high-energy beach STE conveys chemically modified, terrestrial DOM from the inland freshwater lens to the coastal ocean. Terrestrial DOM seems to stem from the groundwater lens, partly being supplemented by vascular plant leachates from the dune belt. Overall, Spiekeroog beach appears to be a very active DOM turnover site, where dissolved, marine, and terrestrial OC can be remineralized with high efficiency, and where microbial degradation are imprinted onto the molecular composition of DOM of exfiltrating porewaters. Based on our data, we suggest that this high-energy beach STE is a net sink for OC from both the terrestrial as well as the marine realm. Furthermore, we propose the East Frisian barrier island beaches may act as efficient "digestors" of organic matter, perhaps respiring DOC also from many other coastal sources (i.e., rivers, tidal flats) found in their vicinity.

We emphasize that our study also revealed several research gaps, which contribute to uncertainties in data interpretation: (1) A characterization of deeper (>1 m) STE layers is needed to constrain endmember hydrochemistry. (2) A thorough investigation of particulate and sedimentary organic matter in the beach is necessary to complete the qualitative and quantitative OC budget. (3) An experimental setup is crucial to derive accurate microbial respiration rates, and to disentangle impacts of electron acceptors *vs.* electron donors on OC remineralization in this dynamic, high-energy environment. (4) An expansion of STE research from micro- and meso- to more macrotidal, exposed, high-energy coastlines is required to confirm the universality and thus global relevance of our findings.

DATA AVAILABILITY STATEMENT

Mass spectrometry and environmental data data are available on the open-access data repository PANGAEA (Waska 2021, Ahrens 2019).

AUTHOR CONTRIBUTIONS

HW designed the study, acquired the data, and wrote the manuscript. HS, SA, JG, JA, SS, and KS acquired the data and contributed to result interpretation and manuscript writing. OZ and TD contributed to study design and manuscript writing. All authors approved the submitted version.

FUNDING

This study was financed by the Niedersächsisches Ministerium für Wissenschaft und Kultur (MWK) in the scope of project "BIME" (ZN3184). SA acknowledges funding from the Max Planck Society.

ACKNOWLEDGMENTS

We would like to thank Swaantje Fock and Carsten Heithecker from Umweltzentrum Wittbülten, and Ulrike Seemann from Quellerdünenheim, for provision of onsite infrastructure. Joachim Ihnken from the Niedersächsische Landesbetrieb für Wasserwirtschaft, Küsten, und Naturschutz (NLWKN), Gregor Scheiffarth, Claus Schulz, and Lars Scheller from the Nationalpark Wattenmeer administration, and Helmo Nicolai from ICBM Terramare are thanked for their support with permits, onsite information, and onsite logistics. We are further grateful to the municipality of Spiekeroog, for accomodating and supporting basic research on the island. HW would like to thank Matthias Friebe, Ina Ulber, and Katrin Klaproth with assistance in field and lab work, and FT-ICR-MS analyses. The two reviewers are thanked for their detailed and constructive comments, which helped to improve this manuscript.

SUPPLEMENTARY MATERIAL

The Supplementary Material for this article can be found online at: https://www.frontiersin.org/articles/10.3389/fmars.2021.607083/full#supplementary-material

REFERENCES

Ahmerkamp, S., Winter, C., Krämer, K., Beer, D. D., Janssen, F., Friedrich, J., et al. (2017). Regulation of benthic oxygen fluxes in permeable sediments of the coastal ocean. *Limnol. Oceanogr.* 62, 1935–1954. doi: 10.1002/lno.10544

Ahrens, J. (2016). *Anorganisch-Geochemische Charakterisierung von Spiekerooger Strandsanden unter Anwendung der Sequentiellen Extraktion Von Eisen-Mineralphasen*. MSc thesis, University of Oldenburg, Oldenburg.

Ahrens, J., Beck, M., Marchant, H. K., Ahmerkamp, S., Schnetger, B., and Brumsack, H. J. (2020). Seasonality of organic matter degradation regulates nutrient and metal net fluxes in a high energy sandy beach. *J. Geophys. Res. Biogeosci.* 125:e2019JG005399.

Anderson, T. R., Rowe, E. C., Polimene, L., Tipping, E., Evans, C. D., Barry, C. D. G., et al. (2019). Unified concepts for understanding and modelling turnover of dissolved organic matter from freshwaters to the ocean: the UniDOM model. *Biogeochemistry* 146, 105–123. doi: 10.1007/s10533-019-00621-1

Anschutz, P., Charbonnier, C., Deborde, J., Deirmendjian, L., Poirier, D., Mouret, A., et al. (2016). Terrestrial groundwater and nutrient discharge along the 240-km-long Aquitanian coast. *Mar. Chem.* 185, 38–47. doi: 10.1016/j.marchem.2016.04.002

Anschutz, P., Smith, T., Mouret, A., Deborde, J., Bujan, S., Poirier, D., et al. (2009). Tidal sands as biogeochemical reactors. *Estuar. Coast. Shelf Sci.* 84, 84–90. doi: 10.1016/j.ecss.2009.06.015

Beck, M., Reckhardt, A., Amelsberg, J., Bartholomä, A., Brumsack, H. J., Cypionka, H., et al. (2017). The drivers of biogeochemistry in beach ecosystems: a cross-shore transect from the dunes to the low-water line. *Mar. Chem.* 190, 35–50. doi: 10.1016/j.marchem.2017.01.001

Benner, R., and Amon, R. M. (2015). The size-reactivity continuum of major bioelements in the ocean. *Ann. Rev. Mar. Sci.* 7, 185–205. doi: 10.1146/annurev-marine-010213-135126

Bianchi, T. S. (2011). The role of terrestrially derived organic carbon in the coastal ocean: a changing paradigm and the priming effect. *Proc. Natl. Acad. Sci. U.S.A.* 108, 19473–19481. doi: 10.1073/pnas.1017982108

Billerbeck, M., Werner, U., Polerecky, L., Walpersdorf, E., DeBeer, D., and Huettel, M. (2006). Surficial and deep pore water circulation governs spatial and temporal scales of nutrient recycling in intertidal sand flat sediment. *Mar. Ecol. Prog. Ser.* 326, 61–76. doi: 10.3354/meps326061

Charbonnier, C., Anschutz, P., Poirier, D., Bujan, S., and Lecroart, P. (2013). Aerobic respiration in a high-energy sandy beach. *Mar. Chem.* 155, 10–21. doi: 10.1016/j.marchem.2013.05.003

Charette, M. A., and Sholkovitz, E. R. (2006). Trace element cycling in a subterranean estuary: Part 2. geochemistry of the pore water. *Geochim. Cosmochim. Acta* 70, 811–826. doi: 10.1016/j.gca.2005.10.019

Couturier, M., Nozais, C., and Chaillou, G. (2016). Microtidal subterranean estuaries as a source of fresh terrestrial dissolved organic matter to the coastal ocean. *Mar. Chem.* 186, 46–57. doi: 10.1016/j.marchem.2016.08.001

D'Andrilli, J., Cooper, W. T., Foreman, C. M., and Marshall, A. G. (2015). An ultrahigh-resolution mass spectrometry index to estimate natural organic matter lability. *Rapid Commun. Mass. Spectrom.* 29, 2385–2401. doi: 10.1002/rcm.7400

Degenhardt, J., Dlugosch, L., Ahrens, J., Beck, M., Waska, H., and Engelen, B. (2020). Seasonal dynamics of microbial diversity at a sandy high energy beach reveal a resilient core community. *Front. Mar. Sci.* 7:869. doi: 10.3389/fmars.2020.573570

Dittmar, T., Koch, B., Hertkorn, N., and Kattner, G. (2008). A simple and efficient method for the solid-phase extraction of dissolved organic matter (SPE-DOM) from seawater. *Limnol. Oceanogr. Methods* 6, 230–235. doi: 10.4319/lom.2008.6.230

Ehlert, C., Reckhardt, A., Greskowiak, J., Liguori, B. T., Böning, P., Paffrath, R., et al. (2016). Transformation of silicon in a sandy beach ecosystem: Insights from stable silicon isotopes from fresh and saline groundwaters. *Chem. Geol.* 440, 207–218. doi: 10.1016/j.chemgeo.2016.07.015

Flerus, R., Lechtenfeld, O. J., Koch, B. P., McCallister, S. L., Schmitt-Kopplin, P., Benner, R., et al. (2012). A molecular perspective on the ageing of marine dissolved organic matter. *Biogeosciences* 9, 1935–1955. doi: 10.5194/bg-9-1935-2012

Froelich, P. N., Klinkhammer, G. P., Bender, M. L., Luedtke, N. A., Heath, G. R., Cullen, D., et al. (1979). Early oxidation of organic matter in pelagic sediments of the eastern equatorial Atlantic: suboxic diagenesis. *Geochim. Cosmochim. Acta* 43, 1075–1090. doi: 10.1016/0016-7037(79)90095-4

Goñi, M. A., and Gardner, I. R. (2003). Seasonal dynamics in dissolved organic carbon concentrations in a coastal water-table aquifer at the forest-marsh interface. *Aquat. Geochem.* 9, 209–232. doi: 10.1023/b:aqua.0000022955.82700.ed

Grasshoff, K., Kremling, K., and Erhardt, M. (1999). *Methods of Seawater Analysis*. Weinheim: Wiley-VCH.

Grünenbaum, N., Greskowiak, J., Sültenfuß, J., and Massmann, G. (2020). Groundwater flow and residence times below a meso-tidal high-energy beach: a model-based analyses of salinity patterns and 3H-3He groundwater ages. *J. Hydrol.* 2020:124948. doi: 10.1016/j.jhydrol.2020.124948

Ibánhez, J. S. P., and Rocha, C. (2016). oxygen transport and reactivity within a sandy seepage face in a mesotidal lagoon (Ria Formosa, Southwestern Iberia). *Limnol. Oceanogr.* 61, 61–77. doi: 10.1002/lno.10199

Itaya, K., and Ui, M. (1966). A new micromethod for the colorimetric determination of inorganic phosphate. *Clin. Chim. Acta* 14, 361–366. doi: 10.1016/0009-8981(66)90114-8

Jiang, S., Zhang, Y., Jin, J., Wu, Y., Wei, Y., Wang, X., et al. (2020). Organic carbon in a seepage face of a subterranean estuary: Turnover and microbial interrelations. *Sci. Total Environ.* 725:138220. doi: 10.1016/j.scitotenv.2020.138220

Kaiser, K., and Guggenberger, G. (2000). The role of DOM sorption to mineral surfaces in the preservation of organic matter in soils. *Organ. Geochem.* 31, 711–725. doi: 10.1016/s0146-6380(00)00046-2

Kim, J., and Kim, G. (2017). Inputs of humic fluorescent dissolved organic matter via submarine groundwater discharge to coastal waters off a volcanic island (Jeju, Korea). *Sci. Rep.* 7, 1–9.

Kim, K. H., Michael, H. A., Field, E. K., and Ullman, W. J. (2019). Hydrologic shifts create complex transient distributions of particulate organic carbon and biogeochemical responses in beach aquifers. *J. Geophys. Res. Biogeosci.* 124, 3024–3038. doi: 10.1029/2019jg005114

Kim, T. H., Waska, H., Kwon, E., Suryaputra, I. G. N., and Kim, G. (2012). Production, degradation, and flux of dissolved organic matter in the subterranean estuary of a large tidal flat. *Mar. Chem.* 142, 1–10. doi: 10.1016/j.marchem.2012.08.002

Koch, B. P., and Dittmar, T. (2006). From mass to structure: An aromaticity index for high-resolution mass data of natural organic matter. *Rapid Commun. Mass Spectrom.* 20, 926–932. doi: 10.1002/rcm.2386

Kwon, E. Y., Kim, G., Primeau, F., Moore, W. S., Cho, H. M., DeVries, T., et al. (2014). Global estimate of submarine groundwater discharge based on an observationally constrained radium isotope model. *Geophys. Res. Lett.* 41, 8438–8444. doi: 10.1002/2014gl061574

Lalonde, K., Mucci, A., Ouellet, A., and Gélinas, Y. (2012). Preservation of organic matter in sediments promoted by iron. *Nature* 483, 198–200. doi: 10.1038/nature10855

Laskov, C., Herzog, C., Lewandowski, J., and Hupfer, M. (2007). Miniaturized photometrical methods for the rapid analysis of phosphate, ammonium, ferrous iron, and sulfate in pore water of freshwater sediments. *Limnol. Oceanog. Methods* 5, 63–71. doi: 10.4319/lom.2007.5.63

Lechtenfeld, O. J., Kattner, G., Flerus, R., McCallister, S. L., Schmitt-Kopplin, P., and Koch, B. P. (2014). Molecular transformation and degradation of refractory dissolved organic matter in the Atlantic and Southern Ocean. *Geochim. Cosmochim. Acta* 126, 321–337. doi: 10.1016/j.gca.2013.11.009

Linkhorst, A., Dittmar, T., and Waska, H. (2017). Molecular fractionation of dissolved organic matter in a shallow subterranean estuary: the role of the iron curtain. *Environm. Sci. Technol.* 51, 1312–1320. doi: 10.1021/acs.est.6b03608

Luijendijk, E., Gleeson, T., and Moosdorf, N. (2020). Fresh groundwater discharge insignificant for the world's oceans but important for coastal ecosystems. *Nat. Commun.* 11, 1–12. doi: 10.1007/1-4020-4738-x_1

Ma, Q., and Zhang, Y. (2020). Global research trends and hotspots on submarine groundwater discharge (SGD): a bibliometric analysis. *Intern. J. Environ. Res. Public Health* 17:830. doi: 10.3390/ijerph17030830

McAllister, S. M., Barnett, J. M., Heiss, J. W., Findlay, A. J., MacDonald, D. J., Dow, C. L., et al. (2015). Dynamic hydrologic and biogeochemical processes drive microbially enhanced iron and sulfur cycling within the intertidal mixing zone of a beach aquifer. *Limnol. Oceanogr.* 60, 329–345. doi: 10.1002/lno.10029

McDonough, L. K., O'Carroll, D. M., Meredith, K., Andersen, M. S., Brugger, C., Huang, H., et al. (2020a). Rainfall recharge drives groundwater dissolved organic matter composition in acoastal sand aquifer. *Water Res.* 169:115201. doi: 10.1016/j.watres.2019.115201

McDonough, L. K., Rutlidge, H., O'Carroll, D. M., Andersen, M. S., Meredith, K., Behnke, M., et al. (2020b). Characterisation of shallow groundwater dissolved organic matter in aeolian, alluvial and fractured rock aquifers. *Geochim. Cosmochim. Acta* 273, 163–176. doi: 10.1016/j.gca.2020.01.022

McDonough, L. K., Santos, I. R., Andersen, M. S., O'Carroll, D. M., Rutlidge, H., Meredith, K., et al. (2020c). Changes in global groundwater organic carbon driven by climate change and urbanization. *Nat. Commun.* 11:1279.

McLachlan, A. (1982). A model for the estimation of water filtration and nutrient regeneration by exposed sandy beaches. *Mar. Environ. Res.* 6, 37–47. doi: 10.1016/0141-1136(82)90006-x

Medeiros, P. M., Seidel, M., Niggemann, J., Spencer, R. G., Hernes, P. J., Yager, P. L., et al. (2016). A novel molecular approach for tracing terrigenous dissolved organic matter into the deep ocean. *Glob. Biogeochem. Cycles* 30, 689–699. doi: 10.1002/2015gb005320

Merder, J., Freund, J. A., Feudel, U., Hansen, C. T., Hawkes, J. A., Jacob, B., et al. (2020). ICBM-OCEAN: processing ultrahigh-resolution mass spectrometry data of complex molecular mixtures. *Analyt. Chem.* 92, 6832–6838. doi: 10.1021/acs.analchem.9b05659

Meredith, K. T., Baker, A., Andersen, M. S., O'Carroll, D., Rutlidge, H., McDonough, L. K., et al. (2020). Isotopic and chromatographic fingerprinting of the sources of dissolved organic carbon in a shallow coastal aquifer. *Hydrol. Earth Syst. Sci.* 24, 2167–2178. doi: 10.5194/hess-24-2167-2020

Moore, W. S. (1999). The subterranean estuary: a reaction zone of ground water and sea water. *Mar. Chem.* 65, 111–125. doi: 10.1016/s0304-4203(99)00014-6

Mostovaya, A., Hawkes, J. A., Dittmar, T., and Tranvik, L. J. (2017). Molecular determinants of dissolved organic matter reactivity in lake water. *Front. Earth Sci.* 5:106. doi: 10.3389/feart.2017.00106

Nelson, C. E., Donahue, M. J., Dulaiova, H., Goldberg, S. J., La Valle, F. F., Lubarsky, K., et al. (2015). Fluorescent dissolved organic matter as a multivariate biogeochemical tracer of submarine groundwater discharge in coral reef ecosystems. *Mar. Chem.* 177, 232–243. doi: 10.1016/j.marchem.2015.06.026

Novitsky, J. A., and MacSween, M. C. (1989). Microbiology of a high energy beach sediment: evidence for an active and growing community. *Mar. Ecol. Prog. Ser.* 52, 71–75. doi: 10.3354/meps052071

Oehler, T., Tamborski, J., Rahman, S., Moosdorf, N., Ahrens, J., Mori, C., et al. (2019). DSi as a tracer for submarine groundwater discharge. *Front. Mar. Sci.* 6:563. doi: 10.3389/fmars.2019.00563

Oksanen, J., Blanchet, F. G., Kindt, R., Legendre, P., McGlinn, D., Minchin, P. R., et al. (2013). Package 'vegan'. *Commun. Ecol. Pack. Vers.* 2, 1–295.

Osterholz, H., Niggemann, J., Giebel, H. A., Simon, M., and Dittmar, T. (2015). Inefficient microbial production of refractory dissolved organic matter in the ocean. *Nat. Commun.* 6, 1–8.

Paffrath, R., Pahnke, K., Behrens, M. K., Reckhardt, A., Ehlert, C., Schnetger, B., et al. (2020). Rare earth element behavior in a sandy subterranean estuary of the southern North Sea. *Front. Mar. Sci.* 7:424. doi: 10.3389/fmars.2020.00424

Reckhardt, A., Beck, M., Greskowiak, J., Schnetger, B., Boettcher, M. E., Gehre, M., et al. (2017). Cycling of redox-sensitive elements in a sandy subterranean estuary of the southern North Sea. *Mar. Chem.* 188, 6–17. doi: 10.1016/j.marchem.2016.11.003

Reckhardt, A., Beck, M., Seidel, M., Riedel, T., Wehrmann, A., Bartholomä, A., et al. (2015). Carbon, nutrient, and trace metal cycling in sandy sediments: a comparison of high-energy beaches and backbarrier tidal flats. *Estuar. Coast. Shelf Sci.* 159, 1–14. doi: 10.1016/j.ecss.2015.03.025

Riedel, T., Biester, H., and Dittmar, T. (2012). Molecular fractionation of dissolved organic matter with metal salts. *Environ. Sci. Technol.* 46, 4419–4426. doi: 10.1021/es203901u

Robinson, C., Gibbes, B., and Li, L. (2006). Driving mechanisms for groundwater flow and salt transport in a subterranean estuary. *Geophys. Res. Lett.* 33:L03402. doi: 10.1029/2005GL025247

Rocha, C. (2008). Sandy sediments as active biogeochemical reactors: compound cycling in the fast lane. *Aquat. Microb. Ecol.* 53, 119–127. doi: 10.3354/ame01221

Röper, T., Kröger, K. F., Meyer, H., Sültenfuss, J., Greskowiak, J., and Massmann, G. (2012). Groundwater ages, recharge conditions and hydrochemical evolution of a barrier island freshwater lens (Spiekeroog, Northern Germany). *J. Hydrol.* 454, 173–186. doi: 10.1016/j.jhydrol.2012.06.011

Roy, M., Martin, J. B., Cherrier, J., Cable, J. E., and Smith, C. G. (2010). Influence of sea level rise on iron diagenesis in an east Florida subterranean estuary. *Geochim. Cosmochim. Acta* 74, 5560–5573. doi: 10.1016/j.gca.2010.07.007

Roy, M., Martin, J. B., Smith, C. G., and Cable, J. E. (2011). Reactive-transport modeling of iron diagenesis and associated organic carbon remineralization in a Florida (USA) subterranean estuary. *Earth Planet. Sci. Lett.* 304, 191–201. doi: 10.1016/j.epsl.2011.02.002

Santos, I. R., Burnett, W. C., Dittmar, T., Suryaputra, I. G. N. A., and Chanton, J. (2009). Tidal pumping drives nutrient and dissolved organic matter dynamics in a Gulf of Mexico subterranean estuary. *Geochim. Cosmochim. Acta* 73, 1325–1339. doi: 10.1016/j.gca.2008.11.029

Santos, I. R., Eyre, B. D., and Huettel, M. (2012). The driving forces of porewater and groundwater flow in permeable coastal sediments: a review. *Estuar. Coast. Shelf Sci.* 98, 1–15. doi: 10.1016/j.ecss.2011.10.024

Sarazin, G., Michard, G., and Prevot, F. (1999). A rapid and accurate spectroscopic method for alkalinity measurements in sea water samples. *Water Res.* 33, 290–294. doi: 10.1016/s0043-1354(98)00168-7

Seibert, S. L., Böttcher, M. E., Schubert, F., Pollmann, T., Giani, L., Tsukamoto, S., et al. (2019a). Iron sulfide formation in young and rapidly-deposited permeable sands at the land-sea transition zone. *Sci. Total Environ.* 649, 264–283. doi: 10.1016/j.scitotenv.2018.08.278

Seibert, S. L., Greskowiak, J., Prommer, H., Böttcher, M. E., and Massmann, G. (2019b). Modeling of biogeochemical processes in a barrier island freshwater lens (Spiekeroog, Germany). *J. Hydrol.* 575, 1133–1144. doi: 10.1016/j.jhydrol.2019.05.094

Seibert, S. L., Holt, T., Reckhardt, A., Ahrens, J., Beck, M., Pollmann, T., et al. (2018). Hydrochemical evolution of a freshwater lens below a barrier island (Spiekeroog, Germany): the role of carbonate mineral reactions, cation exchange and redox processes. *Appl. Geochem.* 92, 196–208. doi: 10.1016/j.apgeochem.2018.03.001

Seibt, M. (2017). *The Molecular Geography of Dissolved Organic Matter in the Atlantic and Southern Ocean*. Ph.D. thesis, University of Oldenburg, Oldenburg.

Seidel, M., Beck, M., Greskowiak, J., Riedel, T., Waska, H., Suryaputra, I. G. N. A., et al. (2015). Benthic-pelagic coupling of nutrients and dissolved organic matter composition in an intertidal sandy beach. *Mar. Chem.* 176, 150–163. doi: 10.1016/j.marchem.2015.08.011

Seidel, M., Beck, M., Riedel, T., Waska, H., Suryaputra, I. G., Schnetger, B., et al. (2014). Biogeochemistry of dissolved organic matter in an anoxic intertidal creek bank. *Geochimi. Cosmochim. Acta* 140, 418–434. doi: 10.1016/j.gca.2014.05.038

Shen, Y., Chapelle, F. H., Strom, E. W., and Benner, R. (2015). Origins and bioavailability of dissolved organic matter in groundwater. *Biogeochemistry* 122, 61–78. doi: 10.1007/s10533-014-0029-4

Sirois, M., Couturier, M., Barber, A., Gélinas, Y., and Chaillou, G. (2018). Interactions between iron and organic carbon in a sandy beach subterranean estuary. *Mar. Chem.* 202:86. doi: 10.1016/j.marchem.2018.02.004

Spiteri, C., Slomp, C. P., Charette, M. A., Tuncay, K., and Meile, C. (2008). Flow and nutrient dynamics in a subterranean estuary (Waquoit Bay, MA, USA): field data and reactive transport modeling. *Geochim. Cosmochim. Acta* 72, 3398–3412. doi: 10.1016/j.gca.2008.04.027

Streif, H. (2002). "The Pleistocene and Holocene development of the southeastern North Sea basin and adjacent coastal areas," in *Climate Development and History of the North Atlantic Realm*, eds G. Wefer, W. Berger, K.-E. Behre, and E. Jansen (Berlin: Springer), 387–397. doi: 10.1007/978-3-662-04965-5_25

Suryaputra, I. G. N. A., Santos, I. R., Huettel, M., Burnett, W. C., and Dittmar, T. (2015). Non-conservative behavior of fluorescent dissolved organic matter (FDOM) within a subterranean estuary. *Continent. Shelf Res.* 110, 183–190. doi: 10.1016/j.csr.2015.10.011

Van Cappellen, P., and Wang, Y. (1996). Cycling of iron and manganese in surface sediments; a general theory for the coupled transport and reaction of carbon, oxygen, nitrogen, sulfur, iron, and manganese. *Ame. J. Sci.* 296, 197–243. doi: 10.2475/ajs.296.3.197

Waska, H., Brumsack, H. J., Massmann, G., Koschinsky, A., Schnetger, B., Simon, H., et al. (2019a). Inorganic and organic iron and copper species of the subterranean estuary: Origins and fate. *Geochim. Cosmochim. Acta* 259, 211–232. doi: 10.1016/j.gca.2019.06.004

Waska, H., Greskowiak, J., Ahrens, J., Beck, M., Ahmerkamp, S., Böning, P., et al. (2019b). Spatial and temporal patterns of pore water chemistry in the inter-tidal zone of a high energy beach. *Front. Mar. Sci.* 6:154. doi: 10.3389/fmars.2019.00154

Webb, J. R., Santos, I. R., Maher, D. T., Tait, D. R., Cyronak, T., Sadat-Noori, M., et al. (2019). Groundwater as a source of dissolved organic matter to coastal waters: insights from radon and CDOM observations in 12 shallow coastal systems. *Limnol. Oceanogr.* 64, 182–196. doi: 10.1002/lno.11028

Yang, L., Chen, C. T. A., Hong, H., Chang, Y. C., and Lui, H. K. (2015). Mixing behavior and bioavailability of dissolved organic matter in two contrasting subterranean estuaries as revealed by fluorescence spectroscopy and parallel factor analysis. *Estuar. Coas. Shelf Sci.* 166, 161–169. doi: 10.1016/j.ecss.2014.10.018

Conflict of Interest: The authors declare that the research was conducted in the absence of any commercial or financial relationships that could be construed as a potential conflict of interest.

The handling editor is currently organizing a Research Topic with one of the authors HW.

Copyright © 2021 Waska, Simon, Ahmerkamp, Greskowiak, Ahrens, Seibert, Schwalfenberg, Zielinski and Dittmar. This is an open-access article distributed under the terms of the Creative Commons Attribution License (CC BY). The use, distribution or reproduction in other forums is permitted, provided the original author(s) and the copyright owner(s) are credited and that the original publication in this journal is cited, in accordance with accepted academic practice. No use, distribution or reproduction is permitted which does not comply with these terms.

frontiers in Marine Science

ORIGINAL RESEARCH
published: 12 June 2020
doi: 10.3389/fmars.2020.00424

Rare Earth Element Behavior in a Sandy Subterranean Estuary of the Southern North Sea

Ronja Paffrath[1], Katharina Pahnke[1], Melanie K. Behrens[1], Anja Reckhardt[2], Claudia Ehlert[1], Bernhard Schnetger[2] and Hans-Jürgen Brumsack[2]*

[1] Marine Isotope Geochemistry, Institute for Chemistry and Biology of the Marine Environment (ICBM), University of Oldenburg, Oldenburg, Germany, [2] Microbiogeochemistry, Institute for Chemistry and Biology of the Marine Environment (ICBM), University of Oldenburg, Oldenburg, Germany

The use of rare earth elements (REEs) as tracers for oceanic processes requires knowledge and quantification of their sources and sinks. Submarine groundwater discharge (SGD) has been suggested to be a potentially important source of REEs and other trace elements to the ocean. To investigate the processes affecting REEs in a subterranean estuary (STE) of a sandy beach system and their contribution to coastal waters of the southern North Sea, we analyzed dissolved REE concentrations in beach pore waters, coastal seawater and fresh groundwater on the barrier island Spiekeroog, German North Sea. The pore waters show variable REE concentrations (Neodymium between 6 and 54 pmol/kg), generally increasing from the upper beach to the shoreline. At the upper beach, mixing of coastal pore water with rainwater and scavenging lead to lower REE concentrations than in coastal seawater and high heavy (HREE) over light (LREE) REE ratios. Close to the low water line, the REE concentrations increase, partly exceeding seawater concentrations and showing a positive deviation from conservative mixing, with shale-normalized light and middle REE-enriched patterns. This is due to the release of light and middle REEs from degrading particulate organic material and potentially dissolution of Fe/Mn-oxides under reducing conditions. Reducing conditions are further supported by the change from a negative Ce-anomaly at the upper beach to no anomaly close to the low water line. Net SGD fluxes of both fresh groundwater and recirculated seawater are a source of light, middle and heavy REEs to the ocean, with a higher contribution of LREEs than HREEs compared to seawater. However, the total amount of REEs added to the North Sea by SGD from the East Frisian Islands is still ~500 times smaller than input from nearby rivers. An anthropogenic Gd signal higher than previously reported is present throughout the pore waters and seawater, indicating increasing accumulation of anthropogenic Gd in the coastal marine environment.

Keywords: rare earth elements, barrier island, North Sea, subterranean estuary, submarine groundwater discharge, Gd-anomaly, Ce-anomaly

OPEN ACCESS

Edited by:
Carlos Rocha,
Trinity College Dublin, Ireland

Reviewed by:
Guebuem Kim,
Seoul National University, South Korea
Peter Wolfgang Swarzenski,
IAEA, Environment Laboratories, Monaco

****Correspondence:***
Ronja Paffrath
ronja.paffrath@uni-oldenburg.de

Specialty section:
This article was submitted to Marine Biogeochemistry, a section of the journal Frontiers in Marine Science

Received: *07 February 2020*
Accepted: *14 May 2020*
Published: *12 June 2020*

Citation:
Paffrath R, Pahnke K, Behrens MK, Reckhardt A, Ehlert C, Schnetger B and Brumsack H-J (2020) Rare Earth Element Behavior in a Sandy Subterranean Estuary of the Southern North Sea. Front. Mar. Sci. 7:424. doi: 10.3389/fmars.2020.00424

INTRODUCTION

Rare earth elements (REEs) are widely used as tracers for oceanic processes like scavenging, redox changes, and provenance of particles or water. The REEs comprise the elements from lanthanum (La) to lutetium (Lu) that all exist in a trivalent oxidation state except for cerium (Ce) and europium (Eu) that can additionally be oxidized (CeIV) or reduced (EuII), respectively (Elderfield and Greaves, 1982). The REEs show similar chemical behavior with small differences due to the consecutive filling of the 4f electron shell with increasing atomic number that leads to a decrease in their ionic radii (e.g., Elderfield, 1988). In seawater, REEs are stabilized by carbonate complexes, with increasing stability of the complexes with increasing atomic number. This results in a decrease in particle reactivity from the light (LREEs) to the heavy REEs (HREEs) (Sholkovitz et al., 1994). The REE concentrations are usually shown in the sequence of increasing atomic number normalized either to a rock reference material (e.g., Post Archean Australian Shale (PAAS), Rudnick and Gao, 2003) or to a reference water mass. The shape of the resulting REE patterns can give insight into the scavenging intensity (high HREE/LREE = strong scavenging) or REE input from e.g., particle (coatings) or lithogenic sources (lower HREE/LREE). Furthermore, anomalies of single elements in comparison to their neighbor elements (all normalized to shale) point to oxic/sub- or anoxic conditions (negative/positive Ce-anomaly), basaltic influence (positive Eu-anomaly) or anthropogenic contamination (highly positive Gd-anomaly).

In order to use the REEs to study biogeochemical processes in the ocean, it is important to understand their input and removal pathways and quantify the respective rates. In the past, rivers were thought to be the main source of REEs to the ocean (Goldstein and Jacobsen, 1988), but based on mass balance calculations for neodymium (Nd), it was found that river input alone cannot account for the observed Nd concentrations and Nd isotope distributions in the ocean (Lacan and Jeandel, 2005). Subsequent studies (e.g., Tachikawa et al., 2003; Johannesson and Burdige, 2007) have suggested submarine groundwater discharge (SGD) as an additional potentially important source of REEs and other trace elements (Windom et al., 2006), nutrients (Anschutz et al., 2009), and contaminants (Bone et al., 2007; Trezzi et al., 2016) to the ocean. Submarine groundwater discharge is defined as the water that is flowing from the seabed on the margins to the overlying water column, including both fresh terrestrial derived groundwater and infiltrated seawater (Burnett et al., 2003). The term SGD is used independent of the mechanisms driving the water discharge like hydraulic gradients, tidal pumping, or current-induced pressure gradients (Burnett et al., 2003). Recent studies have demonstrated the potential of SGD in adding REEs to the ocean in quantities that are similar to or exceed those of either regional river input (e.g., Johannesson and Burdige, 2007; Johannesson et al., 2011; Kim and Kim, 2011; Chevis et al., 2015a), or sediment diffusive fluxes or atmospheric dust input (e.g., Kim and Kim, 2014), depending on the characteristics of the studied region. Particularly, it was suggested that SGD is a source of LREEs and middle REEs (MREEs), but a sink for HREEs (Johannesson et al., 2011; Chevis et al., 2015b). The observed high REE concentrations of SGD are suggested to be linked to the degradation of REE-rich relict terrestrial organic carbon (Duncan and Shaw, 2003) and/or the reduction of Fe-oxides under anoxic conditions in the sediments (Johannesson et al., 2011; Chevis et al., 2015b).

Sandy beach systems, as found on Spiekeroog Island, make up one third of the ice-free coastline worldwide (Luijendijk et al., 2018) and processes in their subterranean estuaries (STEs) may therefore have a major effect on coastal element cycles and global ocean trace element budgets.

It has been shown in many studies that the medical use of gadolinium (Gd) in urban areas results in a positive Gd-anomaly in terrestrial groundwaters (e.g., Knappe et al., 2005; Johannesson et al., 2017), rivers (e.g., Bau and Dulski, 1996; Kulaksiz and Bau, 2011; de Campos and Enzweiler, 2016), and coastal waters (e.g., Kulaksiz and Bau, 2007; Hatje et al., 2016; Pedreira et al., 2018). Due to its paramagnetic properties, Gd has been used in several contrast agents for magnetic resonance imaging (MRI) since the late 1980s (Bau and Dulski, 1996). Since Gd^{3+} is toxic to the human body due to its ionic radius that is similar to that of Ca^{2+} ions (Bourne and Trifaró, 1982), the Gd in the contrast agents is present in complexed form, e.g., gadolinium diethylenetriaminepentaacetic acid (Gd-DTPA) (e.g., Hatje et al., 2016). Because of the high solubility of the Gd complexes, they are not removed in waste water treatment plants and are discharged directly or via rivers into coastal seawater. In an experiment to investigate the behavior of Gd-DPTA during bank filtration, the half-life of Gd-DPTA was determined to be more than 100 days (Holzbecher et al., 2005). However, the authors suggested that different biogeochemical conditions in natural waters (e.g., different concentrations of organic matter) potentially influence the degradation of Gd complexes (Holzbecher et al., 2005). In estuaries, up to 15% of Gd-DPTA can dissociate due to the competition of Mg or Ca ions for DTPA (Schijf and Christy, 2018). Yet, because of the many different complexes in use, their stability may differ under natural conditions and little is known about degradation and transformation of the complexes under natural conditions (Birka et al., 2016).

In this study, we present concentrations of dissolved REEs in pore waters, seawater, and fresh groundwater from a beach site on the northern side of Spiekeroog Island, Germany, facing the open North Sea to investigate the behavior of REEs within the STE and their supply to the coastal waters. Moreover, comparison of natural, complexed, and non-complexed Gd in the STE pore waters and coastal seawater, provides age constraints on the pore waters and additional information on the processes in the STE. The studied STE has previously been shown to be a source of Fe, Mn, Mo, and nutrients to the coastal ocean whereas it is a sink for U, Re, and V (Ehlert et al., 2016; Beck et al., 2017; Reckhardt et al., 2017).

MATERIALS AND METHODS

Study Area and Sampling

The island of Spiekeroog is part of the barrier island chain in the German Wadden Sea about 6.5 km off the German main land (**Figure 1**). The island is subject to a mesotidal regime

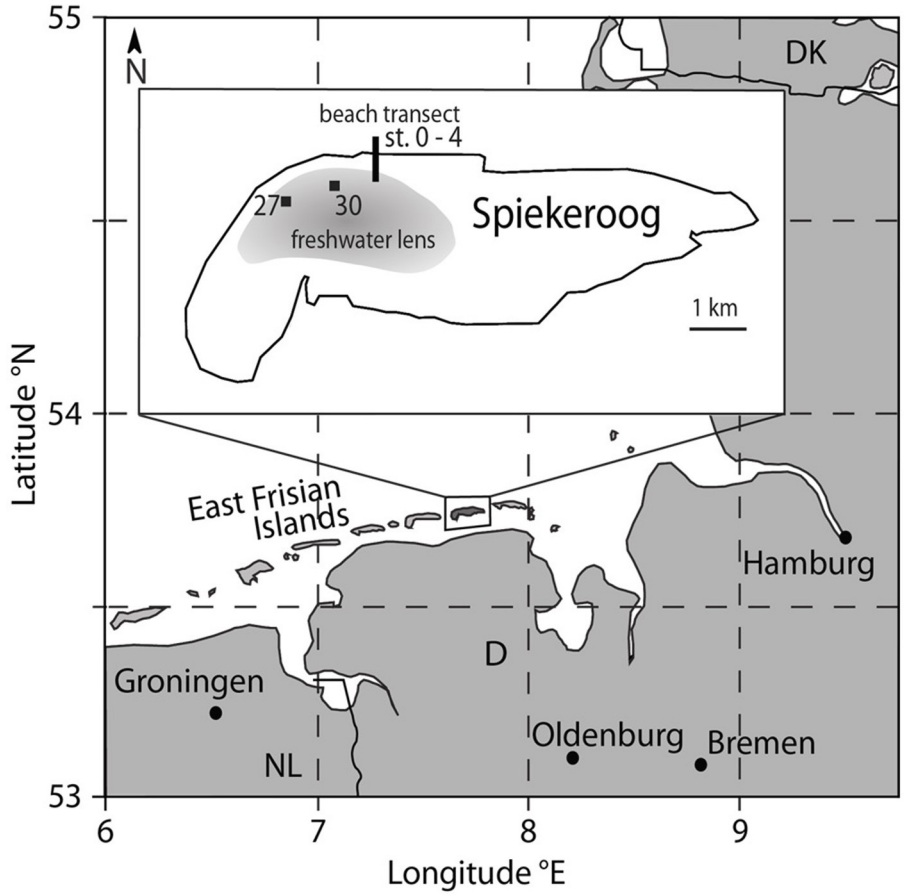


FIGURE 1 | Map of the study area Spiekeroog Island at the German North Sea coast. The beach porewater samples were taken at the north beach (black line, for details see **Figure 2**), freshwater samples from the freshwater lens of the island were collected from two observation wells (27 and 30) in the dune area (black squares).

with a tidal range of approximately 2.6 to 2.8 m (Flemming and Davis, 1994). A freshwater lens in the western part of the island is formed by infiltrating rainwater (Röper et al., 2012). A clay layer at about 50 m below sea level separates the fresh groundwater from the underlying saline groundwater [OOWV (Oldenburg-OstfriesischerWasserverband), 2009]. Moore (1999) defined a coastal aquifer where fresh groundwater mixes with infiltrated seawater and is discharged to the coastal ocean as an STE, similar to a surface estuary (Pritchard, 1967). There are similar reactions altering the composition of the estuarine waters through interactions with particles in surface estuaries and STEs (Moore, 1999). An STE typically encompasses the following zones: an upper saline plume (USP) in the intertidal area where seawater is infiltrated and recirculated back to the coastal ocean, the classical saltwater wedge (SW, density-driven, deeper recirculation cell than the USP) below the mean low water line (MLWL), and confined between the USP and SW a freshwater discharge tube (FDT) that reaches the sediment surface close to the MLWL (Robinson et al., 2007). The STE on Spiekeroog exhibits the typical zonation of STEs with a USP, FDT, and SW as suggested by a hydrological model (Beck et al., 2017) (**Figure 2**).

The upper dune area of the sampled transect (**Figure 2**, stations 0–1) is dominated by low salinities and oxic conditions, indicating recent rain infiltration. In the USP of the intertidal zone (**Figure 2**, station 2), salinities of 27–31.3 reflect the infiltration of seawater, while a drop to 2 % oxygen saturation below 2 m below sediment surface (mbsf) (Beck et al., 2017) indicates a change in redox conditions in the deeper part of the transect. The residence time of the waters in the USP has been modeled and indicated to be weeks to months depending on the depth (Beck et al., 2017; Waska et al., 2019). A small FDT was sampled at 1.5 and 2 mbsf at station 3, as indicated by low salinity, anoxic conditions (Beck et al., 2017) and high dissolved Si concentrations that are also found in the freshwater lens (Ehlert et al., 2016). Near the MLWL at the stations on the ridge (station 3, $\leq$1 mbsf and station 4), seawater is circulated in two small circulation cells, one discharging toward the runnel that separates stations 2 and 3, and one discharging to the open water (**Figure 2**). Most recent modeling results, however, suggest that the FDT on Spiekeroog is split, with parts of the FDT and SW located seaward of the ridge (Waska et al., 2019). Residence times of the pore waters covered by our sampling stations are weeks (saltwater) to years (freshwater) (Beck et al., 2017). The beach

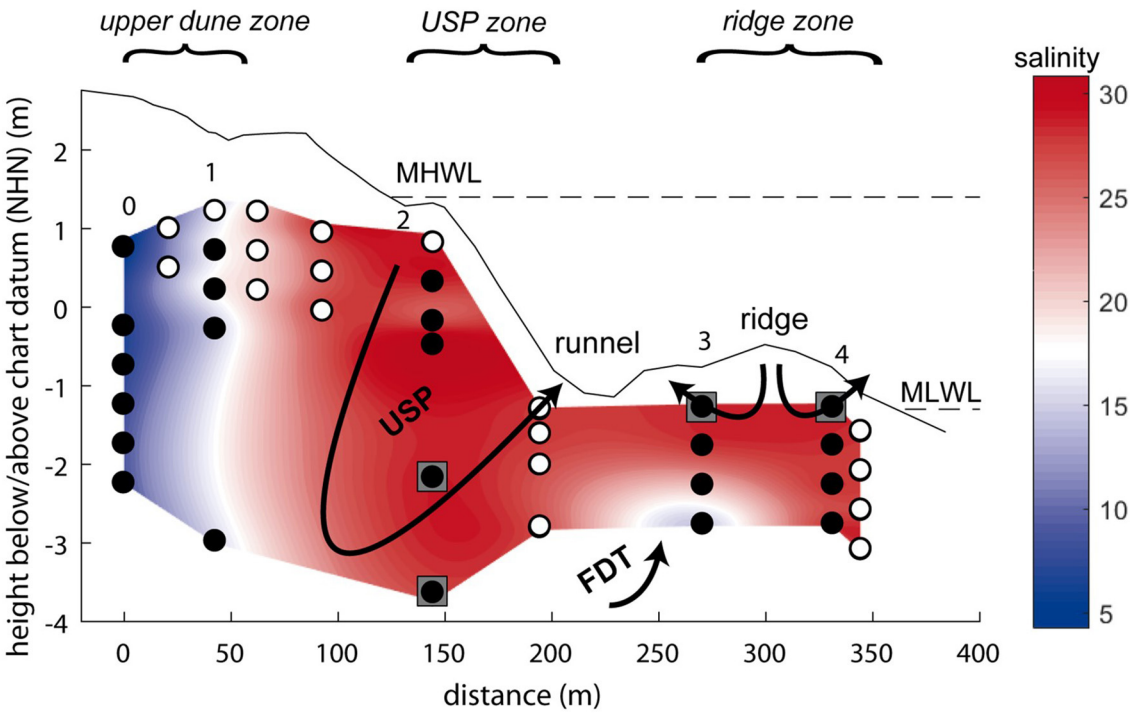


FIGURE 2 | Schematic overview of the subterranean estuary on Spiekeroog with its compartments upper saline plume (USP) and freshwater discharge tube (FDT). Background colors refer to the salinity of the pore waters. Filled circles show sampling depths for REE analyses, open circles indicate additional samples taken for other parameters (salinity, pH, Fe, Mn). Arrows indicate the generalized flow pattern within the STE, gray squares show the representative depths chosen for the flux calculations (representative depths for the FDT in the freshwater lens, not shown). The dashed lines represent the mean low water level (MLWL) and mean high water level (MHWL). Chart datum NHN equals approximately mean sea level. The three areas marked at the top in italics are used in the text for the different compartments of the STE instead of or in addition to the station numbers.

sediments are mainly composed of quarzitic fine to medium grained sand with layers of shells/shell debris, coarser-grained sand, heavy minerals or organic rich mud (Beck et al., 2017).

Beach pore water samples were collected on the northern open North Sea side of the island along a transect from close to the dunes to the MLWL in May 2014 in the framework of an interdisciplinary study (see Beck et al., 2017) (**Figures 1**, **2**). Pore water samples from the beach transect down to 2 mbsf were taken using stainless steel push point samplers, for details see Reckhardt et al. (2015). Sediment depths exceeding 2 mbsf were sampled by elongating a stainless-steel tip stepwise with 90 cm long steel extension rods (outer diameter 15 mm). They were pushed into the sediment by percussion drilling as described in Charette and Allen (2006) and the samples were retrieved through a Teflon tube (inner diameter 5 mm) using a vacuum hand pump and filled into acid-cleaned 500 ml high-density polyethylene (HDPE) bottles. Seawater and runnel samples were taken at ∼0.5 m water depth by submerging a 1 L polycarbonate bottle (Nalgene, acid-cleaned). The samples were filtered (AkroPak200 or 500 filter cartridges, pore size 0.8/0.2 µm) into acid-cleaned HDPE bottles in the lab within 8 h after sampling, acidified with ultra-clean 6N HCl to a pH of ∼2, and stored for further processing in the home laboratory at the ICBM, Oldenburg. Samples from stations 3 and 4 were directly filtered through 0.45 µm surfactant-free cellulose acetate (SFCA) syringe filters into low-density polyethylene (LDPE) bottles and acidified at the sampling location with concentrated, self-distilled HNO_3 to obtain an acid concentration of 1 % (v/v). Samples from the islands freshwater lens were obtained from two observation wells (27 and 30) and two depths per well in the dune area of the island (**Figure 1**) as described in Röper et al. (2012). The samples were filtered directly (AkroPak500 filter cartridges, pore size 0.8/0.2 µm) into acid-cleaned HDPE bottles and acidified immediately in the field.

REE Analyses

The REEs were pre-concentrated from seawater using an automated seaFAST-pico system (Elemental Scientific Inc.) following the method described in Behrens et al. (2016). Briefly, samples were spiked with a multi-element REE isotope spike (DKM, prepared by Gilbert N. Hanson of SUNY Stony Brook) and allowed to equilibrate for at least 48 h before purification and pre-concentration with the seaFAST-pico system. An additional UV/H_2O_2-oxidation was applied for 24 h prior to the pre-concentration step to destroy organic matter and anthropogenic Gd-complexes as degradation of these complexes via hydroxyl radicals has been shown to be very effective (Cyris et al., 2013). The REE concentrations were analyzed and quantified by isotope dilution ICP-MS using a Finnigan Element ICP-MS and a Cetac Aridus II desolvating nebulizer to reduce oxide

formation (<0.04% for Ce). The external reproducibility (1RSD), determined by repeated processing and analysis of seawater samples from North Pacific station SAFe 3,000 m, was <3.4% for all REEs except for Ce (<23%; $n = 6$). Our analyses were well within the 6% range of the consensus values of the SAFe sample (Behrens et al., 2016). Procedural blanks for all REEs except Ce were <4% of the lowest measured REE concentrations and <10% of the lowest measured Ce concentration. All REE concentrations, ratios and anomalies are shown in **Table 1**.

REE Anomalies and Natural and Anthropogenic Gd Concentrations

All REE anomalies were calculated using PAAS-normalized (Rudnick and Gao, 2003) REE concentrations (REE_N): The Ce-anomaly was calculated as

$$\left(\frac{Ce}{Ce^*}\right)_N = \frac{3{*}Ce_N}{2{*}La_N + Nd_N}$$

after German et al. (1995). For the Ce-anomaly, a measured PAAS-normalized Ce concentration is compared with a theoretical PAAS-normalized Ce concentration (Ce*) calculated via neighbor elements. Values >1 indicate a positive Ce-anomaly (higher PAAS-normalized Ce concentrations than expected from interpolation of the neighbor elements), values <1 indicate a negative Ce-anomaly. For all other anomalies of single elements or element groups, the interpretation is accordingly. Ce* or another REE represents the hypothetical Ce value if no anomaly exists. The MREE- and HREE anomalies were calculated after Martin et al. (2010) (for the MREE-anomaly modified by replacing Gd with Eu to avoid inclusion of the high anthropogenic Gd contributions). The Gd-anomaly was calculated in accordance with Bau and Dulski (1996).

Using the Gd-anomaly, the amount of natural Gd (Gd_{nat}) can be calculated as

$$Gd_{nat} = \frac{Gd}{\left(\frac{Gd}{Gd^*}\right)_N}$$

The anthropogenic part (Gd_{anth}) of the total Gd concentration is then the difference between the total Gd concentration and the natural Gd (Gd_{nat}) concentration, neglecting the small natural positive Gd-anomaly that regularly occurs in natural waters due the higher stability of Gd carbonate complexes compared to its neighbor elements (De Baar et al., 1991).

Since it has been shown that hydroxyl radicals can destroy (or destroy to a great extent) the Gd-complexes (Cyris et al., 2013), we re-analyzed three samples without prior UV/H_2O_2 treatment to test whether complexed Gd_{anth} can be readily quantified with our analytical method or whether complexed Gd_{anth} may be lost during pre-concentration.

Flux Calculations

In order to determine the net REE addition/removal of the fluxes from the USP, FDT, and from the ridge to the runnel and from the ridge to the MLWL, we chose samples that represent the REE concentrations of the discharged water (see **Figure 2**, squared symbols) based on the hydrological model of Beck et al. (2017) (see section Study Area and Sampling). We calculate the net fluxes for the USP and ridge, i.e., net addition or removal, in comparison to seawater, because seawater is the source water for the USP and the ridge, by subtracting the REE seawater concentrations from the REE concentrations of the representative samples. The difference in the REE concentrations is then multiplied by the volume of the respective fluxes per day per m shoreline (d*msl), which results in REE addition/removal in pmol per day per m shoreline (**Table 2**) (note that kg and L are used as equivalent here).

$$\text{net flux REE}\left[\frac{\text{pmol}}{\text{d*msl}}\right] = \left(\text{REE conc}\left[\frac{\text{pmol}}{\text{kg}}\right] - \text{REE conc sw}\left[\frac{\text{pmol}}{\text{kg}}\right]\right) * \text{volume flux}\left[\frac{\text{L}}{\text{d*msl}}\right]$$

For the net flux from the FDT the average REE concentrations of the freshwater lens is used, which is the source water for the FDT. The total net flux is the sum of all four net fluxes.

Enrichment factors of the REE concentrations in the compartments compared to seawater REE concentrations are shown in **Table 2** and **Figure 6** and are calculated as follows:

$$EF = \frac{\text{REE conc compartment}}{\text{REE conc sw}}$$

whereby "REE conc compartment" is the (average) REE concentration of the pore water sample(s) representative for the respective flux (**Table 2**) and "REE conc sw" is the average seawater REE concentration (**Table 1**).

RESULTS

Salinity

The salinities are increasing from station 0 (salinity 4.3–9.4) to 2 (salinity 26.0–31.3) and are constant around 28.2–29.0 at stations 3 (<1.5 mbsf depth) and 4 (entire profile). In the deep part of station 3, the salinity decreases to 21.4 at 1.5 and 14.9 at 2 mbsf. The salinity of the nearby seawater is 30.6 (northern beach, 14th May 2014, low tide). Salinities of the freshwater lens are in the range of 0.2 to 0.7.

Redox Conditions and Trace Element Concentrations

Beck et al. (2017) measured oxygen concentrations for stations 1 to 4 during the same sampling campaign. Station 1 is oxic down to 2.2 mbsf with nearly constant oxygen saturations throughout the sampled profile. At station 2, the oxygen saturation decreases from 80% at 0.6 mbsf depth to 2% at 2 mbsf depth. At stations 3 and 4 the oxygen saturation was already at or close to 0 within the first 0.5 mbsf. Previous studies (Beck et al., 2017; Reckhardt et al., 2017) that are based on the same sampling campaign with the same sampling sites and depths used here, showed low Fe and Mn concentrations (<7 μM for Fe, <2 μM for Mn) at stations 0 to 2 and increasing concentrations toward station 3, reaching their maximum at station 4 with 281 μM for Fe and 80 μM for

TABLE 1 | REE and ancillary data of porewaters from the beach transect, seawater, and the freshwater lens on Spiekeroog.

		Depth[a]	pH	Salinity	DOC	Mn	Fe	La	Ce	Pr	Nd	Sm	Eu	Gd	Tb	Dy	Ho	Er	Tm	Yb	Lu	Total Gd_{anth}	Ce/Ce*	Gd/Gd*	MREE/MREE*	HREE/LREE
		(m)	–	–	(μmol/kg)			(pmol/kg)															–	–	–	–
Beach transect																										
Station 0		2.0	8.40	4.3	79	0.1	0.0	13.2	16.0	4.0	16.8	4.3	1.1	13.3	1.0	7.3	1.7	6.0	0.9	6.4	1.1	8.36	0.5	2.7	0.7	5.8
53°46′47.80″ N,		3.0[b]	8.22	7.0	96	0.5	0.1	7.0	9.3	1.7	7.4	1.8	0.5	12.7	0.4	2.9	0.7	2.7	0.4	3.3	0.7	10.7	0.6	6.6	0.6	6.9
7°42′38.63″ E		3.5	8.47	7.2	110	0.1	0.0	6.2	11.4	1.7	7.3	2.1	0.6	20.8	0.5	3.9	1.0	3.6	0.6	4.2	0.9	18.3	0.8	8.1	0.6	8.6
		4.0	8.31	8.5	103	0.2	0.2	6.5	9.8	1.5	7.1	2.0	0.5	20.4	0.5	3.7	0.9	3.4	0.5	4.0	0.8	18.0	0.7	8.4	0.6	8.4
		4.5	8.27	9.4	114	0.3	0.1	15.9	19.8	3.6	15.6	4.2	1.1	21.9	1.0	7.2	1.7	6.0	0.9	6.5	1.2	17.0	0.6	4.4	0.7	6.1
		5.0	8.23	9.2	94	0.2	0.1	5.9	8.4	1.5	6.7	2.1	0.6	16.7	0.6	4.3	1.1	4.0	0.6	4.6	0.9	13.9	0.6	5.9	0.6	9.7
Station 1		1.0	7.51	15.1		2.0	7.0																			
53°46′49.10″ N		1.5	8.03	17.6	87	0.1	0.0	13.5	13.6	2.5	10.9	2.9	0.8	20.4	0.7	5.3	1.4	4.8	0.8	5.6	1.2	16.8	0.5	5.7	0.6	7.3
7°42′39.00″ E		2.0	8.06	18.5	91	0.2	0.1	16.4	19.6	3.4	14.5	3.6	1.0	23.4	0.8	6.5	1.6	5.7	0.9	6.4	1.2	19.2	0.6	5.6	0.6	6.5
		2.5	8.14	15.2	139	0.5	0.2	25.1	34.6	5.3	22.1	5.5	1.4	23.0	1.2	8.2	1.9	6.3	1.0	6.8	1.3	17.0	0.7	3.8	0.8	4.6
		5.2	8.07	15.5	79	0.2	0.1	18.0	19.6	4.0	18.5	4.5	1.3	22.0	1.1	8.3	2.0	7.0	1.1	7.4	1.4	16.4	0.5	3.9	0.7	6.3
Station 2		0.5	7.41	28.8	136	0.2	1.7																			
53°46′52.21″ N		1.0	7.32	29.4	147	0.0	0.2	47.7	47.3	8.8	34.7	7.9	2.0	33.9	1.6	11.0	2.7	9.0	1.3	9.5	1.7	25.6	0.5	4.1	0.7	3.8
7°42′40.25″ E		1.5	7.75	26.0	113	0.0	0.1	27.2	21.8	4.7	19.7	4.9	1.3	22.3	1.1	8.0	2.0	6.5	1.0	7.1	1.3	16.8	0.4	4.0	0.7	5.0
		1.8[b]	7.73	31.3	113	0.1	0.5	48.1	28.7	9.1	38.2	8.2	2.1	28.8	1.5	11.1	2.6	8.3	1.3	8.6	1.5	20.8	0.3	3.6	0.8	3.3
		3.5	7.87	29.1	108	0.8	5.9	11.9	17.1	2.6	12.5	2.8	0.7	23.4	0.6	3.8	1.0	3.4	0.6	4.5	0.9	20.5	0.7	8.0	0.6	5.5
		5.0	8.08	27.0	103	0.2	0.5	20.6	31.8	4.3	19.3	4.7	1.2	29.9	1.0	7.0	1.8	6.9	1.0	7.7	1.5	24.8	0.7	5.9	0.6	6.0
Station 3		0.5	7.78	28.6	147	16.6	6.0	52.2	89.2	10.7	42.5	10.2	2.8	38.9	2.6	14.0	3.4	11.1	1.7	11.7	2.0	25.9	0.9	3.0	0.8	3.9
53°46′56.67″ N		1.0	7.68	28.2	164	18.0	73.3	53.4	79.9	9.8	43.1	10.6	2.7	44.8	2.5	16.6	3.9	12.6	2.0	13.2	2.4	32.4	0.8	3.6	0.8	4.5
7°42′42.48″ E		1.5	7.91	21.4	146	9.1	56.2	29.7	57.7	7.9	34.8	9.8	2.7	25.1	2.5	17.3	4.1	13.5	2.0	13.8	2.4	12.9	0.9	2.1	0.8	6.0
		2.0	8.03	14.9	129	1.2	26.7	38.9	76.8	10.5	44.8	11.8	3.3	21.3	2.9	20.8	4.6	14.5	2.1	14.1	2.4	7.03	0.9	1.5	0.9	4.8
Station 4		0.5	7.67	29.0	164	22.3	74.0	66.1	103.5	12.7	53.8	12.2	3.2	40.8	2.6	18.1	4.0	13.2	2.0	13.3	2.3	27.5	0.8	3.1	0.8	3.7
53°46′57.97″ N		1.0	7.60	28.4	172	45.1	149.1	56.2	99.9	11.8	49.0	12.2	3.2	60.0	2.7	17.9	4.1	13.9	2.2	14.1	2.4	46.4	0.9	4.4	0.8	4.2
7°42′41.22″ E		1.5	7.73	28.3	150	80.2	108.8	32.9	62.7	7.7	33.6	8.7	2.3	54.1	2.1	14.4	3.4	11.5	1.7	11.6	2.1	43.8	0.9	5.3	0.8	5.3
		2.0	7.60	28.4	175	33.7	281.7	29.6	55.5	7.6	33.6	7.2	1.8	29.7	1.3	8.8	2.2	7.8	1.2	8.6	1.6	22.7	0.8	4.3	0.7	4.2
Seawater																										
Seawater high tide					173			31.4	43.0	7.5	30.7	8.0	2.1	31.8	1.9	13.7	3.4	11.8	1.8	12.1	2.1	22.2	0.6	3.3	0.7	5.8
Seawater low tide					187			35.4	44.7	8.0	33.3	8.5	2.3	31.5	2.1	15.4	3.7	12.7	1.9	12.9	2.3	21.2	0.6	3.1	0.7	5.7
Average seawater[C]			**7.9**	**30.6**	**180**	**0.03**	**0.00**	**33.4**	**43.8**	**7.7**	**32.0**	**8.3**	**2.2**	**31.6**	**2.0**	**14.6**	**3.5**	**12.2**	**1.8**	**12.5**	**2.2**	**21.7**	**0.6**	**3.2**	**0.7**	**5.8**
Std dev 1s								2.8	1.2	0.3	1.9	0.4	0.1	0.2	0.1	1.2	0.2	0.6	0.1	0.6	0.1	0.7	0.0	0.2	0.0	0.0
Freshwater lens																										
Station 27																										
53°46′24.6″ N	27A	10.8	8.4	0.3	194	0.4	0.1	54.8	133.5	18.4	82.0	24.1	6.5	29.1	5.0	32.8	7.2	22.4	3.5	22.6	3.9		1.0	1.2	1.0	4.3
07°41′09.8″ E	27B	24.7	8.3	0.2	258	0.0	0.1	161.3	361.2	48.2	213.4	62.6	18.0	95.3	17.4	132.8	32.9	108.1	16.3	103.7	16.8		0.9	1.2	0.8	7.4

(Continued)

TABLE 1 | Continued

	Depth[a]	pH	Salinity	DOC	Mn	Fe	La	Ce	Pr	Nd	Sm	Eu	Gd	Tb	Dy	Ho	Er	Tm	Yb	Lu	Total Gd_{anth}	Ce/Ce*	Gd/Gd*	MREE/MREE*	HREE/LREE
	(m)	–	–	(μmol/kg)			(pmol/kg)															–	–	–	–
Station 30																									
53°46′33.8″ N	30A	10.2	8.4	0.2	427	0.4	1.2	91.6	294.4	41.6	197.0	57.6	14.5	67.9	10.4	64.6	13.6	41.3	6.0	39.4	6.6		1.0	1.1	1.1	3.3
07°41′58.8″ E	30B	35.8	8.1	0.3	206	0.1	0.3	36.9	103.7	16.1	83.7	26.9	7.4	35.9	6.0	39.7	8.9	28.1	4.0	24.6	4.1		0.9	1.1	1.1	4.8
Average freshwater			**8.3**	**0.2**	**271**	**0.2**	**0.4**	**86.2**	**223.2**	**31.1**	**144.0**	**42.8**	**11.6**	**57.0**	**9.7**	**67.5**	**15.6**	**50.0**	**7.4**	**47.6**	**7.8**		**1.0**	**1.2**	**1.0**	**4.9**
Std dev 1s			0.1	0.0	107	0.2	0.5	55.0	124.4	16.2	71.0	20.1	5.6	30.6	5.7	45.6	11.8	39.6	6.0	38.2	6.1		0.1	0.0	0.1	1.7

[a]*beach transect: m below sediment surface; freshwater lense: m below mean sea level.*

[b]*average of three measurements for REEs.*

[c] *pH, DOC, Mn and Fe are measured in one seawater sample, not at low and high tide separately. The bold values are average values for the seawater and freshwater lens, respectively.*

Mn (Fe **Figure 3A**, Mn not shown, Beck et al., 2017; Reckhardt et al., 2017). Concentrations of dissolved organic carbon (DOC) are in the range of 80 to 175 μM with the highest concentrations close to the MLWL (**Figure 3B**, Beck et al., 2017). For details and other parameters see Beck et al. (2017) (nutrients, DOC, sulfate, hydrogen sulfide), Reckhardt et al. (2017) (Mn, Fe, U, Re, Mo, V) and Ehlert et al. (2016) (Si and δ^{30}Si).

Rare Earth Elements

REE Concentrations

Rare earth element concentrations, ratios, and anomalies of beach pore waters, the freshwater lens, and the seawater can be found in **Table 1**. Along the beach pore water transect, REE concentrations show a generally increasing trend from the dunes to the MLWL, ranging from 6.2 to 53.8 pmol/kg for Nd (representative of LREE) and 3.3 to 14.1 pmol/kg for Yb (representative of HREE) (**Figures 3C,D**, for concentrations of other elements see **Table 1**). From the dunes (station 0–1) to the USP (station 2), the REE concentrations increase slightly on average from 12.7 to 24.9 pmol/kg for Nd (5.5 to 7.5 pmol/kg for Yb) and show highest REE concentrations on the ridge (stations 3 and 4) (average of 41.7 pmol/kg for Nd, 12.2 pmol/kg for Yb). Seawater REE concentrations (32.0 pmol/kg for Nd, 12.5 pmol/kg for Yb) are closest to those of the USP (station 2), where salinities indicate the almost pure seawater endmember. Groundwater from the freshwater lens shows generally higher REE concentrations ranging from 82.0 to 213.4 pmol/kg for Nd and 22.6 to 103.7 pmol/kg for Yb.

REE Ratios and Anomalies

PAAS-normalized REE patterns in the upper dune area (stations 0–1) exhibit a strong HREE-enriched pattern with highest HREE/LREE ratios of up to 9.7, compared to 5.8 in coastal seawater (**Figure 3E**). Lower HREE/LREE ratios of 3.6 to 6.6 are found in the USP and ridge area (stations 2 to 4). The range of the MREE-anomaly is from 0.6 to 0.9, with higher values at the ridge stations (**Figures 3F**, **4A**). A negative Ce-anomaly is most pronounced in the upper USP (station 2, 1–1.8 m) and at the duneward stations 0 to 1, whereas only a slight negative Ce-anomaly (0.8 to 0.9) is found on the ridge (**Figure 3H**) and the freshwater lens.

Gadolinium

A pronounced positive Gd-anomaly is present at most stations and depths, with values ranging from 8.4 at station 0 to 1.1 that represents a natural occurring Gd-anomaly at station 3 (**Table 1**). The seawater samples show intermediate Gd-anomalies of about 3.2. Samples from the freshwater lens do not carry an anthropogenic Gd-anomaly, their Gd-anomaly is in the natural range of up to 1.2. Note that normalized to seawater (**Figure 4B**), samples from station 3 and the freshwater lens (that do not show a PAAS-normalized Gd-anomaly) appear to have a negative Gd anomaly, which is due to the positive Gd-anomaly in seawater. The calculated Gd_{nat} concentrations in the pore water samples are in the range of 1.9 to 16.2 pmol/kg, with lowest values at station 0 and highest values at station 4, equivalent to the other REEs. The calculated Gd_{anth}

TABLE 2 | Calculated REE fluxes of SGD on Spiekeroog.

Fluxes from	Modeled SGD fluxes[a] (L/d msl)		La	Ce	Pr	Nd	Sm	Eu	Gd	Tb	Dy	Ho	Er	Tm	Yb	Lu	Samples used for calculation
			(nmol/d msl)														
Upper saline plume	2,800	REE conc (pmol/kg)	16.3	24.4	3.5	15.9	3.8	0.9	26.6	0.8	5.4	1.4	5.1	0.8	6.1	1.2	Average of st.2, 3.5, and 5 m
		Flux	45.5	68.4	9.7	44.4	10.5	2.6	74.6	2.2	15.2	3.8	14.4	2.2	17.1	3.2	
		1s	17.1	29.0	3.3	13.5	3.8	1.0	12.9	0.9	6.2	1.7	6.9	0.9	6.4	1.2	
		Net flux	**−48.0**	**−54.2**	**−12.0**	**−45.2**	**−12.7**	**−3.5**	**−14.0**	**−3.4**	**−25.6**	**−6.1**	**−19.8**	**−2.9**	**−17.9**	**−3.0**	
		EF compared to SW[b]	0.5	0.6	0.4	0.5	0.5	0.4	0.8	0.4	0.4	0.4	0.4	0.4	0.5	0.5	
Fresh-water discharge tube	750	REE conc (pmol/kg)	86.2	223.2	31.1	144.0	42.8	11.6	57.0	9.7	67.5	15.6	50.0	7.4	47.6	7.8	Average of 30A, 30B, 27A, 27B (freshwater lens)
		Flux = net flux	**64.6**	**167.4**	**23.3**	**108.0**	**32.1**	**8.7**	**42.8**	**7.3**	**50.6**	**11.7**	**37.5**	**5.6**	**35.7**	**5.9**	
		1s	41.3	93.3	12.2	53.2	15.1	4.2	23.0	4.2	34.2	8.9	29.7	4.5	28.6	4.6	
		EF compared to SW[b]	2.6	5.1	4.0	4.5	5.2	5.3	1.8	4.9	4.6	4.4	4.1	4.1	3.8	3.5	
Ridge to runnel	500	REE conc (pmol/kg)	52.2	89.2	10.7	42.5	10.2	2.8	38.9	2.6	14.0	3.4	11.1	1.7	11.7	2.0	st.3, 0.5 m
		Flux	26.1	44.6	5.3	21.3	5.1	1.4	19.4	1.3	7.0	1.7	5.6	0.9	5.8	1.0	
		Net flux	**9.4**	**22.7**	**1.5**	**5.3**	**1.0**	**0.3**	**3.6**	**0.3**	**−0.3**	**−0.1**	**−0.5**	**−0.1**	**−0.4**	**−0.1**	
		EF compared to SW[b]	1.6	2.0	1.4	1.3	1.2	1.3	1.2	1.3	1.0	1.0	0.9	0.9	0.9	0.9	
Runnel to low water line	1,000	REE conc (pmol/kg)	66.1	103.5	12.7	53.8	12.2	3.2	40.8	2.6	18.1	4.0	13.2	2.0	13.3	2.3	st. 4, 0.5 m
		flux	66.1	103.5	12.7	53.8	12.2	3.2	40.8	2.6	18.1	4.0	13.2	2.0	13.3	2.3	
		Net flux	**32.7**	**59.7**	**5.0**	**21.8**	**4.0**	**1.0**	**9.1**	**0.6**	**3.5**	**0.4**	**1.0**	**0.1**	**0.8**	**0.1**	
		EF compared to SW[b]	2.0	2.4	1.6	1.7	1.5	1.4	1.3	1.3	1.2	1.1	1.1	1.1	1.1	1.0	
Total STE	5,050	**Total net flux**	**58.7**	**195.5**	**17.7**	**89.9**	**24.3**	**6.4**	**41.5**	**4.7**	**28.2**	**6.0**	**18.1**	**2.8**	**18.2**	**2.9**	
		EF compared to SW[b]	1.2	1.7	1.3	1.4	1.4	1.4	1.1	1.3	1.2	1.2	1.1	1.1	1.1	1.1	

[a] *from Beck et al. (2017).*

[b] *enrichment factor (EF) for the REE concentrations in the respective compartments compared to seawater concentrations, see* ***Figure 6****. The bold values are net fluxes for the respective compartment.*

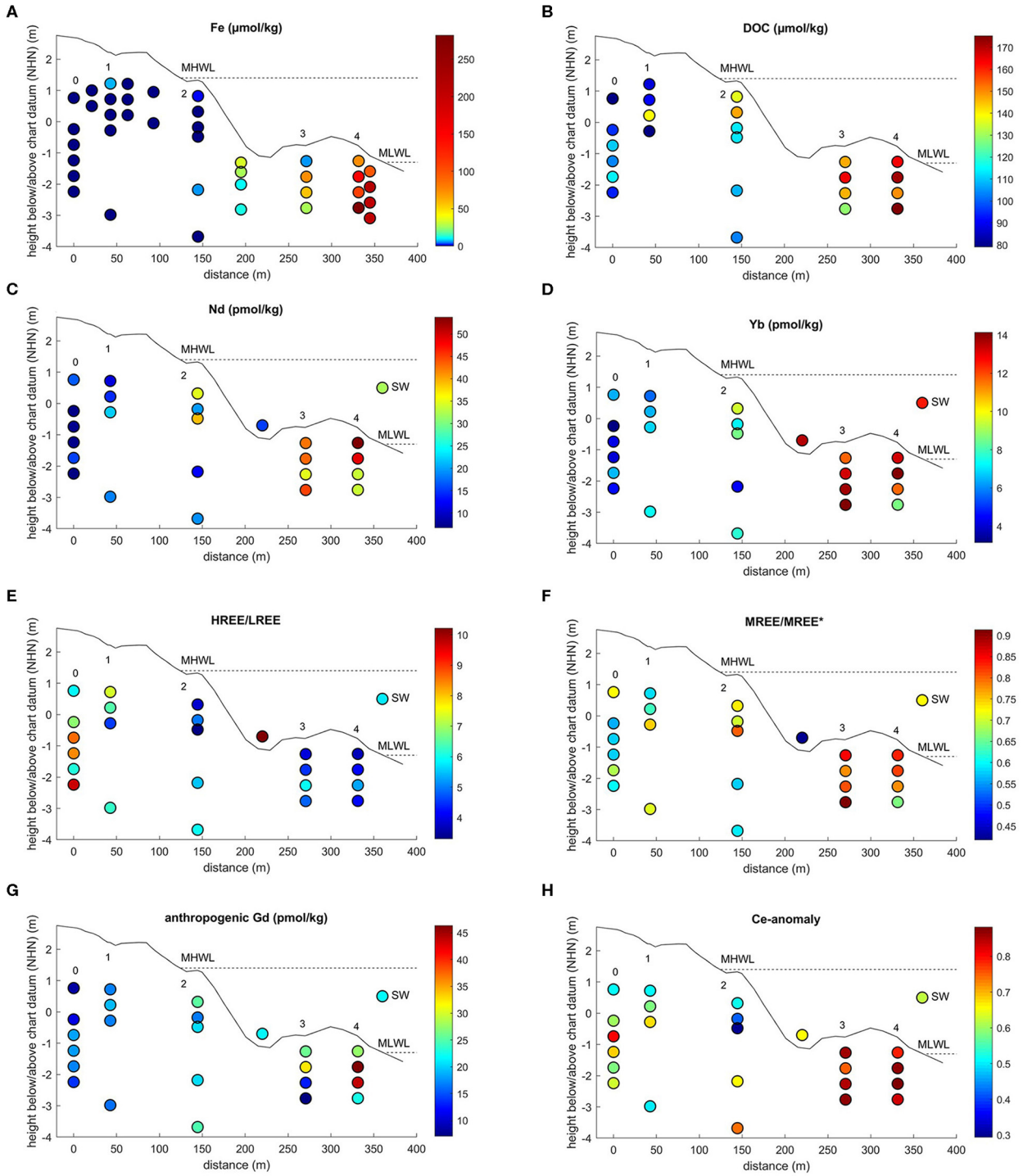


FIGURE 3 | Spatial distribution of **(A)** Fe, **(B)** DOC (Beck et al., 2017), **(C)** Nd concentrations, **(D)** Yb concentrations, **(E)** PAAS-normalized (Rudnick and Gao, 2003) HREE/LREE, **(F)** PAAS-normalized MREE-anomaly, **(G)** anthropogenic Gd concentrations, and **(H)** PAAS-normalized Ce-anomaly (this study) in beach pore waters, the runnel, and seawater (SW) on Spiekeroog Island. Site numbers are from **Figure 2**. The dashed lines indicate the mean high water level (MHWL) and mean low water level (MLWL). Note the non-linear color scales for Fe concentrations. Chart datum NHN equals approximately mean sea level.

concentrations range between 8.4 and 46.4 pmol/kg, again with lowest values at station 0 and highest values at station 4 (**Figure 3G**).

As described above, three samples were analyzed for REE concentrations with and without prior UV/H_2O_2 treatment. The different treatment only affected the measured concentration of

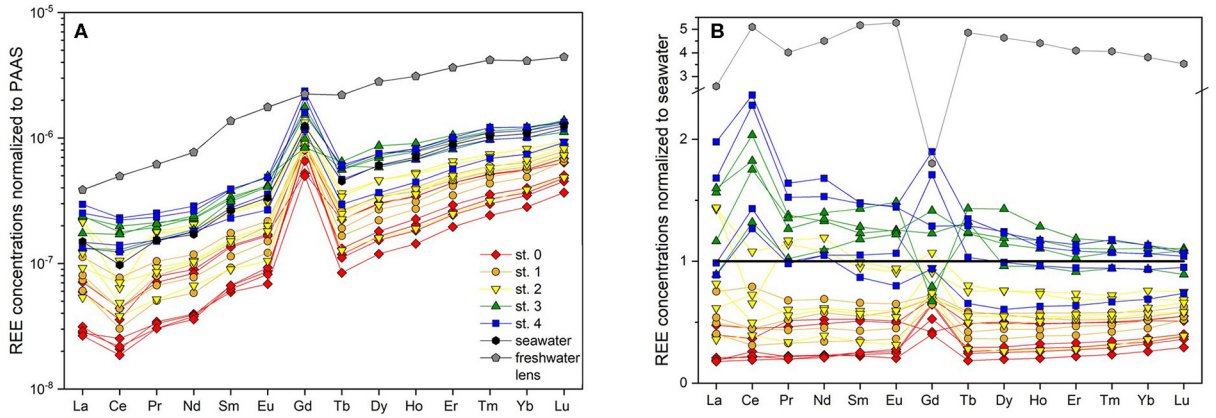


FIGURE 4 | REE concentrations of pore waters and seawater **(A)** normalized to PAAS (Rudnick and Gao, 2003) and **(B)** normalized to seawater.

Gd (**Table 3**), which is higher in the treated compared to the untreated samples by 5.5 to 13.0 pmol/kg Gd, which represents 38 to 49% of the total measured Gd concentration. This additional Gd represents the complexed part of the Gd_{anth} that is only recovered with the ion exchange method used here if the Gd-DTPA complex is destroyed through UV/H_2O_2-treatment prior to pre-concentration.

Fluxes of REEs

The fluxes of REEs for the USP, FDT, and ridge to runnel and ridge to MLWL are listed in **Table 2** as well as enrichment factors of the REE concentrations of these fluxes compared to seawater REE concentrations (see **Figure 6**). We calculated REE fluxes for the different compartments of the STE as REE fluxes from the USP, the FDT, from the ridge to the runnel and from the ridge to the MLWL (water fluxes from Beck et al., 2017). Estimates of the REE net fluxes from the USP reveal that REEs are removed from infiltrating seawater by factors of 0.4 (MREE) and 0.5 (LREE and HREE) (excluding Ce 0.6 and Gd 0.8), resulting in REE removal from seawater of 2.9 (Tm) to 54.2 (Ce) nmol per day per m shoreline. Discharges from the ridge to the runnel and the MLWL, with up to 2.4-fold REE enrichments of pore waters relative to seawater, lead to minimum and maximum net fluxes of −0.1 and 0.1 (Lu) to 22.7 and 59.7 (Ce) nmol per day per m shoreline from the ridge to the runnel and the MLWL, respectively. These fluxes are higher for LREEs and MREEs than for HREEs, with even slightly negative fluxes (removal) of HREEs from the ridge to the runnel. For the FDT that is fed by fresh groundwater, the REE fluxes are net fluxes. They range from 5.6 (Lu) to 167.4 (Ce) nmol per day per m shoreline. Compared to seawater REE concentrations, the REEs are 1.8- to 5.3-fold enriched in the FDT with the highest enrichment for MREEs (except for Ce and Gd). The total net flux for REEs from the STE to the coastal water results in an addition of individual REEs of 2.8 to 195.5 nmol per day per m shoreline, with HREE ≤ MREE ≤ LREE fluxes and varying with natural abundance. The REE concentrations in the total STE flux are enriched compared with seawater, ranging from 1.1 to 1.7 (**Figure 6**, purple line).

DISCUSSION

REE Behavior in the Subterranean Estuary

The zonation of the STE on Spiekeroog into different compartments (**Figure 2**) is also reflected in the distribution of REE concentrations, anomalies, and ratios (**Figure 3**). In all samples, a positive La-anomaly can be found, which is characteristic for seawater as the mean residence time of La is the longest among the LREE and MREE (Alibo and Nozaki, 1999) and is not discussed further. A positive Gd-anomaly can be seen throughout the transect due to anthropogenic input of Gd. The anthropogenic Gd can be present in complexed and non-complexed form whereby the complexed form is not affected by estuarine removal or scavenging processes in general due to its high solubility. Therefore, the complexed Gd behaves differently than the other REEs, which is seen in **Figures 4**, **6**. The behavior of Gd is discussed separately in section Anthropogenic Gd.

Dune Area and Upper Saline Plume

The salinity increases in pore waters from the dune area toward the MHWL and oxic conditions in the dune area imply mixing of rainwater and seawater that may also control the pore water REE composition.

For the samples in the dune area (st. 0 and 1), there is a positive correlation of the REEs with salinity, as rainwater (low salinity and low REE concentrations originating from sea spray) and seawater (salinity 30.6 and higher REE concentrations) mix in the dune area (**Figure 5**). Seawater salinity and REE concentrations fall close to the mixing line of rain- and seawater, suggesting an overall conservative behavior of REEs controlled by mixing of rain- and seawater (**Figure 5**, **Supplementary Figure 1**).

In the USP (station 2), however, we observe small depletions for all REEs in most samples compared to seawater and the theoretical mixing line between seawater and rainwater. This can be either caused by lower REE seawater concentrations at the time of infiltration or by removal processes. Assuming the same REE concentrations in seawater during the time of infiltration and during our sampling, non-conservative removal

TABLE 3 | Effect of UV-treatment prior to pre-concentration on REE concentrations: Comparison of natural Gd (Gd_{nat}) with non-complexed (untreated) and complexed (UV-treated minus untreated) anthropogenic Gd (Gd_{anth}) in porewaters of the beach transect (replicate numbers in brackets, average values in bold).

	La	Ce	Pr	Nd	Sm	Eu	Gd	Tb	Dy	Ho	Er	Tm	Yb	Lu	Gd/Gd*	Gd_{nat}	Gd_{anth}	Complexed Gd_{anth}
	(pmol/kg)														–	(pmol/kg)		
st.0 3 m (1)	5.9	7.6	1.5	6.6	1.7	0.4	6.0	0.3	2.8	0.7	2.7	0.4	3.2	0.6	3.4	1.8	4.2	
st.0 3 m (2)	5.9	7.8	1.4	6.8	1.7	0.4	6.5	0.4	2.8	0.7	2.6	0.4	3.2	0.6	3.5	1.8	4.6	
st.0 3 m (3)	6.3	7.7	1.7	6.3	1.8	0.4	7.6	0.4	2.8	0.7	2.6	0.4	3.3	0.7	4.1	1.9	5.8	
Average	**6.0**	**7.7**	**1.5**	**6.6**	**1.7**	**0.4**	**6.7**	**0.4**	**2.8**	**0.7**	**2.7**	**0.4**	**3.2**	**0.7**	**3.7**	**1.8**	**5.2**	
st.0 3 m UV (1)	7.1	9.6	1.7	7.6	1.8	0.5	12.1	0.4	2.8	0.8	2.6	0.4	3.3	0.6	6.5	1.9	10.2	
st.0 3 m UV (2)	6.5	9.2	1.6	7.2	1.8	0.5	12.9	0.4	2.9	0.7	2.7	0.4	3.2	0.6	6.9	1.9	11.0	
st.0 3 m UV (3)	7.4	9.2	1.8	7.4	2.0	0.4	13.0	0.4	2.9	0.7	2.8	0.4	3.3	0.7	6.3	2.0	10.9	
Average	**7.0**	**9.3**	**1.7**	**7.4**	**1.8**	**0.5**	**12.7**	**0.4**	**2.9**	**0.7**	**2.7**	**0.4**	**3.3**	**0.7**	**6.6**	**1.9**	**10.7**	**5.5**
Runnel (1)	12.1	13.5	2.7	12.0	3.5	1.0	12.3	0.9	7.4	2.0	7.3	1.2	9.0	1.8	2.9	4.3	8.1	
Runnel (2)	11.6	13.3	2.6	12.0	3.4	0.9	13.3	0.9	7.1	2.0	7.3	1.2	9.1	1.8	3.1	4.3	9.0	
Runnel (3)	13.4	13.9	2.8	11.9	3.3	0.9	14.1	0.9	7.3	1.8	7.3	1.1	9.5	1.9	3.3	4.3	9.8	
Average	**12.4**	**13.6**	**2.7**	**12.0**	**3.4**	**0.9**	**13.2**	**0.9**	**7.2**	**1.9**	**7.3**	**1.2**	**9.2**	**1.8**	**3.1**	**4.3**	**9.0**	
Runnel UV (1)	13.0	14.1	2.7	12.8	3.3	0.9	23.3	0.8	7.1	1.9	7.4	1.2	8.6	1.7	5.7	4.1	19.2	
Runnel UV (2)	12.4	14.1	2.8	12.3	3.5	1.0	27.7	0.9	7.0	2.0	7.2	1.2	9.0	1.8	6.5	4.3	23.4	
Runnel UV (3)	12.4	14.3	2.8	12.6	3.4	0.9	27.4	0.9	7.2	2.0	7.2	1.2	8.9	1.8	6.3	4.3	23.1	
Runnel UV (4)	14.3	15.8	3.0	12.8	3.5	1.0	26.6	0.9	7.6	1.8	7.3	1.1	8.6	1.8	5.9	4.5	22.1	
Average	**13.0**	**14.5**	**2.8**	**12.6**	**3.4**	**1.0**	**26.2**	**0.9**	**7.2**	**1.9**	**7.3**	**1.2**	**8.8**	**1.8**	**6.1**	**4.3**	**21.9**	**13.0**
st.2 1.8 m (1)	47.0	27.0	8.7	38.6	8.0	2.1	18.5	1.5	11.0	2.5	8.1	1.2	8.4	1.5	2.3	8.0	10.6*	
st.2 1.8 m (2)	49.0	26.5	8.8	37.8	7.7	2.0	17.7	1.6	11.2	2.6	8.1	1.3	8.3	1.6	2.1	8.4	9.3*	
Average	48.0	26.7	8.8	38.2	7.9	2.1	18.1	1.6	11.1	2.6	8.1	1.2	8.4	1.5	2.2	8.2	9.9*	
st.2 1.8 m UV (1)	47.4	28.0	9.3	38.2	8.5	2.1	27.1	1.5	11.1	2.7	8.4	1.3	8.6	1.5	3.3	8.3	18.8	
st.2 1.8 m UV (2)	51.0	30.8	9.1	38.2	8.1	2.0	29.3	1.5	11.0	2.6	8.1	1.2	8.6	1.5	3.7	7.9	21.4	
st.2 1.8 m UV (3)	45.8	27.2	8.8	38.2	8.0	2.0	30.0	1.5	11.1	2.6	8.4	1.2	8.5	1.5	3.8	7.9	22.1	
Average	**48.1**	**28.7**	**9.1**	**38.2**	**8.2**	**2.1**	**28.8**	**1.5**	**11.1**	**2.6**	**8.3**	**1.3**	**8.6**	**1.5**	**3.6**	**8.0**	**20.8**	**10.8**

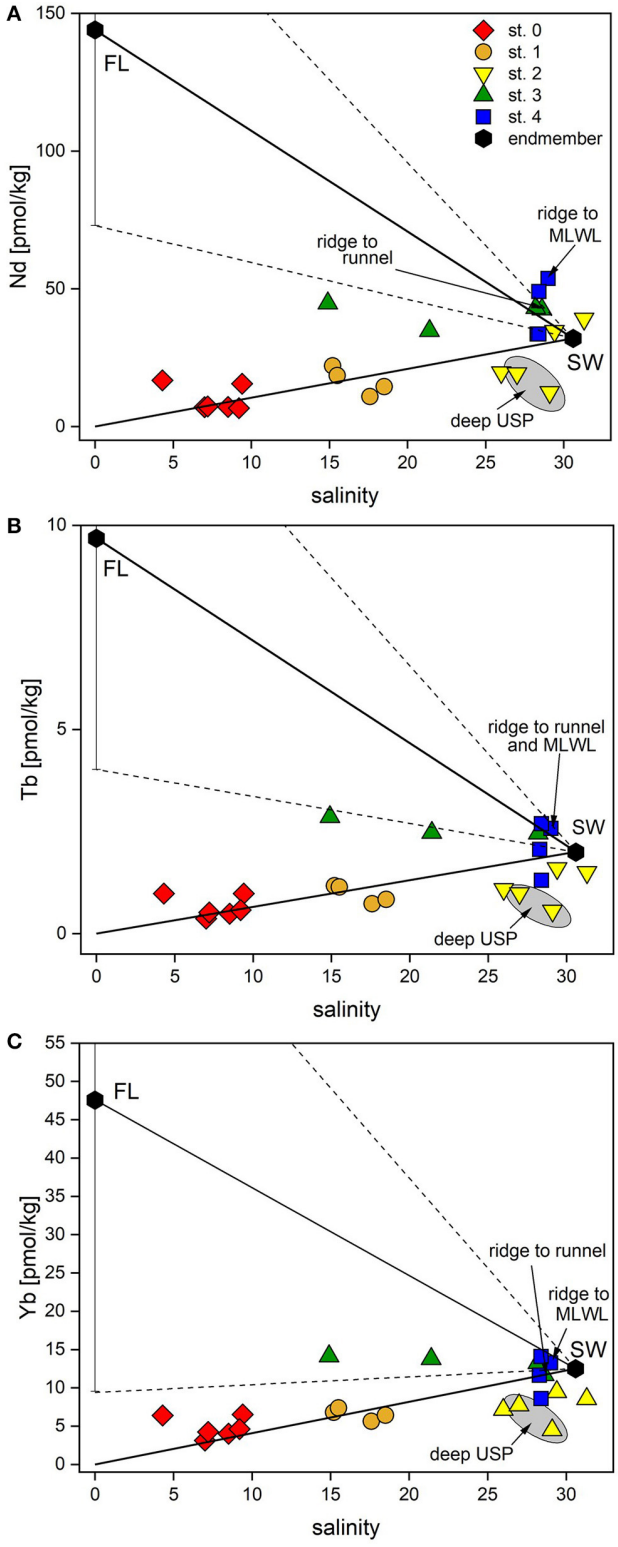


FIGURE 5 | Nd and Yb concentrations vs. salinity of all porewaters and potential endmembers. **(A)** Nd, representing LREEs, vs. salinity, **(B)** Tb, representing MREEs, vs. salinity, **(C)** Yb, representing HREEs, vs. salinity. Black hexagons represent potential endmember compositions of fresh groundwater *(Continued)*

FIGURE 5 | (FL, average of four samples from the freshwater lens) and seawater (SW, average of coastal seawater at high and low tide). Solid lines indicate mixing between the endmembers, dashed lines show the mixing range for the FL (±1SD). Samples used for the calculations of the REE fluxed are labeled.

processes typically effect LREE, MREE and HREE differently: Because of the higher stability of REE-carbonate complexes for HREEs compared to LREEs (Sholkovitz et al., 1994), scavenging of REEs from seawater to e.g., organic material/coatings or to other particles typically leads to a preferential depletion of LREEs relative to HREEs in seawater. Enhanced MREE removal has been suggested to be indicative of Fe-oxide scavenging (Haley et al., 2004). Heavy REEs can be preferentially taken up by bacteria (Takahashi et al., 2005) or scavenged by quartz grains (Byrne and Kim, 1990) or Fe-oxides in form of HREE-carbonate complexes (Dzombak and Morel, 1990; Johannesson et al., 2011). As the sediments at the beach site are mainly composed of quartz and the fraction of reactive Fe that could potentially coat the quartz grains in the beach sediments on Spiekeroog is very low (∼0.01–0.1%) (J. Ahrens, pers. comm., ICBM, July 2018), preferential removal of HREE onto quartz seems a viable process. Furthermore, bacteria binding HREEs to carboxylate and phosphate groups on their cell surfaces, thereby depleting ambient water in HREE (Takahashi et al., 2005), is possible as well.

In the deeper USP (station 2, ≥3.5 mbsf) under suboxic conditions, MREEs are most depleted, probably due du scavenging by Fe-oxides as mentioned above. Iron-oxide formation in the transition zone between the anoxic freshwater of the FDT and the oxic saline waters of the USP has been suggested previously for the STE on Spiekeroog (Linkhorst et al., 2017) and other STEs (e.g., Rouxel et al., 2008). This "iron curtain" has been suggested to act as a temporal storage or even a sink for dissolved organic matter (Linkhorst et al., 2017), which could apply for REEs and also other trace elements.

In summary, REEs in the dune area and partly the USP are dominantly controlled by mixing of rainwater and seawater, while REEs in the deeper USP are additionally affected by REE removal processes that lead to a negative deviation of REE concentrations from conservative mixing lines, particularly for MREEs and HREEs.

The Freshwater Discharge Area

Below 1.5 mbsf at station 3, where salinities are low at 21.4 and 14.9, indicating the presence of the FDT, sub- to anoxic and Fe/Mn-oxide-reducing conditions prevail, as indicated by high pore water Fe and Mn concentrations (Beck et al., 2017; Reckhardt et al., 2017). Ce-anomalies in the FDT and in the freshwater lens of close to 1 indicate that Ce is mostly present in its reduced soluble oxidation state Ce(III), corroborating sub-/anoxic conditions in the FDT (**Figures 3A,H**). Due to the high variability of the freshwater endmember in the freshwater lens of Spiekeroog, conservative mixing (**Figure 5**) is difficult to constrain. However, according to the hydrological model

in Beck et al. (2017), the freshwater that is supplied to the coastal ocean is a mixture from all depths of the freshwater lens, so averaging all the freshwater REE concentrations for the endmember seems appropriate.

The REE concentrations in the FDT are slightly higher (at 2 mbsf) or at the same level (at 1.5 mbsf) as those in coastal seawater (**Table 1**, **Figures 4B**, **5**). Considering a freshwater endmember at the lower end of the REE concentration range found in the freshwater lens, the FDT REE concentrations could be controlled by conservative mixing of water from the freshwater lens and seawater. If the freshwater endmember has REE concentrations at the higher end of the REE concentration range of the freshwater lens, additional removal processes as discussed above must be present.

The Seawater Circulation Cell Below the Ridge

In the suboxic to anoxic seawater circulation cells on the ridge (station 3 $\leq$1 mbsf and station 4), the main source for the pore waters is seawater as reflected by salinities of 28.2–29. All REEs show non-conservative behavior with an enrichment factor of up to 2.4 (for Ce) relative to seawater and generally decreasing enrichment from LREE over MREE to HREE (**Figures 4B**, **6**). The higher REE concentrations at stations 3 and 4 (**Figures 3C,D**), together with higher positive MREE-anomalies (**Figures 3F**, **4A**) and lower HREE/LREE ratios with respect to the coastal seawater, and Ce-anomalies close to 1 (**Figure 3H**) are in line with reducing conditions that lead to the dissolution of Fe/Mn-oxides as indicated by high pore water Fe (**Figure 3A**) and Mn concentrations (Beck et al., 2017; Reckhardt et al., 2017). Possible sources here for the REEs are particulate organic matter (POM), Ce-oxides (source for Ce), and Fe/Mn-oxides. In the following, we will discuss the relevance of the possible sources for the REE concentrations at these stations leading to REE concentrations exceeding those of nearby coastal seawater.

Duncan and Shaw (2003) suggested a relict carbon-rich phase as source for REE enrichment in an STE. This is in agreement with Haley et al. (2004), who also found particulate organic carbon degradation as the main source for REEs in marine pore waters, mostly in oxic and suboxic environments, producing a linear (constant moderate increasing pattern across the REEs) or HREE-enriched PAAS-normalized REE pattern. At our sampling sites on the ridge, the dissolved organic matter (DOM) is mainly of marine origin and is constantly resupplied due to the short residence time of the pore waters (Beck et al., 2017; Waska et al., 2019). In the sediments, degradation of particulate organic matter (POM) may release REEs that were previously scavenged from seawater and potentially contributing to the dissolved REE enrichment on the ridge. As REE scavenging by POM leads to the preferential adsorption of LREEs over HREEs (Sholkovitz et al., 1994), a LREE-enriched pattern would be expected from the dissolution of organic matter. This is in agreement with the elevated LREE over HREE concentrations on the ridge relative to seawater, while the HREE are in the same range as the seawater or even slightly depleted (**Figures 4B**, **5**). If one sample (st. 4, 2 mbsf) with extreme REE and DOC concentrations is excluded, the remaining samples show a positive correlation (R^2 = 0.48 for Nd, 0.23 for Tb and 0.99 for Yb, only significant $p < 0.05$ for DOC vs. Yb) between DOC and REE concentrations (**Supplementary Figure 2**). Due to preferential scavenging of LREE over HREE, the best correlation for the case of POM degradation and associated REE release would be expected for DOC and LREE. However, we cannot distinguish between DOC input with seawater and *in situ* DOC formation through POM degradation and the enrichment (e.g., relative to station 2) is small, which may both affect the correlation. Furthermore, re-adsorption onto sediment particles may affect the REE concentrations after POM degradation and associated REE release. The degradation of an old terrestrial particulate organic carbon pool as suggested for other STEs (e.g., Duncan and Shaw, 2003) is unlikely on Spiekeroog due to the mainly marine origin of the DOM at these sites (Beck et al., 2017). This would also imply that the REEs released here are (at least partly) not "new" fluxes to the ocean but reflect a transient accumulation and subsequent resupply of "marine" REEs to the coastal seawater, as the main source of the released REEs has to be young seawater rather than terrestrial organic or lithogenic material. This is in contrast with other STEs where relict sources or leaching of rocks are the main source for the release of REEs to the terrestrial part of SGD (Duncan and Shaw, 2003; Chevis et al., 2015a; Johannesson et al., 2017).

In the ridge samples, the characteristic negative Ce-anomaly of seawater is nearly absent or clearly less pronounced than in nearby seawater (**Figures 3H**, **4B**) due to Ce-oxide reduction under the suboxic conditions present at the ridge stations (Beck et al., 2017). Below 10 μmol/L oxygen, Ce-oxides are reduced, and Ce behaves like the other trivalent REEs, shifting the Ce-anomaly toward 1 (no anomaly) (Haley et al., 2004).

Under suboxic conditions, Fe/Mn-oxides are reduced, which leads to elevated dissolved Fe and Mn concentrations (Reckhardt et al., 2017) and the release of REEs adsorbed to these oxides. For example, Haley et al. (2004) suggested a positive MREE anomaly as indicative of reductive Fe-oxide dissolution, as Fe-oxides in the water column preferably scavenge MREE. In contrast, Johannesson et al. (2011) found an order of release of REEs under Fe-reducing conditions to follow LREE > MREE > HREE. Here, we observe an MREE- and LREE enrichment for the samples from stations 3 and 4, with a smaller MREE-anomaly (not exceeding 1, **Figure 3F**) than reported by Haley et al. (2004) despite partly higher dissolved Fe concentrations. For SGD in particular, the dissolution of Fe-oxides has been suggested to add REEs to the pore waters (Johannesson et al., 2011; Chevis et al., 2015b). Assuming the dissolution of Fe-oxides as the source for REEs at the ridge stations, there should be a positive correlation between the dissolved Fe and dissolved REE concentrations, which is not observed here. Instead, there is no or a negative correlation between Fe and REE concentrations (**Supplementary Figure 3**) or Fe and the MREE-anomaly (positive MREE-anomaly as an indicator of REE release from Fe-oxides). These correlations are mainly controlled by one (st. 4, 2 mbsf) out of 6 data points with the highest Fe and lowest REE concentrations. There is no positive relationship between REE concentrations or MREE-anomaly with Mn concentrations

either (not shown). This missing correlation between dissolved Fe or Mn and dissolved REE concentrations is in contrast to other studies (Johannesson et al., 2011; Chevis et al., 2015a), suggesting that neither Fe nor Mn-oxide reduction is the dominant source for REEs on the ridge, but can also not be ruled out completely.

In summary, we suggest that remineralization of marine supplied POM is the main source for REE exceeding the concentrations of seawater at the ridge stations supported by the LREE-enriched pattern compared to seawater. We cannot rule out Fe/Mn-oxide reduction as another REE source completely, but no positive correlation with Fe or Mn or the sum of Fe+ Mn exists, though Fe concentrations could be biased by iron sulfide precipitation due to sulfate reduction. The effect on the REE pattern of pore water by Fe/Mn-oxide dissolution is discussed controversially and therefore the pattern shape cannot be used to identify these compounds as a REE source. For Ce, the reduction of Ce-oxides in low oxygenated areas is an additional source.

Estimated Fluxes of REEs From Beach Sediments

Individual REEs behave differently along the beach transect with general depletion of REEs in the USP and general enrichment in the FDT and in the ridge compared to seawater (**Figure 4B**). To investigate if the STE acts as a REE source or a sink for coastal waters, we calculate the element fluxes from the STE into the North Sea using pore water discharge derived from a numerical flow and transport model (Beck et al., 2017) and the REE concentrations of this study (see method section). Briefly, the flux from the FDT is highest for all REEs compared to the other fluxes and higher for LREEs and MREEs compared to HREEs. Note that there is a high variability in the REE concentrations of the FDT as the four samples used to create a mean REE concentration for the FDT show very different REE concentrations (average ± 1SD in **Figure 6**, dashed lines). The net fluxes from the ridge are positive for most REEs and highest for LREEs, whereby the net flux from the ridge to the runnel is slightly negative for HREEs. For the USP, the net flux is negative, resulting in removal of all REEs compared to seawater. The total net flux of all fluxes combined with respect to the discharge of the fluxes is positive for all REEs with HREE $\leq$ MREE $\leq$ LREE and varying with natural abundance.

Cerium fluxes from the FDT and the ridge are higher than those of its neighbor elements due to suboxic conditions in these pore waters that lead to the reduction of the insoluble Ce(IV) to the soluble Ce(III). Gadolinium fluxes differ from the fluxes of its neighbor elements as the representative samples for the fluxes contain different amounts of anthropogenic Gd which is discussed further in section Anthropogenic Gd. The flux calculations, however, do not consider redox changes upon the discharge of SGD into seawater. This may be especially relevant for the pore waters at the ridge and the waters from the suboxic/anoxic freshwater lens and may result in trace element removal to the particulate phase when mixing with oxic seawater. This process has so far not been studied and would also affect the trace element fluxes via SGD that have been reported by other studies where the pore waters are suboxic/anoxic. We also note that our study is potentially missing the flux from the more seaward located salt wedge and another FDT that are predicted from a hydrological model for the deeper sediment column and further seaward on Spiekeroog (Waska et al., 2019). Further studies will have to reveal the contribution of these compartments if their existence is confirmed.

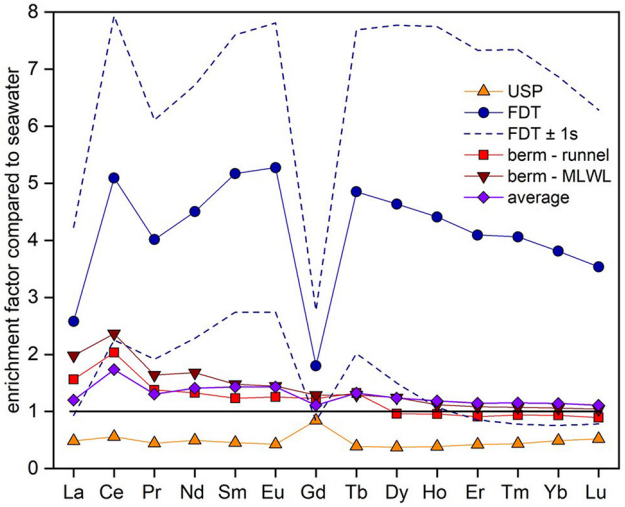


FIGURE 6 | Enrichment factors of the REE concentrations compared to seawater REE concentrations (horizontal black line) for the different compartments of the STE: The freshwater discharge tube (FDT, blue circles), upper saline plume (USP, orange triangles), ridge to the runnel (light red squares) and ridge to the MLWL (dark red inverted triangles). Enrichment factors of total SGD pattern (all concentrations weighted according to their discharge volumes) are shown in purple diamonds. Uncertainties for the FDT (±1SD) that arise from the large range in REE concentrations in the freshwater lens, are shown by blue dashed lines.

To compare the REE fluxes from the beach sediments to the input from rivers, we calculated the total amount of REEs transported by the rivers Weser, Elbe, and Ems to the southern North Sea. Assuming a mean annual discharge of 10.3, 23.7, and 2.5 km^3 per year (Frankignoulle and Middelburg, 2002; Flussgebietsgemeinschaft Weser, 2005) and Nd concentrations of 91.2, 96.7, and 156.5 pmol/L (Kulaksiz and Bau, 2007), the rivers supply 938, 2291, and 391 mol Nd per year, respectively. However, considering a loss of REEs in the river estuaries of ~71% (average Nd removal in river estuaries, Rousseau et al., 2015), the combined river Nd flux to the southern North Sea results in 1,058 mol Nd input per year. The combined REE fluxes from the STE on Spiekeroog extrapolated to a shoreline of 56 km for the East Frisian Islands, amounts to an addition of 1.84 mol Nd per year. Even if the entire shoreline of the southern North Sea (~500 km) is considered, the SGD flux of about 16.4 mol Nd per year is still two orders of magnitude lower than the supply from the rivers. Despite the fact that this must be regarded as a rough estimate, the differences in the REE supply are still significant, suggesting that rivers are the main source of REEs to the southern North Sea. The relative importance of these fluxes, however, may change throughout the year due to changes in river supply, current directions, and precipitation.

Other studies have shown that SGD is the main source for REEs to the ocean with fluxes that are equal to or exceed the supply by local rivers (e.g., Johannesson et al., 2011; Chevis et al., 2015a), by atmospheric contribution or by diffusion from bottom sediments (e.g., Kim and Kim, 2011, 2014). However, in those study areas, overall SGD (water) fluxes exceed local river discharge, the opposite of what is true for the southern North Sea, where river discharge is much higher than the SGD flux by volume. Considering the total estimated Nd input via SGD of 5.03 mmol Nd per day for the East Frisian Islands (56 km shoreline) or 45 mmol Nd per day for the southern North Sea (∼500 km), this is on the same order of magnitude as some other SGD fluxes e.g., for the Indian River Lagoon (9.4 to 100 mmol Nd per day, Johannesson et al., 2011; Chevis et al., 2015b), Pettaquamscutt Estuary, Rhode Island (26 mmol Nd per day, Chevis et al., 2015a) and Kona Coast (1.3–2.6 mmol Nd per day, Johannesson et al., 2017). The SGD REE fluxes estimated for the southern North Sea are as significant as those suggested from other STEs for the global ocean. Yet, if individual SGD fluxes are evaluated with respect to regional river REE input, the significance of SGD for the coastal seawater REE budget varies due to large differences in the river REE contributions. While the rivers to the North Sea are supplying 2.90 mol Nd per day, rivers just add 12.7 mmol Nd per day to the Indian River Lagoon (Johannesson et al., 2011) and 36.7 mmol Nd per day to the Pettaquamscutt Estuary (Chevis et al., 2015a), at the Kona Coast there is no significant river input (Johannesson et al., 2017). These differences in the river input are mainly due to the higher discharge rates of the rivers draining into the North Sea as the Nd concentrations of the rivers are of the same order of magnitude. Two studies from South Korea (Kim and Kim, 2011, 2014) show that the Nd input via SGD is about 1,000 times higher than in the STE presented in this study. This is due to up to two orders of magnitude higher SGD volumes, Nd concentrations in the discharged waters exceeding the concentrations of the pore waters in this study up to 20-fold, and longer shorelines (230 and 130 km, Kim and Kim, 2014). Differences in these factors result in a total input of 120 mol Nd per day (Kim and Kim, 2011) and 58 and 219 mol Nd per day (Kim and Kim, 2014) compared to 5.03 mmol Nd per day for the East Frisian Islands.

All studied estuaries are of a different size and have different catchment areas and the SGD may show seasonal variations. Thus, the total REE inputs are difficult to compare, but they provide an idea of the diversity of the STEs at different locations. One additional important aspect that can lead to large differences is the nature of the aquifer material for the terrestrial groundwater. Here, we compared young basaltic rocks in South Korea (Kim and Kim, 2011) or older glacial deposits derived from Late Proterozoic and Paleozoic rocks on Rhode Island (Chevis et al., 2015a) with fine- to coarse-grained sands and clays that is the source for the young groundwaters in our study. Groundwater contact with different source rocks may result in different REE signatures regarding the total and relative REE concentrations. In addition, the beaches of Spiekeroog have been shown to change the topography, the shoreline, the shape and location of the runnel several times throughout the year (Waska et al., 2019). This could also have an influence on the dimension of the fluxes, the residence times of the waters within the STE and therefore also on the redox conditions in the pore waters. The study presented here therefore has to be seen as representing a snapshot of the current situation, and seasonal and interannual studies are required to confirm the estimated annual REE fluxes.

Anthropogenic Gd

The origin of the Gd_{anth} in the seawater and pore waters is not a local signal from Spiekeroog Island as there is no hospital on the island that could contribute Gd_{anth} to groundwater or coastal waters. The source of Gd_{anth} in coastal seawater must therefore be derived from river discharge (e.g., Weser, Ems, Elbe, Rhine; Kulaksiz and Bau, 2007) or from direct input of effluent waters by (sub)marine outfalls into the North Sea.

Effect of UV/H_2O_2 Treatment on Measured Anthropogenic Gd Concentrations

As described previously, the Gd-complexes are degraded by reaction with hydroxyl radicals via UV/H_2O_2 treatment (Cyris et al., 2013). In order to test whether total Gd (Gd_{nat} and Gd_{anth}) is quantitatively recovered during the pre-concentration of REEs via seaFAST, we measured REE concentrations in samples treated with UV/H_2O_2 and in untreated samples. We suggest that the significantly higher concentrations found for Gd measured in the treated compared to the untreated samples result from the degradation of the Gd-complexes under UV/H_2O_2 conditions and the non-quantitative retention of complexed Gd_{anth} on the chelating resin used for pre-concentration of the REEs. In the following, we therefore discuss the difference in Gd concentrations between UV/H_2O_2 treated and untreated samples as a measure of the difference between complexed and non-complexed Gd_{anth} in the pore waters.

The observed Gd concentration difference between UV/H_2O_2 treated and untreated samples ($n = 3$) of up to 13.0 pmol/kg (**Figure 7**) demonstrates that a large fraction of Gd in the analyzed pore waters is complexed. The percentage of complexed Gd_{anth} of the total Gd_{anth} is in a narrow range of 52 to 59% for the tested samples (st. 0, 3 mbsf, st. 2, 1.8 mbsf, and runnel). This suggests that the samples are roughly of the same age, as it has been shown that there is a degradation of the complexes over time (Holzbecher et al., 2005). Several factors have been found to influence the destabilization of Gd-complexes e.g., transmetallation or competition for binding places of the DPTA complexes by Ca, Mg, or K ions (Schijf and Christy, 2018).

Anthropogenic Gd in the STE on Spiekeroog

The stations in the upper beach zone and the USP suggest strong REE scavenging, whereas the stations on the ridge indicate REE release. As complexed Gd_{anth} is not affected by scavenging/release and stays in the dissolved phase, total Gd-anomalies are misleading, and we will therefore only discuss absolute Gd_{anth} concentrations (**Figure 3G**).

Differences in the total amount of Gd_{anth} in our samples are due to the origin of the waters. At the upper beach (stations 0 and 1), Gd_{anth} is low due to a high proportion of rainwater that contains only minor Gd_{anth} due to the transport of seawater

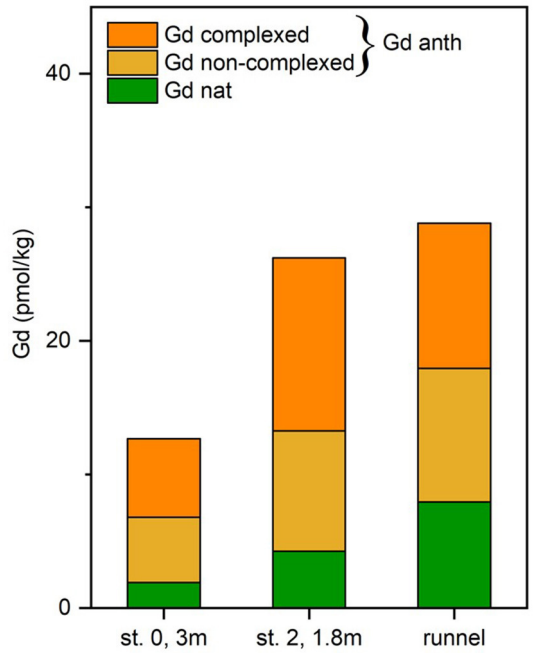


FIGURE 7 | Comparison of natural (Gd nat) and anthropogenic Gd (Gd anth) in pore water and runnel water. The total anthropogenic Gd is separated into a complexed and non-complexed form based on UV-H_2O_2-treated and untreated samples.

aerosols onto land (sea spray). Furthermore, it has to be kept in mind that our study represents a snapshot of a highly variable environment, resulting in uncertainties in the Gd_{anth} concentrations in the endmembers (seawater and rainwater) at the time of infiltration.

The low Gd_{anth} concentrations in the FDT (station 3, 1.5, and 2.0 mbsf) are mostly a result of mixing of fresh groundwater ($Gd_{anth} = 0$) and seawater ($Gd_{anth} = 21.7$ pmol/kg). The samples from the USP (16.8–25.6 pmol/kg Gd_{anth}) and the runnel (21.9 pmol/kg Gd_{anth}) are mainly fed by seawater on a short timescale and therefore show a similar total Gd_{anth} content as the seawater samples. The highest Gd_{anth} concentrations of the transect of up to 46.4 pmol/kg found on the ridge exceed the seawater Gd_{anth} ($Gd_{anth} = 21.7$ pmol/kg) and therefore must be due to release of previously scavenged non-complexed Gd_{anth} (i.e., after degradation of the complex) from seawater. Because of the fact that Gd_{anth} is released from organic matter and/or Fe/Mn-oxides, these possible REE sources have to be younger than the onset of Gd_{anth} discharge to the marine environment (post 1980s). This confirms that the REEs in this study are not derived from relict deposits, as suggested for other STEs (Duncan and Shaw, 2003; Chevis et al., 2015a).

Kulaksiz and Bau (2007) showed positive Gd-anomalies for the North Sea and Weser Estuary. At their closest station to our sampling site (EF5, about 10 km north of Spiekeroog) they found a positive Gd-anomaly of 1.9, compared to 3.0 found in our study for coastal surface waters off Spiekeroog if calculated the same way as Kulaksiz and Bau (2007). This difference of $\Delta Gd/Gd^* = 1.1$ in the anomalies, which is equivalent to 15.7 pmol/kg Gd_{anth}, can in part be attributed to the 9 years timespan between the sampling dates (2005/2014) and reflects the constant increase in input and the accumulation of Gd_{anth} in the North Sea. Additionally, the pre-concentration method used by Kulaksiz and Bau (2007) did not involve a UV/H_2O_2 treatment, suggesting that they did not recover the complexed Gd_{anth} component quantitatively.

CONCLUSIONS

The REE concentrations of a beach transect on Spiekeroog representing an STE have been found to be highly variable. In the upper dune area in oxic, low-salinity pore waters, the REE concentrations are depleted compared to the adjacent seawater due to mixing with rainwater and show a pronounced negative Ce-anomaly due to the oxic conditions. They also show higher HREE/LREE ratios indicating intense scavenging. Moving seawards, the REE concentrations increase due to stronger influence of the seawater. Close to the MLWL with sub-/anoxic redox conditions, confirmed by the near absence of a Ce-anomaly, degradation of POM and possibly also the reduction of Fe/Mn-oxides add REEs to the pore waters and lead to REE concentrations that partly exceed those expected from conservative mixing. Calculated total fluxes from the beach pore waters indicate a net positive addition of all REEs to coastal seawater, with relatively more LREEs than HREEs. This is in line with previous studies that suggested that STEs are a source of LREEs and a sink for HREEs (Johannesson et al., 2011). Compared to nearby rivers, REE addition is of minor importance for the REE budget of the southern North Sea. Compared to most other STEs the observed REE fluxes from the beach sands at Spiekeroog are in the same order of magnitude. The presence of Gd_{anth} throughout the transect displays the increased anthropogenic impact on coastal waters and the accumulation of Gd_{anth} since the first studies that observed Gd_{anth} in the southern North Sea.

DATA AVAILABILITY STATEMENT

All datasets generated for this study are included in the article/**Supplementary Material**.

AUTHOR CONTRIBUTIONS

KP and BS designed the study. RP, CE, AR, and BS took the samples. RP and MB measured REE concentrations. AR measured salinity and Fe and Mn concentrations. RP wrote the manuscript with contributions from the other authors. All authors were involved in the interpretation and discussion of the data.

ACKNOWLEDGMENTS

We thank the Wadden Sea National Park Administration of Lower Saxony for the permission to study the beach site

on Spiekeroog Island and S. Fock and C. Winkelmann from the Research Center Wittbülten on Spiekeroog. We further thank all participants of the sampling campaign in May 2014, especially M. Beck for organization and coordination. J. Ahrens kindly provided information on the Fe-content of beach sands. We further thank H. Nicolai and G. Behrens for the boat transfers and their assistance during planning of the sampling campaign as well as their technical support during sampling. Thanks to the staff of the Lower Saxony Water Management, Coastal Defense and Nature Conservation Agency for transporting the sampling equipment to the study site. Furthermore, we acknowledge M. Schulz for laboratory assistance. This project was financially supported through the Institute for Chemistry and Biology of the Marine Environment (ICBM), Oldenburg, and the Max Planck Institute for Marine Microbiology, Bremen.

SUPPLEMENTARY MATERIAL

The Supplementary Material for this article can be found online at: https://www.frontiersin.org/articles/10.3389/fmars.2020.00424/full#supplementary-material

REFERENCES

Alibo, D. S., and Nozaki, Y. (1999). Rare earth elements in seawater: particle association, shale-normalization, and ce oxidation. *Geochim. Cosmochim. Acta* 63, 363–372. doi: 10.1016/S0016-7037(98)00279-8

Anschutz, P., Smith, T., Mouret, A., Deborde, J., Bujan, S., Poirier, D., et al. (2009). Tidal sands as biogeochemical reactors. *Estuar. Coast. Shelf Sci.* 84, 84–90. doi: 10.1016/j.ecss.2009.06.015

Bau, M., and Dulski, P. (1996). Anthropogenic origin of positive gadolinium anomalies in river waters. *Earth Planet. Sci. Lett.* 143, 245–255. doi: 10.1016/0012-821X(96)00127-6

Beck, M., Reckhardt, A., Amelsberg, J., Bartholom,ä, A., Brumsack, H. J., Cypionka, H., et al. (2017). The drivers of biogeochemistry in beach ecosystems: a cross-shore transect from the dunes to the low-water line. *Mar. Chem.* 190, 35–50. doi: 10.1016/j.marchem.2017.01.001

Behrens, M. K., Muratli, J., Pradoux, C., Wu, Y., Böning, P., Brumsack, H. J., et al. (2016). Rapid and precise analysis of rare earth elements in small volumes of seawater - method and intercomparison. *Mar. Chem.* 186, 110–120. doi: 10.1016/j.marchem.2016.08.006

Birka, M., Roscher, J., Holtkamp, M., Sperling, M., and Karst, U. (2016). Investigating the stability of gadolinium based contrast agents towards UV radiation. *Water Res.* 91, 244–250. doi: 10.1016/j.watres.2016.01.012

Bone, S. E., Charette, M. A., Lamborg, C. H., and Gonneea, M. E. (2007). Has submarine groundwater discharge been overlooked as a source of mercury to coastal waters? *Environ. Sci. Technol.* 41, 3090–3095. doi: 10.1021/es0622453

Bourne, G. W., and Trifaró, J. M. (1982). The gadolinium ion: a potent blocker of calcium channels and catecholamine release from cultured chromaffin cells. *Neuroscience* 7, 1615–1622. doi: 10.1016/0306-4522(82)90019-7

Burnett, W. C., Bokuniewicz, H., Huettel, M., Moore, W., and Taniguchi, M. (2003). Groundwater and pore water inpunts to the coastal zone. *Biogeochemistry* 66, 3–33. doi: 10.1023/B:BIOG.0000006066.21240.53

Byrne, R. H., and Kim, K.-H. (1990). Rare earth element scavenging in seawater. *Geochim. Cosmochim. Acta* 54, 2645–2656. doi: 10.1016/0016-7037(90)90002-3

Charette, M. A., and Allen, M. C. (2006). Precision ground water sampling in coastal aquifers using a direct-push, shielded-screen well-point system. *Gr. Water Monit. Remediat.* 26, 87–93. doi: 10.1111/j.1745-6592.2006.00076.x

Chevis, D. A., Johannesson, K. H., Burdige, D. J., Cable, J. E., Martin, J. B., and Roy, M. (2015b). Rare earth element cycling in a sandy subterranean estuary in Florida, USA. *Mar. Chem.* 176, 34–50. doi: 10.1016/j.marchem.2015.07.003

Chevis, D. A., Johannesson, K. H., Burdige, D. J., Tang, J., Bradley Moran, S., and Kelly, R. P. (2015a). Submarine groundwater discharge of rare earth elements to a tidally-mixed estuary in Southern Rhode Island. *Chem. Geol.* 397, 128–142. doi: 10.1016/j.chemgeo.2015.01.013

Cyris, M., Knolle, W., Richard, J., Dopp, E., Von Sonntag, C., and Schmidt, T. C. (2013). Reaction of gadolinium chelates with ozone and hydroxyl radicals. *Environ. Sci. Technol.* 47, 9942–9949. doi: 10.1021/es402219u

De Baar, H. J. W., Schijf, R. H., and Byrne, R. H. (1991). Solution chemistry of the rare earth elements in seawater. *Eur. J. Solid State Inorg. Chem.* 28, 357–373.

de Campos, F. F., and Enzweiler, J. (2016). Anthropogenic gadolinium anomalies and rare earth elements in the water of Atibaia River and Anhumas Creek, Southeast Brazil. *Environ. Monit. Assess.* 188:281. doi: 10.1007/s10661-016-5282-7

Duncan, T., and Shaw, T. J. (2003). The mobility of rare earth elements and redox sensitive elements in the groundwater/seawater mixing zone of a shallow coastal aquifer. *Aquat. Geochemistry* 9, 233–255. doi: 10.1023/B:AQUA.0000022956.20338.26

Dzombak, D. A., and Morel, F. M. M. (1990). *Surface Complexation Modeling: Hydrous Ferric Oxide*. New York, NY: John Wiley and Sons.

Ehlert, C., Reckhardt, A., Greskowiak, J., Liguori, B. T. P., Böning, P., Paffrath, R., et al. (2016). Transformation of silicon in a sandy beach ecosystem: Insights from stable silicon isotopes from fresh and saline groundwaters. *Chem. Geol.* 440, 207–218. doi: 10.1016/j.chemgeo.2016.07.015

Elderfield, H. (1988). The oceanic chemistry of rare-earth elements. *Philos. Trans. R. Soc. A* 325, 105–126. doi: 10.1098/rsta.1988.0046

Elderfield, H., and Greaves, M. (1982). The rare earth elements in seawater. *Nature* 296, 214–219. doi: 10.1038/296214a0

Flemming, B. W., and Davis, R. A. (1994). Holocene evolution, morphodynamics and sedimentology of the spiekeroog barrier island system (southern North Sea). *Senck. Marit.* 24, 117–155.

Flussgebietsgemeinschaft Weser (2005). *EG- Wasserrahmenrichtlinie. Bewirtschaftungsplan der Flussgebietseinheit Weser*. Bestandsaufnahme.

Frankignoulle, M., and Middelburg, J. J. (2002). Biogases in tidal european estuaries: The BIOGEST project. *Biogeochemistry* 59, 1–4. doi: 10.1023/A:1015544311392

German, C. R., Masuzawa, T., Greaves, M. J., Elderfield, H., and Edmond, J. M. (1995). Dissolved rare earth elements in the Southern Ocean: Cerium oxidation and the influence of hydrography. *Geochim. Cosmochim. Acta* 59, 1551–1558. doi: 10.1016/0016-7037(95)00061-4

Goldstein, S. J., and Jacobsen, S. B. (1988). Rare earth elements in river waters. *Science*, 89, 35–47. doi: 10.1016/0012-821X(88)90031-3

Haley, B. A., Klinkhammer, G. P., and McManus, J. (2004). Rare earth elements in pore waters of marine sediments. *Geochim. Cosmochim. Acta* 68, 1265–1279. doi: 10.1016/j.gca.2003.09.012

Hatje, V., Bruland, K. W., and Flegal, A. R. (2016). Increases in anthropogenic gadolinium anomalies and rare earth element concentrations in San Francisco Bay over a 20 year record. *Environ. Sci. Technol.* 50, 4159–4168. doi: 10.1021/acs.est.5b04322

Holzbecher, E., Knappe, A., and Pekdeger, A. (2005). Identification of degradation characteristics - Exemplified by Gd-DTPA in a large experimental column. *Environ. Model. Assess.* 10, 1–8. doi: 10.1007/s10666-004-4269-x

Johannesson, K. H., and Burdige, D. J. (2007). Balancing the global oceanic neodymium budget: evaluating the role of groundwater. *Earth Planet. Sci. Lett.* 253, 129–142. doi: 10.1016/j.epsl.2006.10.021

Johannesson, K. H., Chevis, D. A., Burdige, D. J., Cable, J. E., Martin, J. B., and Roy, M. (2011). Submarine groundwater discharge is an important net source of light and middle REEs to coastal waters of the Indian River Lagoon, Florida, USA. *Geochim. Cosmochim. Acta* 75, 825–843. doi: 10.1016/j.gca.2010.11.005

Johannesson, K. H., Palmore, C. D., Fackrell, J., Prouty, N. G., Swarzenski, P. W., Chevis, D. A., et al. (2017). Rare earth element behavior during groundwater-seawater mixing along the kona coast of hawaii. *Geochim. Cosmochim. Acta* 198, 229–258. doi: 10.1016/j.gca.2016.11.009

Kim, I., and Kim, G. (2011). Large fluxes of rare earth elements through submarine groundwater discharge (SGD) from a volcanic island, Jeju, Korea. *Mar. Chem.* 127, 12–19. doi: 10.1016/j.marchem.2011.07.006

Kim, I., and Kim, G. (2014). Submarine groundwater discharge as a main source of rare earth elements in coastal waters. *Mar. Chem.* 160, 11–17. doi: 10.1016/j.marchem.2014.01.003

Knappe, A., Möller, P., Dulski, P., and Pekdeger, A. (2005). Positive gadolinium anomaly in surface water and ground water of the urban area Berlin, Germany. *Chem. Erde Geochem.* 65, 167–189. doi: 10.1016/j.chemer.2004.08.004

Kulaksiz, S., and Bau, M. (2007). Contrasting behaviour of anthropogenic gadolinium and natural rare earth elements in estuaries and the gadolinium input into the North Sea. *Earth Planet. Sci. Lett.* 260, 361–371. doi: 10.1016/j.epsl.2007.06.016

Kulaksiz, S., and Bau, M. (2011). Rare earth elements in the Rhine River, Germany: First case of anthropogenic lanthanum as a dissolved microcontaminant in the hydrosphere. *Environ. Int.* 37, 973–979. doi: 10.1016/j.envint.2011.02.018

Lacan, F., and Jeandel, C. (2005). Neodymium isotopes as a new tool for quantifying exchange fluxes at the continent-ocean interface. *Earth Planet. Sci. Lett.* 232, 245–257. doi: 10.1016/j.epsl.2005.01.004

Linkhorst, A., Dittmar, T., and Waska, H. (2017). Molecular fractionation of dissolved organic matter in a shallow subterranean estuary: the role of the iron curtain. *Environ. Sci. Technol.* 51, 1312–1320. doi: 10.1021/acs.est.6b03608

Luijendijk, A., Hagenaars, G., Ranasinghe, R., Baart, F., Donchyts, G., and Aarninkhof, S. (2018). The state of the world's beaches. *Sci. Rep.* 8:6641. doi: 10.1038/s41598-018-24630-6

Martin, E. E., Blair, S. W., Kamenov, G. D., Scher, H. D., Bourbon, E., Basak, C., et al. (2010). Extraction of Nd isotopes from bulk deep sea sediments for paleoceanographic studies on Cenozoic time scales. *Chem. Geol.* 269, 414–431. doi: 10.1016/j.chemgeo.2009.10.016

Moore, W. S. (1999). The subterranean estuary: A reaction zone of ground water and sea water. *Mar. Chem.* 65, 111–125. doi: 10.1016/S0304-4203(99)00014-6

OOWV (Oldenburg-OstfriesischerWasserverband) (2009). *Wasserrechtsantrag. Antrag auf Be Willigung Einer Grundwasserentnahme Über 180.000m3/a für das Wasserwerk Spiekeroog.*

Pedreira, R. M. A., Pahnke, K., Böning, P., and Hatje, V. (2018). Tracking hospital effluent-derived gadolinium in atlantic coastal waters off Brazil. *Water Res.* 145, 62–72. doi: 10.1016/j.watres.2018.08.005

Pritchard, D. W. (1967). "What is an estuary: physical viewpoint," in *Estuaries*, ed G. H. Lauff (Washington, DC: American Association for the Advancement of Science), 3–5.

Reckhardt, A., Beck, M., Greskowiak, J., Schnetger, B., Böttcher, M. E., Gehre, M., et al. (2017). Cycling of redox-sensitive elements in a sandy subterranean estuary of the southern North Sea. *Mar. Chem.* 188, 6–17. doi: 10.1016/j.marchem.2016.11.003

Reckhardt, A., Beck, M., Seidel, M., Riedel, T., Wehrmann, A., Bartholom,ä, A., et al. (2015). Carbon, nutrient and trace metal cycling in sandy sediments: a comparison of high-energy beaches and backbarrier tidal flats. *Estuar. Coast. Shelf Sci.* 159, 1–14. doi: 10.1016/j.ecss.2015.03.025

Robinson, C., Li, L., and Barry, D. A. (2007). Effect of tidal forcing on a subterranean estuary. *Adv. Water Resour.* 30, 851–865. doi: 10.1016/j.advwatres.2006.07.006

Röper, T., Kröger, K. F., Meyer, H., Sültenfuss, J., Greskowiak, J., and Massmann, G. (2012). Groundwater ages, recharge conditions and hydrochemical evolution of a barrier island freshwater lens (Spiekeroog, Northern Germany). *J. Hydrol.* 454–455, 173–186. doi: 10.1016/j.jhydrol.2012.06.011

Rousseau, T. C. C., Sonke, J. E., Chmeleff, J., Beek, P., van, Souhaut, M., Boaventura, G., et al. (2015). Rapid neodymium release to marine waters from lithogenic sediments in the Amazon estuary. *Nat. Commun.* 6:7592. doi: 10.1038/ncomms8592

Rouxel, O., Sholkovitz, E., Charette, M., and Edwards, K. J. (2008). Iron isotope fractionation in subterranean estuaries. *Geochim. Cosmochim. Acta* 72, 3413–3430. doi: 10.1016/j.gca.2008.05.001

Rudnick, R. L., and Gao, S. (2003). "Composition of the continental crust," in *Treatise on Geochemistry,* ed K. K. Turekian (Oxford: Pergamon), 1–64.

Schijf, J., and Christy, I. J. (2018). Effect of Mg and Ca on the stability of the MRI contrast agent Gd-DTPA in seawater. *Front. Mar. Sci.* 5:111. doi: 10.3389/fmars.2018.00111

Sholkovitz, E. R., Landing, W. M., and Lewis, B. L. (1994). Ocean particle chemistry - the fractionation of rare-earth elements between suspended particles and seawater. *Geochim. Cosmochim. Acta* 58, 1567–1579. doi: 10.1016/0016-7037(94)90559-2

Tachikawa, K., Athias, V., and Jeandel, C. (2003). Neodymium budget in the modern ocean and paleo-oceanographic implications. *J. Geophys. Res.* 108:3254. doi: 10.1029/1999JC000285

Takahashi, Y., Châtellier, X., Hattori, K. H., Kato, K., and Fortin, D. (2005). Adsorption of rare earth elements onto bacterial cell walls and its implication for REE sorption onto natural microbial mats. *Chem. Geol.* 219, 53–67. doi: 10.1016/j.chemgeo.2005.02.009

Trezzi, G., Garcia-Orellana, J., Santos-Echeandia, J., Rodellas, V., Garcia-Solsona, E., Garcia-Fernandez, G., et al. (2016). The influence of a metal-enriched mining waste deposit on submarine groundwater discharge to the coastal sea. *Mar. Chem.* 178, 35–45. doi: 10.1016/j.marchem.2015.12.004

Waska, H., Greskowiak, J., Ahrens, J., Beck, M., Ahmerkamp, S., Böning, P., et al. (2019). Spatial and temporal patterns of pore water chemistry in the inter-tidal zone of a high energy beach. *Front. Mar. Sci.* 6:154. doi: 10.3389/fmars.2019.00154

Windom, H. L., Moore, W. S., Niencheski, L. F. H., and Jahnke, R. A. (2006). Submarine groundwater discharge: a large. Previously unrecognized source of dissolved iron to the South Atlantic Ocean. *Mar. Chem.* 102, 252–266. doi: 10.1016/j.marchem.2006.06.016

Conflict of Interest: The authors declare that the research was conducted in the absence of any commercial or financial relationships that could be construed as a potential conflict of interest.

Copyright © 2020 Paffrath, Pahnke, Behrens, Reckhardt, Ehlert, Schnetger and Brumsack. This is an open-access article distributed under the terms of the Creative Commons Attribution License (CC BY). The use, distribution or reproduction in other forums is permitted, provided the original author(s) and the copyright owner(s) are credited and that the original publication in this journal is cited, in accordance with accepted academic practice. No use, distribution or reproduction is permitted which does not comply with these terms.

frontiers in Marine Science

ORIGINAL RESEARCH
published: 21 May 2021
doi: 10.3389/fmars.2021.661201

Does Nitrate Enrichment Accelerate Organic Matter Turnover in Subterranean Estuaries?

J. Severino P. Ibánhez[1,2], Xosé Antón Álvarez-Salgado[2] and Carlos Rocha[1]*

[1] Biogeochemistry Research Group, School of Natural Sciences, Trinity College, Dublin, Ireland, [2] Instituto de Investigacións Mariñas, Consejo Superior de Investigaciones Científicas (IIM-CSIC), Vigo, Spain

Due to the widespread pollution of coastal groundwaters with fertilizers, submarine groundwater discharge (SGD) is often thought to be a large dissolved inorganic nitrogen (DIN) source to the ocean. Whether this N is autochthonous or allochthonous to the subterranean estuary (STE), the availability of large quantities of DIN can nevertheless interact with the cycling of other elements, such as carbon (C). In previous studies, we documented the discharge of large quantities of freshwater and NO_3^- from the mouth of an STE into the Ria Formosa lagoon (SW Iberian Peninsula). For the period covered in this study (2009–2011), the same STE site was dominated by recirculating seawater due to a prolonged fall in piezometric head in the coupled coastal aquifers. Total SGD rates remained similarly high, peaking at 144 cm day^{-1} at the lower intertidal during fall. We observed a progressive increase of NO_3^- availability within the STE associated with the recovery of piezometric head inland. Interestingly, during this period, the highest SGD-derived dissolved organic C and DIN fluxes (112 ± 53 and 10 ± 3 mmol m^{-2} day^{-1}, respectively) originated in the lower intertidal. NO_3^- enrichment in the STE influences the benthic reactivity of fluorescent dissolved organic matter (FDOM): when seawater recirculation drives STE dynamics, only small changes in the benthic distribution of recalcitrant humic-like FDOM are observed (from −2.57 ± 1.14 to 1.24 ± 0.19 10^{-3} R.U. "bulk" sediment h^{-1}) in the absence of DIN. However, when DIN is available, these recalcitrant fractions of FDOM are actively generated (from 1.32 ± 0.15 to 11.56 ± 3.39 10^{-3} R.U. "bulk" sediment h^{-1}), accompanied by the production of labile protein-like FDOM. The results agree with previous studies conducted with flow-through reactor experiments at the same site and suggest that DIN enrichment in the STE enhances the metabolic turnover of sedimentary organic matter up to the point of discharge to surface waters. DIN pollution of coastal aquifers may therefore promote a contraction of the residence time of particulate organic C within the STE, driving carbon from continental storage into the sea.

Keywords: submarine groundwater discharge (SGD), fluorescent dissolved organic matter (FDOM), subterranean estuary, Ria Formosa coastal lagoon, priming effect

OPEN ACCESS

Edited by:
Laura Anne Bristow, University of Southern Denmark, Denmark

Reviewed by:
Andrea Pain, University of Maryland Center for Environmental Science (UMCES), United States
Hannah Karen Marchant, Max Planck Institute for Marine Microbiology (MPG), Germany

****Correspondence:***
J. Severino P. Ibánhez
pinoibaj@tcd.ie

Specialty section:
This article was submitted to Marine Biogeochemistry, a section of the journal Frontiers in Marine Science

Received: *30 January 2021*
Accepted: *27 April 2021*
Published: *21 May 2021*

Citation:
Ibánhez JSP, Álvarez-Salgado XA and Rocha C (2021) Does Nitrate Enrichment Accelerate Organic Matter Turnover in Subterranean Estuaries? Front. Mar. Sci. 8:661201. doi: 10.3389/fmars.2021.661201

INTRODUCTION

The discovery and industrial application of the Haber-Bosch process for fertilizer production from atmospheric N_2 has completely changed the global N cycle. Fertilizer usage, the cultivation of N-fixing crops or biomass, and fossil fuel combustion and subsequent deposition have turned human activities into the largest source of bioavailable N to the biosphere (Vitousek et al., 1997; Galloway et al., 2008). This anthropogenic N enrichment of Earth's ecosystems has dramatically increased N content in freshwater ecosystems and exponentially enhanced N fluxes to the coastal zone (Mackenzie et al., 2002; Boyer et al., 2006; Rivett et al., 2008). There, N enrichment triggers eutrophication, coastal acidification, or environmental degradation (Erisman et al., 2008; Gruber and Galloway, 2008) and interferes with the cycling of other elements such as C and O (Bauer et al., 2013).

The indiscriminate use of fertilizers, together with wastewater and septic tank leaks, industrial spillage, or the use of manure and sewage sludge inland has led to the widespread N pollution of groundwaters (Rivett et al., 2008). Up to 10% of the total 150 Tg N $year^{-1}$ human-derived reactive N applied on the land surface ends in groundwater reservoirs (Schlesinger, 2009). The issue is that continental groundwaters will discharge to the coast whenever a hydraulic connection with a positive pressure head seaward exists (Johannes, 1980; Santos et al., 2012). This discharge of continental groundwater is included in submarine groundwater discharge (SGD; i.e., any source of water with origin in the sediments irrespectively of its origin and composition; Burnett et al., 2003), now recognized as a large source of water to the coastal zone (Kwon et al., 2014; Luijendijk et al., 2020). Land-ocean N fluxes associated with SGD are larger than N transported into the sea by rivers (Cho et al., 2018) on a global scale. Notwithstanding the difficulties in identifying and quantifying this diffusive source of water to the coast, SGD has already been recognized as the dominant source of N to several coastal ecosystems (e.g., Paytan et al., 2006; Leote et al., 2008; Tamborski et al., 2017), and associated with environmentally adverse local effects (Moore, 2010).

During their transit toward the coast, groundwaters can mix with saline groundwaters prior to discharge, developing the subterranean estuary (STE; Moore, 1999). Even if these environments have been largely ignored in coastal monitoring and management (Rocha et al., 2021), they play a crucial role in modulating continental solute transfer to the sea. The sandy exit sites of STEs are locus of a high variety of biogeochemical processes capable of significantly changing solute loads associated with SGD prior to discharge (Moore, 1999; Slomp and Van Cappellen, 2004; Robinson et al., 2018). Due to the need to quantify, predict, and control the SGD-borne N flux to the coastal zone, substantial research has focused on understanding natural N attenuation processes in STEs worldwide (Kroeger and Charette, 2008; Rocha et al., 2009; Erler et al., 2014; Couturier et al., 2017; Ibánhez and Rocha, 2017; Wong et al., 2020).

The availability and quality of organic C is key to understand N cycling in STEs. Low C stocks and the refractory nature of both particulate and dissolved organic matter in the sub-surface land-ocean continuum limit heterotrophic NO_3^- reduction processes and can explain the large NO_3^- concentrations reaching STEs (Hartog et al., 2004; Rivett et al., 2008). On the other hand, fresh marine organic matter brought into the STE at the seepage face fuels a spatially heterogeneous cascade of biogeochemical processes that can determine final N loads to the coast (Ibánhez et al., 2013; Pain et al., 2019; Calvo-Martin et al., 2021). Due to the high mobility of N compounds in the environment and the role N plays in microbial and primary producer metabolism, anthropogenic N enrichment of STEs could also promote alterations on the cycling of other elements such as C. Hence, mobilization of organic C from high residence time reservoirs like peat bogs (Bragazza et al., 2006), the Artic tundra (Mack et al., 2004), or alpine steppes (Chen et al., 2020) is increasingly linked to the enhancement of microbial and enzymatic activity caused by anthropogenic N enrichment. Nevertheless, to our knowledge, the effect of N enrichment on the transformation of organic matter in STEs has only been explored to date in incubation experiments (Ibánhez and Rocha, 2014a). In this study, we use an extensive field dataset collected in an STE seepage face to explore the effects of changing N enrichment within the STE over the quantity and quality of the fluorescent dissolved organic matter (FDOM). The labile and recalcitrant fractions of FDOM are then used as proxies of microbial organic C mineralization at the seepage face.

MATERIALS AND METHODS

Study Site and Sampling Strategy

Five field surveys (from December 2009 until January 2011) were conducted at different times of the year at a seepage face located in the inner intertidal area of the Ancão peninsula (37°00′04″N, 7°58′57″W), in the mesotidal Ria Formosa coastal lagoon (**Figure 1**). NO_3^--rich SGD was documented in the area in a previous series of monthly sampling surveys taking place between 2005 and 2007 (Leote et al., 2008). High NO_3^- concentrations (up to 190 μM) associated with brackish water (16.8 lowest salinity recorded) were identified seeping out at the lower intertidal area of the permeable barrier of the lagoon during low tide (Leote et al., 2008; Rocha et al., 2009). Water stable isotope signatures confirmed that these NO_3^--rich brackish waters derive from mixing of continental groundwater from the Campina de Faro unconfined aquifer system bordering the lagoon (**Figure 1**) and coastal seawater (Rocha et al., 2016). This coastal aquifer was classified as nitrate vulnerable zone in 2005 under the EU's nitrate directive due to large anthropogenic NO_3^- pollution (130 mg NO_3^- L^{-1} in 2010; Rocha et al., 2016). The sampling site was selected within the area previously identified as affected by SGD. The beach is tide-dominated, with a tidal range of 1.5–3.0 m and an averaged beach slope of 10.4% (**Figure 1**).

Extensive characterization of sediments at the sampling site has been made elsewhere (Rocha et al., 2009; Ibánhez et al., 2011; Ibánhez and Rocha, 2014a, 2016). Sediments at the seepage face are classified as medium-coarse sand (d_p = 0.5 mm) with high permeability (1×10^{-3} cm s^{-1}). Porosity peaks close to the

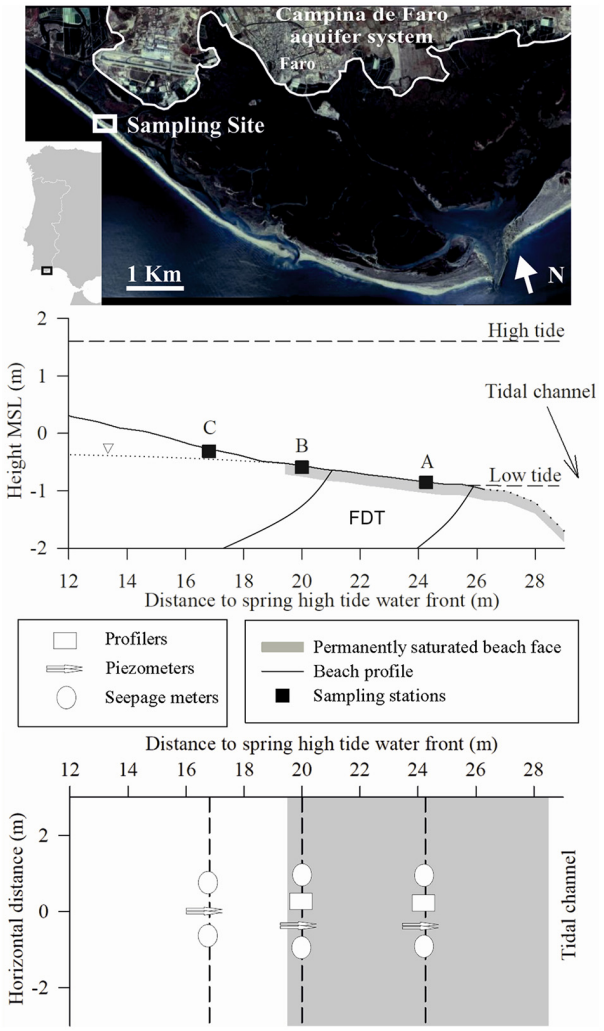


FIGURE 1 | Sampling site location at Ria Formosa coastal lagoon (SW Iberian Peninsula). The location of the three sampling stations (stations A and B within the permanently saturated beach face and station C upward) within the intertidal area of the inner part of Ancão peninsula and the distribution of samplers per station (seepage meters, piezometers, and profilers) are shown. A schematic view of beach water table during low tide, low and high tide marks, and the location of the NO_3^--rich freshwater discharge tube (FDT) observed during the period 2005–2007 (Rocha et al., 2009) at our site are also shown.

sediment–water interface (always >0.3), and then approaches a quasi-asymptotic value of 0.3 with depth, with minimal changes throughout the year. The sediments have low total organic carbon (TOC) content (<0.1%), with the highest values observed at the sediment surface (top 10 cm).

Porewater composition, seepage rate measurements, and associated solute fluxes were investigated during December 2009, April, July, October 2010, and January 2011. Sampling equipment was deployed at the intertidal seepage face during tidal exposure and sampling conducted through the two subsequent tidal cycles, thus leaving the system to re-equilibrate for one tidal cycle after installation. The equipment remained in place for the duration of fieldwork surveys, minimizing disruption to local beach hydraulics (Seeberg-Elverfeldt et al., 2005; Ibánhez et al., 2011). Three sampling stations were established within the beach profile, following identical sampling strategy as in previous studies at the same location (Leote et al., 2008; Rocha et al., 2009; Ibánhez et al., 2011). Two sampling stations (A and B) covered the permanently saturated intertidal seepage face and a third (C) the upper part of the beach profile, situated outside the permanently saturated intertidal zone (**Figure 1**). Station A was situated at the lowest part of the intertidal beach profile where a permanent, well-developed freshwater discharge tube was observed during 2005–2007 (**Figure 1**; Rocha et al., 2009), while B was placed at the upper limit of the permanently saturated seepage face.

Seepage Measurements

Five (six during July and October 2010) Lee-type seepage meters were installed at the beach face (**Figure 1**) to allow direct measurements of seepage rate and solute fluxes across the sediment–water interface (Lee, 1977; Burnett et al., 2006). These were distributed (**Figure 1**) between the three sampling stations, two at A and B and one at C (with an additional seepage meter added to C in July and October 2010). During the survey performed in January 2011, seepage meters were only deployed at station A. Sampling followed the precautions suggested by Cable et al. (1997). Measurements of seepage rate, associated solute fluxes, salinity, and temperature were performed using the water collected with the bags connected to the seepage meters, with aliquots also taken for laboratory determinations.

Porewater and Surface Water Sampling

Four push–pull piezometers (MHE, United States) were installed at each sampling station within the beach profile at screened depths of 28, 66, 84, and 200 cm relative to the sediment surface. Porewater samples were collected periodically with luer-lock syringes (100 mL) attached to the piezometers through tygon tubing and luer stopcocks. The internal volume of the piezometers was flushed three times prior to the collection of any sample.

Soil moisture samplers (Rhizon SMS-10 cm; Rhizosphere, The Netherlands, 0.1 μm pore size) were used to collect *in situ* high-resolution vertical porewater profiles close to the sediment–water interface. The samplers were placed into the sediment at fixed depths with the aid of two acrylic profilers (stations A and B; **Figure 1**) modified from the design of Seeberg-Elverfeldt et al. (2005). Each profiler was buried with 12 Rhizon samplers located horizontally at vertical intervals of 1, 2.5, and 5 cm, covering the first 20 cm depth of the sediment column. Porewater was collected at each depth by connecting Luer-Lock syringes to the Rhizon samplers through the connection tubing protruding from the sediment surface. The first 2 mL of filtered porewater was discarded to avoid contamination due to the dead volume inside the tubing and the samplers and to prevent influence of the NH_4^+ adsorption properties of the membranes (Ibánhez and Rocha, 2014b).

Surface water samples were also collected next to the sampling site during low tide. These were filtered onsite with Rhizon SMS samplers. The final aliquots collected from the seepage meters,

piezometers, the benthic profilers, and the surface seawater were stored at −20°C until analysis. All parameters were analyzed within 1 month of sampling.

Analytical Methods

Porewater, seepage, and surface water samples collected during each field survey were analyzed for NO_3^-, NO_2^- and NH_4^+ content in a Lachat Quickchem 8500 Flow Injection Analysis system following standard colorimetric methods (Grasshoff et al., 1983). Porewater salinity (from both the high-resolution porewater profilers and the piezometers) was measured with an ATAGO hand-held refractometer using single-point calibration with distilled water. Salinity and temperature measurements on the seepage water were performed *in situ* using a YSI 600 (Yellowspring instruments) multiparameter probe following the recommendations of the manufacturer. Dissolved Organic C (DOC) from the seepage meters was determined in a Vario TOC Cube elemental analyzer, after acidification with a 2 M HCl solution to pH < 2 and purge to ensure removal of dissolved inorganic C.

Excitation-Emission Matrix (EEM) Fluorescence of Dissolved Organic Matter (DOM)

A Cary Varian Eclipse fluorescence spectrophotometer was used to obtain a three-dimensional excitation-emission matrix of FDOM in all water and porewater samples (n = 701). The 5 nm excitation and 10 nm emission bandwidths were used. Emission wavelengths for analysis ranged from 290 to 550 nm with a 2 nm interval, and excitation intensities were recorded at wavelengths ranging from 270 to 440 nm with 5 nm intervals. The samples were first placed in a thermostatic bath at 20^{o}C to avoid changes in the spectral intensities caused by temperature differences. Absorbance of the samples in a 1 cm cuvette at 270 nm (the lowest wavelength used in the fluorescence determinations) was generally well below 0.05. The correction of the fluorescence spectra for inner filter effects was therefore deemed unnecessary (Kothawala et al., 2013). Spectra were collected in signal-to-reference mode with instrument-specific excitation and emission corrections applied during collection. Daily recorded Milli-Q water blanks were subtracted from the sample spectra to eliminate water Raman scatter peaks. Subsequently, EEMs were normalized to the integrated area of Milli-Q water Raman peaks to account for potential instrument-dependent intensity factors (Lawaetz and Stedmon, 2009). Results are expressed in Raman units (R.U.). MATLAB with the DOMFluor Toolbox was used to handle first- and second-order Rayleigh scatter peaks and to perform the PARAlel FACtor analysis (PARAFAC) of our samples (Stedmon and Bro, 2008). PARAFAC modeling of EEM fluorescence has been extensively described elsewhere (Andersen and Bro, 2003; Stedmon and Bro, 2008). It allows decomposition of a three-way array of data (the 3-D excitation-emission matrix) into a set of three linear terms and a residual array. Following PARAFAC decomposition, the complex sample EEM yields the individual fluorescence components (fluorophores) within the sample and their individual abundance. PARAFAC analysis was performed on the entire EEM fluorescence dataset discussed here (701 samples). The adequacy of the selected number of components and the uniqueness of the solution were tested by Split Half Analysis (Stedmon and Bro, 2008).

RESULTS

Water and Solute Seepage at the Sampling Site

Seepage rates measured from December 2009 to January 2011 showed a similar discharge pattern to that previously described at the same site (Leote et al., 2008). Seepage rates peaked during ebb tide and were minimal or absent at flood tide (see **Supplementary Material**). Linear vertical porewater velocities in excess of 100 cm day^{-1} were measured at station A in all surveys but April 2010 (**Figure 2**). The highest discharge rates were always measured at this point, followed by station B except during October 2010 where station C showed higher water discharge rates. Although we recorded the highest discharge rates observed between 2009 and 2011 at station A during October 2010 (153 ± 73 cm day^{-1}), the difference in discharge rates obtained during the five sampling periods covering this point of the profile were non-significant (Kruskal–Wallis test, $p > 0.05$).

The salinity of STE outflows only dipped below 35 in April 2010 (**Figure 3**). This contrasts with the 2005–2007 period, when salinities as low as 16.8 were measured (Leote et al., 2008). Nevertheless, the magnitude of the discharge remained very high and comparable to that measured during 2005–2007 (up to 180 cm day^{-1}; Leote et al., 2008).

NO_3^- was generally the predominant dissolved inorganic nitrogen form (DIN = NO_3^- + NO_2^- + NH_4^+; **Supplementary Table 1**) in STE outflow water. The highest DIN concentrations in seepage were recorded during October 2010, even if the lower salinities were measured during April 2010 (**Figure 3**). For the April and October data, DIN was significantly correlated with salinity (**Figure 3**), but with very distinct slopes (April: −7.1x + 261.7, R = 0.80, $p < 0.0001$, n = 46; October: −84.1x + 3041.7, R = 0.86, $p < 0.0001$, n = 71). DOC concentrations in seepage were highest in April (**Figure 3**). DOC fluxes from the beach face at station A, where the highest fluxes were measured, remained year round between 100 and 170 mmol m^{-2} day^{-1} (**Figure 2**). DOC did not covary significantly with salinity, and both DOC and DIN concentrations in the seeped water were generally higher than those measured in the surface seawater during low tide (**Figure 3**).

FDOM Components at the Seepage Face

PARAFAC analysis of our dataset identified five FDOM components (see **Supplementary Material**). These were compared with the OpenFluor database[1] (Murphy et al., 2014). All five components showed high similarity (>0.95 Tucker's congruence) with components identified in several prior studies (C1 present in nine studies, C2 in 18, C3 in 62, C4 in 61, and C5 in 24). Components 1, 2, and 4 (C1, C2, and C4) have characteristic

[1]https://openfluor.lablicate.com; last access 22/12/2020.

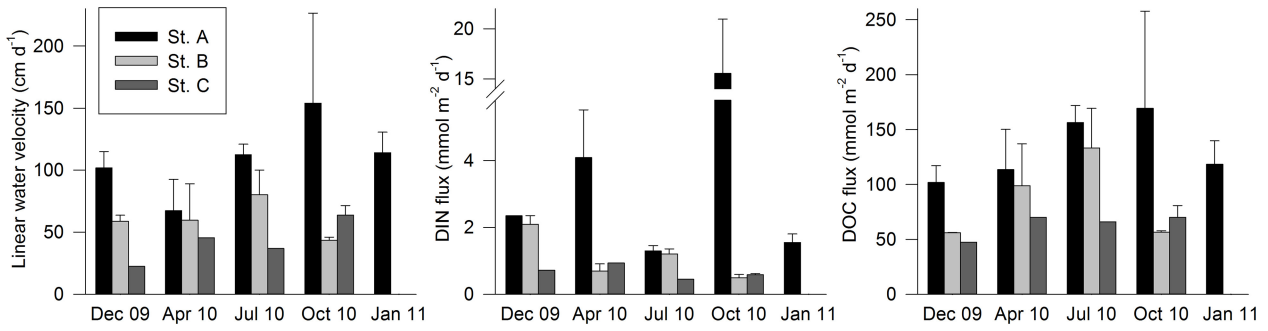


FIGURE 2 | Daily linear porewater velocities, and DIN and DOC fluxes per sampling station calculated over the two consecutive tidal cycles sampled during each survey. Error bars represent the standard error of the estimate.

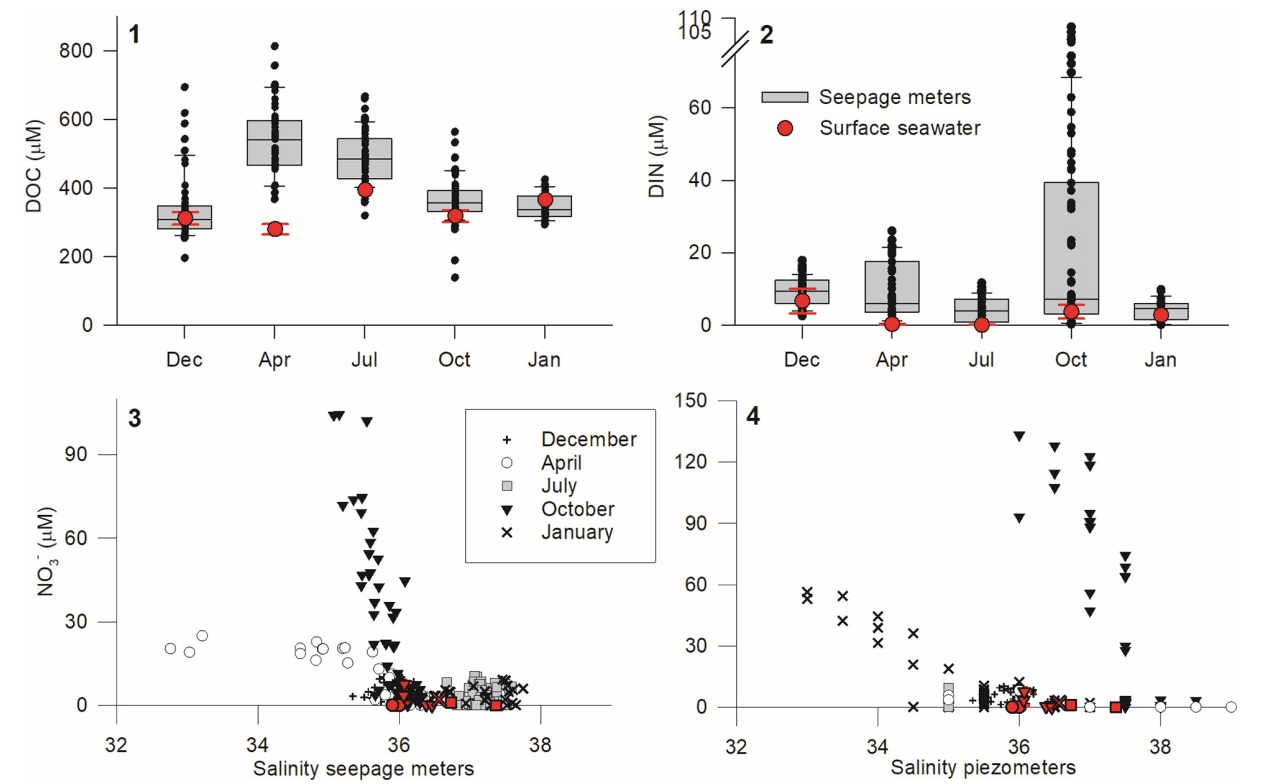


FIGURE 3 | Upper panels: box plot of DOC and DIN concentration range observed in the water samples taken from seepage meters during the five seasonal sampling surveys. Square limits represent the first and the third quartiles, the middle line represents the median, and whiskers are proportional to the interquartile range (IQR) of the data by using 1.58 IQR/$(n)^{1/2}$. Average DOC and DIN concentrations measured in the surface seawater at low tide are shown in red as reference. **Lower panels**: Seasonal NO_3^- concentrations measured in the seeped water (3) and in the porewater samples taken with piezometers (4) as a function of salinity. Symbols denote each survey performed, while red fills are used to include the surface seawater measurements as reference.

emission wavelengths of 296, 340, and 336 nm, typical of protein-like fluorophores. They correspond to peaks T (C2 and C4) and B (C1) in Coble's nomenclature (Coble, 1996) and are associated to labile DOM (Yamashita and Tanoue, 2003; Stubbins et al., 2014). Although they have similar characteristic emission wavelengths, components C2 and C4 differ in their characteristic excitation wavelengths (300 and 280 nm, respectively), suggesting they may correspond to FDOM fractions with different molecular weight (higher in C2; Coble et al., 1998). Components 3 and 5 (C3 and C5) have emission wavelengths of 418 and 466 nm characteristic of humic-like FDOM components (**Supplementary Figure 2**). Component C3 is similar to Coble's peak M, previously identified as a humic-like FDOM component freshly produced in the marine environment by microbial activity. Component C5 corresponds to Coble's peak C and is associated with refractory terrestrial DOM of low bioavailability (Stubbins et al., 2014).

These FDOM components are highly similar to those from an independent PARAFAC analysis run with samples from flow-through reactor experiments conducted with water and sediment collected at the same sampling site (Ibánhez and Rocha, 2014a). Three protein-like (C1, C2, and C5, with characteristic emission wavelengths of 358, 320, and 298 nm, respectively) and two humic-like (C3 and C4, with characteristic emission wavelengths of 464 and 422 nm) FDOM components were also identified then.

Protein-like FDOM component C2 and the two humic-like FDOM components were always present in the seeped water. The predominant FDOM components, on the basis of relative peak intensity, were protein-like component C1 (44.4 ± 1.8%) followed by the marine humic-like component C3 (18.1 ± 0.7%). Over the entire dataset (n = 701), these two components as well as the terrestrial humic-like component C5 were significantly correlated with DOC concentration (C1: R = 0.56, $p < 0.0001$; C3: R = 0.66, $p < 0.0001$; C5: R = 0.26, $p < 0.0001$; n = 251). In contrast, no correlations of FDOM components with salinity or DIN were found. This general pattern in the composition of the FDOM held for each sampling event but October, where FDOM was dominated by the marine humic-like component C3 (28.9 ± 0.9%), followed by the protein-like component C4 (26.9 ± 1.2%) and the terrestrial humic-like component C5 (17.2 ± 0.6%). Despite its ubiquitous presence, protein FDOM component C2 was the lowest contributor to the overall FDOM pool by far (median contribution <8%) and therefore was excluded from the subsequent data analysis.

The FDOM composition of seepage differed along the beach profile. The relative abundance of the two humic-like FDOM components (C3 and C5) was strongly correlated within the permanently saturated beach face (stations A and B), but not in station C (**Figure 4**). Furthermore, this correlation was highly similar across both stations, with very comparable regression slopes (**Figure 4**). Similarly high correlation between the two humic-like FDOM components was observed in surface seawater samples. In contrast, no significant correlations between the relative abundance of the protein-like FDOM components C1 and C4 were found in seepage.

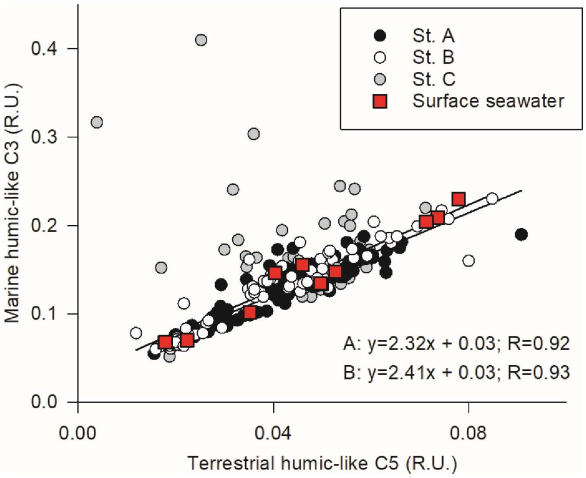


FIGURE 4 | Relationships of the two humic-like FDOM components identified through PARAFAC modeling of our dataset in the samples collected from the seepage meters and those collected from the surface seawater during low tide. Samples from the seepage meters are organized by sampling station.

Porewater Solute Distribution at the Seepage Face

Large spatial solute gradients were found within the beach porewater. **Figures 5**, **6** show a snapshot of solute distribution within the seepage face at the beginning of active seepage (i.e., at the beginning of sediment exposure). In contrast with seepage meter outflows, porewater salinities lower than 35 were only detected in January 2011 (**Figure 3**). These lows were restricted to sampling stations C and B where no seepage meters were installed at the time (**Figure 5.5**). Still, variable vertical salinity gradients are found in almost all the surveys. In stations C and B, the lowest salinity generally corresponds to samples taken from the deepest screened points within the beach aquifer (2 m depth). The exception occurred in January, where the lowest salinities within the beach are found at the shallower screened depths at station B (**Figure 5.5**). At station A, the lower salinity values in seepage water are found in April (**Figure 5.2**) and during July in porewater (salinity = 35; **Figure 5.3**).

NO_3^- was the predominant form of porewater DIN throughout the studied period (**Figure 5**), as expected given the near-saturation of oxygen inside the beach (see **Supplementary Figure 3**; Ibánhez and Rocha, 2016). Significant reductions in oxygen levels during active seepage are only found in association with particulate organic matter (POM) enrichments near the sediment surface (Ibánhez and Rocha, 2016). NO_3^- distribution within the seepage face follows two different patterns during the year: from December 2009 to July 2010, NO_3^- porewater concentrations were lower than 15 μM and generally peaked close to the sediment surface. During October 2010 and January 2011, NO_3^- concentrations in porewaters exceeded 30 μM (up to 133 μM in October; **Figure 3**). In these two surveys, a significant linear relationship between salinity and NO_3^- exists, although with different slopes and intercepts: October: −77.3x + 2923.5, R = 0.81, $p < 0.0001$, n = 44; January: −14.0x + 504.7, R = 0.83, $p < 0.0001$, n = 56 (**Figure 3**). The location of the most NO_3^- enriched porewater was also different during these two surveys: in October, it was found at depth in station B and distributed with depth in station A (**Figure 5.9**). In January, it was found at depth in station C and in the shallower screens for station B piezometer nests (**Figure 5.10**). Ammonium, on the other hand, was permanently low and did not exceed 3 μM with peak concentrations found near the sediment surface (**Figures 5.11–15**).

With regard to the zonation of FDOM components, the highest values for the ratio between abundances of FDOM components C3 and C5 (C3/C5) within the seepage face were generally found in the beach interior (**Figures 6.1–4**), except for January where they could be found in the shallower levels of station A (**Figure 6.5**). On the other hand, the lowest C3/C5 abundance ratios were found during October and January

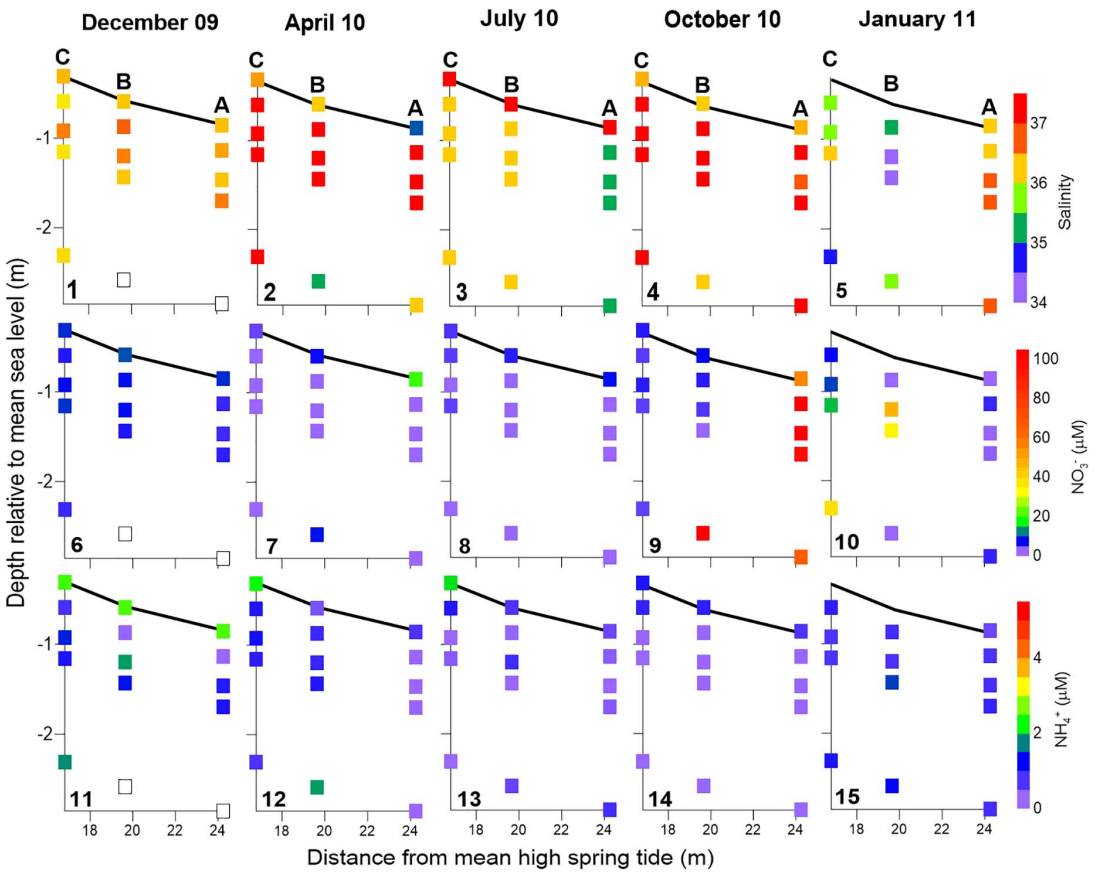


FIGURE 5 | Solute distribution within the seepage face at the beginning of sediment exposure during low tide. Salinity (panels 1–5), NO_3^- (panels 6–10), and NH_4^+ (panels 11–15) are shown for the five surveys presented here. Data are represented on the beach profile, where the dark line represents sediment surface. Samples were collected with piezometers buried at different depths and seepage meters. Seepage meter data corresponding to half an hour around the time of piezometer sampling were integrated at each sampling station and presented at the sediment surface. Sampling stations are labeled in the top panels. White squares mean lack of data.

(**Figures 6.4–5**) and generally matched the location of NO_3^--enriched porewaters (**Figures 5.9–10**). Contrastingly, while FDOM component C1 was more abundant at the sediment surface from December to July (**Figures 6.6–8**), C4 tended to be more prevalent in depth (**Figures 6.11–15**). Nevertheless, no statistical evidence of antithetical association between these protein-like FDOM components was found.

The spatial solute distribution within the seepage face was relatively constant throughout the active seepage period (**Figures 7**, **8**). Salinity gradients within the seepage face remained in place throughout the sampled period (**Figures 7.2–4**), suggesting the active pumping of waters with different origin contributed to support them. Toward the end of sediment exposure, the brackish, NO_3^--enriched porewaters observed in station B during January (**Figures 7.5**, **7.11**) were replaced by low NO_3^-, saline porewaters (**Figures 7.5**, **7.11**). Interestingly, in April, salinity gradients persisted at the deepest beach aquifer zones during tidal exposure (**Figures 7.2–3**) in association with higher NO_3^- concentrations than those in surrounding porewaters (**Figures 7.8**, **7.9**). Furthermore, the spatial patterns identified at the beginning of sediment exposure with regard to FDOM components remained almost unchanged throughout the period of active seepage (**Figure 8**). The lowest C3/C5 ratios were identified in station A during April and stations B and C during January with small changes over time. Labile FDOM component C1 peaked at the sediment–water interface during April and remained so throughout tidal exposure. On the contrary, the highest abundance of the labile FDOM component C4 was found in depth throughout the same period.

The persistence of large, stable solute gradients within the beach aquifer during tidal exposure in spite of high seepage rates highlights the extent of reactive modulation of solute concentrations inside the beach prior to discharge. High-resolution vertical porewater profiles show that the largest vertical solute gradients occur near the sediment surface at the peak of the discharge (**Figures 9**, **10**). These are measured within vertically homogeneous salinity distributions (see **Supplementary Material**), implying that the nitrate gradients are sustained by reaction and not by mixing of different inputs. NO_3^- peaked within the surface 30–50 cm of sediment in station A from December 2009 to July 2010 (**Figure 9**) when large porewater flow rates were measured (**Figure 2**). Considering

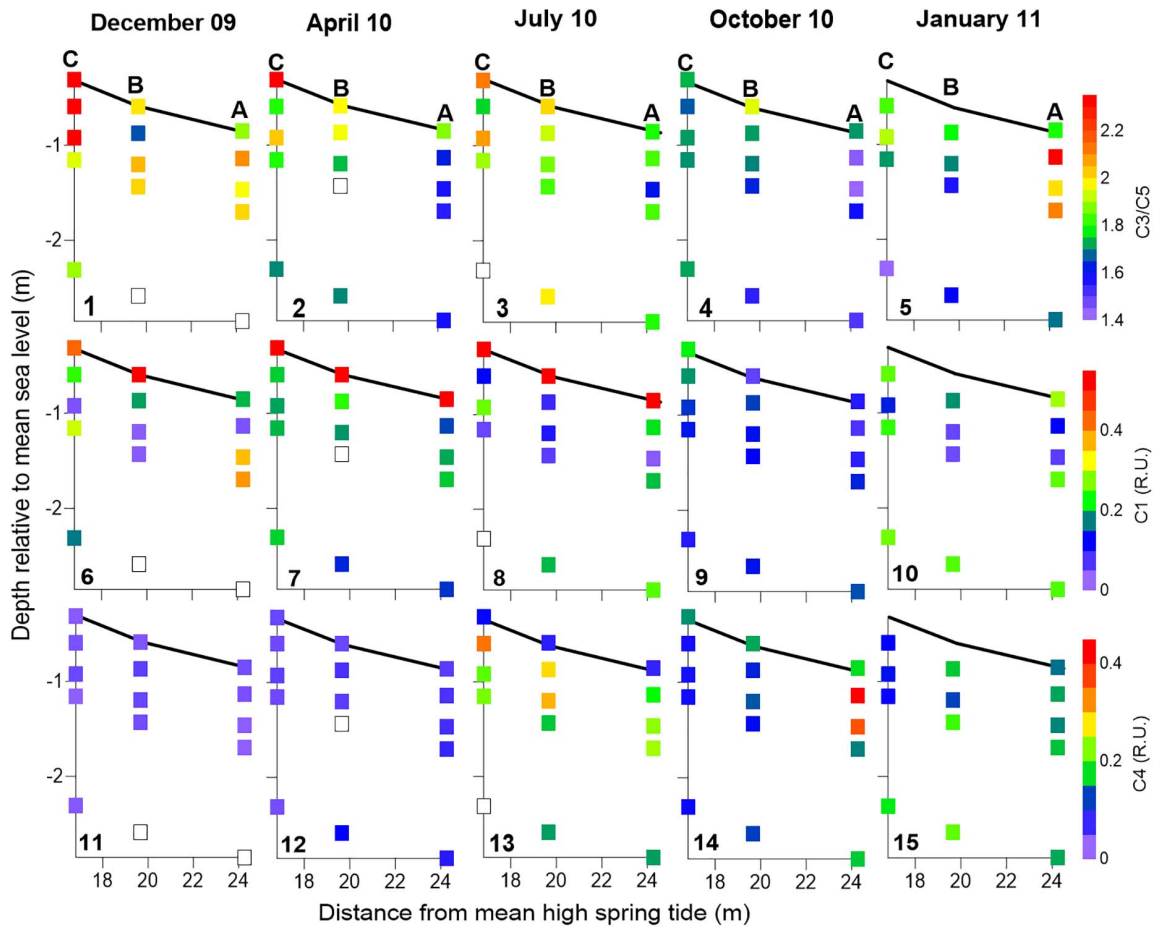


FIGURE 6 | FDOM distribution within the seepage face at the beginning of sediment exposure during low tide. The ratio of FDOM C3/C5 (panels 1–5), C1 (panels 6–10), and C4 (panels 11–15) are shown for the five surveys presented here. Data are represented on the beach profile, where the dark line represents sediment surface. Samples were collected with piezometers buried at different depths and seepage meters. Seepage meter data corresponding to half an hour around the time of piezometer sampling were integrated at each sampling station and presented at the sediment surface. Sampling stations are labeled in the top panels. White squares mean lack of data.

the predominant vertical direction of flow near the sediment surface at our site (Rocha et al., 2009; Ibánhez and Rocha, 2016), these results imply the active production of NO_3^- near the sediment surface at that point of the beach profile. The same is clearly observed at station B in July and October (**Figure 10**). In contrast, NO_3^- is only available at measurable concentrations at depths exceeding 50 cm during December in station B (>3 μM; **Figure 9**), during January in station A and the deepest reaches of station B and during October over the entire sediment column below station A, where NO_3^- concentrations exceeded 100 μM (**Figure 10**). NH_4^+, on the other hand, remained low throughout the entire period of study. The abundance of the two humic-like FDOM components, analyzed individually, was virtually constant with depth throughout the period of study, with very low temporal variability (very small error bars; **Figure 9**). The only notable exceptions to this general pattern were found in January 2011 and quite clearly in October 2010, where the vertical distribution of humic-like FDOM abundance drastically changed over the surface 30 cm of sediment from relative homogeneity with depth (**Figure 10**). There, active production of both C3 and C5 was observed. Protein-like FDOM components C1 and C4 showed higher spatial and temporal variability, although in general the largest changes also occurred at the surface sediment layers.

DISCUSSION

Technical Considerations

Lee-type seepage meters are affected by potential artifacts that influence seepage rate measurements (Shaw and Prepas, 1989). These effects are reduced at high seepage rates, as was the case for the study period (Cable et al., 1997; Leote et al., 2008). Nevertheless, seepage rate measurements reported here were validated with pressure measurements carried out in parallel, in two independent ways: using manual measurements of pore pressure employing the shallow screen piezometers installed every survey, and during April 2010, additional backing provided by continuous pressure measurements made with a ceramic 10M CTD Diver (Schlumberger Water Services, United States)

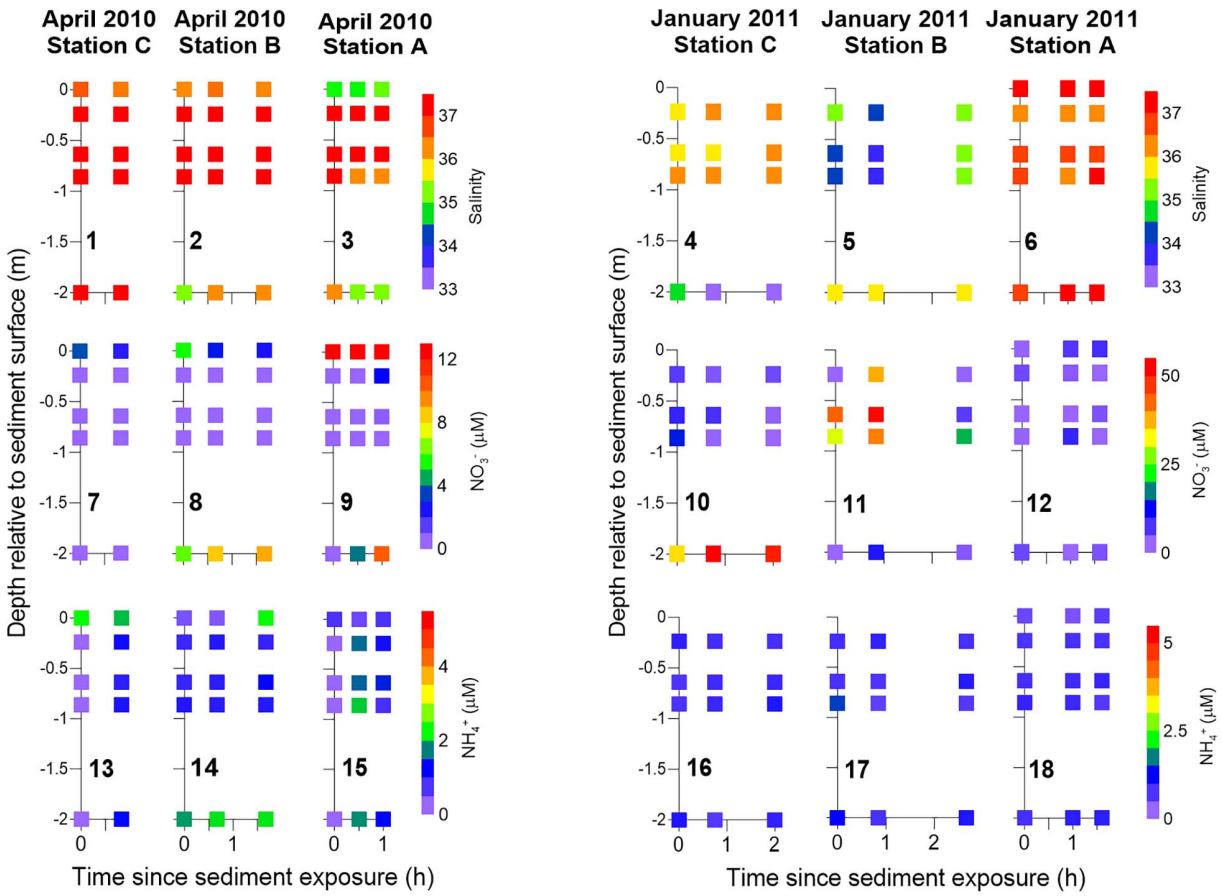


FIGURE 7 | Temporal solute distribution within the seepage face during the period of active seepage, i.e., during sediment exposure, organized by sampling station during April 2010 and January 2011. Porewater salinity (panels 1–6), NO_3^- (panels 7–12), and NH_4^+ (panels 13–18) are shown. Samples were collected with piezometers and seepage meters. Seepage meter data corresponding to half an hour around the time of piezometer sampling were integrated at each sampling station and presented at the sediment surface. White squares represent lack of data. Note the different scale in the NO_3^- concentrations between April and January.

buried at the seepage face for the duration of field sampling (Ibánhez and Rocha, 2016). Intercomparison of results confirmed the correct functioning of our Lee-type seepage meters during sediment exposure and the magnitude of the meter-derived seepage rates. During high tide however, the continuous pressure measurements obtained during April 2010 showed that surface water infiltration occurred within the permanently saturated zone (Ibánhez and Rocha, 2016). Infiltration rates cannot be monitored by Lee-type seepage meters due to their design. While this does not affect the credibility of measured seepage (outflow) rates, it raises concerns regarding the drivers of composition of seepage water collected by these instruments. During high tide, both the entrapped water and the volume of sediment enclosed by Lee-type seepage meters may have been subject to relatively limited ventilation. This would of course affect the solute composition of water collected during the first moments of seepage outflow as this water might be considered the efflux of pore and overlying water stagnating within the chamber for a few hours. Yet, under the prevalent seepage rates, the enclosed volume of water, calculated on the basis of the chamber dimensions (0.1 m^2, 10 cm depth) and the local porosity (~0.3), this potentially stagnant porewater would have been flushed out within less than 30 min of active seepage. Even if this effect is limited over the vast majority of data given the large period covered by the measurements during active seepage stages of the tidal cycle, it might explain the large enrichment in FDOM component C1 found in water samples collected at the beginning of these stages, particularly from December to July (**Figure 6**). The progressive decrease of abundance in FDOM component C1 with time during the active seepage stage shown for April 2010 (**Figure 8**) and the paucity of this FDOM component in porewater profiles collected with our profilers (**Figure 10**) support this interpretation. It follows that composition of seepage water collected with these meters at the very beginning of the outflow stage should be taken with caution when interpreting the overall results.

Compositional Change of SGD at the Sampling Site

Salinities lower than 35 were only measured in seepage water during April, in contrast with the monthly surveys performed

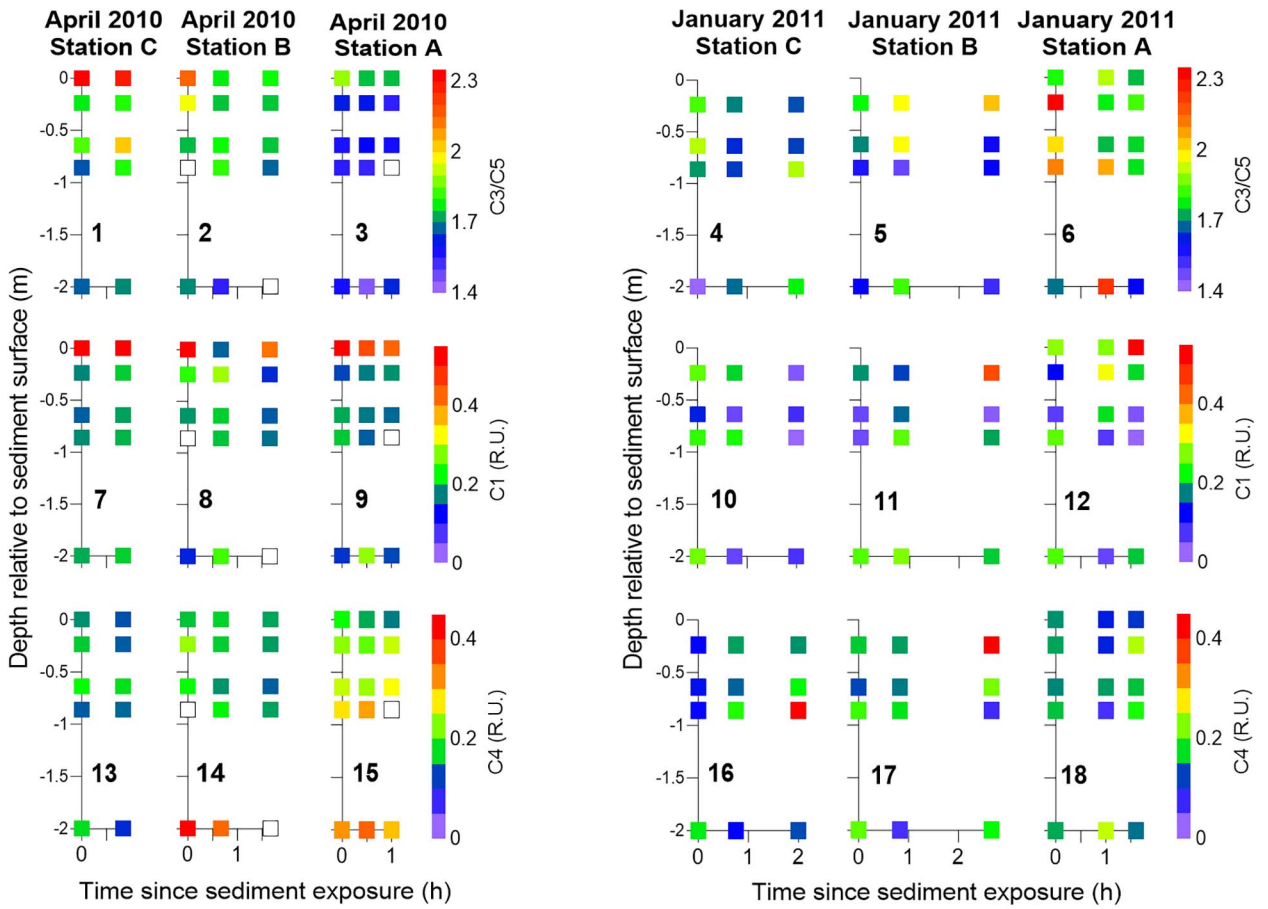


FIGURE 8 | Temporal FDOM distribution within the seepage face during the period of active seepage, i.e., during sediment exposure, organized by sampling station during April 2010 and January 2011. The ratio of FDOM C3/C5 (panels 1–6), C1 (panels 7–12), and C4 (panels 13–18) is shown. Samples were collected with piezometers and seepage meters. Seepage meter data corresponding to half an hour around the time of piezometer sampling were integrated at each sampling station and presented at the sediment surface. White squares represent lack of data.

during 2006–2007 at the same site where measurable fresh groundwater was always present, even if in small quantities during the summer months (Leote et al., 2008; Rocha et al., 2009). Salt budgets (Ibánhez and Rocha, 2016) revealed that fresh groundwater would only account for 2.7 ± 1.8% of the STE outflow at station A during April 2010, while negative salt balances prevailed in the other two stations, due essentially to the accumulation of salt in the unsaturated sediments over low tide (Geng et al., 2016). This drop in salinity during April 2010 is not associated with an influx of NO_3^- to the seepage face as observed during 2006–2007 at the same site, where nitrates and salinity were negatively correlated, suggesting that it might have originated from local rainfall rather than from the subsurface. Thus, SGD was essentially composed of recirculated seawater for this study period. Regardless, seepage rates were comparatively high in comparison to the 2006–2007 period when significant amounts of fresh groundwater were outflowing from the same site. The high hydraulic conductivity (10^{-3} cm s^{-1}), beach slope (10%), and tidal amplitude (1.5–3 m) of the location allow the fast recirculation of seawater through the upper parts of the beach, forming the so-called tidal circulation cell (Robinson et al., 2007a,b) which contributes to sustain the high seepage rates *in situ*.

A sudden, more than threefold increase in SGD-derived NO_3^- fluxes to the lagoon compared to the other months is observed in October 2010. These large NO_3^- fluxes were restricted to sampling station A, where continental groundwater discharge was observed during the period 2005–2007 (Leote et al., 2008). Parallel increases in porewater NO_3^- were not observed in the water collected from the seepage meters installed in January 2011, although the presence of a NO_3^--rich, brackish discharge tube is clearly observed in the beach interior. Beach sands can host large nitrification rates supported by the simultaneous supply of oxygen and organic matter into the beach interior (Schutte et al., 2018). Oxygen transport into our site is driven by the fast infiltration of surface seawater at the unsaturated upper intertidal, explaining the large benthic oxygenation (see **Supplementary Material**; Ibánhez and Rocha, 2016) and therefore could explain the porewater NO_3^- enrichment found during October and January. The substrate for

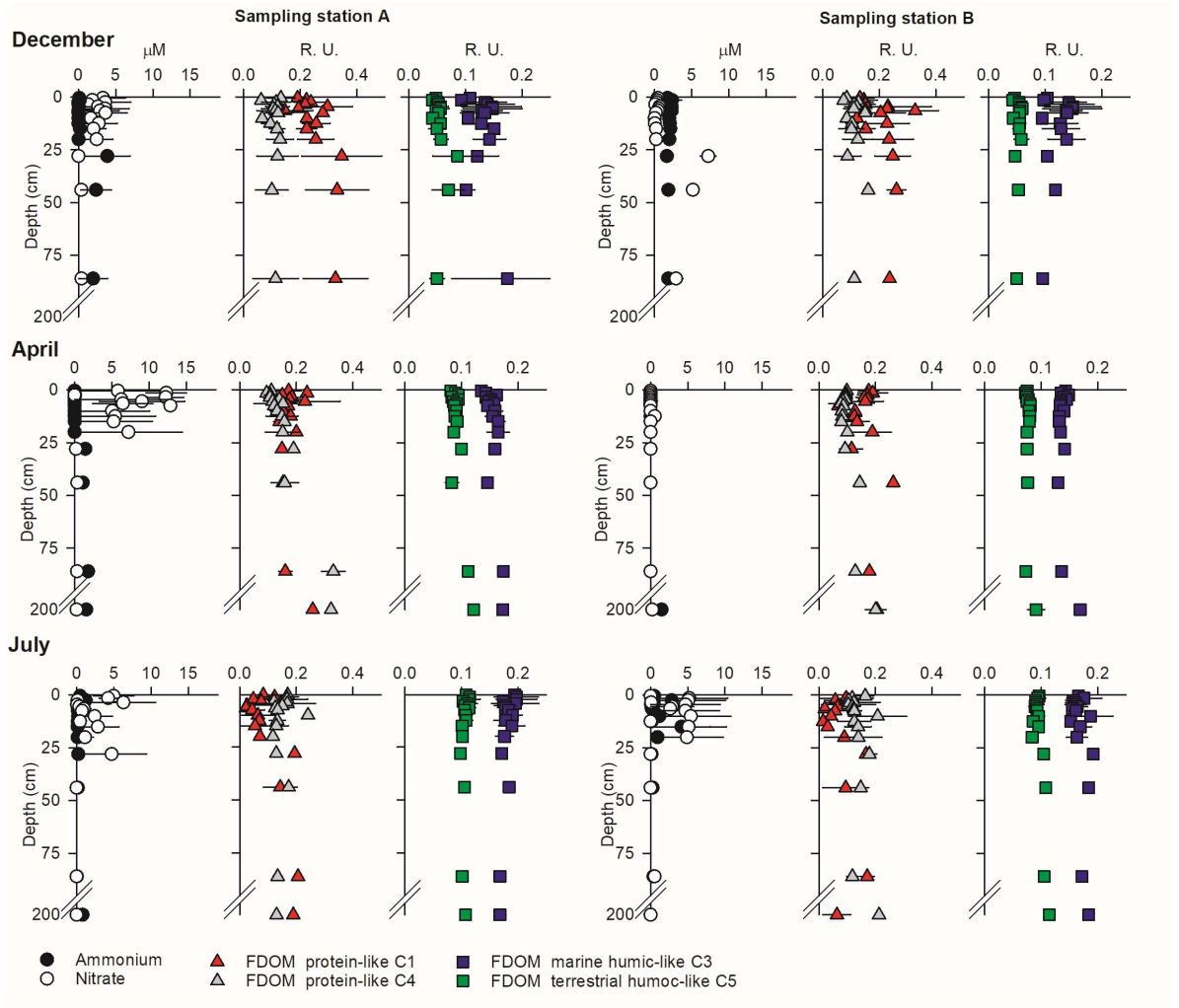


FIGURE 9 | High-resolution vertical porewater profiles of NH_4^+, NO_3^-, and FDOM components during the peak of discharge in stations A and B during December 2009 and April and July 2010. Porewater profiles correspond to the average of those obtained during two consecutive tidal cycles with piezometers and porewater profilers.

benthic autotrophic nitrification, NH_4^+, remained low (generally <3 μM) in porewater (e.g., **Figure 5**). These sediments also have very low NH_4^+ adsorption capacity (Ibánhez and Rocha, 2017). Therefore, to support nitrification rates capable of explaining the observed NO_3^- concentrations, significant benthic organic matter mineralization is required. Two moles of O_2 are needed for the production of one mole of NO_3^- during autotrophic nitrification, and these have to be added to the O_2 consumption fueling aerobic organic matter mineralization. Porewater O_2 levels measured during January in the three sampling stations and throughout the studied sediment column remained near saturation levels (>200 μM; see **Supplementary Material**) at all times, giving no indication of significant benthic O_2 consumption that would support aerobic mineralization coupled to nitrification over the sampling timeframe. This observation supports our previous findings indicating strong organic matter limitation of aerobic respiration (Ibánhez and Rocha, 2016), and implies that the NO_3^- enrichment in porewater found during October and January is not driven by nitrification supported by aerobic respiration within the seepage face. It has to originate elsewhere and is transported toward the seepage face by porewater advection.

The first option is that nitrate originates in subsurface fresh groundwater of continental origin, as suggested by the strong linear correlation of porewater NO_3^- with salinity during both October and January (**Figure 3**) even if porewater salinity below 35 was only found in January. Furthermore, the NO_3^--rich porewater discharge tube observed during these surveys was located in the same area affected by fresh continental groundwater during 2005–2007 (Rocha et al., 2009). These waters originated from the direct mixing of NO_3^--polluted Campina de Faro aquifer system groundwaters and coastal seawater (Rocha et al., 2016). In 2005, a drastic drop in the piezometric head was observed in the coastal aquifer system surrounding Ria Formosa

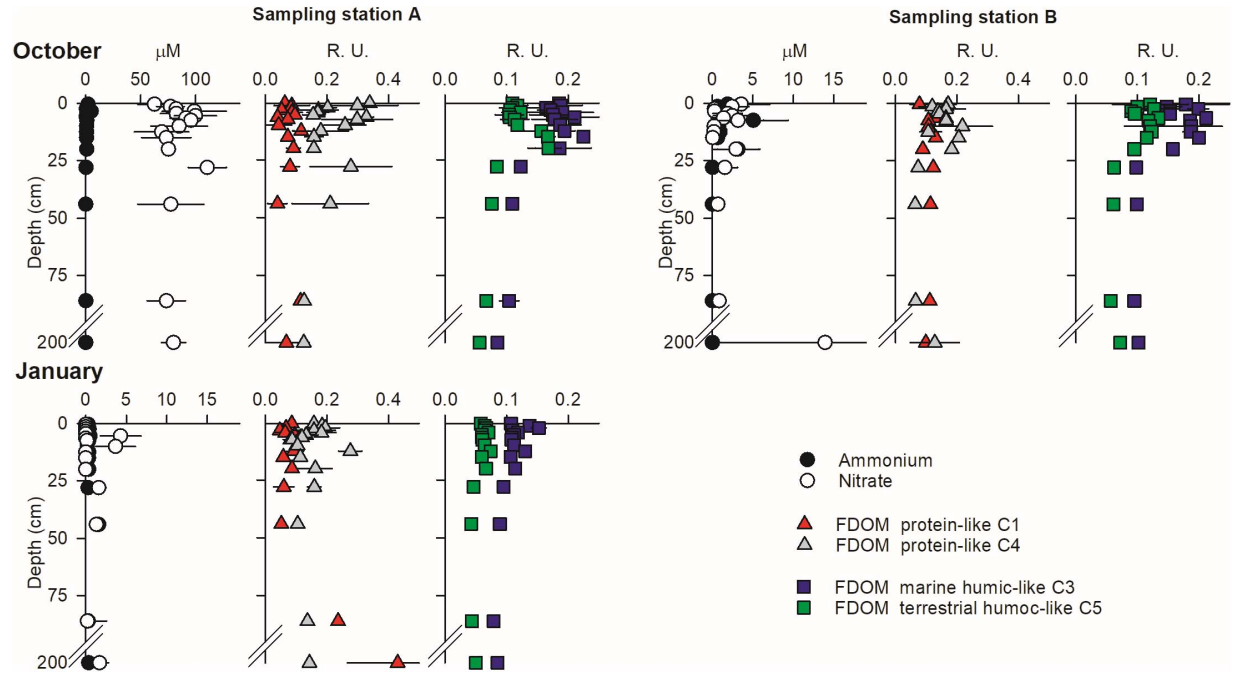


FIGURE 10 | High-resolution vertical porewater profiles of NH_4^+, NO_3^-, and FDOM components during the peak of discharge in stations A and B during October 2010 and January 2011 (only station A). Porewater profiles correspond to the average of those obtained during two consecutive tidal cycles with piezometers and porewater profilers. Note the different scale used in the NO_3^- and NH_4^+ profiles.

(**Figure 11**). The hydraulic gradient to the sea remained very low until the beginning of 2010, when a fast recovery began. This increase in the piezometric head in land during the study period, which reached values at the higher end of those registered for the period 2002–2011, is not immediately translated into higher continental freshwater influx at the site. This suggests that there is a time lag of months from the recovery (or drop during the 2006–2007 period) in the piezometric head inland and the increase (or decrease) of the contribution of continental groundwater to the overall SGD at the site. Alternatively, the water might be diverted or intercepted in transit, and recirculated via irrigation (Hugman et al., 2017) during the spring to fall period. The inland piezometric head further controls the position of the freshwater–seawater interface within the aquifer matrix (Michael et al., 2005; Robinson et al., 2006). Thus, during the prolonged drop in the piezometric head of the coastal aquifer, the freshwater–seawater is displaced inland and surface seawater intrudes de aquifer. There, seawater intrusion completely changes ionic strength (and hence desorption of solutes such as ammonium from the aquifer matrix), pH, DOM content, or oxygen levels within the aquifer and can significantly increase NO_3^- levels through processes such as DOM mineralization, nitrification, and matrix weathering (Slomp and Van Cappellen, 2004; Moore and Joye, 2021; Wan et al., 2021). With the recovery of the piezometric head, this salty groundwater will be displaced toward the seepage face. The displacement of the freshwater–seawater interface and the discharge of the intruded seawater can explain the delay observed between piezometric head recovery and the identification of a fresh groundwater signal at the seepage face but also, can add to the NO_3^- levels observed during October and January. If we take DIN content within the seepage face as a reference however, our data can be separated into two highly distinctive sets: one from December 2009 until July 2010 where porewater in the seepage face is largely dominated by recirculated seawater with low DIN content, and another from October 2010 to January 2011 where the arrival of continental groundwater largely impacted DIN content inside the seepage face.

FDOM as a Proxy of Organic Matter Transport and Reactivity at the Seepage Face

In combination with PARAFAC modeling, FDOM permits to disentangle the cycling of specific fractions of the DOM pool. Compared to the traditional pick-picking technique for identification of FDOM components (e.g., Coble, 1996), PARAFAC allows the fluorescence signals of each fluorophore to be separated, thus avoiding signal overlapping and the ensuing overestimation of fluorophore abundances in concentrated samples (Andersen and Bro, 2003; Stedmon and Bro, 2008). Furthermore, the unique solution produced by PARAFAC modeling of an FDOM dataset allows quantification of the relative abundance of each fluorophore, which is directly proportional to the concentrations of the individual components in the samples (Andersen and Bro, 2003; Murphy et al., 2013).

Previous studies have used FDOM humic-like components identified through PARAFAC analysis to quantify the transport of terrestrial DOM to the coast through SGD (Nelson et al., 2015;

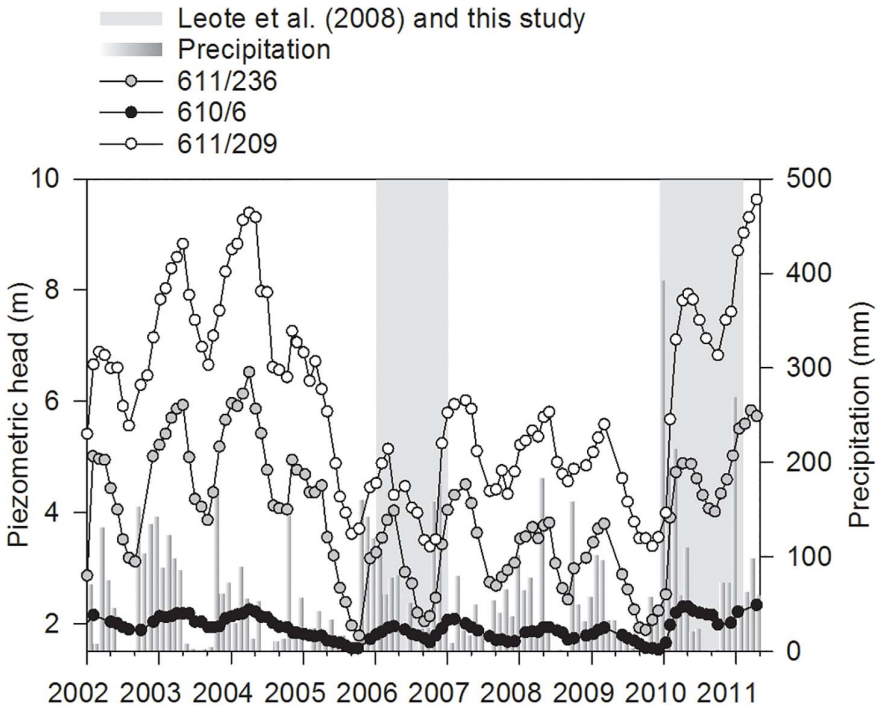


FIGURE 11 | Monthly precipitation as recorded in the meteorological station placed in the airport of Faro (37.02°N, 7.97°W) and piezometric head recorded in the 610/6 (37.02°N, 7.97°W), 611/236 (37.03°N, 7.94°W), and 611/209 (37.05°N, 7.95°W) monitoring wells of the Sistema Nacional de Informação de Recursos Hídricos (SNIRH; Portugal; https://snirh.apambiente.pt) from January 2002 until March 2011. Gray areas denote the temporal coverage of surveys presented in Leote et al. (2008) and in this study.

Kim and Kim, 2017; Cho et al., 2021). In our site, the relative abundances of FDOM humic-like components C3 and C5 were significantly correlated in water seeping out from stations A and B (**Figure 4**), suggesting that the relative abundances of C3 and C5 expressed as a ratio (FDOM C3/C5) could be a reliable tracer of SGD in the Ria Formosa lagoon. Nevertheless, inside the seepage face, the FDOM C3/C5 abundance ratio showed high spatial and temporal variability (**Figures 6**, **8**). During December 2009, at the lowest piezometric level observed inland for this study (**Figure 11**), the FDOM C3/C5 ratio was the highest of the series. A progressive enrichment in FDOM terrestrial humic-like component C5 relative to component C3 is observed afterward, except for July, in coincidence with the seasonal fall of the hydraulic gradient in the coastal aquifer during the summer. During October and January, the lowest C3/C5 ratios (i.e., higher relative contribution of the FDOM terrestrial humic-like component C5) are strongly associated with the NO_3^--rich porewater discharge tube identified (**Figures 5**, **6**), further suggesting the inland origin of the observed porewater NO_3^- enrichment during these last two surveys.

The microbial degradation of both particulate and dissolved organic matter produces humic-like FDOM compounds (Ogawa et al., 2001). Despite the presumable terrestrial origin of FDOM component C5, this humic-like fluorophore was actively produced during October and January near the sediment surface (**Figure 10**). Suryaputra et al. (2015) observed the production of this FDOM component in a microtidal STE associated to marine organic matter degradation. Furthermore, Romera-Castillo et al. (2010, 2011) suggested that humic-like FDOM component C3 is produced by eukaryotes, whereas C5 is produced by prokaryotes that are also able to use FDOM component C3 to produce C5. The blue shift of C5 compared to C3 suggests comparatively higher aromaticity (Coble et al., 1998; Stubbins et al., 2014). Thus, C5 is assumed to have higher resistance to microbial degradation but also that it is produced from more refractory organic matter compared to C3. Its persistence in the environment allows its use to fingerprint water masses with different origins in complex coastal ecosystems (Ibánhez et al., 2019). Combined, humic-like FDOM components C3 and C5 can be linked to the microbial processing of different organic matter fractions.

Protein-like FDOM components are linked to the amino acid content of aquatic ecosystems (Yamashita and Tanoue, 2003; Stubbins et al., 2014). Peptides and both intra and extracellular proteins contribute to the protein-like FDOM pool (Fox et al., 2017). In this study, samples were filtered with Rhizon SMS with a pore size of 0.1 μm, and thus, protein-like FDOM components C1 and C4 can confidently be attributed to the extracellular amino acid content in water samples. Both FDOM components are therefore labile and can feed heterotrophic microbial processes (Stubbins et al., 2014) but also their active production is a reliable proxy of microbial activity (Fox et al., 2017). This is consistent with the highly variable distribution of FDOM components C1 and C4 within the seepage face and

TABLE 1 | NO_3^- and FDOM reaction rates calculated through mass balances of solute distribution in the top 44 cm of sediment in the seepage face, organized by survey and sampling station.

	Station	Velocity	NO_3^-	FDOM protein-like		FDOM humic-like	
				C1	C4	Marine C3	Terrestrial C5
		cm h^{-1}	nmol cm^{-3} bs h^{-1}	10^{-3} R.U. bs h^{-1}			
December 09	A	16.3 ± 2.2	−0.26 ± 0.35	−16.07 ± 5.90	3.69 ± 2.62	0.76 ± 0.16	−2.57 ± 1.14
	B	11.3 ± 1.8	−0.38 ± 0.36	−10.29 ± 4.42	−6.02 ± 1.17	−1.11 ± 0.19	−0.60 ± 0.10
April 10	A	18.6 ± 3.7	0.71 ± 0.83	2.61 ± 0.86	−6.18 ± 2.80	−1.43 ± 0.29	−0.34 ± 0.08
	B	14.3 ± 2.2	0.00 ± 0.00	−8.74 ± 2.25	−4.63 ± 0.97	1.24 ± 0.19	−0.10 ± 0.02
July 10	A	14.6 ± 2.0	0.51 ± 0.26	4.80 ± 4.25	1.13 ± 0.31	−1.22 ± 0.25	−0.89 ± 0.17
	B	9.9 ± 1.6	0.00 ± 0.00	10.93 ± 11.26	1.15 ± 0.32	−1.01 ± 0.21	−0.90 ± 0.17
October 10	A	21.7 ± 2.0	−2.28 ± 1.07	3.72 ± 3.17	19.46 ± 14.14	11.56 ± 3.39	5.09 ± 1.28
	B	8.2 ± 2.7	0.17 ± 0.24	−2.11 ± 1.09	6.18 ± 2.28	4.62 ± 2.38	3.44 ± 2.10
January 11	A	13.3 ± 1.4	−0.12 ± 0.08	3.10 ± 0.95	4.39 ± 0.75	2.20 ± 0.31	1.32 ± 0.15

*Averaged porewater velocity used for these calculations is also shown. Errors are calculated from error propagation of the averaged porewater profiles and the advective velocity used. *bs "bulk" sediment.*

the observation of both apparent production and consumption patterns (**Figures 9**, **10**).

DIN and FDOM Reactivity Within the Seepage Face

Large spatial solute gradients were observed inside the seepage face (**Figures 5**, **6**) that remained stable throughout the period of sediment exposure (**Figures 6**, **7**). Particularly notable are the unstable salinity gradients observed, for instance, in the deepest piezometers of April and in stations C and B in January, that remained in place throughout the period of sediment exposure (**Figure 6**). Vertical density instabilities promote convective turnover and mixing (Rocha, 2000) and thus are not stable over time. Therefore, these unstable density gradients that persist over time must be continuously feed by the complex 3-D transport pathways present inside the beach. Nevertheless, near the sediment–water interface, the magnitude of the measured seepage rates and their validation with pressure measurements that assume vertical porewater transport (Ibánhez and Rocha, 2016), confirm that there, porewater transport is largely dominated by the vertical component.

Using the measured seepage rates during the peak of the discharge and assuming stationary state and vertical seepage (Rocha et al., 2009; Ibánhez and Rocha, 2016), we calculated solute reaction rates from the averaged, high-resolution porewater profiles from the seepage face. To ensure that vertical seepage dominates the sediment horizon studied, solute mass balances were performed with the data from the top 44 cm of sediment. Homogeneous vertical salinity is verified in the selected sediment column throughout the studied period and thus, solute gradients are confidently assigned to the local reactivity (see **Supplementary Material**), calculated as follows:

$$R = \frac{\Delta C\, q}{d} \quad (1)$$

where $\triangle C$ is the change of the target solute verified between 44 cm depth and the sample closest to the sediment surface, q is the Darcy velocity, and d is the length of the studied sediment column (44 cm).

The two different periods identified based on the presence or absence of measurable NO_3^- at the seepage face presented contrasting reactivity (**Table 1**). From December to July, NO_3^- production dominated, while the highest NO_3^- reduction rates are obtained in station A in October, coinciding with the NO_3^- enrichment in the sediment column. These nitrification and NO_3^- reduction rates are at the low end of those determined through diagenetic modeling of *in situ* porewater profiles (Ibánhez et al., 2013) and with flow-through reactor experiments (Ibánhez and Rocha, 2017) at the same site. FDOM protein-like components C1 and C4 showed variable reactivity, with a tendency toward net consumption during the first period sampled and a net production of both components during the second one. Nevertheless, the reactivity of the humic-like FDOM components showed the clearest seasonal pattern. While during the first three surveys humic-like FDOM components remained almost vertically unchanged denoted by the low reaction rates obtained, these were actively produced at high rates coinciding with the observed porewater NO_3^- enrichment at the seepage face. Overall, while during the initial period (December 2009 to July 2010) the seepage face generally acted as a sink of FDOM, during October 2010 and January 2011 net production of the four FDOM components was generally obtained.

DIN Impact Over C Storage and Processing Capacity in the STE

In intertidal sands, pelagic POM transported by seawater infiltration during high tide is trapped near the infiltration surface (de Beer et al., 2005; Rocha, 2008; Jiang et al., 2020). Thus, while solutes such as oxygen or DOC can penetrate the beach interior, POM accumulates in the surface sediments. This was clearly observed at our sampling site during the studied period, where POM content peaked at the sediment surface and decayed with depth (Ibánhez and Rocha, 2014a, 2016). Aerobic respiration and NO_3^- reduction processes at the studied site are

limited by organic C availability, showing strong limitation at depths exceeding 30–40 cm (Ibánhez et al., 2013; Ibánhez and Rocha, 2016). Similarly, intense FDOM reactivity seems to be mainly restricted to the top 30–40 cm of sediment, where FDOM components changed abundance by up to 90% (**Figure 10**).

FDOM component C5 was never actively produced from December 2009 to July 2010 (**Table 1**). This contrasts with the high rates of production of both humic-like FDOM components during October 2010 and January 2011, suggesting an enhanced C processing within the seepage face during this period, including both fresh and older organic matter. This period also showed the highest protein-like FDOM production rates, except for C1 in station B in October, suggesting an enhancement of microbial activity during October and January. Furthermore, the concomitant production of both protein-like and humic-like FDOM suggests that they are primary originated from POM processing rather than from DOC. This is supported by the location of the FDOM production zone, tightly coupled with the distribution of infiltrated pelagic POM that accumulates in the top sediment column of the studied site (Ibánhez and Rocha, 2016). Similar spatial patterns of FDOM reactivity were identified in an STE from Sanggou Bay (China) that receives significant land-derived NO_3^- loads (Jiang et al., 2020). There, the concomitant production of protein-like, humic-like FDOM and DOC under chronic porewater NO_3^- enrichment is observed in the sediment depths where POM is accumulated.

Mechanisms Underlying NO_3^--Driven Organic C Processing Enhancement in the STE

Our results are in high agreement with those presented in Ibánhez and Rocha (2014a). There, a series of flow-through reactor experiments were run with intact sediment columns from the top 12 cm and porewater collected at the study site during October 2010 and January 2011. Under a purely advective regime (15.1 ± 0.2 to 18.8 ± 0.1 cm h^{-1}; Ibánhez and Rocha, 2014a), similar to that found in the field (**Table 1**), the surface sediment metabolism is C-limited and an overall DOC and FDOM sink. Nevertheless, when the circulating porewater is spiked with NO_3^- (>100 μM final concentration), the sediment became a source of DOC, protein-like FDOM, and both humic-like FDOM components identified here, both under oxic (>220 μM O_2) and suboxic conditions (<90 μM O_2). The sudden availability of N stimulates microbial metabolism and its ability to process particulate refractory organic matter, thus mobilizing the stored POM pool. In our field surveys, active FDOM production is mainly restricted to the last two surveys where NO_3^- enrichment is observed within the seepage face. The highest rates of FDOM production are observed in station A during October, directly impacted by this enrichment in NO_3^-. In station B during October and station A during January, this NO_3^- enrichment is not observed at the peak of the discharge. Nevertheless, the lateral displacement of the NO_3^-enriched porewater discharge tube caused by tidal oscillation and mixing during active surface water infiltration during high tide could spread this NO_3^- enrichment within the seepage face, thus promoting the observed enhanced POM processing.

NO_3^- is a powerful oxidant that is used as electron acceptor by different microbial organisms (e.g., Kuypers et al., 2018). In the benthic redox cascade, i.e., the sequential use of electron acceptors by the microbial community based on favorable energy yields, NO_3^- is the most energetically efficient electron acceptor after O_2. Under anoxic conditions, the sudden availability of NO_3^- would feed heterotrophic processes such as heterotrophic denitrification that could promote the observed enhancement of organic C processing at the seepage face. Nevertheless, the sampled beach interior was well oxygenated during the surveyed period and thus, benthic aerobic respiration would not be limited by O_2 availability (see **Supplementary Material**; Ibánhez and Rocha, 2016). NO_3^- reduction under bulk benthic oxic conditions was observed at our site (Ibánhez and Rocha, 2017), and net NO_3^- reduction rates were obtained in the mass balances performed here (**Table 1**). Although aerobic denitrification was reported in permeable marine sediments (Marchant et al., 2017), NO_3^- reduction rates at our site increase when lowering the amount of O_2 in the circulating porewater, suggesting the presence of anoxic microniches within the sediment pore structure that would sustain NO_3^- reduction rates under bulk aerobic conditions (Ibánhez and Rocha, 2017). In the FTR experiments performed in parallel to the surveys presented here (Ibánhez and Rocha, 2014a), the concomitant benthic production of both humic-like and protein-like FDOM components under NO_3^- spiked porewater was similar under both oxic and suboxic conditions. There, a significant increase of the benthic production of humic-like and protein-like FDOM was verified after further adding NH_4^+ to the circulating porewater. These results suggest that, adding to the observed organic C limitation, the local microbial metabolism is also N-limited. With excess electron acceptors in place at the seepage face, porewater N enrichment promotes a priming effect over organic matter mineralization by overcoming stoichiometric constraints of microbial metabolism (Guenet et al., 2010), thus accelerating organic C turnover within the seepage face as observed in other N-deficient systems (e.g., Mack et al., 2004; Bragazza et al., 2006; Chen et al., 2020).

CONCLUSION

The large heterotrophic capacity of permeable coastal sands prevents the accumulation of labile organic matter in the sediment, driving these environments to C limitation. Together with previous research at the same site, our results also indicate that heterotrophic processes are N-limited at the seepage face. Because the progressive recovery of the inland piezometric head observed during the study period resulted in the gradual increase of NO_3^- availability at the seepage face, organic C processing there was completely changed. Sudden N transport to the seepage face appeared to catalyse POM processing, thus reducing C storage. The resulting organic metabolites are then

rapidly transported to surface waters where they become exposed to photolysis and pelagic mineralization. Overall, additional N supplied by the subterranean estuary appears to accelerate particulate organic C turnover within the system. Despite the low standing stocks of POM of these benthic environments, their large volume suggests that this mechanism may have a significant impact on the reactive resilience of the coastal C pool. Validation of these findings by elucidating the role of N supplementation on local microbial and enzymatic activity and generalization of the observations supporting this priming effect to other STEs is yet to occur.

DATA AVAILABILITY STATEMENT

The raw data supporting the conclusions of this article will be made available by the authors, without undue reservation.

AUTHOR CONTRIBUTIONS

JI and CR conceived the study. JI participated in the field and laboratory work and data analysis and elaborated the first draft of the manuscript, which was enriched by contributions of XÁ-S and CR. All authors revised and approved the manuscript.

FUNDING

Data collection and sample analysis were funded by the Portuguese Foundation for Science and Technology (FCT), the EU (FEDER), and the Portuguese Government through grant contract SFRH/BD/39170/2007 and project NITROLINKS [NITROgen loading into the Ria Formosa through Coastal Groundwater Discharge (CGD) – Pathways, turnover, and LINKS between land and sea in the Coastal Zone, PTDC/MAR/70247/2006]. Data analysis and manuscript preparation were funded by project SUBACID [SUBmarine Groundwater Discharge (SGD) impact on coastal ACIDification processes in contrasting European Atlantic Shores: toward securing ecosystem services and food production], funded by the Irish Research Council and the European Union's Horizon 2020 Research and Innovation Program under the Marie Skłodowska-Curie grant agreement no. 713279 through the CAROLINE program (CLNE/2017/210).

ACKNOWLEDGMENTS

The authors are thankful to Inês Alves and Liliana Carbalho (University of Algarve, Portugal) for field support during the December 2009 and April, July, and October 2010 fieldwork surveys and to Mark Kavanagh (Trinity College Dublin, Ireland) for laboratory support. The authors also appreciate the comments made by two reviewers that helped to improve an early version of this manuscript.

SUPPLEMENTARY MATERIAL

The Supplementary Material for this article can be found online at: https://www.frontiersin.org/articles/10.3389/fmars.2021.661201/full#supplementary-material

REFERENCES

Andersen, C. M., and Bro, R. (2003). Practical aspects of PARAFAC modeling of fluorescence excitation-emission data. *J. Chemometr.* 17, 200–215. doi: 10.1002/cem.790

Bauer, J. E., Cai, W.-J., Raymond, P. A., Bianchi, T. S., Hopkinson, C. S., and Regnier, P. A. G. (2013). The changing carbon cycle of the coastal ocean. *Nature* 504, 61–70. doi: 10.1038/nature12857

Boyer, E. W., Howarth, R. W., Galloway, J. N., Dentener, F. J., Green, P. A., and Vörösmarty, C. J. (2006). Riverine nitrogen export from the continents to the coasts. *Glob. Biogeochem. Cycles* 20:GB1S91. doi: 10.1029/2005GB002537

Bragazza, L., Freeman, C., Jones, T., Rydin, H., Limpens, J., Fenner, N., et al. (2006). Atmospheric nitrogen deposition promotes carbon loss from peat bogs. *Proc. Natl. Acad. Sci. U.S.A.* 103, 19386–19389. doi: 10.1073/pnas.0606629104

Burnett, W. C., Aggarwal, P. K., Aureli, A., Bokuniewicz, H., Cable, J. E., Charette, M. A., et al. (2006). Quantifying submarine groundwater discharge in the coastal zone via multiple methods. *Sci. Total Environ.* 367, 498–543. doi: 10.1016/j.scitotenv.2006.05.009

Burnett, W. C., Bokuniewicz, H., Huettel, M., Moore, W. S., and Taniguchi, M. (2003). Groundwater and pore water inputs to the coastal zone. *Biogeochemistry* 66, 3–33. doi: 10.1023/B:BIOG.0000006066.21240.53

Cable, J. E., Burnett, W. C., and Chanton, J. P. (1997). Magnitude and variations of groundwater seepage along a Florida Marine Shoreline. *Biogeochemistry* 38, 189–205. doi: 10.2307/1469004

Calvo-Martin, E., Álvarez-Salgado, X. A., Rocha, C., and Ibánhez, J. S. P. (2021). Reactive solute transport through two contrasting subterranean estuary exit sites in the Ría de Vigo (NW Iberian Peninsula). *Front. Mar. Sci.* 8:626813. doi: 10.3389/fmars.2021.626813

Chen, Q., Yuan, Y., Hu, Y., Wang, J., Si, G., Xu, R., et al. (2020). Excessive nitrogen addition accelerates N assimilation and P utilization by enhancing organic carbon decomposition in a Tibetan alpine steppe. *Sci. Total Environ.* 764:142848. doi: 10.1016/j.scitotenv.2020.142848

Cho, H.-M., Kim, G., Kwon, E. Y., Moosdorf, N., Garcia-Orellana, J., and Santos, I. R. (2018). Radium tracing nutrient inputs through submarine groundwater discharge in the global ocean. *Sci. Rep.* 8:2439. doi: 10.1038/s41598-018-20806-2

Cho, H.-M., Kim, T.-H., Moon, J.-H., Song, B.-C., Hwang, D.-W., Kim, T., et al. (2021). Estimating submarine groundwater discharge in Jeju volcanic island (Korea) during a typhoon (Kong-rey) using humic-fluorescent dissolved organic matter-Si mass balance. *Sci. Rep.* 11:941. doi: 10.1038/s41598-020-79381-0

Coble, P. G. (1996). Characterization of marine and terrestrial DOM in seawater using excitation-emission matrix spectroscopy. *Mar. Chem.* 51, 325–346. doi: 10.1016/0304-4203(95)00062-3

Coble, P. G., Del Castillo, C. E., and Avril, B. (1998). Distribution and optical properties of CDOM in the Arabian Sea during the 1995 Southwest Monsoon. *Deep Sea Res. 2 Top. Stud. Oceanogr.* 45, 2195–2223.

Couturier, M., Tommi-Morin, G., Sirois, M., Rao, A., Nozais, C., and Chaillou, G. (2017). Nitrogen transformations along a shallow subterranean estuary. *Biogeosciences* 14, 3321–3336. doi: 10.5194/bg-14-3321-2017

de Beer, D., Wenzhöfer, F., Ferdelman, T. G., Boeme, S. E., Huettel, M., Beusekom, J. E. E., et al. (2005). *Transport and Mineralization Rates in North Sea Sandy*

Intertidal Sediments, Sylt-Rømø Basin, Wadden Sea. Available online at: http://hdl.handle.net/10013/epic.21375 (accessed December 25, 2008)

Erisman, J. W., Sutton, M. A., Galloway, J., Klimont, Z., and Winiwarter, W. (2008). How a century of ammonia synthesis changed the world. *Nat. Geosci.* 1, 636–639. doi: 10.1038/ngeo325

Erler, D. V., Santos, I. R., Zhang, Y., Tait, D. R., Befus, K. M., Hidden, A., et al. (2014). Nitrogen transformations within a tropical subterranean estuary. *Mar. Chem.* 164, 38–47. doi: 10.1016/j.marchem.2014.05.008

Fox, B. G., Thorn, R. M. S., Anesio, A. M., and Reynolds, D. M. (2017). The in situ bacterial production of fluorescent organic matter; an investigation at a species level. *Water Res.* 125, 350–359. doi: 10.1016/j.watres.2017.08.040

Galloway, J. N., Townsend, A. R., Erisman, J. W., Bekunda, M., Cai, Z., Freney, J. R., et al. (2008). Transformation of the nitrogen cycle: recent trends, questions, and potential solutions. *Science* 320, 889–892. doi: 10.1126/science.1136674

Geng, X., Boufadel, M. C., and Jackson, N. L. (2016). Evidence of salt accumulation in beach intertidal zone due to evaporation. *Sci. Rep.* 6:31486. doi: 10.1038/srep31486

Grasshoff, K., Ehrhardt, M., and Kremling, K. (1983). *Methods of Seawater Analysis*, 2nd Edn. Weinheim: Verlag Chemie.

Gruber, N., and Galloway, J. N. (2008). An Earth-system perspective of the global nitrogen cycle. *Nature* 451, 293–296. doi: 10.1038/nature06592

Guenet, B., Danger, M., Abbadie, L., and Lacroix, G. (2010). Priming effect: bridging the gap between terrestrial and aquatic ecology. *Ecology* 91, 2850–2861. doi: 10.1890/09-1968.1

Hartog, N., van Bergen, P. F., de Leeuw, J. W., and Griffioen, J. (2004). Reactivity of organic matter in aquifer sediments: geological and geochemical controls. *Geochim. Cosmochim. Acta* 68, 1281–1292. doi: 10.1016/j.gca.2003.09.004

Hugman, R., Stigter, T., Costa, L., and Monteiro, J. P. (2017). Modeling nitrate-contaminated groundwater discharge to the ria formosa coastal lagoon (Algarve, Portugal). *Proc. Earth Planet. Sci.* 17, 650–653. doi: 10.1016/j.proeps.2016.12.174

Ibánhez, J. S. P., Arévalo, E., Kelly, T., Papaspyrou, S., Rocha, C., and Nicolaidou, A. (2019). Unraveling the dispersion and environmental impact of anthropogenic discharges in transitional water ecosystems. *Estuar. Coast. Shelf Sci.* 216, 204–217. doi: 10.1016/j.ecss.2017.11.028

Ibánhez, J. S. P., Leote, C., and Rocha, C. (2011). Porewater nitrate profiles in sandy sediments hosting submarine groundwater discharge described by an advection–dispersion-reaction model. *Biogeochemistry* 103, 159–180. doi: 10.1007/s10533-010-9454-1

Ibánhez, J. S. P., Leote, C., and Rocha, C. (2013). Seasonal enhancement of submarine groundwater discharge (SGD)-derived nitrate loading into the Ria Formosa coastal lagoon assessed by 1-D modeling of benthic NO3- profiles. *Estuar. Coast. Shelf Sci.* 132, 56–64. doi: 10.1016/j.ecss.2012.04.015

Ibánhez, J. S. P., and Rocha, C. (2014a). Effects of recirculation of seawater enriched in inorganic nitrogen on dissolved organic carbon processing in sandy seepage face sediments. *Mar. Chem.* 166, 48–58. doi: 10.1016/j.marchem.2014.09.012

Ibánhez, J. S. P., and Rocha, C. (2014b). Porewater sampling for NH 4 + with rhizon soil moisture samplers (SMS): potential artifacts induced by NH 4 + sorption. *Freshw. Sci.* 33, 1195–1203. doi: 10.1086/678483

Ibánhez, J. S. P., and Rocha, C. (2016). Oxygen transport and reactivity within a sandy seepage face in a mesotidal lagoon (Ria Formosa, Southwestern Iberia). *Limnol. Oceanogr.* 61, 61–77. doi: 10.1002/lno.10199

Ibánhez, J. S. P., and Rocha, C. (2017). Kinetics of inorganic nitrogen turnover in a sandy seepage face on a subterranean estuary. *Appl. Geochem.* 87, 108–121. doi: 10.1016/j.apgeochem.2017.10.015

Jiang, S., Zhang, Y., Jin, J., Wu, Y., Wei, Y., Wang, X., et al. (2020). Organic carbon in a seepage face of a subterranean estuary: turnover and microbial interrelations. *Sci. Total Environ.* 725:138220. doi: 10.1016/j.scitotenv.2020.138220

Johannes, R. E. (1980). The ecological significance of the submarine discharge of groundwater. *Mar. Ecol. Prog. Ser.* 3, 365–373. doi: 10.3354/meps003365

Kim, J., and Kim, G. (2017). Inputs of humic fluorescent dissolved organic matter via submarine groundwater discharge to coastal waters off a volcanic island (Jeju, Korea). *Sci. Rep.* 7:7921. doi: 10.1038/s41598-017-08518-5

Kothawala, D. N., Murphy, K. R., Stedmon, C. A., Weyhenmeyer, G. A., and Tranvik, L. J. (2013). Inner filter correction of dissolved organic matter fluorescence. *Limnol. Oceanogr. Methods* 11, 616–630. doi: 10.4319/lom.2013.11.616

Kroeger, K. D., and Charette, M. A. (2008). Nitrogen biogeochemistry of submarine groundwater discharge. *Limnol. Oceanogr.* 53, 1025–1039. doi: 10.4319/lo.2008.53.3.1025

Kuypers, M. M. M., Marchant, H. K., and Kartal, B. (2018). The microbial nitrogen-cycling network. *Nat. Rev. Microbiol.* 16, 263–276. doi: 10.1038/nrmicro.2018.9

Kwon, E. Y., Kim, G., Primeau, F., Moore, W. S., Cho, H.-M., DeVries, T., et al. (2014). Global estimate of submarine groundwater discharge based on an observationally constrained radium isotope model. *Geophys. Res. Lett.* 41, 8438–8444. doi: 10.1002/2014GL061574

Lawaetz, A. J., and Stedmon, C. A. (2009). Fluorescence intensity calibration using the Raman scatter peak of water. *Appl. Spectrosc.* 63, 936–940. doi: 10.1366/000370209788964548

Lee, D. R. (1977). A device for measuring seepage flux in lakes and estuaries. *Limnol. Oceanogr.* 22, 140–147. doi: 10.4319/lo.1977.22.1.0140

Leote, C., Ibánhez, J., and Rocha, C. (2008). Submarine groundwater discharge as a nitrogen source to the Ria Formosa studied with seepage meters. *Biogeochemistry* 88, 185–194. doi: 10.1007/s10533-008-9204-9

Luijendijk, E., Gleeson, T., and Moosdorf, N. (2020). Fresh groundwater discharge insignificant for the world's oceans but important for coastal ecosystems. *Nat. Commun.* 11:1260. doi: 10.1038/s41467-020-15064-8

Mack, M. C., Schuur, E. A. G., Bret-Harte, M. S., Shaver, G. R., and Chapin, F. S. (2004). Ecosystem carbon storage in arctic tundra reduced by long-term nutrient fertilization. *Nature* 431, 440–443. doi: 10.1038/nature02887

Mackenzie, F. T., Ver, L. M., and Lerman, A. (2002). Century-scale nitrogen and phosphorus controls of the carbon cycle. *Chem. Geol.* 190, 13–32. doi: 10.1016/S0009-2541(02)00108-0

Marchant, H. K., Ahmerkamp, S., Lavik, G., Tegetmeyer, H. E., Graf, J., Klatt, J. M., et al. (2017). Denitrifying community in coastal sediments performs aerobic and anaerobic respiration simultaneously. *ISME J.* 11, 1799–1812. doi: 10.1038/ismej.2017.51

Michael, H. A., Mulligan, A. E., and Harvey, C. F. (2005). Seasonal oscillations in water exchange between aquifers and the coastal ocean. *Nature* 436, 1145–1148. doi: 10.1038/nature03935

Moore, W. S. (1999). The subterranean estuary: a reaction zone of ground water and sea water. *Mar. Chem.* 65, 111–125. doi: 10.1016/S0304-4203(99)00014-6

Moore, W. S. (2010). The effect of submarine groundwater discharge on the ocean. *Annu. Rev. Mar. Sci.* 2, 59–88. doi: 10.1146/annurev-marine-120308-081019

Moore, W. S., and Joye, S. B. (2021). Saltwater intrusion and submarine groundwater discharge: acceleration of biogeochemical reactions in changing coastal aquifers. *Front. Earth Sci.* 9:600710. doi: 10.3389/feart.2021.600710

Murphy, K. R., Stedmon, C. A., Graeber, D., and Bro, R. (2013). Fluorescence spectroscopy and multi-way techniques. *PARAFAC. Anal. Methods* 5, 6557–6566. doi: 10.1039/C3AY41160E

Murphy, K. R., Stedmon, C. A., Wenig, P., and Bro, R. (2014). OpenFluor–an online spectral library of auto-fluorescence by organic compounds in the environment. *Anal. Methods* 6, 658–661. doi: 10.1039/C3AY41935E

Nelson, C. E., Donahue, M. J., Dulaiova, H., Goldberg, S. J., La Valle, F. F., Lubarsky, K., et al. (2015). Fluorescent dissolved organic matter as a multivariate biogeochemical tracer of submarine groundwater discharge in coral reef ecosystems. *Mar. Chem.* 177(Pt 2), 232–243. doi: 10.1016/j.marchem.2015.06.026

Ogawa, H., Amagai, Y., Koike, I., Kaiser, K., and Benner, R. (2001). Production of refractory dissolved organic matter by bacteria. *Science* 292, 917–920. doi: 10.1126/science.1057627

Pain, A. J., Martin, J. B., Young, C. R., Huang, L., and Valle-Levinson, A. (2019). Organic matter quantity and quality across salinity gradients in conduit- vs. diffuse flow-dominated subterranean estuaries. *Limnol. Oceanogr.* 64, 1386–1402. doi: 10.1002/lno.11122

Paytan, A., Shellenbarger, G. G., Street, J. H., Gonneea, M. E., Davis, K., Young, M. B., et al. (2006). Submarine groundwater discharge: an important source of new inorganic nitrogen to coral reef ecosystems. *Limnol. Oceanogr.* 51, 343–348. doi: 10.4319/lo.2006.51.1.0343

Rivett, M. O., Buss, S. R., Morgan, P., Smith, J. W. N., and Bemment, C. D. (2008). Nitrate attenuation in groundwater: a review of biogeochemical controlling processes. *Water Res.* 42, 4215–4232. doi: 10.1016/j.watres.2008.07.020

Robinson, C., Gibbes, B., Carey, H., and Li, L. (2007a). Salt-freshwater dynamics in a subterranean estuary over a spring-neap tidal cycle. *J. Geophys. Res.* 112:C09007. doi: 10.1029/2006JC003888

Robinson, C., Gibbes, B., and Li, L. (2006). Driving mechanisms for groundwater flow and salt transport in a subterranean estuary. *Geophys. Res. Lett.* 33:L03402. doi: 10.1029/2005GL025247

Robinson, C., Li, L., and Barry, D. A. (2007b). Effect of tidal forcing on a subterranean estuary. *Adv. Water Resour.* 30, 851–865. doi: 10.1016/j.advwatres.2006.07.006

Robinson, C. E., Xin, P., Santos, I. R., Charette, M. A., Li, L., and Barry, D. A. (2018). Groundwater dynamics in subterranean estuaries of coastal unconfined aquifers: controls on submarine groundwater discharge and chemical inputs to the ocean. *Adv. Water Resour.* 115, 315–331. doi: 10.1016/j.advwatres.2017.10.041

Rocha, C. (2000). Density-driven convection during flooding of warm, permeable intertidal sediments: the ecological importance of the convective turnover pump. *J. Sea Res.* 43, 1–14. doi: 10.1016/S1385-1101(00)00002-2

Rocha, C. (2008). Sandy sediments as active biogeochemical reactors: compound cycling in the fast lane. *Aquat. Microb. Ecol.* 53, 119–127. doi: 10.3354/ame01221

Rocha, C., Ibanhez, J., and Leote, C. (2009). Benthic nitrate biogeochemistry affected by tidal modulation of submarine groundwater discharge (SGD) through a sandy beach face, Ria Formosa, Southwestern Iberia. *Mar. Chem.* 115, 43–58. doi: 10.1016/j.marchem.2009.06.003

Rocha, C., Robinson, C. E., Santos, I. R., Waska, H., Michael, H. A., and Bokuniewicz, H. J. (2021). A place for subterranean estuaries in the coastal zone. *Estuar. Coast. Shelf Sci.* 250:107167. doi: 10.1016/j.ecss.2021.107167

Rocha, C., Veiga-Pires, C., Scholten, J., Knoeller, K., Gröcke, D. R., Carvalho, L., et al. (2016). Assessing land–ocean connectivity via submarine groundwater discharge (SGD) in the Ria Formosa Lagoon (Portugal): combining radon measurements and stable isotope hydrology. *Hydrol. Earth Syst. Sci.* 20, 3077–3098. doi: 10.5194/hess-20-3077-2016

Romera-Castillo, C., Nieto-Cid, M., Castro, C. G., Marrasé, C., Largier, J., Barton, E. D., et al. (2011). Fluorescence: absorption coefficient ratio–Tracing photochemical and microbial degradation processes affecting coloured dissolved organic matter in a coastal system. *Mar. Chem.* 125, 26–38. doi: 10.1016/j.marchem.2011.02.001

Romera-Castillo, C., Sarmento, H., Álvarez-Salgado, X. A., Gasol, J. M., and Marraséa, C. (2010). Production of chromophoric dissolved organic matter by marine phytoplankton. *Limnol. Oceanogr.* 55, 446–454. doi: 10.4319/lo.2010.55.1.0446

Santos, I. R., Eyre, B. D., and Huettel, M. (2012). The driving forces of porewater and groundwater flow in permeable coastal sediments: a review. *Estuar. Coast. Shelf Sci.* 98, 1–15. doi: 10.1016/j.ecss.2011.10.024

Schlesinger, W. H. (2009). On the fate of anthropogenic nitrogen. *Proc. Natl. Acad. Sci.U.S.A.* 106, 203–208. doi: 10.1073/pnas.0810193105

Schutte, C. A., Wilson, A. M., Evans, T., Moore, W. S., and Joye, S. B. (2018). Deep oxygen penetration drives nitrification in intertidal beach sands. *Limnol. Oceanogr.* 63, S193–S208. doi: 10.1002/lno.10731

Seeberg-Elverfeldt, J., Schluter, M., Feseker, T., and Kolling, M. (2005). Rhizon sampling of porewaters near the sediment-water interface of aquatic systems. *Limnol. Oceanogr. Methods* 3, 361–371. doi: 10.4319/lom.2005.3.361

Shaw, R. D., and Prepas, E. E. (1989). Anomalous, short-term influx of water into seepage meters. *Limnol. Oceanogr.* 34, 1343–1351. doi: 10.4319/lo.1989.34.7.1343

Slomp, C. P., and Van Cappellen, P. (2004). Nutrient inputs to the coastal ocean through submarine groundwater discharge: controls and potential impact. *J. Hydrol.* 295, 64–86. doi: 10.1016/j.jhydrol.2004.02.018

Stedmon, C. A., and Bro, R. (2008). Characterizing dissolved organic matter fluorescence with parallel factor analysis: a tutorial. *Limnol. Oceanogr. Methods* 6, 572–579. doi: 10.4319/lom.2008.6.572b

Stubbins, A., Lapierre, J.-F., Berggren, M., Prairie, Y., Dittmar, T., and del Giorgio, P. (2014). What's in an EEM? Molecular signatures associated with dissolved organic fluorescence in boreal Canada. *Environ. Sci. Technol.* 48, 10598–10606. doi: 10.1021/es502086e

Suryaputra, I. G. N. A., Santos, I. R., Huettel, M., Burnett, W. C., and Dittmar, T. (2015). Non-conservative behavior of fluorescent dissolved organic matter (FDOM) within a subterranean estuary. *Cont. Shelf Res.* 110, 183–190. doi: 10.1016/j.csr.2015.10.011

Tamborski, J. J., Cochran, J. K., and Bokuniewicz, H. J. (2017). Submarine groundwater discharge driven nitrogen fluxes to Long Island Sound, NY: terrestrial vs. marine sources. *Geochim. Cosmochim. Acta* 218, 40–57. doi: 10.1016/j.gca.2017.09.003

Vitousek, P. M., Mooney, H. A., Lubchenco, J., and Melillo, J. M. (1997). Human domination of Earth's ecosystems. *Science* 277, 494–499. doi: 10.1126/science.277.5325.494

Wan, J., Tokunaga, T. K., Brown, W., Newman, A. W., Dong, W., Bill, M., et al. (2021). Bedrock weathering contributes to subsurface reactive nitrogen and nitrous oxide emissions. *Nat. Geosci.* 14, 217–224. doi: 10.1038/s41561-021-00717-0

Wong, W. W., Applegate, A., Poh, S. C., and Cook, P. L. M. (2020). Biogeochemical attenuation of nitrate in a sandy subterranean estuary: insights from two stable isotope approaches. *Limnol. Oceanogr.* 65, 3098–3113. doi: 10.1002/lno.11576

Yamashita, Y., and Tanoue, E. (2003). Chemical characterization of protein-like fluorophores in DOM in relation to aromatic amino acids. *Mar. Chem.* 82, 255–271. doi: 10.1016/s0304-4203(03)00073-2

Conflict of Interest: The authors declare that the research was conducted in the absence of any commercial or financial relationships that could be construed as a potential conflict of interest.

Copyright © 2021 Ibánhez, Álvarez-Salgado and Rocha. This is an open-access article distributed under the terms of the Creative Commons Attribution License (CC BY). The use, distribution or reproduction in other forums is permitted, provided the original author(s) and the copyright owner(s) are credited and that the original publication in this journal is cited, in accordance with accepted academic practice. No use, distribution or reproduction is permitted which does not comply with these terms.

frontiers in Marine Science

ORIGINAL RESEARCH
published: 23 June 2021
doi: 10.3389/fmars.2021.642143

Response of Nitrate Processing to Bio-labile Dissolved Organic Matter Supply Under Variable Oxygen Conditions in a Sandy Beach Seepage Face

Shan Jiang[1], Jie Jin[1], Ying Wu[1], Yixue Zhang[1], Yongjun Wei[2], Carlos Rocha[3], Juan Severino Pino Ibánhez[3,4] and Jing Zhang[1,5]*

[1] State Key Laboratory of Estuarine and Coastal Research, East China Normal University, Shanghai, China, [2] Laboratory of Synthetic Biology, Key Laboratory of Advanced Drug Preparation Technologies, Ministry of Education, School of Pharmaceutical Sciences, Zhengzhou University, Zhengzhou, China, [3] Biogeochemistry Research Group, School of Natural Sciences, Trinity College Dublin, Dublin, Ireland, [4] Instituto de Investigacións Mariñas, Consejo Superior de Investigaciones Científicas (IIM-CSIC), Vigo, Spain, [5] School of Oceanography, Shanghai Jiao Tong University, Shanghai, China

OPEN ACCESS

Edited by:
Christian Lønborg, Aarhus University, Denmark

Reviewed by:
Sara Benelli, University of Parma, Italy
Soeren Ahmerkamp, Max Planck Institute for Marine Microbiology (MPG), Germany
Kaijun Lu, University of Texas at Austin, United States

***Correspondence:**
Shan Jiang
sjiang@sklec.ecnu.edu.cn

Specialty section:
This article was submitted to Marine Biogeochemistry, a section of the journal Frontiers in Marine Science

Received: *15 December 2020*
Accepted: *01 June 2021*
Published: *23 June 2021*

Citation:
Jiang S, Jin J, Wu Y, Zhang Y, Wei Y, Rocha C, Ibánhez JSP and Zhang J (2021) Response of Nitrate Processing to Bio-labile Dissolved Organic Matter Supply Under Variable Oxygen Conditions in a Sandy Beach Seepage Face. Front. Mar. Sci. 8:642143. doi: 10.3389/fmars.2021.642143

Supply of bio-labile dissolved organic matter (DOM) has been assumed to be a key factor for the intensity of nitrate (NO_3^-) removal in permeable coastal sediments. In the present study, a series of flow through reactor experiments were conducted using glucose as a N-free bio-labile DOM source to permeable sediments from a sandy beach seepage face to identify its effect on benthic NO_3^- removal. The results revealed a shift from the dominance of NO_3^- production to removal processes when NO_3^- input concentration increased from 10 to 80 μM under oxic conditions. Sediment microbiota information suggests that nitrification (e.g., *Nitrosomonas* and *Nitrososphaera*) and denitrification (e.g., *Marinobacter* and *Bacillus*) were dominant pathways for benthic NO_3^- production and removal in the studied sediment. Compared with the active response of sediment microbiota to NO_3^- additions, the supply of glucose (approximately 300 μM final concentration added) did not significantly change the NO_3^- removal efficiency under aerobic conditions (dissolved oxygen saturation approximately 100%). Similarly, an insignificant increase of NO_3^- removal rate after glucose amendment of the circulating water was obtained when dissolved oxygen (DO) saturation decreased to approximately 70% in the input solution. When DO at the input solution was decreased to 30% saturation (sub-oxic conditions), the removal rate of NO_3^- in the group amended with glucose increased, suggesting that glucose stimulated denitrifiers. These results revealed that NO_3^- removal relied mainly on the anaerobic environment at particle surfaces, with a dependence on the sedimentary organic matter as an electron supplier under bulk aerobic conditions, while the bio-labile DOM was consumed mainly by aerobic respiration instead of stimulating NO_3^- reduction. However, the respiration triggered by the over-supply of bio-labile DOM reduced the

DO in the porewater, likely depressing the activity of aerobic reactions in the permeable sediment. At this point, the benthic microbiota, especially potential denitrifiers, shifted to anaerobic reactions as the key to support nitrogen metabolism. The glucose amendment benefited NO_3^- reduction at this point, under sub-oxic conditions.

Keywords: nitrate, dissolved organic matter, denitrification, subterranean estuary, flow through reactors

INTRODUCTION

Coastal permeable sediments, mainly composed by coarse silicate or carbonate particles with a permeability $>10^{-12}$ m^2, cover more than 70% of global coastal areas (Huettel et al., 2014). In this permeable environment, advection is the dominant pathway for the transport and dispersion of solutes in porewater (Jiang et al., 2021a), and feeds a wide range of biogeochemical reactions (Huettel et al., 2014; Mouret et al., 2020). Bioavailable nitrogen (N) has been intensively introduced into terrestrial ecosystems via different anthropogenic activities. The indiscriminate use of fertilizers, manure and waste sludge in land together with industrial spillages has led to the widespread accumulation of nitrate (NO_3^-) in coastal groundwater on a global scale (Rivett et al., 2008). Coupled with the transport of groundwater from aquifers to coastal oceans driven by hydraulic gradients, a significant portion of land-derived NO_3^- reaches permeable coastal sediments in subterranean estuaries (STEs; defined as the underground mixing zone between continental groundwater and infiltrating seawater; Moore, 1999) prior to discharge to the coast (Jung et al., 2020; Ibánhez et al., 2021a). High groundwater-borne NO_3^- loadings frequently trigger a series of negative feedbacks on coastal ecosystems such as blooms of toxic phytoplankton, accumulation of organic matter, and oxygen depletion (Troccoli-Ghinaglia et al., 2010; Amato et al., 2016; Rocha et al., 2016).

As active reactors in coastal belts, permeable sediments have a strong capability to modulate NO_3^- mass transport via a wide range of biogeochemical reactions, such as autotrophic nitrification, microbial assimilation, and heterotrophic denitrification (Marchant et al., 2014; Kuypers et al., 2018; Ahmerkamp et al., 2020; Jiang et al., 2021c). The main pathway for NO_3^- removal in permeable coastal sediments is frequently identified as denitrification (Ibánhez et al., 2013; Marchant et al., 2014; Ibánhez and Rocha, 2017). Denitrification rates in permeable sediments are deemed to be deeply influenced by environmental factors, including the supply of organic matter, dissolved oxygen (DO) concentration, and advection rate, etc. (Santos et al., 2012; Ibánhez and Rocha, 2017; Ahmerkamp et al., 2020). As a heterotrophic microbial pathway, organic matter availability has widely been acknowledged to be a key factor for benthic denitrification (Crawshaw et al., 2019). In intertidal permeable sediments, the organic matter inventory includes both dissolved organic matter (DOM) and sedimentary organic matter (SOM). There, DOM shows high mobility due to seawater intrusion caused by tidal pumping, wave setup and temperature-driven porewater movement (Suryaputra et al., 2015; Meredith et al., 2020), while the SOM concentration is frequently related to adsorption and retention of particulate organic matter near the infiltration zones (Jiang et al., 2020). Both DOM and SOM can feed carbon-dependent reactions (Weston and Joye, 2005). In terms of denitrification, previous research outcomes frequently assumed that bio-labile DOM would control sediment/soil denitrification capability according to the requirement of electron transfer from carbon compounds (Cornwell et al., 1999; Bernhardt and Likens, 2002; Surey et al., 2020). However, permeable sediments are frequently enriched in DO by porewater exchange with DO saturated seawater and DO diffusion from the atmosphere (Berg et al., 2013; Ibánhez and Rocha, 2016). The bio-labile DOM might be consumed in aerobic mineralization prior to be available for denitrification (Jiang et al., 2018), suggesting a possible spatial isolation between bio-labile DOM enrichment and denitrifiers (e.g., spatial mismatch in coastal aquifers; Siemens et al., 2003). In addition, DO availability might directly hamper the denitrifying bacterial activity, leading to depression of denitrification process rates under oxic conditions (Evard et al., 2012). Alternatively, the consumption of bio-labile DOM in aerobic reactions triggers the decline of DO in porewater (Heiss et al., 2020), creating sub-oxic or anaerobic environments that are suitable for benthic denitrifiers along the porewater transport path (Kessler et al., 2012; Heiss et al., 2020). Nevertheless, our understanding of the interrelations between bio-labile DOM and DO supply and denitrification, i.e., the dominant pathway of NO_3^- removal, in coastal sands is still limited and hinders our understanding of NO_3^- cycling in coastal permeable environments and the resulting NO_3^- fluxes across the land-ocean boundary.

Targeting this knowledge gap, in the present study, a series of laboratory simulations were conducted using flow through reactor (FTR) cells to mimic the dominant advective transport pathways of coastal sands. Glucose was added to the pumped solution as a source of bio-labile DOM to sediment microbes. In addition, the DO concentration in the input solution was adjusted by injecting nitrogen gas. Rates of NO_3^- removal and production were evaluated under different levels of glucose and DO availability. The main hypothesis of the present study was that glucose amendment could significantly stimulate NO_3^- removal rates. The research aim was to test the hypothesis and evaluate the possible mechanisms underlying observed reaction patterns.

MATERIALS AND METHODS

Sample Collection

Permeable coastal sediments were collected from a sandy beach located at the inner part of Sanggou Bay (China). The porosity of the beach sediment was approximately 0.31 and the mean hydraulic conductivity of the sampled sandy sediments was

7.5×10^{-5} m s^{-1}. There, the outflow of low salinity porewater into the bay was verified during ebb tide (Jiang et al., 2020). This brackish water discharge is associated to continental groundwater inputs that also trigger the porewater enrichment in radium isotopes and nutrients (Wang et al., 2014). Around Sanggou Bay, agriculture activities, mainly focused on apples, corn and wheat are intensively developed. These activities lead to a significant accumulation of NO_3^- in the terrestrial groundwaters surrounding the bay, with concentrations >350 μM in coastal wells (Wang et al., 2014). This continental groundwater enriched with NO_3^- reaches the sampled seepage face, leading to a variation of NO_3^- concentration from 20 to 60 μM in porewater. DOC concentrations locally vary between 180 and 390 μM, while the P concentration in the porewater was much lower (below 2 μM) due to adsorption on sandy particles (Wang et al., 2014). Apart from agriculture, the local economy is also supported by intensive marine culture activities conducted in the bay (Fang et al., 2016). High-biomass primary producers, such as diatoms and kelp, introduce a significant amount of pelagic DOM into the bay water via basic metabolism (e.g., secretion), diffusion across the cell membrane and decomposition (Thornton, 2014; Mahmood et al., 2017). This pelagic DOM is injected into the seepage face with seawater infiltration, creating a local mixing zone between bio-labile DOM and terrestrial NO_3^-. Sediment cores (20 cm depth, 10 cm diameter) were collected in the seepage face during ebb tide in April (spring) and October (autumn) 2018. Sediment at the sampling site presented a large accumulation of bivalve debris at the surface originated from the intense bivalve aquaculture in the area. This surface layer of bivalve debris (typically 0–1 cm depth) was removed before the collection of sediment cores.

Laboratory FTR Simulation

Flow through reactor cells were used to mimic *in situ* advective conditions and thus explore benthic reactions in the seepage face (**Figure 1**). FTR cells of 10 cm length and approximately 8 cm of diameter were used (total volume for sediments: 500 cm^3). These include two collimators and fine meshes (pore size: 30 μm) to ensure an even transversal distribution of the pumped solutions through the incubated sediments. After collection, the sediments were gently repacked into the reactor cells after removing large pieces of debris and the inner walls of the cells were scrubbed to increase the contact between sediment particles and the containers and hence to eliminate the build-up of preferential flow paths along the walls. Aluminum foil was wrapped around each cell to eliminate the influence of light exposure on benthic microbial activity or primary producers. After setting up, all FTR cells were placed into a thermo-constant incubator at 20°C, which was comparable to the porewater temperature during both sampled seasons (Jiang et al., 2020). FTR cells were then flushed with seawater overnight (approximately 10 h) at a constant rate of 3 mL min^{-1} (discharge rate as 11.5 cm h^{-1}), equivalent to the advection rate quantified in the seepage face during active seepage (Jiang et al., 2020). With these conditions, porewater retention time was calculated as the quotient of system flow rate and total porewater volume (product of total sediment volume and porosity) in a cell (approximately 52 min). Afterward, the flushed sediment from three reactors was kept for further physico-chemical analyses.

After conditioning of the FTR cells, the working solutions were pumped through the test reactor cells using a high-accuracy peristaltic pump (BT-100, Longer®, China) at the same pumping rate as that used during the flushing period. The series of sediment incubations included seven groups (one control and six treatments) with different levels of NO_3^-, dissolved organic carbon (DOC) and DO in the input solution, as outlined in **Table 1**. The carrier solution used was aged seawater (storage > 100 days) with a salinity of 33 to maintain strict control on the labile DOM content of the circulating porewater. In the six treatments, NO_3^- was kept constant (∼80 μM), while DOC concentrations ranged from ca. 140 (i.e., without amendment) to 480 μM via the addition of glucose. Additionally, three different DO levels in the input solution were employed (**Table 1**). In the DO saturation group (approximately 240 μM), the working solution was bubbled with air before the incubation. For the DO unsaturation groups (70% saturation: nearly 170 μM), nitrogen gas (99.999% purity) was bubbled into the working solution from the bottom of the container at a constant rate for the partial removal of DO. For groups with 30% DO saturation (nearly 75 μM), the input solution was treated in an ultrasonic bath for 3 min prior to the start of the bubbling process. For each treatment, triplicate reactor cells were used. During the experiments, the complete replacement of the porewater inside the FTR cells was determined by dye tracer release-balance (input concentration was identical to output concentration), and it was complete after approximately 3 h at the settled pumping rate (3 mL min^{-1}) based on the input-output balancing experiments using Rhodamine tracer (the input and output balance displayed in **Supplementary Figure 1**). Accordingly, sampling of the input and outflow solutions from each reactor took place after pumping the working solution for 6 h to guarantee solute dispersion in sediments (**Figure 1**). In each reactor, four samplings were conducted at 1 h intervals. The collected samples were filtered with Millipore syringe filters (0.22 μm pore size) and stored in acid prewashed plastic bottles for dissolved inorganic nitrogen (DIN) species and pre-combusted glass vials for DOC and chromophoric dissolved organic matter (CDOM) determinations and kept at −20°C prior to laboratory analyses to avoid potential microbial degradation of the samples (Jiang et al., 2017). Besides the collection of water samples, DO concentrations at both the input solution and the outflow stream were directly measured with a portable probe (WTW Multi 3630). Reaction rates for DIN species, DOC and DO were calculated from the difference in concentration between the input and the output solutions, porewater residence time (52 min) and the sediment volume contained in the FTR cell (500 cm^{-3}) according to Ibánhez and Rocha (2014). Negative reaction rates indicate consumption of the target solute within the sediment, while positive values represent benthic production.

Sediment Physico-Chemical Analyses

Total organic carbon (TOC) content in the sediment samples was determined via a CHNOS Elementar cube (Vario EL III)

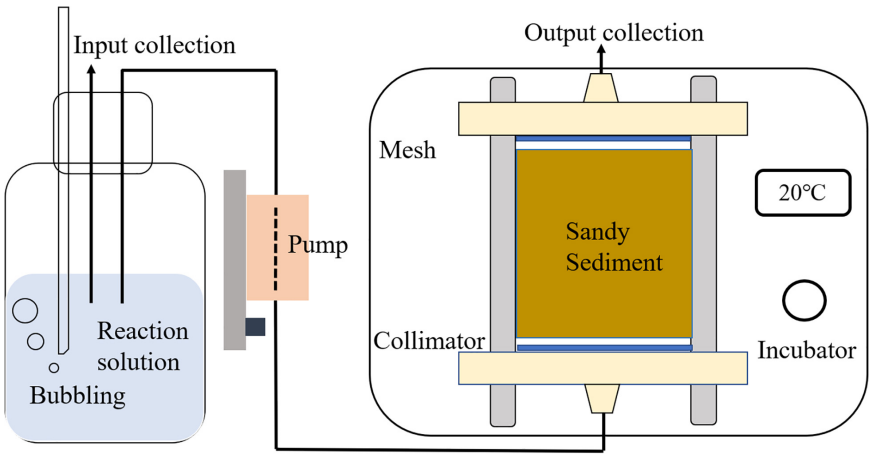


FIGURE 1 | Sketch of flow through reactor (FTR) experiments established in the laboratory. This set highlights the injection of nitrogen gas into the reaction liquid to regulate the oxygen content level. This sketch is modified from Jiang et al. (2018).

TABLE 1 | Initial concentrations of DOC, NO_3^-, and DO in each batch of the flow through reactor (FTR) incubation experiment.

Group	DOC Spring	DOC Autumn	NO_3^- Spring	NO_3^- Autumn	DO Spring	DO Autumn
Low control	142 ± 2.5	133 ± 2.4	10.5 ± 0.2	10.2 ± 0.3	101 ± 1.5	100 ± 2.6
NO_3^--high DO	144 ± 1.9	131 ± 3.5	79.5 ± 0.8	76.8 ± 1.0	99.8 ± 1.2	99.2 ± 2.2
NO_3^--medium DO	141 ± 2.2	135 ± 2.8	77.4 ± 1.1	80.2 ± 1.3	70.4 ± 4.1	71.9 ± 3.9
NO_3^--low DO	145 ± 1.9	132 ± 3.7	79.4 ± 1.9	76.7 ± 1.2	32.7 ± 5.2	35.1 ± 3.4
Glucose-high DO	479 ± 6.1	451 ± 5.2	80.5 ± 1.2	78.2 ± 0.8	100 ± 1.6	99.4 ± 1.9
Glucose-medium DO	486 ± 4.7	455 ± 4.9	79.5 ± 1.2	80.4 ± 1.3	72.4 ± 4.8	73.5 ± 4.4
Glucose-low DO	481 ± 5.8	460 ± 4.8	78.4 ± 1.4	79.6 ± 1.5	30.6 ± 5.7	32.5 ± 4.9

The unit for dissolved organic carbon (DOC) and NO_3^- in the table is μM and unit for dissolved oxygen (DO) is%. It shows the mean ± stand deviation on the basis of triplicate measurements.

after removing inorganic fractions using 2 M hydrochloric acid (Wu et al., 2019). Sediment total nitrogen (TN) concentration was measured with the same equipment without the acid pretreatment. The equipment accuracy for TOC and TN determinations in sandy sediments was approximately 5%. Exchangeable DIN, DOC, and CDOM from sediment particles (approximately 4 g dry weight) was extracted with a 0.5 M potassium chloride (KCl, approximately 40 mL) solution for 12 h under constant agitation, with a rotation rate of 200 rpm (20°C). Subsequently, the supernatant was filtered with syringe filters and kept at −20°C until analysis. Sediment grain size was measured using a Coulter LS 100Q particle analyzer (Coulter Company, United States). The particle size <2 μm was defined as clay, 2–63 μm as silt, and >63 μm as sandy grains (Wu et al., 2019).

Sediment samples from both sampled seasons were also used in a series of adsorption experiments to quantitively determine the influence of adsorption on glucose and NO_3^- concentrations under aerobic conditions. In particular, the sediment used in the adsorption was autoclaved for 30 min at 121°C to eliminate the influence of sediment prokaryotes (Jiang et al., 2018). After gently washing with filtered seawater, the autoclaved sediments (10 g) were mixed with aged seawater (40 mL) spiked with NO_3^- (final concentration: 80 μM) and glucose (final DOC concentration: 480 μM), respectively. The adsorption experiments covered incubation periods ranging from 0.5 to 12 h. The spiked solutions before and after adsorption experiments were collected and stored for laboratory analyses. The adsorbed quantity of glucose and NO_3^- was calculated from the solute concentration difference in these two solutions divided by the sediment dry weight (Ibánhez and Rocha, 2017).

Sediment Microbial Analyses

Total DNA from approximately 0.30 g of sediment was extracted using the DNeasy PowerSoil Kit (Qiagen, Germany). Primers for the V3–V4 regions for 16S rDNA were designated to identify microbial diversity (Wei et al., 2021). The 16S rDNA gene amplicon library from PCR cycling was constructed with the KAPA Hyper Prep Kit (Roche). The built library was paired-end sequenced on an Illumina Miseq system (Illumina). The raw reads have been deposited in the NCBI database. The diversity indices from the spring and autumn samples, including the Shannon index and Equitability, were analyzed with USEARCH alpha_div (Edgar, 2010).

Water Analyses

Dissolved inorganic nitrogen species (NH_4^+, NO_2^-, and NO_3^-) in the samples collected from the FTR experiments, the solutions for extraction of the sediment exchangeable compounds and

adsorption experiments (only NO_3^-) were quantified using a flow injection system (SAN++ plus, SKALAR Analytical B.V., Netherlands). DOC concentrations in these water samples were analyzed by high-temperature catalytic combustion using a Shimadzu TOC-LCPH TOC analyzer (TOC-LCPH, Shimadzu, Japan) with an ASI-L autosampler (Jiang et al., 2020). CDOM of the collected water samples was analyzed on a dual channel spectrophotometer (PERSEE®, China, TU-1901) with ultrapure water as blank (water resistivity: 18.2 MΩ cm). After equipment stabilization, CDOM samples were continuously scanned from 400 to 250 nm on the spectrophotometer with 1 nm intervals. CDOM content in the tested water samples was estimated by the absorption coefficient at 355 nm (a_{355}, Zhang et al., 2007). In addition, the spectral slope from 275 to 295 nm was determined as a proxy of the molecular weight of CDOM ($S_{275-295}$; terrestrial materials frequently show small slopes, while pelagic materials tend to show larger slopes; Zhang et al., 2007). The isotopic composition of NO_3^- ($\delta^{15}N/^{18}O–NO_3^-$) was determined in the collected samples to understand reaction pathways and rates in place (Jiang et al., 2019, 2021b). The isotopic ratios were measured by the bacterial reduction method (Sigman et al., 2001) using a Thermo-Fisher Delta V advantage analyzer coupled with a PreCon system (more details in Jin et al., 2020). The method reproductivity was approximately 0.2‰ for $\delta^{15}N–NO_3^-$ and 0.5‰ for $\delta^{18}O–NO_3^-$.

Statistical Analyses

To explore the effect of glucose supply on NO_3^- removal rate under different DO saturations, a series of one-way ANOVAs and Tukey Honestly Significant Difference (HSD) test were performed with the Minitab software (version 17.0) with the statistical significance as $p < 0.05$. Linear correlation between variables was also explored with Minitab.

RESULTS

Sediment Physico-Chemical Factors and Variability

During the two sampled periods, the mean grain size of the collected sediment, mostly composed by sand, was highly similar (204 μm mean grain size in spring to 199 μm mean grain size during autumn, **Table 2**). The grain skewness was 0.23 in spring and 0.31 in autumn and the kurtosis was ∼2.4 during both seasons. Sediment TOC concentration, determined before the use of the working solutions in the FTR experiments, was 92.5 μmol g^{-1} during spring, and decreased to 72.4 μmol g^{-1} in autumn (**Supplementary Figure 2**). TN content was 7.2 and 5.9 μmol g^{-1} during spring and autumn, respectively. No significant variations of TOC and TN were observed among treatments after the FTR incubations (**Figures 2A,B**). Compared with TN content, concentrations of exchangeable DIN species on sediment particles were much lower (**Table 2**). In addition, the FTR incubations slightly decreased the exchangeable NH_4^+ concentration in the control group as well as DO saturation and 70% saturation treatments during autumn, while the exchangeable NH_4^+ content increased in all the FTR groups containing NO_3^- amended circulating water during spring (groups B–D, **Figure 2C**). Compared with extracted NH_4^+, the exchangeable NO_3^- ($E–NO_3^-$) content was 3–4 times lower (**Supplementary Figure 2**). During spring, the offset in $E–NO_3^-$ became smaller as DO increased, while a reverse trend was found in autumn (**Figure 2D**). As a minor contributor to the DIN pool, extracted NO_2^- concentrations were <1 nmol g^{-1} (**Supplementary Figure 2**).

Solute Adsorption and Heterogeneous Equilibrium in the Studied Sediments

During spring, the adsorbed glucose in the tested sediment was ∼0.03 μmol glucose g^{-1} after 0.5 h incubation regardless of the adsorption of other DOC solutes (**Supplementary Figure 2**). The adsorbed amount logarithmically increased when the incubation time prolonged, reaching 0.14 μmol glucose g^{-1} after 12 h. During autumn, the sediment still retained glucose from the reaction solution via adsorption, similarly to the pattern observed during spring. The NO_3^- content remained relatively constant after 4 h of incubation in spite of the weak NO_3^- adsorption capacity shown by the sediments (**Supplementary Figure 2**), indicating that adsorption was fast.

Dissolved Oxygen and DOM Variation

The DO content in the working solutions was set at three different levels. In the DO saturated group, the DO concentration at the input solution was approximately 230 μM (**Supplementary Figure 3**). After flowing through the sediments, DO concentrations decreased (**Supplementary Figure 3**). In the control group, the outflow stream DO content decreased approximately 30 μM DO, implying benthic respiration rates of 12.9 and 11.6 nmol g^{-1} h^{-1} during spring and autumn, respectively. Introducing NO_3^- did not significantly change the DO consumption rate (group B), while the DO consumption was negatively influenced by the decreasing DO concentration in the input solution (groups C and D). The amendment of the circulating solution with glucose significantly increased DO consumption rates (group E; $p < 0.01$) while a decay in benthic respiration rates at suboxic conditions (groups F and G) was observed for both seasons. Different from DO, the sediment acted as a net source of DOC in the control group, especially during spring (**Figure 3B**). The addition of NO_3^- enhanced the DOC production rate (group B), while decreasing DO in the input solution slightly reduced DOC production rates. In contrast, glucose addition to the circulating solution completely changed the sediment mediation of DOC fluxes into a strong DOC sink due to the rapid consumption of glucose. For CDOM (a_{355}), sediments in all groups showed a production trend (**Figure 3C**), especially at the group B during both seasons (DO saturation, spiked with NO_3^-). After flowing through the sediment, $S_{275-295}$, the index of DOM structure, increased in all groups, revealing increases of small-molecular DOM in the porewater via benthic reactions. The most active addition still occurred at group B during both seasons, while the slowest addition was found at the groups run under suboxic conditions (**Figure 3D**).

TABLE 2 | Sediment physico-chemical characteristics and microbial indices determined during spring and autumn.

		Spring	Autumn
Physico-chemical Factors	Gran size (μm)	204 ± 4.5	199 ± 6.4
	Sandy grains (%)	91.2 ± 1.2	90.7 ± 0.7
	TOC (μmol g^{-1})	92.5 ± 1.6	72.4 ± 1.4
	TN (μmol g^{-1})	7.2 ± 0.3	5.9 ± 0.2
	E-NH_4^+ (nmol g^{-1})	88 ± 2.8	72 ± 1.9
	E-NO_2^- (nmol g^{-1})	0.6 ± 0.02	0.7 ± 0.05
	E-NO_3^- (nmol g^{-1})	19.2 ± 0.6	18.0 ± 0.4
Microbial factors	OTUs	1288	2454
	Shannon	7.33	8.29
	Equitability	0.709	0.736
	Dominant phylum	*Proteobacteria*	*Proteobacteria*
	Opportunistic phylum	*Bacteroidetes*, *Firmicutes*	*Actinobacteria*, *Acidobacteria*
	Key genus	*Sphingobium*	*Nitrosomonas*
		Marinobacter	*Gp10*
		Thioprofundum	*Thioprofundum*
	Potential denitrifiers	*Marinobacter*	*Marinobacter*
		Bacillus	*Bacillus*
		Lactobacillus	*Hyphomicrobium*

Physico-chemical characteristics in the table include the mean ± standard deviation of triplicate measurements. E-NH_4^+/NO_2^-/NO_3^- is the exchangeable NH_4^+/NO_2^-/NO_3^- species extracted from the sediment particles with KCl.

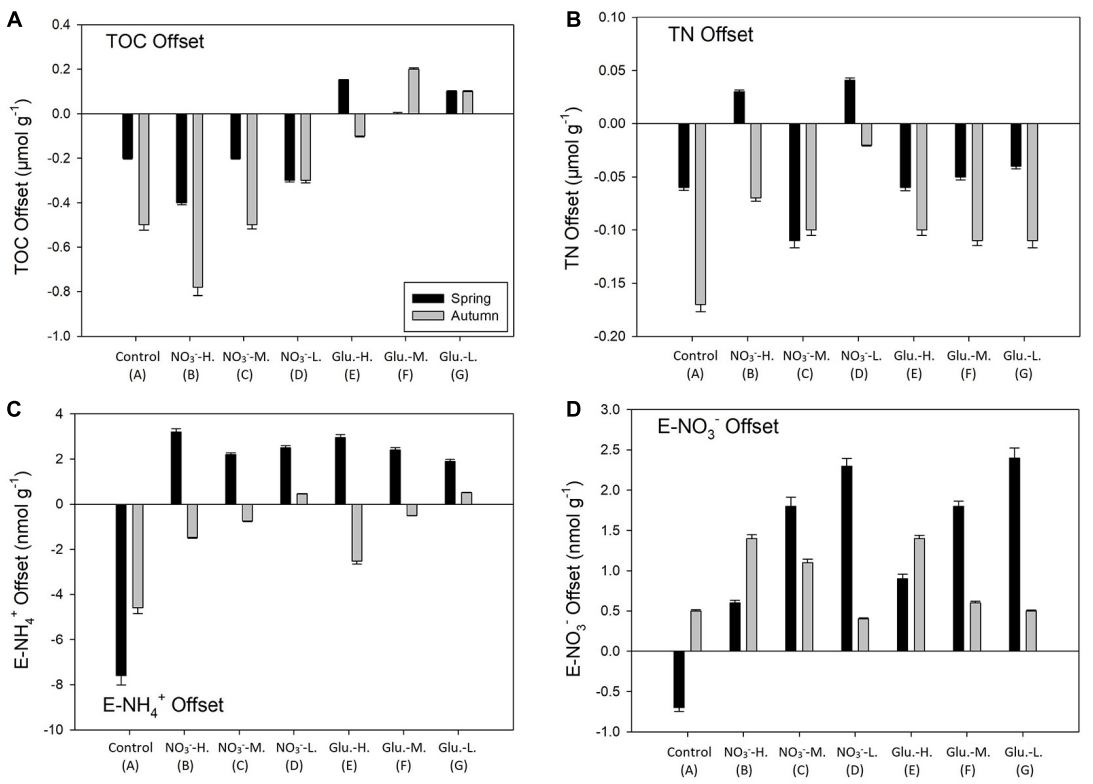


FIGURE 2 | The offset of sediment total organic carbon (TOC) **(A)**, TN **(B)**, exchangeable NH_4^+ (E-NH_4^+, **C**) and exchangeable NO_3^- (E-NO_3^-, **D**) before and after a series of incubations during spring and autumn. Positive values indicate solute concentration increases after incubation and negative is concentration decreases.

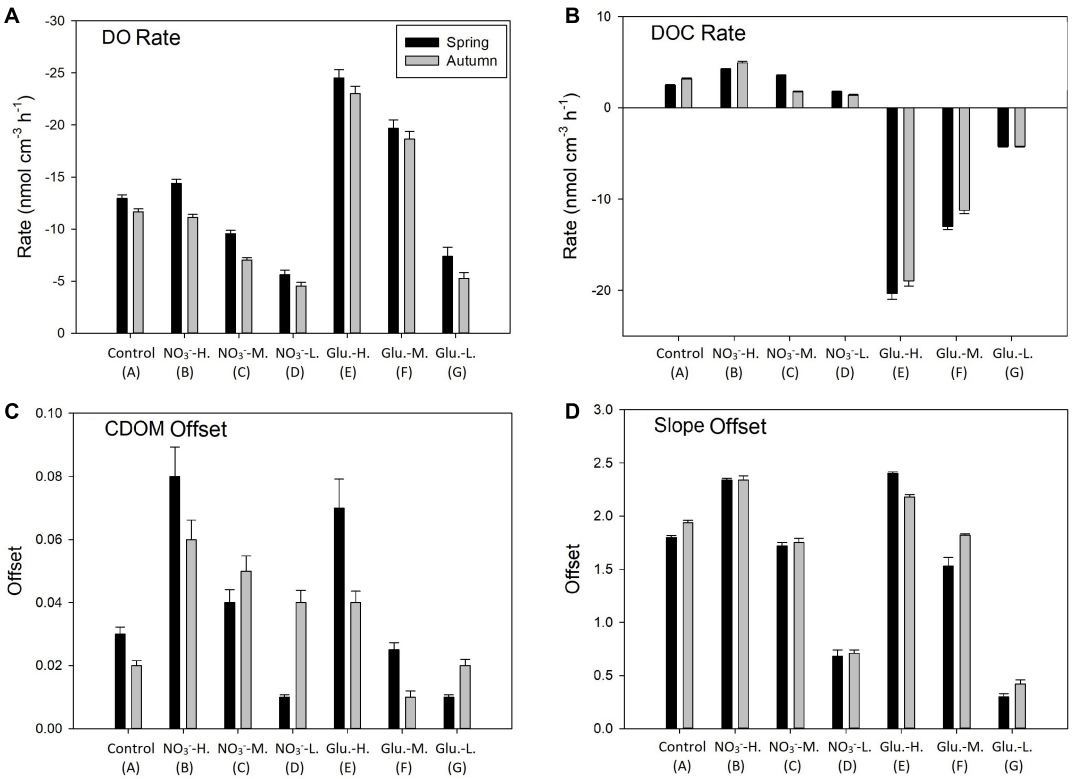


FIGURE 3 | Reaction rates for dissolved oxygen (DO) **(A)** and dissolved organic carbon (DOC) **(B)** during spring and autumn, as well as offsets for chromophoric dissolved organic matter (CDOM) characters (**C** for a_{355}; **D** for $S_{275-295}$) before and after FTR incubations during both seasons. Positive values indicate production/offset enhancement after incubation and negative is removal/offset decrease.

Dissolved Inorganic Nitrogen Species and NO_3^- Isotopes

Similarly, the sediment acted as a net source of NH_4^+ in the control group during both seasons (**Figure 4A**). The amendment of NO_3^- decreased the NH_4^+ production rate during spring, although the sediment still acted as a net NH_4^+ source (group B). The NH_4^+ production was stimulated by NO_3^- addition during autumn. In contrast, the decrease of DO concentration in the input solution significantly decreased the NH_4^+ production rate during both seasons ($p = 0.01$), especially after the concomitant amendment with glucose (group G). Compared with NH_4^+, NO_2^- concentrations in both input and output solutions were much lower, ranging from 0.31 to 0.47 μM (**Supplementary Figure 4**). Such low concentrations led to minor variations among groups (**Figure 4B**).

Different to the mediation of NO_2^- fluxes, the sediment acted as a net source of NO_3^- in the control group during both seasons (**Figure 5A**), leading to a decrease in both $\delta^{15}N$–NO_3^- (**Figure 5B**) and $\delta^{18}O$–NO_3^- (**Supplementary Figure 5**). The sediment became a net NO_3^- sink in response to amendment with NO_3^-, while the NH_4^+ production and DO consumption rates remained similar under oxic conditions (**Figures 4C,D**). Amongst the different treatments, the glucose addition did not significantly decrease the NO_3^- concentration in the output solutions under aerobic conditions (group B vs. E). Accordingly, the isotope offset of both $\delta^{15}N$–NO_3^- and $\delta^{18}O$–NO_3^- (difference between the input and output fractions) was statistically similar between these two groups. Even when the DO concentration in the input solution dropped to 70% saturation, the glucose stimulation of NO_3^- removal rates was still insignificant (group C vs. F) and the isotopic response was similar. In the sub-oxic groups (D and G), NO_3^- removal rates significantly increased compared to the oxic group ($p = 0.01$), leading to a linear relationship between NO_3^- reduction rates and $\delta^{15}N$–NO_3^- increase (**Figure 5C**). In terms of the offset between $\delta^{15}N$–NO_3^- and $\delta^{18}O$–NO_3^- (**Figure 5D**), a linear correlation was observed, suggesting that the dominant NO_3^- consumption pathway remained the same from B to G groups.

Benthic Prokaryotes

During spring, the operational taxonomic units (OTUs) in the sediment were 1,288, increasing to 2,454 during autumn (**Table 2**). Concurrently, the Shannon index and Equitability also increased during autumn. In both periods, the dominant phylum was *Proteobacteria* while important opportunistic groups varied between seasons. The key genera were *Sphingobium*, *Marinobacter*, and *Thioprofundum* during spring, while the relative abundance of *Nitrosopumilus* and *Gp10* increased during autumn. For the potential metabolic functionality (**Supplementary Figure 6**), a wide range of functions were

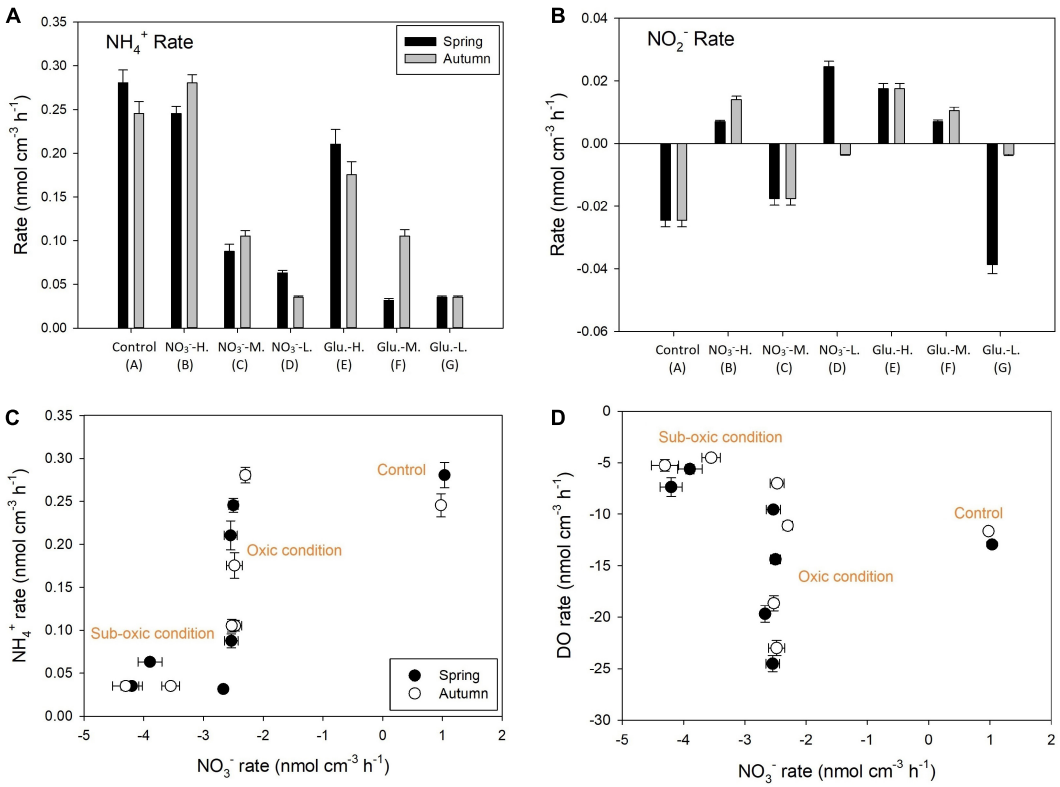


FIGURE 4 | Reaction rates of NH_4^+ **(A)** and NO_2^- **(B)** during spring and autumn. Positive rates indicate production after incubation and negative is removal. It also shows the correlation between NH_4^+ and NO_3^- reaction rates **(C)** and DO and NO_3^- reaction rates **(D)**.

present with benthic carbon, nitrogen and sulfur metabolism, suggesting a significant requirement of electron donors. The nitrogen metabolism was also taken as a key function with a minor seasonal variation. For the microbiota involved in nitrogen transformations, nitrifiers, e.g., *Nitrosopumilus*, were observed in the seepage face. Denitrifying bacteria, characterized at the genus level, such as *Marinobacter*, *Bacillus*, *Hyphomicrobium*, or *Lactobabillus*, were also observed in the sediment (**Table 2**). The microorganisms involved in Anammox and DNRA were not identified at the genus level in the studied seepage face, indicating that NO_3^- removal was mainly conducted by denitrification.

DISCUSSION

Methodological Considerations of the Use of FTR

Flow through reactor simulations under pre-defined environmental conditions, have been identified as an effective tool to quantitively determine nitrogen transformations in permeable coastal sediments, and have been widely applied in many research sites, e.g., Ria Formosa Lagoon, Portugal (Ibánhez and Rocha, 2014, 2016); South Atlantic Bight (Rao et al., 2007) and the North Sea (Marchant et al., 2016). FTR can effectively mimic 1-D advective flow in permeable sediments, adequately simulating the essentially vertical nature of porewater transport in the seepage face during ebbing tide (Ibánhez et al., 2011). The use of FTR with permeable sediments requires a "checklist" prior to laboratory incubations. Apart from flow rate, light exposure and reasonable temperature, the preferential flow paths that might form inside the cells are one of the pivotal factors in FTR simulations, and may lead to uneven transport and dispersion of the target solutes within the reactor cells, questioning the reliability of the reaction rates obtained. In the present study, these environmental variables were constrained at laboratory conditions with limited fluctuations during incubation experiments to reduce the potential errors. To further identify the reliability of our simulation results, a comparison of the obtained reaction rates with *in situ* rates was undertaken. During *in situ* field surveys at the sampling site, the DOC production ranged from 12.5 to 68.9 nmol cm^{-3} h^{-1} during spring and 2.8–62.7 nmol cm^{-3} h^{-1} during autumn, calculated from solute distribution at the seepage face together with measured seepage rates and applying mass balance approaches (data from Jiang et al., 2020). The reaction rates obtained in the FTR experiments were similar to the lower boundary of these *in situ* data. Moreover, on a global scale, the DOC production rates obtained in the present study are in line with the results found in a subterranean estuary seepage face in the Ria Formosa Lagoon, Portugal (FTR experiments; Ibánhez and Rocha, 2014). The DO consumption rate in the control group was 12.9 nmol cm^{-3} h^{-1} during spring, which was in line with

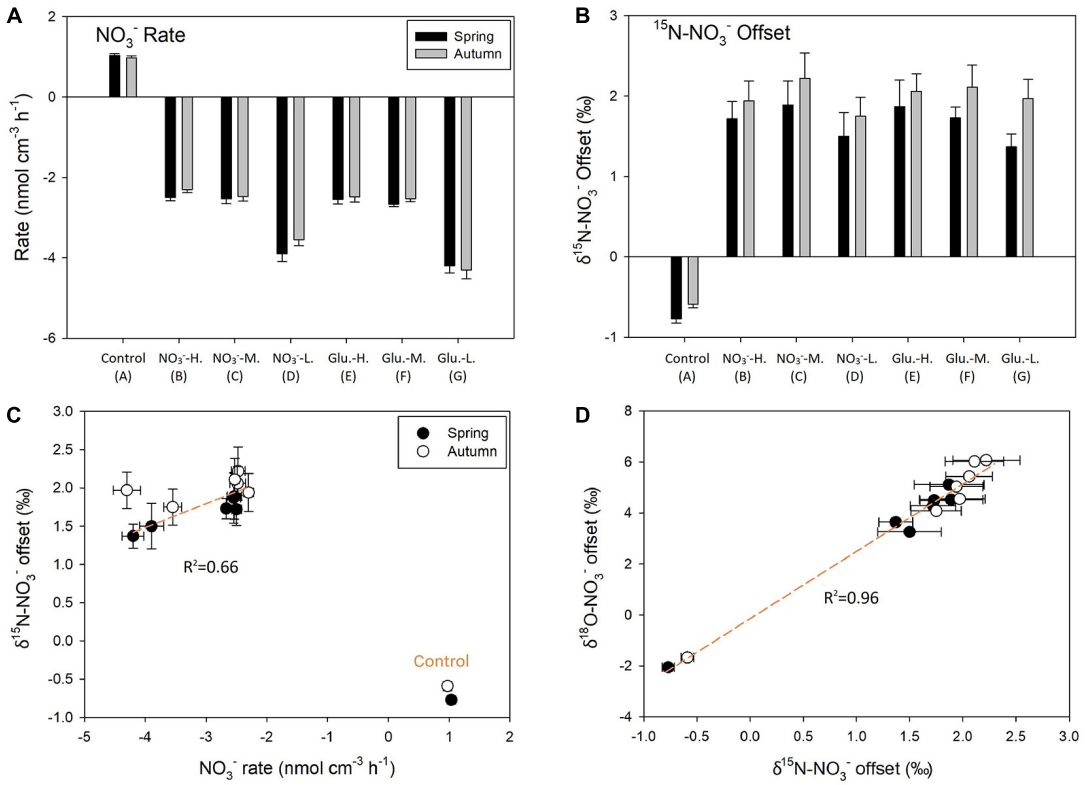


FIGURE 5 | Reaction rates NO_3^- during both seasons **(A)** and offsets for $\delta^{15}N$–NO_3^- from a series of incubations **(B)**. Positive values indicate production/offset enhancement after incubation and negative is removal/offset decrease. It also shows the correlation between NO_3^- reaction rates and $\delta^{15}N$–NO_3^- **(C)** as well as $\delta^{15}N$–NO_3^- and $\delta^{18}O$–NO_3^- offsets **(D)**.

those determined by Rao et al. (2007) in the South Atlantic Bight using FTRs (3.8–16.6 nmol cm^{-3} h^{-1}). The rapid DO consumption in permeable sediments after glucose amendment was also comparable to the results obtained by Rusch et al. (2006) with sediments from the Atlantic Bight (35–57% enhancement). NO_3^- removal rates obtained in the present study are similar to those calculated from field survey data in the same STE (13.6 nmol cm^{-3} h^{-1}, unpublished data) and those measured with FTR in the Ria Formosa Lagoon (0.7–6.8 nmol cm^{-3} h^{-1}; Jiang et al., 2018).

Bio-labile DOM Supply and Benthic NO_3^- Transformations

The effects of bio-labile DOM availability on benthic aerobic respiration and mineralization have been widely documented as a key factor for a wide range of heterotrophic transformations in many coastal permeable environments, such as in Skagerrak, North Sea (Hulthe et al., 1998), St. George Island, Gulf of Mexico (Chipman et al., 2010) or the Ria Formosa Lagoon, Portugal (Ibánhez and Rocha, 2016). In our FTR experiments, the addition of glucose enhanced aerobic respiration rates as expected. Nevertheless, despite DO being more energetically favorable as an electron acceptor than NO_3^- for sediment microbes, net NO_3^- reduction is observed after the addition of NO_3^- to the circulating porewater even at DO saturated conditions, revealing the temporal synchronism of both reactions.

In the present study, nitrogen transformations were identified as a crucial function of sediment microbial metabolism (**Supplementary Figure 6**). Substantial microbial groups were identified as potential nitrifiers and denitrifiers in our sampled site based on the 16S rDNA information. For potential nitrifiers, the dominant genus was *Nitrosomonas* (**Table 2**). During laboratory incubations, *Nitrosomonas* genus showed a significant reliance on the supply of organic carbon during their growth stages in culture solutions despite the autotrophic character of the nitrification process (Clark and Schmidt, 1967). Similarly, the potential key denitrifiers found in the studied seepage face, included *Bacillus*, *Hyphomicrobium*, *Lactobacillus* and several of these were identified as facultative denitrifiers with different metabolism functions at variable DO levels (Ji et al., 2015). They have previously shown strong dependence on organic carbon supply (Harder and Attwood, 1978; Condón et al., 1996; Surono et al., 2008), likely due to their aerobic reaction pathway catalyzed by cytochrome o oxidase (Ji et al., 2015). Often, nitrification and facultative denitrification are closely coupled in coastal sediments (Ouyang et al., 2021) while their reaction rates vary under different environmental settings (Calvo-Martin et al., 2021). Net NO_3^- production in our experiments (group A) reveals the dominance of nitrification, probably fed by organic

matter ammonification with contributions from the adsorbed pool, while NO_3^- removal stimulated by addition likely results from both denitrification and NO_3^- assimilation under such aerobic environment (Jiang and Jiao, 2016), since Anammox-capable microorganisms were not identified here. Given that the biological assimilation of NH_4^+ is more energetically favorable than NO_3^- assimilation, the net NH_4^+ production in all the treatments employed in this study (**Figures 4A,B**) suggests a relatively weak NO_3^- assimilation rate and supports the contention that denitrification may be the dominant NO_3^- removal pathway in place.

However, in contrast to the reliance of denitrifiers on bio-labile DOM reported elsewhere, the addition of glucose under oxic conditions did not lead to a significantly positive response of NO_3^- reduction rates during both seasons (**Figure 5A**). Moreover, the potential denitrifier genera and their relative abundances varied among the two studied seasons, while the response of benthic NO_3^- reduction rates to exogenous DOM remained unchanged under fully oxic conditions. In addition, the isotopic fractionation of NO_3^- (^{15}N–NO_3^-) during net NO_3^- reduction in both glucose-free and glucose-amended groups was similar in the two studied seasons, suggesting that the addition of glucose was in fact not altering NO_3^- reduction rates and pathways (**Figure 5B**). Considering the biological significance of bio-labile organic matter to heterotrophic microbes, the insignificant variation in NO_3^- reduction rates after glucose addition under DO saturated conditions suggests that the added glucose is not used by the denitrifying bacteria as the primary carbon source in these FTR experiments. Despite a significant consumption of glucose by aerobic reactions plus adsorption losses, the outflow porewater still contained substantial quantities of glucose, as evidenced by the measured high DOC concentrations (**Figure 4B**), indicating that the concentration of glucose was not a limiting factor for heterotrophic metabolism throughout the entire sediment column used in the FTR experiments.

In the test sediment, several strains of benthic microbes could be facultative denitrifiers. They may host the function of NO_3^- removal under aerobic conditions, while the processing of NO_3^- removal and glucose consumption might be clearly separated in their metabolism, suggesting that electrons from glucose may flow into the DO respiration in these denitrifiers (cytochrome o; Ji et al., 2015). Alternatively, the presence of active NO_3^- reduction under fully oxic conditions in permeable sediments suggests that porewater transport mechanisms and niches of active denitrifiers on sediment particles would be the key to understand this apparent contradiction. Particularly, in contrast with cohesive sediments, surface permeable coastal sediments are frequently enriched in DO due to the regular porewater flushing with surface seawater together with the periodic undersaturation of intertidal sediments, which permits invasion of the sediment by atmospheric oxygen (Ibánhez and Rocha, 2016). Several strains of *Arthrobacter*, *Pseudomonas*, or *Rhodococcus*, for instance, could actively perform denitrification in aerobic environments (Qiao et al., 2020), a process that has been observed in coastal sites (e.g., the Wadden Sea, Germany, Marchant et al., 2017) and wastewater treatment (Wang et al., 2020). The majority of facultative denitrifiers operate well under a wide range of DO concentrations, while an anaerobic environment favors the expression of *Nir* and *Nor* genes (Ji et al., 2015), suggesting that a fraction of denitrifiers might be closely attached onto the sediment particle surfaces, thus relying on the aerobic microbiota for DO consumption and the creation of anaerobic niches (outlined in **Figure 6**). Though a fraction of denitrifiers might be located outside of these anaerobic niches (niche circularity > 0.8, area < 3 mm^2, Widerlund and Davison, 2007), due to the exposure to DO and the facultative metabolism of denitrifiers (Hayatsu et al., 2008; Wu et al., 2014), denitrification may not be conducted by these DO-exposed denitrifiers, similarly to the results found in oxygen minimum zones in the open ocean (Dalsgaard et al., 2014). The facultative denitrifiers involved in the NO_3^- isotope determinations, e.g., *Pseudomonas aureofaciens*, are usually characterized by variable metabolic functions at different DO concentrations (Sigman et al., 2001). Due to the "isolation" afforded by the "aerobic cover," and sustained by the benthic oxidative metabolism (**Figure 6**), the glucose delivered from the porewater flowing through the sediment would have been consumed by aerobes, such as *Sphingobium* (**Table 2**, active carbon decomposer, Bashir et al., 2013), before reaching active NO_3^- reducers attached to the particle surface. Furthermore, given the difference in molecular weight, the diffusion rate of glucose is much slower than that of DO (regardless of difference in solute concentration gradient), indicating that only a fraction of the microbiota would be fueled by this extra bio-labile DOM source. Accordingly, denitrifying bacteria in permeable sediment micro-niches has to rely on the SOM as a carbon source for NO_3^- reduction (Hong et al., 2010), especially the bio-labile fractions loosely attached on the particle surface (e.g., extractable by KCl solutions, Jiang et al., 2020). This reliance on the SOM provides stability for benthic microbial function and therefore reduces the reaction shock following switching between carbon sources (Wang et al., 2011). In addition, the utilization of SOM during denitrification likely adds DOM content to the porewater. Amendments with NO_3^- increased DOC production rates and added small-molecular DOM into the porewater during both seasons at saturated DO conditions (**Figures 3B–D**). A similar DOC production pattern during net NO_3^- reduction under aerobic conditions was found by Jiang et al. (2018) in intertidal permeable sediments of the Ria Formosa Lagoon, Portugal. On the other hand, Ibánhez et al. (2021b) found that porewater nitrate enrichment accelerates SOM mineralization by overcoming N limitation of the local microbial metabolism, thus shortening SOM turnover times. This priming effect of nitrate over oxic SOM mineralization results in the production of both humic and labile DOM and could also explain the production of labile DOM in our experiments run under oxic conditions. Given the relatively high concentration of SOM compared to DOC (minor SOM concentration variation during the incubations, **Figure 2**), the effects of glucose at the micro-niche scale might require a longer incubation period (e.g., 10 days) to allow for the exhaustion of the labile fractions of SOM, as well as increasing abundance of functional genes (e.g., *nirS* and *nosZ*; Henderson et al., 2010), and thus are not observed under our experimental strategy (10 h of duration).

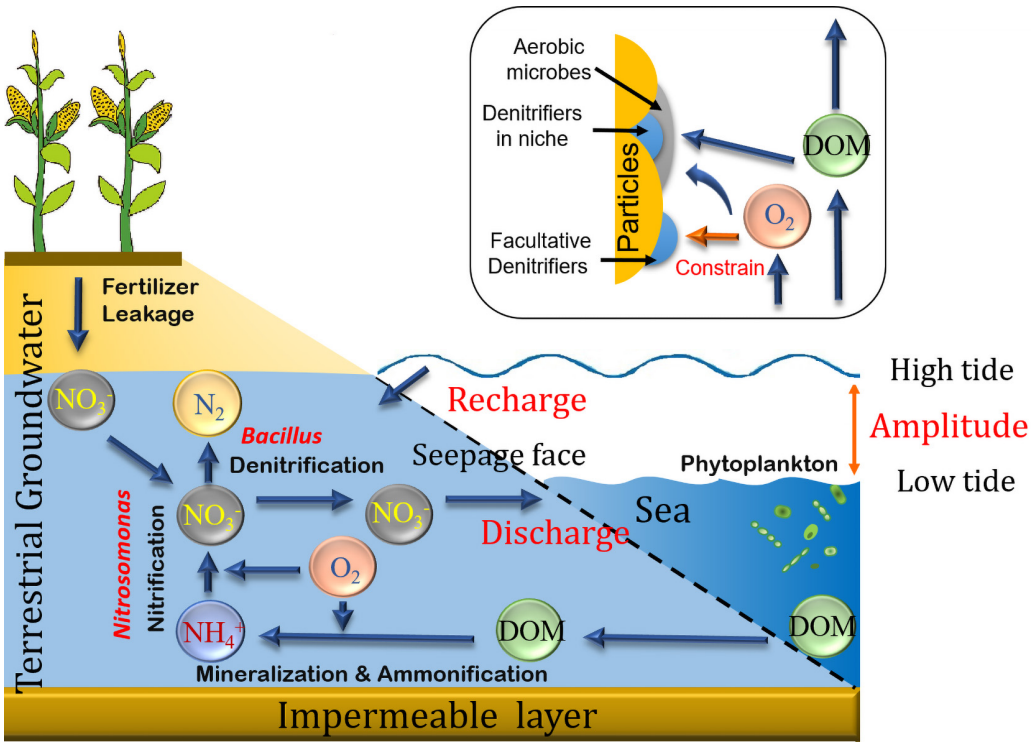


FIGURE 6 | Sketch of the NO_3^- processing in the aerobic seepage face, it highlights the interaction between benthic carbon content [both sedimentary organic matter (SOM) and dissolved organic matter (DOM)] and NO_3^- processing with key microbes. The porewater exchange in the seepage face is mainly driven by the tidal pumping. The *top right* panel is a zoom-in of anaerobic niches in sandy sediments. The majority of denitrifiers in the sediment are facultative denitrifiers, respiring oxygen in the aerobic environment; Nevertheless, the denitrifiers in these niches might be capable for conducting denitrification process due to the anaerobic environment.

When the DO content at the inflow decreased to approximately 70% saturation, the DO concentration in the outflow concurrently dropped to ca. 60% saturation (**Figure 3A**). However, the NO_3^- removal rate remained statistically similar to that under DO saturation conditions (**Figure 5A**). Intriguingly, the consumption of glucose dropped significantly under 70% of DO saturation (DOC consumption rates; $p < 0.01$), indicating that the aerobic mineralization pathways were affected by the decrease in DO (**Figure 3B**). Under these circumstances, the potential amount of bio-labile DOM that could reach denitrifying bacteria via porewater advection should increase. Still, at 70% of DO saturation in the inflowing water, denitrification rates didn't change compared to DO saturation conditions, adding support to the proposed niche structure and the reliance of NO_3^- reducers on SOM rather than bio-labile DOM circulating through the sediment. Delayed reaction of microbial communities to changing metabolite availability was previously discussed by Evard et al. (2012), and can be induced by the changing redox conditions commonly found in permeable sediments.

The significant effect of added bio-labile DOM over benthic NO_3^- consumption rates occurred when the DO concentration at the input solution fell to nearly 30% saturation ($p = 0.01$), while the dominant NO_3^- removal pathway was still deemed to be denitrification based on the linearity in the isotopic fractionation for the remaining NO_3^- (**Figure 5D**). The addition of glucose increased NO_3^- consumption rates compared to the unamended treatment (group D vs. G; approximately 0.32–0.71 nmol NO_3^- cm^{-3} h^{-1} enhancement during both seasons). In the present study, microbial composition was only determined at the initial stage. The more rapid biomass increase at the anaerobic environment during the incubation may lead to the active removal observed at group G. Presuming an insignificant increase for denitrifier biomass during the incubation, the enhancement of NO_3^- consumption rates at lowering DO levels suggest that under these conditions, glucose was reaching the denitrifying community due to the low adsorption potential of NO_3^- onto sediment particles. This delivery further benefited the NO_3^- removal due to the increase of the anaerobic sites on particle surface suitable for NO_3^- consumption at low DO levels. The key genera present at the studied seepage face, including *Sphingobium*, *Gp10* (**Table 2**), are generally adapted to aerobic environments using organic matter as energy supply (Berlendis et al., 2010; Roy et al., 2013). When the DO concentration decreased to nearly 30% saturation, these facultative denitrifiers tend to select NO_3^- as electron acceptor due to the enrichment in porewater (Group D and G). Furthermore, once the DO constraint is removed (30% saturation here), reduced cytochrome from all facultative denitrifiers may resume their function and lead to the increase in NO_3^- reduction (Ji et al., 2015). Consequently, the glucose amendment is linked to the increases

in NO_3^- removal rates in this treatment. Interestingly, in the treatments without glucose addition, the 30% DO saturation at the input solution also triggered a significant enhancement of the denitrification rates. Compared with the aerobic group (100% DO saturation), the increase in NO_3^- removal rates reached approximately 1.3 nmol cm^{-3} h^{-1} (group A vs. D in spring). In addition, the significant linear correlation between $\delta^{15}N$–NO_3^- and $\delta^{18}O$–NO_3^- suggests that the dominant process of NO_3^- removal among different groups remained the same as in the other groups (**Figure 5D**). Such marked increase observed in these treatments suggests that DO levels in the porewater are a strong modulator of denitrification rates because of the shift of terminal electron acceptor in benthic reactions from O_2 (oxic) to NO_3^- (suboxic) during organic matter degradation by microbes (Chen et al., 2017). Generally, denitrification in the open ocean requires DO levels < 2 mg L^{-1}, approximately 28% saturation in the seawater (Codispoti and Christensen, 1985). Correspondingly, the DO input concentration in the sub-oxic treatment could fit this standard and all sediment denitrifying bacteria might be active under these conditions, including the microbiota located outside of the niches (**Figure 6**).

Benthic N and C Interactions and Coastal Management

Coastal permeable sediments in seepage faces are assumed to be active reactors capable of removing terrestrial NO_3^- before it is discharged into coastal waters (Calvo-Martin et al., 2021). Accordingly, denitrification, i.e., the main pathway for a permanent NO_3^- removal (Burgin and Hamilton, 2007), in the exit sites of continental NO_3^- into the sea plays a key role in the coastal NO_3^- inventory. Coastal zones are also an important node for carbon cycling, especially in the production of pelagic organic matter via a wide range of primary producers (Jiang et al., 2020). In the present study, those aerobic metabolic functions (**Figure 6**), likely including reactions of aerobic mineralization and subsequent ammonification and nitrification, were benefited from the addition of bio-labile DOM. In contrast, the significant addition of glucose (nearly 300 μM) did not boost denitrification rates even if the DO concentration in the inputs decreased to approximately 70% saturation. This interaction between the NO_3^- production and DOC supply reveals that the retention of NO_3^- in coastal systems might be higher than previously thought, since the SOM dependent NO_3^- removal capability tends to be stable during the high loading of bio-labile DOM. Within many coastal ecosystems, a large amount of terrestrial NO_3^-, derived from overuse of chemical fertilizer or leakage from sewage pipes, reaches the coastal seawater via the benthic system (Tamborski et al., 2020). Compared with seawater concentration, submarine groundwater discharge-derived NO_3^- concentration was several orders of magnitude higher at our site (e.g., more than 10 times higher in Sanggou Bay, China, Wang et al., 2014). The influx of land-derived NO_3^- frequently triggers the algae blooms at the coast, e.g., Ria Formosa Lagoon, Portugal (Rocha et al., 2016), Jeju Island, Korea (Kang et al., 2019) as well as at our study site (Sanggou Bay, China, Yu et al., 2018). Coupled with cell decay and remineralization of debris, a significant fraction of bio-labile DOM is released into the coastal water and accumulates in subterranean estuaries (Mahmood et al., 2017). This way, STEs in coastal belts may act as catalysts for NO_3^- removal and eliminate the ecological stress caused by excessive NO_3^-, as can be seen from the simulation in group B among two seasons (**Figure 5A**). However, the accumulation of bio-labile DOM could not rapidly lead to the enhancement of denitrification rates in the seepage face in oxic conditions, at least in Sanggou Bay during spring and autumn. DO concentrations in STEs could drop to the saturation level from 20 to 30%, e.g., Ker Chalon beach, France (Mouret et al., 2020), the DO concentration in STE outflow locations, or coastal permeable beaches frequently remains at high-level (Boufadel et al., 2010), e.g., 57–93% in the STE outflow site in Ria Formosa lagoon (Ibánhez and Rocha, 2016) and 87–107% saturation in the Aquitanian coast, France (Charbonnier et al., 2013). Such aerobic environments indicate that denitrification would still not be stimulated on the short term unless conditions reach a specific DO concentration threshold. More importantly, the benthic reduction of NO_3^- may further produce bio-labile DOM via SOM decomposition (non-glucose amendment groups in **Figure 3B**) and drain into coastal seawater (Ibánhez et al., 2021b), potentially increasing the coastal DOM inventory. Consequently, this freshly produced bio-labile DOM could yet yield increases in NO_3^- availability via aerobic nitrification and be made available in the coastal water as a "second-hand" NO_3^-, and stimulating dinoflagellate blooms in the absence of equivalent silicate inflows (Rocha et al., 2002). In Sangou Bay, diatoms and dinoflagellates are often the dominant phytoplankton species (Yuan et al., 2014). Compared to diatoms, dinoflagellates are unfavored food source for consumers, especially for filter-feeders. Notably, frequency of dinoflagellate blooms has increased (Yuan et al., 2014) while aquaculture yields in Sanggou Bay and adjacent areas declined in recent years (local government data[1]), indicating the necessity for considering the feedback loop between NO_3^- and bio-labile DOM in future nutrient management.

CONCLUSION

The present study focused on the interactions between bio-labile DOM supply, DO concentration and NO_3^- removal in STE outflow areas using FTR experiments. Permeable sediments clearly revealed high NO_3^- reduction potential, mainly via denitrification, when the input NO_3^- concentration increased from approximately 10–80 μM. The decrease of DO concentration from 100% saturation to 70% saturation did not trigger a significant increase of the denitrification rate regardless of season, revealing that facultative denitrifiers in the sediment might rely on anaerobic microniches maintained by aerobic reactions. Denitrification rates significantly increased when the DO concentrations decreased to ∼30% saturation, suggesting that NO_3^- reducing potential supported by all facultative denitrifiers present in the sediment came into play then. In such a sub-oxic environment, the addition of glucose also triggered

[1]http://tjj.weihai.gov.cn/

a significant increase in denitrification rate, revealing that a fraction of bio-labile DOM was involved in the denitrification process. However, STE outflow areas are usually characterized by high DO concentration in porewaters. Accordingly, the bio-labile DOM in STEs may not enhance NO_3^- removal, but stimulate aerobic reactions, such as aerobic mineralization and decomposition instead, leading to an increase in NO_3^- availability via nitrification. Accordingly, the land-derived NO_3^- may take part on a self-sustaining vicious cycle supporting the reaction chain "NO_3^-–algae-bio-labile DOM $-NO_3^-$" at the water-sediment interface along coastlines hosting STEs. This overlooked biogeochemical chain in coastal systems requires further attention from coastal managers and stakeholders.

DATA AVAILABILITY STATEMENT

The datasets presented in this study can be found in online repositories. The names of the repository/repositories and accession number(s) can be found below: https://www.ncbi.nlm.nih.gov/, SRX7825212; https://www.ncbi.nlm.nih.gov/, SRX7825225.

AUTHOR CONTRIBUTIONS

SJ: conceptualization, investigation, methodology, writing–original draft, project administration, and funding acquisition. JJ and YZ: investigation. YW: methodology, resources, and writing–original draft. YWe: formal analysis and writing–original draft. CR and JI: methodology and writing–original draft. JZ: conceptualization, resources, writing–original draft, and funding acquisition. All authors contributed to the article and approved the submitted version.

FUNDING

This work was supported by the National Natural Science Foundation of China (Nos. 41706081 and 42111530026) and Scientific Research Foundation of SKLEC (2017RCDW04).

ACKNOWLEDGMENTS

We thank DeepBiome Co., Ltd. for bioinformatic assistance. The comments of three reviewers on an early version of the manuscript are greatly appreciated.

SUPPLEMENTARY MATERIAL

The Supplementary Material for this article can be found online at: https://www.frontiersin.org/articles/10.3389/fmars.2021.642143/full#supplementary-material

REFERENCES

Ahmerkamp, S., Marchant, H. K., Peng, C., Probandt, D., Littmann, S., Kuypers, M. M. M., et al. (2020). The effect of sediment grain properties and porewater flow on microbial abundance and respiration in permeable sediments. *Sci. Rep.* 10:3573.

Amato, D. W., Bishop, J. M., Glenn, C. R., Dulai, H., and Smith, C. M. (2016). Impact of submarine groundwater discharge on marine water quality and reef biota of Maui. *PLoS One* 11:e0165825. doi: 10.1371/journal.pone.0165825

Bashir, S., Fischer, A., Nijenhuis, I., and Richnow, H.-H. (2013). Enantioselective carbon stable isotope fractionation of hexachlorocyclohexane during aerobic biodegradation by *Sphingobium* spp. *Environ. Sci. Technol.* 47, 11432–11439. doi: 10.1021/es402197s

Berg, P., Long, M. H., Huettel, M., Rheuban, J. E., McGlathery, K. J., Howarth, R. W., et al. (2013). Eddy correlation measurements of oxygen fluxes in permeable sediments exposed to varying current flow and light. *Limnol. Oceanogr.* 58, 1329–1343. doi: 10.4319/lo.2013.58.4.1329

Berlendis, S., Cayol, J.-L., Verhé, F., Laveau, S., Tholozan, J.-L., Ollivier, B., et al. (2010). First evidence of aerobic biodegradation of BTEX compounds by pure cultures of *Marinobacter*. *Appl. Biochem. Biotechnol.* 160, 1992–1999. doi: 10.1007/s12010-009-8746-1

Bernhardt, E. S., and Likens, G. E. (2002). Dissloved organic carbon enrichment alters nitrogen dynamics in a forest stream. *Ecology* 83, 1689–1700. doi: 10.1890/0012-9658(2002)083[1689:docean]2.0.co;2

Boufadel, M. C., Sharifi, Y., Van Aken, B., Wrenn, B. A., and Lee, K. (2010). Nutrient and oxygen concentrations within the sediments of an Alaskan beach polluted with the Exxon Valdez oil spill. *Environ. Sci. Technol.* 44, 7418–7424. doi: 10.1021/es102046n

Burgin, A. J., and Hamilton, S. K. (2007). Have we overemphasized the role of denitrification in aquatic ecosystems? A review of nitrate removal pathways. *Front. Ecol. Environ.* 5, 89–96. doi: 10.1890/1540-9295(2007)5[89:hwotro]2.0.co;2

Calvo-Martin, E., Álvarez-Salgado, X. A., Rocha, C., and Ibánhez, J. S. P. (2021). Reactive solute transport through two contrasting subterranean estuary exit sites in the Ría de Vigo (NW Iberian Peninsula). *Front. Mar. Sci.* 8:94. doi: 10.3389/fmars.2021.626813

Charbonnier, C., Anschutz, P., Poirier, D., Bujan, S., and Lecroart, P. (2013). Aerobic respiration in a high-energy sandy beach. *Mar. Chem.* 155, 10–21. doi: 10.1016/j.marchem.2013.05.003

Chen, M., Kim, J., Choi, J., Lee, Y. K., and Hur, J. (2017). Biological early diagenesis and insolation-paced paleoproductivity signified in deep core sediment organic matter. *Sci. Rep.* 7:1581.

Chipman, L., Podgorski, D., Green, S., Kostka, J., Cooper, W., and Huettel, M. (2010). Decomposition of plankton-derived dissolved organic matter in permeable coastal sediments. *Limnol. Oceanogr.* 55, 857–871. doi: 10.4319/lo.2010.55.2.0857

Clark, C., and Schmidt, E. L. (1967). Growth response of *Nitrosomonas europaea* to amino acids. *J. Bacteriol.* 93, 1302–1308. doi: 10.1128/jb.93.4.1302-1308.1967

Codispoti, L. A., and Christensen, J. P. (1985). Nitrification, denitrification and nitrous oxide cycling in the eastern tropical South Pacific ocean. *Mar. Chem.* 16, 277–300. doi: 10.1016/0304-4203(85)90051-9

Condón, S., Palop, A., Raso, J., and Sala, F. J. (1996). Influence of the incubation temperature after heat treatment upon the estimated heat resistance values of spores of *Bacillus subtilis*. *Lett. Appl. Microbiol.* 22, 149–152. doi: 10.1111/j.1472-765x.1996.tb01130.x

Cornwell, J. C., Kemp, W. M., and Kana, T. M. (1999). Denitrification in coastal ecosystems: methods, environmental controls, and ecosystem level controls, a review. *Aquat. Ecol.* 33, 41–54.

Crawshaw, J., O'Meara, T., Savage, C., Thomson, B., Baltar, F., and Thrush, S. F. (2019). Source of organic detritus and bivalve biomass influences nitrogen cycling and extracellular enzyme activity in estuary sediments. *Biogeochemistry* 145, 315–335. doi: 10.1007/s10533-019-00608-y

Dalsgaard, T., Stewart, F. J., Thamdrup, B., De Brabandere, L., Revsbech, N. P., Ulloa, O., et al. (2014). Oxygen at nanomolar levels reversibly suppresses

process rates and gene expression in anammox and denitrification in the oxygen minimum zone off Northern Chile. *mBio* 5:e01966-14.

Edgar, R. C. (2010). Search and clustering orders of magnitude faster than BLAST. *Bioinformatics* 26, 2460–2461. doi: 10.1093/bioinformatics/btq461

Evard, V., Glud, R. N., and Cook, P. L. M. (2012). The kinetics of denitrification in permeable sediments. *Biogeochemistry* 113, 563–572. doi: 10.1007/s10533-012-9789-x

Fang, J., Zhang, J., Xiao, T., Huang, D., and Liu, S. (2016). Integrated multi-trophic aquaculture (IMTA) in Sanggou Bay, China. *Aquac. Environ. Interact.* 8, 201–205. doi: 10.3354/aei00179

Harder, W., and Attwood, M. M. (1978). "Biology, physiology and biochemistry of Hyphomicrobia," in *Advances in Microbial Physiology*, eds A. H. Rose and J. G. Morris (Cambridge, MA: Academic Press), 303–359. doi: 10.1016/s0065-2911(08)60060-0

Hayatsu, M., Tago, K., and Saito, M. (2008). Various players in the nitrogen cycle: diversity and functions of the microorganisms involved in nitrification and denitrification. *Soil Sci. Plant Nutr.* 54, 33–45. doi: 10.1111/j.1747-0765.2007.00195.x

Heiss, J. W., Michael, H. A., and Koneshloo, M. (2020). Denitrification hotspots in intertidal mixing zones linked to geologic heterogeneity. *Environ. Res. Lett.* 15:084015. doi: 10.1088/1748-9326/ab90a6

Henderson, S. L., Dandie, C. E., Patten, C. L., Zebarth, B. J., Burton, D. L., Trevors, J. T., et al. (2010). Changes in denitrifier abundance, denitrification gene mRNA levels, nitrous oxide emissions, and denitrification in anoxic soil microcosms amended with glucose and plant residues. *Appl. Environ. Microboiol.* 76, 2155–2164. doi: 10.1128/aem.02993-09

Hong, S. W., Kim, H. S., and Chung, T. H. (2010). Alteration of sediment organic matter in sediment microbial fuel cells. *Environ. Pollut.* 158, 185–191. doi: 10.1016/j.envpol.2009.07.022

Huettel, M., Berg, P., and Kostka, J. E. (2014). Benthic exchange and biogeochemical cycling in permeable sediments. *Annu. Rev. Mar. Sci.* 6, 23–51. doi: 10.1146/annurev-marine-051413-012706

Hulthe, G., Hulth, S., and Hall, P. O. J. (1998). Effect of oxygen on degradation rate of refractory and bio-labile organic matter in continental margin sediments. *Geochim. Cosmochim. Acta* 62, 1319–1328. doi: 10.1016/s0016-7037(98)00044-1

Ibánhez, J. S. P., Álvarez-Salgado, X. A., Nieto-Cid, M., and Rocha, C. (2021a). Fresh and saline submarine groundwater discharge in a large coastal inlet affected by seasonal upwelling. *Limnol. Oceanogr.* doi: 10.1002/lno.11733

Ibánhez, J. S. P., Álvarez-Salgado, X. A., and Rocha, C. (2021b). Does nitrate enrichment accelerate organic matter turnover in subterranean estuaries? *Front. Mar. Sci.* 8:661201. doi: 10.3389/fmars.2021.661201

Ibánhez, J. S. P., Leote, C., and Rocha, C. (2011). Porewater nitrate profiles in sandy sediments hosting submarine groundwater discharge described by an advection–dispersion-reaction model. *Biogeochemistry* 103, 159–180. doi: 10.1007/s10533-010-9454-1

Ibánhez, J. S. P., Leote, C., and Rocha, C. (2013). Seasonal enhancement of submarine groundwater discharge (SGD)-derived nitrate loading into the Ria Formosa coastal lagoon assessed by 1-D modeling of benthic NO3- profiles. *Estuar. Coast. Shelf Sci.* 132, 56–64. doi: 10.1016/j.ecss.2012.04.015

Ibánhez, J. S. P., and Rocha, C. (2014). Effects of recirculation of seawater enriched in inorganic nitrogen on dissolved organic carbon processing in sandy seepage face sediments. *Mar. Chem.* 166, 48–58. doi: 10.1016/j.marchem.2014.09.012

Ibánhez, J. S. P., and Rocha, C. (2016). Oxygen transport and reactivity within a sandy seepage face in a mesotidal lagoon (Ria Formosa, Southwestern Iberia). *Limnol. Oceanogr.* 61, 61–77. doi: 10.1002/lno.10199

Ibánhez, J. S. P., and Rocha, C. (2017). Kinetics of inorganic nitrogen turnover in a sandy seepage face on a subterranean estuary. *Appl. Geochem.* 87, 108–121. doi: 10.1016/j.apgeochem.2017.10.015

Ji, B., Yang, K., Zhu, L., Jiang, Y., Wang, H., Zhou, J., et al. (2015). Aerobic denitrification: a review of important advances of the last 30 years. *Biotechnol. Bioprocess Eng.* 20, 643–651. doi: 10.1007/s12257-015-0009-0

Jiang, S., Ibánhez, J. S. P., and Rocha, C. (2018). Influence of labile dissolved organic matter on nitrate reduction in a seepage face. *Environ. Sci. Pollut. Res.* 25, 10654–10667. doi: 10.1007/s11356-018-1302-1

Jiang, S., Ibánhez, J. S. P., Wu, Y., and Zhang, J. (2021a). Geochemical tracers in submarine groundwater discharge research: practice and challenges from a view of climate changes. *Environ. Rev.* doi: 10.1139/er-2020-0093

Jiang, S., Jin, J., Jiang, S., Wu, Y., Wang, J., Chen, J., et al. (2021b). Nitrogen in atmospheric wet depositions over the East Indian Ocean and West Pacific Ocean: spatial variability, source identification, and potential influences. *Front. Mar. Sci.* 7:600843. doi: 10.3389/fmars.2020.600843

Jiang, S., Kavanagh, M., Ibánhez, J. S. P., and Rocha, C. (2021c). Denitrification-nitrification process in permeable coastal sediments: an investigation on the effect of salinity and nitrate availability using flow-through reactors. *Acta Oceanol. Sin.* doi: 10.1007/s13131-021-1811-5

Jiang, S., Kavanagh, M., and Rocha, C. (2017). Evaluation of the suitability of vacutainers for storage of nutrient and dissolved organic carbon analytes in water samples. *Biol. Environ. Proc. R. Ir. Acad.* 177B, 33–46. doi: 10.3318/bioe.2017.01

Jiang, S., Müller, M., Jin, J., Wu, Y., Zhu, K., Zhang, G., et al. (2019). Dissolved inorganic nitrogen in a tropical estuary in Malaysia: transport and transformation. *Biogeosciences* 16, 2821–2836. doi: 10.5194/bg-16-2821-2019

Jiang, S., Zhang, Y., Jin, J., Wu, Y., Wei, Y., Wang, X., et al. (2020). Organic carbon in a seepage face of a subterranean estuary: turnover and microbial interrelations. *Sci. Total Environ.* 725:138220. doi: 10.1016/j.scitotenv.2020.138220

Jiang, X., and Jiao, N. (2016). Nitrate assimilation by marine heterotrophic bacteria. *Sci. China Earth Sci.* 59, 477–483. doi: 10.1007/s11430-015-5212-5

Jin, J., Jiang, S., and Zhang, J. (2020). Nitrogen isotopic analysis of nitrate in aquatic environment by cadmium-hydroxylamine hydrochloride reduction. *Rapid Commun. Mass Spectrom.* 34:8804.

Jung, H., Koh, D.-C., Kim, Y. S., Jeen, S.-W., and Lee, J. (2020). Stable Isotopes of Water and Nitrate for the Identification of Groundwater Flowpaths: a Review. *Water* 12:138. doi: 10.3390/w12010138

Kang, J. H., Jang, J. E., Kim, J. H., Byeon, S. Y., Kim, S., Choi, S. K., et al. (2019). Species composition, diversity, and distribution of the genus Ulva along the coast of Jeju Island, Korea based on molecular phylogenetic analysis. *PLoS One* 14:e0219958. doi: 10.1371/journal.pone.0219958

Kessler, A. J., Glud, R. N., Gardenas, M. B., Larsen, M., Bourke, M. F., and Cook, P. L. M. (2012). Quantifying denitrification in rippled permeable sands through combined flume experiments and modeling. *Limnol. Oceanogr.* 57, 1217–1232. doi: 10.4319/lo.2012.57.4.1217

Kuypers, M. M., Marchant, H. K., and Kartal, B. (2018). The microbial nitrogen-cycling network. *Nat. Rev. Microbiol.* 16, 263–276.

Mahmood, T., Fang, J., Jiang, Z., Ying, W., and Zhang, J. (2017). Seasonal distribution, sources and sink of dissolved organic carbon in integrated aquaculture system in coastal waters. *Aquac. Int.* 25, 71–85. doi: 10.1007/s10499-016-0014-0

Marchant, H. K., Ahmerkamp, S., Lavik, G., Tegetmeyer, H. E., Graf, J., Klatt, J. M., et al. (2017). Denitrifying community in coastal sediments performs aerobic and anaerobic respiration simultaneously. *ISME J.* 11, 1799–1812. doi: 10.1038/ismej.2017.51

Marchant, H. K., Holtappels, M., Lavik, G., Ahmerkamp, S., Winter, C., and Kuypers, M. M. M. (2016). Coupled nitrificationŰdenitrification leads to extensive N loss in subtidal permeable sediments. *Limnol. Oceanogr.* 61, 1033–1048. doi: 10.1002/lno.10271

Marchant, H. K., Lavik, G., Holtappels, M., and Kuypers, M. M. (2014). The fate of nitrate in intertidal permeable sediments. *PLoS One* 9:e104517. doi: 10.1371/journal.pone.0104517

Meredith, K. T., Baker, A., Andersen, M. S., O'Carroll, D. M., Rutlidge, H., McDonough, L. K., et al. (2020). Isotopic and chromatographic fingerprinting of the sources of dissolved organic carbon in a shallow coastal aquifer. *Hydrol. Earth Syst. Sci.* 24, 2167–2178. doi: 10.5194/hess-24-2167-2020

Moore, S. (1999). The subterranean estuary: a reaction zone of ground water and sea water. *Mar. Chem.* 65, 111–125. doi: 10.1016/s0304-4203(99)00014-6

Mouret, A., Charbonnier, C., Lecroart, P., Metzger, E., Howa, H., Deflandre, B., et al. (2020). Biogeochemistry in an intertidal pocket beach. *Estuar. Coast. Shelf Sci.* 243:106920. doi: 10.1016/j.ecss.2020.106920

Ouyang, L., Thamdrup, B., and Trimmer, M. (2021). Coupled nitrification and N2 gas production as a cryptic process in oxic riverbeds. *Nat. Commun.* 12:1217.

Qiao, Z., Sun, R., Wu, Y., Hu, S., Liu, X., Chan, J., et al. (2020). Characteristics and metabolic pathway of the bacteria for heterotrophic nitrification and aerobic denitrification in aquatic ecosystems. *Environ. Res.* 191:110069. doi: 10.1016/j.envres.2020.110069

Rao, A. M. F., McCarthy, M. J., Gardner, W. S., and Jahnke, R. A. (2007). Respiration and denitrification in permeable continental shelf deposits on the South Atlantic Bight: rates of carbon and nitrogen cycling from sediment column experiments. *Cont. Shelf Res.* 27, 1801–1819. doi: 10.1016/j.csr.2007.03.001

Rivett, M. O., Buss, S. R., Morgan, P., Smith, J. W. N., and Bemment, C. D. (2008). Nitrate attenuation in groundwater: a review of biogeochemical controlling processes. *Water Res.* 42, 4215–4232. doi: 10.1016/j.watres.2008.07.020

Rocha, C., Galvão, H. M., and Barbosa, A. B. (2002). Role of transient silicon limitation in the development of cyanobacteria blooms in the Guadiana estuary, south-western Iberia. *Mar. Ecol. Prog. Ser.* 228, 35–45. doi: 10.3354/meps228035

Rocha, C., Veiga-Pires, C., Scholten, J., Knoeller, K., Gröcke, D. R., Carvalho, L., et al. (2016). Assessing land-ocean connectivity via submarine groundwater discharge (SGD) in the Ria Formosa Lagoon (Portugal): combining radon measurements and stable isotope hydrology. *Hydrol. Earth Syst. Sci.* 20, 3077–3098. doi: 10.5194/hess-20-3077-2016

Roy, M., Khara, P., Basu, S., and Dutta, T. (2013). Catabolic versatility of *Sphingobium* sp. strain PNB capable of degrading structurally diverse aromatic compounds. *J. Bioremediat. Biodegrad.* 4:173.

Rusch, A., Huettel, M., Wild, C., and Reimers, C. E. (2006). Benthic oxygen consumption and organic matter turnover in organic-poor, permeable shelf sands. *Aquat. Geochem.* 12, 1–19. doi: 10.1007/s10498-005-0784-x

Santos, I. R., Eyre, B. D., and Glud, R. N. (2012). Influence of porewater advection on denitrification in carbonate sands: evidence from repacked sediment column experiments. *Geochim. Cosmochim. Acta* 96, 247–258. doi: 10.1016/j.gca.2012.08.018

Siemens, J., Haas, M., and Kaupenjohann, M. (2003). Dissolved organic matter induced denitrification in subsoils and aquifers? *Geoderma* 113, 253–271. doi: 10.1016/s0016-7061(02)00364-6

Sigman, D. M., Casciotti, K. L., Andreani, M., Barford, C., Galanter, M., and Böhlke, J. (2001). A bacterial method for the nitrogen isotopic analysis of nitrate in seawater and freshwater. *Anal. Chem.* 73, 4145–4153. doi: 10.1021/ac010088e

Surey, R., Schimpf, C. M., Sauheitl, L., Mueller, C. W., Rummel, P. S., Dittert, K., et al. (2020). Potential denitrification stimulated by water-soluble organic carbon from plant residues during initial decomposition. *Soil Biol. Biochem.* 147:107841. doi: 10.1016/j.soilbio.2020.107841

Surono, I. S., Collado, M. C., Salminen, S., and Meriluoto, J. (2008). Effect of glucose and incubation temperature on metabolically active Lactobacillus plantarum from dadih in removing microcystin-LR. *Food Chem. Toxicol.* 46, 502–507. doi: 10.1016/j.fct.2007.08.017

Suryaputra, I. G. N. A., Santos, I. R., Huettel, M., Burnett, W. C., and Dittmar, T. (2015). Non-conservative behavior of fluorescent dissolved organic matter (FDOM) within a subterranean estuary. *Cont. Shelf Res.* 110, 183–190. doi: 10.1016/j.csr.2015.10.011

Tamborski, J., Brown, C., Bokuniewicz, H., Cochran, J. K., and Rasbury, E. T. (2020). Investigating boron isotopes for identifying nitrogen sources supplied by submarine groundwater discharge to coastal waters. *Front. Mar. Sci.* 8:126. doi: 10.3389/fenvs.2020.00126

Thornton, D. C. O. (2014). Dissolved organic matter (DOM) release by phytoplankton in the contemporary and future ocean. *Eur. J. Phycol.* 49, 20–46. doi: 10.1080/09670262.2013.875596

Troccoli-Ghinaglia, L., Herrera-Silveira, J. A., Comín, F. A., and Díaz-Ramos, J. R. (2010). Phytoplankton community variations in tropical coastal area affected where submarine groundwater occurs. *Cont. Shelf Res.* 30, 2082–2091. doi: 10.1016/j.csr.2010.10.009

Wang, M., Cao, G., Feng, N., and Pan, Y. (2020). Bioaugmentation of two-stage aerobic sequencing batch reactor with mixed strains for high nitrate nitrogen wastewater treatment. *Chin. J. Chem. Eng.* 28, 3103–3109. doi: 10.1016/j.cjche.2020.08.014

Wang, X., Du, J., Ji, T., Wen, T., Liu, S., and Zhang, J. (2014). An estimation of nutrient fluxes via submarine groundwater discharge into the Sanggou Bay-A typical multi-species culture ecosystem in China. *Mar. Chem.* 167, 113–122. doi: 10.1016/j.marchem.2014.07.002

Wang, Y., Geng, J., Guo, G., Wang, C., and Liu, S. (2011). N2O production in anaerobic/anoxic denitrifying phosphorus removal process: the effects of carbon sources shock. *Chem. Eng. J.* 172, 999–1007. doi: 10.1016/j.cej.2011.07.014

Wei, Y., Jiang, S., Tian, L., Wei, L., Jin, J., Ibánhez, J. S. P., et al. (2021). Benthic microbial biogeography along the continental shelf shaped by substrates from the Changjiang (Yangtze) river plume. *Acta Oceanol. Sin.* doi: 10.1007/s13131-021-1861-8

Weston, N. B., and Joye, S. B. (2005). Temperature-driven decoupling of key phases of organic matter degradation in marine sediments. *PNAS* 102, 17036–17040. doi: 10.1073/pnas.0508798102

Widerlund, A., and Davison, W. (2007). Size and density distribution of sulfide-producing microniches in lake sediments. *Environ. Sci. Technol.* 41, 8044–8049. doi: 10.1021/es071510x

Wu, B., Lan, T., Lu, D., and Liu, Z. (2014). Ecological and enzymatic responses to petroleum contamination. *Environ. Sci. Process. Impacts* 16, 1501–1509. doi: 10.1039/c3em00731f

Wu, Y., Zhu, K., Zhang, J., Müller, M., Jiang, S., Mujahid, A., et al. (2019). Distribution and degradation of terrestrial organic matter in the sediments of peat-draining rivers, Sarawak, Malaysian Borneo. *Biogeosciences* 16, 4517–4533. doi: 10.5194/bg-16-4517-2019

Yu, R.-C., Lü, S.-H., and Liang, Y.-B. (2018). "Harmful Algal Blooms in the Coastal Waters of China," in *Global Ecology and Oceanography of Harmful Algal Blooms*, eds P. M. Glibert, E. Berdalet, M. A. Burford, G. C. Pitcher, and M. Zhou (Cham: Springer), 309–316. doi: 10.1007/978-3-319-70069-4_15

Yuan, M., Zhang, C., Jiang, Z., Guo, S., and Sun, J. (2014). Seasonal variations in phytoplankton community structure in the Sanggou, Ailian, and Lidao Bays. *J. Ocean Univ. China* 13, 1012–1024. doi: 10.1007/s11802-014-2305-2

Zhang, Y., Qin, B., Zhu, G., Zhang, L., and Yang, L. (2007). Chromophoric dissolved organic matter (CDOM) absorption characteristics in relation to fluorescence in Lake Taihu, China, a large shallow subtropical lake. *Hydrobiologia* 581, 43–52. doi: 10.1007/978-1-4020-6158-5_5

Conflict of Interest: The authors declare that the research was conducted in the absence of any commercial or financial relationships that could be construed as a potential conflict of interest.

Copyright © 2021 Jiang, Jin, Wu, Zhang, Wei, Rocha, Ibánhez and Zhang. This is an open-access article distributed under the terms of the Creative Commons Attribution License (CC BY). The use, distribution or reproduction in other forums is permitted, provided the original author(s) and the copyright owner(s) are credited and that the original publication in this journal is cited, in accordance with accepted academic practice. No use, distribution or reproduction is permitted which does not comply with these terms.

frontiers in Marine Science

ORIGINAL RESEARCH
published: 12 February 2021
doi: 10.3389/fmars.2021.626813

Reactive Solute Transport Through Two Contrasting Subterranean Estuary Exit Sites in the Ría de Vigo (NW Iberian Peninsula)

Elisa Calvo-Martin[1,2], Xosé Antón Álvarez-Salgado[2], Carlos Rocha[3] and J. Severino Pino Ibánhez[2,3]**

[1] Facultade de Ciencias do Mar, Universidade de Vigo, Vigo, Spain, [2] Organic Geochemistry Lab, Department of Oceanography, Instituto de Investigacións Mariñas, Consejo Superior de Investigaciones Científicas (CSIC), Vigo, Spain, [3] Biogeochemistry Research Group, School of Natural Sciences, Trinity College Dublin, Dublin, Ireland

OPEN ACCESS

Edited by:
Johan Schijf,
University of Maryland Center for Environmental Science (UMCES), United States

Reviewed by:
Andrea Pain,
University of Maryland Center for Environmental Science (UMCES), United States
Xiaolong Geng,
New Jersey Institute of Technology, United States
Joseph James Tamborski,
Woods Hole Oceanographic Institution, United States

***Correspondence:**
Elisa Calvo-Martin
elisacalvomartin@gmail.com
J. Severino Pino Ibánhez
pinoibaj@tcd.ie

Specialty section:
This article was submitted to Marine Biogeochemistry, a section of the journal Frontiers in Marine Science

Received: 06 November 2020
Accepted: 25 January 2021
Published: 12 February 2021

Citation:
Calvo-Martin E, Álvarez-Salgado XA, Rocha C and Ibánhez JSP (2021) Reactive Solute Transport Through Two Contrasting Subterranean Estuary Exit Sites in the Ría de Vigo (NW Iberian Peninsula). Front. Mar. Sci. 8:626813. doi: 10.3389/fmars.2021.626813

Subterranean estuaries (STEs), where continental groundwaters and saltwaters meet, are zones of intense biogeochemical reactivity. As such, STEs significantly modify groundwater-borne nutrient fluxes to the coastal zone. Thus, evaluating their reactive role is crucial to anticipate impacts of submarine groundwater discharge (SGD) over coastal ecosystems. Here, we studied the nitrogen biogeochemistry of two STEs with contrasting wave-exposure and redox conditions in Panxón and Ladeira beaches (Ría de Vigo, NW Iberian Peninsula). Seasonal surveys were performed at the permanently saturated zone of both beaches during low tide in February, May, July, and October 2019. Sediment was sampled and porewater samples collected using push-pull piezometers. Salinity, ^{222}Rn and ^{226}Ra activities were used to trace water circulation inside each beach. Porewater nitrate, ammonium, nitrite and dissolved oxygen were used to evaluate the role of these STEs as reactive sinks or sources of inorganic nitrogen. Our results showed a marked seasonal variability of water circulation inside both beaches, with strong salinity gradients in February and May and weakened circulation in July and October. The presence of a gravel layer in Panxón beach completely altered the typical structure of STEs by increasing porewater transport and mixing through the beach interior. As a result, Panxón beach profiles were highly enriched in nitrate and oxygen. Conversely, suboxic, and anoxic conditions were prevalent in Ladeira beach during the study period, with ammonium being the prevailing inorganic nitrogen form. High nitrate concentrations occurred associated to the tidal circulation cell during February and May, being the only effective mechanism of sediment oxygenation in Ladeira beach. Although nitrate reduction and production were observed in both STEs, comparison with averaged conservative mixing porewater profiles showed that Ladeira beach acted as a net nitrogen sink whereas Panxón beach acted as a net nitrogen source. The presence of a gravel layer oxygenates the interior of Panxón beach, thus limiting nitrate reduction and promoting the amplification of groundwater-borne nitrogen fluxes to the coast.

Keywords: subterranean estuary, groundwater discharge, radon, dissolved oxygen, nitrogen cycling, Ría de Vigo

INTRODUCTION

Submarine groundwater discharge (SGD) is defined as any and all water flow on continental margins from the seabed to the coastal ocean, including both the discharge of meteoric groundwater from coastal aquifers (fresh SGD) and the recirculation of seawater through the sea floor (Burnett et al., 2003). The importance of fresh groundwater discharge lies in its usual enrichment in nutrients, trace metals, nitrous oxide, methane, or CO_2 as compared with surface waters (e.g., Leote et al., 2008; Liu et al., 2014; Rodellas et al., 2014; Yang et al., 2015). This general enrichment of biogeochemically active solutes is originated in the degradation of organic matter infiltrated into the aquifer, the percolation of nutrients or the contact with metal-containing aquifer substrates (Slomp and Van Cappellen, 2004; Knee and Paytan, 2012) during the prolonged residence times of groundwaters compared with surface waters. Furthermore, the indiscriminate use of fertilizers in intensive agriculture from the beginning of the twentieth century have provoked an enrichment of nitrogen in aquifers verified worldwide (Valiela et al., 1990; Vitousek et al., 1997; Rivett et al., 2008). This anthropogenic groundwater-borne nitrogen can reach the ocean via different transport processes, including SGD (Beusen et al., 2013), where it has been linked with coastal eutrophication processes (Capone and Slater, 1990; Valiela et al., 1990; Hwang et al., 2005) or harmful algal blooms (Hu et al., 2006; Lee et al., 2010).

Solute flux estimations associated to SGD need to take into account the high biogeochemical reactivity commonly found at the exit sites that can significantly modify the composition of the circulating waters prior to discharge (Slomp and Van Cappellen, 2004; Spiteri et al., 2008; Santos et al., 2008, 2009a,b; Rocha et al., 2009; Ibánhez et al., 2011, 2013; Ibánhez and Rocha, 2014, 2016, 2017; Jiang et al., 2018, 2020). This zone is called subterranean estuary (STE), by analogy with surface estuaries (Moore, 1999; Burnett et al., 2003).

In most tidally driven STEs, three water bodies mix as a result of the interaction between coastal and terrestrial forcings (Robinson et al., 2006; Santos et al., 2012). The infiltration of seawater at the upper intertidal and its exfiltration generally at the low tide mark driven by tidal and wave forcing develops a high salinity zone called tidal circulation cell or upper saline plume (Robinson et al., 2006, 2007b). Secondary cells could also develop backshore due to berm overtopping and the inundation of backshore depressions (Heiss and Michael, 2014). The intrusion of seawater into the seafloor forms a second high salinity zone seaward called salt-wedge, driven by density differences between fresh groundwater from the coastal aquifer and saltwater (Robinson et al., 2006, 2018). Between these two saline zones, the fresh SGD from the coastal aquifer forms a freshwater discharge "tube" (FDT; Robinson et al., 2006). Mixing, flux, and the location of the FDT exit point depend on the hydraulic gradient of the coastal aquifer but also on tidal pumping, wave set-up, density and sediment permeability (Burnett et al., 2003; Santos et al., 2012; Heiss and Michael, 2014; Robinson et al., 2018). The expansion of the tidal circulation cell can make the FDT shallower or non-existent as it causes vigorous saltwater-freshwater mixing due to unstable density distributions inside the beach leading to convective circulation (Robinson et al., 2007a). Spatial sediment heterogeneity within the intertidal zone can alter porewater circulation, creating zones of preferential flux, and complex local-scale mixing rates (Geng et al., 2020a,b).

Biogeochemical reactivity within STEs has been linked to different porewater circulation patterns in numerous studies (Spiteri et al., 2008; Santos et al., 2009a; Ibánhez et al., 2013; Heiss and Michael, 2014; Ibánhez and Rocha, 2016, 2017; Couturier et al., 2017). During high tide, seawater infiltration resupplies the sediment with fresh organic matter, and dissolved oxygen (Ibánhez and Rocha, 2016). Particulate organic matter is retained in the shallower depths, whereas dissolved organic matter penetrates the beach interior driven by the recirculation of seawater though the sediment (Rusch et al., 2000; Santos et al., 2009a; Huettel et al., 2014). The degradation of organic matter can lead to the attenuation of terrestrial groundwater-borne N through nitrate reduction processes within the STE, such as denitrification (Kroeger and Charette, 2008; Thamdrup, 2012). Autotrophic processes, such as anaerobic ammonium oxidation (ANAMMOX), are also important sinks of N and they have been reported in STEs (Kroeger and Charette, 2008; Sáenz et al., 2012; Thamdrup, 2012). In anoxic conditions, the dissimilatory nitrate reduction to ammonium process competes with denitrification for both electron donors and acceptors, although the reduction of nitrate to ammonium seems to be favored at strong reducing conditions (Thamdrup and Dalsgaard, 2008). On the contrary, in oxic STEs, limited N consumption together with the production of ammonium from organic matter mineralization can enhance N loads to surface water bodies (Ibánhez et al., 2013; Ibánhez and Rocha, 2017). The mixing between seawater and meteoric groundwater, together with enhanced transport caused by the permeable nature of STEs, creates a strong biogeochemical zonation that enables the co-occurrence of all these processes in close proximity. However, the modulation role of STEs over land-derived N fluxes to the coast and its controlling factors are still highly uncertain.

For the first time in the Ría de Vigo (NW Iberian Peninsula), two contrasting STEs were examined (**Figure 1**). The evaluation of the mechanisms that control the final SGD N loads to the receiving waters is particularly important in this embayment, as its valuable natural resources depend on the good environmental status of these coastal waters. Both STEs are placed next to each other and yet, they present differential redox conditions. Environmental factors underlying these differences are explored and related to the cycling of the redox-sensitive inorganic N compounds within these STEs. The final objective of this study is to evaluate the factors determining the capacity of STEs to mitigate or amplify groundwater-borne N loads to the receiving waters.

MATERIALS AND METHODS

Study Site

The Ría de Vigo (NW Iberian margin; **Figure 1**) is a large coastal inlet at the northern limit of the Eastern Boundary Upwelling Ecosystem of the Iberian-Canary current (Arístegui et al., 2009).

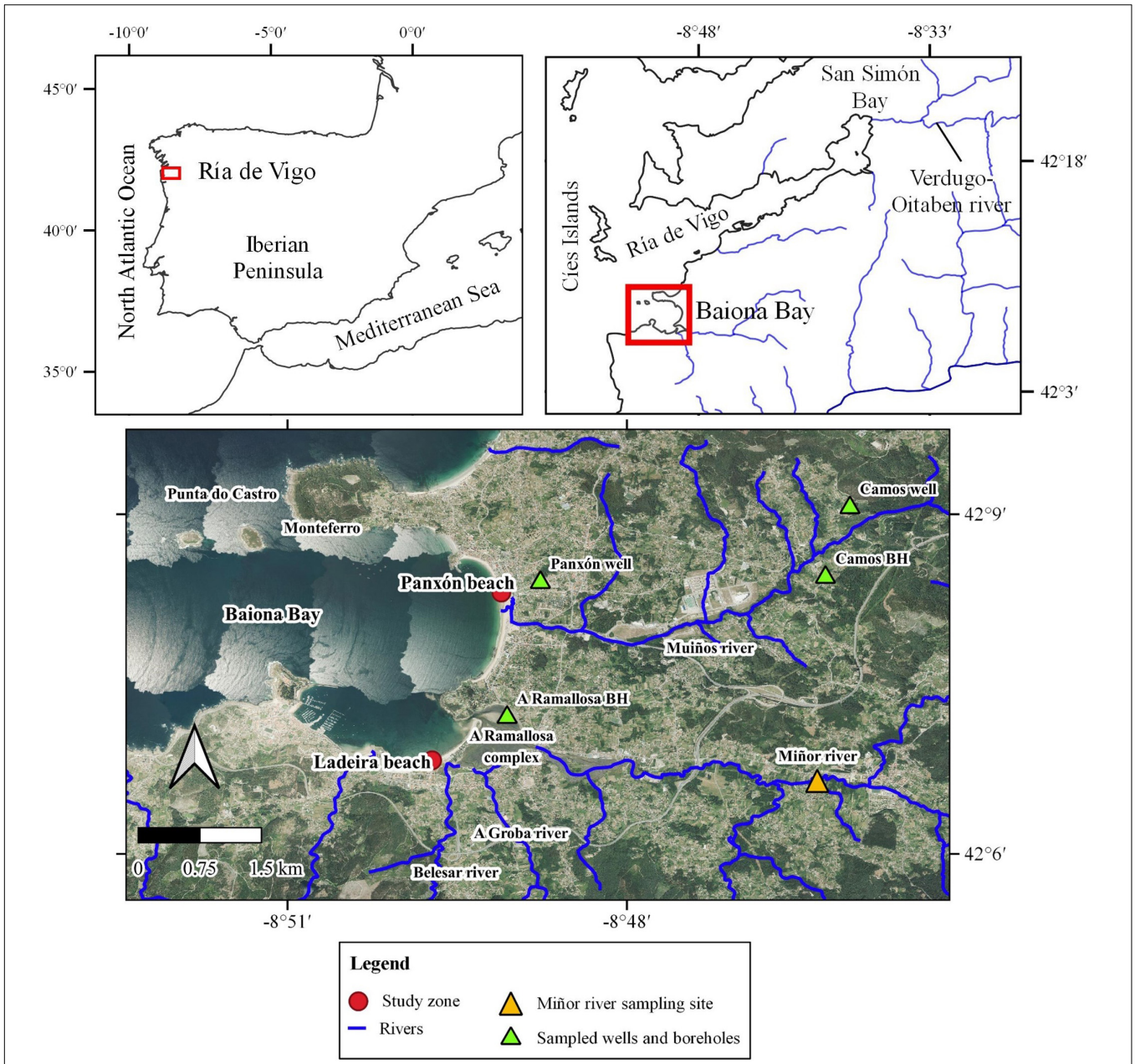


FIGURE 1 | Study area. Sampling sites are identified by red dots. The location of the wells and boreholes used in this study are represented with green triangles, while the location of the Miñor river sampling site is shown with a yellow triangle. These data are obtained from Ibánhez et al. (2019). Orthophoto (taken in 2018) and the mapping of local fluvial courses were obtained from the Instituto Geográfico Nacional (www.ign.es). BH denotes borehole.

Its morphology resembles a funnel oriented SE-NW and protected at its mouth by the Cíes Islands. Depending on the dominance of oceanic or riverine inputs, the Ría can be divided in two zones: an inner estuarine zone, formed by San Simón Bay and Baiona Bay, and an external oceanic zone, which covers the rest of the Ría. Intermittent upwelling of Eastern North Atlantic Central Water during March–April to September–October fertilizes the Ría (Álvarez-Salgado et al., 2003), sustaining intensive mussel aquaculture, shellfish harvesting, and small-scale fisheries in the region (Fernández et al., 2016). The coastal inlets in this area supports 15% of the world's mussel production (around 250,000 tons), billing 112 million € in 2015 and supporting more than 8,000 full-time employees (Labarta and Fernández-Reiriz, 2019).

Using radioisotope tracers, Ibánhez et al. (2019) recently identified and quantified SGD in the Ría de Vigo. San Simón and Baiona Bays (**Figure 1**) were among the most affected zones by this diffusive source of continental water. This study was placed in two wave-dominated beaches located in Baiona Bay: Ladeira and Panxón (**Figure 1**). Baiona Bay is exposed to westerly and southwesterly winds, allowing the most energetic waves to enter

the bay during winter storms. During the summer, the waves are less energetic due to the protection of the bay from northerly winds, making oceanic swell the most important energy source most of the year (Alejo et al., 1999). Tides are semidiurnal, with a range of 3–3.5 m during spring tides and 1.5–2 m during neap tides (Martín Míguez, 2002).

Ladeira beach is located in the inner part of Baiona Bay, protecting the A Ramallosa beach-barrier-lagoon complex. Its sedimentary composition is dominated by siliciclastic sands with carbonate content below 5%, mean grain size of 0.245 mm (Queralt et al., 2002) and little variation in grain size along the beach profile (González-Villanueva et al., 2007). It is influenced by fluvial sediments transported by the Miñor, A Groba and Belesar rivers. These rivers converge at the northern edge of the littoral arrow that connects the A Ramallosa complex and Baiona Bay (**Figure 1**). Backshore and foreshore zones appear well-defined in this beach, with vegetated dunes and beach cusps degraded by human action. Seaweed is accumulated in the intertidal zone during autumn and spring and prevents wave energy dissipation, creating an erosive vortex that develops steeps up to 70 cm high. This type of morphology could be preserved during winter, but it appears covered by sediment the rest of the year (Alejo and Vilas, 1987).

Panxón beach is located in the outer part of Baiona Bay, bounded by Punta do Castro to the North and by the Muiños River to the South (**Figure 1**). This beach is more exposed to wave action compared to Ladeira beach. The backshore ridge of dunes has been altered by human action, and the construction of a pier created a shadow zone in terms of sediment accumulation. Sediment is composed by unimodal fine sands with a medium-high selection, coarser and with poorer selection in more exposed zones of the beach (Álvarez-Vázquez et al., 2003). Mean grain size in Panxón is 0.236 mm with high content in carbonates (60–65%; Queralt et al., 2002).

Both beaches are surrounded by the Monteferro-O Rosal geological complex, which is a metasedimentary formation dominated by shales with intrusions of igneous rocks such as granite, pegmatite, pegmaplite and quartz. This complex is bounded by granitic igneous rocks from the Hercynian age with alkaline affinity to both the East and the West. These crystalline rocks are traditionally considered to have low permeability (Gustafson and Krásný, 1994), but the high fracturing present in the zone alongside with the high weathering of the surface layer (regolith) give them the capacity to store groundwater. Nevertheless, Holocene alluvial and colluvial sedimentary deposits appear associated to the studied beaches and the Monteferro-O Rosal geological complex (Pliego Dones et al., 1978), which further increases groundwater storing capacity in the region. These two beaches were selected attending to their close proximity and yet contrasting characteristics such as wave exposure, organic matter content, oxygenation status, and sediment composition.

Sampling Strategy

Seasonal surveys in Panxón and Ladeira beaches took place on the 20th and 22nd of February, 6th and 8th of May, 2nd and 4th of July and 29th and 30th of October 2019, respectively. These dates were selected to coincide with spring tides and thus, minimize biogeochemical differences caused by changes in the tidal regime. Three sampling stations were selected in the upper, middle and lower limits of the permanently saturated sediments of the intertidal zone (**Figure 2**). At each station, push-pull piezometers (M.H.E. Products, United States; 4 cm of screen-length) were buried at 178, 116, 86, 56, 29, and 10 cm depth within the sediment (the 10 cm depth piezometer was not installed in February). The presence of a gravel layer in Panxón (Álvarez-Vázquez et al., 2003) at a variable depth between 90 and 150 m complicated the installation of the deepest piezometers (116 and 178 cm). As a consequence, the installation depth of the longest piezometer was variable there. Beach profiles in February were measured with a GPS and referenced to the Alicante (SE Spain) datum. The remaining beach profiles from May to October were taken with a scaled rod as the slope from a reference point set at the backshore.

During the four surveys performed at each beach, water sample collection began after the installation of the piezometers during low tide. Porewater samples were collected with air-tight syringes after discarding three times the internal volume of the piezometers. Water samples collected from each piezometer were used to determine salinity, dissolved oxygen (O_2), radon (^{222}Rn),

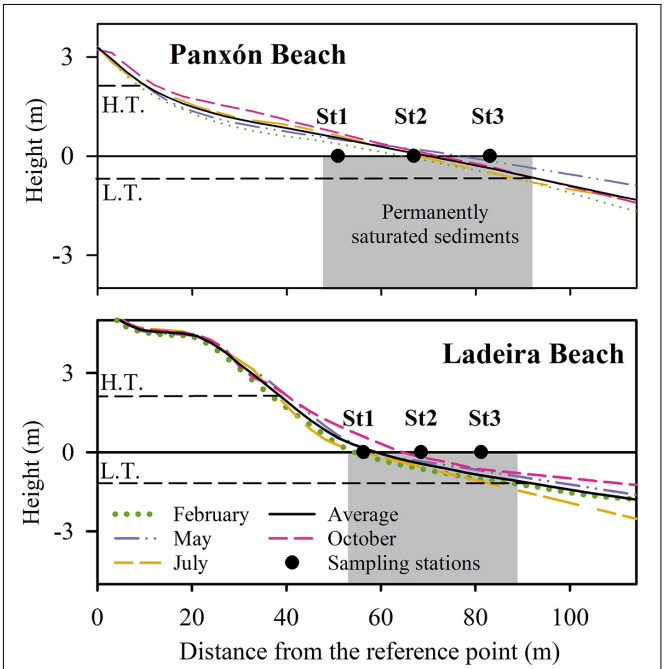


FIGURE 2 | Individual and average beach profiles of Panxón (upper panel) and Ladeira (lower panel). Panxón average beach slope was 3.00% (February: 2.90%, May: 2.44%, July: 3.31%, and October: 3.38%). Ladeira average beach slope was 6.86% (February: 6.71%, May: 7.10%, July: 6.54%, and October: 7.08%). Beach slopes were calculated with the data from the intertidal zone. Black dots represent the averaged location of the three sampling stations. The dark gray area represents the permanently saturated zone. HT, approximate position of high tide; LT, approximate position of low tide.

radium (^{226}Ra), and dissolved inorganic nitrogen (DIN; NO_3^-, NO_2^-, and NH_4^+). Temperature was measured onsite with a thermometer with an accuracy of ± 0.1°C.

Additional sediment samples were taken from the permanently saturated zone of the beach with a PVC minicorer (10 cm long, 2.5 cm of diameter) from the lower and upper sampling stations in May, July and October. In February, sediment samples were taken from the middle station. At each point, two minicorers were collected, sliced onsite into three different depths (0–3, 3–6, and 6–9 cm in February and 0–2, 2–6, and 6–10 cm in the rest of the surveys) and equivalent depths were mixed to reduce spatial variability. The homogenized sediment samples were immediately transferred to the lab and stored at −20°C until further processing. Sediment samples were used to determine water content, organic matter and total nitrogen and organic carbon content.

Analytical Methods

Sample volume collection was limited as much as possible to avoid potential spatial interference between piezometers. Thus, analytical techniques were adapted to low volume water samples. A Guildline Portasal salinometer was used to measure salinity. Nitrate and nitrite were measured following standard colorimetric methods (Grasshoff et al., 1999) on an Alliance Futura segmented flow autoanalyzer. In the case of ammonium the fluorimetric method of Kérouel and Aminot (1997) was used. Dissolved oxygen was measured following the spectrophotometric Winkler method (Labasque et al., 2004) adapted for low sample volumes (25 mL).

Radon activities were measured within 2 days after collection using a Rad7 Radon detector with a RadH2O accessory (Durridge Company, Inc.). The collected samples (70 mL) were transferred into 250 mL flasks and diluted with ^{222}Rn-free water. Readings were corrected for the internal ^{222}Rn decay from the time of collection to analysis. To obtain ^{226}Ra activities, purged samples were stored until ^{222}Rn and ^{226}Ra reached secular equilibrium (∼30 days, i.e., more than 5 times the ^{222}Rn half-life) and measured again. The equipment was purged with an activated carbon ^{222}Rn trap to minimize background activities. The detection limit of our procedure determined from the regular analysis of blanks (n = 36) made with ^{222}Rn-free water (250 mL) was 36 Bq m^{-3}. Thus, the detection limit of ^{222}Rn and ^{226}Ra in our diluted samples is estimated at 128 Bq m^{-3}. Porewater ^{222}Rn equilibrium activities were measured with sediment incubations (∼200 g dry weight; n = 9 for each beach) run with ^{222}Rn-free water (Colbert and Hammond, 2008). After 30–40 days of incubation, ^{222}Rn activities were determined following the same procedure as for field water samples. Results are expressed as the average and the standard error of the 9 equilibrium activities determined.Porosity was approximated to the water content in the sediment as follows:

$$\phi = \frac{V_{pw}}{V_{pw} + V_{sand}}$$

where V_{pw} is the volume of porewater and V_{sand} the volume of sand. Sediment subsamples were dried at 60°C until constant weight was reached. V_{pw} was then calculated using the salinities determined in the shallower depths of each beach. Local dry sediment density was determined (2.599 ± 0.001 kg/L in Panxón and 2.640 ± 0.038 kg/L in Ladeira) and used to calculate V_{sand}. The percentage of organic matter present in the sediment was determined by loss-on-ignition (Ball, 1964). To obtain total N and organic C content, sediment samples were powdered using a laboratory ball mill with natural agate tank during 10–15 min at medium intensity. Then, samples were exposed to HCl flumes during 6 h to remove inorganic C. Afterward, samples were analyzed in a CHN elemental analyzer Perkin Elmer 2400 A.

Statistical Analyses

Statistical analyses presented in this study were carried out in R 4.0.0 with the Rstudio 1.2.5019 editor. Normality of the measured variables was tested with the Shapiro-Wilk test. Spearman correlation analysis was performed using the PerformanceAnalytics 2.0.4 package for R, distinguishing between beaches and among surveys. The Kruskal-Wallis test was applied to verify whether the differences between groups were statistically significant. Principal Component Analysis (PCA) was performed with the "princomp" function from the stats 4.0.0 package and represented using the ggbiplot 0.55 package in R. Variables were scaled before performing the PCA.

Meteorological and Oceanographic Data

Meteorological and oceanographic conditions in the study area were evaluated for a period of 30 days prior to each survey (winter with data from the 20th January to the 22nd February, spring with the data from the 6th April to the 8th May, summer from the 2nd June to the 4th July and autumn from the 30th September to the 30th October; **Supplementary Table 1**). Daily water balance (**Supplementary Table 1**) was obtained from the repository of Meteogalicia[1] using the data from the meteorological platform of Baiona (autumn; 42°6.93′N 8°50.23′W) and Oia (remaining seasons; 41°59.67′N 8°51.97′W). Water balance integrated for the month prior to each survey was calculated as the sum of daily water balances for that period. Water balance is used as a qualitative indicator of groundwater table fluctuations due to the fast aquifer recharge-discharge rates and fast response to environmental conditions verified in the local crystalline aquifers (Raposo et al., 2012). Minimum and maximum wave heights during the studied periods (**Supplementary Table 1**) were obtained from the SIMAR Point (3014003; 42°7.8′N 8°55.2′W) available from Puertos del Estado[2]. Average and standard deviation of sea surface salinity and dissolved oxygen data (**Supplementary Table 1**) were calculated with the data from the INTECMAR repository[3], from the buoy located at the port of Baiona (42°7.26′N 8°50.77′W).

[1] www.meteogalicia.gal

[2] http://www.puertos.es/es-es/oceanografia/Paginas/portus.aspx

[3] www.intecmar.gal

RESULTS

Sampling Site Characterization

Autumn showed the most positive water balance, followed by spring and winter. On the contrary, summer was characterized by low precipitation and a resulting negative water balance (**Supplementary Table 1**). Storm events were recorded in the days prior to the February and May surveys, whereas in July and October calm conditions dominated. Although being the rainiest period, autumn showed the highest averaged salinity within Baiona Bay, followed by summer and winter (**Supplementary Table 1**). Dissolved oxygen levels in surface waters of the bay remained close to saturation throughout the studied period (**Supplementary Table 1**).

The beach profile of Panxón is typical of a dissipative beach, with a leveled morphology caused by high-energy conditions (**Figure 2**). The maximum slope was reached in October (3.38%) and the minimum slope in May (2.44%). Conversely, the beach profiles of Ladeira presented characteristics of a reflective beach, with a well-developed supra-tidal and a marked berm throughout the year (**Figure 2**). This is in accordance with its lower exposure to the dominant waves compared to Panxón beach. The maximum beach slope was reached during May (7.10%) and the minimum in July (6.54%). Following the beach berm, a 50 cm high slope appeared during October and probably caused by storm waves developed in the days prior to this survey (**Supplementary Table 1**). The abnormal storm frequency occurring in summer 2019 caused a switch in the optimum season for the maximum sediment accumulation at both beaches, which occurred in autumn rather than during the summer.

Panxón and Ladeira beaches presented similar porosity (average: 0.47 ± 0.02 in Panxón and 0.46 ± 0.06 in Ladeira; Kruskal-Wallis test p-value > 0.05) but significantly different sedimentary organic matter content (average: 1.33 ± 0.10% dry weight in Panxón and 0.93 ± 0.40% dry weight in Ladeira; Kruskal-Wallis test p-value < 0.01) and C:N molar ratio (average: 3.23 ± 0.81 in Panxón and 10.71 ± 3.48 in Ladeira; Kruskal-Wallis test p-value < 0.01). Organic matter content decreased with depth in both beaches (**Figure 3**), with the exception of the lower station in May and October at Panxón and in February at Ladeira. Organic matter content decline with depth was higher in Ladeira than in Panxón, especially in July (from 1.78 to 0.76% in the lower station and from 1.34 to 0.63% in the upper station; **Figure 3**). C:N molar ratio showed higher average and range in Ladeira (from 7.0 to 21.2; **Figure 3**) than in Panxón (which had a range of 2.1–4.8; **Figure 3**).

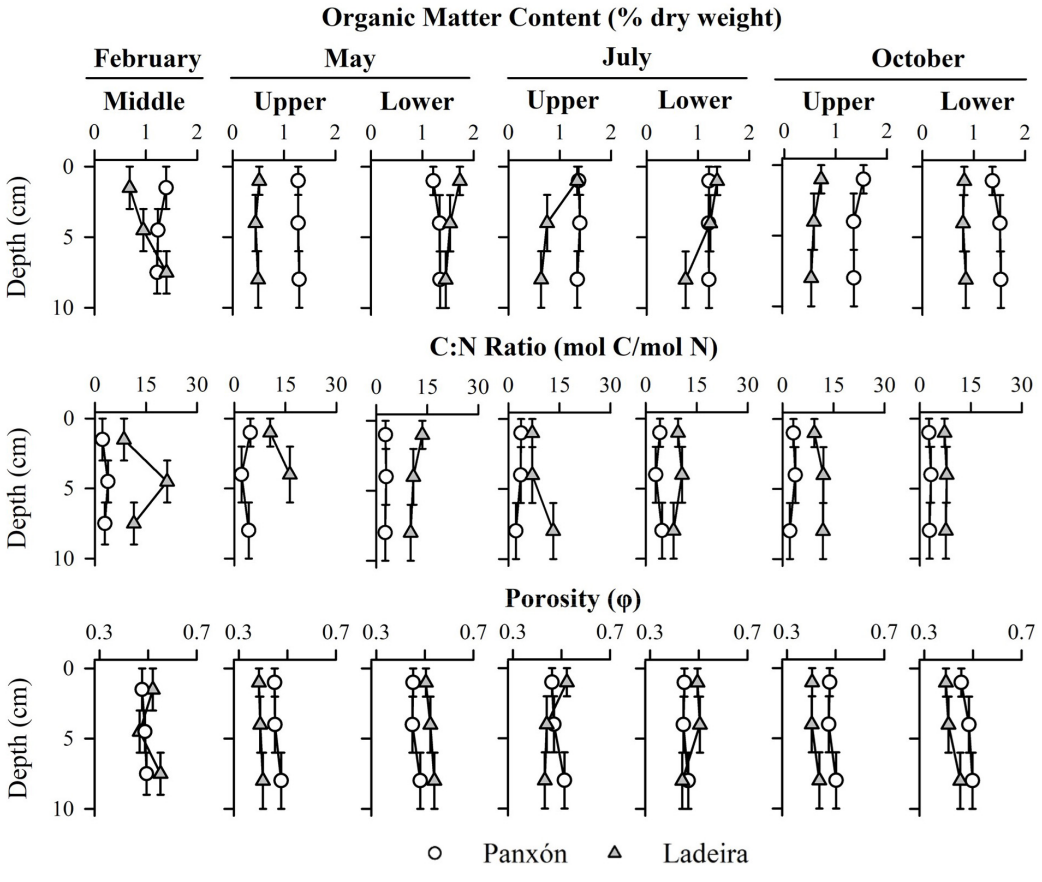


FIGURE 3 | Vertical sediment profiles of organic matter (% dry weight), C:N molar ratio and porosity (ϕ) of each beach and survey at the middle station in February and at the lower and higher sampling stations in the remaining surveys. The vertical error bars represent the length of the sliced sediment samples.

Seasonal differences in the measured sediment properties were only observed in the organic matter content at Panxón beach (Kruskal-Wallis test p-value < 0.05). The lack of organic matter peaks with depth in the collected 10 cm length sediment corers suggests that these differences may be related to seasonal changes in the supply of pelagic organic matter from surface waters rather than seasonal sediment transport along the beach profile.

Porosity and organic matter content appeared significantly correlated in both Panxón ($p < 0.05$, $r = 0.46$, $n = 21$) and Ladeira ($p < 0.001$, $r = 0.76$, $n = 21$). Moreover, Ladeira showed high correlations between porosity and both organic C content ($p < 0.001$, $r = 0.72$, $n = 21$) and total N content ($p < 0.001$, $r = 0.72$, $n = 20$); and between organic matter and both organic C content and total N content ($p < 0.001$, $r = 0.95$, $n = 21$, and $r = 0.95$, $n = 20$, respectively). In Ladeira, total N content and total organic C content also appeared significantly correlated ($p < 0.001$, $r = 0.92$, $n = 20$) although the C:N molar ratio did not show any relationship with the other variables. On the contrary, in Panxón, organic matter content was significantly correlated with total N content ($p < 0.05$, $r = 0.47$, $n = 21$).

Tracing Water Circulation: Salinity, ^{222}Rn and ^{226}Ra Profiles

Porewater salinity was lower than that of Baiona Bay (**Figure 4** and **Supplementary Table 1**) revealing the existence of a freshwater influx to the beach interior. Moreover, high porewater salinity gradients were observed, even in the same month and beach. The high porewater salinity values found in October (30.7 ± 0.7–31.4 ± 1.8) in Panxón did not occur in Ladeira, and the maximum average salinity in Ladeira reported at the lower station of May (32.1 ± 1.1) did not appear reflected in the parallel survey performed in Panxón. This suggests that seasonal salinity changes are specific of each beach, probably due to differences in circulation patterns and freshwater supply.

Porewater ^{222}Rn equilibrium activities determined with sediment incubations were 3698 ± 251 Bq m^{-3} from Panxón sediments and 1610 ± 329 Bq m^{-3} from Ladeira sediments. Porewater ^{222}Rn activities were, in most cases, greater than these ^{222}Rn equilibrium activities, suggesting external inputs of ^{222}Rn to the beach porewaters. Exceptions are found in some sampled porewaters near the sediment surface (**Figure 4**). Average activities of dissolved ^{226}Ra were one order of magnitude lower than the average activities of ^{222}Rn and seasonal and spatial differences were also found.

Vertical gradients of salinity and radioisotopes were observed throughout the four sampling periods (**Figure 4**). Decreases in salinity with depth were recorded in most porewater profiles (e.g., between 29 and 56 cm depth at the middle station of February in Panxón), followed in some of them by new increases (e.g., between 86 and 116 cm depth in the same porewater profile). Temperature variations along the profiles were too small (1–2°C) to cause an increase in density that would support the stability of the salinity profile. Consequently, unstable density profiles were maintained by the flow of the freshwater and seawater bodies that interact in the STE. Only in a few porewater profiles (at the upper station in May, and at the lower and middle station in July, in Panxón) salinity was mostly vertically homogeneous.

In most porewater profiles ^{222}Rn activities were the lowest at shallow depths. Conversely, ^{222}Rn peaks of up to 11234 ± 353 Bq m^{-3} in Panxón and 13551 ± 732 Bq m^{-3} in Ladeira (both at the lower station during October) were registered in depth (**Figure 4**). Besides, increases in ^{222}Rn activity were followed by decreases in salinity at various depths (e.g., at the lower station in October at Panxón). This inverse relationship between salinity and ^{222}Rn activity was significant in May ($p < 0.05$, $r = -0.50$, $n = 17$) and October ($p < 0.01$, $r = -0.62$, $n = 18$) in Panxón and in May ($p < 0.01$, $r = -0.68$, $n = 18$) in Ladeira beach. Peaks of ^{226}Ra activity (> 600 Bq m^{-3}) appeared in some porewater profiles (e.g., at the lower station in July, in Ladeira; **Figure 4**). ^{226}Ra activities were correlated with salinity in July ($p < 0.05$, $r = 0.54$, $n = 18$) in Panxón, and in May ($p < 0.05$, $r = 0.54$, $n = 18$) and July ($p < 0.001$, $r = -0.82$, $n = 18$) in Ladeira.

Tracing Nitrogen Cycling: Nitrate, Nitrite, Ammonium, and Dissolved Oxygen Porewater Profiles

Panxón beach was more oxygenated, with higher profile-averaged concentrations of dissolved oxygen (from 19.8 ± 22.9 μM to 214.2 ± 21.1 μM) than Ladeira (from 0.0 ± 0.0 μM to 22.9 ± 15.2 μM), where suboxic (≤ 4.5 μM) and anoxic conditions dominated (**Figure 5**). These differences in oxygenation were strongly linked to the differences found in inorganic nitrogen speciation in porewaters. Nitrate concentrations were between one and two orders of magnitude higher in Panxón compared to Ladeira. On the contrary, ammonium concentrations were higher in Ladeira (**Figure 5**).

The largest variations in porewater dissolved oxygen concentrations occurred between stations sampled in the same month and beach (**Figure 5**). Upper stations presented, in most cases, higher levels than middle and lower stations. Moreover, the oxygenation in Panxón beach occurred in depth (up to 240 μM), and lowest oxygen levels were found close to the sediment surface (~ 10 μM; **Figure 5**). In Ladeira, increases in dissolved oxygen concentrations appeared both at shallow and at intermediate depths, as shown in the upper porewater profiles of February and May (**Figure 5**).

Nitrate concentration peaks appeared linked to increases in oxygen levels in most porewater profiles. However, nitrate was also present at low concentrations in some of the shallower depths during July and October in Panxón. Dissolved oxygen was significantly correlated with nitrate in February ($p < 0.05$, $r = 0.69$, $n = 14$), May ($p < 0.01$; $r = 0.66$, $n = 17$) and July ($p < 0.01$; $r = 0.66$, $n = 18$) in Panxón beach and in May ($p < 0.05$, $r = 0.59$, $n = 18$) and July ($p < 0.05$, $r = -0.52$, $n = 18$) in Ladeira beach. On the contrary, ammonium generally appeared at shallow depths negatively correlated with oxygen in Ladeira ($p < 0.01$, $r = -0.51$, $n = 69$) and with nitrate in both Panxón ($p < 0.001$, $r = -0.42$, $n = 67$) and Ladeira ($p < 0.001$, $r = -0.24$, $n = 69$). During February and May high ammonium concentrations (>30 μM) were present throughout the entire vertical porewater profile at the lower station in

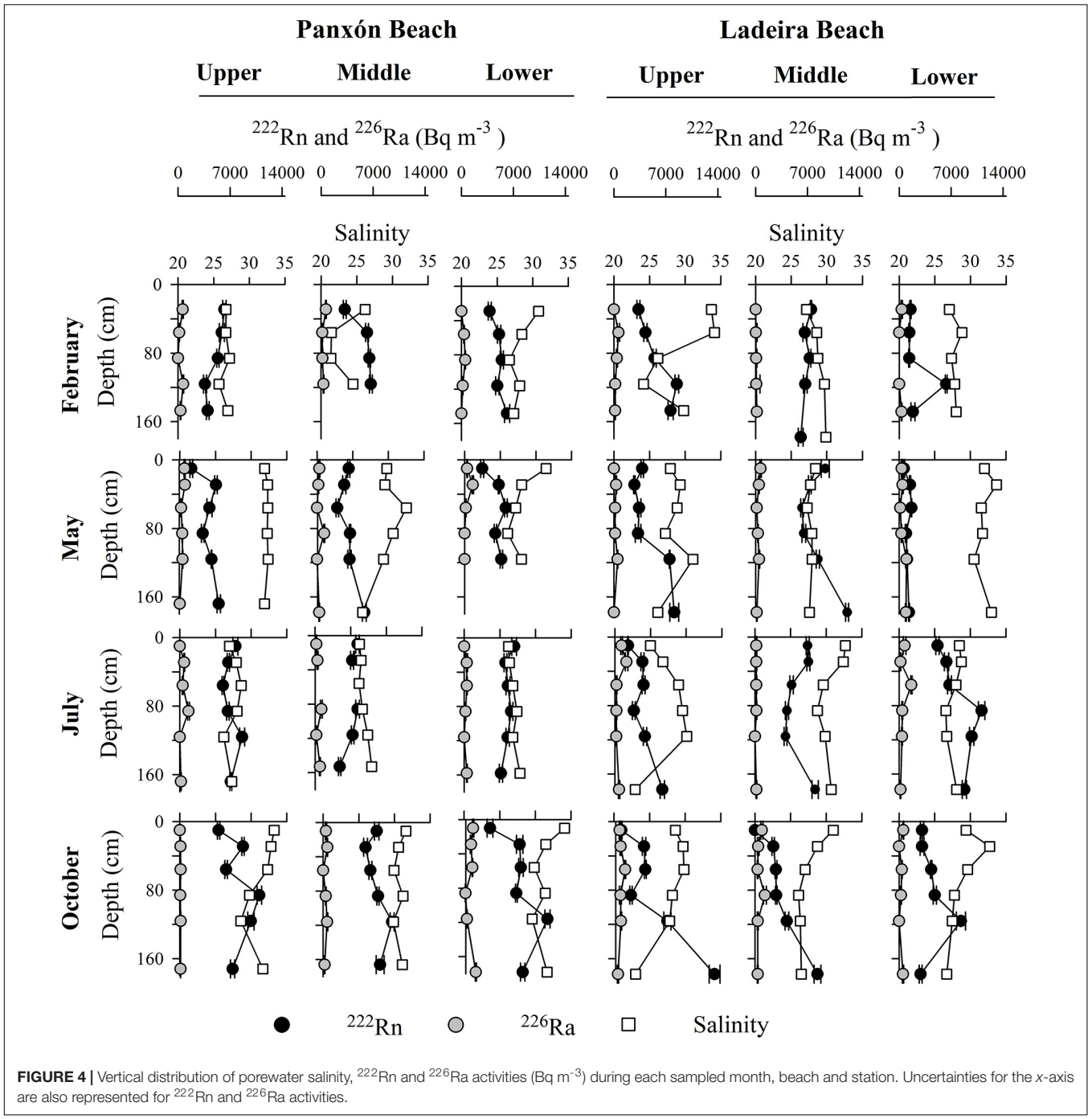


FIGURE 4 | Vertical distribution of porewater salinity, ^{222}Rn and ^{226}Ra activities (Bq m^{-3}) during each sampled month, beach and station. Uncertainties for the *x*-axis are also represented for ^{222}Rn and ^{226}Ra activities.

Ladeira. Nitrite was associated to shallow depths similarly to ammonium, particularly in Panxón beach (**Figure 5**).

Relationships Between Circulation Tracers and Nutrient Profiles

Spearman correlation analysis showed significant relationships between nutrient and internal porewater circulation tracers. In Panxón beach, nitrate and ^{222}Rn ($p < 0.001$; $r = 0.47$, $n = 67$) as well as oxygen and salinity ($p < 0.05$, $r = -0.25$, $n = 67$) were significantly correlated. Furthermore, in October, the month with the most positive water balance (**Supplementary Table 1**), oxygen and ^{222}Rn ($p < 0.05$, $r = 0.57$, $n = 18$), as well as salinity and nitrate ($p < 0.01$, $r = -0.67$, $n = 18$) showed strong correlations. This adds to the correlations found between ^{222}Rn and salinity there and suggests a relationship between nitrate enriched, oxygenated porewater and ^{222}Rn-enriched, low salinity porewater. By contrast, in Ladeira ammonium was significantly correlated with salinity ($p < 0.05$; $r = 0.24$, $n = 69$) and showed negative correlation with ^{222}Rn

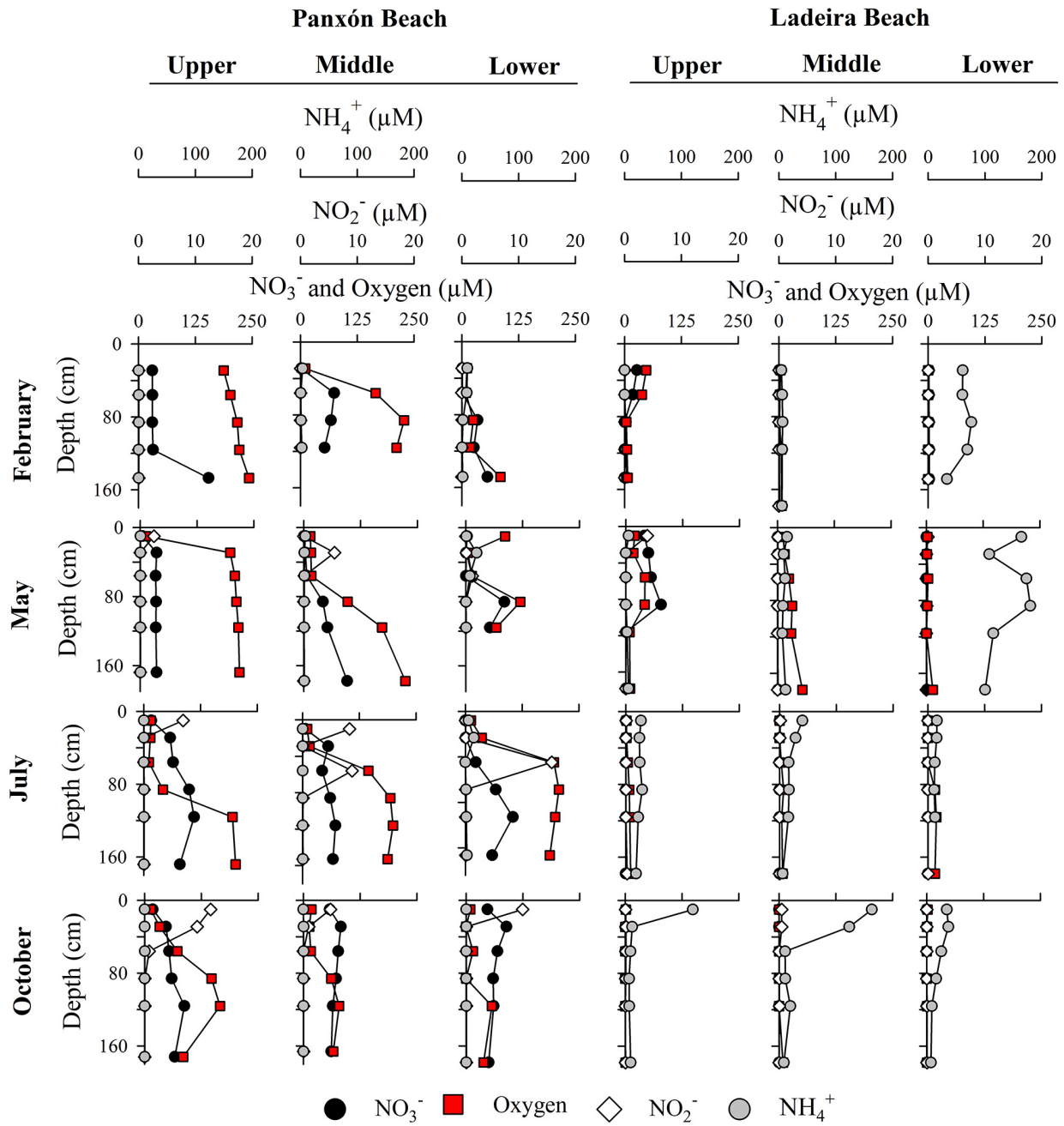


FIGURE 5 | Vertical porewater profiles of nitrate (NO_3^-), nitrite (NO_2^-), ammonium (NH_4^+) and dissolved oxygen concentrations (in μM) organized by sampling station, month and beach.

($p < 0.001$; $r = -0.53$, $n = 69$). Thus, ammonium seems to be related to infiltrated seawater rather than fresh groundwater in Ladeira beach.

A principal component analysis (PCA) of the measured variables in Panxón and Ladeira is presented combined (**Figure 6A**) and individually for each beach (**Figures 6B,C**). Components 1 (C1) and 2 (C2) account for 31.2 and 17.1% of the total variance in the PCA performed with the data from both beaches. There, component C1 is related to the redox conditions, as it is dominated by ammonium (0.51), nitrate (−0.50) and dissolved oxygen (−0.48); whereas Component C2 is more related to transport processes, as it was dominated by ^{222}Rn (−0.52) and salinity (0.47), in addition to dissolved oxygen (0.48) and nitrate (0.46; **Figure 6A**). The data from each beach appeared clustered and well separated from each other in this PCA, giving a different sign of the slope of a linear regression of PCA components 1 and 2 (**Figure 6A**). A more detailed analysis is provided by the individual PCAs.

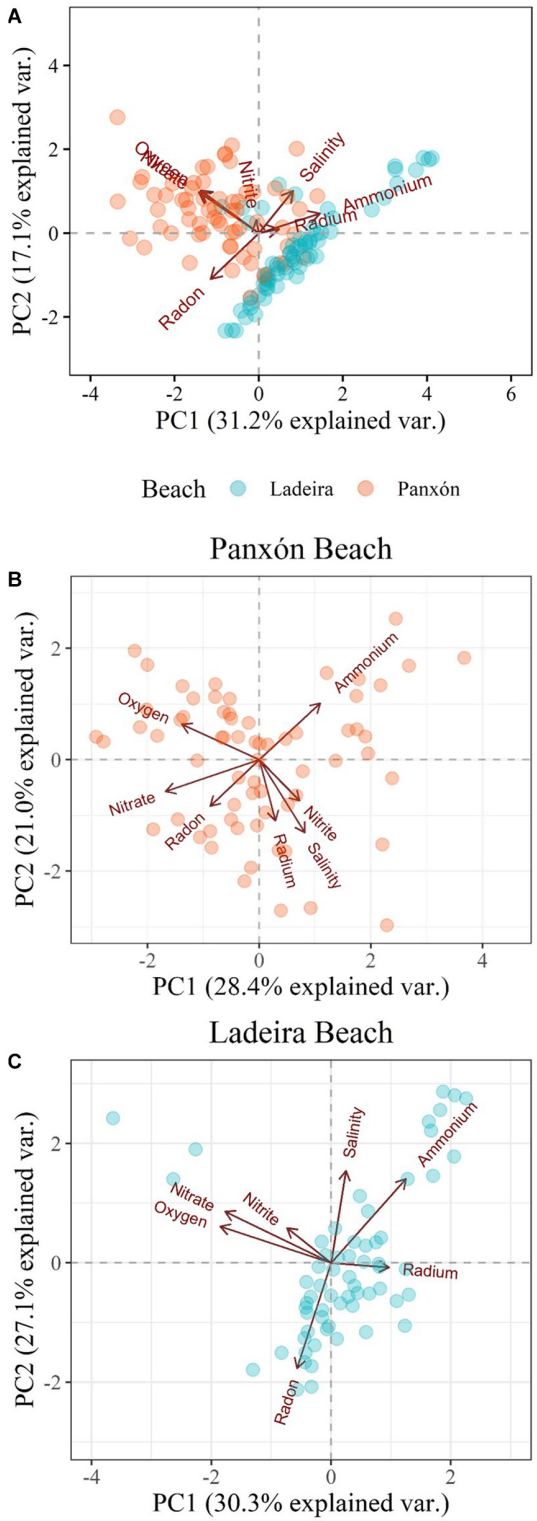


FIGURE 6 | (A) Principal Component Analysis (PCA) performed with the data from both beaches, identified with different colors. Components 1 and 2 were linearly correlated in both beaches: Ladeira: $y = -1.12 + 0.751x$, $R^2 = 0.68$; Panxón: $y = 0.288 - 0.288x$, $R^2 = 0.093$. **(B)** PCA performed with the data from Panxón beach. **(C)** PCA performed with the data from Ladeira beach. Radon and Radium refer to ^{222}Rn and ^{226}Ra activities.

In the PCA performed with the data obtained in Panxón (**Figure 6B**), Components C1 and C2 account for 28.4 and 21.0% of the total variance. Component C1 is dominated by nitrate (−0.59) and oxygen (−0.49), while Component C2 is dominated by salinity (−0.54), ^{226}Ra (−0.45) and ammonium (−0.42). In Ladeira (**Figure 6C**), PCA components C1 and C2 account for 30.3 and 27.1% of the total variance. C1 is dominated by oxygen (−0.59) and nitrate (−0.56) and C2 is dominated by ^{222}Rn (−0.59), salinity (0.52) and ammonium (0.47). Both PCAs confirmed the relationships observed through Spearman correlation analysis.

DISCUSSION

The Source of ^{222}Rn-Rich Porewater

Highly fractured granites and shales dominate the geology of the NW Iberian Peninsula (Llerena et al., 2013) and are part of the Monteferro-O Rosal geological complex (Pliego Dones et al., 1978) that surrounds Baiona Bay. These geological substrates are naturally enriched in isotopes from the ^{228}U decay chain (Tollefsen et al., 2016), such as ^{226}Ra and ^{222}Rn. Therefore, groundwaters contained within these rocks are commonly enriched in these radioisotopes, particularly ^{222}Rn since ^{226}Ra shows very low solubility at low salinities (Gonneea et al., 2008).

Porewater ^{222}Rn equilibrium activities estimated from sediment incubations together with the measured dissolved ^{226}Ra activities (∼130–1,600 Bq m^{-3}) are not sufficient to explain the observed ^{222}Rn enrichment in the sampled porewaters. Furthermore, the negative correlation between ^{222}Rn and salinity found in some of the surveys and the opposite PCA scores between ^{222}Rn and salinity in Ladeira (**Figure 6C**) point toward a freshwater origin for this ^{222}Rn enrichment. Ibánhez et al. (2019) measured radon activities at various freshwater bodies near Baiona Bay (**Table 1**). There, ^{222}Rn activities found in the Miño River (**Figure 1**; $2.7 \pm 0.1 \times 10^3$ Bq m^{-3} in winter/spring and $2.5 \pm 0.1 \times 10^3$ Bq m^{-3} in summer) are one order of magnitude below the maximum ^{222}Rn activities observed in Ladeira. On the other hand, ^{222}Rn activities found in boreholes and wells near the study area (Camos borehole and well, Ramallosa borehole and Panxón well; **Figure 1**) were very high (between $32 \pm 2 \times 10^3$ Bq m^{-3} and $802 \pm 28 \times 10^3$ Bq m^{-3}; **Table 1**). Thus, considering that rainfall has low ^{222}Rn content, the high radon levels found in beach porewaters can only be sourced from groundwater from the coastal aquifers.

Assuming that ^{222}Rn is in secular equilibrium within the coastal aquifer and that no net ^{222}Rn loss occurred during the transit to the studied beaches except from ^{222}Rn decay, the difference between the radon activities found in the proximate groundwaters ($Rn_{aquifer}$; **Table 1**) and those found in the beach porewaters could provide a first estimate of the transit time of groundwater from the terminus of the coastal aquifer to the beach surface. ^{222}Rn activities in excess (Rn_{excess}) are defined as the difference between measured porewater ^{222}Rn activities and those supported by porewater ^{222}Rn equilibrium activities plus porewater dissolved ^{226}Ra activities. We further assume that measured porewater ^{222}Rn equilibrium activities in shallow

TABLE 1 | Temperature, ^{222}Rn and ^{226}Ra activities, dissolved oxygen, dissolved inorganic nitrogen (DIN = $NH_4^+ + NO_2^- + NO_3^-$) and NO_3^- in the Miñor river, wells and boreholes surrounding the sampling beaches during winter/spring and summer/autumn.

			Camos well	Camos BH	Ramallosa BH	Panxón well	Miñor river
	Lat		42.15	42.14	42.12	42.14	42.11
	Lon		−8.76	−8.77	−8.81	−8.81	−8.77
	Depth	M	12	40	40	10	0
Winter/spring	T	°C	16.2	15.4	16.8	n.d.	15.1
	^{222}Rn	10^3 Bq m^{-3}	44 ± 2	341 ± 2	684 ± 16	32 ± 2	2.7 ± 0.1
	^{226}Ra	10^3 Bq m^{-3}	n.d.	n.d.	n.d.	3 ± 0	0.0 ± 0.0
	O_2	μM	n.d.	270	303	n.d.	295
	DIN (NO_3^-)	μM	333 (325)	144 (136)	243 (242)	n.d.	74 (72)
Summer/autumn	T	°C	22	16.6	17.1	20.1	16.9
	^{222}Rn	10^3 Bq m^{-3}	83 ± 4	736 ± 30	802 ± 28	48 ± 2	2.5 ± 0.1
	^{226}Ra	10^3 Bq m^{-3}	0.2 ± 0.0	0.4 ± 0.0	1.7 ± 0.0	0.2 ± 0.0	0.0 ± 0.0
	O_2	μM	n.d.	282	278	n.d.	243
	DIN (NO_3^-)	μM	101 (101)	187 (187)	221 (220)	n.d.	71 (69)

n.d. not determined. BH denotes borehole. Data taken from Ibánhez et al. (2019).

sediments (0–10 cm) are representative of all sampling depths (0–180 cm), since sediment composition is very homogeneous in the studied beaches, with the exception of the gravel layer of Panxón beach (Álvarez-Vázquez et al., 2003; Perez-Arlucea et al., 2005; González-Villanueva et al., 2007). The ^{222}Rn activities in excess recorded during February and July were used to calculate groundwater transit times (t) as follows:

$$t = \frac{\ln\left(Rn_{extrapolated}/Rn_{aquifer}\right)}{\lambda}$$

where λ is the decay constant of ^{222}Rn (0.18 d^{-1}) and $Rn_{extrapolated}$ is the ^{222}Rn activities in excess observed at each beach and extrapolated to 0 salinity. This extrapolation was performed using the percentage of fresh-groundwater ($\%_{fresh}$) and Rn_{excess} in the sample:

$$Rn_{extrapolated} = \frac{100 \cdot Rn_{excess}}{\%_{fresh}}$$

The percentage of fresh-groundwater ($\%_{fresh}$) was obtained using as saltwater endmember the sample with the maximum salinity measured at each beach and survey. Only samples with a percentage of fresh-groundwater above the median of each beach and survey were used to guarantee a Rn_{excess} signal sufficiently high, thus limiting our extrapolations (**Supplementary Table 2**).

Transit times between 3.5 ± 2.6 and 22.8 ± 1.6 days were obtained in Panxón beach and between 1.6 ± 1.6 and 21.4 ± 4.4 days in Ladeira beach, depending on which groundwater endmember is used (**Supplementary Table 2**). These values are in the range of other transit times found elsewhere (Michael et al., 2005; Bokuniewicz et al., 2008). Transit times were higher in summer than winter, probably because higher aquifer residence times result from lower rainfall and higher evaporation, which might have resulted in lower groundwater table during the summer (**Supplementary Tables 1**, **2**). The shortest apparent transit times were calculated when assuming that the coastal aquifer supports Rn levels as those measured in the wells from Camos and Panxón (between 3.4 ± 1.6 and 8.9 ± 4.4 days when using the Camos well, and between 1.6 ± 1.6 and 6.0 ± 1.6 days when using the Panxón well; **Supplementary Table 2**). Radon activities measured in boreholes and wells spans one order of magnitude (**Table 1**) and this strongly affects the calculated transit times.

Transit time calculations performed here assume a steady-state, advection-dominated and homogeneous flow system (Michael et al., 2011). The hydrological Peclet number (P_e) was calculated for each of the transit times to evaluate the assumption of an advection-dominated system (**Supplementary Table 4**):

$$P_e = vL/D_{molec}$$

where L is the characteristic pore length, approximated to the averaged grain size of each beach, D_{molec} is the diffusion coefficient of ^{222}Rn in water and v the groundwater velocity. A D_{molec} of 1.102 × 10^{-5} cm^2/s obtained in seawater at 17°C (Dueñas et al., 1985), i.e., the averaged measured temperatures observed in both STEs, was used. Groundwater velocities (**Supplementary Table 4**) were obtained using the calculated transit times (**Supplementary Table 2**) and the shortest path between each sampling site and the nearest U-enriched body rock (300 m for Panxón beach and 580 m for Ladeira beach; Pliego Dones et al., 1978). In all cases, P_e numbers were higher than 1 (**Supplementary Table 4**), confirming that advection dominates over diffusion regardless of the groundwater endmember used.

A sensitivity analysis was performed to determine the relative importance of $Rn_{aquifer}$ and $Rn_{extrapolated}$ in the calculated transit times as follows (Ibánhez et al., 2011):

$$S(x, y) = (\Delta x/x)/(\Delta y/y)$$

where x is the transit time and y the variable tested ($Rn_{aquifer}$ or $Rn_{extrapolated}$) and Δx and Δy the respective ranges of variation. A 10% of variation was imposed to each variable tested (Δy). Results showed that transit times are very sensitive ($S >> 1$) only at low $Rn_{extrapolated}$ (i.e., at low unsupported ^{222}Rn enrichment in the beach porewaters) and $Rn_{aquifer}$ values ($< 50 \times$

10^3 Bq m^{-3}; i.e., those measured in wells surrounding the study sites). Conceptually, the local aquifers can be approximated to a two-layer aquifer: a surface layer contained within the regolith and the highly fractured surface basement rock where wells are screened, and a deeper layer contained within the fractured basement rock where boreholes are screened (Raposo et al., 2012). Aquifer specific storage and water transmissivities in the study region are orders of magnitude higher in the surface aquifer layer compared to the fractured rock underneath (Raposo et al., 2012 and references therein). These characteristics determine contrasting matrix porosity and groundwater residence times that may explain the differences in ^{222}Rn activities observed between both aquifer layers. Furthermore, these contrasting hydrological characteristics of both aquifer layers suggest the surface layer as the most probable source of continental groundwater to the studied STEs. Nevertheless, further analysis is needed to accurately identify the groundwater endmembers and transit times of both STEs.

Porewater Circulation in the Ladeira and Panxón STEs

The vertical distribution of Rn_{excess} can be used to identify the location of the radon-enriched FDT in the measured porewater profiles (**Figure 7**). For this, homogeneous porewater ^{222}Rn equilibrium activities with depth are assumed. The use of Rn_{excess} to identify the FDT is also limited by internal mixing, that could promote high salinity porewaters associated to high ^{222}Rn activities.

Radon activity "excess" is observed in most of the porewater profiles of Ladeira and Panxón beaches (**Figure 7**). A peak in Rn_{excess} was observed between 86 and 116 cm in the upper station of July and in the three stations of October in Panxón (**Figure 7**). There, the gravel layer detected between 90 and 150 cm likely represents a zone of preferential porewater transport. This modifies the typical porewater circulation structure of STEs, contracting the salt-wedge to shallower depths and increasing mixing, especially in October (**Figure 8**). Secondary peaks of Rn_{excess} (**Figure 7**) could be related to density instabilities (Simmons et al., 2001; Robinson et al., 2006) or to zones with higher permeability with respect to adjacent areas (Geng et al., 2020a,b).

The tidal circulation cell and the salt-wedge can be detected in the measured porewater profiles associated to high salinities (>30; **Figures 4**, **8**), but also to ^{222}Rn activities lower than porewater ^{222}Rn equilibrium (**Figure 8**). This is an indication of porewaters with low residence time, i.e., recently exchanged with surface waters. Porewaters with high salinity and radon activities below equilibrium were found in the upper part of the sampled beaches, identified as the tidal circulation cell, and below the FDT, identified as the salt-wedge (**Figures 4**, **8**).

The seasonal variation of the continental hydraulic gradient and the occurrence of wave events are related with the position of the FDT exit point and the size of the tidal circulation cell in STEs (Robinson et al., 2007b, 2014, 2018; Heiss and Michael, 2014; Xin et al., 2015). High inland water table could cause the narrowing of the tidal circulation cell and the displacement of the FDT exit site landwards (Heiss and Michael, 2014). This seems to be the case during February and May in both beaches (**Figures 4**, **7**), which agrees with the positive water balance observed during these months (**Supplementary Table 1**). Increased wave forcing has been related to strengthen flows in the tidal circulation cell (Robinson et al., 2014; Xin et al., 2015). Apparently, wave events prior to the surveys of February and May (**Supplementary Table 1**) might have influenced the STE (**Figures 4**, **8**), where high salinity and ^{222}Rn activity gradients showed a well-developed tidal circulation cell (**Figures 4**, **8**). Furthermore, the tidal circulation cell penetrated deeper in the upper station of Panxón than in the upper station of Ladeira (**Figure 4**). This suggests that Panxón beach is more sensitive to wave forcing than Ladeira beach, which agrees with its higher wave-exposure. The lower salinities of the FDT in February compared to May might be related to a higher inland hydraulic gradient during February.

July showed vigorous mixing in both beaches, probably caused by a low inland hydraulic gradient and calm wave conditions (**Figure 4**). However, in Panxón, the reduced salinities of the FDT in July suggest a higher fresh groundwater flux, which contrasts with the negative water balance found during the summer (**Supplementary Table 1**) and suggests a time lag between aquifer recharge and discharge. October, which showed the highest water balance of the studied period (**Supplementary Figure 1**), showed a radon-enriched and high salinity FDT in Panxón beach and lower salinity FDT in Ladeira beach (**Figures 4**, **8**). Increased residence times and seawater intrusion into the aquifer due to reduced inland hydraulic gradient during the summer might explain the high salinities and ^{222}Rn activities found in October at Panxón beach. Adsorbed ^{226}Ra at low salinities can be mobilized due to ionic exchange as salinity increases (e.g., during seawater intrusion at low aquifer pressure periods; Dulaiova et al., 2008; Gonneea et al., 2008). With the recovery of the continental groundwater table during autumn, this mobilized ^{226}Ra will then exit the STE as observed during the October survey in Panxón beach. This seems to further support that the high salinity, ^{222}Rn-enriched waters observed during October in Panxón are originated from seawater previously intruded into the aquifer during the summer.

Oxygen and Organic Matter Transfer and Reactivity in the Panxón and Ladeira STEs

In STEs, the tidal circulation cell is, together with the inflow of oxygenated terrestrial groundwater, the main driver of oxygenation of the beach interior (Robinson et al., 2007a; Ibánhez and Rocha, 2016). This is well illustrated by the measured dissolved oxygen porewater profiles at Ladeira beach in February and May. High porewater oxygen concentrations (>20 μM) coincided with radon activities near equilibrium (**Figures 5**, **7**) and with the high salinity zones at the upper station (**Figure 4**), where the tidal circulation cell was active. Conditions became hypoxic in July and October, probably due to the weakening of the tidal circulation cell and/or higher benthic oxygen consumption rates.

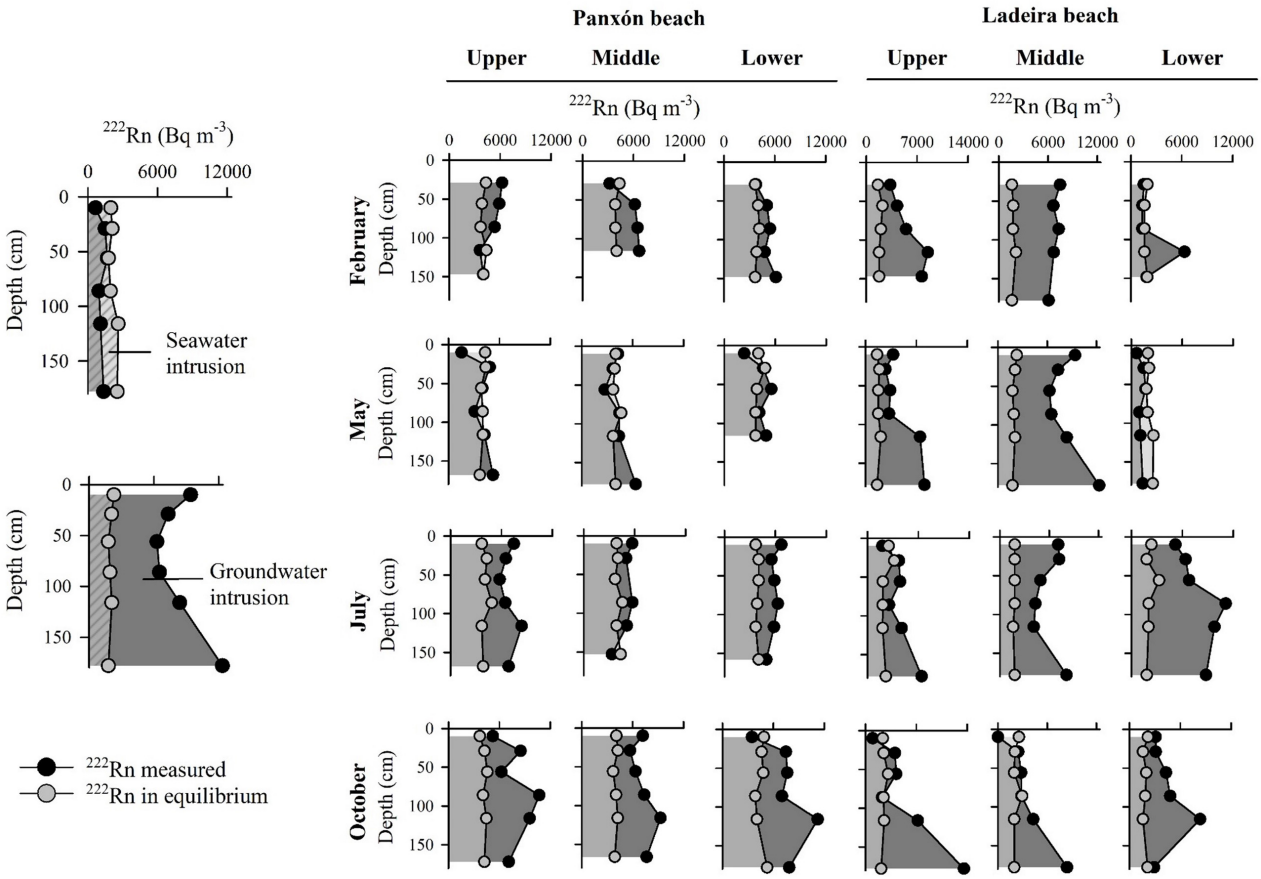


FIGURE 7 | Measured porewater ^{222}Rn activities (black) and equilibrium ^{222}Rn activities (those produced by the sediment in equilibrium + ^{226}Ra activities; gray) per month and beach. When measured ^{222}Rn activities are over the equilibrium activities it is considered an indication of continental groundwater intrusion (dark gray), and when equilibrium activities are higher than those measured, it is considered an indication of recent seawater intrusion (light gray).

The opposite situation occurred in Panxón beach. Very high dissolved oxygen concentrations (> 100 μM) were found in the interior of the beach at the middle and lower stations, showing that beach oxygenation was not only caused by tidal and wave forcing. The inverse correlation between oxygen and salinity and the proximity of oxygen to ^{222}Rn in the PCA (**Figure 6B**) suggest that continental groundwater was, in part, the source of the observed high dissolved oxygen concentrations (**Figure 5**). Moreover, the highest inverse correlation between oxygen and salinity was observed in October ($p < 0.05$, $r = 0.57$, $n = 18$), when the local water balance was the highest of the studied period (**Supplementary Table 1**). This is consistent with the high oxygen levels observed in the nearby continental aquifers (**Table 1**). The salt-wedge, typically assumed anoxic (e.g., Robinson et al., 2007a), presented high oxygen concentrations in Panxón (**Figure 5**). The enhanced water transfer through the gravel layer seems to be the main cause. In Ladeira, low oxygen concentrations appeared at the bottom depths in most profiles (**Figure 5**), suggesting that the FDT was not completely anoxic. Oxygen (and nitrate) consumption in these groundwaters during their transit to the sampled zone of the STE may explain these observations, as none of the surrounding wells had low oxygen concentrations (**Table 1**). Additionally, a certain contribution of the nearby surface freshwater courses to the brackish waters found in the beach interior cannot be discarded, although these would not explain the observed porewater unsupported ^{222}Rn enrichment.

Organic matter to fuel heterotrophic processes in beaches can be sourced by either seawater infiltration (Ibánhez and Rocha, 2016) or fresh groundwater, in particular from contaminated aquifers (Yang et al., 2015). In this study, most of the sediment profiles of particulate organic matter decreased with depth (**Figure 3**). Thus, recirculated seawater may be the main source of particulate organic matter into the beach. The rapid infiltration of seawater during high tide and the accumulation of particulate organic matter in the shallower depths caused a higher consumption of oxygen near the surface than at the interior of the beach, where the only available form of organic matter is dissolved organic carbon (Rusch et al., 2000; Huettel et al., 2014; Ibánhez and Rocha, 2016). In consequence, the consumption of oxygen was reduced in the interior of the beach. This explains the preservation of the oxygen supplied by groundwater in the interior of Panxón and its decrease near the surface (**Figure 5**).

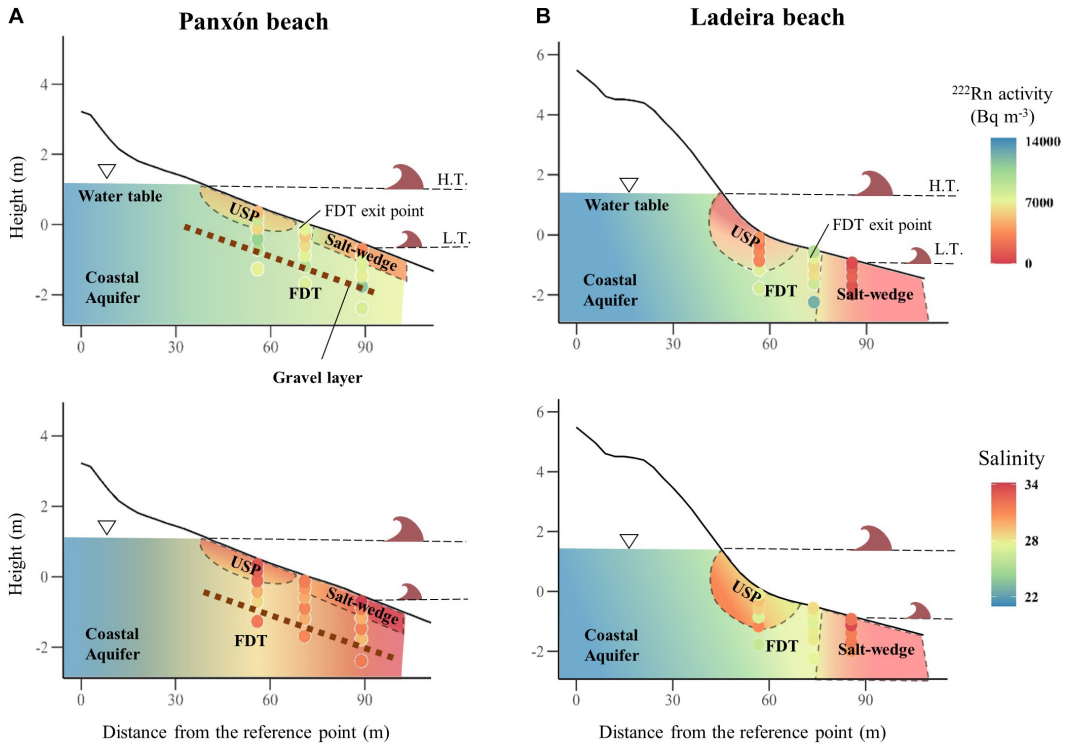


FIGURE 8 | (A) Schematic representation of porewater circulation in Panxón beach, using porewater ^{222}Rn and salinity profiles measured in October. **(B)** Schematic representation of porewater circulation in Ladeira beach, using porewater ^{222}Rn and salinity profiles from May. HT, High Tide; LT, Low Tide; USP, Upper Saline Plume; FDT, Fresh groundwater Discharge Tube.

The organic C: total N elemental ratio was lower than the Redfield ratio (106 C: 16N) in all the profiles of Panxón and higher than it for all the profiles taken in Ladeira (**Figure 3**). In Panxón, this suggests the presence of a large pool of adsorbed N, enhanced by the large content in carbonates of this beach (Rosenfeld, 1979).

Chemical Reactivity of the STEs

Conservative mixing profiles of nitrate, DIN and dissolved oxygen were calculated using salinity and ^{222}Rn as mixing tracers (**Supplementary Figure 1**) to support the analysis of the reactivity of Panxón and Ladeira beaches. For each porewater profile, the samples with the maximum and minimum values of the tracers (salinity or ^{222}Rn activity; **Figure 4**) and their associated nitrate, DIN and dissolved oxygen concentrations (**Figure 5**) were used to construct mixing lines. The slope (m_{eq}) and the Y-intercept (n_{eq}) of these mixing lines were used to calculate the expected values of nitrate, DIN and dissolved oxygen (C_{mix}) for each porewater profile from the distribution of each conservative tracer by using the following equation:

$$C_{mix} = m_{eq} C_{tracer} + n_{eq}$$

where C_{tracer} is the measured salinity or ^{222}Rn activity. The relative change between measured and conservative mixing nitrate, DIN and dissolved oxygen profiles (**Table 2** and **Supplementary Table 3**) was calculated from the vertically integrated areas of each porewater profile (**Supplementary Figure 2**), using the following equation:

$$\%\ Relative\ change = \left(\frac{[C_{measured}]_{int}}{[C_{mix}]_{int}} - 1 \right) \cdot 100$$

where $[C_{measured}]_{int}$ is the vertically integrated nitrate, DIN or dissolved oxygen concentration for each measured profile and $[C_{mix}]_{int}$ is the vertically integrated nitrate, DIN or dissolved oxygen concentration for each conservative mixing profile. These integrals were calculated using the trapezoid approximation.

Large differences were observed whether we used ^{222}Rn or salinity as mixing tracer (**Table 2**), mainly related to mixing processes (Spiteri et al., 2008; Robinson et al., 2018). Moreover, the relative changes of dissolved oxygen (**Supplementary Table 3**) were parallel to the relative changes of DIN (**Table 2**). This could hinder the analysis since these positive values might be partly related to lateral transport, because oxygen cannot be produced in the beach interior. In the following subsections, conservative mixing profiles (**Supplementary Figure 1**), together with circulation tracer profiles (**Figure 4**) and porewater nutrient profiles (**Figure 5**) are examined individually to shed some light on the processes acting in the STEs of Panxón and Ladeira beaches.

TABLE 2 | Apparent percentage of change (%) between the integrated concentrations of dissolved inorganic nitrogen (DIN = $NH_4^+ + NO_2^- + NO_3^-$) and the integrated concentrations of the conservative mixing DIN profiles using ^{222}Rn activities and salinity as conservative tracers.

		Panxón beach		Ladeira beach	
		^{222}Rn	Salinity	^{222}Rn	Salinity
	Lower	−25.47 ± 3.40	−1.99 ± 5.57	36.69 ± 14.85	17.38 ± 5.20
February	Middle	32.03 ± 10.12	14.31 ± 7.45	9.63 ± 3.13	4.10 ± 2.17
	Upper	51.75 ± 4.04	52.34 ± 3.67	−35.96 ± 6.24	−6.61 ± 4.96
	Lower	465.71 ± 48.38	−38.75 ± 6.16	−0.19 ± 6.17	20.65 ± 6.86
May	Middle	2.85 ± 3.52	8.41 ± 7.23	−16.24 ± 3.00	−23.09 ± 3.01
	Upper	23.05 ± 5.48	−4.14 ± 2.67	20.12 ± 4.49	838.93 ± 96.29
	Lower	31.02 ± 6.13	84.55 ± 9.90	−2.54 ± 2.57	−1.29 ± 2.87
July	Middle	−9.96 ± 2.64	1.87 ± 2.31	45.84 ± 17.38	−33.56 ± 6.14
	Upper	−3.78 ± 4.44	−4.85 ± 4.75	4.01 ± 2.12	13.53 ± 2.64
	Lower	7.04 ± 3.97	6.38 ± 3.83	123.66 ± 26.20	8.05 ± 4.20
October	Middle	−5.19 ± 1.66	10.17 ± 3.14	−57.99 ± 1.05	1620.63 ± 80.06
	Upper	39.41 ± 3.76	10.62 ± 4.84	−78.94 ± 0.59	54.03 ± 18.54

Errors are calculated from the analytical errors of measured profiles and standard errors of mixing lines.

Tidal Circulation Cell-Induced Nitrate Profiles in Ladeira Beach

Peak nitrate and dissolved oxygen concentrations appeared at the upper stations of February and May in Ladeira beach, with concentrations above the conservative mixing profiles (**Supplementary Figure 1**). There, the tidal circulation cell was actively pumping oxygen and organic matter into the sand (**Figures 5**, **8**). However, neither PCA nor correlation analysis associated nitrate and salinity in Ladeira. Furthermore, DIN concentrations in the surface waters of the Ría de Vigo or in A Ramallosa Lagoon (Nogueira et al., 1997; Viana and Bode, 2013; Alonso-Pérez and Castro, 2014) are too low to explain the observed peak nitrate concentrations within the tidal circulation cell. Its origin seems to be the ammonification of the organic matter introduced into the sediment and fueled by the parallel transport of oxygen, followed by nitrification of the ammonium produced (Ibánhez and Rocha, 2017). Incomplete nitrification would thus explain the accumulation of nitrite observed near the surface in the upper profile taken in May (**Figure 5**). The absence of nitrate in depth further suggests that the significant nitrate levels measured in continental groundwaters in the studied area (**Table 1**) might be consumed before arriving to Ladeira beach.

Nitrate Reduction and Groundwater Supply in Panxón Beach

The terrestrial fresh groundwater transported through the gravel layer was the main source of nitrate to Panxón beach. This is supported by the high correlation between ^{222}Rn activity and nitrate concentrations and the confluence of nitrate peaks in zones of enhanced transport (**Figures 5**, **7**). Solute transfer was maintained even during the reduced continental groundwater flux of July, observable as an increase of nitrate and oxygen above conservative mixing porewater profiles (**Supplementary Figure 1B**). Scarce availability of fresh (labile) organic matter in the beach interior (Hartog et al., 2004; Slomp and Van Cappellen, 2004) would limit heterotrophic processes and may explain the presence of brackish waters with high oxygen and nitrate content in depth in Panxón. However, at shallower depths, the progressive availability or particulate organic matter trapped in the sediment matrix caused a decrease of oxygen and nitrate over conservative mixing profiles (**Supplementary Figure 1B**). Peaks of nitrite accompanied nitrate consumption (**Figure 5**), which seems to show active nitrate reduction in place (Ibánhez and Rocha, 2017). In the porewater profiles from July to October, organic matter seems to be depleted before nitrate was used as electron acceptor, which resulted in high nitrate concentrations under suboxic conditions (**Figure 5**). Furthermore, the ammonium released by organic matter remineralization was accumulated in the anoxic, shallower layers of some of the vertical porewater profiles (**Figure 5**).

Ammonium Distribution in the Suboxic Sediments of Ladeira Beach

Several processes (terrestrial fresh groundwater and anoxic seawater transport, dissimilatory nitrate reduction to ammonium, desorption from sediments, organic matter decomposition…) can support ammonium content in anoxic STEs (Slomp and Van Cappellen, 2004; Santos et al., 2008). In Ladeira beach, the slight increase in oxygen with depth and the accumulation of ammonium in the shallower depths (**Figure 5**) suggest that ammonium is primarily originated from the remineralization of particulate organic matter trapped near the surface (Huettel et al., 2014; Ibánhez and Rocha, 2016), rather than carried by the FDT or infiltrating seawater. The vertical distribution of ammonium in the porewater seems to be also linked to porewater circulation. The increased mixing observed in July could have been the cause of the nearly homogenous vertical distribution of ammonium in the porewater (**Figure 5** and **Supplementary Figure 1C**). Increased residence times and anoxic conditions could be linked to DIN consumption in the middle station of May, as conservative mixing profiles above measured DIN profiles suggest (**Supplementary Figure 1C**). In the lower sampling station during February and May, high ammonium concentrations ($>30\ \mu M$) were observed throughout

the entire porewater profile (**Figure 5**). The accumulation of seaweed in the low intertidal, observed during these surveys, has been pointed to fuel benthic heterotrophic processes (Santos et al., 2008), leading to the leaching of ammonium into the interior of the beach.

Porewater Circulation and Biogeochemical Reactivity of STEs

The suitability of calculating conservative mixing profiles for the study of the chemical reactivity in STEs has been previously discussed (Spiteri et al., 2008; Rocha et al., 2009). This approach assumes vertical, steady state porewater transport (Rocha et al., 2009). As a result, lateral transport cannot be differentiated from chemical reactivity when following this approach and thus, it is not recommended if the previous assumptions are not fulfilled (Spiteri et al., 2008). In this study, the two endmembers used to define the conservative mixing porewater profiles are local, i.e., the maximum and minimum values of ^{222}Rn and salinity at each porewater profile (**Figures 4**, **5**). Besides, to reduce the possible misinterpretation of deviations of nitrate and DIN concentrations from the calculated mixing lines, conservative mixing profiles of dissolved oxygen were also calculated to identify lateral transport, as oxygen cannot be produced in the interior of the beach. The results discussed in the previous sections showed that oxygen, DIN and nitrate conservative mixing profiles agreed well with the circulation processes defined in section "Porewater Circulation in the Ladeira and Panxón STEs." Although the apparent reaction magnitudes shown in **Table 2** should be taken with caution due to the aforementioned limitations, the approach followed permitted to unveil the sharp biogeochemical zonation of the studied STEs.

This study establishes a necessary link between internal beach hydrodynamics and the biogeochemical processes that regulate the export of nutrients from STEs to the coast. Porewater circulation is the main driver of the strong redox differences found between the studied STEs, thus strongly determining the reactivity of redox-sensitive N compounds (Slomp and Van Cappellen, 2004; Spiteri et al., 2008; Ibánhez et al., 2013; Ibánhez and Rocha, 2016, 2017). Our results highlight the role of the tidal circulation cell over the biogeochemical reactivity of STEs and the seasonality of N speciation observed. Nevertheless, our results further suggest that the different redox conditions found in the FDT are still the main factor to determine N transformations within the STEs. Sediment heterogeneity has been suggested to be particularly important in the establishment of these redox conditions in the FDT (Geng et al., 2020a,b), as it was the main cause of the biogeochemical differences between the two STEs studied here.

CONCLUSION

The biogeochemical reactivity of two contrasting STEs has been studied for the first time in the Ría de Vigo. The three water bodies that typically shape tidally driven STEs were identified in both beaches using salinity, ^{222}Rn and ^{226}Ra as circulation tracers. Large gradients of nitrate, oxygen, and ammonium were observed at both STEs, partially related to porewater circulation. The tidal circulation cell acted as a pump of oxygen and organic matter into the interior of the beaches, inducing the aerobic respiration of organic matter and the nitrification of the ammonium produced. Thus, the tidal circulation cell regulates the transport of regenerated nutrients to the coast. Terrestrial fresh groundwater transported nutrients from the coastal aquifer into the interior of the beaches. Its role in nitrogen processing in Panxón and Ladeira STEs depended principally on the dissolved oxygen levels present at the FDT, which also depended on the different porewater circulation patterns observed in those beaches. Suboxic conditions in the terrestrial fresh groundwater of Ladeira beach caused the dominance of nitrogen reduction processes and the accumulation of ammonium. On the contrary, oxic conditions prevented the consumption of nitrate in the interior of Panxón beach. The layer of increased permeability in depth, besides of having completely altered the circulation structure of the STE, seems to play an important role in enhancing the transport of land-derived nitrate to the coast by limiting nitrate reduction along the flow path but also by fueling nitrification in the beach interior. The degradation of the particulate organic matter trapped near the surface during surface water infiltration (i.e., high tide) caused the consumption of oxygen and groundwater-borne nitrate and the accumulation of ammonium in the shallower depths. As a consequence, our results suggest that the preferential transfer of solutes through the gravel layer together with the oxidation of organic matter within the tidal circulation cell causes Panxón beach to be a net source of N to the coast. In opposition, the suboxic conditions of Ladeira might make this beach a net sink of N.

DATA AVAILABILITY STATEMENT

The raw data supporting the conclusions of this article will be made available by the authors, without undue reservation, to any qualified researcher.

AUTHOR CONTRIBUTIONS

JSPI and CR conceived the study. JSPI, EC-M, and XÁ-S participated in the field and laboratory work. EC-M and JSPI elaborated the first draft of the manuscript, which was enriched by contributions of XÁ-S and CR. All authors revised and approved the manuscript.

FUNDING

This research was supported by the SUBACID project (SUBmarine groundwater discharge (SGD) impact on coastal ACIDification processes in contrasting Atlantic Shores: towards securing ecosystem services and food production) that has received funding from the Irish Research Council and the European Union's Horizon 2020 Research and Innovation

Program under the Marie Skłodowska-Curie grant agreement No. 713279 through the CAROLINE program (CLNE/2017/210).

ACKNOWLEDGMENTS

We are very grateful to Dr. Irene Alejo (University of Vigo) for measuring the beach profiles of February, to Vanesa Vieitez and María José Pazó (Instituto de Investigacións Mariñas-CSIC) for support during sample analysis and to Vanesa Vieitez, Ester Jerusalén (Instituto de Investigacións Mariñas-CSIC) and Uxúe Uribe (University of Vigo) for field support during the surveys. We thank Dr. Álvarez (IEO) for oxygen determinations in samples taken from wells, boreholes and the Miño river. Evaporation and precipitation data of the surveyed period were obtained from the repository of Meteogalicia (www.meteogalicia.gal). Salinity and dissolved oxygen concentrations in surface waters of Baiona Bay were obtained from the repository of INTECMAR (www.intecmar.gal). We are thankful to three reviewers and the editor that helped to improve an early version of the manuscript.

SUPPLEMENTARY MATERIAL

The Supplementary Material for this article can be found online at: https://www.frontiersin.org/articles/10.3389/fmars.2021.626813/full#supplementary-material

REFERENCES

Alejo, I., and Vilas, F. (1987). Ambientes sedimentarios de la ensenada de baiona (Pontevedra). *Cuad. Lab. Xeolóxico Laxe* 12, 11–24.

Alejo, I., Francés, G., Villas, F., and Austin, W. E. N. (1999). Preliminary investigations of the recent foraminifera of Baiona Bay. N.W. Spain. *J. Coast. Res.* 15, 413–427. doi: 10.2307/4298953

Alonso-Pérez, F., and Castro, C. G. (2014). Benthic oxygen and nutrient fluxes in a coastal upwelling system (Ria de Vigo, NW Iberian Peninsula): seasonal trends and regulating factors. *Mar. Ecol. Prog. Ser.* 511, 17–32. doi: 10.3354/meps10915

Álvarez-Salgado, X. A., Figueiras, F. G., Pérez, F. F., Groom, S., Nogueira, E., Borges, A. V., et al. (2003). The Portugal coastal counter current off NW Spain: new insights on its biogeochemical variability. *Prog. Oceanogr.* 56, 281–321. doi: 10.1016/S0079-6611(03)00007-7

Álvarez-Vázquez, R., Bernabeu, A. M., Nombela, M. A., Méndez, G., and Vilas, F. (2003). Evolución morfodinámica de Panxón (Galicia, NO de España). *Geogaceta* 33, 19–22.

Arístegui, J., Gasol, J. M., Duarte, C. M., and Herndld, G. J. (2009). Microbial oceanography of the dark ocean's pelagic realm. *Limnol. Oceanogr.* 54, 1501–1529. doi: 10.1016/j.pocean.2009.07.031

Ball, D. F. (1964). Loss-on-ignition as an estimate of organic matter and organic carbon in non-calcareous soils. *J. Soil Sci.* 15, 84–92. doi: 10.1111/j.1365-2389.1964.tb00247.x

Beusen, A. H. W., Slomp, C. P., and Bouwman, A. F. (2013). Global land-ocean linkage: direct inputs of nitrogen to coastal waters via submarine groundwater discharge. *Environ. Res. Lett.* 8:034035. doi: 10.1088/1748-9326/8/3/034035

Bokuniewicz, H., Taniguchi, M., Ishitoibi, T., Charette, M., Allen, M., and Kontar, E. A. (2008). Direct measurements of submarine groundwater discharge (SGD) over a fractured rock aquifer in Flamengo Bay Brazil. *Estuar. Coast. Shelf Sci.* 76, 466–472. doi: 10.1016/j.ecss.2007.07.047

Burnett, W. C., Bokuniewicz, H., Huettel, M., Moore, W. S., and Taniguchi, M. (2003). Groundwater and pore water inputs to the coastal zone. *Biogeochemistry* 66, 3–33. doi: 10.1023/B:BIOG.0000006066.21240.53

Capone, D. G., and Slater, J. M. (1990). Interannual patterns of water table height and groundwater derived nitrate in nearshore sediments. *Biogeochemistry* 10, 277–288. doi: 10.1007/BF00003148

Colbert, S., and Hammond, D. (2008). Shoreline and seafloor fluxes of water and short-lived Ra isotopes to surface water of San Pedro Bay, CA. *Mar. Chem.* 108, 1–17. doi: 10.1016/j.marchem.2007.09.004

Couturier, M., Tommi-Morin, G., Sirois, M., Rao, A., Nozais, C., and Chaillou, G. (2017). Nitrogen transformations along a shallow subterranean estuary. *Biogeosciences* 14, 3321–3336. doi: 10.5194/bg-14-3321-2017

Dueñas, C., Fernandez, M. C., and de la Torre, M. (1985). Fluxes and Exchange rates of radon and oxygen across an air-sea interface. *Geochem. J.* 20, 61–69. doi: 10.2343/geochemj.20.61

Dulaiova, H., Gonneea, M. E., Henderson, P. B., and Charette, M. A. (2008). Geochemical and physical sources of radon variation in a subterranean estuary-Implications for groundwater radon activities in submarine groundwater discharge studies. *Mar. Chem.* 110, 120–127. doi: 10.1016/j.marchem.2008.02.011

Fernández, E., Álvarez-Salgado, X. A., Beiras, R., Ovejero, A., and Méndez, G. (2016). Coexistence of urban uses and shellfish production in an upwelling-driven, highly productive marine environment: the case of the Ría de Vigo (Galicia, Spain). *Reg. Stud. Mar. Sci.* 8, 362–370. doi: 10.1016/j.rsma.2016.04.002

Geng, X., Heiss, J. W., Michael, H. A., Boufadel, M. C., and Lee, K. (2020b). Groundwater flow and moisture dynamics in the swash zone: effects of heterogeneous hydraulic conductivity and capillarity. *Water Resour. Res.* 56:e2020WR028401. doi: 10.1029/2020WR028401

Geng, X., Holly, A., Michael, Michel, C., Boufadel, Fred, J., et al. (2020a). Heterogeneity affects intertidal flow topology in coastal beach aquifers. *Geophys. Res. Lett* . 47:17.

Gonneea, M. E., Morris, P. J., Dulaiova, H., and Charette, M. A. (2008). New perspectives on radium behavior within a subterranean estuary. *Mar. Chem.* 109, 250–267. doi: 10.1016/j.marchem.2007.12.002

González-Villanueva, R., Costas, S., Alejo, I., and Pérez-Alucea, M. (2007). Morphological changes forced by tidal cycle in a low estuarine beach. *J . Coast. Res. SI* 50, 1010–1014.

Grasshoff, K., Kremling, K., and Ehrhardt, M. (1999). *Methods of Seawater Analysis*, 3rd Edn. Weinheim: Wiley-VCH, doi: 10.1002/9783527613984

Gustafson, G., and Krásný, J. (1994). Crystalline rock aquifers: their occurrence, use and importance. *Appl. Hydrogeol.* 2, 64–75. doi: 10.1007/s100400050051

Hartog, N., Van Bergen, P. F., De Leeuw, J. W., and Griffioen, J. (2004). Reactivity of organic matter in aquifer sediments: geological and geochemical controls. *Geochim. Cosmochim. Acta* 68, 1281–11292. doi: 10.1016/j.gca.2003.09.004

Heiss, J. W., and Michael, H. A. (2014). Saltwater-freshwater mixing dynamics in a sandy beach aquifer over tidal, spring-neap, and seasonal cycles. *Water Resour. Res* . 50, 6747–6766. doi: 10.1002/2014WR015574

Hu, C., Müller-Karger, F. E., and Swarzenski, P. W. (2006). Hurricanes, submarine groundwater discharge, and Florida's red tides. *Geophys. Res. Lett.* 33:L11601. doi: 10.1029/2005GL025449

Huettel, M., Wild, C., Reimers, C., Rusch, A., and Reimers, C. E. (2014). Benthic oxygen consumption and organic matter turnover in organic-poor, permeable shelf sands. *Aquat. Geochem.* 12, 1–19. doi: 10.1007/s10498-005-0784-x

Hwang, D. W., Lee, Y. W., and Kim, G. (2005). Large submarine groundwater discharge and benthic eutrophication in Bangdu Bay on volcanic Jeju Island, Korea. *Limnol. Oceanogr.* 50, 1393–1403. doi: 10.4319/lo.2005.50.5.1393

Ibánhez, J. S. P., and Rocha, C. (2014). Effects of recirculation of seawater enriched in inorganic nitrogen on dissolved organic carbon processing in sandy seepage face sediments. *Mar. Chem.* 166, 48–58. doi: 10.1016/j.marchem.2014.09.012

Ibánhez, J. S. P., and Rocha, C. (2016). Oxygen transport and reactivity within a sandy seepage face in a mesotidal lagoon (Ria Formosa, Southwestern Iberia). *Limnol. Oceanogr.* 61, 61–77. doi: 10.1002/lno.10199

Ibánhez, J. S. P., and Rocha, C. (2017). Kinetics of inorganic nitrogen turnover in a sandy seepage face on a subterranean estuary. *Appl. Geochem.* 87, 108–121. doi: 10.1016/j.apgeochem.2017.10.015

Ibánhez, J. S. P., Leote, C., and Rocha, C. (2011). Porewater nitrate profiles in sandy sediments hosting submarine groundwater discharge described by an

advection-dispersion-reaction model. *Biogeochemistry* 103, 159–180. doi: 10.1007/s10533-010-9454-1

Ibánhez, J. S. P., Leote, C., and Rocha, C. (2013). Seasonal enhancement of submarine groundwater discharge (SGD)-derived nitrate loading into the Ria Formosa coastal lagoon assessed by 1-D modeling of benthic NO3- profiles. *Estuar. Coast. Shelf Sci.* 132, 56–64. doi: 10.1016/j.ecss.2012.04.015

Ibánhez, J. S. P., Rocha, C., Nieto-Cid, M., Casal, L., Wilson, J., and Álvarez-Salgado, X. A. (2019). *Submarine Groundwater Discharge in Ría de Vigo. VI International Symposium on Marine Sciences*. Spain: Vigo.

Jiang, S., Ibánhez, J. S. P., and Rocha, C. (2018). Influence of labile dissolved organic matter on nitrate reduction in a seepage face. *Environ. Sci. Pollut. Res.* 25, 10654–10667. doi: 10.1007/s11356-018-1302-1

Jiang, S., Zhang, Y., Jin, J., Wu, Y., Wei, Y., Wang, X., et al. (2020). Organic carbon in a seepage face of a subterranean estuary: turnover and microbial interrelations. *Sci. Total Environ.* 725:138220. doi: 10.1016/j.scitotenv.2020.138220

Kérouel, R., and Aminot, A. (1997). Fluorometric determination of ammonia in sea and estuarine waters by direct segmented flow analysis. *Mar. Chem.* 57, 265–275. doi: 10.1016/S0304-4203(97)00040-6

Knee, K. L., and Paytan, A. (2012). ". 4, 205–233.

Kroeger, K. D., and Charette, M. A. (2008). Nitrogen biogeochemistry of submarine groundwater discharge. *Limnol. Oceanogr* . 53, 1025–1039. doi: 10.4319/lo.2008.53.3.1025

Labarta, U., and Fernández-Reiriz, M. J. (2019). The Galician mussel industry: innovation and changes in the last forty years. *Ocean Coast. Manag.* 167, 208–218. doi: 10.1016/j.ocecoaman.2018.10.012

Labasque, T., Chaumery, C., Aminot, A., and Kergoat, G. (2004). Spectrophotometric Winkler determination of dissolved oxygen: re-examination of critical factors and reliability. *Mar. Chem.* 88, 53–60. doi: 10.1016/j.marchem.2004.03.004

Lee, Y. W., Kim, G., Lim, W. A., and Hwang, D. W. (2010). A relationship between submarine groundwater borne nutrients traced by Ra isotopes and the intensity of dinoflagellate red-tides occurring in the southern sea of Korea. *Limnol. Oceanogr.* 55, 1–10. doi: 10.4319/lo.2010.55.1.0001

Leote, C., Ibánhez, J. S. P., and Rocha, C. (2008). Submarine groundwater discharge as a nitrogen source to the Ria Formosa studied with seepage meters. *Biogeochemistry* 88, 185–194. doi: 10.1007/s10533-008-9204-9

Liu, Q., Charette, M. A., Henderson, P. B., McCorkle, D. C., Martin, W., and Dai, M. (2014). Effect of submarine groundwater discharge on the coastal ocean inorganic carbon cycle. *Limnol. Oceanogr.* 59, 1529–1554. doi: 10.4319/lo.2014.59.5.1529

Llerena, J. J., Cortina, D., Durán, I., and Sorribas, R. (2013). Impact of the geological substrate on the radiological content of Galician waters. *J. Environ. Radioact* . 116, 48–53. doi: 10.1016/j.jenvrad.2012.08.014

Martín Míguez, B. (2002). *Descripción dinámica de la circulación en dos Rías Baixas: Vigo y Pontevedra*. dissertation/master's thesis Universidade de Vigo: Vigo (IL)

Michael, H. A., Charette, M. A., and Harvey, C. F. (2011). Patterns and variability of groundwater flow and radium activity at the coast: a case study from Waquoit Bay. *Massachusetts. Mar. Chem.* 127, 1–4.

Michael, H. A., Mulligan, A. E., and Harvey, C. F. (2005). Seasonal oscillations in water exchange between aquifers and the coastal ocean. *Nature* 436, 1145–1148. doi: 10.1038/nature03935

Moore, W. S. (1999). The subterranean estuary: a reaction zone of ground water and sea water. *Mar. Chem.* 65, 111–125. doi: 10.1016/S0304-4203(99)00014-6

Nogueira, E., Pérez, F., and Ríos, A. (1997). Seasonal patterns and long-term trends in an estuarine upwelling ecosystem (Ria de Vigo, NW Spain). *Estuar. Coast. Shelf Sci.* 44, 285–300. doi: 10.1006/ecss.1996.0119

Perez-Arlucea, M., Mendez, G., Clemente, F., Nombela, M., Rubio, B., and Filgueira, M. (2005). Hydrology, sediment yield, erosion and sedimentation rates in the estuarine environment of the Ria de Vigo, Galicia, Spain. *J Mar. Syst.* 54, 209–226. doi: 10.1016/j.jmarsys.2004.07.013

Pliego Dones, D., Rubio-Navas, J., and Abril-Hurtado, J. (1978). *Mapa Geológico de España 1:50.000. Instituto Geológico y Minero de España (IGME), Hoja 261 Tuy*. (Madrid: Servicio de publicaciones del Ministerio de Industria y Energía).

Queralt, S., Rodríguez-Fernández, N., Bernabeu, A. M., Rey, D., and Vilas, F. (2002). Características mofrosedimentarias de las playas de la Ría de Vigo: influencia de las condiciones hidrodinámicas. *Geogaceta* 32, 211–214.

Raposo, J. R., Molinero, J., and Dafonte, J. (2012). Parameterization and quantification of recharge in crystalline fractured bedrocks in Galicia-Costa (NW Spain). *Hydrol. Earth Syst. Sci.* 16, 1667–1683. doi: 10.5194/hess-16-1667-2012

Rivett, M. O., Buss, S. R., Morgan, P., Smith, J. W., and Bemment, C. D. (2008). Nitrate attenuation in groundwater: a review of biogeochemical controlling processes. *Water Res* . 42, 4215–4232. doi: 10.1016/j.watres.2008.07.020

Robinson, C. E., Xin, P., Santos, I. R., Charette, M. A., Li, L., and Barry, D. A. (2018). Groundwater dynamics in subterranean estuaries of coastal unconfined aquifers: controls on submarine groundwater discharge and chemical inputs to the ocean. *Adv. Water Resour.* 115, 315–331. doi: 10.1016/j.advwatres.2017.10.041

Robinson, C., Gibbes, B., and Li, L. (2006). Driving mechanisms for groundwater flow and salt transport in a subterranean estuary. *Geophys. Res. Lett* . 33, 3–6. doi: 10.1029/zl025247

Robinson, C., Gibbes, B., Carey, H., and Li, L. (2007a). Salt-freshwater dynamics in a subterranean estuary over a spring-neap tidal cycle. *J. Geophys. Res.* 112:C09007. doi: 10.1029/2006JC003888

Robinson, C., Li, L., and Barry, D. A. (2007b). Effect of tidal forcing on a subterranean estuary. *Adv. Water Resour.* 30, 851–865. doi: 10.1016/j.advwatres.2006.07.006

Robinson, C., Xin, P., Li, L., and Barry, D. A. (2014). Groundwater flow and salt transport in a subterranean estuary driven by intensified wave conditions. *Water Resour. Res.* 50, 165–181. doi: 10.1002/2013WR013813

Rocha, C., Ibanhez, J., and Leote, C. (2009). Benthic nitrate biogeochemistry affected by tidal modulation of Submarine Groundwater Discharge (SGD) through a sandy beach face. Ria Formosa, Southwestern Iberia. *Mar. Chem* . 115, 43–58. doi: 10.1016/j.marchem.2009.06.003

Rodellas, V., Garcia-Orellana, J., Tovar-Sánchez, A., Basterretxea, G., López-Garcia, J. M., Sánchez-Quiles, D., et al. (2014). Submarine groundwater discharge as a source of nutrients and trace metals in a Mediterranean bay (Palma Beach, Balearic Islands). *Mar. Chem.* 160, 56–66. doi: 10.1016/j.marchem.2014.01.007

Rosenfeld, J. K. (1979). Ammonium adsorption in nearshore anoxic sediments. *Limnol. Oceanogr* . 24, 356–364. doi: 10.4319/lo.1979.24.2.0356

Rusch, A., Huettel, M., and Forster, S. (2000). Particulate organic matter in permeable marine sands - Dynamics in time and depth. *Estuar. Coast. Shelf Sci.* 51, 399–414. doi: 10.1006/ecss.2000.0687

Sáenz, J. P., Hopmans, E. C., Rogers, D., Henderson, P. B., Charette, M. A., Schouten, S., et al. (2012). Distribution of anaerobic ammonia-oxidizing bacteria in a subterranean estuary. *Mar. Chem* . 136, 7–13. doi: 10.1016/j.marchem.2012.04.004

Santos, I. R. S., Burnett, W. C., Chanton, J., Mwashote, B., Suryaputra, I. G. N. A., and Dittmar, T. (2008). Nutrient biogeochemistry in a Gulf of Mexico subterranean estuary and groundwater-derived fluxes to the coastal ocean. *Limnol. Oceanogr.* 53, 705–718. doi: 10.4319/lo.2008.53.2.0705

Santos, I. R., Burnett, W. C., Dittmar, T., Suryaputra, I. G. N. A., and Chanton, J. (2009a). Tidal pumping drives nutrient and dissolved organic matter dynamics in a Gulf of Mexico subterranean estuary. *Geochim. Cosmochim. Acta* 73, 1325–1339. doi: 10.1016/j.gca.2008.11.029

Santos, I. R., Dimova, N., Peterson, R. N., Mwashote, B., Chanton, J., and Burnett, W. C. (2009b). Extended time series measurements of submarine groundwater discharge tracers (222Rn and CH4) at a coastal site in Florida. *Mar. Chem.* 113, 137–147. doi: 10.1016/j.marchem.2009.01.009

Santos, I. R., Eyre, B. D., and Huettel, M. (2012). The driving forces of porewater and groundwater flow in permeable coastal sediments: a review. *Estuar. Coast. Shelf Sci* . 98, 1–15. doi: 10.1016/j.ecss.2011.10.024

Simmons, C. T., Fenstemaker, T. R., and Sharp, J. M. (2001). Variable-density groundwater flow and solute transport in heterogeneous porous media: approaches, resolutions and future challenges. *J. Contam. Hydrol.* 52, 245–275. doi: 10.1016/S0169-7722(01)00160-7

Slomp, C. P., and Van Cappellen, P. (2004). Nutrient inputs to the coastal ocean through submarine groundwater discharge: controls and potential impact. *J. Hydrol.* 295, 64–86. doi: 10.1016/j.jhydrol.2004.02.018

Spiteri, C., Slomp, C. P., Tuncay, K., and Meile, C. (2008). Modeling biogeochemical processes in subterranean estuaries: effect of flow dynamics

and redox conditions on submarine groundwater discharge of nutrients. *Water Resour. Res.* 44, 1–18. doi: 10.1029/2007WR006071

Thamdrup, B. (2012). New pathways and processes in the global nitrogen cycle. *Annu. Rev. Ecol. Evol. Syst.* 43, 407–428. doi: 10.1146/annurev-ecolsys-102710-145048

Thamdrup, B., and Dalsgaard, T. (2008). "Nitrogen cycling in sediments," in *Microbial Ecology of the Oceans*, 2nd Edn, ed. D. L. Kirchman (New York, NY: John Wiley & Sons Ltd), 527–568. doi: 10.1002/9780470281840.ch14

Tollefsen, T., De Cort, M., Cinelli, G., Gruber, V., and Bossew, P. (2016). *Data from: 04. Uranium Concentration in Soil*. Brussels: European Commission.

Valiela, I., Costa, J., Foreman, K., Teal, J. M., Howes, B., and Aubrey, D. (1990). Transport of groundwater-borne nutrients from watersheds and their effects on coastal waters. *Biogeochemistry* 10, 177–197. doi: 10.1007/BF00003143

Viana, I. G., and Bode, A. (2013). Stable nitrogen isotopes in coastal macroalgae: geographic and anthropogenic variability. *Sci. Total Environ.* 443, 887–895. doi: 10.1016/j.scitotenv.2012.11.065

Vitousek, P. M., Aber, J. D., Howarth, R. W., Likens, G. E., Matson, P. A., Schindler, D. W., et al. (1997). Technical report: human alteration of the global nitrogen cycle: sources and consequences. *Ecol. Appl.* 7:737. doi: 10.2307/2269431

Xin, P., Wang, S. S. J., Lu, C., Robinson, C., and Li, L. (2015). Nonlinear interactions of waves and tides in a subterranean estuary. *Geophys. Res. Lett.* 42, 2277–2284. doi: 10.1002/2015GL063643

Yang, L., Chen, C. T. A., Hong, H., Chang, Y. C., and Lui, H. K. (2015). Mixing behavior and bioavailability of dissolved organic matter in two contrasting subterranean estuaries as revealed by fluorescence spectroscopy and parallel factor analysis. *Estuar. Coast. Shelf Sci.* 166, 161–169. doi: 10.1016/j.ecss.2014.10.018

Conflict of Interest: The authors declare that the research was conducted in the absence of any commercial or financial relationships that could be construed as a potential conflict of interest.

Copyright © 2021 Calvo-Martin, Álvarez-Salgado, Rocha and Ibánhez. This is an open-access article distributed under the terms of the Creative Commons Attribution License (CC BY). The use, distribution or reproduction in other forums is permitted, provided the original author(s) and the copyright owner(s) are credited and that the original publication in this journal is cited, in accordance with accepted academic practice. No use, distribution or reproduction is permitted which does not comply with these terms.

frontiers in Environmental Science

ORIGINAL RESEARCH
published: 17 January 2022
doi: 10.3389/fenvs.2021.613191

Drivers and Seasonal Variability of Redox-Sensitive Metal Chemistry in a Shallow Subterranean Estuary

Alison E. O'Connor[1,2]*, *Elizabeth A. Canuel*[1] *and Aaron J. Beck*[1,3]

[1]*Virginia Institute of Marine Science, William & Mary, Gloucester Point, VA, United States,* [2]*Ramboll, Beachwood, OH, United States,* [3]*GEOMAR, Kiel, Germany*

The subterranean estuary (STE) has been historically defined in terms of the mixing of saline and fresh water, in an analogy to surface estuaries. However, redox gradients are also a defining characteristic of the STE and influence its role as a source or sink for metals in the environment. Approaching the STE from a redox-focused biogeochemical perspective (e.g., considering the role of microbial respiration and availability of organic matter) provides the ability to quantify drivers of metal transport across spatial and temporal scales. This study measured the groundwater composition of a shallow STE over 2 years and used multiple linear regression to characterize the influence of salinity and redox chemistry on the behavior of redox-sensitive metals (RSMs) including Mo, U, V, and Cr. Molybdenum and uranium were both supplied to the STE by surface water, but differed in their removal mechanisms and seasonal behavior. Molybdenum showed non-conservative removal by reaction with sulfide in all seasons. Sulfide concentrations at this site were consistently higher than required for quantitative reaction with Mo (10 μM sulfide), evidently leading to quantitative removal at the same depth regardless of season. In contrast, U appeared to depend directly on microbial activity for removal, and showed more extensive removal at shallower depths in summer. Both V and Cr were elevated in meteoric groundwater (2.5–297 nM and 2.6–236 nM, respectively), with higher endmember concentrations in summer. Both V and Cr also showed non-conservative addition within the STE relative to conservative mixing among the observed endmembers. The mobility of V and Cr in the STE, and therefore their supply to the coastal ocean, was controlled by the availability of dissolved organic matter and Fe, suggesting V and Cr were potentially complexed in the colloidal fraction. Complexation by different organic matter pools led to seasonal variations in V but greater interannual variability of Cr. These results reveal distinct behaviors of RSMs in response to seasonal biogeochemical processes that drive microbial activity, organic matter composition, and complexation by inorganic species.

Keywords: subterranean estuary, submarine groundwater discharge, coastal groundwater, redox-sensitive metals, oxyanion-forming elements

OPEN ACCESS

Edited by:
Clare Robinson,
Western University, Canada

Reviewed by:
Xueyan Jiang,
Ocean University of China, China
Guebuem Kim,
Seoul National University, South Korea
Gwénaëlle Chaillou,
Université du Québec à Rimouski, Canada

***Correspondence:**
Alison E. O'Connor
alisoneoconnor@gmail.com

Specialty section:
This article was submitted to Biogeochemical Dynamics, a section of the journal Frontiers in Environmental Science

Received: *01 October 2020*
Accepted: *09 December 2021*
Published: *17 January 2022*

Citation:
O'Connor AE, Canuel EA and Beck AJ (2022) Drivers and Seasonal Variability of Redox-Sensitive Metal Chemistry in a Shallow Subterranean Estuary. Front. Environ. Sci. 9:613191. doi: 10.3389/fenvs.2021.613191

1 INTRODUCTION

Submarine groundwater discharge (SGD), advection of water across the seafloor into the coastal ocean, is an important source of nutrients and trace metals to the sea (Spinelli and Fisher 2002; Burnett et al., 2003; Slomp and Van Cappellen 2004; Beck et al., 2009). The chemical composition of SGD is affected by reactions that occur within the subterranean estuary (STE), the mixing zone of fresh and saline water within permeable sediments (Moore 1999; Charette and Sholkovitz 2006; Santos et al., 2009). Recent work has shown that the circulation of water through sandy beaches drives substantial biogeochemical redox reactions (Snyder et al., 2004; Anschutz et al., 2009): the intrusion of oxygenated surface water into the beach face and mixing with outflowing anoxic meteoric groundwater creates a redox interface. Redox reactions within the shallow STE affect the cycling of reduced metabolites (such as Fe(II) and sulfide) as well as redox-active trace metals (Santos et al., 2011; McAllister et al., 2015; O'Connor et al., 2015).

Redox-sensitive metals (RSMs) are characterized by different environmental behavior depending on their redox state. The trace metals Mo, U, V, and Cr form soluble oxyanions under oxidizing conditions, but their reduced species are particle reactive (Bruland and Lohan 2006). Due to their redox-active behavior, these RSMs are widely used as marine paleoproxies to examine oceanic oxygen levels, productivity, and circulation over geologic time scales (e.g., Nameroff et al., 2004; Rimmer et al., 2004; Tribovillard et al., 2006; Algeo et al., 2012). The use of elements like Mo and U as paleoindicators is influenced by material budgets controlling their oceanic concentrations and isotopic composition (Klinkhammer and Palmer 1991; Siebert et al., 2003; Archer and Vance 2008).

The STE may play an important role in controlling RSM budgets in coastal and global oceans; however, the reactions that control RSM concentrations in SGD remain poorly studied. Redox gradients control the porewater concentrations of these elements in both fine-grained sediments (Brumsack and Gieskes 1983; Morford and Emerson 1999; Morford et al., 2005; Scholz et al., 2011), and, although less well studied, in permeable sediments. Uranium removal in the STE has been observed in many locations globally (Duncan and Shaw 2003; Windom and Niencheski 2003; Charette and Sholkovitz 2006; Santos et al., 2011; Riedel et al., 2011). Both non-conservative removal (Windom and Niencheski 2003; Riedel et al., 2011) and addition (Beck et al., 2010) of Mo have been observed in different locations. Although data on V in the STE are limited, both removal and enrichment (Beck et al., 2010; Riedel et al., 2011; Reckhardt et al., 2017) have been observed. Chromium is also poorly studied in the STE, but one study showed non-conservative addition in the mixing zone (O'Connor et al., 2015). In this work, we seek to answer the questions "What biogeochemical processes control RSM distribution in the shallow STE" and "How do these processes change on seasonal and inter-annual time scales".

Mo, U, V, and Cr have been shown to exhibit distinct behaviors in coastal ocean porewaters (Brumsack and Gieskes 1983; Morford et al., 2005; Scholz et al., 2011) as well as within shallow STEs (O'Connor et al., 2015). These elements differ in the redox potential (Eh) at which they are oxidized/reduced and in their responses to geochemical variables such as sorption to reactive metal oxides, complexation with organic matter or sulfide, and the activity of certain microbial species (Rai et al., 1989; Wanty and Goldhaber 1992; Barnes and Cochran 1993; Lovley et al., 1993; Helz et al., 1996). Therefore, seasonal variation in environmental conditions within the STE suggests that RSMs are likely to exhibit seasonally variable behavior within this zone as well. Redox-sensitivity may lead to environmental modulation of the SGD-driven RSM source to the ocean and may therefore represent an unexplored mechanism of variation over time.

2 METHODS

2.1 Study Site

The study site is located on the York River Estuary (YRE) in Gloucester Point, Virginia, United States (37.248884 °N–76.505324 °E) (**Supplementary Figure S1A**). The YRE is a microtidal (0.7–0.85 m tidal range), relatively uncontaminated tributary of the Chesapeake Bay (Moore and Reay 2009). Salinities of YRE surface water overlying the sediments at this study site typically range from 14 in the winter to 25 in the summer (Luek and Beck 2014). The Gloucester Point beach is a narrow (20–30 m wide) sandy beach with a gradual slope (0.2). It is bordered to the east by an upland marsh. Granite breakwaters line the beach ~40 m from the dune line to prevent erosion and stabilize the beach morphology (**Supplementary Figure S1B**). Sediment porosity at the study site ranges from 0.26 to 0.41 (O'Connor et al., 2018).

Previous work at the study site used a Ra budget to estimate seasonally variable SGD volume fluxes to the York River between 93 and 178 L m^{-2} d^{-1} (Luek and Beck 2014), comparable to other SGD fluxes estimated using Ra (Cable et al., 1996; Burnett et al., 2008). Groundwater hydraulic head at the study site is inversely correlated with tidal height (Beck et al., 2016), and seasonal fluctuations in groundwater and sea level control saline water intrusion and groundwater discharge (Luek and Beck 2014). Previous sampling of redox-active constituents at the same mid-tide location showed that advection of water through the sandy sediments drives the formation of a "classic" redox sequence typical of diffusion-dominated fine-grained sediments (O'Connor et al., 2015). Sediments at the mid-tide line (MT; **Supplementary Figure S1C**) are oxic down to ~70 cm depth, exhibit a peak in NO_x between 70 and 100 cm, followed by a peak in dissolved Fe and Mn starting at 100 cm, and increasing sulfide below approximately 140 cm depth (depths relative to the high tide sediment surface level) (O'Connor et al., 2015). The vertical distributions of DOC and reduced metabolites remained consistent over time, but concentrations varied with season (O'Connor et al., 2018). Dissolved organic carbon concentrations were greatest in the summer, and shallow meteoric groundwater supplied the majority of DOC to the STE. Dissolved Fe and Mn were highest in a plume through the middle of the STE (100–140 cm) that was characterized by both higher concentrations and greater non-conservative

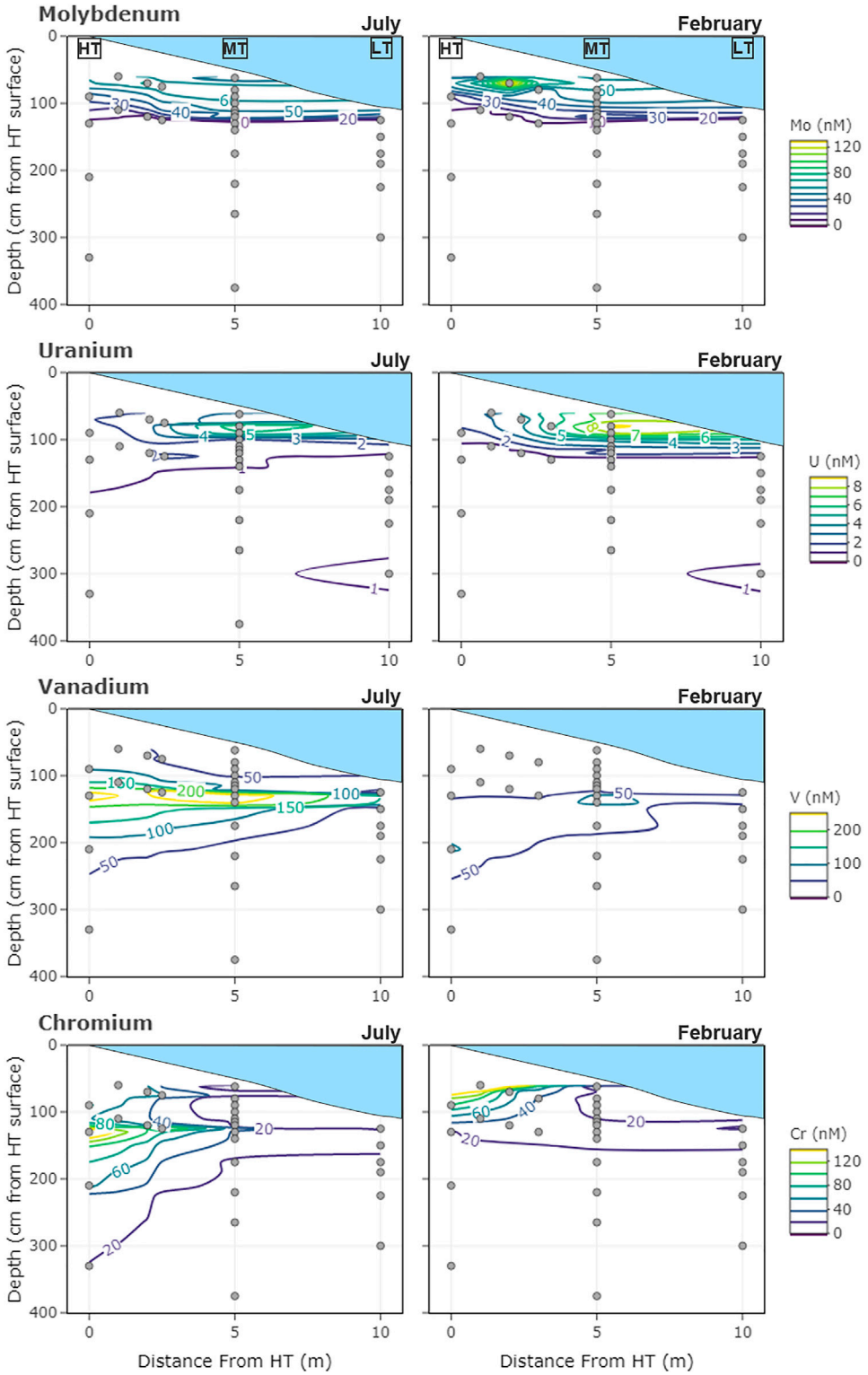


FIGURE 1 | Sampling locations of the subterranean estuary transect and concentrations of dissolved redox-sensitive metals **(A)** Mo **(B)** U **(C)** V, and **(D)** Cr measured in July 2014 and February 2015. Depth profiles were located at the spring high tide (HT), mid-tide (MT), and just below low tide (LT) water levels. Depths are measured relative to the high tide sediment surface (0 cm).

addition in the winter. In contrast, sulfide was higher in summer at depths within the Fe and Mn plume (100–140 cm). The general distributions of RSMs have also been previously described (O'Connor et al., 2015). Both Mo and U were supplied to the STE from overlying estuarine water, and V and Cr had a mid-depth maximum at a sampling profile bisecting the shallow STE (O'Connor et al., 2015).

2.2 Groundwater Collection and Analysis

Sample collection and analyses have been described previously (O'Connor et al., 2018), and will be discussed briefly here. Groundwater samples were collected using permanently installed wells comprising a 1 cm-long stainless steel screened point (AMS, Inc.; e.g., Gonneea et al., 2013) attached to 3 mm diameter No-Ox® PTFE tubing (Supelco/Sigma-Aldrich), or from an all-plastic multi-level sampler (Beck et al., 2007). Low-flow sampling methods were used to minimize oxygen introduction into the sample. Groundwater was pumped from depth using a portable peristaltic pump and filtered through an in-line 0.45 μm Millipore polypropylene capsule filter into sampling containers. Salinity, temperature, and Eh were measured in an included flow-through unit at the time of collection with a hand-held YSI556 multi-probe.

Samples were collected from the mid-tide (MT) profile, located at the center of the shallow saline recirculation cell (**Supplementary Figure S1C**), each month (March 2013 to February 2015) during the week of spring tide at the ebb phase of the tidal cycle. Groundwater samples were also collected from a shore-normal transect (**Figure 1**) during 4 months (April 2014, July 2014, October 2014, and February 2015) to capture variations over a year. Depth profiles were collected along a shore-normal transect, at the locations of average water levels during high tide (HT), MT, and low tide (LT). Additional shallow groundwater samples were collected between the HT and MT locations (**Figure 1**) using a drive-point piezometer to better delineate chemical distributions. To remain consistent between profiles, all depths were calculated relative the sediment surface at the high tide profile (rather than sediment surface at the location of collection).

Groundwater samples for dissolved (<0.45 μm) trace metal analysis (Fe, Mn, Mo, U, V, and Cr) were collected in acid-washed LDPE bottles, acidified immediately after collection, and analyzed by two-fold dilution and direct injection on a Thermo Element 2 inductively-coupled plasma mass spectrometer at the University of Southern Mississippi's Center for Trace Analysis. Isotope dilution was used to account for matrix effects. Detection limits were ≤2 nM (nM). Samples for organic-metal complex measurements (<0.45 μm) were collected during the February seasonal transect sampling in 1 L acid-washed LDPE bottles and immediately frozen. These samples were later thawed and extracted through a Bond Elut C18 column (Agilent, 500 mg bed mass). Columns were acid-washed in dilute trace metal grade HCl and rinsed thoroughly. Before use, columns were conditioned with 100 ml of methanol followed by 500 ml of MilliQ water. Approximately 250 ml of sample was loaded through the column (confirmed by sample mass difference), followed by a 10 ml MilliQ water rinse (Lemaire et al., 2006). The column was dried by pulling air through for 30 minutes, and then elution was done with 10 ml of HPLC-grade methanol. Concentrated ultrapure HNO_3 (100 μL) was added to samples before they were dried under a HEPA-filtered laminar flow hood. Samples were reconstituted with 1 N ultrapure HNO_3 for analysis as described above. This method isolates 20–60% of DOC, primarily hydrophobic species (Lemaire et al., 2006). The amount of DOC recovered in the extractions here is not reported because efforts to prevent metal contamination were prioritized over preventing organic carbon contamination (e.g., collecting eluent in LDPE bottles). The metals extracted along with this organic phase will be referred to here as associated with hydrophobic dissolved organic matter (hDOM). Due to the uncertainty in DOC recovery in hDOM, the association of metals with hDOM can be considered to be a semi-quantitative assessment of how the metals are associated with DOM overall within the STE; comparisons can be made across space, time, and different metals within the study, but caution should be used if comparing precise numbers to other studies. Details for collection and analysis of DOC, humic C, and sulfide can be found in O'Connor et al. (2018).

2.3 Sediment Collection and Analyses

A 4-m long vibracore was collected adjacent to the mid-tide sampling location in May 2013, and processed as described previously (O'Connor et al., 2018). The core was sectioned into 5 cm intervals to evaluate vertical variations in sediment contents. Sequential leaches were performed to isolate the metal oxide and recalcitrant metal fractions (Tessier et al., 1979). Dried and weighed sediments (~1 g) were shaken for 180 min in 5 ml of 1 M hydroxylamine hydrochloride in 25% acetic acid, centrifuged at 3000 g for 10 min. Four milliliters of supernatant were removed to a new, clean tube and diluted in 0.5 M HNO_3 (Aristar Plus, trace metal grade). This represented the fraction liberated upon reductive dissolution of Fe and Mn (hydr)oxides (Tessier et al., 1979), and will be referred to here as the "metal oxide fraction." The leach method used in the current study does not provide the specific information about speciation or redox state of solid-phase metal oxides afforded by other chemical leach methods (e.g., Anschutz et al., 2005; Hyacinthe et al., 2006). The simpler leach method was used here to liberate metals associated with the bulk amorphous oxide pool, comparable to other studies of Fe and Mn cycling in the STE (e.g., Charette et al., 2005). The remaining sediment was shaken in 5 ml aqua regia (1:3 HNO_3:HCl) for 13 h. Samples were centrifuged, and the supernatant removed and diluted with MilliQ water. Metal concentrations in these fractions were analyzed as described for groundwater samples above. This fraction represents more recalcitrant sedimentary phases (but does not dissolve pyrite) and will be referred to as the "recalcitrant fraction" (Tessier et al., 1979; Huerta-Diaz and Morse 1992). Metal concentrations in both fractions were analyzed as described for groundwater samples above.

2.4 Data Analysis

As previously described (O'Connor et al., 2018), this STE is characterized by three endmember mixing between saline, estuarine surface water and two distinct up-gradient

freshwater sources: one shallow and one deep (**Supplementary Figure S1C**). The shallow freshwater endmember is more oxidizing than the deep endmember (Eh around 100 mV compared to < −100 mV) and has higher organic matter contents. Therefore, mixing of chemical elements could not be evaluated only with respect to a single fresh endmember. To evaluate chemical addition or removal along the seasonal STE transects, two mixing lines were inferred on salinity-concentration plots: one between the surface endmember and the shallow fresh endmember, and one between the surface and deep fresh endmember. Points that fall within the triangle created by the two mixing lines were interpreted as resulting from mixing between the three endmembers, while those falling outside result from non-conservative addition or removal.

To quantify the addition or removal of an element at the MT profile over the 2-years time series, we calculated the concentration anomaly relative to conservative mixing. The concentration anomaly is the difference between the measured concentration and the expected concentration given conservative mixing between the endmembers, calculated as:

$$C_{\text{anomaly}} = \left(C_{\text{observed}} - C_{\text{expected}}\right) / C_{\text{expected}}$$

The expected concentration ($C_{expected}$) was calculated using the fractional contributions of the three endmembers. The contribution of each endmember was calculated using salinity and humic carbon as tracers (described in O'Connor et al., 2018).

Multiple linear regression models were used to evaluate the response of the RSEs (Mo, U, V, and Cr) to changes in biogeochemically relevant predictor variables. All analyses were performed using existing functions in R (R Core Team 2015). The goal of these regressions was to determine the effect of major groundwater constituents on the distribution of RSMs, providing insight into how these elements respond to geochemical changes in the STE. These relationships also suggest what major constituents could be used to predict RSM behavior in other coastal groundwaters.

Two sets of regressions were used to understand the responses of redox-sensitive trace metals to other chemical constituents in the STE across time and space. The first used data measured monthly at the MT location and explored seasonal changes over the 2 years of sample collection (referred to here as "time effects"). Time effects regressions were performed on MT profile data separated into summer (May to October) and winter (November to April) of 2013 and 2014 (seasons were differentiated by differences in groundwater temperature; O'Connor et al., 2018). The second set of regressions assessed how RSM responses to predictor variables differed along a shore-normal transect (referred to here as 'space effects'). The space effect regressions were done on the HT, MT, and LT profile data separately (using all 4 months of data at each location) to determine if RSM response to predictor variables differed spatially throughout the STE. Depth ranges included for each well were selected to exclude depths at which a given RSM concentration was consistently below the detection limit (below which any correlation analysis becomes meaningless).

Models using different combinations of geochemically relevant predictor variables were considered. Final models were selected based on p values the Akaike information criterion (AIC). AIC is used to compare the relative quality of potential models, with a lower AIC indicating a higher quality model. The model's p value indicates the chance that the data fit to a model is due to random chance, rather than due to a true relationship in the data. Therefore, a lower p value indicates that a model is statistically significant. Due to the need to select a model that was the best overall fit for several conditions, a hard cut-off for p value was not used. Rather, a combination AIC and p value were evaluated in combination. In reporting model results, all R^2 values reported are the adjusted R^2 of the model which accounts for the sample size.

All response variables (i.e., RSM concentrations), as well as salinity, dissolved Fe, DOC, humic C, and sulfide concentrations were natural log transformed to achieve data normality. Temperature data were normal without transformation. In cases where DOC and humic C were both predictors in a model, collinearity was checked using the variance inflation factor (VIF). The VIF never exceeded 5, the recommended cut-off for multicollinearity in a model (James et al., 2014), so both predictors were retained in these cases.

The biogeochemical rationales for inclusion of various predictor variables considered for inclusion are described here. Salinity was considered for inclusion in all models to account for mixing of fresh and saline waters. Temperature was considered for the space effect models because chemical reactions (both biotic and abiotic) are temperature dependent. The time effects model, already split up by season, accounted for temperature in its design and temperature was therefore not considered as a possible predictor.

Dissolved Fe was considered as a predictor in all Mo and U models because Mo(VI) can sorb to iron oxides, and some Fe reducing bacteria can reduce U. Sulfide was considered in all Mo and U models because sulfide reacts directly with Mo, and because several sulfur-reducing microbial species are capable of reducing U. Although U(VI) can be reduced by Fe(II) (Behrends and Van Cappellen 2005) and sulfide (Hua et al., 2006), the rates of these reactions are comparable to those of enzymatic reduction only under certain conditions (e.g., the ready availability of certain reactive metal hydroxide surfaces; dominance of uranium hydroxide species). Therefore, geochemical associations of U with Fe and S here are generally considered to be proxy relationships for the microbial processes that generate these reduced metabolites, although abiotic reduction may also play a role.

DOC, humic C, and dissolved Fe were considered for all V and Cr models because reduced V and Cr species can be complexed by organic matter (Wehrli and Stumm 1989; Remoundaki et al., 2007) and co-precipitate with iron (hydr)oxides (Rai et al., 1989).

Model results are presented using normalized coefficient plots. For a given model, the coefficients are calculated based on scaled and centered data (using the scale function in R) in order to be comparable across different predictors. Stronger relationships between predictor and response variables are represented by larger (either positive or negative) coefficients. Normalized coefficients and p values can be found in the **Supplementary Material**.

TABLE 1 | Endmember salinities and RSM concentrations used to estimate mixing and concentration anomalies. The notes identify the months corresponding to the endmember concentrations that were used to calculate the conservative mixing lines and concentrations.

	Surface				
	Salinity	**Mo (nM)**	**U (nM)**	**V (nM)**	**Cr (nM)**
April[a]	14.3	54.54	6.47	12.78	3.33
July[b]	18.3	64.56	6.91	41.87	<1
October[c]	20.0	74.26	7.56	42.10	8.61
February[d]	16.6	59.45	7.91	7.24	1.10
	Freshwater–shallow				
	Salinity	Mo (nM)	U (nM)	V (nM)	Cr (nM)
April[a]	0.33	13.42	1.37	2.48	235.55
July[b]	0.33	8.15	1.97	296.87	197.33
October[c]	0.43	5.51	1.04	159.43	58.86
February[d]	1.37	3.93	0.40	45.69	19.37
	Freshwater–deep				
	Salinity	Mo (nM)	U (nM)	V (nM)	Cr (nM)
April[a]	1.94	<1	0.12	12.58	2.56
July[b]	1.96	2.53	0.46	30.73	10.96
October[c]	2.63	<1	<0.01	14.08	9.19
February[d]	2.72	<1	0.17	8.79	3.12

[a]*Mar, Apr.*
[b]*May, Jun, Jul.*
[c]*Aug, Sep, Oct.*
[d]*Nov, Dec, Jan, Feb.*

3 RESULTS

3.1 Groundwater

3.1.1 Molybdenum

The mean concentration of Mo in the shallow freshwater endmember (7.8 ± 4 nM) tended to be higher than for the mean deep freshwater endmember (0.63 ± 1 nM), but both were much lower than estuarine surface water concentrations (63 ± 8 nM) (**Table 1**). Molybdenum was highest in the surface water and shallow STE groundwater, with the 25 nM contour falling between 50 and 150 cm depth, and the 10 nM contour between 100 and 200 cm depth (**Figure 1A**). At MT, concentrations decreased steadily from surface water concentrations (62 ± 11 nM in summer; 57 ± 9 nM in winter) to 24 ± 12 nM at 115 cm depth across all seasons (**Figure 2A**). Below 115 cm depth, Mo declined sharply to less than the detection limit of 1 nM. At LT, Mo was consistently lower than at other locations (3 ± 5 nM) but tended to be highest in the shallowest sampled depth (**Figure 1A**). Concentrations of dissolved Mo associated with hDOM were highest at depths between 50 and 100 cm throughout the STE, reaching 4.5–10.8 nM (**Figure 3A**). The percent of Mo associated with hDOM increased with depth in the STE, from 2.7% in the surface to >50% below 150 cm depth (**Figure 3A**).

In the seasonal transects, samples with sulfide concentration >10 μM showed evidence of non-conservative removal (**Figure 4A**). Most non-sulfidic (shallow groundwater) samples fell within the conservative mixing area or slightly below with the exception of clear non-conservative excess in July. Molybdenum anomalies calculated at the MT profile were near zero in shallow groundwater (<100 cm), and the concentration anomaly dropped to below zero at 130–140 cm (**Figure 5A**).

The time effects linear model selected (based on AIC) for Mo was:

$$\log(\mathrm{Mo}) \sim \log(\mathrm{salinity}) + \log(\mathrm{Fe}) + \log(\mathrm{sulfide})$$

The models for individual seasons explained between 68 and 81% of the variability in Mo concentrations (**Figure 6A**). Molybdenum was correlated negatively with sulfide across all seasons. In seasons where the correlation with sulfide explained a lower percent of Mo variability (summer 2013 and winter 2014), the positive correlation with salinity was stronger.

The space effects linear model selected for Mo was the same as for the time effects model. The models for each location explained between 56 and 62% of the variability in Mo concentrations (**Figure 7A**). Salinity was the best predictor of Mo distribution at LT, whereas Fe and sulfide were better predictors at HT and MT, respectively.

3.1.2 Uranium

The mean U concentration for the shallow freshwater endmember (1.2 ± 0.6 nM) tended to be higher than that for the deep freshwater endmember (0.2 ± 0.2 nM), but both were much lower than estuarine surface water concentrations (7.2 ± 0.6 nM) (**Table 1**).

Dissolved U was highest in the surface water and shallowest parts of the STE. The 1 nM contour fell between 100 and 150 cm in July, and between 150 and 350 cm in February (**Figure 1B**). Summer U concentrations at MT remained relatively constant down to 90 cm (5 ± 3 nM), then decreased to <1 nM by 130 cm (**Figure 2B**). Winter U concentrations at MT remained relatively constant down to 100 cm (6 ± 4 nM), then decreased to <1 nM by 130 cm depth. At LT, U concentrations were consistently low (0.6 ± 0.6 nM), with somewhat higher concentrations evident at the shallowest (125 cm, 0.9 ± 0.2 nM) and deepest (300 cm, 1.6 ± 0.5 nM) sampled depths (**Figure 1B**). Concentrations of dissolved U associated with hDOM were relatively uniform (<0.5 nM) throughout the depth profile, with one sample reaching a maximum 1.4 nM between 300 and 400 cm depth (**Figure 3B**). The percent of U associated with hDOM was low in the surface (2.0%) and reached a maximum in the 200–300 cm depth range (15% ± 12) (**Figure 3B**).

In the seasonal transects, nearly all samples above salinity ~3 showed non-conservative removal (in all months except April) (**Figure 4B**). Greater non-conservative behavior was observed in July than in other months based on the distance of points below the conservative mixing lines (**Figure 4B**) and the consistent negative concentration anomaly at shallower depths (**Figure 5B**). Uranium anomalies calculated at the MT were generally at or below zero from 62 to 115 cm, except in winter 2014, when anomalies were between zero and one, indicating enrichment

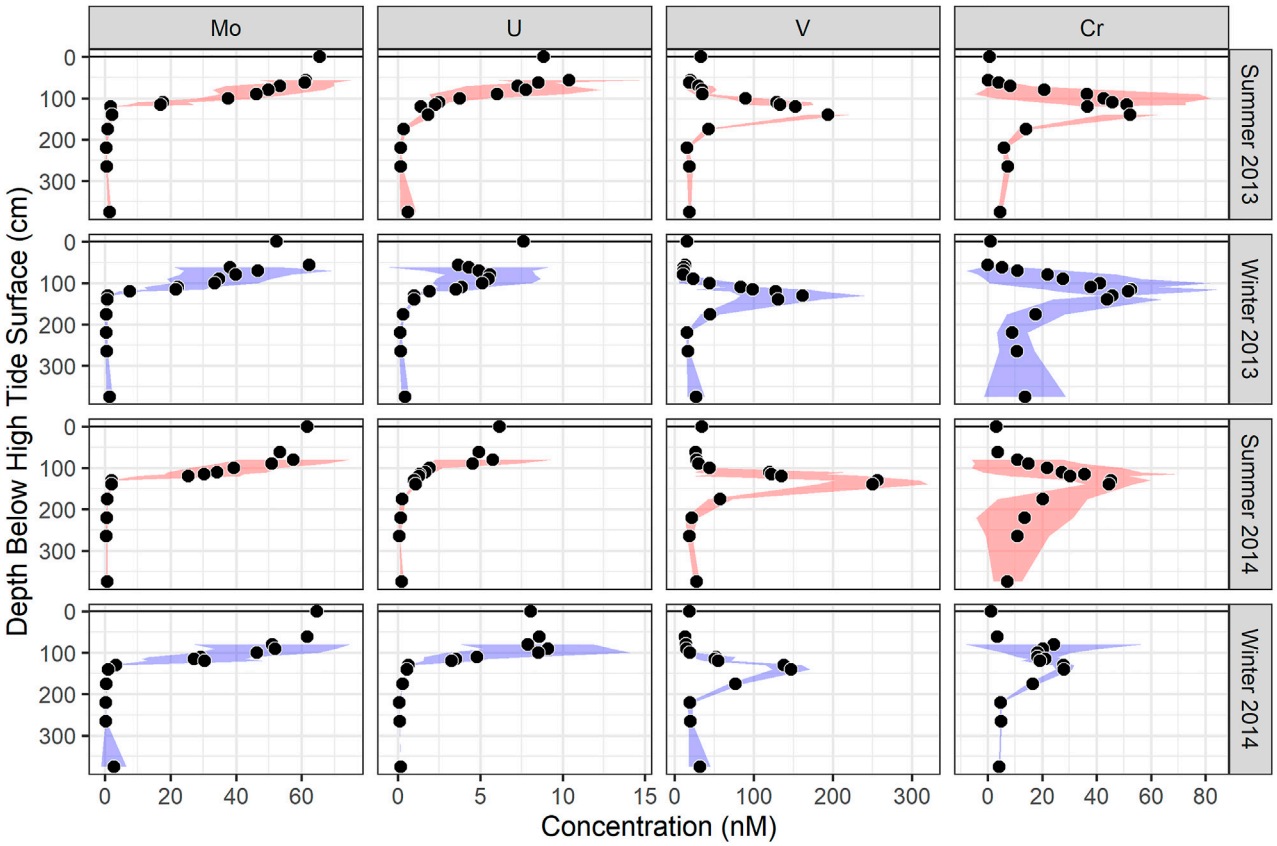


FIGURE 2 | Dissolved **(A)** Mo, **(B)** U, **(C)** V, and **(D)** Cr concentrations from the MT profile over the 2-year time series. Summer is defined as May to October, and winter is defined as November to April. At each depth, the filled circles represent the mean, and shaded areas represent one standard deviation, of all the months sampled in each season.

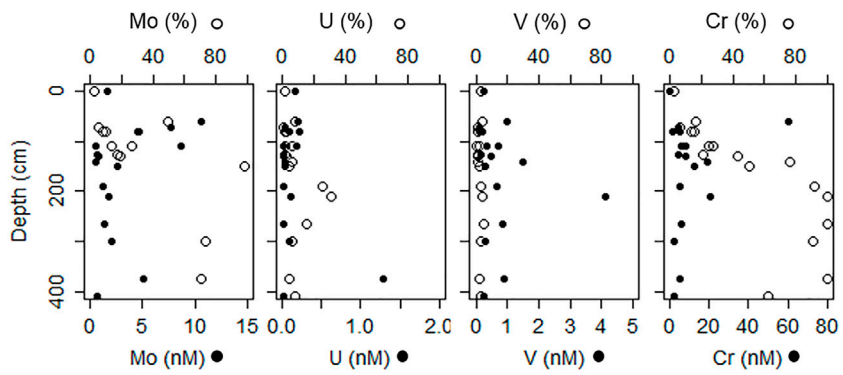


FIGURE 3 | Groundwater depth profiles for concentrations (solid circles; lower axis) and percent of total dissolved metal (open circles; upper axis) associated with hydrophobic organic matter (as determined by extraction on a C18 column). Surface water concentrations are shown at 0 cm depth.

(**Figure 5B**). Non-conservative removal occurred at all depths in summer 2013; at 90 cm and deeper in summer 2014; and at 140 cm and deeper in both winters. The anomalies calculated from three-endmember mixing typically fell between those calculated from mixing between the surface water and either the shallow or deep freshwater endmember.

The time effects linear model selected for U was:

$$\log(\mathrm{U}) \sim \log(\mathrm{salinity}) + \log(\mathrm{Fe}) + \log(\mathrm{sulfide})$$

The models for individual seasons explained between 54 and 84% of the variability in U concentrations (**Figure 6B**). The most statistically significant predictor of U concentrations over the 2-

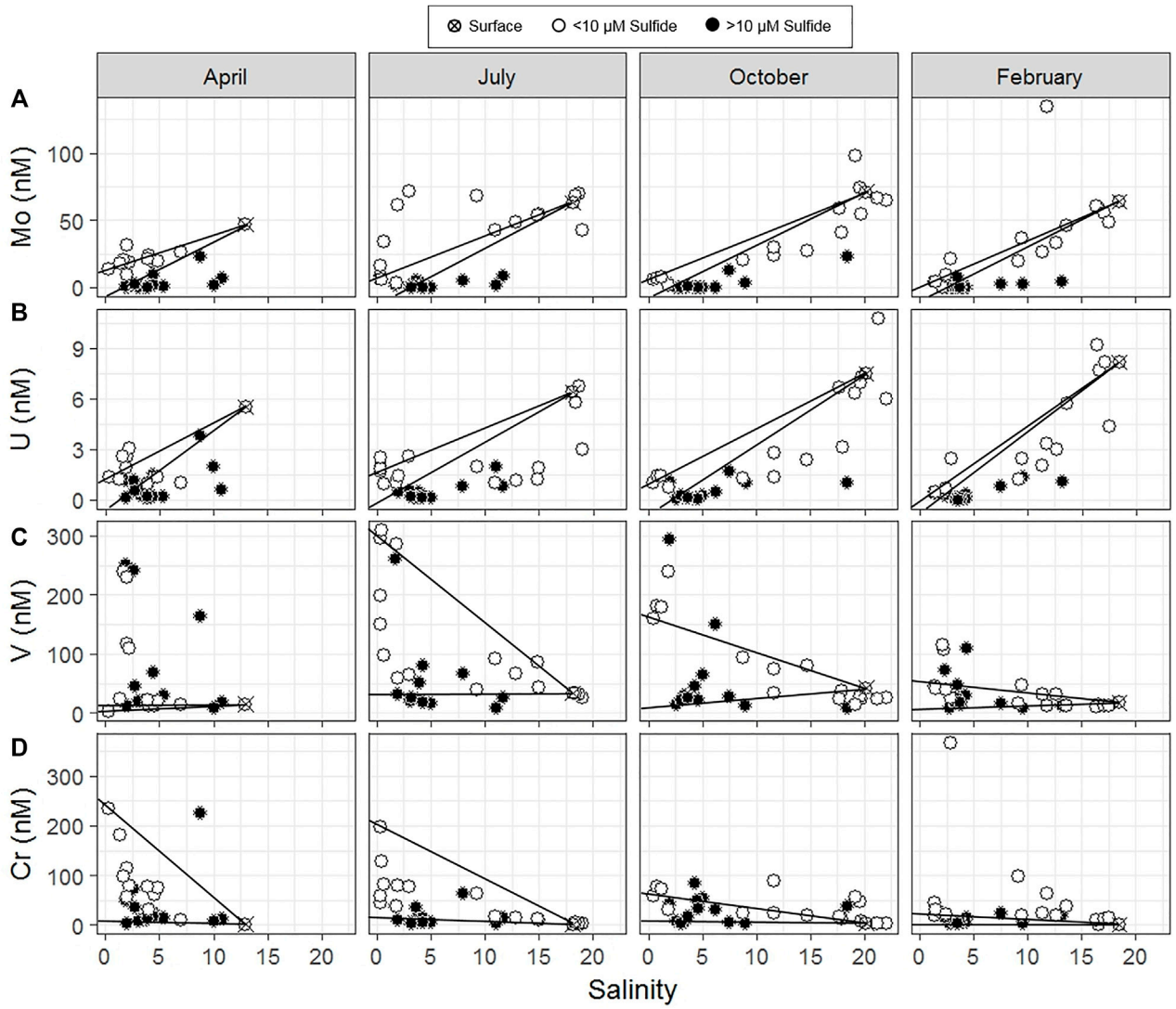


FIGURE 4 | Salinity mixing diagrams of dissolved **(A)** Mo, **(B)** U, **(C)** V, and **(D)** Cr. Solid symbols indicate samples in which sulfide concentrations exceed 10 µM. Conservative mixing lines are drawn between the saline surface water endmember and both the deep and shallow freshwater endmembers (**Table 1**). Samples falling above and below the conservative mixing lines suggest non-conservative addition and removal, respectively.

year sampling period was sulfide (negative correlation), followed by Fe (positive correlation) (**Figure 6B**). In winter 2014, the effect of Fe was not significant, but unlike other seasons, the effect of salinity was statistically significant.

The space effects linear model selected for U was:

$$\log(\mathrm{U}) \sim \log(\mathrm{salinity}) + \log(\mathrm{Fe}) + \log(\mathrm{sulfide})$$

The models for each location explained between 34 and 71% of the variability in U concentrations (**Figure 7B**). The best predictor of U concentration varied between locations. At HT, U was directly proportional to dissolved iron. At MT, U was inversely proportional to dissolved sulfide whereas salinity was the strongest predictor of U concentrations at LT (**Figure 7B**).

3.1.3 Vanadium

Dissolved V showed a mid-depth concentration maximum throughout the STE (**Figure 1C**). The maximum was generally between 50 and 250 cm from HT to MT, and 150–250 cm at LT. Dissolved V concentrations were highest from HT to MT and were never below the detection limit (2 nM) at any location. Within the MT profile maximum (from 100 to 140 cm), V concentrations ranged from a low of 147 ± 24 nM in winter 2014 to a high of 256 ± 54 nM in summer 2014 (**Figure 2C**), with generally higher concentrations in summer than in winter (**Figures 1C**,**2C**; **Supplementary Figure S2**). Concentrations of dissolved V associated with hDOM were typically 1–2 nM at all depths and the fraction of V associated with hDOM was low throughout the surface water and STE (<5%; **Figure 3**).

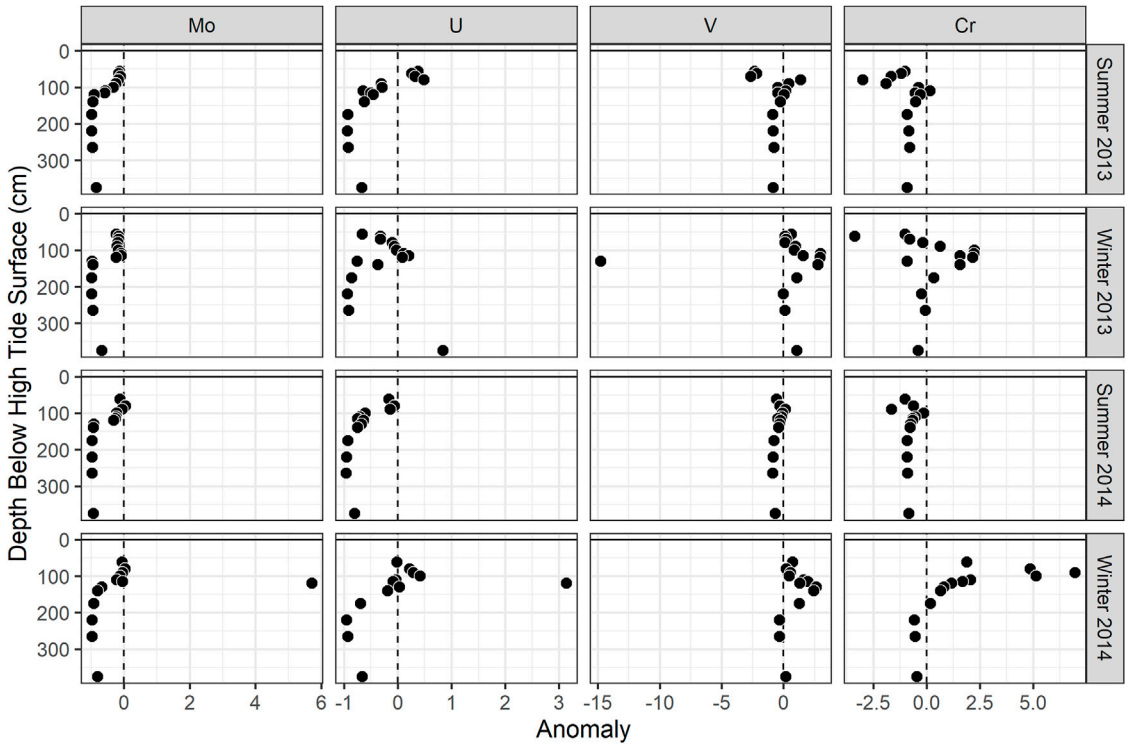


FIGURE 5 | Concentration anomalies (calculated using three endmember mixing as described in the text) of **(A)** Mo, **(B)** U, **(C)** V, and **(D)** Cr at the MT profile. The points shown are the median anomaly values for each season.

On average, vanadium was lowest in the deep freshwater endmember and highest in the shallow freshwater endmember (**Table 1**). The shallow freshwater endmember concentration was variable, increasing by a factor of six between April (2.48 nM) and July (296.9 nM). This shallow freshwater endmember was the primary source of V to the STE (having the highest concentration in all months but April). The deep freshwater endmember varied between a low of 8.8 nM in February to a high of 30.7 nM in July. Surface water concentrations varied between a low of 7.24 in February to a high of 42.1 in October.

In salinity mixing diagrams for the seasonal transects, V generally showed non-conservative addition, although patterns varied by month (**Figure 4C**). In July (with the highest shallow freshwater endmember concentration), most samples showed conservative behavior. In April and February (with lower shallow freshwater endmember concentrations), several sulfidic and non-sulfidic samples showed non-conservative addition. The calculated V anomalies at MT were primarily positive and were greatest between 100 and 175 cm in all seasons, coinciding with the mid-depth V concentration maximum. The concentration anomalies within the peak were higher in winter than in summer (**Figure 5C**). The anomalies within the V concentration maximum from three-endmember mixing typically were lower than those calculated from mixing between the surface water and the shallow or deep freshwater endmember.

The time effects linear model selected for V was:

$$\log(\mathrm{V}) \sim \log(\mathrm{DOC}) + \log(\mathrm{humic}) + \log(\mathrm{Fe})$$

The models for individual seasons explained between 67 and 83% of the variability in V concentrations (**Figure 6C**). Both DOC and Fe were directly correlated with V in most seasons (**Figure 6C**). Humic carbon was a significant predictor of V only in winter.

The space effects linear model selected for V was:

$$\log(\mathrm{V}) \sim \log(\mathrm{DOC}) + \log(\mathrm{humic}) + \mathrm{temperature}$$

Models for each location explained between 40 and 74% of the variability in V concentration (**Figure 7C**). Dissolved organic carbon and temperature were positively correlated with V at MT and LT (**Figure 7C**), whereas V was significantly correlated with only humic carbon at HT. The direct correlation of V with temperature reflects the observed higher V concentrations in summer (**Figures 1C**,**2C**). Salinity was not a predictor of V in either the time effects or space effects models, which is consistent with only one of the freshwater endmembers acting as a primary source of V to the STE (as opposed to the existence of a single consistent fresh or saline source) (**Table 1**).

3.1.4 Chromium

Chromium was lowest in surface water (3 ± 3 nM) and highest in the shallow freshwater endmember (19.4–235.6 nM) (**Table 1**). Similar to V, Cr showed a mid-depth concentration maximum throughout the shallow STE (**Figure 1D**). Maximum Cr

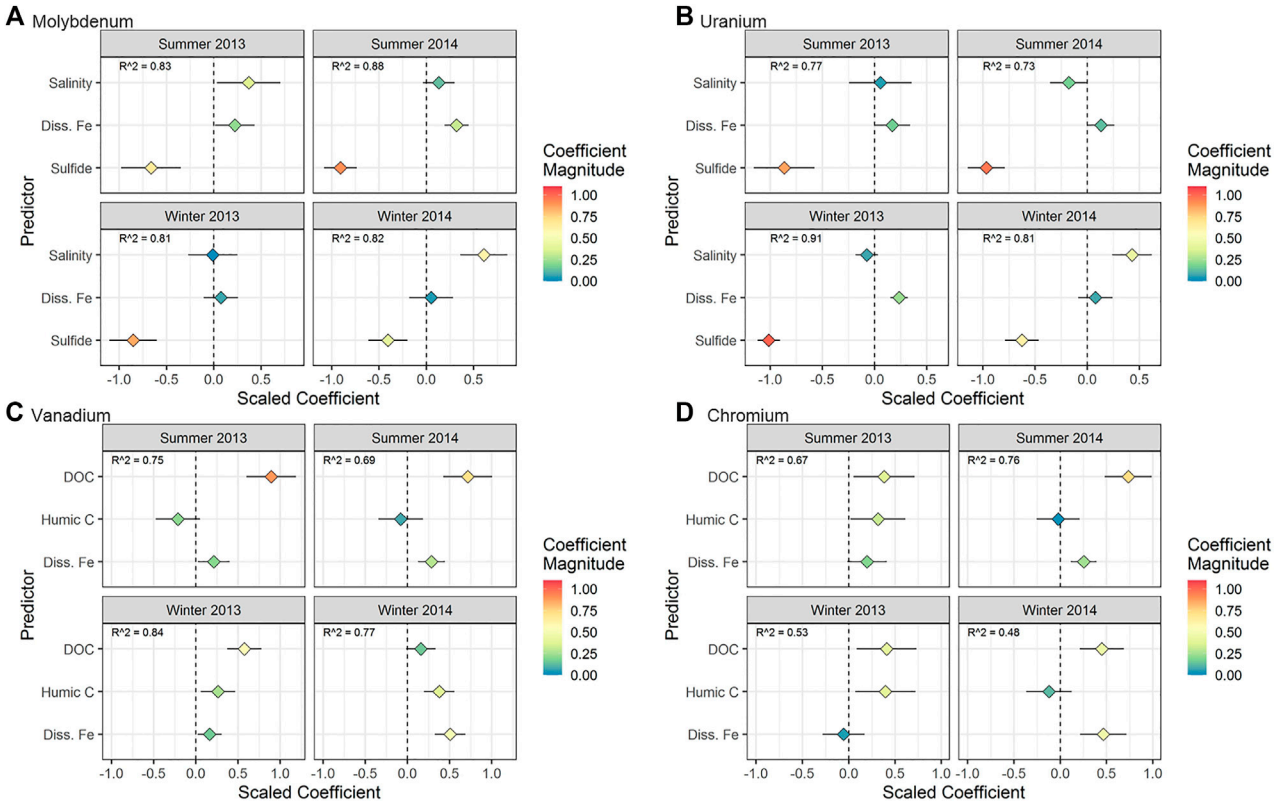


FIGURE 6 | Regression results for **(A)** Mo, **(B)** U, **(C)** V, and **(D)** Cr for the time series taken at the MT sampling location (time effects). The horizontal axis represents the scaled coefficient for each predictor in the multiple linear regression (vertical axis). The color of the points shows the absolute magnitude of the coefficient. More extreme values (positive or negative) represent a stronger relationship between the predictor and the metal concentration. The horizontal line associated with each point represents the 95% confidence interval for the coefficient. For points where the confidence interval does not intersect 0, the *p* value for the coefficient is < 0.05.

concentrations were observed from 90 to 130 cm depth at HT, from 100 to 200 cm depth at MT, and 125–150 cm at LT (**Figure 1D**). Concentrations of Cr were typically highest at HT, with concentrations commonly >100 nM, and up to 235 nM (**Figure 1D**). In the MT time series, Cr concentrations within the maximum ranged from 28 ± 3 nM in winter 2014 to a high of 53 ± 31 nM in winter 2013 (**Figure 2D**). Like V, Cr concentrations were always above the detection limit (1 nM). Concentrations of Cr within the maximum at MT did not show any consistent trends with season, but were higher during 2013 (**Figure 2D**, **Supplementary Figure S2**). Concentrations of dissolved Cr associated with hDOM were highest in the same depth range as the dissolved Cr maximum, between 100 and 200 cm depth (**Figure 3**). The percent of Cr associated with hDOM increased with depth in the STE from the surface water (2.8%) to the 301–410 cm depth interval (81% ± 26; **Figure 3**).

In salinity mixing diagrams for the seasonal transects, Cr concentrations generally exhibited conservative mixing behavior in the summer and non-conservative addition in the fall/winter when shallow freshwater endmember Cr concentrations were lower (**Figure 4D**). Additionally, positive Cr concentration anomalies (indicating addition) were observed at the MT profile, and tended to be higher in winter than summer (**Figure 5D**).

The time effects linear model selected for Cr was:

$$\log(\mathrm{Cr}) \sim \log(\mathrm{DOC}) + \log(\mathrm{humic}) + \log(\mathrm{Fe})$$

The models for individual seasons explained between 45 and 75% of the variability in Cr concentrations (**Figure 6D**). In 2013, Cr was positively correlated with DOC and humic carbon (**Figure 6D**). However, Cr was correlated with DOC and Fe (and not humic carbon) in 2014.

The space effects linear model selected for Cr was:

$$\log(\mathrm{Cr}) \sim \log(\mathrm{salinity}) + \log(\mathrm{DOC}) + \log(\mathrm{Fe})$$

The models for each location explained between 55 and 71% of the variability in Cr concentrations (**Figure 7D**). Chromium was positively correlated with Fe at LT, and correlated with both DOC and Fe at MT. At HT, the predictor closest to statistical significance was Fe ($p = 0.066$). Similar to the linear models of V concentrations, salinity was not a predictor of Cr. However, unlike models for V, temperature was not a predictor of Cr concentrations, reflecting its more constant concentrations between summer and winter (**Figure 2D**).

3.2 Sediment

Metal oxide-associated Mo content in sediments was low (<1.5 μmol/cm^3) in the shallowest sediments, increased to ~4 μmol/cm^3 between

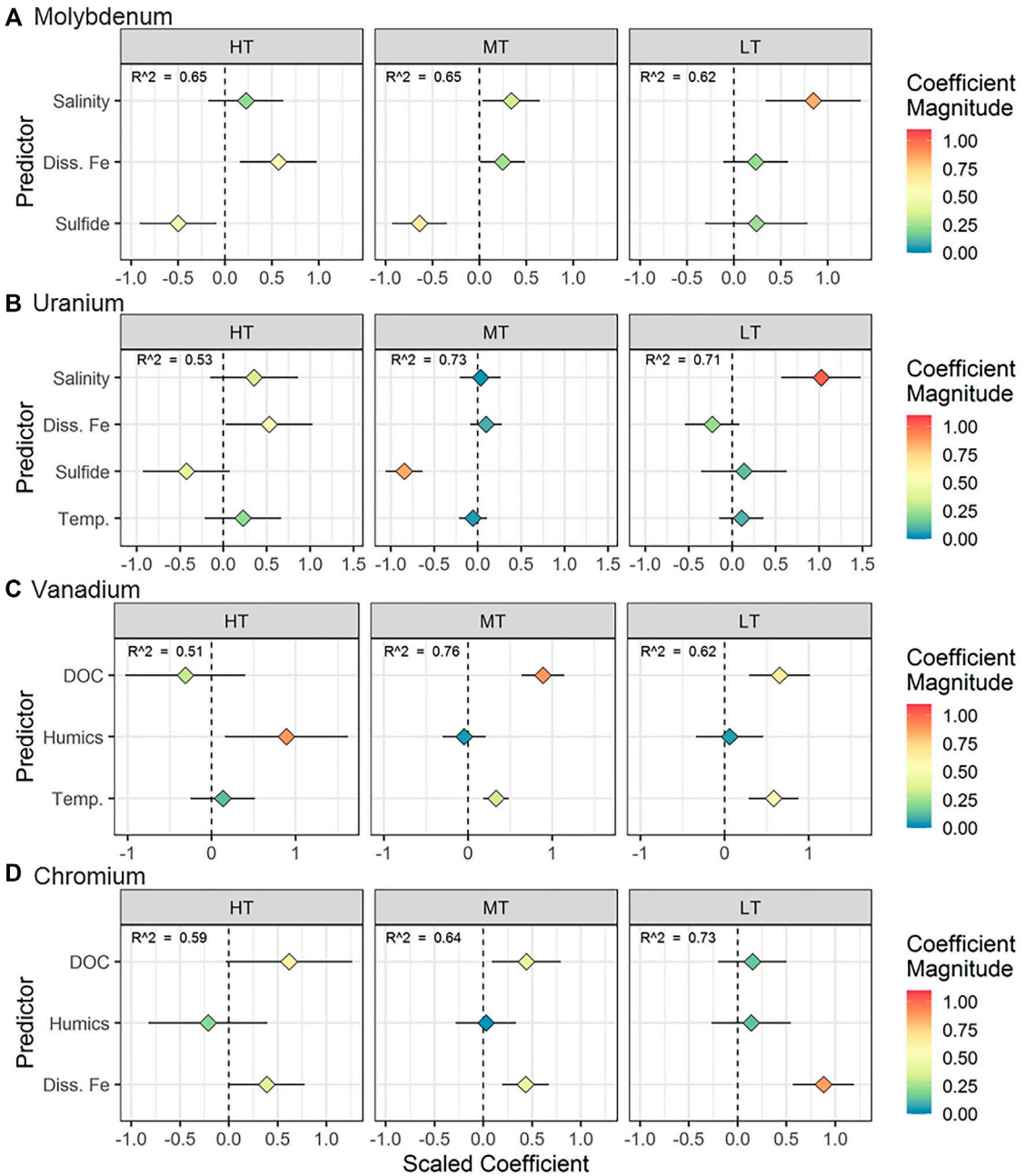


FIGURE 7 | Regression results for **(A)** Mo, **(B)** U, **(C)** V, and **(D)** Cr for measurements taken along the STE transect (space effects). The horizontal axis represents the scaled coefficient for each predictor in the multiple linear regression (vertical axis). The color of the points shows the absolute magnitude of the coefficient. More extreme values (positive or negative) represent a stronger relationship between the predictor and the metal concentration. The horizontal line associated with each point represents the 95% confidence interval for the coefficient. For points where the confidence interval does not intersect 0, the *p* value for the coefficient is < 0.05.

70 and 150 cm, then increased to reach as high as 7.8 μmol/cm^3 at depth (**Figure 8**). Metal oxide-associated U was low (~0.1 μmol/cm^3) down to 45 cm depth, increased to 1–2 μmol/cm^3 between 70 and 250 cm depth, then increased to 5 μmol/cm^3 at the base of the profile. Recalcitrant Mo and U profiles showed similar distributions to their metal oxide fractions.

Metal oxide-associated V and Cr content were highest between 60–90 cm and 190–300 cm depths (**Figure 8**). Sediment concentrations of metal oxide-associated V reached as high as 86 μmol/cm^3 while reducible Cr reached as high as 11 μmol/cm^3. Recalcitrant V and Cr showed similar distributions as the metal oxide fractions, but with a sharper peak at 70 cm depth and similar concentrations.

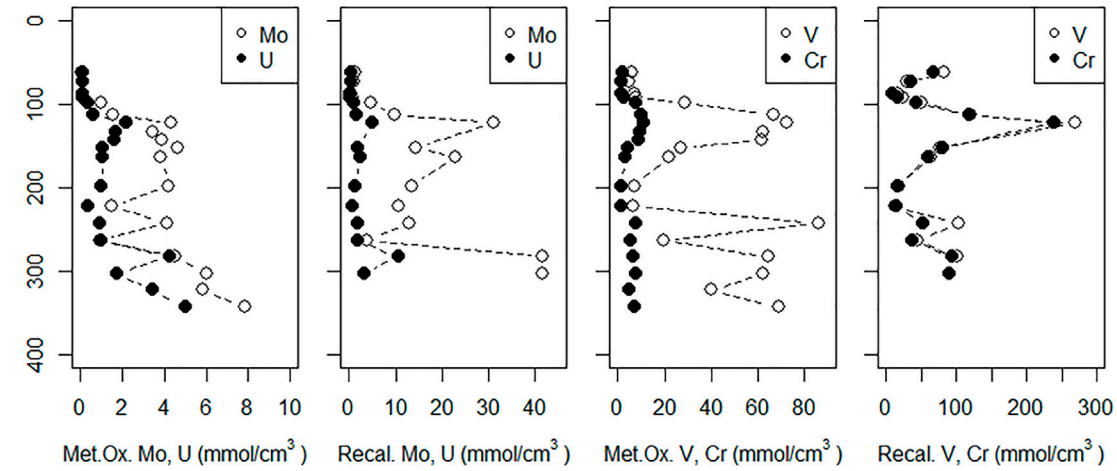


FIGURE 8 | Sediment concentrations of metals dissolved by reducing (Metal Ox.) and aqua regia (recalcitrant [Recal.]) leaches (described in Methods). The sediment core was taken adjacent to the MT profile. The dotted line represents the sediment surface; depths are relative to the sediment surface at HT.

4 DISCUSSION

4.1 Molybdenum

High Mo concentrations in the surface water and shallow STE (compared to freshwater endmembers) showed Mo was supplied to the STE by estuary surface water (**Figures 1A**,**2A**). Once in STE groundwater, Mo was non-conservatively removed during advection into sulfidic portions of the STE (**Figures 4A**, **5A**). Mo in sulfidic samples was always below concentrations expected for conservative mixing (**Figure 4A**), and calculated anomalies showed that Mo was consistently removed from groundwater where dissolved sulfide was first present, between 100 and 140 cm depth at MT (**Figure 4A**; O'Connor et al., 2018). These results are consistent with Mo observations from other STEs globally. Non-conservative removal of molybdenum was observed in several other study sites on the Atlantic and North Sea coasts (Windom and Niencheski 2003; Beck et al., 2008; Reckhardt et al., 2017). Reckhardt et al. (2017) demonstrated that Mo and sulfate depletion were correlated.

Measuring sulfide and using statistical modelling provided quantitative support for previous hypotheses regarding sulfide control on the removal of Mo. Multiple linear regression confirmed a negative correlation between Mo and sulfide throughout the STE (with the exception of the low tide location, discussed below) in all seasons (**Figures 6A**,**7A**). Laboratory and field studies suggest that at a sulfide threshold of ~10 μM a geochemical "switch" is flipped and molybdate quantitatively reacts to form highly particle reactive thiomolybdate (MoS_4^{2-}) (Helz et al., 1996; Erickson and Helz 2000). In this work, we confirm Mo removal primarily occurs where sulfide is present at concentrations higher than 10 μM (**Figure 4A**), consistent with these laboratory results. The negative correlation between Mo and sulfide throughout the 2-year time series suggests the importance of Mo removal by sulfide in every season (**Figure 6A**).

Sulfide concentrations varied seasonally in this STE (O'Connor et al., 2018), with higher concentrations during summer in the depth range where Mo was removed (100–140 cm; **Figure 5A**). However, Mo removal did not appear to be more extensive in summer (**Figures 4A**,**5A**). This may be because sulfide reached sufficiently high concentrations to drive Mo removal (>10 μM) by 140 cm depth in all seasons (O'Connor et al., 2018). Seasonal removal of Mo is more likely to occur in STEs where sulfide concentrations vary around a low-micromolar concentration threshold (e.g., Beck et al., 2008; Morford et al., 2009).

Sediment Mo content was consistent with Mo removal from groundwater to form insoluble compounds. Both metal oxide-associated and recalcitrant Mo increased in the 100–140 cm depth range (**Figure 8**) where sulfide and Mo co-occurred and dissolved Mo was removed (**Figure 5A**). Sediment Mo contents also increased with depth (**Figure 8**) suggests that the Mo-sulfide interface may shift over time, resulting in thiomolybdate compounds sorbing to sediments at different depths.

The pattern of Mo removal differed spatially throughout the STE. At LT, lower Mo concentrations and stronger correlation of Mo with salinity (**Figure 7A**) suggested that Mo removal typically occurs at shallow enough depths (sulfide concentrations were >250 μM at every sampled depth; O'Connor et al., 2018) that increasingly reducing conditions at depth did not drive further changes in Mo. This observation suggests that more seaward portions of shallow STEs may act as a greater Mo sink than intertidal zones.

Modeling done in this study supports a potential mechanism for Mo mobilization from the shallow STE observed by Beck et al. (2010) and in several samples in this study. Because molybdate can sorb to Mn oxides under oxic conditions (Shimmield and Price 1986), Beck et al. (2010) suggested that this may be associated with mobilization of metal (particularly Mn) oxides. This study confirms that dissolved Fe and Mo are correlated in summer months and that metal oxide-associated Mo occurs in shallow STE sediments (**Figure 8**), supporting the hypothesis that under non-sulfidic conditions, Mo cycling may be seasonally controlled by Fe and/or Mn oxidation and reductive dissolution (described in O'Connor et al., 2018).

The distribution of Mo contents in the groundwater and sediment suggests there may be spatial differences in the permanence of sequestration. Increasing concentrations of Mo in sediment occur near the redox interface, and may be mobilized with mixing of saline and oxic surface water into the STE. This mixing depends on the hydraulic gradient between groundwater and surface water (Gonneea et al., 2013; Luek and Beck 2014), which may be disturbed by short-term events such as storm surges or long-term events such as sea level rise. The highest concentrations of Mo in sediment occur at depth, where oxygen intrusion and remobilization are less likely.

4.2 Uranium

Consistent with many other studies (Duncan and Shaw 2003; Windom and Niencheski 2003; Charette and Sholkovitz 2006; Beck et al., 2008; Riedel et al., 2011; Reckhardt et al., 2017), uranium was supplied to the Gloucester Point STE by surface water and showed non-conservative removal with depth (**Figures 1B**, **2B**, **4B**, **5B**). Sampling over several years and seasons showed that non-conservative removal was greater in summer. This is demonstrated by concentrations falling farther below the conservative mixing range in summer (**Figure 4B**) and shallower removal depths in the summer than the winter (**Figure 5B**).

Previous work has found inverse correlations between U and Fe, Mn, and sulfate reduction rate (Riedel et al., 2011; Reckhardt et al., 2017). This inverse relationship is consistent with U reduction coupled to metal oxide or sulfate reduction. Several microbial species, including many iron-reducing bacteria and sulfate/sulfur-reducing bacteria, (e.g., *Geobacter metallireducens* strain GS-15, *Alteromonas putrefaciens, Shewanella putrefaciens, Desulfovibrio desulfuricans, Desulfovibrio vulgaris*), can reduce U to its particle reactive species (Lovley et al., 1991; Lovley and Phillips 1992; Lovley et al., 1993; Fredrickson et al., 2000).

This work expands on these observations by assessing the relative importance of geochemical factors for U removal. Quantifying the relationship between U and other chemical parameters using multiple linear regression, rather than separate regressions, allowed for concurrent assessment of possible influences on U distribution. At the Gloucester Point STE, U was consistently inversely correlated with sulfide, while it showed either no correlation or a positive correlation with Fe (**Figures 6B**,**7B**). This suggests that sulfate/sulfur-reducing bacteria played a greater role in U reduction compared to iron-reducing bacteria at this STE. More extensive U removal in summer may be due to increased activity of sulfate/sulfur-reducing bacteria during warmer temperatures, which is consistent with conclusions drawn in O'Connor et al. (2018).

Similar to Mo, salinity exerted a stronger control on U concentrations at LT than at other locations in this STE (**Figure 7B**). Because redox conditions are largely consistent with depth at LT, U exhibits more conservative behavior compared to parts of the STE with more distinct redox gradients. Despite the strongly reducing conditions observed within the LT profile and consistently low U concentrations, U concentrations were always above the detection limit. Complexation with inorganic or organic ligands, which are both abundant throughout this STE, has been shown to inhibit the rate of microbially-mediated U reduction (Ganesh et al., 1997; Ganesh et al., 1999) and may therefore have led to the presence of soluble U within reducing groundwater.

Although both metal oxide-associated and recalcitrant U increased steadily with sediment depth (**Figure 8**), there was no U peak indicating a single clear depth of removal (as observed by Charette et al., 2005). Additionally, the increase in sediment U content was not as dramatic as the increase of Mo, despite similar contents in shallow (<100 cm) sediments. This may indicate that U removed to the sediments is more susceptible to remobilization during temporary increases in groundwater redox potential.

4.3 Vanadium

Dissolved V concentrations in the STE were highest mid-depth, evidently originating from shallow fresh groundwater (**Figure 2C**). Vanadium concentrations within the maximum (**Figure 2C**) and throughout the STE (**Figure 1C**) were highest in summer. These high summer concentrations appear partly due to higher concentrations of V in the shallow freshwater endmember (**Table 1**). A similar spatial and temporal pattern was observed in a tidal flat by Beck et al. (2008).

Dissolved V tends to be highest in groundwaters that are oxidizing and slightly basic (Wright and Belitz 2010; Pourret et al., 2012), unlike the reducing conditions throughout large portions of this and other coastal groundwater sites where high concentrations of V were measured in fresh water (Beck et al., 2008; Reckhardt et al., 2017). These studies found that V tends to be associated with higher DOC in reducing waters. Our multiple linear regression to model V concentrations found that V was correlated with both DOC and Fe throughout the 2-year time series (**Figure 6A**), suggesting that complexation by an inorganic-organic colloidal phase may have kept particle reactive reduced V species soluble (Pourret et al., 2012; Telfeyan et al., 2015). Only a small percent of V measured was in the hDOM pool at the Gloucester Point STE (**Figure 3C**). Therefore, hydrophilic organic matter (such as fulvic acids) may be important for complexation of V at this site (Stolpe et al., 2013; Telfeyan et al., 2015).

Higher V concentrations and higher DOC concentrations occurred in summer both at the Gloucester Point STE and the tidal flat studied in Beck et al. (2008). As proposed by Beck et al. (2008), this may be due to higher microbial activity in summer generating more labile organic compounds capable of complexing V. Our models found that the pool of organic matter associated with high V concentrations was different in the summer (correlated with DOC) versus the winter (correlated with humic carbon) (**Figure 6A**). This result suggests that, seasonal differences in organic matter concentration and composition could also drive seasonal changes in V concentration, and therefore mobility and eventual flux to the coastal ocean.

In addition to the seasonal variations in meteoric V supply, non-conservative addition of V occurred within the STE itself. Although higher V concentrations occurred in summer, greater non-conservative addition occurred during winter in both years (shown in seasonal transects and MT anomalies; **Figures 4C**,**5C**).

Reduced V can sorb to hydrous metal oxides (Wehrli and Stumm 1989), and V was correlated with dissolved Fe in both winters (**Figure 6C**) at MT (**Figure 7C**). This is consistent with V release during the dissolution of Fe oxides, which occurs just up-gradient of the MT profile (O'Connor et al., 2018). These results suggest that the magnitude of the STE as a V source to the ocean depends on both organic matter source and seasonal redox dynamics.

The primary source of high V in the Gloucester Point STE may be local environmental factors. In inland groundwaters, V tends to be highest in aquifers composed of mafic and ultramafic rocks (Aiuppa et al., 2003; Wright and Belitz 2010; Luengo-Oroz et al., 2014). Sediments in the Chesapeake Bay region are rich in mafic and ultramafic minerals such as ilmenite, epidote, and staurolite (Firek et al., 1977; Darby 1984; Carpenter and Carpenter 1991). Additionally, fossil fuels can contribute to increased V concentrations in the environment (Andrade et al., 2004; Fiedler et al., 2008; Moreno et al., 2011), and coal burning emissions are a major source of contamination to sediments in the Chesapeake Bay region (Dickhut et al., 2000).

4.4 Chromium

Cr (like V) is enriched in minerals associated with mafic and ultramafic rock and in fossil fuels Robles-Camacho and Armienta, 2000 and Oze et al., 2007, which may provide the source of high Cr concentrations in fresh groundwater observed at the Gloucester Point STE. Cr concentrations were highest in a mid-depth maximum originating from shallow fresh groundwater (**Figure 1D**) and in the shallow freshwater endmember (**Table 1**). A similar distribution was observed in a tidal flat by Beck et al. (2008). The presence of dissolved Cr under reducing conditions is unusual given that soluble Cr(VI) is readily reduced to insoluble Cr(III) by Fe(II) (Eary and Rai 1989), organic matter (Bartlett and Kimble, 1976), and sulfide (Smillie et al., 1981), all of which are abundant in the Gloucester Point STE. Additionally, previous equilibrium calculations predict that Cr is reduced and therefore highly particle reactive throughout the STE (O'Connor et al., 2015). Beck et al. (2008) found a correlation between DOC and Cr and proposed that complexation with organic matter kept reduced Cr in solution (Bartlett and James 1983).

The multiple linear regression models for Cr offer more details regarding Cr complexation in the STE. At MT, Cr was correlated with DOC, supporting the hypothesis that complexation with organic matter can solubilize Cr in the STE. At MT, Cr was correlated with either humic carbon (in 2013) or Fe (in 2014) along with DOC (**Figure 7D**). In groundwater, colloids (small particles made up of aluminosilicate, iron (hydr)oxide, and organic components; Buffle et al., 1998) can enhance the transport of particle-reactive metals (Sanudo-Wilhelmy et al., 2002; De Jonge et al., 2004; Kim and Kim 2015). The correlation of Cr with both organic material and Fe at HT and MT suggested either that both Fe and Cr are present in organic complexes (Boggs et al., 1985), or that Cr is bound to mixed organic/inorganic colloidal material. However, Fe was the exclusive and strongest predictor at LT (**Figure 7D**). Colloids based on solid iron oxide material, rather than organic matter, are mobilized at oxic/anoxic interfaces and can transport metals (Pokrovsky and Schott 2002; Hassellov and von der Kammer 2008). As a result, the occurrence of sharp redox interfaces in the STE, including reductive dissolution of Fe oxides (O'Connor et al., 2015), may mobilize Fe-based colloids. This mobilization of Fe colloids may result in a shift from DOC- to Fe-mediated Cr transport moving seaward and shows that colloidal iron may play an important role for metal transport in addition to colloidal organic matter.

Unlike the other redox-active metals in this study, Cr showed interannual, rather that seasonal, variability in concentration. Interannual differences in the association of Cr with DOC, humic carbon, and Fe (**Figure 6D**) may have also contributed to interannual variability in groundwater Cr concentrations. Along with DOC, humic carbon predicted Cr concentrations in 2013, whereas Fe was the significant predictor in 2014, indicating a change in the composition of the material to which Cr was bound. A shift in composition could change binding constants or Cr solubility, resulting in increased concentrations. However, interannual variability was not observed for V. Compared with V, Cr was more strongly associated with the hDOM pool (**Figure 3D**), suggesting that distinct pools of dissolved organic matter complex V and Cr, which may account for differences in seasonal and interannual variability.

Despite not showing differences in concentration with season, Cr showed seasonally dependent non-conservative addition (**Figures 4D**,**5D**). Similar to V, non-conservative addition of Cr was greater in the winter. Because Cr species can sorb to reactive metal (hydr)oxide surfaces, this addition may be due to release upon reductive dissolution of Fe oxides, which is greater in winter in this STE (O'Connor et al., 2018).

5 CONCLUSION

Despite having similar chemical properties, Mo, U, V, and Cr behave differently in the STE due to differences in their sources within the STE and distinct biogeochemical properties. These differences cause seasonal variations in the concentrations and distributions of these elements in coastal groundwater at this study site.

Dissolved Mo and U were supplied to the STE by estuarine surface water and showed non-conservative removal when oxic surface water mixed into the reducing portions of the shallow STE. Molybdenum was removed by reaction with sulfide, but sulfide concentrations at this site were sufficiently high (i.e., in great excess of the 10 μM required to quantitatively react with Mo) that seasonal trends in removal were not evident. In contrast, U removal appeared linked to the activity of sulfate/sulfur-reducing bacteria and showed greater removal during summer (when temperatures are warmer and microbial metabolic rates are higher).

Both V and Cr were primarily supplied to the STE by meteoric groundwater and showed non-conservative addition within the STE. Minerals common to sediments in the region are enriched in V and Cr and were the most likely source of these elements to local groundwater. The mobility of V and Cr within the STE, and

therefore their supply to the coastal ocean, was controlled by association/complexation with groundwater organic matter and Fe-rich colloids. Complexation with different organic matter pools may have led to seasonal variability in the distribution of V, but greater interannual variability of Cr.

Results from this study emphasize the importance of seasonality on biogeochemical cycling in the STE. Although the broader redox structure of the shallow STE was stable over this 2-year study, the magnitude of its source/sink functions changed in predictable ways. For example, studying metals cycling at a seasonal scale revealed greater U removal in summer, which could lead to an overestimation of the STE as a U sink. By simultaneously measuring trace metal concentrations and major redox constituents, seasonal variability in V and Cr concentrations was observed, and these changes could be explained by concomitant variability in DOC and Fe. This result also illustrates that easily measured major redox species such as organic carbon and Fe, which vary seasonally in other STEs, can help explain and even predict the behavior of redox-active trace metals. Understanding these seasonal changes in the distribution of RSMs within the STE can contribute to more accurate estimates of regional or global SGD-driven fluxes of heavy metals.

DATA AVAILABILITY STATEMENT

The original contributions presented in the study are included in the article/**Supplementary Material**, further inquiries can be directed to the corresponding author.

AUTHOR CONTRIBUTIONS

AO and AB contributed to the conception, design, and execution of this study. AO performed the statistical analysis. All authors contributed to manuscript preparation and revision, read, and approved the submitted version.

FUNDING

This work was supported by the National Science Foundation Graduate Research Fellowship Program (grant no: DGE-1444317) and the Virginia Institute of Marine Science.

ACKNOWLEDGMENTS

The authors would like to thank Julie Krask, Leah Fitchett, and Michele Cochran for their invaluable help in the field and laboratory, and Alan Shiller for sample analyses. This article is Contribution 4069 of the Virginia Institute of Marine Science, William and Mary.

SUPPLEMENTARY MATERIAL

The Supplementary Material for this article can be found online at: https://www.frontiersin.org/articles/10.3389/fenvs.2021.613191/full#supplementary-material

REFERENCES

Aiuppa, A., Bellomo, S., Brusca, L., D'Alessandro, W., and Federico, C. (2003). Natural and Anthropogenic Factors Affecting Groundwater Quality of an Active Volcano (Mt. Etna, Italy). *Appl. Geochem.* 18, 863–882. doi:10.1016/s0883-2927(02)00182-8

Algeo, T. J., Morford, J., and Cruse, A. (2012). Reprint of: New Applications of Trace Metals as Proxies in Marine Paleoenvironments. *Chem. Geology.* 324-325, 1–5. doi:10.1016/j.chemgeo.2012.07.012

Andrade, L., Marcet, P., Fernández-Feal, L., Fernández-Feal, C., Covelo, E., and Vega, F. (2004). Impact of the Prestige Oil Spill on Marsh Soils: Relationship between Heavy Metal, Sulfide and Total Petroleum Hydrocarbon Contents at the Villarrube and Lires Marshes (Galicia, Spain). *Cienc. Mar.* 30, 477–487. doi:10.7773/cm.v30i3.281

Anschutz, P., Dedieu, K., Desmazes, F., and Chaillou, G. (2005). Speciation, Oxidation State, and Reactivity of Particulate Manganese in marine Sediments. *Chem. Geol.* 218, 265–279. doi:10.1016/j.chemgeo.2005.01.008

Anschutz, P., Smith, T., Mouret, A., Deborde, J., Bujan, S., Poirier, D., et al. (2009). Tidal Sands as Biogeochemical Reactors. *Estuar. Coast. Shelf Sci.* 84, 84–90. doi:10.1016/j.ecss.2009.06.015

Archer, C., and Vance, D. (2008). The Isotopic Signature of the Global Riverine Molybdenum Flux and Anoxia in the Ancient Oceans. *Nat. Geosci.* 1, 597–600. doi:10.1038/ngeo282

Barnes, C. E., and Cochran, J. K. (1993). Uranium Geochemistry in Estuarine Sediments: Controls on Removal and Release Processes. *Geochim. Cosmochim. Acta* 57, 555–569. doi:10.1016/0016-7037(93)90367-6

Bartlett, R. J., and Kimble, J. M. (1976). Behavior of Chromium in Soils: II. Hexavalent Forms. *J. Environ. Quality* 5, 383–386. doi:10.2134/jeq1976.00472425000500040010x

Bartlett, R. J., and James, B. (1983). Behavior of Chromium in Soils: V. Fate of Organically Complexed Cr(III) Added to Soil. *J. Environ. Qual.* 12, 169–172. doi:10.2134/jeq1983.00472425001200020003x

Beck, A. J., Tsukamoto, Y., Tovar-Sanchez, A., Huerta-Diaz, M., Bokuniewicz, H. J., and Sañudo-Wilhelmy, S. A. (2007). Importance of Geochemical Transformations in Determining Submarine Groundwater Discharge-Derived Trace Metal and Nutrient Fluxes. *Appl. Geochem.* 22, 477–490. doi:10.1016/j.apgeochem.2006.10.005

Beck, M., Dellwig, O., Schnetger, B., and Brumsack, H-J. (2008). Cycling of Trace Metals (Mn, Fe, Mo, U, V, Cr) in Deep Pore Waters of Intertidal Flat Sediments. *Geochim. Cosmochim. Acta* 72 (12), 2822–2840. doi:10.1016/j.gca.2008.04.013

Beck, A. J., Cochran, J. K., and Sañudo-Wilhelmy, S. A. (2009). Temporal Trends of Dissolved Trace Metals in Jamaica Bay, NY: Importance of Wastewater Input and Submarine Groundwater Discharge in an Urban Estuary. *Estuaries Coasts* 32, 535–550. doi:10.1007/s12237-009-9140-5

Beck, A. J., Cochran, J. K., and Sañudo-Wilhelmy, S. A. (2010). The Distribution and Speciation of Dissolved Trace Metals in a Shallow Subterranean Estuary. *Mar. Chem.* 121, 145–156. doi:10.1016/j.marchem.2010.04.003

Beck, A. J., Kellum, A. A., Luek, J. L., and Cochran, M. A. (2016). Chemical Flux Associated with Spatially and Temporally Variable Submarine Groundwater Discharge, and Chemical Modification in the Subterranean Estuary at Gloucester Point, VA (USA). *Estuaries Coasts* 39, 1–12. doi:10.1007/s12237-015-9972-0

Behrends, T., and Van Cappellen, P. (2005). Competition between Enzymatic and Abiotic Reduction of Uranium(VI) under Iron Reducing Conditions. *Chem. Geol.* 220, 315–327. doi:10.1016/j.chemgeo.2005.04.007

Boggs, S., Jr, Livermore, D., and Seitz, M. G. (1985). *Humic Substances in Natural Waters and Their Complexation with Trace Metals and Radionuclides: A Review*. IL (USA): Argonne National Lab.

Bruland, K. W., and Lohan, M. C. (2006). "Controls of Trace Metals in Seawater," in *The Oceans and Marine Geochemistry*. Editors H. D. Hollands, K. K. Turekian, and H. Elderfield (Oxford: Elsevier), 23–47.

Brumsack, H. J., and Gieskes, J. M. (1983). Interstitial Water Trace-Metal Chemistry of Laminated Sediments from the Gulf of California, Mexico. *Mar. Chem.* 14, 89–106. doi:10.1016/0304-4203(83)90072-5

Buffle, J., Wilkinson, K., Stoll, S., Filella, M., and Zhang, J. (1998). A generalized Description of Aquatic Colloidal Interactions: The Three-Colloidal Component Approach. *Environ. Sci. Technol.* 32, 2887–2899. doi:10.1021/es980217h

Burnett, W. C., Bokuniewicz, H., Huettel, M., Moore, W. S., and Taniguchi, M. (2003). Groundwater and Pore Water Inputs to the Coastal Zone. *Biogeochem* 66, 3–33. doi:10.1023/b:biog.0000006066.21240.53

Burnett, W. C., Peterson, R., Moore, W. S., and de Oliveira, J. (2008). Radon and Radium Isotopes as Tracers of Submarine Groundwater Discharge - Results From the Ubatuba, Brazil SGD Assessment Intercomparison. *Estuar. Coast. Shelf Sci.* 76, 501–511. doi:10.1016/j.ecss.2007.07.027

Cable, J. E., Burnett, W. C., Chanton, J. P., and Weatherly, G. L. (1996). Estimating Groundwater Discharge into the Northeastern Gulf of Mexico Using Radon-222. *Earth Planet. Sci. Lett.* 144, 591–604. doi:10.1016/S0012-821X(96)00173-2

Carpenter, R. G., and Carpenter, S. F. (1991). Heavy mineral Deposits in the Upper Coastal plain of North Carolina and Virginia. *Econ. Geol.* 86, 1657–1671. doi:10.2113/gsecongeo.86.8.1657

Charette, M. A., and Sholkovitz, E. R. (2006). Trace Element Cycling in a Subterranean Estuary: Part 2. Geochemistry of the Pore Water. *Geochim. Cosmochim. Acta* 70, 811–826. doi:10.1016/j.gca.2005.10.019

Charette, M. A., Sholkovitz, E. R., and Hansel, C. M. (2005). Trace Element Cycling in a Subterranean Estuary: Part 1. Geochemistry of the Permeable Sediments. *Geochim. Cosmochim. Acta* 69, 2095–2109. doi:10.1016/j.gca.2004.10.024

Darby, D. A. (1984). Trace Elements in Ilmenite: A Way to Discriminate Provenance or Age in Coastal Sands. *Geol. Soc. Am. Bull.* 95, 1208–1218. doi:10.1130/0016-7606(1984)95<1208:teiiaw>2.0.co;2

de Jonge, L. W., Klaergaard, C., and Moldrup, P. (2004). Colloids and Colloid Facilitated Transport of Contaminants in Soils: An Introduction. *Vadose Zo. J.* 3, 321–325. doi:10.2136/vzj2004.0321

Dickhut, R. M., Canuel, E. A., Gustafson, K. E., Liu, K., Arzayus, K. M., Walker, S. E., et al. (2000). Automotive Sources of Carcinogenic Polycyclic Aromatic Hydrocarbons Associated with Particulate Matter in the Chesapeake Bay Region. *Environ. Sci. Technol.* 34, 4635–4640. doi:10.1021/es000971e

Duncan, T., and Shaw, T. J. (2003). The Mobility of Rare Earth Elements and Redox Sensitive Elements in the Groundwater/Seawater Mixing Zone of a Shallow Coastal Aquifer. *Aquat. Geochem.* 9, 233–255. doi:10.1023/b:aqua.0000022956.20338.26

Eary, L. E., and Rai, D. (1989). Kinetics of Chromate Reduction by Ferrous Ions Derived from Hematite and Biotite at 25°C. *Am. J. Sci.* 289, 180–213.

Erickson, B. E., and Helz, G. R. (2000). Molybdenum (VI) Speciation in Sulfidic Waters: Stability and Lability of Thiomolybdates. *Geochim. Cosmochim. Acta* 64, 1149–1158. doi:10.1016/s0016-7037(99)00423-8

Fiedler, S., Siebe, C., Herre, a., Roth, B., Cram, S., and Stahr, K. (2008). Contribution of Oil Industry Activities to Environmental Loads of Heavy Metals in the Tabasco Lowlands, Mexico. *Water Air Soil Pollut.* 197, 35–47. doi:10.1007/s11270-008-9789-6

Firek, F., Shideler, G. L., and Fleischer, P. (1977). Heavy-Mineral Variability in Bottom Sediments of the Lower Chesapeake Bay, VA. *Mar. Geol.* 23, 217–235. doi:10.1016/0025-3227(77)90020-2

Fredrickson, J. K., Zachara, J. M., Kennedy, D. W., Duff, M. C., Gorby, Y. A., Li, S.-M. W., et al. (2000). Reduction of U(VI) in Goethite (Alpha-FeOOH) Suspensions by a Dissimilatory Metal-Reducing Bacterium. *Geochim. Cosmochim. Acta* 64, 3085–3098. doi:10.1016/s0016-7037(00)00397-5

Ganesh, R., Robinson, K. G., Reed, G. D., and Sayler, G. S. (1997). Reduction of Hexavalent Uranium from Organic Complexes by Sulfate- and Iron-Reducing Bacteria. *Appl. Environ. Microbiol.* 63, 4385–4391. doi:10.1128/aem.63.11.4385-4391.1997

Ganesh, R., Robinson, K. G., Chu, L., Kucsmas, D., and Reed, G. D. (1999). Reductive Precipitation of Uranium by Desulfovibri Desulfuricans: Evaluation of Co-contaminant Effects and Selective Removal. *Wat. Res.* 33, 3447–3458. doi:10.1016/s0043-1354(99)00024-x

Gonneea, M. E., Mulligan, A. E., and Charette, M. A. (2013). Seasonal Cycles in Radium and Barium within a Subterranean Estuary: Implications for Groundwater Derived Chemical Fluxes to Surface Waters. *Geochim. Cosmochim. Acta* 119, 164–177. doi:10.1016/j.gca.2013.05.034

Hassellov, M., and von der Kammer, F. (2008). Iron Oxides as Geochemical Nanovectors for Metal Transport in Soil-River Systems. *Elements* 4, 401–406. doi:10.2113/gselements.4.6.401

Helz, G. R., Miller, C. V., Charnock, J. M., Mosselmans, J. F. W., Pattrick, R. A. D., Garner, C. D., et al. (1996). Mechanism of Molybdenum Removal from the Sea and its Concentration in Black Shales: EXAFS Evidence. *Geochim. Cosmochim. Acta* 60, 3631–3642. doi:10.1016/0016-7037(96)00195-0

Hua, B., Xu, H., Terry, J., and Deng, B. (2006). Kinetics of Uranium(VI) Reduction by Hydrogen Sulfide in Anoxic Aqueous Systems. *Environ. Sci. Technol.* 40, 4666–4671. doi:10.1021/es051804n

Huerta-Diaz, M. A., and Morse, J. W. (1992). Pyritization of Trace Metals in Anoxic marine Sediments. *Mar. Chem.* 29, 119–144. doi:10.1016/0016-7037(92)90353-k

Hyacinthe, C., Bonneville, S., and Van Cappellen, P. (2006). Reactive Iron(III) in Sediments: Chemical versus Microbial Extractions. *Geochim. Cosmochim. Acta* 70, 4166–4180. doi:10.1016/j.gca.2006.05.018

James, G., Witten, D., Hastie, T., and Tibshirani, R. (2014). *An Introduction to Statistical Learning: With Applications in R*. New York: Springer Publishing Company, Incorporated.

Kim, I., and Kim, G. (2015). Role of Colloids in the Discharge of Trace Elements and Rare Earth Elements from Coastal Groundwater to the Ocean. *Mar. Chem.* 176, 126–132. doi:10.1016/j.marchem.2015.08.009

Klinkhammer, G. P., and Palmer, M. R. (1991). Uranium in the Oceans: Where it Goes and Why. *Geochim. Cosmochim. Acta* 55, 1799–1806. doi:10.1016/0016-7037(91)90024-y

Lemaire, E., Blanc, G., Coynel, A., and Etcheber, H. (2006). Dissolved Trace Metal – Organic Complexes in the Lot – Garonne River System Determined Using the C18 Sep-Pak System. *Aquat. Geochem.* 12, 21–38. doi:10.1007/s10498-005-0908-3

Lovley, D. R., and Phillips, E. J. P. (1992). Reduction of Uranium by Desulfovibrio Desulfuricans. *Appl. Environ. Microbiol.* 58, 850–856. doi:10.1128/aem.58.3.850-856.1992

Lovley, D. R., Phillips, E. J. P., Gorby, Y. A., and Landa, E. R. (1991). Microbial Reduction of Uranium. *Nature* 350, 413–416. doi:10.1038/350413a0

Lovley, D. R., Widman, P. K., Woodward, J. C., and Phillips, E. J. (1993). Reduction of Uranium by Cytochrome C3 of Desulfovibrio Vulgaris. *Appl. Environ. Microbiol.* 59, 3572–3576. doi:10.1128/aem.59.11.3572-3576.1993

Luek, J. L., and Beck, A. J. (2014). Radium Budget of the York River Estuary (VA, USA) Dominated by Submarine Groundwater Discharge with a Seasonally Variable Groundwater End-Member. *Mar. Chem.* 165, 55–65. doi:10.1016/j.marchem.2014.08.001

Luengo-Oroz, N., Bellomo, S., and D'Alessandro, W. (2014). "High Vanadium Concentrations in Groundwater at El Hierro (Canary Islands, Spain)," in 10th International Hydrogeological Congress, Thessalonik Greece, 8-10 October 2014, 427–435.

McAllister, S. M., Barnett, J. M., Heiss, J. W., Findlay, A. J., Macdonald, D. J., Dow, C. L., et al. (2015). Dynamic Hydrologic and Biogeochemical Processes Drive Microbially Enhanced Iron and Sulfur Cycling within the Intertidal Mixing Zone of a beach Aquifer. *Limnol. Oceanogr.* 60, 329–345. doi:10.1002/lno.10029

Moore, K. A., and Reay, W. G. (2009). CBNERRVA Research and Monitoring Program. *J. Coast. Res.* 57, 118–125. doi:10.2112/1551-5036-57.sp1.118

Moore, W. S. (1999). The Subterranean Estuary: a Reaction Zone of Ground Water and Sea Water. *Mar. Chem.* 65, 111–125. doi:10.1016/s0304-4203(99)00014-6

Moreno, R., Jover, L., Diez, C., and Sanpera, C. (2011). Seabird Feathers as Monitors of the Levels and Persistence of Heavy Metal Pollution after the Prestige Oil Spill. *Environ. Pollut.* 159, 2454–2460. doi:10.1016/j.envpol.2011.06.033

Morford, J. L., and Emerson, S. R. (1999). The Geochemistry of Redox Sensitive Trace Metals in Sediments. *Geochim. Cosmochim. Acta* 63, 1735–1750. doi:10.1016/s0016-7037(99)00126-x

Morford, J. L., Emerson, S. R., Breckel, E. J., and Kim, S. H. (2005). Diagenesis of Oxyanions (V, U, Re, and Mo) in Pore Waters and Sediments from a continental Margin. *Geochim. Cosmochim. Acta* 69, 5021–5032. doi:10.1016/j.gca.2005.05.015

Morford, J. L., Martin, W. R., François, R., and Carney, C. M. (2009). A Model for Uranium, Rhenium, and Molybdenum Diagenesis in marine Sediments Based on Results from Coastal Locations. *Geochim. Cosmochim. Acta* 73 (10), 2938–2960. doi:10.1016/j.gca.2009.02.029

Nameroff, T. J., Calvert, S. E., and Murray, J. W. (2004). Glacial-interglacial Variability in the Eastern Tropical North Pacific Oxygen Minimum Zone Recorded by Redox-Sensitive Trace Metals. *Paleoceanography* 19, 1–19. doi:10.1029/2003pa000912

O'Connor, A. E., Luek, J. L., McIntosh, H., and Beck, A. J. (2015). Geochemistry of Redox-Sensitive Trace Elements in a Shallow Subterranean Estuary. *Mar. Chem.* 172, 70–81. doi:10.1016/j.marchem.2015.03.001

O'Connor, A. E., Krask, J., Beck, A. J., and Canuel, E. (2018). Seasonality of Major Redox Constituents in a Shallow Subterranean Estuary. *Geochim. Cosmochim. Acta* 224, 344–361. doi:10.1016/j.gca.2017.10.013

Oze, C., Bird, D. K., and Fendorf, S. (2007). Genesis of Hexavalent Chromium from Natural Sources in Soil and Groundwater. *PNAS* 104, 6544–6549. doi:10.1073/pnas.0701085104

Pokrovsky, O., and Schott, J. (2002). Iron Colloids/organic Matter Associated Transport of Major and Trace Elements in Small Boreal Rivers and Their Estuaries (NW Russia). *Chem. Geol.* 190, 141–179. doi:10.1016/s0009-2541(02)00115-8

Pourret, O., Dia, A., Gruau, G., Davranche, M., and Bouhnik-Le Coz, M. (2012). Assessment of Vanadium Distribution in Shallow Groundwaters. *Chem. Geol.* 294–295, 89–102. doi:10.1016/j.chemgeo.2011.11.033

R Core Team (2015). *R: A Language and Environment for Statistical Computing*. Vienna, Austria: R Foundation for Statistical Computing. URL: https://www.R-project.org/.

Rai, D., Eary, L. E., and Zachara, J. M. (1989). Environmental Chemistry of Chromium. *Sci. Total Environ.* 86, 15–23. doi:10.1016/0048-9697(89)90189-7

Remoundaki, E., Hatzikioseyian, A., and Tsezos, M. (2007). A Systematic Study of Chromium Solubility in the Presence of Organic Matter: Consequences for the Treatment of Chromium-Containing Wastewater. *J. Chem. Technol. Biotechnol.* 82, 802–808. doi:10.1002/jctb.1742

Reckhardt, A., Beck, M., Greskowiak, J., Schnetger, B., Böttcher, M. E., Gehre, M., et al. (2017). Cycling of Redox-Sensitive Elements in a Sandy Subterranean Estuary of the Southern North Sea. *Mar. Chem.* 188, 6–17. doi:10.1016/j.marchem.2016.11.003

Riedel, T., Lettmann, K., Schnetger, B., Beck, M., and Brumsack, H.-J. (2011). Rates of Trace Metal and Nutrient Diagenesis in an Intertidal Creek Bank. *Geochim. Cosmochim. Acta* 75, 134–147. doi:10.1016/j.gca.2010.09.040

Rimmer, S. M., Thompson, J. a., Goodnight, S. a., and Robl, T. L. (2004). Multiple Controls on the Preservation of Organic Matter in Devonian–Mississippian marine Black Shales: Geochemical and Petrographic Evidence. *Palaeogeogr. Palaeoclimatol. Palaeoecol.* 215, 125–154. doi:10.1016/s0031-0182(04)00466-3

Robles-Camacho, J., and Armienta, M. A. (2000). Natural Chromium Contamination of Groundwater at Leon Valley, Mexico. *J. Geochemical Explor.* 68, 167–181. doi:10.1016/s0375-6742(99)00083-7

Santos, I. R., Burnett, W. C., Dittmar, T., Suryaputra, I. G. N. A., and Chanton, J. (2009). Tidal Pumping Drives Nutrient and Dissolved Organic Matter Dynamics in a Gulf of Mexico Subterranean Estuary. *Geochim. Cosmochim. Acta* 73, 1325–1339. doi:10.1016/j.gca.2008.11.029

Santos, I. R., Burnett, W. C., Misra, S., Suryaputra, I. G. N. A., Chanton, J. P., Dittmar, T., et al. (2011). Uranium and Barium Cycling in a Salt Wedge Subterranean Estuary: The Influence of Tidal Pumping. *Chem. Geol.* 287, 114–123. doi:10.1016/j.chemgeo.2011.06.005

Sañudo-Wilhelmy, S. A., Rossi, F. K., Bokuniewicz, H., and Paulsen, R. J. (2002). Trace Metal Levels in Uncontaminated Groundwater of a Coastal Watershed: Importance of Colloidal Forms. *Environ. Sci. Technol.* 36, 1435–1441. doi:10.1021/es0109545

Scholz, F., Hensen, C., Noffke, A., Rohde, A., Liebetrau, V., and Wallmann, K. (2011). Early Diagenesis of Redox-Sensitive Trace Metals in the Peru Upwelling Area – Response to ENSO-Related Oxygen Fluctuations in the Water Column. *Geochim. Cosmochim. Acta* 75, 7257–7276. doi:10.1016/j.gca.2011.08.007

Shimmield, G., and Price, N. (1986). The Behaviour of Molybdenum and Manganese during Early Sediment Diagenesis — Offshore Baja California, Mexico. *Mar. Chem.* 19, 261–280. doi:10.1016/0304-4203(86)90027-7

Siebert, C., Nägler, T. F., von Blanckenburg, F., and Kramers, J. D. (2003). Molybdenum Isotope Records as a Potential New Proxy for Paleoceanography. *Earth Planet. Sci. Lett.* 211, 159–171. doi:10.1016/s0012-821x(03)00189-4

Slomp, C. P., and Van Cappellen, P. (2004). Nutrient Inputs to the Coastal Ocean through Submarine Groundwater Discharge: Controls and Potential Impact. *J. Hydrol.* 295, 64–86. doi:10.1016/j.jhydrol.2004.02.018

Smillie, R. H., Hunter, K., and Loutit, M. (1981). Reduction of Chromium(VI) by Bacterially Produced Hydrogen Sulphide in a marine Environment. *Water Res.* 15, 1351–1354. doi:10.1016/0043-1354(81)90007-5

Snyder, M., Taillefert, M., and Ruppel, C. (2004). Redox Zonation at the saline-influenced Boundaries of a Permeable Surficial Aquifer: Effects of Physical Forcing on the Biogeochemical Cycling of Iron and Manganese. *J. Hydrol.* 296, 164–178. doi:10.1016/j.jhydrol.2004.03.019

Spinelli, G. A., and Fisher, A. T. (2002). Groundwater Seepage into Northern San Francisco Bay: Implications for Dissolved Metals Budgets. *Water Resour. Res.* 38, 12-1–12-19. doi:10.1029/2001wr000827

Stolpe, B., Guo, L., Shiller, A. M., and Aiken, G. R. (2013). Abundance, Size Distributions and Trace-Element Binding of Organic and Iron-Rich Nanocolloids in Alaskan Rivers, as Revealed by Field-Flow Fractionation and ICP-MS. *Geochim. Cosmochim. Acta* 105, 221–239. doi:10.1016/j.gca.2012.11.018

Telfeyan, K., Johannesson, K. H., Mohajerin, T. J., and Palmore, C. D. (2015). Vanadium Geochemistry along Groundwater Flow Paths in Contrasting Aquifers of the United States: Carrizo Sand (Texas) and Oasis Valley (Nevada) Aquifers. *Chem. Geol.* 410, 63–78. doi:10.1016/j.chemgeo.2015.05.024

Tessier, A., Campbell, P. G. C., and Bisson, M. (1979). Sequential Extraction Procedure for the Speciation of Particulate Trace Metals. *Anal. Chem.* 51, 844–851. doi:10.1021/ac50043a017

Tribovillard, N., Algeo, T. J., Lyons, T., and Riboulleau, A. (2006). Trace Metals as Paleoredox and Paleoproductivity Proxies: An Update. *Chem. Geol.* 232, 12–32. doi:10.1016/j.chemgeo.2006.02.012

Wanty, R. B., and Goldhaber, M. B. (1992). Thermodynamics and Kinetics of Reactions Involving Vanadium in Natural Systems: Accumulation of Vanadium in Sedimentary Rocks. *Geochim. Cosmochim. Acta* 56, 1471–1483. doi:10.1016/0016-7037(92)90217-7

Wehrli, B., and Stumm, W. (1989). Vanadyl in Natural Waters: Adsorption and Hydrolysis Promote Oxygenation. *Geochim. Cosmochim. Acta* 53, 69–77. doi:10.1016/0016-7037(89)90273-1

Windom, H., and Niencheski, F. (2003). Biogeochemical Processes in a Freshwater–Seawater Mixing Zone in Permeable Sediments along the Coast of Southern Brazil. *Mar. Chem.* 83, 121–130. doi:10.1016/s0304-4203(03)00106-3

Wright, M. T., and Belitz, K. (2010). Factors Controlling the Regional Distribution of Vanadium in Groundwater. *Ground Water* 48, 515–525. doi:10.1111/j.1745-6584.2009.00666.x

Conflict of Interest: Author AO was employed by company Ramboll.

The remaining authors declare that the research was conducted in the absence of any commercial or financial relationships that could be construed as a potential conflict of interest.

Publisher's Note: All claims expressed in this article are solely those of the authors and do not necessarily represent those of their affiliated organizations, or those of the publisher, the editors and the reviewers. Any product that may be evaluated in this article, or claim that may be made by its manufacturer, is not guaranteed or endorsed by the publisher.

Copyright © 2022 O'Connor, Canuel and Beck. This is an open-access article distributed under the terms of the Creative Commons Attribution License (CC BY). The use, distribution or reproduction in other forums is permitted, provided the original author(s) and the copyright owner(s) are credited and that the original publication in this journal is cited, in accordance with accepted academic practice. No use, distribution or reproduction is permitted which does not comply with these terms.

frontiers in Environmental Science

REVIEW
published: 26 April 2021
doi: 10.3389/fenvs.2021.653568

The Beach Aquifer Microbiome: Research Gaps and Data Needs

Anand Archana[1]*, *Christopher A. Francis*[2] and *Alexandria B. Boehm*[1]

[1]Department of Civil and Environmental Engineering, Stanford University, Stanford, CA, United States, [2]Department of Earth System Science, Stanford University, Stanford, CA, United States

Beach aquifers, located in the subsurface of sandy beaches, are unique ecosystems with steep chemical and physical gradients resulting from the mixing of terrestrial fresh groundwater and saline groundwater from the sea. While work has rapidly progressed to understand the physics and chemistry in this environment, much less is known about the microorganisms present despite the fact that they are responsible for vital biogeochemical processes. This paper presents a review of the current state of knowledge of microbes within beach aquifers and the mechanisms that control the beach aquifer microbiome. We review literature describing the distribution and diversity of microorganisms in the freshwater-saltwater mixing zone of beach aquifers, and identify just 12 papers. We highlight knowledge gaps, as well as future research directions: The understanding of beach aquifer microorganisms is informed primarily by 16S ribosomal RNA gene sequences. Metagenomics and metatranscriptomics have not yet been applied but are promising approaches for elucidating key metabolic and ecological roles of microbes in this environment. Additionally, variability in field sampling and analytical methods restrict comparison of data across studies and geographic locations. Further, documented evidence on the migration of microbes within the beach aquifer is limited. Taking into account the physical transport of microbes through sand by flowing groundwater may be critical for understanding the structure and dynamics of microbial communities. Quantitative measurements of rates of elemental cycling in the context of microbial diversity need further investigation, in order to understand the roles of microbes in mediating biogeochemical fluxes from the beach aquifer to the coastal ocean. Lastly, understanding the current state of beach aquifers in regulating carbon stocks is critical to foster a better understanding of the contribution of the beach aquifer microbiome to global climate models.

Keywords: subterranean estuary, coastal aquifers, microbiome, sandy beach, groundwater, biogeochemistry

OPEN ACCESS

Edited by:
Carlos Rocha,
Trinity College Dublin, Ireland

Reviewed by:
Gwénaëlle Chaillou,
Université du Québecà Rimouski, Canada
Wenzhi Liu,
Chinese Academy of Sciences, China

***Correspondence:**
Anand Archana
archanaa@stanford.edu

Specialty section:
This article was submitted to Biogeochemical Dynamics, a section of the journal Frontiers in Environmental Science

Received: *14 January 2021*
Accepted: *08 April 2021*
Published: *26 April 2021*

Citation:
Archana A, Francis CA and Boehm AB (2021) The Beach Aquifer Microbiome: Research Gaps and Data Needs. Front. Environ. Sci. 9:653568. doi: 10.3389/fenvs.2021.653568

INTRODUCTION

Oceanic sandy beaches are dynamic environments teeming with life. Sandy beaches represent 31% of the world's unfrozen shoreline (Luijendijk et al., 2018) and are defined as shorelines consisting of permeable, sandy sediments (Charette et al., 2005). Serving as functional links between land and sea, sandy beaches provide numerous invaluable ecosystem services (Rocha, 2008), including coastal protection (Hanley et al., 2014), filtration and purification of water (Brown and McLachlan, 2002), nutrient mineralization (Schlacher et al., 2007), storage and discharge of submarine groundwater (Kim and Heiss, 2021), and the provision of nursery and nesting areas for fish and bird species

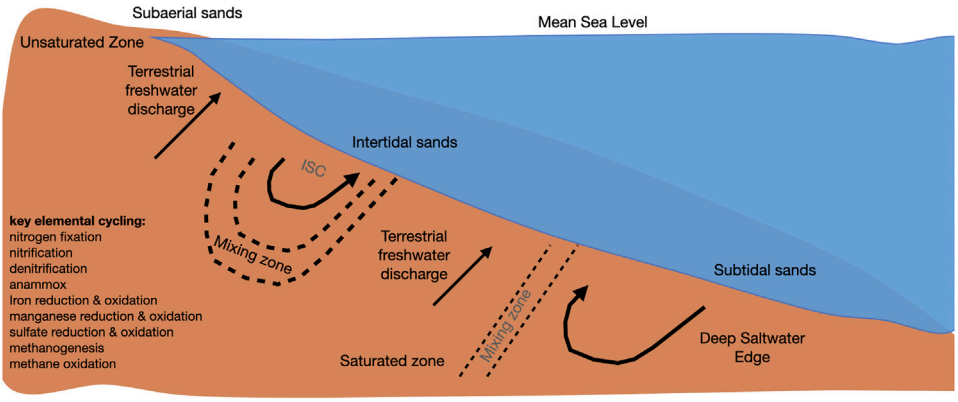


FIGURE 1 | Diagram of a beach aquifer. Adapted from Robinson et al., 2018 and Ruiz-González et al., 2021 (ISC: intertidal saltwater cell).

(Brown and McLachlan, 2002; Defeo et al., 2009). Beaches are also economically important (Hanley et al., 2014; Domínguez-Tejo et al., 2018) because they provide a place for recreation and fishing. In California, a location globally renowned for its beaches, revenue from beach-related tourism is estimated at $17.6 billion per year (Eastern Research Group, 2015).

During the past decade, interest in studying sandy beaches has increased (Dugan et al., 2010). One of the most rapidly progressing research areas at sandy beaches involves the study of beach aquifers (located in the subsurface of beaches) and submarine groundwater discharge from the beach aquifer to the sea (Robinson et al., 2018).

Characteristics of a Beach Aquifer

The beach aquifer is defined as the region below the surface of the sandy beach saturated with groundwater (**Figure 1**). Groundwater in the beach aquifer consists of land-derived freshwater and saline water of marine origin, and can be described by three distinct regions (Abarca et al., 2013): an intertidal saltwater cell (where seawater is flushed through the beach forced by waves and tides) (Robinson et al., 2006; Bakhtyar et al., 2012); an area of terrestrial freshwater (originating from the upland watershed) (Heiss et al., 2017); and a deep saltwater wedge (Heiss and Michael, 2014). The interface between the three water types is termed the subterranean estuary and has steep physical and chemical gradients, similar to a surface water estuary (Moore, 1999). Water that is discharged to the coastal ocean from the beach aquifer is referred to as submarine groundwater discharge (Robinson et al., 2018). Depending in part on the geomorphology of the beach, the relative spatial extents of the different regions in **Figure 1** will vary. For example, the presence of an impermeable layer in the beach aquifer could appreciably affect this conceptual model.

Beach Aquifers as Biogeochemical Reactors and Important Pathways to the Coastal Ocean

The mixing of freshwater and saltwater in beach aquifer was first described in detail in the landmark work by Lebbe (1981). The interplay between physical and chemical gradients set up by the mixing of seawater and freshwater influences the resultant precipitation of minerals in the beach aquifer (Robinson et al., 2018). Although early works have reviewed the physical characteristics of beach aquifers fairly extensively (Michael et al., 2005; Vandenbohede and Lebbe, 2006), in recent years, geochemical and microbial properties of beach aquifer systems are gaining attention (Kim and Heiss, 2021). Physical characteristics such as terrestrial freshwater hydraulic gradients, waves and tidal inputs of seawater, and general geometry of the region influence the mixing of seawater and freshwater within the beach aquifer (Robinson et al., 2007; Beck et al., 2011; Abarca et al., 2013; Kim and Heiss, 2021). Among chemical characteristics within the beach aquifer (Charette and Sholkovitz, 2002; Charette et al., 2005; McAllister et al., 2015), land-derived freshwater can contribute elevated concentrations of nitrate, phosphate, dissolved silica and organic carbon (Abarca et al., 2013; Kim and Heiss, 2021); on the other hand, infiltrating seawater contributes oxygen, salt, sulfate, and organic matter (Kim and Heiss, 2021). The existence of physical and chemical gradients has been documented in several beaches around the world (Santoro et al., 2008; Beck et al., 2011; Robinson et al., 2018).

Within the beach aquifer, microbially mediated biogeochemical processes break down organic matter (Ahrens et al., 2020) thereby changing the oxidation state and form of nutrients (Santoro et al., 2006; Bone et al., 2007; Kroeger and Charette, 2008; McAllister et al., 2015), trace metals (Charette and Sholkovitz, 2002; Charette et al., 2005), carbon (Dorsett et al., 2011) and oxygen (Heiss et al., 2017). In fact, a wide range of biogeochemical reactions has been documented within beach aquifers (Heiss et al., 2017), including but not limited to nitrification (Ullman et al., 2003), denitrification (Santoro, 2010; Wegner et al., 2018), anammox (Slomp and Van Cappellen, 2004; Kroeger and Charette, 2008; Sáenz et al., 2012), iron oxidation-reduction (Charette and Sholkovitz, 2002; Beck et al., 2011; McAllister et al., 2015), manganese oxidation-reduction (Ahrens et al., 2020), sulfate oxidation-reduction (McAllister et al., 2015), organic carbon degradation



FIGURE 2 | Geographic locations of globally sampled beach aquifers. Note - some dots overlap with others (Sources: Santoro et al., 2006; Santoro et al., 2008; McAllister et al., 2015; Ye et al., 2016; Lee et al., 2017; Adyasari et al., 2019; Chen et al., 2019; Jiang et al., 2020; Chen et al., 2020; Adyasari et al., 2020; Degenhardt et al., 2020, Hong et al., 2019).

(Kroeger and Charette, 2008; Sirois et al., 2018), and methanogenesis (Adyasari et al., 2020). Therefore, the beach aquifer can essentially be viewed as a "biogeochemical reactor" (Anschutz et al., 2009) where mixing of freshwater and saltwater has dramatic effects on microbial elemental cycling (Kroeger and Charette, 2008).

Work to date suggests that the above mentioned biogeochemical processes may modulate the flux of chemicals to the coastal ocean (Boehm et al., 2006; Santos et al., 2009; Kim et al., 2012; Santos et al., 2014; Yang et al., 2015; Robinson et al., 2018; Welch et al., 2019; McKenzie et al., 2020) when coupled to the inflow and outflow of groundwater to and from the beach aquifer as well as oceanic forcing (Kim and Heiss, 2021). Indeed some field studies demonstrate elemental fluxes from submarine groundwater discharge of beach aquifers that are on par with those from large nearby river systems (Moore, 2010).

While it is understood that microbes play a role in these various processes in the beach aquifer, there is a paucity of studies describing the distribution, diversity, and function of microbes there. Further, recent work has highlighted the importance of the interplay of physical and chemical processes in controlling the distribution and transformation of chemicals in the beach aquifer, and their flux to the coastal ocean (Robinson et al., 2018), but similar work exploring the added (and critical) role of microbes is scarce. Therefore, the goal of this study is to review the literature on microbes in the beach aquifer to identify knowledge gaps and future research directions. While this paper was in review, a complementary review by Ruiz-González et al. (2021) on the microbial dimension of submarine groundwater discharge was published.

LITERATURE REVIEW

We conducted literature searches on 23rd December 2020 using the web-of-science search terms [(beach or subterranean estuary) and microorganisms] and [submarine groundwater and beach] to identify published studies that have investigated the beach microbiome, and we also identified seemingly relevant references within those papers. Papers were included if they described the microorganisms in the beach aquifer. We excluded papers that were not specifically carried out in the aquifers of sandy beaches. Papers describing research in tidal flats, intertidal beach sands, subtidal sediments, or impermeable sediments were excluded, as they were not within the scope of this study.

We identified only 12 studies that have investigated the distribution, diversity, or function of microorganisms in the beach aquifer (**Figure 2**; **Table 1**). However, we identified a number of papers that examined microbial diversity in subtidal sands (sands consistently bathed in seawater at the bottom of the water column, yet not within the beach aquifer) and in intertidal sands (sands exposed to air at low tide and underwater at high tide, also not within the beach aquifer); we briefly review those papers here, due to their potential relevance to the beach aquifer microbiome given the close proximities of these environments and similar physical characteristics.

In subtidal sands, researchers have identified a diverse group of bacteria capable of many potential metabolic functions (Urakawa et al., 2000; Rusch et al., 2003; Hunter et al., 2006; Sørensen et al., 2007; Mills et al., 2008; Böer et al., 2009; Gaidos et al., 2011; Gobet et al., 2012). They show that despite their low carbon content, subtidal sands could harbor a diverse and robust microbiome. Beck et al. (2011) documented microbial abundance and metabolic rates in sediment cores in a tidal flat to contrast paleo-environmental imprints and modern-day processes.

In intertidal sands, a few studies have characterized the diversity of microbes associated with several potential metabolic functions, as well as potential human pathogens (Yamahara et al., 2007; Cui et al., 2013; Staley and Sadowsky, 2016; Romão et al., 2017). In these studies, the intertidal sands

TABLE 1 | Summary of findings on microbial communities in beach aquifers.

Source	Study site	Main findings	Sample type	Method
Hong et al. (2019)	Gloucester point, VA, United States	1) aerobic-anaerobic transition zone (AATZ) had the highest diversity of microbes 2) AATZ was a hotspot for biogeochemical processes in the subterranean estuary (STE)	Sediment core (100 cm in length), groundwater samples (between 25 cm and 100 cm below surface of sand, adjacent to sediment core)	Target:V4 16S rRNA-based illumina MiSeq sequencing
Jiang et al. (2020)	Beach in sanggou bay national	1) active carbon turnover in the STE 2) seasonality affects microbial activity that stimulates DOC production and removal 3) porewater flow rate influences DOC production and removal by microbes 4) heterotrophic species abundance accelerates carbon transformation rates (in higher temperatures)	Sediment core (22 cm in length), porewater samples (between 0 cm and 20 cm below surface of sand, adjacent to sediment core)	Target: V4-V5 16S rRNA-based illumina MiSeq sequencing — —
Degenhardt et al. (2020)	Spiekeroog island, Germany	1) No clear correlation of the microbial community composition with STE salinity gradients along a sandy high-energy beach 2) equilibrium state of microbial diversity down to a depth of 1 m defined as "core" community 3) prevalence of generalist microorganisms, adapted to quickly changing environmental conditions	Sediment core (100 cm in length), porewater samples (at 0 cm, 10 cm, 30 cm, 50 cm and 100 cm below surface of sand, adjacent to sediment core)	Target: V4-V5 16S rRNA-based illumina MiSeq sequencing —
Chen et al. (2020)	Shengsi island, China	1) diversity of dominant bacteria in coastal well water and porewater is different 2) main species present in sample types participate in the degradation of organic pollutants and utilization of nitrate in STEs	Well water, pore water (100 cm from surface)	Target: V4-V5 16S rRNA-based illumina MiSeq sequencing
Adyasari et al. (2020)	Mobile bay, gulf of Mexico	1) higher microbial diversity was found in the coastal pore water than the surface water samples 2) distinct archaeal communities dominated the peat-dominated and sandy-dominated SGD samples	Sediment core (150 cm from surface of sand), river water (from surface), inland groundwater (300 cm from surface), coastal pore water (2500 cm from surface), bay water (from surface)	Target: V4-V5 16S rRNA-based illumina MiSeq sequencing
Adyasari et al. (2019)	Jepara, Indonesia	1) microbial community composition varied with salinity 2) fecal indicators and potential pathogens were identified 3) microbial community composition varied with hydrology	Dug wells, pore water, seepage meters, river water, seawater (pore water and seepage meter samples were categorized as submarine groundwater discharge samples). All samples were collected with vertical profiles between 0 cm to 20 cm below surface of sand	Target: V4-V5 16S rRNA-based illumina MiSeq sequencing —
Chen et al. (2019)	Qinzhou bay, China	1) microbial community composition varied with size fraction 2) some key microbial groups from the two size fractions were utilized in the transformation of carbon, nutrients and iron 3) microbial communities have important roles in carbon, nitrogen and iron cycling in STEs	Well water (at 4 m depth below surface of sand)	Target: V4-V5 16S rRNA-based illumina MiSeq sequencing —
Lee et al. (2017)	Gongcheonpo beach, jeju island, korea	1) less diverse microbial groups were detected in seawater-dominated samples when compared with groundwater-dominated samples 2) significant relationships between environmental factors and microbial communities were observed 3) community composition varied significantly with tidal fluctuation	Coastal water samples, and black sand samples (collected according to tidal stage)	Target: V1-V3 16S rRNA gene-based pyrosequencing —

(Continued on following page)

TABLE 1 | (*Continued*) Summary of findings on microbial communities in beach aquifers.

Source	Study site	Main findings	Sample type	Method
Ye et al. (2016)	Yellow sea coast, China	1) less diverse bacterial groups were detected in well water samples when compared with those detected in pore water samples 2) well water samples were associated with bacterial communities that were involved in nitrate cycling, while brackish porewater samples were associated with microbes involved in ammonium cycling 3) bacterial communities were correlated with the salinity gradient 4) distinct bacterial communities were detected among different porewater samples	Pore water in unconsolidated deposits (15 m from surface of sand), bedrock fissure water (0.3–0.4 m from surface of sand), beach coarse sand pore water (0.5 m–1.5 m from surface of sand)	Target: V4-V5 16S rRNA-based illumina MiSeq sequencing — —
McAllister et al. (2015)	Cape shores, lewes, Delaware	1) microbial communities significantly influenced Fe and S mineralization 2) hydrological fluctuations affect the location of Fe & S mineralization	Porewater samples from long-term multilevel sampling wells (390 cm–3600 cm from surface of sand)	Target: V1-V3 SSU; 454 pyrosequencing
Santoro et al. (2006)	Huntington beach, California, United States	1) first study characterizing N-cycling functional genes and denitrifier community composition in the beach aquifer system 2) geochemistry (nitrate and salinity) plays an important role in shaping denitrifying bacterial communities 3) nonequilibrium state of coastal aquifers is likely playing a vital role in shaping the microbial community	5 cubic cm of sediment, pore water	Target: *nirK*, *nirS* ABI 3100 or ABI 3730 capillary sequencer (PE applied biosystems) —
Santoro et al. (2008)	Huntington beach, California, United States	1) pioneering study documenting the abundance and community composition of both AOA and AOB (and nitrification genes) in the beach aquifer 2) salinity appeared to be responsible for the shift from an AOA-dominated community at low-salinities to an AOB-dominated community at the most marine site 3) AOA diversity was high at all sites and time points, while AOB was extremely low	5 cubic cm of sediment, pore water	Target: Bacterial *amoA*, archaeal *amoA* ABI 3730XL capillary sequencer (PE applied biosystems) —

sampled were from a location where one might place a beach towel; many of these studies sought primarily to understand whether human pathogens are present in beach sands.

Below we summarize the 12 papers on microbial distribution, diversity, and function in the beach aquifer. Our summary is guided by the following questions 1) what do we know about the beach aquifer microbiome? 2) what are the biggest challenges for characterizing and reporting microbial communities and associated metabolisms in beach aquifers? and 3) which future research directions warrant attention?

WHAT DO WE KNOW ABOUT THE BEACH AQUIFER MICROBIOME?

Microbial Community Characteristics in the Beach Aquifer

Nine of the 12 studies investigated the microbial community using 16S rRNA amplicon sequencing (**Table 2**) and these studies found that *Proteobacteria* dominated all samples. *Chloroflexi* and *Bacteroidetes* were the next most dominant phyla. Other documented phyla were *Planctomycetes*, *Acidobacteria*, *Actinobacteria*, *Firmicutes*, and *Vernucomicrobia*. Within *Proteobacteria*, genus-level identification revealed members belonging to *Alphaproteobacteria*, *Betaproteobacteria* and *Gammaproteobacteria*, which varied in proportion among saline groundwater and brackish/fresh well water samples. Less commonly observed were genera belonging to *Epsilonproteobacteria* and *Zetaproteobacteria* (only noted in McAllister et al. (2015)). More commonly observed genera were *Sphingobium, Pseudoalternomonas, Flavobacterium, Limnohabitans, Rhodobacter, Aquiluna, Pseudomonas, Marinobacterium,* and *Nitrospira*. Although some genera were consistently observed globally, at the species-level, data were not provided in all the publications.

Four of the 12 studies characterized archaea in the beach aquifer. Santoro et al. (2008) characterized the archaeal community composition in a beach aquifer, focusing specifically on ammonia-oxidizing *Thaumarchaeota*. Other studies (Chen et al., 2019; Hong et al., 2019; Jiang et al., 2020) characterized the archaeal community composition in addition to the bacterial community composition using amplicon sequencing. Hong et al. (2019) documented *Crenarchaeota* (60%), *Euryarchaeota* (30%) as the dominant archaeal phyla

TABLE 2 | Summary of microbial communities in beach aquifers. The organisms listed were extracted from figures and tables provided in the original study, the lists include all the organisms in the study.

Study	Bacteria	Archaea	Taxonomic classification level
Hong et al. (2019)	*Proteobacteria, Chloroflexi, Planctomycetes, Bacteroidetes, Acidobacteria, Cyanobacteria, unclassified phyla*	*Crenarchaeota, Euryarchaeota, Parvarchaeota, and unclassified phyla*	Phylum
Jiang et al. (2020)	*Proteobacteria, Actinobacteria, Bacteroidetes, and Firmicutes*	—	Phylum
	Pseudoalteromona, Marinobacter, Colwellia, Sphingobium, Thioprofundum, Gp10, and Ilumatobacter	*Nitrosopumilus*	Genus
Degenhardt et al. (2020)	*Acidobacteria, Actinobacteria, Chloroflexi, Planctomycetes, Proteobacteria, Verrucomicrobia, Bacteroidetes, Latescibacteria, and Firmicutes*	—	Phylum
	Gillisia, Lewinella, Aquibacter, Sediminicola, Winogradskyella, Nitrospira, Fuerstia, Sulfurifustis, Persicirhabdus, Planococcus, Bacillus and Planomicrobium, and several unclassified genera	—	Genus
Chen et al. (2020)	*Gemmatimonadetes, Armatimonadia, Elusimicrobia, Cyanobacteria, SAR202_clade, Nitrospira, Acidobacteria, Planctomycetacia, Sphingobacteriia, deltaproteobacteria, cytophagia, Gammaproteobacteria, Flavobacteriia, Actinobacteria, Alphaproteobacteria, Betaproteobacteria*	—	Class
	Marivivens donghaensis, Pseudoalteromonas hodoensis, Pseudomonas pseudoalcaligenes, Acinetobacter populi, Pelagibacterium nitratireducens, Enterobacter tabaci, Flavobacterium jejuense, Erythrobacter citreus, Halomonas zhaodongensis, Vibrio toranzoniae, Acidovorax soil strain BL21, Rhodobacter ovatus, Novosphingobium naphthae	—	Species (OTUs with >98% similarity)
Adyasari et al. (2020)	*Acidimicrobiia, Actinobacteria, Alphaproteobacteria, Anaerolineae, Bacteroidia, Dehaloccoidia, Deltaproteobacteria, Gammaproteobacteria, Holophagae, Methanomicrobia, Oxyphotobacteria, Parcubacteria, Planctomycetacia, Thermodesulfovibrionia, Thermoleophilia, Verrucomicrobiae, unclassified*	—	Class
	Acinetobacter, Catenococcus, Cutibacterium, Cyanobium, Flavobacterium, Gaiellales, Massilia, Mesorhizobium, Methylobacter, Nocardioides, Pirellulaceae, *Polynucleobacter, Rheinheimera, Sphingomonas, Spirosoma, Turicella, Verrucomicrobium, Vogesella, unclassified*	—	Genus
Adyasari et al. (2019)	*Gammaproteobacteria, Alphaproteobacteria, Bacteroidia, Oxyphotobacteria, Actinobacteria*	—	Class
	Burkholderiaceae, *Novosphingobium, Limnohabitans, Pseudarcicella, Sediminibacterium, Methylomonas,* Methylomonaceae, *Flavobacterium, Marivivens, Acidovorax, Synechococcus, Marinobacterium, Halomonas*	—	Genus
Chen et al. (2019)	*Limnohabitans, Gallionella, Terrimonas, Perlucidibaca, Ferruginibacter, Sphingobium, Polynucleobacter, Pseudomonas, Sphingopyxis, Simiduia, Flavobacterium, Novosphingobium*	*Methanobacterium, Methanosaeta, unclassified Parvarchaeota, unclassified Bathyarchaeota, unclassified Woesearchaeota*	Genus
	Limnohabitans australis, Limnohabitans parvus, Novosphingobium pentaromativorans, Sphingopyxis soli, Flavobacterium chungnamense, Flavobacterium columnare, Polynucleobacter necessarius, Pseudomonas extremorientalis, Perlucidibaca piscinae, Acinetobacter vivianii, Caulobacter virbioides, Sphingobium cupriresistens, Ferruginibacter profundus, Terrimonas lutea, Methanococcus mairipludis	*Methanosaeta concilli, Methanobacterium lacus, Nitrosopumilus maritimus,* several other OTUs with > 98% similarity with clones found in groundwater from studies listed in Chen et al. (2019)	Species (OTUs with >98% similarity)

(Continued on following page)

TABLE 2 | (*Continued*) Summary of microbial communities in beach aquifers. The organisms listed were extracted from figures and tables provided in the original study, the lists include all the organisms in the study.

Study	Bacteria	Archaea	Taxonomic classification level
Lee et al. (2017)	*Alphaproteobacteria, Gammaproteobacteria, Flavobacteria, Betaproteobacteria, Sphingobacteria, Planctomycetacia, Deltaproteobacteria, Chloracidobacterium, Chroobacteria, Anaerolineae, Acidimicrobiia, Rhotdothermus, Bacteroidia, Coscinodiscophyce, Actinobacteria, Unclassified*	—	Class
	Loktanella, Pelagibacter, Roseovirus, Polaribacter, Shwanella, Pseudomonas, Flavobacterium, Sterolibacterium, Blastocella, Dechloromonas	—	Genus
Ye et al. (2016)	*Proteobacteria, Actinobacteria, Bacteroidetes, Planctomycetes, Acidobacteria, Cyanobacteria*	—	Phylum
	Comamonas, Limnohabitans, Flavobacterium, Flectobacillus, Novosphingobium, Rhodobacter, Sediminibacterium, Perlucidibaca, Aquabacterium, Hydrogenophaga, Simplicispira, Fluviicola, Pseudarcicella, Polynucleobacter, Winogradskyella, Chryseolinea, Blastopirellula, Acinetobacter, Prochlorococcus, Rhodopirellula, Nitrospira, Lentibacter, Erythrobacter, Leisingera, Loktanella, Glaceicola	—	Genus
	Rhodoluna lacicola, Rhodoluna limnophila, Aquiluna rubra, Polynucleobacter acidophobus, Calothrix desertica, Karenia brevis, Prochlorococcus marinu, Vibrio splendidus, Pseudoalteromonas marina, Rhodopirellula baltica	—	Species (OTUs with >98% similarity)
McAllister et al. (2015)	*Deltaproteobacteria, Epsilonproteobacteria, Gammaproteobacteria, Betaproteobacteria, Zetaproteobacteria*	—	Class
	Desulfovibrio, Desulfopila, Desulfurispora, Geopsychobacter, Geobacter, Sulfurimonas, Acidiferrobacter, Ferritrophicum, Thioclava, Mariprofundus, Ferritrophicum	—	Genus
Santoro et al. (2008)	*Betaproteobacteria* (*Nitrosospira*-like)	*Thaumarchaeota* (*Nitrosopumilus*- and *Nitrosarchaeum*-like)	*amoA*-based OTUs with >95% identity
Santoro et al. (2006)	*Unknown denitrifiying bacteria. Sequences were more closely related to other environmental sequences than known cultivated denitrifiers*	—	*nirK* or *nirS*-based OTUs with >95% identity

and *Parvarchaeota* as a minor phylum at the study site. Chen et al. (2019) also noted *Euryarchaeota* as a dominant archaeal phylum, in addition to *Bathyarchaeota*, *Woesearchaeota* and *Parvarchaeota*. Jiang et al. (2020) noted a change in the abundance of *Thaumarchaetoa* to changing seasons in comparison with the major phylum–*Proteobacteria*.

Adyasari et al. (2019) documented the first evidence of the distribution of potential pathogens (1%-10% of total microbial community composition recorded) in beach aquifers, with potential implications on the water quality of the coastal ocean. The dominant genera were *Vibrio*, *Prevotella*, *Staphylococcus*, *Leptospira*, and members of the family *Enterobacteriaceae*.

To date, there is no evidence for the presence of endemic microbes in beach aquifer systems, although previous work on terrestrial aquifers suggests this may be a strong possibility (Anantharaman et al., 2016).

Functional Characteristics of the Beach Aquifer Microbiome

Five of the twelve studies (Santoro et al., 2006; Santoro et al., 2008; McAllister et al., 2015; Chen et al., 2019; Hong et al., 2019) aimed to provide substantive insights into the functional diversity of microbes in the beach aquifer. Two of those (Santoro et al., 2006; Santoro et al., 2008) investigated microorganisms involved in the nitrogen cycling using quantification and/or sequencing of functional genes involved in denitrification and nitrification, and three (McAllister et al., 2015; Chen et al., 2019; Hong et al., 2019) inferred microbial function from 16S rRNA amplicon sequencing.

Nitrogen cycling was investigated in the beach aquifer extensively by Santoro et al. (2006), Santoro et al. (2008). Santoro et al. (2006) characterized the diversity of denitrifying bacteria by sequencing *nirS* and *nirK* nitrite reductase genes (using Sanger sequencing). Little community compositional overlap between sampling sites was observed, suggesting high denitrifier diversity along small spatial scales (<40 m). Santoro et al. (Santoro et al., 2008) investigated the relative diversity and abundance of betaproteobacterial ammonia-oxidizing bacteria (AOB) and ammonia-oxidizing archaea (AOA) in the same beach aquifer using sequencing and quantitative polymerase chain reaction (qPCR) analysis of the functional gene encoding ammonia monooxygenase subunit A (*amoA*). Interestingly, a clear transition from an AOB-dominated community to an AOA-dominated community was observed

TABLE 3 | Relationships between beach aquifer microbiota and environmental parameters (Empty grey cells refer to measured environmental data, Grey cells with "X" indicates authors reported, statistically significant relationship between microbiome community composition and the environmental parameter; Empty white cells indicate parameters that were not measured by a given study. DO = dissolved oxygen, Temp = Temperature, ORP = Oxidation-Reduction Potential, Size fraction = Chen et al. (2019) was the only study that used cellulose acetate filters to generate two size fractions: 0.2–0.45 μm and >0.45 μm and study its relationship with the environment, N = nitrogen concentration, P = phosphorous concentration, C = carbon concentration, Fe = iron concentration, S = sulfide concentration, Si = silicate concentration).

Study	DO	Salinity	pH	Temp	ORP	Size fraction	N	P	C	Fe	S	Si
Hong et al 2020	X				X							
Jiang et al 2020				X					X			
Degenhardt et al 2020	X						X		X			
Chen et al 2020		X										
Adyasari et al 2020	X	X					X	X				
Adyasari et al 2019		X		X								
Chen et al 2019						X						
Lee et al 2017	X	X	X	X			X	X				
Ye et al 2016		X					X		X			
McAllister et al 2015	X	X								X	X	
Santoro et al 2008	X	X										
Santoro et al 2006		X		X			X					

as the location of the brackish mixing zone in the beach aquifer shifted seaward with a change in the season. This study also revealed a striking difference in relative bacterial and archaeal *amoA* gene diversity at all stations and time points. The study demonstrated an intimate link between microbial community composition, physicochemical gradients (e.g., especially salinity), and groundwater hydrology.

A broad suite of microbially mediated elemental cycling in the beach aquifer was investigated by McAllister et al. (2015), Hong et al. (2019), and Chen et al. (2019). McAllister et al. (2015) identified putative iron-cycling microbes (2.5% of the groundwater community) and sulfur-cycling microbes (29% of the groundwater community) based on the metabolic characteristics of the closely related (>98% OTU similarity) microbes documented in literature in other habitats. Hong et al. (2019) inferred metabolic functions (nitrogen, methane, and sulfur metabolism) from classified 16S rRNA OTUs using the bioinformatics program, PICRUSt (Phylogenetic Investigation of Communities by Reconstruction of Unobserved States), along a redox gradient in the beach aquifer. Their results indicated the presence of an erobic-anaerobic transition zone where microbial diversity was the highest. Chen et al. (2019) also noted the dominance of the archaeal phylum *Bathyarchaeota,* which may play a significant role in anaerobic carbon metabolism in groundwater.

Linkages Between Environmental Factors and Microbial Community Composition in the Beach Aquifer

Among the 12 papers, authors investigate associations between the microbial community and various physical (temperature, size fraction, sediment lithology and sample retrieval depth) and chemical properties (pH, salinity, concentrations of dissolved oxygen, nitrogen, phosphorous, iron, silica, sulfur, and carbon) of the sampling location (summarized in **Table 3**).

Among the physical properties, authors presented evidence of links between the microbial community and sample retrieval depth from surface (Hong et al., 2019), size fraction (Chen et al., 2019), sediment lithology (Adyasari et al., 2020) and temperature (Santoro et al., 2006; Lee et al., 2017; Adyasari et al., 2019; Jiang et al., 2020). Temperature was the most commonly investigated physical parameter. Adyasari et al. (2019) found that temperature explained the patterns of microbial diversity. Lee et al. (2017) also observed a significant positive correlation between microbial community composition and temperature measurements, but only for groundwater samples collected at low tide. Although Santoro et al. (2006) measured temperature in the groundwater samples, selection for microbial communities and nitrogen cycling genes based on this variable was not apparent. Temperature might also be linked to other environmental parameters such as subsurface salinity gradients (Geng et al., 2016). Complementarily, Jiang et al. (2020) observed a link between sediment microbial activity and carbon transformations in groundwater samples with higher temperatures.

Among the chemical properties, which were more extensively investigated compared to the physical properties, two of the most commonly reported factors that affected the composition of the microbiome were salinity and oxygen. Eight of the 12 studies (**Table 3**) reported a significant relationship between salinity and microbial community composition. Contrastingly, Degenhardt et al. (2020) did not observe a correlation between microbial community composition and salinity gradients in the aquifer of a sandy high-energy beach in Spiekeroog Island. Hong et al. (2019) also did not observe clear patterns of bacterial or archaeal community shifts with variation in salinity. Chen et al. (2019) and Jiang et al. (2020) measured salinity, but neither study reported any significant relationships with microbes within the beach aquifer systems. In this case, salinity could be tightly linked to other environmental parameters such as concentration of organic matter, temperature, and pH (Rath et al., 2019). For

example, when salinity decreases, it promotes the adsorption of dissolved organic carbon to sediment and may cause a reduction in groundwater dissolved organic carbon concentration (Setia et al., 2013; Jiang et al., 2020). Contrastingly, when salinity increases, groundwater dissolved organic carbon concentration may increase (Setia et al., 2013; Jiang et al., 2020).

Six of the 12 studies (**Table 3**) concluded that dissolved oxygen plays a vital role in regulating microbial distribution and function. Three studies highlighted the importance of dissolved oxygen in governing the distribution of bacterial communities (Santoro et al., 2008; McAllister et al., 2015; Degenhardt et al., 2020). One study (Hong et al., 2019) showed a dissolved oxygen profile drove the distribution of distinct erobic microbial groups (*Gammaproteobacteria*, *Betaproteobacteria*, *Acidobacteria*, *Flavobacteria*, *Thaumarchaeta*) and anaerobic microbial groups (sulfate-reducing bacteria, methanogenic archaea). Adyasari et al. (2020) also observed changes in microbial community composition with oxygen distribution. Lastly, Lee et al. (2017) showed that microbial community composition was significantly correlated to dissolved oxygen concentration, but only in samples collected at high tide.

WHAT ARE THE BIGGEST KNOWLEDGE GAPS AND DATA NEEDS FOR CHARACTERIZING AND REPORTING MICROBIAL COMMUNITIES AND ASSOCIATED METABOLISMS IN BEACH AQUIFERS?

Lawton (1999) stated "although details of single organisms matter and are of great interest, ecologists would profit most from uncovering underlying patterns, rules and laws". Beach aquifers are vulnerable global hotspots for microbe-mediated biogeochemical cycling. Yet, there are limited studies to-date that characterize the microbial community ("who is there?") in the beach aquifer. Questions that remain unanswered are "what are they doing there?" and "how did they get there?" Further, biogeochemical cycling estimates in beach aquifers remain fragmented. Therefore, the biggest challenge is the lack of data on the controls of the beach aquifer microbiome, or the "rules of life" of this environment. For the purpose of this study, we have identified knowledge gaps informed by our review and highlight corresponding data needs that warrant attention for future research.

Going Beyond Community Characteristics

Although the 12 studies identified in our review are extremely valuable, there is plenty of room for further investigation into the "potential function" of the microbiome using metagenomics (where the total community DNA is sequenced) and the "actual function" (or "expressional activity") of the microbiome using metatranscriptomics (where the total community mRNA is sequenced). Recently, Anantharaman et al. (2016) applied metagenomic sequencing, assembly, and binning approaches to examine the genetic and metabolic potential of sediment and groundwater bacteria and archaea within a shallow aquifer near the Colorado River. Results demonstrating tremendous novelty in the aquifer system highlight the potential of this approach for biological discovery in subsurface beach aquifers as well. Moran et al. (2013) argued that instantaneous inventories of mRNA can be highly informative about ecologically relevant processes. When metagenomics is coupled with metatranscriptomics, these approaches can advance beach aquifer microbial diversity/function research.

Complexities in Sampling

Among the studies identified in our review, there was considerable variability in the sample type, sampling method, frequency, depth, location, and storage. First, the studies reviewed undertook sampling at different points along the shoreline (defined as mean sea level). Most samples were collected within ±50 m from the shoreline. Only a few studies sampled beyond ±100 m from the shoreline (Ye et al., 2016; Chen et al., 2019; Degenhardt et al., 2020). Second, several types of samples were collected for microbial community analysis with varying terminologies–e.g., well water, groundwater, pore water, sediment. Well water, groundwater, and pore water represent water collected from within the porous media of the beach aquifer which we refer to as "groundwater" here. Third, samples were collected at varying depths beneath the surface of the sand. Often, when sediment cores were used to sample sediment, water adjacent to the sediment core was also sampled at varying depths. Sediment cores were usually 100 cm in length, except in Jiang et al. (2020) where they were 22 cm in length. Groundwater was extracted from anywhere between 0 cm and 3600 cm below the sand surface and were obtained using push-point piezometers and peristaltic pumps or pre-rinsed polyethylene syringes (Charette and Allen, 2006), except one study that used an *in-situ* profiler (0–20 cm) (Ibánhez et al., 2011). Fourth, the frequency of sampling varied–from hourly to weekly and monthly. Finally, once collected, samples were stored at −20°C (Ye et al., 2016; Adyasari et al., 2019; Chen et al., 2020; Degenhardt et al., 2020; Jiang et al., 2020), or −80°C (Santoro et al., 2006; Santoro et al., 2008; McAllister et al., 2015; Chen et al., 2019; Hong et al., 2019) or −70°C (Lee et al., 2017) for downstream analysis.

Free-Living Versus Attached Microbes in Beach Aquifer Systems

Among the papers we reviewed, the microbial ecology of the beach aquifers targeted prokaryotes in both groundwater (free-living) and sediments (attached). However, to date there are no direct comparisons between the free-living and attached microbial communities documented in coastal aquifer systems (Ruiz-Gonzalez et al., 2021). Specifically, no study has directly compared groundwater and sediment microbial communities in beach aquifer systems. Some works did report differences in the microbial communities with changes in particle size fraction (for example: Chen et al., 2019). Therefore, addressing the difference in the microbial diversity of suspended versus attached communities will form an

important part of future microbiome research in beach aquifer systems.

Variability in Analytical Methods

The papers we reviewed relied heavily on 16S rRNA gene amplicon sequencing. Downstream analysis for microbial community composition and functional characteristics consistently targeted the hypervariable V4-V5 region of the 16S rRNA gene on the MiSeq Illumina sequencing platform, except McAllister et al. (2015) and Lee et al. (2017), which adopted tagged pyrosequencing of the V1-V3 region. However, the fusion-primers targeting the regions were different among the papers reviewed. We observed consistency in the usage of forward primers (515F: (Ye et al., 2016; Adyasari et al., 2019; Chen et al., 2019; Hong et al., 2019; Chen et al., 2020). However, the same studies used different reverse primers (926R–(Adyasari et al., 2019, 2020); 907R–(Ye et al., 2016; Chen et al., 2019, 2020); 541R–(Lee et al., 2017); 806R–(Hong et al., 2019)). Degenhardt et al. (Degenhardt et al., 2020) used a unique set of forward and reverse primers as per Klindworth et al. (2013). Overall, this variability in the primers and variable regions used for 16S rRNA amplicon sequencing makes comparisons across studies (and field sites) challenging. To date, no published studies have used metagenomics or metatranscriptomics to characterize the beach aquifer microbiome. Such studies have the potential to yield extremely valuable and unprecedented information on the metabolic functions of microbes in the beach aquifer, rather than relying solely on inferences made using 16S rRNA gene amplicon sequencing.

Metadata Reporting

Metadata reporting, including site description, access to the sediment, and relevant properties of the beach aquifer system, were fragmented or inconsistent across many of the studies identified in our review. For instance, not all studies report groundwater flow rate and/or velocity, and properties of the sand (such as texture, grain size) were often not mentioned. In cases where sediments are not homogenous and contain iron-containing minerals, it might not be possible to isolate the effect of groundwater chemistry on the microbiome, since sediment mineral composition co-varies with groundwater chemistry (Luo et al., 2018). Detailed sediment and site characterization can help document potential confounding effects.

Taxonomic Levels of Classification of Microbial Data

Some studies have chosen to report microbial community data only at the phylum or class level. While this provides high-level details regarding microbiome composition of beach aquifers, in the future, whenever possible it will be important to document evidence at the genus and/or species level to provide more insight into the function of microbiome. For example, there is increasing evidence to suggest the presence of aquifer microbes that are distinct from other microbes found in sediments or surface waters (e.g., iron-cycling, sulfur-cycling microbes; (Anantharaman et al., 2016; Probst et al., 2017; Probst et al., 2018; Kadnikov et al., 2020). Yet, it continues to remain unclear as to whether these differences are apparent at the genus and/or species level, as studies often report data at higher taxonomic levels of classification. Moreover, some phyla (e.g., *Proteobacteria*) are known to be extremely diverse with numerous members when compared to other phyla. Therefore, phylum-level classification may not provide a fine enough description of the community composition.

Microbial Transport Within the Beach Aquifer

It is likely that the microbiome is readily transported with water as it moves over wave-, tidal- and seasonal time scales through the beach aquifer. To date, experiments on microbial transport in the subsurface have focused primarily on the movement of pathogens in relation to the protection of water resources (de Sieyes et al., 2016). Boehm et al. (2014) tested whether the microbiome can be transported from seawater through unsaturated, intertidal sands and the vadose or unsaturated zone to the aquifer. While the groundwater surrounding the sediment may contain the same microorganisms as the sediment (suggesting a constant exchange of microbes between the sediment and groundwater), this does not mean that microorganisms in the groundwater can be readily transported through the subsurface. Surface-surface interactions caused by electrostatic, hydrophobic, and steric forces between sediments and microorganisms, or straining, may impede their transport through the porous media and cause their transport to be retarded (Bradford et al., 2002; Bradford et al., 2003; Bradford et al., 2013). Therefore, even if there is exchange of microbes between sediment and groundwater, this does not imply microbial transport can occur. Indeed, investigation into the potential for immigration of microbes between different regions (via transport through sands and adaptations to changes in groundwater chemistry) in the beach aquifer is required to understand the mechanisms controlling microbial structure.

Quantifying Rates of Elemental Cycling Within Beach Aquifer Systems

Data on the rates of key microbially mediated biogeochemical processes (e.g., nitrification/denitrification) in beach aquifer systems is lacking. For example, denitrification (the transformation of nitrate to nitrogen gas) in the beach aquifer is vital to reduce the nitrogen load in groundwater that gets discharged to the coastal ocean (Galloway et al., 2003). Organic carbon mineralization is tightly linked to nitrate-rich freshwater denitrification (Anschutz et al., 2009) and quantifying the reduction of sulfate to sulfide is also important, as sulfur cycling is closely linked to nitrogen cycling (Heiss et al., 2017). Therefore, nuances of the reactive and dynamic nature of the beach aquifer (quantitative measurements of rates of elemental cycling) in the context of its microbial diversity needs further investigation.

Beach Aquifers and the Global Carbon Budget

One of the emergent issues in beach aquifers is the behavior and lability of terrestrially derived dissolved organic matter, as well as

the source-sink dynamics of carbon (Waska et al., 2021). In a thorough review on groundwater, Griebler and Lueders (2009) highlighted the important association between microbial communities and dissolved organic carbon as a driver of free-living versus attached communities in addition to other variables such as the availability of nutrients, sediment grain size and minerology. Further, Dittmar et al. (2001) noted that subsurface fluxes of organic matter are significant, yet quantitative estimates of transformations of organic matter through microbially mediated cycling need further investigation. This highlights the importance of beach aquifers as potential sources of organic and inorganic carbon and their need to be incorporated into global climate system models. It is possible that investigating carbon cycling in beach aquifers can potentially alter the global estimates of CO_2 outgassing to the atmosphere, as current budgets underestimate the flux of CO_2 from groundwater to the atmosphere (Ward et al., 2017).

CONCLUSION

Although there has been advancement in the knowledge and understanding of beach aquifer systems, there is presently a paucity of data on the beach aquifer microbiome. The mechanisms that control the beach aquifer microbiome or the "rules of life" for this environment need attention. Specifically, the extent to which the environment (groundwater chemistry, sediment characteristics) controls the beach aquifer system and the ability of the microbiome present naturally in the beach sediments to be transported to other locations in the aquifer remains largely unknown. Beach aquifer microbiome research will directly benefit society by furthering the understanding of the ecosystem services provided by beaches in terms of biogeochemical cycling. As beaches are threatened by changing environmental conditions such as sea-level rise, this information is essential to anticipate the overall contribution of beaches to biogeochemical cycling on the planet.

AUTHOR CONTRIBUTIONS

AB conceptualized the framework for the review. AA wrote the manuscript. AB, CF and AA reviewed the manuscript and analysis. All authors contributed to the article and approved the submitted version.

FUNDING

We are grateful to the National Science Foundation (NSF Emerging Frontiers Award Number:2024504) for funding the project "The sandy beach microbiome: physical, chemical and biological controls on diversity and function".

REFERENCES

Abarca, E., Karam, H., Hemond, H. F., and Harvey, C. F. (2013). Transient Groundwater Dynamics in a Coastal Aquifer: The Effects of Tides, the Lunar Cycle, and the Beach Profile. *Water Resour. Res.* 49, 2473–2488. doi:10.1002/wrcr.20075

Adyasari, D., Hassenrück, C., Montiel, D., and Dimova, N. (2020). Microbial Community Composition across a Coastal Hydrological System Affected by Submarine Groundwater Discharge. *PLoS One* 15, e0235235. doi:10.1371/journal.pone.0235235

Adyasari, D., Hassenrück, C., Oehler, T., Sabdaningsih, A., and Moosdorf, N. (2019). Microbial Community Structure Associated with Submarine Groundwater Discharge in Northern Java (Indonesia). *Sci. Total Environ.* 689, 590–601. doi:10.1016/j.scitotenv.2019.06.193

Ahrens, J., Beck, M., Marchant, H. K., Ahmerkamp, S., Schnetger, B., and Brumsack, H. J. (2020). Seasonality of Organic Matter Degradation Regulates Nutrient and Metal Net Fluxes in a High Energy Sandy Beach. *J. Geophys. Res. Biogeosci.* 125. doi:10.1029/2019JG005399

Anantharaman, K., Brown, C. T., Hug, L. A., Sharon, I., Castelle, C. J., Probst, A. J., et al. (2016). Thousands of Microbial Genomes Shed Light on Interconnected Biogeochemical Processes in an Aquifer System. *Nat. Commun.* 7, 13219. doi:10.1038/ncomms13219

Anschutz, P., Smith, T., Mouret, A., Deborde, J., Bujan, S., Poirier, D., et al. (2009). Tidal Sands as Biogeochemical Reactors. *Estuarine, Coastal Shelf Sci.* 84, 84–90. doi:10.1016/j.ecss.2009.06.015

Bakhtyar, R., Barry, D. A., and Brovelli, A. (2012). Numerical Experiments on Interactions between Wave Motion and Variable-Density Coastal Aquifers. *Coastal Eng.* 60, 95–108. doi:10.1016/j.coastaleng.2011.09.001

Beck, M., Riedel, T., Graue, J., Köster, J., Kowalski, N., Wu, C. S., et al. (2011). Imprint of Past and Present Environmental Conditions on Microbiology and Biogeochemistry of Coastal Quaternary Sediments. *Biogeosciences* 8, 55–68. doi:10.5194/bg-8-55-2011

Boehm, A. B., Paytan, A., Shellenbarger, G. G., and Davis, K. A. (2006). Composition and Flux of Groundwater from a California Beach Aquifer: Implications for Nutrient Supply to the Surf Zone. *Continental Shelf Res.* 26, 269–282. doi:10.1016/j.csr.2005.11.008

Boehm, A. B., Yamahara, K. M., and Sassoubre, L. M. (2014). Diversity and Transport of Microorganisms in Intertidal Sands of the California Coast. *Appl. Environ. Microbiol.* 80, 3943–3951. doi:10.1128/AEM.00513-14

Böer, S. I., Hedtkamp, S. I. C., van Beusekom, J. E. E., Fuhrman, J. A., Boetius, A., and Ramette, A. (2009). Time- and Sediment Depth-Related Variations in Bacterial Diversity and Community Structure in Subtidal Sands. *Isme J.* 3, 780–791. doi:10.1038/ismej.2009.29

Bone, S. E., Charette, M. A., Lamborg, C. H., and Gonneea, M. E. (2007). Has Submarine Groundwater Discharge Been Overlooked as a Source of Mercury to Coastal Waters?. *Environ. Sci. Technol.* 41, 3090–3095. doi:10.1021/es0622453

Bradford, S. A., Morales, V. L., Zhang, W., Harvey, R. W., Packman, A. I., Mohanram, A., et al. (2013). Transport and Fate of Microbial Pathogens in Agricultural Settings. *Crit. Rev. Environ. Sci. Tech.* 43, 775–893. doi:10.1080/10643389.2012.710449

Bradford, S. A., Simunek, J., Bettahar, M., van Genuchten, M. T., and Yates, S. R. (2003). Modeling Colloid Attachment, Straining, and Exclusion in Saturated Porous Media. *Environ. Sci. Technol.* 37, 2242–2250. doi:10.1021/es025899u

Bradford, S. A., Yates, S. R., Bettahar, M., and Simunek, J. (2002). Physical Factors Affecting the Transport and Fate of Colloids in Saturated Porous Media. *Water Resour. Res.* 38, 63–71. doi:10.1029/2002WR001340

Brown, A. C., and McLachlan, A. (2002). Sandy Shore Ecosystems and the Threats Facing Them: Some Predictions for the Year 2025. *Envir. Conserv.* 29, 62–77. doi:10.1017/S037689290200005X

Charette, M. A., and Allen, M. C. (2006). Precision Ground Water Sampling in Coastal Aquifers Using a Direct-Push, Shielded-Screen Well-Point System. *Groundwater Monit. Remediation* 26, 87–93. doi:10.1111/j.1745-6592.2006.00076.x

Charette, M. A., Sholkovitz, E. R., and Hansel, C. M. (2005). Trace Element Cycling in a Subterranean Estuary: Part 1. Geochemistry of the Permeable Sediments.

Geochimica et Cosmochimica Acta 69, 2095–2109. doi:10.1016/j.gca.2004.10.024

Charette, M. A., and Sholkovitz, E. R. (2002). Oxidative Precipitation of Groundwater-Derived Ferrous Iron in the Subterranean Estuary of a Coastal Bay. *Geophys. Res. Lett.* 29, 85–91. doi:10.1029/2001GL014512

Chen, X., Ye, Q., Du, J., and Zhang, J. (2019). Bacterial and Archaeal Assemblages from Two Size Fractions in Submarine Groundwater Near an Industrial Zone. *Water* 11, 1261. doi:10.3390/w11061261

Chen, X., Ye, Q., Sanders, C. J., Du, J., and Zhang, J. (2020). Bacterial-derived Nutrient and Carbon Source-Sink Behaviors in a Sandy Beach Subterranean Estuary. *Mar. Pollut. Bull.* 160, 111570. doi:10.1016/j.marpolbul.2020.111570

Cui, H., Yang, K., Pagaling, E., and Yan, T. (2013). Spatial and Temporal Variation in Enterococcal Abundance and its Relationship to the Microbial Community in Hawaii Beach Sand and Water. *Appl. Environ. Microbiol.* 79, 3601–3609. doi:10.1128/aem.00135-13

de Sieyes, N. R., Russell, T. L., Brown, K. I., Mohanty, S. K., and Boehm, A. B. (2016). Transport of Enterococci and F+ Coliphage through the Saturated Zone of the Beach Aquifer. *J. Water Health* 14, 26–38. doi:10.2166/wh.2015.290

Defeo, O., McLachlan, A., Schoeman, D. S., Schlacher, T. A., Dugan, J., Jones, A., et al. (2009). Threats to Sandy Beach Ecosystems: A Review. *Estuarine, Coastal Shelf Sci.* 81, 1–12. doi:10.1016/j.ecss.2008.09.022

Degenhardt, J., Dlugosch, L., Ahrens, J., Beck, M., Waska, H., and Engelen, B. (2020). Seasonal Dynamics of Microbial Diversity at a Sandy High Energy Beach Reveal a Resilient Core Community. *Front. Mar. Sci.* 7, 573570. doi:10.3389/fmars.2020.573570

Dittmar, T., Lara, R. J., and Kattner, G. (2001). River or Mangrove? Tracing Major Organic Matter Sources in Tropical Brazilian Coastal Waters. *Mar. Chem.* 73, 253–271. doi:10.1016/S0304-4203(00)00110-9

Domínguez-Tejo, E., Metternicht, G., Johnston, E. L., and Hedge, L. (2018). Exploring the Social Dimension of Sandy Beaches through Predictive Modelling. *J. Environ. Manage.* 214, 379–407. doi:10.1016/j.jenvman.2018.03.006

Dorsett, A., Cherrier, J., Martin, J. B., and Cable, J. E. (2011). Assessing Hydrologic and Biogeochemical Controls on Pore-Water Dissolved Inorganic Carbon Cycling in a Subterranean Estuary: A 14C and 13C Mass Balance Approach. *Mar. Chem.* 127, 76–89. doi:10.1016/j.marchem.2011.07.007

Dugan, J. E., Defeo, O., Jaramillo, E., Jones, A. R., Lastra, M., Nel, R., et al. (2010). Give Beach Ecosystems Their Day in the Sun. *Science* 329, 1146. doi:10.1126/science.329.5996.1146-a

Eastern Research Group (2015). "The National Significance of California's Ocean Economy." 2015. https://coast.noaa.gov/data/digitalcoast/pdf/california-ocean-economy.pdf (Accessed January 11, 2021).

Gaidos, E., Rusch, A., and Ilardo, M. (2011). Ribosomal Tag Pyrosequencing of DNA and RNA from Benthic Coral Reef Microbiota: Community Spatial Structure, Rare Members and Nitrogen-Cycling Guilds. *Environ. Microbiol.* 13, 1138–1152. doi:10.1111/j.1462-2920.2010.02392.x

Galloway, J. N., Aber, J. D., Erisman, J. W., Seitzinger, S. P., Howarth, R. W., Cowling, E. B., et al. (2003). The Nitrogen Cascade. *BioScience* 53, 341. doi:10.1641/0006-3568(2003)053[0341:TNC]2.0.CO;2

Geng, X., Boufadel, M. C., and Jackson, N. L. (2016). Evidence of Salt Accumulation in Beach Intertidal Zone Due to Evaporation. *Sci. Rep.* 6, 31486. doi:10.1038/srep31486

Gobet, A., Böer, S. I., Huse, S. M., van Beusekom, J. E. E., Quince, C., Sogin, M. L., et al. (2012). Diversity and Dynamics of Rare and of Resident Bacterial Populations in Coastal Sands. *Isme J.* 6, 542–553. doi:10.1038/ismej.2011.132

Griebler, C., and Lueders, T. (2009). Microbial Biodiversity in Groundwater Ecosystems. *Freshw. Biol.* 54, 649–677. doi:10.1111/j.1365-2427.2008.02013.x

Hanley, M. E., Hoggart, S. P. G., Simmonds, D. J., Bichot, A., Colangelo, M. A., Bozzeda, F., et al. (2014). Shifting Sands? Coastal Protection by Sand Banks, Beaches and Dunes. *Coastal Eng.* 87, 136–146. doi:10.1016/j.coastaleng.2013.10.020

Heiss, J. W., and Michael, H. A. (2014). Saltwater-freshwater Mixing Dynamics in a Sandy Beach Aquifer over Tidal, Spring-Neap, and Seasonal Cycles. *Water Resour. Res.* 50, 6747–6766. doi:10.1002/2014WR015574

Heiss, J. W., Post, V. E. A., Laattoe, T., Russoniello, C. J., and Michael, H. A. (2017). Physical Controls on Biogeochemical Processes in Intertidal Zones of Beach Aquifers. *Water Resour. Res.* 53, 9225–9244. doi:10.1002/2017WR021110

Hong, Y., Wu, J., Wilson, S., and Song, B. (2019). Vertical Stratification of Sediment Microbial Communities along Geochemical Gradients of a Subterranean Estuary Located at the Gloucester Beach of Virginia, United States. *Front. Microbiol.* 9, 3343. doi:10.3389/fmicb.2018.03343

Hunter, E. M., Mills, H. J., and Kostka, J. E. (2006). Microbial Community Diversity Associated with Carbon and Nitrogen Cycling in Permeable Shelf Sediments. *Appl. Environ. Microbiol.* 72, 5689–5701. doi:10.1128/aem.03007-05

Ibánhez, J. S. P., Leote, C., and Rocha, C. (2011). Porewater Nitrate Profiles in Sandy Sediments Hosting Submarine Groundwater Discharge Described by an Advection-Dispersion-Reaction Model. *Biogeochemistry* 103, 159–180. doi:10.1007/s10533-010-9454-1

Jiang, S., Zhang, Y., Jin, J., Wu, Y., Wei, Y., Wang, X., et al. (2020). Organic Carbon in a Seepage Face of a Subterranean Estuary: Turnover and Microbial Interrelations. *Sci. Total Environ.* 725, 138220. doi:10.1016/j.scitotenv.2020.138220

Kadnikov, V. V., Mardanov, A. V., Beletsky, A. V., Karnachuk, O. V., and Ravin, N. V. (2020). Microbial Life in the Deep Subsurface Aquifer Illuminated by Metagenomics. *Front. Microbiol.* 11, 572252. doi:10.3389/fmicb.2020.572252

Kim, K. H., and Heiss, J. W. (2021). Methods in Capturing the Spatiotemporal Dynamics of Flow and Biogeochemical Reactivity in Sandy Beach Aquifers: A Review. *Water* 13, 782. doi:10.3390/w13060782

Kim, T.-H., Waska, H., Kwon, E., Suryaputra, I. G. N., and Kim, G. (2012). Production, Degradation, and Flux of Dissolved Organic Matter in the Subterranean Estuary of a Large Tidal Flat. *Mar. Chem.* 142-144 (144), 1–10. doi:10.1016/j.marchem.2012.08.002

Klindworth, A., Pruesse, E., Schweer, T., Peplies, J., Quast, C., Horn, M., et al. (2013). Evaluation of General 16S Ribosomal RNA Gene PCR Primers for Classical and Next-Generation Sequencing-Based Diversity Studies. *Nucleic Acids Res.* 41, e1. doi:10.1093/nar/gks808

Kroeger, K. D., and Charette, M. A. (2008). Nitrogen Biogeochemistry of Submarine Groundwater Discharge. *Limnol. Oceanogr.* 53, 1025–1039. doi:10.4319/lo.2008.53.3.1025

Lawton, J. H. (1999). Are There General Laws in Ecology?. *Oikos* 84, 177. doi:10.2307/3546712

Lebbe, L. (1981). The Subterranean Flow of Fresh and Salt Water Underneath the Western Belgian Beach. 7th Salt Water Intrusion Meeting, Uppsala. Sveriges Geologiska Underso kning Rapporter och Meddelanden, 27, 193–219.

Lee, E., Shin, D., Hyun, S. P., Ko, K.-S., Moon, H. S., Koh, D.-C., et al. (2017). Periodic Change in Coastal Microbial Community Structure Associated with Submarine Groundwater Discharge and Tidal Fluctuation. *Limnol. Oceanogr.* 62, 437–451. doi:10.1002/lno.10433

Luijendijk, A., Hagenaars, G., Ranasinghe, R., Baart, F., Donchyts, G., and Aarninkhof, S. (2018). The State of the World's Beaches. *Sci. Rep.* 8, 6641. doi:10.1038/s41598-018-24630-6

Luo, W., Gao, X., and Zhang, X. (2018). Geochemical Processes Controlling the Groundwater Chemistry and Fluoride Contamination in the Yuncheng Basin, China-An Area with Complex Hydrogeochemical Conditions. *PLoS One* 13, e0199082. doi:10.1371/journal.pone.0199082

McAllister, S. M., Barnett, J. M., Heiss, J. W., Findlay, A. J., MacDonald, D. J., Dow, C. L., et al. (2015). Dynamic Hydrologic and Biogeochemical Processes Drive Microbially Enhanced Iron and Sulfur Cycling within the Intertidal Mixing Zone of a Beach Aquifer. *Limnol. Oceanogr.* 60, 329–345. doi:10.1002/lno.10029

McKenzie, T., Holloway, C., Dulai, H., Tucker, J. P., Sugimoto, R., Nakajima, T., et al. (2020). Submarine Groundwater Discharge: A Previously Undocumented Source of Contaminants of Emerging Concern to the Coastal Ocean (Sydney, Australia). *Mar. Pollut. Bull.* 160, 111519. doi:10.1016/j.marpolbul.2020.111519

Michael, H. A., Mulligan, A. E., and Harvey, C. F. (2005). Seasonal Oscillations in Water Exchange between Aquifers and the Coastal Ocean. *Nature* 436, 1145–1148. doi:10.1038/nature03935

Mills, H. J., Hunter, E., Humphrys, M., Kerkhof, L., McGuinness, L., Huettel, M., et al. (2008). Characterization of Nitrifying, Denitrifying, and Overall Bacterial Communities in Permeable Marine Sediments of the Northeastern Gulf of Mexico. *Appl. Environ. Microbiol.* 74, 4440–53. doi:10.1128/aem.02692-07

Moore, W. S. (2010). A Reevaluation of Submarine Groundwater Discharge along the Southeastern Coast of North America. *Glob. Biogeochem. Cycles* 24, a–n. doi:10.1029/2009GB003747

Moore, W. S. (1999). The Subterranean Estuary: a Reaction Zone of Ground Water and Sea Water. *Mar. Chem.* 65, 111–125. doi:10.1016/S0304-4203(99)00014-6

Moran, M. A., Satinsky, B., Gifford, S. M., Luo, H., Rivers, A., Chan, L.-K., et al. (2013). Sizing up Metatranscriptomics. *ISME J.* 7, 237–243. doi:10.1038/ismej.2012.94

Probst, A. J., Castelle, C. J., Singh, A., Brown, C. T., Anantharaman, K., Sharon, I., et al. (2017). Genomic Resolution of a Cold Subsurface Aquifer Community Provides Metabolic Insights for Novel Microbes Adapted to High CO_2concentrations. *Environ. Microbiol.* 19, 459–474. doi:10.1111/1462-2920.13362

Probst, A. J., Ladd, B., Jarett, J. K., Geller-McGrath, D. E., Sieber, C. M. K., Emerson, J. B., et al. (2018). Differential Depth Distribution of Microbial Function and Putative Symbionts through Sediment-Hosted Aquifers in the Deep Terrestrial Subsurface. *Nat. Microbiol.* 3, 328–336. doi:10.1038/s41564-017-0098-y

Rath, K. M., Fierer, N., Murphy, D. V., and Rousk, J. (2019). Linking Bacterial Community Composition to Soil Salinity along Environmental Gradients. *ISME J.* 13, 836–846. doi:10.1038/s41396-018-0313-8

Robinson, C. E., Xin, P., Santos, I. R., Charette, M. A., Li, L., and Barry, D. A. (2018). Groundwater Dynamics in Subterranean Estuaries of Coastal Unconfined Aquifers: Controls on Submarine Groundwater Discharge and Chemical Inputs to the Ocean. *Adv. Water Resour.* 115, 315–331. doi:10.1016/j.advwatres.2017.10.041

Robinson, C., Gibbes, B., Carey, H., and Li, L. (2007). Salt-freshwater Dynamics in a Subterranean Estuary over a Spring-Neap Tidal Cycle. *J. Geophys. Res.* 112, C09007. doi:10.1029/2006JC003888

Robinson, C., Gibbes, B., and Li, L. (2006). Driving Mechanisms for Groundwater Flow and Salt Transport in a Subterranean Estuary. *Geophys. Res. Lett.* 33, L03402. doi:10.1029/2005GL025247

Rocha, C. (2008). Sandy Sediments as Active Biogeochemical Reactors: Compound Cycling in the Fast Lane. *Aquat. Microb. Ecol.* 53, 119–127. doi:10.3354/ame01221

Romão, D., Staley, C., Ferreira, F., Rodrigues, R., Sabino, R., Veríssimo, C., et al. (2017). Next-generation Sequencing and Culture-Based Techniques Offer Complementary Insights into Fungi and Prokaryotes in Beach Sands. *Mar. Pollut. Bull.* 119, 351–358. doi:10.1016/j.marpolbul.2017.04.036

Ruiz-González, C., Rodellas, V., and Garcia-Orellana, J. (2021). The Microbial Dimension of Submarine Groundwater Discharge: Current Challenges and Future Directions. *FEMS Microbiol. Rev.* doi:10.1093/femsre/fuab010

Rusch, A., Huettel, M., Reimers, C. E., Taghon, G. L., and Fuller, C. M. (2003). Activity and Distribution of Bacterial Populations in Middle Atlantic Bight Shelf Sands. *Fems Microbiol. Ecol.* 44, 89–100. doi:10.1111/j.1574-6941.2003.tb01093.x

Sáenz, J. P., Hopmans, E. C., Rogers, D., Henderson, P. B., Charette, M. A., Schouten, S., et al. (2012). Distribution of Anaerobic Ammonia-Oxidizing Bacteria in a Subterranean Estuary. *Mar. Chem.* 136-137 (137), 7–13. doi:10.1016/j.marchem.2012.04.004

Santoro, A. E., Boehm, A. B., and Francis, C. A. (2006). Denitrifier Community Composition along a Nitrate and Salinity Gradient in a Coastal Aquifer. *Aem* 72, 2102–2109. doi:10.1128/aem.72.3.2102-2109.2006

Santoro, A. E., Francis, C. A., de Sieyes, N. R., and Boehm, A. B. (2008). Shifts in the Relative Abundance of Ammonia-Oxidizing Bacteria and Archaea across Physicochemical Gradients in a Subterranean Estuary. *Environ. Microbiol.* 10, 1068–1079. doi:10.1111/j.1462-2920.2007.01547.x

Santoro, A. E. (2010). Microbial Nitrogen Cycling at the Saltwater-Freshwater Interface. *Hydrogeol J.* 18, 187–202. doi:10.1007/s10040-009-0526-z

Santos, I. R., Bryan, K. R., Pilditch, C. A., and Tait, D. R. (2014). Influence of Porewater Exchange on Nutrient Dynamics in Two New Zealand Estuarine Intertidal Flats. *Mar. Chem.* 167, 57–70. doi:10.1016/j.marchem.2014.04.006

Santos, I. R., Burnett, W. C., Dittmar, T., Suryaputra, I. G. N. A., and Chanton, J. (2009). Tidal Pumping Drives Nutrient and Dissolved Organic Matter Dynamics in a Gulf of Mexico Subterranean Estuary. *Geochim. Cosmochim. Acta* 73, 1325–1339. doi:10.1016/j.gca.2008.11.029

Schlacher, T. A., Dugan, J., Schoeman, D. S., Lastra, M., Jones, A., Scapini, F., et al. (2007). Sandy Beaches at the Brink. *Divers. Distributions* 13, 556–560. doi:10.1111/j.1472-4642.2007.00363.x

Setia, R., Rengasamy, P., and Marschner, P. (2013). Effect of Exchangeable Cation Concentration on Sorption and Desorption of Dissolved Organic Carbon in Saline Soils. *Sci. Total Environ.* 465, 226–232. doi:10.1016/j.scitotenv.2013.01.010

Sirois, M., Couturier, M., Barber, A., Gélinas, Y., and Chaillou, G. (2018). Interactions between Iron and Organic Carbon in a Sandy Beach Subterranean Estuary. *Mar. Chem.* 202, 86–96. doi:10.1016/j.marchem.2018.02.004

Slomp, C. P., and Van Cappellen, P. (2004). Nutrient Inputs to the Coastal Ocean through Submarine Groundwater Discharge: Controls and Potential Impact. *J. Hydrol.* 295, 64–86. doi:10.1016/j.jhydrol.2004.02.018

Sørensen, K. B., Glazer, B., Hannides, A., and Gaidos, E. (2007). Spatial Structure of the Microbial Community in Sandy Carbonate Sediment. *Mar. Ecol. Prog. Ser.* 346, 61–74.

Staley, C., and Sadowsky, M. J. (2016). Regional Similarities and Consistent Patterns of Local Variation in Beach Sand Bacterial Communities throughout the Northern Hemisphere. *Appl. Environ. Microbiol.* 82, 2751–2762. doi:10.1128/aem.00247-16

Ullman, W. J., Chang, B., Miller, D. C., and Madsen, J. A. (2003). Groundwater Mixing, Nutrient Diagenesis, and Discharges across a Sandy Beachface, Cape Henlopen, Delaware (USA). *Estuarine, Coastal Shelf Sci.* 57, 539–552. doi:10.1016/S0272-7714(02)00398-0

Urakawa, H., Yoshida, T., Nishimura, M., and Ohwada, K. (2000). Characterization of Depth-Related Population Variation in Microbial Communities of a Coastal Marine Sediment Using 16S rDNA-Based Approaches and Quinone Profiling. *Environ. Microbiol.* 2, 542–554. doi:10.1046/j.1462-2920.2000.00137.x

Vandenbohede, A., and Lebbe, L. (2006). Occurrence of Salt Water above Fresh Water in Dynamic Equilibrium in a Coastal Groundwater Flow System Near De Panne, Belgium. *Hydrogeol J.* 14, 462–472. doi:10.1007/s10040-005-0446-5

Ward, N. D., Bianchi, T. S., Medeiros, P. M., Seidel, M., Richey, J. E., Keil, R. G., et al. (2017). Where Carbon Goes when Water Flows: Carbon Cycling across the Aquatic Continuum. *Front. Mar. Sci.* 4. doi:10.3389/fmars.2017.00007

Waska, H., Simon, H., Ahmerkamp, S., Greskowiak, J., Ahrens, J., Seibert, S. L., et al. (2021). Molecular Traits of Dissolved Organic Matter in the Subterranean Estuary of a High-Energy Beach: Indications of Sources and Sinks. *Front. Mar. Sci.* 8, 607083. doi:10.3389/fmars.2021.607083

Wegner, C.-E., Gaspar, M., Geesink, P., Herrmann, M., Marz, M., and Küsel, K. (2018). Biogeochemical Regimes in Shallow Aquifers Reflect the Metabolic Coupling of the Elements Nitrogen, Sulfur, and Carbon. *Appl. Environ. Microbiol.* 85, e02346–18. doi:10.1128/AEM.02346-18

Welch, E. M., Dulai, H., El-Kadi, A., and Shuler, C. K. (2019). Submarine Groundwater Discharge and Stream Baseflow Sustain Pesticide and Nutrient Fluxes in Faga'alu Bay, American Samoa. *Front. Environ. Sci.* 7, 162. doi:10.3389/fenvs.2019.00162

Yamahara, K. M., Layton, B. A., Santoro, A. E., and Boehm, A. B. (2007). Beach Sands along the California Coast Are Diffuse Sources of Fecal Bacteria to Coastal Waters. *Environ. Sci. Technol.* 41, 4515–4521. doi:10.1021/es062822n

Yang, L., Chen, C.-T. A., Hong, H., Chang, Y.-C., and Lui, H.-K. (2015). Mixing Behavior and Bioavailability of Dissolved Organic Matter in Two Contrasting Subterranean Estuaries as Revealed by Fluorescence Spectroscopy and Parallel Factor Analysis. *Estuarine, Coastal Shelf Sci.* 166, 161–169. doi:10.1016/j.ecss.2014.10.018

Ye, Q., Liu, J., Du, J., and Zhang, J. (2016). Bacterial Diversity in Submarine Groundwater along the Coasts of the Yellow Sea. *Front. Microbiol.* 6, 1519. doi:10.3389/fmicb.2015.01519

Conflict of Interest: The authors declare that the research was conducted in the absence of any commercial or financial relationships that could be construed as a potential conflict of interest.

Copyright © 2021 Archana, Francis and Boehm. This is an open-access article distributed under the terms of the Creative Commons Attribution License (CC BY). The use, distribution or reproduction in other forums is permitted, provided the original author(s) and the copyright owner(s) are credited and that the original publication in this journal is cited, in accordance with accepted academic practice. No use, distribution or reproduction is permitted which does not comply with these terms.

frontiers in Environmental Science

ORIGINAL RESEARCH
published: 22 April 2021
doi: 10.3389/fenvs.2021.642098

The Three Domains of Life Within the Discharge Area of a Shallow Subterranean Estuary at a High Energy Beach

Julius Degenhardt[1], Sahar Khodami[2], Felix Milke[1], Hannelore Waska[1], Bert Engelen[1] and Pedro Martinez Arbizu[2]*

[1] Institue for Chemistry and Biology of the Marine Environment, University of Oldenburg, Oldenburg, Germany, [2] German Centre for Marine Biodiversity, Senckenberg am Meer, Wilhelmshaven, Germany

Subterranean estuaries (STEs) play an important role in linking nutrient cycling between marine and terrestrial systems. As being the primary drivers of nutrient cycling, the composition of microbial communities and their adaptation toward both, terrestrial and marine conditions are of special interest. While bacterial communities of STEs have received increasing scientific attention, archaeal and meiofaunal diversity was mostly neglected. Previous studies at the investigated sampling site, the STE of a mesotidal beach at the German North Sea island of Spiekeroog, focused on spatial and seasonal patterns of geochemical and bacterial diversity. By additionally investigating the archaeal and meiofaunal diversity and distribution, we now aimed to fill this gap of knowledge to understand the microbial response to submarine groundwater discharge (SGD). The topography of Spiekeroog beach and associated geochemical gradients in porewater displayed a distinct cross-shore zonation, with seawater infiltration on the upper beach at the high water line (HWL), and saline and brackish porewater exfiltration (SGD) at the ridge-runnel structure and the low water line (LWL) on the lower beach. This led to a higher evenness of prokaryotic communities in lower beach areas impacted by SGD compared to unimpacted areas. *Archaea* contributed 1–4% to the 16S rRNA gene sequence dataset. Those were dominated by *Nitrosopumilaceae*, corresponding well to higher concentrations of NH_4^+ in the discharge area of the STE. The unimpacted sites had elevated abundances of *Wosearchaeia*, which were also detected previously in impacted areas of an STE at Mobile Bay (Gulf of Mexico). While a large proportion of prokaryotes were present in the entire intertidal area, meiofaunal community compositions were site specific and dominated by nematodes. Nematode communities of the high-water line differed distinctively from the other sites. Overall, our data indicates that the three domains of life display distinctly different adaptations when facing the same conditions within the STE. Therefore, distribution patterns of any domain can only be understood if all of them, together with basic environmental information are investigated in an integrated context.

Keywords: *Archaea*, bacteria, intertidal area, meiofauna, microbial diversity, North Sea, sandy beach, SGD

OPEN ACCESS

Edited by:
Ross Thompson,
University of Canberra, Australia

Reviewed by:
Guillaume Grosbois,
Université du Québec en Abitibi Témiscamingue, Canada
Daniele Kasper,
Federal University of Rio de Janeiro, Brazil

****Correspondence:***
Bert Engelen
engelen@icbm.de

Specialty section:
This article was submitted to Freshwater Science, a section of the journal Frontiers in Environmental Science

Received: *16 December 2020*
Accepted: *07 April 2021*
Published: *22 April 2021*

Citation:
Degenhardt J, Khodami S, Milke F, Waska H, Engelen B and Martinez Arbizu P (2021) The Three Domains of Life Within the Discharge Area of a Shallow Subterranean Estuary at a High Energy Beach. Front. Environ. Sci. 9:642098. doi: 10.3389/fenvs.2021.642098

INTRODUCTION

Sandy beaches are highly permeable, advection driven systems (Anschutz et al., 2009), receiving labile organic matter (OM), oxygen, sulfate (Huettel et al., 2014) and seasonally nitrate (Ahrens et al., 2020) by seawater infiltration. Therefore, beaches have been compared to bioreactors exhibiting high microbial activity, despite their relatively low OM content (Anschutz et al., 2009). An extreme example are high energy beaches, which are prone to strong physical forcing by waves and tides, enhancing the recharge of nutrients and substrates to deeper sediment depths. This increases the magnitude of exchange between sediments and the coastal ocean compared to less permeable sediments, or those with a lower energy input (Webster and Taylor, 1992; Reckhardt et al., 2015). Additionally, constant sediment reallocation prevents stable biogeochemical conditions, resulting in a weaker redox zonation than usually observed along the depth profile of marine sediments (Froelich et al., 1979).

Another process impacting the redox zonation of coastal sediments around the globe is submarine groundwater discharge (SGD) (Moore, 1996; Paerl, 1997; Santos et al., 2009; Rodellas et al., 2014; Anschutz et al., 2016; Cho et al., 2018). SGD introduces fresh meteoric groundwater as well as recirculated sea water into the marine sediments, lowering the salinity and introducing reduced chemical compounds like ammonium and dissolved iron (Moore et al., 2008; Kwon et al., 2014). These compounds are either re-oxidized along the flow path or discharged into the coastal ocean (Riedel et al., 2011; Reckhardt et al., 2015; Beck et al., 2017; Kim et al., 2017). The outflow marks the discharge area of the so called subterranean estuary (STE) which exhibits a horizontal redox zonation toward the low water line (Moore, 1999). The constant resupply of oxygen and labile OM from the ocean in combination with a steady supply of reduced chemicals by SGD creates niches for many microorganisms. Thus, mixing of terrestrial and marine constituents within the STE leads to elevated microbial activities (Anschutz et al., 2009; Gao et al., 2012; Charbonnier et al., 2013) and result in physiological diversity maxima in the oxic-anoxic transition zone (Hong et al., 2018).

Several microbiological studies have been conducted on sandy beaches from regional (Boehm et al., 2014) to global scales (Staley and Sadowsky, 2016), detecting a cosmopolitan core within the bacterial communities of sandy beaches. Site specific studies on bacterial diversity in sandy STE's reported contrasting findings mostly caused by differences in the physical energy input. On the one hand, STE's discharging at low energy beaches exhibit horizontal redox zonation with bacterial communities adapted to the different zones (McAllister et al., 2015). On the other hand, at high energy beaches, this zonation is constantly disrupted and thus pronounced weaker. Most likely, this physical reworking also overprints visible effects of SGD on the bacterial communities. In our previous study on the bacterial diversity at the high energy beach of Spiekeroog Island (Northern Germany), we have shown that these dynamics appear to result in bacterial communities of adapted generalists (Degenhardt et al., 2020).

Except for a recent study by Adyasari et al. (2020), almost all previous investigations focused on bacterial communities of sandy beaches and STEs, neglecting archaeal diversity. In the last decade, knowledge about archaeal diversity was greatly enhanced by cultivation independent techniques like single-amplified genomes (SAG) or metagenomics (Brochier-Armanet et al., 2011; Rinke et al., 2013). Ecological studies started to shed light on distribution patterns (Auguet et al., 2010; Hugoni et al., 2015; MacLeod et al., 2019), yet knowledge about the ecological roles of most *Archaea* remains scarce (Meng et al., 2014; Castelle et al., 2015). Aquatic *Archaea* are known from a wide variety of habitats like costal (Rios-Del Toro et al., 2018) and deep sea sediments (Lloyd et al., 2013), freshwater (Ortiz-Alvarez and Casamayor, 2016) and pelagic environments (Karner et al., 2001). In most benthic environments, they are less abundant than bacteria, yet their numbers seem to increase with sediment depth (Lipp et al., 2008). Physiologically, they are known for their role in processes like methanogenesis (Thauer et al., 2008) but also in ammonia oxidation (Könneke et al., 2005), anaerobic ammonia oxidation (Rios-Del Toro et al., 2018), or anaerobic oxidation of methane (Boetius et al., 2000). Their involvement in the nitrogen cycle and elevated abundances in oxygen minimum zones (Rios-Del Toro et al., 2018; Muck et al., 2019) might make them important players at the oxic-anoxic interface of STE's. Information on archaeal diversity of Spiekeroog beach will broaden the knowledge about their role in shaping biogeochemical processes within the STE and the intertidal area of a high energy beach.

Another often overlooked fraction of interstitial life are eukaryotes belonging to the so called meiofauna, which is one of the most diverse group of small organisms, unicellular protists and multicellular metazoans that live in aquatic sediments (Giere, 2009). Meiofauna is a collective name for organisms of 20 different phyla that pass through a 1 mm mesh sieve and are retained in a 32 μm sieve. Inhabiting various marine, brackish and freshwater environments (Higgins and Thiel, 1988; Giere, 2009), they are the most suitable candidates in terms of monitoring ecological changes (Zeppilli et al., 2014) and serve as indicators for environmental variabilities (Jessup et al., 2004; Nascimento et al., 2012; Bonaglia et al., 2014). Limited body size and mobility make those organisms very susceptible to changes in sediment and porewater biochemistry, which may influence their abundance and diversity (Kennedy and Jacoby, 1999). The majority of meiobenthic communities in most marine habitats consists of nematodes and harpacticoid copepods (Gallucci et al., 2012; Losi et al., 2013; Semprucci et al., 2015). Their communities are uniquely sensitive to temperature, pH, dissolved oxygen, redox potential and heavy metal content of the sediment matrix (Moreno et al., 2011; Vanaverbeke et al., 2011; Meadows et al., 2015). Thus, nematodes have been identified as indicators of environmental pollution and dynamic changes in marine systems (Losi et al., 2013; Semprucci et al., 2015). They were frequently reported by both, morphological and molecular studies, as the most abundant taxa among marine meiobenthos communities followed by harpacticoids (Huys et al., 1992; Karanovic and Cooper, 2012; Zeppilli et al., 2015; de Faria et al., 2018). Despite their importance, meiofauna were included only recently into ecosystem functioning investigations, due to difficulties arising from the small size of the examined

animals. This limits differentiation on the species level to a few highly skilled taxonomists (Huys, 1996). Furthermore, due to their high abundance and diversity, working through each sample is very time-consuming, making a high sample throughput difficult. Additionally, high-throughput sequencing techniques for meiofauna have only emerged in the past few years and lack behind on respective studies on prokaryotic diversity (Taberlet et al., 2012; Haenel et al., 2017).

As SGD shapes the physical environment by altering (i) grain size distribution of bottom sediments and (ii) altering the vertical position of redox and pH gradients, it affects the distribution of meiofauna within the sediments (Miller and Ullman, 2004; Zipperle and Reise, 2005). However, investigations of SGD-affected areas have shown variable community responses with regards to of diversity and abundance. Studies from the coast of France and Portugal e.g., found no impact of SGD on meiofaunal abundance (Ouisse et al., 2011), but enhanced metabolism (Migné et al., 2011) and increased diversity (Encarnação et al., 2013). Contrastingly, in a study from the Polish coast lower abundances were found in areas influenced by SGD as well as distinctively different communities between affected and unaffected sites (Kotwicki et al., 2014). In an investigation at the coast of Long Island, a lower diversity among nematode genera was detected at impacted sites compared to a generally higher diversity in areas unimpacted by SGD (Grzelak et al., 2018). Overall, these studies show that SGD does influence meiofaunal community structure, yet in different ways depending on the characteristics of the respective sites. However, all abovementioned studies from SGD affected areas were based on morphological investigations, while no molecular studies are available, yet.

In the present study, we attempt to cover the entire microbial diversity in the discharge area of a shallow STE and to unravel putative interactions between all three domains of life. The study site is located at Spiekeroog Island, which harbors a freshwater lens that fuels the STE. The discharge area at Spiekeroog beach has previously been subject of intensive multidisciplinary research (Beck et al., 2017; Waska et al., 2019b; Degenhardt et al., 2020; Grünenbaum et al., 2020a,b). Investigations on its hydrogeology, porewater geochemistry and bacterial diversity gave a solid insight into the coupling of benthic processes. The strongest gradients of porewater chemistry within the discharge area of the STE were found in cross-shore direction (Waska et al., 2019b). The whole discharge area of the beach was divided into multiple zones of pore water in- and exfiltration which were not fixed in position throughout the year. The high water line (HWL) and the low water line (LWL) were physico-chemically most distinct, likely due to relatively stable in- and exfiltrating conditions. The zones in between showed strong spatial and temporal heterogeneity, possibly due to extensive morphological changes of the beach, which in turn influenced their hydrochemistry (Waska et al., 2019b). Seasonal variations of seawater constituents were found to influence the pathways of bacterial organic matter degradation (Ahrens et al., 2020). During colder seasons, porewater conditions within the STE were predominantly oxic or nitrate reducing and shifted to manganese and iron reduction during warmer seasons. As a result, the discharge area changed from a dissolved inorganic nitrogen (DIN) sink in spring to a source in late summer. Bacterial communities within those sediments were shown to be highly uniform down to a depth of 1 m and over the whole intertidal area (Degenhardt et al., 2020). Since this was observable throughout the year, this assemblage has been dubbed the bacterial core community of the investigated sediments.

Based on these findings, we revisited Spiekeroog beach in March 2019 and sampled the same cross-shore transect as investigated previously (Waska et al., 2019b; Ahrens et al., 2020; Degenhardt et al., 2020), in order to fill the knowledge gaps on the entire microbial diversity. We hypothesize that (i) there is a large archaeal and meiofaunal core community and (ii) the conditions in the discharge area of the STE favor the presence of those *Archaea* involved in nitrogen cycling. We further hypothesize that (iii) the harsh high-energy conditions at Spiekeroog beach result in a nematode dominated community over a copepod dominated community. In general, our investigation will enhance the understanding of correlations between all three microbial domains within the intertidal area.

METHODS

Site Description

The Island of Spiekeroog is part of the East Frisian Barrier Island chain located in the German North Sea, with the Wadden Sea in its back barrier region. The island harbors a freshwater lens, which is formed by rain and separated from the surrounding sea water by a density gradient. The freshwater lens partially discharges through a subterranean estuary within the intertidal area along the northern shore of the island. This intertidal area is located on a sandy, mesotidal, high energy beach with a runnel-ridge system. A schematic of the investigated area is shown in the supplements (**Supplementary Figure 1**). The runnel-ridge system is not stationary but frequently relocated within the intertidal area due to wind and wave action. Areas above the mean sea-level are characterized as sea-water infiltration zones, while areas below the sea level are net discharge areas of the STE (Grünenbaum et al., 2020a). Due to the aforementioned strong morphodynamics, these in- and exfiltration areas are not static and the discharge is more diffusive than observed for other STEs. Detailed descriptions of hydrogeochemistry (Beck et al., 2017; Waska et al., 2019b; Grünenbaum et al., 2020a,b), geochemistry (Ahrens et al., 2020) and bacterial diversity (Degenhardt et al., 2020) can be found in previous studies investigating the Spiekeroog STE.

Sediment Sampling

Samples were collected in March 2019 at the North beach of Spiekeroog Island. Sediment cores were recovered with aluminum core liners (80 mm diameter) along a transect between the high- and low water line. Four cores were taken along the transect at the specific topographical features: the HWL, runnel, ridge and LWL. The cores were subsampled for prokaryotic diversity analyses at 0–2, 10–12, 30–32, 50–52, and 100–102 cm depth using sterile cut-off syringes. The different depths will be

referred hereafter as 0, 10, 30, 50, and 100 cm. Samples were stored frozen at −20°C until further processing. Meiofauna was sampled individually by transferring sediments of the upper 10 cm taken in close vicinity of the long sediment cores into plastic containers. Five replicates were fixed with ethanol, another five were fixed with a solution containing dimethyl sulfoxide, disodium EDTA, and saturated NaCl (DESS) (Yoder et al., 2006). The ethanol fixed samples were re-fixed after 12 h and all samples were stored at 4°C until further processing.

Porewater samples were obtained by using stainless steel push-point samplers and pre-rinsed polyethylene syringes, and were processed according to Ahrens et al. (2020) for NO_3^-, NO_2^-, NH_4^+, Fe, and Si. PO_4^{3-} was determined photometrically, following the methods of Itaya and Ui (1966) for samples with concentrations below 2.1 μM and Laskov et al. (2007) for samples exceeding 2.1 μM PO_4^{3-}. DOC samples were treated and processed according to Waska et al. (2019a).

In order to extract the meiofauna, sediment samples were sieved through a 32 μm sieve and centrifuged using Kaolin and Levasil (Kurt Obermeier GmbH & Co., KG, Bad Berleburg, Germany) following McIntyre and Warwick (1984). A total number of 150 nematode specimens (when available) were sorted out from each meiofauna sample in one separate vial for each sample. In case of samples with less than 150 specimens, all nematodes were taken into account. The remaining meiofauna was filtered using glass filters (1.6 μm particle size). Ethanol was used to wash the extracted meiofauna from DESS residues. The filters (containing meiofauna) were dried using a speed-vacuum system for 1 h at 45°C and stored in a sterile 1.5 ml Eppendorf mini-tube for DNA extraction.

DNA-Extraction, Amplification, and Sequencing

Genomic DNA for prokaryotic samples was extracted by using a modified phenol-chloroform protocol (Gabor et al., 2003; Lueders et al., 2004). A one step PCR attaching Illumina adaptors and barcodes was performed in 50 μl setups. The master mix contained 34.4 μl PCR grade water, 10 μl Phusion-Polymerase Buffer, 0.75 μl (10 pmol/μl) of each primer published by Parada et al. (2016) 0.2 μL $MgCl_2$ (50 mM), 1 μl BSA (25 mg/ml), 0.4 μl dNTPs (10 mM each) and 0.5 μl Phusion Polymerase (1 U/μl) per reaction. Reactions were performed in 96 well plates (Eppendorf) using 2 μl template. Cycler settings included an activation step at 98°C for 1 min, followed by 32 cycles of denaturation at 98°C or 45 s, annealing at 50°C for 45 s, elongation at 72°C for 30 s and a final elongation step at 72°C for 5 min.

DNA extraction from meiofauna and nematode samples was carried out using the E.Z.N.A.® Mollusc DNA Kit (Omega BIO-TEK) following their protocol. The genomic DNA was eluted in 100 μl of nuclease-free water for each library (sample). Two PCRs were performed to amplify the V1 and V2 hypervariable regions of the 18S rRNA from each meiofauna and nematode library and bind the Illumina Unique Dual Nextera XT Indexes and compatible adapters. The first PCR was performed using the SSU universal primers F04 and R22 (Blaxter et al., 1998) tagged by the first part of the Illumina adapters in total volume of 20 μl containing 10 μl of Phusion Green Hot Start II High-Fidelity PCR Master Mix (ThermoFisher), 0.5 μl of each primer (10 pmol/μl), 2 μl of genomic DNA and 7 μl of molecular grade water. Cycler settings for the first PCR encompassed an initial denaturation step at 98°C for 2 min, 20 cycles of denaturation at 98°C for 15 s, annealing at 60°C for 30 s, elongation at 72°C for 30 s and a final elongation at 72°C for 2 min. Five microliter of the first PCR products were purified using 2 μl of ExoSAP-IT PCR Product Cleanup Reagent (ThermoFisher). A two-step PCR was carried out to bind the Nextera XT Indexes and Illumina adapter overhang according to Illumina 16S Metagenomic Sequencing Library Preparation guide (15044223Rev.B), using 7 μl of DNA template (purified first PCR product), 10 μl of Phusion Green Hot Start II High-Fidelity PCR Master Mix, 1 μl of molecular grade water and 1 μl of each index primers from Nextera XT Indexes. The cycler setting contained an initial denaturation step at 98°C for 2 min, 15 cycles of denaturation at 98°C for 15 s, annealing and elongation at 72°C for 35 s, and a final elongation at 72°C for 2 min. The PCR products were checked on a 1.5% agarose gel containing 1% GelRed to check the amplification and target fragment length. Two to ten microliter of the 2nd PCR products have been pooled into one Eppendorf tube and purified using AMPure XP Beads for PCR Purification (Beckman Coulter) in the volume of 60%. The pooled library was denatured and 20% PhiX control was added before performing a test run using the MiSeq Reagent Nanokit v2 (150-cycles paired end), and a final sequencing run with the MiSeq Reagent kit v3 (300-cycles paired end). Sequencing was performed at the DZMB Metabarcoding lab in Wilhelmshaven (Germany) on an Illumina MiSeq platform. The sequences were deposited at the European Nucleotide Archive under the accession number PRJEB42988.

Bioinformatics and Statistical Analysis of Prokaryotic Sequence Data

Prokaryotic 16S rRNA gene sequences were processed according to the pipeline of Yeh et al. (2019). First, primers were trimmed from reads using cutadapt and all reads missing forward or reverse primer sequences were discarded. The error threshold within the primer sequence was set to 20% to account for mismatches to the primers, primer sequences including higher error rates were discarded. Trimmed reads were matched against a curated 16S/18S database originating from SILVA132 (Quast et al., 2013) and PR2 (Guillou et al., 2013). Eukaryotic sequences were discarded.

All 16S rRNA gene sequences were further processed using QIIME2 (Bolyen et al., 2019) and its q2-dada2 plugin. Low quality ends of the reads were removed and denoised using DADA2 (Callahan et al., 2016). After removal of chimeric reads, prokaryotic sequences were classified using the classify-sklearn plugin of QIIME2 against a curated SILVA132 database, which was fitted to the V4-V5 primer region. Plastidal sequences were reclassified using the PhytoRef database (Decelle et al., 2015). Finally, count tables were exported from QIIME for further statistical analysis. To account for erroneous sequences, amplicon sequence variants (ASVs) were filtered according to Milici et al. (2016): Only those ASVs that had an abundance of >0.001%

within the complete dataset and (i) were present in relative abundance of >1% in at least one sample or (ii) had an abundance of >0.1% within a sample in at least 2% of all samples or (iii) were present in >5% of all samples in any abundance were kept. This strict abundance filter was mainly used because DADA2 retained lots of very rare sequences that inflated the amount of ASVs found in each sample. All further analyses were based on this dataset. Samples were rarefied to 14,885 counts for alpha-diversity analyses, which was the lowest count number found among all samples. Barplots were drawn with an abundance threshold of 0.5% by which groups were sorted into "others." Principal coordinate analysis (PCoA) was performed using Bray-Curtis transformed community distances. Venn-Diagrams were used to show the separation of ASV richness between locations. All analyses were done using R statistical software (R Core Team, 2019) and its package vegan (Oksanen et al., 2019).

Bioinformatics and Statistical Analysis of Eukaryotic Sequence Data

The NGS reads were demultiplexed by indexes and trimmed from the sequencing primers prior to analyses using BBmap. The DADA2 pipeline (Callahan et al., 2016), a divisive amplicon de-noising algorithm for correcting Illumina errors, was used to analyze the sequence reads from meiofauna and nematode libraries in which the Illumina reads were de-noised based on the error rate of the data. They were filtered by length and quality scores, chimera detected and de-replicated to high resolution ASVs. The ASVs were further processed using a custom script (SGN Metabarcoding pipeline) where all sequences shorter than 320 bp were eliminated and each ASV was blasted against the database NCBI in which the 10 best blast hits were retrieved and pooled with our own 18S reference library (available from DNA barcode archive of the DZMB institute). This merged dataset was used as final blast database to assign the best and closest taxonomical assignment to each ASV. The ASV table containing taxonomical assignments, percentage identities, query coverage and number of reads per library were analyzed using a custom post-processing script Dada2pp implemented in the R statistical software and by using the vegan package for eliminating contaminations, short or non-target sequences, determining target meiofaunal groups and detailed diversity analyses and comparisons. Above mentioned analyses were performed on nematode sequence libraries at the genus level.

RESULTS

A total of 20 sediment samples from four designated stations of the intertidal area of the North beach of Spiekeroog Island were analyzed to identify the bacterial and archaeal diversity by next generation sequencing (NGS). Those were taken in cross-shore direction at the HWL, the runnel, ridge and the LWL at five different depths (0, 10, 30, 50, and 100 cm). Additionally, shorter cores (0–10 cm) were taken in five replicates at each location to investigate meiofaunal diversity. As microscopic investigation revealed the dominance of nematodes within the meiofaunal community, those were analyzed separately.

Porewater Geochemistry of the Beach

The discharge areas of the Spiekeroog beach STE were marked by brackish salinities at the ridge and the LWL (**Figure 1**). This was complemented by elevated concentrations in total dissolved nitrogen (TDN), NH_4^+, PO_4^{3-}, Si and Mn at the LWL in comparison to the other sampling sites. Additionally, porewaters from deeper sediment depths of the ridge (30 and 100 cm) had elevated concentrations of Fe(II), indicating reducing conditions. Porewaters from the LWL and the HWL were generally low in Fe(II), as well as in NO_3^- and NO_2^-. The shallow porewaters from the runnel (0 and 10 cm) were characterized by higher amounts of NO_3^- and slightly elevated concentrations of DOC in comparison to the other sites. This can be interpreted as a sign for infiltrating conditions. Since some sediments were too dry to obtain porewaters for the respective analyses, they were marked by gray bars in the heatmap (**Figure 1**).

Composition of the Sequence Data Set

Sequencing of prokaryote samples resulted in a total of 3,079,547 reads, recovering a total diversity of 13,568 different ASVs. After applying the abundance filter, the majority of 2,967,880 reads was left representing a final diversity of 6944 ASVs within the dataset. Samples were deeply sequenced with a mean of 148,394 reads per sample. Amplicon sequencing of the V1 and V2 hypervariable region of 18S rRNA gene yielded a total of 3,537,703 reads and 1,263 ASVs belonging to 50 eukaryote groups based on NCBI taxonomic assignment. After filtering a total of 3,408,572 reads and 846 ASVs were classified as 11 target meiofaunal groups.

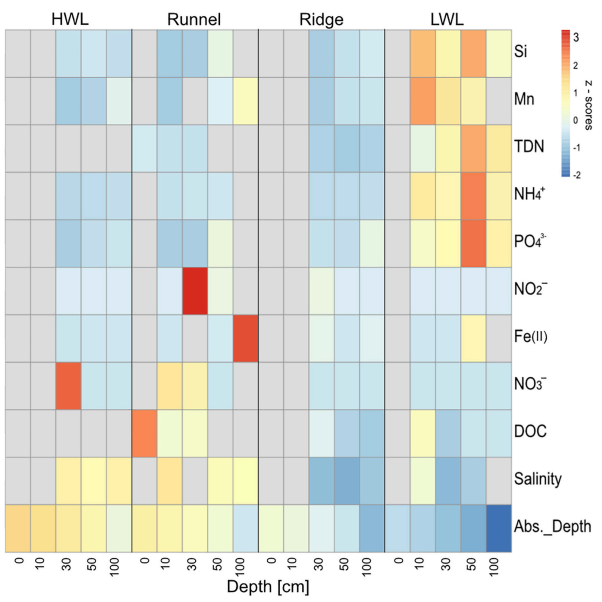


FIGURE 1 | Normalized porewater constituents (z scores) across the transect. Colder colors indicate lower, warmer colors higher z scores, respectively. Gray bars indicate missing values caused by porewater scarcity. depth, absolute depth above or below sea level; DOC, dissolved organic carbon; TDN, total dissolved nitrogen.

From the nematode samples, 18 NGS libraries yielded a total of 2,214,455 reads and 1,455 ASVs where 1,680,256 reads and 255 ASVs were detected as nematode encompassing 43 different species and 25 genera. Two libraries were excluded from the nematode dataset as they did not contain enough sequencing reads.

Microbial Diversity Patterns

The presence and absence of ASVs at the different stations were compared to identify horizontal patterns among prokaryotic and eukaryotic community compositions along the investigated transect (**Figure 2**). For prokaryotes, a large proportion of ASVs was shared among all stations (14%), which is in accordance with the previously detected bacterial core community (Degenhardt et al., 2020). Yet, every station still harbored a number of site specific ASVs (10–16%), which was largest among the HWL samples (16%). In contrast, meiofaunal communities only shared a small amount of ASVs among all stations (3%) and large proportions of site specific ASVs at every station. The highest number of unique ASVs was detected in the runnel (26%) followed by the ridge (24%), the LWL (16%) and the HWL (15%), respectively. In comparison to all other sites, the percentage of ASVs shared between runnel and ridge was comparably high (6%).

Principle coordinate analysis (PCoA) distance matrices were used to compare community compositions across the intertidal area (**Figure 3**). The prokaryotic community structures differed between the individual sampling sites. Especially, all samples taken at the runnel clustered apart from the other sites yet were quite dissimilar among each other. In contrast, the LWL and the ridge communities were highly similar. The HWL community exhibited large differences with depth, while all other sites showed no coherent vertical patterns. The eukaryotic communities also showed a strong site-specific ordination within the PCoA. Here, all communities of the LWL replicates were rather similar, which was also the case for the communities of the runnel replicates, yet they were forming groups clearly separated from the rest. Both, the ridge and HWL communities showed a higher scatter among the replicates.

Prokaryotic Community Composition

The dominant part of the prokaryotic community was composed of 11 different bacterial phyla. Yet, 25–40% of the community were attributed to rare taxa, here summarized as "others" (**Figure 4A**). Those include most *Archaea* due to their low abundances within the dataset. Summarized, archaeal relative abundances reached 1–4%. The dominant phyla exhibiting by far the largest amount of internal diversity, were the *Bacteroidetes* and the *Proteobacteria*, represented by 12 genera, each. Within the *Proteobacteria*, most ASVs were related to *Deltaproteobacteria*, indicating sub- to anoxic conditions. The only other phyla represented by more than one genus were the *Acidobacteria* and *Planctomycetes*, represented by two genera, each. The other bacterial phyla detected were *Actinobacteria*, *Calditrichaeota*, *Gemmatimonadetes*, *Kiritimatiellaeota*, *Latescibacteria,* and *Nitrospirae*. The only archaeal phylum detected with an abundance above our filter criteria were *Thaumarchaeota* of the family *Nitrosopumilaceae*. Differences between the sampling sites could be explained by varying abundances of individual taxa. The HWL differed mostly due to higher relative abundances of *Bacteroidetes*, which additionally increased in abundance with depth. This increase was attributed to the genera *Muriicola*, *Portibacter* and unknown members of the *Rhodotermaceae* and *Saprospiraceae*. These genera were also detected at the other sites, but in lower relative abundances. The distinct community composition of the runnel samples can be attributed to increased relative abundances of members of the *Proteobacteria* and *Sediminicola* (*Bacteriodetes*).

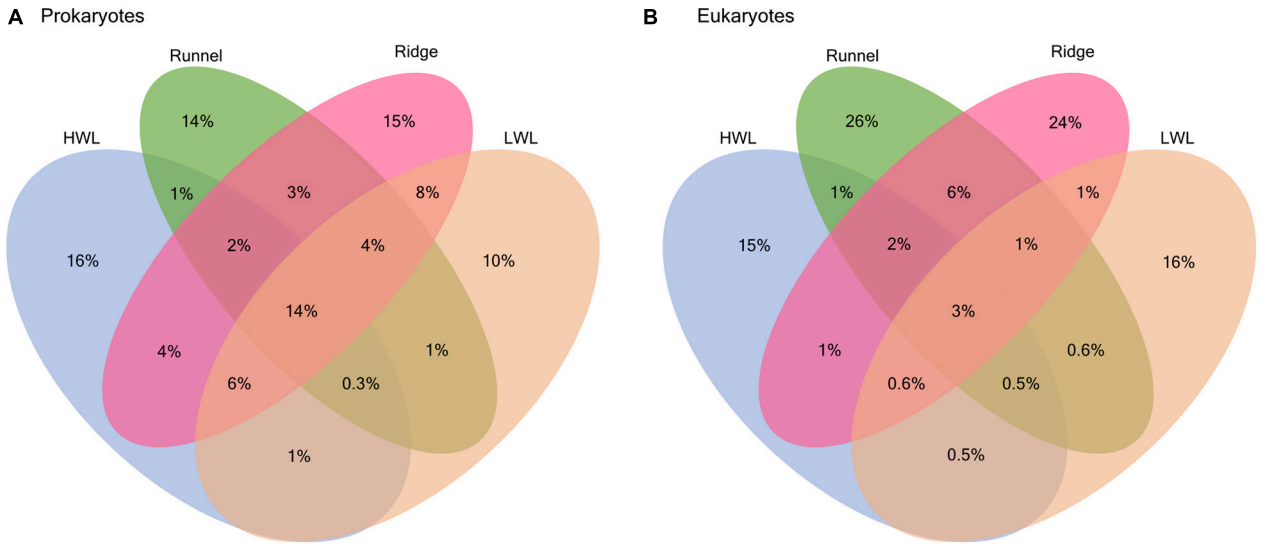


FIGURE 2 | Venn diagrams showing the percentage of shared ASVs between different stations for **(A)** prokaryotic and **(B)** eukaryotic communities.

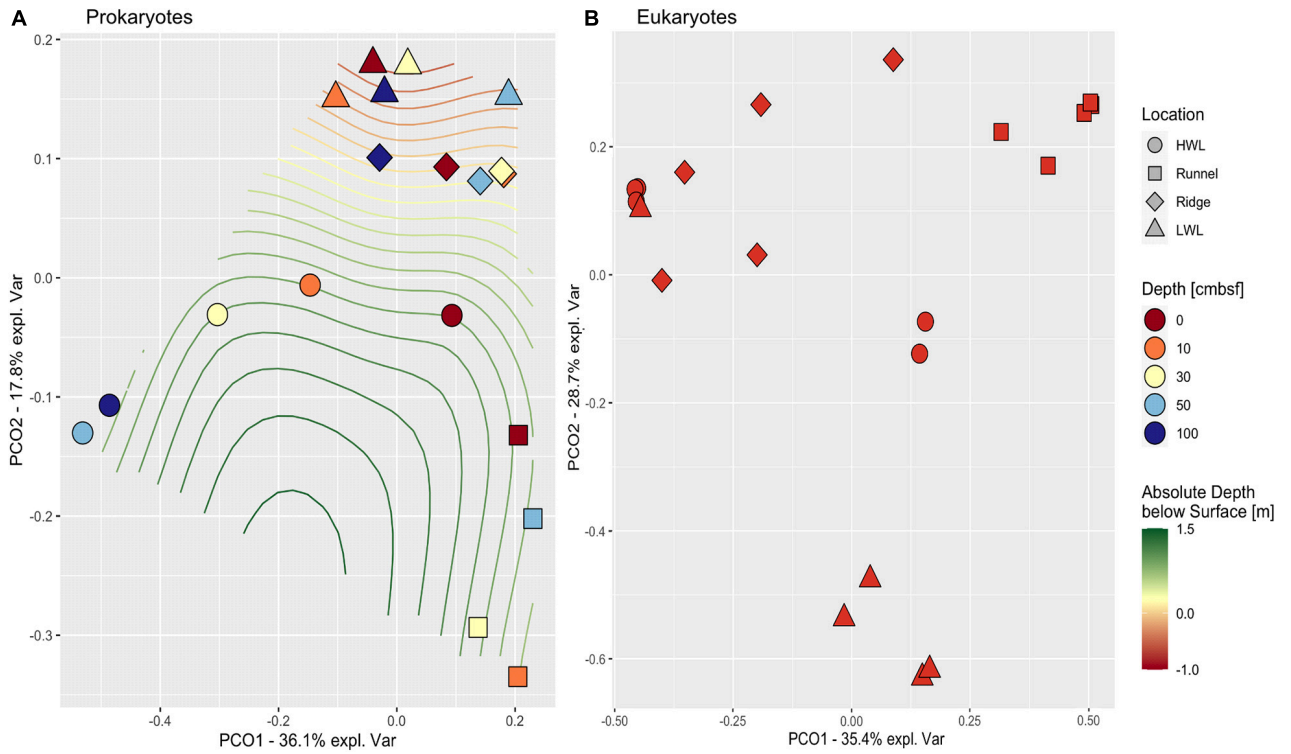


FIGURE 3 | PCoA of prokaryotic **(A)** and eukaryotic **(B)** communities. The PCoA plots depict the similarities between samples based on community composition comparing the four locations (symbols) and depths (colors). Absolute depth above or below sea level is indicated by isoclines. Depth is showed in centimeters below sea floor (cmbsf).

Surprisingly, most members of this class were represented by ASVs of unknown genera with the exceptions of *Woseia* and *Cupriavidus*. The latter was present in high relative abundances, which was unexpected since that genus is not typically found in marine sediments. The community composition of the LWL and the ridge samples appeared to be an intermediate version of the two other sites.

Despite their low relative abundances, the intra-archaeal diversity could be unraveled, due to deep sequencing (**Figure 4B**). The community was dominated by ASVs related to unknown *Nitrosopumilaceae*, with relative abundances between 60 and 80% of all detected *Archaea*. The *Woesearchaeia*, represented by *Candidatus Stazkawiczbacteria* and unknown *Wosearchaeia*, were far less abundant. The phyla *Bathyarchaeota* and *Odinarchaeota* were also detected in most samples in relatively low abundances. The amount of completely unknown archaeal ASVs or those grouped into "others" was surprisingly low with about 5%, only. Relative abundances of unknown *Wosearchaeia* were higher at the HWL and runnel (infiltration areas) than at the LWL and Ridge (exfiltration area). Additionally, they were increasing with depth at the HWL. The shallower depths of the HWL as well as the runnel and Ridge sites showed elevated abundances of unknown *Bathyarchaeia*. The distribution of *Odinarchaeia* was patchy with elevated relative abundances at the Ridge.

Eukaryotic Community Composition

A total number of 10 meiofaunal groups was detected in this study comprising Nematoda, Crustacea, Platyhelminthes, Annelida, Gastrotricha, Chaetognatha, Mollusca, Bryozoa, Tardigrada and Nemertea (**Figure 5A**; rare taxa are categorized as others). Considering the diversity and relative number of ASVs per taxon (**Figure 5A**), meiofaunal composition differed greatly among the studied sites. In general, the HWL appeared to be the least diverse site. Interestingly, two of the HWL replicates were dominated by Annelida, while with nematodes being the most abundant taxa in the other three replicates. While all replicates of the runnel were dominated by the genus *Archiola* de Beauchamp, 1910, four replicates of the LWL showed a high relative abundance of *Nematoplana*, 1938, both Platyhelminthes. In contrast, the ridge was again dominated by nematodes, with two replicates also showing increased relative abundances of Platyhelminthes.

Detailed community analysis of the relative number of picked nematode ASVs (**Figure 5B**) showed certain differences among the HWL and LWL compared to the runnel and ridge at the genus level. All HWL replicates and three LWL samples revealed a high nematode diversity with the most dominant genera being *Xyala* Cobb, 1920 or *Omicronema* Cobb, 1920 followed by *Oxyonchus* Filipjev, 1918 and *Neochromadora* Micoletzky, 1924. All ridge samples showed a low nematode diversity at

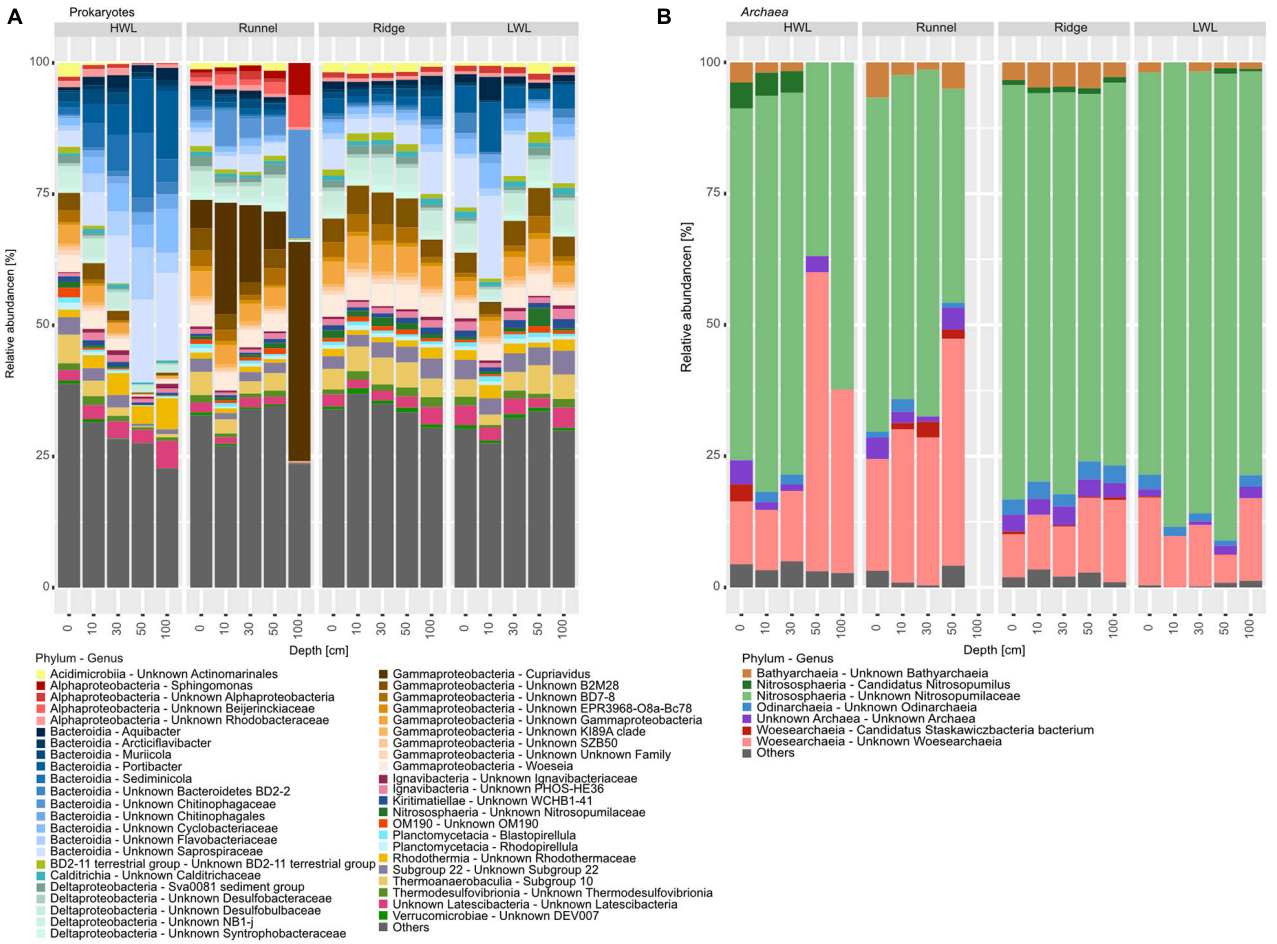


FIGURE 4 | Barplots of prokaryotic communities along the transect depicted on phylum and genus level. **(A)** Shows total prokaryotic diversity, while **(B)** zooms into the *Archaeal* diversity, due to their low relative abundances. Taxa below the abundance threshold were summarized as "others."

genus level with 4–6 genera present in each library, greatly dominated by *Enoplolaimus* de Man, 1893. The runnel stations, however, were represented by a maximum of two nematode genera in each replicate, being *Enoplolaimus* and *Xyala* within three replicates *Neochromadora* and *Daptonema* Cobb, 1920 in one of them. In general, a low nematode diversity and a prevalence of specimens of the genus *Enoplolaimus* may indicate their successful adaptation to this habitat.

DISCUSSION

Adaptation of Prokaryotic Communities to the Effect of SGD

The prokaryotic community composition within the exfiltration areas of the STE was more evenly distributed compared to the seawater infiltration sites of the beach. Furthermore, the archaeal community at the exfiltration sites was dominated by members the ammonia oxidizing *Nitrosopumilaceae*, which can be interpreted as an effect of increased ammonium supply through the STE. In our previous investigation on the same cross-shore transect, we described a dominant bacterial core community across all sites, depths and seasons, which was disrupted by a subsurface bloom during spring (Degenhardt et al., 2020). In the current study, we could confirm the presence of a prokaryotic core community, but in a weaker pronunciation. Surprisingly, distinctive communities were observed at every site with almost equal proportions. This might be due to different environmental conditions such as changing beach topographies and a stronger impact of SGD, reflected by distinctively lower salinities in comparison to those measured in our previous sampling campaigns (Waska et al., 2019b; Ahrens et al., 2020; Degenhardt et al., 2020). Furthermore, the chosen sequencing approach allowed to simultaneously investigate bacterial and archaeal diversity (Parada et al., 2016), yet direct comparisons with our previous findings might not be valid.

Due to the effects of SGD, environmental conditions across the intertidal area showed a drop in salinity at the ridge and LWL compared to the HWL and runnel. Additionally, enhanced concentrations of reduced compounds clearly mark these two stations as discharge areas of the STE. This is

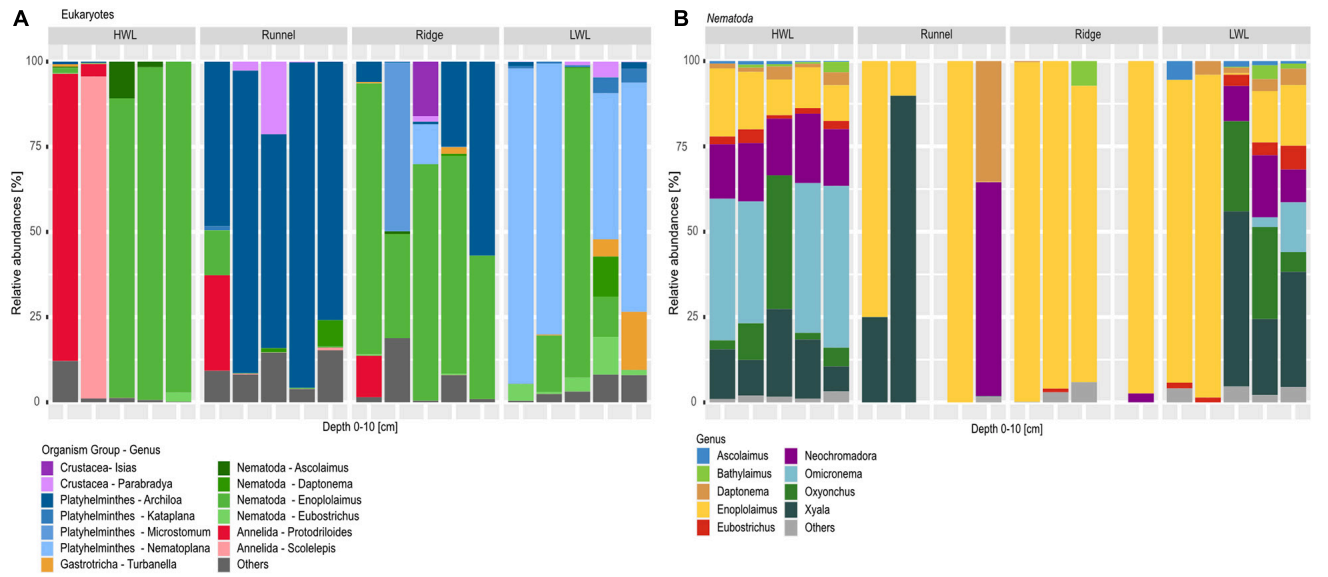


FIGURE 5 | Barplots of eukaryotic communities along the transect depicted on phylum and genus level. **(A)** Shows total meiofauna diversity, while **(B)** zooms into nematode diversity, due to their high relative abundances within the dataset and during morphological investigation. Taxa below the abundance threshold were summarized as "others." One replicate from the runneland Ridge were excluded from the nematode libraries analyses due to low numbers of reads.

reflected in the prokaryotic community structures, exhibiting similarities between the ridge and LWL communities were more similar to each other, despite differences over all sites. In our preceding study we could not detect an adaptation of the bacterial community to the effects of SGD, concluding that those were overprinted by the high energy conditions of Spiekeroog beach. Since the discharge area of the STE is chemically much clearer defined in the present study, its effect may previously have been underestimated (Waska et al., 2019b; Degenhardt et al., 2020). Instead of being negligible due to being overprinted, SGD might be an additional factor in forming stable and diverse communities. The significance of this effect could vary depending on differences in time scales for physical disturbances, porewater flowpaths, and community adaptations.

All detected bacterial genera have originally been reported to thrive in marine sediments, except for *Cupriavidus*, which reached high relative abundances within the runnel samples. Isolates of this genus are highly versatile and were cultured from different habitats, such as soils (Cuadrado et al., 2010) plants (Platero et al., 2016), anthropogenic environments (Mergeay, 2015), but also from freshwater sediments (Qian et al., 2010; Nguyen and Lee, 2014). Since the salinity at the runnel was clearly marine, a possible explanation for their high relative abundance could be the detection of an uncultured marine representative of this genus. Environmental disturbances like the burial of plant material by winter storms might be an alternative explanation for their occurrence. The second genus that distinguished the prokaryotic community of the runnel from the other sites of the transect was *Sediminicola*. This bacterium is a facultative anaerobe, capable of nitrate reduction and known from coastal and deep sea sediments (Khan et al., 2006). The HWL community differed from the other sites by high relative abundances of *Muriicola* (Kahng et al., 2010) and *Portibacter* (Yoon et al., 2012) which are both aerobes, with *Muriicola* also being capable of nitrate reduction. The common features of both sites, the HWL and runnel, are a higher elevation above sea-level and higher salinity values, indicating marine conditions, which are typically more oxygenated. These characteristics have been described for those sites at Spiekeroog beach (Waska et al., 2019b; Ahrens et al., 2020; Degenhardt et al., 2020). The dominant genera found at the HWL and runnel could also be detected at the ridge and LWL, yet in lower relative abundances. Overall, the communities of the latter sites, located in the discharge area of the STE, showed a higher evenness in the relative abundances of the different taxa.

During our previous investigation, we detected increased relative abundances of members of the *Bacteroidetes* (*Gillisia*) and *Firmicutes* (*Planococcus* and *Planomicrobium*) at the same month and sampling sites, which we described as a "subsurface bloom." In the current investigation, members of the *Firmicutes* could only be detected in relative abundances ranging from 0.1 to 0.2%, only. While we did not detect the genus *Gilisia* in high numbers, other *Bacteroidetes* were present in every sample and elevated relative abundances at the HWL. Known relatives of the genera with increased abundances are aerobes, capable of nitrate reduction. In our preceding study we attributed the "subsurface bloom" to elevated concentrations and penetration depths of oxygenated compounds like nitrate. As these conditions were not found during this sampling campaign, the right settings for a bloom might not have been present. We conclude that we either sampled the same month but under different geochemical conditions, or that we previously

sampled an irregular, rather than a regularly occurring event (Degenhardt et al., 2020).

Adaptation of Archaeal Communities

Within the archaeal community, cross-shore differences appeared as a decrease in relative abundances of *Wosearchaeia* and an increase of *Nitrosopumilaceae*. The dominance of *Nitrosopumilaceae* within the discharge area of the STE is very likely related to increased ammonium concentrations, as members of this phylum are known for ammonia oxidation (Nakagawa and Stahl, 2013; Shafiee et al., 2019). Thus, *Nitrosopumilus* might outcompete other archaea when high ammonium concentrations are present. On the other hand, *Wosearchaeia* are known for having very small genomes and a symbiotic or fermentation based lifestyle (Castelle et al., 2015). This might be beneficial at high energy beaches a steady resupply of seawater constituents and metabolites, explaining why they are the second most abundant archaea at Spiekeroog beach. Especially in the infiltration zones, this constant resupply might foster competitive advantages they may have due to their streamlined genomes. Another archaeal group observed within most of our samples, but in low abundances are the *Bathyarchaeia*. They are known to be globally distributed generalists, which are often found in anoxic sediments (Zhou et al., 2018). Additionally, a rather enigmatic archaeal taxon, the *Odinarchaeia*, were detected in very low, but increased abundances at the ridge. Since not much is known about their lifestyle, their role within the discharge area of the STE remains to be investigated.

In general, our results on the diversity and relative abundances of *Archaea* at the Spiekeroog STE are in accordance with findings by Adyasari et al. (2020), the only study that also investigated archaeal diversity within an STE at several geochemically different discharge areas. Within the porewaters of two SGD hotspots in Mobile Bay (Gulf of Mexico), the authors found different archaeal communities with varying abundances, depending on the investigated site. At an anoxic site, the archaeal community was dominated by *Wosearchaeia* and constituted 4–8% of the microbial community. Another discharge area within that study was more similar to our sampling site. It was characterized by coarse sand and less reducing conditions, caused by higher hydraulic conductivity. Under these conditions, the *Archaea* made up 1% of the microbial community and were dominated by ammonia oxidizing *Thaumarchaea,* which fits to our observations.

Meiofaunal Communities Are Structured Site-Specifically

In contrast to the prokaryotes, meiofauna exhibited almost no core community across all sampling sites, but large site-specific assemblages and a high spatial distribution between the replicates. A possible explanation for this could be their narrower tolerance range for different environmental conditions in comparison to prokaryotes, such as oxygen concentrations and salinity. Additionally, being much more mobile than prokaryotes, they possibly migrate toward preferred conditions, forming site specific communities.

We detected a large variance in community composition between replicates taken at the respective sites. However, cross shore differences could be observed between the HWL and the other sites due to the distinct differences in the community compositions. The relative number of ASVs per group are indicative for a high abundance of nematodes in three replicates from the HWL, whereas the runnel was mainly dominated by platyhelminthes. The LWL and ridge, however, showed a difference within the meiofaunal community composition of the two other sites, where either platyhelminthes or nematodes were the most abundant taxa in the different replicates. These results are in agreement with the study of Grzelak et al. (2018), in which the diversity of nematodes was significantly higher at the saline HWL at the coast of Long Island compared to the areas with lower salinities. Although the LWL and ridge (as the discharge area of the STE) showed similar prokaryotic communities, this effect is not pronounced for the investigated eukaryotes. Different composition of meiofaunal communities within SGD affected and non-affected areas may be an indication of a non-adaptation toward the effect of SGD. The presence of crustaceans (mainly copepods) was only perceptible in the runnel replicates. Also, morphological observations did not recognize many copepod specimens within the samples. This may also be an indication of their seasonal variabilities as the sampling took place in early spring. Seasonal variations of seawater alter the organic matter input and the associated degradation by bacteria. Therefore, the STE areas are lower in the amount of inorganic nitrogen in early spring compared to late summer (Ahrens et al., 2020) which could explain the overall low abundance and diversity of harpacticoid copepods in our study.

The overwhelming majority of meiofauna detected during morphological investigation were nematodes. Thus, the relatively high proportions of reads belonging to other groups such as annelids and platyhelminthes may be caused by the higher biomass of those taxa, the presence of their appendages or environmental DNA. Although the abundance of certain meiofaunal groups such as nematodes was higher at the HWL, the relative diversity was greater in the runnel, ridge and LWL samples. This was caused by the presence of rare taxa such as marine Tardigrada, Chaetognatha, Nemertea and Bryozoa (included in "others" in **Figure 5**) which were not detected at the HWL. This was probably due to the lower salinity that turns the environmental condition intolerable for the addressed taxa. In general, we detected different meiofaunal community compositions between all four study sites. This is in agreement with Kotwicki et al. (2014), indicating the strong effects of environmental conditions on meiofaunal communities even within SGD-impacted areas of high-energy beaches.

In contrast to the overall meiofaunal diversity, nematode diversity did not follow the described cross-shore trend. At the HWL and LWL, the nematode communities were much more diverse in comparison to the runnel and ridge, where the dominating genera were *Enoplolaimus* and *Xyala*. We detected *Xyala* in high relative abundance at every site, implying an

adaptation to the conditions of the intertidal area. When investigating three beaches impacted by SGD at the Long Island peninsula (California, United States), at every station Grzelak et al. (2018) also detected Xyalidae Chitwood, 1951, which includes the genera *Xyala* and *Theristus* Bastian, 1865. Furthermore, the authors described the presence of *Enoplolaimus* sp., an omnitrophic predatory genus, which was distinctive for areas unaffected by SGD at one of the beaches studied. Yet, it was also found at impacted sites of another beach they investigated.

In our study, we detected *Enoplolaimus* at the LWL, the discharge area of the STE, with clearly brackish salinities. Thus, SGD alone may not affect the presence of this genus. This is in accordance to another study on nematode diversity within the intertidal area of two sandy beaches in Italy and Poland (Gheskiere et al., 2005). Furthermore, in our study, *Enoplolaimus* ASVs showed high relative abundances at every zone of the beach, agreeing with Gheskiere et al. (2005) where 7–10% of the detected nematodes were *Enoplolaimus,* with a more consistent presence at the beach exhibiting higher energy input. Since Spiekeroog beach is characterized by even stronger physical forcing, the high relative abundances of *Enoplolaimus* ASVs in our dataset could indicate an adaptation to high energy environments. Furthermore, we detected a lower nematode diversity at the runnel and ridge sites of Spiekeroog beach. Our findigs again fit to those of Gheskiere et al. (2005), also indicating a lower nematode diversity and evenness at the investigated swash and breaker zones, which are comparable to our runnel and ridge sites. A possible explanation for this might be the greater physical stress due to the high wave action in these zones. In both, our and their study, a maximum of nematode diversity was detected at the HWL. This is probably caused by the presence of taxa which are related to more terrestrial environments within the transition zone between the terrestrial and the marine environment.

Genera typical for brackish conditions like *Bathylaimus* Cobb, 1894 and *Tryploides* de Man, 1886 (Gheskiere et al., 2005) were also detected at the HWL and LWL of Spiekeroog beach with low relative abundances (both genera are marked as "others" in **Figure 5**). At the same stations, we also found *Microlaimus* de Man, 1880 (categorized as "others" in **Figure 5**) which have been found exclusively at sites unaffected or affected by SGD, respectively (Grzelak et al., 2018). While the flowpath and exfiltration zones of the Spiekeroog STE are usually patchy and heterogeneous, beaches investigated by Grzelak et al. (2018) had distinct areas affected or unaffected by SGD. Yet, especially during our campaign, the LWL showed a reliable chemical signal of SGD and brackish salinities, probably caused by a beach topography which was unusually stable for the stormy winter/spring season.

Potential Influence of Nematode Diversity on Prokaryotic Diversity

We found that nematode communities significantly correlated with changes in bacterial communities, while the overall meiofauna did not. However, due to the different sampling strategies for prokaryote and eukaryote diversity analyses, a statistically valid testing could not be applied. Since only a few studies have targeted community level interactions between these domains of life and none of them investigated the specific role of STE's, our study could be a starting point for this kind of investigations. Co-occurrences between bacteria and nematodes e.g., were detected in submarine deep-sea canyons and correlated to physiological needs of the respective bacterial taxa (Rzeznik-Orignac et al., 2018). For example, taxa like *Eubostrichus*, which has also been detected in our study, might serve as "shuttles" fur sulfur- and ammonia oxidizers between oxic and anoxic sediment layers, due to their tolerance for anoxic conditions (Schiemer et al., 1990). This form of interaction is probably less prevalent at Spiekeroog beach since it exhibits much stronger recharge of seawater constituents and a less stable redox zonation compared to deep-sea sediments. Yet, the authors also found several predatory taxa, which are expected to have an influence on bacterial diversity. Furthermore, while there is no direct study on interactions between *Archaea* and nematodes, members of *Nitrosopumilus* were detected within single nematode individuals in an extensive study on the microbiomes of free living marine nematodes (Schuelke et al., 2018). Even though we could not detect significant correlations between the variances of nematode and archaeal communities in Spiekeroog beach sediments, *Nitrosopumilus* was still the dominant archaeal taxon.

CONCLUDING REMARKS

In this study we expected to (i) detect a large archaeal and meiofaunal core community within the discharge area of the Spiekeroog beach STE. We detected a core-community of prokaryotes, yet less dominant than previously observed. This is possibly related to a previously unobserved stability of the beach morphology, which has been shown to govern the hydrogeochemical conditions within the STE. Regarding the meiofauna, we did not find a core community, but dominant site-specific communities and a cross shore difference between the HWL and all other sites. We attribute this to the higher motility and narrower tolerance range of meiofauna to environmental parameters. We further hypothesized, that (ii) the conditions in the discharge area of the STE favor the presence of those *Archaea* involved in nitrogen cycling. We could confirm this by detecting an overwhelming dominance of *Nitrosopumliaceae* ASVs in the entire intertidal area, which increased at the ridge and LWL, marked as exfiltration zones by geochemical (NH_4, salinity) and topography data. Lastly, we hypothesized, that (iii) the harsh high-energy conditions a Spiekeroog beach result in a nematode dominated community over a copepod dominated community. This also holds true, as the vast majority of meiofauna detected by morphological analysis were nematodes, which also dominated the sequence dataset. Contrary to a previous investigation of the Spiekeroog STE we could detect an influence of SGD on prokaryotic communities, which was visible as a higher evenness at SGD-impacted sites (ridge, LWL) compared to unimpacted sites (HWL, runnel). This influence is probably related to the weaker pronunciation of the runnel-ridge system and a rather

dissipative morphology of the beach. Yet, correlations between prokaryotic and meiofaunal communities remain to be explored in greater detail.

DATA AVAILABILITY STATEMENT

The data presented in the study are deposited in the European Nucleotide Archive (https://www.ebi.ac.uk/ena), accession number PRJEB42988.

AUTHOR CONTRIBUTIONS

JD performed sampling, molecular biological lab work, and wrote the manuscript. SK performed Illumina sequencing, bioinformatics, and writing. FM did bioinformatics. HW performed geochemical analysis. BE secured funding and wrote the manuscript. PM did eukaryotic data analysis and writing. All authors read and approved the manuscript.

FUNDING

This study was financed by the Niedersächsisches Ministerium für Wissenschaft und Kultur (MWK) in the scope of project "BIME" (ZN3184).

ACKNOWLEDGMENTS

We want to thank the BIME research consortium and especially Frank Meyerjürgens, for their help during sampling. We would also like to thank Helmo Nikolai and Gerrit Behrends for providing logistics and equipment, and Heike Simon and Ina Ulber for support with sampling and DOC analyses. Further, we thank Jannik Schnier for sorting and picking meiofauna samples and preparing them for sequencing. Also, we thank Carola Lehners, Eleonore Gründken, Heike Simon, Ina Ulber and Matthias Friebe for their support with porewater nutrient and DOC analysis. Likewise, we would like to acknowledge the Niedersächsischer Landesbetrieb für Wasserwirtschaft, Küsten- und Naturschutz (NLWKN), Svante Pitters, the Umweltzentrum Wittbülten, and the Quellerdünen hostel, for on-site logistics and infrastructure. This is publication No 75 of the Senckenberg am Meer Metabarcoding Laboratory.

SUPPLEMENTARY MATERIAL

The Supplementary Material for this article can be found online at: https://www.frontiersin.org/articles/10.3389/fenvs.2021.642098/full#supplementary-material

Supplementary Figure 1 | Location of the sampling site at Spiekeroog beach, modified after Ahrens et al. (2020) and Degenhardt et al. (2020). Displayed is a cross-section through the beach, including hydrological flow paths and beach morphology. The squares mark the sampling sites across the intertidal area. MHWL, mean high water line; MSL, mean sea-level; MLWL, mean low water line.

REFERENCES

Adyasari, D., Hassenruck, C., Montiel, D., and Dimova, N. (2020). Microbial community composition across a coastal hydrological system affected by submarine groundwater discharge (SGD). *PLoS One* 15:e0235235. doi: 10.1371/journal.pone.0235235

Ahrens, J., Beck, M., Marchant Hannah, K., Ahmerkamp, S., Schnetger, B., and Brumsack, H. J. (2020). Seasonality of organic matter degradation regulates nutrient and metal net fluxes in a high energy sandy beach. *J. Geophys. Res. Biogeosci.* 125:e2019JG005399.

Anschutz, P., Charbonnier, C., Deborde, J., Deirmendjian, L., Poirier, D., Mouret, A., et al. (2016). Terrestrial groundwater and nutrient discharge along the 240-km-long Aquitanian coast. *Mar. Chem.* 185, 38–47. doi: 10.1016/j.marchem.2016.04.002

Anschutz, P., Smith, T., Mouret, A., Deborde, J., Bujan, S., Poirier, D., et al. (2009). Tidal sands as biogeochemical reactors. *Estuar. Coast. Shelf Sci.* 84, 84–90. doi: 10.1016/j.ecss.2009.06.015

Auguet, J. C., Barberan, A., and Casamayor, E. O. (2010). Global ecological patterns in uncultured Archaea. *ISME J.* 4, 182–190. doi: 10.1038/ismej.2009.109

Beck, M., Reckhardt, A., Amelsberg, J., Bartholoma, A., Brumsack, H. J., Cypionka, H., et al. (2017). The drivers of biogeochemistry in beach ecosystems: a cross-shore transect from the dunes to the low-water line. *Mar. Chem.* 190, 35–50. doi: 10.1016/j.marchem.2017.01.001

Blaxter, M. L., De Ley, P., Garey, J. R., Liu, L. X., Scheldeman, P., Vierstraete, A., et al. (1998). A molecular evolutionary framework for the phylum Nematoda. *Nature* 392, 71–75. doi: 10.1038/32160

Boehm, A. B., Yamahara, K. M., and Sassoubre, L. M. (2014). Diversity and transport of microorganisms in intertidal sands of the California coast. *Appl. Environ. Microbiol.* 80, 3943–3951. doi: 10.1128/aem.00513-14

Boetius, A., Ravenschlag, K., Schubert, C. J., Rickert, D., Widdel, F., Gieseke, A., et al. (2000). A marine microbial consortium apparently mediating anaerobic oxidation of methane. *Nature* 407, 623–626. doi: 10.1038/35036572

Bolyen, E., Rideout, J. R., Dillon, M. R., Bokulich, N. A., Abnet, C. C., Al-Ghalith, G. A., et al. (2019). Reproducible, interactive, scalable and extensible microbiome data science using QIIME 2. *Nat. Biotechnol.* 37, 852–857.

Bonaglia, S., Nascimento, F. J., Bartoli, M., Klawonn, I., and Bruchert, V. (2014). Meiofauna increases bacterial denitrification in marine sediments. *Nat. Commun.* 5:5133.

Brochier-Armanet, C., Forterre, P., and Gribaldo, S. (2011). Phylogeny and evolution of the archaea: one hundred genomes later. *Curr. Opin. Microbiol.* 14, 274–281. doi: 10.1016/j.mib.2011.04.015

Callahan, B. J., McMurdie, P. J., Rosen, M. J., Han, A. W., Johnson, A. J., and Holmes, S. P. (2016). DADA2: high-resolution sample inference from illumina amplicon data. *Nat. Methods* 13, 581–583. doi: 10.1038/nmeth.3869

Castelle, C. J., Wrighton, K. C., Thomas, B. C., Hug, L. A., Brown, C. T., Wilkins, M. J., et al. (2015). Genomic expansion of domain archaea highlights roles for organisms from new phyla in anaerobic carbon cycling. *Curr. Biol.* 25, 690–701. doi: 10.1016/j.cub.2015.01.014

Charbonnier, C., Anschutz, P., Poirier, D., Bujan, S., and Lecroart, P. (2013). Aerobic respiration in a high-energy sandy beach. *Mar. Chem.* 155, 10–21. doi: 10.1016/j.marchem.2013.05.003

Cho, H. M., Kim, G., Kwon, E. Y., Moosdorf, N., Garcia-Orellana, J., and Santos, I. R. (2018). Radium tracing nutrient inputs through submarine groundwater discharge in the global ocean. *Sci. Rep.* 8:2439.

Cuadrado, V., Gomila, M., Merini, L., Giulietti, A. M., and Moore, E. R. B. (2010). *Cupriavidus pampae* sp. nov., a novel herbicide-degrading bacterium isolated from agricultural soil. *Int. J. Syst. Evol. Microbiol.* 60, 2606–2612. doi: 10.1099/ijs.0.018341-0

de Faria, L. C., Di Domenico, M., Andrade, S. C. S., dos Santos, M. C., Fonseca, G., Zanol, J., et al. (2018). The use of metabarcoding for meiofauna ecological patterns assessment. *Mar. Environ. Res.* 140, 160–168. doi: 10.1016/j.marenvres.2018.06.013

Decelle, J., Romac, S., Stern, R. F., Bendif, E. M., Zingone, A., Audic, S., et al. (2015). PhytoREF: a reference database of the plastidial 16S rRNA gene of

photosynthetic eukaryotes with curated taxonomy. *Mol. Ecol. Resour.* 15, 1435–1445. doi: 10.1111/1755-0998.12401

Degenhardt, J., Dlugosch, L., Ahrens, J., Beck, M., Waska, H., and Engelen, B. (2020). Seasonal dynamics of microbial diversity at a sandy high energy beach reveal a resilient core community. *Front. Mar. Sci.* 7:573570.

Encarnação, J., Leitão, F., Range, P., Piló, D., Chícharo, M. A., and Chícharo, L. (2013). The influence of submarine groundwater discharges on subtidal meiofauna assemblages in south Portugal (Algarve). *Estuar. Coast. Shelf Sci.* 130, 202–208. doi: 10.1016/j.ecss.2013.04.013

Froelich, P. N., Klinkhammer, G. P., Bender, M. L., Luedtke, N. A., Heath, G. R., Cullen, D., et al. (1979). Early oxidation of organic matter in pelagic sediments of the eastern equatorial Atlantic: suboxic diagenesis. *Geochimica et Cosmochimica Acta* 43, 1075–1090. doi: 10.1016/0016-7037(79)90095-4

Gabor, E. M., Vries, E. J., and Janssen, D. B. (2003). Efficient recovery of environmental DNA for expression cloning by indirect extraction methods. *FEMS Microbiol. Ecol.* 44, 153–163. doi: 10.1016/s0168-6496(02)00462-2

Gallucci, F., Hutchings, P., Gribben, P., and Fonseca, G. (2012). Habitat alteration and community-level effects of an invasive ecosystem engineer: a case study along the coast of NSW. Australia. *Mar. Ecol. Prog. Ser.* 449, 95–108. doi: 10.3354/meps09547

Gao, H., Matyka, M., Liu, B., Khalili, A., Kostka, J. E., Collins, G., et al. (2012). Intensive and extensive nitrogen loss from intertidal permeable sediments of the Wadden Sea. *Limnol. Oceanogr.* 57, 185–198. doi: 10.4319/lo.2012.57.1.0185

Gheskiere, T., Vincx, M., Urban-Malinga, B., Rossano, C., Scapini, F., and Degraer, S. (2005). Nematodes from wave-dominated sandy beaches: diversity, zonation patterns and testing of the isocommunities concept. *Estuar. Coast. Shelf Sci.* 62, 365–375. doi: 10.1016/j.ecss.2004.09.024

Giere, O. (2009). Synecological perspectives in meiobenthology. *Meiobenthology* 373–415. doi: 10.1007/978-3-540-68661-3_9

Grünenbaum, N., Ahrens, J., Beck, M., Gilfedder, B. S., Greskowiak, J., Kossack, M., et al. (2020a). A multi-method approach for quantification of in- and exfiltration rates from the subterranean estuary of a high energy beach. *Front. Earth Sci.* 8:571310.

Grünenbaum, N., Greskowiak, J., Sültenfuß, J., and Massmann, G. (2020b). Groundwater flow and residence times below a meso-tidal high-energy beach: a model-based analyses of salinity patterns and 3H-3He groundwater ages. *J. Hydrol.* 587:124948. doi: 10.1016/j.jhydrol.2020.124948

Grzelak, K., Tamborski, J., Kotwicki, L., and Bokuniewicz, H. (2018). Ecostructuring of marine nematode communities by submarine groundwater discharge. *Mar. Environ. Res.* 136, 106–119. doi: 10.1016/j.marenvres.2018.01.013

Guillou, L., Bachar, D., Audic, S., Bass, D., Berney, C., Bittner, L., et al. (2013). The protist ribosomal reference database (PR2): a catalog of unicellular eukaryote small sub-unit rRNA sequences with curated taxonomy. *Nucleic Acids Res.* 41, D597–604. doi: 10.1093/nar/gks1160

Haenel, Q., Holovachov, O., Jondelius, U., Sundberg, P., and Bourlat, S. J. (2017). NGS-based biodiversity and community structure analysis of meiofaunal eukaryotes in shell sand from Hallo island, Smogen, and soft mud from Gullmarn Fjord, Sweden. *Biodivers. Data J.* 5:e12731. doi: 10.3897/bdj.5.e12731

Higgins, R. P., and Thiel, H. (1988). *Introduction to the Study of Meiofauna*. Washington, DC: Smithsonian Institution Press.

Hong, Y., Wu, J., Wilson, S., and Song, B. (2018). Vertical stratification of sediment microbial communities along geochemical gradients of a subterranean estuary located at the gloucester beach of virginia, united states. *Front. Microbiol.* 9:3343.

Huettel, M., Berg, P., and Kostka, J. E. (2014). Benthic exchange and biogeochemical cycling in permeable sediments. *Ann. Rev. Mar. Sci.* 6, 23–51. doi: 10.1146/annurev-marine-051413-012706

Hugoni, M., Domaizon, I., Taib, N., Biderre-Petit, C., Agogue, H., Galand, P. E., et al. (2015). Temporal dynamics of active archaea in oxygen-depleted zones of two deep lakes. *Environ. Microbiol. Rep.* 7, 321–329. doi: 10.1111/1758-2229.12251

Huys, R. (1996). *Marine and Brackish Water Harpacticoid Copepods*. Shrewsbury: Field Studies Council.

Huys, R., Herman, P. M. J., Heip, C. H. R., and Soetaert, K. (1992). The meiobenthos of the North Sea: density, biomass trends and distribution of copepod communities. *ICES J. Mar. Sci.* 49, 23–44. doi: 10.1093/icesjms/49.1.23

Itaya, K., and Ui, M. (1966). A new micromethod for the colorimetric determination of inorganic phosphate. *Clin. Chim. Acta* 14, 361–366. doi: 10.1016/0009-8981(66)90114-8

Jessup, C. M., Kassen, R., Forde, S. E., Kerr, B., Buckling, A., Rainey, P. B., et al. (2004). Big questions, small worlds: microbial model systems in ecology. *Trends Ecol. Evol.* 19, 189–197. doi: 10.1016/j.tree.2004.01.008

Kahng, H. Y., Lee, S. S., Kim, J. M., Jung, J. Y., Lee, M. Y., Park, W., et al. (2010). *Muriicola jejuensis* gen. nov., sp. nov., isolated from seawater. *Int. J. Syst. Evol. Microbiol.* 60, 1644–1648. doi: 10.1099/ijs.0.015313-0

Karanovic, T., and Cooper, S. J. B. (2012). Explosive radiation of the genus Schizopera on a small subterranean island in Western Australia (Copepoda:Harpacticoida): unravelling the cases of cryptic speciation, size differentiation and multiple invasions. *Invertebrate Syst.* 26, 115–192. doi: 10.1071/is11027

Karner, M. B., DeLong, E. F., and Karl, D. M. (2001). Archaeal dominance in the mesopelagic zone of the Pacific Ocean. *Nature* 409, 507–510. doi: 10.1038/35054051

Kennedy, A. D., and Jacoby, C. A. (1999). Biological indicators of marine environmental health: meiofauna - a neglected benthic component? *Environ. Monit. Assess.* 54, 47–68.

Khan, S. T., Nakagawa, Y., and Harayama, S. (2006). Sediminicola luteus gen. nov., sp. nov., a novel member of the family flavobacteriaceae. *Int. J. Syst. Evol. Microbiol.* 56, 841–845. doi: 10.1099/ijs.0.64047-0

Kim, K. H., Heiss, J. W., Michael, H. A., Cai, W.-J., Laattoe, T., Post, V. E. A., et al. (2017). Spatial patterns of groundwater biogeochemical reactivity in an intertidal beach aquifer. *J. Geophys. Res. Biogeosci.* 122, 2548–2562. doi: 10.1002/2017jg003943

Könneke, M., Bernhard, A. E., de la Torre, J. R., Walker, C. B., Waterbury, J. B., and Stahl, D. A. (2005). Isolation of an autotrophic ammonia-oxidizing marine archaeon. *Nature* 437, 543–546. doi: 10.1038/nature03911

Kotwicki, L., Grzelak, K., Czub, M., Dellwig, O., Gentz, T., Szymczycha, B., et al. (2014). Submarine groundwater discharge to the Baltic coastal zone: impacts on the meiofaunal community. *J. Mar. Syst.* 129, 118–126. doi: 10.1016/j.jmarsys.2013.06.009

Kwon, E. Y., Kim, G., Primeau, F., Moore, W. S., Cho, H. M., DeVries, T., et al. (2014). Global estimate of submarine groundwater discharge based on an observationally constrained radium isotope model. *Geophys. Res. Lett.* 41, 8438–8444. doi: 10.1002/2014gl061574

Laskov, C., Herzog, C., Lewandowski, J., and Hupfe, M. (2007). Miniaturized photometrical methods for the rapid analysis of phosphate, ammonium, ferrous iron, and sulfate in pore water of freshwater sediments. *Limnol. Oceanogr. Methods* 4, 63–71. doi: 10.4319/lom.2007.5.63

Lipp, J. S., Morono, Y., Inagaki, F., and Hinrichs, K. U. (2008). Significant contribution of Archaea to extant biomass in marine subsurface sediments. *Nature* 454, 991–994. doi: 10.1038/nature07174

Lloyd, K. G., Schreiber, L., Petersen, D. G., Kjeldsen, K. U., Lever, M. A., Steen, A. D., et al. (2013). Predominant archaea in marine sediments degrade detrital proteins. *Nature* 496, 215–218. doi: 10.1038/nature12033

Losi, V., Ferrero, T. J., Moreno, M., Gaozza, L., Rovere, A., Firpo, M., et al. (2013). The use of nematodes in assessing ecological conditions in shallow waters surrounding a Mediterranean harbour facility. *Estuar. Coast. Shelf Sci.* 130, 209–221. doi: 10.1016/j.ecss.2013.02.017

Lueders, T., Manefield, M., and Friedrich, M. W. (2004). Enhanced sensitivity of DNA- and rRNA-based stable isotope probing by fractionation and quantitative analysis of isopycnic centrifugation gradients. *Environ. Microbiol.* 6, 73–78. doi: 10.1046/j.1462-2920.2003.00536.x

MacLeod, F., Kindler, G. S., Wong, H. L., Chen, R., and Burns, B. P. (2019). Asgard archaea: diversity, function, and evolutionary implications in a range of microbiomes. *AIMS Microbiol.* 5, 48–61. doi: 10.3934/microbiol.2019.1.48

McAllister, S. M., Barnett, J. M., Heiss, J. W., Findlay, A. J., MacDonald, D. J., Dow, C. L., et al. (2015). Dynamic hydrologic and biogeochemical processes drive microbially enhanced iron and sulfur cycling within the intertidal mixing zone of a beach aquifer. *Limnol. Oceanogr.* 60, 329–345. doi: 10.1002/lno.10029

McIntyre, A., and Warwick, R. (1984). *Methods for the Study of Marine Benthos*. Oxford: Blackwell.

Meadows, A. S., Ingels, J., Widdicombe, S., Hale, R., and Rundle, S. D. (2015). Effects of elevated CO2 and temperature on an intertidal meiobenthic

community. *J. Exp. Mar. Biol. Ecol.* 469, 44–56. doi: 10.1016/j.jembe.2015.04.001

Meng, J., Xu, J., Qin, D., He, Y., Xiao, X., and Wang, F. (2014). Genetic and functional properties of uncultivated MCG archaea assessed by metagenome and gene expression analyses. *ISME J.* 8, 650–659. doi: 10.1038/ismej.2013.174

Mergeay, M. (2015). *The History of Cupriavidus Metallidurans Strains Isolated from Anthropogenic Environments*. Berlin: Springer.

Migné, A., Ouisse, V., Hubas, C., and Davoult, D. (2011). Freshwater seepages and ephemeral macroalgae proliferation in an intertidal bay: II. effect on benthic biomass and metabolism. *Estuar. Coast. Shelf Sci.* 92, 161–168. doi: 10.1016/j.ecss.2010.12.023

Milici, M., Deng, Z. L., Tomasch, J., Decelle, J., Wos-Oxley, M. L., Wang, H., et al. (2016). Co-occurrence analysis of microbial taxa in the atlantic ocean reveals high connectivity in the free-living bacterioplankton. *Front. Microbiol.* 7:649.

Miller, D. C., and Ullman, W. J. (2004). Ecological consequences of ground water discharge to delaware bay, united states. *Ground Water* 42, 959–970. doi: 10.1111/j.1745-6584.2004.tb02635.x

Moore, W. S. (1996). Large groundwater inputs to coastal waters revealed by 226Ra enrichments. *Nature* 380, 612–614. doi: 10.1038/380612a0

Moore, W. S. (1999). The subterranean estuary: a reaction zone of ground water and sea water. *Mar. Chem.* 65, 111–125. doi: 10.1016/s0304-4203(99)00014-6

Moore, W. S., Sarmiento, J. L., and Key, R. M. (2008). Submarine groundwater discharge revealed by 228Ra distribution in the upper Atlantic Ocean. *Nat. Geosci.* 1, 309–311. doi: 10.1038/ngeo183

Moreno, M., Semprucci, F., Vezzulli, L., Balsamo, M., Fabiano, M., and Albertelli, G. (2011). The use of nematodes in assessing ecological quality status in the Mediterranean coastal ecosystems. *Ecol. Indic.* 11, 328–336. doi: 10.1016/j.ecolind.2010.05.011

Muck, S., De Corte, D., Clifford, E. L., Bayer, B., Herndl, G. J., and Sintes, E. (2019). Niche differentiation of aerobic and anaerobic ammonia oxidizers in a high latitude deep oxygen minimum zone. *Front. Microbiol.* 10:2141.

Nakagawa, T., and Stahl, D. A. (2013). Transcriptional response of the archaeal ammonia oxidizer nitrosopumilus maritimus to low and environmentally relevant ammonia concentrations. *Appl. Environ. Microbiol.* 79, 6911–6916. doi: 10.1128/AEM.02028-13

Nascimento, F. J. A., Näslund, J., and Elmgren, R. (2012). Meiofauna enhances organic matter mineralization in soft sediment ecosystems. *Limnol. Oceanogr.* 57, 338–346. doi: 10.4319/lo.2012.57.1.0338

Nguyen, V. K., and Lee, J.-U. (2014). Antimony-oxidizing bacteria isolated from antimony-contaminated sediment – a phylogenetic study. *Geomicrobiol. J.* 32, 50–58. doi: 10.1080/01490451.2014.925009

Oksanen, J., Blanchet, F. G., and Friendly, M. (2019). *Vegan: Community Ecology Package*.

Ortiz-Alvarez, R., and Casamayor, E. O. (2016). High occurrence of Pacearchaeota and Woesearchaeota (Archaea superphylum DPANN) in the surface waters of oligotrophic high-altitude lakes. *Environ. Microbiol. Rep.* 8, 210–217. doi: 10.1111/1758-2229.12370

Ouisse, V., Riera, P., Migné, A., Leroux, C., and Davoult, D. (2011). Freshwater seepages and ephemeral macroalgae proliferation in an intertidal bay: i effect on benthic community structure and food web. *Estuar. Coast. Shelf Sci.* 91, 272–281. doi: 10.1016/j.ecss.2010.10.034

Paerl, H. W. (1997). Coastal eutrophication and harmful algal blooms: importance of atmospheric deposition and groundwater as "new" nitrogen and other nutrient sources. *Limnol. Oceanogr.* 42, 1154–1165. doi: 10.4319/lo.1997.42.5_part_2.1154

Parada, A. E., Needham, D. M., and Fuhrman, J. A. (2016). Every base matters: assessing small subunit rRNA primers for marine microbiomes with mock communities, time series and global field samples. *Environ. Microbiol.* 18, 1403–1414. doi: 10.1111/1462-2920.13023

Platero, R., James, E. K., Rios, C., Iriarte, A., Sandes, L., Zabaleta, M., et al. (2016). Novel cupriavidus strains isolated from root nodules of native uruguayan mimosa species. *Appl. Environ. Microbiol.* 82, 3150–3164. doi: 10.1128/aem.04142-15

Qian, Y., Shi, J., Chen, Y., Lou, L., Cui, X., Cao, R., et al. (2010). Characterization of phosphate solubilizing bacteria in sediments from a shallow eutrophic lake and a wetland: isolation, molecular identification and phosphorus release ability determination. *Molecules* 15, 8518–8533. doi: 10.3390/molecules15118518

Quast, C., Pruesse, E., Yilmaz, P., Gerken, J., Schweer, T., Yarza, P., et al. (2013). The SILVA ribosomal RNA gene database project: improved data processing and web-based tools. *Nucleic Acids Res.* 41, D590–D596.

R Core Team (2019). *R: a Language and Environment for Statistical Computing*. Vienna: R Foundation for Statistical Computing.

Reckhardt, A., Beck, M., Seidel, M., Riedel, T., Wehrmann, A., Bartholomä, A., et al. (2015). Carbon, nutrient and trace metal cycling in sandy sediments: a comparison of high-energy beaches and backbarrier tidal flats. *Estuar. Coast. Shelf Sci.* 159, 1–14. doi: 10.1016/j.ecss.2015.03.025

Riedel, T., Lettmann, K., Schnetger, B., Beck, M., and Brumsack, H.-J. (2011). Rates of trace metal and nutrient diagenesis in an intertidal creek bank. *Geochimica et Cosmochimica Acta* 75, 134–147. doi: 10.1016/j.gca.2010.09.040

Rinke, C., Schwientek, P., Sczyrba, A., Ivanova, N. N., Anderson, I. J., Cheng, J. F., et al. (2013). Insights into the phylogeny and coding potential of microbial dark matter. *Nature* 499, 431–437. doi: 10.1038/nature12352

Rios-Del Toro, E. E., Valenzuela, E. I., Ramírez, J. E., López-Lozano, N. E., and Cervantes, F. J. (2018). Anaerobic ammonium oxidation linked to microbial reduction of natural organic matter in marine sediments. *Environ. Sci. Technol. Lett.* 5, 571–577. doi: 10.1021/acs.estlett.8b00330

Rodellas, V., Garcia-Orellana, J., Tovar-Sánchez, A., Basterretxea, G., López-Garcia, J. M., Sánchez-Quiles, D., et al. (2014). Submarine groundwater discharge as a source of nutrients and trace metals in a Mediterranean bay (Palma Beach, Balearic Islands). *Mar. Chem.* 160, 56–66. doi: 10.1016/j.marchem.2014.01.007

Rzeznik-Orignac, J., Puisay, A., Derelle, E., Peru, E., Le Bris, N., and Galand, P. E. (2018). Co-occurring nematodes and bacteria in submarine canyon sediments. *PeerJ* 6:e5396. doi: 10.7717/peerj.5396

Santos, I. R., Burnett, W. C., Dittmar, T., Suryaputra, I. G. N. A., and Chanton, J. (2009). Tidal pumping drives nutrient and dissolved organic matter dynamics in a Gulf of Mexico subterranean estuary. *Geochimica et Cosmochimica Acta* 73, 1325–1339. doi: 10.1016/j.gca.2008.11.029

Schiemer, E., Novak, R., and Ott, J. (1990). Metabolic studies on thiobiotic free-living nematodes and their symbiotic microorganisms. *Mar. Biol.* 106, 129–137. doi: 10.1007/bf02114683

Schuelke, T., Pereira, T. J., Hardy, S. M., and Bik, H. M. (2018). Nematode-associated microbial taxa do not correlate with host phylogeny, geographic region or feeding morphology in marine sediment habitats. *Mol. Ecol.* 27, 1930–1951. doi: 10.1111/mec.14539

Semprucci, F., Losi, V., and Moreno, M. (2015). A review of Italian research on free-living marine nematodes and the future perspectives on their use as ecological indicators (EcoInds). *Mediterr. Mar. Sci.* 16, 352–365. doi: 10.12681/mms.1072

Shafiee, R. T., Snow, J. T., Zhang, Q., and Rickaby, R. E. M. (2019). Iron requirements and uptake strategies of the globally abundant marine ammonia-oxidising archaeon, *Nitrosopumilus maritimus* SCM1. *ISME J.* 13, 2295–2305. doi: 10.1038/s41396-019-0434-8

Staley, C., and Sadowsky, M. J. (2016). Regional similarities and consistent patterns of local variation in beach sand bacterial communities throughout the northern hemisphere. *Appl. Environ. Microbiol.* 82, 2751–2762. doi: 10.1128/aem.00247-16

Taberlet, P., Coissac, E., Pompanon, F., Brochmann, C., and Willerslev, E. (2012). Towards next-generation biodiversity assessment using DNA metabarcoding. *Mol. Ecol.* 21, 2045–2050. doi: 10.1111/j.1365-294x.2012.05470.x

Thauer, R. K., Kaster, A. K., Seedorf, H., Buckel, W., and Hedderich, R. (2008). Methanogenic archaea: ecologically relevant differences in energy conservation. *Nat. Rev. Microbiol.* 6, 579–591. doi: 10.1038/nrmicro1931

Vanaverbeke, J., Merckx, B., Degraer, S., and Vincx, M. (2011). Sediment-related distribution patterns of nematodes and macrofauna: two sides of the benthic coin? *Mar. Environ. Res.* 71, 31–40. doi: 10.1016/j.marenvres.2010.09.006

Waska, H., Brumsack, H.-J., Massmann, G., Koschinsky, A., Schnetger, B., Simon, H., et al. (2019a). Inorganic and organic iron and copper species of the subterranean estuary: origins and fate. *Geochimica et Cosmochimica Acta* 259, 211–232. doi: 10.1016/j.gca.2019.06.004

Waska, H., Greskowiak, J., Ahrens, J., Beck, M., Ahmerkamp, S., and Boning, P. (2019b). Spatial and temporal patterns of pore water chemistry in the inter-tidal zone of a high energy beach. *Front. Mar. Sci.* 6:154.

Webster, I. T., and Taylor, J. H. (1992). Rotational dispersion in porous media due to fluctuating flows. *Water Resour. Res.* 28, 109–119. doi: 10.1029/91wr02323

Yeh, Y.-C., McNichol, J. C., Needham, D. M., Fichot, E. B., and Fuhrman, J. A. (2019). Comprehensive single-PCR 16S and 18S rRNA community analysis validated with mock communities and denoising algorithms. *bioRxiv [preprint]* doi: 10.1101/866731

Yoder, M., De Ley, I. T., King, I. W., Mundo-Ocampo, M., Mann, J., Blaxter, M., et al. (2006). DESS: a versatile solution for preserving morphology and extractable DNA of nematodes. *Nematology* 8, 367–376. doi: 10.1163/156854106778493448

Yoon, J., Matsuo, Y., Kasai, H., and Yokota, A. (2012). Portibacter lacus gen. nov., sp. nov., a new member of the family Saprospiraceae isolated from a saline lake. *J. Gen. Appl. Microbiol.* 58, 191–197.

Zeppilli, D., Bongiorni, L., Serrao Santos, R., and Vanreusel, A. (2014). Changes in nematode communities in different physiographic sites of the condor seamount (north-East atlantic ocean) and adjacent sediments. *PLoS One* 9:e115601. doi: 10.1371/journal.pone.0115601

Zeppilli, D., Sarrazin, J., Leduc, D., Arbizu, P. M., Fontaneto, D., Fontaneto, C., et al. (2015). Is the meiofauna a good indicator for climate change and anthropogenic impacts? *Mar. Biodivers.* 45, 505–535.

Zhou, Z., Pan, J., Wang, F., Gu, J. D., and Li, M. (2018). Bathyarchaeota: globally distributed metabolic generalists in anoxic environments. *FEMS Microbiol. Rev.* 42, 639–655. doi: 10.1093/femsre/fuy023

Zipperle, A., and Reise, K. (2005). Freshwater springs on intertidal sand flats cause a switch in dominance among polychaete worms. *J. Sea Res.* 54, 143–150. doi: 10.1016/j.seares.2005.01.003

Conflict of Interest: The authors declare that the research was conducted in the absence of any commercial or financial relationships that could be construed as a potential conflict of interest.

Copyright © 2021 Degenhardt, Khodami, Milke, Waska, Engelen and Martinez Arbizu. This is an open-access article distributed under the terms of the Creative Commons Attribution License (CC BY). The use, distribution or reproduction in other forums is permitted, provided the original author(s) and the copyright owner(s) are credited and that the original publication in this journal is cited, in accordance with accepted academic practice. No use, distribution or reproduction is permitted which does not comply with these terms.

frontiers in Environmental Science

ORIGINAL RESEARCH
published: 13 May 2021
doi: 10.3389/fenvs.2021.670914

Changes in Organic Matter Deposition Can Impact Benthic Marine Meiofauna in Karst Subterranean Estuaries

David Brankovits[1], Shawna N. Little[2], Tyler S. Winkler[3], Anne E. Tamalavage[3], Luis M. Mejía-Ortíz[4], Christopher R. Maupin[5], German Yáñez-Mendoza[6] and Peter J. van Hengstum[1,3]*

[1]Department of Marine and Coastal Environmental Science, Texas A&M University at Galveston, Galveston, TX, United States, [2]Department of Marine Biology, Texas A&M University at Galveston, Galveston, TX, United States, [3]Department of Oceanography, Texas A&M University, College Station, TX, United States, [4]Biospeleology & Carcinology Lab, University of Quintana Roo, Cozumel, Mexico, [5]Department of Geography, Texas A&M University, College Station, TX, United States, [6]Circulo Espeleológico del Mayab A.C., Cozumel, Mexico

OPEN ACCESS

Edited by:
Hannelore Waska, University of Oldenburg, Germany

Reviewed by:
Luisa Bergamin, Higher Institute for Environmental Protection and Research (ISPRA), Italy
Andrea Pain, University of Maryland Center for Environmental Science (UMCES), United States

***Correspondence:**
David Brankovits
dbranko@tamu.edu

Specialty section:
This article was submitted to Biogeochemical Dynamics, a section of the journal Frontiers in Environmental Science

Received: *22 February 2021*
Accepted: *26 April 2021*
Published: *13 May 2021*

Citation:
Brankovits D, Little SN, Winkler TS, Tamalavage AE, Mejía-Ortíz LM, Maupin CR, Yáñez-Mendoza G and van Hengstum PJ (2021) Changes in Organic Matter Deposition Can Impact Benthic Marine Meiofauna in Karst Subterranean Estuaries. Front. Environ. Sci. 9:670914. doi: 10.3389/fenvs.2021.670914

Subsurface mixing of seawater and terrestrial-borne meteoric waters on carbonate landscapes creates karst subterranean estuaries, an area of the coastal aquifer with poorly understood carbon cycling, ecosystem functioning, and impact on submarine groundwater discharge. Caves in karst platforms facilitate water and material exchange between the marine and terrestrial environments, and their internal sedimentation patterns document long-term environmental change. Sediment records from a flooded coastal cave in Cozumel Island (Mexico) document decreasing terrestrial organic matter (OM) deposition within the karst subterranean estuary over the last ~1,000 years, with older sediment likely exported out of the cave by intense storm events. While stable carbon isotopic values ($\delta^{13}C_{org}$ ranging from −22.5 to −27.1‰) and C:N ratios (ranging from 9.9 to 18.9) indicate that mangrove and other terrestrial detritus surrounding an inland sinkhole are the primarily sedimentary OM supply, an upcore decrease in bulk OM and enrichment of $\delta^{13}C_{org}$ values are observed. These patterns suggest that a reduction in the local mangrove habitat decreased the terrestrial particulate OM input to the cave over time. The benthic foraminiferal community in basal core sediment have higher proportions of infaunal taxa (i.e., *Bolivina*) and *Ammonia*, and assemblages shift to increased miliolids and less infaunal taxa at the core-top sediment. The combined results suggest that a decrease in terrestrial OM through time had a concomitant impact on benthic meiofaunal habitats, potentially by impacting dissolved oxygen availability at the microhabitat scale or resource partitioning by foraminifera. The evidence presented here indicates that landscape and watershed level changes can impact ecosystem functioning within adjacent subterranean estuaries.

Keywords: subterranean estuaries, groundwater, karst, caves, mangroves, organic matter, benthic ecology

INTRODUCTION

Karst subterranean estuaries (KSEs), areas in coastal carbonate aquifers where seawater, saline groundwater, and fresh meteoric waters mix, are biogeochemical reaction zones between the land and the sea that provide habitat to characteristic biological communities. Global coastlines are ~25% karst landscapes (Ford and Williams, 2013), which account for ~12% of global submarine groundwater discharge (Beck et al., 2013). Dissolution and diagenesis of eogenetic carbonate landscapes create abundant cave networks and sinkholes that can become subsequently inundated through sea-level rise. This geologic setting simultaneously enhances seawater intrusion that impacts groundwater resources inland on carbonate landscapes (Perry et al., 2002; Coronado-Álvarez et al., 2011) and land-to-sea material transport through conduits and submarine springs (e.g., Fleury et al., 2007). The terms "anchialine cave" and "marine cave" have been widely applied to describe the habitat of cave-adapted biological communities living in the freshwater, mixing zone, brackish water, and also in the marine sector of karst and volcanic subterranean estuaries in the Mediterranean (e.g., Sket, 1996; Bergamin et al., 2020; Chen et al., 2020), the Tropical North Atlantic Ocean (e.g., Rubio et al., 2015; van Hengstum et al., 2019), and elsewhere (Holthuis, 1973; Stock et al., 1986; Iliffe and Kornicker, 2009; Bishop et al., 2015; Riera et al., 2018). Given modern challenges of coastal urbanization, seawater nutrient loading, and porosity of karst landscapes, there is a growing need to better understand organic matter delivery and carbon exchange between the ocean and subsurface within KSEs.

Bulk organic matter (OM) can be an important sedimentary constituent and an essential carbon source in KSEs. Direct openings to the surface facilitate particulate organic matter (POM) transport from eroding terrestrial soils and aquatic/marine primary producers into flooded coastal caves and sinkholes that are flooded by the subterranean estuary (van Hengstum et al., 2010; Gregory et al., 2017). As a result, changing terrestrial vegetation, such as wetland colonization, can impact local POM inputs to KSEs (Collins et al., 2015; Tamalavage et al., 2018). Refractory POM is either exported from the coastal aquifer or accumulates along the land-sea environmental continuum in submerged sinkholes and caves (e.g., Gabriel et al., 2009; Collins et al., 2015; Tamalavage et al., 2018; van Hengstum et al., 2020). POM distribution and accumulation in the sediment is also affected by horizontal groundwater flow through the caves (Gabriel et al., 2009; van Hengstum et al., 2010; Winkler et al., 2016). In addition, chemoautotrophic primary producers can supply *in-situ* POM to the benthos in the form of sinking material in marine caves (Airoldi and Cinelli, 1996). The bioavailable fraction of OM fuels biogeochemical cycling and food webs in coastal caves and sinkholes in KSEs (Pohlman et al., 1997; Socki et al., 2002; Seymour et al., 2007; Brankovits et al., 2017). However, an important question remains: Do changes in the source of sediment OM actually influence benthic meiofaunal communities in KSEs?

This study presents a 1,000-year stratigraphic record of organic matter and benthic meiofaunal community change from a flooded coastal cave on Cozumel in Mexico. Bulk OM and benthic foraminiferal community shifts were used to investigate how changes related to the sources and quantity of sedimentary OM impacted benthic meiofauna over time. The results indicate that 1) a sinkhole allows terrestrial OM to enter a subsurface stream of brackish to saline groundwater before its discharge to the coastal sea, 2) the influx of OM from mangroves in the adjacent sinkhole have decreased over the last millennium, and 3) changes in benthic foraminiferal assemblages through time are most likely related to changes in the source and decreased supply of OM.

MATERIALS AND METHODS

Study Site

The island of Cozumel is located approximately 20 km from the northeastern coast of the Yucatán Peninsula in Mexico (**Figure 1**) and separated by the Cozumel Channel (>400 m in water depth). Cozumel and the northeastern Yucatán coast have similar Pleistocene sea-level histories and carbonate lithology (Spaw, 1978), and the flooded caves filled with speleothems (e.g., stalactites, stalagmites, columns) indicate that regional caves were in the vadose zone during previous glacial episodes (Spaw, 1978; Richards et al., 1994). The region's tropical climate has dry (from December to April/May) and wet seasons (from May to November) (Curtis et al., 1996; Kottek et al., 2006). Like the nearby mainland, the carbonate island of Cozumel is topographically flat (mean 5 m in elevation) and the absence of fluvial systems means rainfall either directly evapotranspires or infiltrates into the unconfined aquifers (Perry et al., 2002; Beddows et al., 2007; Gondwe et al., 2010). Abundant sinkholes and well-developed cave networks impact subsurface hydrologic transport depending on seasonal rainfall and storms (Frausto-Martínez et al., 2018; Frausto-Martinez et al., 2021), which may change groundwater discharge rates and associated constituent transport to the coastal sea like on the Yucatán Peninsula (Young et al., 2008; Gonneea et al., 2014; Null et al., 2014). The region experiences microtides that span 0.1–0.2 m (Kjerfve, 1981), which also impacts daily groundwater table elevation. Tourism is driving rapid regional development and urbanization, which threatens groundwater resources (Coronado-Álvarez et al., 2011), groundwater-dependent habitats (Bauer-Gottwein et al., 2011), and other native ecosystems, like coral reefs and coastal vegetation (e.g., mangroves, seagrass) (Muckelbauer, 1990).

The sinkhole (cenote) entrance to Aerolito Cave (N 20.47°, W 86.98°; 71 m by 21 m) (**Figure 2**) provides access to 6.1 km of mapped cave passages traversing both inland (upstream) and seaward (downstream), and red mangroves (*Rhizophora mangle*) are present along its northern periphery (Frontana-Uribe and Solis-Weiss, 2011). There is a ~240 m long subsurface connection from the sinkhole to a marine bay. These marine and terrestrial openings facilitate direct detritus inputs to the cave (Mejía-Ortíz et al., 2007). These conduits hydrographically connect the sea and the aquifer as meteoric freshwater flows to the coast mixing with oceanic seawater intruding into the aquifer. Downstream passages are well-mixed and resemble typical marine conditions, whereas the water column in the open pool of the sinkhole and the

upstream passages is stratified. Here, a sharp mixing zone (halocline) between brackish (~15 psu) and saline (~37 psu) water masses occurs typically at ~7 m water depth (Mejía-Ortíz et al., 2007; Calderón-Gutiérrez et al., 2018). Shifts in the depth and thickness of the mixing zone in response to high-intensity rain events have been documented in Aerolito (Calderón-Gutiérrez et al., 2018), similar to the mainland Yucatán Peninsula (Coutino et al., 2017; Brankovits et al., 2018). Previous local research includes documenting endemic cave fauna (Mejía et al., 2008; Mejía-Ortíz et al., 2017; Olesen et al., 2017) and marine invertebrate ecology (Mejía-Ortíz et al., 2007; Pisanty et al., 2010; Frontana-Uribe and Solis-Weiss, 2011; Ortiz and Winfield, 2015; Márquez-Borrás et al., 2016; Calderón-Gutiérrez et al., 2018; Gómez and Calderón-Guitérrez, 2020).

Sediment Core Collection

Sediment cores were obtained from Aerolito using cave diving procedures in July 2014 following safety protocols outlined by the American Academy of Underwater Sciences (AAUS). Sediment cores were collected using 5 or 8 cm diameter clear polycarbonate pipes along a land-sea transect. Four cores were collected proximal to the inland cenote pool (Core 1 to Core 4, collectively referred to as the upstream sites) and four cores between the terrestrial opening and the ocean (Core 5 to Core 8, referred to as the downstream sites) (**Figure 2**). All coring drives ceased at a hardground that is most likely the host carbonate platform. This observation suggests that the cores sampled the complete sedimentary accumulation at each location. The water table elevation is assumed to be sea-level, given the core sites and oceanic proximity. Core collection depths are measured with respect to the modern groundwater table (~sea-level) at the time of sampling using scuba diver depth gauges (vertical accuracy ±0.3 m). Collection depths were not corrected for local microtidal variability. The sediment water interface was located at 10.5 and 6 m below sea-level in the upstream and downstream passages, respectively (**Figure 2**; **Supplementary Table S1**). Sediment cores were then transported back to the laboratory to be split lengthwise, photographed, stratigraphically described, x-radiographed to image downcore density, and continuously stored at 4°C until further analysis.

Lithological Analysis and Radiocarbon Dating

To characterize changes in the coarse carbonate sedimentary fraction, the volumetric mass of sedimentary particles greater than 63 µm was measured in all cores using the Sieve-first Loss-on-Ignition procedure (Sieve-first LOI) (van Hengstum et al., 2016). This approach was chosen because of the known challenges associated with measuring particle size distributions of carbonate sediments using different methods (Murray, 2002). Contiguous 1-cm sediment sub-samples, with a standardized initial volume of 2.5 cm^3 (1.25 cm^3 for smaller diameter cores), were first sieved wet over a 63-µm mesh, dried for 12 h in an oven at 80°C, and weighed to determine the final coarse sediment residue that included both coarse organic particles and mineral matter. Thereafter, desiccated coarse sediment residues were ignited in a muffle furnace at 550°C for 4.5 h to re-mineralize coarse organic matter particles. Remaining sediment residues were then re-weighed to determine a final concentration in milligrams of coarse sedimentary particles exceeding 63 µm in diameter per unit cm^3 (expressed throughout as $D_{>63\mu m}$ mg cm^{-3}). Finally, new sediment sub-samples were obtained at contiguous 1-cm intervals downcore and subjected to a Classic LOI procedure to determine variation in bulk OM content, as per standard methods (550°C for 4.5 h) and reported as weight percent (%) of the original sediment mass (Dean, 1974; Heiri et al., 2001). Uncertainty on laboratory replicates using the Classic LOI approach is typically less than ±1%.

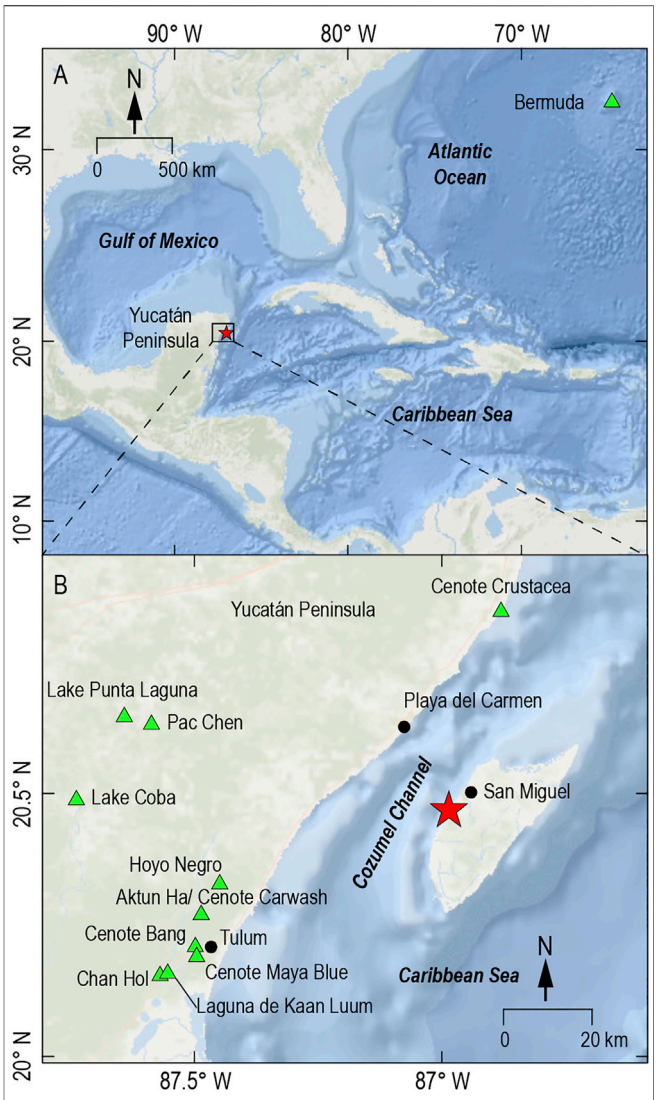


FIGURE 1 | Cozumel Island located east of the Yucatán Peninsula, Mexico. Aerolito Cave (red star) is located on the west coast of Cozumel. Other common research sites in karst subterranean estuaries are also shown (green triangles) in Bermuda (Cresswell and van Hengstum, 2021) and the Yucatán region, such as Hoyo Negro (Kovacs et al., 2017), Carwash (Gabriel et al., 2009), Yax Chen (Collins et al., 2015), Maya Blue (Pohlman et al., 1997), and Cenote Bang (Brankovits et al., 2017).

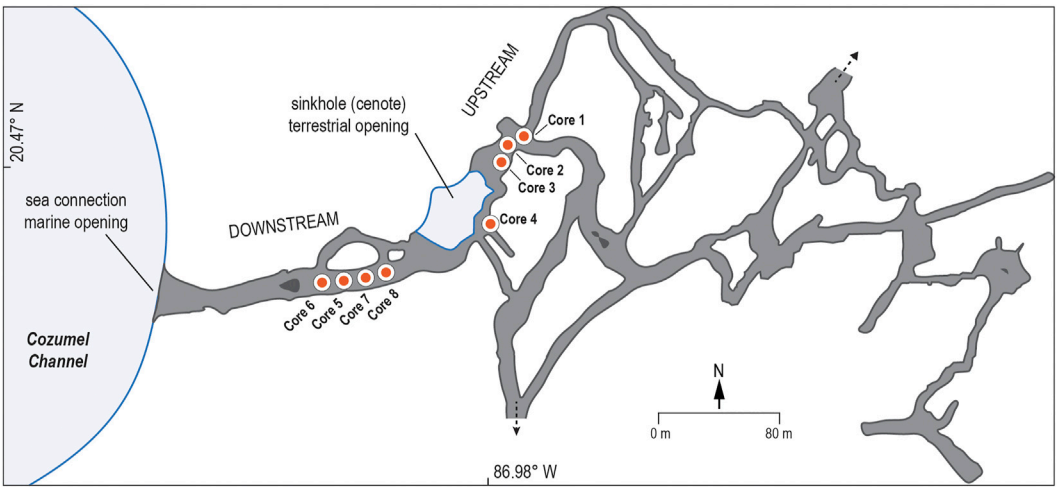


FIGURE 2 | Map of Aerolito Cave in Cozumel Island. Located below sea-level, the cave network promotes seaward material transport and a hydrologically interconnected environment between the sea and the aquifer, providing access to the subterranean estuary. The terrestrial sinkhole opening, colloquially known as Cenote El Aerolito, is partially surrounded by mangroves. Sediment cores (orange circles) were obtained from downstream (Core 5, Core 6, Core 7, and Core 8) and upstream (Core 1, Core 2, Core 3, and Core 4) passages. Map is adapted after Mejía-Ortíz et al. (2007).

Age constraint was provided by radiocarbon dating bulk sedimentary OM particles and, when available, terrestrial plant macrofossils (e.g., twigs). Biogenic carbonates were deemed inappropriate for age purposes because hardwater and marine reservoir effects create problems for calibrating conventional radiocarbon results from marine invertebrates into sidereal years. Six radiocarbon dates were obtained across four cores: Core 1 (2 bulk sedimentary OM), Core 5 (2 terrestrial plant macrofossils), and Core 7 (2 terrestrial plant macrofossils; **Supplementary Table S2**). Material sampled for radiocarbon dating was rinsed with deionized water, dried, weighed, and then submitted for radiocarbon determination at the National Ocean Sciences Accelerator Mass Spectrometry (NOSAMS) Facility at Woods Hole Oceanographic Institution. Conventional radiocarbon dates were calibrated to calendar years before present (cal yrs BP) using IntCal20-NH (Reimer et al., 2020) calibration curves using CALIB 8.2 (Stuiver et al., 2021) (**Supplementary Table S2**).

Stable Carbon Isotope and C:N Ratio Analysis of Organic Matter

Seven cores (Core 1 to Core 7) were sampled contiguously downcore to determine the stable carbon isotopic ratio of bulk organic matter ($\delta^{13}C_{org}$) and the C:N ratio. In coastal settings, $\delta^{13}C_{org}$ and C:N measured from sediment cores can diagnose the organic matter sources deposited through time (e.g., Gonneea et al., 2004; Lamb et al., 2006; Tamalavage et al., 2018; Gonneea et al., 2019). For our cores, a 5 mm sub-sample was obtained every 1 or 2 cm downcore for the entire length (n = 222). Approximately 1.25 cm^3 of sediment was directly acidified with ~8 ml of 1 M hydrochloric acid for 24 h, or until effervescence ceased, then desiccated at 50°C and homogenized into a powder. Determination of $\delta^{13}C_{org}$ and C:N ratio occurred at the Texas A&M University Stable Isotope Geoscience Facility using an Erba NA 1500 Elemental Analyzer that is coupled to a Thermo Scientific DELTA^{plus} isotope ratio mass spectrometer. Final isotopic ratios are reported relative to the standard Vienna Pee Dee Belemnite (VPDB) for carbon in per mil (‰). Analytical precision for two international standards, USGS 40 and 41a which represent a range of $\delta^{13}C$ values for a two-point calibration, are within 0.2‰ (1σ) $\delta^{13}C$. Additional internal standards were used as an internal check for reproducibility. The residual organic carbon %C (acidified residue) was divided by %N (acidified residue) to calculate C:N ratio.

A simple two-source mixing model using $\delta^{13}C_{org}$ values (Fry, 2007) calculated an estimate for the relative terrigenous versus marine supply to sedimentary OM through the terrestrial versus marine openings. This calculation was based on the assumptions that: 1) OM in the cave sediments is derived from two main sources (marine-derived OM transported landward through the marine cave opening and terrestrial-derived OM eroding into the cave through interconnected sinkholes) and 2) the endmember values are preserved with no or minimal changes after burial. We recognize that a two-source mixing model grossly oversimplifies the organic carbon sources delivered to coastal settings because it does not account for the complexity of variable OM sources and diagenesis. For example, potential sedimentary OM sources in coastal settings include primary producers, C3 and C4 plants of coastal vegetation, terrestrial vegetation, and marine and freshwater algae (e.g., Fourqurean et al., 2005; Lamb et al., 2006). Moreover, diagenesis (i.e., biological, chemical, and physical processes) can affect sedimentary OM composition, including $\delta^{13}C_{org}$ values, after burial (e.g., Fogel et al., 1989; Benner et al., 1991; Gonneea et al., 2004). Despite the complexities, this approach can provide a first-order estimate for the relative contribution of terrigenous versus marine sources to the sediment OM in a dark cave setting that facilitates carbon exchange between the land and the sea.

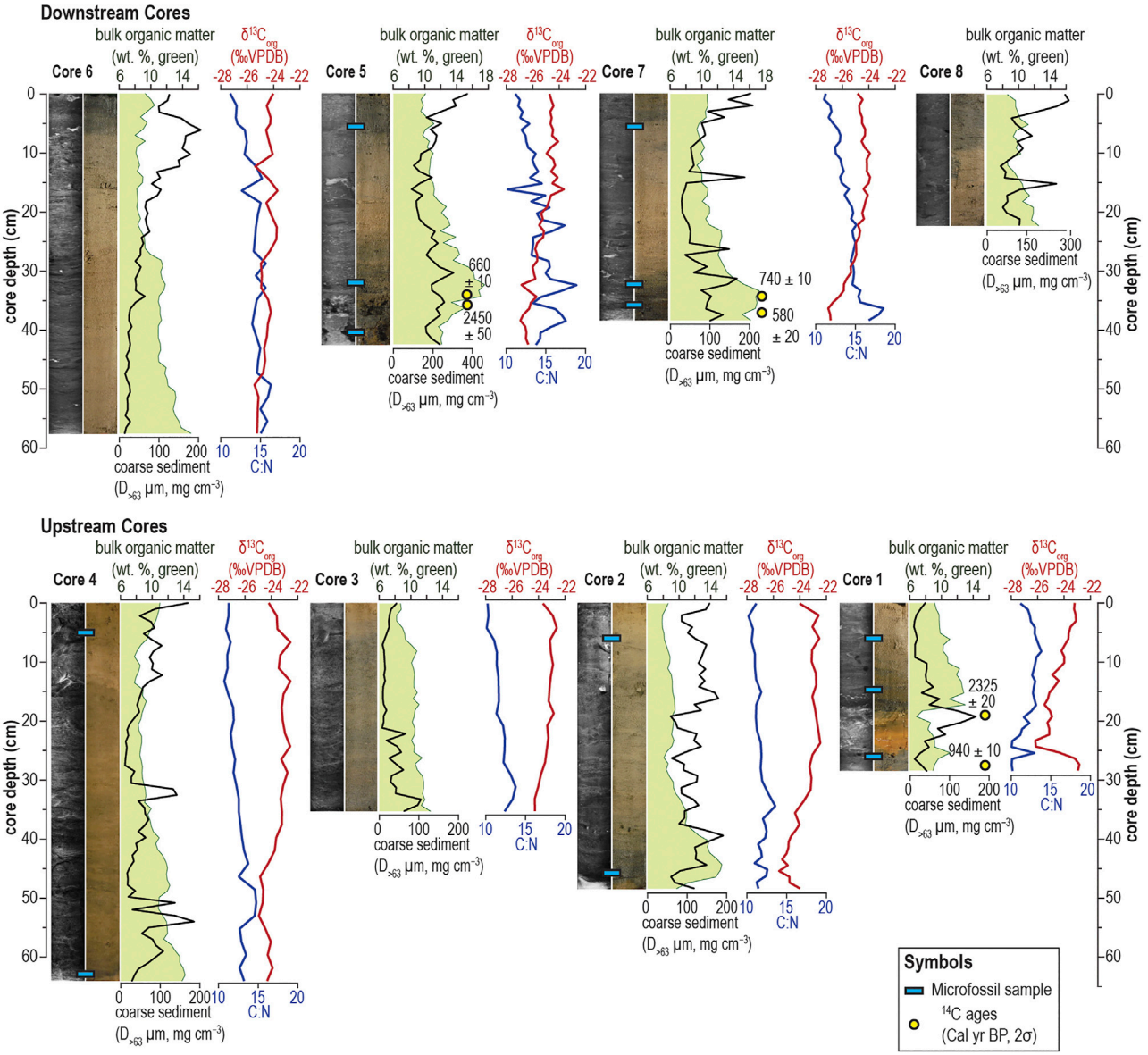


FIGURE 3 | Detailed photographs and x-radiographs of sediment cores are shown with downcore coarse-grained particle deposition (Sieve-first LOI, $D_{>63}$ µm), bulk organic matter (Classic LOI, weight %), stable carbon isotopic values ($\delta^{13}C_{org}$), and C:N ratios. Radiocarbon and microfossil sample positions are marked on relevant cores.

Considering the habitats adjacent to Aerolito, we assume that terrestrially derived OM primarily includes mangrove-derived detritus, other terrestrial and wetland plants, and, in this case, even some biomass from aquatic primary producers in the sinkhole. The assumption that sediment OM was a mix of marine and terrigenous sources can be expressed mathematically by:

$$f_{terrestrial} + f_{marine} = 1, \quad (1)$$

where $f_{terrestrial}$ and f_{marine} are the fractions of OM from the two different sources. To calculate $f_{terrestrial}$, the following equation (**Eq. 2**) was used:

$$f_{terrestrial} = \frac{\delta_{sediment} - \delta_{marine}}{\delta_{terrestrial} - \delta_{marine}}, \quad (2)$$

where $\delta_{sediment}$ is the measured $\delta^{13}C_{org}$ value of the sediment sample, $\delta_{terrestrial}$ is the average $\delta^{13}C_{org}$ value measured across a variety of mangrove plants from multiple habitats in the Yucatán Peninsula (−28.24‰; Gonneea et al., 2004), δ_{marine} is the average $\delta^{13}C_{org}$ value of POM measured from the sea along the coastline in the nearby Cozumel Channel (−20.1‰; Brankovits et al., 2017) which is assumed to represent the isotopic content of marine algae and other components of the coastal marine POM pool. The determined fraction contribution of a source will only reflect the

component of the OM that is preserved and not the original flux to the sediment.

Benthic Foraminifera

Subfossil benthic foraminifera can provide a physical record of changing benthic environmental conditions, such as changes in groundwater salinity, dissolved oxygen concentrations, or organic matter supply (Caralp, 1989; Kaiho, 1994; Gooday, 2003; Jorissen et al., 2007). As such, benthic foraminifera were the model organism used to provide a proxy for any long-term changes in the benthic meiofaunal community in the passages proximal to the ocean of Aerolito Cave. After an assessment of the radiocarbon results (discussed further below), our research design included: 1) sampling both the oldest (basal core samples) and youngest (core-tops) parts of the stratigraphic record (n = 13), and 2) comparing Aerolito foraminiferal assemblages to the dataset of recent benthic foraminifera in Bermudian underwater caves (Cresswell and van Hengstum, 2021; n = 125).

Foraminifera were sampled from Core 1, Core 2, Core 4, Core 5, and Core 7 (n = 13, **Figure 3**). Core-top samples (n = 5) were collected from 5 to 7 cm core depths to ensure that both epifaunal (living at or near the sediment water interface) and infaunal (living deeper in the sediment) foraminiferal taxa would be represented, along with any taxonomic smoothing imparted by local taphonomic effects (e.g., currents or any bioturbation in oxygenated marine settings) or patchiness in local benthic foraminiferal communities. Samples were also collected near the base of the selected cores (n = 8). For each sample, a 1-cm wide interval of 0.63 cm^3 of sediment was obtained from the core and rinsed over a >63-μm sieve to concentrate benthic foraminiferal tests. Benthic foraminifera were counted with a minimum census of 300 individuals per sample (Patterson and Fishbein, 1989; Fatela and Taborda, 2002; Schönfeld et al., 2012). In one sample, 0.63 cm^3 of sediment was insufficient to reach our minimal census count goal and additional sediment was sieved from the same stratigraphic level, resulting in sample volumes spanning 0.63–3.13 cm^3. To promote counting efficiency, four samples were split into representative aliquots using a wet-splitter prior to census counting (Scott and Hermelin, 1993). Foraminifera were wet counted and identified to the species level, with taxonomic identification based on taxonomic literature (Cushman, 1933; Loeblich and Tappan, 1987) and previous studies on cave foraminifera in Bermuda (van Hengstum and Scott, 2011; Little and van Hengstum, 2019; Cresswell and van Hengstum, 2021). The raw foraminiferal database of census counts from the 13 samples from Aerolito included 40 taxonomic units identified to the species level from 60 genera. The resulting dataset was subjected to both unconstrained Q-mode and R-mode cluster analysis to observe any natural groupings between the samples using R Studio software (version 1.1.423; R Core Team, 2020). Using a similarity profile analysis (SIMPROF), 1000 permutations of the cluster analysis were performed to yield a dendrogram with significant clusters (p < 0.05). First, the proportional abundance of each taxa was calculated using the "decostand" function in the "vegan" package (Oksanen et al., 2019) and bubble plots were generated using "ggplot2" (Wickham, 2016). Cluster diagrams and SIMPROF were produced in the "vegan" and "clustsig" (Whitaker and Christman, 2014) packages, using the proportional abundance values, Bray-Curtis dissimilarity index, and UPGMA cluster algorithms. Taxa were excluded from cluster analyses if the calculated standard error was greater than the proportional abundance for a taxonomic unit in all samples.

The foraminiferal results from Aerolito (n = 13) were then compared to dataset of recent foraminiferal distributions in surface samples from Bermudian marine caves (n = 125, Cresswell and van Hengstum, 2021) to create a new composite dataset of 138 samples. Taxonomic differences were evaluated at the genus level in the composite dataset to 1) promote equitable comparison between regions, and 2) taxonomic bias imparted by separate microscopists. While the genera *Patellina* and *Patellinoides* were originally differentiated in the samples from Aerolito Cave, they were subsequently grouped into a pseudo-*Patellina* genus for comparison to Bermuda (see discussion in Cresswell and van Hengstum, 2021). Biodiversity indices [Shannon-Weiner Index (H') and Fisher's Alpha (α)] for each sample was calculated from the raw counts in the final database using the "vegan" package. Species richness (S_{rare}) was calculated using rarefaction with the "rarefy" function in "vegan" because of the spread in the number of individuals counted between samples (ranging from 377 to 1,151). The sub-sample size was set to 377 individuals, which is the minimum sample size observed. Finally, ternary diagrams were generated using the "ternary" package in R (Smith, 2017) with respect to: 1) the proportions of wall structure and life mode (epifaunal versus infaunal), and 2) the $\delta^{13}C_{org}$ value of bulk OM. These ternary plots compared the total percent miliolid taxa (epifaunal and infaunal) to the remaining epifaunal (hyaline and agglutinated) and infaunal taxa (hyaline and agglutinated). Since agglutinated taxa were not common in the dataset from these shallow, tropical carbonate settings, this ternary division best highlighted structural differences in the miliolid-dominated dataset. Designation of hyaline and agglutinated taxa as epifaunal or infaunal primarily followed: Corliss and Chen (1988), Corliss and Emerson (1990), Corliss (1991), Jorissen and Wittling (1999), Murray (2003), with additional references to Rathburn and Corliss (1994), Alve and Bernhard (1995), Gooday (1996), Bernhard and Bowser (1999), Fontanier et al. (2002), and van Hengstum and Scott (2012).

RESULTS

Lithology and Chronology

Sediment in Aerolito is dominated by carbonate materials and organic matter, with negligible contributions from siliciclastic minerals and mean sediment accumulation is just 107 ± 19 cm (eight cores, range: 77–135 cm, **Supplementary Table S1**). Qualitatively, the sediment presents as fine carbonate matrix (e.g., micrite), with inclusions of coarse-grained shell material (bivalves and gastropods), carbonate fecal pellets, and sponge spicules that could be readily observed through stereomicroscopy of wet-sieved sediment (over a >63-μm mesh). In general, basal core sediment was dark brown in color versus the core-tops, and

orange-colored iron-rich sediment appears at the base of Core 2 and Core 4, and from 25–17 cm in Core 1 (**Figure 3**). This sedimentary unit is separated with a sharp interface from overlying carbonate sediments and has decreased bulk organic matter content. Lastly, sedimentary bedding in the carbonate mud was not immediately visible in photographs, but linear bedding could be observed in x-radiographs (**Figure 3**). These observations indicate minimal (<3 cm) vertical post-depositional sediment mixing from bioturbation. However, bedding structures cannot be assumed to indicate long periods of continuous sedimentation because similar sedimentary structures can be rapidly generated following current dissipation and re-dissipation of suspended sediment load after an intense storm (e.g., hurricane).

The downstream passages have generally more bulk OM than the upstream passages (**Figure 3**). Downstream sites have highest bulk OM content toward the base of the core (up to 17.7%) with a gradual upcore decrease at an average rate of −0.11% OM cm^{-1}. This upcore decrease in bulk OM is also present in upstream core sites (Core 2, Core 4, above 17 cm in Core 1), but with a lower rate of −0.04% OM cm^{-1}. The lightest-shaded sedimentary layers in the greyscale radiographs document the densest layers, which typically correspond to iron-rich sediments or relatively higher fractional abundance of coarse sediment grains ($D_{>63\mu m}$ mg cm^{-3}) that have the lowest measured bulk OM content (as low as 7.8% OM in Core 4). For instance, the coarser-grained iron oxide rich layer from 16 to 23 cm in Core 1 has a mean $D_{>63\mu m}$ of 100 mg cm^{-3} ± 40, whereas the rest of the 22 cm core has a mean $D_{>63\mu m}$ is 28 mg cm^{-3} ± 15. Coarse sediment mass generally increases upcore in the downstream cores, but there are no consistent trends in the upstream section (**Figure 3**). Spatially, the downstream cave areas between the sinkhole and the ocean are typically coarser than the upstream, with mean $D_{>63\mu m}$ values of 116 mg cm^{-3} ± 79 (n = 163 cm) versus 67 mg cm^{-3} ± 47 (n = 178 cm) upstream. Sediment with higher bulk OM that is typically near the base of the cores is hereafter referred to as OM-enriched deposits, whereas sediment with lower bulk OM is hereon referred to as OM-limited deposits.

Six radiocarbon dates broadly constrain the onset of sedimentation (**Figure 3**; **Supplementary Table S2**). The basal date from Core 1 has a probable 1σ age of 940 ± 10 cal yrs BP at 27–28 cm, which represents the oldest reliable date for the *minimum* onset of *preserved* sediment accumulation within Aerolito. The second date from Core 1 that is higher in the succession at 19–20 cm dates older to 2325 ± 20 cal yrs BP. However, this date was pulled from an interval with relatively high coarse-grained sediment content (>63 μm), which is perhaps dominated by older sediments reworked by a high energy hydrologic event and were subsequently incorporated into the radiocarbon dated bulk OM. In the downstream passage at Core 5, a date at 36–37 cm is aged to 2450 ± 50 cal yrs BP, but a date just 2 cm higher at 34–35 cm is 660 ± 10 cal yrs BP when bulk OM content increases to ~18%. If the deeper date from Core 5 is accurate, it would suggest ~1,800 years of non-deposition at this core site. Sediments from the basal 35–43 cm interval in Core 5 have relatively low bulk OM (12.9% ± 1.1), which is not represented in other downstream cores. Alternatively, the date at 36–37 cm in Core 5 was obtained on an older plant fragment that became deposited in the cave long after the plant died. The dated plant fragment deeper in Core 7 at 37–38.5 cm is 580 ± 20 cal yrs BP, but the dated plant fragment higher in the succession at 33.5–34 cm has an age of 740 ± 10 cal yrs BP. Again, this shallower and older date is likely a reworked plant fragment from the terrestrial surface that was deposited long after the original plant died. Based on the youngest possible dates in Core 1 (940 ± 10 cal yrs BP, 27–28 cm), Core 5 (660 ± 10 cal yrs BP, 34–35 cm), and Core 7 (580 ± 20 cal yrs BP, 37–38.5 cm), the sediment sampled by the cores accumulated in the last millennium, which is long after the cave was first flooded by Holocene sea-level rise.

Stable Carbon Isotopic Values and C:N Ratios

The $\delta^{13}C_{org}$ values across all core samples (n = 222) range from −22.5 to −27.1‰, and the C:N values vary from 9.9 to 18.9. There is a general upcore decrease in C:N ratios, and $\delta^{13}C_{org}$ values become more enriched (i.e., positive) (**Figure 3**). As a result, the OM-limited sedimentary sections near the top are relatively ^{13}C-enriched and lower in their C:N values compared to the core bottoms. Spatially, sediment archived in downstream passages are characterized with relatively depleted $\delta^{13}C_{org}$ values (mean: −25.0 ± 0.8‰, ranging from −23.6 to −27.1‰) and high C:N ratios (mean: 14.1 ± 1.6, ranging from 10.2 to 18.9). In contrast, sediments located upstream from the terrestrial opening show more enriched $\delta^{13}C_{org}$ values (mean: −23.8 ± 0.9‰, ranging from −22.5 to −26.2‰) and lower C:N ratios (mean: 12.0 ± 1.0, ranging from 9.9 to 14.8).

In general, the two-source mixing model based on $\delta^{13}C_{org}$ values indicates that ^{13}C-depleted OM sources (e.g., terrestrial plants, mangroves), deliver a considerable portion of the organic carbon to the sediment (dataset range: 29–85%). However, there is generally greater terrigenous contribution at the base rather than at the core-tops (**Figure 4**). These patterns suggest that terrestrial organic carbon delivery to the sediment was greater in the past (basal core sediment) than in the present (core-top). Comparing the measured $\delta^{13}C_{org}$ and C:N values with previously reported values of potential OM sources (Lamb et al., 2006) further indicates that organic carbon preserved in the Aerolito sediment is derived from two primary sources: vascular C3 plants and marine POM/algae (**Figure 5A**). In comparison to similar coastal caves in Bermuda (Cresswell and van Hengstum, 2021), sediment in Aerolito preserved less marine-sourced organic carbon, like from marine algae (**Figure 5A**). Interestingly, sedimentary OM closer to the marine opening (downstream) received greater contributions from vascular plant detritus than those near the terrestrial opening (upstream) (**Figure 5**). Moreover, higher bulk OM accumulation (up to 17.7% OM) was associated with greater contribution of percent terrestrial organic carbon (up to 85%) (**Figure 5B**).

Foraminiferal Communities

Benthic foraminifera were abundant in sediment from sampled areas in Aerolito (**Figure 2**). Two groupings can be identified in

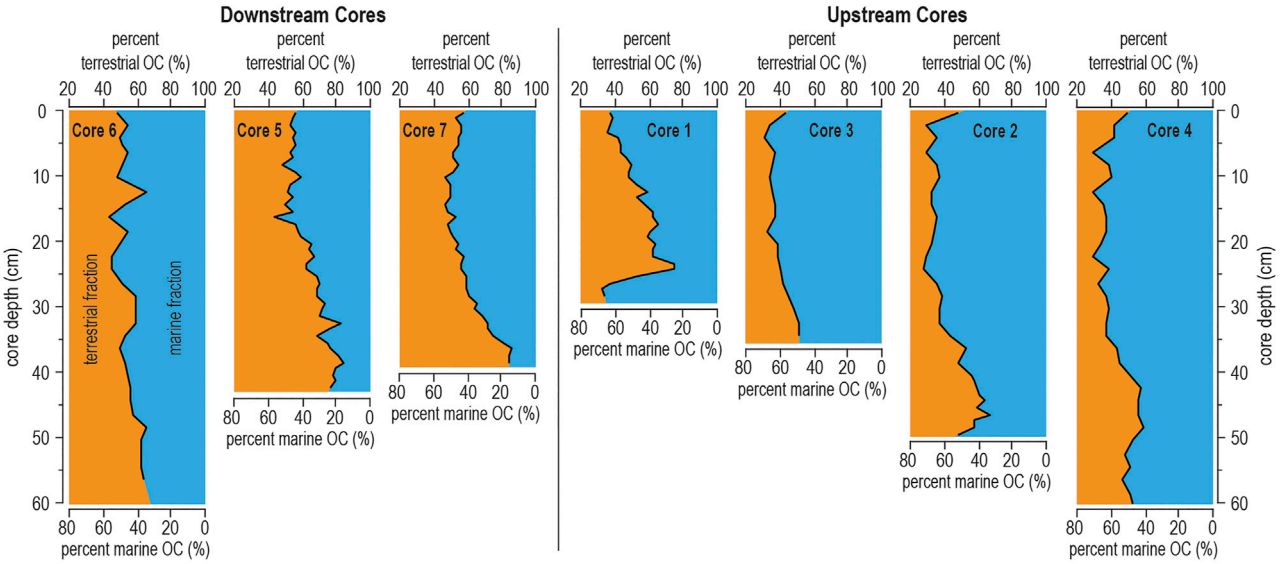


FIGURE 4 | Isotope mixing model results. Downcore trends in the percent terrestrial organic carbon (OC) as calculated from the $\delta^{13}C_{org}$ values using a simple two-source mixing model. The terrestrial endmember value is $\delta^{13}C_{org}$ = −28.2‰, as the mangrove vegetation reported by Gonneea et al. (2004), while the marine endmember is $\delta^{13}C_{org}$ = −20.1‰, as the marine POM along the coast of the Cozumel Channel reported by Brankovits et al. (2017).

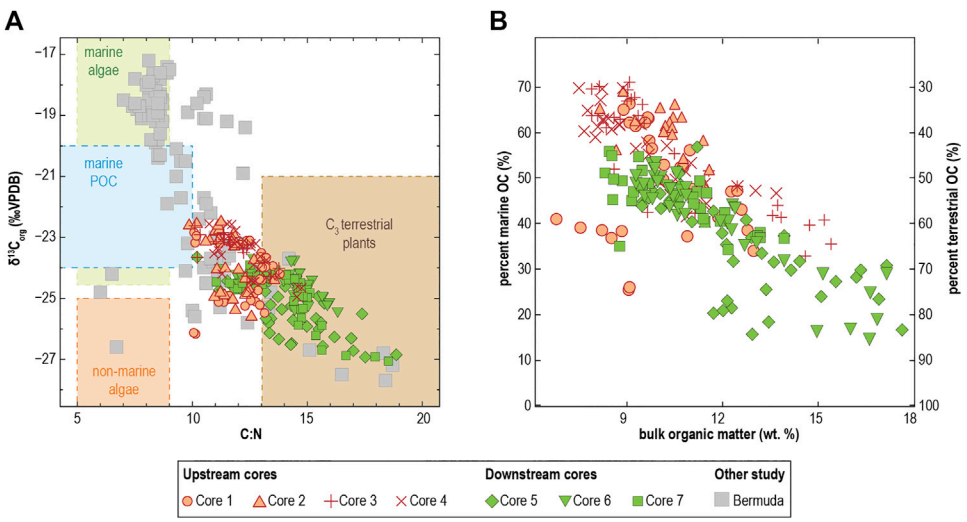


FIGURE 5 | (A) Cross-plot between stable carbon isotopic values ($\delta^{13}C_{org}$) and C:N ratio of bulk organic matter in Aerolito Cave (this work) and Bermuda caves (Cresswell and van Hengstum, 2021). **(B)** Cross-plot between bulk organic matter content (Classic LOI, weight %) and the percent marine/terrestrial organic carbon as calculated from the two-endmember mixing model based on $\delta^{13}C_{org}$ values.

the dendrogram produced from unconstrained Q-mode cluster analysis (**Figure 6**), which generally separates core-top samples (i.e., less bulk OM, more depleted $\delta^{13}C_{org}$ values) from the bottom of the cores (i.e., higher bulk OM, more enriched $\delta^{13}C_{org}$ values). The two communities are hereafter referred to as the OM-limited Community (recent) and the OM-enriched Community (past) (**Figure 6**). There is little taxonomic difference between the two communities identified by Q-mode cluster analysis, which indicates negligible long-term changes in water column structure in the sampled areas.

However, the relative abundance of infaunal (i.e., *Bolivina*) versus miliolid taxa differentiates the two foraminiferal communities, along with the proportions of shared common taxa (**Figure 6**). In the OM-limited Community (core-tops), the dominant fauna (>10%) are the porcelaneous miliolid taxa (33.1%; e.g., *Quinqueloculina*, *Triloculina*, *Spirophthalmidium*)

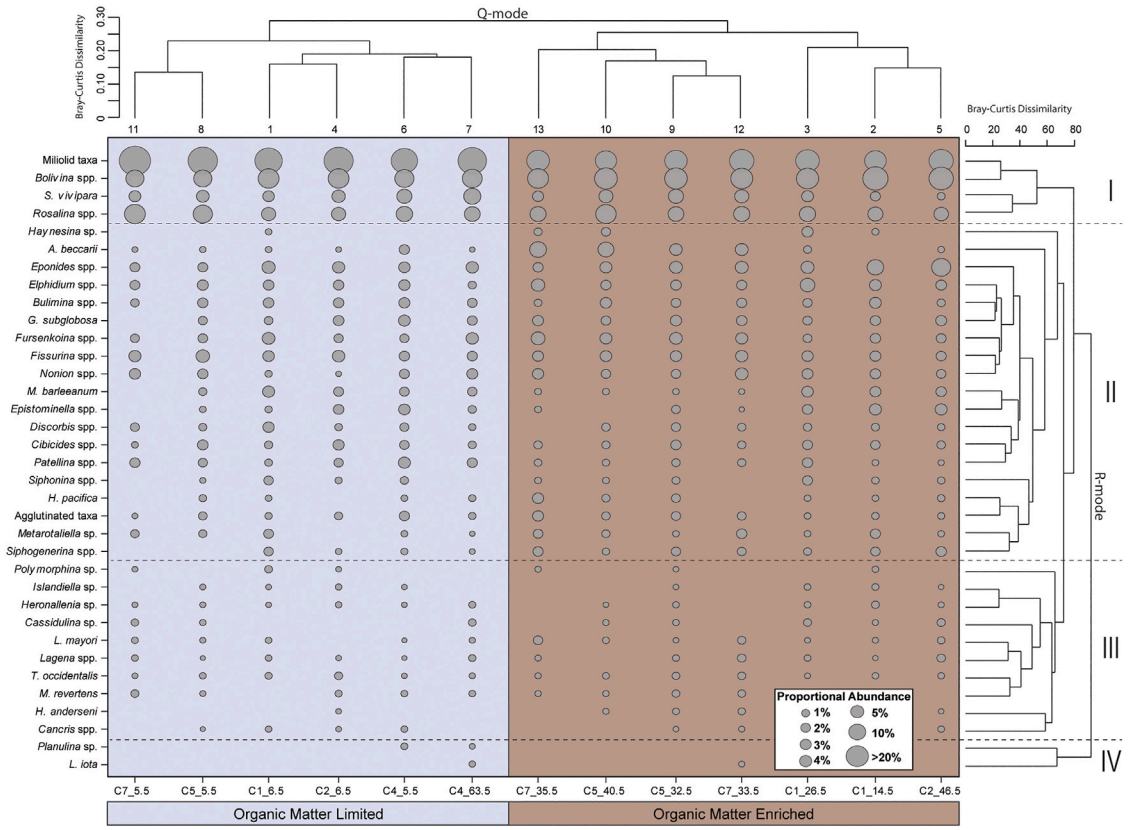


FIGURE 6 | Dendrogram produced from two-way hierarchical cluster analysis of the benthic foraminiferal data in Aerolito. The Q-mode cluster analysis identifies two main groups: OM-limited Community (purple field) and OM-enriched Community (brown). The R-mode cluster analysis highlights dominant (Group I), common (Group II), rare (Group IV), and very rare taxa (Group IV). Sample codes (bottom row) are based on the core ID followed by sample depth in cm (e.g., C7_5.5 was sampled from Core 7 at 5.5 cm core depth).

and the infaunal hyaline genus *Bolivina* (14.1%). Other common taxa (>5%) include *Rosalina* spp. (mean: 10.0%) and *Spirillina* (mean: 5.7%) (**Supplementary Table S3**). In contrast, the OM-enriched Community (basal sediments) has an increased abundance of *Bolivina* (20.7%), decreased miliolids (21.2%), and common occurrences of *Rosalina* (9.0%) and *Eponides* (6.1%). Foraminiferal density is also higher in the OM-limited Community (mean: 4357 individuals cm^{-3}) than the OM-enriched Community (mean: 915 individuals cm^{-3}), though both communities have a similar diversity (H'_{OML}: 2.36; H'_{OME}: 2.62).

The R-mode cluster analysis identifies four groups of species (**Figure 6**). Group I contains the top four dominant taxa (mean: ≥5%) present in both communities from the unconstrained Q-mode cluster analysis: miliolid taxa, *Bolivina*, *Rosalina*, and *S. vivipara*. Group II comprises the greatest number of taxonomic units ($n = 19$), which are common to both communities and includes taxa such as the infaunal taxa *Bulimina*, *Ammonia*, and rare agglutinated fauna. *Ammonia* is rare in the OM-limited Community (mean: <1%), but it achieves a higher proportion in the OM-enriched Community (mean: 4.7%). Group III ($n = 10$) contains rare taxa (mean: <2%) that are present in nearly every sample, whereas Group IV consists of only two genera which occur in only two samples (mean: <1%).

The two communities also exhibit differences in foraminiferal test structure and morphology (**Figure 7**; **Supplementary Table S4**). The ternary diagrams depict an overall increase in miliolid taxa in the core-top (i.e., youngest) versus bottom (i.e., oldest), and differences in the proportions of infaunal taxa versus epifaunal taxa. The older OM-enriched Community (numbered brown data points on **Figure 7A**) has more infaunal taxa (mean: 46.5%; range: 42.5–52.1%), such as *Bolivina*, *Buliminella*, and *Fursenkoina*, with decreased miliolid abundance (20.7%; range: 17.3–23.7%) and epifaunal taxa (mean: 31%; range: 27.6–38.4%). The younger OM-limited Community (numbered purple data points on **Figure 7A**) has higher miliolid abundances (mean: 20.7%; range: 17.3–23.7%), epifaunal species (mean: 28.7%; range: 23.8–38.4%), and decreased infaunal taxa (mean: 34.4%; range: 26.1–43.5%).

DISCUSSION

Integrity of Sedimentation

Based on the radiocarbon ages, the basal age result of ~940 cal yrs BP from Core 1 most likely constrains the earliest possible onset of modern sedimentation. An overall young (i.e., last millennium

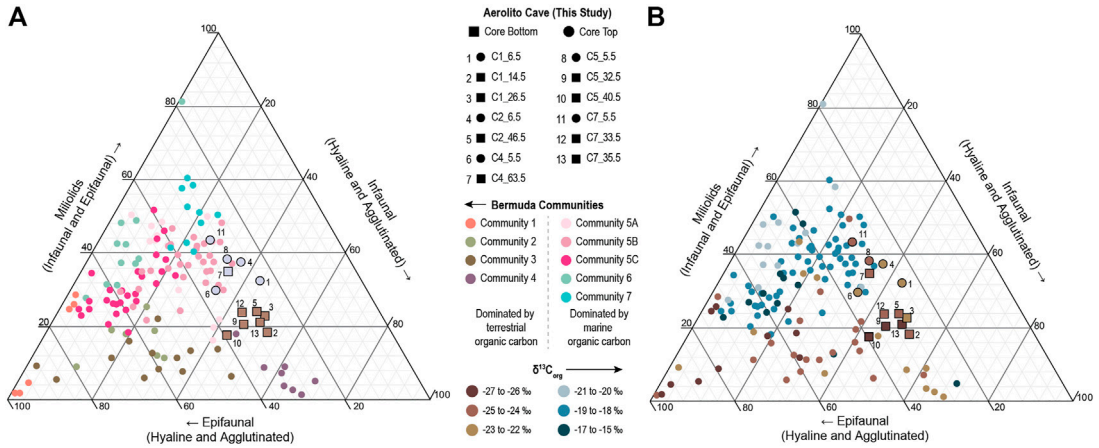


FIGURE 7 | Ternary diagrams depicting the proportion of benthic foraminiferal taxa in each sample organized into miliolid, non-miliolid epifaunal, and non-miliolid infaunal taxa. Results from this study (numbered circles and squares) are compared to benthic foraminifera from karst subterranean estuaries in Bermuda (smaller circles) (Cresswell and van Hengstum, 2021). Samples in the ternary diagram are color coded **(A)** by community designation (Aerolito Cave OM-limited Community in purple and OM-enriched Community in brown), and **(B)** by $\delta^{13}C_{org}$ values of sediment OM.

at most) age for the recovered stratigraphy from this part of Aerolito Cave is also supported by the young basal age from Core 7 of 580 ± 20 cal yrs BP at 37–38.5 cm. Parts of the western North Atlantic margin experienced increased intense hurricane activity from 2600 to 1000 cal yrs BP (Donnelly and Woodruff, 2007; van Hengstum et al., 2016). Thus, it is possible that any older than ~1,000 years old sedimentary deposits were washed out from the cave when more frequent intense hurricane activity repetitively increased the velocity of groundwater flow.

Although an assessment of temporal change is tempered by potential impacts to the stratigraphic integrity by more recent high-energy storm events, the recovered cores do preserve a record of long-term environmental change in Aerolito during the last millennium. Older radiocarbon dated material (e.g., ~2450 and 2325 cal yrs BP in Core 5 and Core 7) could either have been transported and deposited into the cave after death of the original plant, or potentially indicate re-suspension of preexisting sedimentary material in the cave following a hurricane. Occasional increase in coarse-grained sediment content in the cores collectively suggest that modern sedimentation has likely been affected by episodic hydrologic events like hurricanes. However, distinctive coarse-grained tempestite beds were not visible in the stratigraphy despite the available sediment supply (e.g., shell material), and the upcore stratigraphic trends are not characterized by repetitive fining upward sequences that commonly develop from hurricane-induced suspension and redeposition of sediment in marine environments (Kuenen and Migliorini, 1950; Wanless, 1981; Bentley et al., 2002; Toomey et al., 2013). The original horizontal bedding imaged by the x-radiographs and the intact iron-rich sedimentary deposit in Core 1, with sharp contacts with overlying and underlying carbonate sediment, all lend further support that the sediments can be used to evaluate long-term environmental trends (**Figure 3**). While some bioturbation is expected, these sedimentary structures indicate that complete vertical post-depositional sediment mixing and homogenization from bioturbation or groundwater currents have not occurred. Taken together, these observations lend confidence that the recovered cores preserve, at least, a low-resolution record of long-term environmental change in Aerolito.

Iron Oxide Sediment

Sedimentary layers with increased iron oxide concentrations occur both intercalated within a core (Core 1) and at the base of cores (Core 2 and Core 4; **Figure 3**). The intercalated iron-rich sedimentary unit in Core 1, which has decreased bulk OM content, is separated with a sharp interface from overlying sediments. It is highly likely that Cozumel experiences some Saharan dust deposition from atmospheric transport (Prospero and Nees, 1986; Prospero and Lamb, 2003; Muhs et al., 2007). However, the recovered iron-rich sediments are likely not derived from Saharan dust deposition because these sediments are most likely less than 1,000 years old (see above), and Aerolito and other caves flanking the Cozumel Channel at similar elevations would have already been flooded by Holocene sea-level rise (Gabriel et al., 2009; Milne and Peros, 2013; Khan et al., 2019).

An alternative hypothesis is that these iron-rich sedimentary deposits have an *in situ*, subaquatic origin. In siliciclastic subterranean estuaries, the oxidative precipitation of dissolved Fe(II) from the mixing of seawater and groundwater causes iron oxide deposition in the subsurface (Charette and Sholkovitz, 2002). Similar iron-rich deposits have been observed in Palm Cave (van Hengstum et al., 2019) and Green Bay Cave (van Hengstum et al., 2011) in Bermuda, where it has been hypothesized that they originate from the oxidative precipitation of Fe(II)-rich minerals in an "iron curtain" along a redox gradient at the sediment-water interface as anoxic saline groundwater upwells into the oxygenated caves within carbonate platforms (van Hengstum et al., 2011; van Hengstum et al., 2019). We speculate that a similar mechanism is also occurring in

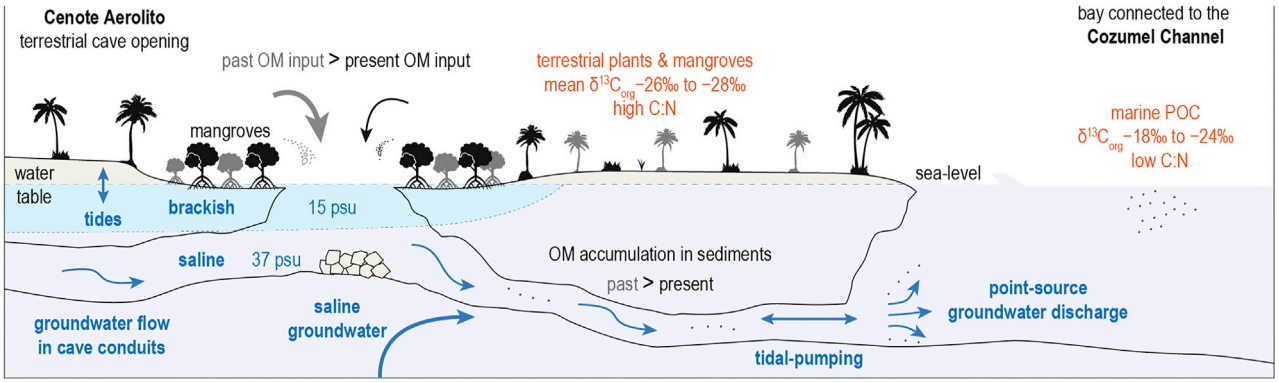


FIGURE 8 | Landscape-level conceptual model summarizing organic matter (OM) dynamics in the karst subterranean estuary (KSE). Hydrologic forcing (blue arrows) through cave conduits accelerates the transport and exchange of material between the terrestrial and marine environments. These processes are especially amplified during episodic events (e.g., hurricanes). OM inputs from mangroves and terrestrial vegetation into the KSE were greater in the past (gray arrow) than in the present (black arrow), resulting in a decrease in the accumulated OM in the caves over time. Reduced OM inputs likely caused a shift in biogeochemical conditions which prompted a change in the benthic foraminifera communities. Higher terrestrial OM accumulation near the marine opening is from persistent seaward material transport during the last millennium.

Aerolito Cave, but further work is required to assess these geochemical processes in KSEs.

Evidence for Reduction in Organic Matter Inputs From a Mangrove Habitat

Based on the simplistic two-endmember mixing model, the terrestrial-sourced OM contributions to the sediment OM pool vary from 29 to 85% (**Figure 5B**). Although the proportion of ^{13}C-depleted OM has decreased over time, its sources continued to contribute to the sediments throughout the record (**Figure 4**). These patterns are most likely a result of mixed OM supply from the mangroves or other vegetation surrounding the terrestrial opening, similar to observations in the Yucatán Peninsula (van Hengstum et al., 2010; Collins et al., 2015), The Bahamas (Tamalavage et al., 2018; Björnerås et al., 2020), and Bermuda (van Hengstum et al., 2011; Little and van Hengstum, 2019). Globally, mangrove ecosystems are important carbon reservoirs (Donato et al., 2011) and a major source of organic carbon to the oceans (Dittmar et al., 2006; Maher et al., 2013), and they clearly contribute considerable organic carbon to tropical KSEs. POM with low C:N ratios and ^{13}C-depleted isotopic values, which is indicative of *in-situ* biomass production by freshwater algae in the flooded sinkhole, is another likely source of OM that fluxes into the cave environment (Tamalavage et al., 2018). It is possible that the higher C:N ratios in basal core sediment is partly from diagenetic alteration of OM from the preferential loss of nitrogen (e.g., Fogel et al., 1989; Benner et al., 1991; Gonneea et al., 2004; Lamb et al., 2006). However, increased C:N values in the basal sediments are associated with high bulk OM content and depleted $\delta^{13}C_{org}$ values, which suggests that OM inputs from the terrestrial sinkhole were higher in the past than in the present.

An upcore decrease in bulk OM is present in all cores and is associated with an overall decline in C:N ratios, increasing $\delta^{13}C_{org}$ values, and consequent decrease in terrestrially derived OM contribution as estimated by the two-source mixing model (**Figure 4**). Because the joint shifts in bulk OM, C:N ratios, and $\delta^{13}C_{org}$ values are most likely a result of lessening OM supply by mangrove vegetation through the sinkhole pool, it is possible that the mangrove habitat on the adjacent surface have shrunk in the last ~1,000 years (**Figure 8**). One may consider that increased POM inputs from the marine algae (with more enriched $\delta^{13}C_{org}$ values) could also explain the decrease in the fraction of terrestrially derived OM in the sediments. However, the OM-enriched sediment in Aerolito has depleted $\delta^{13}C_{org}$ values and relatively high C:N ratios, which suggests that the observed shift in OM accumulation was primarily driven by changing supplies from wetland and/or terrestrial plants. Shifts in OM supply may affect biogeochemical cycling in KSEs, which could impact the composition of the discharged groundwater (Moore, 1999; Moore, 2010), but how this change in OM supply impacted elemental cycling in Aerolito through time remains unknown.

Bulk OM content is generally higher near the marine opening that is downstream from the sinkhole, versus core sites that are proximal to and upstream from the sinkhole. Higher bulk OM has also been documented downstream from inland sinkholes (i.e., cenotes) on the Yucatán Peninsula (van Hengstum et al., 2009; Collins et al., 2015). Higher OM content downstream is associated with high C:N and depleted $\delta^{13}C_{org}$ values (**Figure 3**) and, thus, likely receives larger contributions from terrestrial sources (**Figures 4**, **5B**). Tidal-pumping of seawater between the ocean and karst aquifer facilitates the inland transport of marine-derived OM through the caves up to 400 m from the marine opening (**Figure 4**). At the same time, the general land-to-sea direction of fresh groundwater flow in the region promotes the seaward transport of non-marine POM delivered to the flooded cave environment through the terrestrial opening, rather than upstream from the terrestrial opening. This scenario is consistent with our observations *in situ*. During sample collections, sediment accumulation was negligible in the conduits further inland from the upstream sampling locations. Extreme hydrologic events (e.g., hurricanes) can

amplify the seaward groundwater transport and subsurface currents, which may further influence POM distribution in the conduits. Hydrodynamic sorting may also contribute to the dissemination of terrigenous POM during hydrologic transport (Keil et al., 1994; Goñi et al., 1997).

In summary, evidence for continuous accumulation of terrestrially derived OM in the downstream passages confirms that the conduits have facilitated land-to-sea transport of OM during the last millennium (**Figure 8**). These observations support findings in other KSEs that the type of surface vegetation and the presence of terrestrial openings are key factors regulating POM inputs to coastal sinkholes (e.g., van Hengstum et al., 2010; van Hengstum et al., 2011; Collins et al., 2015; Gregory et al., 2017; Tamalavage et al., 2018; Little and van Hengstum, 2019). Such high POM inputs can promote eutrophic KSE sub-habitats that are in contrast with oligotrophic cave areas distant from openings (Pohlman, 2011; Brankovits et al., 2017) and the greater aquifer (groundwater-rock matrix) with limited connectivity to the surface. Open sinkholes, however, are known to exert a clear biogeochemical influence on the subterranean realm on tropical carbonate landscapes, and their influence is transmitted to oligotrophic caves and to the ocean by groundwater flow. For example, quantitative evidence from time-series data have shown the importance of rainfall-induced hydrological transport of OM from inland mangroves to the coastline through cave networks (Coutino et al., 2020). Although karst platforms account for a substantial percentage of certain trace element inputs to the ocean globally (Beck et al., 2013; Gonneea et al., 2014; Mayfield et al., 2021), point-sources of groundwater discharge only represents a (likely small) portion of these inputs. Point-source discharge, however, can influence coral reefs (Crook et al., 2012) and other local ecosystems (Moosdorf et al., 2015) while contributing to the heterogeneity of land-to-sea material fluxes along global coastlines (Luijendijk et al., 2020; Moore and Joye, 2021; Rocha et al., 2021).

Broader Comparison of Benthic Foraminifera Communities

Aerolito Cave contains benthic foraminiferal taxa that are similar to flooded coastal caves in Bermuda (Cresswell et al., 2017; Cresswell and van Hengstum, 2021). However, the foraminiferal communities of Aerolito have a lower proportion of epifaunal taxa and increased infaunal taxa. For example, non-miliolid epifaunal taxa reach proportions as high as >80% in Bermuda while the maximum proportion recorded in Aerolito is only 38.4% (**Figure 7**). The OM-enriched Community of Aerolito is most similar to foraminiferal communities from Bermuda that are also found in sediments with depleted $\delta^{13}C_{org}$ values (likely because of increased terrestrial OM input), such as Community 4 from Green Bay Cave (GBC), as both contain a larger proportion of infaunal taxa ($mean_{OME}$: 46.5%; $mean_{GBC}$: 33.7%) and decreased miliolids ($mean_{OME}$: 20.7%; $mean_{GBC}$: 12%) (**Figure 7**). Aerolito's OM-limited Community (core-top) is more similar to Community 5B in Green Bay Cave, as both foraminifera communities have similar abundances of miliolid taxa ($mean_{OML}$: 35.6%; $mean_{GBC}$: 36.2%). Green Bay Cave's well-oxygenated water column is exposed to regular tidally forced groundwater-seawater exchange.

Overall sediment $\delta^{13}C_{org}$ values in Aerolito are more depleted than observed in Bermuda marine caves (**Figures 5A**, **7B**), which suggests that marine POM provides a larger contribution to the sedimentary OM pool in Bermuda KSEs than in Aerolito. Like Bermuda, sediments with a higher proportion of miliolid taxa in Aerolito tend to have more enriched $\delta^{13}C_{org}$ values (**Figure 7B**), which suggests that marine-derived POM delivery is beneficial to miliolid taxa in these environments. Sediment $\delta^{13}C_{org}$ values in Aerolito are most similar to the terrestrially influenced regions of Green Bay Cave (mean: −24.37‰) and Cow Cave (mean: −25.93‰) in Bermuda. More broadly, the presence of *Spirophthalmidium emaciatum* is also consistent with marine caves in Spain (Bergamin et al., 2020) and Bermuda (Cresswell and van Hengstum, 2021). Future comparisons to marine caves elsewhere in the tropical North Atlantic, such as Giant Cave in Caye Caulker (Fosshagen and Iliffe, 1991), could provide further insight into the differential impacts of OM delivery on cave benthic meiofaunal communities. It remains unknown how variation in the relative contributions from marine and terrigenous OM sources cascades and impacts the subterranean food webs in Bermuda versus Aerolito, but perhaps these differences contribute to regional biogeographical variances in higher-order cave fauna.

Benthic Foraminifera Respond to Organic Matter Changes

Foraminiferal community shifts suggest that decreasing OM inputs from a mangrove habitat over time impacted the benthic meiofaunal community in Aerolito Cave. Benthic foraminiferal communities are significantly controlled by OM quantity and source (e.g., terrestrial versus marine), both as a food source and by impacting bottom water and pore-water oxygenation (Corliss and Chen, 1988; Gooday and Turley, 1990; Bernhard, 1992; Jorissen et al., 1995; Belanger et al., 2020; Dimiza et al., 2020). The environmental control of OM supply on benthic foraminiferal communities has been documented in a variety of coastal environments such as the Mediterranean (Dimiza et al., 2020) and the Bay of Biscay (Fontanier et al., 2002), as well as the deep sea (Corliss and Chen, 1988; Jorissen et al., 1995). OM effects on benthic foraminiferal microhabitats have been previously explored within the KSEs of Bermuda (van Hengstum and Scott, 2011; Cresswell et al., 2017; Little and van Hengstum, 2019; Cresswell and van Hengstum, 2021), where habitats with more increased terrestrial-based OM (depleted $\delta^{13}C_{org}$ values) are favored by certain taxa (e.g., *Helenina, Bolivina*, *Rosalina*).

In Aerolito, the basal part of the cores that have increased bulk OM and depleted $\delta^{13}C_{org}$ values are associated with increased infaunal benthic foraminifera (e.g., *Bolivina*, *Bulimina*, *Fursenkoina*) and *Ammonia beccarii* (mean: 4.7% versus <1% in core-tops, **Figures 6**, **7**). However, there was likely *no* widespread or long-term change in the physicochemical characteristics of the water column (e.g., dissolved oxygen and salinity). While increased *Ammonia* and infaunal taxa can be

related to decreased dissolved oxygen concentration (Moodley and Hess, 1992; Jorissen et al., 1995; Sen Gupta et al., 1996), miliolid foraminifera are generally intolerant to long-term suboxic to anoxic conditions (<1.5 ml/L dissolved oxygen; Kaiho, 1994) and they are abundant in all Aerolito samples examined. In addition, the lack of agglutinated taxa (e.g., *Trochammina*, *Entzia, Miliammina*) associated with brackish water in caves and sinkholes (van Hengstum et al., 2008; Little and van Hengstum, 2019; Cresswell and van Hengstum, 2021) indicates that brackish conditions at the sediment-water interface were not persistent over the last 1,000 years in Aerolito. These results suggest that despite observations for short-term water column changes in Aerolito from increased freshwater discharge during hurricanes (Calderón-Gutiérrez et al., 2018), the conditions rebound back to the pre-storm conditions fairly quickly. Alternatively, subtle changes in OM sourcing and supply may alter: 1) the dissolved oxygen concentrations in the benthic foraminifera microhabitats, in turn impacting foraminiferal distributions, or 2) OM resource allocation and exploitation by different foraminifera genera in KSEs (Cresswell and van Hengstum, 2021). While *in-situ* microcosm experiments could help resolve the precise mechanisms, these findings indicate that changes in OM delivery into Aerolito over time have impacted benthic meiofaunal communities.

CONCLUSION

- Only young sediment from the last 1,000 years is preserved in Aerolito, despite the fact that the cave was flooded by the coastal aquifer thousands of years prior from deglacial sea-level rise. More frequent intense hurricane activity prior to 1,000 years ago may have exported older sediment out of the cave from constant increases in groundwater flow and discharge rates.
- The source and quantity of OM exported from the subterranean estuary to adjacent ocean is not constant through time, and its export is linked to: 1) changes in adjacent aquatic and terrestrial habitats and 2) potentially large storm events. In contrast, the coastal caves have allowed marine-derived OM to enter the aquifer in spite of the net land-to-sea hydrologic transport from the discharge of coastal groundwater.
- Over the last millennium, a decrease in terrestrial OM deposition (reduction in C:N ratios and increase in $\delta^{13}C_{org}$ values) in the cave suggests that the magnitude of OM inputs from adjacent subaerial environments has decreased. We hypothesize that the contribution of ^{13}C-depleted OM from mangroves in the adjacent sinkhole has changed through time, caused by a decrease in the areal extent of the mangroves in the area.
- Benthic foraminiferal community changes reveal an ecological response to decreased OM supply to the cave through time. In the past, when OM supply was higher and dominated by non-marine sources (i.e., depleted $\delta^{13}C_{org}$ values), the benthic foraminiferal community in Aerolito was composed of taxa preferentially found in sediment with ^{13}C-depleted bulk OM in Bermudian caves that have well-oxygenated water columns. The hypothesized cause of these community shifts is a change in food resource partitioning between foraminiferal genera through time.

DATA AVAILABILITY STATEMENT

The original contributions presented in the study are included in the article/**Supplementary Material**, further inquiries can be directed to the corresponding author.

AUTHOR CONTRIBUTIONS

The project was conceived by PvH and LMM-O. PvH, TW, and GY-M collected the samples. DB, SL, TW, AT, and CM completed the laboratory activities. DB and SL conducted data analyses. DB, TW, and SL generated the artwork. All authors contributed to data interpretation, and DB wrote the manuscript with contributions from all.

FUNDING

Funding for DB was provided by the Texas A&M University at Galveston Postdoctoral Fellowship.

ACKNOWLEDGMENTS

John W. Pohlman and Fernando Calderón-Gutiérrez provided valuable feedback during the writing. Two reviewers are thanked for comments to improve the final manuscript.

SUPPLEMENTARY MATERIAL

The Supplementary Material for this article can be found online at: https://www.frontiersin.org/articles/10.3389/fenvs.2021.670914/full#supplementary-material

REFERENCES

Airoldi, L., and Cinelli, F. (1996). Variability of Fluxes of Particulate Material in a Submarine Cave with Chemolithoautotrophic Inputs of Organic Carbon. *Mar. Ecol. Prog. Ser.* 139, 205–217. doi:10.3354/meps139205

Alve, E., and Bernhard, J. M. (1995). Vertical Migratory Response of Benthic Foraminifera to Controlled Oxygen Concentrations in an Experimental Mesocosm. *Mar. Ecol. Prog. Ser.* 137–151.

Bauer-Gottwein, P., Gondwe, B. R. N., Charvet, G., Marín, L. E., Rebolledo-Vieyra, M., and Merediz-Alonso, G. (2011). Review: The Yucatán Peninsula Karst Aquifer, Mexico. *Hydrogeol J.* 19, 507–524. doi:10.1007/s10040-010-0699-5

Beck, A. J., Charette, M. A., Cochran, J. K., Gonneea, M. E., and Peucker-Ehrenbrink, B. (2013). Dissolved Strontium in the Subterranean Estuary - Implications for the Marine Strontium Isotope Budget. *Geochimica et Cosmochimica Acta* 117, 33–52. doi:10.1016/j.gca.2013.03.021

Beddows, P. A., Smart, P. L., Whitaker, F. F., and Smith, S. L. (2007). Decoupled Fresh-Saline Groundwater Circulation of a Coastal Carbonate Aquifer: Spatial Patterns of Temperature and Specific Electrical Conductivity. *J. Hydrol.* 346, 18–32. doi:10.1016/j.jhydrol.2007.08.013

Belanger, C. L., Sharon, J., Du, J., Payne, C. R., and Mix, A. C. (2020). North Pacific Deep-Sea Ecosystem Responses Reflect Post-glacial Switch to Pulsed Export Productivity, Deoxygenation, and Destratification. *Deep Sea Res. Oceanographic Res. Pap.* 164, 103341. doi:10.1016/j.dsr.2020.103341

Benner, R., Fogel, M. L., and Sprague, E. K. (1991). Diagenesis of Belowground Biomass of Spartina Alterniflora in Salt-Marsh Sediments. *Limnol. Oceanogr.* 36, 1358–1374. doi:10.4319/lo.1991.36.7.1358

Bentley, S. J., Keen, T. R., Blain, C. A., and Vaughan, W. C. (2002). The Origin and Preservation of a Major Hurricane Event Bed in the Northern Gulf of Mexico: Hurricane Camille, 1969. *Mar. Geol.* 186, 423–446. doi:10.1016/s0025-3227(02)00297-9

Bergamin, L., Taddei Ruggiero, E., Pierfranceschi, G., Andres, B., Constantino, R., Crovato, C., et al. (2020). Benthic Foraminifera and Brachiopods from a Marine Cave in Spain: Environmental Significance. *Medit. Mar. Sci.* 21, 506–518. doi:10.12681/mms.23482

Bernhard, J. M. (1992). Benthic Foraminiferal Distribution and Biomass Related to Pore-Water Oxygen Content: Central California Continental Slope and Rise. *Deep Sea Research Part A. Oceanographic Res. Pap.* 39 (3-4), 585–605. doi:10.1016/0198-0149(92)90090-g

Bernhard, J. M., and Bowser, S. S. (1999). Benthic Foraminifera of Dysoxic Sediments: Chloroplast Sequestration and Functional Morphology. *Earth Sci. Rev.* 46 (1-4), 149–165. doi:10.1016/s0012-8252(99)00017-3

Bishop, R. E., Humphreys, W. F., Kršinić, F., Sket, B., Iliffe, T. M., Žic, V., et al. (2015). 'Anchialine' Redefined as a Subterranean Estuary in a Crevicular or Cavernous Geological Setting. *J. Crustacean Biol.* 35, 511–514. doi:10.1163/1937240x-00002335

Björnerås, C., Škerlep, M., Gollnisch, R., Herzog, S. D., Ugge, G. E., Hegg, A., et al. (2020). Inland Blue Holes of the Bahamas–chemistry and Biology in a Unique Aquatic Environment. *Fundam. Appl. Limnol.* 95–106. doi:10.1127/fal/2020/1330

Brankovits, D., Pohlman, J. W., Ganju, N. K., Iliffe, T. M., Lowell, N., Roth, E., et al. (2018). Hydrologic Controls of Methane Dynamics in Karst Subterranean Estuaries. *Glob. Biogeochem. Cycles* 32, 1759–1775. doi:10.1029/2018gb006026

Brankovits, D., Pohlman, J. W., Niemann, H., Leigh, M. B., Leewis, M.-C., Becker, K. W., et al. (2017). Methane-and Dissolved Organic Carbon-Fueled Microbial Loop Supports a Tropical Subterranean Estuary Ecosystem. *Nat. Commun.* 8, 1835. doi:10.1038/s41467-017-01776-x

Calderón-Gutiérrez, F., Sánchez-Ortiz, C., and Huato-Soberanis, L. (2018). Ecological Patterns in Anchialine Caves. *PLoS ONE* 13. doi:10.1371/journal.pone.0202909

Caralp, M. H. (1989). Size and Morphology of the Benthic Foraminifer Melonis Barleeanum; Relationships with Marine Organic Matter. *J. Foraminiferal Res.* 19 (3), 235–245. doi:10.2113/gsjfr.19.3.235

Charette, M. A., and Sholkovitz, E. R. (2002). Oxidative Precipitation of Groundwater-Derived Ferrous Iron in the Subterranean Estuary of a Coastal Bay. *Geophys. Res. Lett.* 29, 8585–9184. doi:10.1029/2001gl014512

Chen, X., Cukrov, N., Santos, I. R., Rodellas, V., Cukrov, N., and Du, J. (2020). Karstic Submarine Groundwater Discharge into the Mediterranean: Radon-Based Nutrient Fluxes in an Anchialine Cave and a Basin-wide Upscaling. *Geochimica et Cosmochimica Acta* 268, 467–484. doi:10.1016/j.gca.2019.08.019

Collins, S. V., Reinhardt, E. G., Werner, C. L., Le Maillot, C., Devos, F., and Rissolo, D. (2015). Late Holocene Mangrove Development and Onset of Sedimentation in the Yax Chen Cave System (Ox Bel Ha) Yucatan, Mexico: Implications for Using Cave Sediments as a Sea-Level Indicator. *Palaeogeogr. Palaeoclimatol. Palaeoecol.* 438, 124–134. doi:10.1016/j.palaeo.2015.07.042

Corliss, B. H., and Chen, C. (1988). Morphotype Patterns of Norwegian Sea Deep-Sea Benthic Foraminifera and Ecological Implications. *Geol* 16 (8), 716–719. doi:10.1130/0091-7613(1988)016<0716:mponsd>2.3.co;2

Corliss, B. H., and Emerson, S. (1990). Distribution of Rose Bengal Stained Deep-Sea Benthic Foraminifera from the Nova Scotian Continental Margin and Gulf of Maine. *Deep Sea Res. A. Oceanographic Res. Pap.* 37 (3), 381–400. doi:10.1016/0198-0149(90)90015-n

Corliss, B. H. (1991). Morphology and Microhabitat Preferences of Benthic Foraminifera from the Northwest Atlantic Ocean. *Mar. Micropaleontol.* 17 (3-4), 195–236. doi:10.1016/0377-8398(91)90014-w

Coronado-Álvarez, L., Gutiérrez-Aguirre, M. A., and Cervantes-Martínez, A. (2011). Water Quality in Wells from Cozumel Island, Mexico. *Trop. Subtropical Agroecosystems* 13, 233–241.

Coutino, A., Stastna, M., Kovacs, S., and Reinhardt, E. (2017). Hurricanes Ingrid and Manuel (2013) and Their Impact on the Salinity of the Meteoric Water Mass, Quintana Roo, Mexico. *J. Hydrol.* 551, 715–729. doi:10.1016/j.jhydrol.2017.04.022

Coutino, A., Stastna, M., and Reinhardt, E. G. (2020). Interaction of Mangrove Surface Coverage and Groundwater Inputs on the Temperature and Water Level Near Tulum, Quintana Roo, Mexico: Observations and Modelling. *J. Hydrol.* 583, 124566. doi:10.1016/j.jhydrol.2020.124566

Cresswell, J. N., and van Hengstum, P. J. (2021). Habitat Partitioning in the Marine Sector of Karst Subterranean Estuaries and Bermuda's Marine Caves: Benthic Foraminiferal Evidence. *Front. Environ. Sci.* 8, 249. doi:10.3389/fenvs.2020.594554

Cresswell, J. N., van Hengstum, P. J., Iliffe, T. M., Williams, B. E., and Nolan, G. (2017). Anthropogenic Infilling of a Bermudian Sinkhole and its Impact on Sedimentation and Benthic Foraminifera in the Adjacent Anchialine Cave Environment. *Int. J. Speleol.* 46 (3), 7. doi:10.5038/1827-806x.46.3.2128

Crook, E. D., Potts, D., Rebolledo-Vieyra, M., Hernandez, L., and Paytan, A. (2012). Calcifying Coral Abundance Near Low-pH Springs: Implications for Future Ocean Acidification. *Coral Reefs* 31, 239–245. doi:10.1007/s00338-011-0839-y

Curtis, J. H., Hodell, D. A., and Brenner, M. (1996). Climate Variability on the Yucatan Peninsula (Mexico) during the Past 3500 years, and Implications for Maya Cultural Evolution. *Quat. Res.* 46, 37–47. doi:10.1006/qres.1996.0042

Cushman, J. A. (1933). Some New Recent Foraminifera from the Tropical Pacific. *Contrib. Cushman Lab. Foraminiferal Res.* 9, 77–95.

Dean, W. E. (1974). Determination of Carbonate and Organic Matter in Calcareous Sediments and Sedimentary Rocks by Loss on Ignition; Comparison with Other Methods. *J. Sediment. Res.* 44, 242–248. doi:10.1306/74D729D2-2B21-11D7-8648000102C1865D

Dimiza, M. D., Fatourou, M., Arabas, A., Panagiotopoulos, I., Gogou, A., Kouli, K., et al. (2020). Deep-sea Benthic Foraminifera Record of the Last 1500 Years in the North Aegean Trough (Northeastern Mediterranean): A Paleoclimatic Reconstruction Scenario. *Deep Sea Res. Part Topical Stud. Oceanography* 171, 104705. doi:10.1016/j.dsr2.2019.104705

Dittmar, T., Hertkorn, N., Kattner, G., and Lara, R. J. (2006). Mangroves, a Major Source of Dissolved Organic Carbon to the Oceans. *Glob. Biogeochem. Cycles* 20, a–n. doi:10.1029/2005gb002570

Donato, D. C., Kauffman, J. B., Murdiyarso, D., Kurnianto, S., Stidham, M., and Kanninen, M. (2011). Mangroves Among the Most Carbon-Rich Forests in the Tropics. *Nat. Geosci* 4, 293–297. doi:10.1038/ngeo1123

Donnelly, J. P., and Woodruff, J. D. (2007). Intense Hurricane Activity over the Past 5,000 Years Controlled by El Niño and the West African Monsoon. *Nature* 447, 465–468. doi:10.1038/nature05834

Fatela, F., and Taborda, R. (2002). Confidence Limits of Species Proportions in Microfossil Assemblages. *Mar. Micropaleontol.* 45 (2), 169–174. doi:10.1016/s0377-8398(02)00021-x

Fleury, P., Bakalowicz, M., and de Marsily, G. (2007). Submarine Springs and Coastal Karst Aquifers: a Review. *J. Hydrol.* 339, 79–92. doi:10.1016/j.jhydrol.2007.03.009

Fogel, M. L., Kent Sprague, E., Gize, A. P., and Frey, R. W. (1989). Diagenesis of Organic Matter in georgia Salt Marshes. *Estuarine, Coastal Shelf Sci.* 28, 211–230. doi:10.1016/0272-7714(89)90067-x

Fontanier, C., Jorissen, F. J., Licari, L., Alexandre, A., Anschutz, P., and Carbonel, P. (2002). Live Benthic Foraminiferal Faunas from the Bay of Biscay: Faunal Density, Composition, and Microhabitats. *Deep Sea Res. Part Oceanographic Res. Pap.* 49 (4), 751–785. doi:10.1016/s0967-0637(01)00078-4

Ford, D., and Williams, P. D. (2013). *Karst Hydrogeology and Geomorphology*. West Sussex: John Wiley & Sons.

Fosshagen, A., and Iliffe, T. M. (1991). A New Genus of Calanoid Copepod from an Anchialine Cave in Belize. *Bull. Plankton Soc. Jpn.* 27. 339-350.

Fourqurean, J. W., Escorcia, S. P., Anderson, W. T., and Zieman, J. C. (2005). Spatial and Seasonal Variability in Elemental Content, δ13C, and δ15N ofThalassia Testudinum from South Florida and its Implications for Ecosystem Studies. *Estuaries* 28, 447–461. doi:10.1007/bf02693926

Frausto-Martínez, O., Castillo, J. F. R., and Olivares, O. C. (2021). Morphometry of Karst Depressions at Detailed Scale: El Cedral, Cozumel, Mexico. *Trop. Subtropical Agroecosystems* 24.

Frausto-Martínez, O., Zapi-Salazar, N. A., and Colin-Olivares, O. (2018). Identification of Karst Forms Using LiDAR Technology: Cozumel Island, Mexico. *Trends Geomatics-an Earth Sci. Perspective* 11. doi:10.5772/intechopen.79196

Frontana-Uribe, S., and Soli's-Weiss, V. (2011). First Records of Polychaetous Annelids from Cenote Aerolito (Sinkhole and Anchialine Cave) in Cozumel Island. *Jcks* 73, 1–10. doi:10.4311/jcks2009lsc0107

Fry, B. (2007). *Stable Isotope Ecology*. New York: Springer Science & Business Media.

Gabriel, J. J., Reinhardt, E. G., Peros, M. C., Davidson, D. E., van Hengstum, P. J., and Beddows, P. A. (2009). Palaeoenvironmental Evolution of Cenote Aktun Ha (Carwash) on the Yucatan Peninsula, Mexico and its Response to Holocene Sea-Level Rise. *J. Paleolimnol* 42, 199–213. doi:10.1007/s10933-008-9271-x

Gómez, P., and Calderón-gutiérrez, F. (2020). Anchialine Cave-Dwelling Sponge Fauna (Porifera) from La Quebrada, Mexico, with the Description of the First Mexican Stygobiont Sponges. *Zootaxa* 4803, 125–151. doi:10.11646/zootaxa.4803.1.7

Gondwe, B. R. N., Lerer, S., Stisen, S., Marín, L., Rebolledo-Vieyra, M., Merediz-Alonso, G., et al. (2010). Hydrogeology of the South-Eastern Yucatan Peninsula: New Insights from Water Level Measurements, Geochemistry, Geophysics and Remote Sensing. *J. Hydrol.* 389, 1–17. doi:10.1016/j.jhydrol.2010.04.044

Goñi, M. A., Ruttenberg, K. C., and Eglinton, T. I. (1997). Sources and Contribution of Terrigenous Organic Carbon to Surface Sediments in the Gulf of Mexico. *Nature* 389, 275–278. doi:10.1038/38477

Gonneea, M. E., Charette, M. A., Liu, Q., Herrera-Silveira, J. A., and Morales-Ojeda, S. M. (2014). Trace Element Geochemistry of Groundwater in a Karst Subterranean Estuary (Yucatan Peninsula, Mexico). *Geochimica et Cosmochimica Acta* 132, 31–49. doi:10.1016/j.gca.2014.01.037

Gonneea, M. E., Maio, C. V., Kroeger, K. D., Hawkes, A. D., Mora, J., Sullivan, R., et al. (2019). Salt Marsh Ecosystem Restructuring Enhances Elevation Resilience and Carbon Storage during Accelerating Relative Sea-Level Rise. *Estuarine, Coastal Shelf Sci.* 217, 56–68. doi:10.1016/j.ecss.2018.11.003

Gonneea, M. E., Paytan, A., and Herrera-Silveira, J. A. (2004). Tracing Organic Matter Sources and Carbon Burial in Mangrove Sediments over the Past 160 Years. *Estuarine, Coastal Shelf Sci.* 61, 211–227. doi:10.1016/j.ecss.2004.04.015

Gooday, A. J. (2003). Benthic Foraminifera (Protista) as Tools in Deep-Water Palaeoceanography: Environmental Influences on Faunal Characteristics. *Adv. Mar. Biol.* 46, 1–90. doi:10.1016/s0065-2881(03)46002-1

Gooday, A. J. (1996). Epifaunal and Shallow Infaunal Foraminiferal Communities at Three Abyssal NE Atlantic Sites Subject to Differing Phytodetritus Input Regimes. *Deep Sea Res. Part Oceanographic Res. Pap.* 43 (9), 1395–1421. doi:10.1016/s0967-0637(96)00072-6

Gooday, A. J., and Turley, C. M. (1990). Responses by Benthic Organisms to Inputs of Organic Material to the Ocean Floor: a Review. *Philosophical Trans. R. Soc. A* 331 (1616), 119–138. doi:10.1098/rsta.1990.0060

Gregory, B. R. B., Reinhardt, E. G., and Gifford, J. A. (2017). The Influence of Morphology on Sinkhole Sedimentation at Little Salt Spring, Florida. *J. Coastal Res.* 332, 359–371. doi:10.2112/jcoastres-d-15-00169.1

Heiri, O., Lotter, A. F., and Lemcke, G. (2001). Loss on Ignition as a Method for Estimating Organic and Carbonate Content in Sediments: Reproducibility and Comparability of Results. *J. Paleolimnol.* 25, 101–110. doi:10.1023/a:1008119611481

Holthuis, L. B. (1973). Caridean Shrimps found in Land-Locked Saltwater Pools at four Indo-West Pacific Localities (Sinai Peninsula, Funafuti Atoll, Maui and Hawaii Islands), with the description of one new genus and four new species. *Zoologische Verhandelingen* 128 (1), 1–48.

Iliffe, T. M., and Kornicker, L. S. (2009). Worldwide Diving Discoveries of Living Fossil Animals from the Depths of Anchialine and Marine Caves. *Smithsonian Contrib. Mar. Sci.* 38, 269–280.

Jorissen, F. J., de Stigter, H. C., and Widmark, J. G. (1995). A Conceptual Model Explaining Benthic Foraminiferal Microhabitats. *Mar. Micropaleontol.* 26 (1-4), 3–15. doi:10.1016/0377-8398(95)00047-x

Jorissen, F. J., Fontanier, C., and Thomas, E. (2007). Chapter Seven Paleoceanographical Proxies Based on Deep-Sea Benthic Foraminiferal Assemblage Characteristics. *Dev. Mar. Geol.* 1, 263–325. doi:10.1016/s1572-5480(07)01012-3

Jorissen, F. J., and Wittling, I. (1999). Ecological Evidence from Live–Dead Comparisons of Benthic Foraminiferal Faunas off Cape Blanc (Northwest Africa). *Palaeogeogr. Palaeoclimatol. Palaeoecol.* 149 (1-4), 151–170. doi:10.1016/s0031-0182(98)00198-9

Kaiho, K. (1994). Benthic Foraminiferal Dissolved-Oxygen Index and Dissolved-Oxygen Levels in the Modern Ocean. *Geol* 22 (8), 719–722. doi:10.1130/0091-7613(1994)022<0719:bfdoia>2.3.co;2

Keil, R. G., Tsamakis, E., Fuh, C. B., Giddings, J. C., and Hedges, J. I. (1994). Mineralogical and Textural Controls on the Organic Composition of Coastal Marine Sediments: Hydrodynamic Separation Using SPLITT-Fractionation. *Geochimica et Cosmochimica Acta* 58, 879–893. doi:10.1016/0016-7037(94)90512-6

Khan, N. S., Vane, C. H., Engelhart, S. E., Kendrick, C., and Horton, B. P. (2019). The Application of δ13C, TOC and C/N Geochemistry of Mangrove Sediments to Reconstruct Holocene Paleoenvironments and Relative Sea Levels, Puerto Rico. *Mar. Geol.* 415, 105963. doi:10.1016/j.margeo.2019.105963

Kjerfve, B. (1981). Tides of the Caribbean Sea. *J. Geophys. Res.* 86, 4243–4247. doi:10.1029/jc086ic05p04243

Kottek, M., Grieser, J., Beck, C., Rudolf, B., and Rubel, F. (2006). World Map of the Köppen-Geiger Climate Classification Updated. *metz* 15, 259–263. doi:10.1127/0941-2948/2006/0130

Kovacs, S. E., Reinhardt, E. G., Chatters, J. C., Rissolo, D., Schwarcz, H. P., Collins, S. V., et al. (2017). Calcite Raft Geochemistry as a Hydrological Proxy for Holocene Aquifer Conditions in Hoyo Negro and Ich Balam (Sac Actun Cave System), Quintana Roo, Mexico. *Quat. Sci. Rev.* 175, 97–111. doi:10.1016/j.quascirev.2017.09.006

Kuenen, P. H., and Migliorini, C. I. (1950). Turbidity Currents as a Cause of Graded Bedding. *J. Geol.* 58, 91–127. doi:10.1086/625710

Lamb, A. L., Wilson, G. P., and Leng, M. J. (2006). A Review of Coastal Palaeoclimate and Relative Sea-Level Reconstructions Using δ13C and C/N Ratios in Organic Material. *Earth-Science Rev.* 75, 29–57. doi:10.1016/j.earscirev.2005.10.003

Little, S. N., and van Hengstum, P. J. (2019). Intertidal and Subtidal Benthic Foraminifera in Flooded Caves: Implications for Reconstructing Coastal Karst Aquifers and Cave Paleoenvironments. *Mar. Micropaleontol.* 149, 19–34. doi:10.1016/j.marmicro.2019.03.005

Loeblich, A. R., Jr, and Tappan, H. (1987). *Foraminiferal Genera and Their Classification*. New York: Springer.

Luijendijk, E., Gleeson, T., and Moosdorf, N. (2020). Fresh Groundwater Discharge Insignificant for the World's Oceans but Important for Coastal Ecosystems. *Nat. Commun.* 11, 1–12. doi:10.1038/s41467-020-15064-8

Maher, D. T., Santos, I. R., Golsby-Smith, L., Gleeson, J., and Eyre, B. D. (2013). Groundwater-derived Dissolved Inorganic and Organic Carbon Exports from a Mangrove Tidal Creek: The Missing Mangrove Carbon Sink?. *Limnol. Oceanogr.* 58, 475–488. doi:10.4319/lo.2013.58.2.0475

Márquez-Borrás, F., Solís-Marín, F. A., Bribiesca-Contreras, G., and Laguarda-Figueras, A. (2016). First Record of *Ophiura Ljungmani* (Echinodermata: Ophiuroidea) from an Anchialine Cave in the Mexican Caribbean. *Revista Mexicana de Biodiversidad* 87, 1127–1130. doi:10.1016/j.rmb.2016.07.006

Mayfield, K. K., Eisenhauer, A., Ramos, D. P. S., Higgins, J. A., Horner, T. J., Auro, M., et al. (2021). Groundwater Discharge Impacts Marine Isotope Budgets of Li, Mg, Ca, Sr, and Ba. *Nat. Commun.* 12, 1–9. doi:10.1038/s41467-020-20248-3

Mejía, L., Zarza, E., and López, M. (2008). *Barbouria Yanezi* Sp. nov., a New Species of Cave Shrimp (Decapoda, Barbouriidae) from Cozumel Island, Mexico. *Crustaceana* 81, 663–672. doi:10.1163/156854008784513474

Mejía-ortíz, L. M., Yañez, G., and López-Mejía, M. (2017). Anchialocarididae, a New Family of Anchialine Decapods and a New Species of the Genus Agostocaris from Cozumel Island, Mexico. *Crustac* 90, 381–398. doi:10.1163/15685403-00003657

Mejía-Ortíz, L. M., Yánez, G., and López-Mejía, M. (2007). Echinoderms in an Anchialine Cave in Mexico. *Mar. Ecol.* 28, 31–34. doi:10.1111/j.1439-0485.2007.00174.x

Milne, G. A., and Peros, M. (2013). Data-model Comparison of Holocene Sea-Level Change in the Circum-Caribbean Region. *Glob. Planet. Change* 107, 119–131. doi:10.1016/j.gloplacha.2013.04.014

Moodley, L., and Hess, C. (1992). Tolerance of Infaunal Benthic Foraminifera for Low and High Oxygen Concentrations. *Biol. Bull.* 183 (1), 94–98. doi:10.2307/1542410

Moore, W. S., and Joye, S. B. (2021). Saltwater Intrusion and Submarine Groundwater Discharge: Acceleration of Biogeochemical Reactions in Changing Coastal Aquifers. *Front. Earth Sci.* 9. doi:10.3389/feart.2021.600710

Moore, W. S. (2010). The Effect of Submarine Groundwater Discharge on the Ocean. *Annu. Rev. Mar. Sci.* 2, 59–88. doi:10.1146/annurev-marine-120308-081019

Moore, W. S. (1999). The Subterranean Estuary: a Reaction Zone of Ground Water and Sea Water. *Mar. Chem.* 65, 111–125. doi:10.1016/s0304-4203(99)00014-6

Moosdorf, N., Stieglitz, T., Waska, H., Dürr, H. H., and Hartmann, J. (2015). Submarine Groundwater Discharge from Tropical Islands: a Review. *Grundwasser* 20, 53–67. doi:10.1007/s00767-014-0275-3

Muckelbauer, G. (1990). The Shelf of Cozumel, Mexico: Topography and Organisms. *Facies* 23, 201–239. doi:10.1007/bf02536714

Muhs, D. R., Budahn, J. R., Prospero, J. M., and Carey, S. N. (2007). Geochemical Evidence for African Dust Inputs to Soils of Western Atlantic Islands: Barbados, the Bahamas, and Florida. *J. Geophys. Res. Earth Surf.* 112. doi:10.1029/2005jf000445

Murray, J. W. (2003). An Illustrated Guide to the Benthic Foraminifera of the Hebridean Shelf, West of Scotland, with Notes on Their Mode of Life. *Palaeontol. Electronica* 5 (1), 31.

Murray, M. R. (2002). Is Laser Particle Size Determination Possible for Carbonate-Rich Lake Sediments?. *J. Paleolimnol.* 27 (2), 173–183. doi:10.1023/a:1014281412035

Null, K. A., Knee, K. L., Crook, E. D., de Sieyes, N. R., Rebolledo-Vieyra, M., Hernández-Terrones, L., et al. (2014). Composition and Fluxes of Submarine Groundwater along the Caribbean Coast of the Yucatan Peninsula. *Continental Shelf Res.* 77, 38–50. doi:10.1016/j.csr.2014.01.011

Oksanen, J., Guillaume Blanchet, F., Kindt, R., Legendre, P., McGlinn, D., Minchin, P. R., et al. (2019). Vegan: Community Ecology Package. Retrieved from https://CRAN.R-project.org/package=vegan (Accessed January 24, 2021).

Olesen, J., Meland, K., Glenner, H., van Hengstum, P. J., and Iliffe, T. M. (2017). *Xibalbanus Cozumelensis*, a New Species of Remipedia (Crustacea) from Cozumel, Mexico, and a Molecular Phylogeny of Xibalbanus on the Yucatán Peninsula. *Eur. J. Taxonomy* 316, 1–27. doi:10.5852/ejt.2017.316

Ortiz, M., and Winfield, I. (2015). A New Amphipod Species (Peracarida: Amphipoda: Ampithoidae) Collected from Cenote Aerolito, Cozumel Island, Quintana Roo. *Revista Mexicana de Biodiversidad* 86, 332–336. doi:10.1016/j.rmb.2015.04.008

Patterson, R. T., and Fishbein, E. (1989). Re-examination of the Statistical Methods Used to Determine the Number of Point Counts Needed for Micropaleontological Quantitative Research. *J. Paleontol.* 63 (02), 245–248. doi:10.1017/s0022336000019272

Perry, E., Velazquez-Oliman, G., and Marin, L. (2002). The Hydrogeochemistry of the Karst Aquifer System of the Northern Yucatan Peninsula, Mexico. *Int. Geol. Rev.* 44, 191–221. doi:10.2747/0020-6814.44.3.191

Pisanty, D. T., Solis, E. M. C., Weiss, V. S., and Salazar, M. H. (2010). Peracarids (Crustacea: Malacostraca) from Cenote Aerolito, Cozumel, Mexican Caribbean. *Cahiers de Biologie Mar.* 51, 177–180.

Pohlman, J., Iliffe, T., and Cifuentes, L. (1997). A Stable Isotope Study of Organic Cycling and the Ecology of an Anchialine Cave Ecosystem. *Mar. Ecol. Prog. Ser.* 155, 17–27. doi:10.3354/meps155017

Pohlman, J. W. (2011). The Biogeochemistry of Anchialine Caves: Progress and Possibilities. *Hydrobiologia* 677, 33–51. doi:10.1007/s10750-011-0624-5

Prospero, J. M., and Lamb, P. J. (2003). African Droughts and Dust Transport to the Caribbean: Climate Change Implications. *Science* 302, 1024–1027. doi:10.1126/science.1089915

Prospero, J. M., and Nees, R. T. (1986). Impact of the North African Drought and El Niño on Mineral Dust in the Barbados Trade Winds. *Nature* 320, 735–738. doi:10.1038/320735a0

R Core Team (2020). *RStudio: Integrated Development for R*. USA: RStudio, Inc. Boston. 423.

Rathburn, A. E., and Corliss, B. H. (1994). The Ecology of Living (Stained) Deep-Sea Benthic Foraminifera from the Sulu Sea. *Paleoceanography* 9 (1), 87–150. doi:10.1029/93pa02327

Reimer, P. J., Austin, W. E. N., Bard, E., Bayliss, A., Blackwell, P. G., Bronk Ramsey, C., et al. (2020). The IntCal20 Northern Hemisphere Radiocarbon Age Calibration Curve (0-55 Cal kBP). *Radiocarbon* 62, 725–757. doi:10.1017/rdc.2020.41

Richards, D. A., Smart, P. L., and Lawrence Edwards, R. (1994). Maximum Sea Levels for the Last Glacial Period from U-Series Ages of Submerged Speleothems. *Nature* 367, 357–360. doi:10.1038/367357a0

Riera, R., Monterroso, Ó., Núñez, J., and Martínez, A. (2018). Distribution of Meiofaunal Abundances in a Marine Cave Complex with Secondary Openings and Freshwater Filtrations. *Mar. Biodiv* 48, 203–215. doi:10.1007/s12526-016-0586-y

Rocha, C., Robinson, C. E., Santos, I. R., Waska, H., Michael, H. A., and Bokuniewicz, H. J. (2021). A Place for Subterranean Estuaries in the Coastal Zone. *Estuarine, Coastal Shelf Sci.* 250, 107167. doi:10.1016/j.ecss.2021.107167

Rubio, F., Rolán, E., Worsaae, K., Martínez, A., and Gonzalez, B. C. (2015). Description of the First Anchialine Gastropod from a Yucatán Cenote, *Teinostoma Brankovitsi* N. sp. (Caenogastropoda: Tornidae), Including an Emended Generic Diagnosis. *J. Molluscan Stud.* 82, 169–177. doi:10.1093/mollus/eyv049

Schönfeld, J., Alve, E., Geslin, E., Jorissen, F., Korsun, S., and Spezzaferri, S. (2012). The FOBIMO (FOraminiferal BIo-MOnitoring) Initiative-Towards a Standardised Protocol for Soft-Bottom Benthic Foraminiferal Monitoring Studies. *Mar. Micropaleontol.* 94-95, 1–13. doi:10.1016/j.marmicro.2012.06.001

Scott, D. B., and Hermelin, J. O. R. (1993). A Device for Precision Splitting of Micropaleontological Samples in Liquid Suspension. *J. Paleontol.* 67 (01), 151–154. doi:10.1017/s0022336000021302

Sen Gupta, B. K., Eugene Turner, R., and Rabalais, N. N. (1996). Seasonal Oxygen Depletion in Continental-Shelf Waters of Louisiana: Historical Record of Benthic Foraminifers. *Geol* 24 (3), 227–230. doi:10.1130/0091-7613(1996)024<0227:sodics>2.3.co;2

Seymour, J., Humphreys, W., and Mitchell, J. (2007). Stratification of the Microbial Community Inhabiting an Anchialine Sinkhole. *Aquat. Microb. Ecol.* 50, 11–24. doi:10.3354/ame01153

Sket, B. (1996). The Ecology of Anchihaline Caves. *Trends Ecol. Evol.* 11, 221–225. doi:10.1016/0169-5347(96)20031-x

Smith, M. R. (2017). Ternary: An R Package for Creating Ternary Plots. *Zenodo* 10. doi:10.5281/zenodo.1068996

Socki, R. A., Perry, E. J. C., and Romanek, C. S. (2002). Stable Isotope Systematics of Two Cenotes from the Northern Yucatan Peninsula, Mexico. *Limnol. Oceanogr.* 47, 1808–1818. doi:10.4319/lo.2002.47.6.1808

Spaw, R. H. (1978). Late Pleistocene Carbonate Bank Deposition: Cozumel Island, Quintana Roo, Mexico. *Gulf Coast Assoc. Geol. Societies Trans.* 28, 601–619.

Stock, J. H., Iliffe, T. M., and Williams, D. (1986). The Concept of Anchialine Reconsidered. *Stygologia* 2, 90–92.

Stuiver, M., Reimer, P. J., and Reimer, R. W. (2021). CALIB 8.2. Retrieved from http://calib.org (Accessed January 24, 2021).

Tamalavage, A. E., van Hengstum, P. J., Louchouarn, P., Molodtsov, S., Kaiser, K., Donnelly, J. P., et al. (2018). Organic Matter Sources and Lateral Sedimentation in a Bahamian Karst Basin (Sinkhole) over the Late Holocene: Influence of Local Vegetation and Climate. *Palaeogeogr. Palaeoclimatol. Palaeoecol.* 506, 70–83. doi:10.1016/j.palaeo.2018.06.014

Toomey, M. R., Curry, W. B., Donnelly, J. P., and van Hengstum, P. J. (2013). Reconstructing 7000 Years of North Atlantic Hurricane Variability Using Deep-Sea Sediment Cores from the Western Great Bahama Bank. *Paleoceanography* 28, 31–41. doi:10.1002/palo.20012

van Hengstum, P. J., Cresswell, J. N., Milne, G. A., and Iliffe, T. M. (2019). Development of Anchialine Cave Habitats and Karst Subterranean Estuaries since the Last Ice Age. *Scientific Rep.* 9, 1–10. doi:10.1038/s41598-019-48058-8

van Hengstum, P. J., Donnelly, J. P., Fall, P. L., Toomey, M. R., Albury, N. A., and Kakuk, B. (2016). The Intertropical Convergence Zone Modulates Intense Hurricane Strikes on the Western North Atlantic Margin. *Scientific Rep.* 6, 1–10. doi:10.1038/srep21728

van Hengstum, P. J., Reinhardt, E. G., Beddows, P. A., and Gabriel, J. J. (2010). Linkages between Holocene Paleoclimate and Paleohydrogeology Preserved in a Yucatan Underwater Cave. *Quat. Sci. Rev.* 29, 2788–2798. doi:10.1016/j.quascirev.2010.06.034

van Hengstum, P. J., Reinhardt, E. G., Beddows, P. A., Huang, R. J., and Gabriel, J. J. (2008). Thecamoebians (Testate Amoebae) And Foraminifera From Three Anchialine Cenotes in Mexico: Low Salinity (1.5-4.5 Psu) Faunal Transitions. *J. Foraminiferal Res.* 38 (4), 305–317. doi:10.2113/gsjfr.38.4.305

van Hengstum, P. J., Reinhardt, E. G., Beddows, P. A., Schwarcz, H. P., and Gabriel, J. J. (2009). Foraminifera and Testate Amoebae (Thecamoebians) in an Anchialine Cave: Surface Distributions from Aktun Ha (Carwash) Cave System, Mexico. *Limnol. Oceanogr.* 54, 391–396. doi:10.4319/lo.2009.54.1.0391

van Hengstum, P. J., and Scott, D. B. (2011). Ecology of Foraminifera and Habitat Variability in an Underwater Cave: Distinguishing Anchialine versus Submarine Cave Environments. *J. Foraminiferal Res.* 41 (3), 201–229. doi:10.2113/gsjfr.41.3.201

van Hengstum, P. J., Scott, D. B., Gröcke, D. R., and Charette, M. A. (2011). Sea Level Controls Sedimentation and Environments in Coastal Caves and Sinkholes. *Mar. Geol.* 286, 35–50. doi:10.1016/j.margeo.2011.05.004

van Hengstum, P. J., and Scott, D. B. (2012). Sea-level Rise and Coastal Circulation Controlled Holocene Groundwater Development in Bermuda and Caused a Meteoric Lens to Collapse 1600years Ago. *Mar. Micropaleontol.* 90-91, 29–43. doi:10.1016/j.marmicro.2012.02.007

van Hengstum, P. J., Winkler, T. S., Tamalavage, A. E., Sullivan, R. M., Little, S. N., MacDonald, D., et al. (2020). Holocene Sedimentation in a Blue Hole Surrounded by Carbonate Tidal Flats in the Bahamas: Autogenic versus Allogenic Processes. *Mar. Geol.* 419, 106051. doi:10.1016/j.margeo.2019.106051

Wanless, H. R. (1981). Fining-upwards Sedimentary Sequences Generated in Seagrass Beds. *J. Sediment. Res.* 51, 445–454. doi:10.1306/212F7CA2-2B24-11D7-8648000102C1865D

Whitaker, D., and Christman, M. (2014). Clustsig: Significant Cluster Analysis. Retrieved from https://CRAN.R-project.org/package=clustsig (Accessed January 24, 2021). doi:10.4324/9781315855226

Wickham, H. (2016). *Ggplot2: Elegant Graphics for Data Analysis*. Springer.

Winkler, T. S., van Hengstum, P. J., Horgan, M. C., Donnelly, J. P., and Reibenspies, J. H. (2016). Detrital Cave Sediments Record Late Quaternary Hydrologic and Climatic Variability in Northwestern Florida, USA. *Sediment. Geol.* 335, 51–65. doi:10.1016/j.sedgeo.2016.01.022

Young, M. B., Gonneea, M. E., Fong, D. A., Moore, W. S., Herrera-Silveira, J., and Paytan, A. (2008). Characterizing Sources of Groundwater to a Tropical Coastal Lagoon in a Karstic Area Using Radium Isotopes and Water Chemistry. *Mar. Chem.* 109, 377–394. doi:10.1016/j.marchem.2007.07.010

Conflict of Interest: The authors declare that the research was conducted in the absence of any commercial or financial relationships that could be construed as a potential conflict of interest.

Copyright © 2021 Brankovits, Little, Winkler, Tamalavage, Mejía-Ortíz, Maupin, Yáñez-Mendoza and van Hengstum. This is an open-access article distributed under the terms of the Creative Commons Attribution License (CC BY). The use, distribution or reproduction in other forums is permitted, provided the original author(s) and the copyright owner(s) are credited and that the original publication in this journal is cited, in accordance with accepted academic practice. No use, distribution or reproduction is permitted which does not comply with these terms.

frontiers in Environmental Science

ORIGINAL RESEARCH
published: 09 March 2021
doi: 10.3389/fenvs.2020.594554

Habitat Partitioning in the Marine Sector of Karst Subterranean Estuaries and Bermuda's Marine Caves: Benthic Foraminiferal Evidence

Jacquelyn N. Cresswell[1] *and Peter J. van Hengstum*[2,3]*

[1] *Department of Marine Biology, Texas A&M University at Galveston, Galveston, TX, United States,* [2] *Department of Marine and Coastal Environmental Science, Texas A&M University at Galveston, Galveston, TX, United States,* [3] *Department of Oceanography, Texas A&M University, College Station, TX, United States*

Karst subterranean estuaries (KSEs) are created from the two- and three-way mixing of saline groundwater, rain, and oceanic water in the subsurface on carbonate landscapes, and this hydrographic framework promotes unique physical processes, biogeochemical cycling, and biological communities. Here we provide evidence that the source and quantity of particulate organic matter (POM) that is delivered to the benthos strongly correlates to benthic habitat partitioning in the oxygenated marine sectors of KSEs. A dataset of benthic foraminifera at 128 different locations from several large flooded cave systems in Bermuda were compiled and evaluated against common environmental characteristics (e.g., tidal exposure, substrate particle size, bulk organic matter, C:N, total organic carbon, and $\delta^{13}C_{org}$). Benthic areas receiving more carbon isotopically depleted organic matter sources (mean $\delta^{13}C_{org}$ values $< -23.2‰$, C:N ratios >11), most likely from the terrestrial surface and some marine plankton, were dominated by *Trochammina inflata*, *Bolivina* spp., and *Helenina anderseni*. In contrast, benthic areas receiving more carbon isotopically enriched organic matter sources (mean $\delta^{13}C_{org}$ values $> -21.6‰$, C:N ratios <10), most likely from marine plankton transported through marine cave openings cave from adjacent coastal waters, were dominated by *Spirophthalmidium emaciatum*, *Spirillina vivipara*, *Patellina corrugata*, and *Rotaliella arctica*. The benthic foraminifera most distal from any cave entrances were dominated by taxa also known from the deep-sea (e.g., *Rotaliella*, *Spirophthalmidium*) in sediment with the lowest bulk organic matter content (mean: 6%), or taxa that prefer hard substrates and are potentially living attached to cave walls (*Patellina*, *Spirillina*). While physical groundwater characteristics (e.g., salinity, dissolved oxygen) are expected drivers of benthic ecosystems in KSEs, these results suggest that POM source, quantity, and delivery mechanisms (e.g., groundwater-seawater circulation mechanisms, terrestrial flux) play an important role in benthic habitat partitioning and the spatial variability of biogeochemical cycles in the oxygenated marine sector of KSEs.

Keywords: anchialine, marine cave, submarine cave, Bermuda, karst, subterranean estuaries, foraminifera, subterranean ecology

OPEN ACCESS

Edited by:
Carlos Rocha,
Trinity College Dublin, Ireland

Reviewed by:
Luisa Bergamin,
Higher Institute for Environmental Protection and Research (ISPRA), Italy
John Pohlman,
United States Geological Survey (USGS), United States

***Correspondence:**
Peter J. van Hengstum
vanhenp@tamug.edu

Specialty section:
This article was submitted to Biogeochemical Dynamics, a section of the journal Frontiers in Environmental Science

Received: *13 August 2020*
Accepted: *06 November 2020*
Published: *09 March 2021*

Citation:
Cresswell JN and van Hengstum PJ (2021) Habitat Partitioning in the Marine Sector of Karst Subterranean Estuaries and Bermuda's Marine Caves: Benthic Foraminiferal Evidence. Front. Environ. Sci. 8:594554. doi: 10.3389/fenvs.2020.594554

INTRODUCTION

Karst subterranean estuaries (KSEs) are an environment created from the two- and three-way mixing of saline groundwater, rain, and oceanic water in the subsurface on carbonate landscapes, and this hydrographic framework promotes unique physical processes, biogeochemical cycling, and biological communities. Research on subterranean estuaries has significantly increased in the last 20 years (Moore, 1999; Gonneea et al., 2014; Brankovits et al., 2017, 2018; Pain et al., 2019, 2020; Duque et al., 2020). Traditionally, the biologic-focused study (fauna and ecosystems) of caves that are flooded by a KSE have been described with the adjectives *anchialine* or *marine cave* environments (Iliffe et al., 1983, 1984; Stock et al., 1986; Bishop et al., 2015). Since the groundwater-ocean dynamics that create KSEs are linked to sea level, KSEs also vertically migrate in the subsurface in response to orbitally-forced changes in eustatic sea level (van Hengstum et al., 2019) and this is represented in the fossil record (Proctor and Smart, 1991; van Hengstum et al., 2009; Rosso et al., 2015, 2018; Guido et al., 2017). Despite advances in the last decades, there still is considerable uncertainty regarding ecosystem functioning in modern KSEs, including the impact of organic carbon on benthic community ecology (**Figure 1**).

Benthic foraminifera are useful for investigating environmental variability and benthic habitat partitioning in KSEs in both modern and ancient settings (Balduzzi and Cattaneo, 1985; Proctor and Smart, 1991; van Hengstum et al., 2008, 2009; Omori et al., 2010; Guido et al., 2017; Bergamin et al., 2018, 2020; Romano et al., 2018, 2020). Benthic foraminifera are eukaryotic protists that live among the meiofauna (0.062–0.5 mm in size) in most marine settings, and they exhibit ecological zonation from physical environmental gradients (e.g., salinity, organic matter flux, dissolved oxygen). In the deep-sea, benthic foraminifera they can account for 50% of eukaryotic biomass in sediment (Gooday et al., 1992). Foraminifera are heterotrophs that eat phytodetritus, terrestrial detritus, prokaryotes, among other trophic strategies, with only a few species living in symbiotic relationships with photosynthetic algae (Gooday, 1988, 1993; Goldstein and Corliss, 1994; Linke et al., 1995; Nomaki et al., 2005; Dupuy et al., 2010). Individual foraminifera produce a simple shell, or test, that remains within the sediment after death, so statistically significant populations can be sampled by SCUBA divers during routine ecological surveys, or their fossil remains can preserve a record of prehistoric KSEs.

Here we document how benthic foraminiferal communities correlate with particulate organic carbon source, quantity, and delivery mechanisms in Bermuda's horizontally expansive submerged caves, which represent areas of KSEs where salinity and dissolved oxygen are not limiting factors. Bermuda is a ∼35 million year old volcanic seamount in the North Atlantic Ocean, that is capped by 30–80 m of limestone interspaced by paleosols (Pirsson and Vaughn, 1917; Woolard and Ewing, 1939; Plummer et al., 1976; Palmer et al., 1977; Vacher et al., 1995). The limestone units deposited during Quaternary sea-level high stands have weathered into a mature karst landscape (Mylroie et al., 1995), with abundant cave-related karst development in the oldest carbonate formations that are concentrated in the northeastern part of the island (Land et al., 1967; Plummer et al., 1976; Palmer et al., 1977; Vacher and Rowe, 1997). Bermuda is an ideal location for this study because the flooded caves are an established biodiversity hot spot of endemic anchialine fauna (Iliffe et al., 1983), and its surrounding marine environments have been the focus of long-term oceanographic study (e.g., Woolard and Ewing, 1939; Neumann, 1965; Morris et al., 1977) and foraminiferal work (Carmen, 1927; Steinker and Clem, 1984; Javaux and Scott, 2003). This study provides the broadest geographic perspective yet available for benthic foraminiferal distributions in the KSE habitat for any global island by combining foraminiferal census data from 28 new samples from

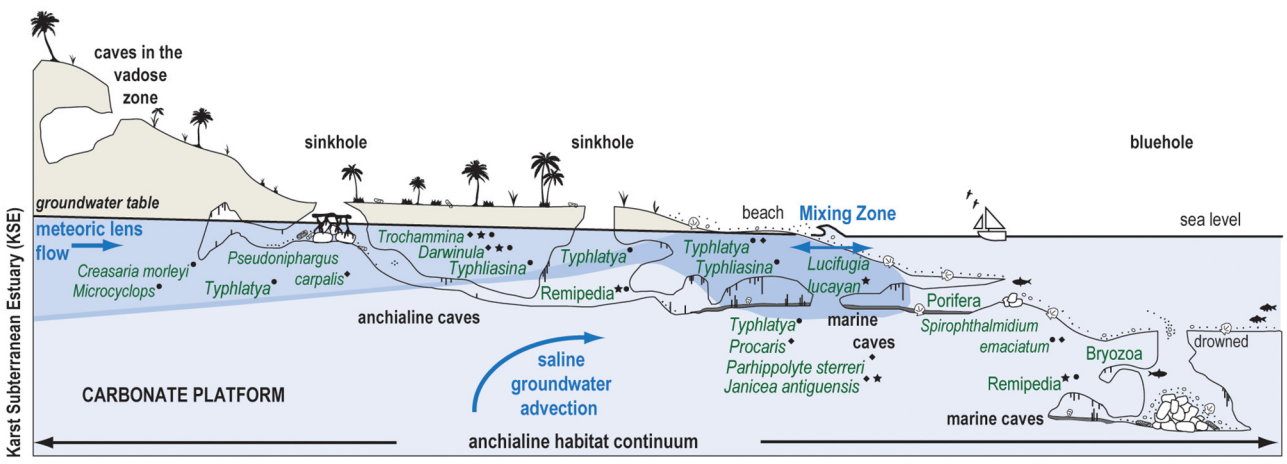


FIGURE 1 | Conceptual model of a karst subterranean estuary (KSE) and the anchialine habitat continuum created by subsurface groundwater variability (van Hengstum et al., 2019). Western North Atlantic anchialine fauna (e.g., fish, shrimps, decapods, ostracodes, foraminifera, marine Porifera, and Bryozoa) are positioned in their typical groundwater habitat based on observations from several localities, including The Bahamas (★), Yucatan Peninsula (●), and Bermuda (♦). *Typhlatya* shrimp exemplify habitat and resource partitioning in the KSE (Chávez-Solís et al., 2020).

the 2nd largest flooded cave (Palm Cave) into a new dataset with 100 samples from previously studied caves in Bermuda (Deep Blue, Cow Cave, Green Bay Cave).

MATERIALS AND METHODS

Research Design and Study Sites

Submerged caves in Bermuda are most abundant in the oldest geologic formations (e.g., Walsingham Formation) between Castle Harbor and Harrington Sound, and between North Shore Lagoon and Harrington Sound (**Figure 2**). The volcanic-limestone contact has not yet been observed in any flooded cave, and cave passages are generally shallower than ∼23 m below sea level. This study focuses on two large caves with physical connections into Harrington Sound (i.e., Green Bay Cave, Palm Cave), and two cave entrances that are slightly more inland (Cow Cave, Deep Blue). Harrington Sound is a shallow coastal embayment that is ∼5 km^2, with a mean depth of 14.5 m below sea level, and a maximum depth of ∼25 m below sea level in the southwest (Parsons et al., 2015). It is estimated that the seawater residence time in the mixed layer of Harrington Sound is ∼30 days from tidal exchange of seawater through the narrow channel at Flatts Inlet (Morris et al., 1977), but effective tidal mixing can be as long as 4 months (Parsons et al., 2015). Harrington Sound experiences seasonal hypoxia or anoxia from water column stratification in summer (Coull, 1969; Bates, 2017), which causes benthic sedimentary and ecological zonation: a sandy shallow zone with sea grass and macroalgae (0–10 m), the *Oculina* coral zone (10–19 m), and the subthermocline zone (19–26 m) (Neumann, 1965). Seasonal dysoxia or anoxia have not been observed or documented in Bermuda's caves, and previous work documents that surficial foraminiferal distributions in Bermuda's caves are not typical of those observed in open ocean hypoxic to anoxic settings (Sen Gupta et al., 1996; Bernhard and Sen Gupta, 1997; Levin et al., 2009). This suggests that tidal pumping of seawater from the mixed layer in Harrington Sound into the caves is the dominant source of seawater. Tidal pumping also causes microtidal variability (<0.5 m) in the local groundwater table elevation (i.e., water table, Martin et al., 2012), which can be measured in the shallow pools that provide access to the flooded caves (Palmer et al., 1977; van Hengstum et al., 2015; Little and van Hengstum, 2019).

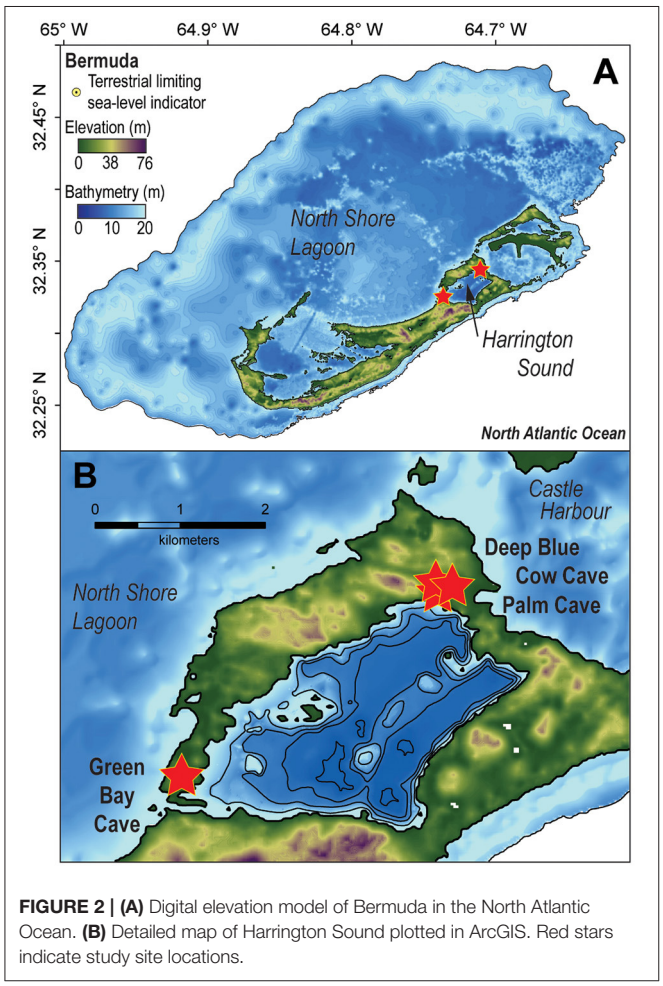


FIGURE 2 | (A) Digital elevation model of Bermuda in the North Atlantic Ocean. **(B)** Detailed map of Harrington Sound plotted in ArcGIS. Red stars indicate study site locations.

Bermuda's caves offer a great location for investigating the marine sector of a KSE on a carbonate platform that is nearly flooded by eustatic sea-level rise. The commonly-studied flooded caves in Bermuda *do not* discharge a meteoric lens toward the ocean like caves on larger carbonate landscapes in the Mediterranean area (Radolović et al., 2015; Romano et al., 2020) or Yucatan Peninsula (Suárez-Morales et al., 2004; Chávez-Solís et al., 2020). This is in part because Bermuda is currently in a late stage of carbonate platform flooding relative to the position of global sea level (van Hengstum et al., 2019), and local meteoric water masses in Bermuda are spatially diminished. On the carbonate platforms of The Bahamas, for example, landmass area and mean annual rainfall alone can be used to predict meteoric lens thickness on different islands (Cant and Weech, 1986). Bermuda does have five modest meteoric lenses located in geologically-recent lithologies (Vacher, 1978), but these are not located in the primary area of cave development on the isthmus between Castle Harbor and Harrington Sound (Walsingham Formation, highest porosity: Land et al., 1967). In northeastern Bermuda where the Walsingham Formation is located, only a thin (<50 cm), seasonal and ephemeral brackish cap occurs in some cave-collapse entrances, and a limited meteoric lens can form near the "Letterbox" area of Green Bay Cave that does not directly contact the sediment-water interface, or discharge water through marine exit into Harrington Sound (see map in van Hengstum and Scott, 2011). The mineralogy of sediment in Bermuda's caves is dominated by carbonates, along with localized deposits of paleosol eroding into cave from the terrestrial surface above. Lastly, while large carbonate platforms in the Bahamas and the Yucatan frequently have large sinkholes that host extensive primary productivity and are interconnected to flooded caves (Schmitter-Soto et al., 2002; Tamalavage et al., 2018), the most comparable geomorphologic feature in Bermuda is Cliff Pool Sinkhole in the Green Bay Cave System. Even then, Cliff Pool still only supports a thin (<0.5 m) brackish water mass whose salinity depends upon seasonal rainfall and aridity.

Two of the largest cave systems in Bermuda, Palm Cave (primary entrance: 32.34°N, 64.71°W) and Green Bay Cave (primary entrance: 32.33°N, 64.74°W), were targeted for analysis of recent foraminiferal distributions (uppermost 5 cm of sediment) and compared to the impact of tidal variability on foraminiferal distributions at cave entrances to the Walsingham Cave System at Deep Blue (32.347°N, 64.711°W) and the entrance to Cow Cave (32.34°N, 64.71°W). Green Bay Cave also has the largest direct connection to the sea at Harrington Sound. According to measurements of Iliffe (2008), 1,960,000 m^3 of seawater flows into Green Bay Cave at a cross sectional area of 25.5 m^2 during a flood tidal cycle. In contrast, Palm Cave has multiple, small subaerial entrances to the forest landscape in the Walsingham Nature Preserve, and one direct connection to Harrington Sound at Cripple Gate (cross sectional area: 0.6 m^2) that permits ∼1,000 m^3 of seawater exchange during a flood tidal cycle (Iliffe, 2008). Both Palm Cave and Green Bay Cave have seagrass meadows (e.g., *Thalassia testudinium, Syringodium filiforme*) within 100 m of their marine entrances (Iliffe, 2008), in the shallow sandy benthic ecological zone in Harrington Sound (Neumann, 1965).

Benthic Foraminiferal Processing From Palm Cave

28 new surface (<5 cm depth, >30 cm^3 of sediment) sediment samples were collected from various depths and locations throughout Palm Cave in August 2015 (**Figure 3**). At each sample station, a separate 50 mL centrifuge tube was filled with sediment by a SCUBA diver employing advanced technical cave diving procedures. Collecting this volume of sediment permitted separate sediment sub-samples from each station to be individually processed for benthic foraminifera, textural analysis, Loss-on-Ignition (LOI), and bulk organic geochemistry. The total assemblages of benthic foraminifera were analyzed at each sampling station, as some workers perceive this to be most reflective of long-term distributions (Buzas, 1968; Scott and Medioli, 1980; Debenay and Guillou, 2002). Benthic foraminifera were concentrated by wet sieving sediment sub-samples (0.63–5 cm^3) over a standard 63 μm screen mesh, with the remaining coarse sediment residues sub-divided into representative aliquots using a wet splitter to enable representative census counts of ∼300 individuals per sample (Patterson and Fishbein, 1989; Scott and Hermelin, 1993). While van Hengstum and Scott (2011) used a 45 μm sieve to concentrate benthic foraminifera in their study of Green Bay Cave, Little and van Hengstum (2019) documented negligible difference between resultant foraminiferal communities from Bermudian caves using 45 vs. 63 μm mesh sizes. Individual benthic foraminifera were wet picked onto micropaleontological slides and identified to the species level in most cases. Taxonomy was confirmed by comparing scanning electron microscopy of representative individuals to literature comparisons (Carman, 1933; Bermúdez, 1949; Loeblich and Tappan, 1987; van Hengstum and Scott, 2011; Little and van Hengstum, 2019). This produced a new dataset for benthic foraminifera from Palm Cave of 28 samples x 111 taxonomic observations (see **Supplementary Material**).

Sediment Texture and Organic Geochemistry

Sediment texture (i.e., mean particle size) in Palm Cave was examined in separate sediment sub-samples using standard laser diffraction particle size analysis and loss on ignition (LOI) procedures. Organic matter was recorded as percent-lost relative to the original total sample weight after LOI at 550°C for 4.5 h (Heiri et al., 2001). Mean particle size for sediment sub-samples was measured with a Malvern Mastersizer 2000S laser particle size analyzer (Sperazza et al., 2004), with individual particles disaggregated in a sodium hexametaphosphate dispersant prior to analysis. The stable carbon isotopic value ($\delta^{13}C_{org}$) and C:N ratio of bulk sediment was measured on separate sediment sub-samples from the new sediment samples collected from Palm Cave ($n = 28$). In general, $\delta^{13}C_{org}$ values of bulk sedimentary organic matter reflect the relative contributions of marine, terrestrial and pelagic organic carbon sources in coastal environments (Lamb et al., 2006; Khan et al., 2019). Terrestrial plants that preferentially use the C3 photosynthetic pathway produce organic tissues that are ^{13}C-depleted and nitrogen-poor, with $\delta^{13}C_{org}$ values generally ranging between −32 and −21‰ (Lamb et al., 2006). Sea grasses and macroalgae are common in the shallow waters from 0 to 10 m of Harrington Sound (sandy zone with seagrass and macroalgae of Neumann, 1965) where Palm Cave and Green Bay Cave have entrances (Wefer and Killingley, 1986; Fourqurean et al., 2015). Seagrasses are also important contributors of carbon isotopically enriched organic matter to the sediment in nearshore environments relative to marine plankton (Fry et al., 1977; Anderson et al., 1992; Kennedy et al., 2010). Based on measurements on plant tissues around Bermuda coastal waters, seagrasses (e.g., *Syringodium* and *Thalassia:* mean of −7.4‰, $n = 455$) and macro algae like *Halimeda* (mean of −14.3‰, $n = 60$) also have relatively more ^{13}C-enriched $\delta^{13}C_{org}$ values (see Table 1 in Burgett et al., 2018). The $\delta^{13}C_{org}$ values of particulate organic carbon (POC) in the Sargasso Sea are similar to elsewhere in the tropical North Atlantic and range from ∼-21 to −23‰ (Jeffrey et al., 1983; Altabet, 1990), and these values primarily reflect the ranges of marine planktonic algae (France, 1995). For samples from Palm Cave, carbonates were first digested with 1.0 M HCl for 12 h, and the remaining sediment residue was rinsed, desiccated, powdered, and weighed into silver capsules. Stable carbon isotope ratios ($\delta^{13}C_{org}$) were measured against international standards at Baylor University Stable Isotope Laboratory on a Thermo-Electron Delta V Advantage Isotope Ratio Mass Spectrometer. Final isotopic ratios are reported relative to the standard delta (δ) notation relative to Vienna Pee Dee Belemnite (VPDB) for carbon (expressed as parts per mil: ‰) with an uncertainty of ± 0.1‰, with the C:N ratio and total organic carbon (TOC, weight %) calculated from the analysis of the residual sediment fraction after acidification.

Data Analysis

A final dataset was compiled for further multivariate statistical analysis that contained 128 total samples: (a) the 28 new samples from Palm Cave (this study), 74 samples from

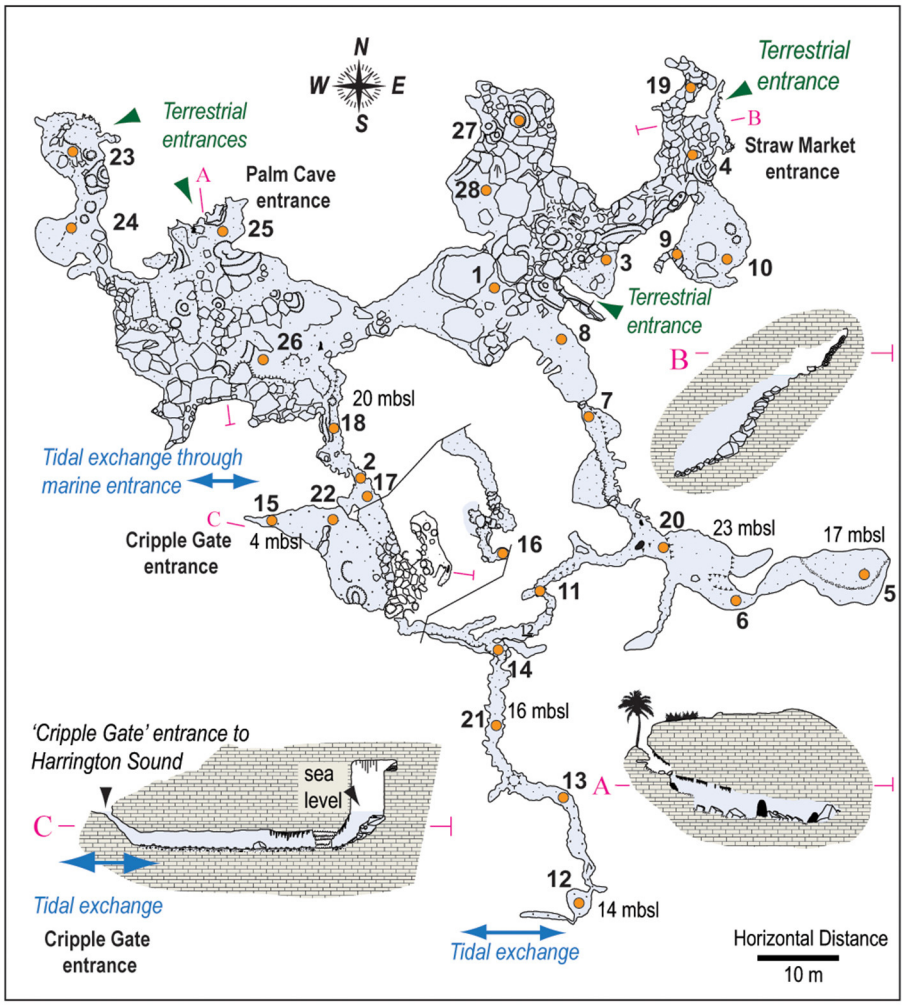


FIGURE 3 | Detailed wall map of Palm Cave, showing explored cave passages that provide direct access to the subterranean estuary, with locations of surface sediment samples (orange circles) and cave entrances (adapted from original survey of Jason Richards). Maps and surface sample locations for Green Bay Cave, and Cow Cave and Deep Blue are provided elsewhere (van Hengstum and Scott, 2012; Little and van Hengstum, 2019).

Green Bay Cave (van Hengstum and Scott, 2011), 18 samples from Cow Cave (Little and van Hengstum, 2019), and 7 samples from Deep Blue (Little and van Hengstum, 2019). From Little and van Hengstum (2019), we use the >45 μm database, which has higher census counts and thus likely better represents the sampled areas. All taxonomic observations were grouped to the generic level to limit the impact of taxonomic bias imparted by different microscopists at the species level. The exception was the brackish water indicator *Trochammina inflata*, which was left at specific level to differentiate from co-generic marine taxa (e.g., *T. globularis*). Also, the final dataset amalgamated the taxonomically similar genera *Pattelina*, *Heteropatellina*, and *Patellinoides* (all members of the order Spirillinida). These genera were differentiated by Little and van Hengstum (2019, Deep Blue and Cow Cave), but lumped together by van Hengstum and Scott (2011, Green Bay Cave). The final combined dataset was 128 samples by 89 taxonomic units at the generic level (see **Supplementary Material**).

Numerical analyses were completed in R Studio software (version 1.1.383; R Studio, 2016). The final combined dataset of benthic foraminifera was used to calculate rarefied species richness (*S*) and the Shannon-Wiener Diversity Index (H), using the "rarefy" and "diversity" functions in the R package "vegan" (Gotelli and Colwell, 2011; Oksanen et al., 2013), and raw counts were converted to proportional abundances using the "decostand" function in the "vegan" package. Unconstrained Q-mode cluster analysis was used to help divide the dataset into ecologically meaningful benthic foraminiferal communities by grouping statistically similar populations (Legendre and Legendre, 1998). Prior to cluster analysis, the proportional abundances were square root transformed to minimize the impact of dominant species and to better compare community structure (Legendre and Legendre, 1998). Samples

were then subjected to hierarchical cluster analysis using an unweighted paired group averaging algorithm and the Bray-Curtis dissimilarity index using the "simprof" function in the "clustsig" package (Clarke et al., 2008; Whitaker and Christman, 2014), and the "vegdist" function in the "vegan" package (Oksanen et al., 2013). The proportion of dominant taxa in the dendrogram (5% proportional abundance in at least 1 sample) were illustrated between the different samples by generating a vertical stratigraphic plot using the "stratplot" function in the "rioja" package (Juggins, 2015). Finally, physical environmental parameters were graphically summarized in box-and-whisker plots: $\delta^{13}C_{org}$, C:N, bulk organic matter-LOI, TOC, mean particle size, and mean groundwater depth, and compared to the benthic foraminiferal communities grouped by unconstrained Q-mode cluster analysis.

RESULTS: BENTHIC FORAMINIFERAL COMMUNITIES

Similar to other Bermudian caves investigated (Green Bay Cave, Deep Blue, and Cow Cave), Palm Cave has abundant benthic foraminifera with a mean concentration of 7256 individuals per cm^3 of sediment (range: 458–14,603). No new endemic species of foraminifera are described, but the identified benthic foraminiferal communities differ from those found in other Bermudian coastal environments (e.g., mangroves, carbonate lagoons, or reefs: see Javaux and Scott, 2003). Seven communities of benthic foraminifera can be recognized at a dissimilarity index of 0.44 on the dendrogram produced from unconstrained Q-mode cluster analysis (**Figure 4**), but this division increases to nine groupings if Community 5 is subdivided at a dissimilarity of index of ∼0.36 (discussed below). Two samples were plotted at the bottom of the dendrogram and were deemed most dissimilar to the other samples: ISC-72 and CC5-ITA. From the original dataset, however, the very high relative abundance of *Spirophthalmidium emaciatum* (70%) in ISC-72 suggests this sample is most closely related to Community 6. Similarly, CC5-ITA had a very high abundance of *Trochammina*, *Entzia*, and *Miliammina* relative to other samples in Community 1. With currently available data, we consider that the samples CC5-ITA and ISC-72 are just endmember examples in Community 6 and 1, respectively.

Community 1 characterizes the intertidal zone of Cow Cave, and this lower diversity ($H = 2.2$) community is dominated by taxa known to tolerate periodic aerial exposure related to tides, high quantities of bulk organic matter in the sediment, and lower salinities. Dominant taxa include *Trochammina inflata* (mean: 18.3%), *Miliammina fusca* (mean: 13.1%), and *Entzia macrescens* (mean: 8.7%; **Table 1**). Tidal variability of the water table causes periodic exposure of these shallow benthic areas (**Figure 5**), and this community likely also experiences repeated brackish conditions from rain and surface runoff (Little and van Hengstum, 2019). Community 1 is characterized by the highest bulk organic matter content (mean: 25.5%), which is predominantly derived from terrestrial sources based on the mean $\delta^{13}C_{org}$ values and C:N ratio (mean: −25.9‰, mean C:N ratio: 18.3; **Figure 6**).

Community 2 includes subtidal areas of Deep Blue in the saline groundwater mass that are exposed to normal sunlight. The benthos has lower bulk organic matter (mean: 18.8%) than Community 1, but the organic carbon remains primarily sourced from the adjacent terrestrial surface (mean: −26.1‰, C:N ratio mean: 11.1; **Table 1**). This community has higher species richness ($S = 28$) and diversity ($H = 2.7$) than Community 1, which is most likely because these benthic area are constantly submerged. This community is dominated by the infaunal genus *Bolivina* (mean: 16.6%), *T. inflata* (mean: 12.2%), and *H. anderseni* (mean: 7.5%, **Table 1**). *Rosalina* is also dominant (mean: 10.5%), which is primarily *Rosalina globularis*, and small-sized *Triloculina oblonga* (mean: 12.2, **Supplementary Material**).

Communities 3 and 4 occur in a transect of increasing depth into the saline groundwater at Cliff Pool Sinkhole within the Green Bay Cave (AC-04 to AC-11 of van Hengstum and Scott, 2011), and include the shallowest samples from Cliff Pool Sinkhole (ML-1, ML-2, ML3). The shallow sinkhole itself receives direct sunlight, and shallow sampling sites have taxa that must be tolerant of brackish conditions. Communities 3 and 4 start in open water, and form a transect down into the aphotic zone of Green Bay Cave. Community 3 is dominated by *Bolivina* spp. (mean: 20.2%), *H. anderseni* (mean: 21.4%), and *Rosalina* spp. (mean: 11%). While *Ammonia* (mean: 11.6%) has been grouped to the generic level, van Hengstum and Scott (2011) observed that Community 3 was characterized by *Ammonia beccarii* var. tepida. In contrast, Community 4 has higher species richness ($S = 30$) and diversity ($H = 2.6$), and *Bolivina* spp. (mean: 26%) and *Rosalina* spp. (mean: 11%) remain dominant (**Figure 4**; **Table 1**). However, Community 4 also includes other taxa like phytodetritus feeding *Melonis barleeanum* (mean: 5.8%), *Siphogenerina columellaris* (mean: 4.9%), *Siphonina* (mean: 4.2%), and *Nonionella* (mean: 4.7%, **Figure 4**). Community 3 contains a mean of 14.1% of bulk organic matter, and a mean $\delta^{13}C_{org}$ value of −24.2‰ and a mean C:N ratio of 11 (**Table 1**), whereas Community 5 has higher bulk organic matter (mean 17.5%) content.

Most of the samples collected from throughout Palm Cave, Cow Cave, and Green Bay Cave collectively form Community 5 at a Bray-Curtis dissimilarity index of 0.44. Community 5 is located in benthic areas that: (i) are only impacted by saline groundwater, (ii) are not subaerially exposed anytime during the tidal cycle, and (iii) are in the aphotic zone. While all the areas characterized by Community 5 samples have similarities, important differences emerge with the physical environmental characteristics that warrant dividing further at a Bray-Curtis dissimilarity index of 0.36 (**Figure 4**). For example, Communities 5A, 5B, and 5C show a trend toward more enriched $\delta^{13}C_{org}$ values and decreasing bulk organic matter content (**Figure 5**). Community 5A is located in the subtidal areas of the roofed Cow Cave, and is located in shallow subtidal pools that are proximal to the adjacent terrestrial landscape. Except for the samples collected specifically in Cliff Pool Sinkhole (ML-1, ML-2, and ML-3), most of Communities 5B and 5C are located deeper in the saline groundwater. Community 5A is

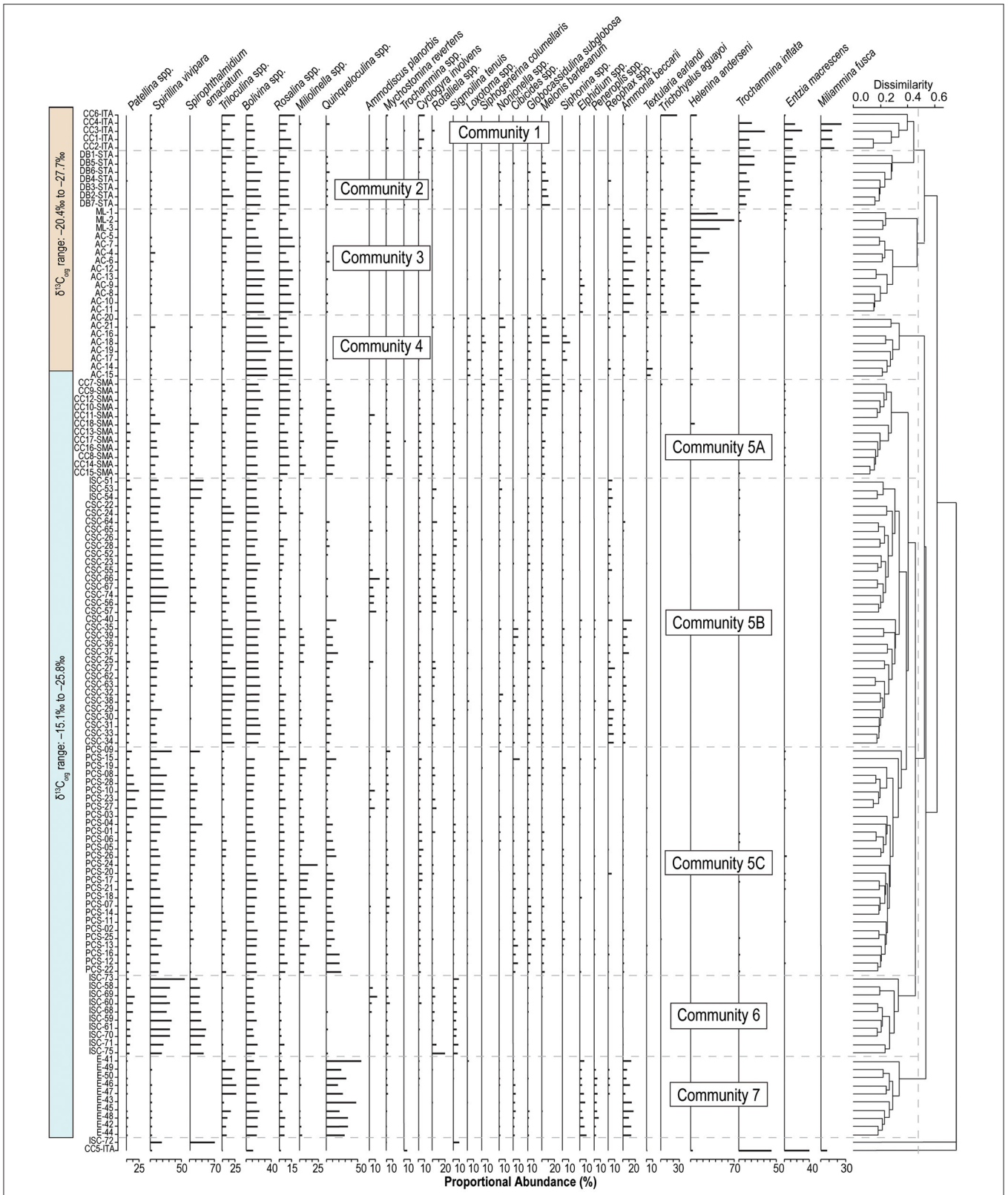


FIGURE 4 | Benthic foraminiferal communities in Palm Cave, Green Bay, Cow Cave, and Deep Blue as defined by groupings in a dendrogram produced from Q-mode cluster analysis. A 7-cluster (dissimilarity 0.44) or a 9-cluster division (dissimilarity 0.36) of the dendrogram correlates well with the measured environmental variables. Only taxa with >5% in at least one sample are shown to emphasize significant fauna.

TABLE 1 | Selected summary statistics for environmental characteristics, and arithmetic mean of the percent abundance of dominant taxa in each benthic foraminiferal community.

	Dominated by Terrestrial Organic Matter (TOM) Sources				Dominated by Marine Organic Matter (MOM) Sources				
Benthic foraminiferal community	**1**	**2**	**3**	**4**	**5A**	**5B**	**5C**	**6**	**7**
Community name	**Intertidal**	**TOM shallow subtidal**	**TOM high carbon**	**TOM lower carbon**	**MOM shallow subtidal**	**MOM high carbon–finer**	**MOM high carbon–coarser**	**Low carbon marine**	**Marine Cave entrance**
Sample count	6	7	13	8	12	33	28	11	10
$\delta^{13}C_{org}$ (‰) average	−25.9	−26.1	−24.2	−23.2	−21.6	−18.6	−20	−17.6	−18.6
$\delta^{13}C_{org}$ (‰) standard deviation	1.2	1.6	1.5	0.7	3.2	0.2	1.7	0.4	0.5
$\delta^{13}C_{org}$ (‰) range	−27.5 to −24	−27.7 to −23	−26.7 to −20.4	−24.4 to −21.7	−25.8 to −17.8	−19.2 to −17.8	−23.7 to −15.1	−18.6 to −16.8	−19.6 to −17.9
C:N average	18.3	11.1	11.2	11	10.1	8.2	9.1	8.6	8.1
C:N standard deviation	11.7	7.3	1.7	0.9	2.1	0.3	1.3	0.5	0.4
C:N range	3.4–28.7	1.1–18.6	8.5–15.1	9.5–12.1	6–12.4	7–8.7	7.8–14.2	8.1–10.2	7.5–8.6
Bulk organic matter (% LOI) average	25.5	18.7	14.1	17.5	13.4	8.1	8.6	6	10
Bulk organic matter (% LOI) standard deviation	6.5	6.1	8.8	4.4	4.8	1.9	2.6	2.3	6
Bulk organic matter (% LOI) range	18.2–36.3	11.6–28.2	6.7–40.8	11–23.2	9–20.5	4–12	2.4–12.5	2.5–9.3	3.2–20
TOC (%) average	7.4	4.5	23.9	12.5	5.5	15.3	12.4	5.1	30
TOC (%) standard deviation	5.1	2.4	8.9	6.3	1.2	4.5	5.7	2.2	4.2
TOC (%) range	2.6–16.2	1.5–7.8	11.4–41.3	4.1–22.6	4–8.4	5.8–26.7	2.6–25	1.8–9.6	24.3–35.4
Particle size (mm) average	16.2	43.8	271.2	149.6	14.3	20.7	39.7	5.9	311.3
Particle size (mm) standard deviation	6	27.4	52.8	109	2.6	43.6	34.9	1.3	113.9
Particle size (mm) range	9.2–24.7	23–99.3	190.5–370.4	13.5–333.8	9.7–19.6	1.1–218.1	13–169	4.1–7.9	86.7–459.4
Depth (m) average	−0.1	0.5	3	17.5	0.7	15.9	13.5	15.4	5.3
Depth (m) standard deviation	0	0.2	3.2	1.6	0.3	3.4	7	3	2.4
Depth (m) range	−0.3 to −0.1	0.2–0.9	0.2–10.7	13.7–18.7	0.1–1.2	5.2–20.1	2.4–22.6	9.6–18.6	2.7–10
Foraminiferal concentration (tests per cm^3) average	1811.8	595.4	322.3	1521.6	3507.2	3227.7	7415.5	2569.5	3480
Shannon-Weiner Diversity Index (*H*) average	2.2	2.7	2.1	2.6	3	2.9	2.9	2.1	2.5
Rarefied species richness average	21	28	18	30	34	35	34	23	30
Dominant taxa–percent abundance (%, average)									
Ammodiscus	-	1.3	-	-	1.3	2.1	-	2.3	-
Ammonia	-	-	11.6	1.4	-	2.2	-	-	9.7
Bolivina	3.7	16.6	20.2	29.2	12.5	11.4	5.4	4.3	11
Cibicides	-	-	-	-	-	1.1	1.8	-	1.9
Cyclogyra	3.9	-	-	-	2.8	1.6	2.5	-	-
Elphidium	-	-	1.9	-	1	-	-	-	4.7
Entzia	8.7	1.8	-	-	-	-	-	-	-
Globocassidulina	-	2	-	3.1	2.3	2	2.4	-	-
Helenina	2.9	7.5	21.4	-	-	-	-	-	-
Loxostomum	-	-	-	2.5	-	-	-	-	-
Melonis	-	7	-	5.8	5.1	1.6	1.9	-	-
Miliammina	13.1	1	-	-	-	-	-	-	-
Average of Miliolinella	-	-	1	-	4	2.2	7.2	-	1.6
Mychostomina	-	-	-	-	2.9	-	1.6	1.7	-
Nonionella	-	1.7	-	4.7	2.8	1.4	-	-	-

(Continued)

TABLE 1 | Continued

	Dominated by Terrestrial Organic Matter (TOM) Sources				Dominated by Marine Organic Matter (MOM) Sources				
Benthic foraminiferal community	**1**	**2**	**3**	**4**	**5A**	**5B**	**5C**	**6**	**7**
Community name	**Intertidal**	**TOM shallow subtidal**	**TOM high carbon**	**TOM lower carbon**	**MOM shallow subtidal**	**MOM high carbon–finer**	**MOM high carbon–coarser**	**Low carbon marine**	**Marine Cave entrance**
Peneroplis	-	-	-	-	-	-	-	-	3
Pseudo-*Patellina* (*Pattelina*-like taxa)	-	-	-	-	3.3	5.6	7.8	7.2	1.6
Quinqueloculina	1.4	3.1	1.5	-	9.2	4.1	8.2	-	27.5
Reophax	-	1.4	1.2	1.4	-	3.1	-	-	1
Rosalina	11.2	10.5	12.5	10.5	9.5	3.7	5.4	1.6	4.8
Rotaliella	-	-	-	-	1	1.6	-	2.5	-
Sigmoilina	-	-	-	-	1.4	1.8	1.2	5.9	-
Siphogenerina	-	-	-	4.9	1.8	-	-	-	-
Siphonina	-	-	-	4.2	1	1	1.5	-	-
Spirillina	1.1	-	1.4	-	5.8	10.9	13	24.3	1.1
Spirophthalmidium	-	-	-	2.2	7.6	8.3	10	31.5	-
Textularia	-	1.7	3.9	3.3	-	-	-	-	3.2
Trichohyalus	4.7	2.2	6.3	-	-	-	-	-	-
Triloculina	14.3	12.2	7.7	2.2	5.5	13	3.7	1.1	12.9
Trochammina	-	3.6	-	-	1.2	2.3	4.6	2.4	-
Trochammina inflata	18.3	12.2	-	-	-	-	-	-	-

Species with a mean percent abundance of <1% are marked with a dash to emphasize dominant taxa. The data from samples CC5-ITA and ISC-72 were averaged into Community 1 and 6, respectively. TOC, total organic carbon; LOI, Loss-on-Ignition.

also a transition between benthic foraminiferal communities characterized by more depleted $\delta^{13}C_{org}$ values (Communities 1–4) vs. more enriched $\delta^{13}C_{org}$ values (Communities 5B, 5C, 6, and 7), and similarly with C:N ratios (**Figure 5**). Despite a general linear trend in the $\delta^{13}C_{org}$ values of the sediment (**Figure 5**), there is a distinct change in the benthic foraminiferal communities from the dominance of *Bolivina* and *Rosalina* in Community 5A to *Spirophthalmidium*, *Spirillina*, and *Pattelina*-like genera (*Patellina*, *Heteropatellina*, *Patellinoides*) dominating Communities 5B and 5C (**Figure 4**; **Table 1**).

Community 6 is located in areas most distal to any cave exit (either terrestrial or marine). Relative to most other areas, Community 6 is characterized by enriched $\delta^{13}C_{org}$ values (mean: −18.5‰) and lower C:N ratios (mean: 8.6). The sediment where Community 6 is found has the lowest total organic carbon content (mean: 5.1 ± 2.2%) and bulk organic matter observed (mean: 6 ± 2.3%). While all cave areas are dominated by carbonate and organic matter, Community 6 is dominated by fine-grained carbonate particles (fine silt: 5.9 ± 1.3 μm, **Table 1**). Community 6 is less diverse than Community 5 ($S = 22$, $H = 2.1$), and is dominated by *Spirophthalmidium emaciatum* (mean 20.4%), *Spirillina vivipara* (mean: 19.6%), *Patellina* (mean: 9.6%), and *Bolivina* (mean: 4.3%).

Community 7 occurs in a transect from open water in the shallow (0–10 m) sandy ecological zone in Harrington Sound (E-47, E-48, E-49, and E-50), through the marine cave entrance into Green Bay Cave and stops at the Rat Trap area (see **Figure 2** in van Hengstum and Scott, 2011). This community is characterized by lower bulk organic matter on average (mean: 10%), but high variability (range: 3.2–20%) depending upon the spatial variability in carbonate sand content (mean particle size: 311 μm, **Table 1**). The $\delta^{13}C_{org}$ values (mean: −18.6‰) of the sediment are more enriched relative to Communities 1–4, with a lower C:N ratio (mean: 8.1). This community of benthic foraminifera has a higher diversity ($H = 2.5$) and species richness ($S = 29$), and is dominated by common carbonate lagoon genera *Quinqueloculina* (mean: 26%), but also *Bolivina* (mean: 12%), and *Triloculina* (mean: 11.4%).While *Ammonia* (mean: 9.7%) has been grouped to the generic level, van Hengstum and Scott (2011) observed that Community 7 was characterized by *Ammonia beccarii* var. parkinsoniana.

DISCUSSION: DRIVERS OF FORAMINIFERAL DISTRIBUTIONS

Our previous work (i.e., van Hengstum and Scott, 2011) divided the benthic foraminiferal communities in Green Bay Cave into those that were termed anchialine (terrestrially-dominated) vs. submarine (marine-dominated). This was based on the ideas of "terrestrial vs. marine influence" that were originally presented in Stock et al. (1986, more specifically), see the footnotes on page 91). This partly reflects the challenges faced by early workers with evaluating environmental and biological differences

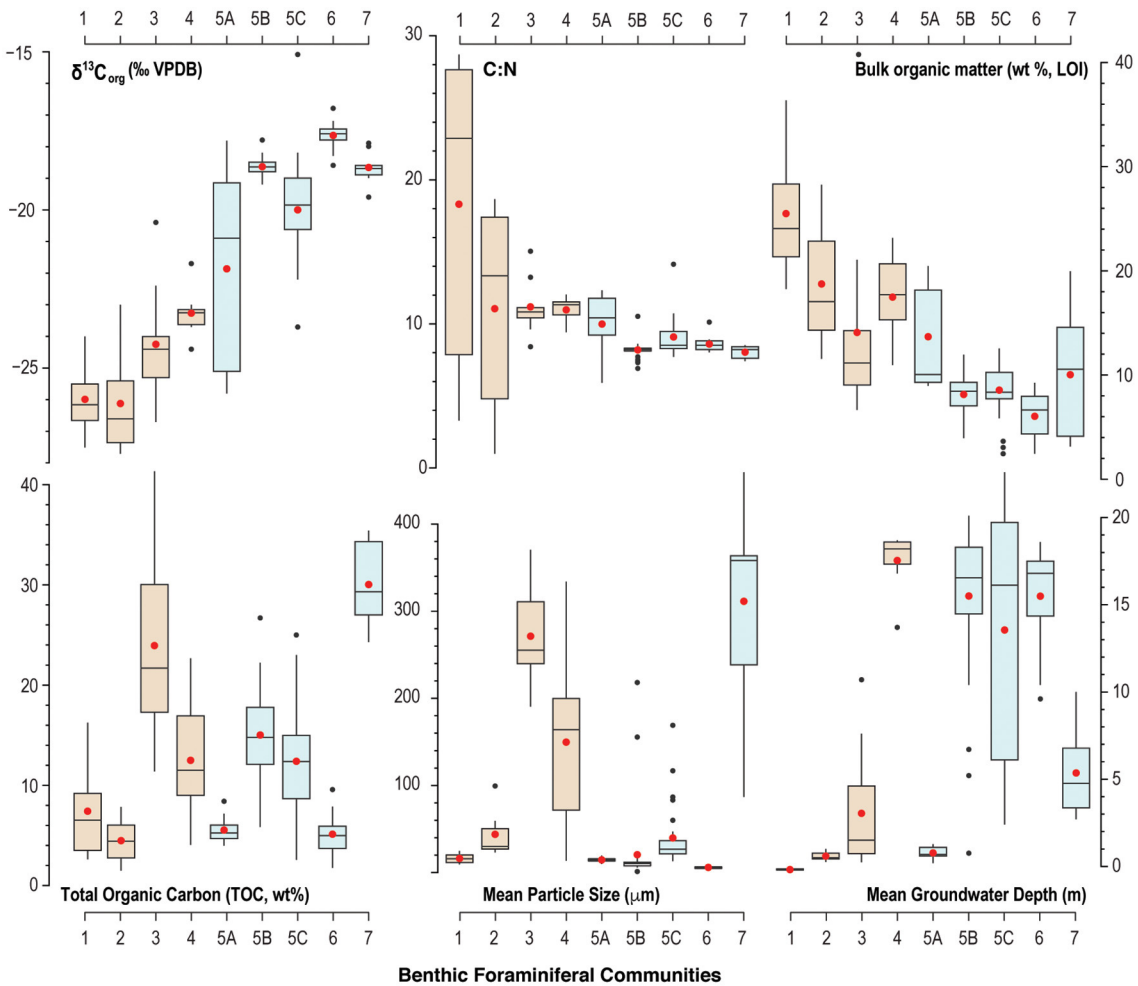


FIGURE 5 | Box-and-whisker plot of summary statistics (mean is red dot, median is central line) for benthic environmental characteristics associated with each benthic foraminiferal community. Despite the trend or gradient observed in $\delta^{13}C_{org}$ values, C:N ratios, and bulk organic matter content, the brown (blue) colored boxes identify benthic foraminiferal communities that prefer terrestrial (marine) organic matter sources delivered to the benthos.

between: marine flooded caves like those found in northeastern Bermuda that have negligible meteoric lenses, vs. (ii) those with extensive meteoric lens development such as observed in caves the Yucatan Peninsula. However, a "terrestrial vs. marine" distinction is too simple for describing both benthic and pelagic habitat partitioning in subterranean estuaries, and the dependance of physical processes, biological communities, and biogeochemical cycles on specific groundwater masses (Brankovits et al., 2017, 2018; Chávez-Solís et al., 2020) that must vertically migrate through geologic time (Riedl and Ozretić, 1969; van Hengstum et al., 2019). For example, recent work with *Typhlatya* shrimp surveyed over a large area in the Yucatan Peninsula clearly documents pelagic habitat partitioning with respect to groundwater masses and carbon sources (see Figure 2 in Chávez-Solís et al., 2020). After applying broader environmental concepts of a KSE (**Figure 1**), the sampled marine caves of Bermuda include only the marine sector of KSEs that are not oxygen or salinity limited. As discussed below, modern benthic foraminiferal communities in the marine sector of KSEs in Bermuda's can be correlated with exposure caused by tidal variability of the water column, and the quantity, source, and transport mechanisms of particulate organic matter that is delivered to the benthos.

Marine Benthic Habitats Dominated by Terrestrial-Sourced Organic Carbon

In general, benthic foraminiferal Community 1 (mean: −25.9‰), 2 (mean: −26.1‰), 3 (mean: −24.2‰), and 4 (mean: −23.2‰) all occupy sediment that has more depleted $\delta^{13}C_{org}$ values and lower C:N ratios (**Figures 5**, **6**). Based on a comparison with literature values, this likely indicates that terrestrial organic matter is the dominant source of organic carbon delivered to these areas. In opposite, Communities 5, 6, and 7 occupied sediment with more enriched $\delta^{13}C_{org}$ values (mean: −21.6 to −17.6‰, **Table 1**), which suggests that marine carbon sources are more dominant. The proximity between sample stations and cave

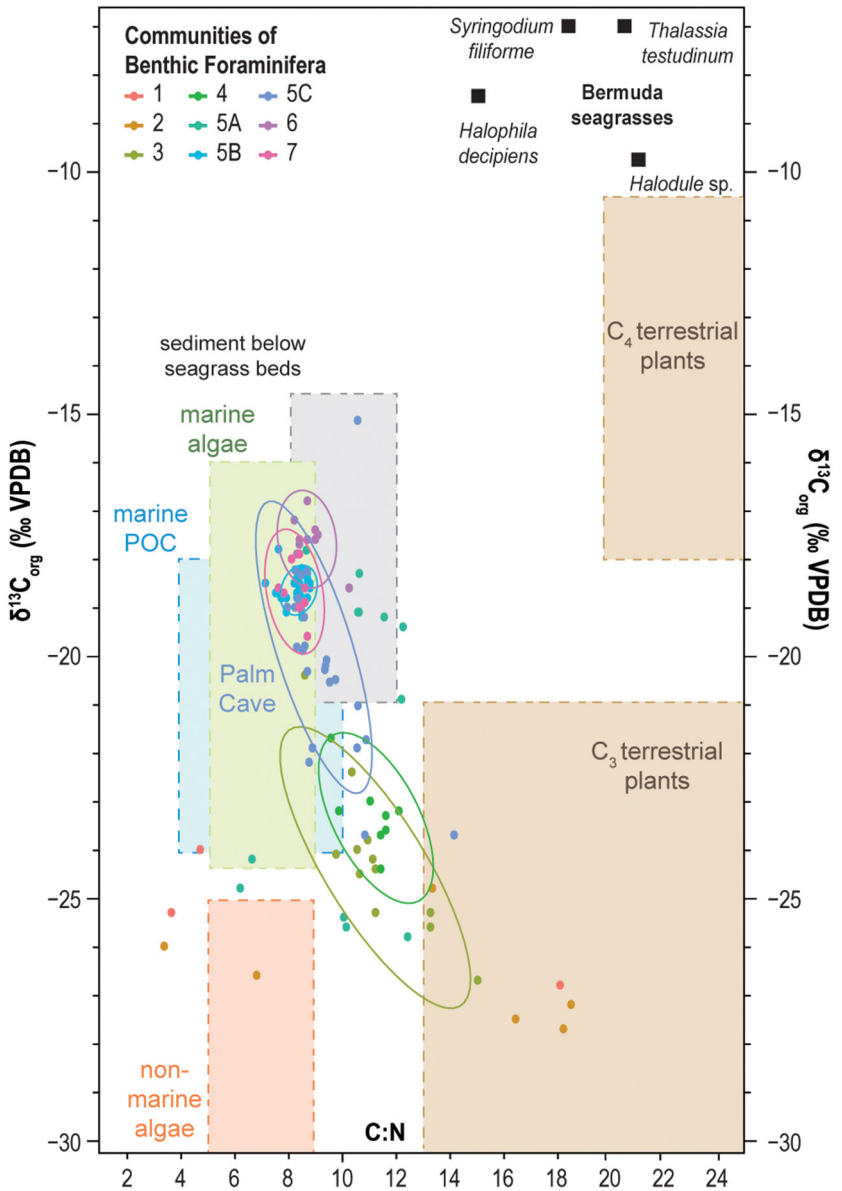


FIGURE 6 | Crossplot of $\delta^{13}C_{org}$ values and C:N ratio of bulk sediment from the Palm Cave (this work), Green Bay Cave (van Hengstum and Scott, 2011), Cow Cave, and Deep Blue (Little and van Hengstum, 2019). Samples are grouped according to their benthic foraminiferal communities. Colored ellipses correspond to 95% confidence intervals around the mean values for selected groups. The values of $\delta^{13}C_{org}$ and the C:N ratio of other organic carbon pools are compiled from the literature (Lamb et al., 2006; Kennedy et al., 2010; Fourqurean et al., 2019).

openings (i.e., exits) to the forest landscape is clearly impacting organic matter delivery to the benthos. Detrital carbon is a key resource for benthic foraminifera in marine environments (Gooday, 1993; Jorissen et al., 1995), so it is unsurprising that foraminifera are also responding to different carbon sources in flooded marine caves. Cave exits provide a point source for terrestrial sedimentation into an otherwise marine environment, and diverse organic carbon pools increase the opportunity for resource partitioning and foraminiferal diversity. While terrestrial detritus eroding into the caves from the adjacent landscapes is likely a dominant carbon source for Communities 1–4 ($\delta^{13}C_{org}$ values: −26.1 to −23.2‰), we cannot rule out the contribution of organic matter from marine plankton in the water column at Cliff Pool Sinkhole (Green Bay Cave) as also impacting the proximal Communities 3 and 4. Since marine POC from marine plankton has a $\delta^{13}C_{org}$ value of −21 to −23‰ (Jeffrey et al., 1983; Altabet, 1990; France, 1995), the $\delta^{13}C_{org}$ value of benthic sediment alone cannot differentiate the relative contributions of carbon from terrestrial detritus vs. marine plankton. Deposition of POC from marine plankton

can also explain the modestly lower and stabilized C:N values in Communities 3 and 4 relative to Communities 1 and 2 (**Figure 5**). This is because vascular terrestrial detritus typically has much higher C:N ratios (Lamb et al., 2006), which is likely to collect in cave pools closer to the forest, whereas the deeper water column at Cliff Pool Sinkhole can support higher primary productivity. The uncertainty in these results is an opportunity to use more specific organic biomarkers to resolve carbon source contributions to the benthos. Overall, the more carbon isotopically depleted samples suggest an increased proportion of terrestrial detritus in Communities 1–4 relative to Communities 5–7, as all areas likely receive inputs of POC from marine plankton in response to active seawater-groundwater circulation between Harrington Sound and the caves (discussed below).

Similar to the result of Little and van Hengstum (2019), benthic habitats dominated by terrestrial organic carbon deposition can be further separated by tidal exposure: Community 1 is exposed to tidal variability of the water column, whereas Communities 2, 3, and 4 are all subtidal (**Figure 5**). The micro-tidal changes to the water table elevation at Cow Cave are sufficient to expose Community 1 during low tides (**Figure 5**, Little and van Hengstum, 2019). Community 1 is dominated by agglutinated, brackish-tolerant species *Trochammina inflata, Miliammina fusca*, *Entzia macrescens*, and *Helenina anderseni* (**Table 1**). These taxa are common in marshes, which also experience tidal exposure (Hayward et al., 1999; Javaux and Scott, 2003; Camacho et al., 2015). Community 1 likely also experiences intermittent brackish conditions from runoff during pluvial events given the close proximity of Community 1 to the terrestrial landscape (**Figure 7**). Taxa like *E. macrescens* and *Miliammina fusca* are useful sea-level indicators due to their significant correlation with tidal elevation (Scott and Medioli, 1978; Guilbault et al., 1995; Gehrels and van de Plassche, 1999). In the studied Bermuda caves, *Miliammina fusca* is the primary taxon in intertidal areas dominated by terrestrial organic carbon, with *E. macrescens* occurring in both intertidal (Community 1) and subtidal (Community 2) areas (**Figure 4**).

Subtidal benthic areas dominated by the deposition of terrestrially-sourced organic carbon could be further divided by light exposure, depth into the subsurface, and particle size (Communities 2, 3, and 4, **Figure 7**). None of the recovered benthic foraminifera in the caves employ photosymbionts (e.g., *Amphistegina*), therefore, foraminifera are all feeding on materials delivered to, or otherwise available in, the substrate (e.g., algae, bacteria, detritus, or dissolved organic matter). While these communities are all dominated by *Rosalina* and *Bolivina* (**Table 1**), differences in the secondary taxa are relevant to the community structure. It is important to note that Cliff Pool Sinkhole has a water column open to sunlight, and eyewitnesses report that the sinkhole can appear seasonally greenish from primary productivity. This potentially explains faunal differences between Cliff Pool Sinkhole (increased abundance of *Trichohyalus aguayoi* and *Helenina* in Community 3) vs. Deep Blue (increased abundance of *Trochammina* and *Entzia* in Community 2, **Figure 4**), with the potential for increased resource partitioning and foraminiferal diversity deeper into the saline groundwater mass at Cliff Pool Sinkhole (Communities 3 and 4). Other secondary taxa that are also present include *Melonis barleeanum* (Caralp, 1989) and *Globocassidulina subglobosa*, both of which are known to respond favorably to seasonal delivery of phytodetritus in the open ocean. Their increased

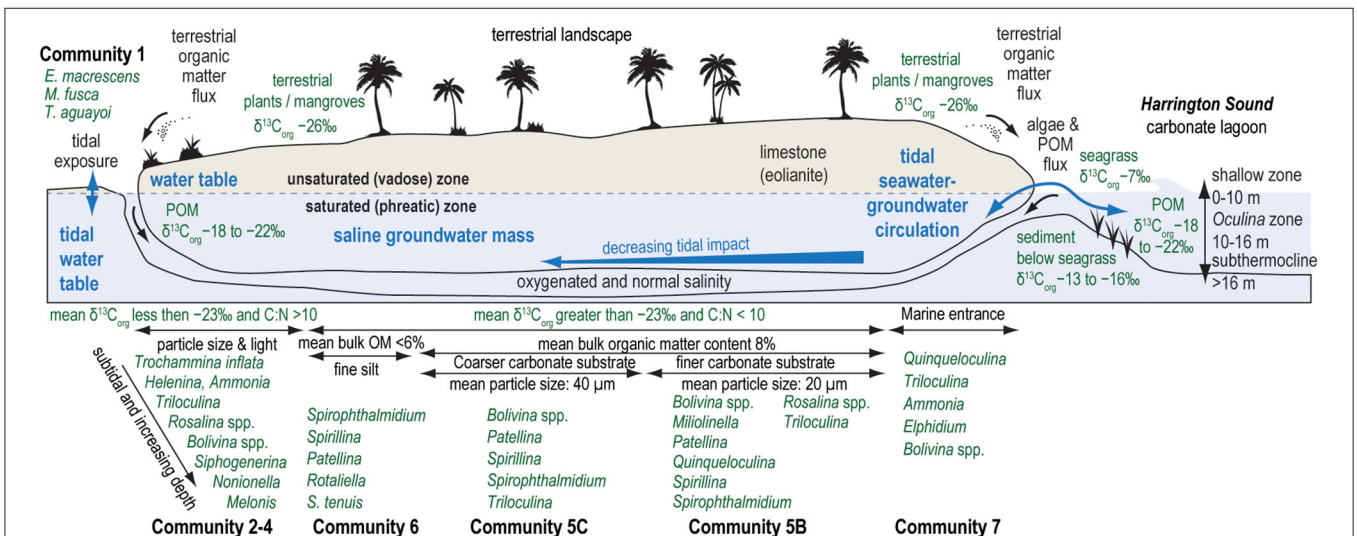


FIGURE 7 | Conceptual model of idealized benthic foraminiferal communities in the marine sector of karst subterranean estuaries in Bermuda, along with idealized changes in stable carbon isotopic value of bulk organic matter ($\delta^{13}C_{org}$), organic matter quantity, mean particle size of substrate, tidal exposure in subaerial pools, and the magnitude of nutrient and particle delivery from ocean-groundwater exchange through marine cave openings. Representative values of $\delta^{13}C_{org}$ values for source organic matter summarized from the literature (Goericke and Fry, 1994; Kennedy et al., 2010; Fourqurean et al., 2019), and ecological zones in Harrington Sound from Neumann (1965).

percent abundance in Communities 3 and 4 proximal to Cliff Pool Sinkhole is likely related this additional food resource produced in the dimly-lit water column, and is supported by modestly lower C:N ratios (**Figure 5**). This likely indicates that additional environmental variables are impacting the benthic foraminiferal communities that are not quantified in this study (i.e., dissolved nutrients at the sediment-groundwater interface, pore water chemistry). Based on experimental cultures, the epifaunal *Rosalina globularis* prefers warm and saltier waters (optimal: 27°C, >25 psu) for reproduction (Saraswat et al., 2011, 2015), which are found in the relatively shallow (<20 m depth) marine habitats in Bermuda's caves. The most abundant genus is the infaunal *Bolivina,* which is likely capitalizing on any available food resource in the benthos. While the impact of particle size on benthic foraminifera in other environments remains a debated issue (Debenay et al., 2001; Diz et al., 2004; Armynot du Châtelet et al., 2009), our results suggest that substrate texture in KSEs may also be influencing benthic habitat variability and foraminiferal community structure. Community 3 was associated with coarser substrates (mean particle size: >271.2 μm) compared with Community 4 (mean particle size: 149.6 μm).

These results now clearly inform the environmental conditions of Pleistocene-aged KSEs that were colonized by benthic foraminifera, which have been subsequently preserved in fossil cave deposits. For example, Proctor and Smart (1991) documented fossil benthic foraminifera in elevated caves in England, which are most likely dated Marine Isotope Stage 11 (424,00–374,000 years ago). Detailed foraminiferal counts were not provided, but fine textured sediment contained echinoid spines, *Ammonia beccarii*, *Cassidulina*, and *Bolivina.* On the Yucatan Peninsula in Mexico, van Hengstum et al. (2009) described *Bolivina*-dominated foraminiferal communities in Carwash Cave (older than Last Glacial Maximum 20,000 years ago), and there are *Helenina*- and B*olivina*-dominated Pleistocene-aged foraminiferal deposits in Maya Blue Cave and Vaca-Ha (van Hengstum and E. Reinhardt, unpublished observations). Based on modern benthic foraminiferal communities in Bermuda, these examples of fossil benthic foraminifera were all living in sediment that was dominated by terrestrial organic matter inputs, with additional taxonomic variability in the Pleistocene foraminiferal community most likely related to the salinity of the contemporaneous groundwater mass flooding that specific cave.

Marine Benthic Habitats Dominated by Marine-Sourced Organic Carbon

Communities 5, 6, and 7 occur in benthic habitats that primarily receive marine sources of organic carbon, which is most likely from marine plankton based on the $\delta^{13}C_{org}$ values from −22.3 to −15.1‰ and C:N ratios of 8–10 (**Figures 6**, **7**). Marine particulate organic carbon generally has values from −18 to −23‰ in lower latitudes (Jeffrey et al., 1983; Altabet, 1990; Goericke and Fry, 1994). An important component of particulate organic matter is marine plankton, which has a much lower C:N ratio (<10) relative to terrestrial organic carbon (Lamb et al., 2006; **Figure 6**). Seagrasses and macroalgae are abundant in the shallow sandy ecological zone of Harrington Sound (upper 10 m; Neumann, 1965), and consistent with global trends (Kennedy et al., 2010), seagrasses in Harrington Sound have enriched $\delta^{13}C_{org}$ values and C:N ratios exceeding 18 (Fourqurean et al., 2019). Two locally common seagrass species, for example, *Thalassia testudium* has a mean $\delta^{13}C_{org}$ value of −7.5‰ ($n = 351$) and a mean C:N ratio of 21 ($n = 364$), and *Syringodium filiforme* has a mean $\delta^{13}C_{org}$ value of −6.3‰ ($n = 369$) and a mean C:N ratio of 18 ($n = 362$) (Fourqurean et al., 2019; **Figure 6**). Sediment below seagrass in Harrington Sound is estimated to have a C:N ratio of 11, and $\delta^{13}C_{org}$ value of −13 to −16‰, based on a global mean $\Delta^{13}C_{seagrass-sediment}$ value of 6.3‰ (Kennedy et al., 2010). While some contribution of organic matter from seagrasses and macroalgae cannot be ignored, the low C:N ratios associated with Communities 5, 6, and 7 (∼8–10, **Figure 7**; **Table 1**) indicates that a more nitrogen-rich organic matter source like marine plankton is likely being delivered to these communities.

Community 7 is located in the main tunnel in Green Bay Cave that is closest to Harrington Sound, and extends from open water into an area colloquially referred to as the "Rat Trap" (see map in van Hengstum and Scott, 2011). This tunnel is characterized by attenuating light availability (disphotic zone), and past the Rat Trap is the aphotic zone. This tunnel is dominated by *Quinqueloculina, Ammonia, Elphidium*, and *Peneroplis* (**Figure 6**), which are common taxa in the shallow carbonate lagoons throughout the tropical North Atlantic Ocean (Javaux and Scott, 2003). While this study grouped all taxa at the genus level, van Hengstum and Scott (2011) noted that Community 7 is associated with *Ammonia beccarii* var. parkinsoniana. This tunnel coincides with areas that receive classic taxonomic investigation in marine caves, where strong gradients in light and tidal currents exist. The coarser substrate is likely promoted by winnowing-away of finer sediment particles in response to the large volume of seawater circulating through this tunnel during each tidal cycle (∼1,960,000 m^3: Iliffe, 2008). Coarser substrates also occur in other Mediterranean marine caves with higher current velocities from tidal action (Radolović et al., 2015). It is likely that tidal and storm currents also have transported some benthic foraminifera tests from Harrington Sound into the cave tunnel, however, current velocities notably decrease through the rest of Green Bay Cave past the narrowing of cave passage at the Rat Trap. Interestingly, PCS-15 from Palm Cave was not similar to Community 7, despite its proximity to the opening with Harrington Sound (i.e., Cripple Gate). Perhaps this is related to the much smaller connection of Palm Cave to Harrington Sound at "Cripple Gate," and the much lower volume of water exchanged with Harrington Sound during tidal cycles impacting benthic habitat conditions.

Community 6 is most distal from any cave entrance (or exit, **Figure 7**), is associated with areas where endemic anchialine cave animals (e.g., *Procaris chacei*) are more likely to be observed, and the fine-grained substrate (mean particle size: 5.3 μm) has the lowest bulk organic matter content (mean: 6%) and TOC (mean: 5%). Community 6 has the highest percent abundance of *Spirophthalmidium emaciatum,* members of the order Sprillinida

(e.g., *Patellina, Spirillina*, and *Mychostomina*), and *Rotaliella arctica*. Observation of *Spirophthalmidium emaciatum* outside of marine caves is limited, and includes New Guinea (Haig, 1988), the Mediterranean (Kuhnt et al., 2007), and the deep Pacific (Brady, 1884). In general, the thin-walled and fragile test of *S. emaciatum* is unlikely to endure taphonomic reworking. This taxon is very closely related (or a ecophenotypic variant) of *S. acutimargo*, which constitutes up to 3% of communities in deep-marine carbonate oozes (>2000 m water depth) from the North Atlantic Ocean near the Azores (Hermelin and Scott, 1985). While common in Community 6 (mean water depth: 15.4 m), *Rotaliella arctica* is also observed at 4450 m water depth on the Bermuda Rise (Pawlowski, 1991), and at 1980 m water depth in the Arctic (Scott and Vilks, 1991). Interestingly, dominant taxa in Community 6 (*Rotaliella*, Spirillinids, and *Spirophthalmidium*) are not common in carbonate sediments from shallower locations (300–1000 m) off the Little Bahama Bank in The Bahamas (Martin, 1988), or on the shallow (10–40 m) flooded carbonate Serranilla Bank (Triffleman et al., 1991) elsewhere in the Tropical North Atlantic Ocean. In caves, a deep-sea affinity is well-known in higher taxonomic groups like crustaceans (Iliffe et al., 1983). In the Mediterranean, *S. emaciatum* has been recently described in benthic foraminiferal communities from a marine cave with carbonate sedimentation on the Murica coastal region in Spain (Cueva Gemelas: Bergamin et al., 2020), but not in marine caves on eastern Sardinia with siliciclastic sedimentation and evidence for the discharge of meteoric water (Romano et al., 2018, 2020). On the island of Cozumel (Mexico) where Aerolito Cave is located (Mejía-Ortiz et al., 2007a,b; CalderóN-GutiéRrez et al., 2018), caves passages flooded with oxygenated saline groundwater and benthic carbonate sediment also host populations of *S. emaciatum* (van Hengstum, personal observation). Murray (2006) states that *Spirillina* and *Patellina* prefer hard substrates, so it remains possible that the cave walls/ceiling may be providing an ideal natural hard substrate for these taxa. However, our research design is unable to assess this possibility (sampling benthic sediment, not cave walls). As suggested by Fichez (1991), perhaps complex organic matter is a critical resource for Community 6, which can only be evaluated by resolving biogeochemical cycling of nutrients in these areas (Fichez, 1990, 1991; Airoldi and Cinelli, 1996; Jian et al., 2020). Finally, Community 6 also occurs very close to the shoreline in Green Bay Cave (samples ISC-61 or ISC-73 See fig 2 in van Hengstum and Scott, 2011), yet does not receive enough nutrients to promote higher diversity and species richness like Community 5 from direct seawater transfer through the limestone pores. From a conservation perspective, these results indicate that any introduced physical cave openings from anthropogenic activity will change nutrient supply and communities of benthic meiofauna in marine sectors of KSEs.

Community 5 (including: 5A, 5B, and 5C) is colonizing benthic habitats experiencing more regular tidal groundwater-seawater exchange and likely higher sedimentation rates (Community 5B and 5C) or some terrestrial input (Community 5A). This is likely providing increased nutrient availability, and in turn is promoting higher species richness and diversity than benthic habitats colonized by Community 6 (**Table 1**). Community 5 is not primarily influenced by: (i) strong tidal currents and attenuating light availability like Community 7, (ii) exposure from water table variability like Community 1, or (iii) increased organic matter input from the adjacent terrestrial landscape like Communities 2–4. Dominant taxa in Community 5 include *Globocassidulina subglobosa* that commonly occurs in carbonate sediments >1000 deep of the Little Bahama Bank (Martin, 1988), and *Melonis barleeanum* who is successful in areas with regular delivery of marine organic matter (Caralp, 1989). In Green Bay Cave, Community 5 is proximal to the large entrance (exit) into Harrington Sound. Tintinnid loricas (pelagic ciliates) are also deposited in the sediment with Community 5 in Green Bay Cave, and they were likely transported into the cave and settled out of the suspended sedimentary load. This observation supported the hypothesis that Community 5 in Green Bay Cave receives increased deposition of suspended sediments as the velocity of groundwater currents caused by tidal flow attenuate in the subsurface (van Hengstum and Scott, 2011), similar to what has been observed in marine caves on the Mediterranean coast of France (Fichez, 1991). An important taxonomic caveat is that small miliolids identified as *Triloculina* in Bermuda caves are not well-developed adult specimens with clear phenotypic characteristics like those common in subtidal marine carbonate lagoons (Javaux and Scott, 2003). Thus, it cannot be ruled-out that these are juvenile *Quinqueloculina* (Schnitker, 1967). Overall, these smaller cave miliolids are perhaps responding to a nutritional deficiency that is not constrained in this study.

Further evaluation of the physical environmental characteristics (**Table 1**; **Figures 5–7**) supports a tripartite division of the dendrogram (**Figure 4**, Bray-Curtis Similarity Index: 0.36). As previously discussed, the subtidal benthic foraminifera in Cow Cave (Community 5A, Cow Cave) is transitional between the foraminiferal communities that favor primary inputs from marine vs. terrestrial organic matter (**Figure 5**). While these samples are from shallow subtidal settings, benthic areas in Cow Cave receive protection from direct terrestrial sedimentation by the rock roof of the cave (i.e., geomorphology). Faunistically, samples from Palm Cave (Community 5C) closely compare with benthic areas in Green Bay Cave (Community 5B, **Figure 4**). However, finer substrates (Community 5B) had a greater abundance of *Reophax* spp. (mean: 3.1%) and *Bolivina* spp. (mean: 11.4%), while coarser substrates (Community 5C) had a greater abundance of *Spirillina vivipara* (mean: 13%) and *Patellina*-like taxa (mean: 7.8%). However, a careful evaluation of the cross plot between $\delta^{13}C_{org}$ and C:N (**Figure 6**) indicates that organic matter in Palm Cave (Community 5C) is slightly more carbon isotopically depleted with higher C:N values than Green Bay Cave (Community 5B). At least two hypotheses emerge to explain these differences between Community 5C and 5B that are related to cave morphology: either (i) proportionally less carbon isotopically enriched organic matter (e.g., seagrass, algae) is transported into Palm Cave through the smaller opening at Cripple Gate vs. the large marine opening of Green Bay Cave (**Figure 3**), or (ii) more ^{13}C-depleted terrestrial organic matter is eroding into Palm Cave through its more numerous

openings (exits) to the terrestrial landscape above (**Figure 2**). This suggests that differences in tidal exchange of seawater and particulate organic carbon transport through Cripple Gate (Palm Cave) and Green Bay Entrance (Green Bay Cave) may be influencing benthic habitat partitioning between caves, but other geochemical proxies are required to resolve these uncertainties. The collective role of cave geometry and volumetric exchange of seawater during tidal cycles between saline groundwater and Harrington Sound appear important for generating differences in the benthic foraminiferal community structures, and by corollary, benthic habitats in the oxygenated marine sectors of KSEs.

CONCLUSIONS

- Benthic foraminifera in the marine sector of karst subterranean estuaries (KSEs) in Bermuda can be grouped into 9 different communities that are correlated to organic matter source and quantity, tidal exposure, texture of the carbonate sediment substrate (i.e., mean particle size size), proximity to cave exits, and the relationship between cave morphology and tidally-forced circulation between coastal seawater and saline groundwater.
- The source and quantity of particulate organic carbon delivered to the benthos is significantly correlated to benthic foraminiferal community structure. A primary division emerges in foraminiferal communities correlated with organic carbon inputs primarily from the terrestrial surface with some marine plankton (mean $\delta^{13}C_{org}$ values <-23.2‰, C:N ratios >11), vs. organic carbon inputs dominantly from marine plankton (mean $\delta^{13}C_{org}$ values >-21.6‰, C:N ratios <10) that are transported into the caves from groundwater-seawater circulation from the adjacent carbonate lagoon (i.e., Harrington Sound).
- Benthic areas with more depleted $\delta^{13}C_{org}$ values of sediment are dominated by *Rosalina*, *Bolivina*, and *Triloculina*. In contrast, benthic areas with more enriched $\delta^{13}C_{org}$ values of sediment are dominated by *Patellina*, *Spirillina*, *Rotaliella*, *Miliolinella*, and *Spirophthalmidium*.
- Benthic areas with the least amount of organic carbon in the sediment (mean: TOC 5.1%, mean bulk organic content: 6%) are the least diverse, and dominated by *Spirophthalmidium emaciatum* (mean: 31%, maximum: 70%).
- Differences in the size and morphology of direct connections between Harrington Sound and Palm Cave vs. Green Bay Cave are impacting benthic foraminiferal community structure.

DATA AVAILABILITY STATEMENT

The original contributions presented in the study are included in the article/**Supplementary Material**, further inquiries can be directed to the corresponding author.

AUTHOR CONTRIBUTIONS

PvH designed the research. JC collected the samples from Palm Cave and completed laboratory activities. PvH and JC jointly interpreted that data, generated the artwork, and co-wrote the final manuscript. All authors contributed to the article and approved the submitted version.

FUNDING

This work was funded by student research grants from the American Academy of Underwater Sciences (JC, 2016), the Geologic Society of America (JC), the Bermuda Aquarium, Museum and Zoo (JC), and resources for publishing from Texas A&M University at Galveston.

ACKNOWLEDGMENTS

We acknowledge the support of S. R. Smith, G. Nolan, B. Williams, with sample collections approved through the support of a Special Permit (2015, Number 150301) issued to PH from the Department of Environmental Protection in the Bermuda Government. This research is only possible through the long-term support from the Tucker family, the Bermuda National Trust, and members of the Bermuda Zoological Society. Additional technical support was provided by S. Little, A. Tamalavage, R. Sullivan, T. Winkler, T. Iliffe, and T. van Hengstum. A constructive evaluation by two reviewers and D. Brankovits improved the final manuscript.

SUPPLEMENTARY MATERIAL

The Supplementary Material for this article can be found online at: https://www.frontiersin.org/articles/10.3389/fenvs.2020.594554/full#supplementary-material

REFERENCES

Airoldi, L., and Cinelli, F. (1996). Variability of fluxes of particulate material in a submarine cave with chemolithoautotrophic inputs of organic carbon. *Mar. Ecol. Prog. Ser.* 139, 205–217. doi: 10.3354/meps139205

Altabet, M. A. (1990). Organic C, N, and stable isotopic composition of particulate matter colelcted on glass-fiber and aluminum oxide filters. *Limnol. Oceanogr.* 35, 902–909. doi: 10.4319/lo.1990.35.4.0902

Anderson, B., Scalan, R. S., Behrens, E. W., and Parker, P. L. (1992). Stable carbon isotope variations in sediment from Baffin Bay, Texas, U.S.A.: evidence for cyclic changes in organic matter source. *Chem. Geol. Isotope Geosci. Sect.* 101, 223–233. doi: 10.1016/0009-2541(92)90004-O

Armynot du Châtelet, É., Bout-Roumazeilles, V., Riboulleau, A., and Trentesaux, A. (2009). Sediment (grain size and clay mineralogy) and organic matter quality control on living benthic foraminifera. *Rev. Micropaléontol.* 52, 75–84. doi: 10.1016/j.revmic.2008.10.002

Balduzzi, A., and Cattaneo, R. (1985). Estimation par relèvements photographiques de la distribution de *Miniacina miniacea* (Sarcomastigophora, Foraminifera) dans une grotte sous-marine du Golfe de Naples. *Rapp. P. V. Comm. Int. Explor. Sci. Mer Méditerr.* 29, 127–129.

Bates, N. R. (2017). Twenty years of marine carbon cycle observations at Devils Hole Bermuda provide insights into seasonal hypoxia, coral reef calcification, and ocean acidification. *Front. Mar. Sci.* 4:372. doi: 10.3389/fmars.2017.00036

Bergamin, L., Marassich, A., Provenzani, P., and Romano, E. (2018). Foraminiferal ecozones in two submarine caves of the Orosei Gulf (Sardinia, Italy). *Rend. Lincei Sci. Fis. Nat.* 29, 547–557. doi: 10.1007/s12210-018-0700-0

Bergamin, L., Taddei Ruggiero, E., Pierfranceschi, G., Andres, B., Costantino, R., Crovato, C., et al. (2020). Benthic foraminifera and brachiopods from a marine cave in Spain: environmental significance. *Mediterr. Mar. Sci.* 21, 506–518. doi: 10.12681/mms.23482

Bermúdez, P. J. (1949). *Tertiary Smaller Foraminifera of the Dominican Republic*. Cushman Laboratory for Foraminiferal Research Special Publication, 25, 1–322.

Bernhard, J. M., and Sen Gupta, B. K. (1997). "Foraminifera of oxygen-depleted environments," in *Modern Foraminifera*, ed B. K. Sen Gupta (Boston, MA: Kluwer Academic Press), 201–216. doi: 10.1007/0-306-48104-9_12

Bishop, R. E., Humphreys, W. F., Cukrov, N., Žic, V., Boxshall, G. A., Cukrov, M., et al. (2015). "Anchialine" redefined as a subterranean estuary in a crevicular or cavernous geological setting. *J. Crust. Biol.* 35, 511–514. doi: 10.1163/1937240X-00002335

Brady, H. B. (1884). Report on the foraminifera dredged by the H.M.S. Challenger during the years 18731–1876: reports on the scientific results of the Voyage of the H.M.S. Challenger during the years 18731–1876. *Zoology* 9:814.

Brankovits, D., Pohlman, J. W., Ganju, N. K., Iliffe, T. M., Lowell, N., Roth, E., et al. (2018). Hydrologic controls of methane dynamics in karst subterranean estuaries. *Global Biogeochem. Cycles* 32, 1759–1775. doi: 10.1029/2018GB006026

Brankovits, D., Pohlman, J. W., Niemann, H., Leigh, M. B., Leewis, M. C., Becker, K. W., et al. (2017). Methane- and dissolved organic carbon-fueled microbial loop supports a tropical subterranean estuary ecosystem. *Nat. Commun.* 8:1835. doi: 10.1038/s41467-017-01776-x

Burgett, C. M., Burkholder, D. A., Coates, K. A., Fourqurean, V. L., Kenworthy, W. J., Manuel, S. A., et al. (2018). Ontogenetic diet shifts of green sea turtles (*Chelonia mydas*) in a mid-ocean developmental habitat. *Mar. Biol.* 165:33. doi: 10.1007/s00227-018-3290-6

Buzas, M. A. (1968). On the spatial distributionof foraminifera. *Contrib. Cushman Found. Foraminiferal Res.* 19, 1–11.

Calderón-GutiéRrez, F., SáNchez-Ortiz, C. A., and Huato-Soberanis, L. (2018). Ecological patterns in anchialine caves. *PLoS ONE* 3:e0202909. doi: 10.1371/journal.pone.0202909

Camacho, S., Moura, D., Connor, S., Scott, D., and Boski, T. (2015). Ecological zonation of benthic foraminifera in the lower Guadiana Estuary (southeastern Portugal). *Mar. Micropaleontol.* 114, 1–18. doi: 10.1016/j.marmicro.2014.10.004

Cant, R. V., and Weech, P. S. (1986). A review of the factors affecting the development of Ghyben-Hertzberg lenses in the Bahamas. *J. Hydrol.* 84, 333–343. doi: 10.1016/0022-1694(86)90131-9

Caralp, M. H. (1989). Size and morphology of the benthic foraminifera *Melonis barleeanum*: relationships with marine organic matter. *J. Foraminiferal Res.* 19, 235–245. doi: 10.2113/gsjfr.19.3.235

Carman, K. W. (1933). *The Shallow-Water Foraminifera of Bermuda*. Cambridge, MA: Massachusetts Institute of Technology.

Carmen, K. W. (1927). *The Shallow-Water Foraminifera of Bermuda*. Cambridge, MA: Massachusetts Institute of Technology.

Chávez-Solís, M., Solís, C., Simões, N., and Mascaró, M. (2020). Distribution patterns, carbon sources, and niche partitioning in cave shrimps (Atyidae: Typhlatya). *Sci. Rep.* 10:12812. doi: 10.1038/s41598-020-69562-2

Clarke, K. R., Somerfield, P. J., and Gorley, R. N. (2008). Testing of null hypotheses in exploratory community analyses: similarity profiles and biota-environment linkage. *J. Exp. Mar. Biol. Ecol.* 366, 56–69. doi: 10.1016/j.jembe.2008.07.009

Coull, B. (1969). Hydrographic control of meiobenthos in Bermuda. *Oecologia* 14, 953–957. doi: 10.4319/lo.1969.14.6.0953

Debenay, J.-P., Tsakiridis, E., Soulard, R., and Grossel, H. (2001). Factors determining the distribution of foraminiferal assemblages in Port Joinville Harbor (Ile d'Yeu, France): the influence of pollution. *Mar. Micropaleontol.* 43, 75–118. doi: 10.1016/S0377-8398(01)00023-8

Debenay, J. P., and Guillou, J. J. (2002). Ecological transitions indicated by foraminiferal assemblages in paralic environment. *Estuaries* 6A, 1107–1120. doi: 10.1007/BF02692208

Diz, P., Francés, G., Costas, S., Souto, C., and Alejo, I. (2004). Distribution of benthic foraminifera in coarse sediments, Ría de Vigo, NW Iberian margin. *J. Foraminiferal Res.* 34, 258–275. doi: 10.2113/34.4.258

Dupuy, C., Rossignol, L., Geslin, E., and Pascal, P. Y. (2010). Predation of mudflat meio-macrofaunal metazoans by a clacareous foraminifer, *Ammonia tepida* (Cushman 1926). *J. Foraminiferal Res.* 40, 305–3012. doi: 10.2113/gsjfr.40.4.305

Duque, C., Michael, H. A., and Wilson, A. M. (2020). The subterranean estuary: technical term, simple analogy, or source of confusion? *Water Resour. Res.* 56:e2019WR026554. doi: 10.1029/2019WR026554

Fichez, R. (1990). Decrease in allochthonous organic inputs in dark submarine caves, connection with lowering in benthic community richness. *Hydrobiologia* 207, 61–69. doi: 10.1007/BF00041441

Fichez, R. (1991). Suspended particulate organic matter in a Mediterranean submarine cave. *Mar. Biol.* 108, 167–174. doi: 10.1007/BF01313485

Fourqurean, J. W., Manuel, S. A., Coates, K. A., Kenworthy, W. J., and Boyer, J. N. (2015). Water quality, isoscapes, and stoichioscapes of seagrasses indicate general P limitation and unique N cycling in shallow water benthos of Bermuda. *Biogeosciences* 12, 6235–6249. doi: 10.5194/bg-12-6235-2015

Fourqurean, J. W., Manuel, S. A., Coates, K. A., Massey, S. C., and Kenworthy, W. J. (2019). Decadal monitoring in Bemruda shows a widespread loss of seagrasses attributable to overgrazing by the green sea turtle *Chelonia mydas*. *Estuaries Coasts* 42, 1524–1540. doi: 10.1007/s12237-019-00587-1

France, R. L. (1995). Carbon-13 enrichment in benthic compared to planktonic algae: foodweb implications. *Mar. Ecol. Prog. Ser.* 124, 307–312. doi: 10.3354/meps124307

Fry, B., Scalan, R. S., and Parker, P. L. (1977). Stable carbon isotope evidence for two sources of organic matter in coastal sediments: seagrasses and plankton. *Geochem. Cosmochim. Acta* 41, 1875–1877. doi: 10.1016/0016-7037(77)90218-6

Gehrels, W. R., and van de Plassche, O. (1999). The use of Jadammina macrescens (Brady) and Balticammina pseudomacrescens Brönnimann, Lutze, and Whittaker (Protozoa: Foraminiferida) as sea-level indicators. *Palaeogeogr. Palaeoclimatol. Palaeoecol.* 149, 89–101. doi: 10.1016/S0031-0182(98)00194-1

Goericke, R., and Fry, B. (1994). Variations of marine plankton delta-13-C with latitude, temperature and dissolved CO2 in the world ocean. *Global Biogeochem. Cycles* 8, 85–90. doi: 10.1029/93GB03272

Goldstein, S. T., and Corliss, B. H. (1994). Deposit feeding in selected deep-sea and shallow-water benthic foraminifera. *Deep Sea Res.* 41, 229–241. doi: 10.1016/0967-0637(94)90001-9

Gonneea, M. E., Charette, M. A., Liu, Q., Herrera-Silveira, J. A., and Morales-Ojeda, S. M. (2014). Trace element geochemistry of groundwater in a karst subterranean estuary (Yucatan Peninsula, Mexico). *Geochim. Cosmochim. Acta* 132, 31–49. doi: 10.1016/j.gca.2014.01.037

Gooday, A. J. (1988). A response by benthic foraminifera to the deposition of pytodetritus in the deep sea. *Nature* 332, 70–73. doi: 10.1038/332070a0

Gooday, A. J. (1993). Deep-sea benthic foraminiferal species which exploit phytodetritus–characteristic features and controls on distribution. *Mar. Micropaleonol.* 22, 187–205. doi: 10.1016/0377-8398(93)90043-W

Gooday, A. J., Levin, L. A., Linke, P., and Heeger, T. (1992). The role of benthic foraminifera in deep-sea food webs and carbon cycling. *Deep Sea Food Chains Global Carbon Cycle* 360, 63–91. doi: 10.1007/978-94-011-2452-2_5

Gotelli, N. J., and Colwell, R. K. (2011). "Estimating species richness," in *Biological Diversity: Frontiers in Measurement and Assessment*, eds A. E. Magurran and B. J. Mcgill (Oxford: Oxford University Press), 39–54.

Guido, A., Rosso, A., Sanfilippo, R., Russo, F., and Mastandrea, A. (2017). Microbial biomineralization in biotic crusts from a pleistocene marine cave (NW Sicily, Italy). *Geomicrobiol. J.* 34, 864–872. doi: 10.1080/01490451.2017.1284283

Guilbault, J.-P., Clague, J. J., and Lapointe, M. (1995). Amount of subsidence during a late Holocene earthquake—evidence from fossil tidal marsh foraminifera at Vancouver Island, west coast of Canada. *Palaeogeogr. Palaeoclimatol. Palaeoecol.* 118, 49–71. doi: 10.1016/0031-0182(94)00135-U

Haig, D. W. (1988). Miliolid foraminfiera from the inner neritic sand and mud facies of the Papuan Lagoon, New Guinea. *J. Foraminiferal Res.* 18, 203–236. doi: 10.2113/gsjfr.18.3.203

Hayward, B. W., Grenfell, H. R., and Scott, D. B. (1999). Tidal range of marsh foraminifera for determining former sea-level heights in New Zealand. *N. Z. J. Geol. Geophys.* 42, 395–413. doi: 10.1080/00288306.1999.9514853

Heiri, O., Lotter, A. F., and Lemcke, G. (2001). Loss on ignition as a method for estimating organic and carbonate content in sediments: reproducibility and comparability of results. *J. Paleolimnol.* 25, 101–110. doi: 10.1023/A:1008119611481

Hermelin, J. O. R., and Scott, D. B. (1985). Recent benthic foraminifera from the central North Atlantic. *Micropaleontology* 31, 199–220. doi: 10.2307/1485542

Iliffe, T. M. (2008). Groundwater pollution and its impact on Bermuda's reefs and inshore water, NOAA Coral Reef Conservation Grant–Final Report, National Oceanic and Atmospheric Administration.

Iliffe, T. M., Hart, C. W. J., and Manning, R. B. (1983). Biogeography and the caves of Bermuda. *Nature* 302, 141–142. doi: 10.1038/302141a0

Iliffe, T. M., Wilkens, H., Parzefall, J., and Williams, D. (1984). Marine lava cave fauna: composition, biogeography, and origins. *Science* 225, 309–311. doi: 10.1126/science.225.4659.309

Javaux, E., and Scott, D. B. (2003). Illustration of modern benthic foraminifera from Bermuda and remarks on distributions in other subtropical/tropical areas. *Paleontol. Electron.* 6:29. Available online at: http://palaeo-electronica.org/paleo/2003_1/benthic/issue1_03.htm

Jeffrey, A. W. A., Pflaum, R. C., Brooks, J. M., and Sackett, W. M. (1983). Vertical trends in particulate organic carbon 13C:12C ratios in the upper water column. *Deep Sea Res.* 30, 971–983. doi: 10.1016/0198-0149(83)90052-3

Jian, S., Zhang, Y., Jin, J., Wu, Y., Wei, Y., Wang, X., et al. (2020). Organic carbon in a seepage face of a subterranean estuary: turnover and microbial interrelations. *Sci. Tot. Environ.* 725:138220. doi: 10.1016/j.scitotenv.2020.138220

Jorissen, F. J., De Stigter, H. C., and Widmark, J. G. V. (1995). A conceptual model explaining benthic foraminifera microhabitats. *Mar. Micropaleontol.* 26, 3–15. doi: 10.1016/0377-8398(95)00047-X

Juggins, S. (2015). *Rioja: Analysis of Quaternary Science Data. R-Package 0.9-5*. Available online at: https://cran.r-project.org/web/packages/rioja/index.html

Kennedy, H., Beggins, J., Duarte, C. M., Fourqurean, J. W., Holmer, M., Marba, N., et al. (2010). Seagrass sediments as a global carbon sink: Isotopic constraints. *Global Biogeochem. Cycles* 24:2010GB4026. doi: 10.1029/2010GB003848

Khan, N. S., Vane, C. H., Englehart, S. E., Kendrick, C., and Horton, B. P. (2019). The application of δ13C, TOC, and C/N geochemistry of mangrove sediments to reconstruct Holocene paleoenvironments and relative sea levels, Puerto Rico. *Mar. Geol.* 415:105963. doi: 10.1016/j.margeo.2019.105963

Kuhnt, T., Schmiedl, G., Ehrmann, W., Hamann, Y., and Hemleben, C. (2007). Deep-sea ecosystem variability of the Aegean Sea during the past 22 kyr as revealed by benthic foraminifera. *Mar. Micropaleontol.* 64, 141–162. doi: 10.1016/j.marmicro.2007.04.003

Lamb, A. L., Wilson, G. P., and Leng, M. J. (2006). A review of coastal palaeoclimate and relative sea-level reconstructions using δ13C and C/N ratios in organic material. *Earth Sci. Rev.* 75, 29–57. doi: 10.1016/j.earscirev.2005.10.003

Land, L. S., Mackenzie, F. T., and Gould, S. J. (1967). Pleistocene history of Bermuda. *Geol. Soc. Am. Bull.* 78, 993–1006. doi: 10.1130/0016-7606(1967)78[993:PHOB]2.0.CO;2

Legendre, P., and Legendre, L. (1998). Numerical ecology: developments in environmental modelling. *Dev. Environ. Model.* 20, 1–853.

Levin, L. A., Ekau, W., Gooday, A. J., Jorissen, F. J., Middelburg, J. J., Naqvi, S. W. A., et al. (2009). Effects of natural and human-induced hypoxia on coastal benthos. *Biogeosciences* 6, 2063–2098. doi: 10.5194/bg-6-2063-2009

Linke, P., Altenbach, A. V., Graf, G., and Herger, T. (1995). Response of deep-sea benthic foraminifera to a simulated sedimentation event. *J. Foraminiferal Res.* 25, 75–82. doi: 10.2113/gsjfr.25.1.75

Little, S. N., and van Hengstum, P. J. (2019). Intertidal and subtidal benthic foraminifera in flooded caves: implications for reconstructing coastal karst aquifers and cave paleoenvironments. *Mar. Micropaleontol.* 149, 19–34. doi: 10.1016/j.marmicro.2019.03.005

Loeblich Jr, A. R., and Tappan, H. (1987). *Foraminiferal Genera and Their Classification*. Boston, MA: Springer.

Martin, J. B., Gulley, J., and Spellman, P. (2012). Tidal pumping of water between Bahamian blue holes, aquifers, and the ocean. *J. Hydrol.* 416–417, 28–38. doi: 10.1016/j.jhydrol.2011.11.033

Martin, R. E. (1988). Benthic foraminiferal zonation in deep-water carbonate platform margin environments, northern Little Bahama Bank. *J. Paleontol.* 62, 1–8. doi: 10.1017/S0022336000017935

Mejía-Ortiz, L. M., Yánez, G., and López-Mejía, M. (2007a). Echinoderms in an anchialine cave in Mexico. *Mar. Ecol.* 28, 31–34. doi: 10.1111/j.1439-0485.2007.00174.x

Mejía-Ortiz, L. M., Yánez, G., López-Mejía, M., and Zarza-Gónzales, E. (2007b). Cenotes (anchialine caves) on Cozumel Island, Quintana Roo, Mexico. *J. Cave Karst Stud.* 69, 250–255.

Moore, W. S. (1999). The subterranean estuary: a reaction zone of ground water and sea water. *Mar. Chem.* 65, 111–125. doi: 10.1016/S0304-4203(99)00014-6

Morris, B., Barnes, J., Brown, F., and Markham, J. (1977). *The Bermuda Marine Environment: A Report of the Bermuda Inshore Waters Investigations 1976–1977*. St. Georges: Bermuda Biological Station.

Murray, J. (2006). *Ecology and Applications of Benthic Foraminifera*. London: Cambridge University Press.

Mylroie, J. E., Carew, J. L., and Vacher, H. L. (1995). "Karst development in the Bahamas and Bermuda," in *Terrestrial and Shallow Marine Geology of the Bahamas and Bermuda*, eds H. A. Curran and B. White (Boulder, CO: Geologic Society of America), 251–267.

Neumann, A. C. (1965). Processes of recent carbonate sedimentation in Harrington Sound, Bermuda. *Bull. Mar. Sci.* 15, 987–1035.

Nomaki, H., Heinz, P., Hemleben, C., and Kitazato, H. (2005). Behavior and response of deep-sea benthic foraminifera to freshly supplied organic matter: a laboratory feeding experiment in microcosm environments. *J. Foraminiferal Res.* 35, 103–113. doi: 10.2113/35.2.103

Oksanen, J., Blanchet, F. G., Kindt, R., Legendre, P., Minchin, P. R., O'hara, R. B., et al. (2013). *Vegan: Community Ecology Package. R Package Version 3*. Available online at: https://cran.r-project.org/web/packages/vegan/index.html

Omori, A., Kitamura, A., Fujita, K., Honda, K., and Yamamoto, N. (2010). Reconstruction of light conditions within a submarine cave during the past 7000 years based on the temporal and spatial distribution of algal symbiont-bearing large benthic foraminifers. *Palaeogeogr. Palaeoclimatol. Palaeoecol.* 292, 443–452. doi: 10.1016/j.palaeo.2010.04.004

Pain, A. J., Martin, J. B., and Young, C. R. (2019). Sources and sinks of CO2 and CH4 in siliciclastic subterranean estuaries. *Limnol. Oceanogr.* 64, 1500–1514. doi: 10.1002/lno.11131

Pain, A. J., Martin, J. B., Young, C. R., Valle-Levinson, A., and Mariño-Tapia, I. (2020). Carbon and phosphorus processing in a carbonate karst aquifer and delivery to the coastal ocean. *Geochimi. Cosmochim. Acta* 269, 484–495. doi: 10.1016/j.gca.2019.10.040

Palmer, A., Mv, P., and Jm, Q. (1977). "Geology and origin of the caves in Bermuda," in *Proceeding of the 7th International Speleological Congress* (Sheffield), 336–339.

Parsons, R. J., Nelson, C. A., Denman, C. C., Andersson, A. J., Kledzik, A. L., Vergin, K. L., et al. (2015). Marine bacterioplankton community turnover within seasonally hypoxic waters of a subtropical sound: Devil's Hole, Bermuda. *Environ. Microbiol.* 17, 3481–3499. doi: 10.1111/1462-2920.12445

Patterson, R. T., and Fishbein, E. (1989). Re-examination of the statistical methods used to determine the number of point counts needed for micropaleontological quantitative research. *J. Paleontol.* 63, 245–248. doi: 10.1017/S0022336000019272

Pawlowski, J. (1991). Distribution and taxonomy of some benthic tiny foraminifers from the Bermuda rise. *Micropaleontology* 37, 163–172. doi: 10.2307/1485556

Pirsson, L. V., and Vaughn, T. W. (1917). A deep Boring in Bermuda Island. *Am. J. Sci. Ser.* s4–36, 70–71. doi: 10.2475/ajs.s4-36.211.70

Plummer, L. N., Vacher, H. L., Mckenzie, F. T., Bricker, O. P., and Land, L. S. (1976). Hydrogeochemistry of Bermuda: a case history of ground-water diagenesis of biocalcarenites. *Geol. Soc. Am. Bull.* 87, 1301–1316. doi: 10.1130/0016-7606(1976)87<1301:HOBACH>2.0.CO;2

Proctor, C. J., and Smart, P. L. (1991). A dated sediment record of Pleistocene transgressions on Berry Head, Southwest England. *J. Quat. Sci.* 6, 233–244. doi: 10.1002/jqs.3390060306

Radolović, M., Bakran-Petricioli, T., Petricioli, D., Surić, M., and Perica, D. (2015). Biological response to geochemical and hydrological processes in a shallow submarine cave. *Mediterr. Mar. Sci.* 16, 305–324. doi: 10.12681/mms.1146

Riedl, R., and Ozretić, B. (1969). Hydrobiology of marginal caves. Part 1: general problems and introduction. *Int. Rev. Gesamten Hydrobiol. Hydrogr.* 54, 661–683. doi: 10.1002/iroh.19690540503

Romano, E., Bergamin, L., Di Bella, L., Frezza, V., Marassich, A., Pierfranceschi, G., et al. (2020). Benthic foraminifera as proxies of marine influence in the Orosei marine caves (Sardinia, Italy). *Aquat. Conserv. Mar. Freshwater Ecosyst.* 30, 701–716. doi: 10.1002/aqc.3288

Romano, E., Bergamin, L., Pierfranceschi, G., Provenzani, C., and Marassich, A. (2018). The distribution of benthic foraminifera in Bel Torrente submarine cave (Sardinia, Italy) and their environmental significance. *Mar. Environ. Res.* 133, 114–127. doi: 10.1016/j.marenvres.2017.12.014

Rosso, A., Sanfilippo, R., Bonfiglio, L., Richards, D. A., and Nita, D. C. (2018). Exceptional Pleistocene vermetid crusts preserved in a cave located 130 m above sea level near Taormina (NE Sicily). *Boll. Soc. Paleontol. Ital.* 57:134. doi: 10.4435/BSPI.2018.09

Rosso, A., Sanfilippo, R., Ruggieri, R., Maniscalco, R., and Vertino, A. (2015). Exceptional record of submarine cave communities from the Pleistocene of Sicily (Italy). *Lethaia* 48, 133–144. doi: 10.1111/let.12094

Saraswat, R., Kouthanker, M., Kurtarkar, S. R., Nigam, R., Naqvi, S. W. A., and Linshy, V. N. (2015). Effect of salinity induced pH/alkalinity changes on benthic foraminifera: a laboratory culture experiment. *Estuar. Coast. Shelf Sci.* 153, 96–107. doi: 10.1016/j.ecss.2014.12.005

Saraswat, R., Nigam, R., and Pachkhande, S. (2011). Difference in optimum temperature for growth and reproduction in benthic foraminifer Rosalina globularis: implications for paleoclimatic studies. *J. Exp. Mar. Biol. Ecol.* 405, 105–110. doi: 10.1016/j.jembe.2011.05.026

Schmitter-Soto, J. J., Comín, F. A., Escobar-Briones, E., Herrera-Silveira, J., Alcocer, J., Suárez-Morales, E., et al. (2002). Hydrogeochemical and biological characteristics of cenotes in the Yucatan Peninsula (SE Mexico). *Hydrobiologia* 467, 215–228. doi: 10.1023/A:1014923217206

Schnitker, D. (1967). *Variation in Test Morphology of Triloculina linneiana d'Orbigny in Laboratory Cultures. Contributions from the Cushman Foundation for Foraminiferal Research, Vol.* 18, 85–86.

Scott, D. B., and Hermelin, J. (1993). A device for precision splitting of micropaleontological samples in liquid suspension. *J. Paleontol.* 67, 151–154. doi: 10.1017/S0022336000021302

Scott, D. B., and Medioli, F. S. (1978). Verticle zonation of marsh foraminifera as accurate indicators of former sea levels. *Nature* 272, 528–531. doi: 10.1038/272528a0

Scott, D. B., and Medioli, F. S. (1980). Living vs. total foraminiferal populations: their relative usefulness in paleoecology. *J. Paleontol.* 54, 814–813.

Scott, D. B., and Vilks, G. (1991). Benthonic foraminifera in the surface sediments of the deep-sea Arctic Ocean. *J. Foraminiferal Res.* 21, 20–38. doi: 10.2113/gsjfr.21.1.20

Sen Gupta, B. K., Turner, R. E., and Rabalais, N. N. (1996). Seasonal oxygen depletion in continental-shelf waters of Louisiana: historical record of benthic foraminifers. *Geology* 24, 227–230. doi: 10.1130/0091-7613(1996)024<0227:SODICS>2.3.CO;2

Sperazza, M., Moore, J. N., and Hendrix, M. S. (2004). High-resolution particle size analysis of naturally occurring very fine-grained sediment through laser diffractometry. *J. Sediment. Res.* 74, 736–743. doi: 10.1306/031104740736

Steinker, D. C., and Clem, K. V. (1984). Some nearshore foraminiferal assemblages from phytal substrates and bottom sediments, Bermuda. *Compass* 61, 98–115.

Stock, J. H., Iliffe, T. M., and Williams, D. (1986). The concept "anchialine" reconsidered. *Stygologia* 2, 90–92.

Suárez-Morales, E., Reid, J. W., Fiers, F., and Iliffe, T. M. (2004). Historical biogeography and distribution of the freshwater cyclopine copepods (Copepoda, Cyclopoida, Cyclopinae) of the Yucatan Peninsula, Mexico. *J. Biogeogr.* 31, 1051–1063. doi: 10.1111/j.1365-2699.2004.01053.x

Tamalavage, A. E., van Hengstum, P. J., Louchouarn, P., Kaiser, K., Donnelly, J. P., Albury, N. A., et al. (2018). Organic matter sources and lateral sedimentation in a Bahamian karst basin (sinkhole) over the late Holocene: influence of local vegetation and climate. *Palaeogeogr. Palaeoclimatol. Palaeoecol.* 506, 70–83. doi: 10.1016/j.palaeo.2018.06.014

Triffleman, N. J., Hallock, P., Hine, A. C., and Peebles, M. W. (1991). Distribution of foraminfieral tests in sediments of Serranilla Bank, Nicaraguan Rise, Southwestern Caribbean. *J. Foraminiferal Res.* 21, 39–47. doi: 10.2113/gsjfr.21.1.39

Vacher, H., Hearty, P., and Rowe, M. (1995). *Terrestrial and Shallow Marine Geology of the Bahamas and Bermuda*. Boulder, CO: Geological Society of America.

Vacher, H., and Rowe, M. (1997). *Geology and Hydrogeology of Carbonate Islands*. Amsterdam: Elsevier.

Vacher, H. L. (1978). Hydrogeology of Bermuda—significance of an across-the-island variation in permeability. *J. Hydrol.* 39, 207–226. doi: 10.1016/0022-1694(78)90001-X

van Hengstum, P. J., Cresswell, J. N., Milne, G. A., and Iliffe, T. M. (2019). Development of anchialine cave habitats and karst subterranean estuaries since the last ice age. *Sci. Rep.* 9:11907. doi: 10.1038/s41598-019-48058-8

van Hengstum, P. J., Donnelly, J. P., Kingston, A. W., Williams, B. E., Scott, D. B., Reinhardt, E. G., et al. (2015). Low-frequency storminess signal at Bermuda linked to cooling events in the North Atlantic region. *Paleoceanography* 30, 52–76. doi: 10.1002/2014PA002662

van Hengstum, P. J., Reinhardt, E. G., Beddows, P. A., Huang, R. J., and Gabriel, J. J. (2008). Thecamoebians (testate amoebae) and foraminifera from three anchialine cenotes in Mexico: Low salinity (1.5–4.5 psu) faunal transitions. *J. Foraminiferal Res.* 38, 305–317. doi: 10.2113/gsjfr.38.4.305

van Hengstum, P. J., Reinhardt, E. G., Beddows, P. A., Schwarcz, H. P., and Garbriel, J. J. (2009). Foraminifera and testate amoebae (thecamoebians) in an anchialine cave: surface distributions from Aktun Ha (Carwash) cave system, Mexico. *Limnol. Oceanogr.* 54, 391–396. doi: 10.4319/lo.2009.54.1.0391

van Hengstum, P. J., and Scott, D. B. (2011). Ecology of foraminifera and habitat variability in an underwater cave: distinguishing anchialine versus submarine cave environments. *J. Foraminiferal Res.* 41, 201–229. doi: 10.2113/gsjfr.41.3.201

van Hengstum, P. J., and Scott, D. B. (2012). Sea-level rise and coastal circulation controlled Holocene groundwater development and caused a meteoric lens to collapse 1600 years ago in Bermuda. *Mar. Micropaleonol.* 90–91, 29–43. doi: 10.1016/j.marmicro.2012.02.007

Wefer, G., and Killingley, J. S. (1986). Carbon isotopes in organic matter from a benthic alga *Halimeda incrassata* (Bermuda): effect of light intensity. *Chem. Geol. Isotope Geosci. Sect.* 59, 321–326. doi: 10.1016/0168-9622(86)90081-3

Whitaker, D., and Christman, M. (2014). *Sigclust: Significant Cluster Analysis. R Package Version 1, 2.4–2*. Available online at: https://cran.r-project.org/web/packages/sigclust/

Woolard, G. P., and Ewing, M. (1939). Structural geology of the Bermuda Islands. *Nature* 143:898. doi: 10.1038/143898a0

Conflict of Interest: The authors declare that the research was conducted in the absence of any commercial or financial relationships that could be construed as a potential conflict of interest.

Copyright © 2021 Cresswell and van Hengstum. This is an open-access article distributed under the terms of the Creative Commons Attribution License (CC BY). The use, distribution or reproduction in other forums is permitted, provided the original author(s) and the copyright owner(s) are credited and that the original publication in this journal is cited, in accordance with accepted academic practice. No use, distribution or reproduction is permitted which does not comply with these terms.

Advantages of publishing in Frontiers

OPEN ACCESS
Articles are free to read for greatest visibility and readership

FAST PUBLICATION
Around 90 days from submission to decision

HIGH QUALITY PEER-REVIEW
Rigorous, collaborative, and constructive peer-review

TRANSPARENT PEER-REVIEW
Editors and reviewers acknowledged by name on published articles

Frontiers
Avenue du Tribunal-Fédéral 34
1005 Lausanne | Switzerland

Visit us: www.frontiersin.org
Contact us: frontiersin.org/about/contact

REPRODUCIBILITY OF RESEARCH
Support open data and methods to enhance research reproducibility

DIGITAL PUBLISHING
Articles designed for optimal readership across devices

FOLLOW US
@frontiersin

IMPACT METRICS
Advanced article metrics track visibility across digital media

EXTENSIVE PROMOTION
Marketing and promotion of impactful research

LOOP RESEARCH NETWORK
Our network increases your article's readership